publicaciones técnicas

Full-scale Engineered Barriers Experiment

Updated Final Report

1994-2004

enresa

publicación técnica 05-0/2006

FEBEX

Full-scale Engineered Barriers Experiment

Updated Final Report

1994-2004

ENRESA
Dirección de División Técnica. Departamento de Coordinación de Proyectos e I+D
Emilio Vargas nº 7
28043 Madrid - España
Tfno.: 915 668 100
Fax: 915 668 169
www.enresa.es

Diseño y producción: TransEdit
Imprime: GRAFISTAFF, S.L.
ISSN: 1134-380X
D.L.: M-53195-2006
Diciembre de 2006

This report has been drawn up on behalf of ENRESA.
This report has been drawn up within the context of the FEBEX project. Its contents represent only the opinions of the authors, which do not necessarily coincide with those of the other participants in the said project.

AUTHORS

F. Huertas (1), P. Fariña (2), J. Farias (3), J.L. García-Siñériz (3), M.V. Villar (4),
A.M. Fernández (4), P.L. Martín (4), F.J. Elorza (5), A. Gens (6), M. Sánchez (6),
A. Lloret (6), J. Samper (7), M.A. Martínez (8)

(1) ENRESA, Spain
(2) DM Iberia S.A., Spain
(3) AITEMIN, Spain
(4) CIEMAT, Spain
(5) UPM, Spain
(6) UPC – DIT, Spain
(7) UDC, Spain
(8) SGS Technos S.A., Spain

ACKNOWLEDGMENTS

The project was carried out with the contributions from the persons listed below:

AITEMIN, Spain
J.L. Fuentes-Cantillana, I. Bárcena, J.J. Franco, A. Pérez, J. Obis

ANDRA, France
F. Jullien, B. Vignal

BRGM, France
J.C. Gourry

CEG-CTU, Check Republic
J. Pacovsky, E. Hynková, Z. Cechova

CIEMAT, Spain
P. Rivas, T. Missana, J. Pardillo, M. García, M.J. Turrero, J. Alberdi, J.M. Barcala, R. Campos, E. Gamero, P. Gómez, A. Hernández, A Illera, A.M. Melón, F. Ortuño, M. Mingarro, M. Pelayo

CLAY TECHNOLOGY, Sweden
L. Börgesson

CSIC-Zaidín, Spain
J. Linares, E. Caballero, J. Cuadros, F. Huertas, F.J. Huertas, C. Jiménez de Cisneros

EIG EURIDICE, Belgium
J. Verstricht

EUROGEOMAT, France
J.C. Robinet

G·3S, France
B. Bazargan- Sabet, M. Ghoreychi

GRS, Germany
N. Jockwer, K. Wieczorek

INASMET, Spain
V. Madina, I. Azkárate

INPL, France
E. Montarges-Pelletier, K. Devineau, F. Villieras

NAGRA, Switzerland
W. Kickmaier, P. Marschall

Posiva, Finland
J-P. Salo

PSI, Switzerland
B. Baeyens, M.H. Bradbury

SKB, Sweden
C. Svemar

UAM, Spain
J. Cuevas

UDC, Spain
P. Carretero, Z. Dai, J. Delgado, R. Juncosa, J. Molinero, A. Ruiz, A. Vázquez, L. Montenegro, L. Zheng

UPC-DIT, Spain

E. Alonso, J. Carrera, A.J. García-Molina, J. Guimerá, L. do N. Guimaraes, L. Martínez, S. Olivella, X. Pintado

UPM, Spain
J.L. Borregón, I. Cañamón, R. Rodríguez, J.C. Pérez

VBB VIAK, Sweden
I. Rhén

VTT, Finland
A. Muurinen

Thanks also to be given to B. Haijtink and C. Davies, technical officers from the European Commission, for their continuous support and advice. The authors are also thankful to J. E. Kennedy (TLS) for the English translation and editing work.

Contents

Contents

LIST OF SOME ABBREVIATIONS/ACRONYMS USED

A/D	Analog/digital
AENOR	Asociación Española de Normalización y Certificación, Spain *(Spanish association of standardization and certification)*
AGP	Almacenamiento Geológico Profundo *(Deep geological storage)*
AGP Granito	Almacenamiento Geológico Profundo en Granito *(Deep geological storage in granite)*
ANDRA	Agence Nationale pour la gestion des Déchets Radioactifs, France *(French national agency for the management of radioactive waste)*
AITEMIN	Asociación para la Investigación y Desarrollo Industrial de los Recursos Naturales, Spain *(Spanish association for industrial research and development of natural resources)*
BGR	Bundesanstalt fuer Geowissenschaften und Rohstoffe, Germany *(Federal Institute for Geosciences and Natural Resources)*
BRGM	Bureau de Recherches Géologiques et Minières, France *(Agency for Geological and Mining Research)*
CEA	Commissariat à l'Énergie Atomique, France *(French atomic energy commission)*
CEC	Cation Exchange Capacity
CEG-CTU	České Vysoké Učceni Techniké v Praze, Czech Republic *(Czech Technical University - Faculty of Civil Engineering)*
CIEMAT	Centro de Investigaciones Tecnológicas, Energéticas y Medio Ambientales, Spain *(Spanish center of technology, energy, and environmental research)*
CIMNE	Centro Internacional de Métodos Numéricos en Ingeniería, Spain *(Spanish international center of numerical methods in engineering)*
CSIC-Zaidín	Consejo Superior de Investigaciones Científicas—Estación experimentestal del Zaidín, Spain *(Spanish Council for Scientific Research — Zaidín Experimental Station)*
CT	Clay Technology AB, Sweden
DAS	Data Acquisition System
DDL	Diffuse Double Layer
EBS	Engineered Barriers System
EC	European Commission
EFTA	European Free Trade Association
ENRESA	Empresa Nacional de Residuos Radiactivos, S.A., Spain *(Spanish national company for radioactive waste)*
EU	European Union
EUG	Euro-Géomat Consulting, France
FEBEX	Full-scale Engineered Barriers Experiment in Crystalline Host Rock

FTP	File Transfer Protocol
G.3S	Groupement pour l'Étude des Structures Souterraines de Stockage, France *(French group for the study of subterranean storage structures)*
GRS	Gesellschaft für Anlagen-und-Reaktorsicherheit mbH, Germany *(German company for the security of reactors and systems)*
GTS	Grimsel Test Site, Switzerland
HCS	Heater Monitoring and Control Systems
HLW	High-Level Radioactive Waste
I/O	Input/Output
INPL.LEM	Institut National Polytechnique de Lorraine, France *(Polytechnic National Institute at Lorraine)*
IPP	Inspection Point Program
KWO	Kraftwerke Oberhasli AG, Switzerland (*Swiss electric company of Oberhasli*)
LVDT	Linear Voltage Differential Transformer
MIP	Mercury Intrusion Porosimetry
NAGRA	Nationale Genossenschaft für die Lagerung Radioaktiver Abfälle, Switzerland *(Swiss national cooperative for the storage of radioactive wastes)*
PA	Performance Assessment
PFA	Polymer perfluor-alkoxide
PID	Proportional, Integral, and Derivative Controller
PLC	Programmable Logic Control
POSIVA	Posiva Oy, Finland
PRACLAY	ESV Praclay Gie, Belgium *(European Underground Research Infrastructure for Disposal of Nuclear Waste in Clay Environment - Economic Interest Grouping between ANDRAF/NIRAS and SCK/CEN)*
PSD	Pore Size Distribution
PSI	Paul Scherrer Institut, Switzerland
QA	Quality Assurance
R&D	Research and Development
RMC	Remote Monitoring Center
RTD	Resistance Temperature Detector
SCADA	Supervision, Control, And Data Acquisition software
SEM	Scanning Electron Microscope
SKB	Svensk Kärnbränslehantering AB, Sweden (*The Swedish Nuclear Fuel and Waste Management Company*)

ST	Secretaría Técnica del Proyecto FEBEX (*Technical Secretariat of FEBEX*)
SWECO	SWECO, AB, Sweden
TBM	Tunnel Boring Machine
TDR	Time Domain Reflectometry
THG	Thermo-Hydro-Geochemical
THM	Thermo-Hydro-Mechanical
UAM	Universidad Autónoma de Madrid, Spain (*Spanish Autonomous University of Madrid*)
ULC	Universidad de La Coruña, Spain (*Spanish University of La Coruña*)
UDC	Universidade da Coruña (*Spanish University of La Coruña*)
UPC-DIT	Universidad Politécnica de Cataluña— Departamento de Ingeniería del Terreno, Spain (*Spanish Polytechnical University of Cataluña—Geotechnical Engineering and Geosciences*)
UPM	Universidad Politécnica de Madrid, Spain (*Spanish Polytechnical University of Madrid*)
UPS	Uninterrupted Power System
VTT	Valtion Teknillinen Tutkimuskeskus, Finland (*Technical Research Center of Finland*)
XRD	X-ray diffraction

Sinopsis

Sinopsis

FEBEX tiene el múltiple objeto de demostrar la factibilidad de fabricar, manejar y montar las barreras de ingeniería y de desarrollar modelos numéricos y códigos para la evaluación del comportamiento termo-hidro-mecánico y termo-hidro-geoquímico del campo próximo de un repositorio geológico profundo de residuos radiactivos de alta actividad. Estos objetivos requieren un trabajo integrado de desarrollo teórico y experimental. El trabajo experimental consiste en tres partes: un ensayo "in situ", un ensayo en "maqueta", y una serie de ensayos de laboratorio. El experimento está basado en el concepto de referencia español para roca cristalina en el que las cápsulas de residuo se emplazan horizontalmente en galerías, rodeadas por una barrera de bloques de bentonita compactada a gran densidad. En los dos ensayos a gran escala, el efecto térmico del residuo se simula mediante calentadores (dos calentadores en cada ensayo); la hidratación es natural en el ensayo "in situ" y controlada en la "maqueta". Los ensayos a gran escala, con sus sistemas de monitorización, están en funcionamiento desde principios de 1997 y continuarán durante un tiempo todavía no definido, aunque desde el año 2002 (en que se desmontó parcialmente) el ensayo "in situ" tiene un solo calentador. La demostración se ha conseguido en el ensayo "in situ", durante su construcción y desmantelamiento parcial. Los modelos numéricos desarrollados describen bastante bien el comportamiento del campo próximo, como se ha comprobado por comparación con los datos de monitorización y del desmantelamiento parcial del ensayo "in situ". No obstante, todavía existen algunas discrepancias entre los modelos y los datos de monitorización que será necesario investigar en el futuro.

Abstract

Abstract

FEBEX has the multiple objective of demonstrating the feasibility of manufacturing, handling and assembling the engineered barriers and of developing numerical models and codes for assessment of the thermo-hydro-mechanical and thermo-hydro-geochemical behaviour of the near field of a deep geological disposal facility for high level radioactive waste. These objectives require integrated theoretical and experimental development efforts. The experimental work comprises three parts: an "in situ" test, a "mock-up" test and a series of laboratory tests. The experiment is based on the Spanish reference concept for crystalline rock, in which the waste canisters are emplaced horizontally in drifts, surrounded by a barrier of high density compacted bentonite blocks. In the two large-scale tests, the thermal effect of the waste is simulated by means of heaters (two heaters in each test); hydration is natural in the "in situ" test and controlled in the case of the "mock-up". The large-scale tests, with their monitoring systems, have been in operation since the beginning of 1997 and will continue into the future for a period that has yet to be defined, although since 2002 (when partial dismantling took place) the "in situ" test has had a single heater. Demonstration has been achieved in the "in situ" test during construction and partial dismantling. The numerical models developed describe quite well the behaviour of the near field, as has been verified by comparison with the data from monitoring and the partial dismantling of the "in situ" test. Nevertheless some discrepancies between the data monitored and computed still need to be investigated.

Preface

Preface

The FEBEX project aims to demonstrate the technical feasibility and study the behaviour of the near-field components of a high level radioactive waste repository in crystalline rock. The project consists of an "in situ" test, a "mock-up" test and a series of complementary laboratory tests, as well as modelling work.

The project was co-ordinated by ENRESA (Spain), assisted for certain aspects by NAGRA (Switzerland), and the work was carried out by the following organisations:

In the initial phase:

- ❑ CIEMAT, AITEMIN, UPC-DIT (CIMNE), ULC, CSIC-Zaidín, and UPM (SPAIN)
- ❑ ANDRA and G.3S (FRANCE)
- ❑ GRS (GERMANY)

In addition to the organisations mentioned above, the following joined the project during the second phase:

- ❑ SKB, Clay Technology and SWECO VIAK (Sweden)
- ❑ POSIVA and VTT (Finland)
- ❑ CEG-CTU (Czech Republic)
- ❑ EURIDICE GIE (Belgium)
- ❑ BGR (Germany)
- ❑ PSI (Switzerland)
- ❑ INPL, Eurogeomat and BRGM (France)

The project was co-founded by the European Commission.

This report includes a summary description of the project from its conception until more than seven years after completion of the installation of the two large-scale tests (from the middle of 1994 to the beginning of 1997 -pre-operational stage- and operational stage and partial dismantling up to 30th December 2004). The project is described in detail in a series of specific reports.

Although each participating group wrote the sections on their particular work, this report is the result of the technical review and editing carried out by P. Fariña and J. Farias (Technical Secretariat, ST) under the direction of F. Huertas (Project Director, ENRESA); however, in the text, the contribution made by each responsible participating group is indicated.

In addition to this preface, and the following executive summary, the report is structured on the basis of eleven chapters, the general contents of which are indicated below.

Chapter 1 describes, in general terms, the different parts of the project, as well as the justification, objectives, expected results, and anticipated uncertainties. This chapter has been written by the ST, with the collaboration of CIEMAT, but the ideas are those of all the participating groups.

Chapter 2 contains a synthesis of the results from the characterisation tests performed on the FEBEX bentonite used in the construction of the clay barriers for the two large-scale tests, and in the laboratory tests. CIEMAT, CSIC-Zaidín, and UPC-DIT performed the characterisation tests, but CIEMAT contributed most of the data.

Chapter 3 includes a description of the "mock-up" test. CIEMAT was responsible for the design, manufacturing, assembly and operation of the test.

Chapter 4 refers to the "in situ" test. This chapter includes the design, fabrication and installation of the physical components of the test, test operation and partial dismantling. This part of the project was the responsibility of AITEMIN. The chapter also includes the hydrogeological and hydrochemical characterisation of the rock mass surrounding the FEBEX drift; the hydrogeological study was performed by UPC-DIT, with CIEMAT contributing to its geological content and undertaking responsibility for sampling and chemical analysis of the water.

Chapter 5 includes the laboratory tests performed on the FEBEX bentonite to obtain the constitutive laws and parameters required for thermo-hydro-mechanical (THM) and thermo-hydro-geochemical (THG) modelling, along with those carried out on samples extracted during dismantling, both bentonite and other materials. Most of these tests were performed by CIEMAT and UPC-DIT, with important contributions from CSIC-Zaidín and also the collaboration of UAM, PSI, CEG-CTU, INPL, GRS, ULC, Euro-Géomat, EIG EURIDICE, INASMET and AITEMIN.

Chapters 6 and 7 summarise the THM and THG modelling, respectively. The first was carried out by UPC-DIT, and the second by ULC.

Chapter 8 refers to the EDZ (Excavation Damaged Zone) studies in the "in situ" test gallery. These were performed by CIEMAT, BRG, G·3S and UPM.

The Quality Assurance Programme applied to the project is described in Chapter 9. The programme was based on the ENRESA Quality Assurance system, and was extended to include the participating institutions during performance of the work. The ENRESA Quality Management Department drew up the general procedures for the groups and managed the implementation of the programme.

Chapter 10 includes the overall conclusions drawn in relation to the objectives of the project.

Chapter 11 consists of a list of references, including the specific reports detailing the various tasks performed during the project.

Executive summary

Executive summary

Introduction

The FEBEX (Full-scale Engineered Barriers Experiment) consists of an "in situ" test performed under natural conditions and at full scale; a "mock-up" test, at almost full scale; a series of laboratory tests to complement the information from the two large-scale tests; and modelling work.

The aim of the project was to study the behaviour of the near-field components for a high level radioactive waste repository in crystalline rock. The following three objectives were established:

- ❑ First: Demonstration of the feasibility of handling and constructing an engineered barriers system.
- ❑ Second: Study of the thermo-hydro-mechanical (THM) processes in the near field.
- ❑ Third: Study of the thermo-hydro-geochemical (THG) processes in the near field.

The complexity of the project is justified because – following studies of the characterisation of the granite rock mass and of the thermal, hydraulic, mechanical, and geochemical behaviour of the materials for the clay barrier, in previous R&D Plans – ENRESA arrived at the conclusion that relevant progress in knowledge of the behaviour of the near-field could be achieved only by means of a very complete experiment, such as FEBEX.

The demonstration objective was expected to be attained primarily in the "in situ" test. The THM and THG processes also needed to be studied in the "in situ" test, since it is a representation of a real repository. However, the study of processes and variables and the development, verification, and validation of the numerical models require less complex systems than the natural one: the "mock-up" test and very simplified and controlled laboratory tests.

The experiment was based on the Spanish reference concept for the disposal of radioactive waste in crystalline rock (AGP Granito), in which the canisters enclosing the conditioned waste are placed horizontally in drifts and surrounded by a clay barrier constructed of highly-compacted bentonite blocks.

The project was initially scheduled for a period of 7 years (1994 to 2001). However, in view of the experience acquired after two years of heating (1999), the decision was taken to extend the project, finally, to the end of the year 2004. Its performance has been divided into four stages: pre-operational (planning, design, characterisation of the bentonite, installation, and modelling); operational (heating, monitoring, cooling, and verification of predictions); dismantling (extraction, inspection, sampling and study of the materials); and final evaluation of the results and verification of the models. The decision was taken to dismantle only Heater #1 of the "in situ" test, allowing the large-scale tests to continue.

This report covers the work performed during the pre-operational stage (from the middle of 1994 to the beginning of 1997) and the operational and partial dismantling stages, up to December 2004.

Bentonite

The bentonite used in FEBEX comes from the Cortijo de Archidona deposit, exploited by Minas de Gádor, S.A., in the zone of Serrata de Níjar (Province of Almería, Spain). ENRESA has an extensive database on this deposit, developed from the many studies carried out prior to FEBEX. Some 300 tons of duly homogenised and conditioned bentonite were acquired for the fabrication of the blocks for the barriers of the two large-scale tests and for all the laboratory tests.

The following are some of the properties that characterise this bentonite:

Montmorillonite content (%)	92 ± 3
Liquid limit (%)	102 ± 4
Specific weight	2.70 ± 0.04
Average swelling pressure for a dry density of 1.60 g/cm^3	5 MPa
Average saturated hydraulic conductivity for a dry density of 1.60 g/cm^3	4 x 10^{-14} m/s

The raw material prepared for the fabrication of the blocks is a granulate of bentonite with less than 5% of the grains greater than 5 mm, with more than 85% of the grains less than 74 μm, and with a water content of 12.5% to 15.5%.

"Mock-up" test

The "mock-up" test has been and continues to be conducted at the facilities of CIEMAT (Madrid). The physical components of the test consist of five basic units: the confining structure, with its hydration system; the heating system; the clay barrier; the instrumentation and the systems for data acquisition and for heater control.

Predictive modelling has been carried out on THM and THG behaviour during the pre-operational stage, along with modelling during the operational stage and contrasting with the test monitoring values.

Confining structure and hydration system

The aim of the confining structure with its hydration system is to simulate the drift with water make-up from the surrounding rock mass, but under well-known and controlled conditions.

The confining structure is a cylindrical steel body with an internal diameter of 1.62 m and an effective length of 6.00 m. The hydration system, which supplies granitic water under pressure to the periphery of the clay barrier, consists of two tanks and related piping connecting to 48 nozzles in the confining structure. To uniformly apply the water to the surface of the clay barrier, the confining structure is lined with various layers of geotextile.

Heating system

Two electrical heaters have been installed in the test, separated by 0.75 m and placed concentrically in the confining structure in direct contact with the bentonite, i.e. without the steel liner used in the “in situ” test. Each heater measures 1.625 m in length, 0.340 m in diameter, and has a mass of about 600 kg.

Each heater has three heating elements capable of supplying a thermal power of 930 W each, i.e. a total power of 2800 W per heater. In this test a constant temperature of 100°C is maintained at the heater-bentonite interface by means of the heater control system. The system is redundant: each heating element is capable of supplying a higher thermal power than is strictly required.

Clay barrier

The clay barrier is composed of highly compacted bentonite blocks, weighing about 25 kg each. The fabricated blocks have weighted average values of 13.6% and 1.77 g/cm^3 of water content and dry density, respectively. The average dry density of the constructed barrier is 1.65 g/cm^3 and the barrier has a percentage of construction gaps of 6.25. There were 908 blocks placed in 48 slices with a total mass of 22.5 t. Immediately following its construction, the “mock-up” test had a systematic gap between the clay barrier and the geotextile liner that reaches a maximum 1.5 cm at the top.

Instrumentation

Within the clay barrier and the rest of the components of the test, 507 sensors were installed to measure the following variables: temperature, humidity, fluid pressure, total pressure, deformation of the confining structure and injection pressure of the water.

Samples of different metals were placed in the bentonite near the heaters to study corrosion. In addition, at different points in the clay barrier and in the injection water, both conservative and non-conservative chemical tracers were added to study geochemical processes and transport mechanisms.

Data acquisition and heater control systems

The data acquisition system (DAS) is made up of all the electric and/or electronic components and the computer programs required for the supervision, registration and storage on a secure magnetic device (disk) of the data obtained from the test, in an autonomous form. The system is capable of storing, analysing and displaying the data obtained.

The heater control system (HCS) is made up of all the electric and/or electronic components and computer programs required to accomplish the following functions: supervision of heater operation and control of the power supply, data acquisition and transfer to the DAS and activation of the processes and alarms in the event of component failure.

Installation

After installation in the annex to Building 19 at the CIEMAT facilities, which was especially constructed for this test, the confining structure was lined with various layers of geotextile.

The clay barrier was constructed manually, in complete slices, using appropriate blocks, such that there was an enclosed space for each heater in its assigned place. As the slices were installed, the sensors and their corresponding cables were placed in their pre-assigned positions in mechanically made holes and grooves within the appropriate bentonite blocks. The cables exited the confining structure through 186 hermetically sealed perforations.

A table with rollers was used to align the heater with its prepared space, and the heater was then inserted under pressure.

The components of the DAS are installed in an area adjacent to, and above, the confining structure.

The fabrication of the components and their installation has been subjected to a quality assurance program.

Operational stage of the test

Following a series of tests and initial hydration (flooding of the gaps in the clay barrier), definitive heating and hydration (operational stage) began on 4th February 1997. The instrumentation and the hydration and heating systems have operated satisfactorily. However, as a result of a malfunction towards the end of November 2000 (day 1391), the control program supplied the total heating power (around 2700 W/heater) for more than 36 hours, until the temperature at the sensors in the heaters reached the resistance safety value (300°C). This overheating was automatically stopped, but not before the temperature within the bentonite had achieved values of around 240°C. More than 90% of the sensors continue to be operative after more than seven years of heating and the few incidents that have occurred have been promptly corrected, without any consequences for the data.

A database containing the values of all the variables measured is available. Furthermore, monitoring reports have been published every three months, these having been distributed to all the working groups.

“In situ” test

The “in situ” test was installed within a new drift, which was excavated in the northern zone of the underground laboratory (GTS) managed by NAGRA at Grimsel (Switzerland). The physical components of the test consist of five basic units: the drift, the heating system, the clay barrier, the instrumentation, and the monitoring and control system. In the second phase of the project, the “in situ” test was partially dismantled.

As in the case of the “mock-up” test, predictive modelling has been carried out in relation to THM and THG behaviour during the pre-operational stage, and modelling was performed during the operational stage, the values obtained being contrasted with those arising from test monitoring and partial dismantling. In order to obtain the hydraulic data on the rock mass required for modelling, a hydrogeological study was performed of the area surrounding the drift.

Hydrogeological characterisation

The first phase of this study had the following three objectives: to determine the location of the drift, within a zone previously assigned in the northern part of GTS; to establish the test zone, and consequently, the length of the drift, by observing the actual hydrological conditions of the drift during excavation; and to determine the parameters, initial conditions and boundary conditions of the hydraulic system of the rock mass, necessary for THM and THG modelling.

The study includes and is supported by the GTS database, by boreholes drilled for this purpose (in which hydraulic tests were performed), by observations made in the drift itself, by measurement of the piezometric levels and by a geological study.

The analysis was performed by means of a three-dimensional numerical model capable of predicting the infiltration in the drift and the surrounding hydraulic pressures.

The results of the study indicate that $5 \cdot 10^{-11}$ to $8 \cdot 10^{-11}$ m/s is the equivalent hydraulic conductivity of the assumed homogeneous rock mass, while that of the matrix is of the order of $1 \cdot 10^{-11}$ m/s. The infiltration into the drift was between 7 and 12 L/day and the initial hydraulic pressure at the level of the drift was 0.7 MPa.

Samples of water were taken in representative boreholes and subjected to chemical analysis.

During the second phase of the project, a new hydraulic testing campaign was carried out. The programmed tests comprised long-term tests, short duration tests and pulse type tests. The objective was to check the evolution of the hydraulic parameters during heating. The main conclusion was that no changes were detected.

Drift

The drift is 70.40 m long and 2.28 m in diameter. It was excavated, between 25th September and 30th October 1995, with a tunnel boring machine (TBM) in a predominately granite mass. In the last 17.4 m of the drift (test zone), two heaters, the clay barrier, and the instrumentation were installed. This zone was closed with a concrete plug. Between the concrete plug and the portal of the drift was the service zone, where the monitoring and control system were installed. In the second phase, the concrete plug and part of the clay barrier were excavated and one heater extracted. The new test area was closed again with a shotcrete plug.

Heating system

During the first phase, the main elements of the heating system were two heaters, separated horizontally by one metre, which simulate full-sized canisters. The heaters were placed inside a cylindrical steel liner, which had been installed concentrically with the drift. Each heater is made of carbon steel, measures 4.54 m in length and 0.90 m in diameter, has a wall thickness of 0.10 m and weighs 11 tons. In the second phase, one heater was extracted.

The objective of the heating was to constantly maintain a maximum temperature of 100°C at the steel liner/bentonite interface. This is the temperature anticipated in the reference concept, AGP Granito. Each heater has three independent electrical heating elements, with the capacity to provide a thermal power of 4300 W per element. This is the nominal power required to reach a temperature of 100°C in a period of less than two months, with a factor of safety, considering the most unfavourable case of bentonite saturation. The system had redundancies to increase the probability of its functioning throughout the planned duration of the test.

The other basic elements of the heating system consist of the equipment and procedures regulating the power of the heaters to maintain the specified temperature.

Clay barrier

The clay barrier was formed by blocks of highly compacted bentonite weighing 20 to 25 kg each. The weighted average values of the dry density and water content of all the blocks fabricated were 1.70 g/cm^3 and 14.4%, respectively. 5331 blocks were used in construction of the barrier, corresponding to a mass of 115.7 t. In place, the barrier had an average dry density of 1.60 g/cm^3, determined during construction, and a volume, when installed, of construction gaps (separations of variable magnitude) of 5.53%. The gaps existed: between blocks of the same slice; between slices; between the blocks and the steel liner and, systematically, between the clay barrier and the rock, where a gap of increasing width, up to as much as 3 cm, extends from the lower part to the crown. In the second phase, the clay barrier around the extracted heater was dismantled.

Instrumentation

A total of 632 sensors of diverse types were installed in the clay barrier, the rock mass, the heaters, and the service zone to measure the following variables: temperature, humidity, total pressure, displacement, water pressure, etc.

In addition, a system of porous ceramic pipes was installed to capture gases, measure their pressures, and take samples for chemical analysis. Samples of different metals were placed near the heaters, embedded in the bentonite blocks, to study corrosion. Conservative and non-conservative chemical tracers were placed at different locations within the bentonite barrier to obtain information on geochemical processes and transport mechanisms. The instruments located in the dismantled clay barrier were retrieved for its analysis.

Monitoring and control

There are two systems: the “local system”, situated in the GTS, and the “remote system”, situated at the Remote Monitoring Centre (RMC) in Madrid. The two systems are connected by modem, with the remote system acting as the master by furnishing control rules and commands to the local system.

The local system consists of all the electric and/or electronic components and computer programs for autonomous data acquisition, supervision, and control of the test. The remote system consists of all the hardware and software for the supervision and control of the test from a distance, and for data storage, analysis and display.

Installation

Following excavation of the drift, the infrastructure was prepared: ventilation, electrical supply, water supply, and construction of a concrete sill within the drift. This sill was extended, forming an exterior platform to be used as a loading and unloading dock and as a depot for the auxiliary equipment for the handling and transport of materials.

In the test zone, 19 boreholes were drilled from the interior of the drift for the installation of the instruments for rock mass measurements. The boreholes were 7 m to 22 m in length, with a total of 233 m of drilling.

The clay barrier was installed manually, by slices. In the heater zones, the steel liner was first installed with a provisional support to provide correct alignment; then the barrier was constructed around it, in complete slices, until the space for the heater was enclosed. As the slices were installed, the sensors and their corresponding cables were placed in their pre-assigned positions in mechanically made holes and grooves within the appropriate bentonite blocks. The cables were channelled radially to be gathered into four bundles. Within the test zone, each of these bundles was channelled along the rock face at the crown, invert, and both springlines.

For insertion of the heaters, a special transport and insertion car with a pushing mechanism was designed and constructed. This car ran on rails designed to prevent transverse movement and maintain correct alignment between the car and the rails. Each heater, mounted on the car anchored to the rails and facing the mouth of the steel liner, was pushed into its final position by means of the pushing mechanism. The correct alignment of the steel liner and the proper installation of the rails allowed this to be accomplished, since the critical factor during heater insertion is the correct alignment of the inner lower part of the steel liner with the outer lower part of the heater located on the transport and insertion car.

The plug, which closes the test zone, was concreted in three sections with the mixture being pumped from outside the drift. This method did not allow for good concreting of the key, where a void remained; this was later filled by injection. The bundles of cables pass through the concrete plug within four plastic pipes.

Test zone installation commenced on 1st July and terminated on 15th October 1996.

In the service zone of the drift, the monitoring and control equipment was installed, the cables were connected, and the functional tests were completed on 27th February 1997. That same day, heating started, i.e. the operational stage began.

A quality assurance program was applied to the fabrication of the components as well as to their installation.

Dismantling

Before starting the dismantling, a detailed design and planning of dismantling and sampling activities were performed. Also the heater car, the winch and transport wagon were modified for extraction of the heater and removal of the clay barrier.

The shutdown of Heater #1, carried out on 28th February 2002, initiated the countdown for dismantling. The dismantling works started after two months of cooling.

After the controlled demolition of the concrete plug, the clay barrier was then removed and sampled up to the front of Heater #1, in accordance with the previously written sampling plan. Then the heater was extracted, sent to Spain and sampled for corrosion analysis. The dismantling and sampling of the bentonite continued to completion on July 23rd 2002.

A temporary section of the new shotcrete plug, measuring one metre in length, was finished on July 25th.

Before constructing the second section of the plug, the following tasks were performed: new gas injection and collection pipes were installed in the buffer for gas sampling and permeability measurements; new instruments for water sampling, humidity and temperature sensors, total pressure cells and thermocouples were installed in boreholes; and four cable connection boxes filled with resin were installed at the rock surface in the area corresponding to the second section of the plug, before shotcreting, to introduce the instrument cables without jeopardising the water tightness of the system.

Finally the second stage of the plug, measuring two metres in length, was built at the end of June 2003.

A quality assurance program was applied throughout the entire activity, from the tasks previous to the start of dismantling up to the end of construction of the plug.

Operational stage of the test

Apart from a series of short tests, the heating stage (operational stage) began on 27th February 1997. The sensors, heaters and data acquisition and control systems have shown highly satisfactory behaviour, as has the remote control system (AITEMIN offices in Madrid). There have been minor operating events, which have been easily solved and have had no influence on the data. 80% of the sensors continue to be operative.

A complete database is available, containing the values for all the variables measured. In addition to the database on magnetic support media, used by the modelling groups, quarterly graphic reports have been drawn up showing the evolution of all the variables, and have been distributed among the different working groups.

Laboratory tests

In addition to the two large-scale tests, FEBEX had a specific laboratory program, which included basic characterisation and thermo-hydro-mechanical and thermo-hydro-geochemical testing. Although the determination of certain basic parameters requires new testing techniques and methods, the last two groups show the greatest experimental innovation.

In this program, the most noteworthy tests are those performed in thermohydraulic cells, the oedometric and triaxial tests with suction and temperature control and those aimed at determining ion exchange and transport parameters.

A set of laboratory tests was carried out on bentonite samples taken during dismantling, with the aim of characterising the actual state of the bentonite and to determine the possible changes that might have occurred during the experiment. No changes were observed.

THM and THG modelling

Three THM modelling runs have been carried out between the beginning of the project and the end of the first phase, using CODE_BRIGHT. The first, for the design, was performed using few real data, but made it possible to understand the THM processes, determine heater power and define the distribution of the sensors. The second modelling was performed at the end of the pre-operational stage ("blind" prediction) using laboratory data for bentonite barrier characterisation. This modelling made it possible to identify the laws and parameters with the most critical influence on the results, and thus enabled a laboratory testing program better suited to the demands of the model to be developed. Furthermore, the objective of this "blind" prediction was to produce results that would subsequently be contrasted with the monitoring data. The "blind" prediction has reproduced all the processes well, albeit with quantitative deviations with respect to the monitoring data, due to the fact that when the modelling was performed there were no adequate laboratory testing results available for certain critical parameters. The last modelling of the first phase has basically consisted of achieving the best possible fit with the monitoring data, establishing the condition that the values of the parameters were within the range of those obtained in the laboratory tests. This modelling served to demonstrate that CODE_BRIGHT was capable of reasonably approximating the results of the measurements performed. Although uncertainties still existed, there was a significant increase in the degree of confidence in the predictive capacity of the code.

The results of the first modelling performed at the beginning of the second phase, provided an unexpected surprise. It became clear that, as from day 900 from the initiation of hydration, the results of the prediction differed from the monitoring data in several hydraulic aspects. During this second phase modifications were made to the model, resulting in a better fit between the prediction and the data, although a difference in trends persists. This will require further investigation if it is not shown to be irrelevant.

During the first phase, two THG codes have been developed and verified: CORE-LE and FADES-CORE-LE. During the pre-operational stage of the modelling this was limited to analysis of the transport of the chemical tracers placed in the clay barrier. However, the results obtained and the work performed on the models led to the drawing up of an integrated laboratory testing program by the experimentalists and modellers. During the operational stage, the codes developed were applied to the analysis and interpretation of the laboratory tests and to modelling of the large-scale tests. From this application it was concluded that the codes reproduced fairly well the geochemical behaviour patterns observed in a large number of laboratory tests, this having generated high expectations as regards their predictive capacity.

During the second phase, the THG codes have been continuously improved, this leading to development of the most recent and powerful version: INVERSE-FADES-CORE. The improved codes have been applied to the analysis of laboratory tests and to modelling of the large-scale tests and contrasted with the chemical results obtained from the laboratory analyses of samples taken during partial dismantling of the "in situ" test. From the aforementioned application of the codes it may be concluded that, in general, they reproduce fairly well most of the observed patterns of geochemical behaviour, this generating confidence in their predictive capacity.

However, there are still discrepancies between the modelling results and measurements, which will require the inclusion of other processes not considered to date. There are high expectations that by doing what is recommended it might be possible to construct numerically verified, scientifically sound and thoroughly tested THG computer codes and numerical models.

Quality assurance

Generally, R&D projects are not subjected to quality assurance programs, but ENRESA decided that such programs should be applied to FEBEX for various reasons: the results may be input data for the performance assessment of a repository, the impossibility of repairing/replacing certain components in the large-scale tests following installation, the complex interrelations existing between the participating working groups and the high cost of the project.

The program was applied when design of many of the components was either well under way or had been completed; nevertheless, the program was very useful for management of the project and for quality control of the fabrication, acquisition, installation of the components of the two large-scale tests and partial dismantling and sampling.

Conclusions

The following conclusions have been drawn from analysis of the results obtained during the preoperational stage, about seven years of the operational stage and partial dismantling of the "in situ" test (these are briefly summarised below):

- ❑ The feasibility of constructing engineered barriers for the horizontal storage of canisters placed in drifts has been demonstrated. Specifically it has been demonstrated that the manufacturing and handling of bentonite blocks is feasible at industrial scale and that the clay barrier may be constructed with a specified average dry density, in order to achieve the permeability and swelling pressure required for the barrier. Furthermore, highly useful information has been obtained for the design of a repository, in relation to the size of the drifts, the specifications and procedures for the manufacturing and handling of the bentonite blocks and the basic characteristics of the equipment for construction of the clay barrier and insertion of the waste canisters. In addition, useful information has been obtained regarding the behaviour of the instrumentation system, of which only 10% in the "mock-up" and 20% in the "in situ" test of the sensors have failed to date. It has also been demonstrated that a Quality Assurance System is applicable, not only to manufacturing and installation of the physical components of the experiment, but also for the research work on processes, parameters and modelling.
- ❑ The CODE_BRIGHT numerical THM model is capable of predicting the THM behaviour of the clay barrier and near field of the rock. During the project, formulation of the model and the code were modified and significantly improved, although the core, based on a solid formulation of physical laws, has not required any change. Fundamental progress has been made in the development of laboratory apparatus, techniques and methods for the determination of the constitutive laws and parameters required by the model. Thus, although complete validation is never possible, the checks performed have significantly increased the degree of confidence in the capacity of the model for the performance assessment of the THM behaviour of a repository near field. However, some discrepancies between the model and monitoring data still persist, which it will be necessary to investigate in the future.
- ❑ Great progress has been made in the development of THG numerical tools and analysis methods, from both the experimental and modelling points of view. The THG codes have been continuously improved, from TRANQUI to the latest INVERSE-FADES-CORE. These codes reproduce fairly well most of the observed patterns of geochemical behaviour of a large number of laboratory tests and data of partial dismantling of the "in situ" test, this generating confidence in their predictive capacity. Nevertheless, some discrepancies between predictions and measured data have been observed and some relevant processes have not been addressed in the project. Experimental data as well as numerical analyses on the role of these processes should be undertaken in the future. There are major expectations that, by so doing, it might be possible to construct models capable of predicting with confidence the THG behaviour of the near field. Important progress has been made in laboratory testing in relation to the determina-

tion of sorption and transport processes and parameters and in the chemical analysis of pore water. Particularly important is the demonstration that montmorillonite is not transformed into illite, at least up to 80 °C, and that the properties of permeability and swelling of the bentonite is not modified as a result of hydration and heating.

1. Introduction

1. Introduction

1.1. General

The aim of FEBEX (Full-scale Engineered Barriers Experiment) has been to study the behaviour of components in the near field for a high-level radioactive waste (HLW) repository in crystalline rock, by means of an integrated theoretical and experimental approach. The experimental work has consisted of three main parts:

1) an "in situ" test, under natural conditions and at full scale [1];
2) a "mock-up" test, at almost full scale [2]; and
3) a series of laboratory tests to complement the information from the two large-scale tests [3, 4].

The project is based on the Spanish disposal reference concept for radioactive waste in crystalline rock (AGP Granito): the waste canisters are placed horizontally in drifts and surrounded by a clay barrier constructed from highly compacted bentonite blocks [5].

The project was initially planned to last some 7 years (1994 to 2001) and its performance was divided into four successive stages, defined by the main tasks to be performed in the two large-scale tests. These stages are: pre-operational (planning, design, characterisation of the clay, installation, and modelling); operational (heating, monitoring, cooling, and verification of predictions); dismantling (extraction, inspection, sampling, and study of the materials); and final evaluation of the results and verification of the models.

During the period 1996 to 1999 the project was co-funded by the European Commission (EC) as part of the 4th Euratom framework programme (1994-98) and a final report was produced, EUR 19147, 2000. However, in view of the conclusions drawn from integral analysis more than two years after the initiation of heating, the decision was taken to extend the experiment by two or three more years and to dismantle only Heater # 1 of the "in situ" test, allowing the experiment to continue. The extension of the experiment, also co-financed by the EC, began in September 2000 and concluded in 2004.

This report is an integrated summary of the work performed during the pre-operational stage (from the middle of 1994 to the beginning of 1997), and the operational and partial dismantling stage up to December 2004.

The experiment was justified because the engineered barriers (waste, canister, and clay barrier) are key elements in the final disposal concept for HLW. The matrix of the spent fuel acts as a reducing barrier that minimises solubility; the canister isolates the wastes for a certain time and contributes to the reducing environment. The clay barrier has the multiple purpose of providing mechanical stability for the canister, by absorbing stress and deformations; of sealing discontinuities in the adjacent rock and retarding the arrival of groundwater at the canister and of retaining/retarding the migration of the radionuclides released, once failure of the canister and lixiviation of the spent fuel have occurred.

The behaviour of a HLW repository is determined, to a large extent, by the characteristics of the design and construction of the engineered barriers and especially by the changes that may occur in the mechanical, hydraulic, and geochemical properties as a result of the combined effects of heat generated by the radioactive decay and of the water and solutes contributed by the surrounding rock. Therefore, it has been considered of fundamental importance that the processes taking place in the near field be understood and quantified, for the evaluation of long-term behaviour.

In previous R&D plans, ENRESA had studied the sources of supply of materials to be used in the clay barrier, as well as their thermal, hydraulic, mechanical, and geochemical behaviour. Integral characterisation studies of granite masses had also been carried out. As a result of these studies, and given the fact that there had not been any large-scale experiment in granite with the waste canisters emplaced horizontally in drifts, ENRESA reached the conclusion that the next step, in establishing the viability of the concept and in progressing in the comprehension and evaluation of the behaviour of the near-field (especially of the clay barrier), was the performance of a very complete experiment, such as FEBEX.

Therefore, the FEBEX experiment has the multiple objectives of demonstrating the feasibility of fabricating and assembling the engineered barriers and of developing methodologies and models for evaluation of the thermo-hydro-mechanical (THM) and thermo-hydro-geochemical (THG) behaviour of the near field. These objectives are to be attained through the combination of the "in situ", "mock-up", and laboratory tests.

Fundamentally, the objective of the demonstration was expected to be attained in the "in situ" test, which operates under natural conditions with components constructed with the actual design dimensions of a repository drift. The demonstration objective has less importance in the "mock-up" test.

The objectives of checking the predictive capacities of the THM and THG numerical models have been supported by the program of laboratory tests designed to obtain parameters and to study and comprehend the processes that take place in the clay barrier under simple and controlled conditions and to develop the governing equations. The "mock-up" test, performed at almost full scale and with well-known geometry, along with well-controlled initial and boundary conditions, serves to verify the predictive capacity of the coupled numerical models and serves also as a reference for the evaluation of discrepancies, if they exist, and for adjustment of the models predicting the behaviour of the clay barrier under more heterogeneous conditions, such as those in the existing natural system of the "in situ" test.

The underground laboratory managed by NAGRA (Grimsel, Switzerland) was selected for performance of the "in situ" test, due to the similarity of the Spanish and Swiss reference concepts for the repository and the suitable laboratory conditions for this test. The "mock-up" test is still being performed at the CIEMAT facilities (Madrid, Spain). The laboratory programs were performed at various research facilities: initially UPC-DIT, CSIC-Zaidín, CIEMAT and GRS, to which were added PST, VTT and others during the prolongation of the experiment.

1.2. Spanish reference concept, AGP Granito

Figure 1.1 shows a longitudinal section of a disposal drift in the Spanish reference concept, AGP Granito [5]. The specifications of the reference concept that are pertinent to the FEBEX project are briefly described below.

The waste canisters, separated by one meter, are stored horizontally in drifts measuring 2.40 m in diameter within a continuous steel liner installed concentrically with the drift. The canisters measure 4.54 m in length and 0.90 m in diameter, and weigh 12 t. The inner diameter of the steel liner is 2 cm larger than the outer diameter of the canisters.

The reference concept specifies various forms of bentonite blocks, with weights of more than 200 kg

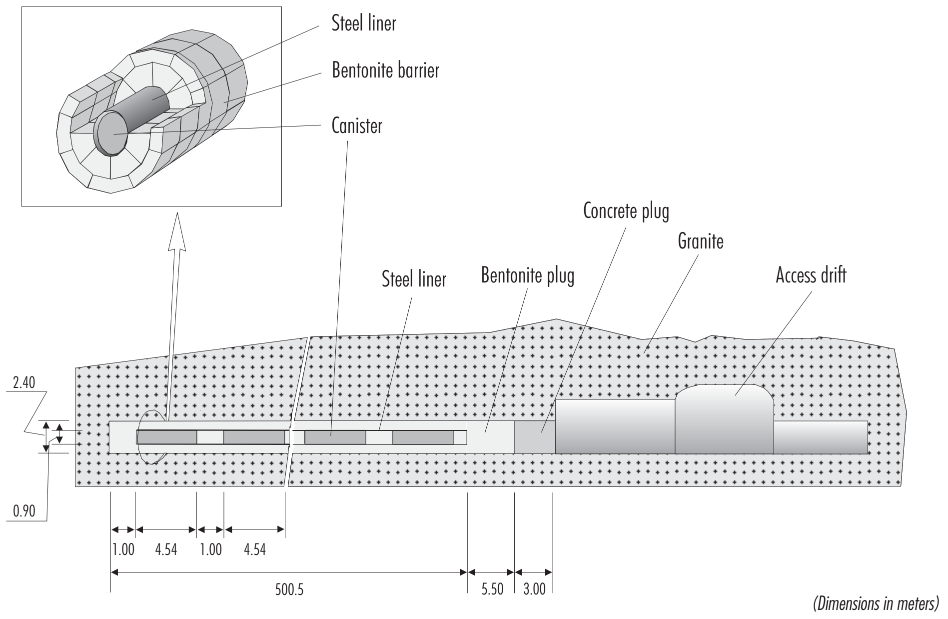

Figure 1.1: Longitudinal section of a disposal drift in the Spanish reference concept, AGP Granito.

each. Other relevant specifications are that the maximum temperature at the clay barrier/steel liner interface is to be 100°C and that the swelling pressure of the clay barrier is to be of the order of 5 MPa (for the FEBEX bentonite this implies an average dry density of 1.60 t/m^3) [5].

1.3. Previous experimentation–clay barrier

As pointed out above, the material of the clay barrier was selected and investigated in the laboratory within the framework of previous ENRESA R&D plans. Industrial characterization and the feasibility of fabricating and installing the blocks in drilled wells were also studied.

A brief summary of the previous experimentation and modelling by ENRESA, on which the objectives and planning of FEBEX [6] were based, is presented below.

1.3.1. Studies of Spanish smectite clays

These studies were performed by CSIC-Zaidín, UAM and CIEMAT. The most important sources of smectite clay are basically associated with two areas: Cabo de Gata (Almería) and the Tajo Basin (Toledo). The materials studied from the area of Cabo de Gata are montmorillonite bentonites originating from volcanic materials altered by hydrothermal processes. The materials from the Tajo Basin are saponite bentonites of sedimentary origin resulting from the geochemical evolution of the basin.

Of all the sources studied, two were selected: Cortijo de Archidona (in the Serrata de Níjar, Almería) and Cerro del Águila-Cerro del Monte (Toledo). They were selected for their mineralogical purity, high values of specific surface, liquid limits, proportions of the fraction of less than 2 mm, acceptable thermal conductivity and good compactability.

1.3.2. Selection of candidate material

After the Cortijo de Archidona and Cerro del Monte bentonites were selected as the best materials, CIEMAT continued thermal, hydraulic, mechanical, and geochemical characterization. The montmorillonite bentonite of Cortijo de Archidona was selected because of its better compactability, although both bentonites met the requirements for the barrier material.

1.3.3. Evaluation of fabrication and construction of the clay barrier

Evaluation of the fabrication and construction of the clay barrier to be made from the selected bentonite (Cortijo de Archidona) was carried out in collaboration by ENRESA, CIEMAT and CEA.

The mould and the fabrication system for the compacted clay blocks, as well as the method of installation, were designed using the methodology employed by the French. Their corresponding “in situ” investigative test was carried out in drilled wells measuring 1.50 m in diameter and 6.00 m in depth, in an abandoned mine of Cogema (Fanay-Silord, France), and is well documented in the report EUR 14.185.

1.3.4. Longevity Studies

The integrity of the clay barrier is fundamental for the long-term performance of a repository; consequently, the changes that the clay undergoes during the lifetime of a repository must be studied. The changes are controlled by thermal impact, hydration water and the chemical environment. An important change that the clay barrier may undergo is the possible transformation of montmorillonite to illite, with the resulting deterioration of its mechanical, swelling, and retention properties.

The materials were tested in the CSIC-Zaidín, UAM and CIEMAT laboratories, at various concentrations of salinity, temperatures, and time intervals, to determine the reaction kinetics. CSIC-Zaidín established an equation that governs the transformation of montmorillonite to illite; the equation indicates that, at a temperature of less than 120°C, transformation takes place over a period from hundreds of thousands to millions of years, depending on the quantity of potassium available in the environment. The UAM studies did not find any relevant transformation that would affect the saponite for temperatures of below 200°C, but did establish kinetic equations that control the transformation of the accessory minerals (sepiolite) into saponite and that indicate that transformation occurs in decades.

CSIC studied the bentonite of Almería to obtain thermodynamic and kinetic information on the process of dissolution/precipitation.

1.3.5. Studies of the processes generated by thermohydraulic flow

CIEMAT performed an experimental program aimed at identifying the processes originated by thermohydraulic flow in compacted bentonite specimens and at determining the consequences for its properties and behaviour [7]. Conclusions were drawn in reference to temperature distribution within the clay; the velocity of water intake; the distribution of moisture and density; mechanisms for the transport of salts (of those, three were distinguished: advection, advection/convection, and diffusion) and the influence of heating on the exchange complex, the specific surface, porosity and the composition of the pore water.

1.3.6. Studies of thermo-hydro-mechanical behaviour

CIEMAT studied the thermo-hydro-mechanical behaviour of the compacted bentonite by means of laboratory tests with controlled suction, and UPC-DIT performed the modelling. A determination has been made of the relation between suction and water content and of how it is influenced by the initial dry density and moisture of the clay. Oedometric tests with controlled suction were performed on samples with equal initial conditions; the samples were subjected to various loading and suction paths, allowing for definition of state surfaces.

1.4. Objectives

As has been pointed out above, the aim of the FEBEX project is multiple. The objectives have been classified according to their importance for the waste management programme and their probability of achievement, in the following way:

First *Demonstration of the feasibility of constructing the engineered barriers system (EBS).* The demonstration consists of: verifying the feasibility of fabricating, handling and installing the components of the engineered barriers, including the industrial fabrication of highly-compacted bentonite blocks; the development and application of a satisfactory Quality Assurance/Quality Control (QA/QC) programme and the development and use of an acceptable instrumentation system. Experience was to be acquired and criteria developed for the techniques of waste disposal, not only during the construction of the large-scale tests but also during dismantling, by observation and study of the barriers. Furthermore, there was an opportunity to study the capacity of non-destructive tools (geophysical) for the characterisation of a rock mass, by comparing the conditions encountered in the boreholes and in the FEBEX drift with the results of the geophysical studies performed in the area during previous investigations.

Second *Study of the thermo-hydro-mechanical (THM) processes in the near field*. The aim of the project has been to study the THM processes in the near field, especially in the clay barrier, and to improve, verify and validate the existing codes and constitutive relations.

Third *Study of the thermo-hydro-geochemical (THG) processes in the near field*. The aim of the study was to identify, evaluate and model the possible mineralogical and geochemical alterations in the clay barrier, caused by high temperatures, mass transport and water flow. Also the effect of these alterations on the hydrodynamic, mechanical and hydrochemical properties of the bentonite have been studied. This objective also includes study of the generation and transport of gas as well as the corrosion of metals.

It was thought that the first objective had a high probability of being attained; nevertheless, it would not be a complete demonstration. A complete demonstration would require a replica of a repository in a test section. FEBEX does not meet this requirement as the bentonite blocks in the reference concept are 10 times larger than those used in the experiment, and the installation of the different elements would be by robot in a repository, whereas in the FEBEX installation it has been manual. For obvious reasons, neither the size of the blocks nor the installation system could be equal to that of the reference concept; nevertheless, it was thought that the proposed objective could be achieved and the planned demonstration would provide very useful information for the design and operation of a real repository.

Full achievement of the second and third objectives would mean the complete development and validation of THM and THG numerical models realistically describing the behaviour of the near field. It was thought that these objectives would have a lower probability of being achieved than the demonstration objective; also it was thought that in view of the greater complexity and lower degree of current development of the THG modelling, compared to THM, the degree of success would be higher for THM modelling than for THG.

The prolongation of FEBEX as initially designed has not meant any change in the objectives, but merely in the period for performance and in certain activities. Indeed, it arose from analysis after two years of heating, when the measuring instruments and heating system were seen to have functioned well in the two large-scale tests. This analysis led to the conclusion that the THM and THG numerical models promised high expectations, inasmuch as sufficient confidence in their capacity to predict behaviour in the near field might be forthcoming. In order to achieve such confidence, it was necessary to continue theoretical development of the models and to carry out new laboratory tests to obtain parameters and validate the constitutive laws. It was considered particularly important to extend the period of experimentation in order to achieve more advanced states of hydration. For this reason the experiment extension is not considered to be complete; rather the strategy is to extend it as much as possible over time, depending on the performance of the experimental system.

The objective of the demonstration, which was to be complemented with the dismantling of the "in situ" test –with observation of the state of the clay barrier and of the measuring instruments– was accomplished with partial dismantling of the area of Heater # 1.

Two further studies were also added: one on a potential EDZ in the FEBEX gallery and its evolution throughout the experiment, and the second on modification of the original hydraulic properties of the rock in the near field.

1.5. General description of FEBEX

The project includes experimental and modelling work. The experimental work consists of an "in situ" test, a "mock-up" test, and a series of laboratory tests. The objective of the modelling work is the development and validation of THM and THG models for performance assessment of the near-field behaviour.

1.5.1. "In situ" test

The "in situ" test was installed in a drift excavated in the northern zone of the underground laboratory at Grimsel (Grimsel Test Site, GTS). Figure 1.2 represents the test schematically as initially built. The physical components of the test consist of five basic units: the drift, the heating system, the clay barrier, the instrumentation, and the monitoring and control system.

The drift has a length of 70.4 m and a diameter of 2.28 m, and is excavated in a granite rock mass. In the last 17.4 m of the drift, the basic elements of the test were installed and the section was sealed with a concrete plug.

The main elements of the heating system are two heaters located within a steel liner installed concentrically with the drift. The heaters simulate the canisters at real size. Each heater has the following characteristics:

- Material: Carbon steel
- Outer diameter: 0.90 m
- Length: 4.54 m
- Wall thickness: 0.10 m
- Weight: 11 t

The clay barrier is formed from blocks of highly compacted bentonite. The blocks were fabricated with an average water content of 14.4% and an average dry density of 1.70 t/m^3. The clay barrier has an average dry density of 1.60 t/m^3 and a percentage of construction gaps of 5.53.

The instrumentation includes the sensors installed in the heaters, clay barrier, and surrounding rock. The variables measured are: temperature, humidity, stress, total pressure, displacement, and water pressure. In addition, the generation and transport of gas is being measured.

Two systems, connected by modem, are being used for monitoring and control: the "local system" situated in the FEBEX drift and the "remote system" located in Madrid.

Partial dismantling has consisted of extracting one heater and corresponding clay barrier and of sealing the remaining section of the test with a new concrete plug.

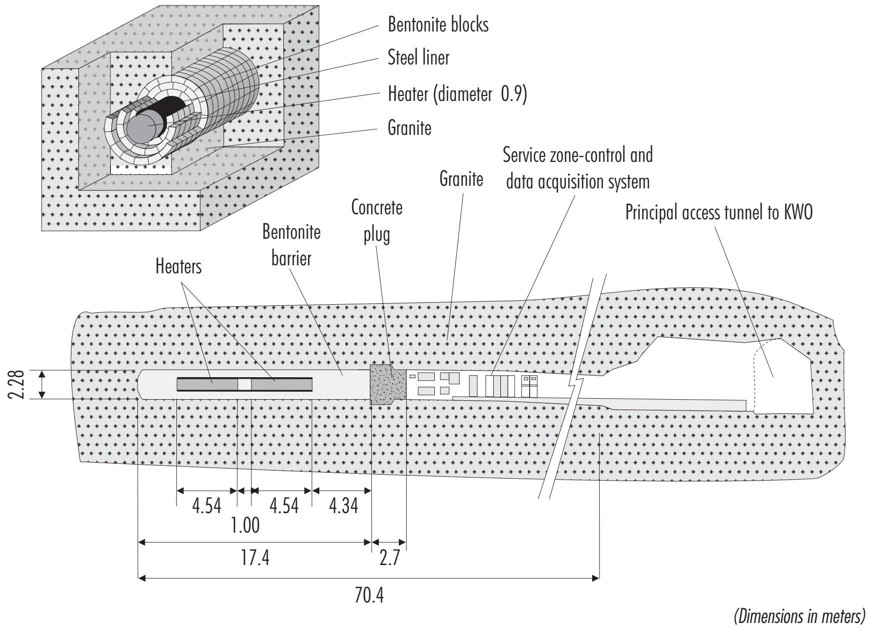

Figure 1.2: General scheme of the "in situ" test.

1.5.2. "Mock-up" test

The "mock-up" test is located in an annex to Building 19 at the CIEMAT facilities in Madrid. The physical components of the test consist of five basic units: the confining structure with its hydration system, the heating system, the clay barrier, the instrumentation, and the systems for data acquisition and for heater control. Figure 1.3 shows the test schematically.

The confining structure is a cylindrical steel body with an effective length of 6.00 m and an inner diameter of 1.62 m. The hydration system, that supplies granitic water under pressure to the periphery of the clay barrier, consists of two tanks with their connections to the confining structure.

The main elements of the heating system are two heaters located concentrically in the confining structure and horizontally separated by 0.75 m. Each heater has a length of 1.625 m and a diameter of 0.340 m. In this test, there is no steel liner between the clay barrier and the heaters.

The clay barrier is formed from highly compacted bentonite blocks. The blocks were fabricated with an average water content of 13.6% and an average dry density of 1.77 t/m^3. As constructed, the barrier has an average dry density of 1.65 t/m^3 and a percentage of construction gaps of 6.25.

Basically, the instrumentation includes the sensors installed in the clay barrier, heaters, and confining structure. The variables measured are: temperature, humidity, fluid pressure, total pressure, deformation of the confining structure, and injection pressure of the water.

The components of the data acquisition and heater control systems are located in a space adjacent to the confining structure.

1.5.3. Laboratory tests

In addition to the two large-scale tests, FEBEX has included a specific programme of laboratory tests. This programme has consisted of basic characterisation, as well as thermo-hydro-mechanical and thermo-hydro-geochemical research tests, gas generation and corrosion tests and sensor analyses; research tests require a great deal of experimentation

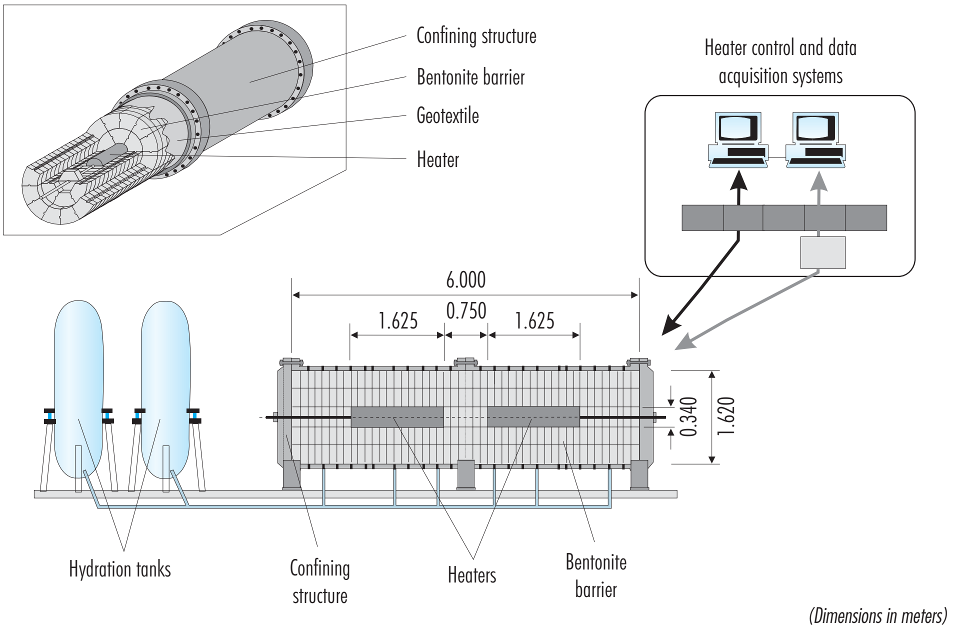

Figure 1.3: General scheme of the "mock-up" test.

and of innovation in experimental techniques. Some tests performed to obtain the basic parameters also required new techniques and testing methodologies. An important part of the testing programme consisted of jointly contemplating the thermal, hydraulic, mechanical and geochemical aspects of the system.

Attention should be brought to the tests performed in thermohydraulic cells, the oedometric and triaxial tests with controlled suction and temperature and tests to determine transport and ion exchange parameters.

These tests have been performed in parallel to the large-scale tests.

The characterisation tests have continued throughout the dismantling of Heater # 1 in order to analyse the possible changes occurring in the bentonite barrier.

1.5.4. Modelling work

Ideally, the objective of the modelling work is to achieve THM and THG numerical models that are verified and sufficiently validated for the performance assessment of the near field of a repository.

This activity requires interactive work on the theoretical development of models and on their application to the different types of tests performed in the project, especially the large-scale tests.

The THM and THG modelling work is not only an objective in itself, it is also the tool that makes it possible to understand the processes occurring in the near field, and has consequently been a basic guideline for the design of the two large-scale tests and for planning of the laboratory testing programme.

Theoretical development has been an on-going task throughout the project. The application to the tests was carried out in the different stages of the project, using the models in their stage of development at each moment and the available parameters.

The THM CODE-BRIGHT code was used for the distribution of the instrumentation for the two large-scale tests, albeit with a limited availability of actual parameters for the FEBEX bentonite. Subsequently, at the end of the pre-operational stage, a "blind" prediction was made of the behaviour of the two large-scale tests. This prediction was checked against the data from monitoring of the first operational stage. Subsequent modelling exercises have been performed simultaneously with the monitoring, and a final modelling has been carried out on completion of the project.

The initial THG code TRANQUI was used during the pre-operational stage, allowing a laboratory testing programme to be developed for analysis of the processes and parameters. Two more complete codes have been developed during the first operational stage, CORE-LE and FADES-CORE-LE, and have been used for the modelling of a series of laboratory tests and for predictions regarding the two large-scale tests. Development of the models has continued throughout the project and a final modelling has been carried out to compare the calculation results with the laboratory test data on samples taken during the partial dismantling of Heater #1 of the "in situ" test.

1.6. Results expected from the experiment

It was thought that, on the one hand, FEBEX would supply valid information for the design and construction of the clay barrier, as well as criteria for the emplacement of the canisters. On the other hand, it was expected that FEBEX would provide a better understanding of the THM and THG processes occurring in the near field and the capacity for quantitative prediction of these processes by numerical models. Specifically, it was hoped that the experiment would supply the following:

- ❑ Knowledge of the properties of the raw bentonite necessary for the fabrication of the blocks.
- ❑ Procedures for conditioning and quality control of the bentonite, from excavation to preparation as a raw material with the required properties.
- ❑ Criteria for the design of the clay barrier, including geometry, dry density, water content and dimensions of the blocks.
- ❑ Methods and techniques for the fabrication of the blocks and procedures for quality control.
- ❑ Procedures for the storage, transport and handling of the blocks, to prevent their deterioration.
- ❑ Criteria for the installation of the engineered barriers (canister and clay barrier), including the methods, appropriate auxiliary means and environmental conditions in the drift, to prevent deterioration of the blocks.
- ❑ Criteria for the selection of measuring instruments for experiments of this type.
- ❑ Criteria for the design of the transport and handling equipment for the repository components to be installed in drifts of reduced section.
- ❑ Criteria for the design and construction of the concrete plugs for drift sealing.
- ❑ Information on the characteristics of the clay barriers before and after the period of hydration/heating: gaps between the different blocks, between blocks and other elements of the barriers and between the heaters and the steel liner; state of the barriers immediately after their emplacement; state of the barriers after the operational stage of the experiment; degree of homogeneity of the clay barrier after the operational stage; sealing of rock fissures; behaviour of the concrete plug and of the adjacent zone of rock; etc.
- ❑ Improvement in the knowledge of the predictive capacity of geophysical methods for the characterization of rock masses.
- ❑ A database of the variables measured by the instruments as a function of time, as well as parameters obtained by means of the laboratory tests.
- ❑ More advanced numerical models than the current ones, including constitutive equations for the prediction of the THM behaviour of the near field.
- ❑ A match of the measured values from the hydraulic system of the rock mass with the values calculated using the hydrogeological model. As a result, evaluation of the methods and instruments for the acquisition of the hydraulic parameters and of the predictive capacity of the numerical model.
- ❑ A match of the results of the hydrogeological modelling of the rock mass with the THM modelling in the isothermal hydromechanical mode for the states prior to installation of the engineered barriers; and evaluation of both models from the point of view of prediction of the hydrodynamic behaviour of the rock mass.

- A match of the results of THM modelling with the values measured in the laboratory heating tests in cells and in the "mock-up" test, as well as evaluation of the match.
- A match of the results of THM modelling with the values measured in the "in situ" test; evaluation of the match and a definition of the areas that should be the subject of future investigations.
- Laboratory instruments designed, constructed and checked for the determination of the parameters of the bentonite required by the most advanced THM constitutive laws.
- Evaluation of the possible transformation of montmorillonite to illite due to the effects of temperature, water flow and time. The evaluation will be based on the series of laboratory tests performed to investigate ion exchange and its kinetics in samples of bentonite with different compositions of granitic water, various temperatures and different testing times.
- Analysis of the geochemical changes (migration of salts, modification of the exchange complex and modification of the pore water) occurring in the bentonite, by means of hydration and heating-in-cells tests.
- Evaluation of the effects produced by the geochemical changes on the mechanical, hydraulic and transport properties of the bentonite.
- Results of the physico-chemical, mineralogical and hydromechanical characterisation of the clay barrier before and after the operational stage of the "mock-up" and "in situ" tests; and evaluation of the modifications occurring.
- More advanced THG numerical models than those currently available, including the laws governing THG behaviour.
- A match of the results obtained from THG numerical calculations with the results from the laboratory tests and geochemical analysis of the samples obtained from the clay barrier during the dismantling stage; evaluation of the match and definition of the areas that should be the subject of future investigations.
- A global evaluation of the progress provided by the FEBEX project as regards criteria for design and construction, the development of THM and THG numerical models for the evaluation of the behaviour of the near field and definition of the areas that should be investigated in the future.

1.7. Problem areas

The results hoped for in this experiment have been listed in the previous section; nevertheless, it was recognized that there were problem areas and areas of uncertainty. Some results could not, therefore, be obtained and, as a result, the corresponding objective would not be attained (partially or totally). The most important problem areas that were identified are the following:

- *Heating system (heaters, temperature sensors, and cables)*. If, after installation, the system had ceased to function, it would not have been possible to repair it due to its inaccessibility. To minimise the risk of malfunctioning, two heaters were installed in each of the large-scale tests and three independent heating elements in each heater; and a careful review was made of the complete system design, as well as of its fabrication and installation. However, it was impossible to guarantee functioning, especially during the scheduled three years of the original operational stage. It was clear that if the heating system totally failed in a relatively short period of time, the test would not contribute to the second and third objectives, but would still contribute to the demonstration objective (although only partially, since the changes due to heating would not be obtained). Nevertheless, an isothermal test could be operated that would provide important information relative to hydration. It was hoped however that with the redundancies designed and the quality control performed there would be a high probability of achieving heating throughout the operational stage of the test. Fortunately, these concerns proved to be unfounded and, in fact, the experiment continues today after almost eight years of operation (five more than originally foreseen) due to the good performance of its elements.
- *Instrumentation system (sensors and cables) in the test zone*. Problems similar to those for the heating system were thought to exist for these parts of the instrumentation system. The instrument suppliers did not guarantee their products for the full operational stage initially foreseen (3 years) in such a harsh environment. Although the cables and their connections are

also elements of uncertainty, reasonable measures were taken to reduce the possibility of failure. In any case, a large number of sensors were installed with the hope of obtaining an acceptable level of information. Even in the event that a large number of sensors failed, but the heaters functioned correctly, the demonstration objective would be achieved and the other two objectives would have been partially attained since, even if a significant quantity of intermediate data would have been lost, the initial and final states would still be available; the final state will be defined by the laboratory tests on samples of bentonite taken during dismantling.

- *Hydraulic properties*. An area of uncertainty in the validation of the THM and THG numerical models for the "in situ" test relates to the properties of the rock mass: the initial and boundary conditions; the properties of the zone disturbed by excavation of the drift; and the effects of desaturation produced by ventilating the drift during the installation of the physical elements of the test. Although a detailed hydrogeological characterisation was made of the zone adjacent to the drift, it was thought probable that there would be uncertainties due to undefined effects in the far field, to the previous existence of the access tunnel, the drifts of the laboratory, the investigative boreholes and the heterogeneity of the rock mass itself; consequently, the accuracy of the hydraulic data would be limited. Since study of the zone disturbed by the excavation of the drift was not an objective initially, its properties and extent have been assumed based on experiments performed elsewhere for most of the analyses. These uncertainties are not found in the "mock-up" test; on the contrary, the initial and boundary hydraulic conditions of the clay barrier are controlled and, therefore, well defined.
- *Numerical models*. There were problems inherent to the improvement, extension, verification, and validation of the THM and THG numerical models. Certainly, the capacity of the initial models to describe the geometry, processes, etc. would be improved and extended; however, not only was it impossible to define "a priori" the degree of fit that the improved models would have with the measurements actually made in the two large-scale tests, but there were also uncertainties in the degree of improvement to be achieved in the mathematical formulation itself, especially with respect to the behavioural laws of the materials and the modelling of anisotropy and heterogeneities.
- *Samples*. Another problem area identified was the acquisition of representative samples of the clay barrier immediately before the initiation of cooling, in the large-scale tests. The aim of taking these samples was to analyse the changes that have occurred during heating, which might be masked during the cooling phase.

2. FEBEX bentonite

2. FEBEX bentonite

2.1. Origin and manufacturing

The FEBEX bentonite (also called "Serrata" clay in some FEBEX reports) was extracted from the Cortijo de Archidona deposit, exploited by Minas de Gádor, S. A., in the zone of Serrata de Níjar (Almería, Spain). This deposit was selected in the ENRESA R&D plans previous to the FEBEX project as the most suitable material for the backfilling and sealing of a HLW repository, the reasons for this selection being its very high content of montmorillonite, large swelling pressure, low permeability, acceptable thermal conductivity, good retention properties and ease of compaction for the fabrication of blocks.

Over several years prior to FEBEX, and following the selection of this deposit as the reference bentonite (called bentonite S-2 in reports and publications), numerous characterisation and behaviour (thermal, hydraulic, mechanical, and geochemical) studies were performed. As a result, there was an extensive database on the properties of this bentonite. Comparison of the results of the two sets of characterisation tests —S-2 bentonite and FEBEX bentonite, obtained from the same deposit but in two study phases separated by more than five years— indicates that the deposit is very homogeneous. However, there are some differences between the average values of the properties from the two sets of tests, which allow the range of variations to be evaluated. This evaluation may be used to establish realistic limits in modelling sensitivity analyses, and, thus gain insight into the consequences for the PA of a repository.

In the following sections, several general conclusions on the properties of the bentonite from this deposit are summarised.

2.1.1. Geological setting

The Cortijo de Archidona deposit is located at the SE end of the Serrata de Níjar, 12 km SE of the village of the same name (Almería). The Serrata de Níjar is made up of a succession of small hills running in the NE-SW direction and measuring some 11 km in length and 1.5 km in width on average. The area is located in quadrant III of the 1:25.000 scale IGN map "Fernán Pérez".

Along with the Sierra de Cabo de Gata, the Serrata de Níjar constitutes the volcanic region of Cabo de Gata. The origin of this volcanism is associated with the geotectonic dynamics of the Western Mediterranean during the Neogene. The radiometric dating of the volcanic episodes, which are calco-alkaline in type, indicates ages of between 15 and 17 million years [8]. This volcanism frequently occurred under shallow submarine conditions. Episodes of both emersion and immersion of the volcanic complexes subsequently took place, as is shown by the interlayering of paleosoils, bioclastic limestones and reef materials. For this reason, the volcanic rocks have been exposed to the action of both meteoric and marine waters, in both cases linked to hydrothermal systems caused by the volcanic activity itself. The action of these fluids at different temperatures contributed to the alteration of the volcanic rocks, giving rise to silica, alunite, jarosite, kaolinite or bentonites, depending on the composition of the solutions.

The Serrata de Níjar is a volcanic complex that forms part of an intensely fractured horst, bound by two fractures running parallel in the NE-SW direction. Figure 2.1 shows the location of the zone within the context of the southeastern Iberian Peninsula.

The Cortijo de Archidona deposit is located to the south of the Serrata de Níjar, and is reflected on sheet 1046 of the IGME 1:50.000 scale Geological Map, corresponding to Carboneras. Figure 2.2 shows a geological diagram of the deposit that illustrates the arrangement of the different materials. From the oldest to the most modern, these materials are as follows [9]:

- ❑ Betic substrate, constituted fundamentally by a breccoid limestone of Jurassic age, in addition to Triassic dolomites and filites.
- ❑ Volcanic rocks, including polygenic and dacytic tuffs, amphibolic dacytes, riodacytic vitrophyres, pyroclastic breccia of dacyte and andesite and vitrophyres.
- ❑ Sedimentary covering, formed by Pliocenic and Quaternary materials and constituting the SE limit of the bentonitised zone, with which it enters in contact by means of a major fault.

The geometry of the quarry from which the mineral is extracted runs in two directions of maximum alteration, coinciding with areas of fracturing. The main mass of bentonite coincides with a fault running NW-SE, which is where the most important mining work has been carried out. A second zone, where the volume of altered material is smaller, coincides with a fault running NE-SW.

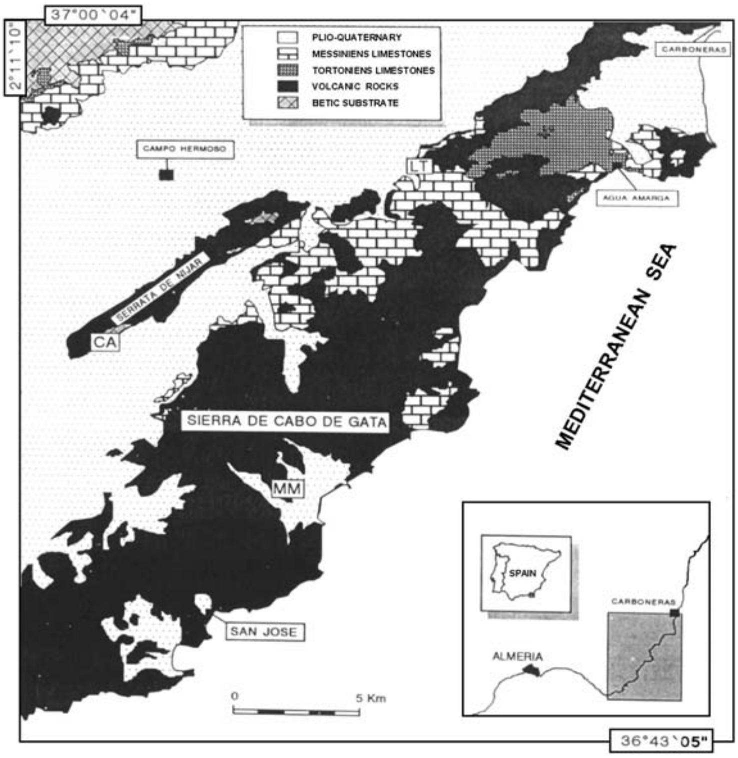

Figure 2.1: Location of the Cortijo de Archidona (CA) deposit in the context of SE Spain (from Delgado 1993).

2.1.2. Selection and conditioning

Approximately 300 tons of suitably homogenised and conditioned bentonite was stocked for FEBEX. Based on the experience acquired in the aforementioned studies, the selected raw bentonite was required to meet the following specifications:

- Fraction of particles of more than 5 mm, less than 5 percent, and fraction of particles smaller than 74 μm, greater than 85 percent.
- Liquid limit greater than 90 percent.
- Swelling pressure between 3 MPa and 7 MPa, for a dry density of 1.60 g/cm^3.
- Water content, after conditioning, between 12.5 and 15.5 percent.

The conditioning of the bentonite in the quarry, and later in the factory, was strictly mechanical (homogenisation, rock fragment removal, drying, crumbling of clods, and sieving) to obtain a granulated material with the specified characteristics of grain size distribution and water content. A quality assurance (QA) program was applied to the conditioning process. The conditioned material was packaged in large waterproof bags (1300 kg each). During the packaging, a sample of 8 to 10 kg was taken every 2.5 tons of bentonite. From each sample 6 kg were taken and they were all mixed by shovelling to obtain a homogeneous reference sample, 70-IMA-3-4-0 –from hereon FEBEX–, which was subsequently quartered and sent to different laboratories.

2.2. Mineralogy and geochemistry

2.2.1. Mineralogical composition

The bentonite from the Cortijo de Archidona deposit has a very high content of montmorillonite-type

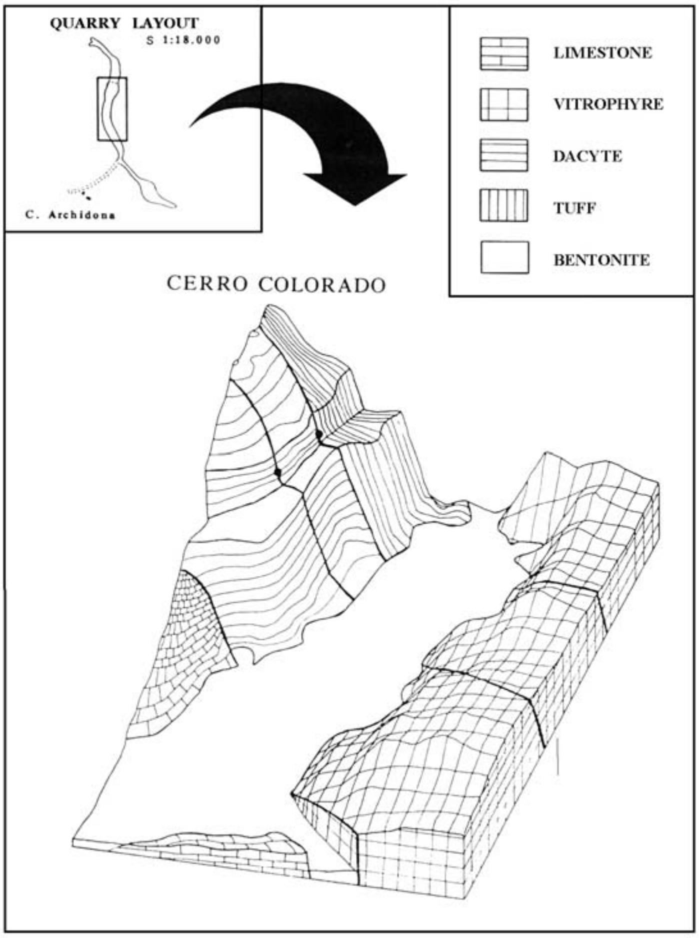

Figure 2.2: Diagram of the Cortijo de Archidona deposit and associated materials (from [9]).

dioctahedric smectite. Furthermore, from the mineralogical point of view, the deposit is very homogeneous, since the montmorillonite content of the bentonites (S-2 and FEBEX) varies only between 89 and 96 percent.

The mineralogical composition of the bentonite has been studied by X-ray diffraction (Figure 2.3, Figure 2.4 and Table 2.1). The smectitic phases of the FEBEX bentonite are actually made up of a smectite-illite mixed layer with ~11 percent of illite layers ($\Delta 2\theta$=5.502). The thickness of FEBEX smectite quasicrystals is around 102±5 Å, and the quasicrystals of saturated FEBEX smectite consist of 6 lamellae or layers stacked along the crystallographic c-axis. The Biscaye index of smectite crystallinity is 0.97. The parameters of the crystallographic unit cell are: a=5.156 Å (a=5.196 Å, theoretically), b=9.0 Å, and c=14.3 Å (room conditions) or c=16.9 Å (saturated atmosphere) [10, 11].

In spite of its high smectite content, the bentonite contains numerous accessory minerals, either neoformed or remains of the original volcanic rock nearly unaltered. The bentonite contains variable quantities of quartz, plagioclase, K-feldspar, calcite and opal-CT (cristobalite-tridymite) (Table 2.1). Other accessory minerals are mica (biotite, sericite, muscovite), chlorite, non-differentiated silicates of Al, K, Fe, Mg and Mn, augite-diopside, hypersthene, horn-

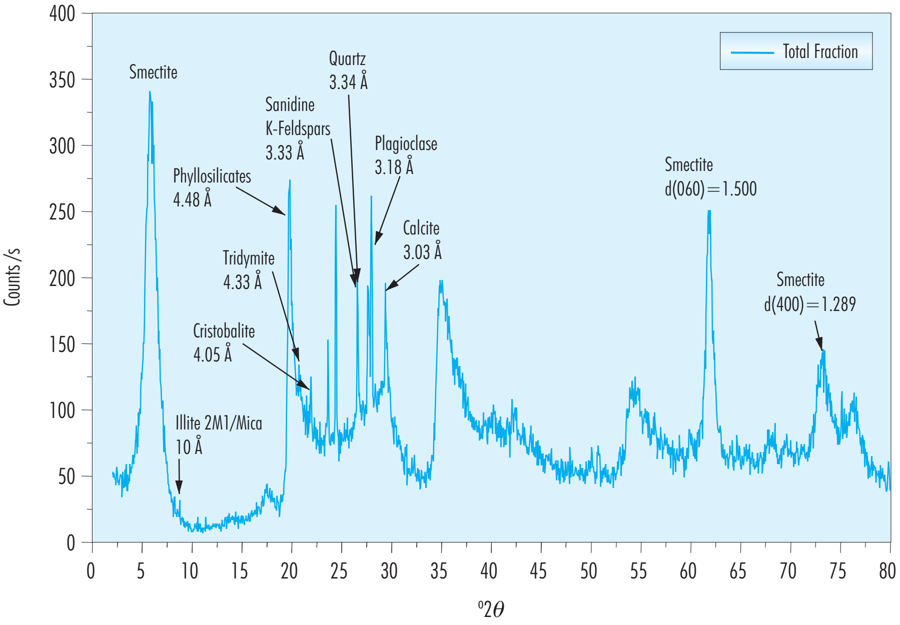

Figure 2.3: XRD pattern of a random powder of the FEBEX bentonite.

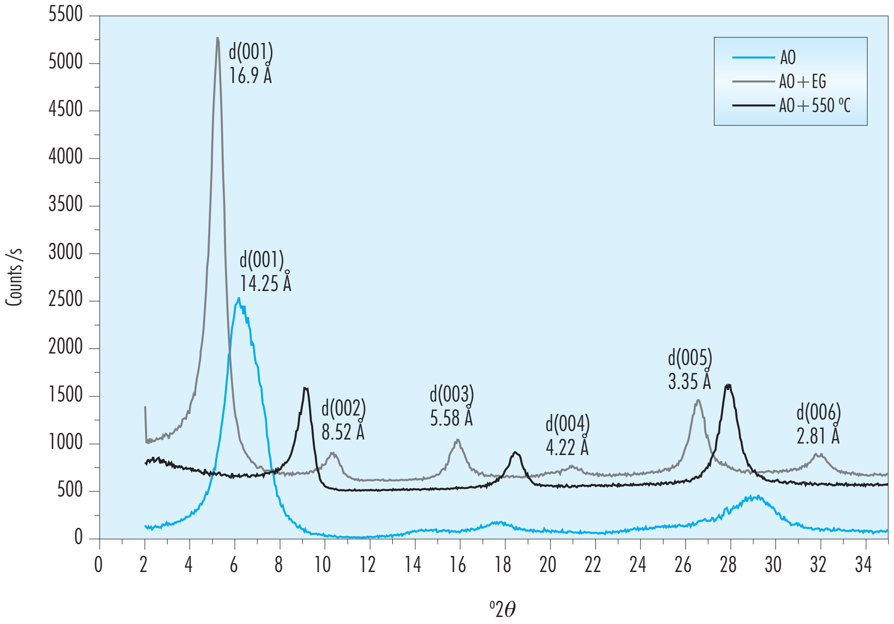

Figure 2.4: XRD pattern of an oriented powder of the FEBEX bentonite at room conditions (AO), after saturation with ethylene glycol (AO+EG), and after heating at 550ºC (AO+550ºC).

blende, oxides (ilmenite, rutile, magnetite, Fe-oxides), phosphates (apatite, xenotime, monacite) and non-differentiated silicates of titanium and rare earths, which have been determined by weight from dense concentrates and SEM identification. Their total amount is 0.8 percent. Some minerals, such as carbonates, chlorides and sulphates, have been determined by a normative calculation and SEM identification (Table 2.2). The poorly ordered minerals have been determined by selective chemical methods (Table 2.3). Most of the accessory minerals are in the sand and coarse silt fractions, although there

Table 2.1
Content of the main minerals obtained by X-ray diffraction analysis, in %

Mineral	Bentonite S-2	FEBEX Bentonite
Smectite	92 ± 4	92 ± 3
Quartz	2 ± 1	2 ± 1
Plagioclase (Na, Ca)	3 ± 1	3 ± 1
Cristobalite	2 ± 1	2 ± 1
K-Feldspars	—	Traces
Calcite	1 ± 1	1 ± 0.5

Table 2.2
Accessory minerals of the FEBEX bentonite determined by a normative calculation and SEM identification, in %

Mineral	Content (%)
Organic Matter (expressed as CO_2)	0.35 ± 0.05
Carbonates (calcite, dolomite)	0.60 ± 0.13
Soluble sulphates (gypsum)	0.14 ± 0.01
Low soluble sulphates (barite, celestite)	0.019 ± 0.04
Sulphides (pyrite)	0.02 ± 0.01
Chlorides (halite)	0.13 ± 0.02

Table 2.3
Poorly ordered minerals of the FEBEX bentonite determined by selective chemical methods, in %

Amorphous Phases	CSIC-Zaidín	CIEMAT
SiO_2	1.48 ± 0.11	0.038 ± 0.005
Al_2O_3	0.035 ± 0.005	0.035 ± 0.005
Fe_2O_3	0.105 ± 0.009	0.105 ± 0.009

are some traces in the fractions of smaller size. Different accessory minerals detected by SEM may be seen in Figure 2.5 and Figure 2.6.

2.2.2. Chemical composition

Table 2.4 shows the average content values of the major elements of the FEBEX and S-2 bentonite. Generally speaking, the content of the major elements obtained at the CIEMAT and CSIC-Zaidín laboratories is very similar for both types of bentonite. Thus, a high degree of homogeneity is observed in the chemical composition of the different samples analysed.

Table 2.5 shows the average values of the minor and trace elements of the FEBEX bentonite [10]. The content of chlorides and sulphates is worthy of mention.

Based on chemical analyses, the structural formula or unit-cell formula of the Ca conditioned FEBEX smectite is:

$$(Si_{7.78}\,Al_{0.22})^{IV}\,(Al_{2.78}\,Fe^{3+}{}_{0.33}\,Fe^{2+}{}_{0.02}\,Mg_{0.81}Ti_{0.02})^{VI}$$
$$O_{20}\,(OH)_4\,(Ca_{0.50}Na_{0.08}K_{0.11})$$

Tetrahedral charge: -0.22, Octahedral charge: -0.97, interlayer charge: +1.19

The formula weight per 22 atoms of oxygen is 752.46 g. 19 percent of the charge arises from tetrahedral substitution, and 81 percent from octahedral substitution. This indicates that this dioctahedral smectite (montmorillonite) is of the Tatatila and Chambers type (Newman 1987). According to chemical analysis, the theoretical exchange capacity is 1.05 eq/kg and therefore, the total charge per unit-cell is 0.79. The 0.11 potassium ions per formula unit are not exchangeable and belong to the 11 percent illitic layers of the smectite-illite mixed layers [10, 11].

2.2.3 Soluble salts

The total soluble salts were analysed in aqueous extract solutions at low solid to liquid (S:L) ratios. Ground samples were placed in contact with deionised and degassed water, shaken end-over-end at 1:4 S:L ratio and allowed to react for 2 days under room conditions. After phase separation by centrifuging (30 minutes at 15000 rpm), the supernatant solutions were analysed. The results obtained by the two laboratories are shown in Table 2.6. The differences observed between the two laboratories are due to the heterogeneity of the FEBEX bentonite.

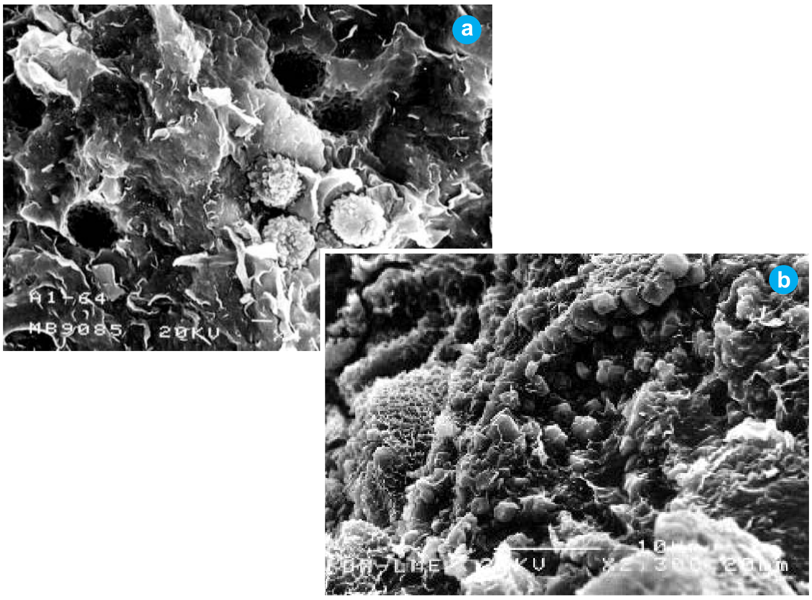

Figure 2.5: Carbonates: a) calcite as micritic crystals, and b) crystals of carbonates surrounded by smectite.

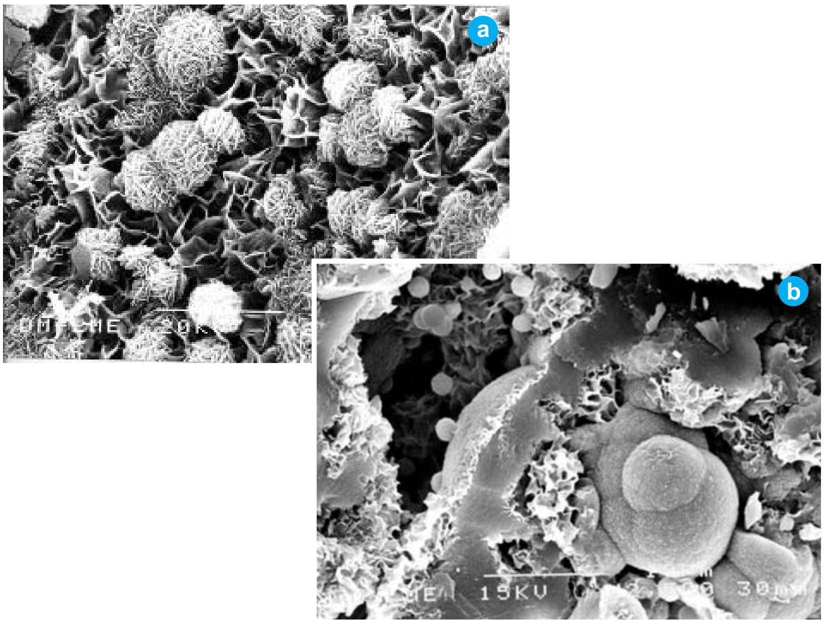

Figure 2.6: a) Spheres of crystallized silica (cristobalite), and b) silica with a botryoidal shape (opal).

The chloride and sulphate inventories of the FEBEX bentonite, *i.e.* the element amount per kg of oven-dried clay mass, are shown in Table 2.7. These values are the average of different tests performed at high and low S:L ratios [11, 12] (see Section 5.2.1).

2.3. Physico-chemical properties

2.3.1. Identification properties

The data presented in Table 2.8 are the so-called identification properties (according to the terminology of geotechnical engineering) this being because on the basis of simple tests they give an initial idea of the type of physico-chemical behaviour to be expected in clay.

Regardless of the differences in the grain-size distributions between the S-2 and FEBEX bentonite, it should be noted that the results obtained from CIEMAT and UPC-DIT differ considerably as regards the content of the $< 2\ \mu$m fraction (clay size). The proportion of the clay size fraction obtained depends on the previous treatment of the bentonite for the determination of its grain-size distribution. The differences may be explained by the fact that a very strong dispersion procedure, including ultrasounds, was used by CIEMAT, whereas UPC-DIT employed standard geotechnical techniques.

It must be taken into account that the external specific surface (BET) value is very dependent on the experimental conditions of the determination and even on the method chosen for the interpretation of the isotherm. With respect to the total specific surface, the value calculated for the FEBEX bentonite on the basis of the unit cell parameters and the unit weight is 746 m^2/g.

The low content of the $< 2\ \mu$m fraction had already been noticed in the first studies performed on the S-2 bentonite. It was proposed at that time that the smaller particles were agglutinated or cemented with colloidal silica (during alteration of the original volcanic material). This would make dispersion of the clay, and consequently separation of the $< 2\ \mu$m fraction, more difficult. This argument is supported since most of the silt-sized material, and some of the sand-sized material, is formed by "pseudomorphs"

Table 2.4
Chemical composition of S-2 and FEBEX bentonite, in %

Oxides	Bentonite S-2		FEBEX Bentonite	
	CSIC-Zaidín	CIEMAT	CSIC-Zaidín	CIEMAT
SiO_2	59.90	57.30	58.92 ±1.74	57.89 ± 1.55
Al_2O_3	18.70	19.60	19.48 ±1.05	17.95 ± 0.71
Fe_2O_3	$3.60^{(3)}$	$3.90^{(3)}$	$3.48 \pm 0.63^{(3)}$	2.84 ± 0.12
FeO				0.25 ± 0.10
MgO	5.80	4.70	4.83 ± 0.27	4.21 ± 0.21
MnO	___	<0.03	0.06 ± 0.02	0.04 ± 0.00
CaO	2.00	2.90	2.51 ± 0.09	1.83 ± 0.10
Na_2O	2.20	1.90	2.28 ± 0.11	1.31 ± 0.09
K_2O	0.70	1.40	1.21 ± 0.08	1.04 ± 0.05
TiO_2	___	0.30	0.27 ± 0.06	0.23 ± 0.01
P_2O_5	___	0.10	0.06 ± 0.02	0.03 ± 0.01
$H_2O^{-\,(1)}$	___	___	___	8.66 ± 2.88
$H_2O^{+\,(2)}$	6.70	5.70	5.07 ± 0.76	4.31 ± 0.41
CO_2 organic	$0.70^{(4)}$	0.19	0.19 ± 0.04	0.35 ± 0.05
CO_2 inorganic		0.20	0.52 ± 0.07	0.26 ± 0.06
SO_2 total	___	0.05	___	0.21 ± 0.10
F^-	___	0.16	0.21 ± 0.03	0.18 ± 0.01

$^{(1)}$ determined at 220ºC; $^{(2)}$ structural water; $^{(3)}$ Fe_2O_3 total; $^{(4)}$ $CO_{2\ total}$

Table 2.5
Minor and trace elements of the FEBEX bentonite, in ppm

Ba	Sr	Ce	Co	Cr	Cu	La	Ni	V	Y	Zn	Zr	U	Th	Rb	Li	Cl^-	SO_4^{2-}
164 ±25	220 ±23	74 ±6	9 ±3	8 ±2	25 ±9	40 ±3	20 ±3	16 ±2	25 ±3	65 ±4	43 ±0	2.0 ±0.5	19 ±1	41 ±2	54 ±3	774 ±144	984 ±65

Table 2.6
Main chemical species concentrations in the 1:4 S:L aqueous phase, in mmol/100g of dried clay

Parameter	pH	Cl^-	SO_4^{2-}	HCO_3^-	Na^+	K^+	Mg^{2+}	Ca^{2+}	Sr^{2+}	Fe^{3+}	Al^{3+}	SiO_2
CIEMAT$^{(1)}$	8.73	1.98	0.98	1.18	5.02	0.073	0.055	0.050	$0.4 \cdot 10^{-3}$	$1.7 \cdot 10^{-3}$	0.013	0.145
UAM$^{(2)}$	7.93	2.03	1.84	1.56	6.04	0.062	0.146	0.067				

$^{(1)}$ Fernández (2003); $^{(2)}$ ENRESA (2000): As, V, Br, Sr, Ti, Mn, Fe, Ni, Cu, Zn and Y in concentrations lower than 10^3 mmol/100g

Table 2.7
Cl^- and SO_4^{2-} inventories of FEBEX bentonite

Size fraction	Cl^- (mmol/100g)	SO_4^{2-} (mmol/100 g)
Total	2.185 ± 0.396	1.026 ± 0.068
< 63 µm	2.269 ± 0.314	0.987 ± 0.081

Table 2.8
Identification properties

Property	Bentonite S-2		FEBEX Bentonite		
	CSIC-Zaidín	CIEMAT	CSIC-Zaidín	CIEMAT	UPC-DIT
Water content in equilibrium with the air in the laboratory, in %	—	10 to 13	—	13.7 ± 1.3	13.3 ± 1.3
Liquid limit, in %	—	105 ± 10	—	102 ± 4	93 ± 1
Plastic limit, in %	—	—	—	53 ± 3	47 ± 2
Plasticity index	—	—	—	49 ± 4	46 ± 2
Specific weight	—	2.78	—	2.70 ± 0.04	—
Grain-size distribution, in %					
Fraction less than 74 µm	93 ± 3	86	—	92 ± 1	87
Fraction less than 2 µm	82 ± 6	65 ± 1	—	68 ± 2	45
Specific surface, in m^2/g					
Total	614 ± 74(1)	516 ± 37(2)	649 ± 5(1)	725 ± 47(1)	—
External, BET	—	37	—	32 ± 3 (3) 56-62 (4)	—

(1) Determined by the Keeling hygroscopicity method; (2) Determined by the methylene blue method; (3) [13] ; (4) [11]

of volcanic grains transformed into smectite (see Section 2.3.3). The "pseudomorphs" are relatively stable and would moderate the physical behaviour of the bentonite: they behave as smectite from a chemical point of view, but do not have the physical effects of the bentonite.

2.3.2. Pore size distribution

A clay may develop three kinds of pores: i) interlamellar pores within the primary particles (1-10 Å), ii) intra-aggregate pores, usually of less than 0.002 µm in size delineated by the boundaries of primary particles within the aggregates, and iii) inter-aggregate pores (0.002 to several micrometers in size). Classifications based only on pore size [14] consider pores smaller than 0.002 μm to be micro pores, and the limit between meso and macro pores is set at 0.05 μm. In the case of compacted FEBEX bentonite, a family of large intergranular pores, which are located between grains resulting from the physical treatment of the clay at the quarry and the factory, may be defined. Pore size distribution was determined in different types of samples of the FEBEX bentonite using two techniques. Bentonite powder, ground to a grain size of less than 1 mm, was examined by N_2-adsorption isotherms, and bentonite compacted at different densities was tested by mercury intrusion porosimetry (MIP). The main difference between both techniques is the different range of accessible pore sizes, which is between 0.006 and 480 μm diameters for mercury, and between 0.001 and 0.8 μm diameters for nitrogen. Other differences relate to the diverse preliminary preparation of the samples and to the possible effect of the intrusion of the fluid on the clay structure.

The results obtained by CIEMAT are shown in Table 2.9 and Table 2.10. In the latter table it may be observed that when compaction increases the percentage of large pores decreases, as does their size mode, whereas the percentage of smaller pores increases.

Figure 2.7 shows the pore size distribution (PSD) obtained by UPC-DIT in samples compacted to different values of dry density (from 1.4 g/cm^3 to 1.68 g/cm^3) and hygroscopic water content, in terms of logarithmical increment of void ratio ($\Delta e/\Delta \log_{10}$ pore diameter). It may be observed that the pore size distribution in the range tested is bimodal: a dominant size around 10 nm, and a larger pore size, which depends on the compaction dry density and ranges from 20 μm (for ρ_d=1.68 g/cm^3) to 30 μm (for ρ_d=1.4 g/cm^3). These larger voids would correspond to the inter-granular pores. The boundary between both pore size families may be situated at around 150-200 nm, as pores smaller than this size do not appear to be affected by the magnitude of the compaction load. The samples differ only in the proportion of macro pores having a diameter bigger than 2 μm.

Similar conclusions concerning macro porosity may be achieved considering the samples compacted at low water content (3-4 percent) [15]. Figure 2.8 presents a summary of the inter-granular pore sizes

Table 2.9
Pore size distribution of the bentonite powder obtained by nitrogen adsorption (1)

Pore diameter (μm)	Quantity (%)
0.150 to 0.045	36±8
0.045 to 0.020	25±4
0.020 to 0.006	20±4
0.006 to 0.003	11±4
<0.003	8±2

(1) The pore size distribution has been calculated to add 100%

Table 2.10
MIP results for samples compacted with hygroscopic water content at different dry densities (1)

ρ_d (g/cm^3)	Macropores				Mesopores	
	200-6 μm diameter		6-0.1 μm diameter		0.1-0.006 μm diameter	
	%	Mode (μm)	%	Mode (μm)	%	Mode (μm)
1.55 (2)	66	42	3	1.88	31	0.026
1.65 (2)	31	32	21	1.72	48	0.016
1.75 (3)	23±6	18±4	26±6	0.76±0.56	54±10	0.016±0.006

(1) The pore size distribution has been calculated to add 100%; (2) One sample; (3) Average of 45 samples taken from blocks compacted for the mock-up test

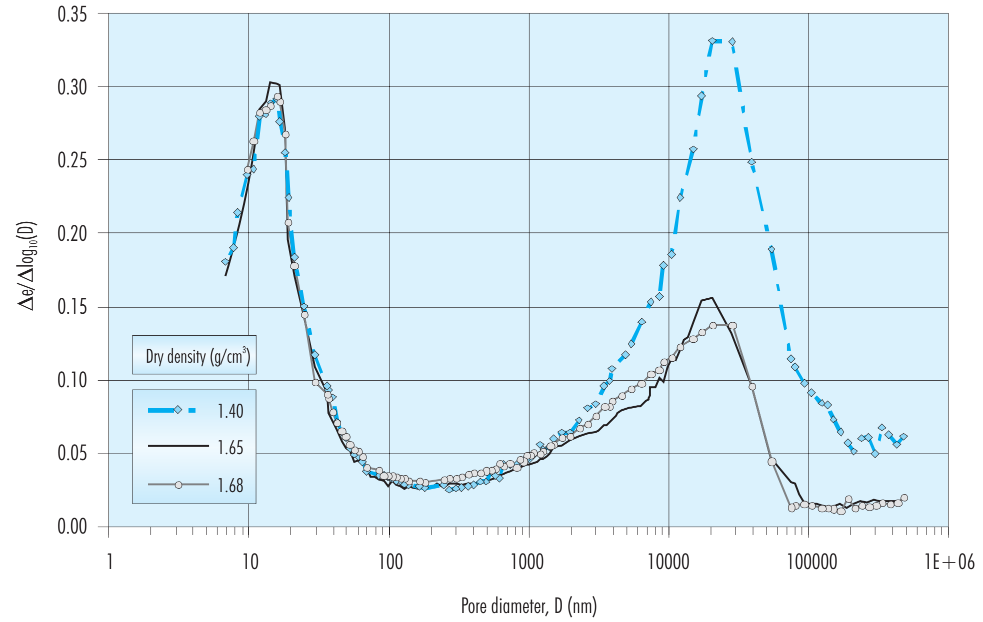

Figure 2.7: Porosimetry of samples compacted to different dry densities with a water content of about 13 percent.

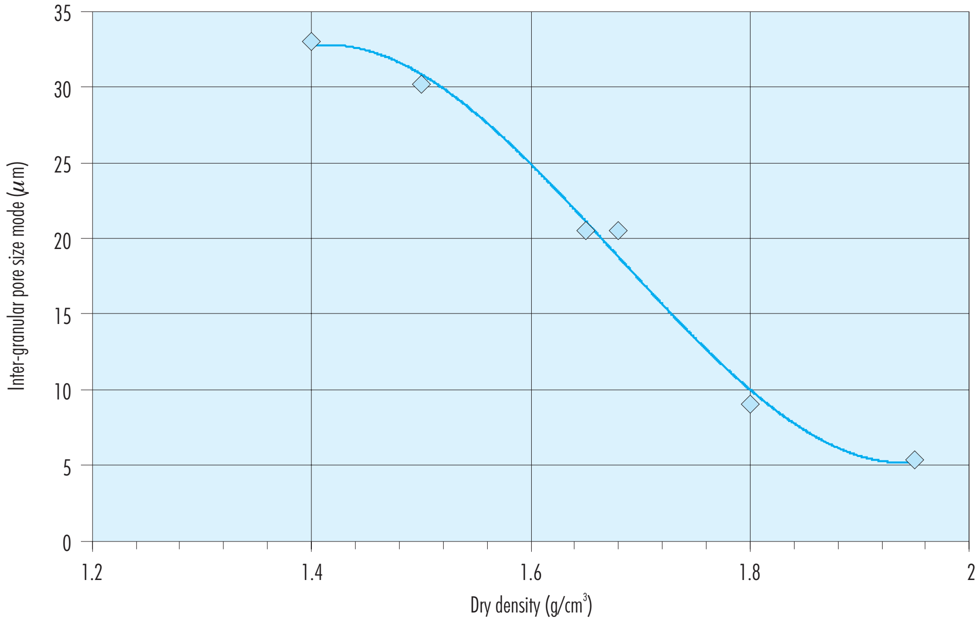

Figure 2.8: Pore size mode for the inter-granular voids as a function of dry density.

as a function of the dry density for samples compacted with hygroscopic water content.

Figure 2.9 shows the relationship between pore diameter and intruded pore volume for two samples compacted at dry densities of 1.40 g/cm^3 and 1.68 g/cm^3. It may be appreciated that there is a significant pore volume into which the mercury could not penetrate or that has a diameter larger than the resolution of the equipment. In the case of the sample with a dry density of 1.68 g/cm^3, this pore volume corresponds mostly to pores smaller than 6 nm (e=0.24), but in the case of the sample with a dry density of 1.40 g/cm^3, part of this volume corresponds also to pores bigger than 480 μm. Assuming that the magnitude of the pore volume associated with pores of diameter smaller than 6 nm (not intruded by mercury) is the same for the two specimens, the volume of pores with a diameter larger than 480 μm that is not reflected in the curve of the less dense specimen, is about 0.15. Indeed, the volume of pores smaller than 200 nm is very similar for the two samples, with void ratio values of around 0.41. The remaining of the pore space corresponds, therefore, to inter-aggregate and inter-granular pores, accounting for about 55 percent of the voids (e=0.51) in the sample with a dry density of 1.40 g/cm^3, and about 33 percent of the voids (e=0.20) in the sample with a dry density of 1.68 g/cm^3.

2.3.3. Fabric

Thin sections of compacted FEBEX bentonite were prepared for study by polarising optical microscopy. The textural heterogeneity itself is the main feature in the sample. The FEBEX bentonite is mainly composed of clay aggregates (81±19 %) that may occur as dark isotropic poorly crystalline crystals and/or present a preferred orientation and relatively large (sub-micrometric) bright crystals. There are also glassy materials (1.4 %), volcanic rock fragments (1.2 %) and single accessory minerals (quartz and feldspars, up to 5 %). Calcite (0.9 %) is usually present as esparitic crystals, which replace feldspars, and less frequently as isolated micritic cements. Figure 2.10 shows the general appearance of the untreated air-dried compacted clay.

The microfabric studies on powder material by SEM microscopy show that, in general, the FEBEX bentonite is mainly composed of variable size aggregates of smectite, usually higher than 2 µm. These

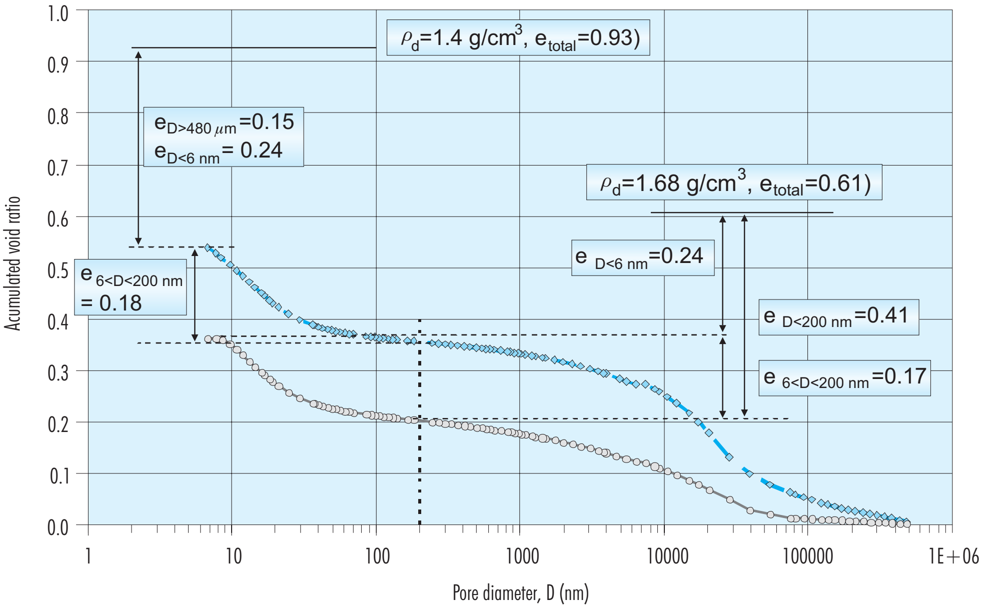

Figure 2.9: Relationship between pore diameter and intruded pore volume for two samples compacted at different dry densities.

Figure 2.10: Unsaturated appearance of the compacted FEBEX clay (x 37.5).

aggregates, of high stability, present a dense granular arrangement without any preferential orientation. The aggregates are pseudomorphs of the original and inherited minerals from which they were originated, such as volcanic glass, feldspars, pyroxenes and amphiboles [16]. Inside the aggregates, the clay particles have a honeycomb texture, characterised by an edge-edge and edge-face clay platelet group interaction (Figure 2.11). This leads to three-dimensional voluminous card-house structures giving place to a globular microfabric type.

2.3.4. Exchange capacity

The cation exchange capacity (CEC) is the numerical value of the ion-exchange capability of the clay minerals. For the FEBEX bentonite it is 102±4 meq/100g. To determine this capacity, the exchange sites of the sample were saturated with sodium. The adsorbed sodium was then displaced by successive extractions with 1 *M* ammonium acetate at pH=7.0 [17, 18].

Table 2.11 shows the average content values of the exchangeable cations obtained by two laboratories. These values were obtained by using the 1 *M* NH_4AcO pH 7.0 method [18], after washing the bentonite soluble salts with deionised water at 1:4 S:L ratio (CIEMAT) or with a 1:1 acetone/water mixture (CSIC).

However, some uncertainties in the amount of exchangeable cations were detected when measured with the NH_4AcO pH 7.0 method. The FEBEX bentonite contains carbonates and sulphates as accessory minerals. The possible solubilisation of these minerals must be taken into account when selecting the interchange reactive. Furthermore, a previous washing of soluble salts may alter the true concentrations of the exchangeable cations. An uncontrolled dissolution of calcite during the extraction of the exchangeable cations was observed at low S:L ratios [12]. This produced over- and underestimations of the exchangeable calcium and sodium values, respectively.

To overcome this uncertainty, new methods were used to determine the accurate amount of exchangeable cations, based on: 1) the incorporation of solvents less polar than water in the extracted solution (such as ethanol), 2) the use of a solution with high pH (~8.2), and 3) the use of an index cation whose adsorption affinity is much higher than for all

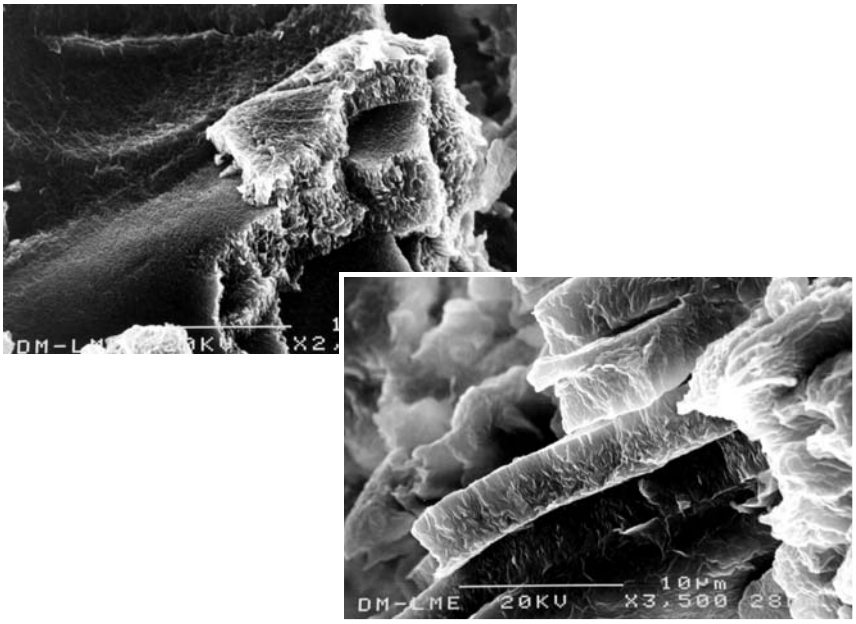

Figure 2.11: SEM microphotographs: three-dimensional voluminous card-house structures arising a pseudoglobular microfabric type with face to face associations of the clay plates.

ions commonly present in clays, such as NH_4 or Cs [19, 20].

From the new results obtained (see Section 5.2.1.4.), the 0.5 M $CsNO_3$ at pH 7 method at 1:8 S:L ratio and without previous washing of the soluble salts was finally selected. Table 2.12 shows the reference values of the cation occupancies for the FEBEX bentonite selected from among all the results obtained [11]. It includes also the values extrapolated from aqueous extracts determinations at different S:L ratios (see Section 5.2.1.1.).

2.3.5. Surface charge density

The retention and release of elements by smectite is controlled by the adsorption and desorption of anions and cations on the charged surfaces (interlamellar surfaces and the surface functional groups).

The permanent structural charge of the FEBEX smectite expressed as a *surface charge density* (σ), *i.e.* the excess of non-balanced charge per unit surface area of this smectite with a charge of 0.79 electrons per $O_{20}(OH)_4$, is 0.136 C/m^2 [10]. This permanent structural charge is due to isomorphic substitutions in the clay lattice and the deficit of positive charge within the sheet is balanced by interlamellar cations. Thus, the surface charge density has been calculated by taking into account the cation exchange capacity, the specific surface, the elementary charge, the unit cell parameters, and the formula weight.

2.3.6. Redox capacity

The Redox buffering capacity or the total reducing capacity of the FEBEX bentonite has been determined experimentally by oxidising the sample with potassium dichromate in the presence of concentrated sulphuric acid. The total reducing capacity (TRC) evaluated by this method is 0.23±0.19 meq/g. The values of organic carbon and organic matter content are 0.07±0.06 and 0.12±0.10 percent, respectively [11].

From the chemical analysis of the bentonite, the calculated TRC – which is related to the amount of reduced species (sulphide, ammonium, oxidisable or-

Table 2.11
Average values of exchangeable cations initially determined, in meq/100g [13]

Exchangeable cations	Bentonite S-2		FEBEX Bentonite	
	CSIC-Zaidín	CIEMAT	CSIC-Zaidín	CIEMAT
Ca^{2+}	31 ± 6	41 ± 7	43 ± 5	42 ± 3
Mg^{2+}	33 ± 6	31 ± 7	32 ± 3	32 ± 2
Na^{+}	30 ± 3	22 ± 3	24 ± 4	25 ± 2
K^{+}	3.0 ± 1.0	2.5 ± 1.0	2.1 ± 0.2	2.5 ± 0.3

Table 2.12
Summary of the cation occupancies (in meq/100 g) for the FEBEX bentonite

Cation	Cs method$^{(1)}$	Extrapolated $^{(2)}$
Ca^{2+}	34.8±2.4	34.6
Mg^{2+}	31.0±3.1	34.0
Na^{+}	27.1±0.2	31.2
K^{+}	2.6±0.4	1.9
$Sr2^{+}$	0.4±0.1	—
CEC (as Σcations)	95.8±0.2	102 ± 4

(1) Determination without previous washing of soluble salts, the soluble cations were subtracted by using Cl and SO_4^{2-} inventories [11]
(2) Extrapolated from results of aqueous extracts [12].

ganic carbon, Fe (II) and Mn(II) – is 0.59±0.12 meq/g. In these calculations the amount of sulphates (SO_4^{2-}) in total S has been subtracted, and the amount of NH_4^+ has not been taken into account.

There are some uncertainties in the chemical determination of the sulphides content. This might explain the difference between the two methods. In any case, the Redox buffering capacity of the FEBEX bentonite is low.

3. “Mock-up” test design, construction and operation

3. “Mock-up” test design, construction and operation

3.1. General description

The "mock-up" test simulates, at almost full scale, the components of the engineered barriers system (EBS) in accordance with the ENRESA AGP Granito reference concept.

In this test, the heterogeneities of the natural system (granite formation) are avoided, the hydration process is controlled and the boundary conditions are better defined than in the "in situ" test. This facilitates the verification of the predictive capacity of the numerical codes developed for analysis of the behaviour of the near field, as only the behaviour of the clay barrier is considered. This verification by comparison only with the behaviour of the clay barrier is a necessary step prior to comparing the model results with the behaviour of the natural conditions, as in the "in situ" test.

The components of the test are similar to those of the "in situ" test: two electric heaters, a 0.64 m-thick clay barrier, instrumentation, automatic control of heaters and a data acquisition system for the data generated. Although the conceptualisation of the two large-scale tests is very similar, there are certain major differences: the "mock-up" test has a clay barrier with an unlimited availability of hydration water, supplied at constant pressure; and has a steel structure (instead of the heterogeneous granite mass of the "in situ" test), installed in a room maintained at a practically constant temperature.

The clay barrier was constructed of highly compacted bentonite blocks. The total bentonite mass installed was 22.5 t.

The test is being performed at the CIEMAT facilities (Madrid), in a building constructed for this purpose.

The heating and hydration (operational) stage commenced in February 1997, and was planned to last about three years. According to new plans (Chapter 1), the operational stage has been prolonged for several years, as has been the FEBEX Project. In fact the test still continues with the EC Integrated Project NF-PRO. The test is functioning automatically, regulated by the heater control system (HCS), and produces information from approximately 500 installed sensors. The information is being stored and managed by the data acquisition system (DAS).

At the end of the operational stage, it is planned to proceed to the dismantling stage – extraction, inspection, sampling, and study of all the installed materials. The aim is to use the results from the dismantling stage to gain insight into the final state of the instruments, the intensity of the corrosion induced in the metals and, especially, the geochemical modifications produced in the bentonite.

A summary description of the design, fabrication, and installation of the physical components of the test is presented in this chapter. It also includes a summary of the operational stage of the test, from the begining up to now (more than seven years). CIEMAT performed all the work, and the detailed description is in references [21] and [22].

3.2. Components of the test

The test is installed in an annex, constructed exclusively for this purpose, to Building 19 at the CIEMAT facilities in Madrid, Spain. The building is air-conditioned, such that the temperature is maintained almost constant (20±2°C).

The infrastructure of the test consists of five basic units, represented in Figure 3.1: the confining structure with its hydration system, heating system, clay barrier, instrumentation, and systems for data acquisition (DAS) and heating control (HCS).

Specimens of different metals were installed in the clay barrier to complement the study of the corrosion affecting the metallic components of the system (heaters and sensors). In addition, artificial chemical tracers were installed to facilitate understanding of the geochemical processes of the water/bentonite interaction and of mass transport.

3.2.1. Confining structure and hydration system

3.2.1.1 Confining structure

The structure that encloses the clay barrier is a cylinder of carbon steel with an interior cladding of stainless steel. It consists of two cylindrical bodies joined by a central flange and closed by two metallic end covers, of the same materials. The confining structure is supported by three metallic legs.

The main characteristics of the confining structure are as follows:

- ❑ Inner diameter: 1.615 m
- ❑ Inner length: 6.00 m

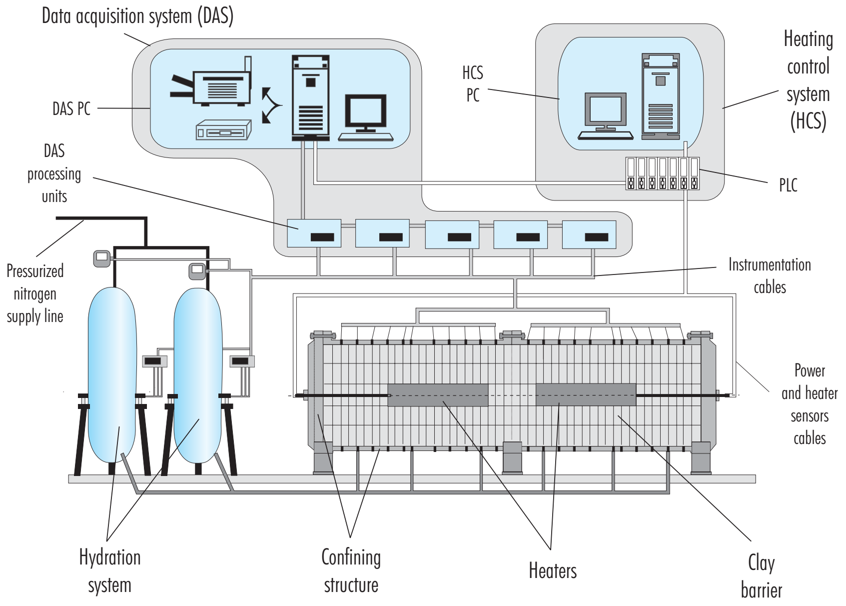

Figure 3.1: General scheme of the "mock-up" test.

- ❑ Wall thickness: 0.070/0.005 m of carbon/ stainless steel
- ❑ Design pressure: 9 MPa
- ❑ Total empty mass (estimated): 30 000 kg

Each end cover is fitted with a penetration for the power and temperature sensor cables from the heaters. The cylindrical surface of the confining structure is perforated at 234 points: 48 for water injection and 186 for the exit of sensor cables.

The materials used were received with their corresponding quality certificates.

CIEMAT performed the inspections and tests considered necessary to monitor and control the materials and construction techniques used. The most significant examinations were by X-rays and penetrant liquids, the acceptance of an inspection point program (IPP) and the performance of two hydraulic tests, one structural in character and the other to detect leaks (performed with water under pressure, up to 112 bars).

3.2.1.2. Hydration system

This system supplies water for hydration of the bentonite mass at a constant and controlled pressure.

The system consists of two tanks with a total capacity of approximately 1.3 m^3, under pressure from the top nitrogen supply line, with water supplied via a network of pipes joined to the 48 water injection nozzles in the confining structure.

Each one of the tanks is supported on three metallic legs, which are the bases of the weighing system used to measure the mass of water injected. The tanks are located as close as possible to the confining structure, in order to reduce the dead volume of the system (Figure 3.1).

The basic elements of the system are as follows:

- ❑ Nitrogen line under 4.0 MPa pressure
- ❑ Two tanks, under pressure, each with the following characteristics:
  - ➪ Material: Stainless steel
  - ➪ Height: 3.0 m
  - ➪ Diameter: 0.8 m
  - ➪ Wall thickness: 0.012 m
  - ➪ Working pressure: 3.5 MPa
  - ➪ Internal volume (estimated): 0.660 m^3
  - ➪ Total empty mass (estimated): 550 kg

- Weighing system for measurements
- Network of pipes to the confining structure
- Filters and geotextile for the protection of the water injection points (nozzles) and geotextile lining of the interior surface of the confining structure. The purpose of the geotextile lining is to homogenise the water supply around the periphery of the clay barrier.

The parts of the system in contact with the water are of stainless steel, AISI 304L.

The materials were supplied with their corresponding quality certificates.

The hydration tanks have been subjected to a hydraulic test at 1.5 times the rated design pressure (4.0 MPa) and 100% of the welds have been examined.

Connection to the confining structure

The connection between the hydration system and the confining structure is made by means of 48 injection points distributed in six sections, each section with eight injection nozzles distributed at 45° and connected to a pipe ring. To avoid clogging by the clay, the injection nozzles are protected by two filters of stainless steel, one stainless steel mesh disk, and one geotextile disk.

The internal surface of the confining structure is covered with four layers of geotextile to facilitate the homogeneous hydration of the clay barrier. The properties of compressibility and permeability of the geotextile have been verified by laboratory tests.

Type of water

For hydration, a commercial granitic water is being used, due to the ease of supplying the necessary quantity of chemically stable water throughout the entire test period. Furthermore, this is the water that has been used in the laboratory tests in recent years and its composition is known and stable.

Iodine and deuterium were added to the water as tracers; Table 3.1 shows the composition of the resulting water. It has a pH of 8.1 and an electrical conductivity of 278 µS/cm.

Monitoring and control of the hydration water supply

Load cells and pressure sensors control the mass and injection pressure of the water supplied to the confining structure. The values obtained are sent directly to the data acquisition system (DAS).

The mass of water introduced into the system is measured by continuously weighing the hydration tanks. The weighing system for each tank is made up of the following elements:

- Three flexural load cells HBM Z6FC3/500 (500 kg, connected to 6 wires, 2 mV/V, precision C3, protection IP67), with assembly modulus K-Z6/MS550KG (anti-spin, anti-overturning, and overload protection).
- Shunt connection box HBM VKK2, to add the three load cells.
- Measurement amplifier/indicator HBM MVD2510 (0.1% precision) with analogue output (from 0 to 10 VDC) directly connected to the DAS.

Each tank is suspended by three metallic lugs, located at 120°, on the tank body. These lugs are over the load cells, which are seated on the three legs (Figure 3.2).

Using the values from the weighing system and the nitrogen pressure of the hydration tanks, the injected water mass is determined and registered in the DAS.

The injection pressure at the exit of the tanks and the pressures at the hydration surface in each half of

Table 3.1
Composition of the hydration water, in mg/l

Element	Ca^{2+}	Mg^{2+}	Na^{+}	K^{+}	Cl^{-}	I^{-}	HCO_3^{-}	NO_3^{-}	SO_4^{2-}
Concentration	38	9.4	14	1.3	15	2.1	152	5.0	15
Element	SiO_2	Ba	Cd	Mn	Ni	Pb	Sr	Zn	Al
Concentration	21.8	0.05	0.05	0.05	0.04	0.07	0.09	0.12	0.09

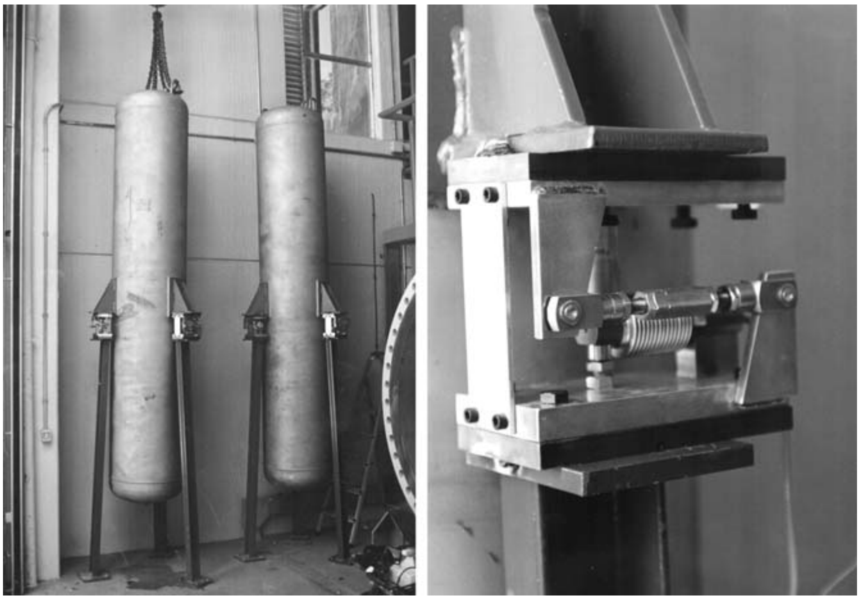

Figure 3.2: Hydration tanks. Details of weighing system.

the confining structure are continuously logged. The measured values are registered directly by the DAS. The measuring system is composed of the following elements:

- ❑ Digital manometer HBM Digibar 300 (20 bar) on the exit line from the tanks.
- ❑ Two transmitters DRUCK PCX1400 (20 bar, 4-20 mA) installed in two orifices of the cable exits, one in each half of the confining structure.

3.2.1.3. Quality assurance/quality control

The design of the confining structure and hydration system was developed by CIEMAT. The confining structure was constructed by Talleres VICALDE, Llodio (Álava, Spain). The hydration tanks were manufactured by TAM, S.A., Madrid (Spain) and the nitrogen line and connections between the tanks and the confining structure were made by DTA, S.L., Madrid (Spain).

The following activities were carried out in accordance with the quality assurance program applied: issuing of the IPP and performance of inspections during manufacturing; drafting of the quality report on the confining structure; obtaining certification from the Ministry of Industry for the hydration tanks and performance of the hydraulic and leakage tests for both systems.

3.2.2. Clay barrier blocks

The clay barrier was constructed with highly compacted bentonite blocks. The same bentonite was used throughout the FEBEX project, its properties having been described in Chapter 2. Section 3.3.3 describes the construction of the barrier.

Reference [6] describes in detail the processing of the bentonite into blocks.

3.2.2.1. Design

Figure 3.3 shows the geometry of the barrier in two representative sections, one in the heater area and the other in the non-heater area. This geometry is made with four types of blocks: A, B, C, and E. Figure 3.4 and Table 3.2 show the shapes and dimensions of these different blocks.

The dry density specified for the design of the blocks is 1.77 g/cm^3. This density is based on considering the anticipated volume of construction gaps and a final dry density of the clay barrier of 1.65 g/cm^3. This final dry density value corresponds to the design criterion of the AGP Granito. The water content of the blocks is that specified for the raw bentonite, from 12.5% to 15.5%.

3.2.2.2. Fabrication

Moulds were designed and manufactured for fabrication of the block types A and B. Some of the B-type blocks were machined to have a plane inner face, thus forming C-type blocks. The B mould was then modified (protrusions were removed) to obtain intermediate blocks (D-type), which were subsequently machined to obtain E-type blocks.

A single-acting, uniaxial hydraulic press was used to fabricate the blocks, the compaction force being provided by three successive strokes of 40 MPa to 50 MPa pressure. Both fabrication of the moulds and compaction of the blocks were performed by Jesús Castro, S.L., Torrejón de Ardoz (Madrid, Spain).

The quality assurance program was applied to the fabrication process: in each block the weight, dimensions, external appearance, dry density and water content were controlled.

Table 3.3 shows the average values of the characteristics of the different types of blocks.

In total, 25870 kg of bentonite were compacted to manufacture 1012 blocks. The average weighted values for water content and dry density were 13.6% and 1.77 g/cm^3, respectively.

3.2.2.3.. Packaging, transporting, handling, and storing

Laboratory tests indicated that the blocks deteriorate rather quickly when exposed to a high humidity en-

Table 3.2
Construction dimensions of the blocks

Block	Radius mm					Angle degrees	Dimension mm			Thickness mm
	R	r	e	r_1	r_2		a	b	c	
A	795	480	645	26	25	30	$411^{\pm 2}$	$248^{\pm 2}$	$315^{\pm 2}$	$124^{\pm 1}$
B	475	170	325	26	25	60	$475^{\pm 2}$	$170^{\pm 2}$	$305^{\pm 2}$	$124^{\pm 1}$
C	475		645	26	25	60	$473^{\pm 2}$	$250^{\pm 2}$	$225^{\pm 2}$	$124^{\pm 1}$
D						60	$450^{\pm 2}$	$225^{\pm 2}$	$225^{\pm 2}$	$124^{\pm 1}$

Table 3.3
Average values of the physical properties and number of blocks fabricated

	Type of block		
	A	B+C	D(E)
Weight per block (kg)	25.8	25.2	25.3 (D)
Average water content (%)	14.2	13.2	13.1
Dry density (g/cm^3)	1.77	1.76	1.82
Number of fabricated units	598	322	92
Total weight (kg)	15428	8114	2328

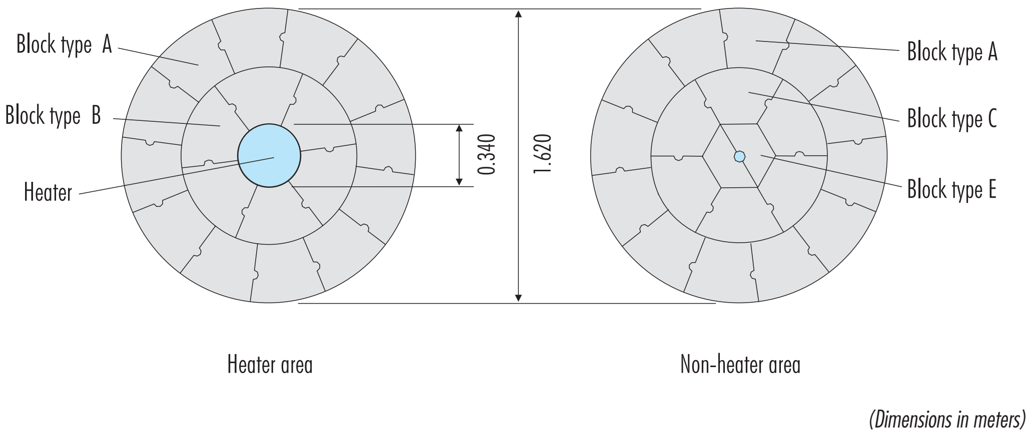

Figure 3.3: Geometry of the barrier.

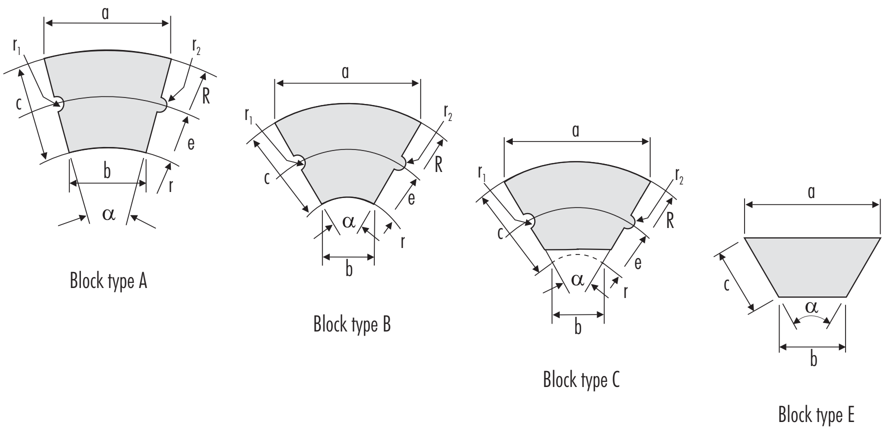

Figure 3.4: Shapes and dimensions of the blocks.

vironment. Consequently, the blocks were protected with plastic sheets, then packed in wooden boxes until used.

The temperature and relative humidity in the interior of the confining structure were controlled during construction. No major variations in the average ambient conditions (temperature of 20°C and relative humidity of 60%) were observed.

There was no deterioration of the blocks produced by excessive dampness; some were rejected due to damage during handling. The percentage of rejected blocks during machining and installation was less than the expected 10%.

3.2.3. Heating system

The system consists of two cylindrical heaters and corresponding monitoring and control systems. Each heater has three internal electrical heating elements (resistors), capable of individually supplying the thermal power necessary to maintain a temperature of 100°C at the heater/bentonite interface, in accordance with the AGP Granito requirements.

The criterion of heater operation is that a constant superficial temperature (a relatively simple control) is to be maintained, but with the possibility of providing for constant power operation.

3.2.3.1. Heaters

General characteristics

The basic premises used in designing the heaters were that there would be no possibility of performing repairs/replacements after installation and that the maximum temperature at the heater/bentonite contact must be 100°C, distributed as homogeneously as possible.

In this test, the heaters are in direct contact with the bentonite, with a 0.75-m horizontal separation between them. The electrical heating elements were selected on the basis of the following criteria: efficiency, homogeneous distribution of the heat, power density, cost of installation, lifetime of the elements, and safety aspects.

The external dimensions of the heaters (1.625 m long and 0.34 m in diameter) were selected taking into account the thickness of the bentonite blocks (0.125 m) and the relation between the area of the cylindrical surface and the area of the surface of a reference waste canister (4.54 m long and 0.90 m in diameter).

The maximum power to be supplied was set at 900 W per heater, based on different analyses and modelling exercises performed during the design phase of the test. This level of power will maintain the specified temperature in the heater even during the most unfavourable condition of the bentonite that is being saturated.

Mechanical characteristics

The design calculations considered the maximum pressure on the heaters to be 9 MPa, with a maximum difference in temperature of 20°C to be allowed between two points of the heater (for thermal stress).

Each heater consists of a carbon steel core (reel), with a wall thickness of 0.012 m and an outer diameter of 0.3 m, into which the resistors are inserted. A carbon steel casing (0.02 m thick and 0.34 m in external diameter), closed with two end covers (welded at the back end and fixed by screws at the front end), protects the set (reel and resistors).

The principal characteristics of each heater are as follows:

- ❑ External diameter: 0.34 m
- ❑ Length: 1.625 m
- ❑ Material: Carbon Steel
- ❑ Wall thickness: 0.04 m (interior of the core to the exterior of sheet casing) and 0.06 m (end covers)
- ❑ Working pressure: 9.0 MPa
- ❑ Elements: Metal casing and end covers, reel, 3 heating elements (max. 930 W/unit), and 9 temperature control points
- ❑ Nominal maximum power: 2800 W
- ❑ Total empty mass (estimated): 475 kg

The sealing of the exterior casing was accomplished using Viton O-rings and epoxy.

Electrical characteristics

The heating elements selected are shielded resistors, THERMOCOAX ZEZ Ac 25/600-2600-600/2 CM 25 (2.5 mm ∅, resistance 2.0 Ω/m, 220 VAC/50 Hz). The total length of the elements is 38 m (6 m of cold ends and 26 m of hot zone). They are protected by a stainless steel sheath, AISI 304L, with external connections of CM25 type (150 W/m, to 200 °C).

The heating core is composed of Ni/Cr 80/20 and the cold zones of Cu/Zr. The maximum working temperature in the hot zone is 600 °C. The core is insulated from the sheath by MgO powder, which increases dielectric resistance, heat transfer and the lifetime of the element.

To ensure a high probability of power being supplied throughout the entire test, each heater has three resistors, each having the capacity to supply the nominal power required. The resistors of each heater are controlled as a set. In the event of failure of one, the remaining resistors supply the equivalent power. Full safety elements for protection of the personnel and minimisation of the possibility of danger to the equipment were installed.

The electrical supply to the heaters is insulated from the general network by grounded insulating transformers.

Machining

The following aspects of the machining of the heaters should be highlighted:

Reel and casing: special attention has been given to the tolerance between the reel and the casing, to obtain an optimum fit.

Resistor location: three semicircular channels or grooves measuring 3 mm in width and depth run along the reel in a helical path, with a total length of 25 m.

Power control temperature sensor locations: perforations were made in both the reel and the casing; the former measure 10 mm in diameter, while those in the casing are threaded M12. The sensors are distributed in three sections: one in the central area and another section near the end where the cables exit (front end cover), each of which have four locations distributed at 90°. The section at the other end has only one location.

Assembly

Assembly was performed carefully in a sequential process, since the resistors are particularly fragile. At each step, the functioning of the assembled components was verified:

Reel winding: the three resistors in each heater are wound helicoidally in the grooves machined on the reel of the heater, with a separation of 18.66 mm between centres and with a total of 27 turns per element. The separation between spirals on any one element is 56 mm. This should give a uniform thermal power distribution along the hot zone of the heater. Loctite Output, an adhesive of high thermal conductivity used in electronics, was then applied to the resistors with light pressure until they adhered to the reel.

Encasing: the insertion of the reel into the casing was accomplished with the help of an anti-corrosion grease (Loctite 7671 anti-seize), applied on the reel to make sliding easier and to ensure a good thermal contact between the two parts.

Installation of the temperature sensors: the power control temperature sensors were installed in locations machined in the reel and in the casing, inserted in specifically designed screws. Once the perforations of the casing and reel were correctly aligned, the screws were installed from the exterior of the casing.

Power supply and sensor cable penetration through the front end cover: following installation of all the sensors, the ends of the resistors and temperature sensor signal cables, each appropriately identified, were passed through a protective pipe exiting the heater. The length of the cold ends of the heating elements is sufficient to exit the casing of the heater, pass through the protection pipe and reach the junction box to the control unit located outside the confining structure.

Heater closure: after the cables were passed through the pipe, the front-end cover was affixed. The sealing of the front-end cover was obtained by closing it with a special Viton O-ring and a triangular washer for each of the joining screws.

3.2.3.2. Heater monitoring and control systems (HCS)

The HCS consists of all the electrical and/or electronic components and computer programs for autonomous supervision of the operation and control of the power supply to the heaters, data acquisition (including sending the measurements of the parameters to the DAS) and activation of the processes and alarms in the event of failure of any of the components (heater resistor, electronics, etc.).

The system is based on a closed loop control with a Programmable Logic Control (PLC) that manages the assembly and regulates the power supply by means of a triac breaker and associated electronics. The triac shot is made to coincide with the passage of the wave through zero, so as to avoid fatigue in the resistors. The three resistors of each heater are controlled as a set.

The control parameter for the heating is either the temperature or the supplied power. In the event of failure of any of the heating elements, the control system compensates by using the rest of the heating elements. The nine sensors installed in each heater allow the internal temperature distributions to be observed.

Main elements of the heater control system

The HCS is composed of the following subsystems:

- ❑ Programmable Logic Control (PLC)

  The PLC receives the setpoint values from the test control and switches to operation in an autonomous mode, transforming the nominal control parameters to the power supplied to the heater during automatic operation.

  The PLC measures the temperatures in each heater (at nine points) and controls the average temperature value at the four points in the central section, such that it is equal to the setpoint value. The control program makes the calculations, regulates the power by the auxiliary electronics and sends the temperature and instantaneous power data as demanded by the DAS.

- ❑ Temperature sensors

  These sensors are included to provide the temperature from the area closest to the heater/bentonite interface to the heater element control. The assembly has been described above. The sealing of the body, where the sensors are inserted, is by means of a high-temperature resistant anaerobic retainer/sealer.

- ❑ Electronic power regulation system

  This system is designed to control the electrical power supplied to the resistors by a redundant system. The control parameters may be a programmed value of temperature or of power.

  The PLC controls the triac, which acts as an interrupter, via the associated power electronics, regulating conduction time and, consequently, the power supplied to the heater. Conduction time regulation is accomplished by packages of complete cycles, with triggering occurring when the triac passes through zero, followed by a waiting period prior to sending of the next package; this arrangement reduces the number of coupling/uncoupling cycles and prolongs the life of the resistors.

- ❑ Heater protection system

  There is an alarm system designed to detect the possible failure of either of the heating elements or the critical elements of the power electronics. This is accomplished by detecting variations in the power consumption of any single element.

  In the event of failure of a resistor, the system activates the alarm and automatically compensates for the loss. In the event of triac failure, the system activates the alarm and a relay opening signal is sent, preventing overheating.

Control procedure

Any variations occurring in the heater power regime, changes in the control strategy, etc. must be transmitted to the PLC by secure programs, allowing access only by authorised persons.

In this test, two heater power regulation regimes have been applied:

- ❑ *Initial heating*. The aim in this phase was to reach the setpoint temperature in the shortest possible time. To simplify modelling, this initial heating was accomplished in constant power steps.
- ❑ *Constant temperature heating*. Once the temperature neared the setpoint temperature (100°C) at any point in the heater/bentonite interface, the regulation mode was switched to a constant temperature mode, implying continuous power regulation in response to system demands.

As has already been pointed out, all the heating elements are used simultaneously. This approach provides the advantage of not subjecting any of the resistors to excessive loads, which is important in view of the anticipated duration of the test and the guaranteed mean lifetime of these resistors. This approach also allows for an instantaneous increase in power without there being an excessive increase in temperature in each resistor.

3.2.3.3. Quality assurance

CIEMAT designed and constructed the heaters and also assembled the different elements. The heating elements were made by THERMOCOAX (France), a firm that provides the appropriate quality certificates. Installation of the temperature sensors in the special screws was performed by HERTEN, S.L. (Spain), with inspection by CIEMAT. The solid end covers of the heaters were welded by a specialist firm holding the required certifications.

The requirements of the project quality assurance program were applied and met: robust and redundant design, selection of suppliers, procurement and verification of materials, assembly and verification of components and performance of preliminary tests.

3.2.4. Instrumentation and data acquisition system (DAS)

In order to gain insight into the continuous evolution of the variables in the test, the components of the system (heaters, clay barrier, hydration system, confining structure, and enclosing building annex) were instrumented with the appropriate temperature, total pressure, fluid pressure, humidity, and deformation sensors. To acquire information on the geochemical processes, different tracers and metal specimens were installed.

The DAS visualises the set of sensors, performs data conversion and stores the data on a disk. This system is controlled by a SCADA program running on a personal computer. The system is autonomous and independent of the HCS.

3.2.4.1 Sensors

The working conditions (pressure ≥ 5 MPa, temperature up to 100°C, and harsh saline environment) made it advisable to select sensors without active electronic components. The same requirements have been established for the cables and their connections to the sensors. As a precautionary measure, the cable length is such that it is the minimum required to reach the processing units of the DAS located outside the confining structure.

Table 3.4 summarises the number and type of sensors, the parameters measured, and the area in which they are located. Even though 507 sensors or instruments were installed, there are 484 signals automatically registered, while another 19 signals, relating to deformation, are obtained manually. A further four values are obtained from the PLC calculations. Thus the final number of signals is 547, as there is the possibility of measuring humidity and temperature with the 40 relative humidity sensors.

These signals correspond to either the sensors installed in the interior of the confining structure (in the clay barrier or in the heaters) or to the external sensors and instruments.

The specific characteristics of the sensors are as follows:

- ❑ *Temperature:* thermo-resistance Pt100, Heraus, installed with four wires and measured with a limited current flow to avoid overheating the sensor. Installed in a sheath of Inconel or in special screws sealed with epoxy and connected to a silicone or Teflon cable, respectively.
- ❑ *Total pressure:* semiconductor strain gages, Kulite 0234, 50 bar SG range, 200% overpressure, range compensated for temperatures -20°/100°C. Constructed of AISI 316L steel with Teflon cable and high pressure cable gland.
- ❑ *Fluid pressure:* semiconductor strain gages, Kulite HKM375, 50 bar SG range, 200% overpressure, range compensated for temperatures -20°/100°C. Constructed of AISI 316L steel with Teflon cable and high pressure cable gland. Outer protection of AISI 316L with filter.
- ❑ *Relative humidity:* temperature and RH transmitter, Vaisala HPM233, with capacitive sensor HUMICAP (0 to 100% RH range) and temperature sensor Pt100 1/3 (to 120°C). Constructed in ABS plastic with AISI 316L filter and Teflon cable. Outer protection of AISI 316L steel and epoxy.
- ❑ *Exterior strain gages:* strain gages, HBM; 350 Ω impedance, length of 6 mm, 12 DC volt excitation. Located at 90° and in a ½ bridge configuration. Protected by a sheet of PVC and aluminium.

The instrumentation associated with the hydration and heater control systems has been described above.

3.2.4.2. Sensor distribution

The test has been divided into two zones, one including Heater A (Zone A) and the other Heater B (Zone B). The sensors in the clay barrier have been grouped into 25 sections—12 in each lateral zone, and one section AB, which coincides with the central vertical plane. The lateral instrumented section is called Ann or Bnn, depending on the zone (A or B) and on the distance from the central vertical plane, where nn is the ordinal number of the placement.

Figure 3.5 shows the distribution of the instrumented sections, with the two zones shown on the appropriate sides of the central plane.

Other sensors have been installed in the confining structure and in the exterior auxiliary systems (such as the temperature probes and the strain gages on the structure), as well as in the hydration and heater control systems (registering the injected water pressure and mass, as well as the heater temperatures).

Table 3.4
Installed instrumentation

Parameter	Type of sensor or instrument	Area			Total
		Bentonite	CS*	Exterior	
Temperature	RTD Pt100	328	20		348
Room temperature	RTD Pt100			1	1
Injection pressure					
manometer	DIGIBAR II			1	1
water pressure	DRUCK 1400PTX		2		2
Mass of hydration tanks	MVD 2510				
Total pressure					50
radial	KULITE BG0234	14			
tangential	KULITE BG0234	14			
axial	KULITE BG0234	22			
Fluid pressure	KULITE HKM375	20			20
RH + temperature	VAISALA HMP233	40			40
Deformation (strain gages)	HBM		19		19
PLC values					
temperature	RTD Pt100			18	18
average temperature	calculated			2	2
power	calculated			2	2
DC voltage				2	2
Totals		438	41	28	507

**CS is the confining structure*
RH is relative humidity

3.2.4.3. Sensor coding

Cylindrical coordinates were selected to describe the distribution of the sensors within each instrumented section. In this coordinates system (R, θ, and Z), the point of origin O has been taken as the intersection of the central vertical plane AB with the longitudinal axis of the confining structure (axis Z). In accordance with the rules of this coordinates system, values of R increase from axis Z, values of θ increase from the reference radius (upper vertical radius of each section) and Z increases from the point of origin O to Zone B (Figure 3.6).

The entire sensor coding follows these general rules with a few exceptions. A distinction has been made between four main groups of sensors: in the clay barrier, in the heaters, on the surface of the confining structure, and outside the confining structure.

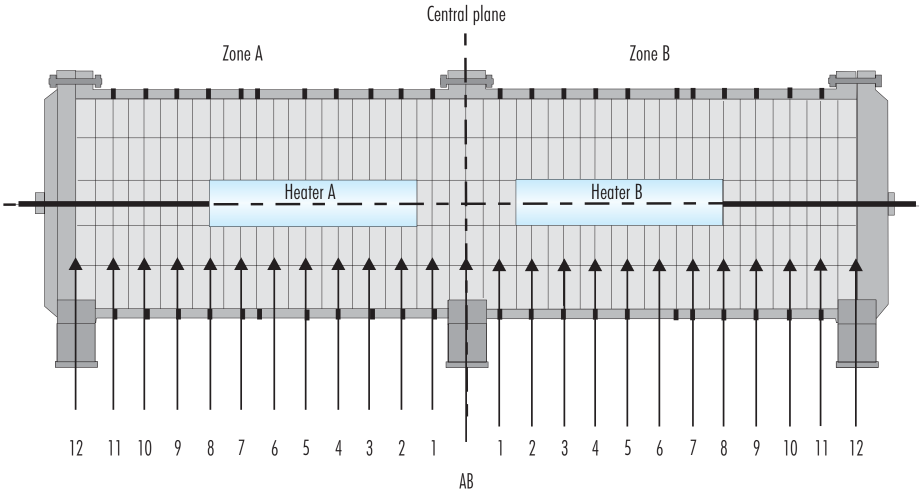

Figure 3.5: Distribution of instrumented sections.

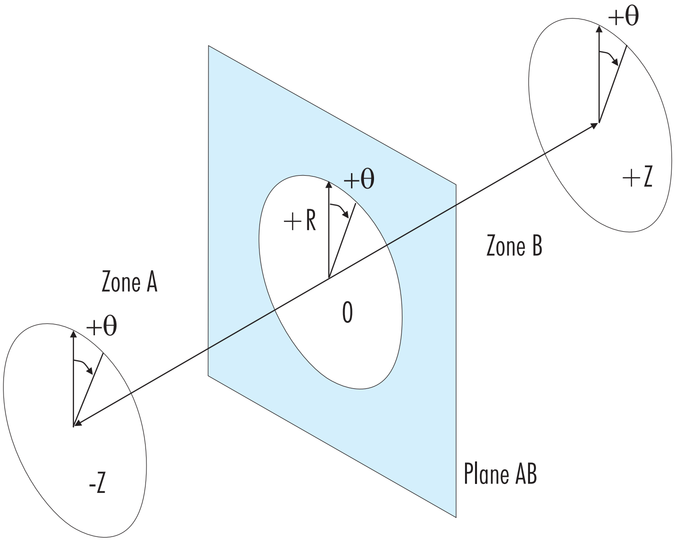

Figure 3.6: "Mock-up" test coordinate system.

Sensors in the clay barrier

The sensor coding used in the clay barrier is indicated below. Each installed sensor is identified by an alphanumeric code of the following type:

$$\alpha\alpha\_\beta\beta\_nn\_k\_l$$

$\alpha\alpha$: Sensor type – T (temperature), PR (total radial pressure), PT (total tangential pressure), PZ (total axial pressure), H (fluid pressure), and V (relative humidity and temperature).

$\beta\beta$: Designation of the location – A (Zone A), B (Zone B), and AB (central plane AB).

nn: Numbering of instrumented section as installed in each zone – from 1 to 12, increasing with distance from the central plane AB.

k: Numbering of the radial order within the corresponding instrumented section – from 1 to 4, increasing with increasing radius. In the distribution of the pressure sensors, as a special case, the maximum number is 3, corresponding to the different areas within the instrumented section: core (1), interior crown (2) and exterior crown (3).

l: Numbering of the angular order within the corresponding instrumented section – from 0 to 7, increasing with increasing angle. In the distribution of the pressure sensors, as a special case, the maximum number is 1 or 2.

Temperature sensors on the heaters

These sensors are located on the surface of the heater and are distributed in three sections located near the front-end cover (sensors numbered 1 to 4), in the control zone (sensors numbered 5 to 8) and in the solid end cover (sensor number 9). The sensors are distributed at 90° in each section, in a strip measuring less than 0.02 m in width. The control zone is in the central area of the heater and is used to provide the average temperature value used in calculating the power to be supplied to the heater.

These sensors do not follow the general coding rule; they are identified by the following alphanumeric code:

$$C\_PT\#\_\alpha$$

C_PT: Temperature point on the heater

#: Numbering of order of installation on the heater, from 1 to 9

α: Heater – Heater A (Zone A) or Heater B (Zone B)

Temperature sensors on the surface of the confining structure

Following initiation of the test, 20 temperature sensors were placed on the outer surface of the confining structure at locations associated with the position of the deformation measuring points.

These sensors do not follow the general coding rule, and are identified by the alphanumeric code.

$$T\_\alpha\_\#$$

T: Temperature

α: A or B corresponding to Zone A or Zone B

#: Numbering of order of installation, from 1 to 10

Sensors, instruments, and measurements outside the confining structure

These sensors include all those not dealt with above, such as for example those measuring room temperature, water pressure at the inner surface of the structure and the hydration system—injection pressure and weight of the tanks. The calculated values (injected volume of water, average control temperature and supplied power) are included in this group. A different coding system, not included here, is being used for these values.

3.2.4.4. Metallic specimens for corrosion study

Metallic specimens —carbon steel, stainless steel, titanium, copper, and welds of the same materials— were placed in the clay barrier to analyse their possible corrosion under conditions that may be considered close to those expected in a repository. The specimens were prepared by INASMET (San Sebastián, Spain) and were mounted on a Teflon rack.

3.2.4.5. Tracers

To obtain complementary information on the hydration in the clay barrier, on water/ bentonite interaction and on the transport processes, tracers were installed by various means: dissolved in the hydration water or placed in the bentonite within compacted clay plugs, porous metal capsules and impregnated filter paper. Both conservative and non-conservative tracers were used. The profiles of concentration and distribution of the tracers will be studied during dismantling. (Information on the tracers used, placement, location, etc. is given in Chapter 7.)

3.2.4.6. Data acquisition system (DAS)

The DAS includes all the electrical/electronic components, as well as the software necessary to autonomously supervise, register and store on a disk the set of data obtained from the test. It provides conversion of the analogue signals from the transducers into numerical data and performs data analysis, display and storage over the long time period (years) that the data are acquired.

The system is expected to acquire, adapt, display and register all the data generated by the installed instrumentation in real time; to cause the test to function automatically, without full-time personnel; and to generate a master database of the test.

This is a commercial system based on processing units connected one to the next by means of a high velocity RS-422 serial link, and with a PC by an RS-232C serial link. Each processing unit has its own analogue/digital converter and controls the nearest signals.

DAS elements

The DAS is composed of the following main elements:

- ❑ Processing units of the DAS

  These consist of a FLUKE extended system consisting of five HELIOS I processing stations (a master, Model 2289, and four slaves, model 2281). The system (Figures 3.7 and 3.8), has the following characteristics:

  - ➪ 18-bit analogue/digital converter,
  - ➪ 140 channels for measuring DC voltage, and
  - ➪ 400 channels for measuring thermoresistances.

  The stations have a microprocessor with both RAM and ROM memory, providing local intelligence. This intelligence increases the capability and facilitates the control function of the PC.

- ❑ DAS personal computer (DAS PC)

  The central control of the DAS consists of a PC. There is an identical PC on stand-by for possible failures, duplicating the equipment and program configurations. In the stand-by PC the database is periodically reproduced, as is indicated in the following section.

  The DAS PC is connected simultaneously with the main processing unit of the DAS and with the PLC of the HCS (Figure 3.9) to obtain and register information from the heater. An uninterrupted power supply (UPS) is used to guarantee the stability of the electricity supply and to secure the data against power surges or failures.

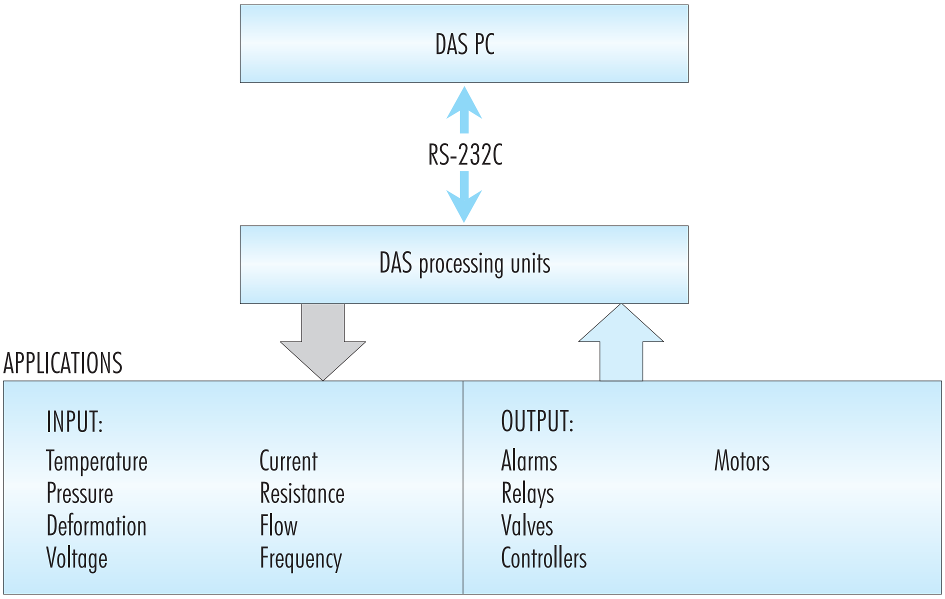

Figure 3.7: Structure of DAS processing units: interface application – Control PC.

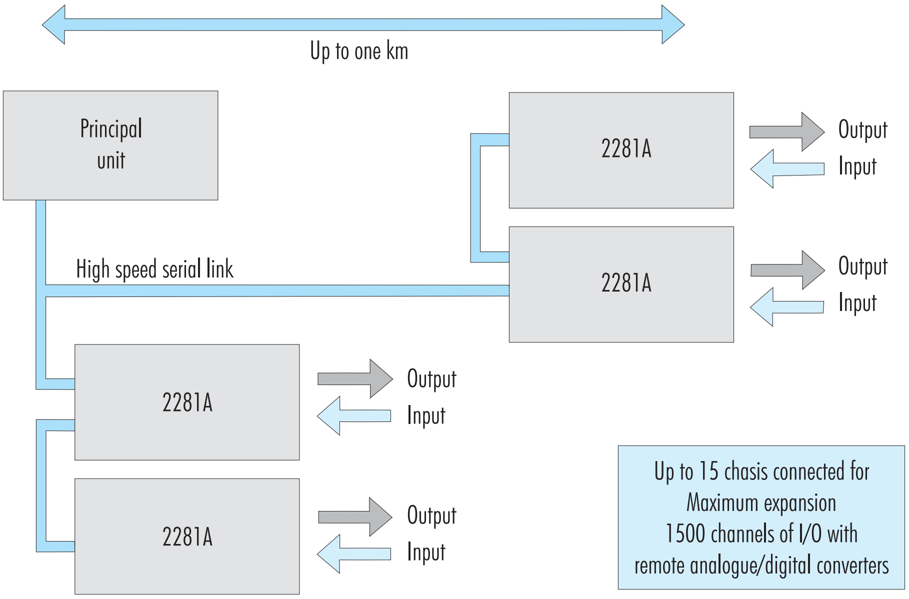

Figure 3.8: DAS structure: general system configuration.

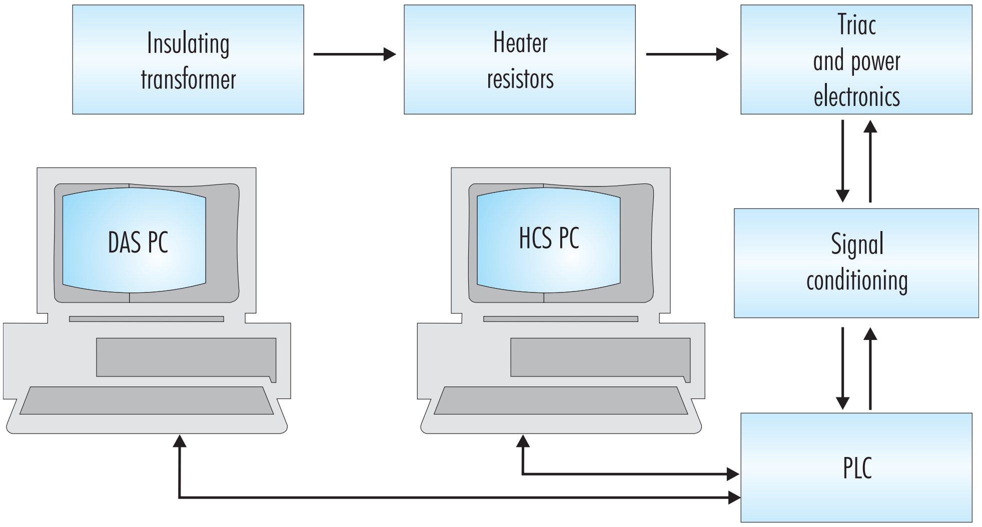

Figure 3.9: General schematic diagram of the heater control system (HCS).

The DAS PC functions independently, although periodically it is connected to a local network to allow for maintenance and file transfer operations.

- ❑ Signal conditioning, surge protection and/or electricity supply systems

The basic data acquisition system accepts inputs/outputs (I/O) in standard format (stress, current, thermoresistances) and is connected directly to the DAS PC by a special serial link. Some sensors require specifically adapted signal conditioning subsystems.

The electrical protection of the instrumentation against supply line surges is obtained by means of a UPS. Furthermore, each piece of signal conditioning equipment has an adequate protection against surges: each of the metallic elements is connected to its own ground line.

The UPS used is the COMET 511 5 kVA by MERLIN-GERIN. This equipment functions in accordance with an "in line" scheme; i.e., the output voltage is filtered and isolated from that of the input and has batteries as a buffer. This approach reduces disturbances of the network to a minimum. The UPS has been designed to operate under normal conditions at 10% of its nominal power, and has a set of auxiliary batteries to maintain autonomy for approximately two hours in the event of power failure.

- ❑ Communication system

Data transfer between the DAS computer, the DAS processing units and the HCS is accomplished via two conventional RS-232C serial links. The communication between the DAS PC and the HCS transmits the control values. The communication between the different processing units of the DAS is accomplished by a special high-speed RS-422 serial link.

The HCS PLC has another serial port connected to another PC (for control of the heaters), which displays the alarms and other parameters of the PLC that are not transmitted to the DAS. This PC is equipped with software for the transmission of instructions directly to the PLC, as well as of a new work program for autonomous operation.

A generic file transfer protocol (FTP) is used for the transmission of data between the DAS PC and other computers, for subsequent processing.

- ❑ Software

Monitoring and control are performed by a generic commercial client-server system SCADA (Supervision, Control, And Data Acquisition) called FIX DMACS by INTELLUTION, Inc. (USA). In addition, the FIX DMACS also performs the following functions to provide all the data:

Test supervision and display

The graphical characteristics of FIX DMACS allow for the creation of personalised screens to display the test parameters and to supervise the test. These screens may be reproduced to document the processes, and other information such as parameters in real time, alarm summaries, histograms, and other graphics may be included on them. Figures 3.10 and 3.11 show two examples of these screens.

Data storage and report generation

The data are stored in files generated by SCADA, gathering data obtained over four hours (six files per day) with a minimum frequency of 30 minutes (SCADA does not permit readings to be stored for a longer period of time). The program has its own internal database that is periodically reproduced in identical form in the stand-by computer.

The characteristics of FIX DMACS allow for the multiple activities of processing, transmitting, and backing up of historic data without destroying either the data log or the alarm management in progress.

The historic files allow for the logging, storage and display of process data and analysis of the relationships between variables. The stored data are distributed as periodic reports for the study of processes.

The transferred data are treated with the MICROSOFT EXCEL 5.0 program.

- ❑ Communications

Specific protocols have been developed for communication between the DAS PC, the main station of the DAS and the PLC of the HCS.

3.2.4.7. Quality assurance and quality control

CIEMAT installed the instrumentation and the DAS.

The processing units are from the firm FLUKE (USA), which holds the pertinent quality certificates. The manufacturer of the DAS supplied the characteristics certifi-

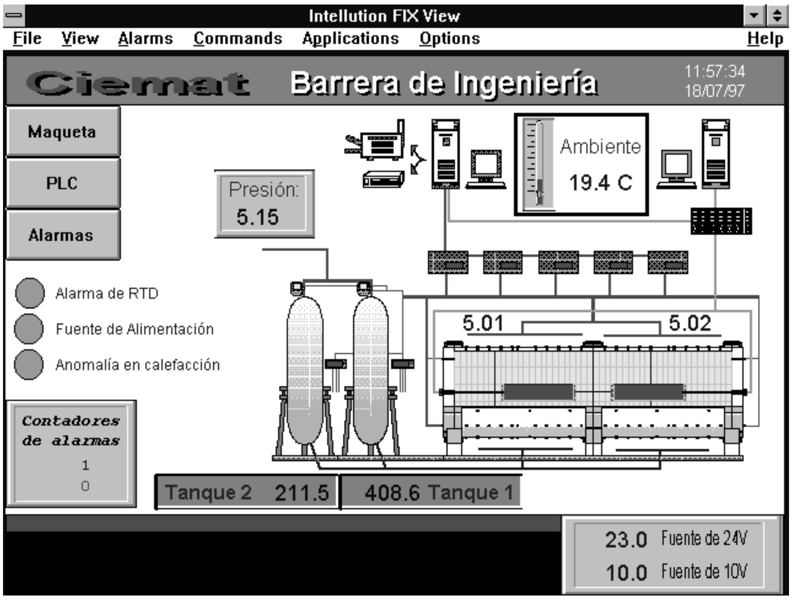

11:57:34
18/07/97

Presión: 5.15

Ambiente 19.4 C

Alarma de RTD
Fuente de Alimentación
Anomalía en calefacción

Contadores de alarmas
1
0

5.01 5.02

Tanque 2 211.5
408.6 Tanque 1

23.0 Fuente de 24V
10.0 Fuente de 10V

Figure 3.10: Example of test control screen: data and accessible elements.

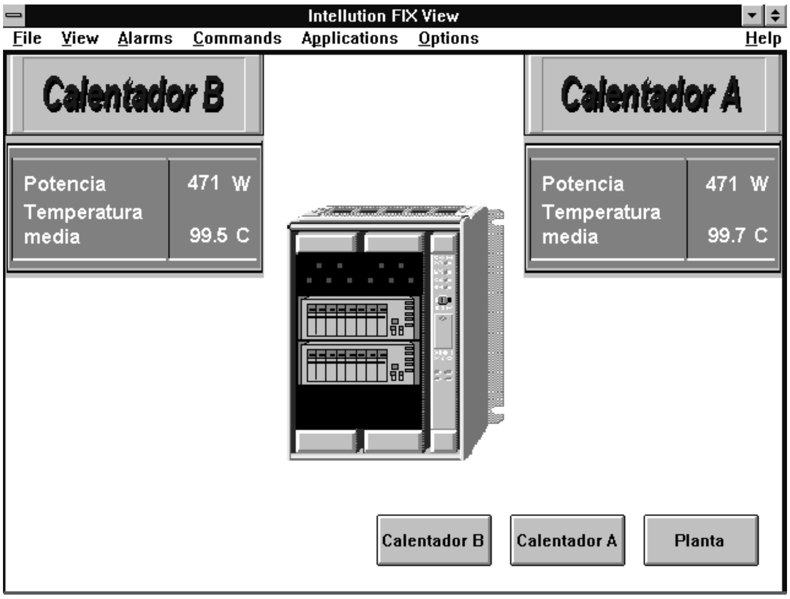

Calentador B	
Potencia	471 W
Temperatura media	99.5 C

Calentador A	
Potencia	471 W
Temperatura media	99.7 C

Figure 3.11: Example of screen showing data and accessible elements of heaters.

cate, guaranteeing that the equipment meets the specifications. Annual verifications are anticipated.

Verification or calibration certificates were provided for the sensors. The protections for the temperature sensors were installed by HERTEN, S. L. and inspected by CIEMAT.

No systematic calibration of the equipment was performed, but the majority were received with calibration certificates from the manufacturer or the supplier.

Each sensor was inspected on reception. At least one point of measurement was checked in the laboratory and immediately after each sensor was connected to the DAS. If any problem was detected, another sensor was installed in its place. The connection between each cable and sensor was checked in the laboratory during verification of the sensor, or in a specific test.

The quality control criteria and procedures approved for the project have been applied and the required documents have been issued.

3.3. Test installation

3.3.1. Building and infrastructure

The infrastructure and general services were installed during the construction of the building annex, which was designed especially for the test. A foundation plate of special characteristics was constructed, this having the capacity to support the forces induced by the total mass of the "mock-up" test, approximately 60 t. Three metallic supporting legs, which were levelled prior to the placement of the confining structure, were seated on the foundation plate.

3.3.2. Confining structure

This section describes the operations performed before the installation of the clay barrier.

3.3.2.1. Transportation and installation

The two parts forming the confining structure were assembled and then transported by road to CIEMAT. The positioning of the structure on the three supporting legs was accomplished by means of a 35-t crane (Figure 3.12). The positioning operation was carried out before the annex building front end was completed, due to the size and difficulty in handling the confining structure.

3.3.2.2. Cleaning

In accordance with the IPP, and in view of the condition of the confining structure on delivery (it was subjected to welding finishing, pressure and leakage tests), cleaning of the structure was performed after it was installed.

During the cleaning process, detergents and water under pressure were used to eliminate all residues of adhering liquids, greases, and solids, especially on the inner surface and in the perforations. After cleaning, the structure was protected with plastic sheets until installation of the internal components began.

3.3.2.3. Connection of hydration system and leak testing

After the external elements of the hydration system were connected to the confining structure, at the injection nozzles, leakage testing of the system was performed with nitrogen under pressure, up to 35 kg/cm^2. By increasing the pressure (to 38 kg/cm^2), the discharge of the safety valves was also verified.

3.3.2.4. Nozzle cleaning

The 48 injection nozzles were cleaned by blowing nitrogen under high pressure, using the same nitrogen as for the leakage tests.

Following this, the tanks were filled with water and then emptied, under pressure, through the nozzles. This filling allowed the total capacity of the system (660 litres each tank) to be checked, along with the response of the load cells used to control the mass of water injected.

3.3.2.5. Positioning of the filter system

To protect the hydration nozzles from possible plugging by the bentonite as it swells, four layers of filter disks were placed over each nozzle: two filters (6.25 mm ∅ stainless steel with equivalent pores of 100 and 60 microns, respectively); covered by a 20 mm ∅ stainless steel disk, of mesh 100; and finally, by another disk, 25 mm ∅, of the same geotextile used to line the interior of the confining structure.

3.3.2.6. Hydration surface

The last item in the preparation of the confining structure was the lining of its interior with geotextile. The geotextile is to homogenise the hydration of the clay barrier.

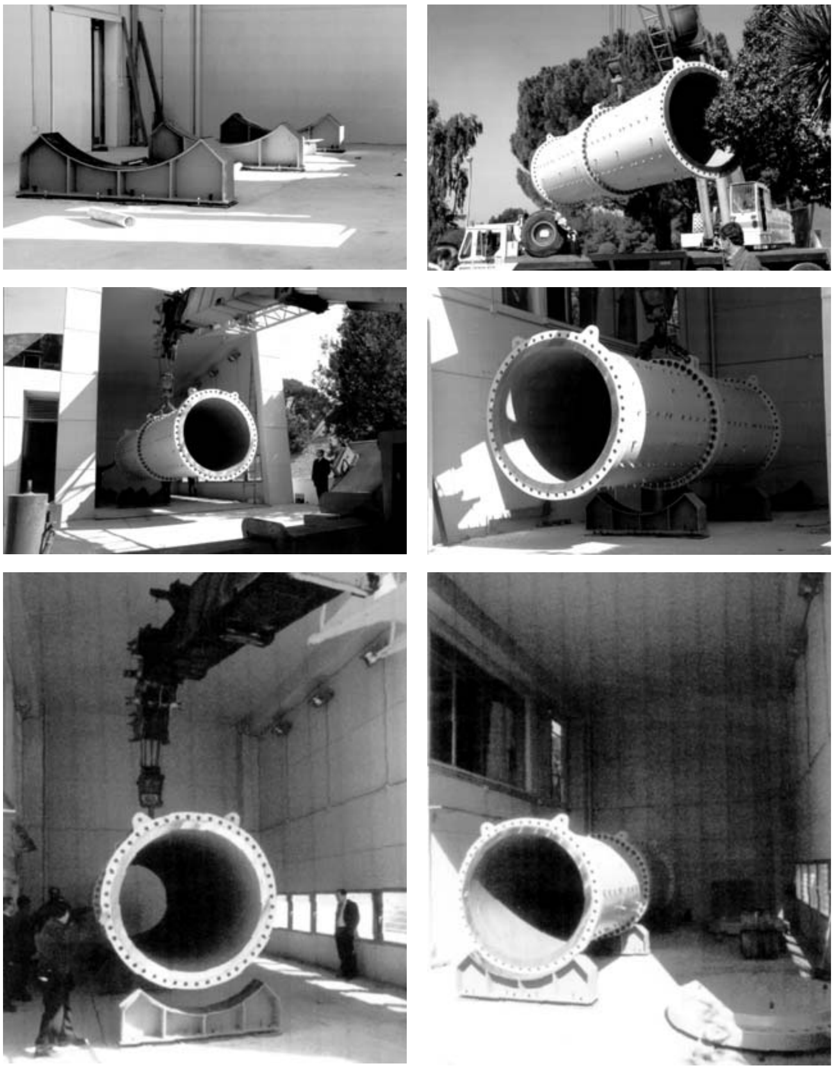

Figure 3.12: Installation of confining structure.

The geotextile lining of the inner cylindrical surface of the confining structure has a thickness of some 6 mm and is composed of four overlapping, alternating layers designed to avoid both the formation of preferential paths for the water and for the exit of the bentonite.

During installation, supports were used to maintain the cylindrical configuration of the geotextile lining and its contact with the inner surface of the confining structure. Special care was taken to avoid contamination of the geotextile during installation, a protective cover being used in all cases and progressively removed as the process advanced.

The geotextile had perforations made with a sawtooth bit (30 mm ⌀) matching those (same location) in the confining structure. These perforations have served as a guide for the correct location of each slice of bentonite blocks, allowing alignment to be controlled, with awareness and correction of any possible deviations during the installation of the clay barrier.

3.3.3. Installation of clay barrier

3.3.3.1 Preliminary trials

Before starting the installation of the clay barrier, some preliminary installation trials were performed, these serving to: optimise the positioning process and assembly of the blocks; check the stability of the bentonite slices; decide on how to initiate the installation and evaluate the diametrical gap that accumulates in the upper area of the barrier due to the effects of weight and of the sequence of placement (from bottom to top) of the blocks. This gap in the upper area reached some 15 mm between the barrier and the geotextile, measured in the radial direction.

3.3.3.2 Central prop for the initiation of block installation

From the preliminary trials it was seen that a rigid support was needed as a prop for the initial blocks, in order to guarantee the verticality of the first slice of blocks and to ensure that they were in the central plane.

For the rigid support, a circular piece of wood with a diameter equal to the interior of the confining structure was constructed and installed in the central plane, AB. Once the verticality of the support was adjusted, it was fixed to the structure and then the Zone A installation was initiated. The support was maintained until the installation of the blocks began in Zone B.

3.3.3.3. Installation of bentonite block slices

The installation was carried out manually, one slice of blocks at a time. For the installation of each slice, the block positioning sequence was as indicated by the numbers in Figure 3.13. In accordance with this sequence, the blocks were first placed in the lower part of each ring, followed by the external ring, closure of the interior ring, completion of the external ring and finally closure of the core in the non-heater areas.

Each of the 48 slices of blocks that make up the clay barrier is identified by its location within the zone (A or B) corresponding to one of the two heaters, and by its order number from plane AB to the corresponding end of the confining structure (from 1A to 24A and from 1B to 24B). In total, there were 908 blocks, with a total mass of bentonite amounting to almost 22 500 kg.

The slices were installed in the crown in alternating directions, to counter their possible inclination (Figure 3.14).

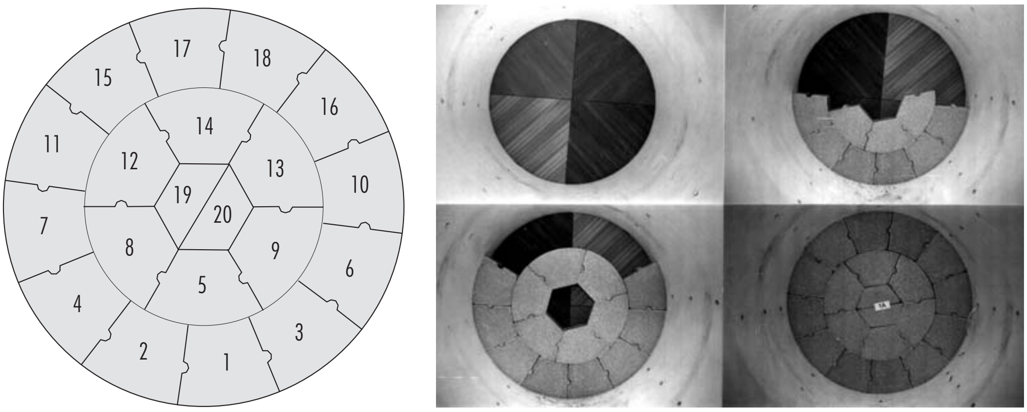

Figure 3.13: Sequence of installation of a slice of bentonite blocks.

Slices in non-heater areas, between heaters

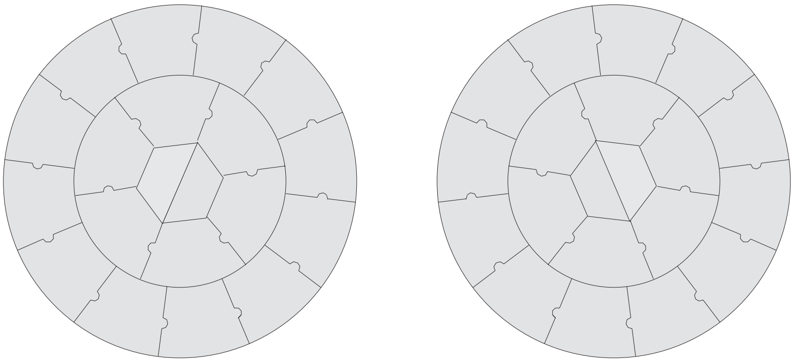

Slices #1 and #3

Slice #2

Slices in heater areas

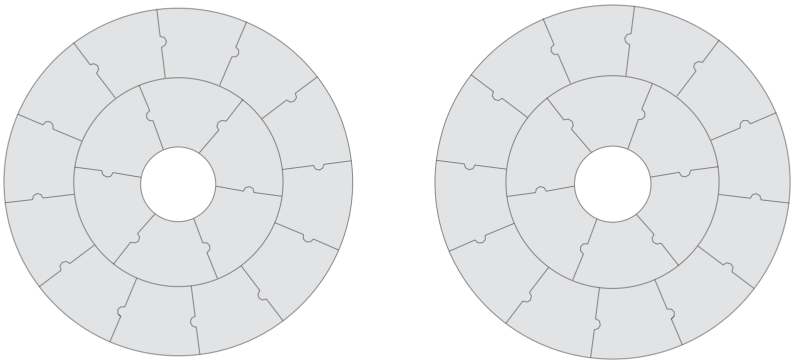

Slices #4, #6, #8, #10, #12, #14 and #16

Slices #5, #7, #9, #11, #13 and #15

Slices in non-heater areas, between heaters and ends of confining structure

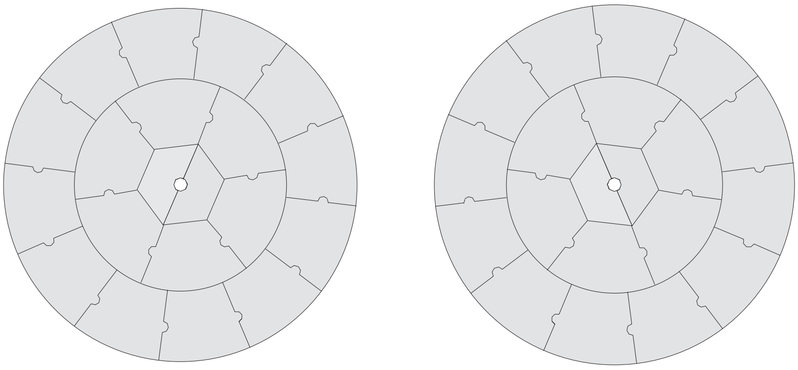

Slices #17, #19, #21 and #23

Slices #18, #20, #22 and #24

Figure 3.14: Installation method for slices of blocks.

3.3.4. Heater installation

For the insertion of the heaters, each weighing some 600 kg, a table with rollers was constructed, allowing the heater to be aligned with its location in the clay barrier and facilitating insertion by sliding. Figure 3.15 shows various moments of the insertion process and the good fit between the heater and its location in the clay barrier.

Given the inevitable irregularities in the enclosed space for the heater, and the friction between the heater and the bentonite blocks, it was necessary to apply force by mechanical means to insert the heaters.

3.3.5. Sensor installation

The sensors were installed in their assigned positions on completion of the corresponding slice of blocks. For each sensor, the location was machined into the bentonite, keeping the orifice to a minimum. All the space surrounding the sensor was filled with bentonite powder.

The cables were guided through the channels machined into the surface of the blocks. The cables were placed so as to avoid sharp curves or sharp edges and were not tightened, in order to reduce problems from movements due to the swelling of the bentonite.

The cables exit the confining structure in groups (four cables for each temperature sensor and two for each of the rest) by way of a mechanism for hermetic sealing in each of the 186 pre-drilled perforations. The majority of the sensor cables are located in the contact between the bentonite blocks.

The pressure sensors installed on the outside of the blocks and in the contact between blocks were placed such that they could measure the swelling pressure generated by the clay barrier in the three directions of the selected coordinates system (identified as PR, PT, and PZ). They are grouped at the same radial distance and a fluid pressure sensor is associated with each group (Figure 3.16).

3.3.6. Installation of metallic specimens for corrosion studies

Two complete sets of these specimens are located in the central and lower area near a heater (Heater B),

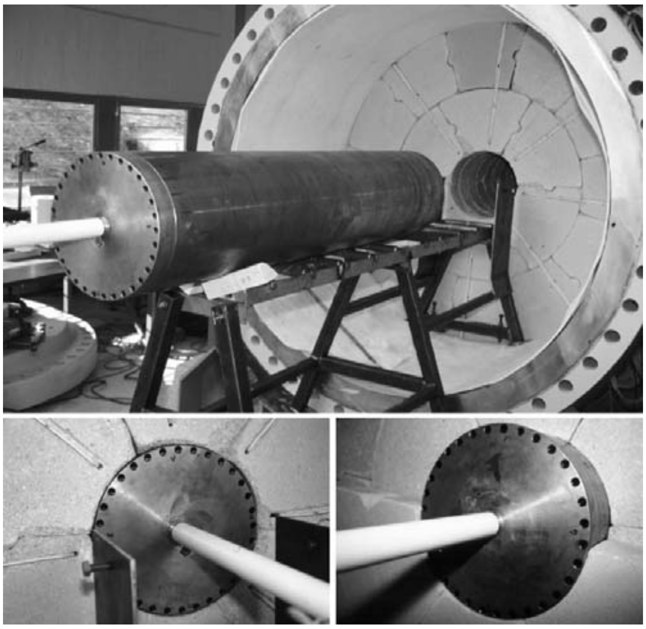

Figure 3.15: Heater insertion: table with rollers (top), Heater A (bottom left) and Heater B (bottom right).

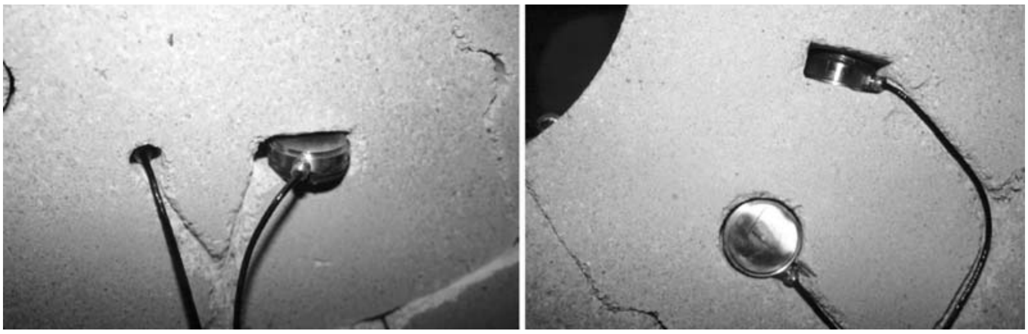

Figure 3.16: Installation detail of pressure sensors.

where the conditions of humidity and temperature may be more critical. As with sensor positioning, the corresponding blocks (in slices B9 and B10) were machined to place the racks containing the specimens, and the resulting spaces were later filled with bentonite powder (Figure 3.17).

3.3.7. Tracer installation

The tracers in impregnated filter paper were installed at the contact surfaces between blocks (external and internal crowns), while those in sintered metal capsules or incorporated in compacted bentonite plugs (a quasi-point location) were located in very small boreholes in the bentonite blocks (Figure 3.18), in a direction parallel to the longitudinal axis of the confining structure.

3.3.8. Quality assurance and quality control

The installation of the clay barrier was performed and controlled by CIEMAT, in accordance with the approved procedure.

The average dry density of the clay barrier has been considered fundamental, both as a parameter for the control of swelling pressures—so as not to exceed the swelling pressure used in the calculations for the components (6 MPa for a dry density of 1.65 t/m^3) nor go below the minimum considered tolerable of 1.4 t/m^3—and because it is a basic parameter in modelling.

To obtain the specified density, the mass of the blocks installed has been controlled and logged, and the loss of mass due to machining, drilling, and perforating of the blocks for installation of the sensors and corrosion specimens, the passage of the cables and the adjustment of the blocks was deducted. This has made it possible to calculate the average dry density and the volume of the gaps of each slice within the clay barrier. Therefore, the variations of these parameters are known throughout the length of the clay barrier, as represented in Figure 3.19, and the average values for the entire barrier were calculated: dry density of 1.65 g/cm^3 and volume of gaps of 6.25%. These values are in accordance with the initial expectations.

The positions of all the sensors were recorded, such that the database contains the actual installation coordinates.

Following installation a visual control was performed to check each slice, register anomalies and make a photographic record.

3.4. Operational stage of the test

The two fundamental processes during the operational stage of the test are the hydration and heating of the clay barrier. The following tasks were per-

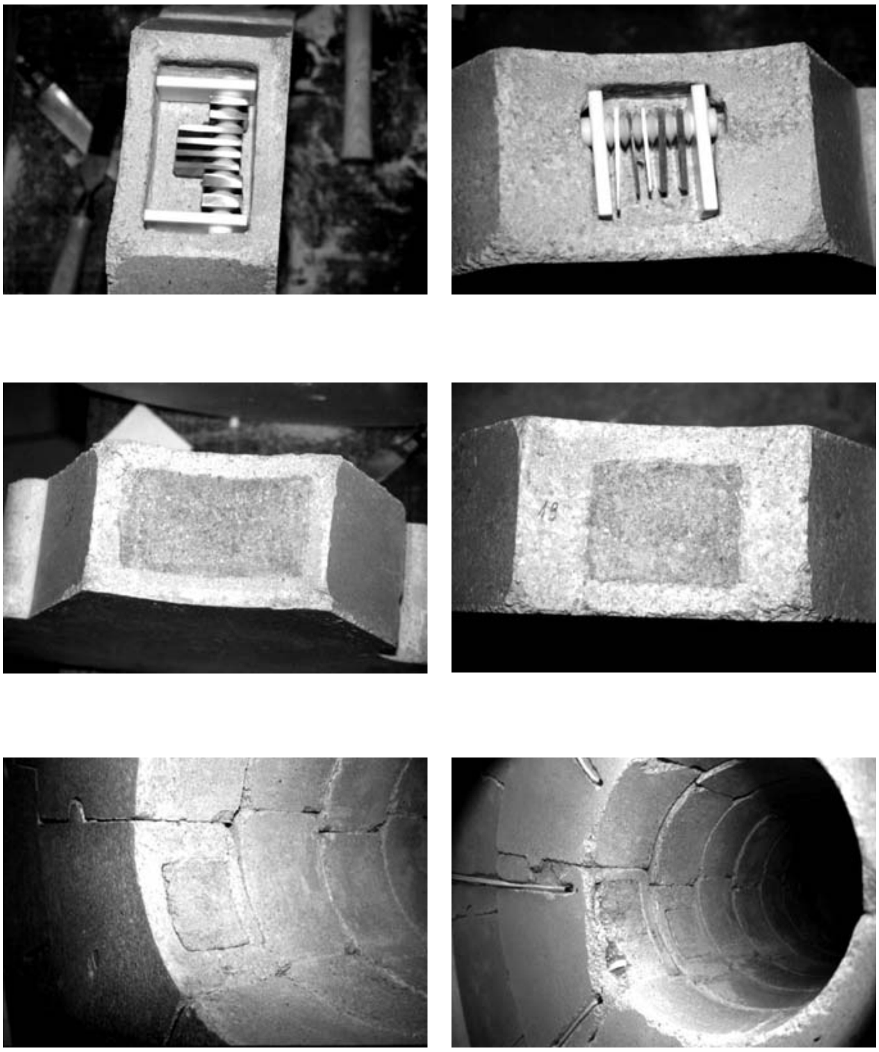

Figure 3.17: Installation of corrosion specimens.

formed prior to the establishment of the operational conditions for both systems (hydration and heating).

3.4.1. Hydration of the clay barrier

Unlike the "in situ" test, the "mock-up" test has allowed the initiation of the hydration of the clay barrier to be controlled. Actions were planned to eliminate the greatest possible number of heterogeneities and to obtain detailed insight into the initial and stable boundary conditions. In keeping with these objectives, actions were taken to eliminate the air existing between blocks and between these and the structure, to eliminate or reduce the discontinuities due to the configuration of the clay barrier (slices of blocks juxtaposed), and to obtain a gradual and radial hydration towards the heaters.

3.4.1.1. Preliminary tests

A leakage test was performed using gas to check the sealing of the sensor cable passages in the confining structure.

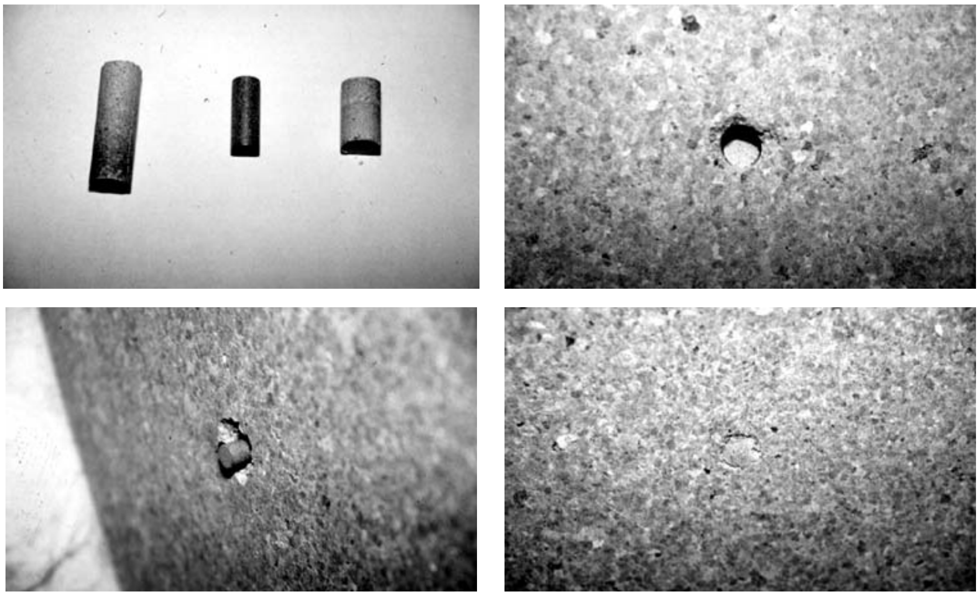

Figure 3.18: Method of installation of tracers in capsules.

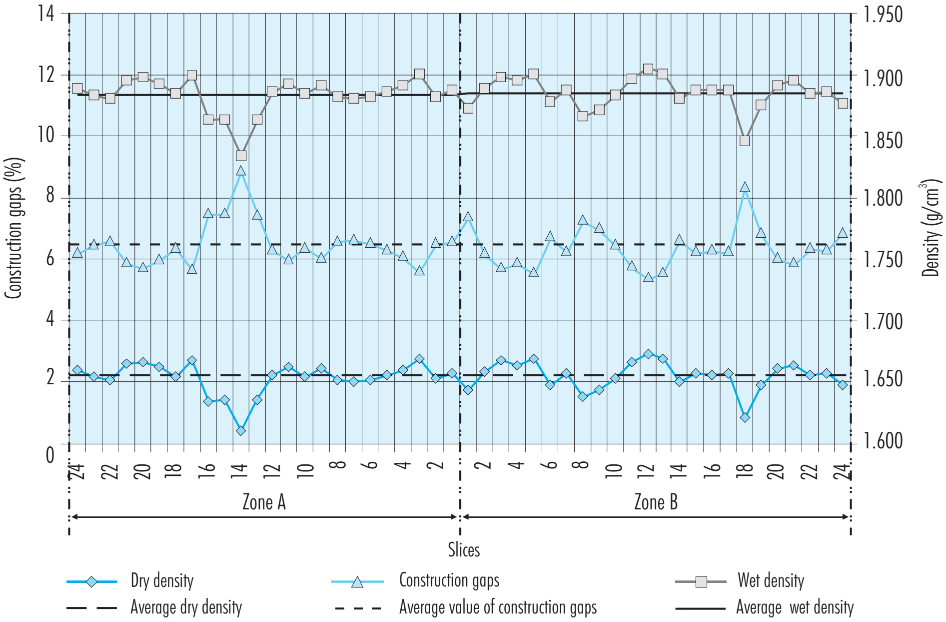

Figure 3.19: Distribution of density and volume of construction gaps in clay barrier.

Prior to initiating the hydration operation, the behaviour of the hydration system under the maximum operating pressure was verified, including all the mechanical components (manometers, valves, pipes, and connections), the electronic components (digital manometer and weighing system) and the safety elements.

To establish the relation between the pressure applied in the tanks and the water flow that enters the hydration rings, the water flow was gauged at the origin of the rings. From the curves obtained it was determined that the pressure in the tank should be 15 bars for this initial phase, to provide an average water flow of 5 l/min. This flow was considered sufficient to fill the free volume in a time period that would allow the water to enter the majority of the joints and thus ensure their sealing.

3.4.1.2. Filling of the tanks

The hydration tanks were filled with 1.3 m^3 (0.65 m^3 per tank) of granitic water, a greater volume than was necessary to fill the estimated free volume in the clay barrier. This assures the water supply is of the same composition during the initial phase of the test.

The tracers iodine and deuterium were added to the water. To fill the tanks, the water was pumped, by means of a GRUNDFOS model MP1 pump, with a flow of 3 l/min, and the upper valves of the tanks were opened to allow for the passage of the water and the exit of air from the interior, while the rest of the system valves remained closed.

3.4.1.3. Initial hydration

For initial hydration (filling of the joints), only one of the tanks was used (Tank 1). The first operation consisted of filling the hydration piping and rings, followed by purging of the system via the upper valves. In these upper valves, water samples were taken to control the tracers added.

The hydration sequence following purging of the piping is described in the following paragraphs. The valves connecting the tank and the piping network were closed, and the tank pressurised by applying 15 bars of nitrogen pressure. When pressure equilibrium was reached in the tank, the valve between the tank and the piping network was opened, and the pressure was then stabilised once more.

A mechanical regulator installed in the mouth of the bottle controls the pressure in the nitrogen supply line. A digital manometer installed at the connection to the piping network displays the pressure at the tank exit. This pressure value is recorded (and stored) in the DAS.

Once the pressures were stabilised, the system was ready for the initiation of water injection. This operation was performed by simultaneously opening all the lower valves (2 per hydration ring, 12 in total) and leaving two upper valves open to purge the system. When the water reached the upper valves, the lower valves and the valve connecting the tank to the distribution network were closed and two pressure sensors were installed in the valves that had been used for purging. These sensors will indicate the hydration water pressure in the confining structure during the test.

The operation described (filling of the joints) lasted 180 minutes and 634 litres of water were injected, which was in accordance with the previously performed calculation of the volume of gaps. On completion of this operation, all the valves were closed and the tank used was depressurised and refilled.

During the aforementioned operation, the general data acquisition system (DAS) registered the signals sent by the sensors distributed within the confining structure, by the conditioning modules of the tank weighing system and by the digital manometer. The water mass injected is obtained from the weight values of the tanks after depressurisation.

The system was maintained for three days under the conditions existing at the end of the previous operation. This time period was considered sufficient to have the injected water cause swelling of the bentonite blocks and, as a result, closing of the joints.

3.4.1.4. Definitive hydration

Following this three-day period the actual hydration and heating (operational stage) that the clay barrier would be subjected to throughout the entire testing period was initiated.

The injection pressure of the water was established between 5.0 and 5.5 bars. This value has been be maintained practically constant throughout the entire operational stage.

Given that the hydration system was purged after initial hydration, hydration proceeded as follows: application of the established nitrogen pressure pressurised the tank; the connection between the tank and the distribution network was opened and the pressures were stabilised. After pressure stabilisation, the entry valves to the confining structure were successively opened, from the lower to the upper end of each hydration ring, this completing the initiation of definitive hydration.

The data acquisition system (DAS) continuously gathers the values sent by the sensors, the manometer and the weighing system.

The instantaneous values of the weight of water injected are corrected for the injection pressure of the nitrogen. The maximum correction is less than 0.5% of the water mass at pressures of up to 5 bars.

The fundamental controls established consist of maintaining the injection pressure and periodically inspecting the system. The objective of this inspection is to detect any leak that may be produced by failures in connections or in the seals at the cable exits.

3.4.2. Heating

The heating and the hydration of the clay barrier are the basic operations of the "in situ" and "mock-up" tests. Consequently, precautions were taken to ensure correct operation of the heating system throughout the scheduled test period, with redundancy in the heating elements, the establishment of regulation and control processes allowing for the immediate detection of failures, the maintenance of a stable thermal level surrounding the heaters, the availability of the historic record of the thermal and power regimes of the heaters and regulation of the temperature in the test room, to obtain stable initial and boundary conditions.

This section describes the preliminary open-air operational testing of the heaters and their control system, initial heating at constant power and the constant temperature (operational) heating, automatically controlled as a function of the temperature at the heater/clay barrier interface.

The components of the heating system were subjected to various heating tests in the open air: with constant power to 1 kVA, automatic power control and instantaneous maximum power (3 kVA); with alternate operation, followed by simultaneous functioning of all the heating elements and deliberate shutdown of the electricity supply.

3.4.2.1. Preliminary tests

Preliminary tests were performed to check the correct operation of the different components (PLC, electronics, temperature sensors, and resistors); the values of safety-related electrical parameters (electrical insulation and grounding) and the operation of the acoustic overheating alarms. These alarms complement the optical alarms of the HCS.

In addition to these tests, and with the heaters already installed in the clay barrier, brief heating tests were performed prior to the initiation of operational heating.

3.4.2.2. Initial heating

The plan was to reach the 100 °C constant temperature of the operational stage by progressive heating in power steps, in order to reduce the risk of damaging the heating elements and to obtain data on constant power heating, to help in the modelling and interpretation of the process.

Given that the power estimated in the modelling was 500 W/heater, it was considered that initial heating could be accomplished in only two steps. The first step, at 50% (250 W) power, was maintained until temperature stabilisation was almost achieved (6 days); then in a second step, the power was increased to 100% (500 W). The second step lasted 4 days, until the temperature in the control zone of the heaters reached 95°C. From that moment on, the temperature at the heater/bentonite interface regulated the power control, and the power supply was automatically modified in accordance with the control program.

The heating and hydration of the operational stage of the test started on February 4, 1997.

3.4.2.3. Constant temperature heating

As has been pointed out, after a temperature of 95°C was reached at the heater/bentonite interface, the HCS was switched to the automatic control mode. The initial power value was reduced by 5%, to 475 W/heater, to avoid overheating, and from that moment on the HCS was maintained at a constant temperature of 100 °C, with slight variations in the power and with a tendency to slowly increase.

The HCS performs the control function by varying the conduction time in the resistors, depending on the power desired. If, with this power, the temperature does not reach 100 °C, the program changes the value of the conduction time and therefore increases the power in accordance with its internal algorithm; this process is repeated until 100 °C is obtained. If any of the heating elements fail, the rest maintain heating power.

3.4.2.4. Anticipated emergencies

Accidental shutdowns

The electricity supply for the PLC and the associated electronics passes through an uninterrupted power supply system (UPS); therefore, it is not anticipated that a failure will occur in the supply. Shutdown of the HCS, for maintenance or other reasons, for time periods of up to several hours is not considered to be a problem as regards the integrity of the test because of its thermal inertia.

The only accidental shutdown of the HCS foreseen would be a general failure in the CIEMAT electricity supply (external or internal) or damage to the HCS itself. No consideration is given either to the total destruction of the three resistors of a heater, because it is impossible to repair or replace them, or to possible failures in the data acquisition system. The HCS has already experienced an accidental shutdown, with a duration estimated at 20 minutes, with no mishap.

Reset

Should the HCS be shut down, either accidentally or voluntarily, the procedure to restart the heating will be the same as previously described for initiation. The only variation would be that the last values of power and temperature registered in the DAS would be used.

3.4.2.5. Maintenance

Periodic checks

For maintenance of the HCS, periodic checks of component operation have been specified, for correction in the event of failure. These checks include:

- ❑ Observing that the temperature of the electronics of the control unit do not exceed the ambient temperature by more than 20 °C. Although the electronics are designed to function up to 40 °C, it is very important, as a safety measure, that the ventilation works without malfunctions.
- ❑ Observing the illuminated indications at the front of the control panel of the PLC, taking into account that the lights of all indicators must be off, except for the central light that indicates that the equipment is operating. Flashing lights indicate the existence of alarms, located in the DEBUG of the PLC, where they are recorded.
- ❑ Observing the red lights marked R1, R2, and R3. If these are lit, it is an indication that the corresponding resistor is out of service; in this case, the resistor circuit and the ground must be reviewed in accordance with the established procedures. The number of the operating resistors is registered on the DEBUG panel.
- ❑ Observing the power indications on the DEBUG panel or the DAS screen. If the value is zero and there are no resistors in operation, the protection fuses must be reviewed and the relays inspected in accordance with the established procedures.

Calibration

Although, due to their location, it is not possible to calibrate the temperature sensors, the program notes and discards the use, by the control system, of any sensor with a reading, which is clearly different from the rest of the group. Nevertheless, periodic calibration of the power measurement is performed, since for power determination the program uses an algorithm in which are included the following: the number and value of the resistors in service, the period between heating processes, the heating time and the voltage value. All of these are parameters determined in this calibration.

Prior to the HCS being switched to the automatic mode, a calibration was made allowing the slight variation in temperature observed between the two heaters to be corrected. This correction in power has been less than 1%.

The calibrations will be made in accordance with the operating and calibrating procedure of the HCS.

3.4.3. Data management

The data generated by the test are recorded every 30 minutes. This record may be interactively modified, depending on test requirements. The software described above manages the data and copies are distributed to all the participants.

3.4.3.1. Database

The internal database contains all the data relative to each of the instruments (identification, description, signals or data provided, physical position in the DAS, conversions, etc.) and the readings are stored with the sensor reference, date, and time. The program allows the historical records to be consulted as a function of the sensor characteristics and/or the dates/times that the data were recorded.

The following standards have been adopted to keep the size of the database from increasing unnecessarily, taking into account the gradual evolution of the parameters controlled: a complete reading, taken every half hour from all the sensors is stored; the reading corresponding to the one taken at 12 noon daily is being used as the test datum; and the evolution of a parameter is analysed in greater detail from the recorded values, if necessary.

3.4.3.2. Data transfer

The data are transferred in ASCII format by means of a program from the database generated by the SCADA.

For data transmission between computers, a generic FTP-based file transfer program was used, the files passing through the network installed in the building (Ethernet). All the computers used the same program versions, adapted to the operating system installed in each. Access to each computer was protected by means of a password.

3.4.3.3. Data processing

Finally the data were filed in MS-EXCEL format. From these files, paper reports were generated semi-automatically. CIEMAT distributed copies of these reports to the groups participating in the project.

These reports present the evolution of the variables in graphic form, grouping the variables by sections and types of sensors (in this order), and were issued every six months.

Upon request, the numerical data in the database – in MS-EXCEL – for the group of sensors and/or time period might also be sent to the working groups. This might be accomplished on magnetic support or by electronic mail.

3.4.4. Operational management

The operational stage of the “mock-up” test (heating and hydration) started on February 4, 1997, “day 0” on the time scale, with the sequence described above.

The major events and incidents that have occurred since that date are described below, along with the main results of the experiment in relation to the data, sensor performance and the related conclusions.

3.4.4.1. Operation test control

Power supply

The power supplied to maintain the temperature at 100 °C at the heater-clay interface has remained almost constant throughout the initial months of the experiment. Following a minor decrease during the initial period (120 days), to 425 W/heater, the average value has ranged from 450 to 475 W/heater. From day 650 onwards, the power supplied increased to an average value of about 550 W/heater, within variations lower than 10%. Important changes in the external temperature have led only to minor increases in heating power during this phase.

Finally, for the last two years, and due to problems with the isolation of the electric resistances that occurred after several cooling-heating incidents, the heater has been operated at constant power supply (700W/heater) with a temperature close to the target (Figure 3.20).

Hydration

An increase of nitrogen pressure has been necessary on occasions to regulate the injection pressure in the hydration line. Because of the observed changes in this value, due to external temperature variations, it was decided to set the pressure close to 6 bars to obtain a more constant pressure value. Finally, a pressure-controller was installed to establish the nominal value, 0.53 MPa (Figure 3.21).

The hydration system has not been affected by any major changes. The spare tank, with only 400 l, replaced the water tank in operation during day 300. The total volume injected from the start-up of the test (1024.3 l on 08/07/2004) is shown in Figure 3.22,. No variations were observed in the hydration asymptotic trend.

Data acquisition and communications

The DAS has worked as expected. The data set has been recorded as foreseen.

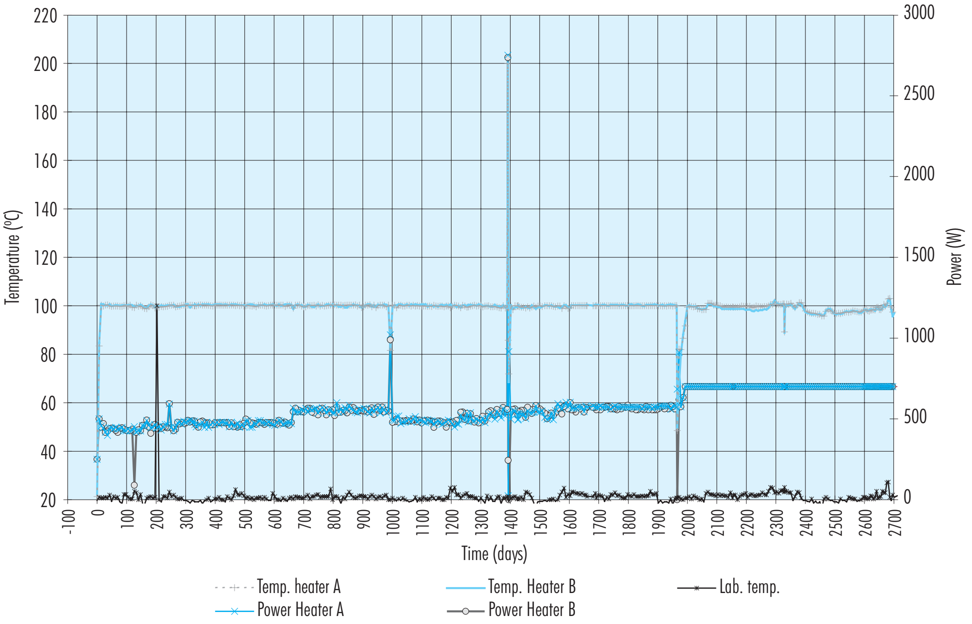

Figure 3.20: Evolution of heater and room temperatures, and power supply.

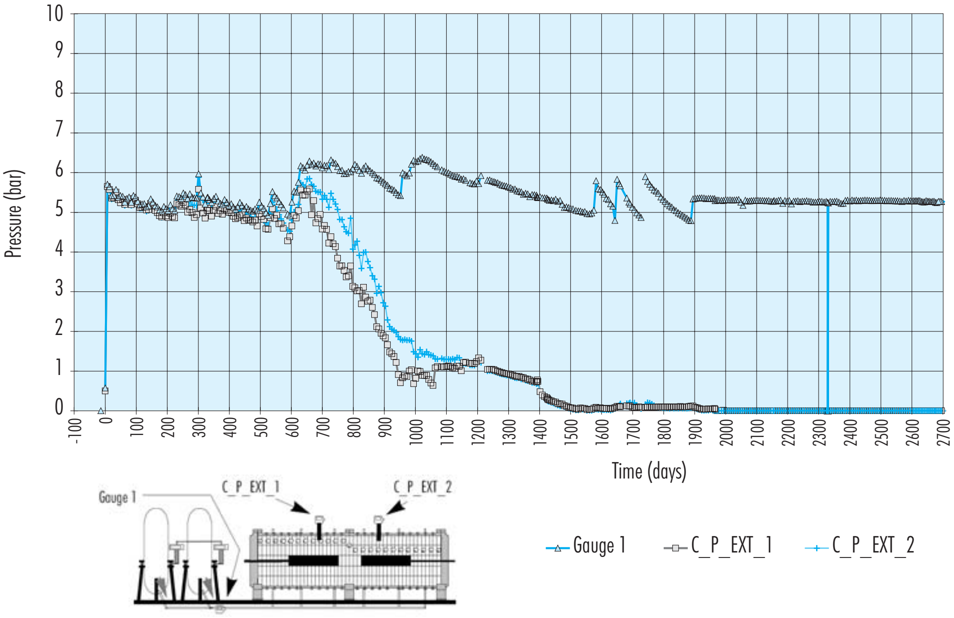

Figure 3.21: Evolution of injection pressure and water pressure within the geotextile.

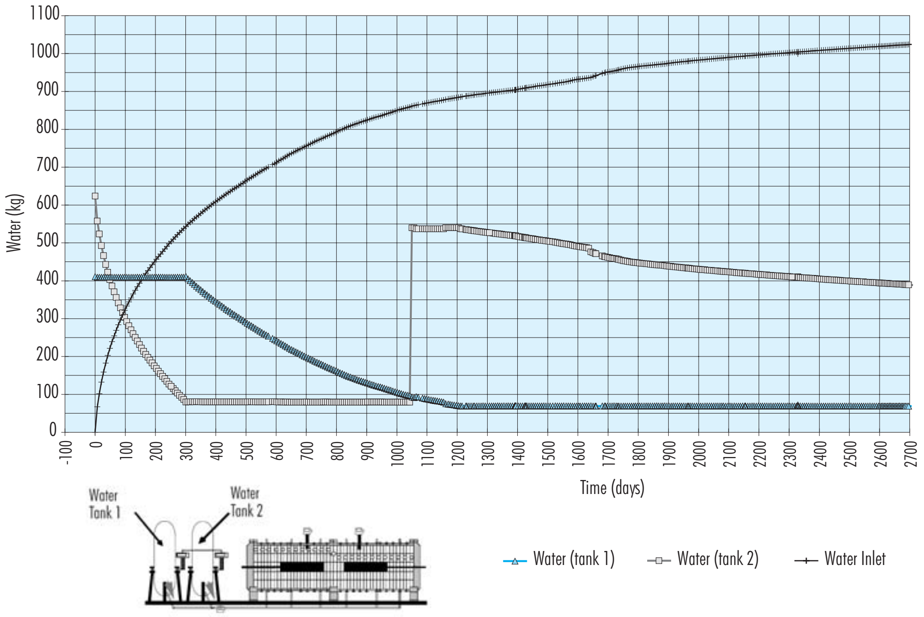

Figure 3.22: Evolution of injected water volume.

3.4.4.2. Incidents

Power supply

The heating system has experienced minor failures in the general power supply, with a loss of less than 10°C. There were no major consequences and these failures do not appear in the daily readings.

After the start-up of the test, the Industry Authorities required an annual check of the general power supply and electrical systems inside CIEMAT. The major incidents were produced by these annual technical shutdowns, required to obtain the corresponding authorisations.

In order to cope with these minor events, the reset procedure of the heating system was performed, in order to reach the target temperature as soon as possible. In general, this objective was accomplished so quickly that it does not appear in the 12 P.M. data.

Several cooling-heating incidents have been long enough to be recorded in the database. Some electrical problems have caused the UPS to discharge completely, turning the DAS and control system off. As was foreseen, when the power supply returned, the DAS and the system control started to operate once more, while the protections of the heating system prevented overheating by keeping the resistances turned off. This operation caused a loss of heating power for several hours, without major consequences. This was the case around days 240, 670 and 990 of the experiment (Figures 3.20 and 3.23)

Due to a malfunction that occurred towards the end of November 2000 (day 1391), the control program supplied the total heating power (around 2700 W/heater) for more than 36 hours, until the temperature at the sensors in the heaters reached the resistance safety value (300°C). This overheating was halted automatically, but the temperature within the bentonite reached values of around 240°C. Consequently, the bentonite around the heaters was dried and a thermal pulse was generated followed by a cooling-heating cycle [23] (Figures 3.20 and 3.24).

Finally, due to certain problems with the isolation of the electrical resistances, it was necessary to stop

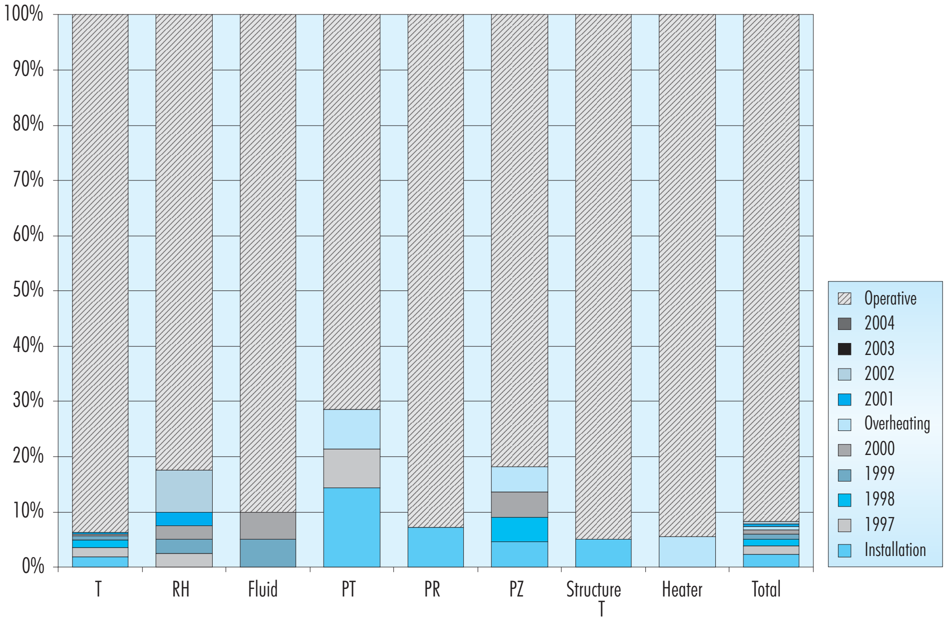

Figure 3.23: Evolution of sensor breakdown (operative sensors in striped pattern).

the system for two weeks, around day 1975, causing a loss of 50°C (Figure 3.20).

Hydration

There were no problems with the behaviour of the hydration system, except minor variations in the value of injection pressure.

The pressure measurements in the injection line and from the sensors on the hydration surface were similar, until certain deviations were observed after 500 days. The explanation for this might be the filling of pipes by clay, sealing off pressure transmission (Figure 3.21).

In order to confirm the THM behaviour of the barrier, some tests were performed on the injection nozzles to confirm the water inflow through the geotextile into the clay. New instrumentation was also installed to measure the water flow in the lines of the hydration system.

Data acquisition and communications

Most of the incidents were caused by loss of communication between the DAS, the PLC or the control PC, due to transmission errors. Resetting of the DAS mainframe, as established in the operating procedures, recovered the communications and solved the problem. This objective was accomplished in a few minutes. Three kinds of incidents are described below:

- ❑ *Minor incidents* were due to failures in initialisation off the data files. The data lag is estimated at one data file (4 hours). The system was capable of overcoming the problem by itself.
- ❑ *Intermediate incidents* did not indicate communication failures between the DAS frames and the control PC. These failures produced minor data lags, lasting from several hours to several days.
- ❑ *Major events* did not cause any communication failure signal and caused extensive data lag up to the next routine control (one or two weeks).

One hardware breakdown occurred during the first year of the test. Several heavy electrical storms during the summer of 1997 caused the PLC serial port to break down, with loss of communication between the DAS and the control PC. This did not affect the functioning of the PLC and the DAS, but transmission between them was impossible. Replacing the serial port in the PLC solved the problem.

These incidents do not pose a major problem because of the duration of the test and the slow trend that it presents.

3.4.4.3. Sensor performance

Almost all the sensors installed currently continue to operate, after having been in the bentonite for more than eight years. The sensors work correctly in spite of the harsh environmental conditions.

Most of the faulty sensors are temperature sensors and have been removed from the database. The faulty pressure and RH sensors remain in the database, in case they might be recovered after some time and pending confirmation of their failure.

Figure 3.23 shows the evolution of sensor breakdown, by type and year (including events such as installation and overheating). More than 90% of the total number of sensors remain operative, but this percentage is 70% for tangential pressure (PT) and 80% for axial pressure (PZ) and RH. It is not possible to guarantee their future behaviour.

The instruments associated with the hydration are operating without problems. The heating system has lost one sensor in heater A.

3.4.4.4. Sensor data from the clay barrier

The readings from the sensors within the bentonite, reported in reference [24], are plotted by groups of measured parameters (temperature, RH, total pressure and fluid pressure), in order to facilitate comparison between the sensors of the same kind at different sections.

Temperature

After the first two weeks, the test continued in a quasi-stationary temperature state. The slight temperature waves are caused by variations due to the difficulty of conditioning the test room. These fluctuations are evident in the sensors placed in the outer radii, as expected.

In general the data show good homogeneity throughout the test. The initial variations observed between sensors placed on the same radial distance are less than 2°C.

The average measurements from section A5 are shown in Figure 3.24 as an example of temperature data.

Relative Humidity

The data show good homogeneity throughout the test. The variations observed between sensors placed at the same radial distance are not significant (Figure 3.25).

A representative evolution of the RH measurements is presented in Figure 3.26, for section A4.

In general, a drying-wetting process is observed, with a maximum of three phases. These phases are different, both in duration and in drying-wetting rates, depending on the location of the RH measurement (distance to the hydration surface and thermal gradient imposed on the sensor):

- ❑ First, sharply increasing RH values appear, related to the vapour phase generated by the heating. Water vapour migrates through the buffer from the heater to the colder zones. This phase presents a maximum value that seems to be due to the limited source of vapour within the clay. As was expected, the shorter the distance to the heater surface, the sharper the RH peak observed (Figures 3.25 and 3.26).
- ❑ Second, heat transfer from the heaters causes drying of the clay, leading to decreasing RH values. The higher the distance to the hydration surface, the longer the duration of the drying phase (Figures 3.25 and 3.26). No drying phase is observed for the external sensors (radius =70 cm).
- ❑ Third, after some time with almost steady RH values, hydration reaches the dried zone and overcomes the drying process, increasing the RH values measured. Wetting returns. The greater the distance to the hydration surface, the lower the wetting rate (Figures 3.25 and 3.26), as expected.

The synchronous evolution of the different RH sensors (Figure 3.25) indicates that their behaviour is a real process and not an artefact in the RHE (relative humidity of equilibrium) evolution of the material. This evolution is shown as a decrease of magnitude in the more saturated zones of the external ring in the barrier. From above, the water inflow is radial and homogeneous, modified only by the intrinsic THM behaviour of the barrier. This was a specification of the design.

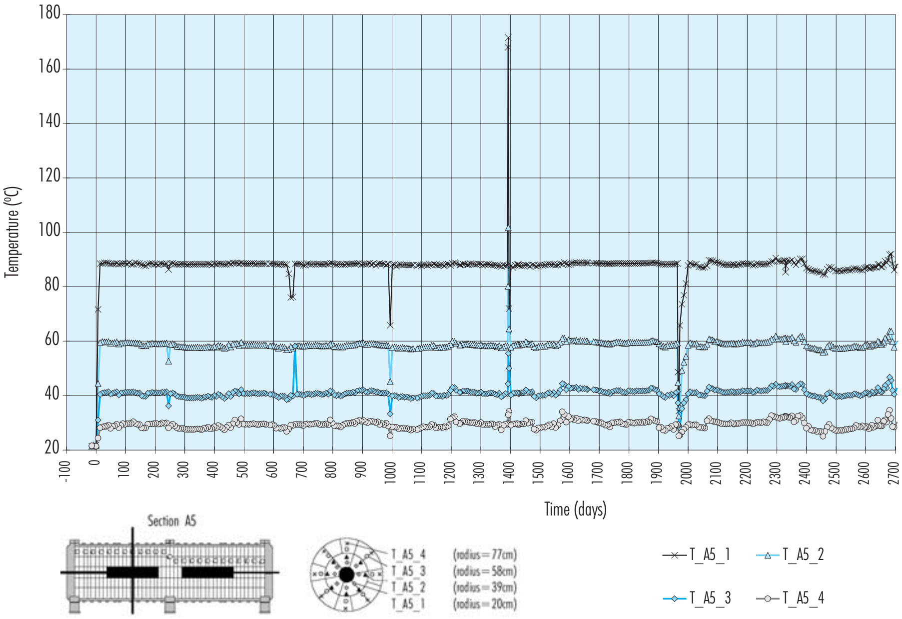

Figure 3.24: Evolution of temperatures (average values) in section A5.

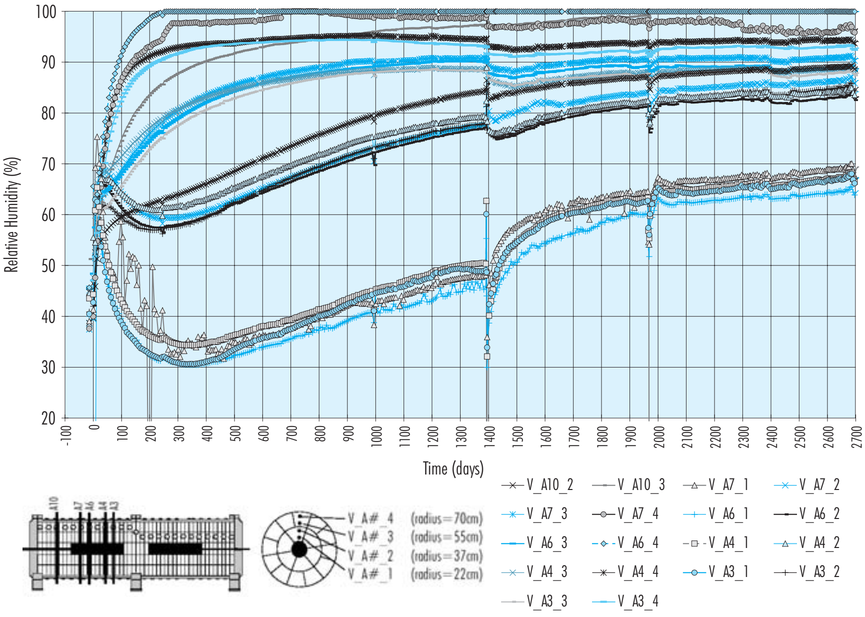

Figure 3.25: Evolution of relative humidity in zone A.

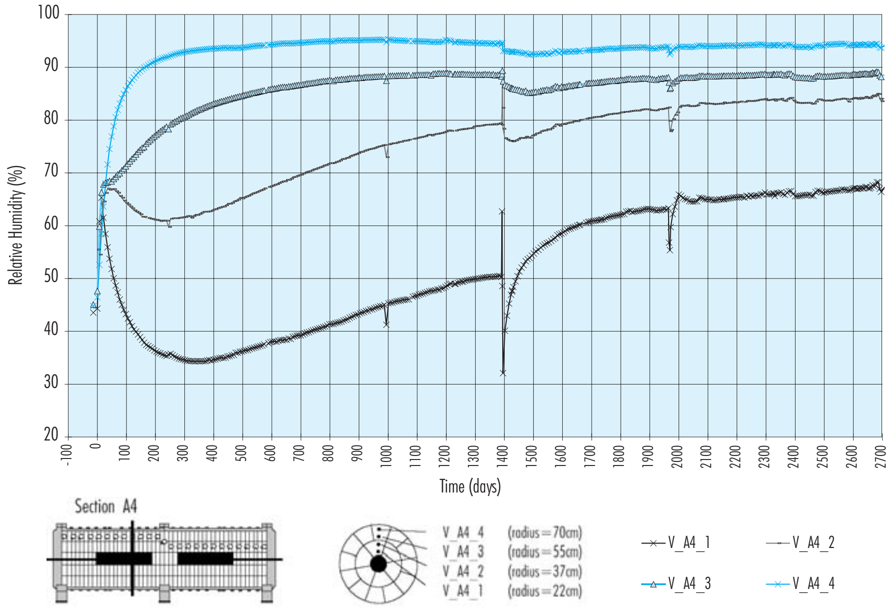

Figure 3.26: Evolution of relative humidity in section A4.

Major variations in RH values (Figures 3.25 and 3.26), not in trends, are associated with the more important cooling-heating incidents mentioned above: day 975, over-heating (day 1390) and heating breakdown (day 1975).

At present (more than 7 years from the initial hydration), the "4" sensors (r=70 cm) show a steady state with values close to 100%. The so-called "3", "2" and "1" sensors (r=55, 37 and 22 cm, respectively) are being affected by the wetting process, with slightly different hydration rates.

The values from the sensors placed close to the surface of the structure suggest that the bentonite in this external zone is fully saturated. In some cases, this saturation seems to affect the measurement.

Total pressure

Under hydration, the bentonite develops a mechanical pressure by swelling recorded by the total pressure sensors located at selected radial distances (35.0 cm and 66.5 cm), and orientated in the three main directions. The pressures are in accordance with the swelling pressure values of the bentonite measured in the laboratory.

The higher-pressure values are located within the outer ring due to the evolution of the saturation front. Indeed, the average-pressure values in this zone and their gradual increase might indicate a high degree or full saturation and, therefore, high swelling in the outer part of the buffer. Here, axial pressure ranges from 5.0 to 10.0 MPa (Figure 3.27), radial pressure has converged in a narrow range from 7.5 to 8.5 MPa (Figure 3.28) following the important variations induced by overheating in the heater zones, and tangential pressure ranges from 6.0 to 9.0 MPa (Figure 3.29).

On the other hand, the wider range of values and the lack of pressure uniformity in the inner rings might indicate two different processes: mechanical stressing of the buffer by the swelling pressures in the outer rings or the extension of saturation (Figures 3.25 and 3.26) into this zone.

The entire data set for the inner ring is presented, with axial pressure ranging from 2.0 to 11.0 MPa (Figure 3.30), radial pressure from 3.0 to 12.0 MPa

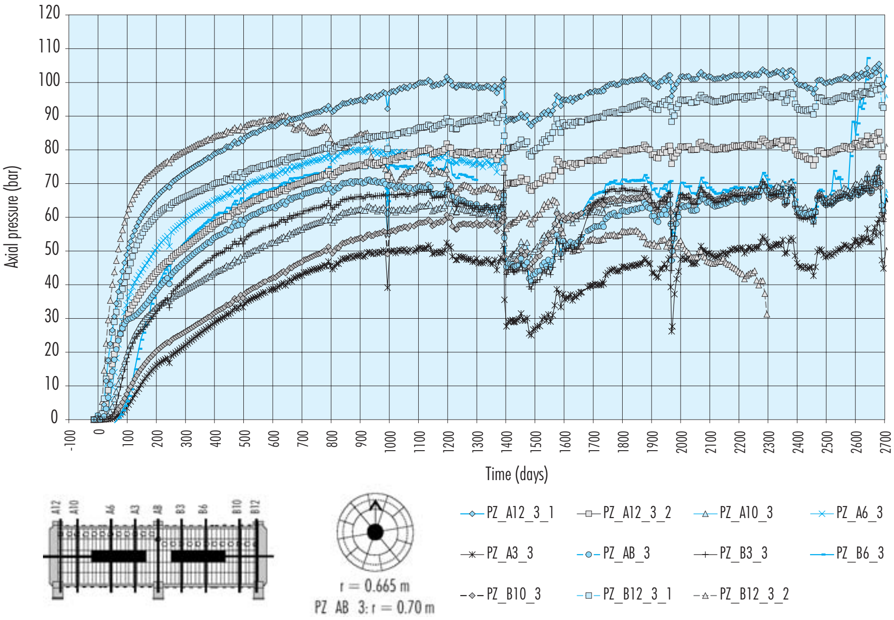

Figure 3.27: Evolution of Z axial pressure in the outer ring.

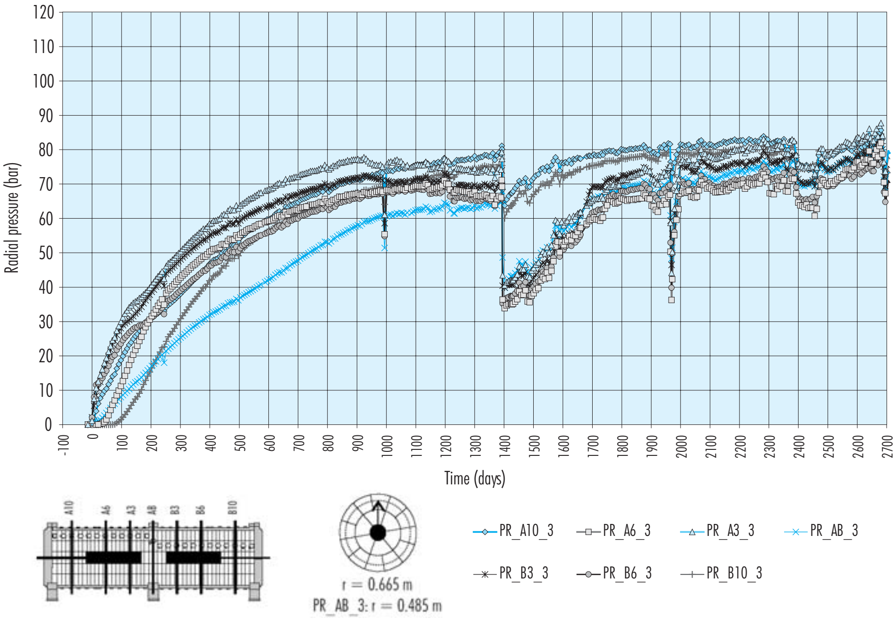

Figure 3.28: Evolution of radial pressure in the outer ring.

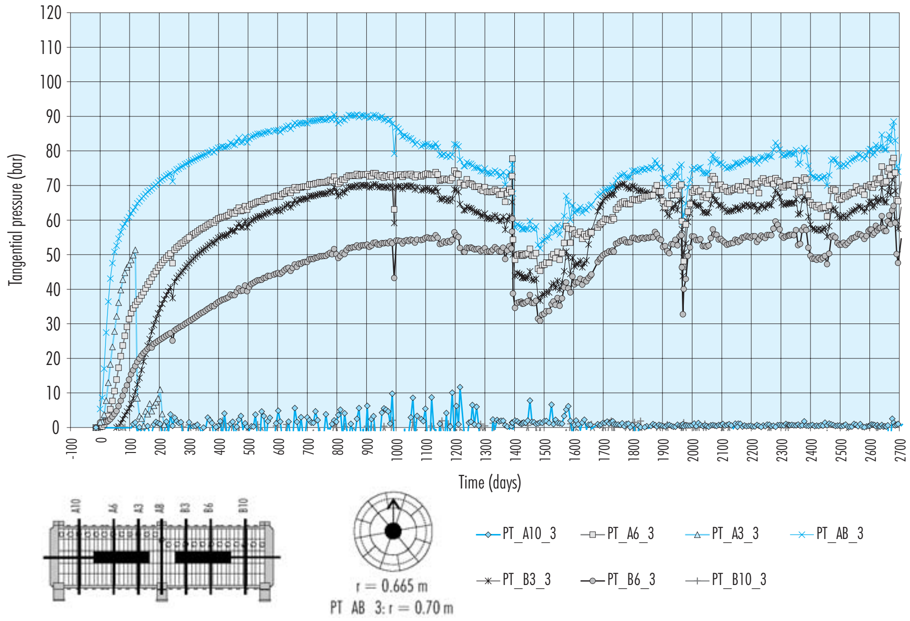

Figure 3.29: Evolution of tangential pressure in the outer ring.

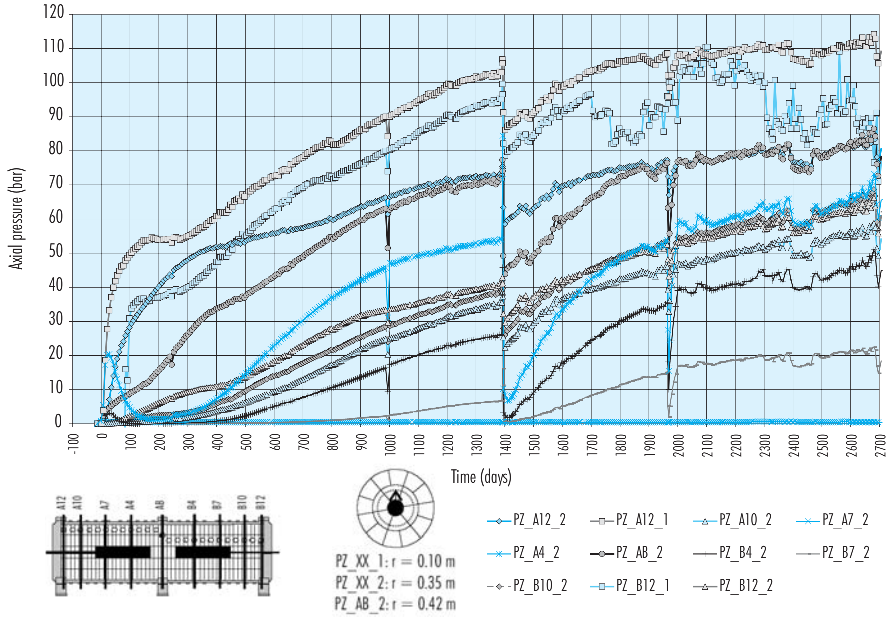

Figure 3.30: Evolution of Z axial pressure in the inner ring.

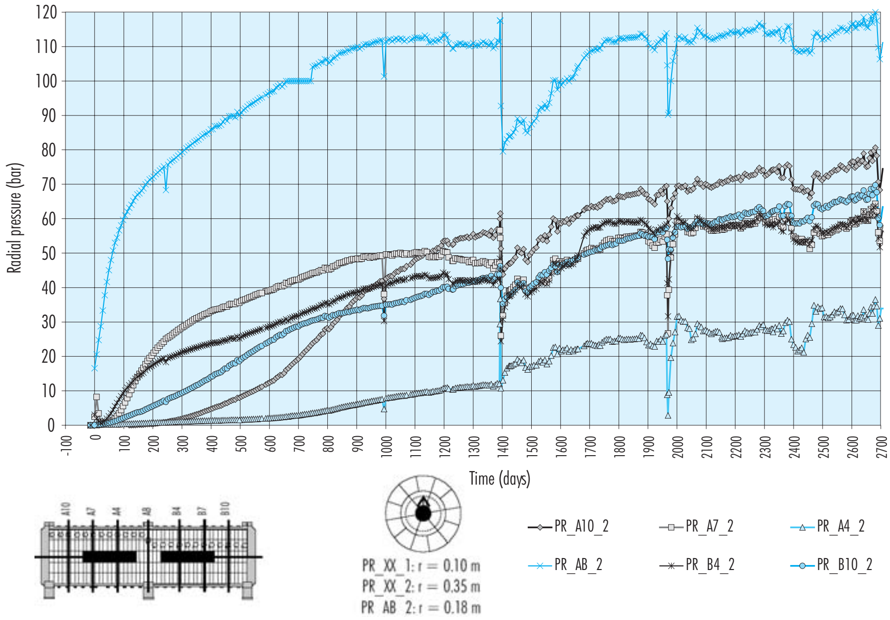

Figure 3.31: Evolution of radial pressure in the inner ring.

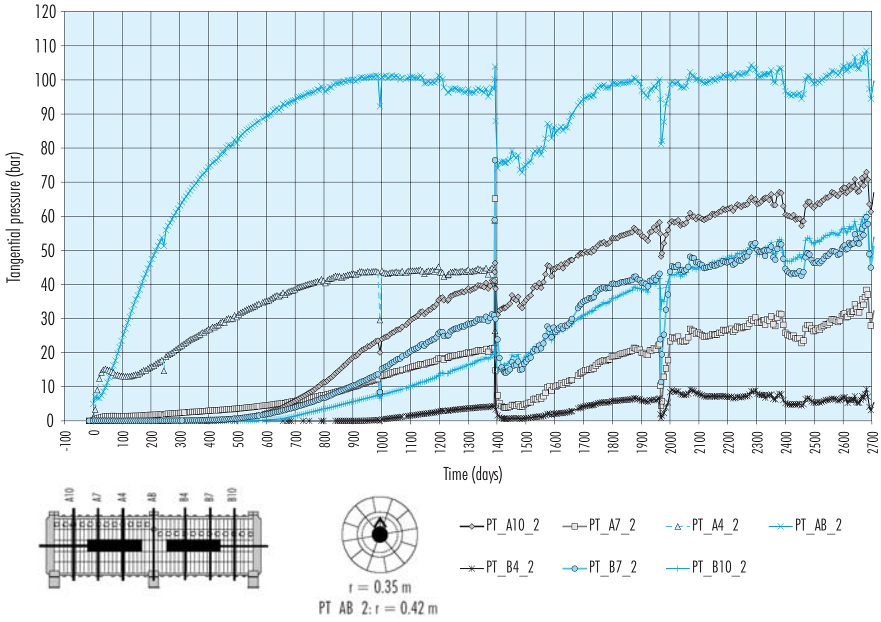

Figure 3.32: Evolution of tangential pressure in the inner ring.

(Figure 3.31) and tangential pressure from 1.0 to 11.0 MPa (Figure 3.32). Lower values and higher relative variations after overheating are encountered in the zones around the heaters.

Different behaviours may be observed between the bentonite sections that include the heaters (hot sections): A3, A4, A6, A7, B3, B4, B6 y B7) and those without heaters (cold sections): A12, A10, AB, B12 y B10.

Fluid pressure

At the beginning of the test, the measurements are so low that no conclusion may be drawn. They might be considered as fluctuations of the equipment.

As the test continues, the measured values cannot be assigned to water or gas pressure without uncertainty, mainly in the inner ring. Only some variations seem to be related to the arrival of water, always for sensors located in the outer rings. In all cases, the fluctuations seem to be related to temperature variations (Figure 3.33).

The thermally induced behaviour mentioned above is also seen in the fluid pressure sensors, separating the two zones as a function of the temperature field. Approximately 700 days are required for any increase to be observed in the fluid pressure within the outer rings. This gradual pressure increment, which produces higher and more stable values in the hot zones (Figure 3.33), might show a dependence on fluid temperature (through water viscosity); for their part the internal rings show a similar behaviour in both zones, hot and cold (Figure 3.34) and up to 900 days are required for any appreciable increase to be observed.

Taking all these facts into account, it seems that the physico-chemical processes controlling the evolution of the measured parameters undergo deviations related to the temperature field generated in the barrier, either as thermal gradient-driven processes (thermo-hydraulic coupled phenomena), or as processes relating to the increased temperature rate (chemical or of the Arrhenius type).

3.4.4.5. Other sensor data

Temperature sensors on the surface of the heaters

The readings from the sensors installed on the surface of the heaters are close to 100°C in the control zone (Figure 3.20), and close to 90°C in the end zones.

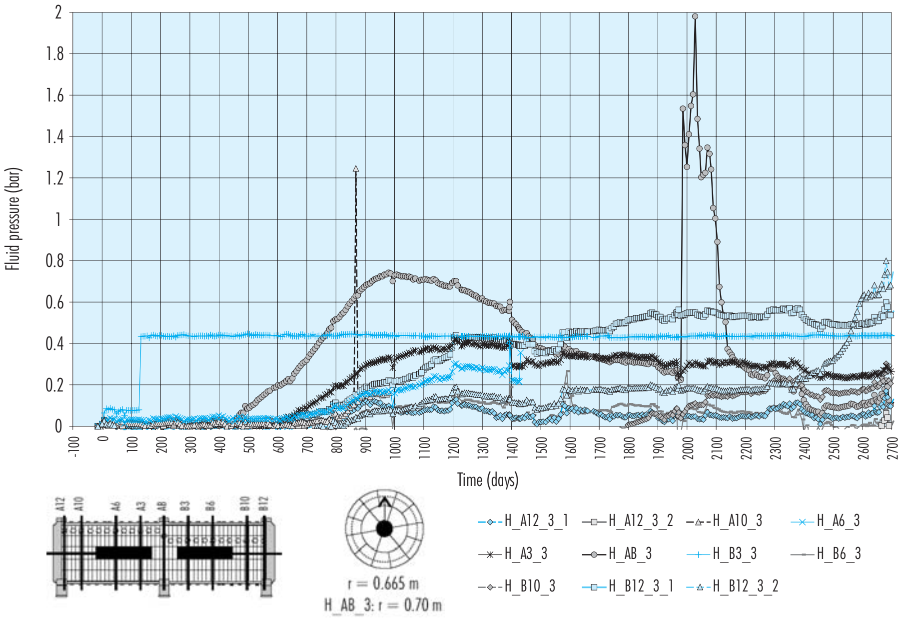

Figure 3.33: Evolution of fluid pressure in the outer ring.

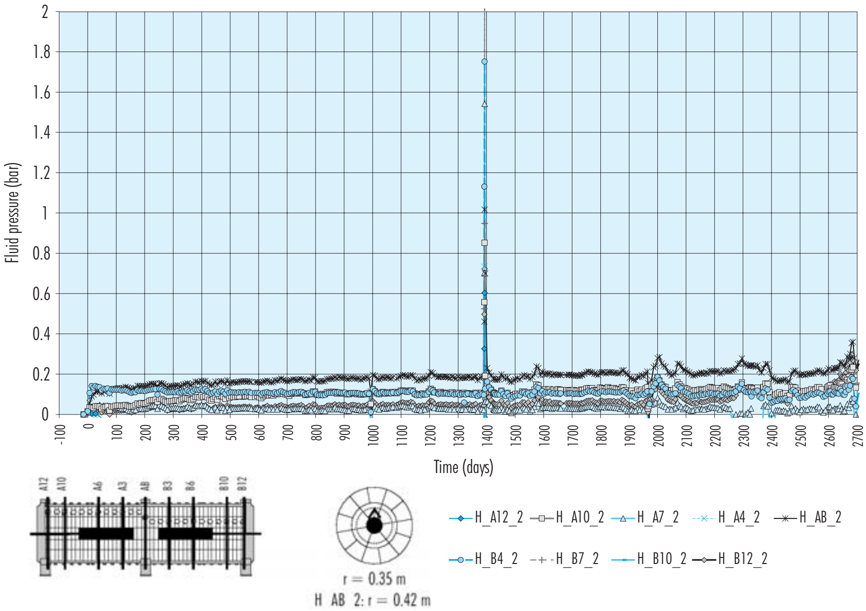

Figure 3.34: Evolution of fluid pressure in the inner ring.

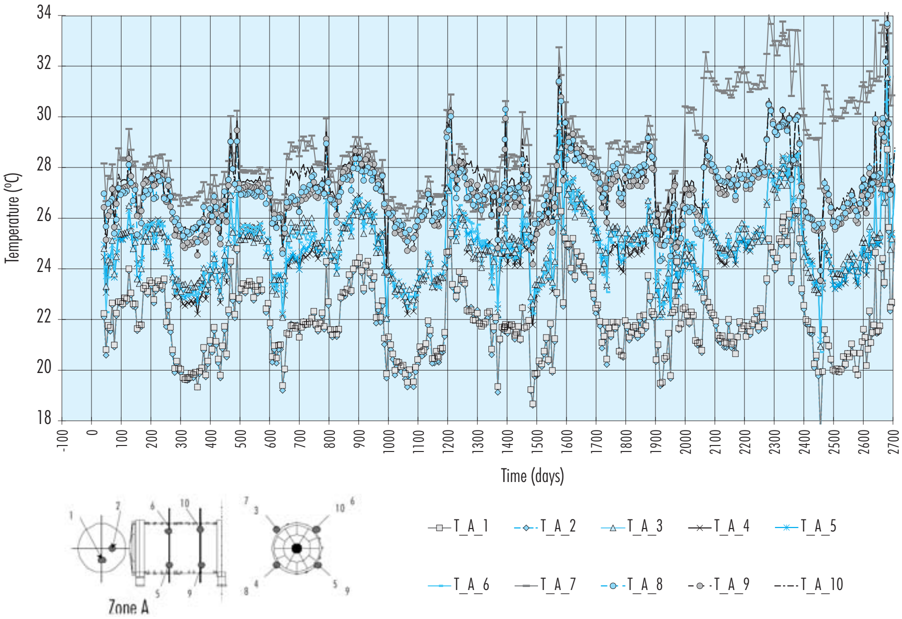

Figure 3.35: Evolution of external temperatures on the confining structure.

Temperature sensors on the surface of the structure

In general, the changes in the temperature are due to important and sudden variations in natural climate conditions. The arrival of summer produces higher daily temperature variations, which are not completely compensated for by the air-conditioning system (within the +4°C difference).

With these exceptions, the temperature waves on the structure are within the ±2.0°C difference, as required (Figure 3.35).

External sensors and instruments

This section includes the values from the hydration system: injection pressure in the hydration line, injection pressure on the hydration surface, the mass of the tanks, and the volume injected (Figures 3.21 and 3.22).

This entire set of parameters has been controlled within the requirements of the experiment. Since day 500, the only major variation has been the anomalous increasing deviation between the sensors measuring the injection pressure at the hydration surface and the injection pressure in the hydration line.

The temperature of the test room is also measured close to the PLC rack (Figure 3.20).

3.4.4.6. Measured THM-parameter distributions

From the data set, distributions of temperature and RH have been estimated at several different times; the distribution of suction was also calculated at these times. The estimates are made by constructing a regular grid using a linear kriging method with an anisotropy factor (Figures 3.36 to 3.38).

The thermodynamic relationship between soil suction, partial vapour pressure of the pore water and temperature is [25]:

$$\psi = -\frac{RT}{v_{w0}\omega_v}\ln\left(\frac{\overline{u}_v}{u_{v0}}\right)$$

where:

ψ	Total suction (kPa)
R	Gas universal constant [8.31432 (J/mol·K)]
T	Absolute temperature [$T=273.16+t^0$ (K)]
t^0	Temperature (°C)
v_{w0}	Specific volume of water [$1/\rho_w$ (m^3/kg)]
ρ_w	Water density (998 kg/m^3 a 20°C)
w_v	Molecular weight of water (18.016 kg/kmol)
u_v	Partial vapour pressure of pore water (kPa)
u_{v0}	Saturated vapour pressure of pore water over a plane surface at the given temperature.

In calculation, the value inside the ln() operator is replaced by the estimate obtained from the measured RHs, the absolute temperature values are estimated from the measured distribution of temperatures and water density is taken as a constant. The suction is calculated in an element-to-element scheme and converted to MPa.

Due to the temperature distribution (Figure 3.36), the zones adjacent to the heater have lost water, which moves away towards the structure in both the radial and longitudinal directions. At the same time, water is coming from the structure (liquid hydration front, Figure 3.37). The combined effects of these processes modify the state of total water potential (suction) within the barrier (Figure 3.38): modification of the temperature and the suction gradients, possible chemical effects on the pore water potential, irreversible changes in material structure, etc.

Furthermore, in the hot zones, the vapour migrates towards colder zones where it may condensate to form almost saturated zones (at least inasmuch as it is impervious to vapour flow) at intermediate positions within the barrier. Consequently, the effect is the reduction of the geometry and the local suction gradient, precisely in the zone where the core barrier extracts water from periphery. This process might diminish water-driving potentials (Figure 3.38) and the associated water intake as the test goes on.

3.5. Test behaviour evaluation and conclusions

The FEBEX "Mock-up" test run at CIEMAT will continue for several years, within the EC Integrated Project NF-PRO, prior to being dismantled. At present, certain conclusions may be drawn in relation to the following:

3.5.1. Operational behaviour of the components of the experiment

The "mock-up" test is functioning correctly and with most of the sensors still in operation, even though its operative design lifetime (3 years) has more than been exceeded:

- The reliability of the instruments is fairly good. More than 90% of the sensors remain operative. However, it is not possible to guarantee their future behaviour.
- The reliability and performance of the heaters are sufficiently high. The change in the functioning of the heaters (one resistance with filtered power supply) should extend their life expectancy and prevent any further damage from occurring.
- The data acquisition and control systems are working satisfactorily.

3.5.2. Conclusions on the measurement of THM parameters

Though seven and a half years have passed since the beginning of the operational phase of the test, its final evaluation will be performed only after it is dismantled. However, some qualitative conclusions may be established, mainly concerning the differences in the behaviour between the “hot” and “cold” zones of the buffer, indicating major implications of the thermal aspects in the transport processes. Also, some large-scale THM couplings have been identified.

3.5.2.1 Temperature

- The thermal regime is homogeneous and symmetric; both with respect to the central section and the longitudinal axis. Fluctuations are observed near the structure and are due to external temperature variations.
- The temperature distribution is controlled by thermal conduction, due to the slow rate of the transport processes involved in saturation of the buffer material.
- The temperature calculation based on thermal conductivity, tuned by saturation of the material, fits well with the data (Chapters 6 and 7).
- A limited number of sensors are enough to display the temperature distribution and evolution.

3.5.2.2. Relative humidity

- The RH capacitive sensors work well within the RH and temperature ranges of the test. This allows for monitoring of the hydration process throughout this experiment.
- The saturation of the bentonite barrier is behaving as expected, although with slower rates than foreseen in the preliminary calculations.
- Both, water inflow and water vapour outflow, occur mainly in a radial direction.
- The saturation of the bentonite barrier is apparently controlled by the hydraulic properties of the bentonite and the thermal gradient imposed by heating.

3.5.2.3. Total pressure

- The measurement of total pressure depends on the swelling pressure built up in the outer ring and on the heterogeneous distribution of stresses in a buffer formed by blocks, with limited swelling in the inner ring.
- The pressure increases seem to be associated with the arrival of the hydration front. The measured values become stable as the buffer material saturates and the material reaction changes its structure.
- Values for the different directions (PR, PZ and PT) are converging in narrow ranges.

3.5.2.4. Fluid pressure

- The values registered are so close to zero that they are strongly affected by the fluctuations of the external temperatures and the thermal waste due to natural convection on the structure.
- The fluid pressure measurements seem to be due to the presence of liquid in the external rings and to the presence of gas in the internal rings. It would be necessary to have sufficient free water (full saturation) within the inner rings of the buffer material for this pressure value to be considered as water pressure.

3.5.3. Interaction with models

- In a first phase of the test, hydration advanced throughout the entire barrier, with higher rates in the outer ring, apparently controlled by the hydraulic properties of the bentonite affected by the local temperatures. The regime was regular and symmetric and the data and models show good agreement.
- As the system evolved, there were clear differences in hydration between the “hot” and

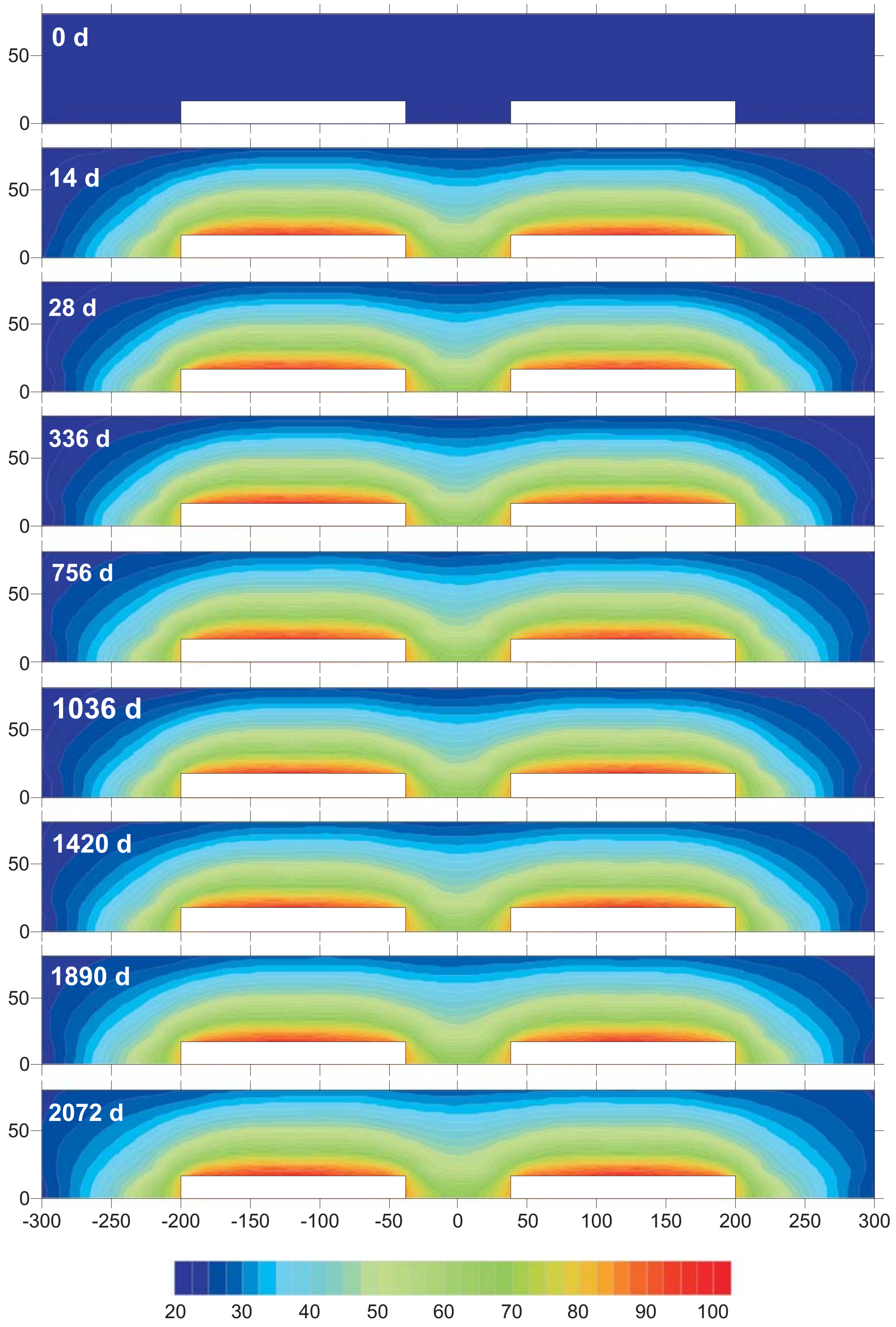

Figure 3.36: Temperature evolution (ºC) during the experiment.

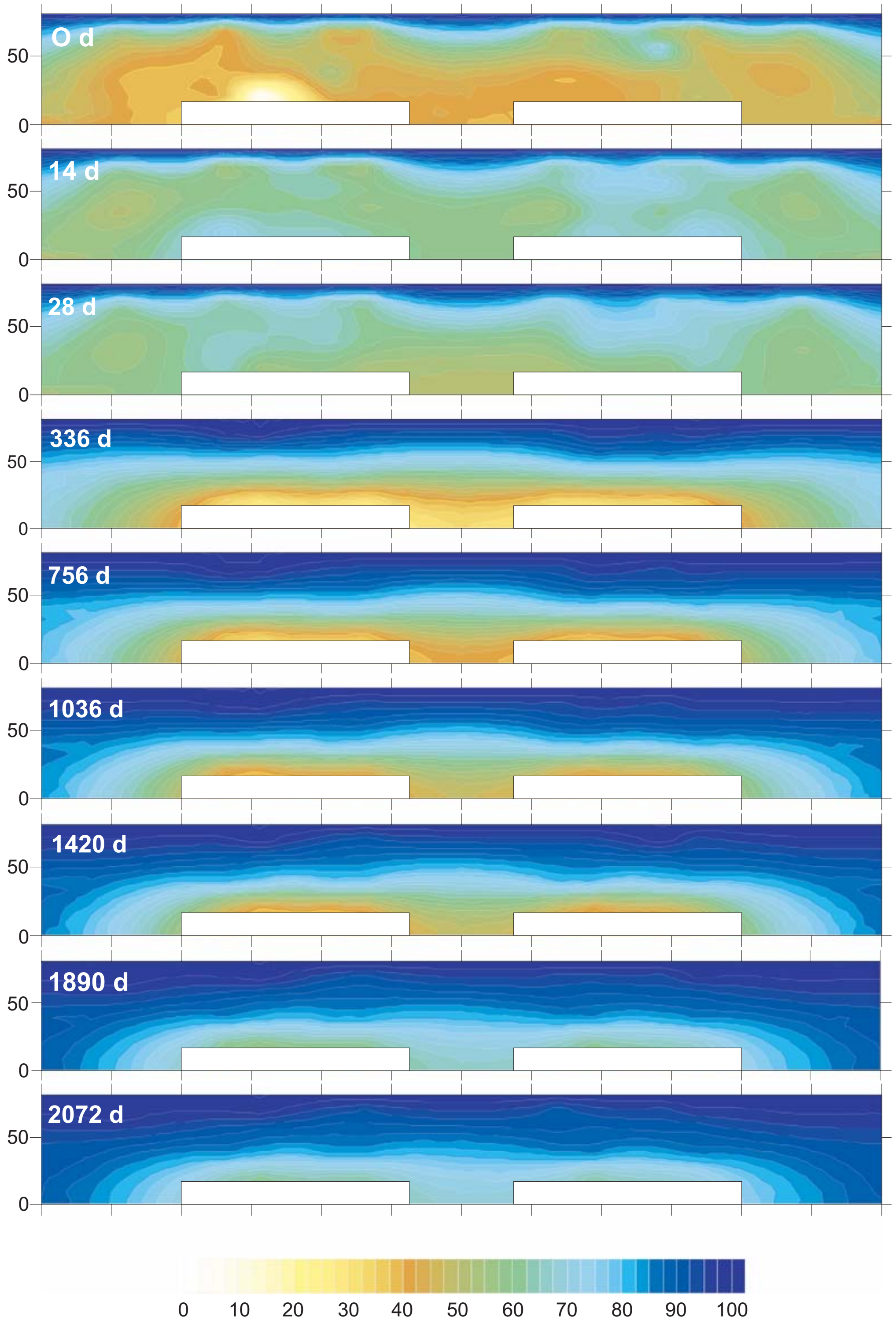

Figure 3.37: RHE evolution (%) during the experiment.

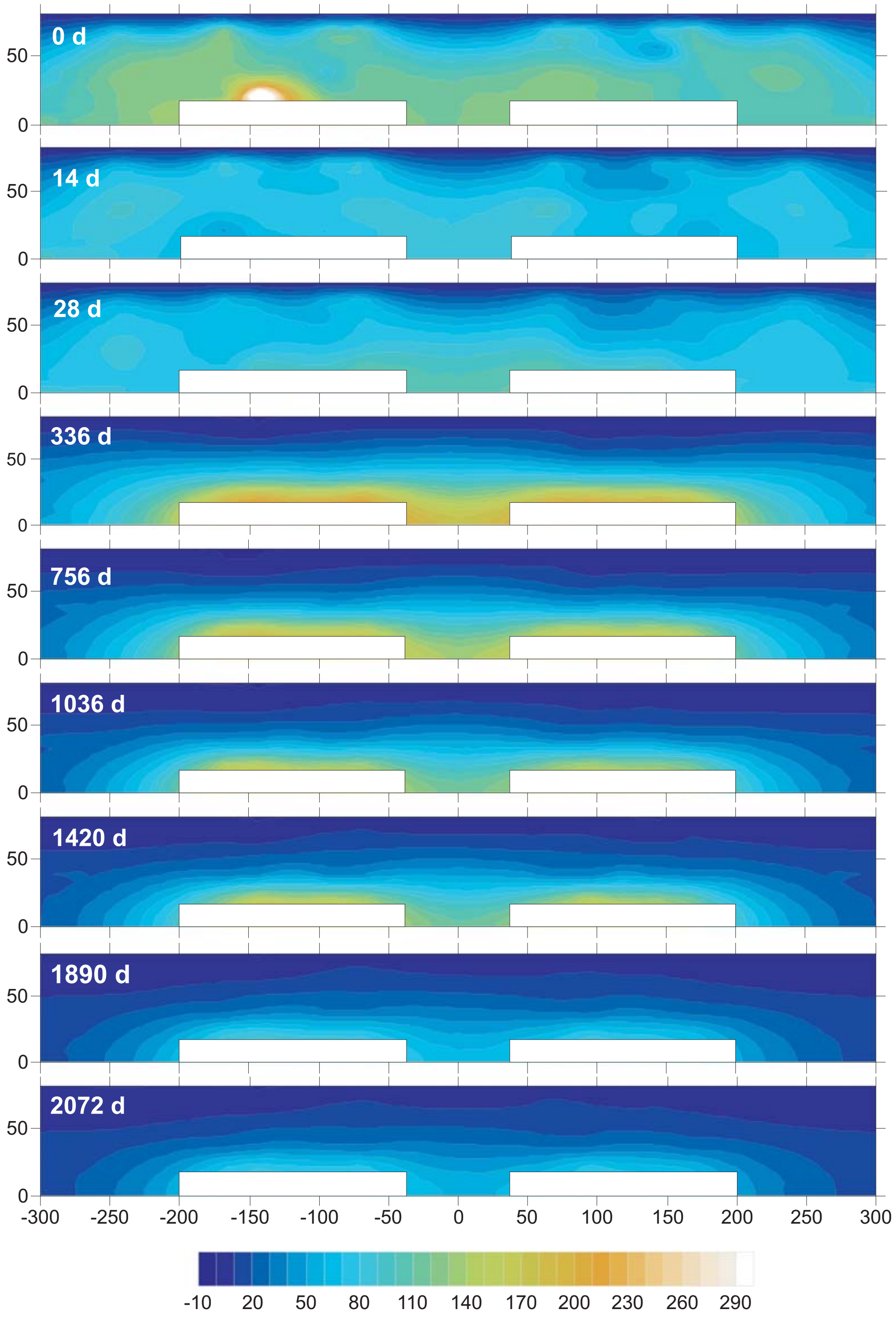

Figure 3.38: Suction evolution (MPa) during the experiment.

"cold" zones of the buffer, verified with measurements of the injected flow. The regime is regular and symmetric, except for the difference in magnitude. Modifications of the model are required to take this behaviour into account.

- A detailed revision of the test has not detected any artefacts that might modify the response of the sensors. Statistical tools have demonstrated that the observed signals are representative of the THM behaviour of the system [26, 27].

3.5.4. Database and instrumentation

- The database generated in the "mock-up" is valuable by itself. In particular, it has verified most of the hypothesis regarding the THM processes in the saturated/non-saturated transition phase of the barrier material, with water vapour.
- Comparison with actual values obtained from dismantling of the test will be the definitive trial of the THM instrumentation in the test, but the performance of the sensors and the results obtained encourage the continuation of the test for as long as possible.
- Furthermore, the measurement of relative humidity might provide information on the chemical evolution of the pore water within the barrier, to be validated with the chemical codes, allowing better understanding to be obtained as regards their implication on the HM properties of the saturated bentonite.

4. “In situ” test

4. “In situ” test

4.1. General description

The "in situ" test consisted of a full-scale simulation of a HLW disposal facility, in keeping with the ENRESA AGP Granito (Deep Geological Disposal, Granite) reference concept [5]. Performance of this test implied the placing of two electrical heaters, of dimensions and weight equivalent to those of the canisters in the concept, in a 2.28 m diameter drift excavated in granite, the entire space surrounding the heaters being filled with blocks of compacted bentonite to complete the 17.4 m of barrier for the test section. This test zone was closed with a concrete plug.

The test was installed in the underground laboratory managed by NAGRA, located in Grimsel (Switzerland), because it has an excellent infrastructure for large-scale tests, and because of the similarity between the Spanish and Swiss reference concepts.

In addition to the clay barrier, made up of 5331 bentonite blocks with a total mass of 115.7 t, and the heaters, 632 sensors of very diverse types were installed. The sensors were installed to monitor the different thermo-hydro-mechanical processes that occur in both the clay barrier and the surrounding rock throughout the entire life of the test. A series of artificial chemical tracers, specimens of different metals and gas collectors were installed in the test zone for the study of corrosion and transport phenomena.

A drift was specifically excavated for this test, in an area previously selected in accordance with the existing Grimsel laboratory database. To provide additional information, two exploratory boreholes were drilled in the area, practically parallel to the planned trace of the drift.

Following excavation of the drift, a detailed reconnaissance of its geometry and geology was performed and 19 boreholes were drilled from its interior, to instrument the rock mass.

A detailed hydrogeological study of the rock mass surrounding the drift was performed, using data taken from the existing boreholes in the area, the two boreholes made for the study, the walls of the drift and the 19 boreholes drilled from the interior of the drift.

The test was designed to function in an autonomous mode. Supervision, monitoring, and control were accomplished remotely from Madrid.

The first operational phase comprised five years of uninterrupted heating at constant temperature, and finished with the disconnection of the heater closest to the plug (Heater # 1). The corresponding part of the test zone was dismantled after a short cooling period and the remaining part was sealed with a new sprayed concrete plug. New sensors were installed in the buffer, and a second operational phase with the modified layout was started.

The FEBEX "in situ" test included an important component of demonstration; therefore, special attention was paid to the design and fabrication of the components (heaters, bentonite blocks, etc.), to transportation and handling within a space of reduced dimensions, to excavation of the drift, to the installation of all the components and to their sampling and status analysis following the first operational phase.

One objective of the test was to check the predictive capacity of the THM and THG models, based on the results from this test. There were, nevertheless, uncertainties relating to the hydraulic system of the rock mass: heterogeneity, parameters and initial and boundary conditions. These uncertainties were the underlying reason for performance of the "mock-up" test (Chapter 3).

This chapter presents a summarised description of the design, fabrication, installation, partial decommissioning and status analysis of the physical components of the test. It also includes a summary of the two operational phases of the test. The work is described in detail in references [28, 29, 30, 31, 32, 33, 34, 35, 36].

Also included are summaries of the hydrogeological characterisation and chemical analyses of the water at Grimsel, described in detail in references [37, 38].

4.1.1. Grimsel Test Site

The "in situ" test has been carried out at the Grimsel Test Site (GTS), operated by NAGRA and located at an elevation of 1725 m in the Swiss Alps, near the Grimsel Pass (Figure 4.1).

The laboratory consists of a series of excavated experimental drifts and caverns connecting with the main access tunnel for two underground hydroelectric power plants owned by the electricity company KWO.

The GTS starts at 1.02 km from the portal of the main access tunnel, at a depth of some 400-m relative to the surface of the terrain. The laboratory has a general service area and is equipped with the in-

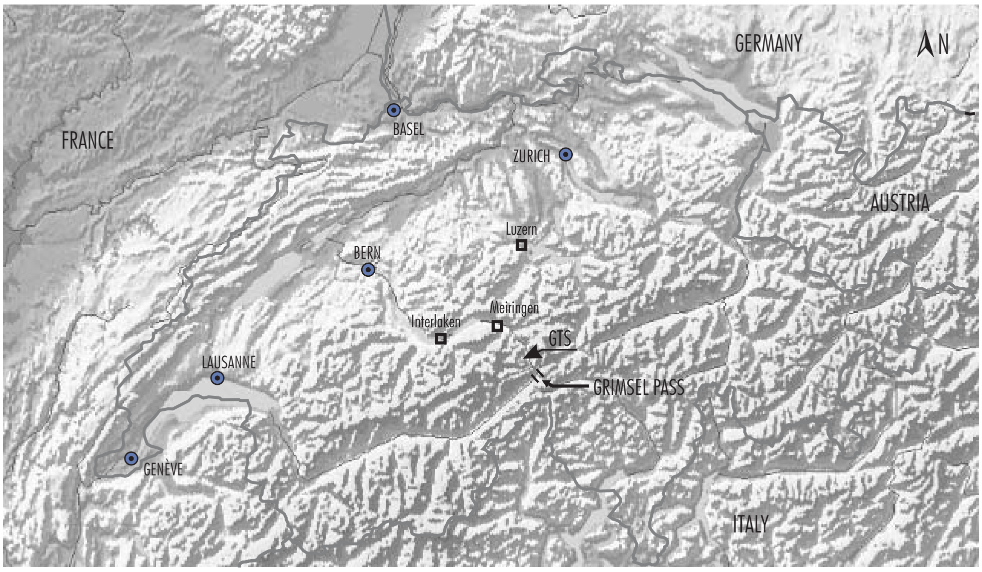

Figure 4.1: Location map of GTS.

frastructure required for the performance of large-scale tests.

Figure 4.2 shows a general view of the laboratory and the location of the FEBEX drift within it.

The GTS is accessible by road only from approximately May/June to October/November, depending on the year. For the rest of the year access is accomplished via the KWO service cable car, this limiting the transportation of heavy loads. This greatly affected the planning of the different phases of the project—the timing of all the installation and dismantling operations and, especially, the loading and unloading of materials and/or the use of heavy equipment—which had to be adjusted to the periods during which the GTS was accessible by road.

4.1.2. Test location and layout

4.1.2.1. Location and geometry

The FEBEX drift starts from the northern entrance of the GTS (Figure 4.2). The location of the drift portal was selected with a view to having an area allowing for the access of heavy equipment with relative ease. The alignment and length were selected to provide a test area that would contribute at least a minimum amount of water (Section 4.2) and thus provide the greatest possible degree of saturation in the bentonite during test performance.

The drift is circular in section with an average diameter of 2.28 m, has a length of 70.4 m, and was excavated with an ascending slope of 1% to permit natural drainage. The test zone is located in the last (dead-end) 17.4 m of the drift (Figure 4.3).

4.1.2.2. Excavation

The drift was excavated using a tunnel-boring machine (TBM) with a nominal diameter of 2.27 m. This diameter, slightly less than the 2.40 m of the AGP Granito reference concept, was dependent on the availability of this type of machine at the time the drift was to be excavated.

The drift was excavated between 25 September 1995 and 30 October 1995. Following the excavation, the actual diameters and roughness of the rock surface were measured with a laser profiler [29], the result for the test zone being an average diameter of 2.28 m, with a variation of ± 1 cm.

A mechanical rotating saw was used to enlarge the drift to the extent required for the concrete plug (Figure 4.3), to prevent damaging the rock around the drift. The enlargement was achieved by making a series of cuts perpendicular to the axis of the drift, using a circular saw, and then removing the intervening rock manually by means of wedges.

4.1.2.3. Test zone

Figure 4.3 shows the final arrangement of some of the main elements of the test following their installation in the drift, including the instrumented sections.

During the first operational phase, all the electrical and electronic equipment for heater power control and data acquisition and logging was located in the area known as the service zone. In this zone a concrete sill was constructed to facilitate the transportation and installation of the materials and equipment.

Between the service zone and the concrete plug is an intermediate zone of 3.5 m in length, designed to collect possible infiltration water from the test zone.

4.2. Test site characterisation

4.2.1. Hydrogeological characterisation

This section contains a summary description of the hydrogeological study of the rock mass in the area surrounding the FEBEX drift.

The goal of the study was to determine the parameters and the initial and boundary conditions of the hydraulic system of the rock mass, necessary for the THM and THG modelling of the test.

The analyses were performed using a three-dimensional numerical model capable of predicting infiltration flow into the drift and the piezometric levels of the surrounding area [37].

The hydrogeological study included and was based on the following information:

- *Geology*. This part of the study is based, fundamentally, on the mapping of the tunnels and on the logs of the borehole cores (observations of fracturing, water circulation, etc.) [39].
- *Geophysics*. Two radar surveys were carried out, one between boreholes BOUS-85.001 (BOUS-1), BOUS-85.002 (BOUS-2), and BOUS-85.003 (BOUS-3), and another between FEBEX-95.001

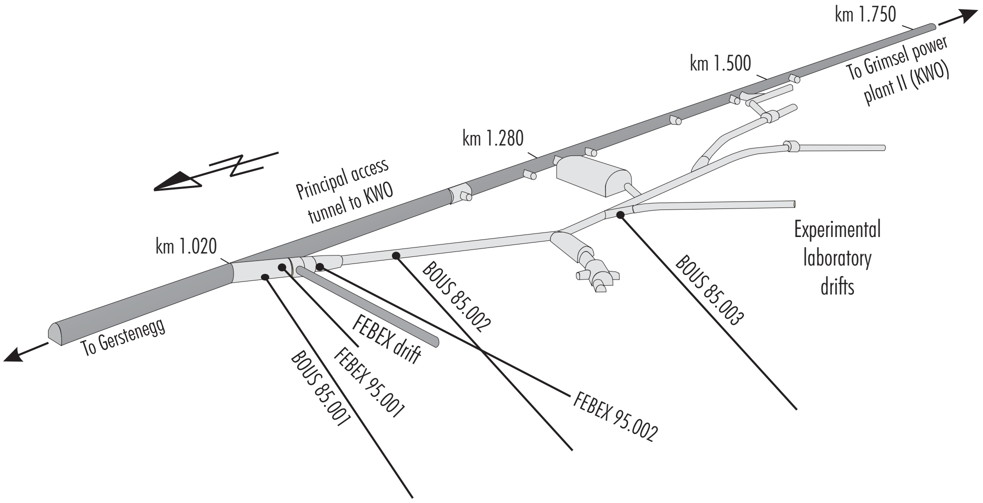

Figure 4.2: Schematic representation of the Grimsel underground laboratory

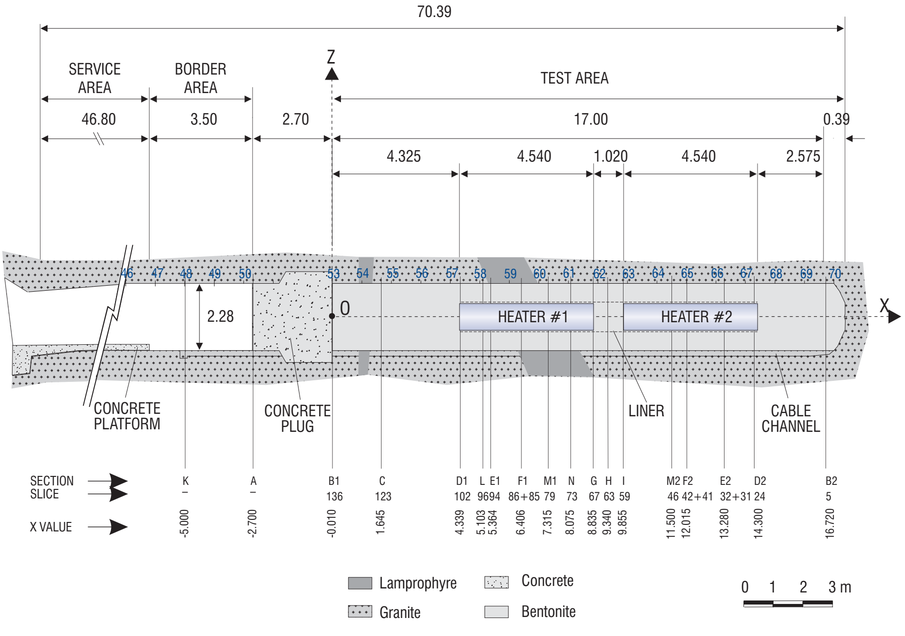

Figure 4.3: General layout of certain main elements in the test zone after installation, including instrumented sections.

(FBX-1) and FEBEX-95.002 (FBX-2). The locations of the boreholes are indicated in Figure 4.2. Also, seismic tomography was used between boreholes, on the plane defined by the alignment of boreholes BOUS-1, BOUS-2, and BOUS-3 and the wall of the longitudinal drift of the laboratory.

- *Hydraulic tests*. During the different phases of the project, a great number of hydraulic tests were performed (in single boreholes and between boreholes) with different duration times. The hydraulic tests were performed in sections isolated by packers, not only in boreholes BOUS (1 and 2) and FBX (1 and 2), but also in certain of the 19 boreholes drilled from the interior of the FEBEX drift (Figure 4.23).
- *Water flow gauging*. Water flow measurements were made at selected points in the drift area, as well as in the walls of the drift.
- *Piezometric level measurements*. All the sections (intervals) of the boreholes between packers were equipped with pressure sensors. The pressure history during the different phases of the study was obtained using a datalogger, and this will continue throughout the entire test.

4.2.1.1. GTS geology

The GTS is excavated in a predominately granite and granodiorite rock mass that has been affected by various episodes of fracturing [39]. The following geologic features may be noted to be relevant to the regional water flow (Figure 4.4):

- Shear zones S1+ S2, of azimuth of the dip/dip 140-150 / 80-90
- Shear zones K and lamprophyre dikes, of azimuth of the dip/dip 205-220 / 80

The shear zones in this area have a thickness of 5 m to 20 m and oozing may be observed at their intersection with the walls of the tunnels, indicating their relevance as areas of preferential flow. The lamprophyre dikes are also thick (up to several meters), but their role with respect to the flow is not as important as that of the shear zones. The area of preferential flow in the dikes is the contact surface between the lamprophyre and the host rock; it is not surprising, therefore, that a large number of locations of ooz-

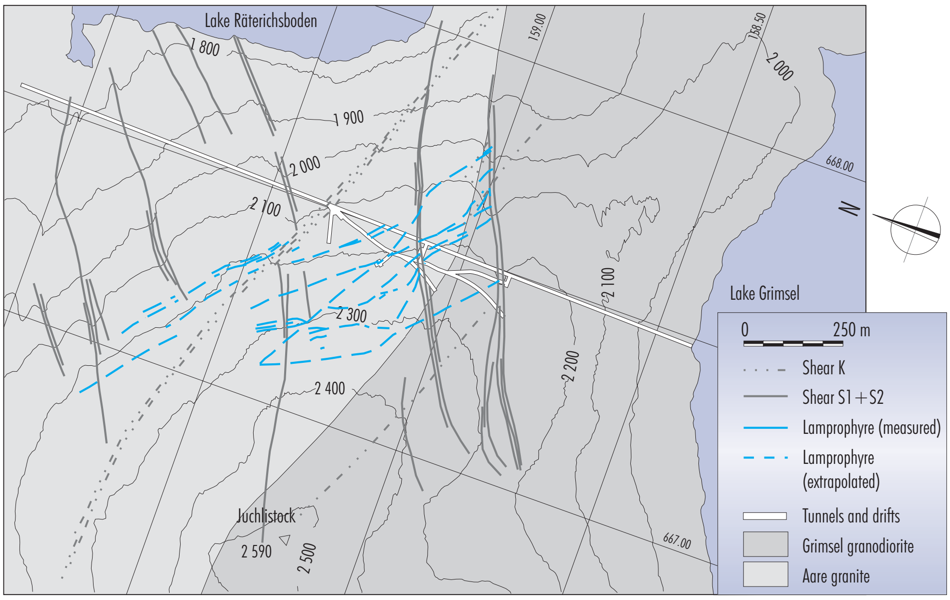

Figure 4.4: Simplified regional geologic map.

ing should be found at the intersections of the dikes with the walls of the tunnels. Minor fractures parallel to the principal direction have been observed in some of the thicker lamprophyre dikes. These fractures increase hydraulic conductivity in the direction of their planes and decrease it in the direction perpendicular to them. Consequently, the hydraulic conductivity of the dikes is anisotropic.

The most relevant shear zones and lamprophyre dikes may be superficially mapped. Figure 4.5 shows a geologic cut from the surface to the elevation of the tunnels. The FEBEX drift, found in the extreme northern part of the GTS, is limited by two main shear zones (Figure 4.4 and Figure 4.5).

4.2.1.2. FEBEX drift geology

Figure 4.6 shows a geological map of the drift, where the last 17.4 m corresponds to the test zone. This zone (between meters 53 and 70 along the drift) is broadly characterised by a medium-high density of fracturing, together with lamprophyre dikes and open fractures.

At about meter 20, the drift cuts a set of fractures with the same azimuth as the shear zones. This set of fractures is considered to constitute another shear zone (unmapped at the surface) because of its high conductivity (with water flow of the order of 30 ml/min for the set of fractures, which is considered high for the GTS and comparable to other shear zones).

4.2.1.3. Estimation and measurement of water flow into the FEBEX drift

The specifications of the project required that the test zone be selected such that the flow of water into it would be between 5 and 15 ml/min.

Estimation of flow prior to excavation of the drift

Boreholes FBX-1 and FBX-2 were drilled during the summer of 1995 for investigation of the area surrounding the planned drift location, in order to fix its definitive position. Hydraulic tests were carried out in the boreholes. The results of the tests were used to estimate the anticipated flow of water to the drift. The flow of water estimated from FBX-2 (between

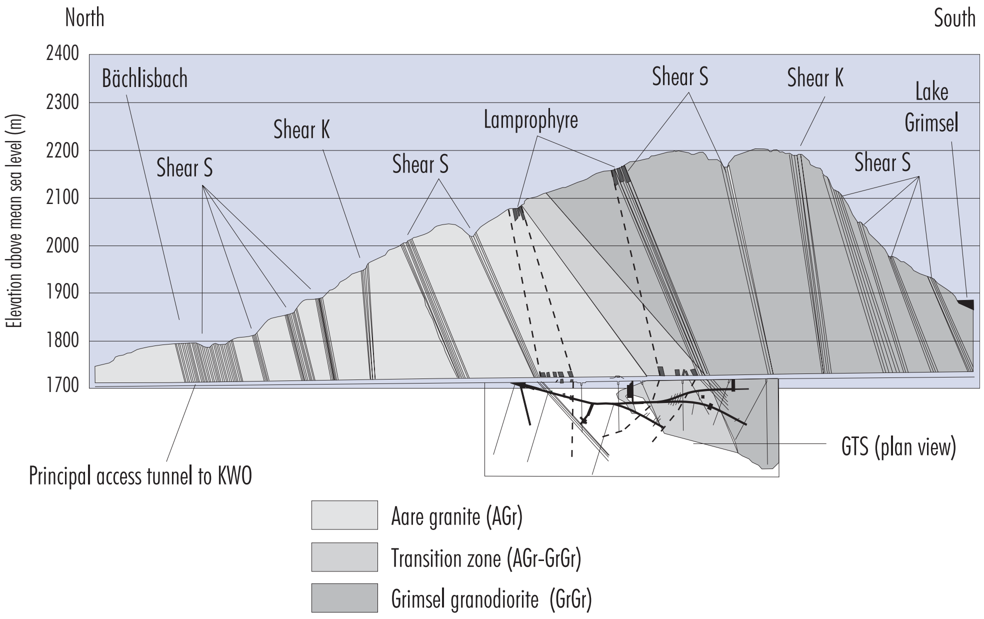

Figure 4.5: Geologic section of the Grimsel area, showing the major geological structures and their positions relative to the KWO and GTS tunnels.

meters 62 and 74), interval 3 data, was the one that best met the requirements of the project, as a result of which it was decided that the FEBEX drift should be located in the vicinity of this borehole.

Measurement of drift inflow

As a basic datum for the hydrogeological study, it was necessary to measure the actual flow of water into the drift following excavation. It was also fundamentally important that flow be measured during excavation, to determine the actual conditions, and that excavation be terminated when a length (test zone) with the required flow had been reached.

The traditional methods of measuring flow were inadequate for the excavation phase. Therefore, a new method was developed to measure the moisture from the walls of the drift. This method consisted of placing an absorbent material of known weight on the wall; this material absorbed water over a known period of time and was then re-weighed. The flow of water was the difference in weights divided by the measured time. The method is quick and of proven reliability; furthermore, it is relatively inexpensive. Its disadvantages are the dependence of the results on the properties of the material used, on initial water content and the duration of the measurements, on the variability of the atmospheric conditions and on the reliability of extrapolating the values to long-term conditions [37].

Considering the various uncertainties inherent to the method, the range of variations in the values of the different measurements performed in the 17.4 m (test zone) of the drift was small from the practical point of view, 4.5 ml/min to 8.5 ml/min.

4.2.1.4. Hydrogeological analysis and modelling

The conceptual model included an area of Aare granite mass, limited by two shear systems (together called the shear system S1+ S2). These two systems were taken as boundaries, because of their high transmissivity and on the assumption that they attenuate the effects of all the tests carried out between them. The rest of the boundaries were selected on the basis of the same criteria (Figure 4.7).

Fundamentally, the following structures have been included in the conceptual model:

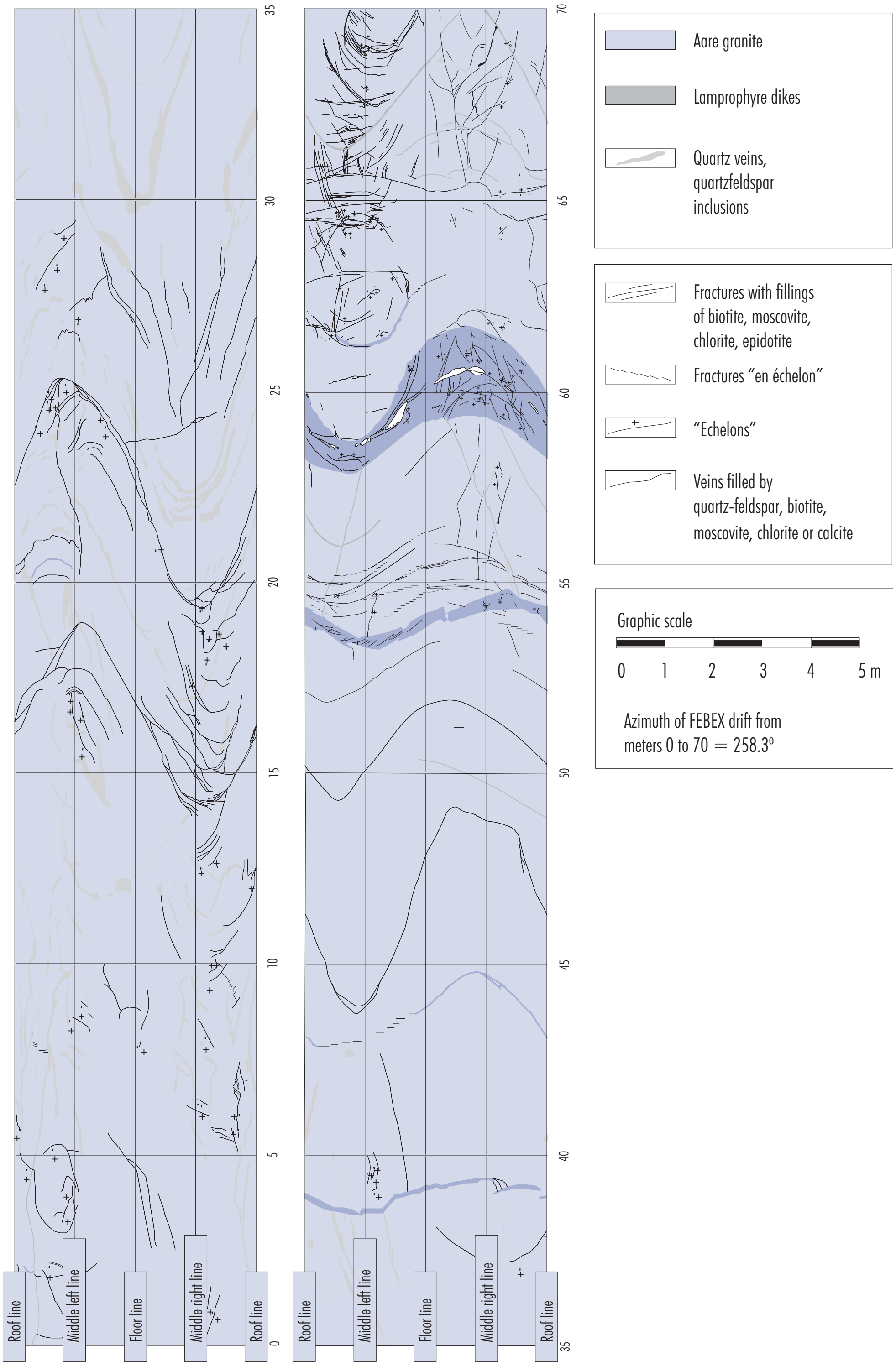

Figure 4.6: Geological map of FEBEX drift.

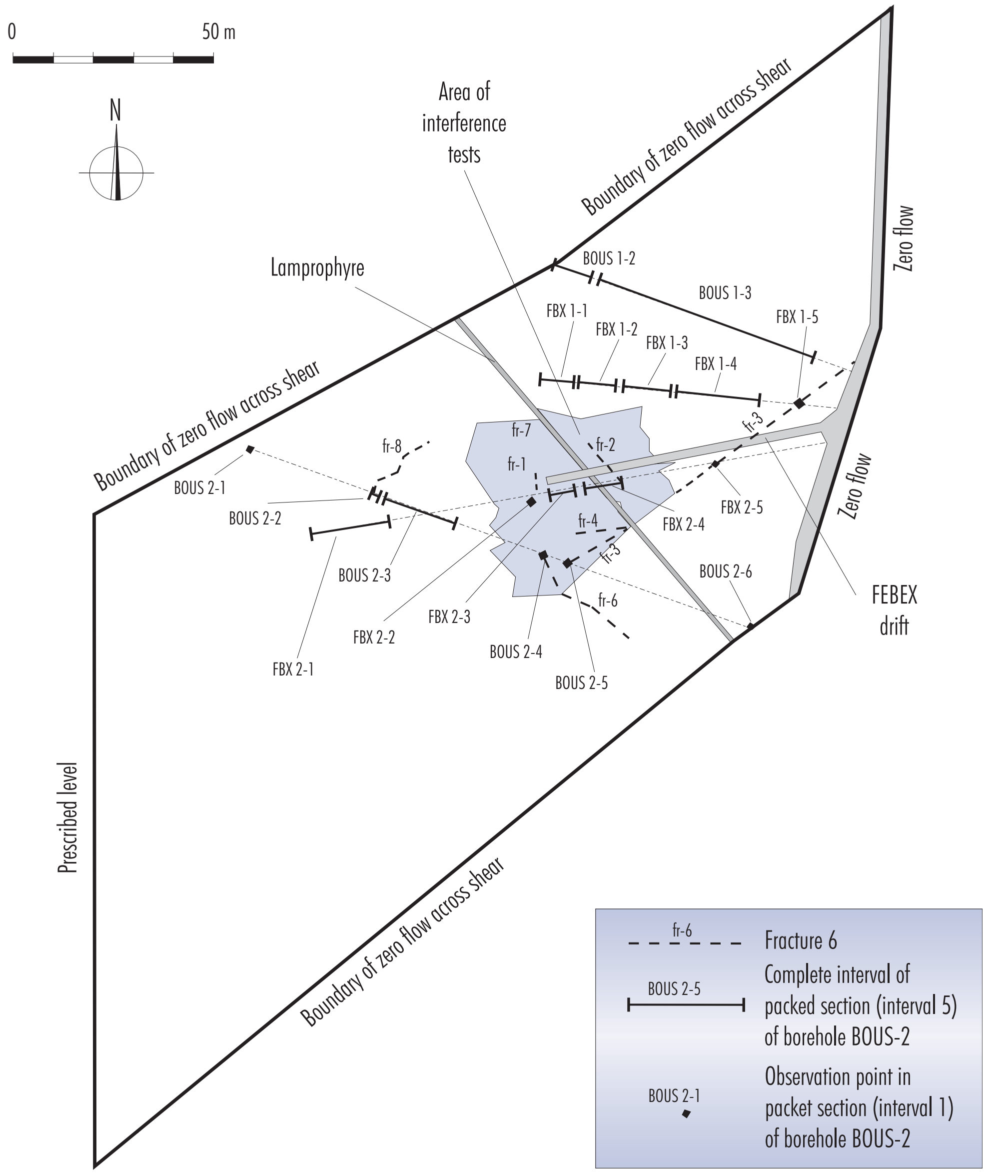

Figure 4.7: Plan view of structures represented in the flow models. Boundary conditions.

- Lamprophyre dikes. These are structures of regional scale, identified from geological mapping, hydraulic testing, geophysics, etc. It was observed, with the help of the tests, that the areas of contact with the host rock are planes of major transmissivity, this confirming a marked direction of anisotropy.

- Fracture 1 (fr-1). This fracture was identified in the hydraulic tests and is located a few meters from the dead-end of the drift.

- Fracture 2 (fr-2). As in the previous case, this fracture was identified during hydraulic testing, and also in the geologic mapping of the drift. It is the “en échelon” fracture.

- Fracture 3 (fr-3). The available data (hydraulic testing, geophysics, mapping) point to this fracture being large scale, although it is not continuous as has been represented in the model.

Five 3-D models were developed previously, using this conceptual model, for calibration of the five tests of interference performed in the boreholes drilled from the interior of the drift. These models are known as “interference tests”.

In addition to the aforementioned structures, there are others (fr-4, fr-6, fr-7, and fr-8), of a more local character, that have been identified fundamentally from hydraulic testing and with the help of the borehole cores.

Taking this conceptual model as a basis, four different models were calibrated, these corresponding to the four different water flows defined by the following conditions:

- Temporary conditions—two different periods of the project, before and after excavation of the FEBEX drift.
- Geometric conditions—heterogeneity of the shear planes used as boundaries. This heterogeneity is manifested in areas of less transmissivity closer to the FEBEX drift.

The four models are called as follows:

- LAR-SIN—homogeneous shear planes, without drift
- COR-SIN—heterogeneous shear planes, without drift
- LAR-CON—homogeneous shear planes, with drift
- COR-CON—heterogeneous shear planes, with drift

In the post-drift phase excavation models, a specific area measuring 15 m in radius around the test zone was included. For this area, the results of the interference test models were included directly, these having served to better identify the structures, due to the large quantity of information available for this area. The rest of the model has been represented as an equivalent porous medium (rock matrix), with superposition of the few identified fractures (fractures 6 and 8, see Figure 4.7). In this case, the hydraulic conductivity of the rock matrix engulfs that of the rest of the existing fractures not included in the model. In both areas, the rock matrix has been treated as anisotropic.

Discretisation

The model has been discretised using:

- Triangular prisms for the rock blocks
- Tetrahedral for adaptation of the boundaries of the tunnel borders
- Triangles in 2-D to represent planes (fractures, faults, and shear zones)
- One-dimensional elements to represent the boreholes

After developing a 2-D projection of the entire geometry to be represented, a 3-D mesh was generated (Figure 4.8).

Calibration

The results used as initial parameters and preliminary information for calibration were those obtained from the models of the interference tests. For the structures that do not appear in the interference tests, the results used were those obtained from interpretation of the hydraulic test in which they do appear.

The models were calibrated assuming steady-state conditions. A standard deviation of 1 was assigned for all levels, except for those that are supposed not to have reached the steady state.

The lines of equal piezometric level, as well as the differences between the measured and calculated levels, are shown in Figures 4.9 and 4.10 (for the pre-drift excavation models) and in Figures 4.12 and 4.13 (for the post-drift excavation models). Figures 4.11 and 4.14 show the 3-D calculated levels for the pre and post-excavation models, respectively.

Discussion and results

The parameters obtained with the models are coherent. The number of unknown parameters is relatively high compared to the measured levels, which would have caused the model to produce an unstable estimate if a good hydraulic characterisation had not previously been accomplished. In fact, the quantitative data at regional scale and in the vertical direction are scarce, since the majority of the information is found near the horizontal plane that passes through the FEBEX drift.

The quality of the models must be examined by comparing them at different scales—drift and regional. The piezometric levels in the vicinity of the drift are well reproduced. Furthermore, the hydraulic

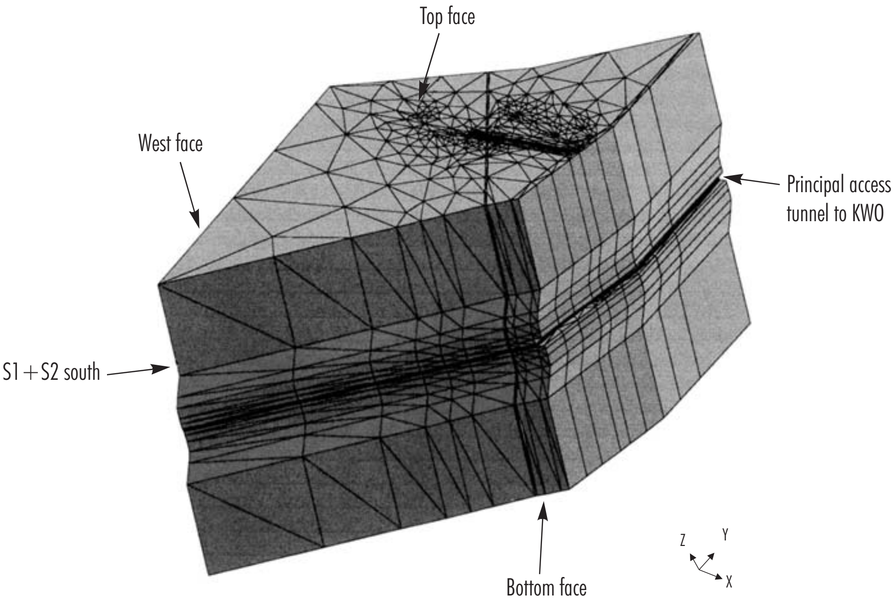

Figure 4.8: 3-D mesh.

parameters estimated under different conditions of flow in the large-scale models (LAR-SIN, COR-SIN, LAR-CON, and COR-CON) are very close one to the other and with respect to those derived from the interference tests. The calculated flows of water for the FEBEX drift are within the range of those measured, even though they were not used in the calibration.

The distribution of piezometric levels in the vicinity of the drift is radial, with local heterogeneities arising as a result of the more transmissive fractures. The piezometric gradient at the dead-end of the drift is very large as the infiltration flows concentrate at this point and decrease toward the entrance.

The contact planes of lamprophyre/host rock are areas of preferential flow, as may be observed in their intersections with the drift. Direct observations show a strong anisotropy in the geologic structure, such anisotropy having been taken into account in the large-scale models.

Two questions are posed in the performance assessment (PA) exercises: the possibility of changes in the value of hydraulic conductivity in a ring around the drift, and the effect of a “flow barrier” formed by the desaturation front in the area immediately surrounding the drift wall. The answer to these questions was not within the scope of this study, but some indirect results have been obtained. Firstly, in the repetition of tests at intervals following excavation of the drift, the distribution of pressures and the interpretation of the interference tests point to a decrease in hydraulic conductivity in the area surrounding the wall of the drift, although this reduction is not particularly large (less than an order of magnitude). Secondly, the ventilation of the drift produces immediate responses in the intervals that are better connected with it. From these data it may be inferred that the desaturation front is unlikely to act as a “flow barrier”; it is more likely that the barrier effect might be attributed to mechanical effects.

The parameters of the rock mass, the relevant geological features and the water flow into the drift have been estimated by means of different models, at different scales. The piezometric levels and the measured flow of water into the drift are well reproduced by these local parameters; thus it may be concluded that the characterisation is robust.

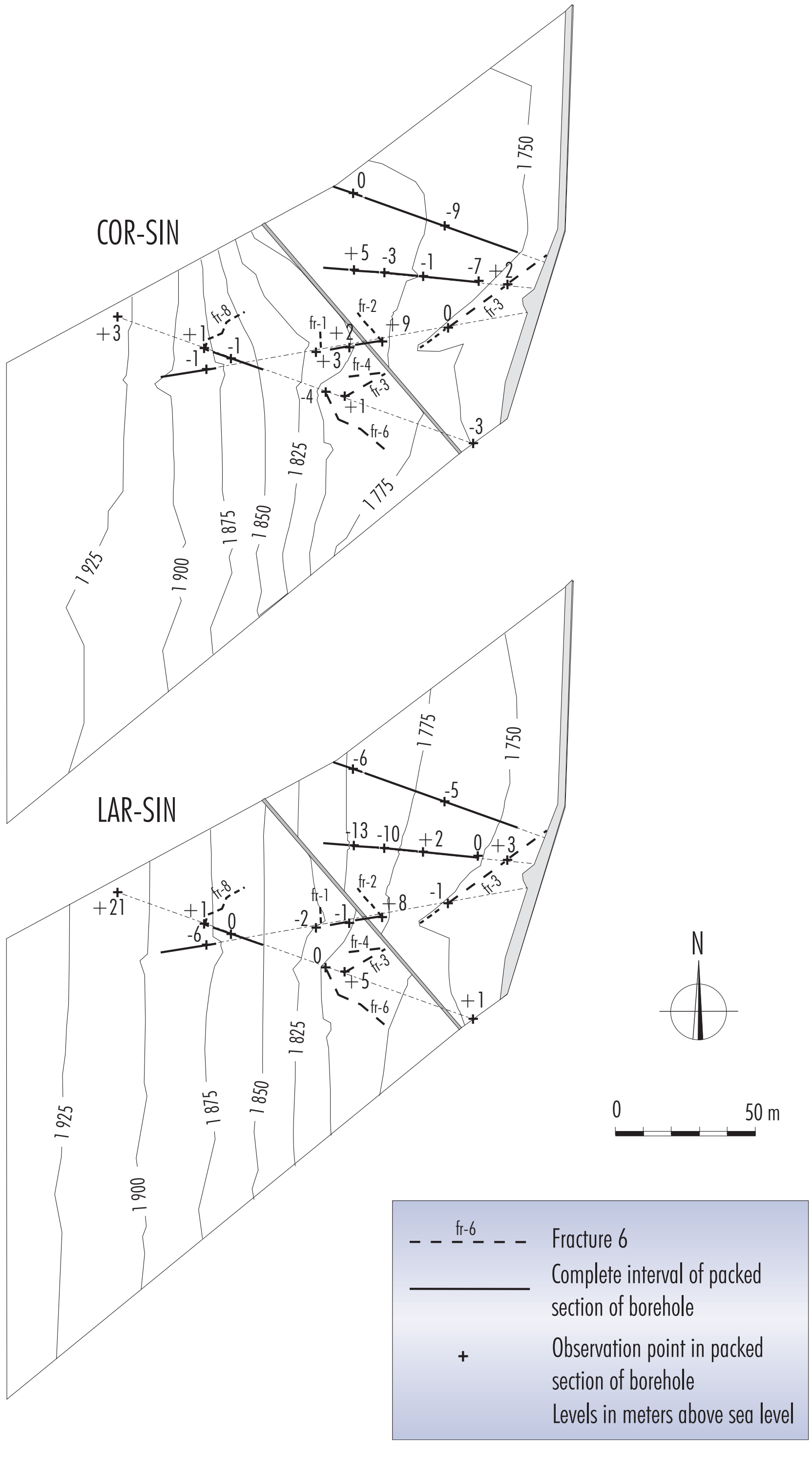

Figure 4.9: Curves of equal piezometric levels and residuals (differences between the measured and calculated levels) obtained with the LAR-SIN (bottom) and COR-SIN (top) models (plan view, at elevation of drifts).

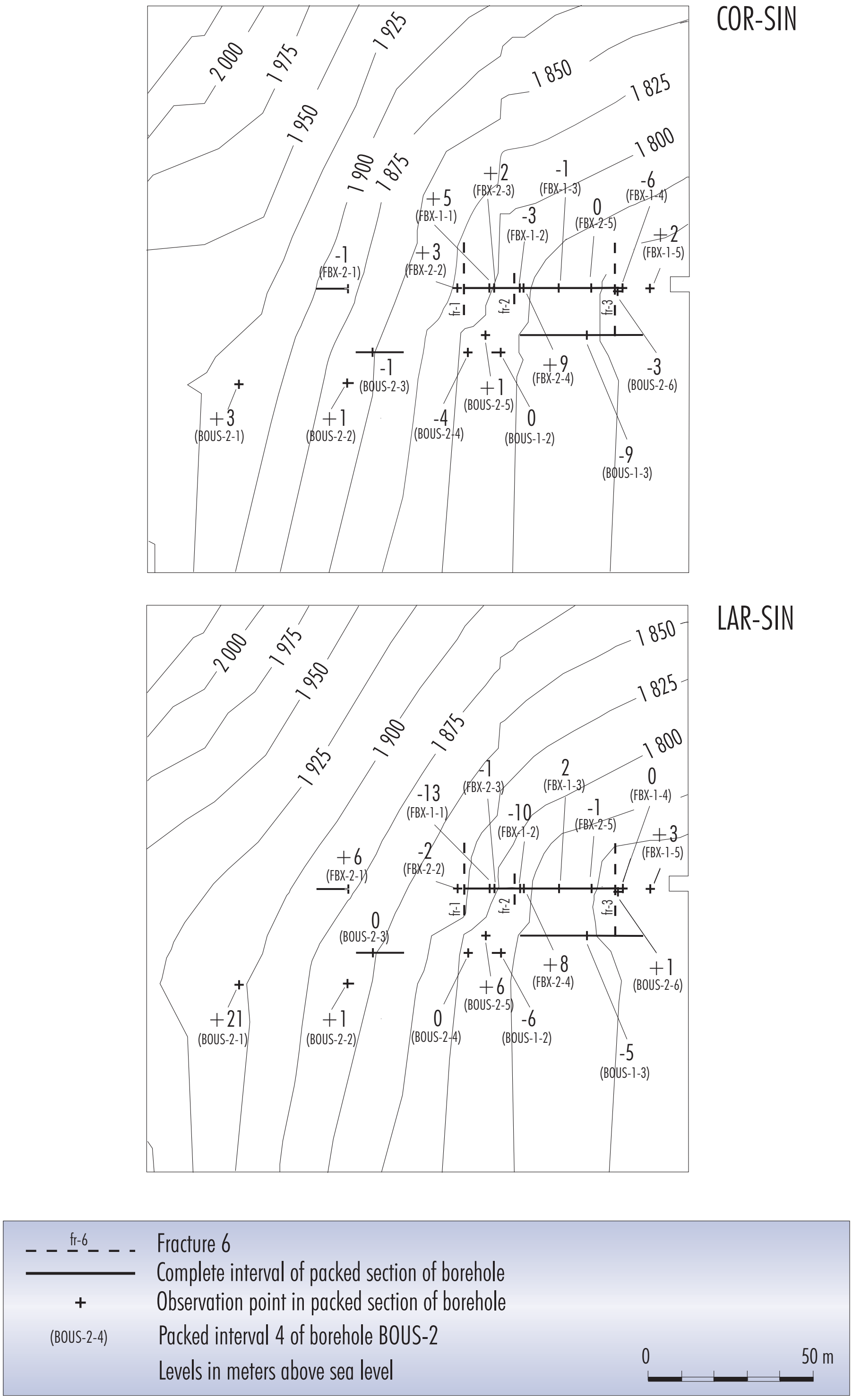

Figure 4.10: Curves of equal piezometric levels and residuals calculated for the LAR-SIN (bottom) and COR-SIN (top) models (vertical section, passing through the axis of the FEBEX drift).

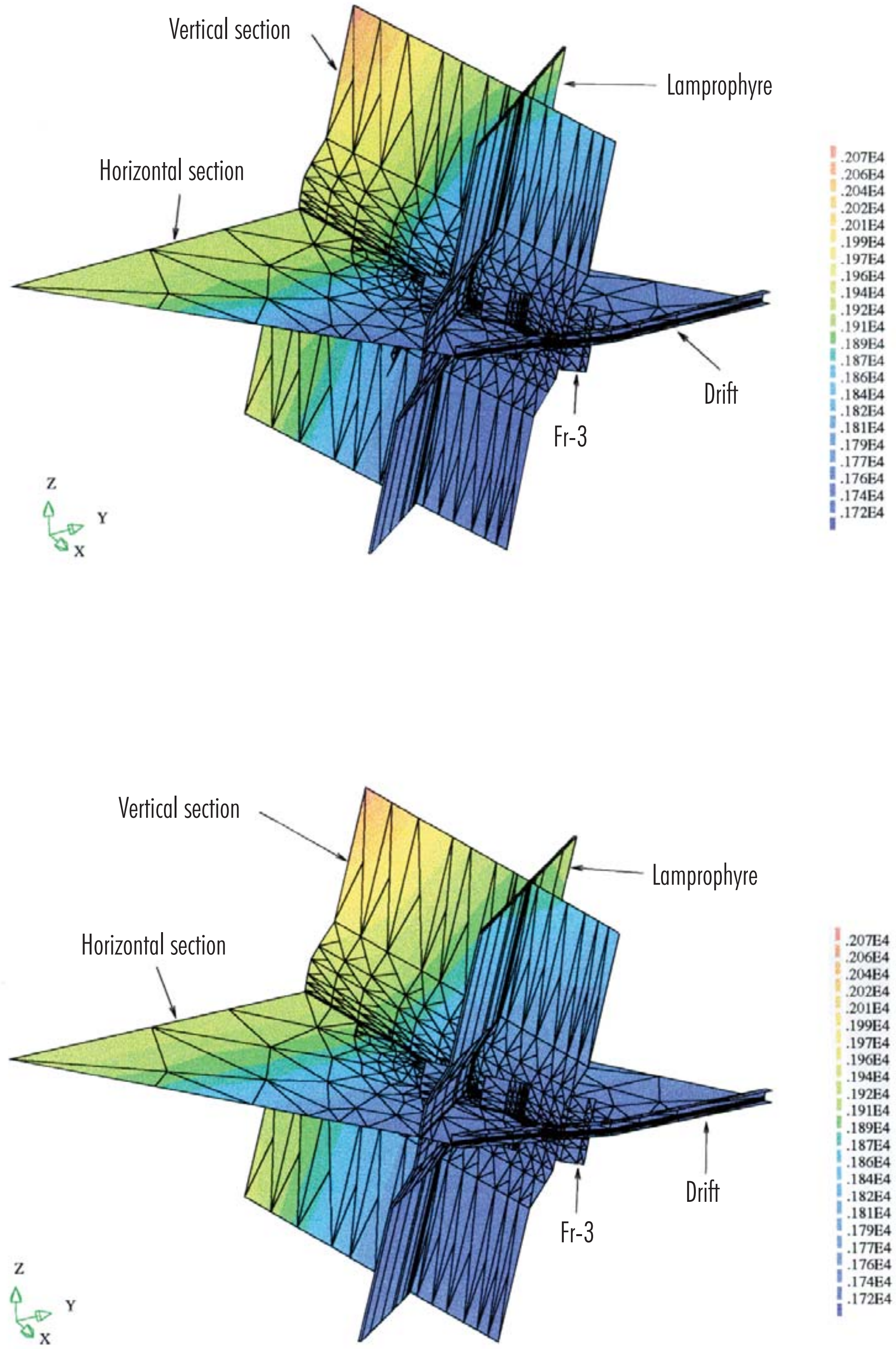

Figure 4.11: Calculated piezometric levels with COR-SIN (top) and LAR-SIN (bottom) models

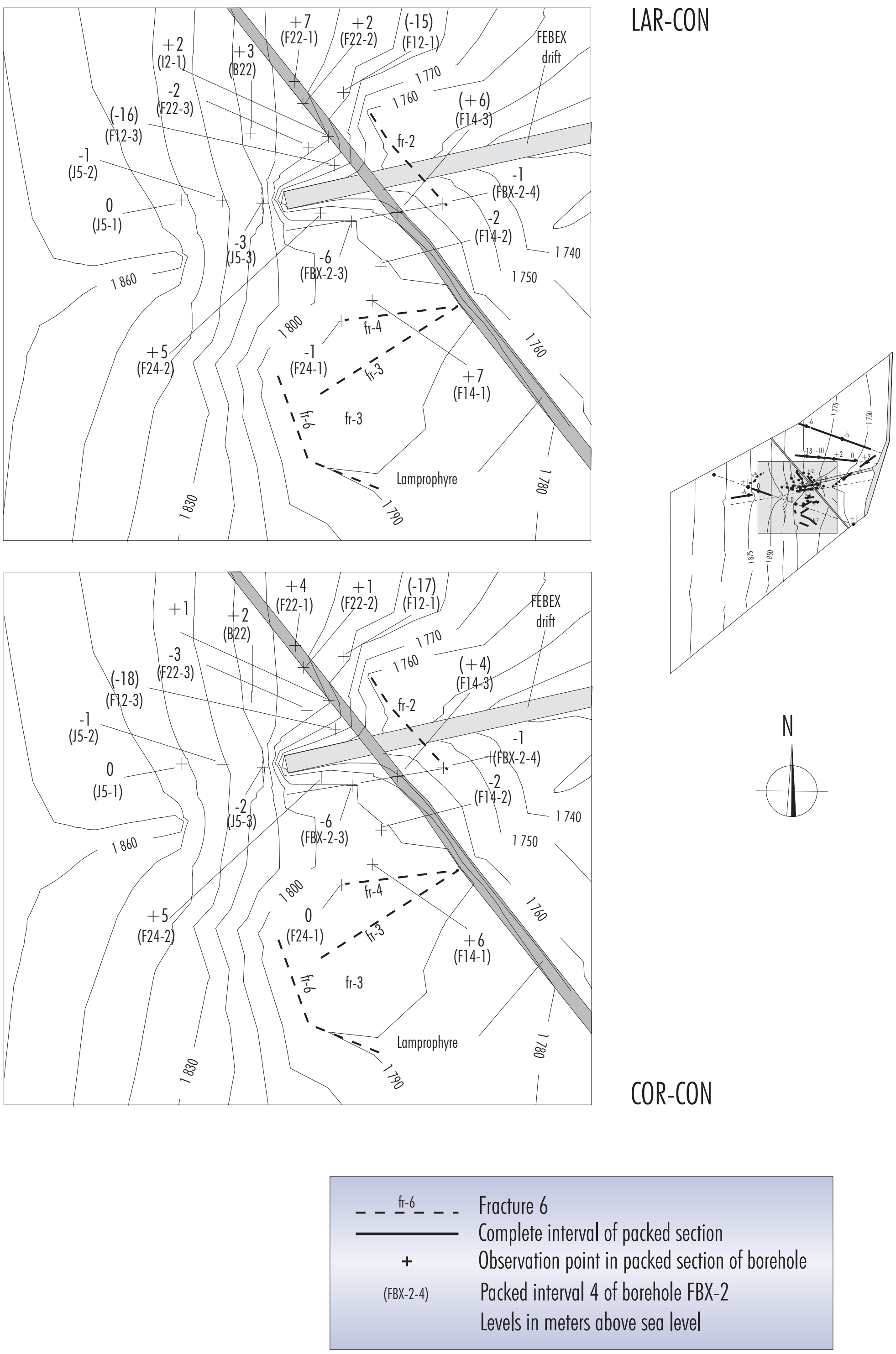

Figure 4.12: Plan view of the calculated piezometric levels and residuals with the models COR-CON (bottom) and LAR-CON (top). The numbers within brackets are non-stabilised measurements.

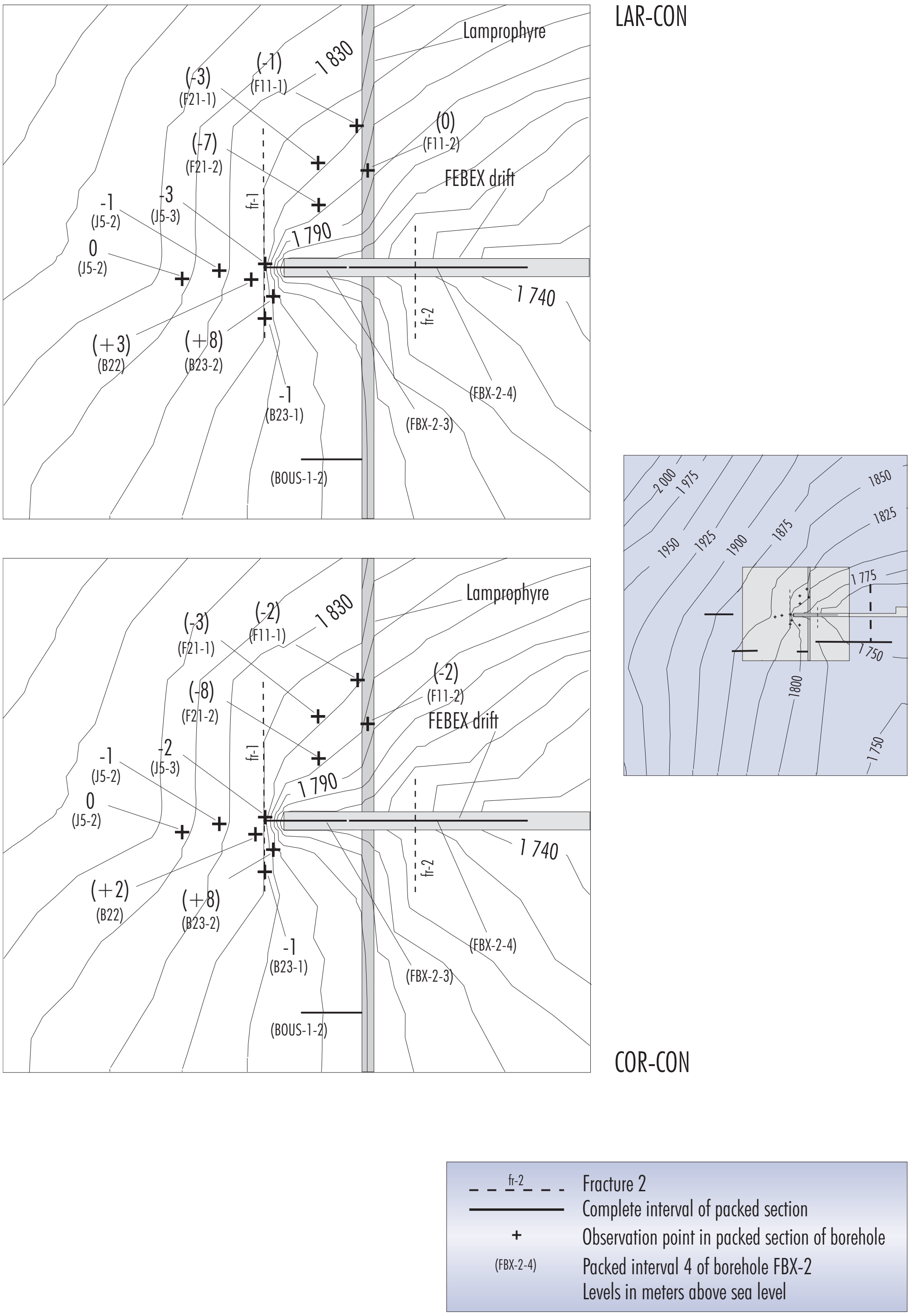

Figure 4.13: Vertical section with calculated piezometric levels and residuals, with the COR-CON (bottom) and LAR-CON (top) models. The numbers between brackets are non-stabilised measurements.

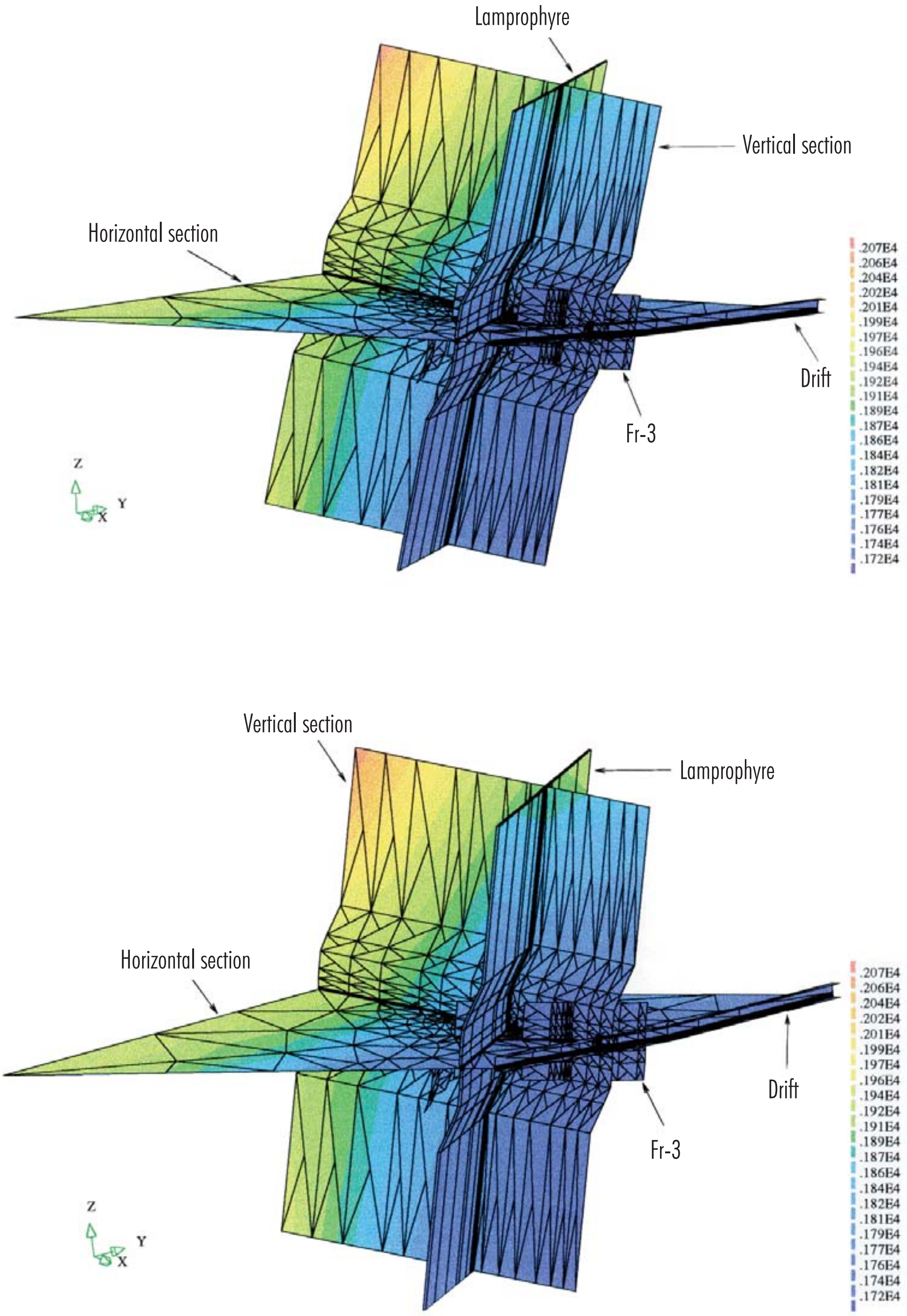

Figure 4.14: Calculated piezometric levels with the LAR-CON (top) and COR-CON (bottom) models.

4.2.1.5. Conclusions

The hydraulic regime in the area immediately surrounding the drift (<10 m) is clearly radial and, in the more homogeneous sections, may be considered quasi 2-D. At a distance of 10-20 m from the wall of the drift (in boreholes drilled from the interior of the drift), the distribution of the piezometric levels loses part of its "two-dimensionality", even in the more homogeneous boreholes. At a distance of 50 m from the drift the flow is oriented in accordance with the local regime (Jüchlistock mountain and Aare river), where the Grimsel tunnels play an important role in drainage. The vertical and horizontal hydraulic gradients are very high, as corresponds to the mountainous characteristics of the area and to the low permeability of the medium.

At a distance of 50 m, the hydraulic pressure along a horizontal plane through the axis of the drift may be considered as amounting to 0.7 MPa.

The most frequent hydraulic conductivity value in the tests was $1 \cdot 10^{-11}$ m/s. This value may be considered as representing the hydraulic conductivity of the rock matrix.

The main heterogeneities intersecting the drift in the test zone are as follows, measured from the concrete plug (along the left wall of the drift): a fractured area at 16.0 m, the lamprophyre dike at 7.0 m and the "en échelon" fracture at 2.5 m.

The total flow of water calculated for the entire test zone (17.4 m) varies from 5 ml/min (in the COR-CON model) to 8.2 ml/min (in the LAR-CON model). These values are similar to the measured flows. The flow into the drift is dependent on the more important heterogeneities and on the rock matrix (including the microfractures). The equivalent hydraulic conductivity required to generate these flows, assuming a homogeneous rock mass surrounding the drift, may range from $5 \cdot 10^{-11}$ to $8 \cdot 10^{-11}$ m/s.

4.2.2. Hydrochemical characterisation

The water from some of the boreholes drilled from the interior, or in the vicinity, of the FEBEX drift, was characterised [38]. Sampling of the hydraulically active areas identified in the hydrogeological study was carried out in July 1996. The boreholes selected were: SF14-3[1] (representative of the water in the area of the lamprophyre dike), SF24-1, SB23-1 and SJ5-3 (representative of the water in the area of Heater #2) and the horizontal borehole BOUS-2-2 (representative of the water in the fractured area). The locations of the boreholes are indicated in Figures 4.2 and 4.23.

The boreholes were drilled into little-altered Aare granite, and cut some lamprophyre, quartz, and aplite dikes. The discontinuities between the granite and the lamprophyre are, in principle, the more significant structures, both hydraulically and chemically.

During sampling, precautions were taken to minimise alterations to the natural condition of the water: sampling was performed in a sealed chamber with a controlled nitrogen (99.9999% pure) atmosphere; with pumping from each interval isolated by packers until the volume of extracted water was equivalent to at least three times the volume between the packers; and measurement of the physico-chemical parameters pH, Eh, electric conductivity, dissolved oxygen, and temperature, until stability was reached.

The analytical results of the samples are presented in Table 4.1. The water is diluted with low contents of dissolved salts (<100 μS/cm) and has a pH close to 9. The composition of the water is bicarbonate-fluoride sodic-calcic, in accordance with the major components.

4.2.3. Other rock characterisation data

4.2.3.1. Deformability and strength

During the pre-operational stage, unconfined compression tests were carried out on samples taken from the boreholes drilled from the interior of the FEBEX drift. The results are shown in Table 4.2.

4.2.3.2. Retention curve

The retention curves for three granite and two lamprophyre samples extracted from the boreholes drilled from the interior of the FEBEX drift were determined. For both materials, air entry values of between 0.5 MPa and 5.0 MPa were deduced. The retention curves obtained are shown in Figure 4.15.

The porosity accessible to the water, deduced from the water content in saturated conditions, is of the

---

[1] *The first number forms part of the identification of the borehole, and the second indicates the interval between packers where the sample was taken.*

Table 4.1
Chemical composition of water from boreholes drilled from the interior, or in the vicinity, of the FEBEX drift

	SF24-1	SB23-1	BOUS-2-2	SJ5-3	SF14-3
Date, in July 1996	11	12	15	16	18
Temperature, in ºC	14.3	15.1	13.8	17.4	17.6
pH-laboratory	8.6	8.4	8.4	8.2	7.3
pH-"in situ"	9.1	9.1	9.3	9.4	8.9
CE "in situ", in μS/cm	76.3	80.3	83.7	82.7	194.3
CE laboratory, in μS/cm	71.3	74.7	72.7	75.7	86.3
CE calculated, in μS/cm	69.3	72.0	69.5	73.3	79.5
Eh, in mV	15.3	55.3	101.3	84.0	418.0
Alkalinity, in mg/l $CaCO_3$	19.7	20.0	20.1	19.8	19.5
HCO_3^-, in ppm	24.0	24.4	24.5	24.1	23.5
Total dissolved solids	61.4	63.9	61.4	63.3	65.3
log P(CO_2)	-4.789	-4.781	-5.006	-5.104	-4.6045
I(x10^{-3}), in M	1.035	1.08	1.04	1.11	1.105
Charge balance	-3.545	-3.31	-3.07	-4.06	0.29
F^- , in ppm	3.87	4.47	3.97	4.37	4.23
Cl^-, in ppm	0.36	0.56	0.37	0.52	3.93
NO_2^-, in ppm	<0.1	<0.1	<0.1	<0.1	<0.1
NO_3^-, in ppm	<0.1	<0.1	<0.1	<0.1	1
NH_4^+, in ppm	<0.1	<0.1	<0.1	<0.1	<0.1
PO_4^{3-}, in ppb	<10	<10	<10	<10	<10
SO_4^{2-}, in ppm	7.37	7.30	7.03	7.80	7.37
Br^-, in ppm	0.021	0.056	<0.01	<0.01	0.01
I^-, in ppm	<0.02	<0.02	<0.02	<0.02	<0.02
SiO_2, in ppm	9.53	9.83	9.43	9.67	9.10
Al, in ppm	<0.05	<0.05	<0.05	<0.05	<0.05
As, in ppb	0.62	0.42	0.42	0.30	0.26
Ba, in ppb	0.95	0.90	0.82	1.10	1.90
Be, in ppb	<0.1	<0.1	<0.1	<0.1	<0.1
Bi, in ppb	<0.1	0.8	<0.1	<0.1	0.32
B, in ppm	<0.05	<0.05	<0.05	<0.05	<0.05

Table 4.1 (continuation)
Chemical composition of water from boreholes drilled from the interior, or in the vicinity, of the FEBEX drift

	SF24-1	SB23-1	BOUS-2-2	SJ5-3	SF14-3
Cd, in ppb	0.50	0.53	0.61	1.00	0.45
Ce, in ppb	<0.1	<0.1	<0.1	<0.1	<0.1
Ca, in ppm	7.17	7.43	6.73	7.40	7.13
Co, in ppb	0.29	0.13	0.10	0.17	<0.1
Cr, in ppb	0.45	0.31	0.12	0.38	0.29
Cu, in ppb	1.7	0.7	1.5	0.4	1.5
Hg, in ppb	<0.2	<0.2	<0.2	<0.2	<0.2
La, in ppb	<0.1	<0.1	<0.1	<0.1	<0.1
Fe^{2+}, in ppb	<50	<50	<50	<50	<50
Fe^{3+}, in ppb	<50	<50	<50	<50	<50
K, in ppm	0.21	0.40	0.26	0.33	2.90
Li, in ppb	3.6	3.9	4.5	4.0	4.0
Mg, in ppb	23.3	35.7	38.0	36.0	77.3
Mn, in ppm	<0.03	<0.03	<0.03	<0.03	<0.03
Mo, in ppb	52.0	50.0	49.0	51.0	53.0
Na, in ppm	8.4	8.9	9.0	8.8	8.9
Ni, in ppb	1.7	1.0	0.8	1.0	8.0
Pb, in ppb	<0.1	<0.1	<0.1	<0.1	<0.1
Rb, in ppb	2.3	2.3	1.8	2.1	4.6
Sb, in ppb	0.5	1.9	0.3	0.6	0.6
Se, in ppb	<1	<1	<1	<1	<1
Sn, in ppb	0.6	0.89	0.12	0.2	0.44
Sr, in ppm	0.21	0.23	0.2	0.22	0.24
Th, in ppb	<0.1	<0.1	<0.1	<0.1	<0.1
Ti, in ppb	0.5	0.7	0.64	0.86	0.81
Zn, in ppb	20.0	4.6	9.7	7.0	37.0
TOC, in mgC/l	0.6	0.67	<0.5	1.10	5.43
V, in ppb	0.16	0.26	0.39	0.2	0.17
U, in ppb	<0.1	<0.1	2.30	0.53	<0.1
Y, in ppb	<0.1	0.16	0.22	0.18	0.11

Table 4.2
Results of unconfined compression tests on the Grimsel rock, performed during the pre-operational stage

Identification	Distance to the drift wall m	Young's Modulus E_{50} GPa	Unconfined compressive strength MPa
Granite (borehole SF22)	0.17 to 0.27	61.6	193.5
Granite (borehole SF22)	0.85 to 0.95	50.8	110.0
Lamprophyre (borehole SF22)	12.16 to 12.26	49.8	142.0
Lamprophyre (borehole SF22)	0.70 to 0.80	35.7	85.4

order of 0.4% for the lamprophyre and 0.8% for the granite.

4.3. Test components

This section includes a summary of the most important features of the test components, as well as the most relevant aspects of their design and construction processes.

4.3.1. Bentonite blocks

The blocks used to construct the clay barrier were fabricated from FEBEX bentonite, the properties of which are described in Chapters 2 and 5. The construction of the barrier is described in Section 4.4.2.

See report 70-IMA-M-3-3 (Bentonite: Origin, Properties, and Fabrication of Blocks) [6] for details.

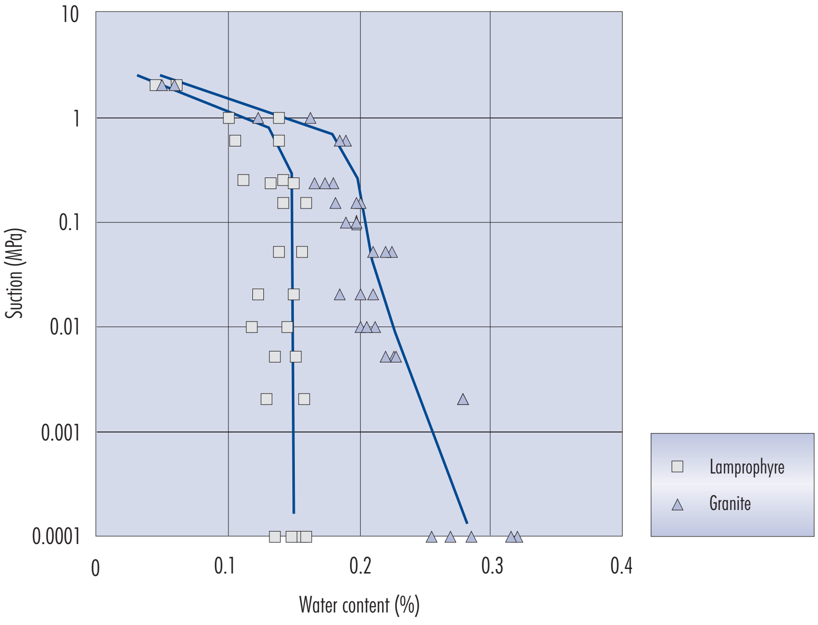

Figure 4.15: Retention curves of granite and lamprophyre, near the FEBEX drift.

4.3.1.1. Design

Figure 4.16 shows the geometry of the barrier in the heater and non-heater areas. In both areas, the three exterior rings of blocks are equal; in the heater area the interior crown of this group is in contact with the steel liner, while, in the non-heater area, the interior crown is in contact with a core of blocks.

Five types of blocks form this barrier geometry: BB-G-01, BB-G-02, BB-G-03, BB-G-04, and BB-G-05. Figure 4.17 and Table 4.3 show respectively the shapes and dimensions of the block types.

The dry density specified in the design of the blocks was 1.70 g/cm^3. This density was determined by taking into account the probable volume of the construction gaps and the need to have a barrier with an average dry density of 1.60 g/cm^3. For a dry density of 1.60 g/cm^3, the swelling pressure is of the order of 5 MPa, which is the value proposed in the AGP Granito. The water content of the blocks is that specified for the raw bentonite, 12.5% to 15.5% (Chapter 2).

4.3.1.2. Fabrication

For the fabrication of blocks BB-G-01, BB-G-02, BB-G-03, and BB-G-04 it was necessary to design and manufacture moulds, whereas block BB-G-05 was obtained from BB-G-04 by machining the curved face with a saw. The blocks were fabricated in the REFRACTA, S. A. plant at Quart de Poblet (Province of Valencia, Spain), by compaction in a uniaxial hydraulic press under a pressure of 40 MPa to 45 MPa. A quality assurance program was applied in fabrication of the blocks: external appearance, dimensions, water content, and dry density were controlled.

Table 4.4 shows the average values for the characteristics and the number of blocks fabricated for each type.

Taking into account the dimensions of the blocks of each type, the average values of water content and dry density are 14.4% and 1.69 g/cm^3, respectively. A total of 7568 blocks were fabricated, with a total weight of 165076 kg.

4.3.1.3. Packing, handling, transport and storage

Laboratory tests and the study of some blocks placed in the tunnels of the GTS showed that the blocks deteriorate quite rapidly when exposed to an environment of high humidity. For this reason, the blocks were packed in boxes appropriately protected by sheets of plastic. Although the blocks have a good mechanical consistence, they were packed

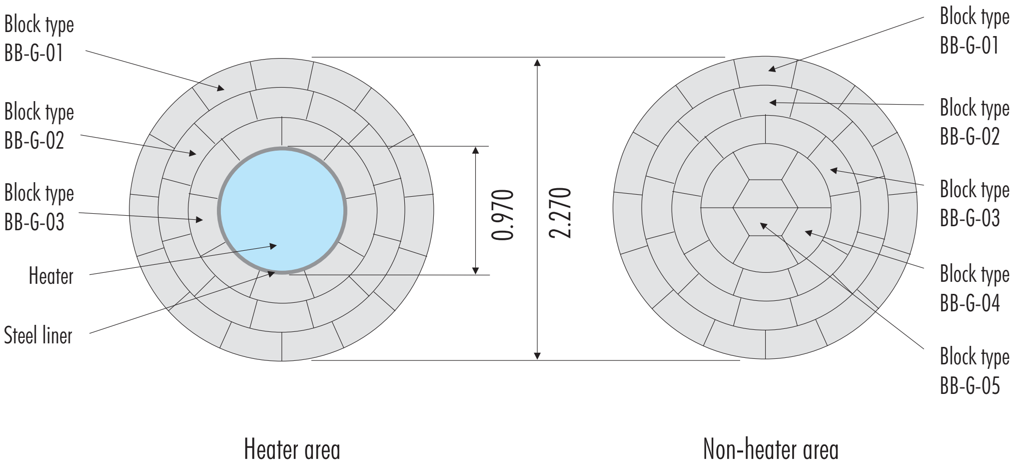

Figure 4.16: Geometry of the clay barrier.

Table 4.3
Dimensions for block fabrication

Type	a mm	b mm	c mm	Thickness mm	R mm	r mm	α
BB-G-01	$470.0^{+2.0}_{-5.0}$	$380.0^{+2.0}_{-4.0}$	$214.0^{+2.0}_{-3.0}$	$125.0^{+2.0}_{-2.0}$	1133	919	24º
BB-G-02	$473.0^{+2.0}_{-5.0}$	$361.0^{+2.0}_{-4.0}$	$214.0^{+2.0}_{-3.0}$	$125.0^{+2.0}_{-2.0}$	917	703	30º
BB-G-03	$478.0^{+2.0}_{-5.0}$	$330.0^{+2.0}_{-3.0}$	$214.0^{+2.0}_{-3.0}$	$125.0^{+2.0}_{-2.0}$	701	487	40º
BB-G-04	$483.0^{+2.0}_{-5.0}$	$240.0^{+2.0}_{-3.0}$	$240.0^{+2.0}_{-3.0}$	$125.0^{+2.0}_{-2.0}$	485	-	60º
BB-G-05	$483.0^{+2.0}_{-5.0}$	$240.0^{+2.0}_{-3.0}$	$240.0^{+2.0}_{-3.0}$	$125.0^{+2.0}_{-2.0}$	-	-	60º

in boxes inside quilted plastic wrapping to avoid impact damage during their handling and transport.

The appropriately packed blocks were stored away from the GTS, in a warehouse with controlled temperature and humidity. During the construction of the barrier, the FEBEX drift was dried, heated, and ventilated to keep relative humidity low. Also the work was scheduled such that in the work area at the portal of the drift, where relative humidity is high, the time of exposure was compatible with the stability of the blocks.

These precautions were effective since no damage was observed in the blocks.

4.3.2. Heating system

4.3.2.1. Heaters

General characteristics

The test used two electrical heaters inserted within a steel liner. The heaters reproduced the mechanical characteristics of the AGP Granito canister, simulating the thermal effects of the waste nuclear fuel.

The external dimensions of the heater were identical to those of the canister anticipated in the AGP Granito concept (a cylinder measuring 4.54 m in

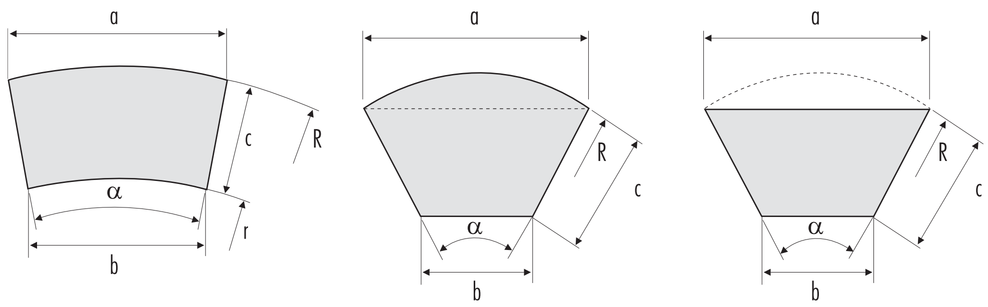

Block types BB-G-01, BB-G-02, and BB-G-03

Block BB-G-04

Block BB-G-05

Figure 4.17: Shapes of the blocks.

Table 4.4
Average values of the physical properties and number of blocks fabricated

	Type of block				
	BB-G-01	BB-G-02	BB-G-03	BB-G-04	BB-G-05
Weight per block (kg)	22.1	21.8	21.3	23.1	18.0
Average water content (%)	14.49	14.07	14.87	13.69	13.07
Average dry density (g/cm^3)	1.69	1.69	1.69	1.70	1.70
Number of units fabricated	2898	2310	1614	562	184
Total weight (kg)	64046	50358	34378	12982	3312

length with a diameter of 0.90 m) and the weight was of the same order (11 t). Both the material and the shape of the exterior body of the heaters were similar to those anticipated for the canister: carbon steel plate measuring 100 mm in thickness.

As regards the thermal aspect, the aim of the test was to subject the bentonite, at the point of contact with the steel liner, to a maximum constant temperature of 100°C, which is the maximum value anticipated in the reference concept. Nevertheless, in order to reach this value in a period of time compatible with the duration of the test, and maintain it in an isolated drift, it was necessary to increase the power of the heaters beyond the value anticipated in the AGP Granito concept for the maximum residual thermal power of the canisters, that is 1200 W [5]. Following different analyses and modelling exercises, performed during the design phase of the test [1], the nominal power was fixed at 4300 W per heater. This power would be the maximum required in the most unfavourable case of the clay barrier being totally saturated, with a certain margin of safety.

Mechanical characteristics

Figure 4.18 shows a general view of the final design of the heater. The exterior casing consisted of a forged tube with a wall thickness of 100 mm, and two welded end covers of metal plate, each measuring 150 mm in thickness. The casing was of carbon steel without any treatment or covering, except sandblasting of the exterior surface. The mechanic part of these units was manufactured by the Spanish company ENSA at its facilities in Maliaño (Santander, Spain).

Inside the casing, the heating elements (electrical resistances) were wound around a tube or reel measuring 660.4 mm in diameter and 12.7 mm in thickness. The assembly – reel and resistances – was covered with a copper sheet measuring 3 mm in thickness. This covering served to distribute the temperatures more uniformly along the heater and to provide mechanical protection for the heating elements during heater assembly.

The thickness and shape of the end covers were based simply on convenience during assembly of the interior elements of the heater and did not correspond to the reference concept. The front-end cover had a total of 24 perforations to allow for the exit of cables (6 for heating elements and 18 for control thermocouples) and was fitted with a cylindrical, bolted box on the exterior for mechanical protection of the cable exits. On the front-end cover there were two key notches located at 36°, to allow for coupling with the pushing mechanism of the insertion system. The other end cover was solid, and its outer edge was chamfered to facilitate insertion into the liner.

The cable exits were sealed with Viton gaskets and filled with epoxy resin in order to seal the casing hermetically.

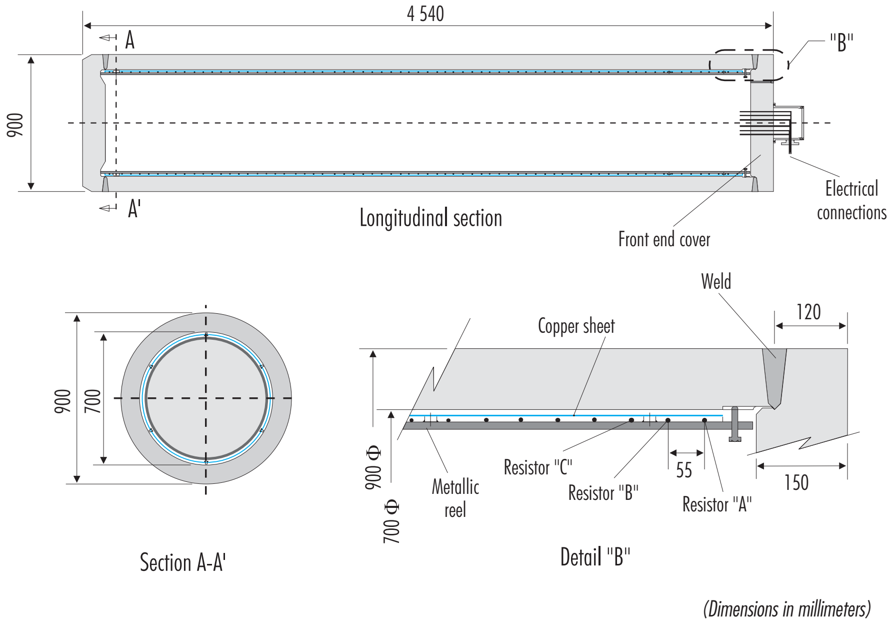

Figure 4.18: Construction aspect of the heaters.

Electrical characteristics

In order to increase reliability, the system was redundant. Each heater had three independent heating elements, each of which was capable of supplying individually the nominal required power of 4300 W. The elements were of the shielded resistor type and their main characteristics are summarised in Table 4.5.

4.3.2.2. Steel liner

The AGP Granito reference concept considers the existence of a continuous steel liner, common to all the canisters emplaced in the same drift. This steel liner consists of a perforated steel tube measuring 15 mm in thickness, the only aim being to provide, during the installation, the space into which the canister is inserted, so no consideration is given to possible deformation due to swelling of the bentonite.

The steel liner required for the test had a length of 10 m, corresponding to the length of the two heaters plus a one-metre separation between them. Thus, 11 segments of one metre each were made, designed to be coupled by means of a male/female conical coupling measuring 100 mm in length, machined in the ends of each segment (Figure 4.19). The material of the steel liner was conventional alloyed steel of the type used for boilers and pressure vessels.

The inner diameter of the liner was 940 mm; thus there were 40 mm of play with respect to the outer diameter of the heaters, a value that was considered sufficient for correct insertion of the heaters, taking into account the normal errors of alignment in an installation of this type.

4.3.2.3. Power regulation system

Regulation equipment

The power of each of the heating elements was controlled by a static single-phase power regulator based on thyristors, regulating the effective voltage applied to the element by adjusting the wave phase angle.

Each heater had an associated power regulation control unit consisting of three independent regulation channels, one for each heating element. For

Table 4.5
Characteristics of the heating elements

Active conductor	Material of the conductor core	Ni-Cr 80/20
	Length	52 ±3% m
	Supply voltage	400 V AC
	Nominal power	4300 ±10 % W
	Insulation	MgO
	Sheath material	Inconel 600
	External diameter	4.6 mm
Cold terminals	Conductor section	6 mm^2
	Sheath material	AISI 304 L
	External diameter	6.4 mm

greater security, each of the channels was galvanically segregated from the main network.

Each power regulator was governed by a PID-type controller that received a setpoint assigned from the test control system. This system allowed for constant power or constant temperature control, depending on the control desired at each moment.

Control procedures

The test consisted of two clearly differentiated phases in which the power regulation of the heaters was controlled:

1) Initial heating

   In this initial phase, the goal was to reach the constant temperature of 100 °C in a time pe-

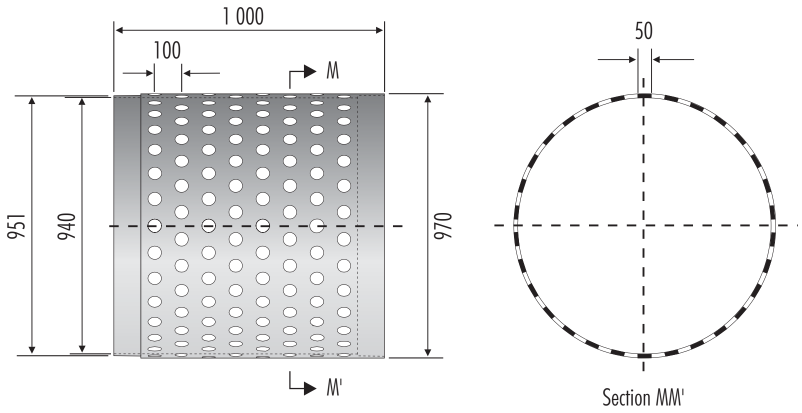

(Dimensions in millimeters)

Figure 4.19: Steel liner.

riod of a few weeks, compatible with the total duration of the test. With a view to simplifying modelling and allowing for identification of the thermal response of the system, this initial heating was performed at constant power, in various steps.

2) Heating at constant temperature

   Once a temperature of 100 °C was reached at some point in the steel liner/bentonite interface, the goal was to maintain that temperature constant, with the lowest fluctuations possible, this implying continuous power regulation. To accomplish this, a PID-type algorithm was applied, which was adjusted in accordance with the empirical identification of the thermal response of the system.

In principle, given the overdimensioning and redundancy of the heating elements, only one element in each heater was used, the other two remaining in stand-by.

4.3.2.4. Quality Assurance (QA) program

The detailed engineering of the mechanical components and their construction were carried out in Maliaño, in accordance with a QA program. A similar QA program was carried out for all the components of the power regulation system.

Additionally, the heater was subjected to a helium test following welding of the end covers. This test was to check the welding of the front-end cover and the sealing of the cable exit penetrations. The gas was left in the interior of the heater both to improve the thermal conductivity of the internal atmosphere and to provide some corrosion protection.

4.3.3. Instrumentation and control

4.3.3.1. Sensors

Types and locations

A total of 632 sensors were installed. Table 4.6 indicates the variables measured, the types of sensors used and the locations of the sensors, distributed by areas.

The sensors in the clay barrier were grouped in a series of cross-sections, as indicated in Figure 4.3: sections A, B1, B2, C, D1, D2, E1, E2, F1, F2, G, H, I, K, L, M1, M2 and N. The sections with the same letter had similar sensor configurations.

The boreholes BOUS-1, BOUS-2, FBX-1, and FBX-2 were used, along with the 19 boreholes drilled from the interior of the drift, for the instrumentation in the rock, in particular for hydrogeological and mechanical variations (Section 4.4.1.2). Other sensors, such as psychrometers and TDR probes were installed in shorter boreholes, drilled from the drift in areas closer to the wall (up to 2.5 m).

An example of the location of sensors in the clay barrier is shown in Figure 4.20. Each sensor was identified by a code of the type:

AA-BCn-DD

where

AA: Code of sensor type (see Table 4.6)

B: Designation of location type: rock, instrumented section, etc. (see Table 4.6)

C Designation of section or borehole code

n: Order number of section (where applicable), borehole or heater

DD: Order number within the section, borehole, heater, or service area

Characteristics

The sensors, cables and connections between them were selected to conform to the conditions expected in each area. The sensors installed in the bentonite barrier had to withstand the harshest environment – temperature up to 100°C, pressure up to 5 MPa, and highly corrosive (more than 6000 ppm of Cl^- in some points).

For the same reason, the incorporation of elements containing active electronics (amplifiers, signal conditioning, etc.) was avoided in the test zone. To accomplish this, the cables were made sufficiently long for the associated electronics of the sensors to be installed in the service zone, which together with the required lifetime made it necessary in some cases to use especially designed and protected sensors.

4.3.3.2. Instrumentation for gas measurement

Gas is generated in the test zone due to the effects of corrosion and the presence of microorganisms

Table 4.6
Sensors installed during the first phase

Sensor code	Variable (or instrument)	Type of sensor	Designation of area (*)				Total
			B	S	H	A	
T	Temperature	Thermocouple	62	91	36		189
P	Total pressure in borehole in rock (3-D)	Vibrating wire	4				4
P	Total pressure on rock surface	Vibrating wire	30				30
P	Total pressure on heater	Vibrating wire		6			6
Q	Hydraulic pressure in borehole in rock	Piezoresistive	62				62
PP	Packer pressure in borehole	Piezoresistive	62				62
Q	Pore pressure in bentonite	Vibrating wire		52			52
WC	Water content	Capacitive		58		1	59
WP	Water content	Psychrometer	28	48			76
WT	Water content	TDR	4	20			24
S	Extensometer in rock	Vibrating wire	2x3				6
SH	Heater displacement	Vibrating wire		9			9
SB	Expansion of bentonite block	Vibrating wire		8			8
S	Displacement within the bentonite barrier	Potentiometer		2x3			6
IT	Clinometer	LVDT		6x2			12
3S	Crack meter	LVDT	1x3				3
GP	Gas pressure in the bentonite barrier	Magnetic		4			4
GF	Gas flow	Manual measure		6			6
AP	Atmospheric pressure	Piezoresistive				1	1
A	Velocity of ventilation air	Hot wire				1	1
C	Resistor intensity	Electric converter				6	6
V	Resistor voltage	Electric converter				6	6
	TOTALS		261	320	36	15	632

(*) B: granite; S: instrumented section in bentonite; H: heater; A: service zone

in the bentonite. The pressure of the gas generated, as well as the permeability of the barrier to this gas, was measured, and samples were taken for study. For this purpose, two sets of porous ceramic pipes measuring 0.20 m and 3 m in length respectively were installed at various points in the granite/bentonite interface, at the steel liner surface and in boreholes drilled within the intermediate zone of the barrier. All the ten pipes installed were connected by plastic conduits to the measuring and sampling equipment located in the service zone of the drift.

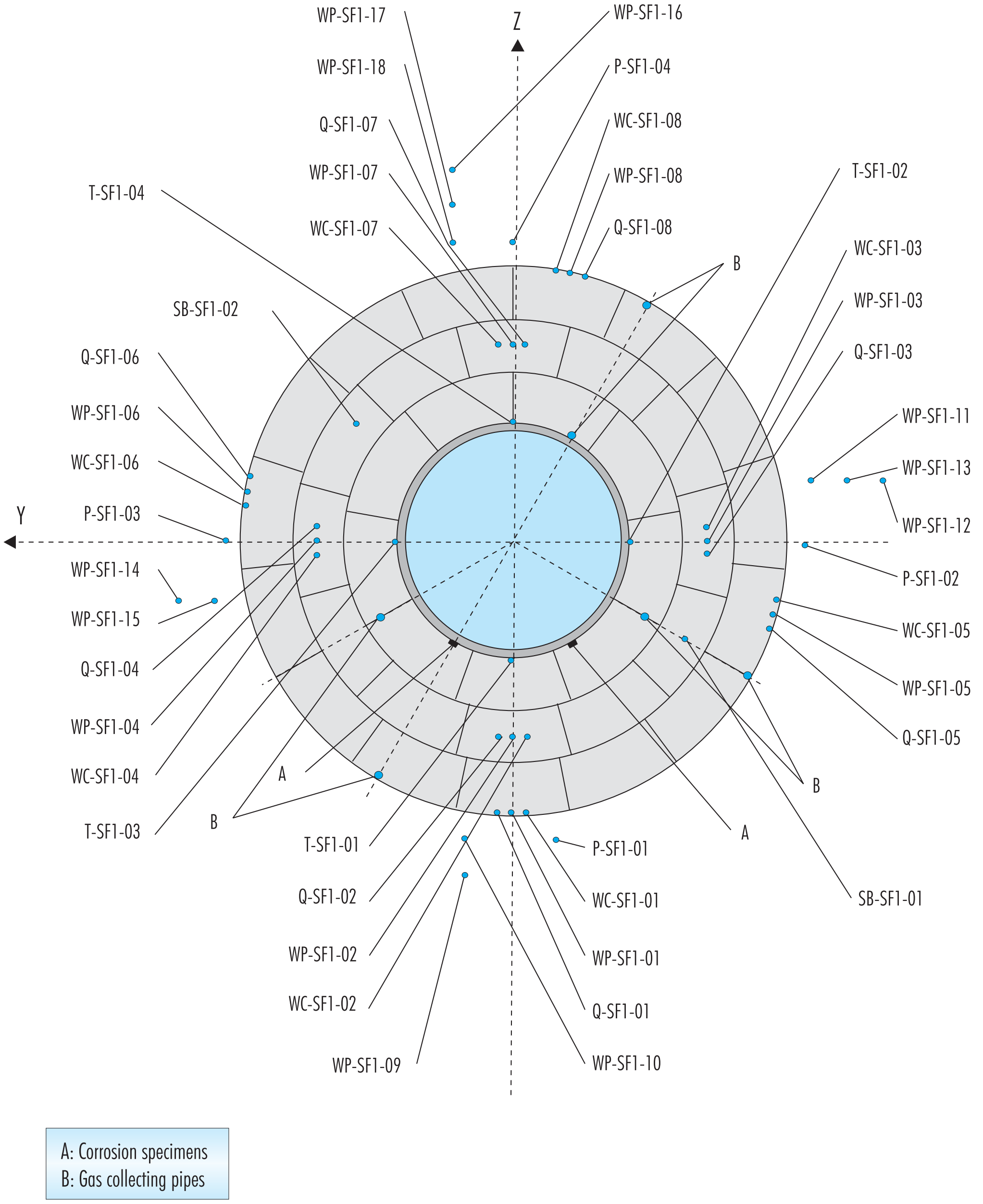

Figure 4.20: Final location of sensors in instrumented cross-section F1.

4.3.3.3. Specimens for the corrosion study

To analyse corrosion behaviour under close to actual conditions, specimens of different metallic materials were placed in the clay barrier, at points within the bentonite situated very close to the heaters (Figure 4.20). The specimens were of various types of steel (both carbon and stainless), titanium, and copper, as well as welds of the same materials.

4.3.3.4. Chemical tracers

With a view to the dismantling stage, conservative and non-conservative chemical tracers were placed at single points in the bentonite barrier and distributed along its periphery to obtain information on the geochemical processes and transport mechanisms.

4.3.3.5. Monitoring and control

Goals and structure

The monitoring and control systems were made up of two sub-systems: the "local system", located in the FEBEX drift at the GTS, and the "remote system", located at the AITEMIN office in Madrid, each one comprising all the necessary electrical and/or electronic components, computers, and computer programs.

The main goals of the monitoring and control of the "in situ" test were: 1) to control the heater power and to acquire, convert, display and store all the raw data generated by the instrumentation, all this being performed in an automatic operation mode by the "local system", and 2) to allow, from the "remote system", the remote supervision and strategic command of the test via modem, and the analysis, display and storage of the data obtained into a master database of the test.

Local system

The local system was composed of the following elements:

- ☐ Surge protection
- ☐ Uninterrupted supply system (UPS)
- ☐ Specific systems for signal conditioning
- ☐ Main data acquisition system (DAS)
- ☐ Two industrial type computers for supervision and control (PC1 and PC2)
- ☐ Power regulation units for the heaters
- ☐ Communication system.

Given the remoteness of the test and the seasonal difficulty of access, the system was designed to function automatically without the need for local personnel and with a high degree of reliability. To achieve this, the critical components were duplicated when possible (see Figure 4.21).

The system was governed by the two main computers (PC1 and PC2) functioning in a master/slave setup, with automatic switching in the event of failure of the master, and running a software application of the SCADA type (Supervision, Control, And Data Acquisition). This software was configured to perform the functions required for data display and storage and for heater power control.

Figure 4.22 show an example of the type of visual data display supplied by this system. To store the data, each computer saved a log of all the readings of the sensors in its database every-half hour.

Two additional computers (GRS PC and NAGRA PC) were installed. The GRS PC was used for the acquisition of gas pressure and flow instrumentation data, while the NAGRA PC was used for TDR data acquisition and processing.

Remote system

In the remote system, the master database was built upon MS-ACCESS. In view of the gradual evolution of the parameters, and in order not to increase excessively the size of the database, only one reading for each variable was stored daily, this corresponding to a measurement made at approximately noon. To create the database, the data stored in the local system were transferred periodically, on demand from the remote system and including the TDR data from NAGRA PC. The data stored in the GRS PC was collected from the GRS offices in Germany.

Periodic data reports were generated semi-automatically from the database, and distributed to all the project participants. These reports represented graphically the evolution of all the controlled variables. In addition, numerical data were supplied to the participants requesting them for different purposes, as modelling, analysis of sensors performance, etc.

Communications

A conventional telephone network conducted the data transmission between the remote system and the local system by means of modems. In the local system, two independent exterior telephone lines were used, connected to a dedicated telephone switchboard for the test.

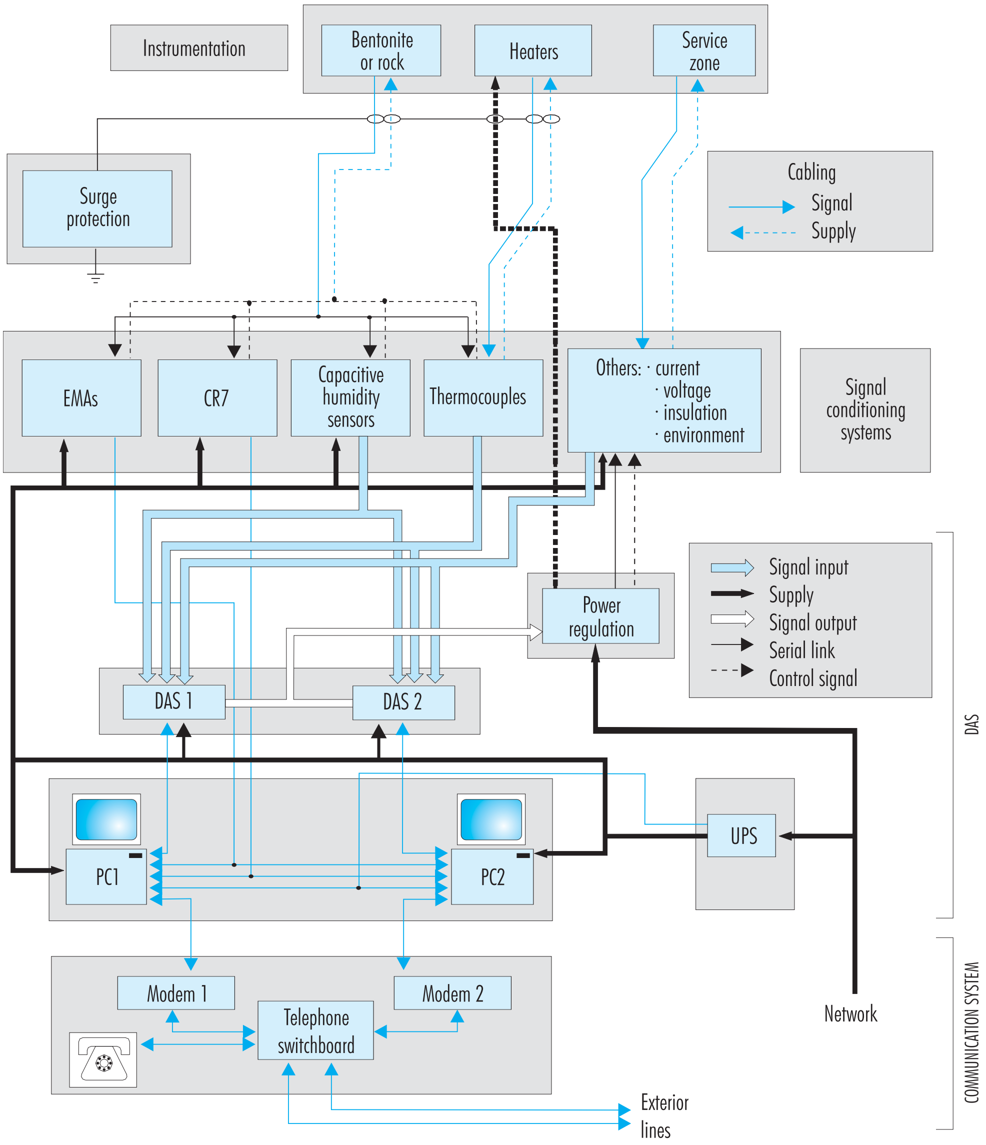

Figure 4.21: Local monitoring and control system.

4.3.3.6. Quality assurance and quality control procedures

With the goal of ensuring the quality and the traceability of the measurements made by the instrumentation, specific quality assurance and quality control procedures were applied in all the phases relating to the supply, tests, and installation of the instrumentation.

Given the short period of time available, no systematic calibration of the instrumentation was performed; however, most of the instrumentation was supplied with calibration certificates from the manufacturer or supplier, and in all cases 100% of the sensors were subjected to reception tests, with at least one point of measurement being checked with the calibration certificate.

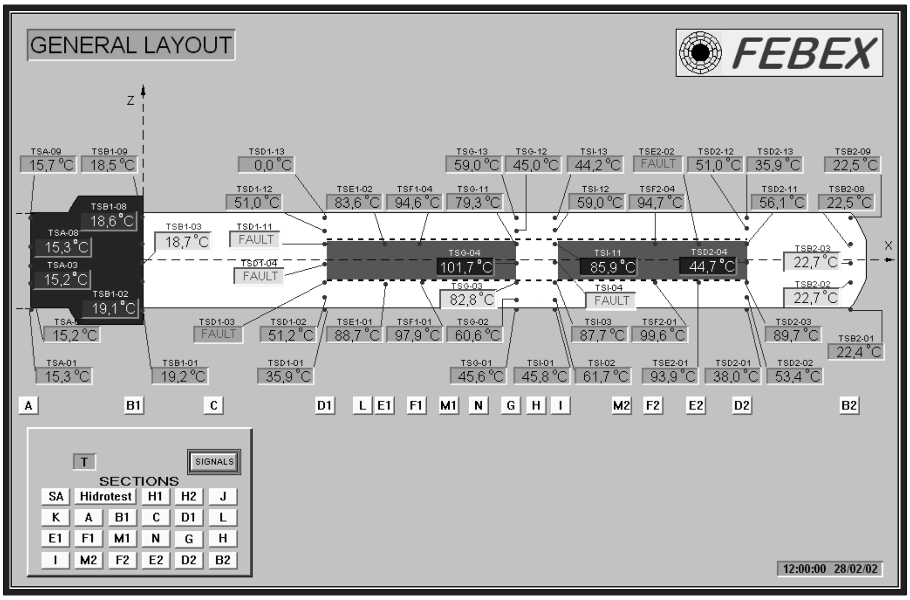

Figure 4.22: Visual data display (longitudinal section of temperatures).

4.4. Installation

4.4.1. Preparatory works

4.4.1.1. Basic services

The supplies of ventilation, electricity, and water were taken from those already existing at the GTS.

The air from the GTS central ventilation system has a controlled temperature and humidity (approximately 15 °C and 30% to 40%, respectively). Therefore, the largest possible airflow was taken to dry the interior of the drift. A dry environment was necessary to minimise the risks of bentonite block deterioration by adsorption of the ambient humidity. To further dry (and heat) the environment, two electrical convectors were employed at the working area.

4.4.1.2. Boreholes

Nineteen boreholes were drilled in the test zone from the interior of the drift, for the placement of the instrumentation in the surrounding rock mass. The orientation and length of these boreholes were established as a function of the specified positioning for each instrument, and especially of those relative to the hydraulic parameters. The length of the boreholes varied between 7 m and 22 m, with a total of 233 m drilled. Figure 4.23 shows the positions of these boreholes. Boreholes SG1 and SG2, where total pressure triaxial cells were installed, measure 146 mm in diameter; the rest, for the hydraulic instrumentation, having a diameter of 66 mm.

4.4.1.3. Concrete sill and platform

In the service zone of the drift, a concrete sill was constructed to permit the installation of the transportation system and to facilitate the passage of personnel. This sill was extended 13 m from the portal of the drift, forming a platform outside it, to facilitate the loading and unloading of equipment and to station the materials handling and transportation equipment (Figure 4.24).

4.4.2. Clay barrier construction

Due to the lack of previous experience in an installation of this type, especially in placing the engi-

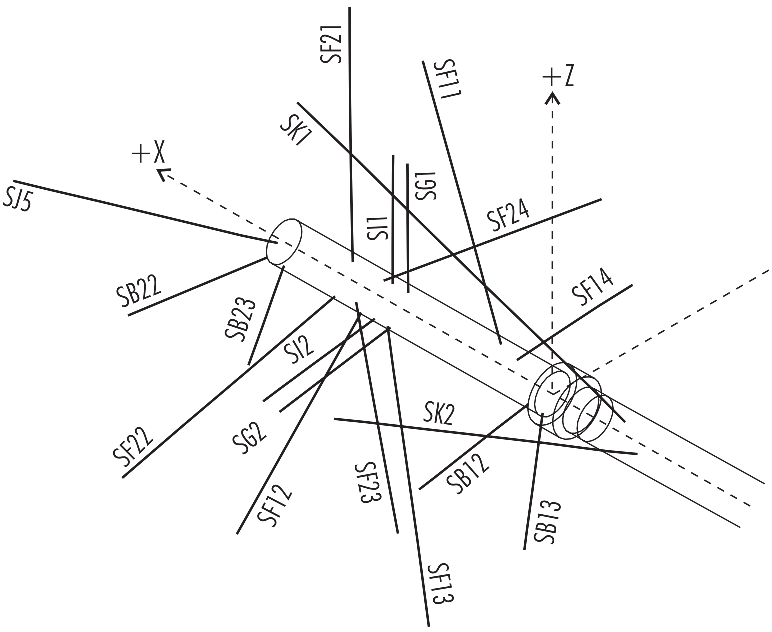

Figure 4.23: Boreholes drilled from the interior of the drift.

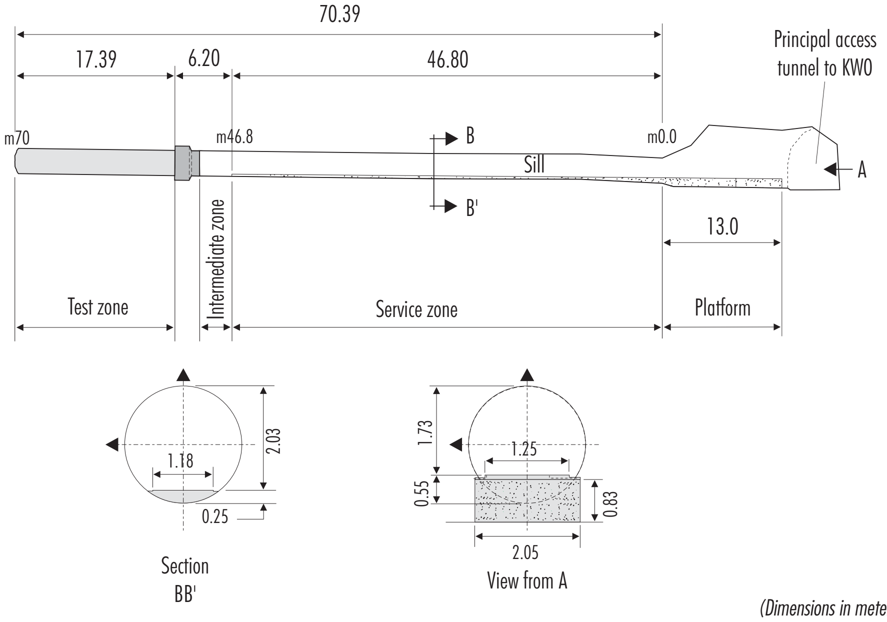

(Dimensions in meters)

Figure 4.24: Concrete sill and platform.

neered barriers in a horizontal position, a test installation was set up in a simulated drift of concrete at the AITEMIN facilities in Toledo (Spain). This test was very useful, and served to detect certain important aspects associated with the installation. In particular, these aspects were the stability of the bentonite slices and the accumulative effects of the play between the blocks themselves and the blocks and the drift.

The effects of mechanical degradation of the bentonite blocks due to the humidity of the environment and/or a film of water at the rock surface were studied by laboratory tests and in a tunnel at the GTS. As a result of these experiences, the decision was taken to protect the packages of blocks against humidity; to dry the working area within the drift to the extent possible and to minimise the time the blocks were exposed to the GTS environment, where the relative humidity is practically 100%.

4.4.2.1. Installation procedures

The barrier was constructed manually, in accordance with the scheduled procedure. The sequence of installation is shown on Figure 4.25. First the steel liner was placed on a provisional support; second, the alignment with the axis of the drift was checked and adjusted; and finally the barrier was constructed around the steel liner, in complete vertical slices.

The correct alignment of all the segments of the steel liner, with respect to one another and to the drift, is critical as regards avoiding difficulties in inserting the heaters. Initially, once aligned, some points were welded in the joint between the liner segments, to ensure and maintain their correct position until the heater was inserted. Later it was decided that it was easier to ensure this alignment by introducing the steel liner into the drift already joined; as a result, up to three joined segments were installed. Figure 4.26 shows the deposition hole, after being enclosed by the construction of the barrier around the steel liner.

In some cases, and especially for the first slices of the installation, it was necessary to wedge the top blocks against the rock to ensure the stability of the slices using granite pieces.

On the other hand, all the play existing between the blocks, both by design and as a result of manufacturing tolerances, accumulates at the top part of each slice, resulting in this case in a gap of approximately 2 to 3 cm. Figure 4.27 represents a typical cross-section of the drift. It may be seen that, for these reasons, the axis of the steel liner is off-centre, displaced some 15 mm. Consequently, the heater is off-centre by some 35 mm, the exact deviation depending on the actual diameter of the drift at each point.

4.4.2.2. Sensor installation and cabling

The sensors in granite were emplaced before the clay barrier was installed, whereas the sensors in bentonite were installed in mechanically made holes at their pre-assigned positions within the blocks on completion of each slice.

The cables were carried radially from each sensor to the rock surface in a machined groove or channel in the bentonite. All the cables, including those from the sensors in the granite, were grouped into four bundles. The bundles were carried along the rock surface at the crown, the invert, and both springlines of the drift. To carry each bundle along the rock face and through the bentonite blocks, a channel equal to the size of the bundle was made in each slice. At the crown and the two springlines, the bundles were fastened to the granite. In the invert, a channel previously made along the entire length of the test zone was used to carry the heater power cables and the rest of cables from that zone; this arrangement also avoided high initial compression on the cables from the weight of the bentonite barrier. Once all the cables were placed in the invert channel, it was filled with bentonite powder.

4.4.2.3. Quality assurance and quality control

Control of the dry density of the clay barrier was fundamental to its construction. The average dry density was not to be more than 1.60 t/m^3, in order not to exceed the maximum swelling pressure of 5 MPa used in the calculations for the test components. On the other hand, it was required not to be less than the minimum considered tolerable, 1.4 t/m^3. Furthermore, knowledge of the actual dry density obtained was necessary for modelling, as well as for the interpretation of the test results. For this reason, during the construction of the clay barrier, the real mass of bentonite placed and the volume of the drift occupied by each vertical slice of blocks was determined. From these values, the global dry density as well as the percentage of construction gaps for each slice were calculated (Figure 4.28).

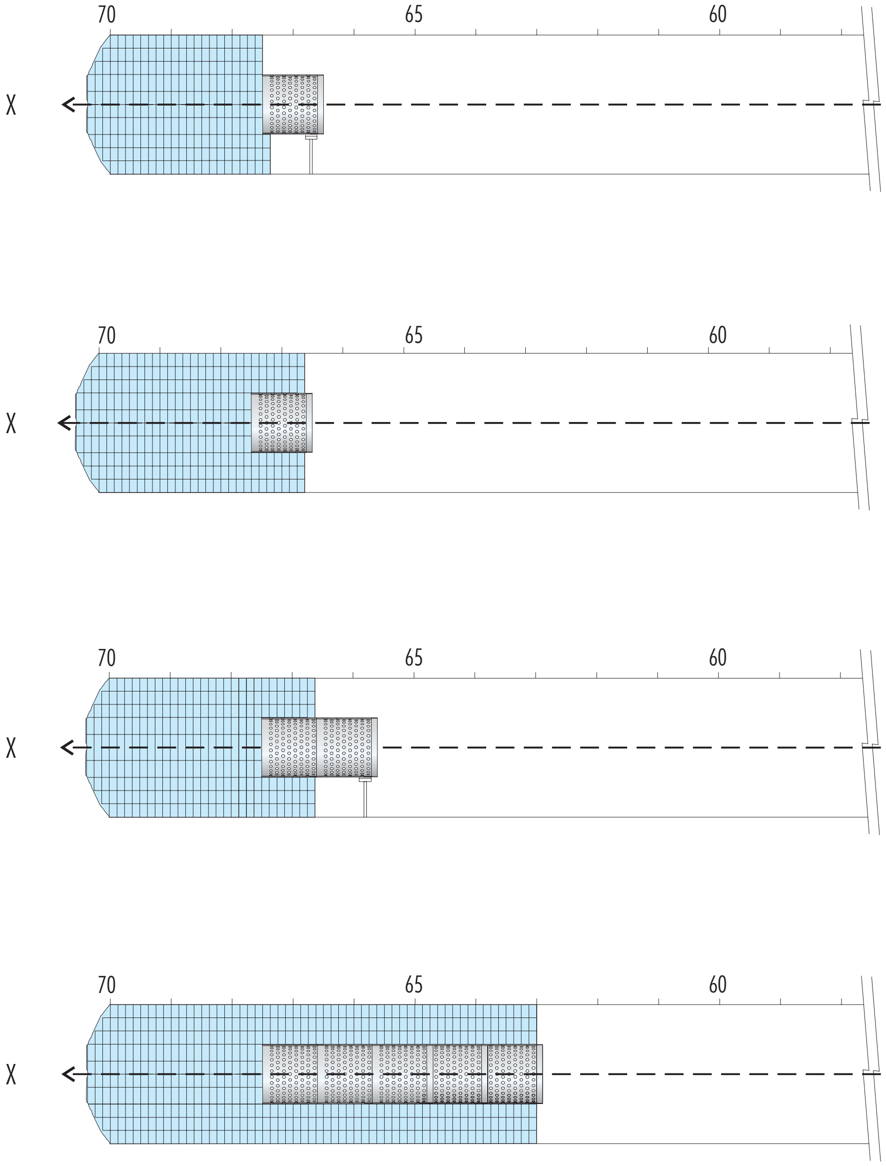

Figure 4.25: Sequence of clay barrier construction.

A total of 136 slices were installed, made up of 5331 blocks and having an overall mass of 115716 kg of bentonite. The average values of the barrier were a dry density of 1.60 t/m^3 and a volume of construction gaps of 5.53%. It was assumed that the barrier maintained the water content (an average of 14.4%) from the fabrication of the blocks.

4.4.3. Insertion of heaters

For the transportation of the heaters along the drift and their insertion into the deposition hole, a specific piece of equipment (heater transport and insertion car) was designed and constructed, in accordance with the scheme shown in Figure 4.29. Basi-

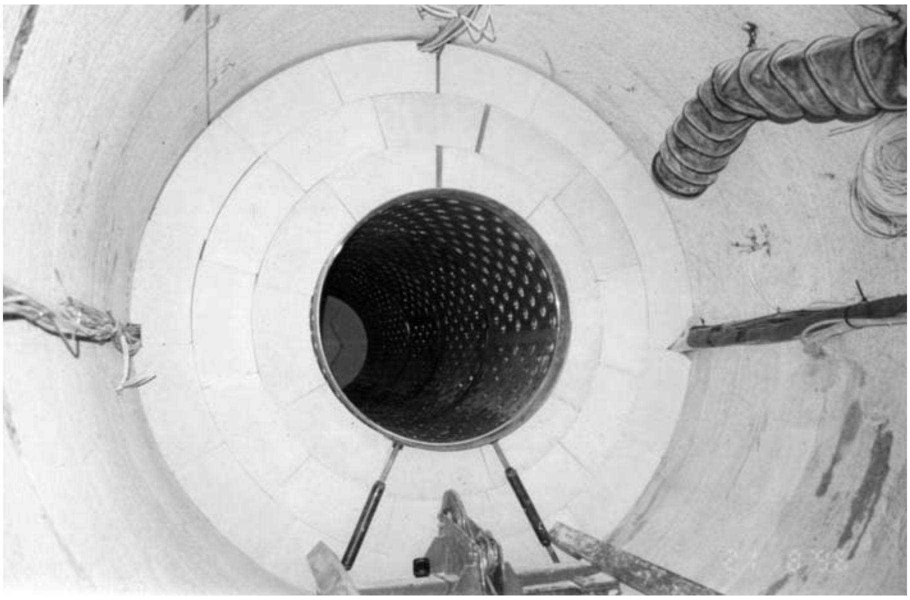

Figure 4.26: Enclosed space for the heater, after construction of the clay barrier.

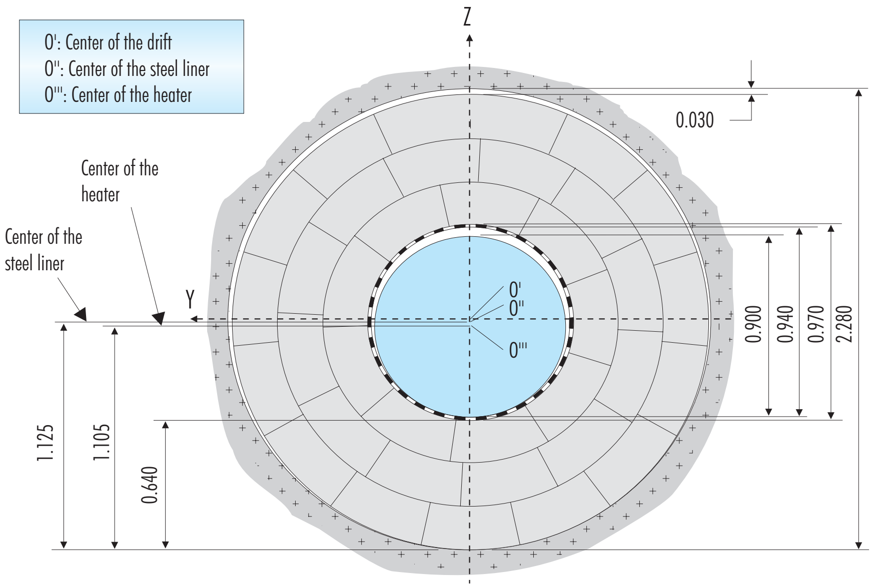

(Dimensions in meters)

Figure 4.27: Typical cross section of the clay barrier.

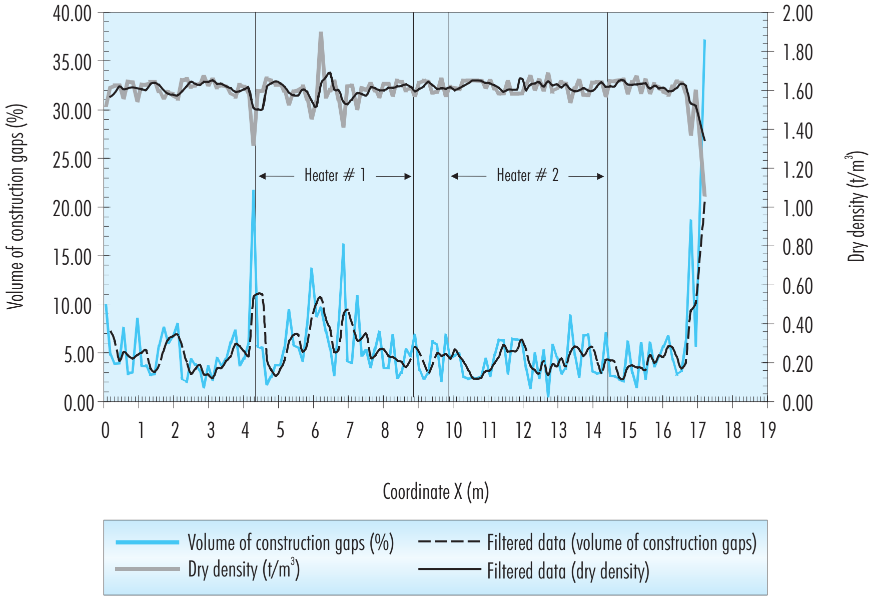

Figure 4.28: Profiles of dry density and volume of construction gaps in the clay barrier.

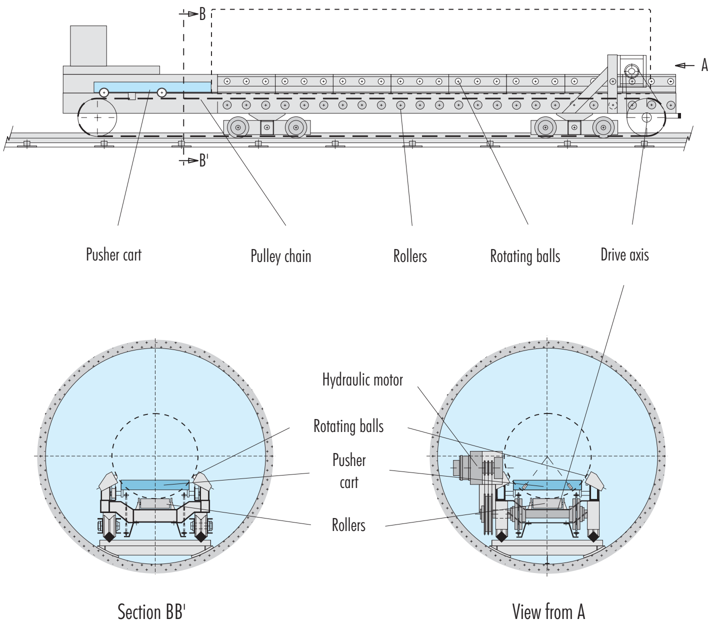

Figure 4.29: Heater transport and insertion car.

cally, this piece of equipment was a car composed of a main frame supporting lines of rollers and rotating balls, which formed a trough of dimensions fitting those of the heater. This transport and insertion car ran along a rail system installed along the entire length of the drift.

The transport and insertion car incorporated a pushing system, made up of a cart pulled by chains and moved by four flanged wheels running along guides existing in the chassis or main frame. Two flanges on the face of the pusher cart coupled the machined notches to the front-end cover of the heater, avoiding spinning during transportation and insertion of the heater.

The pusher cart was driven by a hydraulic motor mounted on the transport and insertion car itself. This unit had a regulation system that allowed the speed of the pusher cart to be continuously varied. The hydraulic equipment also made it possible to reverse the direction of motor rotation, such that the same system may be used to extract the heater from its space, if that became necessary.

The rails had a square cross section and were fitted with an edge up to minimize lateral movements of the car and ensure correct alignment between the car and the rails. In the service zone, the rails were mounted directly on the concrete sill, while in the test zone, they were laid on metallic ties fixed to the rock by bolts, allowing them to be easily retrieved as the next slices of bentonite were placed.

Movement of the transport and insertion car over the rails was accomplished by means of a cable pulled by an electrically powered winch located outside the drift, with a return pulley situated at the other end of the rails.

Table 4.7 shows the main characteristics of the car and winch.

Heater insertion was performed following the sequence shown in Figure 4.30. The heater, mounted on the transport and insertion car, was placed in front of the deposition hole; the transport and insertion car was anchored to the rails; and then, by means of the pusher cart, the heater was slid into its proper emplacement.

Figure 4.31 shows a heater already in place and also a partial view of the transport and insertion car.

The critical factor for the insertion manoeuvre was the correct alignment, in the three spatial directions, of the rolling surface of the trough of the transport and insertion car with the internal lower surface of the steel liner. This was accomplished by proper alignment of the steel liner and satisfactory installation of the rails.

4.4.4. Concrete plug

The test zone was closed with a concrete plug, the geometry of which is shown in Figure 4.32. The plug was designed to resist the swelling pressure of the bentonite. No specification was included for the water tightness or gas tightness of the concrete plug.

The plug was constructed with plane concrete, without any reinforcement, to facilitate subsequent dismantling. It was designed to withstand a total force of 2000 t, which corresponds to a swelling pressure of the bentonite of 5 MPa [29].

The concrete used had a low value of hydration heat and minimum shrinkage. Table 4.8 shows the proportions used for the concrete mix.

Table 4.7
Transport and insertion car and winch data

Car	Total weight	5.2 t
	Power of the hydraulic pusher unit	2.98 kW
	Pushing force	21560 kN
	Maximum velocity of pusher cart	1 m/min
Winch	Pulling force	19600 kN
	Velocity of movement	1.6/10 m/min
	Power of electric motor	0.67/4.10 kW

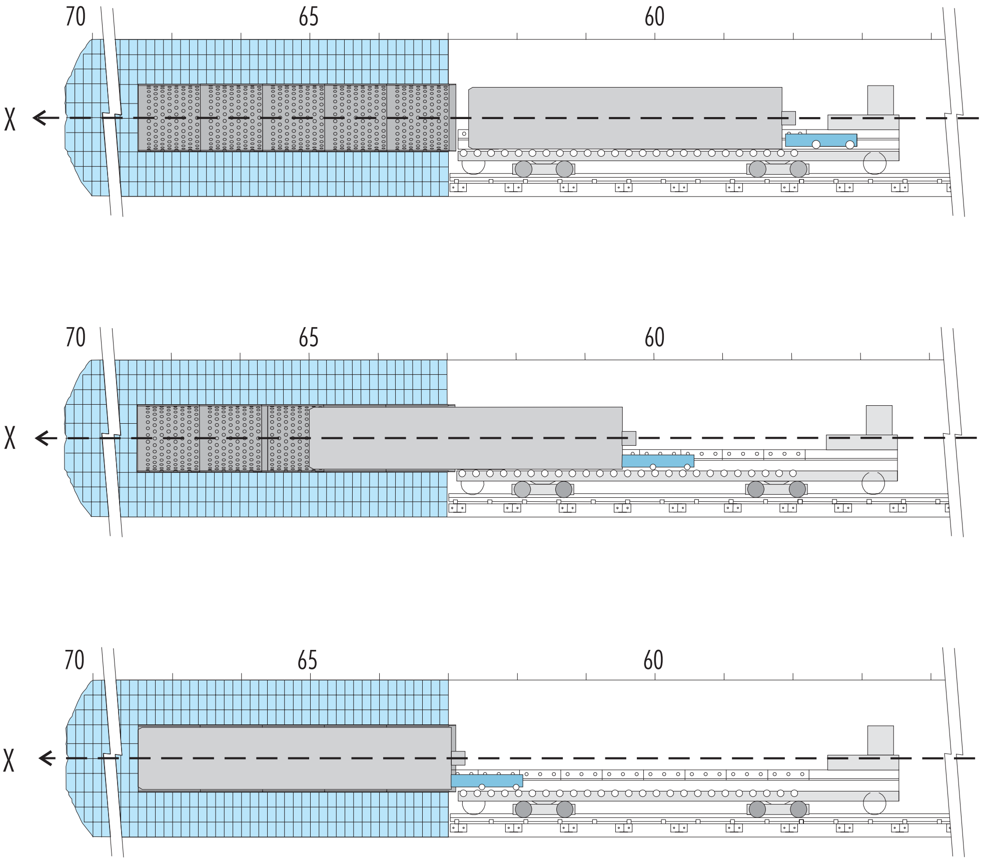

Figure 4.30: Heater insertion manoeuvre.

The plug was concreted in three sections perpendicular to the axis of the drift, such that the filling of the upper part could be checked, at least for a part of the plug. The concrete was pumped from outside the drift and was compacted by vibration. This method did not allow for good concreting of the key, where a void remained, this subsequently being filled by means of injection. Table 4.9 shows the results obtained from the concrete control tests.

The four bundles of cables pass through the concrete plug inside 200 mm-diameter plastic pipes. The pipes were later filled with fine mortar.

4.4.5. Comments on the installation phase

The FEBEX "in situ" test was the first real-scale test of a horizontal disposal of HLW, and for this reason some simplifications were introduced in relation with the real case, the most important being the size of the bentonite blocks and their method of emplacement.

Different systems and pieces of equipment have been used for the canister handling operations, such as transport along the drift and insertion. This equipment was especially designed and constructed for this project, and do not represent the equipment required in a future repository, as the engineering aspects in the reference concept AGP are not yet well defined. The construction of some of the components was a valuable experience, which has generated an important amount of data and know-how for the future.

The successful setting-up of the test was by itself a preliminary demonstration of the feasibility of the AGP reference concept in granite, and provided

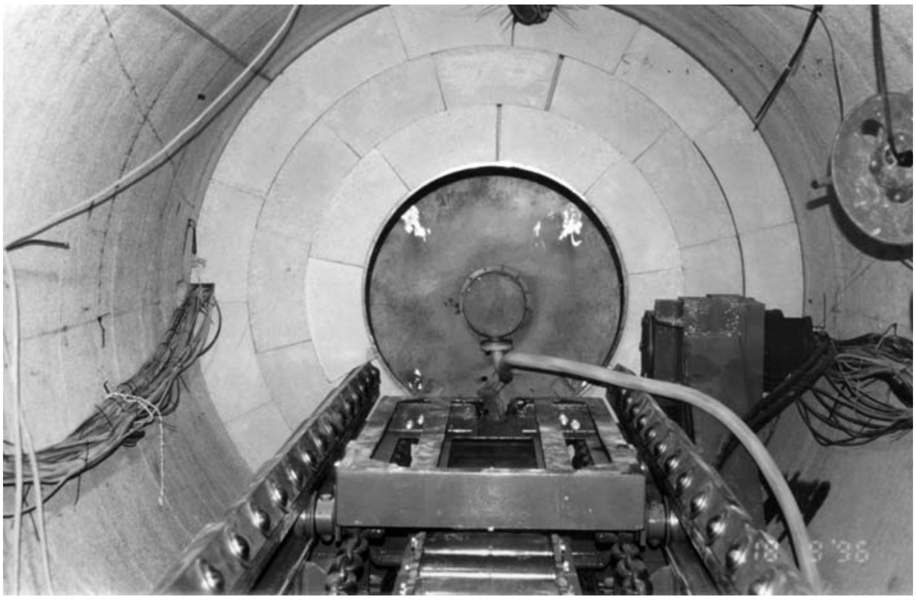

Figure 4.31: View of final position of a heater.

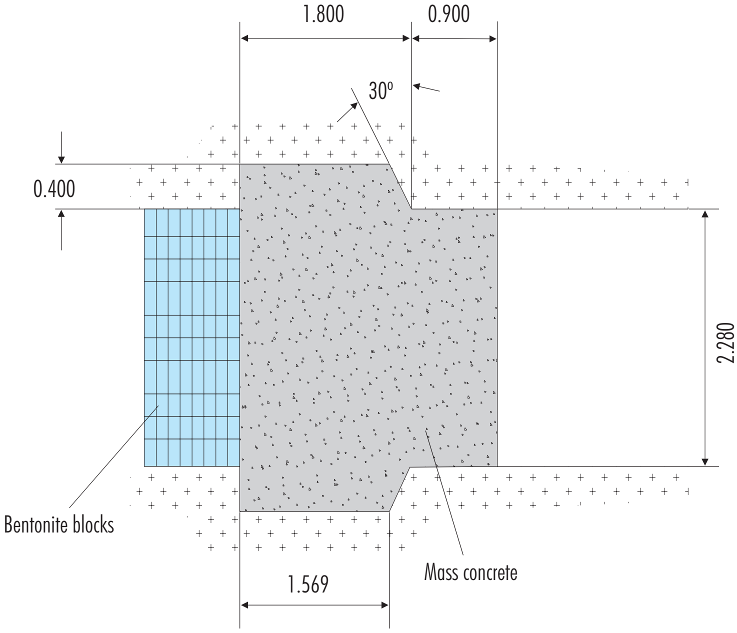

(Dimensions in meters)

Figure 4.32: Longitudinal section of concrete plug.

Table 4.8
Concrete mix proportions used in plug construction

Component	Type	Proportions kg/m^3
Cement	PCO “Sulfacem” (CEM I 32.5 HS)	160
Silica fume	Sikafume HR	60
Fine aggregate	Grimsel granite, 4 to 8 mm	660
Coarse aggregate	Grimsel granite, 8 to 16 mm	430
Sand	Quartz 0.1 to 5.6 mm	800
Filler	Limestone	170
Water	City network	155
Superplasticiser	Sikament-12 +	13

Table 4.9
Results of concrete control tests

Water/Cement ratio	0.99
Water/total hydraulic materials ratio	0.72
Slump	44 mm
Density (fresh concrete)	2394 kg/m^3
Air content (fresh concrete)	0.4 %
28-day strength	47.1 MPa

very useful information on potential problem areas and aspects still requiring improvement.

4.5. First operational phase

This operational phase extended from 27 February 1997, the date identified as “day 0” on the time scale, to 28 February 2002, identified as “day 1827”. These dates correspond to the switching on of both heaters, and the switching off of Heater #1.

4.5.1. Start-up procedure

The mechanical installation tasks, which were the critical phase from the point of view of accessing the GTS by road, were completed in 16 weeks between 1 July 1996 and 15 October 1996, two weeks ahead of schedule. Given that they were not time critical issues, the assembly and setting up of the data acquisition and control systems were prolonged longer than anticipated, until 27 February 1997, with 11 weeks of effective work in this period.

Apart from some short duration tests, the heating (first operational) stage began on 27 February 1997, the date identified as “day 0” on the time scale. The sequence of initiation was as follows (Figure 4.33, corresponding to Heater # 1):

- ❑ Throughout an initial period of 20 days a constant power of 1200 W per heater was applied, with the aim of identifying the thermal response of the system and adjusting the control algorithms.

- ❑ Over the next 33 days the power was increased to 2000 W per heater and maintained constant to approximate the temperature of 100 °C desired at the surface of the steel liner, but with a limitation on the rate of power increase to reduce thermally-induced stresses.
- ❑ Finally, on 21 April 1997 (day 53) the system was switched to the constant temperature control mode, allowing the power to fluctuate freely. Over a period of 8 days, three subsequent steps were performed to adjust the parameters of the control algorithm, the setpoints of the system being established successively at 95 °C, 99 °C, and 100 °C.

4.5.2. Control and monitoring process

4.5.2.1. Heating control. Operation and events

From day 61 onwards, the power control system automatically regulated the power in the two heaters independently, so as to maintain a constant temperature of 100 °C at the hottest point of the steel liner/bentonite interface, as originally planned.

The reference used by the power control algorithm was the highest temperature value in the sensors located at the surface of the steel liner, which was always at the centre of the bottom line of the heater (Figure 4.34). Due to the shape of the heater casings, temperatures over 100 °C were observed at the lids, but these were discarded, as they were considered to be unique points.

Only one of the three elements per heater, identified as Resistor A, was used on each heater on a permanent basis, the other two being kept in stand-by. The underlying reason for this was to check the operational life of these elements, which is inversely proportional to their external temperature. In any case, there were no failures of the elements throughout the first operational phase. Figure 4.34 shows the temperatures on the surface of the different elements at the end of this phase, immediately before the disconnection of Heater #1 on 28 February 2002.

The power required to maintain a constant temperature of 100 °C at the bottom of the steel liner showed some minor variations throughout the first operational phase. Initially being about 2280 W for Heater #1 and 2430 W for Heater #2 (it was always higher for Heater #2, which was located

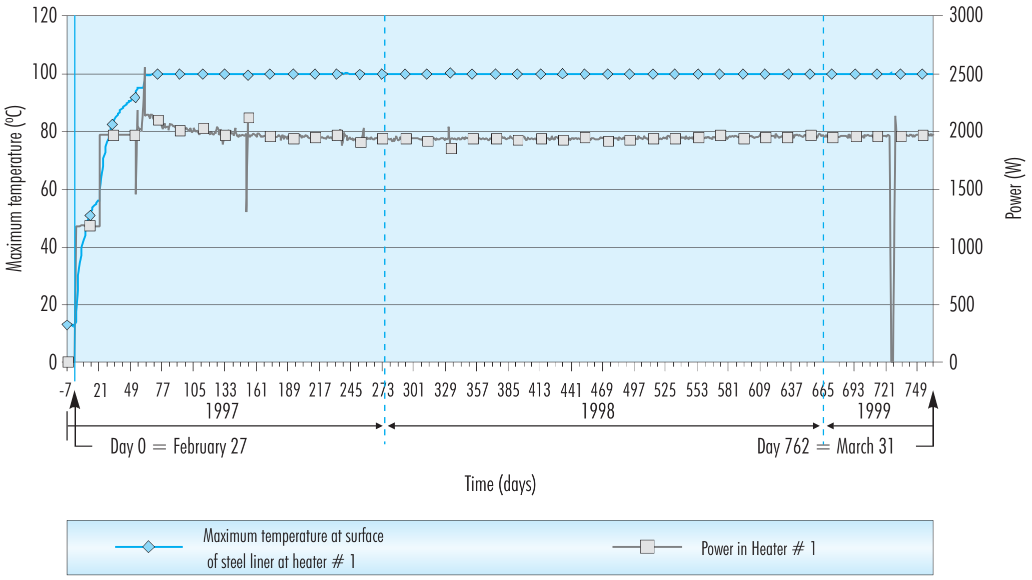

Figure 4.33: Log of temperature and power in Heater #1 during the first 762 days.

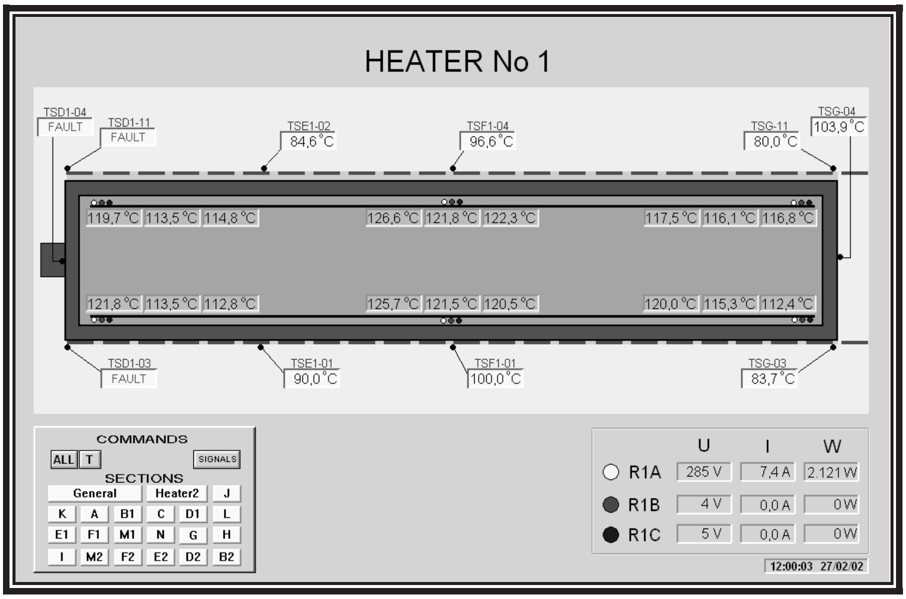

TSD1-04 FAULT
TSD1-11 FAULT
TSE1-02 84,6 °C
TSF1-04 96,6 °C
TSG-11 80,0 °C
TSG-04 103,9 °C

119,7 °C 113,5 °C 114,8 °C
126,6 °C 121,8 °C 122,3 °C
117,5 °C 116,1 °C 116,8 °C

121,8 °C 113,5 °C 112,8 °C
125,7 °C 121,5 °C 120,5 °C
120,0 °C 115,3 °C 112,4 °C

TSD1-03 FAULT
TSE1-01 90,0 °C
TSF1-01 100,0 °C
TSG-03 83,7 °C

	U	I	W
○ R1A	285 V	7,4 A	2.121 W
● R1B	4 V	0,0 A	0 W
● R1C	5 V	0,0 A	0 W

12:00:03 27/02/02

Figure 4.34: View of internal and external temperatures in Heater #1 at the end of the first operational phase.

deeper in the rock mass), it slowly decreased during the first 2 years of the first operational phase to 1940 W and 2175 W respectively. This was probably due to the drying of the section of the clay buffer located close to the heaters, which implied a lower thermal conductivity. The process was inverted afterwards, as deeper parts of the buffer progressively gained in humidity, resulting in a slow, constant increase of power in both heaters up to 2121 W and 2265 W, respectively, at the end of the first operational phase.

4.5.2.2. Monitoring and information processing

The test was remotely monitored and controlled from the Remote Monitoring Centre (RMC), located at the AITEMIN main office in Madrid, throughout the entire operational stage. Connections via modem were made periodically, about twice per week, to check system status and transfer data from the GTS computers to the Master Database generated at the Madrid system.

The Master Database stored one datum value per day and instrument, corresponding more or less to the value read at noon. At the end of the first operational phase, after 1827 days of heating, it contained some 1650000 records, with a total file extension of over 270 Mbytes. To simplify data transfer and handling by all the participating groups, the Master Database was built using MS-ACCESS.

Data could be retrieved from the Database in various forms for analysis and interpretation. A Sensor Data Report containing plots of the evolution of data from all the operative sensors was produced by AITEMIN every three months, and was distributed among all the project participants. During this phase, numerical data were also supplied by AITEMIN in electronic format to the other groups, as requested, for further processing.

4.5.3. Incidences

No major events occurred during the first operational stage in relation to heating control. The most relevant incidents are as follows:

- ❑ One current transducer in Heater #2 started to give an erroneous indication on 14 October 1997 (day 299). This caused a power increase up to a maximum value of 103 °C at some points of the liner/bentonite interface. The faulty transducer was replaced and the normal power level was restored.

- On 20 June 1999 (day 843), the power in Heater #1 was automatically switched off when one of the thermocouples in the control loop failed, providing a temperature reading over 100 °C. The power was restored after 24 h. The temperature dropped to 92 °C at the hot-test point of this heater during this short cut.
- Two main power failures occurred on 22 February 1999 (day 725) and 20 February 2000 (day 1088). In both cases the fault lasted less than one hour and no effect was noticed on the temperatures.

Other relevant events are listed below:

- Routine maintenance visits were made to the GTS about three times per year during the first operational phase. No really important actions were carried out during these visits, other than an overall check of the system and the replacement of certain minor faulty parts.
- From February to May 2001, relocation and rewiring operations of the Local Monitoring and Control System were carried out at the test site as one of the preparatory works for the partial dismantling operation to be carried out at the end of the first operational phase (see Section 4.6.3).
- Other preparatory works carried out in autumn 2001 were the installation of the equipment required for the handling and transport of components during dismantling, and the reconfiguration and upgrading of the DAS.

Mentions should also be made of the fact that, during this operational phase, water leaked from the system through the tubes used to pass the cable bundles through the concrete plug (especially through the bottom and right-hand tubes), and also along the inside of certain of the cables (especially the psychrometer cables, since these sensors were not watertight). The amount of water was measured periodically, and ranged from a minimum of 1.5 l/day to a peak value of 3.9 l/day. In principle this represented a significant amount of the estimated total water inflow into the drift (about 10 l/day), but it should be taken into account that this estimate was made before the instrumentation boreholes were drilled, and, as was observed during the installation operation, most of the water channelled along the cable bundles was coming from borehole SI-2.

4.5.4. Evolution of parameters

A great deal of information was obtained from the sensors installed in the system, since most of them remained operative at the end of the first operational phase. Independently of the specific analysis of these data carried out within the modelling (Chapters 6 and 7), a global, qualitative assessment of system behaviour may be derived from the sensor data, for the main monitored parameters.

4.5.4.1. Temperature

The temperature trend was quite uniform throughout the first operational phase, and this was the parameter showing the best symmetry throughout the test. A longitudinal section of the test, with the temperatures reached after 1827 days of heating, is shown in Figure 4.22.

In general, the temperatures in the clay barrier (buffer) around the heaters reached a stable value in a short time, whereas those points located far from the heaters showed a more gradual rising trend. Some examples are given in Figure 4.35.

Except for the control algorithm reference point, which was kept constant at 100 °C at all times, the temperatures at the surface of the steel liner decreased slowly during approximately the first two years of heating. The trend was then inverted to a slow increase, reaching at the end of the first operational phase values similar to the initial ones, and even higher in some cases (curves 1, 2 and 3 in Figure 4.35). This behaviour might be coupled with the slow initial decrease and subsequent increase of the applied power. Temperature differences of up to almost 20 °C were observed along the surface of the heaters (Figure 4.34).

In the intermediate part of the buffer, temperatures soon reached values in the range of 50-60 °C (depending on position) and remained quite stable, or increasing very slowly at this level (curves 4 and 5, Figure 4.35).

At the outer part of the buffer (rock contact), the temperature continued to increase gradually (curves 6, 7 and 8, Figure 4.35). Temperatures in the bottom part of the drift were higher than those in the roof, in correlation with the temperatures at the bottom and top surfaces of the steel liner.

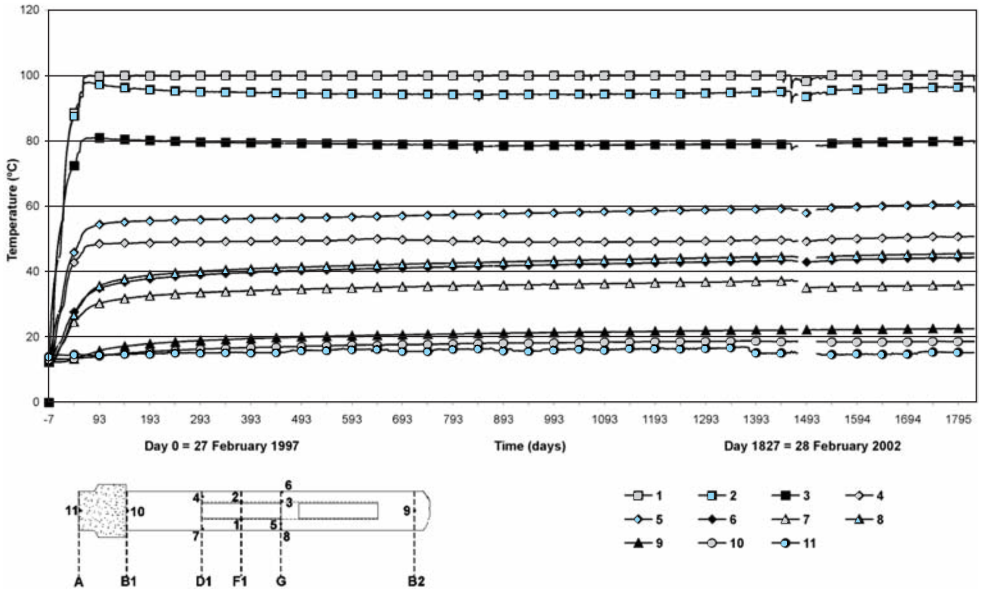

Figure 4.35: Evolution of temperature in the buffer during the first operational phase.

In the buffer sections located further from the heaters, temperatures were much lower but still showed a gradual rising trend (curves 9 and 10, Figure 4.35).

Within the rock mass, the temperature field was quite regular. Temperatures depended on the distance to the drift, and those points located closest to it showed a fast temperature rise at the beginning, later showing a gradual increase. Points located deeper in the rock, on the other hand, showed a more uniform rise trend, although their absolute values were lower.

4.5.4.2. Humidity

A good correlation was found between the readings provided by the three different methods used to monitor changes of humidity within the buffer: capacitive sensors, psychrometers, and TDR (Time Domain Reflectometry).

The evolution of humidity was not as symmetric as that seen for temperature. However, a common pattern could be seen in different cross-sections along the length of the buffer, and this is shown for example in Figure 4.36, corresponding to the capacitive sensors in the instrumented cross-section E1:

- ❑ The points located in the outer periphery of the buffer quickly reached high humidity values[2] especially on the right-hand side[3] (sensor 07) and in the top part (sensor 10). The bottom part (sensor 01) also reached a high humidity in a short time. On the left-hand side (sensor 08), hydration progressed at a slower rate but after two years it also practically reached the level of the other sensors in the buffer periphery.
- ❑ The points located close to the heaters (sensors 03 and 04) dried up quickly as soon as heating started, but after about one year they started a slow process of hydration that continued until the end of the first operational phase.

---

[2] It should be taken into account that the concrete plug was built almost 5 months before Day 0.

[3] The main water inflow, borehole SI2, is located in the cable channel on the right-hand side.

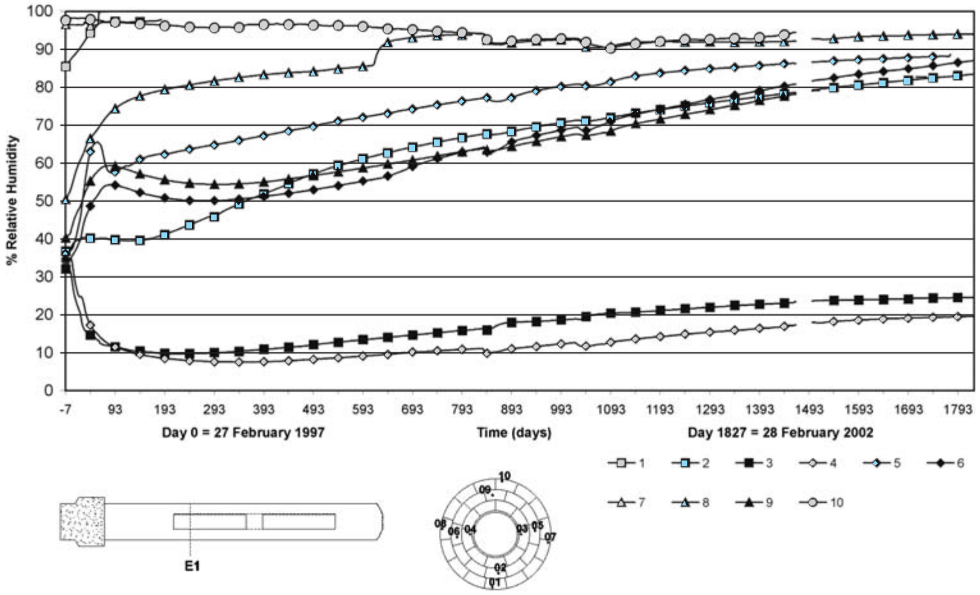

Figure 4.36: Evolution of buffer relative humidity at section E1 in the first operational phase.

- ❑ The points located in an intermediate position of the buffer (sensors 02, 05, 06 and 09) showed an oscillating behaviour, with alternating drying and wetting periods for approximately the first year, this having been explained by the two-phase flow in this zone. After that period, they all showed a steady increase in humidity content.

As mentioned above, this pattern was quite repetitive along the entire length of the buffer, as a result of which the following conclusions could be drawn:

- ❑ The radial channels for the cables of sensors introduced in the inner buffer, and the joints between blocks, which could have been a preferential path for water inflow, were sealed very soon.
- ❑ The system irregularities (local water inflows, air gaps, cable channels, etc) might have played an important role in producing hydration asymmetries, especially during the first year, but these were practically limited to the outer ring of blocks. After that period, the humidity field trended to a more uniform situation.

On the other hand, the humidity sensors placed in the granite (psychrometers and TDRs) did not yield any indication of de-saturation in the rock. On the contrary, many psychrometer readings showed an increase of saturation in the rock, from the initial situation of partial de-saturation (the drift was dried during the installation operation). In the same way, the readings from TDRs in granite, which were reinterpreted manually after the partial dismantling, showed an increase in the water content of the rock.

4.5.4.3. Total pressure

There were certain doubts as to the absolute values of the data provided by these sensors from the start of the test. In fact, the recalibration carried out on some of them after the partial dismantling operation made it possible to apply an offset correction to their data sets.

Regardless of the above, the general trend of total pressure developed within the buffer may be seen in Figure 4.37. Following, in some cases, an initial period during which negative readings were obtained, probably due to an installation problem, the pres-

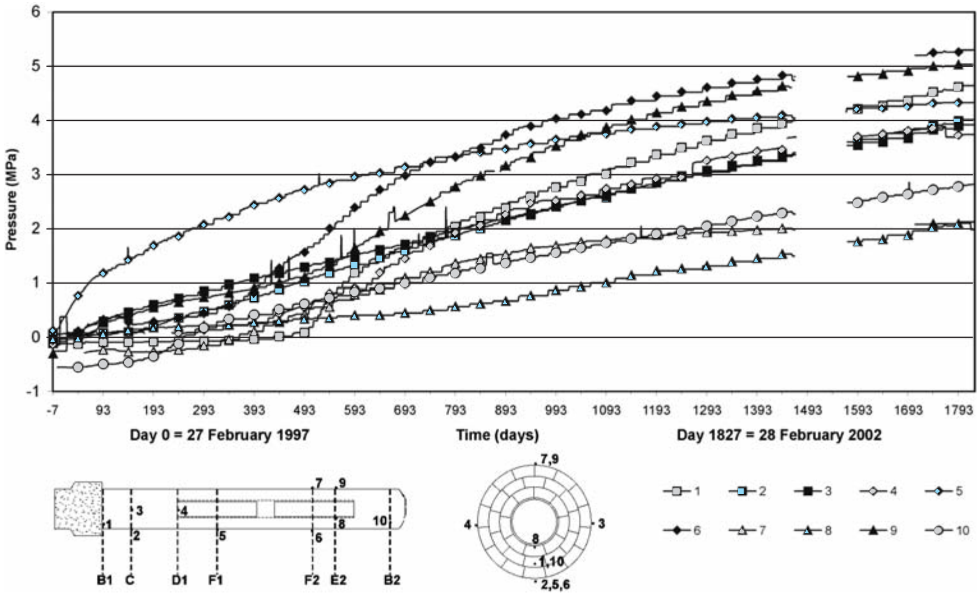

Figure 4.37: Evolution of total pressure in the buffer during the first operational phase.

sures increased continuously throughout the first operational phase, in parallel with the general increase of the degree of saturation observed in the buffer.

The highest pressures were observed at the bentonite/rock interface, and normally at the bottom part, reaching peak values over 5 MPa at the end of the first operational phase. Values in this range were also observed at the drift roof in section E2 and at the inner side of the concrete plug (Figure 4.37). At the drift end and the inner side of the concrete plug, some points reached some 3 MPa. Lower values, in the range of 2 MPa, were measured at the surface of the liner, although this might be explained by the arch effect of the ring of dry blocks in contact with the heater.

The cells installed within the rock mass, in boreholes SG1 and SG2, showed a general trend of increasing total pressures, with some fluctuations, reaching peak values in the range of up to 5.6 MPa. The evolution was, however, very different depending on the specific location and orientation of each cell.

4.5.4.4. Other parameters

Pore pressure in bentonite

In general, these sensors provided very low readings. Some positive pore pressure values, in the range of 0.4 MPa, were observed at those parts of the buffer having a higher degree of saturation, such as for instance the outer ring of blocks on the right-hand side.

Hydraulic pressure in the rock

The hydraulic pressures measured in the radial boreholes during the first operational phase showed a general trend of gradual but steady recovery of water heads in the rock mass, with some fluctuations in some boreholes.

In the boreholes located outside the drift (BOUS 1 and 2, FBX 1 and 2), no significant variations were observed in general, and the pressure levels remained quite stable throughout the period, apart from one temporary drop, probably due to valve misuse.

A hydrotesting campaign and a water sampling campaign were carried out during the first operational phase, their effects being registered as fast pressure drops and recoveries in the affected intervals.

Displacements

A number of instruments were introduced in the system to monitor different kinds of displacements within the buffer [29] and [32].

Heater displacements. For those measurements, nine high sensitivity linear displacement transducers were used; they were fixed at one end to the rock and at the other end to the liner. The sensors provided indications of movements in the range of several mm in different directions during this operational phase, but the confidence on the readings obtained from these sensors was poor. Finally, the readings did not match with the measures taken during partial dismantling, and the displacement transducers removed were found to be severely damaged by corrosion.

Crackmeter. This was a set of three highly sensitive displacement sensors installed over a fracture in the gallery wall in section F2. In principle they allowed opening, shearing and reject movements of the crack to be measured, but they failed in an early stage of the first operational phase due to flooding of the electronics with water. The data recorded before the failure showed significant values of displacement, which reached a relative magnitude of two millimetres.

Clinometer. This was a set of six twin-axis capacitive transducers assembled inside steel cylinders, and installed horizontally and vertically at the front end of Heater #1. In principle they allowed rotation along the cylinder axis and around its centre of gravity to be measured, but they failed along with the crackmeter. The measurements taken by the clinometers inside the bentonite blocks prior to failure showed very small dip angle values, of less than 0.5 degrees during the 150 first days. This value corresponded to a differential displacement of about one millimetre.

Extensometers. Two extensometers were installed in horizontal and vertical positions at the front end of Heater #1. Each extensometer consisted of three resistive transducers allowing individual bentonite block displacements to be measured in relation to the gallery wall. The extensometers failed along with the crackmeter and clinometer. The readings recorded prior to failure showed that the displacements in the horizontal position were greater than the vertical ones, of the order of 20 mm. The trends detected pointed to a swelling of the external blocks (close to the wall) due to hydration, shrinkage of the inner blocks (close to the heater) due to drying, and minor variations of the intermediate blocks, in good correlation with the readings from floating displacement transducers and also with the variation of the water content of the intermediate blocks.

Gas generation, release and migration

Sampling and analysis of gases in the "in situ" test, performed by GRS [28], started in December 1996, almost three months prior to switching on of the electrical heaters, and was continued until June 1999 almost monthly. The main result concerns hydrogen concentrations resulting from corrosion of metallic components, which were observed before the start of the heating. These decreased after switching on of the heaters, this indicating that the hydrogen already present might have escaped through the non-gastight concrete plug. Afterwards, the concentration increased again, pointing to a continuation of the corrosion processes, as was finally observed in the metallic components located at the most humid parts of the barrier during partial dismantling.

Posterior increases and decreases in the hydrogen concentration, detected in the measurements taken between 2000 and 2002, might have been caused by variations both in the level of activities carried out within the service area of the drift and in the ventilation regime, given the non-gas tightness of the plug.

The investigation also indicated that the draining pipes located close to the rock walls were flooded, while those in the intermediate ring of the barrier and in contact with the liner were filled with gas at atmospheric pressure. This was checked again during partial dismantling: those pipes close to the rock were found to have been crushed by the bentonite swelling force, while the rest maintained their integrity.

4.5.5. Performance of components

According to the historical records of the test, the behaviour of the heating system and of the DAS during the first operational phase was excellent and only some irrelevant failures were registered.

The data collected from the sensors throughout this period allowed for the creation of a large database, which was used to validate the modelling codes. The results were very positive, with a good correlation between the model predictions and real data.

Most of the sensors passed well beyond their expected operational lifetime. By March 2002, before the partial dismantling of the tests, more than 85 % of the sensors remained operative, after more than 5 years of operation. At that time it was possible to make a qualitative assessment of sensor performance:

a) Temperature sensors (thermocouples): the data obtained seemed to be accurate when compared with measurements from temperature sensors incorporated in other instruments and with the expected evolution provided by the models.

b) Humidity (capacitive type, psychrometers and TDRs): Capacitive type sensors provided very valuable data and in general, the readings provided by each sensor type matched quite well with the others and also with the prediction from the models.

   The psychrometers signals in bentonite became difficult to interpret and only some of them at the outer buffer ring reached the measurement range (above 95 % RH). The psychrometers in the granite gave reasonable readings (very low suction).

   The readings from the TDRs installed in the buffer were good, although these sensors provided an integrated measurement. The performance of the TDRs installed in granite was not so accurate, as they were operating at the limit of their resolution.

c) Vibrating wire sensors: the rest of the instruments were mostly vibrating wire type. These sensors were used to measure pore pressure in the bentonite, total pressure in the bentonite, at the rock interface or in boreholes (also called 3D cells), displacements in rock (extensometers), heater displacements and displacement in bentonite blocks.

   In general, their behaviour was as good as expected, that is: high accuracy, long-term stability, reduced temperature drift and no hysteresis. The only difficulty came from the weakness of the embedded thermistor, which failed in some cases. That thermistor was used for temperature compensation of the vibrating wire signal. Fortunately in all events it was possible to substitute that temperature with the reading from another temperature sensor (thermocouple) located sufficiently close by.

d) Hydraulic pressure in rock boreholes: internal packer pressures and borehole interval pressures were measured by means of conventional pressure transducers installed outside the sealed area, at the end of nylon type plastic tubes. These sensors worked under standard conditions and could be checked or replaced if necessary, as was the case with some of them.

e) 100 % of the LVDT type clinometers and potentiometers for displacement between the bentonite barrier (also called experimental sensors) failed due to some of them being completely flooded up to the associated electronics.

4.5.6. Comments and observations on the first operational phase

The first operational phase lasted exactly five years, from the switching-on of both heaters, on 28 February 1997, to the switching-off of Heater #1 on 28 February 2002. During this period the test ran in a continuous mode, with no significant interruptions, and the information provided by the installed instruments was collected, creating a large experimental database. Only 12 % of the installed sensors failed during the first operational phase. In fact, the good performance of the system components was one of the reasons supporting the decision to extend the operational phase of the test.

In relation to the evolution of the test itself, a number of observations were extracted at this point from the sensor readings (see Section 4.5.4):

- ❑ The temperature field was not yet stabilised after five years of heating, except for zones very close to the heaters.
- ❑ The hydration of the buffer was in progress at all points at the end of the period, even in zones in contact with the heater, which had showed a drying process during an initial period lasting about 200 days. Apparently, saturation was being reached only in zones close to the rock, and seemed to be faster in the bottom part.
- ❑ Total pressures increased in general throughout the test, especially at the rock-bentonite contact, and more quickly in the bottom part, this being in accordance with the observations from the humidity sensors.
- ❑ The important differences in humidity values observed from the very beginning between

points located relatively close each other confirmed that all the construction gaps and cable channels sealed very soon.

- This saturation pattern was quite uniform throughout the entire test, with no relevant differences between zones of the drift that were initially considered as being more humid or more dry, this indicating that the hydration process was being controlled by the bentonite itself. No signs of de-saturation were observed in the rock mass close to the buffer.

4.6. Partial dismantling

4.6.1. Concept

The partial dismantling extended from 28 February 2002 to 26 July 2002. These dates correspond to the switching off of Heater #1, and the end of the construction of the first part of the shotcrete plug.

The works consisted basically of removing one of the heaters, leaving the other in operation for an as yet undefined period. They were initially planned for the summer of 2001, but an apparent divergence was observed in the “mock-up” test between the model predictions and certain measured parameters, such as water intake, humidity, and total pressure. The works were postponed for one year in order to study this problem and to compare the evolution of the “mock-up” with that of the “in situ” test, and also to check whether if the “in situ” test were left for a longer period it would behave in the same manner. The partial dismantling took place in the summer of 2002.

The design and planning of the partial dismantling was conditioned by three basic objectives:

1. To carry out an intensive sampling programme in the test components (bentonite, rock, metals, instruments, etc) located in the area of Heater # 1. Samples should be taken with minimum alterations.
2. To perform a canister retrieval exercise in such a way that information be provided on the potential technological problems that may be found in an operation of this kind in the real case.
3. To re-construct the test, with the necessary amendments and improvements, in order to continue the heating and hydration phase with the second heater over a longer timescale.

During dismantling, a large number of samples from different materials (rock, concrete, bentonite, water, chemical tracers and metals) were taken for analysis. The detailed design and planning of the partial dismantling was undertaken by AITEMIN in close cooperation with all the partners, and especially with NAGRA. As result, by March 2001 an initial version of a Sampling Plan [40] was issued, describing the samples to be taken during the dismantling and the procedures to be adhered to. Similarly, a document entitled “Sample Identification and Control within the FEBEX Project” [41] was produced, the aim of which was to simplify and provide a uniform sample labelling procedure throughout the entire project.

The initial plan was to remove the buffer and all components up to a distance of one metre from Heater #2 (Section G in Figure 4.3). However, and in view of the risk of disturbing the non-dismantled area, it was finally decided to leave one additional metre of buffer, as a result of which the dismantling was carried out up to the longitudinal coordinate x = 7.882 (Figure 4.38). A dummy steel cylinder with a length of one metre was inserted in the void left by Heater #1 in the centre of the buffer. Some new sensors were installed in that one additional metre of bentonite buffer.

New instruments were installed in the remaining part of the test, in order to increase the density of measurements in the buffer, and also to extend the life expectancy of the instrumentation system. These sensors were introduced in boreholes drilled in the buffer parallel to the drift.

To simplify this activity, the new concrete plug was constructed in two phases: An initial temporary plug measuring just one metre in length, which was built immediately after dismantling, and a second section to complete the plug length to the three metres planned in the design of the test. Unlike the first plug, the new one was a parallel plug, without keys excavated in the rock, and was constructed by shotcreting.

The configuration of the test, after completing the dismantling operation and construction of the full plug length, is shown in Figure 4.38.

4.6.2. Overall sequence of activities

Very schematically, the sequence of the main operations carried out during the partial dismantling operation was as follows:

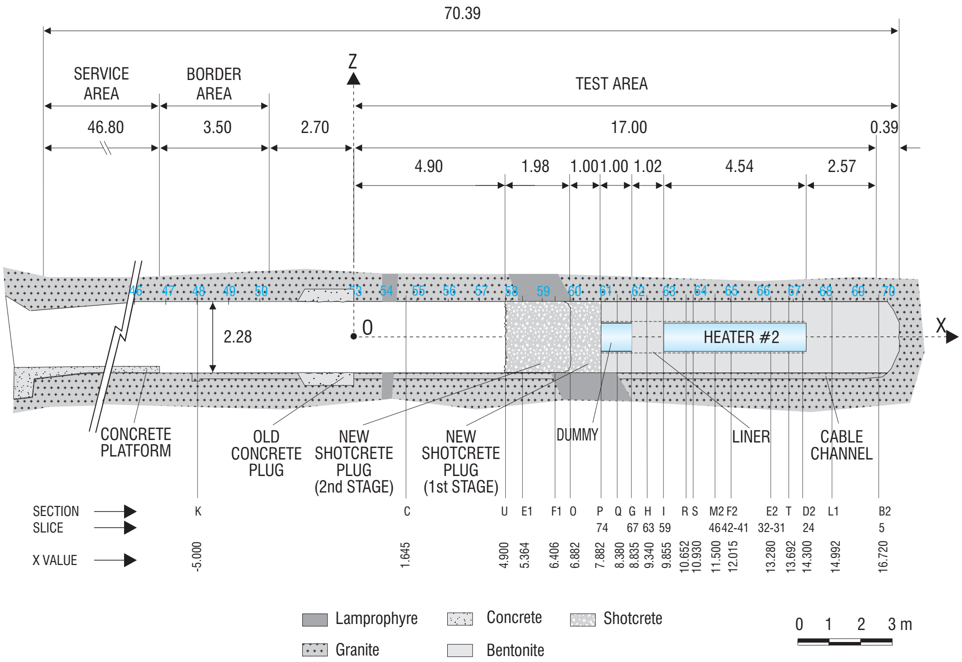

Figure 4.38: "In situ" test configuration after dismantling of Heater #1.

a) Preliminary tests

Due to a lack of experience regarding some aspects of the planned operations, a number of tests were carried out during a preliminary phase in order to provide inputs for the design of the operation and to minimise the risks involved to the extent possible. The most relevant tests were the following:

- Cable dismantling tests, focused on the problem of dismantling without damaging the instrumentation cables, which were grouted and embedded in resin into the tubes crossing the plug.
- Bentonite sampling tests, intended to determine adequate sampling procedures for the bentonite, at different degrees of saturation.
- Bentonite mass extraction tests, necessary to identify the most operative procedures for removal of the bentonite buffer and to estimate dismantling times.
- Shotcreting tests, to assess the feasibility of constructing a shotcrete plug and obtain parameters for its design.

b) Preparatory works

A number of works were carried out prior to the dismantling operation itself, the most important being:

- Removal of all electrical and electronic systems installed in the FEBEX drift, which were moved to a nearby location so as to clear the drift for the dismantling.
- Installation of a new drift hauling system, including a new winch and transport and handling vehicles.
- Upgrading of the DAS.

These works are described in more detail in Section 4.6.3.

c) Dismantling

The dismantling itself was carried out according to the following sequence:

1. Switching off of Heater #1, one month in advance of plug demolition
2. Rock sampling in the service area
3. Demolition of the concrete plug (sampling)

4. Removal of bentonite up to the front of the Heater # 1 (sampling)
5. Extraction of Heater #1
6. Removal of liner and bentonite buffer up to the target point (sampling)
7. Insertion of a one-metre dummy steel cylinder in the central hole
8. Installation of part of the new instruments
9. Construction of the first section of the shotcrete plug
10. Installation of additional instruments in the buffer
11. Completion of the shotcrete plug to a total length of three metres

4.6.3. Preparatory works

Removal of electrical and electronic systems

Previous to any other operation, some of the larger electrical and electronic systems in the service area of the FEBEX drift were disconnected, removed, transported to a new area at the main entrance of the GTS and reconnected, in order to provide sufficient room for the dismantling operation in the drift. This included computers, data acquisition systems, UPS and heater power regulation units.

This was done from February to May 2001, during the first operational phase. The operation was carried out in such way that both the period of power interruption and of data loss between disconnection and reconnection of the sensor cables were minimised.

Installation of handling and transport equipment

New equipment was required for the handling and transport of components during dismantling. This included a new vehicle required to extract the heater from the deposition hole, a side dump wagon to transport concrete and bentonite outside the drift and a new winch to be installed on the concrete platform outside the drift. This equipment was transported to the GTS and installed at the FEBEX drift in autumn 2001.

New hauling system. The main difference with respect to the system used during installation is that in this case the new winch had fully independent drums for each direction of movement, with separate electric drives and braking system electronically regulated in order to compensate the tension and speed in both cable lines (pull/release). The pulling cable was also renewed and a number of additional track sections were taken to the GTS, as they were required to extend the track system during dismantling.

Side dump car. This was designed and constructed to transport the bentonite and the concrete debris along the drift. It was equipped with a bucket with an approximate capacity of 1 m^3 that could turn on one side so as to discharge the material along a ramp fixed to the concrete platform outside the drift.

Reconfiguration and upgrading of the DAS

The DAS had to be reconfigured for the specific conditions of the second operational phase (single heater, new distribution of sensor interfaces and reduced number of instruments, but longer cable distances). This required certain modifications to be made to its structure, adding new components and/or changing the previous configuration of the system and upgrading the obsolete ones.

This was done in autumn 2001. The main works carried out were:

- ❑ The main data-logging unit of the test (IMC) was divided in several parts to simplify the cabling of sensors, using the IMC distributed bus capability.
- ❑ The two control computers were completely renewed and the software packages were upgraded.
- ❑ An additional computer was included for demonstration purposes. This computer was linked with the control system, but could be operated by non-skilled personnel, such that the status of the test at every moment might be easily demonstrated to GTS visitors.
- ❑ A local network linked the two control computers and the third one for GTS visitors.

4.6.4. Sampling

4.6.4.1. Design and objectives

The sampling and analysis (see Section 5) of the area around Heater #1 was aimed at several objectives:

- ❑ To assess the behaviour and current state of the different elements in the "in situ" test after five years of heating and hydration, and to further understand the processes that took place within.

- ❑ To evaluate the reliability of the data obtained from the instrumentation by calibrating the retrieved sensors, and to compare these data with the observations made from the samples taken. The assessment of the data will ultimately serve for comparison with the model predictions.
- ❑ To confirm the expected behaviour of the barrier under heating and hydraulic load.
- ❑ To study the corrosion processes in the capsule, liner, "ad hoc" coupons and sensors.

Different analyses, requiring specific samples to be collected, were proposed by the participants in the project in order to achieve those objectives. All the sampling requirements were put together and combined into an intensive and coherent Sampling Plan [40], which was agreed to by all the participants. This plan included sampling protocols to be fulfilled for each type of sample, with precise indications regarding the type of collection.

The plan was organised in 32 sampling sections perpendicular to the gallery axis, and located in the service area, the concrete plug and the zone of the barrier to be dismantled. A layout of the gallery with all the sampling sections and the purpose of the samples included in each may be seen in Figure 4.39.

Samples from diverse materials were collected with the following purposes:

- ❑ Concrete cores were extracted from the shear stress zone and from the interfaces with bentonite and with rock, in order to study the mechanical behaviour of the material and the potential alterations undergone.
- ❑ Bentonite samples of different shapes, from blocks to cores of various diameters and lengths, were taken to analyse the physical and chemical changes experienced, the chemical evolution of the bentonite porewater and the flow paths of the different types of chemical tracers that were installed during the installation phase (glass ampoules, tracer coupons and doped filter papers), and also to calibrate some of the sensors installed in the barrier (TDR), according to the measurements made during the dismantling (water content).

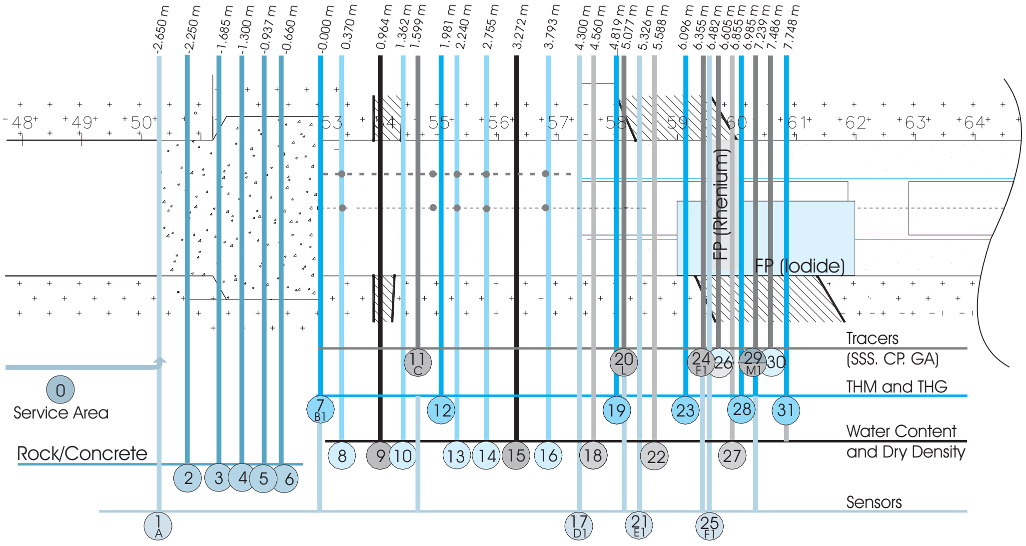

Figure 4.39: Sampling sections.

- Rock cores were collected to analyse the evolution of the physical, mechanical, hydraulic and geochemical properties of the granite and lamprophyre in contact with the clay barrier, with particular reference to the EDZ.
- Heater #1, liner sections and the corrosion coupons placed during the installation were collected as metal samples to analyse the different corrosion processes occurred.
- All the accessible instrumentation within the dismantled barrier was collected to perform different analyses and recalibrations, in order both to assess the reliability of the data stored throughout the first operational phase and analyse the causes of the failures.

An appropriate labelling procedure was necessary to identify each sample by its material, shape and location. Except for the sensors removed, which maintained their original labelling as sample code, each sample collected was identified by a code of the type:

T-Y-NN-ZZ

where

T:	Code of material: B (bentonite), C (concrete), R (rock), M (metal), or a combination of two (C/R, C/B)
Y:	Sample shape: H (heater), L (liner), B (block), T (rock core), S (any other shape including core except for rock)
NN:	Sampling section number: S0 to S31
ZZ:	Correlative sample number for same type of samples in each section

4.6.4.2. Sampling works

The sampling work started in the service area on 2 April 2002, with the extraction of granite cores perpendicular to the gallery axis as blank samples for comparison with rock affected by the test.

At the concrete plug, concrete and concrete/rock cores were extracted using the same technique at the foreseen sections as the demolition operation progressed. Before finishing dismantling of the plug, cores from the concrete/bentonite interface were extracted. The instruments installed on both sides of the plug were also collected. This sampling was completed on 28 May 2002, when the plug demolition was finished.

The sampling of the clay barrier was carried out subsequently. Each section had been assigned to a bentonite slice of interest, so that one section per day was sampled after removing the bentonite slices previous to the assigned one. Cores of several diameters were extracted from all parts of the barrier (Figure 4.40). Many of these cores were analysed "in situ" immediately following extraction, in order to obtain a profile of the actual water content and dry density of the barrier at the moment of the dismantling. The rest of the cores, as well as complete bentonite blocks and other types of samples, were packed immediately after collection according to the established procedures, and sent to the involved participants for laboratory analysis. Rock cores from granite and lamprophyre were also extracted, after the gallery was cleared from bentonite.

In those sampling sections corresponding to instrumented sections all the accessible sensors were removed and packed.

The complexity of the sampling may be observed in Figure 4.40, which shows the sampling plan for a given section and the bentonite slice after the sampling was completed.

The sampling plan was fully accomplished with minor modifications decided in agreement with the involved partners. Several remarks may be made in relation to the work:

- The sampling section at the concrete/bentonite interface had to be reconfigured in order to avoid the mercury spilled by two damaged total pressure cells (see Section 4.6.5.2).
- The sensors and their cables were found to be in good contact with the bentonite and those close to the rock walls were highly pressed towards the rock. Some of them were found to be damaged due to this pressure, and also with rust build up in some cases. No noticeable changes in sensor positions were found.
- Some of the sensors in the bentonite were found to be severely corroded, especially at the front end of Heater #1 (Figure 4.41). Subsequent analysis showed that this corrosion had been produced by sulforeducing bacteria (see Section 5.4).

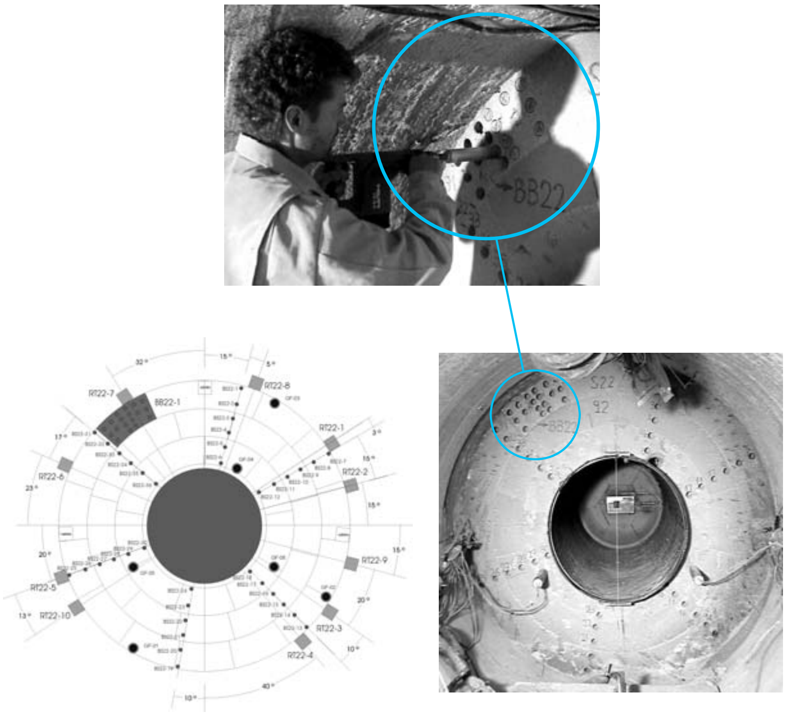

Figure 4.40: Example of sampling section plan and its appearance upon completion.

- The ceramic gas flow pipes at the bentonite/rock interface, as well as the gas pressure sensor, were found to be broken and squashed by the pressure of the bentonite. The pipes at the heater surface were broken only in large fragments, and those protected in metallic tubes remained intact.

Table 4.10 contains a breakdown of all the collected samples, by materials and zones.

4.6.4.3. Quality assurance and quality control

The entire activity was carried out under a Quality Assurance Programme supervised and approved by the FEBEX Project Quality Assurance service.

All the sampling was adequately documented: logs were produced for each section sampled and for each sample collected, containing all the relevant information. In addition, quality records containing

Table 10
Breakdown of samples

Zone	Section	Rock	Concrete	Bentonite	Sensors	Metal	Subtotal
Service area	S0	10					10
Concrete plug	S1 – S7		56	15	23		94
Clay barrier	S8 – S31	23		623	141	6	793
TOTAL		33	56	638	164	6	897

Figure 4.41: Corrosion effects in a linear displacement transducer at the front end of Heater #1.

the results from the "in situ" analysis carried out were produced.

The temperature and humidity conditions of both the gallery and the sample storage area were measured and registered throughout the works.

Finally, all the relevant aspects of the works performed were graphically documented with digital photos and video.

4.6.5. Dismantling of concrete plug and buffer

4.6.5.1. Switch-off of Heater #1

Throughout the first operational phase of the project, the temperature at the liner/bentonite interface was maintained at 100 °C. One of the main constraints of the dismantling works was the intention to minimise the effect of such works in the part of the test that was to remain in place. Therefore, it was decided to perform the dismantling keeping Heater #2 in operation at all times.

Temperatures in the area affected by the dismantling had to be reduced to a level compatible with manual work, in the range of 25 °C to 30 °C. Therefore, in accordance with the results obtained from the modelling of several cooling options, the power of Heater #1 was switched off on 28 February 2002, one month before the start of the dismantling works.

4.6.5.2. Dismantling of concrete plug

The demolition of the plug was carried out with a hydraulic splitter. This method was selected instead of blasting so as to minimise the risk of damaging the instrument cables passing via tubes through the plug, and also to disturb the system as little as possible.

Figure 4.42: Intermediate phase of plug demolition.

Before starting the concrete breaking, a first borehole was drilled up to the bentonite for pressure release. No gas or water outbursts were observed. Figure 4.42 shows the plug at an intermediate phase of demolition.

Two total pressure cells located at the contact with the bentonite were damaged during the final stage of the demolition. Part of the mercury contained in them was spilled, so a mercury decontamination process was required. Special measures were taken to avoid damaging the remaining cells at that interface, and also to control the mercury content in the working environment until the demolition was completed on 28 May 2002.

A total of 11 m^3 (26.5 t) of concrete was removed. No flows of water were observed coming from the bentonite or from the rock. The concrete presented a homogeneous and dry appearance, with no cracks and few pores. Two constructive joints could be observed, corresponding to the three sections into which the plug construction was divided (section 4.4.4). No special weakness was observed at those joints, even in the cores that crossed them.

4.6.5.3. Dismantling of buffer

Dismantling up to Heater #1

The first task carried out after the removal of the plug was a long drilling test. The aim was to assess the feasibility of drilling horizontal boreholes of up to 8 m in length into the non-dismantled buffer without significant deviations. These boreholes would be needed to insert new sensors and gas pipes into the barrier with a view to the second operational phase. The test was successful.

The dismantling works performed from this point on were carried out as quickly as possible in order to reduce the potential changes in the sampled materials, but without jeopardising the quality of the collected samples. The ventilation in the working area was limited, to avoid excessive evaporation of the water contained in the bentonite.

During the first stage, until reaching the heater front, approximately 4.3 metres of buffer were removed. All the bentonite slices were dismantled one by one by hand (Figure 4.43).

The bentonite not required for analysis was transported along the drift using the side dump wagon

Figure 4.43: Dismantling of bentonite slice.

described in Section 4.6.3. up to a large container outside the drift. When filled up, this container was transported by truck to an authorised dumpsite in the area. About 54 t of bentonite were dumped during the entire dismantling process.

The actual x coordinates from each bentonite slice, close to the left and right walls, were registered by means of two laser meters located at the $x=0$ coordinate. Also, each bentonite slice was graphically documented.

Dismantling in the heater zone

After the extraction of Heater #1, the buffer dismantling continued up to the planned final position, that is, two metres ahead of Heater #2. During this part of the works, approximately 3.5 m of buffer length were dismantled. As in the case of the previous part, the slices were dismantled one by one by hand, but due to the space constraint, this part was more difficult to complete (Figure 4.44). Three and a half sections of liner were removed during this part of the dismantling.

As for the previous buffer dismantling, the x local coordinate for each bentonite slice was registered at both sides of the gallery, and each slice was also graphically documented.

Observations

The following observations from the dismantling have been made:

- The measured x coordinates were some centimetres smaller than the ones taken during the construction phase. Small longitudinal grooves in the direction of the gallery axis could be observed on the bentonite surfaces in contact with the rock. All these observations might suggest a displacement or expansion of the buffer, at least at its exposed part, towards the drift entry.
- In general, no free water was observed at the bentonite/rock interface, or in the exposed rock, except for a local water inflow located at the right-hand side of the large lamprophyre dyke.
- The bentonite showed a solid appearance, even in the area close to the rock. No mud or gel was found. The blocks seemed to be quite dry in the centre, producing dust when drilled, and more humid in the outer ring, with a noticeably darker colour (Figure 4.45).

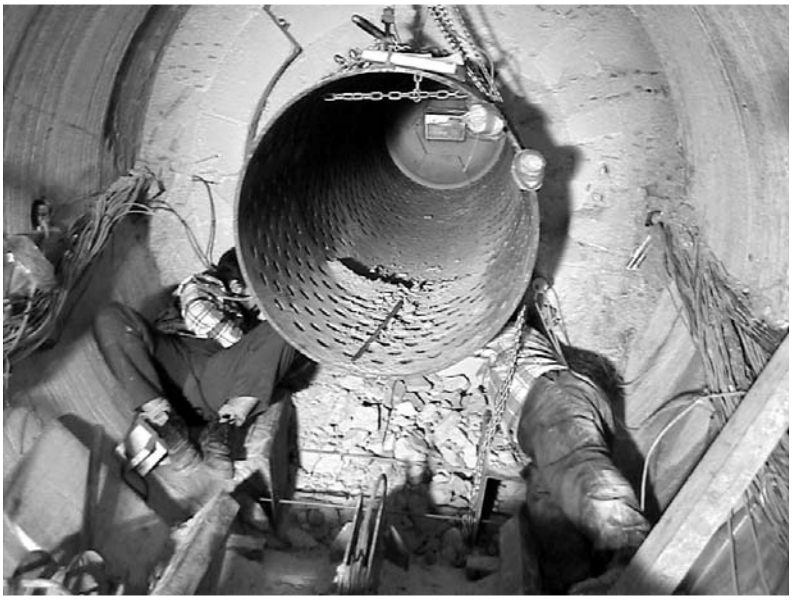

Figure 4.44: Dismantling works in the heater section.

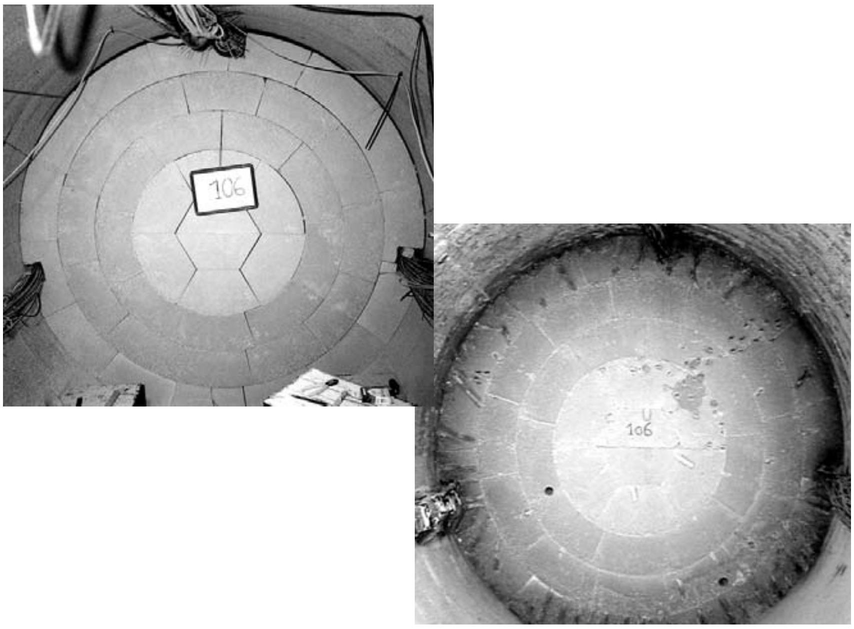

Figure 4.45: Appearance of the same bentonite slice during construction (left) and before dismantling (right).

- All the construction gaps were completely closed, including the 4-5 cm gap in the top of the buffer and the different gaps between blocks, around cable channels, and around sensors (Figure 4.45).
- The boundaries of the blocks were clearly visible, except for some joints between those of the outer ring, which were difficult to observe in some parts. In any case, even in these zones the blocks could be separated at the joints and showed considerable mechanical integrity.
- Deformation could be appreciated in all the liner sections: The horizontal diameter was about 5 mm less than the nominal, and the vertical diameter was about 10 mm in excess of it. This was an elastic deformation that disappeared when the surrounding bentonite was removed.
- All welding cords between liner sections, about 10 cm long, were found to be broken. The liner sections themselves showed a separation of between 5 mm and 10 mm. The oxidation at the breaking surface of the welding cord suggested that the break was not recent.

4.6.6. Heater retrieval

4.6.6.1. Equipment

Design criteria

The equipment used for the extraction and handling of Heater #1 was designed and constructed specifically for this task. Many structures and components of the equipment used in 1996 for the test installation were used again [42], albeit with important modifications. The main modifications refer to the replacement of the hauling winch located on the concrete platform outside the drift for a new unit, and to the re-engineering of the heater car so as to adapt it for the extraction.

When designing the extraction system, a number of potential problems that might occur during the extraction were considered:

- The cross-sectional position of the heater might have changed due to differential swelling of the bentonite buffer.

  The vertical displacement transducers fixed to the liner had showed an apparent sinking of about 10 mm, but the reliability of these readings was doubtful [43]. On the other hand, according to the signals provided throughout the operational phase by the humidity sensors and the total pressures against the rock, it was considered that the movement, if any, would most probably be upwards, with a maximum displacement of the order of the construction gaps existing at the top of the buffer (around 5 cm). It was therefore decided to provide a height adjustment capability in that range for the heater extraction equipment. For larger displacements it might also be possible to adjust the position and height of the track system.
- The corrosion of the heater and liner might require a large pulling force to separate them.

  Only limited corrosion was expected, as the humidity in the inner part of the buffer had been rather low throughout the entire operational phase. On the other hand, additional problems might be caused by bentonite parts entering into the perforated liner. The potential risk of the liner being deformed by the swelling pressure of the bentonite was not considered, since the pressure values recorded at the liner contact were relatively low (0.4 MPa). In any case, it was decided to construct a robust extraction system with a pulling capacity of 15 t, which should be sufficient to cope with this kind of problem (the total weight of the heater is 11 t).

A description of the main characteristics of this equipment is given in the following sections.

Heater retrieval car

The machine used for extraction of the heater from the deposition hole and for its transport along the drift was based on the same piece of equipment that was used for emplacement (see Section 4.4.3), which was modified for this new task. The modifications included replacement of the originally installed pushing mechanism for a new system, prepared in this case for pulling from the heater, and the introduction of some capability to adjust the height of the machine, as mentioned above.

A schematic view of the modified equipment is shown in Figure 4.46. The chassis, which was basically the same one that was used for the emplacement, was modified in the bogies zone, in order to incorporate the possibility of regulating the height of the rolling bed base line. Instead of having a fixed connection, the link between the bogies and the chassis consisted of a series of studs (16 in total) that provided a height variation capability of ap-

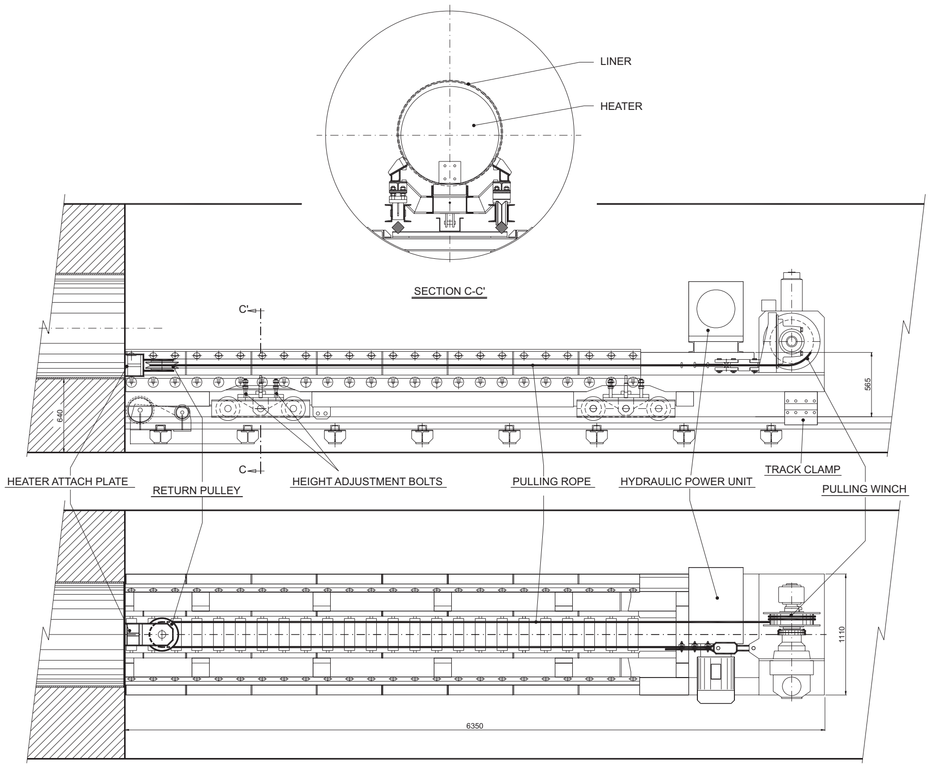

Figure 4.46: Schematic diagram of the heater extraction equipment.

proximately ± 25 mm, in relation to the original reference level. Also the clamps used to fix the vehicle to the tracks were made more robust, in order to absorb the potential reaction forces that might have been generated during the extraction.

The pulling system was simple and robust, and was based on a hydraulic winch installed on board the vehicle that pulled the heater using a steel rope and a return pulley (Figure 4.46 and Figure 4.47). The return pulley was attached to the heater by means of four M20 bolts, using the four threaded holes already existing at the bottom part of the heater front cover, and the winch pulled it using a steel rope fixed at the other end to the main chassis.

The hydraulic power group, which was also installed on board the vehicle, allowed for continuous regulation of the pulling force of the winch, such that it was possible to adjust it to the minimum value required to extract the heater. A tensile load sensor was installed at the rope attachment point in order to measure this force.

The main characteristics of the heater extraction vehicle are shown in Table 4.11.

4.6.6.2. Heater extraction

The extraction of Heater #1 took place on 19 June 2002, and was carried out without any specific problem.

The heater appeared to be dry and with little corrosion. Surfaces ground during installation still appeared to be bright, and only some red dust covered the body of the heater, together with particles of bentonite fallen from the buffer on top of it. In the lower sector, the bentonite had penetrated the liner perforations and was clearly visible from the inner part of the liner.

The liner did not show any relevant corrosion damage. No significant differences were found as re-

Figure 4.47: Heater extraction vehicle. The heater attachment plate is visible on top of the front rollers.

gards the position of the liner (and heater), the distance to the rock floor being basically the same as recorded during installation.

Under these conditions, no special difficulties were identified for extraction of the heater, so the last segment of tracks, reaching up to the bentonite front, was installed, levelled to the reference position and fixed to the rock floor with spit bolts. The height of the heater extraction car was adjusted to the nominal level, and it was then introduced into the drift and taken to its position in front of the deposition hole. Once in position, it was fixed to the tracks using the clamp located at the rear part (Figure 4.46).

The return pulley of the pulling system was fixed to the front cover of the heater by means of screws. To increase the safety of the attachment, the end plate of the return pulley assembly was welded at some points to the front cover of the heater.

Once the return pulley assembly was safely fixed, the pulling system was put into operation and the heater

Table 4.11
Main characteristics of the heater extraction equipment

Length	4720 mm
Wide	1110 mm
Pulling force (max.)	15000 Kg
Pulling cable diameter	20 mm
Pulling cable speed	0.01 m/s
Electrical power	11 KW

was extracted without problems (Figure 4.48). The peak pulling force recorded was about 2 t at the moment of mobilisation, but decreased later to about 1 t during the rest of the extraction.

4.6.7. Additional instrumentation

In order to improve the amount of information to be collected during the second operational phase, it was decided to install some new additional sensors in the buffer front before the construction of the first part of the plug, and subsequently install through this part of the plug more instrumentation and new gas pipes within the buffer.

The location of all the boreholes to be drilled into the buffer was carefully chosen to avoid damaging the existing sensors. A projection of all the existing sensors in the remaining test zone and the position of the new instruments may be seen in Figure 4.49.

A list of all the additional instrumentation installed, including the sensors installed in the new plug (see Section 4.6.8.4) and the gas collection pipes, is given in Table 4.12. A brief description of the installation of sensors in the barrier is given in the following sections.

4.6.7.1. New instrumentation in the buffer front

The first step of this task was carried out immediately after the dismantling of the last slice of bentonite buffer, before spraying the shotcrete onto it. Three relative humidity sensors were placed in the buffer at half a metre from the new plug, and two total pressure sensors were installed at the bentonite/plug interface (Figure 4.49). Another total pressure sensor was installed at the rear end of the void left by Heater #1.

4.6.7.2. Dummy insertion

Immediately after inserting the total pressure sensor, the void was filled with the dummy canister. This was a one-metre long carbon steel dummy cylinder with the same diameter as the heater, designed to support a maximum swelling pressure of 8 MPa. After the insertion, a thin steel plate was welded to the liner to prevent the ingress of shotcrete during construction of the new plug.

Figure 4.48: Heater extraction.

Table 4.12
Additional sensors installed

Sensor code	Variable (or instrument)	Type of sensor	Designation of area (*)				Total
			B	S	H	A	
T	Temperature	Thermocouple	1	8			9
P	Total pressure	Vibrating wire	4	9			13
WC	Water content	Capacitive		21			21
SP	Plug displacement	LVDT	4				4
GF	Gas flow	Manual measure		6			6
WS	Water sampling	Filter		18			18
TOTALS			9	62			71

(*) B: granite or concrete; S: instrumented section in bentonite; H: heater; A: service zone

Figure 4.50 shows the final appearance of the bentonite front with the new instrumentation and the steel lid welded to the liner.

4.6.7.3. Gas injection/collection pipes

After the first part of the new plug was constructed, three new gas injection and collection pipes were installed in the buffer, in April 2003. Unlike those of the first operational phase, which were ceramic, these were plastic pipes featuring two stainless steel sintered filters, one of them measuring three metres in length and another shorter one at the end of the pipe. They were inserted in boreholes drilled across the first part of the plug and into the buffer parallel to the drift axis, so that the long filter remained centred with Heater #2, as shown in Figure 4.51.

Stainless steel tubing runs from the filters to the valve panel in the service area, for gas extraction and injection [44].

4.6.7.4. New instrumentation within the buffer

Following the installation of the gas pipes, the rest of the instrumentation was installed. This instrumentation consisted of 18 relative humidity sensors, 8 total pressure sensors and 8 thermocouples, as well as 18 water sampling devices, all of them installed in plastic pipes and again inserted into boreholes drilled parallel to the drift axis across the first part of the plug and into the bentonite buffer, up to the central point of Heater #2 (instrumented section F2).

Pipes with total pressure sensors and thermocouples were installed in the inner and intermediate bentonite rings, while those including relative humidity sensors and water sampling devices were installed in the three rings (Figure 4.49 and Figure 4.52). These devices (filters in contact with the bentonite) were connected to a valve panel in the service area by means of plastic tubing, in order to allow water sampling for chemical analysis at any time during the second operational phase.

4.6.8. Shotcrete plug

4.6.8.1. Plug design and construction phases

The concrete plug used for the confinement of the remaining part of the FEBEX “in situ” test was designed as a parallel plug, without keys or anchors in the rock, constructed by the shotcreting technique. The justification of this design, the preliminary tests carried out, and the mechanical model of this type of solution, are described in [45].

The basic design of the plug is shown in Figure 4.53. It was constructed in two stages: a first section with a thickness of one metre, and a second of two metres, up to a total width of three metres. The first section served as a temporary plug during the pe-

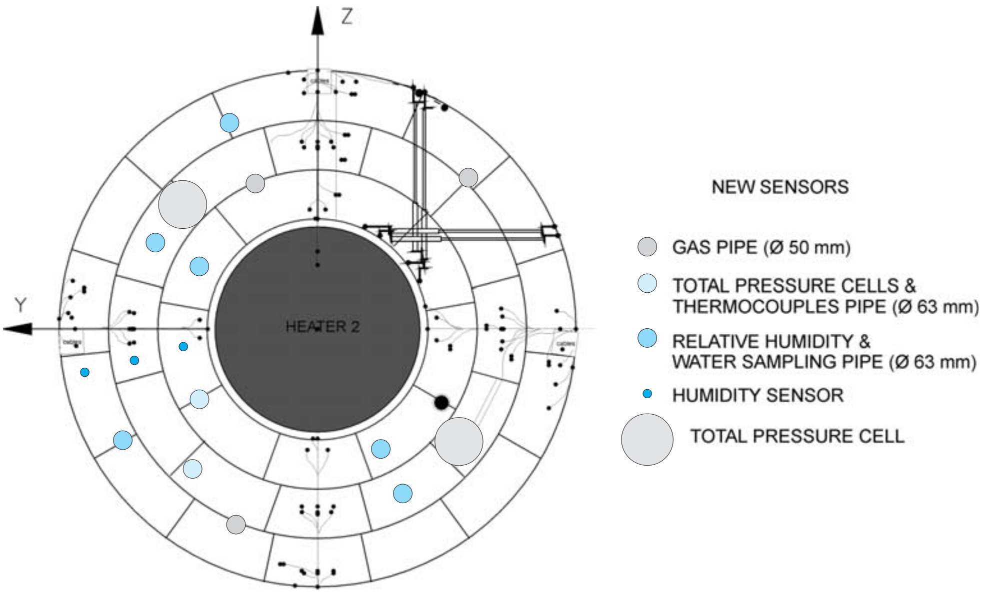

Figure 4.49: Projection of all sensors already existing in the buffer.

Figure 4.50: New instrumentation on the bentonite front and steel lid welded to the liner, before the shotcreting of the plug.

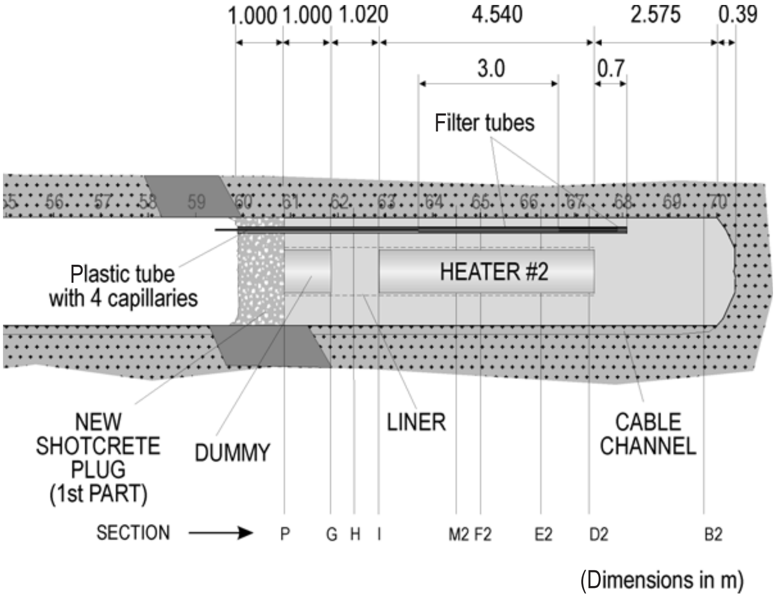

Figure 4.51: Structure of pipes for gas injection and collection (only one pipe is represented).

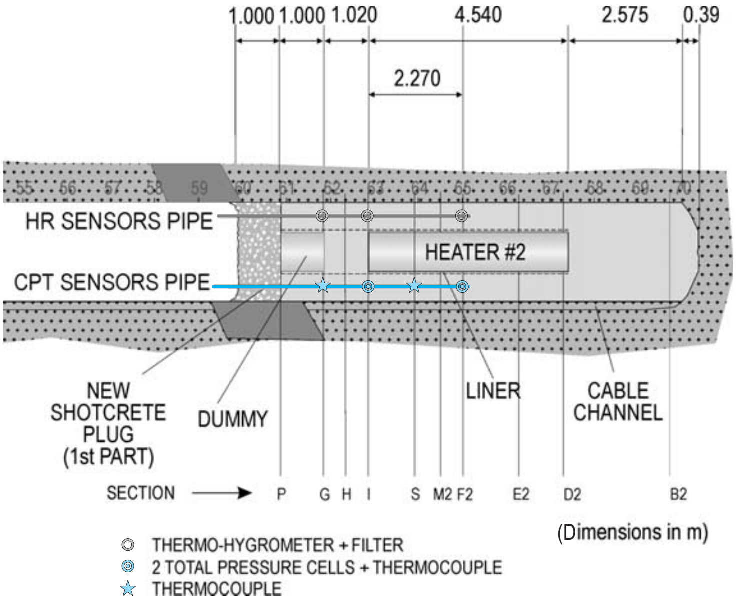

Figure 4.52: Locations for new sensors installed in the buffer (only one pipe of each type is represented).

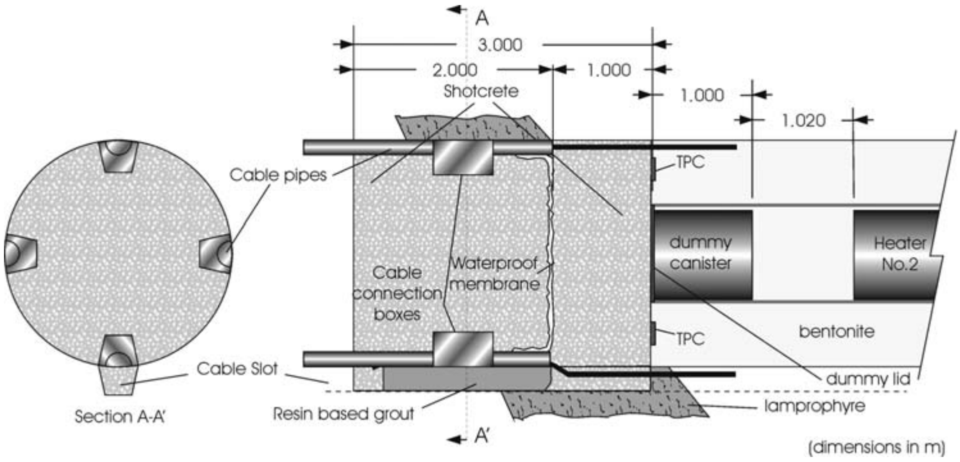

Figure 4.53: Design of the new shotcrete plug for FEBEX.

riod required to prepare the cable connection boxes and the new instruments to be installed in the remaining part of the buffer.

4.6.8.2. Construction of first plug section

The first section of the shotcrete plug was constructed in two days, on 23-24 July 2002. The construction was performed according to the specification 70-AIT-H-6-03_Rev.2 [46], with some minor modifications that are discussed below.

The formulation of the material used for shotcreting is shown in Table 4.13. This mix was prepared at Aarekies Brienz AG in Brienz, and transported to the FEBEX site in concrete mixer trucks. The concrete was applied using a wet shotcreting pump located at the entrance of the FEBEX area, the total pumping length being approximately 80 m.

The initial plan was to build a total of four shotcrete layers with a thickness of about 25 cm each, making two layers per day, with a delay of about four hours between each. However a number of problems appeared during the shotcreting:

- The first batch of fresh shotcrete delivered at the site had too high a W/C ratio (0.6) and was inadequate for shotcreting. Only a thin shotcrete layer of about two centimetres could be made with this material. Consequently, the other three layers were made thicker (approximately 39, 25, and 30 cm), so as to give a total average thickness of about 95 cm.
- Problems were detected with the homogeneity of the accelerant agent in the mix, due to the type of pump used and the long pumping distance. This generated a large amount of rebound material, which made it very difficult to work in such a reduced dimension gallery (Figure 4.54). It was therefore decided to increase the dosage of accelerant agent to about 8 %. This made it possible to complete the work, but also generated some degree of heterogeneity in the final result.

4.6.8.3. Cable passes through the plug

A total of 388 cables, corresponding to the instruments installed in the remaining test zone, had to be passed through the plug, without jeopardising the water tightness of the system.

As in the case of the initial concrete plug, an individual solution for each cable (for instance the use of compression glands) was not possible, as a result of space constraints. Therefore, it was decided to install four “cable connection boxes” filled with resin, which were installed at the rock surface in the area corresponding to the second section of the plug, before shotcreting (Figure 4.53).

Table 4.13
Shotcrete formulation in the first plug section

CEM II A-L 32,5 R	430 Kg/m^3
Nanosilica MEYCO MS 660	30 Kg/m^3
Steel fibres Dramix ZP 306	50 Kg/m^3
Polypropylene fibres	800 g/m^3
Superplasticiser GLENIUM T803	1.5 %
W/C	0.40
Aggregate 0-8 mm	1700 Kg/m^3
Curing compound MEYCO TCC 735	1 %
Accelerant MEYCO SA 160 E	6 %

Each box comprised a metallic plate measuring 1.6 m in length, which was bolted and grouted to the drift wall to prevent water flow in between. The cable connection box was fixed to this plate at its middle position, and cable pipes protected the cable bundles on both sides (Figure 4.55).

Metal-sheathed cables passed through the box without alteration, but in the case of plastic tubing (polyamides), the external surface was activated using a special chemical compound to guarantee a good contact with the resin, and a compression gland was installed on each tubing to increase the resin con-

Figure 4.54: First layer of shotcrete onto the bentonite front.

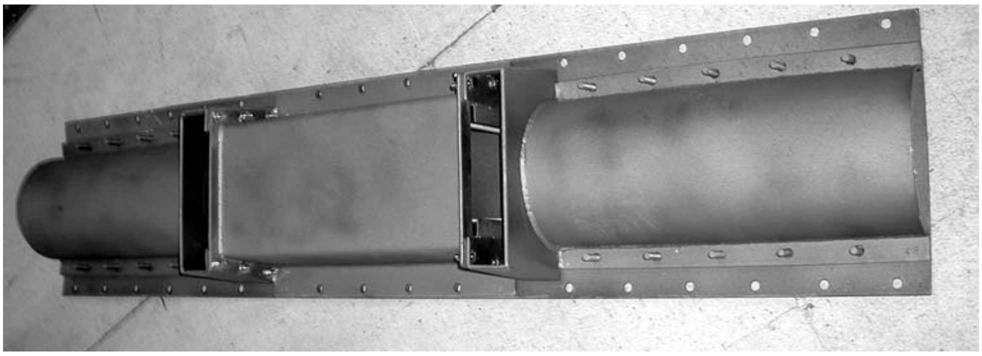

Figure 4.55: Cable pass assembly with connection box and cable pipes.

tact. Plastic coated cables were peeled off inside the box to guarantee a good copper/resin contact and prevent water leakage across the inner part of the cables.

Figure 4.56 shows the final appearance of the four boxes once installed. The front end of the first part of the plug with the cable outlets from the new instruments installed in the buffer, and the sampling boreholes (see Section 4.6.8.5) may also be observed.

4.6.8.4. Concrete plug-final section

New shotcrete formulation and trial tests

For the construction of the second section of the concrete plug, both the steel and polypropylene fibres were eliminated from the shotcrete formulation, as in principle fibres would not be accepted in a real repository, because of the difficulties for the long-term safety assessment of such components.

Before constructing the plug, a new trial test was performed in May 2003 at the contractor's facilities in Lungern, in order to test the modified shotcrete formulation and also to solve the operational problems encountered when constructing the first part of the plug. In this test, a piston-type shotcreting pump with integrated electronic control for accelerant dosage was used.

Tests were carried out in a circular section room constructed with prefabricated concrete tube having a similar cross-section to the FEBEX drift, with the pump located at a distance of 70 m.

As a result of this test, the shotcrete formulation was slightly modified, to prevent problems of material segregation along the pipe flow. The formulation finally adopted is shown in Table 4.14. The test also revealed the possibility of constructing shotcrete layers with thicknesses in excess of 40-50 cm in one step without problems.

The construction of a 1.20 m long plug was done without any incident, including very little rebound. Up to eight cores were drilled after 28 days of hardening. The shotcrete appeared to be very homogeneous. Mechanical and hydraulic testing performed on these cores provided mean values of 26.33 MPa for mechanical strength and of 8.7 E-11 m/s for permeability. This test was successful [46].

Plug construction

The second section of the plug was constructed at the FEBEX drift during the period 23-27 June 2003. The equipment used, as well as the operating staff, were the same as in the trial test performed in Lungern in May 2003 (see previous section).

A layer of MASTERSEAL X345 was first applied on top of the existing temporary plug. This material is a sprayable polymer product especially developed for the impermeabilisation of shotcrete lined tunnels, and should improve the water and gas tightness of the

Table 4.14
Shotcrete specification in the second plug section

CEM II A-L 32,5 R	475 Kg/m^3
Nanosilica MEYCO MS 660	60 Kg/m^3
Superplasticizer GLENIUM T803	1.5 %
W/C	0.46
Aggregate 0-8 mm	1700 Kg/m^3
Curing compound MEYCO TCC 735	1 %
Accelerant MEYCO SA 160 E	6 %

test. A layer of approximately 3-4 cm was sprayed, with the final appearance shown in Figure 4.57.

The shotcrete was then applied in five layers up to a total plug length of about 1.95 m. The first two layers were made rather thick (43 and 67 cm respectively), but this was later reduced to about 30 cm as some minor retraction cracks were observed in the thicker layers. The specification of the shotcrete was in all cases the same as that used in the Lungern trial of May 2003, shown in Table 4.14.

The construction process was much more efficient than during the first section of the plug in July 2002 (see section 4.6.8.2), with very little rebound material and a very good uniformity of the shotcrete.

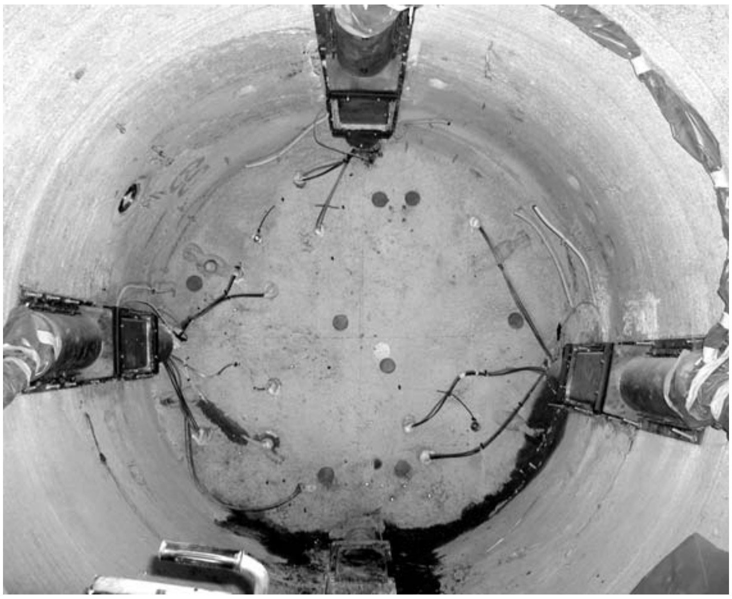

Figure 4.56: Cable connection boxes and pipes after installation.

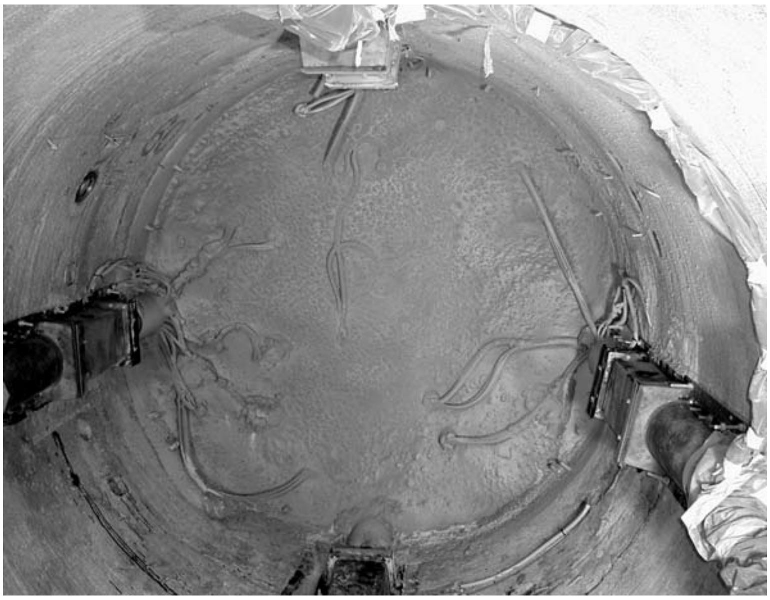

Figure 4.57: Impermeable layer on top of the first part of the plug.

Some additional instrumentation was installed in the final section of the plug. Namely, two pressure cells in the contact between the two sections of the plug, installed before spraying the impermeable layer, one thermocouple embedded in the centre of the last shotcrete layer, and four extensometers in the final front, anchored to the rock to measure potential movements of the plug (these had been also temporary installed in the first part of the plug). The final appearance of the plug with these sensors is shown in Figure 4.58.

4.6.8.5. Quality control

The quality of every fresh shotcrete batch was controlled, either on site or at the concrete plant, by an independent laboratory.

The hardening of each shotcrete layer was controlled with a penetrometer before starting the next. In the case of the first part, some areas showed very fast hardening due to the high proportion of accelerant in these zones. However, the results in the final part of the plug showed a very uniform hardening, with a calculated compressive strength of approximately 0.2 MPa after one hour following the application of each layer.

Cores were drilled for testing in the first part of the shotcrete plug after 28 days of hardening. In the case of the final part of the plug, cores were extracted from sample boxes made from every layer.

The cores from the first part of the plug showed the presence of some voids and poor quality areas, although they were limited to a few localised zones. The test results also showed some dispersion in the strength values, with a mean value of 32 MPa.

Cores from the final part of the plug showed a higher compressive strength, with a mean value of 39.66 MPa. This is about 50 % higher than the one obtained in cores drilled at the test in Lungern, which may be due to the different methods of sampling, but may also be an indication of the sensitivity of the shotcreting technique to small changes in the process.

Regarding permeability, tests made on cores from the first section of the plug showed a mean value of 4.3 E-11 m/s, which is in the same order of magnitude as that estimated for the granite matrix, which is 1 E-11 m/s [47]. Results from the final part of the plug show a higher mean value, 9.4 E-11 m/s, which is similar to the value obtained at the Lungern test and again comparable to the granite matrix.

The shear strength of the shotcrete/rock interface of the first part of the plug was also tested using an "in situ" testing method, at four points on the edge of the last shotcrete layer of the plug. Although the results obtained were relatively low compared to the values obtained during the preliminary shotcrete trials, they were still acceptable.

4.6.9. Comments and observations on partial dismantling

The partial dismantling carried out in the FEBEX "in situ" test was the first experience of this kind in a large-scale experiment. The work was complex, because of the intensive sampling programme and also because of the need to minimise its impact on the rest of the test. There was also a significant level of risk involved, due to the lack of previous experience, and to the uncertainties existing in areas such as the actual state of certain components, the behaviour of the bentonite buffer during excavation or the effectiveness of the new concept of shotcrete plug. In this sense, perhaps the most important outcome is that the work was carried out as planned, with no unexpected events, and without affecting to the rest of the test, which remains fully operative.

The work cannot be considered to be a true demonstration of the retrievability aspects of the AGP concept, due to the relatively low degree of saturation of the inner part of the buffer, however some interesting experience has been acquired in this field.

The main observations that may be drawn from the partial dismantling are:

- ❑ With this degree of saturation, the buffer showed good mechanical consistency and stability, and was excavated easily using conventional means.
- ❑ The humidity content observed in the buffer was consistent with the readings provided by the instruments during the operational phase: The inner part was still dry, whereas the periphery zone was more humid. The outer ring of blocks was practically saturated. All construction gaps were closed. Joints between blocks were still visible, but sealed.

Figure 4.58: Final appearance of the plug, with displacement sensors installed.

- Corrosion processes were limited to the areas in which there was a combination of high humidity and relatively high temperature. According to the analysis performed, the corrosion has in this case an important microbial component.
- The heater was extracted without problems. The limited corrosion in the heater area, and the mechanical integrity of the liner, simplified this task.
- Shotcreting has been demonstrated as an alternative method for the construction of concrete plugs. Some practical problems found during the construction process were solved satisfactorily. This construction technique may have significant practical advantages in some situations, also in a real repository.
- The effects of cooling were clearly visible in the area to be dismantled: the total pressures dropped drastically after the switching off of Heater #1, and also a redistribution of humidity in the inner and intermediate bentonite rings was observed.
- Nevertheless, the disturbance caused by partial dismantling on the remaining part of the experiment has been very small. No significant alterations have been observed in parameters such as temperature or humidity. Some displacement of the buffer towards the open space was observed, but seemed to be limited to the zone close to the free face. The most important variations have occurred in the stress field, especially in areas closer to the new plug, in which a decrease of the total pressure values was observed. These values recovered after the construction of the new plug, over a period that depends on the distance to the plug (slower at closer points).
- The new instruments installed in the bentonite buffer will increase the amount of information that may be obtained from the experiment in the coming years.

4.7. Second operational phase

The second operational phase started on 26 July 2002, identified as “day 1975” on the time scale. This date correspond to the end of the construction of the first part of the shotcrete plug.

4.7.1. Control and monitoring process

4.7.1.1. Modifications in the DAS

In addition to the changes introduced in the DAS previous to dismantling (described in section 4.6.3), it was necessary to introduce certain modifications and improvements in this system in order to adapt it to the new configuration of the test:

- Upgrading of the Remote Monitoring System: a more powerful computer was installed in Madrid to store and manage the test Master Database.
- Changes in the supervision software:
    - The monitoring screens were adapted to the new test configuration, introducing the new sensors and eliminating the removed ones.
    - Additional temperature sensors were introduced in the heater power control loop at the start of the second operational phase, in order to compensate for the failed ones. Given the risk of failure of these sensors, the control algorithm was modified in the summer of 2004 so as to perform the regulation by using the heater internal thermocouples instead of the external temperature sensors.
    - A limitation was introduced in the power control algorithm to avoid overheating in the event of sensor failure. The power limit was set to 2600 W.
- Development of the FEBEX website: a website of the test was created within AITEMIN’s site. Every project participant was provided with a user name and password for access to it. The main features were the possibility of directly downloading data from selected sensors and time span, the downloading of quarterly Data Reports and other relevant documents and access to the monitoring screens of all the instrumented sections displaying data from any desired date.

The monitoring was carried out upon the same basis as during the first operational phase, with remote monitoring from the RMC via modem connection, and quarterly reports were distributed to all the participants.

4.7.1.2. Heating control

After the disconnection of Heater #1, the power requirements to keep a constant temperature of 100

°C at Heater #2 increased by about 5 % (100 W) in two months. This increase was slightly smaller than predicted by the modelling exercise carried out in advance, which pointed to a value of 10 %.

During the second operational phase, the applied power has continued to increase but at a very slow rate, such that in two years another 100 W rise has been registered.

4.7.2. Incidences and corrective measures

The following incidents and corrective measures were registered during this operational phase:

- ❑ Short power switch-offs in the heater occurred on 28 October 2002 (day 2069), and from 19 to 21 November 2003 (day 2456 to day 2458), due to failure of thermocouples in the control loop, which provided temperature readings over 100 °C. In the first case the temperature dropped to about 80 °C at the hottest point of the heater, and the power was restored after 29 h. In the second case, the temperature decreased to 93 °C.
- ❑ On 6 February 2003 (day 2170) the power was cut off in all the GTS due to a snow avalanche that also blocked the access by road. The cut off lasted more than the autonomy of the Uninterrupted Power System supporting the Data Acquisition and Control System. This produced a total discharge of the batteries, which were damaged, as a result of which the power was not automatically restored to the computers. Hence, the heating was not restarted until it was possible to switch it on manually on 13 February 2003. No data were registered during that period. The temperature used for control, which had decreased to about 50 °C, recovered quickly.
- ❑ In order to make adjustments in the temperature control loop, the power was manually decreased to about 1750 W on 13 November 2002 (day 2085). Three days later it was increased again to a constant power of about 2365 W. After finishing the adjustments in the temperature control loop, the applied power was set to temperature control on 27 January 2003 (day 2160).
- ❑ Some tests were carried out in April and May 2004, in order to tune the power regulation for use of the heater internal thermocouples instead of the external temperature sensors. These tests produced some oscillations in the applied power [48].

4.7.3. Evolution of parameters

As expected, the disconnection of Heater #1 and subsequent dismantling produced a transient period of the main monitored parameters in the zone around this heater, while small effects were noticed around Heater #2. A detailed description of the evolution of the system during this period and in the second operational phase follows.

4.7.3.1. Temperature

In general the disconnection of Heater #1 caused the system to start behaving as a single-heater system, with a central plane of symmetry on Heater #2: at the front side of Heater #2 (closer to Heater #1) temperatures decreased noticeably to equal those of their equivalent points at the back side, in section D2. Figure 4.59 shows the evolution of the temperature at different points of the buffer from January 2002 to August 2004. Three milestones are marked, corresponding to the switching off of Heater #1, the start of the partial dismantling operations and the start of the second operational phase.

After this short transient period, temperatures stabilised throughout the buffer, from the heater surface to the rock, and also at the most distant points. Apart from that, the temperatures in the bottom part of the drift continued to be higher than those in the sides and upper part for each section.

The new thermocouples installed within the buffer showed values that were coherent with the old ones.

Temperatures in the rock registered only some decreases after the disconnection of Heater #1, especially in boreholes in its area of influence and at intervals closer to the drift. Afterwards, the values stabilised in general.

4.7.3.2. Humidity

As predicted in the preliminary modelling exercises, the humidity values around Heater #1 were affected by the cooling period. The change in the thermal field caused a redistribution of the water content in the clay buffer, by inversion of the two-phase flow mechanisms. This was reflected in a decrease of values in the intermediate bentonite ring and a fast increase in the inner bentonite ring.

In the buffer around Heater #2, the water content continued to increase in general at all points during the second operational phase, with no influence from the cooling and dismantling period.

The new capacitive type sensors installed in the outer part of the buffer reached almost maximum values in a short period of time, regardless of their location with respect to the heater.

The values of those installed in the intermediate ring of blocks also increased, but at a different rate depending on whether they were located in the heater area or outside the heater zone.

The sensors installed closer to the heater also showed an increasing trend value, especially on the lower right hand side and outside the heater zone.

Figure 4.60 shows the values in the inner ring from the start of the second operational phase to August 2004.

The TDR sensors and psychrometers in the buffer confirmed the previous observations. The TDR sensors installed in granite, which had showed a constant increase in the water content of the rock during the first operational phase, also showed a decrease as an effect of the dismantling, this being more accused in those sensors installed in the area of influence of Heater #1. The trend towards increasing values was resumed during the second operational phase, although at a lower rate.

4.7.3.3. Total pressure

The switching off of Heater #1 produced a major drop in the pressure readings around it, and the remaining pressure was released as the dismantling operation progressed. Sensor 1 in Figure 4.61 exemplifies this phenomenon. Again the same three milestones as for temperature are marked. In the zone of Heater #2, the stress field was almost unaffected by the cooling and dismantling period.

During the second operational phase, pressures rose in general throughout the buffer, although at different rates, reaching values in general of between 3 MPa and 5 MPa. A brief analysis follows:

- ❑ By the end of the first operational phase, the pressures in the contact bentonite/rock (sensors 7 and 9 in Figure 4.61) had reached values in the

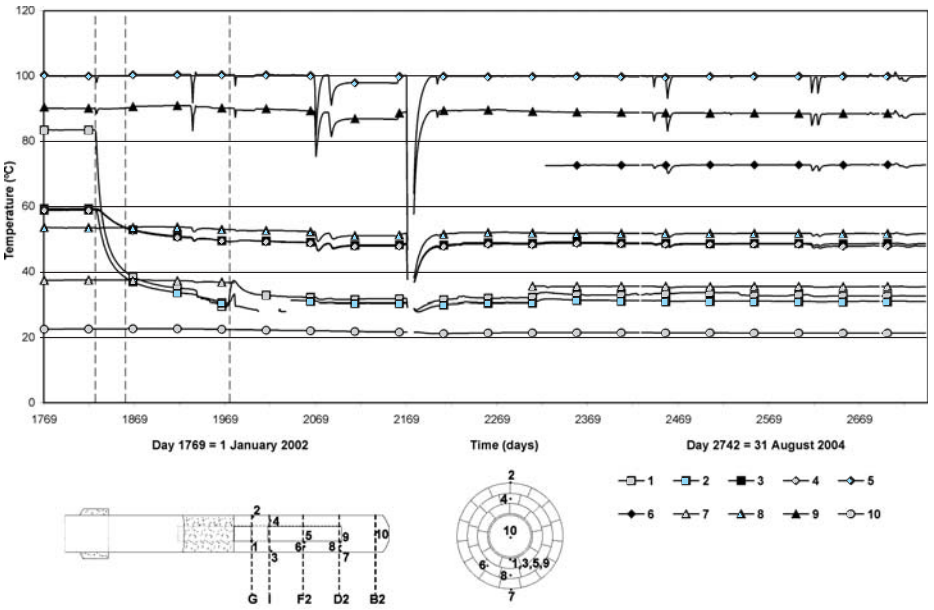

Figure 4.59: Evolution of temperature in the buffer during the second operational phase.

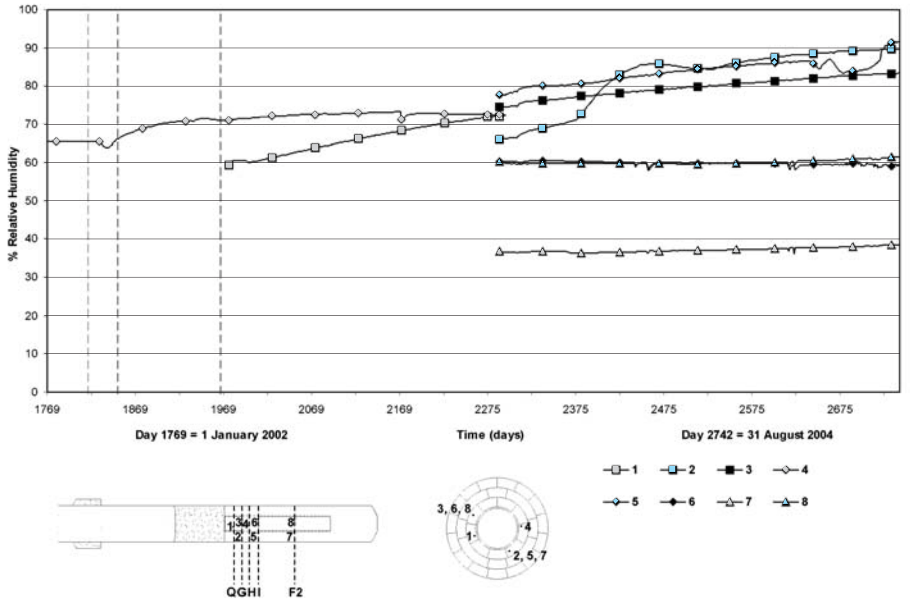

Figure 4.60: Evolution of humidity in inner bentonite ring in the second operational phase.

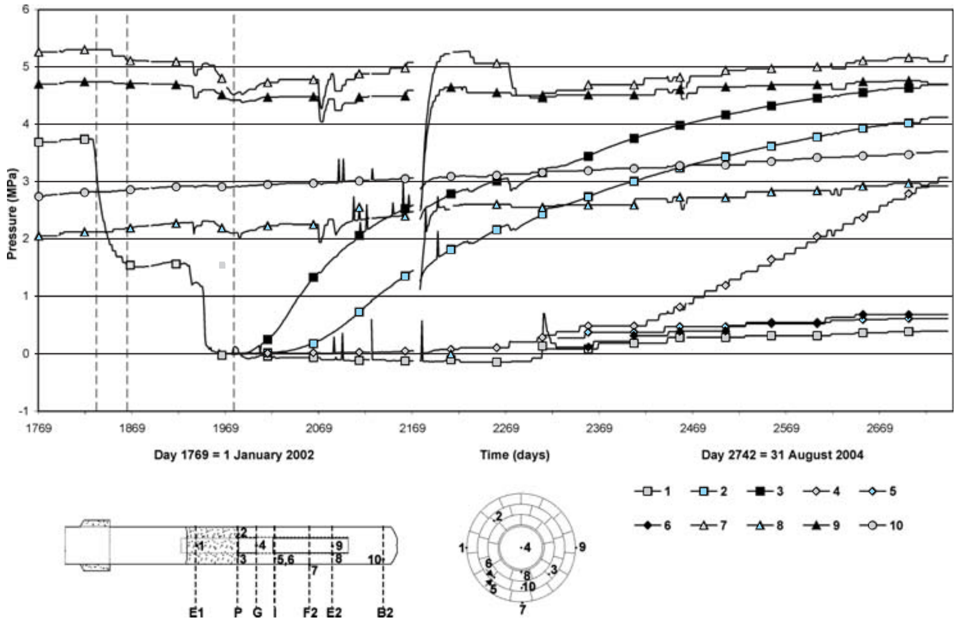

Figure 4.61: Evolution of pressure in the buffer during the second operational phase.

range of 5 MPa. During the second operational phase, very slow increases were registered.

- At the heater/bentonite contact, pressures also continued to increase, reaching a value of 3 MPa in instrumented section E2 by August 2004 (sensor 8).
- The pressures in the buffer rose at high rates in some cases, as is the case of the rear end of the dummy canister, and at the most distant points from the heater, with values in the range of 3 MPa (sensors 4 and 10 respectively). While the new total pressure cells installed in the inner bentonite ring in 2003 still showed no pressure build up by August 2004, those in the intermediate bentonite ring started to provide low readings with slow increasing rates, this probably being caused by their emplacement method in plastic pipes inserted in boreholes excavated in the buffer (sensors 5 and 6).
- After the construction of the first part of the plug, pressures at the concrete/ bentonite contact started to rise at a very high rate, and kept increasing two years later, reaching values of between 4 MPa and 5 MPa, higher at the lower right hand.
- The pressure cells still in operation in the bentonite/rock contact around Heater #1 were left in place after the dismantling, being covered by the new shotcrete plug. During the second operational phase, these cells started to register some pressure, in the range of 0.4 MPa. This may have been caused by the transmission of the pushing force from the bentonite swelling throughout the concrete mass towards the rock walls.

The two pressure cells installed between the two sections of then new shotcrete plug had not registered any pressure build up by summer 2004.

Pressures in the rock mass decreased during the cooling period. This decrease was faster for sensors closer to the drift, and it became even faster during bentonite dismantling. Subsequently, this trend reversed to a general rise by all the sensors, this being maintained during the second operational phase.

4.7.3.4. Other parameters

Pore pressure in bentonite

All the pore pressure sensors providing positive readings during the first operational phase, mainly located at the right-hand side, dropped to zero around both heaters during cooling and dismantling.

During the second operational phase, the pressures registered by those sensors at the right-hand side rose again at a slow rate, with maximum values of the order of 0.2 MPa by summer 2004, and some positive values also in the rest of the outer bentonite ring.

Hydraulic pressure in the rock

A general decrease of hydraulic pressures was noticed during the cooling and dismantling period. No clear trends can be detected during the second operational phase, with pressure stabilised in many of the boreholes, and increasing slowly in some.

As in the first operational phase, two hydrotesting campaigns and another two water sampling campaigns were carried out during the second operational phase. Again, these produced fast pressure drops and recoveries in the affected intervals.

Displacements

Heater displacements. No effects were noticed from the cooling and dismantling period. The trends from the first operational phase were maintained.

Plug displacement. The four displacement sensors placed at the front end of the shotcrete plug registered no displacements prior to August 2004.

Gas generation, release and migration

Three gas sampling campaigns were performed between October 2003 and May 2004. The results from the analysis of the gas samples showed that concentrations of the gas components hydrogen, carbon dioxide and hydrocarbons decreased drastically with time from the values measured in the first samples.

In addition to the above, no significant increase of gas pressure was observed in the draining pipes. All this might indicate that the plug or the surrounding host rock is not gas tight.

4.7.4. Performance of components

A total of 188 sensors were removed during the partial dismantling operation, and another 52 new ones were installed afterwards for the second operational phase. Therefore, for this phase 10 % of the sensors were new and the rest had been in operation since the start of the test. Nevertheless, by mid 2004, the percentage of operative sensors was still over 80 %, which may be considered a very good performance in general, and particularly for the original sensors.

Regarding the new sensors installed within the barrier, they provided readings that were coherent both one with respect to the next and also with respect to the old sensors, as was the case for the humidity sensors. This is an important issue since it proves that the method of emplacement did not have a significant effect on the readings obtained. As this method consisted of installing the sensors in plastic pipes inserted in boreholes drilled in the barrier, it may be inferred that the bentonite sealed the gap around the plastic pipes, providing a good contact with sensors. The positive values from the total pressure cells are the clearest evidence of this.

The pressure cells installed at the bentonite/concrete interface also provided good readings, with pressures rising very strongly.

4.7.5. Comments and observations on the second operational phase

At the moment of preparing this report (October 2004), the second operational phase had lasted two years and three months, which is the time elapsing since the construction of the first section of the new plug, in July 2002. In fact, this second phase is a continuation of the first, since there has not been any power interruption in the remaining heater from the beginning of the experiment. In total, the remaining part of the test had been in operation for seven years and eight months at the moment of preparing this report.

The information provided by the instruments during the second operational phase basically confirms the observations made at the end of the first phase (see Section 4.5.6). However, the THM processes have progressed during this period, and also some new instruments were added after the dismantling.

The specific observations in this second phase are the following:

- ❑ Having only one heater, the system is trending to a more symmetric structure in the thermal field.
- ❑ Humidity is progressing at all points, at a similar rate as in the first period. However, points located close to the heater are not yet saturated. The information given by the new instruments suggests that humidity is also increasing at these points, but still at a very gradual pace.
- ❑ The disturbances caused in the stress field by the partial dismantling operation were compensated for over a period of between 100 and 300 days, depending on the proximity to the new plug. Apparently the original values and trends have now recovered at all points.
- ❑ The total pressure measured at the inner face of the plug has increased rapidly. No displacement has been measured in the plug front.
- ❑ The pressure at the concrete/rock interface in the plug position has increased significantly, showing that the plug is transmitting the thrust of the bentonite buffer to the rock mass, as expected.
- ❑ The water tightness capacity of the new plug is not easy to assess. No leaks are observed through the cables, which would suggest that the cable connection boxes are performing well. However, some water is present at the gallery bottom close to the plug, although this water might also come from the rock around the plug.
- ❑ Gas measurements in the buffer show that the system is tighter.

4.8. Conclusions

4.8.1. Performance of test components

The overall performance of the test components has been excellent, including that of those with a short expected lifetime. This reflects the major effort taken in planning, selection and design of these components, the quality requirements, and the redundancy introduced in the most critical aspects.

Specifically:

Heaters

The heaters have proven to be very reliable, and no leaks have been detected in the heater body, the power cables, or the internal resistors.

Through the conservative design of the resistors and the stable and smooth operation of the power regulation system, a long operational life has been achieved. In fact, after more than seven years of operation, only one of the three redundant sets of resistors existing on each heater has so far been used.

Handling equipment

The systems used in FEBEX are only an initial approach to the problem, since very relevant aspects such as radiation protection, productivity and durability have not been considered in their design.

However, the experience has been positive, the different operations have been carried out without problems, despite the lack of previous tests, and valuable information has been obtained for the future design of the equipment required in a real repository.

Instruments

The initial assumptions regarding the expected lifetime of many of the instruments, have proven to be very conservative. The initial estimates were based on the guarantee given by the manufacturers – which is usually conservative – and also on the predictions for an extremely harsh working environment in terms of temperature, pressure, or corrosion potential, which, in fact, have been only found together in some parts of the test.

There have been a wide variety of instruments installed in the test, both in terms of measuring principles and types of construction. The large majority of the instruments have worked well, and have been operational for periods much longer than initially expected. This fact was indeed one of the main reasons supporting the decision to extend the duration of the test.

Most of the sensors installed in the buffer and the rock were standard, well proven products, although in some cases they were customised by the manufacturer for this specific application, for instance modifying the casing material or the type of cable. This is the case of the thermocouples and of the sensors measuring total pressure, pore pressure, and relative humidity. It is with these sensors that the experience has been most positive, both in terms of durability and accuracy.

The experience has been not so good with sensors especially developed or adapted for the test, as the case for some of the linear transducers, crack meters, or inclinometers. Also the mechanical protection used for psychrometers proved to be ineffective. A more intensive testing before installation would have been convenient in these cases. On the positive side, the TDR system developed for measuring water content worked well in the buffer, although the information provided during the test had to be recalculated after carrying out the post-mortem calibration. In any case, it allowed for a crosscheck with other sensors, such as those used for relative humidity.

The density of measurements has proven to be more or less adequate, both for the modellers and for the overall appraisal of system behaviour. However, additional redundancy would have been necessary in some critical points, such as for example the external temperature in the middle of the heaters, which is the reference point for the power control algorithm. On the other hand, some other instruments, such as the linear displacement ones installed to detect the movement of the heaters or of individual bentonite blocks, have provided little usable information, in some cases due to poor installation.

Monitoring and control system

Given the remote location of the test site, the monitoring and control system was especially designed to enable automatic mode operation with remote supervision via modem from AITEMIN's office in Madrid. For this reason, hardware and software components were selected on the basis of their quality and reliability, and redundancy was introduced in the most critical aspects.

The system has shown excellent performance during the test, providing continuous control of the heating system and generating a large experimental database that includes more than 115 M records of instrument data, at a rate of one datum every 30 minutes. The few incidents that have occurred were caused by external factors, and in particular by lengthy power shutdowns that exceeded the capacity of the back-up batteries embedded in the system. Nevertheless, these incidents did not have any real impact on the experiment control nor on the continuity of the database.

The power control algorithm developed to keep a constant temperature of 100 °C at the hottest point of the heater surface has been very effective, providing a smooth operation of the heaters and a good adaptation to the changes occurring in the heaters´ environment, such as for instance the progressive hydration of the buffer or the partial dismantling operation.

The experience so far has been excellent, and as a result of this, the FEBEX philosophy for control and monitoring has subsequently been applied in other underground tests.

4.8.2. Behaviour of the bentonite buffer

An overall assessment of the behaviour of the bentonite buffer may be made on the basis of the data provided by the sensors during the experiment, on direct observations during partial dismantling and on the analysis carried out on samples taken during this activity. The conclusions in all cases are the same, this in itself being a very important conclusion and a validation of the experimental procedure.

In general terms the behaviour of the buffer has been as expected. That is, the hydration is progressing from the outer part in contact with the rock to the inner and hotter part, and this hydration has produced the closure of all the gaps and joints existing after installation. Furthermore, these closed very soon at a relatively low degree of saturation. The rate of hydration was very much in accordance with the one initially predicted by THM models during the initial phases of the experiment; however, after about the first three years, the hydration seems to progress at a slower rate than predicted, which means that models must yet be improved to match reality.

The hydration process seems to be controlled by the bentonite itself, as the saturation pattern became quite uniform throughout the test after an initial period of less than one year, with no real differences between humid and dry areas of the test drift. Given the low relevance of the EDZ under FEBEX conditions, this means that the rock is able to supply the amount of water required by the suction from the bentonite at all points, without causing dehydration in the granite.

4.8.3. Experiences gained and future developments

The FEBEX "in situ" test was not planned as a full demonstration experiment, but has provided an initial practical experience of many aspects related to the construction of an underground repository according to the Spanish reference concept AGP-Granite. It has also allowed for the identification of the most critical features for construction and emplacement, and has shown the way in which future developments must be oriented.

In this respect, the main lesson learned during the project is that the Spanish reference concept in granite AGP is feasible from the construction point of view; however, some aspects require improvement and others must yet be developed. A more detailed discussion of the experiences gained and the developments required for the future follows:

1. All the different processes involved in *the manufacturing of bentonite blocks* starting from raw clay material have been developed and demonstrated, including the quality control procedures. This experience will be extremely valid for the future, even if a different type of bentonite is used. However the experience has been limited to small size blocks, and therefore future developments should focus on the manufacturing of larger blocks, which may have specific problems for compaction and mould extraction.

2. *The buffer construction* method used in the experiment has been adapted to the specific test constraints and needs, and does not represent the real case, in which larger blocks must be used. The future emplacement method must be designed and developed in parallel with the definition of the shape and size of the real blocks. Handling of these large blocks in a reduced cross-section drift is not a trivial task, especially if the process must be robotised or remotely operated.

   Ambient humidity has a high degree of influence on the mechanical integrity of the bentonite blocks, and this must be taken into account in the design of the storage, handling, and emplacement process. Construction gaps in the buffer do not seem to be a problem, at least if they are kept at the same level as in the FEBEX experiment. In the test conditions, these gaps closed very quickly, preventing the creation of preferential flow paths for the water. However, the presence of water in the drift during the emplacement operation may be a serious problem, which can even make construction of the buffer impossible. The experience in FEBEX has shown that a small amount of water is manageable, but the upper limits for this are not known.

3. A set of methods and equipment has been developed *for the transport of the heaters along the drift and the insertion* in the deposition hole. The design and construction of these systems have been very specific to the testing requirements and do not necessarily reflect the methods to be used in the real case. However,

the experience has provided interesting information that will be very useful for the design of the future systems. These include aspects such as alignment, applied forces and speeds, frictions and reactions and the management of contingencies.

In this sense, the role of the steel liner must be discussed. The experience obtained shows that liner alignment is a critical aspect during the canister emplacement operation, and from this point of view the liner may be a complication more than an aid. If larger size blocks are used, the deposition hole may be mechanically stable and the liner may not be necessary. Possible irregularities in the sliding surface of the deposition hole might be smoothed by machining the bentonite blocks after emplacement.

4. The external case of *the heaters* was the same as the one planned for the real canister. The construction of this steel body, carried out under strict quality control, has been a valuable experience.

5. The *hydration of the buffer* has progressed more or less as predicted, although the rate of hydration after approximately the first three years became slower than initially predicted by the THM models. Several explanations have been given for this, and some of them might explain this divergence, however this needs to be checked over a longer period of time.

   The hydration pattern is quite uniform along the test length, with no major differences between dry or more humid parts of the rock. This would show that, at least in this case, the amount of water available in the rock is greater than what is being taken by the buffer, and that therefore it is the bentonite that is controlling the process.

6. The extraction of Heater #1 carried out during *the partial dismantling* of the test was an interesting experience, was very easy and posed no special problems, given the low degree of saturation in the inner part of the buffer. For this reason it cannot really be considered as being a representative retrieval operation. In the case that the buffer is fully saturated the situation may be quite different and it would probably be necessary to adopt a completely different approach, possibly requiring the removal of all bentonite in the top part to free the canister.

7. A very important *sampling* programme was carried out during partial dismantling. Different sampling techniques were tested and in some cases improved. This is also a valuable experience for other experiments and for the future final dismantling of the test.

8. *The corrosion processes* have been very limited to areas with a high degree of humidity and high temperature. Therefore little corrosion has been observed in the canister and the corrosion probes emplaced close to it. However some knowledge has been gained in this area through the analysis of instruments recovered during dismantling.

9. Important experience and know-how have been gained in the construction of two different types of *concrete plugs*. In particular, the shotcrete method has a number of advantages that make it a potential candidate for many different applications in a real repository, and should be further developed and tested.

10. Regarding the *monitoring and management of the test*, the experience with the test instrumentation has made it possible to establish a number of criteria for the selection of sensors and transducers in future experiments. The cable entries into the system might be a problem in the event that the future repository has to be monitored. Future research must be oriented to wireless instruments or remote sensing systems.

    Also the automatic operation of the test with remote supervision via modem has been excellent. Some minor changes should be introduced in this concept to improve the reliability and the fault-tolerance capacities of the monitoring and control equipment.

    The management of the data generated by the experiment has been another valuable aspect of the project. The adopted data display and reporting formats have been very well accepted by the different users, and in fact the FEBEX formats have later been used in other underground experiments. The methods used for the distribution of data and reports, and the facilities developed for downloading data via the Internet, have proven to be efficient and convenient.

5. Laboratory tests

5. Laboratory tests

As has been pointed out in Chapter 1, the experimental work performed during the FEBEX Project has consisted of three main parts: "in situ" testing, testing on a "mock-up" and a large series of laboratory tests.

The laboratory tests may be classified in the following types: characterisation tests, thermo-hydro-mechanical (THM) tests, thermo-hydro-geochemical (THG) tests, gas generation and migration tests, corrosion studies and the recalibration of sensors.

The basic characterisation tests for the selection and preparation of the FEBEX bentonite have been described in Chapter 2, FEBEX BENTONITE. This chapter includes all the other laboratory tests carried out during the project.

Some gas generation THM and THG tests were performed in order to study and understand the processes occurring in the clay barrier under simple and controlled conditions and to develop the governing equations, and required extensive experimental work and the innovation of experimental techniques. Certain of the tests performed to obtain the basic parameters also required new testing techniques and methodologies.

Most of the previous tests were performed during the pre-operational and operational stages.

Furthermore, characterisation tests were performed during partial dismantling of the "in situ" test in order to study the possible change in the bentonite generated by hydration and heating, this being accomplished by comparing the results with those obtained from the same tests on untreated material. Corrosion studies were carried out on the samples of metal extracted during dismantling, and a conditions analysis and recalibration on the sensors recovered.

5.1.THM tests

5.1.1. Thermal properties

5.1.1.1. Specific heat

Specific heat was determined only for bentonite S-2 [6]. The relationship between specific heat and temperature fits the following equation, in a range of temperatures of between 45 and 150°C:

$$c_s = 1.38 \cdot T + 732.5 \qquad (5.1)$$

where c_s is the specific heat, in J/kg°C, and T is the temperature, in °C.

5.1.1.2. Thermal conductivity

The superficial thermal conductivity of the FEBEX bentonite was determined at laboratory temperature in compacted specimens at various nominal dry densities and with different water contents. From these measurements, it was found that thermal conductivity (λ W/m·K) may be related exponentially to water content (w %) in the interval studied. This empirical relation, which also includes the contribution made by dry density (ρ_d g/cm^3), is expressed as follows:

$$\ln \lambda = \ln (0.8826\, \rho_d - 0.8909) + 0.0333\, w \qquad (5.2)$$

Figure 5.1 shows the regression curves of the values of superficial thermal conductivity as a function of the degree of saturation, for bentonites S-2 [6] and FEBEX [16, 49]. A good correlation of the sigmoidal type (Boltzmann) was obtained for the two bentonites by means of the following equation:

$$\lambda = A_2 + \frac{A_1 - A_2}{1 + e^{(Sr - x_0)/d_x}} \qquad (5.3)$$

where λ is the thermal conductivity, in W/m·K, S_r is the degree of saturation, A_1 is the value of λ for $S_r = 0$, A_2 is the value of λ for $S_r = 1$, x_0 is the degree of saturation for which the thermal conductivity is the average value between the extreme values, and d_x is a parameter.

The parameters obtained in the fitting of the curves are as follows:

	S-2 Bentonite	FEBEX bentonite
A_1	0.39 ± 0.08	0.57 ± 0.02
A_2	1.34 ± 0.06	1.28 ± 0.03
x_0	0.54 ± 0.03	0.65 ± 0.01
d_x	0.15 ± 0.03	0.10 ± 0.02

There is a difference between the curves, this being more noticeable with lower values for the degree of saturation. However, taking into account all the points, there would seem to be very little difference between the two bentonites as regards this parameter.

5.1.1.3. Coefficient of linear thermal expansion

Measurements of thermal expansion were carried out on 12 samples of compacted FEBEX bentonite with an initial dry density of between 1.57 and 1.72 g/cm^3

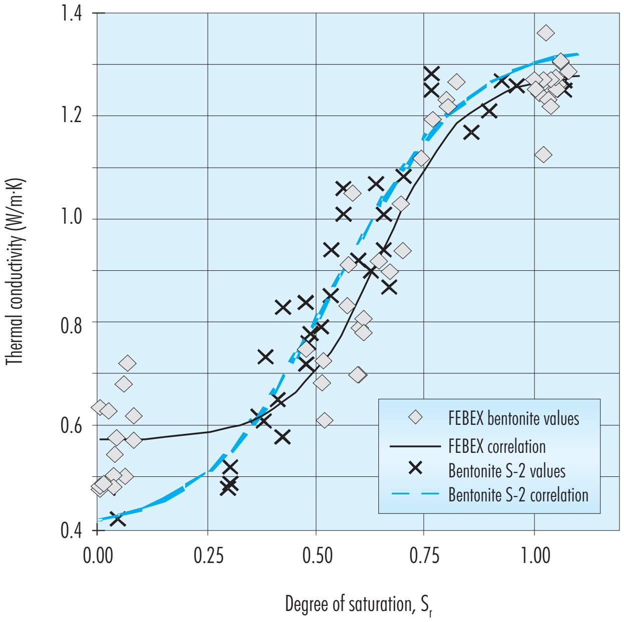

Figure 5.1: Thermal conductivity as a function of degree of saturation for S-2 and FEBEX bentonite.

and a water content of between 12.5 and 25.1 percent [50]. The specimens were located in an isothermal bath with controlled temperature. A latex membrane kept the overall water content of the soil constant throughout the heating and cooling processes. Temperature varied between 25 and 70 °C. In each test, several cycles of heating and cooling were applied to the sample.

The vertical strains in the first heating path were higher than the strains measured during the second and subsequent cycles. In addition, in each cycle the strains measured during the heating process are higher than those observed throughout the cooling path and, as a result, an accumulation of irreversible strains is observed. The slope of the relationship between temperature and strain is shown in Figure 5.2. This slope increases slightly with temperature. The following correlations for the linear thermal expansion coefficient have been obtained from this figure:

$$\Delta\epsilon_z/\Delta T = -\ 0.118\cdot 10^{-4}\ +\ 6.5\cdot 10^{-6}\ T \qquad (5.4)$$

(first heating)

$$\Delta\varepsilon_z/\Delta T = -\ 1.265\cdot 10^{-4}\ +\ 6.5\cdot 10^{-6}\ T \qquad (5.5)$$

(subsequent heating paths)

$$\Delta\varepsilon_z/\Delta T = -\ 1.538\cdot 10^{-4}\ +\ 6.5\cdot 10^{-6}\ T \qquad (5.6)$$

(cooling paths)

where ε_z is the linear strain and T the temperature in °C. At temperatures higher than 55°C, an increase in the dispersion of the results is observed, due to experimental difficulties.

5.1.2. Hydraulic properties

5.1.2.1. Water permeability

Saturated permeability

An empirical relationship was obtained, using saturated specimens, for the coefficient of permeability of the FEBEX bentonite as a function of dry density, this being expressed by the following equations:

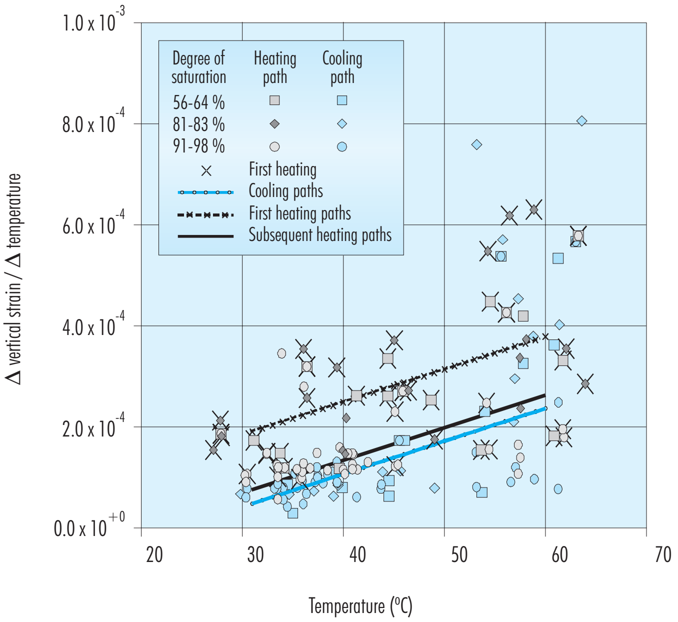

Figure 5.2: Linear thermal expansion as a function of temperature.

$$\log k_w = -6.00\, \rho_d - 4.09 \qquad (5.7)$$

$r^2 = 0.97$, for ρ_d between 1.30 and 1.47 g/cm^3

$$\log k_w = -2.96\, \rho_d - 8.57 \qquad (5.8)$$

$r^2 = 0.70$, for ρ_d between 1.47 and 1.84 g/cm^3

where k_w is the coefficient of permeability for distilled water, in m/s, and ρ_d is the dry density, in g/cm^3 [16, 49]. The variation of the values actually obtained with respect to these fittings is of the order of 30 percent. This should be evaluated taking into account that the values of the coefficient of permeability are very small, of the order of 10^{-14}.

Figure 5.3 shows the regression lines for the coefficient of permeability of FEBEX bentonite shown above and the points obtained in different determinations. The influence of the water used as a permeant was tested, as well as the repercussion of the direction of the measurement, parallel or perpendicular to compaction effort, in the value of the coefficient of permeability. None of these aspects seems to be relevant, with the exception of the use of saline water (8 g/L), which yields a higher hydraulic conductivity.

The data indicate that the FEBEX bentonite is less permeable than the bentonite S-2 [6]. However, this is a very small difference: in some cases it is even less than the scattering shown in the same set of tests.

The effect of salinity on water conductivity, when the salt concentration is high, is shown in Figure 5.4 [15]. The values of permeability to salt solutions have been estimated from oedometric tests on samples saturated with different solutions. These values have been compared with the values of the permeability at the same void ratio, measured directly using deionised water.

The permeability increases slightly in a logarithmic manner with temperature, as expected from the decrease in water kinematic viscosity (Figure 5.5, [15]). The error bars shown were obtained from equations (5.7) and (5.8) shown above.

Laboratory tests have shown that the saturated permeability of compacted bentonite remained constant for 700 days, and for more than 4 years when

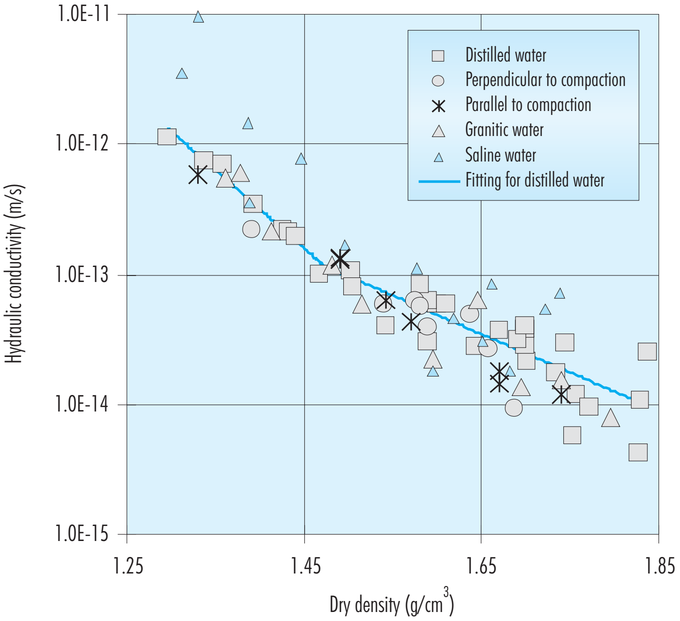

Figure 5.3: Saturated hydraulic conductivity as a function of dry density.

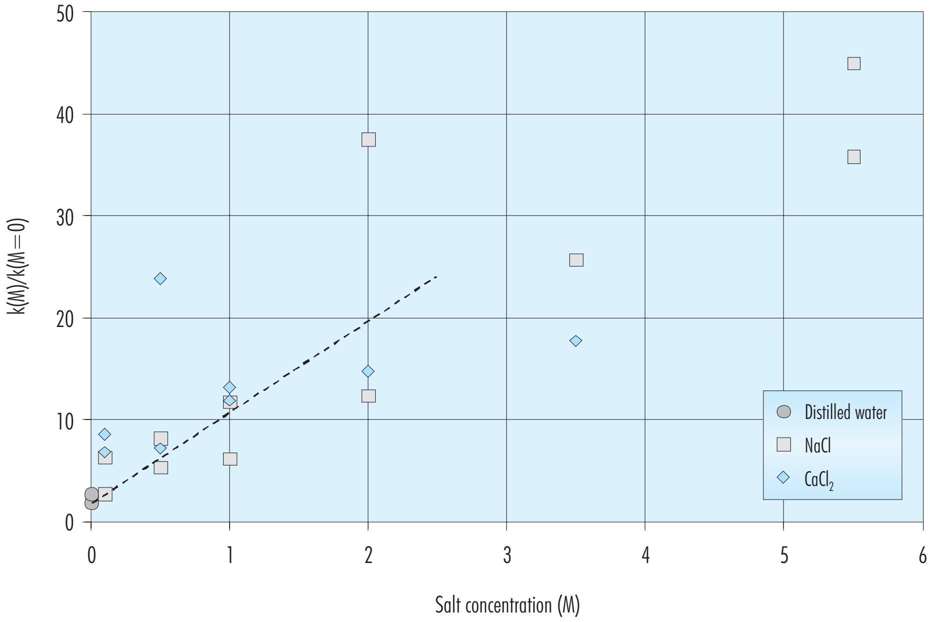

Figure 5.4: Relationship between the values of permeability obtained using salt solutions and deionised water.

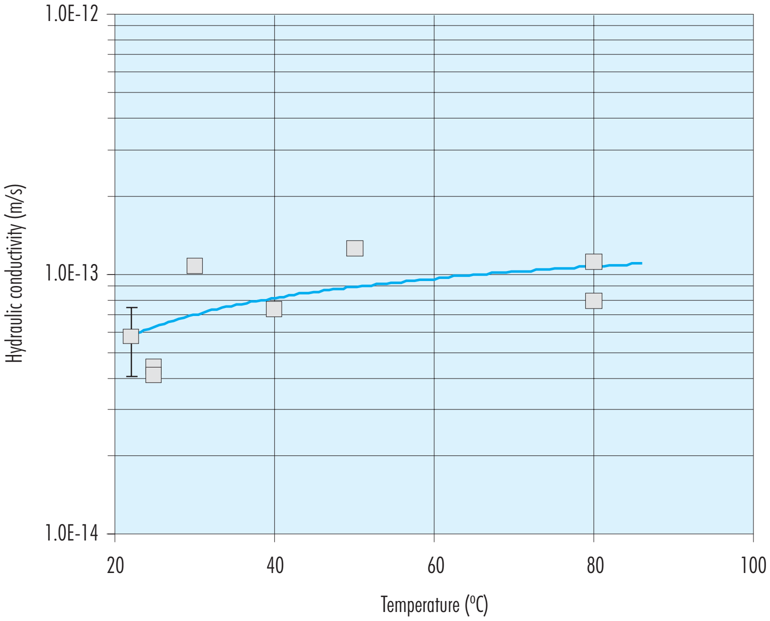

Figure 5.5: Hydraulic conductivity as a function of temperature for saturated FEBEX clay compacted to dry density 1.58 g/cm³ (the error bars correspond to samples tested at laboratory temperature).

it was measured under high hydraulic gradients [15].

The analysis of the bentonite permeability tests proves the independence between the hydraulic gradient applied and the hydraulic conductivity obtained in the range of gradients used in the tests (between 5000 and 25000). However, there seems to be a tendency to find gradients higher than 0 to have a measurable flow, around 5000, and even higher, in the case of the highest densities, which would point out the existence of a threshold gradient.

Relative permeability and tortuosity factor

Unsaturated hydraulic conductivity is highly dependent on the degree of saturation (S_r) and may be expressed as the product of relative permeability (k_r) times the saturated hydraulic conductivity (k_w). The dependence on the degree of saturation is usually expressed by means of a potential law for the relative permeability: $k_r=S_r^n$.

The water infiltration tests provide data allowing unsaturated hydraulic conductivity and its dependence on the degree of saturation to be obtained. The calibration of numerical models and the adjustment of parameters have been done by the back-analysis of the infiltration tests. In the infiltration tests, compacted blocks of clay are introduced in hermetic cells and saturated through the top, while thermal gradients may be applied. After a pre-fixed time, the cell is disassembled and the water content of clay is determined at different distances from the hydration front. By means of parameter identification techniques similar to those used in groundwater engineering and geophysics, intrinsic permeability and the exponent of the law used to obtain the relative permeability may be estimated.

From the water infiltration tests carried out by CIEMAT in Teflon cells (Section 5.1.4.1), the value of intrinsic permeability obtained was $2.95\cdot10^{-21}$ m^2 and the exponent of the relative permeability law was 4.64, for samples with an initial dry density of 1.75 g/cm^3.

Similar infiltration tests were carried out at UPC-DIT. In this case, in order to study the possibility of desaturation of the surrounding rock at the interface between the bentonite and the granite, a hydraulic gradient was prescribed across a specimen of granite in contact with another of bentonite (Section 5.1.4.2). From the analysis of these tests, the exponent of the relative permeability law obtained was 3.5, for samples of dry density of 1.76 g/cm^3.

From the water infiltration tests described in Sections 5.1.4.1, 5.1.4.2 and 5.1.4.3, the value of intrinsic permeability obtained was $1.9{\cdot}10^{-21}$ m^2 and the exponent of the relative permeability law was 3, in the case of samples with an initial porosity of 0.4 (dry density 1.6 g/cm^3).

On the other hand, if the infiltration test is performed under thermal gradients, the tortuosity factor that is involved in vapour flux modelling may also be obtained or validated. Using parameter identification techniques, values of tortuosity factor between 0.5 and 2 have been obtained from seven thermo-hydraulic tests [50]. However, in most of the cases the measurements can be well reproduced using a value of this parameter of 0.8.

5.1.2.2. Gas permeability

The gas permeability of the compacted clay has been determined by CIEMAT using nitrogen gas as a fluid, injected at a low pressure [16, 49]. Specimens of nominal dry densities ranging from 1.50 to 1.70 g/cm^3 and with different water contents have been tested. The values obtained are plotted in Figure 5.6, together with the fitting obtained (valid only for the degree of saturation between 25 and 80 %):

$$k_g = 3.164{\cdot}10^{-6}\ (e\ (1-S_r))^{4.3}$$
$$(r^2=0.82,\ 39\ \text{points}) \qquad (5.9)$$

where k_g (m/s) is the gas permeability, e the void ratio and S_r the degree of saturation.

The gas permeability for the same degree of saturation is a function of dry density and, for the same dry density, decreases with the degree of saturation. In tests performed with the bentonite with hygroscopic water content compacted to different dry densities it was observed that gas permeability decreases logarithmically with increasing dry density.

In all the tests performed, the values of intrinsic permeability obtained (ranging between 10^{-16} and 10^{-12} m/s) are much higher than those obtained when intrinsic permeability is calculated from hydraulic conductivity tests conducted with the clay under saturated conditions (Figure 5.7). This is due to the different structural disposition of the saturated and unsaturated specimens, caused by swelling of the clay as it hydrates. In water flow tests performed under saturated and confined conditions, the bentonite tries to swell and fill the inter-aggregate pores. Under these conditions, mean pore diameter is close to intra-aggregate pore size (see Section 2.3.2 and 5.1.5). In the case of gas flow under dry conditions, this flow takes place through inter-granular pores with a diameter of more than 0.2 μm. This difference in accessible pore size may explain the different values of intrinsic permeability that have been derived from water and gas flow.

GRS determined the gas permeability of the bentonite in cores machined from bentonite blocks similar to those used in the "in situ" test. These cores were installed in a modified Hassler cell to determine permeability as a function of gas humidity and confining pressure. The values obtained vary in the range between $5{\cdot}10^{-16}$ to $8{\cdot}10^{-15}$ m^2. When the confining pressure is increased from 1 to 11 MPa, the permeability decreases by almost one order of magnitude due to porosity reduction.

5.1.2.3 .Water retention capacity

Tests on unconfined samples

CIEMAT carried out suction/water content tests for the FEBEX bentonite, both in compacted and in trimmed samples. Suction was imposed either by controlling the relative humidity of the atmosphere in which the specimens were placed (for suctions between 400 and 3 MPa) or by applying the axis translation technique in membrane cells (suctions between 2 and 0.1 MPa). The relationship between suction and water content was determined in compacted samples for three different suction values and, also following wetting, drying and wetting after drying paths. UPC-DIT tested specimens at suctions between 3 MPa and 500 MPa following similar wetting and drying paths. Figure 5.8 shows the tests results grouped according to initial dry density (ρ_{d0}). Tests with a dry density of 1.67 and 1.75 g/cm^3 were performed by CIEMAT and tests with a dry density of 1.64 g/cm^3 were performed by UPC-DIT [50]. The relationship between suction (s, MPa) and water content (w, %) changes, taking into account the initial dry density (ρ_{d0}, g/cm^3), may be fitted to the following equation [50]:

$$w = (45.1\ \rho_{d0}-39.2)-(18.8\rho_{d0}-20.34)\log s \qquad (5.10)$$

The volume variations observed with changing suction are important. Figure 5.9 shows the relationship between the dry density and the change in suc-

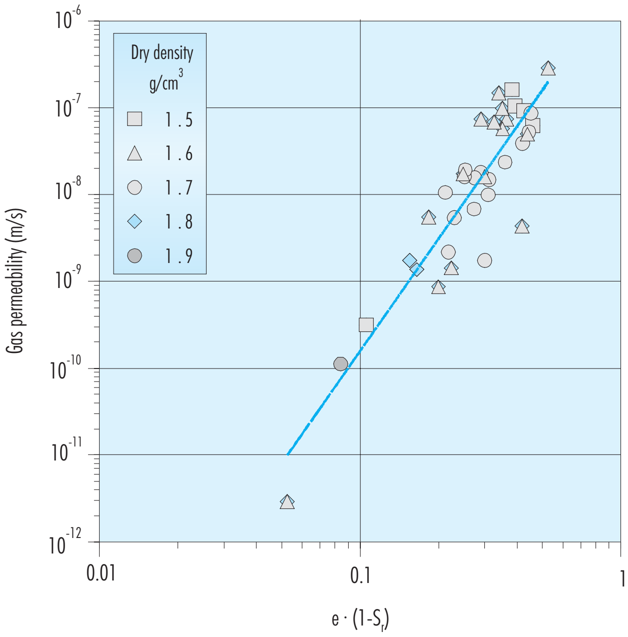

Figure 5.6: Gas permeability measured in specimens of FEBEX bentonite compacted to different dry densities and with varying water content.

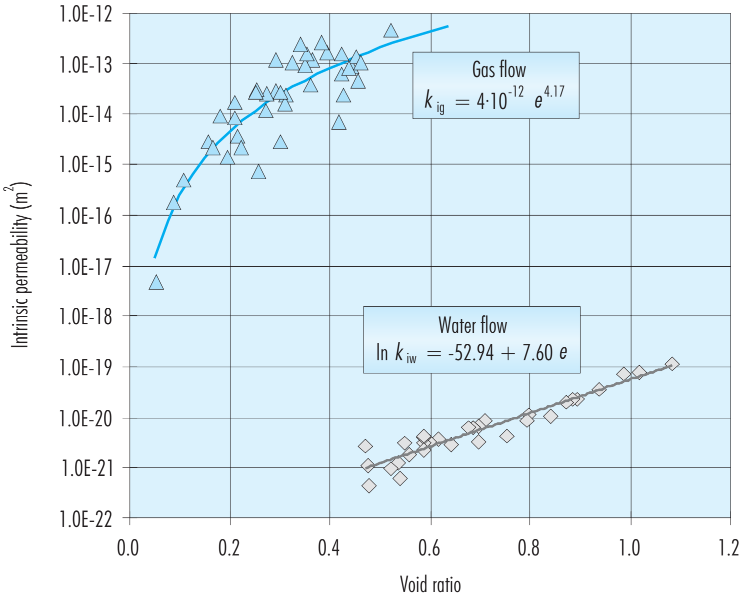

Figure 5.7: Intrinsic permeability of the compacted clay obtained from saturated water flow and from unsaturated gas flow tests.

tion for the different samples tested, grouped according to their initial dry densities. The dry density for values of suction ranging from 400 to 0.1 MPa may be obtained through the following expression:

$$\rho_d = 1.15\, s^{0.13\rho_{d0}} - 0.15 \qquad (5.11)$$

where ρ_{do} is the initial dry density in g/cm^3 and s is the suction in MPa.

For suctions of between 2.0 MPa and 385.0 MPa, an empirical equation was determined for the bentonite S-2, independent of initial dry density (ENRESA 1998)

$$w = 36.1 - 12.0 \log s$$
$$(r^2 = 0.94,\ 191\ \text{points}) \qquad (5.12)$$

where w is the water content in %, and s the suction in MPa.

Figure 5.10 shows the regression curves for the bentonites (S-2 and FEBEX) and the points obtained by CIEMAT and UPC-DIT for each bentonite. The differences between the two curves are very small, one or two percentage points in the water content, depending on the suction value. Nevertheless, it may be said that exists a difference that is reflected in the water content in equilibrium with the laboratory conditions, as was indicated in Table 2.8. For all practical purposes, the differences between the two bentonites are very small, as far as the PA is concerned.

Tests on confined samples

In unconfined tests, the dry density and structure of the bentonite undergo important changes during the hydration process. However, volume changes are small in a bentonite barrier, and knowledge of the relationship between suction/water content at constant dry density (characteristic or water retention curve) is essential to predict the hydration process of the barrier.

The determination of the retention curve at constant volume was initially performed by two different kind of tests. CIEMAT used suction controlled oedometers to hinder swelling of the clay, by adding the appropriate loads [16, 49]. UPC-DIT designed containers made from sintered metal to fix the volume of the sample, while the water vapour in the clay changes with the atmosphere in which the capsule is

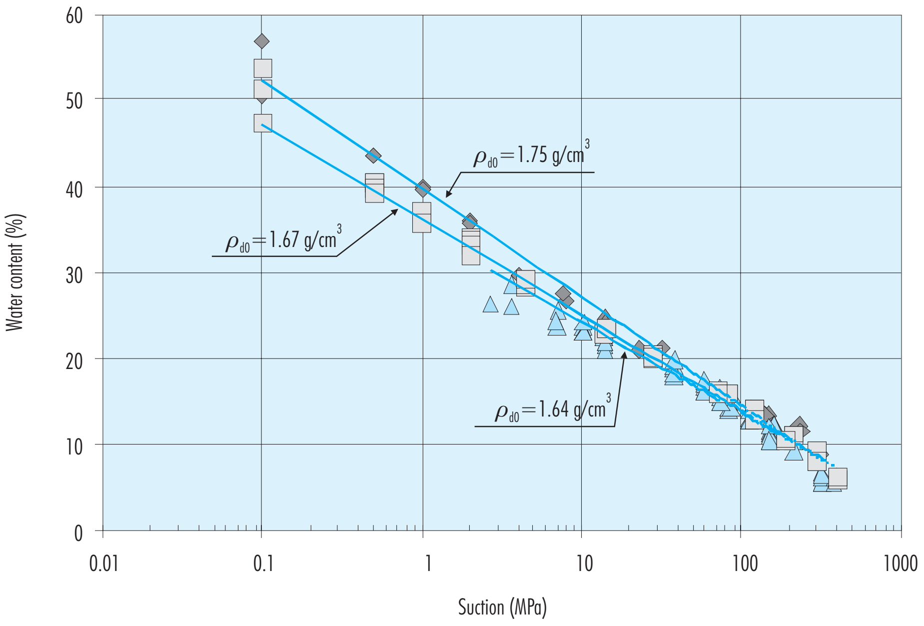

Figure 5.8: Suction/water content relationship in tests on unconfined samples, for FEBEX bentonite.

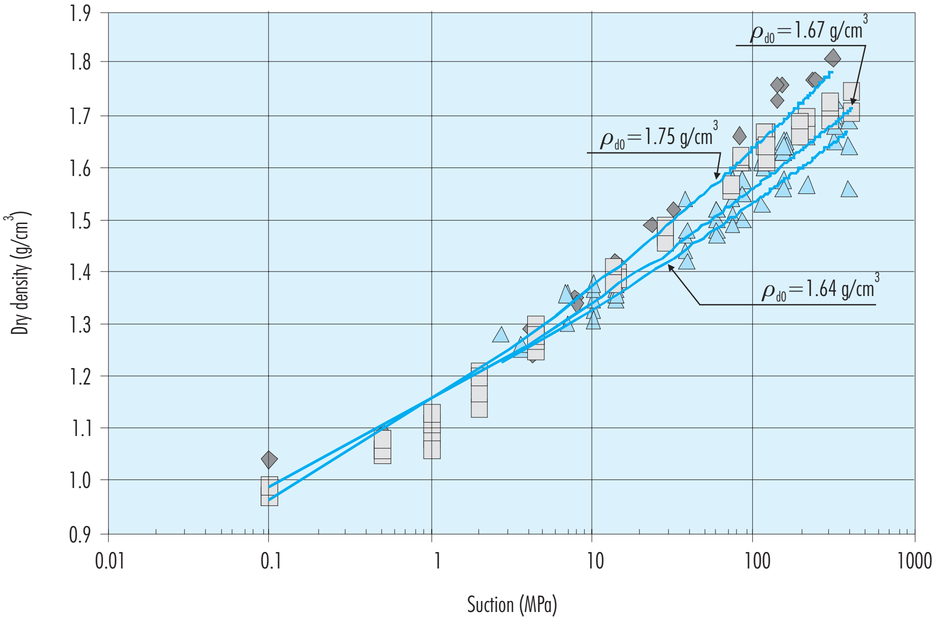

Figure 5.9: Relationship between dry density and suction in tests on unconfined samples, for FEBEX bentonite.

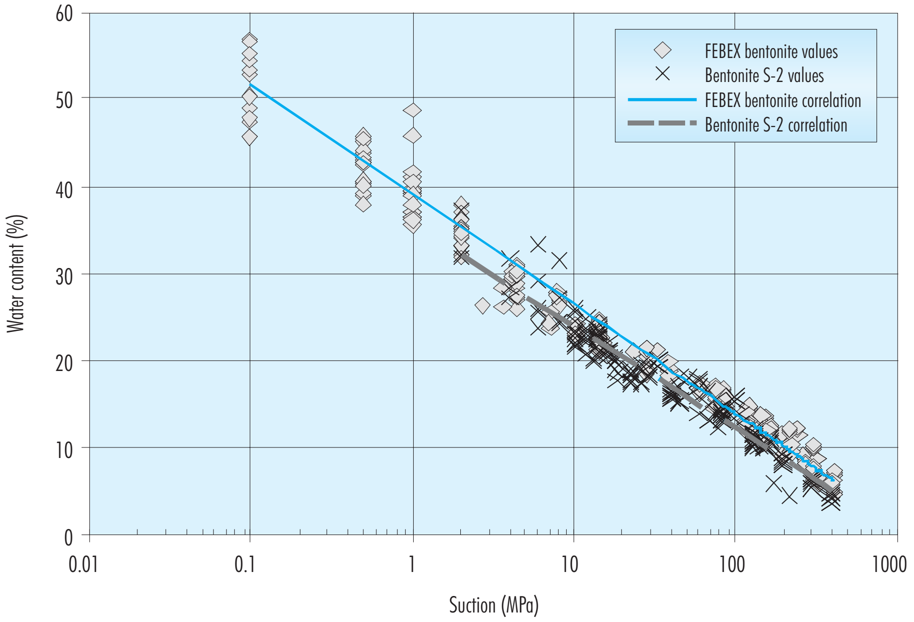

Figure 5.10: Suction/water content relationship in tests on unconfined samples, for S-2 and FEBEX bentonites.

placed [50]. In both cases, minor volume changes occurred.

The retention curves may be fitted to the van Genuchten expression:

$$S_r = S_{r_0} + (S_{r_{max}} - S_{r_0})\left[1+\left(\frac{s}{P_0}\right)^{\frac{1}{1-\lambda}}\right]^{-\lambda} \qquad (5.13)$$

or to a modification of this expression that is more suitable for higher values of suction:

$$S_r = S_{r_0} + (S_{r_{max}} - S_{r_0})\left[1+\left(\frac{s}{P_0}\right)^{\frac{1}{1-\lambda}}\right]^{-\lambda}\left[1-\frac{s}{P'_0}\right]^{\lambda'} \qquad (5.14)$$

where S_{r0} and S_{rmax} are the residual and maximum degree of saturation and P_0 (MPa), P'_0 (MPa), λ and λ' are material parameters.

On approaching saturation, the degrees of saturation obtained were higher than one, because they were computed by considering the density of the water as 1.00 g/cm^3, what has been shown to be untrue for high plasticity materials (see Section 5.1.2.4). The values of degree of saturation higher than one, have been made equal to one for fitting the curves obtained.

Table 5.1 shows the parameters fitted for the wetting paths, which are plotted together with the experimental points in Figure 5.11 [50]. Changes in dry density took place during wetting due to the swelling that could not be completely counteracted. The first column of the table gives the range of dry densities for each curve. These parameters must not be considered exclusive, because the curves can be fitted also with slightly different combinations of parameters.

Figure 5.12 shows the hysteresis effect on samples that have reached saturation and have subsequently been dried. The parameters used in the curves reflected in this figure are shown in Table 5.2.

The methodology initially used to determine curves at constant volume presented technical limitations that made it difficult to perform the tests without failures. In addition, the possible change of dry density during wetting was a major drawback. For this reason, special cells were designed at the end of the first phase, what allowed to determine the retention curves for different dry densities in a systematic way.

The cell shown in Figure 5.13 consists of a cylindrical body measuring 0.5 cm in thickness, with two perforated covers joined by bolts. The cell is placed in a desiccator with a sulphuric acid solution and vacuum is created. The suction control method is, therefore, through the control of relative humidity. The porous stone and the perforated covers allow for the exchange of water in the vapour phase between the clay and the atmosphere of the desiccator. This process is very slow – slower than when the retention curve under free volume conditions is determined in the desiccator – not only because not the entire surface of the sample acts as an exchange surface (but only the upper and lower parts) but also because the process is performed at constant volume. Once the water content of the clay is stable, the cell is weighed and the solution in the desiccator

Table 5.1
Parameters for fitting of the retention curves in wetting paths

Dry density range g/cm^3	Kind of equation (no. in Figure 5.11)	P_0 MPa	λ	S_{r0}	S_{rmax}	P'_0 MPa	λ'
1.75-1.65	van Genuchten (1)	90	0.45	0.00	1.00	-	-
1.75-1.65	modified van Genuchten (2)	100	0.45	0.01	1.00	1500	0.05
1.65-1.60	van Genuchten (3)	30	0.32	0.10	1.00	-	-
1.65-1.60	modified van Genuchten (4)	35	0.30	0.01	1.00	1500	1.50
1.60-1.53	van Genuchten (5)	5	0.17	0.00	1.00	-	-
1.60-1.53	modified van Genuchten (6)	2	0.10	0.01	0.99	1000	1.30

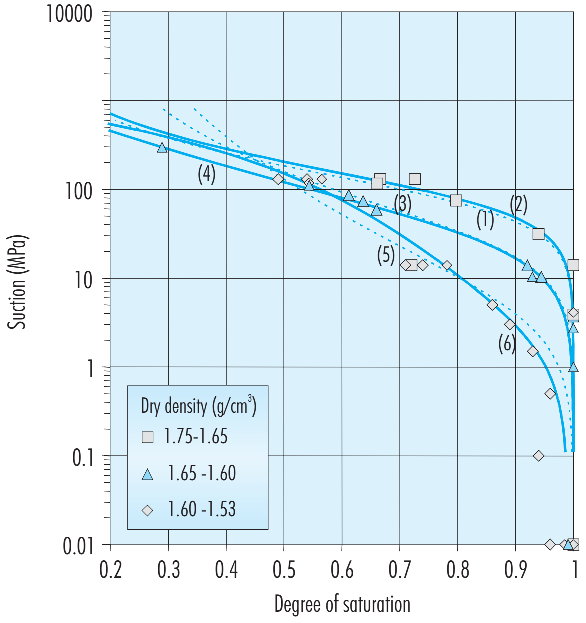

Figure 5.11: Retention curves in wetting paths performed on confined samples. In parentheses the number of the van Genuchten equation used in Table 5.1.

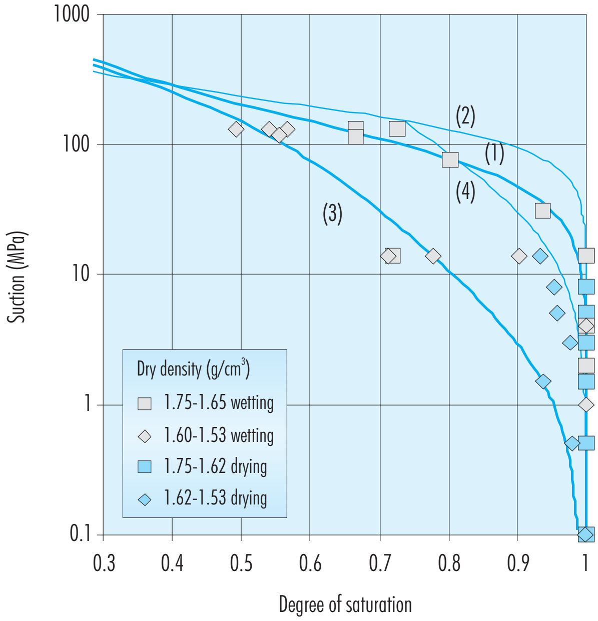

Figure 5.12: Hysteresis effect on the wetting-drying paths under confined conditions. In parentheses the numbers of the curves indicated in Table 5.2.

Table 5.2
Parameters for fitting of the drying paths after saturation

Dry density range g/cm^3	Kind of equation (no. in Figure 5.12)	P_0 MPa	λ	S_{r0}	S_{rmax}	P'_0 MPa	λ'
1.75-1.65 wetting	Modified van Genuchten (1)	100	0.45	0.01	1.00	1500	0.05
1.75-1.62 drying	van Genuchten (2)	180	0.62	0.00	1.00	-	-
1.60-1.53 wetting	Modified van Genuchten (3)	2	0.10	0.01	0.99	1000	1.30
1.62-1.53 drying	van Genuchten (4)	30	0.15	0.00	1.00	-	-

is changed by a lower concentration one in order to perform a wetting path.

The device shown in Figure 5.14 has been designed by UPC-DIT. In order to reduce the time needed to reach equilibrium following suction changes, a flow of humid air is induced across the porous plates by means of a peristaltic pump. The humidity of the air is controlled by means of saturated salt solutions.

CIEMAT carried out the determination of the retention curve at constant volume following a wetting path from 130 to 1 MPa, followed by a drying path up to 130 MPa for dry densities of 1.60, 1.65 and 1.70 g/cm^3. The determination was performed at 20°C. The initial water content of the samples was the hygroscopic content (about 14 percent). The results obtained are plotted in Figure 5.15 [15]. Although there are no major differences between the water content curves for the different dry densities – probably due to the fact that they are very close values – at the beginning of hydration the water content of the samples with a higher dry density is

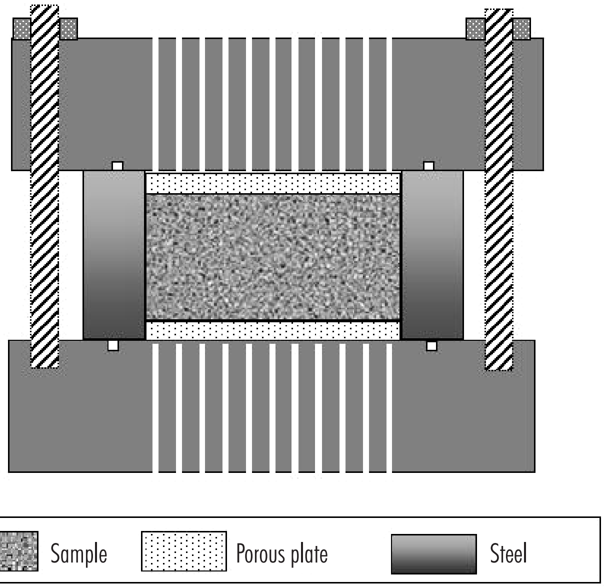

Figure 5.13: Non-deformable cell for the determination of the retention curve (CIEMAT).

greater for the same values of suction. However, when lower values of suction are reached, the water content of the denser samples is lower. This occurs because the volume of small pores is higher in samples with a higher dry density, due to the fact that the volume of large pores is reduced during compaction, as a result of which the sample takes up more water at the beginning of hydration. However, as suction decreases and water content increases, the lower total porosity of the samples of greater density limits their possibility for water uptake [16]. Consequently, the repercussion of initial dry density on the value of water content reached becomes more obvious as suction decreases. On the other hand, the difference between the wetting and drying paths is significant, although it should be taken into account that the density change cannot be controlled during the drying sequence and increases as the sample dries.

UPC-DIT has used the new cells (Figure 5.14) to determine the water retention curves at 22°C on specimens compacted with hygroscopic water content at dry densities of 1.55 and 1.65 g/cm^3. Figure 5.16 shows the results obtained in terms of suction-water content relationship.

The retention curves for wetting paths obtained by the two laboratories using the methodologies employed during the two phases of FEBEX (results of Figure 5.11, Figure 5.15 and Figure 5.16) are plotted together in Figure 5.17. Although the results are consistent, those obtained at the beginning – using a less highly developed methodology – are more scattered.

Figure 5.18 shows how the retention curve differs significantly, for the same initial conditions of the material, depending on the volume restriction imposed on the sample during determination. The water content for a given suction is much higher if the sample is allowed to swell freely than if its volume change is constrained.

Influence of solutes

The retention curves of compacted bentonite samples were obtained following wetting paths. The water content of the samples was increased progressively by adding three types of fluid: distilled water and NaCl solutions with concentrations of 2.5 and 5.5 M. At each step the total suction was measured using an SMI transistor psychrometer (approximate measure-

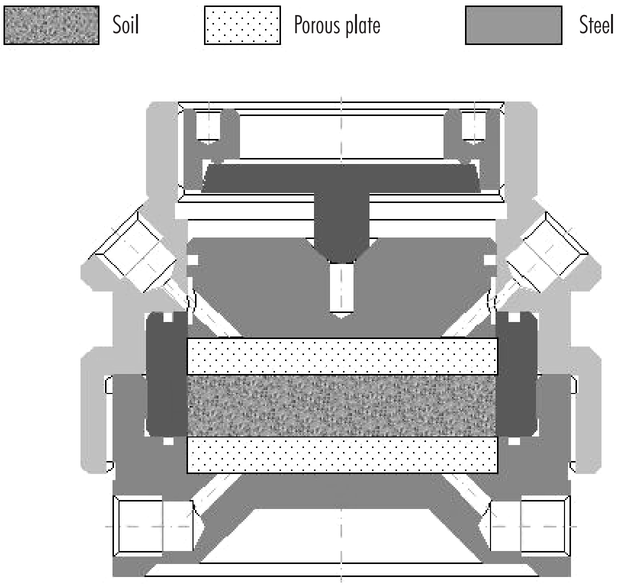

Figure 5.14: Cell designed by UPC-DIT to determine retention curves at constant volume.

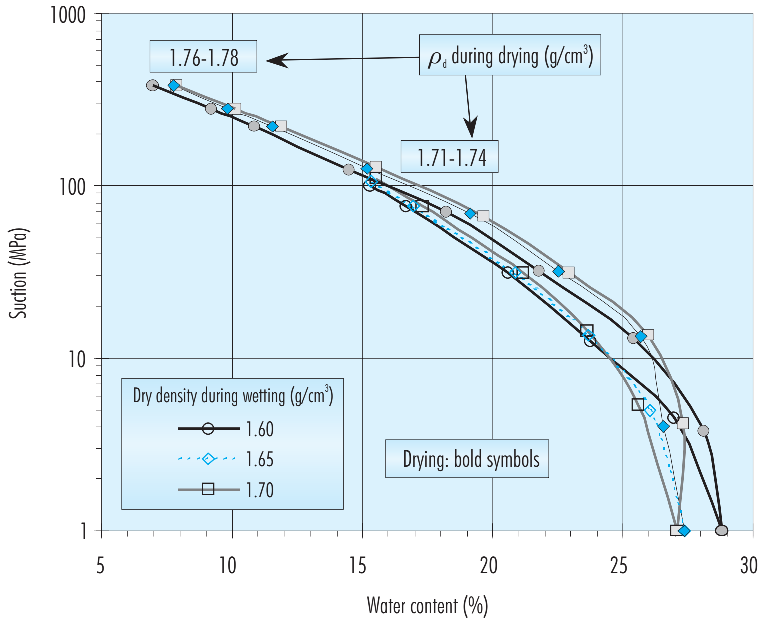

Figure 5.15: Retention curves at constant volume and at 20ºC in wetting/drying paths (CIEMAT).

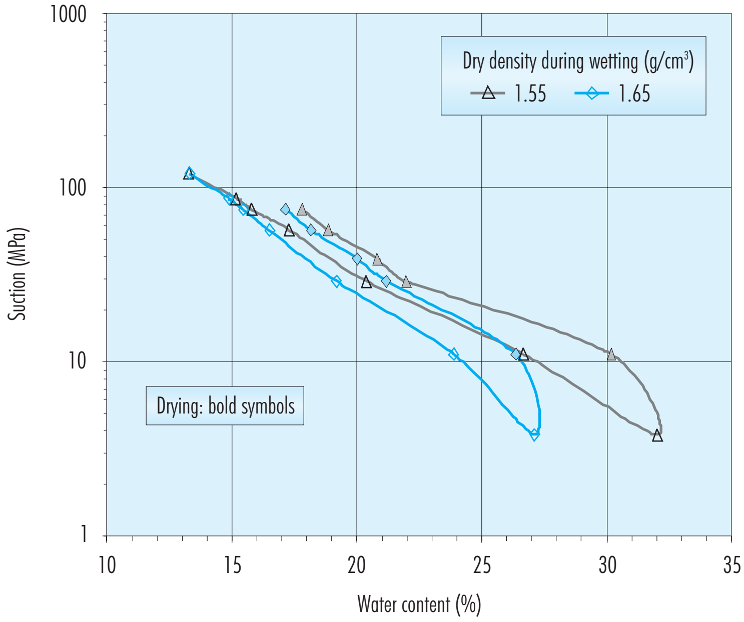

Figure 5.16: Retention curve at constant volume and at 22ºC in a wetting/drying path (UPC-DIT).

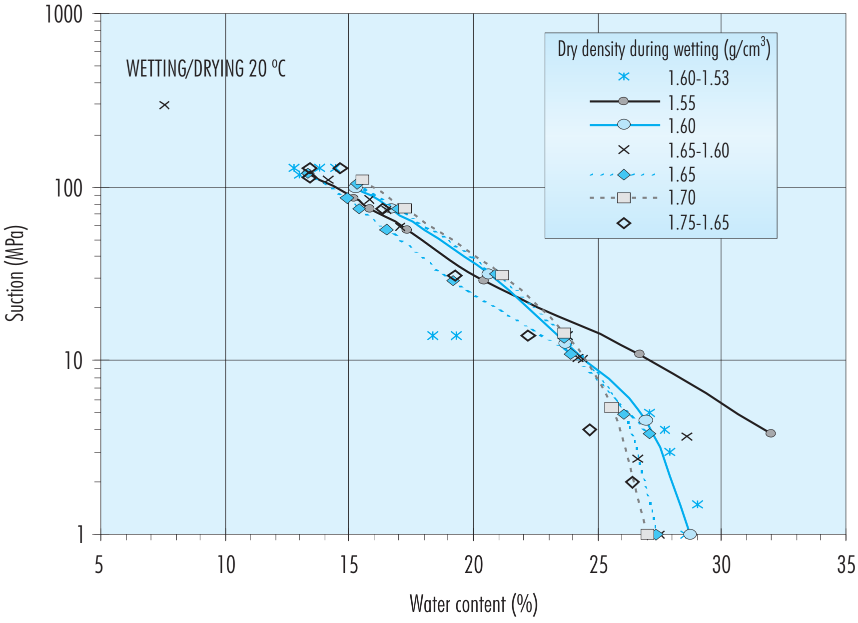

Figure 5.17: Retention curves at constant volume obtained using two different methodologies during the first phase (points) and during the second phase (lines and points) of FEBEX.

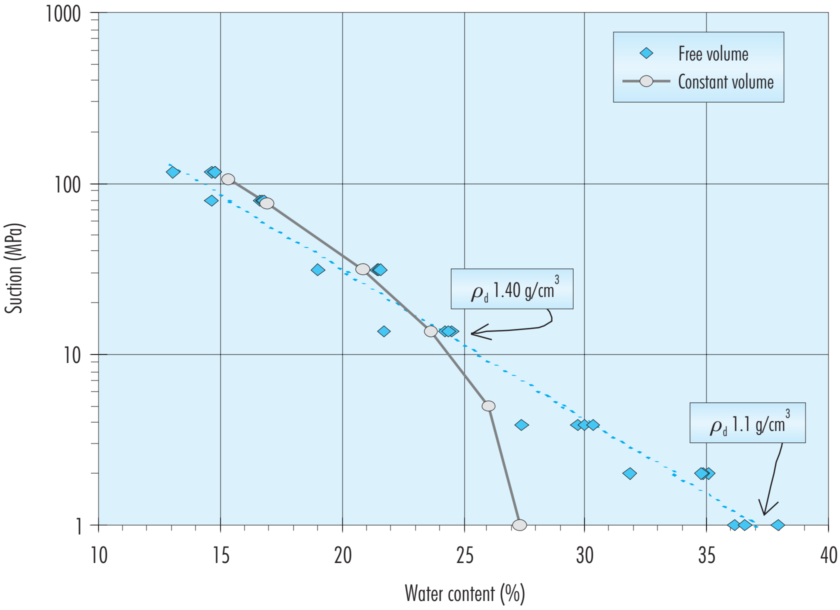

Figure 5.18: Retention curves of bentonite samples of initial dry density 1.65 g/cm³ wetted under free and constant volume conditions. The average dry density of the samples wetted at free volume is indicated.

ment range between 100 MPa and 0.5 MPa). The samples were initially compacted with hygroscopic water content to a dry density of 1.65 g/cm^3. During the wetting process, the samples were confined only laterally in the psychrometric chamber and the volume changes were not measured. Two types of paths were performed; in the first (Figure 5.19), the samples were wetted starting from the hygroscopic water content and in the second (Figure 5.20), the samples were dried after compaction in order to start the wetting process from an almost zero water content. In the samples wetted with saline solutions, at saturation, the total measured suction tends towards the osmotic pressure induced by each solution (33 MPa in the case of 5.5 *M* NaCl and 12.2 MPa in the case of 2.5 *M* NaCl). Assuming that the osmotic suction, due to the salinity of natural bentonite water, is small, it is possible to estimate the matric suction in the tests. The retention curve computed using this matric suction tends towards the retention curve obtained in the sample wetted with distilled water. Also included in the figures is the empirical expression to describe the retention curves under unconfined conditions (Equation 5.10). It should be noted that at low suctions the water content is affected by the important volume increment of the samples that were not measured in the tests; these volume changes and the measurement errors of the equipment in the low range of suctions may explain the discrepancies observed between the retention curve obtained using the estimated matric suction and the retention curve measured with distilled water.

Influence of temperature

The suction/water content relationship was determined both in confined and unconfined samples under different temperatures. Although the sealing material will be unconfined only in the outer part of the barrier, where a void exists between the compacted blocks and the host rock, the determination of the suction/water content relationship in unconfined samples is justified because, being much easier to determine, it will still be useful in identifying the influence of temperature.

The retention curve following a drying/wetting path was determined by CIEMAT in unconfined samples for temperatures of 80 and 60°C [15]. In terms of water content, there are no differences regarding

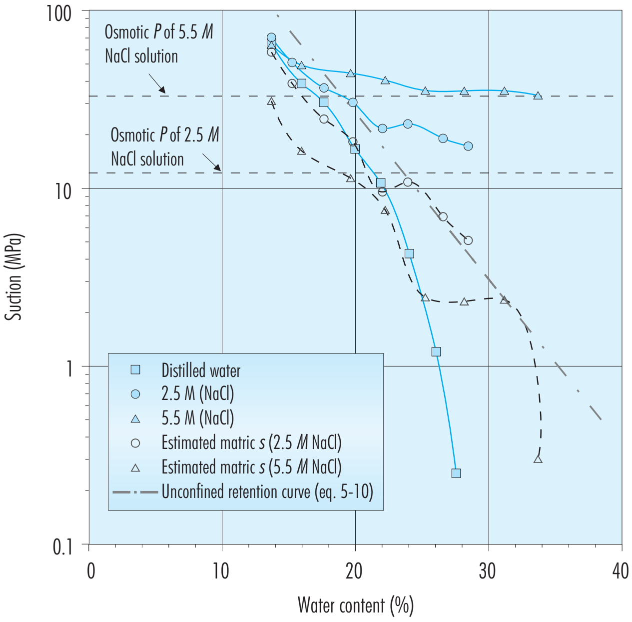

Figure 5.19: Retention curves of bentonite in wetting paths using water of different salinity (starting from the hygroscopic state).

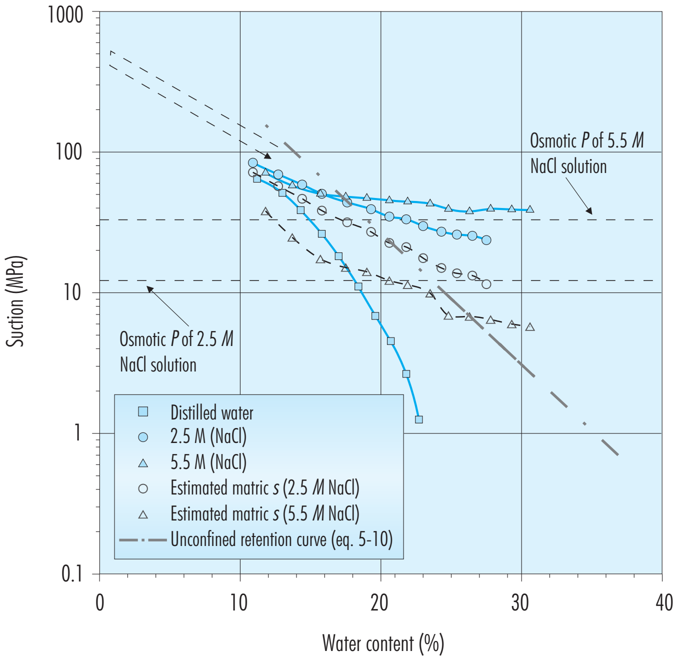

Figure 5.20: Retention curves of bentonite in wetting paths using water of different salinity (starting from the dried state).

initial dry density; however there are differences in terms of the degree of saturation (Figure 5.21): for a given temperature and suction, the higher the initial dry density, the higher the degree of saturation. The curves obtained show hysteresis, the water contents in the wetting paths being lower than those reached for the same suction with previous drying. Figure 5.22 shows the results obtained for a dry density of 1.65 g/cm^3, compared with those obtained at 20°C (see above) for a similar dry density. The retention capacity is higher for the samples tested at laboratory temperature, although no difference may be appreciated in the drying path between the samples tested at 60 and 80°C. The lower retention capacity at higher temperature is clearer in the case of the wetting after drying path.

Figure 5.23 shows the changes in dry density experienced by specimens with an initial dry density of 1.65 g/cm^3 during the determination of retention curves under unconfined conditions. For suctions higher than 100 MPa, volume changes are small and do not depend on temperature. However, for suctions lower than 100 MPa, the decrease in dry density in the wetting path becomes increasingly important and different for each temperature. Swelling is greater for specimens tested at room temperature, in accordance with the results presented in Section 5.1.3.6.

The retention curve at constant volume was determined by CIEMAT for dry densities of between 1.60 and 1.70 g/cm^3 and temperatures of between 20 and 80°C. The curves followed a wetting path, from suction at 130 MPa to 0.1 MPa, and afterwards, a drying path to 130 MPa. The initial water content of the samples was hygroscopic (approximately 14 percent). To hinder the swelling of clay during the determination, the samples were compacted in the cells shown in Figure 5.13. These cells were introduced in vacuum desiccators with a sulphuric acid solution, which were in turn placed in an oven at controlled temperature.

The results obtained are plotted in Figure 5.24 [15]. The results show the hysteretic behaviour of clay, the water contents reached during drying being higher than those obtained during previous wetting. On the other hand, the retention capacity at higher temper-

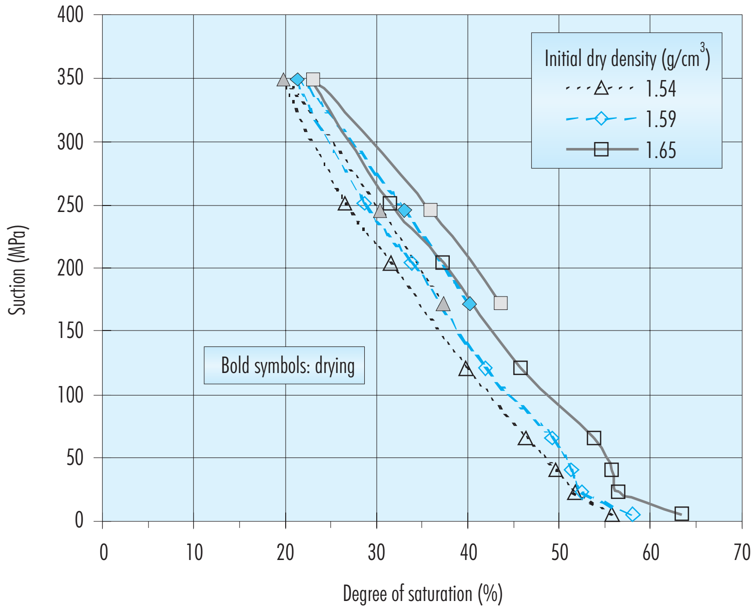

Figure 5.21: Retention curves following drying/wetting paths determined at 80° C for unconfined samples of different initial dry density (CIEMAT).

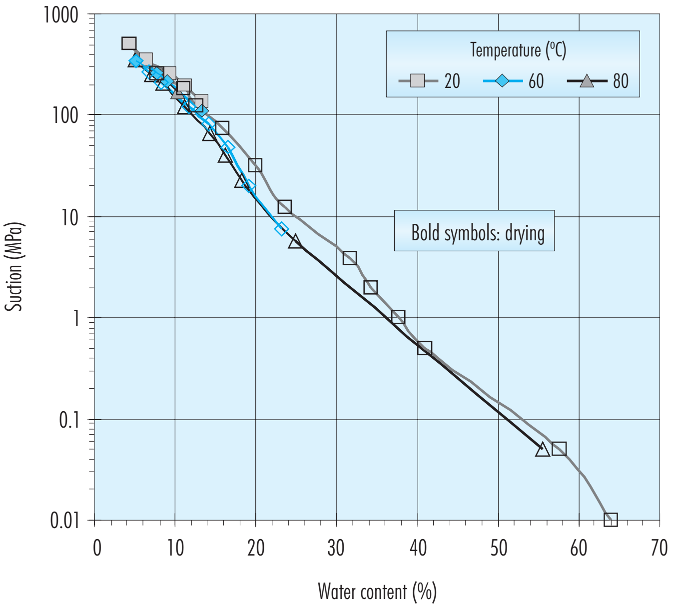

Figure 5.22: Retention curves following drying/wetting paths determined in unconfined samples with an initial nominal dry density of 1.65 g/cm^3 at different temperatures (CIEMAT).

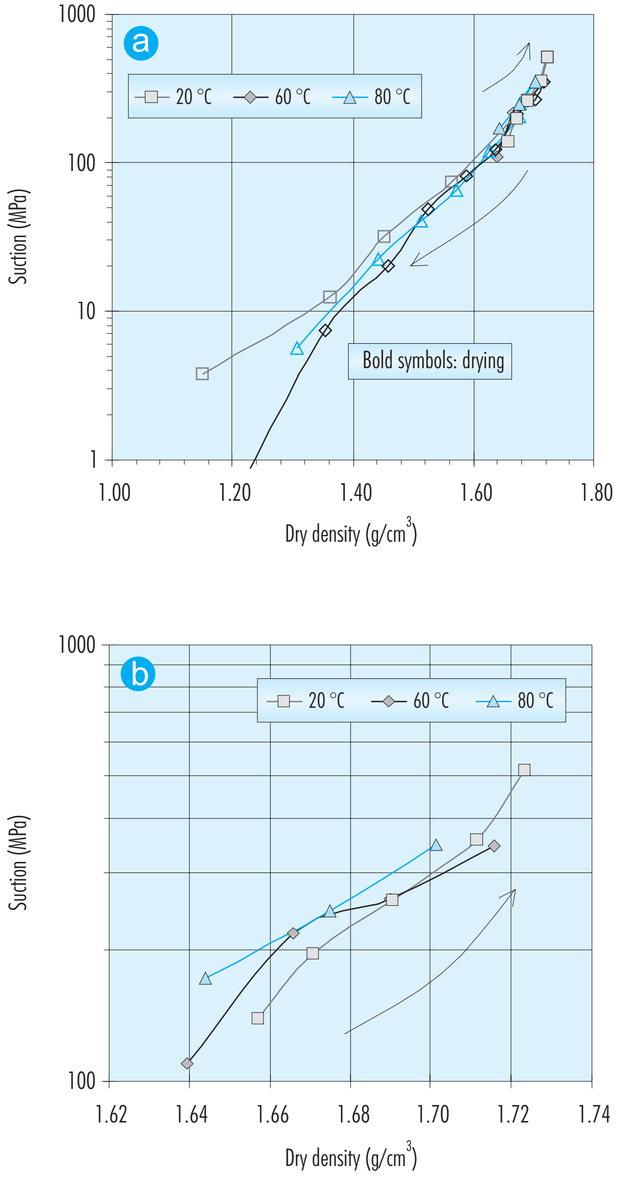

Figure 5.23: Evolution of dry density in the retention curves in unconfined specimens of bentonite compacted at an initial dry density of 1.65 g/cm^3; a: drying/wetting paths, b: enlargement of drying paths.

ature seems to be slightly lower. This is seen in Figure 5.25, where only the wetting curves have been plotted.

By applying an approach similar to that presented by Sánchez [51] to fit the data from these laboratory determinations, the following empirical equation may be obtained:

$$w = (a + bn)\left[1 + \left(\frac{s}{P_0 e^{-\eta(n-n_0)} e^{\alpha(T-T_0)}}\right)^{\frac{1}{1-\lambda}}\right]^{-\lambda} \qquad (5.15)$$

where w is the water content in percentage terms, n the porosity, s the suction in MPa, and T the temperature in °C. The values of the fitted parameters a, b,

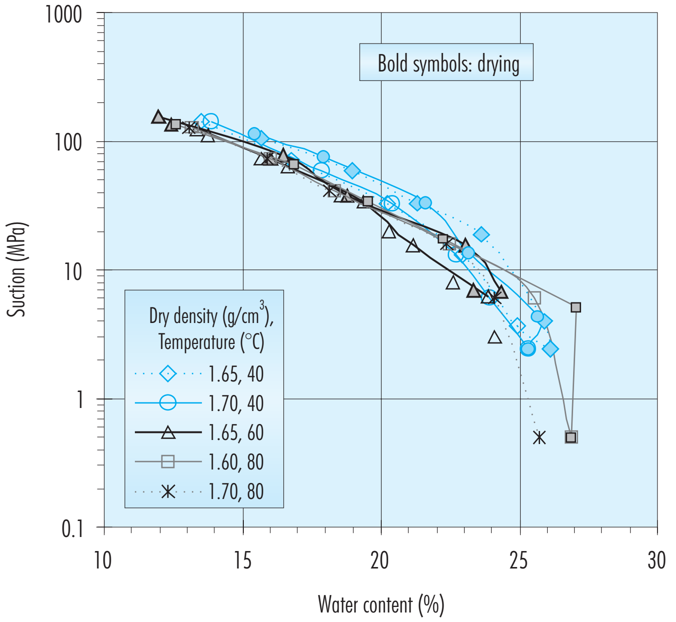

Figure 5.24: Retention curves at constant volume and at different temperatures on a wetting/drying path (CIEMAT).

P_0, λ, η, n_0, α, and T_0 are 10.4, 41.89, 12.68 MPa, 0.211, 7.97, 0.4, 0.00647 °C^{-1} and 20°C, respectively.

5.1.2.4 .Water density

During the experimentation with the FEBEX bentonite it was systematically observed that, at the end of the hydration tests under confined conditions, the measured water contents were higher than those corresponding to the water content for saturated conditions, assuming that the specific density of the mineral particles is 2.7 and the water density 1.0 g/cm^3. The degrees of saturation obtained are higher than 100 percent because they were calculated considering the density of the water to be 1.00 g/cm^3, which was shown to be untrue for high plasticity materials since the water in them is usually adsorbed [16, 52, 53, 54, 55]. The values of average water density obtained are represented in Figure 5.26, which shows that this parameter increases when the volume of pores, and consequently the amount of free water, decreases. The water contents measured may be explained by considering that the microstructural void ratio is about 0.46, and that the average water density in the microstructure is about 1.2 g/cm^3. From measurements of specific surface and basal spacing, Fernández [10] has obtained values for water density varying from 1.13 to 1.51 g/cm^3 for different states of adsorbed water in FEBEX bentonite (see Section 5.2.1.3).

5.1.3. Mechanical properties

5.1.3.1. Elastic shear modulus

UPC-DIT determined the elastic shear modulus, G, at minor deformations ($10^{-6} \leq \gamma \leq 10^{-4}$) for the FEBEX bentonite. The tests were performed in a resonant column on 10 specimens compacted at various dry densities and degrees of saturation [6]. The results are shown in Table 5.3.

5.1.3.2. Strength: unconfined compression and triaxial tests

In the years previous to FEBEX, strength was determined only on samples of bentonite S-2 [6]. Some

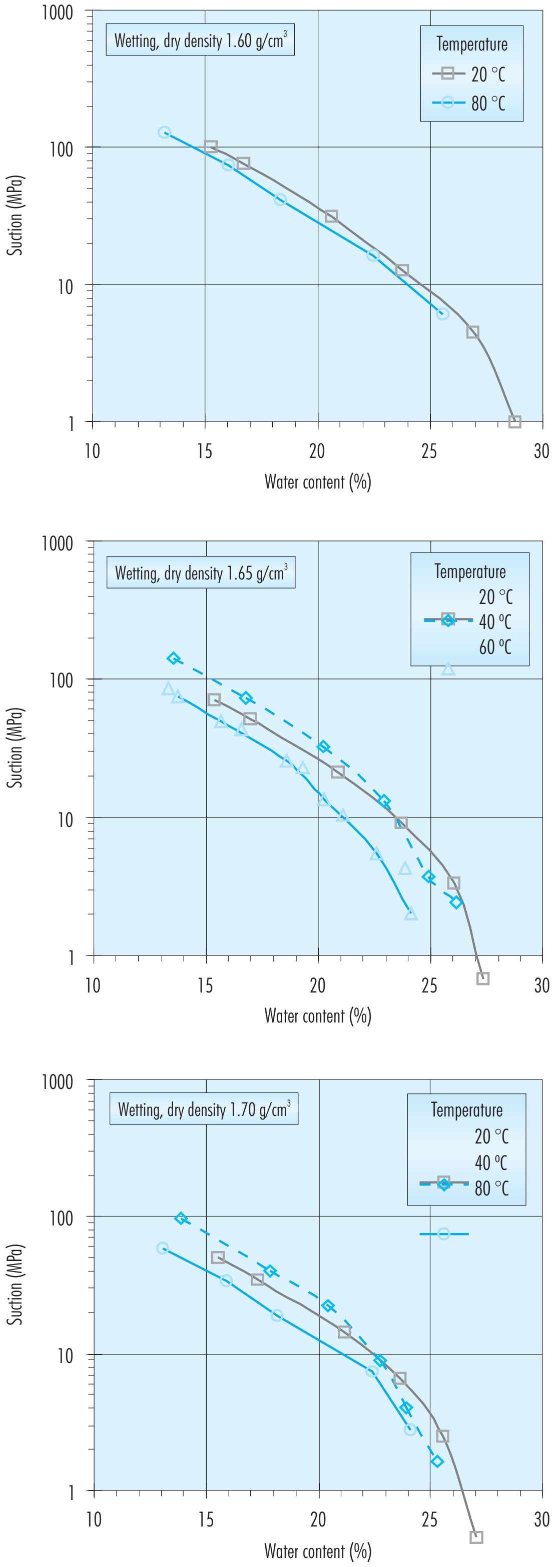

Figure 5.25: Retention curves at constant volume for different temperatures and dry densities .

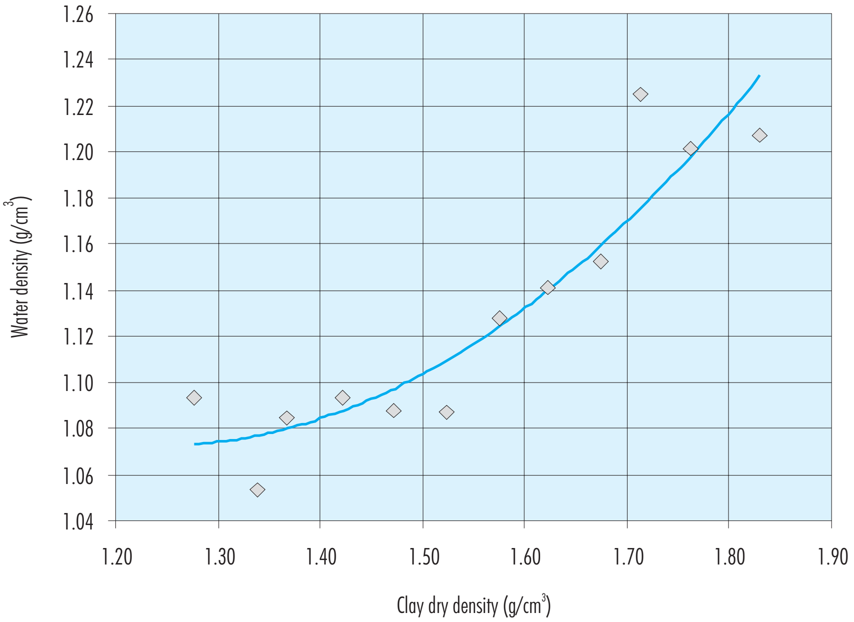

Figure 5.26: Values of average density of adsorbed water calculated for specimens of bentonite of different dry density saturated with distilled water at constant volume [49]).

Table 5.3
Elastic shear modulus obtained in resonant column tests

Dry density g/cm^3	Water content %	Degree of saturation %	Void ratio	Elastic shear modulus, *G*, in MPa				
				σ_3=0.01 MPa	σ_3=0.1 MPa	σ_3=0.2 MPa	σ_3=0.4 MPa	σ_3=0.8 MPa
1.58	14.7	54	0.757	140	207	245	300	370
1.66	13.6	57	0.668	211	223	270	---	---
1.54	3.4	12	0.802	78	106	174	208	326
1.56	2.8	10	0.777	89	106	138	---	---
1.62	24.6	95	0.717	240	270	---	331	336
1.66	21.3	87	0.677	252	296	370	429	502
1.65	4. 7	19	0.685	74	90	137	190	310
1.72	10.4	47	0.615	200	219	293	381	429
1.68	3.7	16	0.652	61	89	141	200	290
1.62	12.7	50	0.713	122	180	240	299	387

of these data are presented herein for informative purposes.

The unconfined compressive strength is 2.5 MPa for samples prepared with hygroscopic water content at a density of 1.70 g/cm^3. It was found that unconfined compressive strength increases exponentially with dry density.

Various types of triaxial tests were performed, using saturated and unsaturated samples. Table 5.4 shows the results from the unconsolidated, undrained tests performed with unsaturated samples, prepared at different dry densities with the water content at equilibrium with the laboratory conditions.

5.1.3.3. Swelling pressure

Swelling pressure tests were performed using conventional oedometers on samples saturated with deionised water. A regression curve was developed as a function of dry density for the swelling pressure of the FEBEX bentonite, as shown in Figure 5.27, and expressed by the equation [16, 49]

$$P_s = \exp\,(6.77\,\rho_d - 9.07) \qquad (5.16)$$

where P_s is the swelling pressure, in MPa, and ρ_d is the dry density, in g/cm^3. The deviation of the experimental values with respect to this fitting may be as high as 25 percent. The dispersion observed in the values is larger for higher dry densities, this probably being due to technical limitations, as the load capacity of the oedometers is almost exceeded by the swelling pressure.

The repercussion of the direction of the measurement – parallel or perpendicular to the compaction effort – on the value of swelling pressure has also been tested (trimmed samples), as has the use of granitic instead of deionised water. None of these aspects seems to be relevant.

The swelling pressure values and the regression curve for bentonite S-2 are also shown in Figure 5.27. The difference in the swelling pressures of the S-2 and the FEBEX bentonites may be considered to be negligible for all practical purposes in the PA of a repository.

5.1.3.4. Swelling capacity

The saturation (or swelling) under load test makes it possible to determine the strain capacity of the soil when it saturates under a previously established pressure. These tests were performed using conventional oedometers on samples of the FEBEX bentonite.

Table 5.4
Strength parameters obtained in triaxial tests on unsaturated specimens of bentonite S-2 prepared with hygroscopic water content and at different initial dry densities

ρ_d g/cm^3	Initial S_r %	Range of σ_3 MPa	Cohesion MPa	Friction angle Degrees
1.6	41 - 47	0.5-3.0	0.7	25
1.6	41 - 47	3.0-10.0	2.8	14
1.6	41 - 47	10.0-30.0	4.4	14
1.7	49 - 60	0.5-3.0	0.8	30
1.7	49 - 60	3.0-10.0	1.0	26
1.7	49 - 60	10.0-30.0	3.5	16
1.8	53 - 59	3.0-10.0	4.3	16
1.8	53 - 59	10.0-30.0	3.6	18
1.9	65 - 79	3.0-10.0	4.5	19

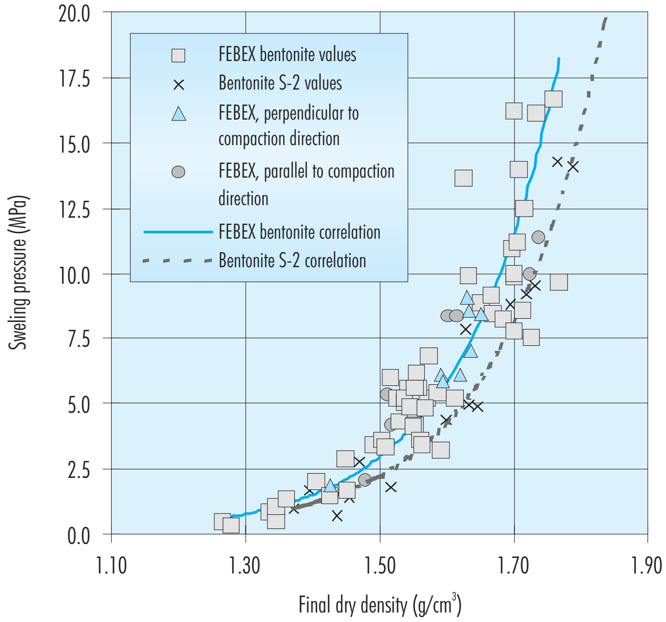

Figure 5.27: Swelling pressure as a function of dry density.

Influence of vertical load and initial dry density

CIEMAT carried out tests on specimens with an initial nominal dry density of 1.50, 1.60 and 1.70 g/cm^3 saturated with deionised water under vertical loads of between 0.1 and 3.0 MPa [15]. The initial water content of the bentonite was hygroscopic. Taking into account all the results, the following fitting between final swelling strain (ϵ, %) and vertical pressure (σ, MPa), as a function of initial dry density (ρ_d, g/cm^3), was found:

$$\epsilon = (5.40\,\rho_d - 1.32)\ln\sigma + (-48.25\,\rho_d + 63.69) \qquad (5.17)$$

UPC-DIT performed 21 flooding-under-load tests on specimens prepared at various dry densities of between 1.57 g/cm^3 and 1.87 g/cm^3, with an initial water content of 11.7 percent (water content at equilibrium with laboratory conditions). The specimens were saturated with distilled water while being subjected to a predetermined load of between 0.01 MPa and 10 MPa [50]. The strain (ϵ, %) induced after saturation may be approximately expressed by the equation

$$\epsilon = 46.9 + 19.4\log\sigma - 36.6\,\rho_d \qquad (5.18)$$

where σ is the vertical load in MPa and ρ_d is the initial dry density in g/cm^3.

As expected, both in the tests performed by CIEMAT and those carried out by UPC-DIT, the strain undergone by the specimens on saturation is higher the lower the load applied. Likewise, swelling capacity increases with increasing initial dry density.

Influence of the kind of water

In addition, tests were performed by CIEMAT using both granitic and saline water for saturation of the sample. The nominal initial dry density of the FEBEX specimens was 1.50, 1.60 and 1.70 g/cm^3, and they were saturated under vertical loads of between 0.1 and 3.0 MPa [15]. The initial water content of the bentonite was hygroscopic. A commercial granitic water was used, identical to the one used for saturation in the “mock-up” test. The saline water is a synthetic product having a chemical composition similar to that of the bentonite interstitial water, but simplified to include only the major elements. The chemical composition of both is shown in Table 5.5.

Final strains as a function of vertical pressure are represented in Figure 5.28, for the nominal dry density of 1.50 g/cm^3, in Figure 5.29, for the nominal dry density of 1.60 g/cm^3, and in Figure 5.30, for the nominal dry density of 1.70 g/cm^3. The fittings obtained for the different types of water are also shown in these figures. Taking into account all the results, the following fittings between final swelling strain (ϵ, %) and vertical pressure (σ, MPa), as a function of initial dry density (ρ_d, g/cm^3), were found:

For saline water:

$$\epsilon = 6.47 \ln \sigma + (-48.71 \rho_d + 66.13) \quad (5.19)$$

For granitic water:

$$\epsilon = (-6.49 \rho_d + 16.53) \ln \sigma + (-43.59 \rho_d + 58.14) \quad (5.20)$$

The final values of strain do not seem to be particularly dependent on the kind of water, although in the tests performed with saline water they are somewhat higher than in those performed with granitic water, the values for deionised water being the highest. This difference becomes less apparent for higher vertical pressures.

In order to evaluate the effect of salinity on swelling strains, UPC-DIT performed tests with the FEBEX bentonite compacted to a dry density of 1.65 g/cm^3 and soaked under a load of 0.5 MPa using different solutions. After soaking, the bentonite was loaded under oedometric conditions up to 2 MPa, in order to evaluate its stiffness and permeability. Figure 5.31 shows the results of the soaking under load tests in terms of changes in vertical strain. Swelling capacity decreases significantly with salinity. On the other hand, samples wetted with $CaCl_2$ solutions swell slightly more than those wetted with NaCl. If the osmotic pressure of the solution is considered, the effect of changes in salt concentration may be compared with the changes measured in suction controlled oedometers (Section 5.1.3.5): in fact, the volume changes measured in the suction controlled oedometer tests during the suction reduction stages are comparable to the volume changes measured in soaking tests using salt solutions [15].

On the other hand, the settlements measured upon application of a vertical load on the saturated sam-

Table 5.5
Chemical composition and pH of the water used in the tests (mg/L)

Dissolved ions and pH	Granitic	Saline
Cl^-	13.1	3550.0
SO_4^{2-}	14.4	1440.0
Br^-	0.1	—
NO_3^-	4.8	—
HCO_3^-	144.0	—
SiO_2 (aq)	22.2	—
Mg^{2+}	9.4	360.0
Ca^{2+}	44.9	400.8
Na^+	11.0	253.9
K^+	1.0	—
Sr^{2+}	0.09	—
pH	8.3	7.0

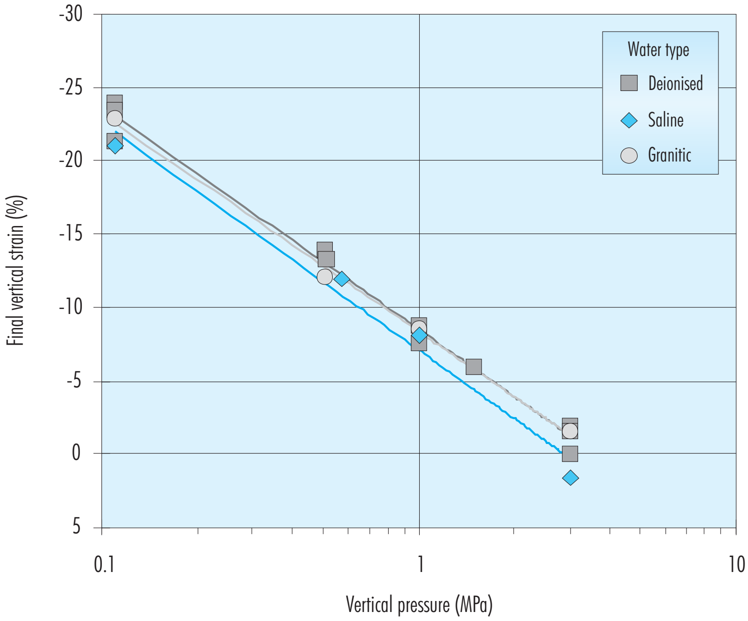

Figure 5.28: Final strain of samples with a dry density of 1.50 g/cm³ saturated under different vertical pressures with different waters (CIEMAT).

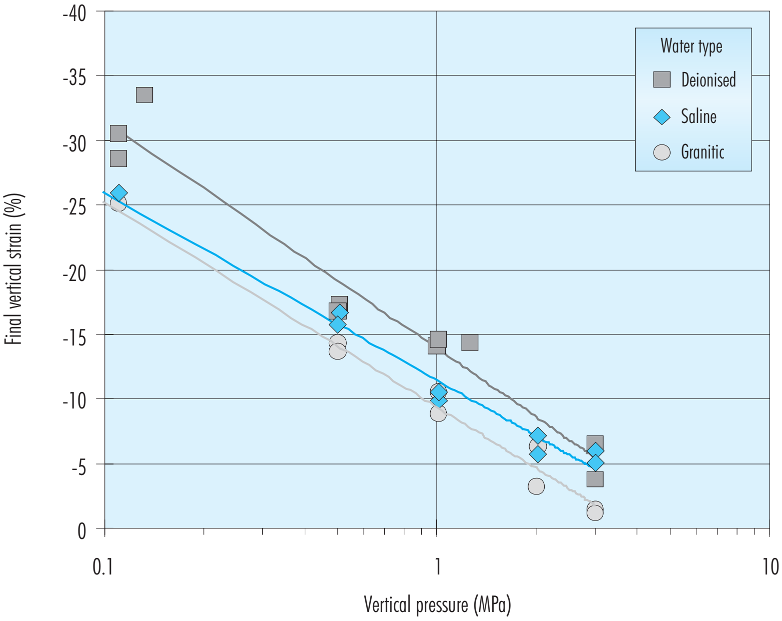

Figure 5.29: Final strain of samples with a dry density of 1.60 g/cm³ saturated under different vertical pressures with different waters (CIEMAT)

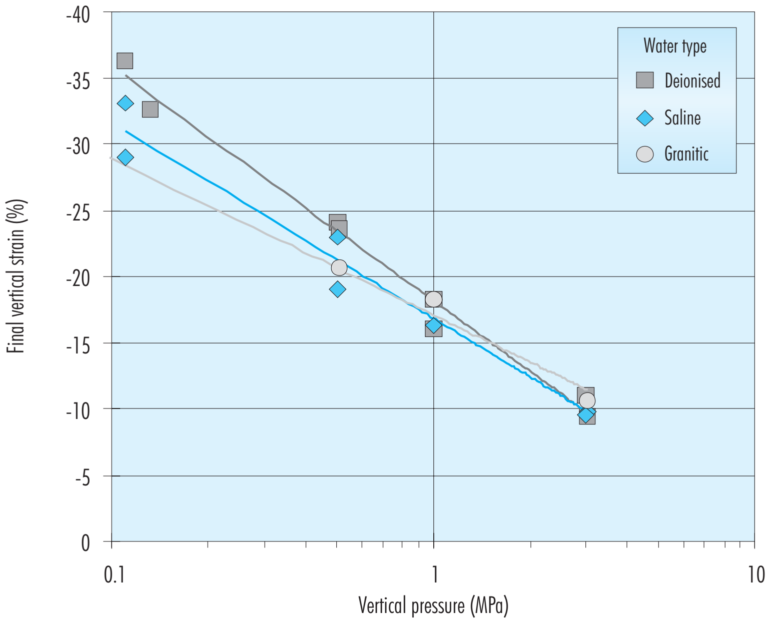

Figure 5.30: Final strain of samples with a dry density of 1.70 g/cm^3 saturated under different vertical pressures with different waters (CIEMAT)

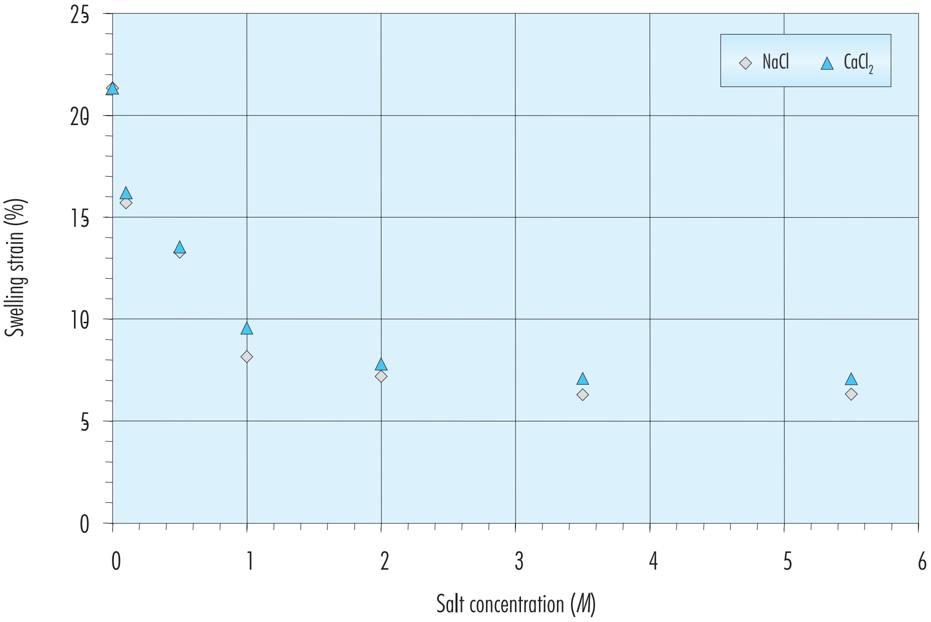

Figure 5.31: Variation of swelling strains due to wetting with different solutions under a vertical stress of 0.5 MPa (initial dry density of 1.65 g/cm^3).

ples show that the samples saturated with solutions containing high concentrations are less deformable and consolidate more rapidly than the samples saturated with low salinity solutions. Using the Terzaghi's 1D consolidation theory it is possible to obtain the consolidation coefficient (c_v), the confined elastic modulus (E_m) and the permeability of the water (k_w); in addition, from the same curves, the secondary consolidation coefficient (C_α) may be measured. The values obtained for these parameters are summarised in Figure 5.32. The increase with salinity of the consolidation coefficient, water permeability and stiffness cannot be attributed only to solute effects; in fact, the different structure (void ratio) of the samples after saturation plays a significant role in the value of these parameters. The influence of salinity on water conductivity has been discussed in Section 5.1.2.1.

Influence of initial water content

The influence of the initial water content of the bentonite on its swelling capacity was tested by means of soaking tests similar to those described above. The granulated bentonite with its hygroscopic water content (about 14 percent) was mixed with deionised water in different proportions in order to obtain different initial water contents: of 17, 20 and 22 percent. This material was compacted to nominal dry densities of 1.50, 1.60 and 1.70 g/cm^3. Once in the oedometer, vertical pressures of 0.1, 0.5, 1.0 and 3.0 MPa were applied to the samples.

The final strains reached by specimens compacted at different initial dry densities upon saturation with deionised water under different vertical pressures are plotted as a function of initial water content in Figure 5.33. From the results obtained, an empirical relation was found between swelling strain (ε,, %), initial dry density (ρ_d, g/cm^3), initial water content (w, %) and vertical pressure (σ, MPa), the prediction capacity being rather good:

$$\epsilon = [(-12.12 \ln \rho_d + 1.89) \ln \sigma + (36.81 \rho_d - 53.59)] \ln w + (38.27 \ln \rho_d - 1.25) \ln \sigma + (-149.05 \rho_d + 211.42) \tag{5.21}$$

5.1.3.5. Hydro-mechanical behaviour observed in suction controlled tests

An extensive programme of suction controlled oedometer tests was performed, the results being taken into account in the numerical modelling performed during the project [50]. Suction controlled oedometer tests were performed at CIEMAT (24 tests) and UPC-DIT (5 tests) on compacted bentonite with hygroscopic water content and at nominal dry densities of 1.70 and 1.65 g/cm^3, respectively. Three types of paths were followed. In the first type, simulating the behaviour of a point near the heater, initial drying was followed by loading, the bentonite finally being saturated. In the second type, simulating a point near the external boundary, an initial path of suction decrease is followed by an increase in load. Figure 5.34 shows the measured volume changes in the tests of these two types. In order to use a logarithmic scale, a constant value of 0.1 MPa was added to all suction values plotted in this Figure. The same convention was used in the rest of the section. In the third case, aimed at reproducing a swelling pressure test, an attempt was made to maintain the height of the sample constant during the suction reduction path by applying increments of vertical load. Suction is applied, with the relative humidity of the air on the sample being controlled by means of sulphuric acid or salt solutions in the high suction range, and by the axis translation technique in the case of suctions ranging from 0 to 14 MPa.

Paths with constant vertical stress or constant suction

Table 5.6 presents the initial conditions and the stress paths of five tests performed at CIEMAT in which a combination of loading paths at constant suction and suction change paths at constant load were applied [16, 49, 56]. The various load or suction changes were applied in stages, as shown in Figure 5.35. All the tests started at an applied vertical stress of 0.1 MPa and at a compaction suction of about 125 MPa. Subsequently, a variation of suction was applied under constant load, except for one specimen in which suction was kept unchanged. Following this the load was increased, also under constant suction, this being followed by wetting until saturation (zero suction) was reached. The maximum vertical stresses under saturated conditions were either 5 MPa or 9 MPa.

Figure 5.36a shows the variation of void ratio during the initial stage of suction modification and subsequent loading. The starting points for the loading stages are very different because of the large dependence of volumetric strain on the suction applied at low loads. On loading, the stiffness of the bentonite (*i.e.* the slope of the void ratio *vs.* the vertical stress line plotted on a semi-logarithmic scale) reduces slightly as the suction applied during loading

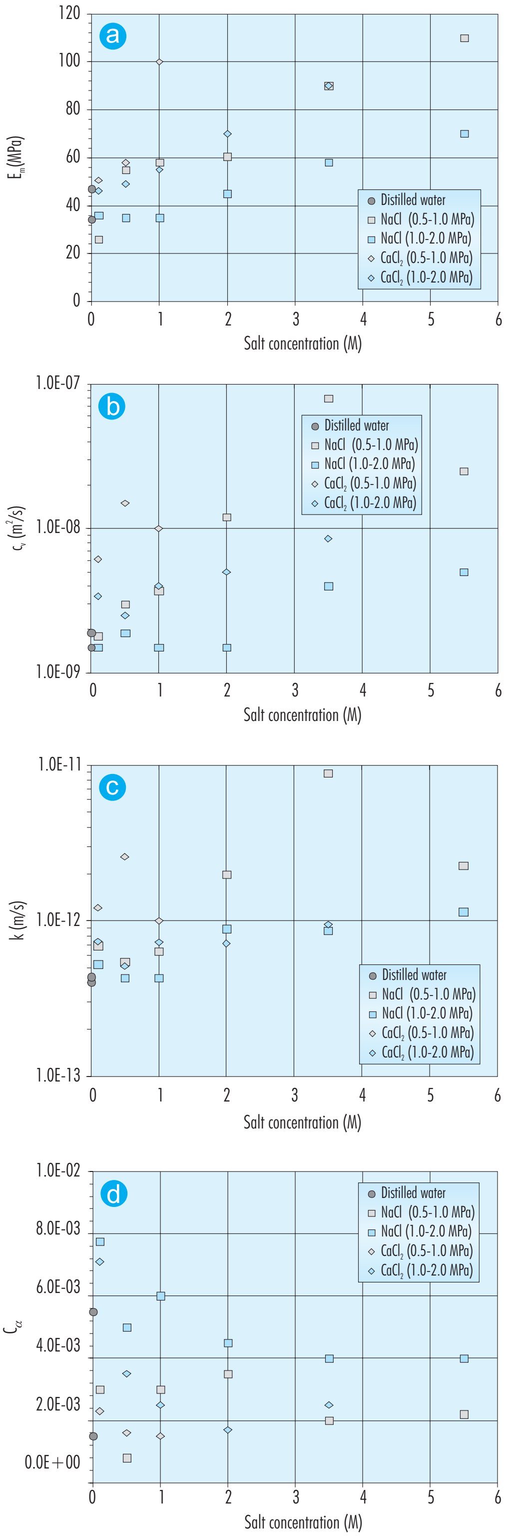

Figure 5.32: Variation with salinity of parameters obtained from oedometric tests on samples saturated with different solutions (initial dry density of 1.65 g/cm^3).

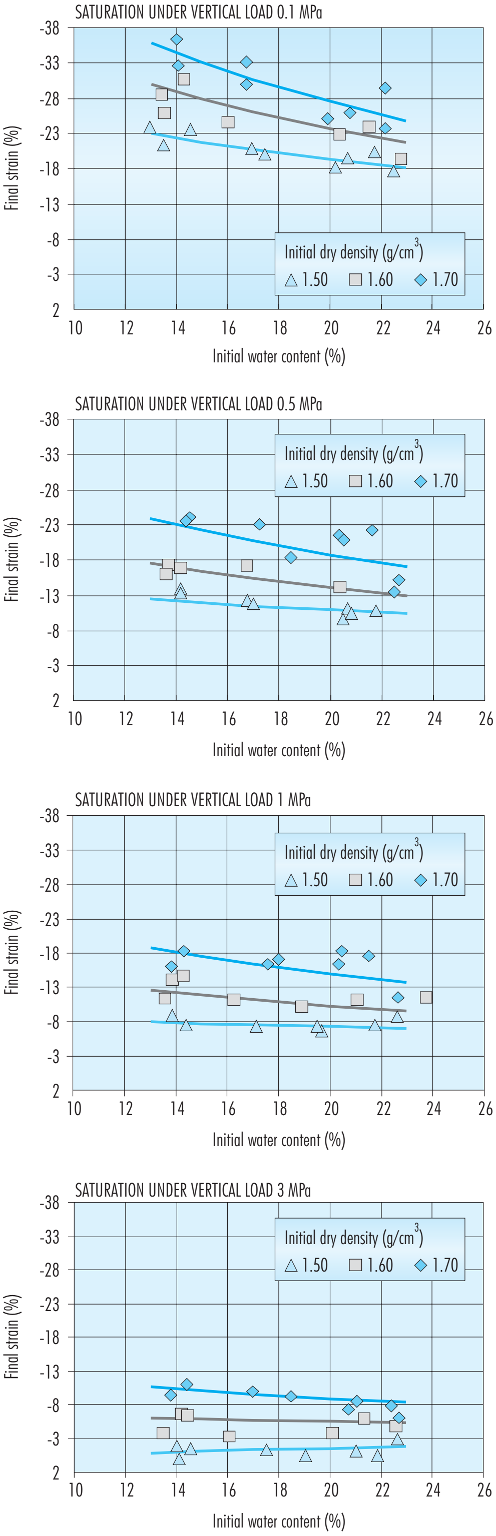

Figure 5.33: Final strains reached in soaking tests under different vertical pressures for specimens compacted at different initial dry density and water content.

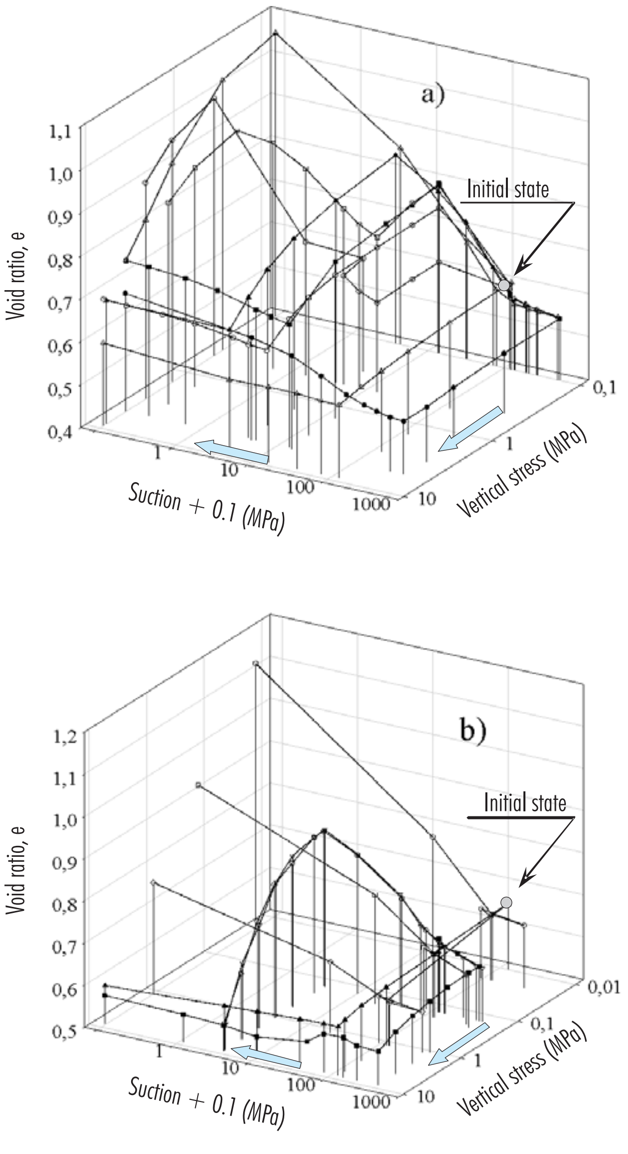

Figure 5.34: Results of suction controlled oedometer tests. a) Initial dry density 1.70 g/cm^3, b) initial dry density 1.65 g/cm^3.

increases. However, the most noticeable effect of suction is the shifting of the point at which there is a change in the slope of these lines, indicated by a vertical arrow in Figure 5.36a. In the framework of elasto-plasticity, this change is interpreted as the crossing of a yield surface, and the load at which it takes place may be considered as being an apparent preconsolidation pressure. Figure 5.36b shows the dependence of this preconsolidation pressure on suction. Large preconsolidation pressure reductions are apparent at low suction values. According to the conceptual model of Gens & Alonso [57], the reduction of the yield point is due to the irreversible macrostructural strains induced by microstructural deformations occurring during the swelling to low suction values. Yielding was not reached in tests S1 and S2, and in the plot of Figure 5.36b it is assumed that the preconsolidation stress corresponds approximately to the vertical stress value reached during static compaction, about 18 MPa.

The variations in void ratio during the subsequent stages, at which the vertical stress is maintained constant and suction is reduced, are presented in Figure 5.37a. Large void ratio changes are observed in the specimens where wetting takes place at 0.1 MPa, whereas in the samples where wetting takes place at 5.1 MPa and, especially, at 9 MPa load, the volume changes are quite small. Figure 5.37b summarises this information in terms of the slope of the swelling line (on a semi-logarithmic plot) with the vertical stress applied during wetting. The effects of applied load are very noticeable.

One of the samples (S5) was subjected to drying to a suction of 500 MPa before being wetted to a suction of 0.1 MPa. The measured void ratio changes are plotted in Figure 5.38. It may be seen that the drying produces very small volumetric strains. However, when wetting is continued towards smaller suction values a large increase in swelling strains is observed, signalling a significant change of behaviour. Comparison of the results of this test with those of test S4, which did not undergo this initial drying/wetting cycle, suggests that such a suction cycle does not have any noticeable effects on subsequent behaviour.

An important feature of behaviour concerns the possible stress path dependency or independency of the material under generalised stress including suction. In non-saturated non-expansive soils, it is often found that behaviour is independent of the stress path if the trajectories include only loading and wetting (suction reduction) stages [58]. However, Gens & Alonso [57] argued that, in expansive soils, there would be irreversible macrostructural rearrangements caused by the swelling of the microstructure on wetting of the samples. This interaction would be higher when applied stresses are low. As a result, such macrostructural changes might result in stress path dependency of volume changes, even in those cases in which only wetting paths are involved. This issue was examined in this experimental programme.

Figure 5.39a shows the void ratio variation for two specimens that share initial and final stress points but that have followed different stress paths. It may be appreciated that the final state is different, so there is a measure of stress path dependency. As observed in other expansive clays, the final void ratio of the sample wetted under low stresses is higher. The disruption of the macrostructure would be more severe in this case because of the larger swelling strains developed during wetting, inducing large macrostructural volume changes that cannot be recovered upon subsequent loading. Figure 5.39b shows a similar plot for a further three specimens with the same initial and final points, where, again, it may be appreciated that the final void ratio

Table 5.6
Stress paths of the tests in which a combination of loading paths at constant suction and suction change paths at constant load were applied. Tests performed at CIEMAT [16, 49]

Test	Initial conditions		Path σ_v (MPa), s (MPa)									
	ρ_d (g/cm^3)	w (%)	I		II		III		IV		V	
			σ_v	s	σ_v	s	σ_v	s	σ_v	s	σ_v	s
S1	1.72	13.0	0.1	138	0.1	550	5.1	460	5.1	0	0.1	0
S2	1.68	13.7	0.1	126	-	-	9.1	127	9.1	0	0.1	0
S3	1.69	14.2	0.1	121	0.1	14	9.0	14	9.0	0	0.1	0
S4	1.71	12.9	0.1	119	0.1	3.7	8.4	4.1	8.4	0	0.1	0
S5	1.72	13.2	0.1	138	0.1	520	0.1	0	5.0	0	0.01	0

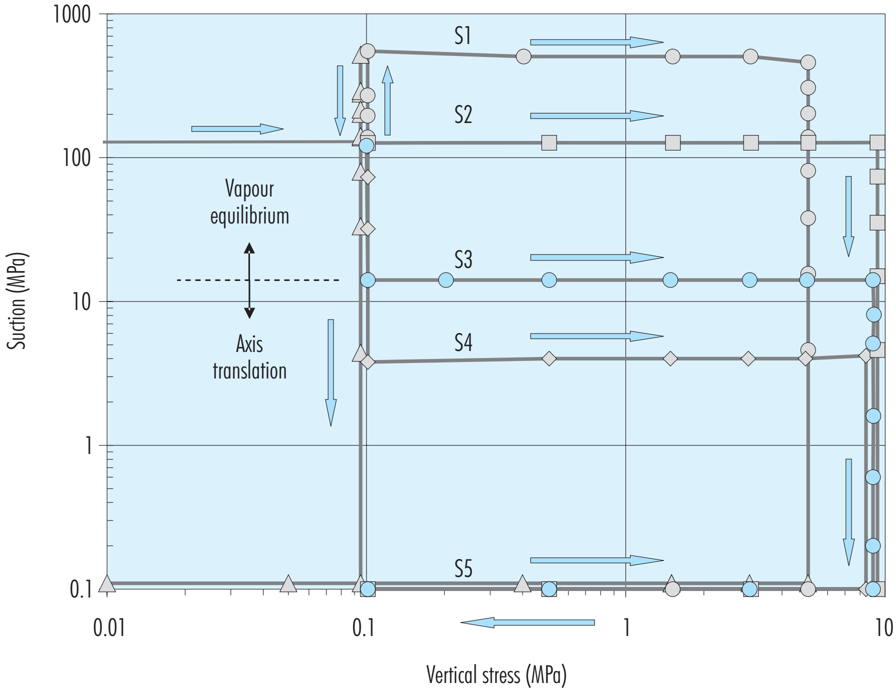

Figure 5.35: Generalised stress paths followed by tests S1 to S5.

values do not coincide. As before, the sample that was wetted at the lower applied vertical stress (4 MPa) reaches the highest final void ratio.

Constant volume paths

The main features of the swelling pressure tests performed in the UPC-DIT laboratory are presented in Table 5.7 [59, 56]. Initially a suction change is applied to three of the samples in order to achieve a range of initial conditions for the next testing stage. During the swelling pressure phase a condition of no volume change is prescribed and suction is reduced in stages under controlled conditions. In this way it is possible to follow the stress path, in terms of suction *vs*. vertical stress throughout the tests, as shown in Figure 5.40.

Three zones may be distinguished (Figure 5.40). The first corresponds to the stage of high suction and low applied loads. In this region the vertical stress remains below the preconsolidation stress (in elasto-plastic terms, the stress state has not reached the yield locus) and the stress path is defined by the increase of load required to compensate the small swelling strains due to suction reduction.

Once the preconsolidation pressure (yield locus) is reached, the second zone is entered and a drastic change of slope ensues. If the load is sufficiently high, a collapsing of the macrostructure occurs and the value of vertical stress tends to reduce to compensate for the compressive strains associated with this collapse. Naturally, the microstructural swelling strains also contribute to the compensation of collapse deformation but at this stage they may not be large enough to offset the reduction of vertical stress.

The points indicating the preconsolidation stress identified in the suction reduction tests under constant stress have been added to Figure 5.40 for reference. In fact, a close coincidence of yield points from the two types of tests should not be expected because of the different stress paths followed, which lead to different magnitudes of irreversible strains and, therefore, to somewhat different yield surfaces. Generally,

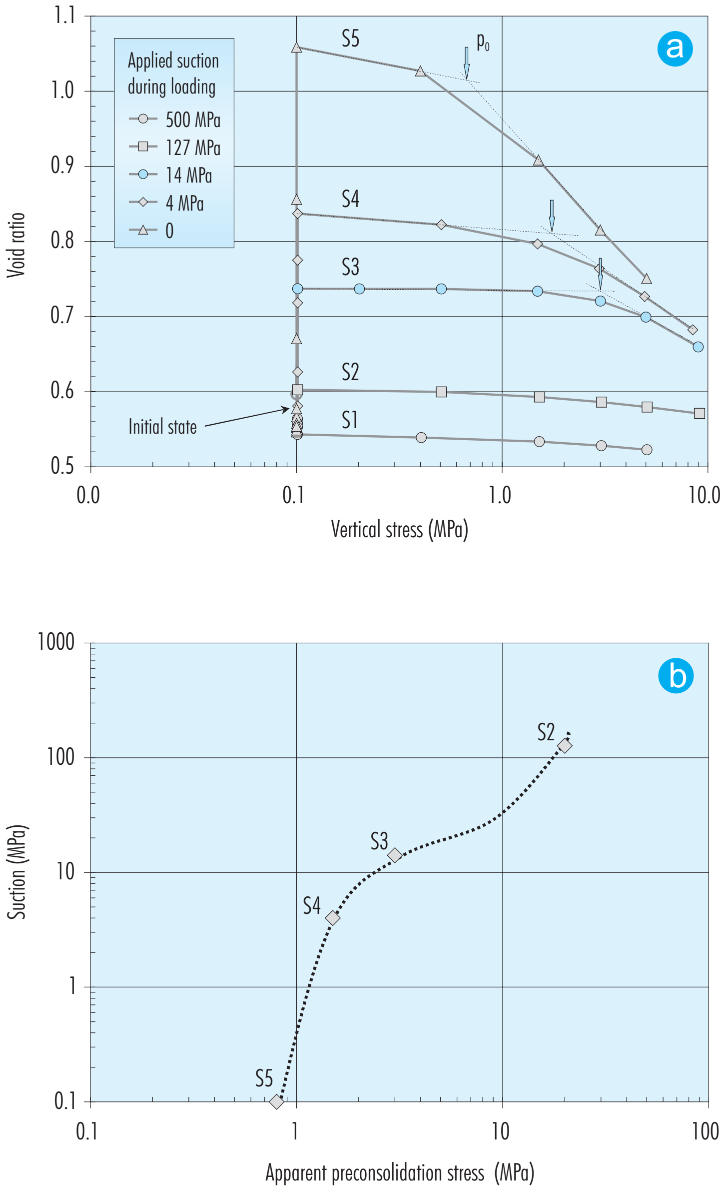

Figure 5.36: a) Variation of void ratio during the initial stage of suction variation and subsequent loading for tests S1 to S5. b) Relationship between the apparent preconsolidation stress and applied suction identified in the loading stages of tests S3, S4 and S5. The preconsolidation stresses of samples S1 and S2 are assumed to be approximately equal to the static compaction stress.

in the constant load tests, the larger swelling strains should lead to smaller sizes of yield loci.

Finally, zone III corresponds to the region of low suctions where microstructural swelling strains exhibit their largest magnitude. Now microstructural strains overcome any possible collapse strains and the vertical stress must rise again to compensate for the large swelling strains. It is interesting to note that even the rather complex behaviour displayed by the compacted bentonite during the swelling pressure tests may be readily explained in the context of a

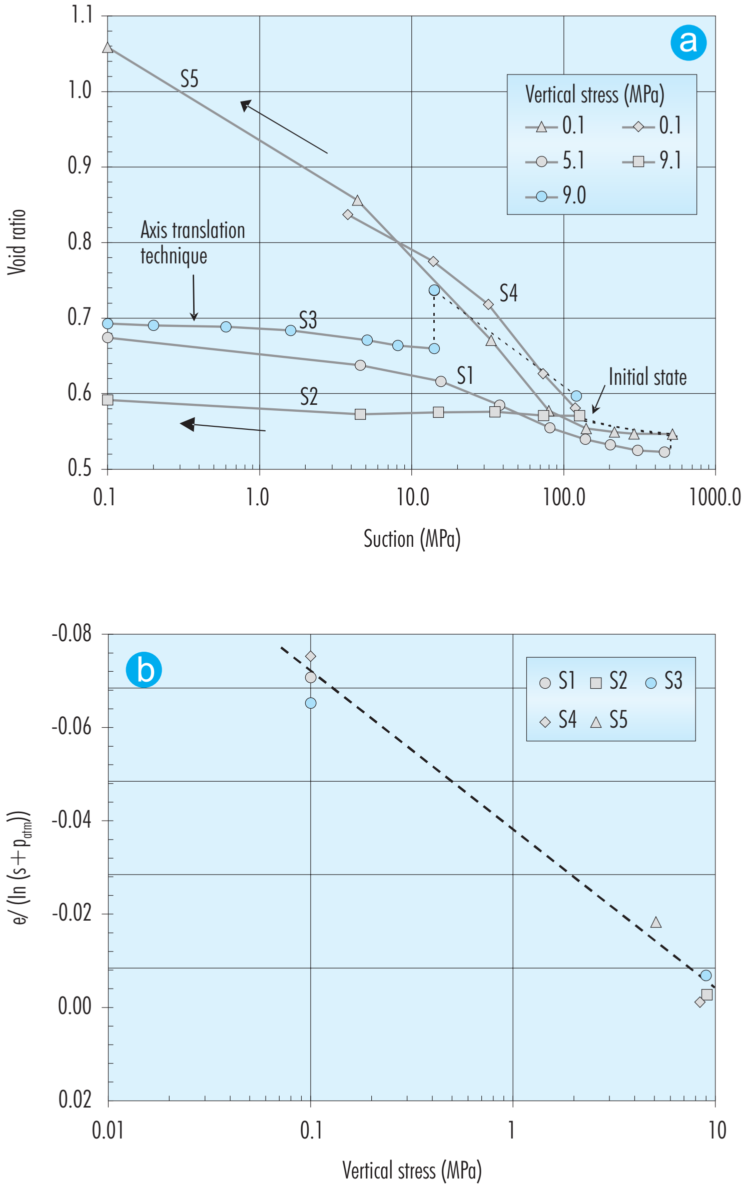

Figure 5.37: a) Variation in void ratio during the stages at which vertical stress is maintained constant and suction reduced in tests S1 to S5. b) Influence of applied vertical stress on the slope of the swelling line measured on wetting.

conceptual framework that considers the interaction between microstructure and macrostructure.

The values of swelling pressure obtained in suction-controlled equipments agree with those obtained in the conventional tests described in Section 5.1.3.3.

5.1.3.6. Effect of temperature on hydro-mechanical behaviour

Temperature changes affect the mechanical response of the material, which has important implications for the design of the repository. The experimental information on the effect of temperature on

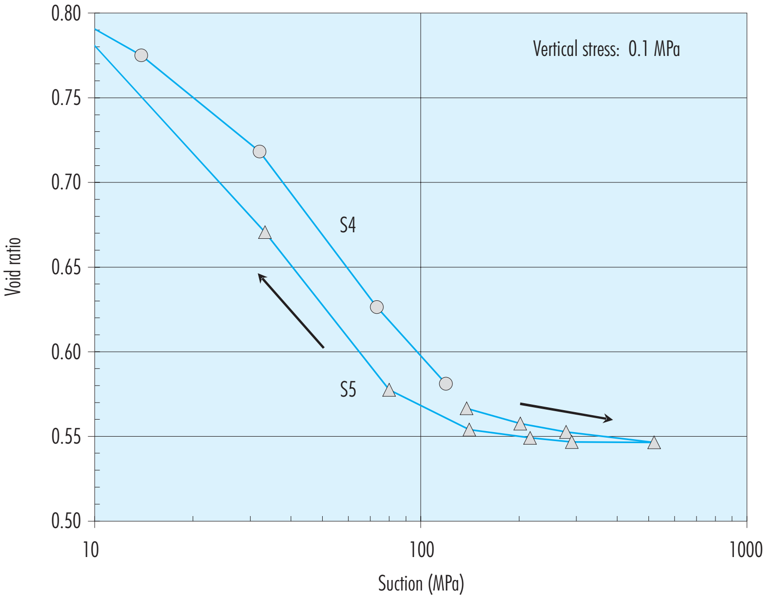

Figure 5.38: Variation of void ratio with suction of test S5 during an initial drying/wetting cycle and subsequent wetting. The results of test S4 are included for comparison.

the behaviour of expansive materials is still scarce, and for this reason this issue was addressed during the last phase of FEBEX [54, 55, 15, 60].

Swelling capacity

The influence of temperature on the swelling capacity of clay was checked by tests of swelling under vertical load. These tests were performed by CIEMAT using an oedometer whose cell is placed in a thermostatic bath with controlled temperature. The samples had an initial water content of 14 percent and a dry density of 1.60 g/cm^3. After reaching stabilisation at the target temperature, vertical pressures of 0.1, 0.5, 1.5 and 3.0 MPa were applied to the samples. Immediately afterwards, the samples

Table 5.7
Main features of the swelling pressure tests performed at the UPC laboratory [59]

Test	Initial conditions		Path before swelling pressure test σ_v (MPa), s (MPa)				Dry density before swelling pressure test
			I		II		
	ρ_d (g/cm^3)	w (%)	σ_v	s	σ_v	s	ρ_d (g/cm^3)
SP1	1.62	14.6	0.11	128	0.11	424	1.65
SP2	1.63	13.2	0.15	146			1.63
SP3	1.62	14.6	0.16	128	0.16	70	1.57
SP4	1.63	14.2	0.15	128	0.15	39	1.50

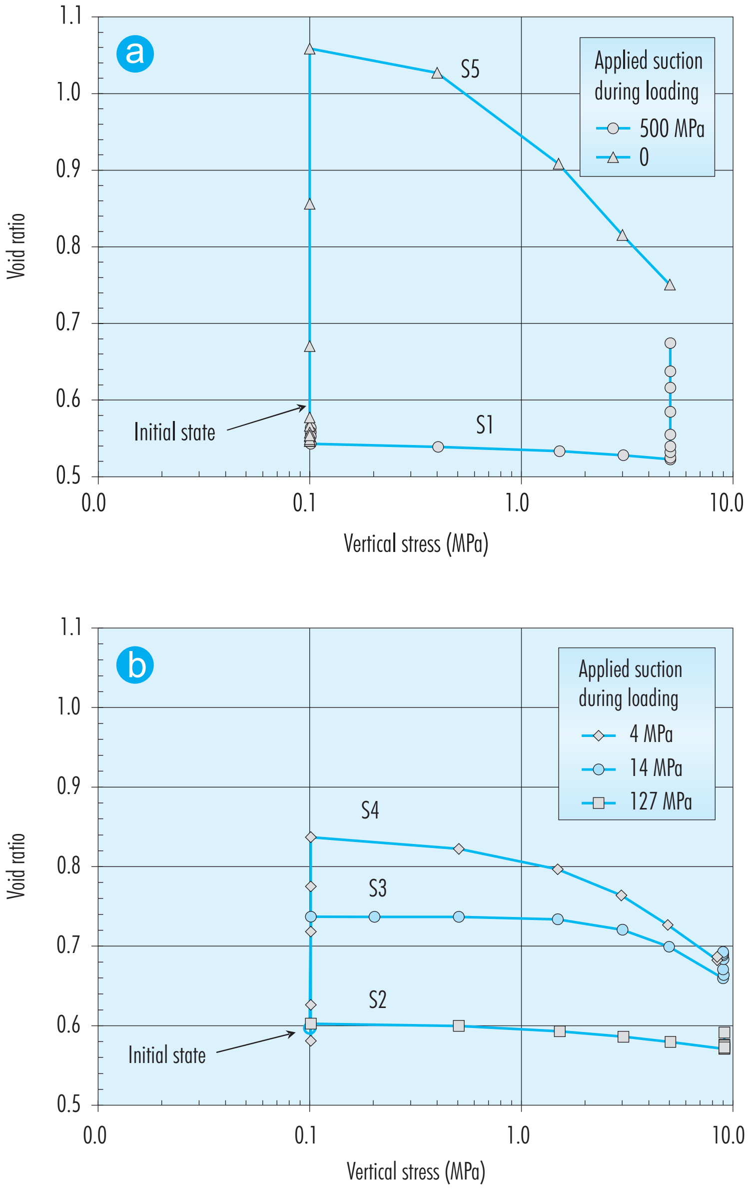

Figure 5.39: Variation of void ratio observed in tests with the same initial and final stress states. a) Tests S1 and S5. b) Tests S2, S3 and S4.

were soaked with deionised water at atmospheric pressure from the bottom porous plate. The swelling strain experienced by the specimens on saturation was recorded as a function of time to stabilisation.

The final strains reached are plotted as a function of the temperature and vertical pressure in Figure 5.41. The strain percentage is calculated as the increase in height with respect to the initial height of the sample, the negative values indicating swelling strains. As shown in the Figure, the swelling capacity decreases with temperature and linear fittings may be drawn between swelling strain and pressure. Although the fittings come from tests performed at

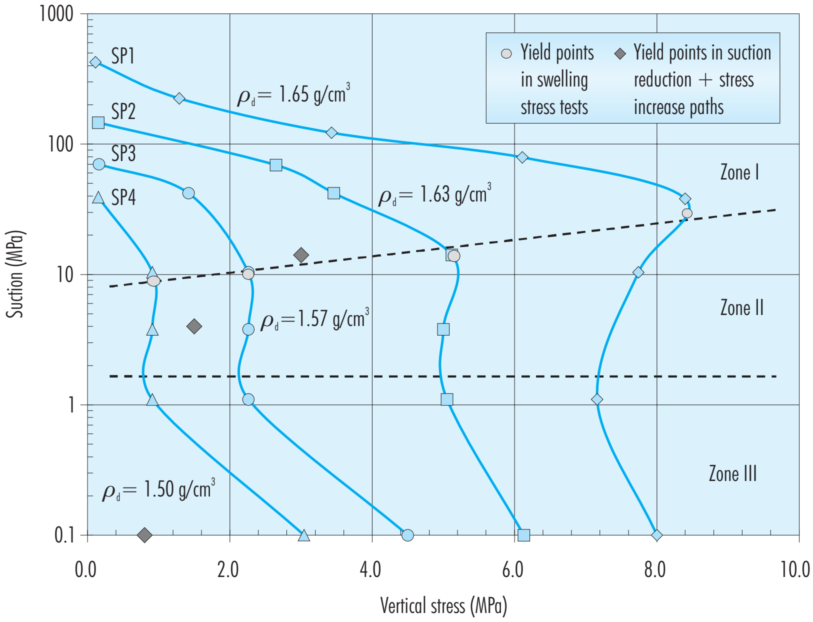

Figure 5.40: Generalised stress paths observed in the swelling pressure tests.

temperatures ranging from 30 to 80°C, the extrapolation of lines towards higher temperatures would appear to indicate that the swelling capacity would stand for temperatures of around 100°C.

Swelling pressure

The determination of the swelling pressure as a function of temperature was performed by CIEMAT in a new high-pressure oedometer (Figure 5.42). The granulated clay with its hygroscopic water content was compacted uniaxially and statically at room temperature, to nominal dry densities of 1.60 and 1.50 g/cm^3. The oedometer allows for the saturation of the specimen at constant volume and for the measurement of swelling pressure, water intake and axial strain.

The swelling pressure results are plotted in Figure 5.43, where the dispersion of data may be attributed mainly to the variations in dry density (whose average value was in fact 1.58 g/cm^3). The error bars shown in the figure were obtained from values measured in tests performed at laboratory temperature (Section 5.1.3.3). A decrease in swelling pressure, as a function of temperature, is observed. This would be in accordance with the results obtained in soaking under load tests, which predict a decrease in swelling capacity with temperature. However, the extrapolation of the logarithmic correlation towards higher temperatures would indicate that swelling pressures higher than 1 MPa would be developed even for temperatures of 100°C.

Oedometric behaviour under suction control

CIEMAT performed suction and temperature controlled tests in oedometers in which suction is controlled by means of sulphuric acid solutions. The equipment experienced recurring breakdowns: some of the results of the tests performed at high temperature must be considered preliminary. On the other hand, the possible effect of sulphuric vapour on the behaviour of the bentonite is unknown.

The initial dry density of the specimens was 1.70 g/cm^3 (except for test EDSC_1, compacted at 1.60 g/cm^3). Once in the oedometer cell, the samples were initially heated under a suction of 130 MPa (corresponding to the relative humidity of the laboratory)

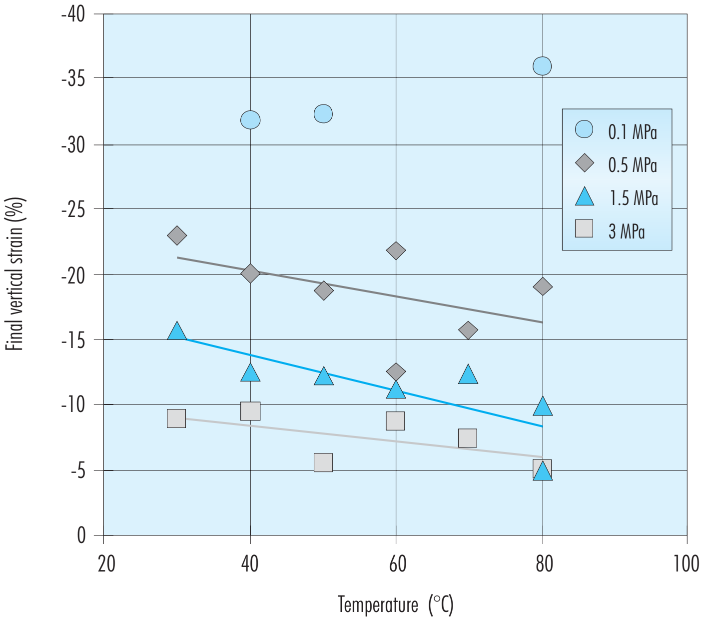

Figure 5.41: Final strain of samples compacted to a dry density of 1.60 g/cm³ saturated with deionised water under different vertical pressures and temperatures.

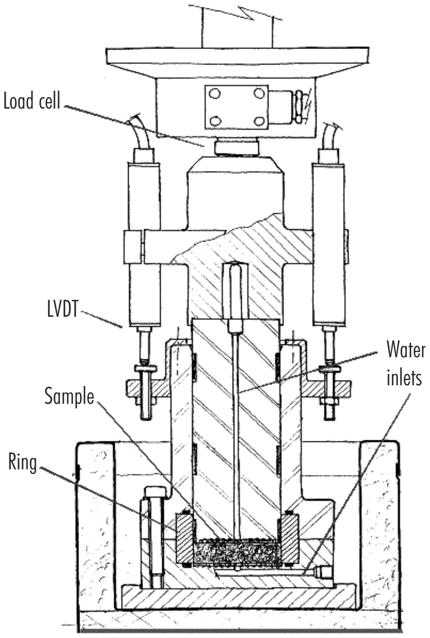

Figure 5.42: Schematic layout of the oedometric cell inside the thermostatic bath (CIEMAT).

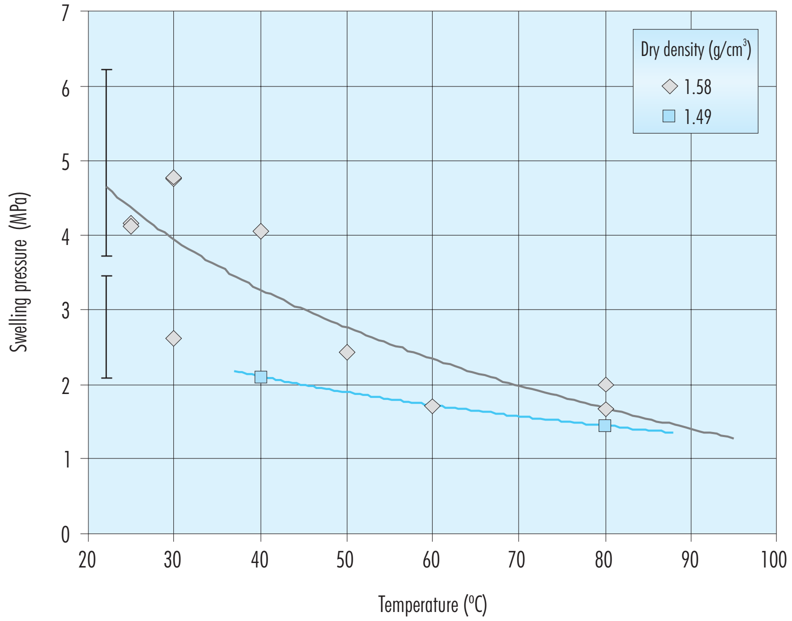

Figure 5.43: Swelling pressure as a function of temperature for saturated FEBEX clay compacted to different nominal dry densities (the error bars correspond to samples of the same dry density tested at laboratory temperature).

and a vertical pressure of 0.1 MPa. Afterwards, the two different stress paths shown in Figure 5.44 were followed.

Path E5 starts by stabilising the sample at the suction corresponding to its equilibrium water content (130 MPa) under a minor load (0.1 MPa). The void ratio of the tests performed at 50°C increases during this first step, which does not happen in the tests performed at 20°C. There is no clear explanation for this observation, which might be due to the thermal expansion of the soil or to an experimental artefact. This initial difference determines the subsequent behaviour of the samples during the tests, which is shown in Figure 5.45. Although the stiffness of the soil, when loaded under hygroscopic conditions, becomes evident for all the temperatures, the compressibility during loading of samples tested at 50°C is higher than for samples tested at 20°C. This may be simply a result of the different void ratio at the beginning of compression. In saturated materials it has been observed that temperature increases the compressibility of bentonite. As in saturated soils, a reduction in the size of the elastic domain with temperature may be observed [61], the apparent preconsolidation stress being lower when the temperature is 50ºC than when it is 20ºC.

The behaviour of the samples during wetting under a high vertical load was diverse and apparently not determined by temperature. Overall the initial void ratios are recovered, although two tests (EDS1_10 and EDSC_8) experienced minor collapse at the beginning of wetting.

The results of the tests performed following path E6 are plotted in Figure 5.46. The increase in void ratio during the initial wetting under a low vertical load is important in all tests. No different behaviour may be observed as a consequence of temperature. In the subsequent loading, the initial void ratio is not recovered in any test, due to the irreversible macrostructural strains induced by the microstructural deformations that occurred during the previous swelling to low suction values. The comparison of the curves obtained during loading at different temperatures and constant suction (tests EDS3_11 at 20°C and EDSC_3 at 60°C) suggests once more that temperature increases the compressibility of bentonite and that some reduction in the size of the elastic domain with temperature takes place.

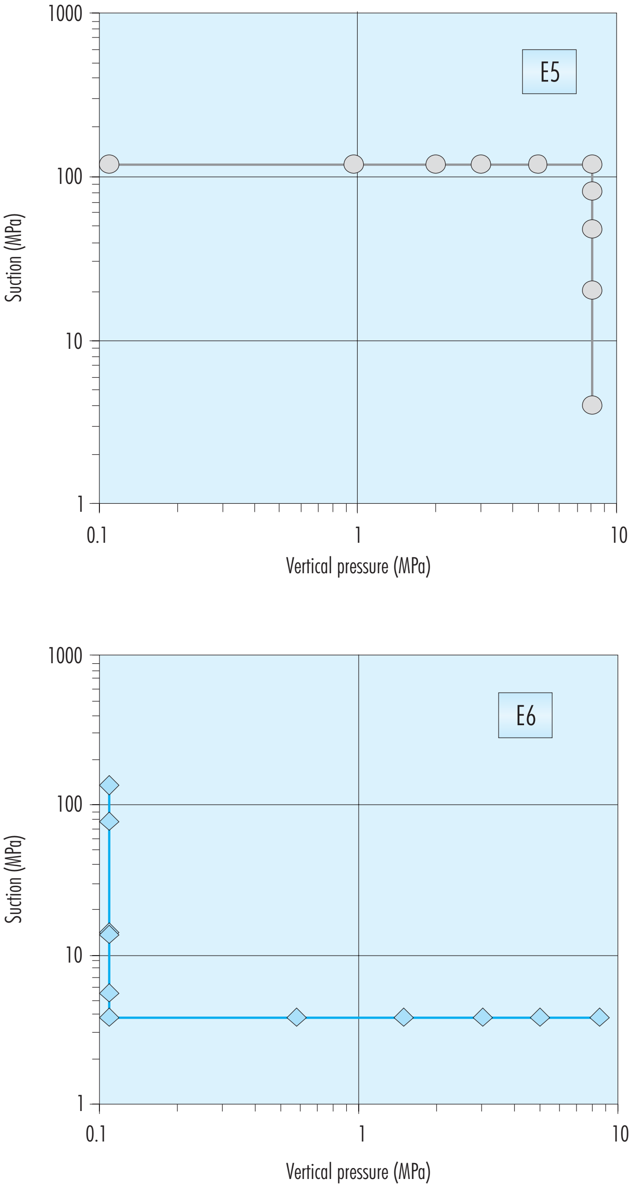

Figure 5.44: Stress paths for the suction and temperature controlled oedometric tests.

The two paths tested have approximately the same initial and final states as regards suction and vertical stresses. In particular, for test EDS1_13 the path followed consisted of loading up to 8 MPa under a constant suction of 130 MPa and then wetting under this high vertical load (path E5). For test EDS3_11, the path followed (E6) consisted of wetting under a constant vertical load of 0.1 MPa, followed by loading to 9 MPa under a constant suction of 3 MPa. In Figure 5.47 the final void ratio of each step of the two tests is plotted against the corresponding suction or vertical load. As both variables have the same units, they are represented on the same axis (wetting paths are indicated by bold sym-

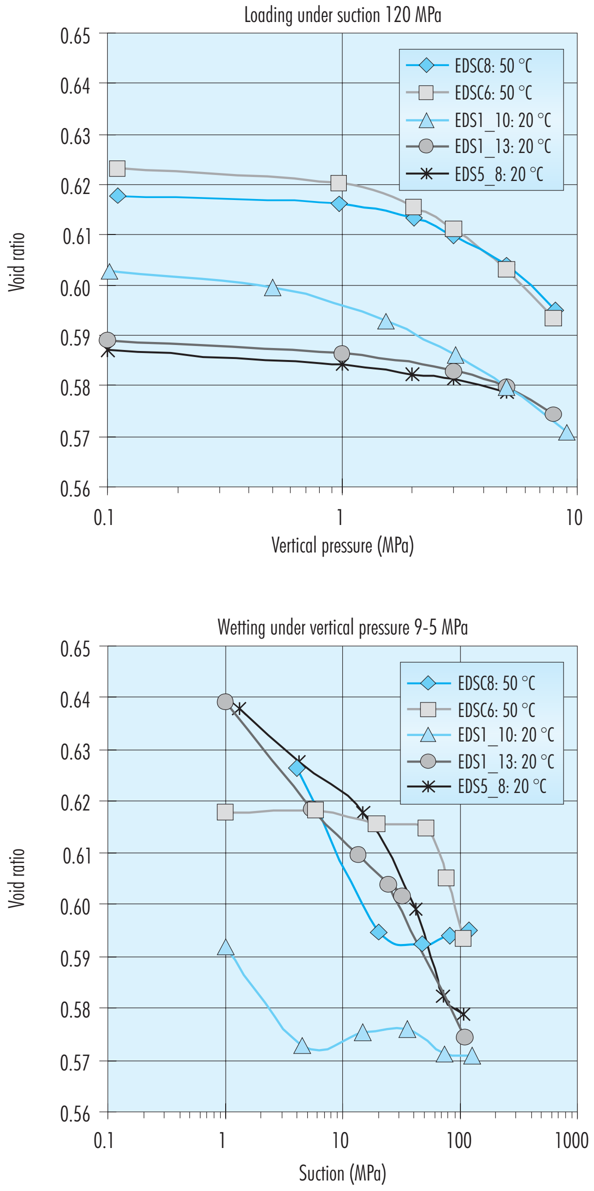

Figure 5.45: Evolution of void ratio in the different steps of the loading and wetting paths performed in suction controlled oedometers at different temperatures following path E5 (initial nominal dry density 1.70 g/cm^3).

bols). It becomes clear that when wetting takes place under a low vertical load (test EDS3_13), a large increase in void ratio occurs and the external load subsequently applied is unable to counteract this swelling. However, if swelling during saturation is prevented by previous loading (test EDS1_11), the final volume change is smaller. These tests are an example of the irreversible macroscopic deformation induced by micro-structural swelling, the magnitude of which (plastic deformation) is stress path-dependent [57].

The same remarks might be made when comparing the results of tests EDSC_8 (path E5) and EDSC_3 (path E6), plotted in Figure 5.48. These tests were performed at temperatures of 50 and 60°C, re-

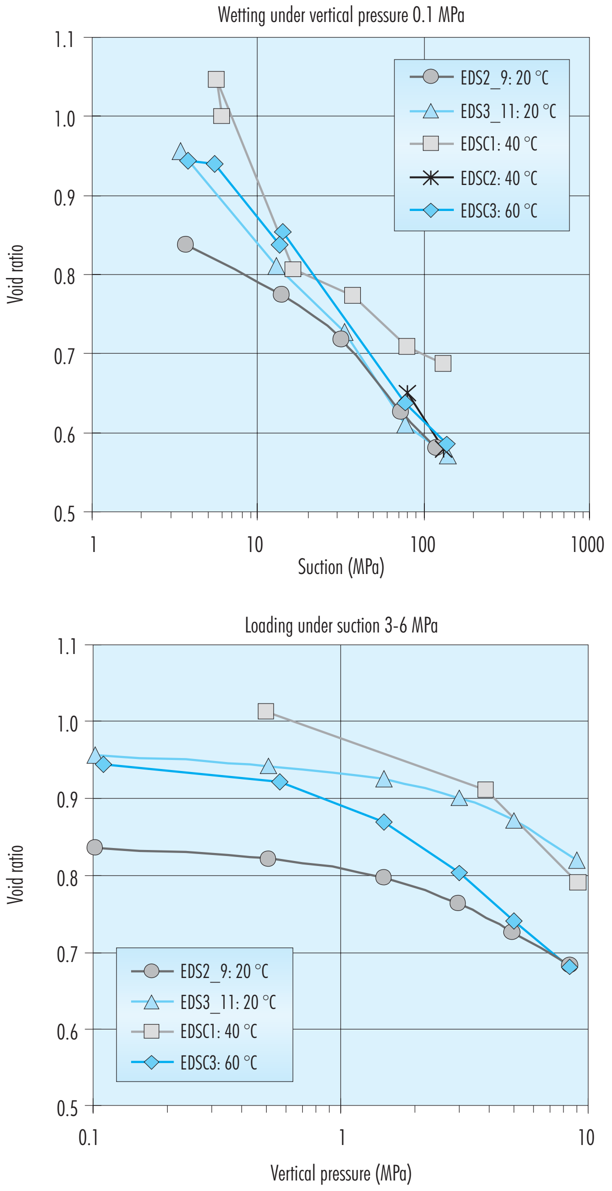

Figure 5.46: Evolution of void ratio in the different steps of the wetting and loading paths performed in suction controlled oedometers at different temperatures following path E6 (initial nominal dry density 1.70 g/cm^3, except for EDSC1: 1.60 g/cm^3).

spectively. The behaviour of bentonite at high temperature is similar to that observed at 20°C (Figure 5.47), which would suggest that the repercussion of the stress path on bentonite deformation is higher than that of temperature. The only significant difference between the tests performed at laboratory temperature and those performed at high temperature, is the higher compressibility of quasi-saturated bentonite upon loading at high temperature (test EDSC_3 with respect to test EDS3_11), which has been commented on above.

On the other hand, UPC-DIT performed suction and temperature controlled tests on two bentonite samples compacted at a dry density of 1.7 g/cm^3. The

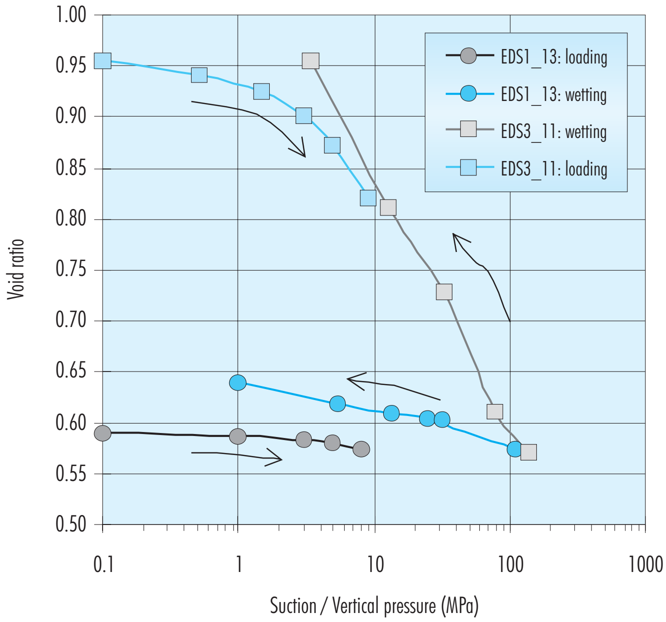

Figure 5.47: Comparison of void ratios at the end of each step of paths E5 (test EDS1_13) and E6 (test EDS3_11) performed in oedometers with control of suction at 20° C.

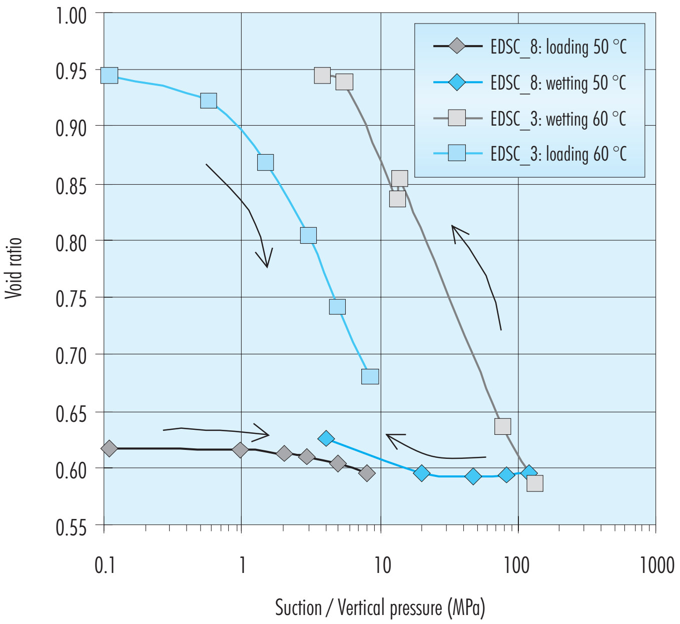

Figure 5.48: Comparison of void ratios at the end of each step of paths E5 (test EDSC_8, 50° C) and E6 (test EDSC_3, 60° C) performed in oedometers with control of suction at high temperature.

tests were performed in controlled-suction oedometer cells specifically designed for accurate temperature control (Figure 5.49). Soil suction was applied by prescribing a value of the relative humidity of the atmosphere in contact with the sample by the use of solutions of sulphuric acid at various concentrations or of saturated solutions of various salts. Figure 5.50 shows the generalised stress paths followed in the experimental programme in a three-dimensional stress-suction-temperature space.

The vertical strains measured during the different stages of the two tests are shown in Figure 5.51. From the evolution of vertical strains and temperature during the heating stage at constant water content (stage B-B', 22 to 70 °C), and if the volume changes due to suction variation are not taken into account, a value of the linear coefficient of thermal expansion (α) of $4 \cdot 10^{-4}$ is obtained. This value is similar to those obtained in the unconfined tests performed during the first phase of the FEBEX project (Section 5.1.1.3). During the equalisation of suction at 110 MPa, negligible vertical strains were measured in the sample tested at 22°C. However in the sample tested at 70°C, an important shrinkage was observed (vertical strain of 3.5%). This shrinkage compensates the initial thermal swelling and the resulting dry density is higher than the dry density of the sample tested at 22°C.

Afterwards, it may be observed than the compressibility of the bentonite is similar at both temperatures (stages B'-C). However it must be pointed out that the sample loaded at 70°C has an initial dry density of 1.72 g/cm^3, whereas the sample tested at 22°C has a dry density of 1.70 g/cm^3. Therefore, the increase of compressibility due to temperature that was observed in other tests is compensated by the reduction due to the increase in dry density.

During the subsequent suction reduction (stages C-E), swelling strains were higher in the sample wetted at low temperature. This behaviour agrees with the results obtained in the swelling capacity tests.

The sample that was loaded and saturated at 22°C, was finally heated up to 78 °C (stage E-F). In this case, due to the higher vertical stress applied (8.6 MPa), the thermal expansion is smaller than that observed under a vertical stress of 0.1 MPa. In the present case, the linear thermal expansion coefficient is only about $0.4 \cdot 10^{-4}$.

5.1.4. Thermo-hydraulic tests in cells

The thermo-hydraulic (TH) tests in cells consist of subjecting the bentonite simultaneously to heating and/or hydration, in opposite directions, for different periods of time. The back-analysis of infiltration tests allows for the calibration of numerical models and the adjustment of parameters that are difficult to obtain by direct measurement. In the infiltration tests, compacted blocks of clay are introduced in a hermetic cell and saturated through the top, while thermal gradients may be applied. After a pre-fixed time, the cell is disassembled and the water content of the clay is determined at different distances from the hydration front. If the infiltration test is performed with thermal gradients, the tortuosity factor that is involved in vapour flux modelling may also be obtained or validated.

The response of the FEBEX bentonite under the small-scale test conditions is very complex, due to the physical processes and interactions that take place during the simultaneous heating and hydration of clay under conditions of practically constant volume. For this reason, coupled THM analysis becomes a requirement, in order to simulate this problem. The THM formulation proposed by UPC-DIT [62], was adopted as a general framework for analysis, and the finite element code CODE_BRIGHT [63] was used to analyse small-scale tests as a boundary value problem. The simulations aim to reproduce the evolution of the main variables of the tests (water intake and temperature) and also the experimental data arising from the post-mortem study. Regarding these studies, it is important to highlight that most of the constitutive laws and parameters considered in the analyses are the same as those adopted for the Operational Base Case (OBC) model of the 'mock-up' test (Chapter 6). In this sense, the results obtained in this study are model predictions that allow for increased confidence in the constitutive equations and parameters used.

On the other hand, the TH tests make it possible to analyse the properties of the bentonite and its behaviour under conditions similar to those that will be found in a repository, and to clarify what processes and geochemical changes occur. These processes may influence the retention and the thermo-hydro-mechanical properties of the clay barrier.

5.1.4.1. Infiltration tests in Teflon cell

CIEMAT performed isothermal infiltration tests in a cylindrical cell (diameter of 53 mm and height of 101 mm) made out of Teflon [15]. Four small blocks (2.5-cm thick) compacted to dry densities of 1.60 or 1.75 g /cm^3 were placed in the cell. The tests were performed at 20 and 60°C. Figure 5.52 shows the

1) Silicone oil bath and heater; 2) Soil sample; 3) and 4) Coarse porous disc

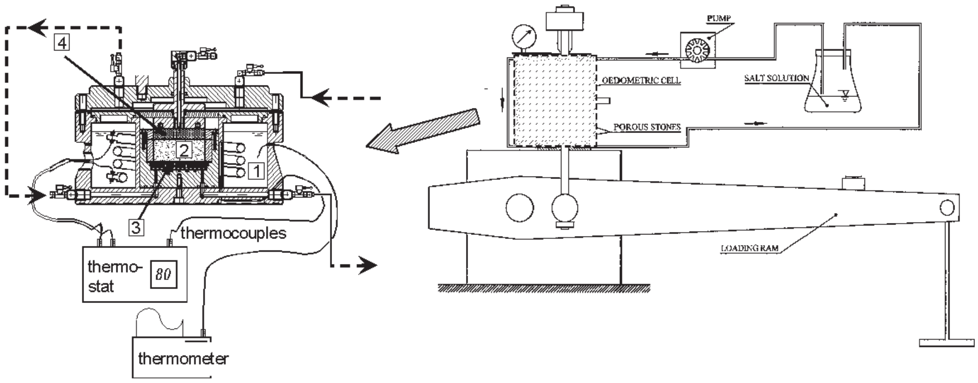

Figure 5.49: Schematic layout of the experimental system with simultaneous control of suction and temperature (UPC-DIT).

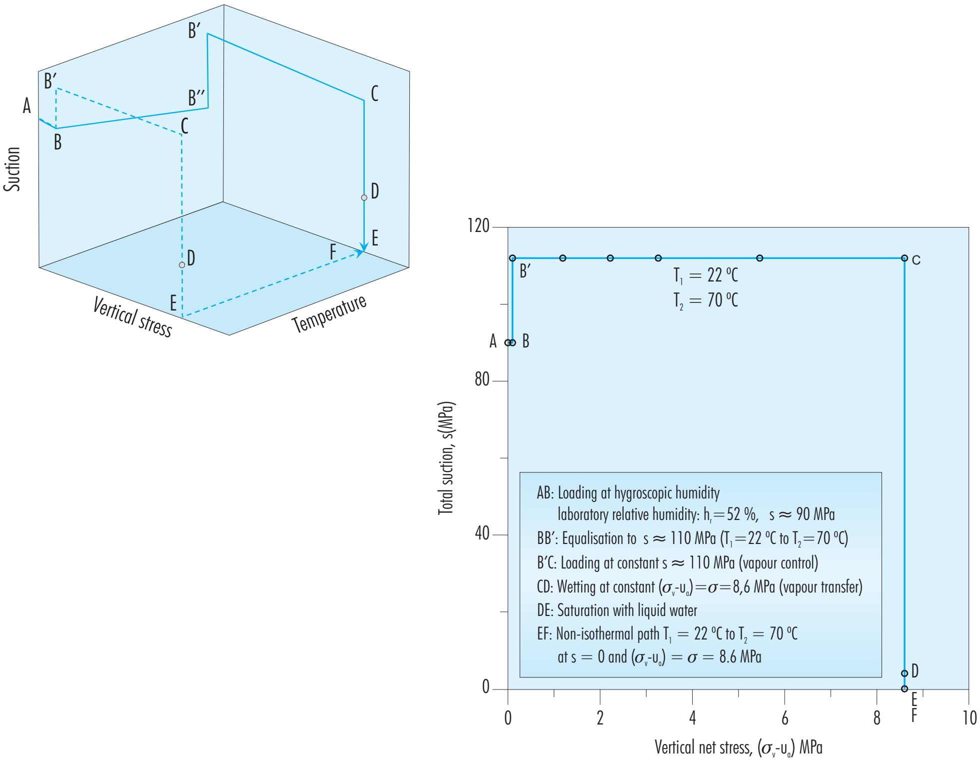

Figure 5.50: Generalised stress paths followed in the testing programme of UPC-DIT.

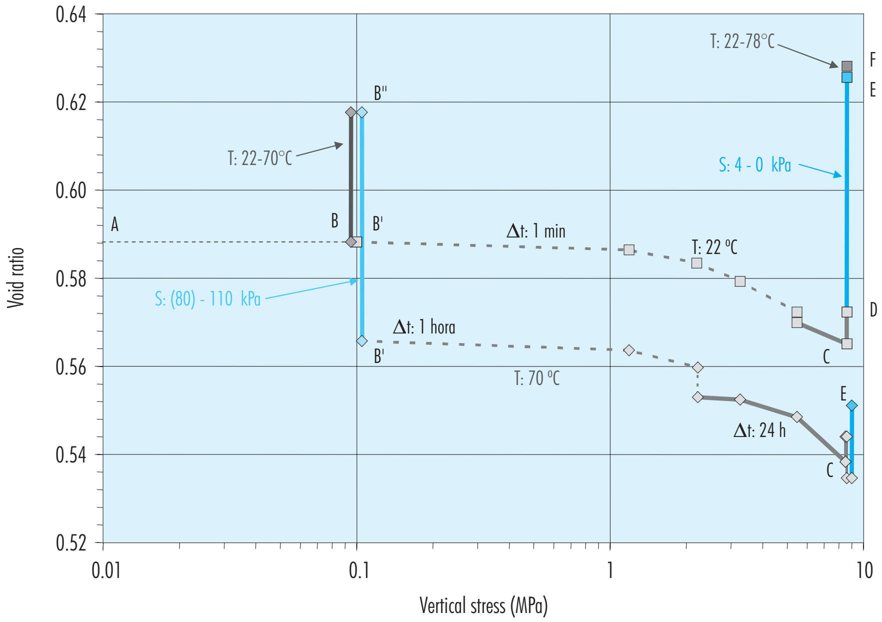

Figure 5.51: Summary of volume change experienced by two samples tested in a suction and temperature controlled oedometer .

evolution of water intake in the tests. At the beginning of the test a rapid infiltration flow was measured, which is associated with the water required to fill the void existing between the small bentonite blocks and the cell walls. During hydration the initial dry density of the bentonite decreased, due to the existence of these voids and to the deformability of the cell. The measurement of profiles of dry density and water content at the end of different tests (Figure 5.53) allowed for the determination by back analysis of hydraulic parameters, such as the exponent *n* in the relative permeability law ($k_r = S_r^{\ n}$) or the value of intrinsic permeability. A value of $n = 4.64$ was obtained from the tests performed at 20°C with an initial dry density of 1.75 g/cm^3.

5.1.4.2. Infiltration tests in triaxial cell

Infiltration tests were carried out at UPC-DIT on bentonite specimens (diameter 38 mm, height 76 mm) compacted with hygroscopic water content at a dry density of 1.65 g/cm^3 and confined in a triaxial cell with a confinement pressure of 0.8 MPa. In order to study the possibility of de-saturation of the rock in contact with the bentonite, a hydraulic gradient was prescribed across a specimen of granite in contact with another of bentonite. During the test no change in water content was detected in the granite, which acted as a porous interface. At the end of the granite specimen a backpressure of 0.6 MPa was applied. Using the parameters derived from the identification process ($n = 3.5$), Figure 5.54 shows that a good agreement between measurements and numerical model predictions is obtained.

5.1.4.3. Tests of prescribed heat flow with constant water content

A testing device was developed by UPC-DIT to obtain the data required for the identification of certain thermo-hydraulic parameters [64]. A controlled heat flux is applied at one end of a cylindrical specimen (38 mm in diameter, 76 mm long) while the other end is maintained at constant temperature. A latex membrane, which allows for deformation and keeps overall water content constant, and a 5.5-cm thick heat insulating deformable dense foam material surrounds the specimen. In order to ensure knowledge of the heat flux crossing the sample, two specimens symmetrically placed with respect to the heater are used in the tests.

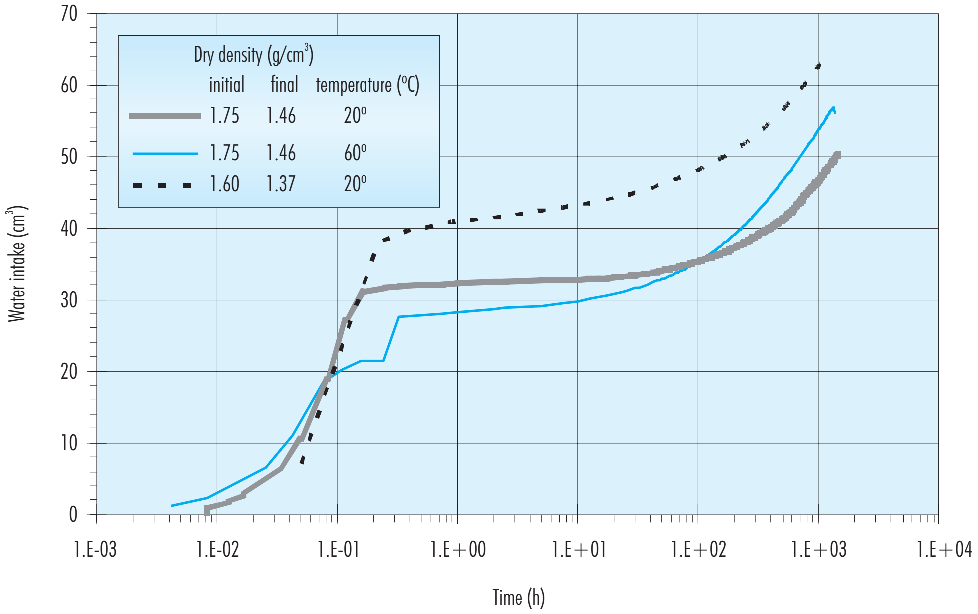

Figure 5.52: Evolution of water intake in the isothermal tests performed in small Teflon cells.

The heater is a copper cylinder (38 mm diameter, 50 mm long) containing five small electrical resistances. A constant power of 2.6 W has been used in the tests, allowing steady temperatures in the range of 70-80°C to be reached at the hotter end of the specimen. At the cold end, a constant temperature of 30°C is maintained by flowing water in a stainless steel head in contact with the soil. Figure 5.55 shows the scheme of the equipment used in the tests.

Axisymmetric analyses performed using CODE-BRIGHT allowed the effect of lateral loss of heat to be evaluated, this having been estimated at 60 percent of total heater power. This indicates the importance of performing a 2D analysis of the experiment.

Three specimens of bentonite compacted at a dry density of 1.68 g/cm^3 and with water contents of 15.3, 16.9 and 17.1 percent were tested. During the tests, the temperatures at both ends of the specimen and at three equidistant internal positions are monitored. At the end of the tests, changes in specimen diameter were measured. Finally, the soil samples were cut in six small cylinders and the water content of each was determined.

A fully coupled thermo-hydraulic model was used to simulate the experiment. The temperatures obtained under steady-state conditions and the water content measured at the end of the test have been considered as input data. In each test, three parameters have been identified: the thermal conductivity of saturated bentonite, λ_{sat}, needed to obtain the unsaturated thermal conductivity ($\lambda=(\lambda_{sat})^{Sr}\,(\lambda_{dry})^{(1-Sr)}$); the tortuosity, τ; and the exponent n for the unsaturated (relative) permeability law ($k_r=S_r^{\,n}$). The thermal conductivity under dry conditions (λ_{dry}) is fixed at 0.47 W/m·K. The parameters obtained during the identification process are similar but not identical in the three tests, as shown in Table 5.8. The values are within the normal range of these parameters. In addition, the identification technique provides a systematic and consistent procedure allowing the parameters that best reproduce the measurements for the selected model to be found. The method also provides insight into the model structure and allows the dependence and coupling between parameters to be detected. In this type of test, analysis of the model

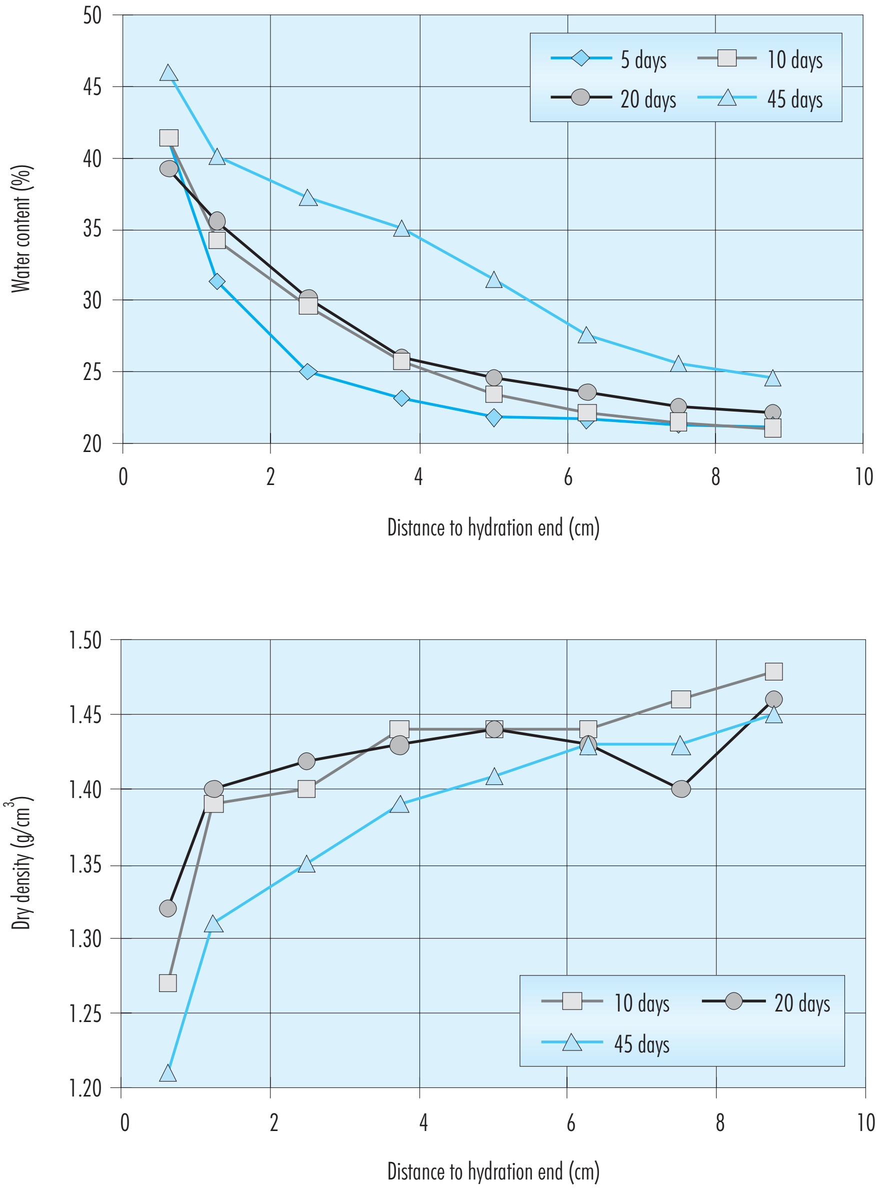

Figure 5.53: Water content and dry density profiles measured at different times in isothermal infiltration tests in Teflon cells (initial dry density 1.6 g/cm^3, temperature 20ºC).

structure shows that the values obtained for the parameter *n* entail a higher degree of uncertainty than the values for the other parameters. This is in accordance with the relative influence of water flow in liquid and vapour phases.

The optimisation procedure showed that there are a few combinations of parameters that give similar results in terms of the objective function. This is reasonable, as measured water content is a global quantity, and it is difficult to distinguish between water transported by liquid flow (controlled by *n*) and by vapour diffusion (controlled by τ).

Figure 5.56 shows the objective function in terms of the tortuosity factor (τ) and the exponent from the

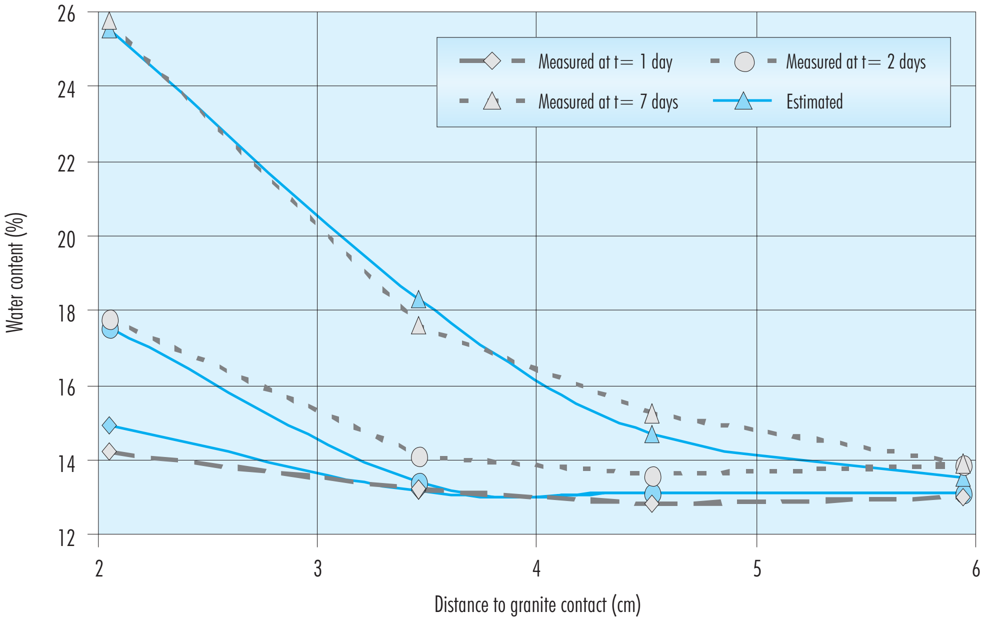

Figure 5.54: Measured and computed final water content after infiltration tests in triaxial cells.

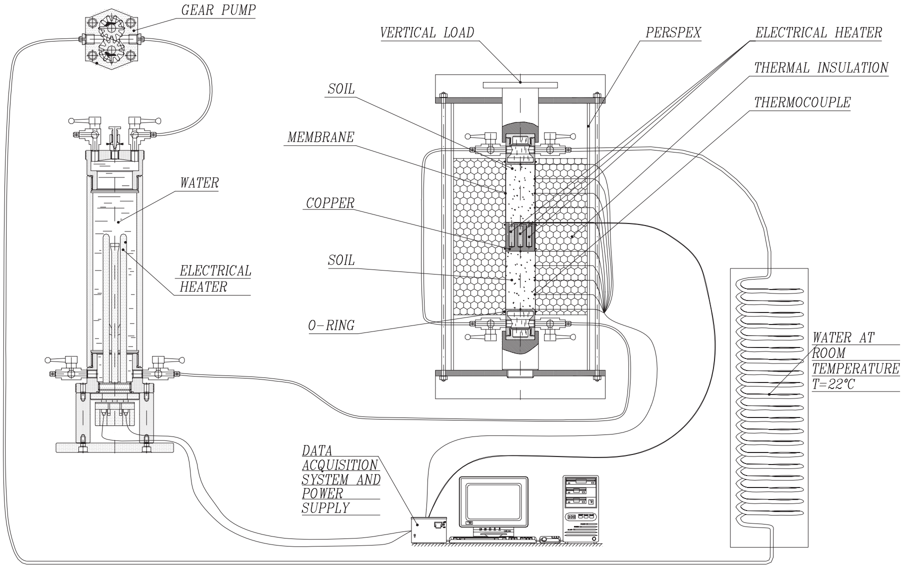

Figure 5.55: Scheme of the experimental device used in the prescribed heat flow tests with constant water content.

Table 5.8
Parameters obtained from different thermal flow tests

Test	Water content	Exponent in relative permeability law, *n*	Tortuosity factor, τ	Saturated thermal conductivity λ_{sat} W/m·K
1	15.5	3.06	0.56	1.19
2	16.9	1.10	0.74	1.31
3	17.1	1.68	0.90	1.18

relative permeability law (*n*), for one of the controlled heat flow tests. In order to give the same importance to the sets of measurements for temperature and water content, a weighting procedure has been used to define the objective function. Contours are isolines of the objective function with different combinations of the parameters. The parameter values obtained by back analysis are located at the minimum of the objective function. The same figure includes points representing the values of the parameters obtained in the other back-analysed tests. In the case of the hydraulic tests described previously, only the exponent *n* is known. In all cases, the representative points are located in the same area of the objective function, with similar values of error. The following set of parameters and laws was selected for a bentonite porosity of 0.4 taking all the tests into account:

$$k_w = 2 \cdot 10^{-21}\ m^2;\ \ k_r = S_r^3;\ \tau = 0.8;$$
$$\lambda(W/m{\cdot}K) = 0.47^{1-Sr}\ 1.15^{Sr}$$

This set of parameters (together with the rest of parameters used in numerical modelling of the "mock-up" and "in situ" tests) was used to solve the direct problem and to simulate the water infiltration and heat flow tests. The agreement between the measurements and the model predictions is satisfactory.

5.1.4.4. Tests in ceramic cell

A new device was developed by UPC-DIT (Figure 5.57) in order to run infiltration tests. In order to avoid the volume changes due to the deformability of Teflon cells and to reduce the lateral thermal losses of metallic cells, the sample was confined laterally by a cylinder with a ceramic wall. It was possible to measure the temperatures and swelling stresses (vertical and radial) developed during the infiltration process at several positions of the cell by means of thermocouples, a load cell and three total pressure sensors, respectively.

In the preliminary test performed, distilled water was injected from the top of the cell under a hydraulic pressure of 0.1 MPa. The initial dry density of the specimen (70 mm in diameter and 140 mm in height) was 1.62 g/cm^3, and the initial water content was 13.5 percent. The test was carried out under isothermal conditions at ambient temperature (22°C).

Figure 5.58 shows some results of the first preliminary test performed with this cell. The ceramic cylinder, where the soil sample was located during the test, was broken after approximately seven days from the beginning of the infiltration process, because the ceramic did not resist the swelling pressures of the bentonite.

Figure 5.58a shows that the swelling vertical stress increased sharply; the stress increases more quickly than in other cases ("mock-up" and "in situ" tests). This was due to the inexistence of gaps between bentonite blocks or between the bentonite and the cell walls.

The test was modelled using the same numerical approach used to model the operational phase of the "in situ" and "mock-up" tests. Regarding the mechanical problem, the constitutive model known as *BBM* (Barcelona Basic Model) was adopted. The model parameters were identified in the preoperational stage of the FEBEX project [47]. Vertical and lateral mechanical confinement was imposed up to failure of the ceramic wall; following this, the radial stresses were reduced in order to simulate the loss of lateral confinement. Table 5.9 and Table 5.10 show the model parameters used in the analysis.

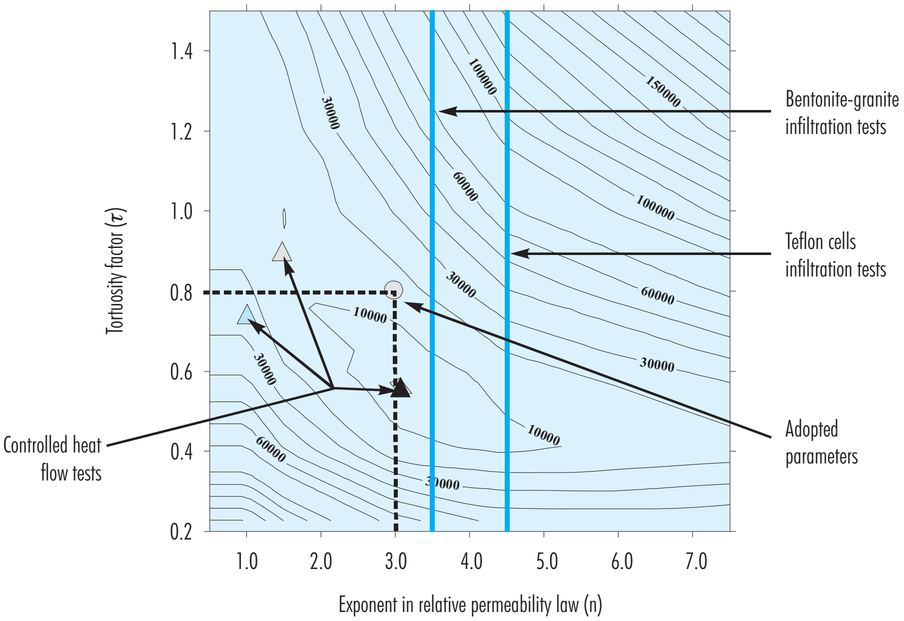

Figure 5.56: Contour map of objective function in the case of thermal flow test 1 (see details in Table 5.8). The same graph shows the parameter values obtained by back analysing different tests.

Table 5.9
Model parameters related to the thermo-hydraulic problem in the infiltration test in ceramic cell

Intrinsic permeability $k=k_o\,e^{(b(\phi-\phi_o))}$	k_o (m^2)	b	Reference porosity, Φ_o	
	$1.9\cdot10^{-21}$	30	0.40	
Relative permeability $k_{rl}=S_e^n$ $S_e=\frac{S_l-S_{lr}}{S_{ls}-S_{lr}}$	n	S_{lr}	S_{ls}	
	3	0	1	
Retention curve $S_l=\left[1+\left(\frac{s}{P_o}\right)^{\frac{1}{1-\lambda_o}}\right]^{-\lambda_o} f_d$ $f_d=\left(1-\frac{s}{P_d}\right)^{\lambda_d}$	P_o (MPa)	λ_o	P_d (MPa)	λ_d
	15	0.18	1100	1.1
Vapour diffusion	Tortuosity, τ			
	0.8			

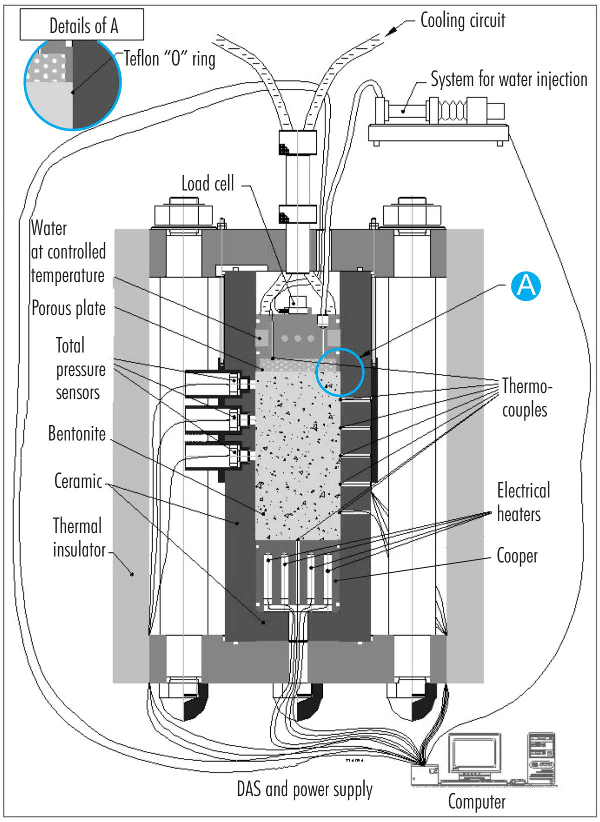

Figure 5.57: Schematic representation of the ceramic cell designed by UPC-DIT to perform infiltration tests at different temperatures.

Table 5.10
Model parameters (BBM model) related to the mechanical problem in the infiltration tests in the ceramic cell (see definition of parameters in Chapter 6)

κ	0.05	κ_s	0.38
ν	0.4	α_{is}	-0.008
α_{sp}	-0.147	α_{ss}	0.00
α_o	$1.5 \cdot 10^{-4}$ ºC^{-1}	α_2	0.00
λ_0	0.15	p_c	0.10 MPa
p_o*	14 MPa	α	0.395
r	0.75	β	0.05
M	1.5	T_o	20ºC
k	0.1	ρ	0.2

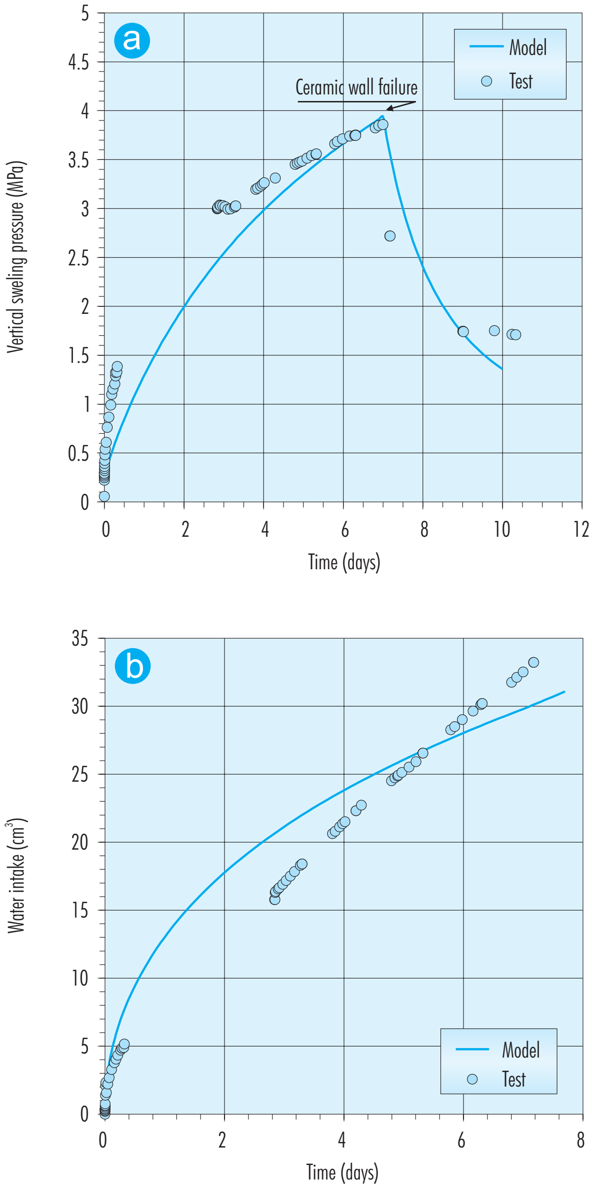

Figure 5.58: Evolution of swelling pressure and accumulated water intake in an infiltration test performed in the ceramic cell.

The evolution of computed vertical swelling stress and water intake is shown in Figure 5.58, whereas Figure 5.59 shows the profiles of water content and dry unit weight. A reasonable agreement is obtained between measured and computed values of the different variables. In particular, the decrease in vertical swelling pressure after the failure of the confining cylinder was properly reproduced.

5.1.4.5. Tests in 60-cm long cells

These tests were performed by CIEMAT in cylindrical cells with an inner length of 60 cm and a diameter of 7 cm ([65], Figure 5.60). The cells are made from Teflon in order to prevent lateral heat conduction to the extent possible and are externally covered with steel semi-cylindrical pieces to avoid the

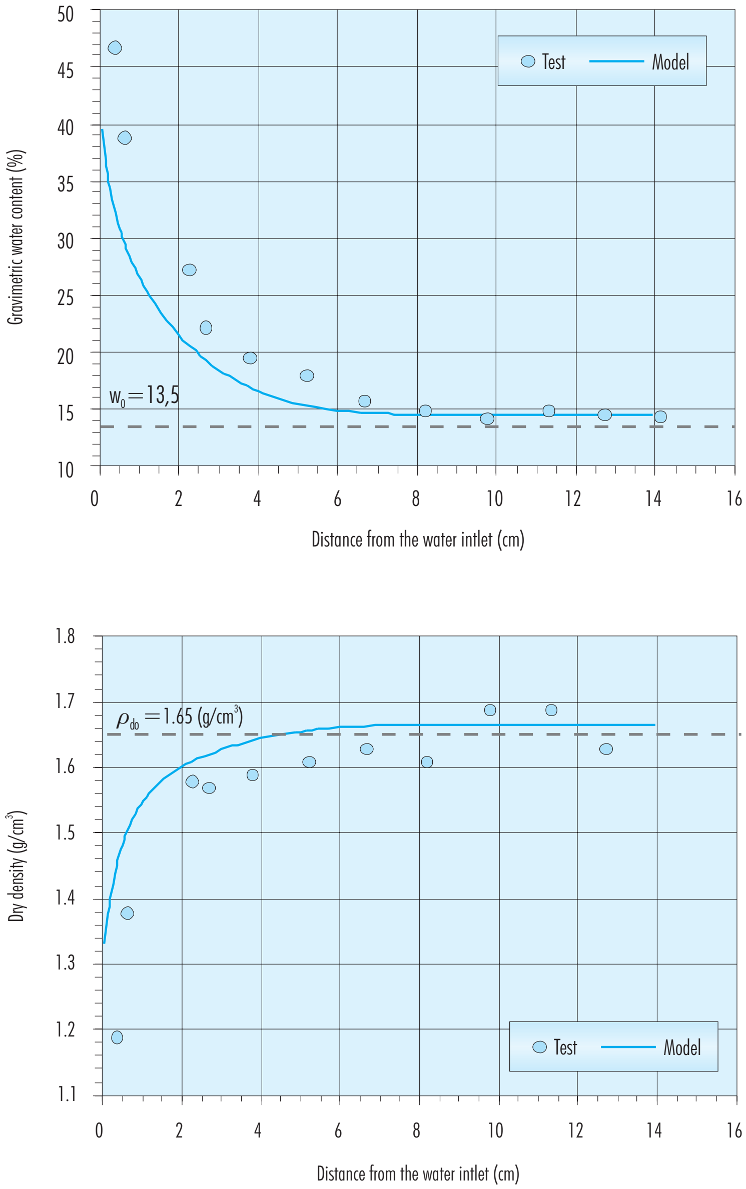

Figure 5.59: Water content and dry density profiles at the end of the infiltration test performed in the ceramic cell.

deformation of the cell by bentonite swelling. Inside the cells, six compacted blocks of bentonite were piled, giving a total length similar to the thickness of the bentonite barrier in the "mock-up" test. To produce these blocks, the clay with its hygroscopic water content (around 14 percent) was uniaxially compacted at a dry density of 1.65 g/cm^3.

The bottom part of the cell is a plane heater whose temperature is fixed at 100°C. Above the upper lid of the cell there is a tank in which water circulates at constant temperature (20-30°C). In this way, a constant gradient of 1.1-1.3°C/cm between the top and bottom of the sample is imposed. Granitic water with a salinity of 0.02 percent (Table 5.5) is injected through the upper lid of the cell at a pressure of 1.2 MPa. This simulates the water that saturates the barrier in a repository excavated in granitic rock, and is the same as that employed to saturate the "mock-up" test.

The duration of the tests was of 6, 12 and 24 months (tests FQ1/2 and HI1/2, FQ1 and HI1 and FQ2 and HI2, respectively). During the tests, the temperatures at different positions inside the clay were measured by means of thermocouples and recorded, along with the volume of water intake. The 5 thermocouples, T1 to T5, were placed at 50, 40, 30, 20 and 10 cm from the heater. At the end of the thermo-hydraulic treatment, the cell was dismounted and the clay blocks extracted. As the blocks were extracted, they were cut into cylindrical sections of 2.5 cm in thickness in which dry density and water content, among others, were determined. A total of 24 sections were obtained.

The evolutions of temperature at different locations inside the clay and of the water intake during one of the 24-month tests are shown in Figure 5.61. The repercussion of the laboratory temperature on the temperatures inside the clay was noticeable. The average temperatures recorded by each thermocouple for the period between 1000 hours after the beginning of the test and the end of the test are plotted in Figure 5.62 for three tests of different duration. There is a sharp temperature gradient in the vicinity of the heater, the temperature decreasing from 100°C at the heater surface to 50°C at a distance of 10 cm from it inside the clay. Furthermore, a decrease in temperature with saturation (longer tests) is observed, especially in the wetter zones, *i.e.* within the 20 cm closest to the hydration surface. This is due to the higher heat dissipation of wet clay.

The final distribution of water content for three tests is shown in Figure 5.63. The water content reduction due to the temperature effect is similar for the three tests, which means that desiccation takes place rather quickly and affects only the 18 cm closest to the heater, where the water contents are lower than the initial ones, which were around 14 percent. In the 6-month test, there is a central zone, between 20 and 40 cm, in which the initial water content is barely modified. The effect of hydration, which is evident only in the 20 cm closest to the hydration surface in the 6-month test, is noticeable in the upper 40 centimetres at 12 months. Over the next 12 months, the water content increases in these upper 40 centimetres, but does not change in the 18 cm closest to the heater, probably because in this zone the thermal effect is still predominant.

The final distribution of bentonite dry density is plotted in Figure 5.64. Dry density decreases from the heater towards the hydration surface, showing an approximately linear tendency. In the zones affected by hydration, dry density decreases below the initial value (1.65 g/cm^3), due to the expansion caused by saturation. On the contrary, near the heater, dry density increases, due to the shrinkage caused by desiccation. Despite the dispersion of data –caused by the initial non-homogeneities and by the determination method–, it may be observed that the densities reached near the hydration surface are lower in the longer tests, due to the fact that the saturation and, consequently, the swelling deformation are higher. Due to this density decrease, the degrees of saturation are lower than what might be expected in view of the high water content. In fact, a degree of saturation higher than 90 percent is reached only in the 3 cm closest to the hydration surface after 6 months of TH treatment, in 8 cm after 12 months and in 10 cm after 24 months. On the other hand, near the heater (18 cm) the density remains the same from 6 to 24 months, and the degrees of saturation decrease from the initial 55-60 percent to values of around 25 percent in the vicinity of the heater. An overall decrease of dry density was observed, since the average value measured was 1.57 g/cm^3 for the 6 and 12-month tests and 1.55 g/cm^3 for the 24-month tests, whereas the initial dry density of the blocks was 1.65 g/cm^3. This is due to the fact that the cells are made of Teflon, a material that deforms slightly because it is not able to withstand the high swelling pressure developed by the clay as it saturates. This overall decrease of dry density is linked to the hydration of clay, and for this reason, is more important for the longer tests that have reached a higher degree of saturation.

Modelling of the TH behaviour

1-D axisymmetric models have been used in the analysis of the 24-month test. As in the case of the infiltration test in the ceramic cell, the test was modelled using the same numerical approach used to model the operational phase of the "in situ" and "mock-up" tests. The parameters corresponding to the hydraulic and mechanical aspects of the model are the same as those indicated in Table 5.9 and Table 5.10 respectively, except that a value of 28 MPa has been taken for P_0, 0.04 for κ, 0.25 for κ_s, and -0.003 for α_{is}.

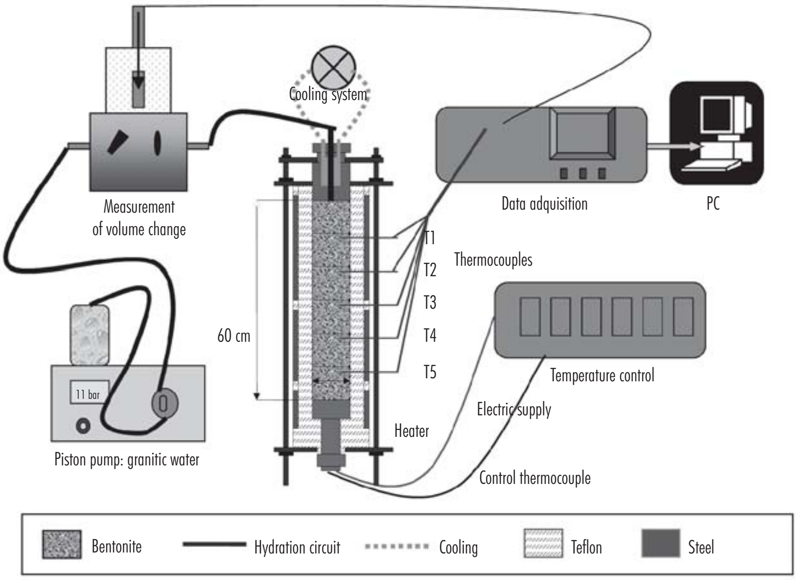

Figure 5.60: Experimental setup for the 60-cm long thermo-hydraulic tests (CIEMAT).

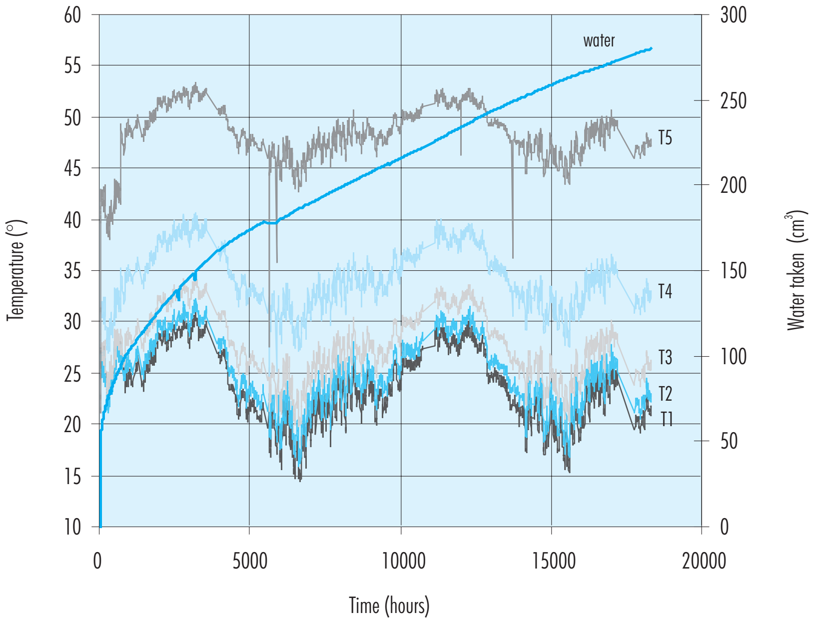

Figure 5.61: Evolution of temperatures at different locations inside the clay (T1 to T5, 50 to 10 cm from the heater) and of water intake in the 24-month test FQ2.

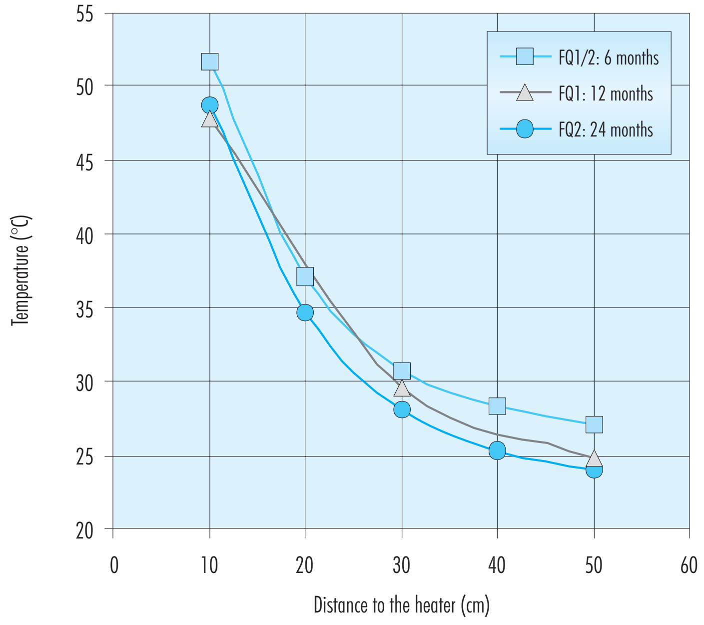

Figure 5.62: Average steady temperatures at different positions for three tests of different duration.

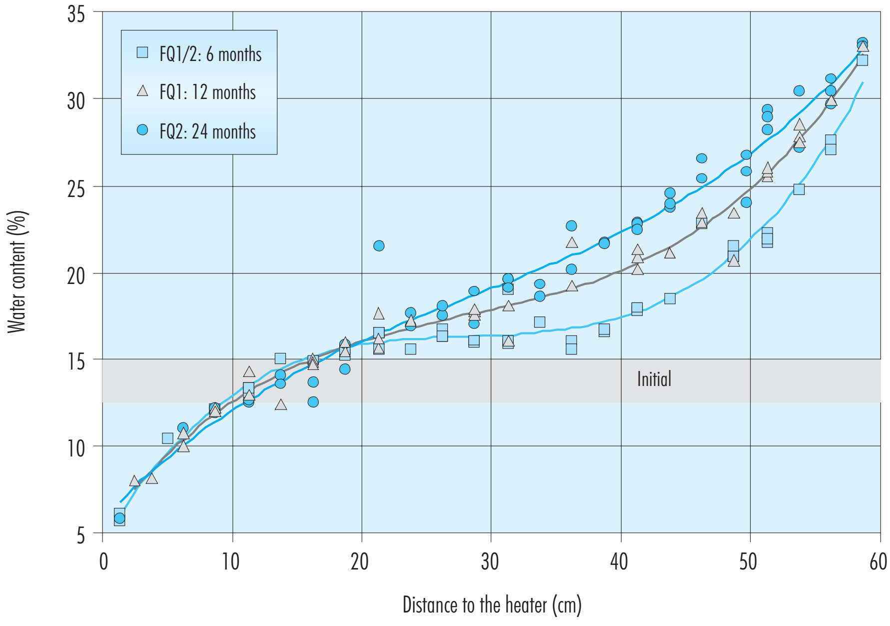

Figure 5.63: Final distribution of water content for tests of different duration.

Figure 5.64: Final distribution of dry density for tests of different duration.

The numerical results relating to the hydraulic problem are good, as may be seen in Figure 5.65, in terms of cumulative water intake and of water intake rate. As regards the comparisons related to the post-mortem analyses, Figure 5.66 presents the distribution of temperatures along the sample at the end of the test. The comparisons related to the distribution of the water content along the cell (Figure 5.67) show that the results are not particularly good, especially in zones close the heater. It is important to highlight that the simulation does not take into account the cooling phase to which the samples were submitted during the dismantling of the test (before the determination of the water content values). It is possible that these hot zones might be those most affected by the omission of this cooling stage. In any case, the simulations capture this variable well qualitatively. The effect of the wetting in the lower part of the sample (approximately 10 cm) due to the condensation of the water vapour coming from the bottom of the cell (where the heater is located) may be observed.

Figure 5.68 shows the measured values of clay dry density together with the model results. A clear density reduction may be observed in zones close to the hydration front (due to swelling of the clay), and higher densities as the distance to the heater diminishes. The model captures the overall trend of the test qualitatively; however, as for the case of water content, the agreements between the model results and measurements are not good in the zones close to the heater. The omission of the cooling and unload phases in the analyses might be the main reason for the discrepancies in this case also.

Modification of hydro-mechanical properties

At the end of the thermo-hydraulic treatment, the cells were dismounted and the clay blocks extracted and cut into 2.5-cm thick cylindrical sections, which were used for the following determinations: dry density, water content, swelling capacity, swelling pressure and permeability. All of these determinations were performed once the samples had cooled down. Geochemical, mineralogical and fabric studies – described in Section 5.2.2.3 and in [66] – were also performed.

For the determination of hydro-mechanical (HM) properties, the specimens were trimmed from the bentonite blocks to fit the ring of the permeability or

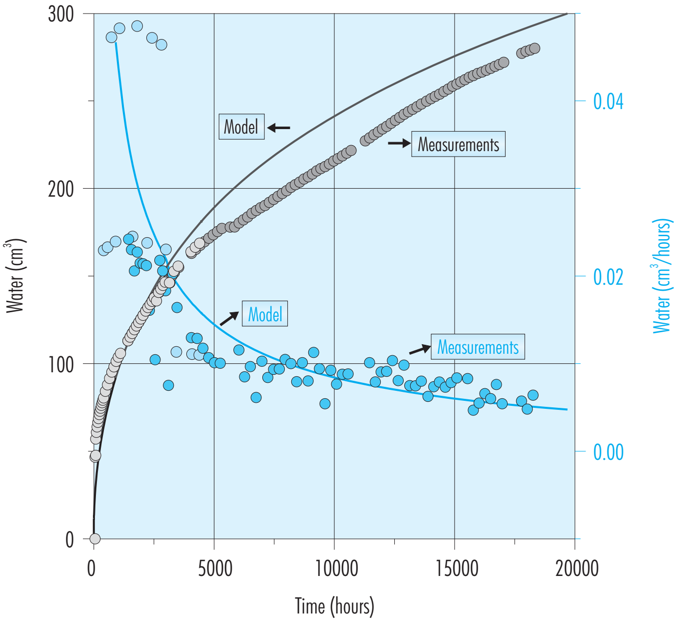

Figure 5.65: Computed versus measured values of cumulative water intake and rate of water intake.

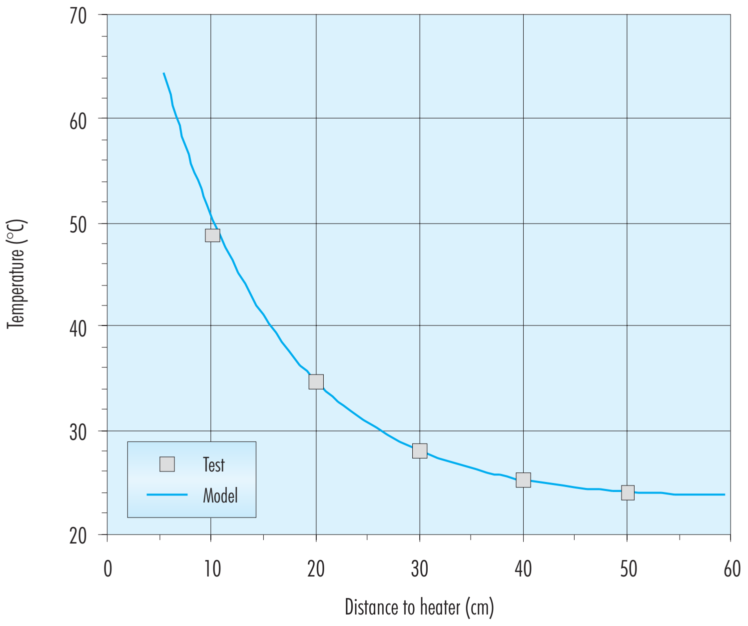

Figure 5.66: Distribution of temperature along the cell at the end of the 24-month test FQ2 (measured and computed values).

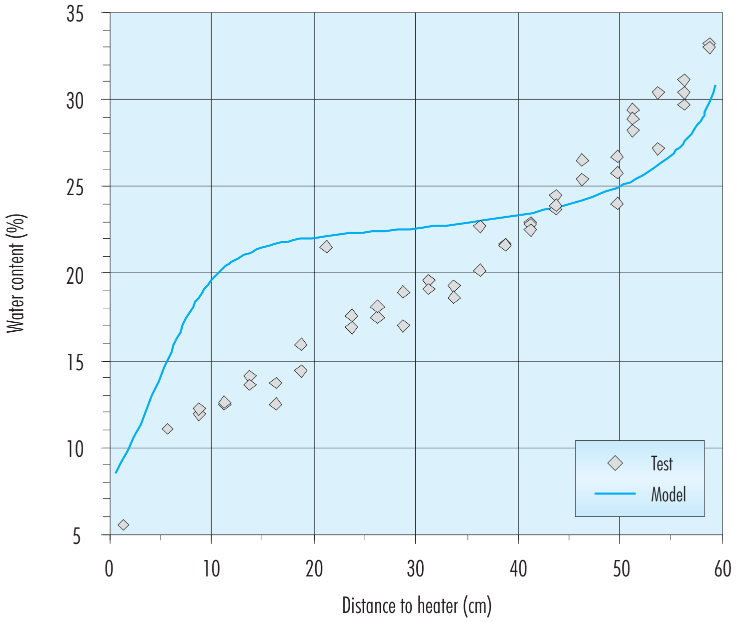

Figure 5.67: Distribution of water content along the cell at the end of the 24-month test FQ2 (measured and computed values).

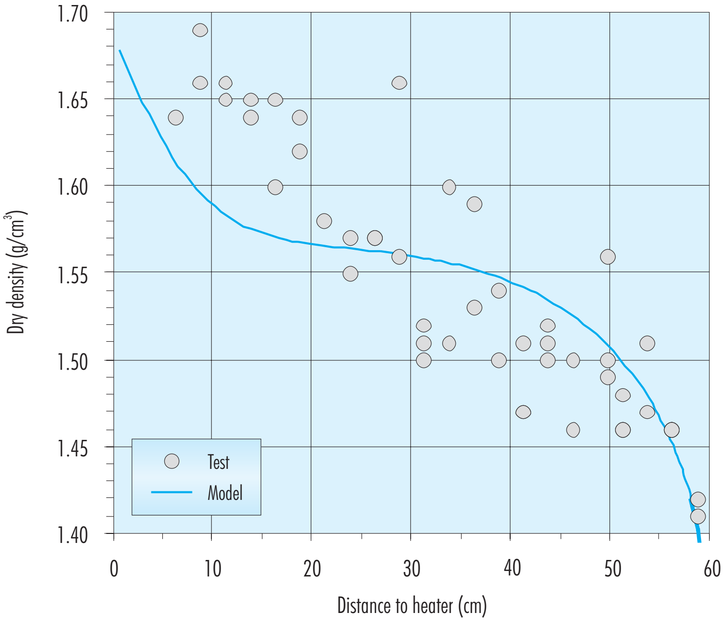

Figure 5.68: Distribution of dry density along the cell at the end of the 24-month test FQ2 (measured and computed values).

oedometer cell, dry density and water content being preserved as on completion of the TH treatment. As a result, the specimens from different positions had different density and water content values at the beginning of the HM determinations, this highly influencing the values obtained [65, 67]. Thus, the analysis of the hydro-mechanical properties of the clay after TH treatment is technologically complicated and difficult to interpret. On the one hand, once the sample is extracted from the TH cell, it loses its stress conditions, and on the other the hydro-mechanical properties of the clay are modified by dry density and water content, which differ depending on the position of the sample inside the cell. Consequently, it is difficult to determine whether the modifications observed are caused by the TH treatment – and related geochemical variations – or just by the changes in dry density and water content, which are merely transitory. To overcome the uncertainties related to these initial differences, some samples were also tested after remoulding, *i.e.* dried under laboratory conditions, ground and compacted at a dry density of 1.6 g/cm^3 [65]. However, this technique proved to be inadequate for study of the potential modifications, as it increases the swelling capacity of the clay. Consequently, to evaluate the variation of hydro-mechanical properties after TH treatment, it is necessary to have a complete database on the influence of density and water content on the properties to be tested.

The measurements of saturated hydraulic conductivity performed after the TH treatment revealed an increase of saturated permeability with respect to the untreated sample (although this continued to be very low) and a strong dependence on dry density (Figure 5.69).

The swelling pressure and swelling capacity of the treated clay are influenced by its initial dry density and water content, and remain at values similar to those of the untreated clay (Figure 5.70). There is a suggestion that the swelling capacity under a low vertical load (swelling under load tests) might be reduced after desiccation [67].

5.1.4.6. Tests in 40-cm long cells

These tests were performed by CIEMAT in the cylindrical Teflon cells described in the previous section. The cells were modified in order to give them a final

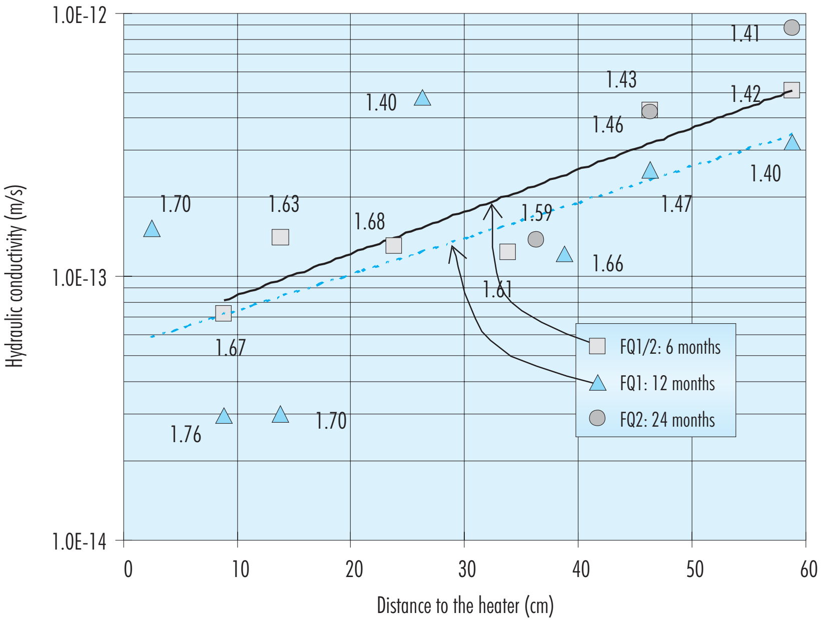

Figure 5.69: Hydraulic conductivity values obtained after thermo-hydraulic treatment over different periods of time as a function of the distance to the heater (the dry density of each specimen is shown in g/cm^3).

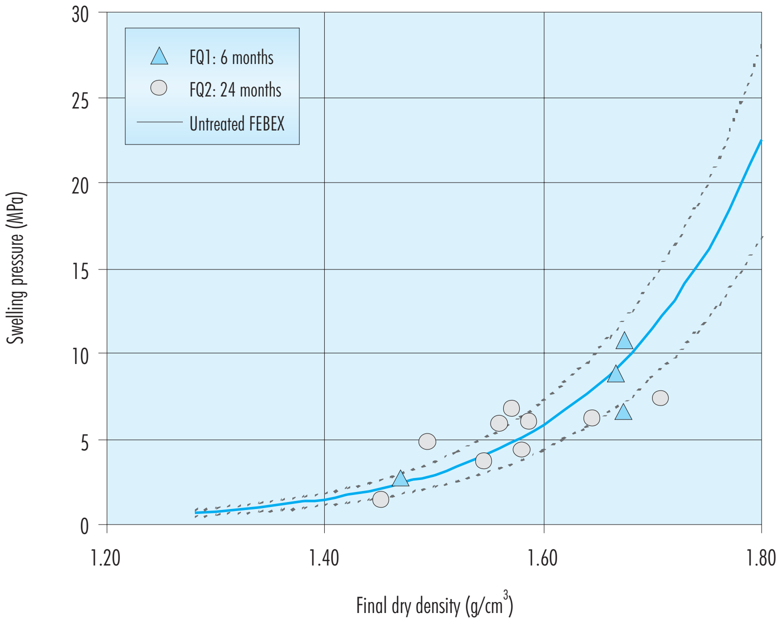

Figure 5.70: Swelling pressure of clay subjected to TH treatment over different periods of time as a function of dry density. The curve for untreated FEBEX was obtained with Equation 5.16.

internal length of 40 cm. Blocks of FEBEX clay compacted with hygroscopic water content at an initial nominal dry density of 1.65 g/cm^3 were piled inside each cell. Hydration with granitic water takes place through the upper surface under an injection pressure of 1.2 MPa. In one of the tests the clay is heated through the bottom surface at a temperature of 100°C, whereas the other test is carried out under isothermal conditions (laboratory temperature). The water intake and the relative humidity and temperature evolution at different levels inside the clay are measured as a function of time. The two cells in operation are shown in Figure 5.71.

The evolution of temperature and relative humidity in the test performed under a thermal gradient (GT40) is shown in Figure 5.72, and under isothermal conditions (I40) in Figure 5.73. Test GT40 showed that the permeability to water vapour of dry bentonite is very high, since a quick redistribution of water took place when the thermal gradient was established. The initial hydration of compacted bentonite would seem to take place more quickly under a thermal gradient (test GT40) than at laboratory temperature (test I40), since the increase in humidity registered by the upper sensor (RH1) is higher in test GT40 than in test I40, whereas the sensor placed in the middle (RH2) starts to perceive the humidity increase much earlier in the case of infiltration under a thermal gradient than in the case of infiltration at laboratory temperature. However, in the case of test GT40, the humidity recorded by sensor RH2 might originate in the form of water vapour from the lower part of the column. Otherwise, the increase in hydraulic conductivity with temperature would account for this possible initial quicker hydration of the test under the thermal gradient.

However this behaviour is reversed as saturation proceeds and later the water intake is higher for the sample tested at room temperature because the hot zones of the sample tested under a thermal gradient remain desiccated for a long time. After 27000 hours (more than 3 years) of hydration, the average relative humidity recorded by the three sensors in test GT40 is 68 percent, and in test I40 is 85 percent. In fact, the relative humidity inside the bentonite submitted to the thermal gradient has remained quite constant from 20000 hours up to now (28000 hours), whereas the average relative humidity of the

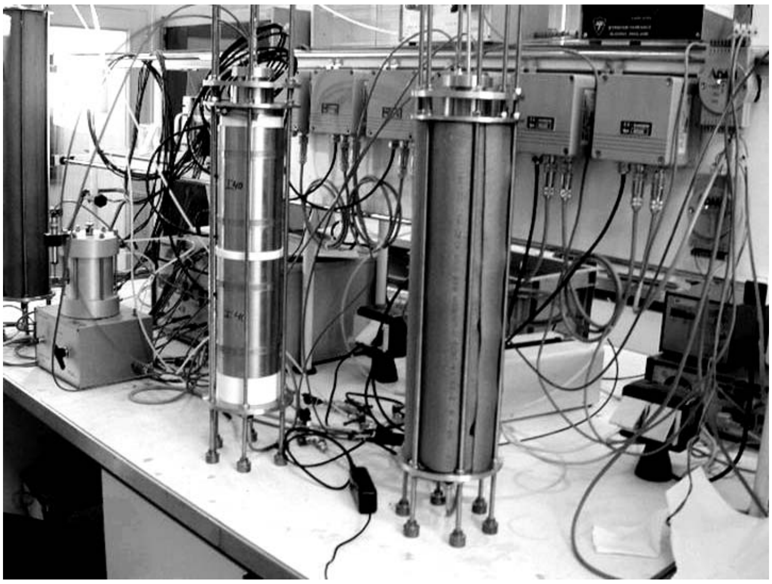

Figure 5.71: Infiltration cells in operation: isothermal (left) and with thermal gradient (right).

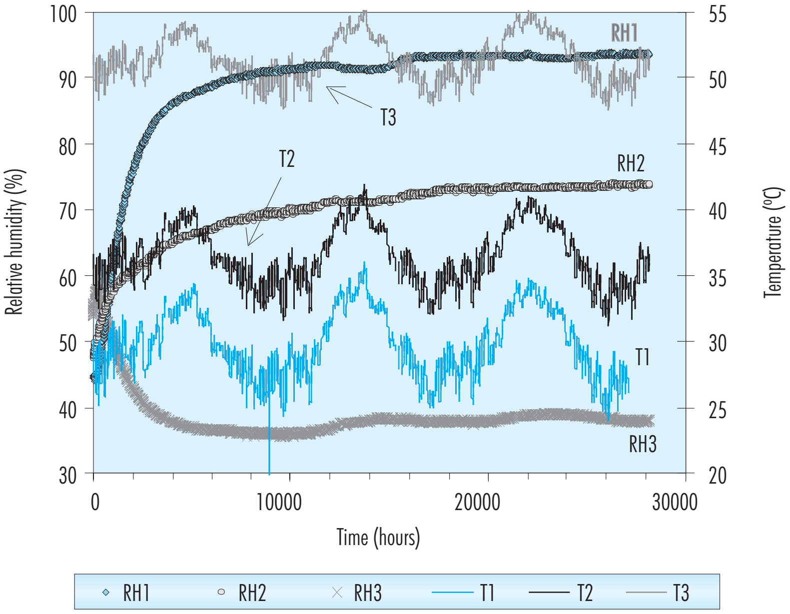

Figure 5.72: Evolution of temperature and relative humidity in the test performed under a thermal gradient (GT40) during infiltration (sensor 1 placed 30 cm from the bottom, sensor 2 at 20 cm and sensor 3 at 10 cm).

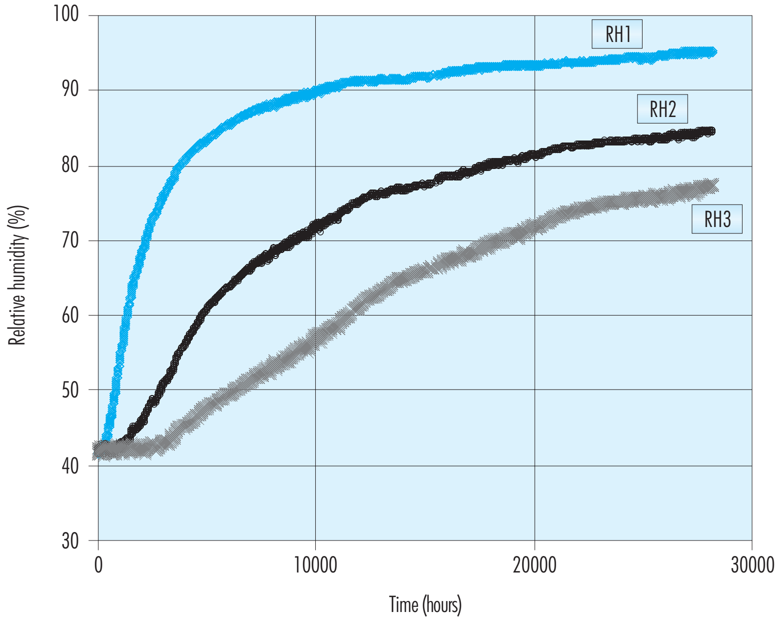

Figure 5.73: Evolution of relative humidity in the test performed under isothermal conditions (I40) during infiltration (sensor 1 placed 30 cm from the bottom, sensor 2 at 20 cm and sensor 3 at 10 cm).

sample hydrated under isothermal conditions is still slowly but steadily increasing.

5.1.5. Microstructural changes upon loading and wetting

The data on the pore size distribution (PSD) of samples compacted with hygroscopic water content presented in Section 2.3.2 indicate a clear presence of two structural levels in the material: a microstructure inside the aggregates and a macrostructure, constituted by the ensemble of aggregates and inter-aggregates pores. Microstructure features appear to be largely independent from compaction effort. Additional information on the soil fabric may be inferred from the examination of retention curves obtained under free swelling and constant volume conditions (Figure 5.18). It may be observed that the water retained at suctions higher than about 15 MPa is independent from the total void ratio (or dry density). It seems plausible that the water retained at those high suctions belongs to the intra-aggregate pores, where total porosity plays no relevant role [68].

In addition, the influence of various mechanical (loading) and hydraulic (wetting/drying) stress paths on the pore size distribution of compacted bentonite was analysed by MIP [15]. Figure 5.74 shows the porosimetry of a specimen obtained by loading a bentonite slurry to 1.5 MPa. After the loading/unloading path the dry density of the specimen was around 1.15 g/cm^3. The PSD function displays a clear dominant pore size mode at 430 nm. It may be observed that inter-granular pores disappear due to the slurry condition of the sample.

The evolution of the PSD function on wetting specimens initially compacted to 1.65 and 1.40 g/cm^3 is presented in Figure 5.75 and Figure 5.76, respectively. The different final dry densities of the materials are indicated in the figures. It may be seen that an intermediate pore size mode emerges. Simultaneously, and as a result of the constant volume condition during wetting, inter-granular porosity is reduced, tending towards occlusion. Due to the limitations of the method, the evolution of the intra-aggregate pore size mode, which is expected to increase on wetting, cannot be registered. The emerging pore mode displays values of between 350 and

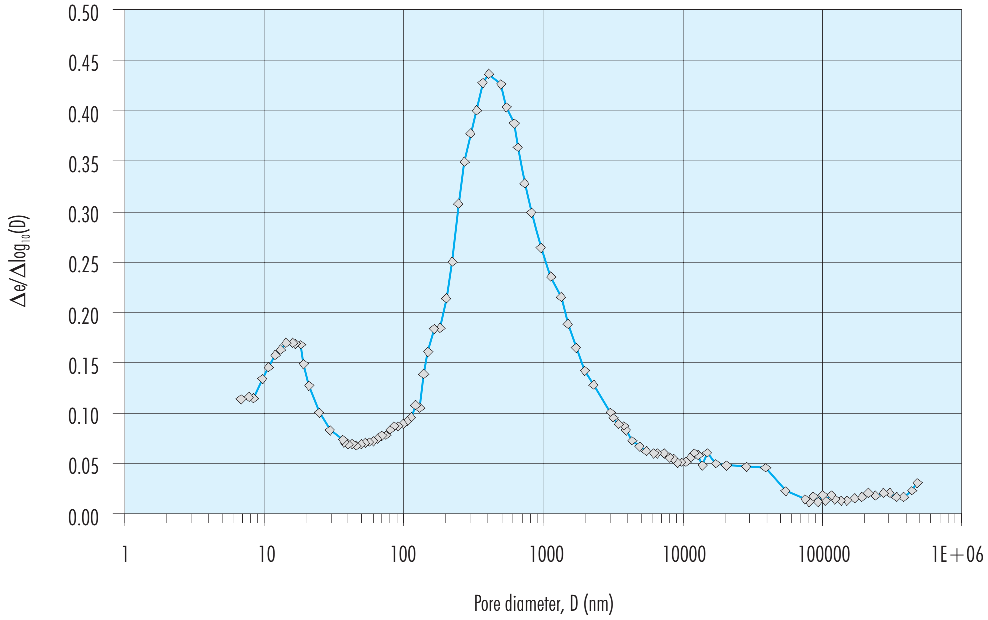

Figure 5.74: Porosimetry of consolidated slurry; dry density 1.15 g/cm^3.

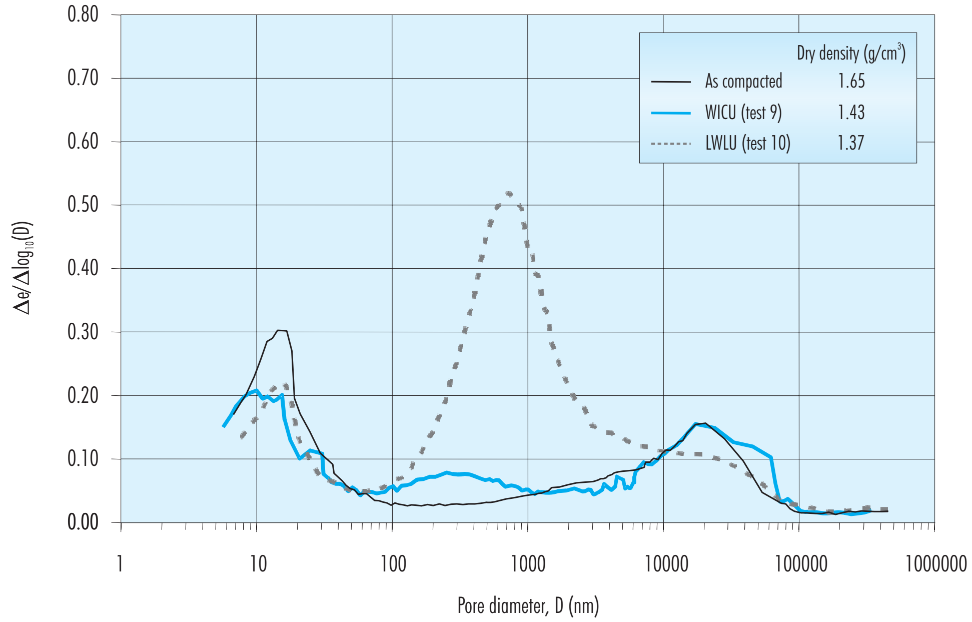

Figure 5.75: Evolution of PSD functions on wetting a bentonite specimen with an initial dry density of 1.65 g/cm^3 under constant vertical net stress (test 10) and under constant volume (test 9).

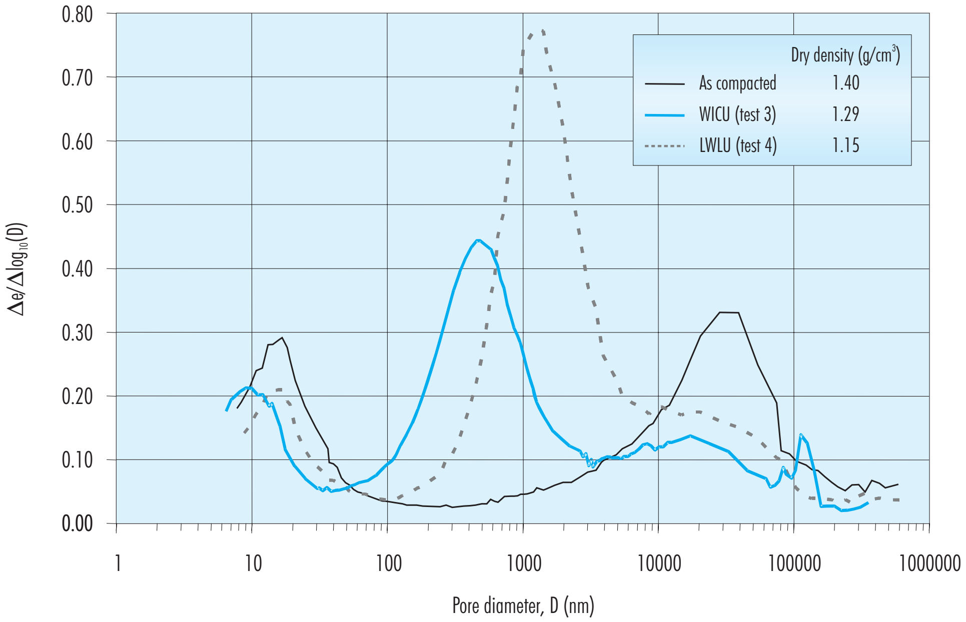

Figure 5.76: Evolution of PSD functions on wetting a bentonite specimen with an initial dry density of 1.40 g/cm³ under constant vertical net stress (test 4) and under constant volume (test 3).

1100 nm, similar to those observed in the slurry. It appears that wetting induces the progressive splitting of the original structure of the pseudomorphs, which are purely smectitic piles (Section 2.3.3). The progressive subdivision causes an increase in the number of reactive surfaces and the emerging intermediate porosity. The changes due to wetting are more evident in samples with a lower density.

A systematic observation of specimens used for the MIP tests was performed by means of an environmental scanning electron microscope (ESEM) [15]. Although the observations mainly provide qualitative information, the use of this technique is of interest since it enhances knowledge of the structural changes due to the wetting and drying paths. Using the capabilities of the equipment, the microphotographs were made under different environmental conditions of temperature and relative humidity.

The effect of sample preparation may be observed in Figure 5.77, where the images of a consolidated slurry and a sample compacted at hygroscopic water content are presented with the same magnification. The consolidated slurry possesses a more uniform and homogeneous structure (matrix structure), in which aggregates are not clearly distinguished, in agreement with the MIP results, which show a clear predominant pore size of 0.4 μm diameter (Figure 5.74). The compacted sample, displaying an aggregated structure, shows denser aggregates separated by pores of greater dimensions (inter-granular pores).

The effect of compaction intensity may be observed in Figure 5.78, where the microphotographs of samples compacted to 1.40 and 1.65 g/cm^3 with hygroscopic water content are presented. The size of the inter-granular pores is larger in the less dense sample. At larger magnification, the differences between the two samples are less evident.

The structural changes caused by the progressive wetting of bentonite compacted at an initial dry density of 1.65 g/cm^3 may be observed in Figure 5.79. Suction changes in isochoric conditions were applied before the observation in the ESEM. The differences in final dry density are due to the rebound experienced by the bentonite after unloading. The progressive occlusion of inter-granular pores due to particle swelling is qualitatively appreciable.

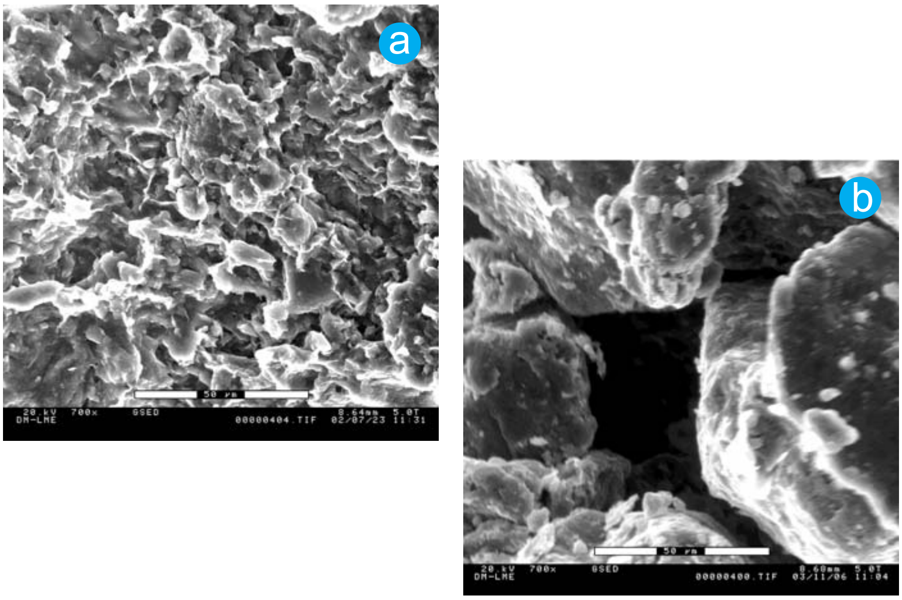

Figure 5.77: Fabric of bentonite samples. a) Consolidated slurry (ρ_d=1.15 g/cm^3); b) Compacted bentonite with hygroscopic water content (ρ_d=1.40 g/cm^3).

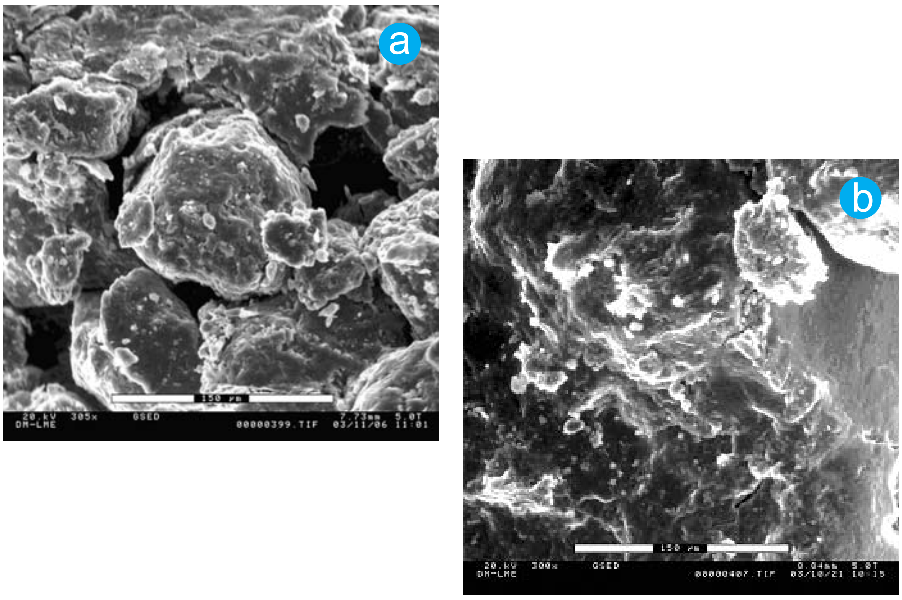

Figure 5.78: ESEM images of bentonite compacted with hygroscopic water content. a) ρ_d=1.40 g/cm^3; b) ρ_d=1.65 g/cm^3.

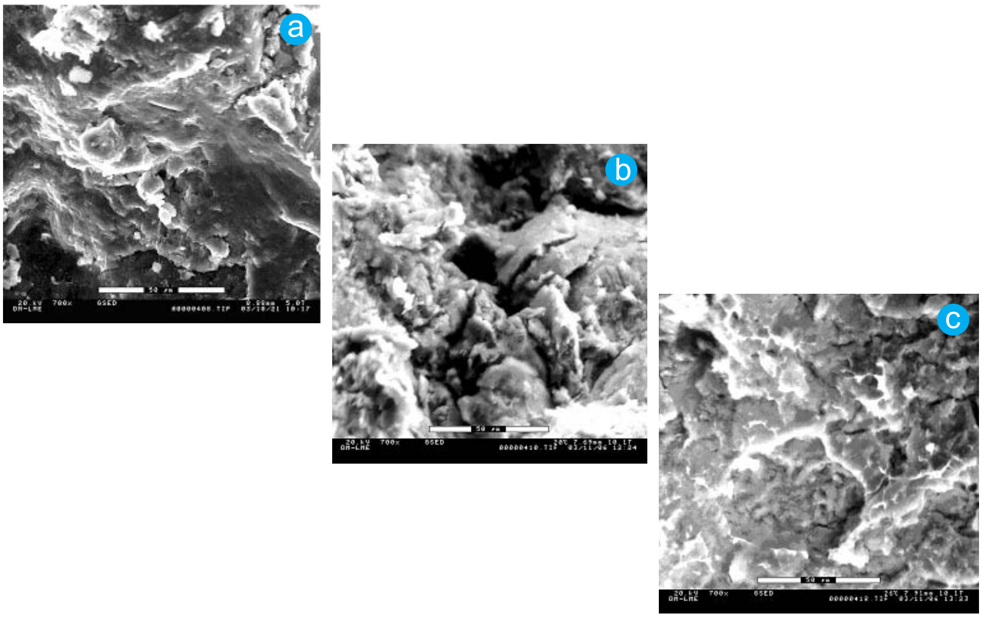

Figure 5.79: ESEM images of bentonite initially compacted with hygroscopic water content at ρ_d*=1.65 g/cm*^{3}*: a) as compacted; b) after application of a suction of 10 MPa under isochoric conditions (*$\rho_{d\ final}$*=1.46 g/cm*^{3}*); and c) after saturation under isochoric conditions (*$\rho_{d\ final}$*=1.43 g/cm*^{3}*).*

In the context of the study of swelling clay behaviour, the most relevant feature of the ESEM device is the possibility of changing the relative humidity of the microscope chamber in order to change the total suction of clay. Nevertheless, it should be taken into account that during the observation the samples are not confined, which makes it difficult to observe the occlusion of inter-granular pores due to the expansion of clay aggregates. Figure 5.80 shows the appearance of clay aggregates in a sample compacted at a dry density of 1.70 g/cm^3 and observed under a relative humidity of 50 percent. This sample was progressively hydrated for 5 hours in the microscope chamber by increasing relative humidity while keeping the temperature constant. Figure 5.80 also shows the final appearance of the same sample under a relative humidity of 100 percent. A decrease in the size of some voids may be observed.

Additional photographs of high-density fabrics were carried out in order to complement the information on aggregate swelling/shrinkage in a wetting/drying path (Figure 5.81). Measurements of volume changes in ESEM images were calculated using digital imaging techniques, as indicated in Figure 5.82. The swelling/shrinkage results were complemented with wetting and drying paths, performed at macroscale, (specimen with a diameter of 16 mm) using the vapour equilibrium technique. The reversible and irreversible features of both micro and macroscales are clearly observed in Figure 5.82 for the same high-density fabric. At microscale, strains are almost reversible, due to the reversibility of the physical and chemical phenomena that take place at particle level.

5.1.6. Joint behaviour

5.1.6.1. Hydration tests

Hydraulic tests were performed on specimens with joints, with a view to gaining insight into the influence of the joints of the clay barrier on its hydraulic behaviour [50]. The analysis included mainly the influence of joints on hydration rate, their sealing capacity and the modification that they induce in hydraulic conductivity. Different cylindrical cells with

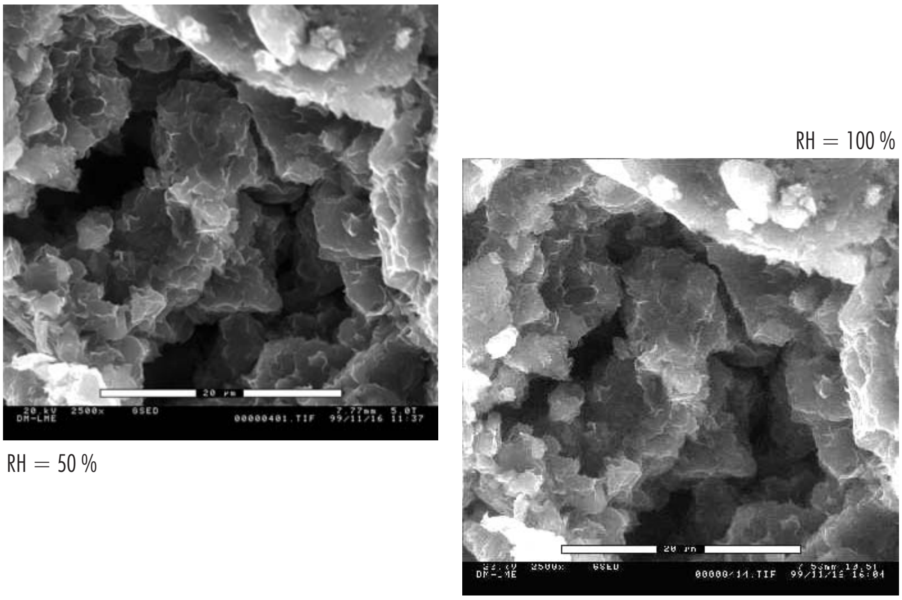

RH = 50 %

RH = 100 %

Figure 5.80: Image analysis evolution of volume change behaviour referring to a compacted bentonite sample at ρ_d*=1.7 g/cm*^{3}*.*

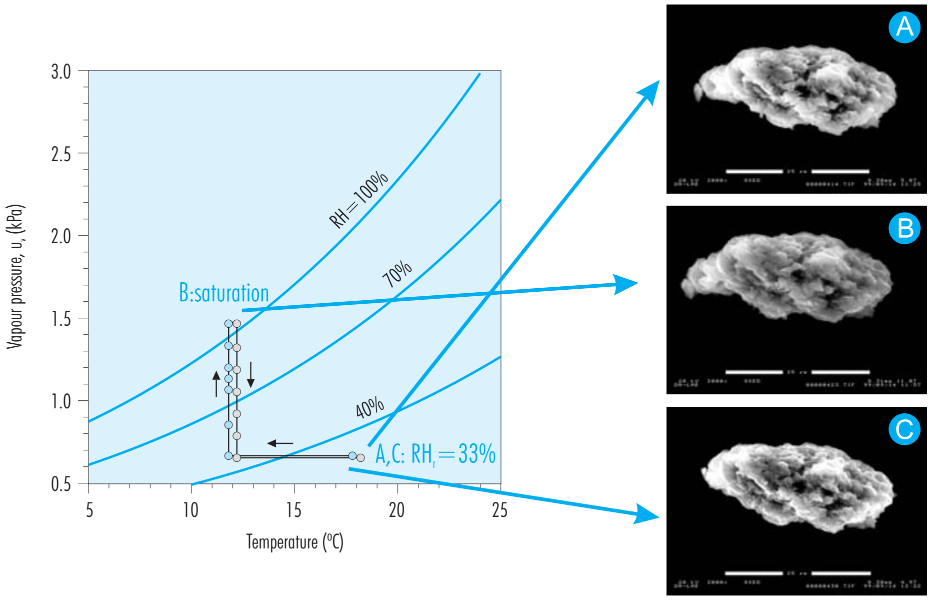

Figure 5.81: Relative humidity paths followed in the ESEM. Images of high-density fabrics at different relative humidity values.

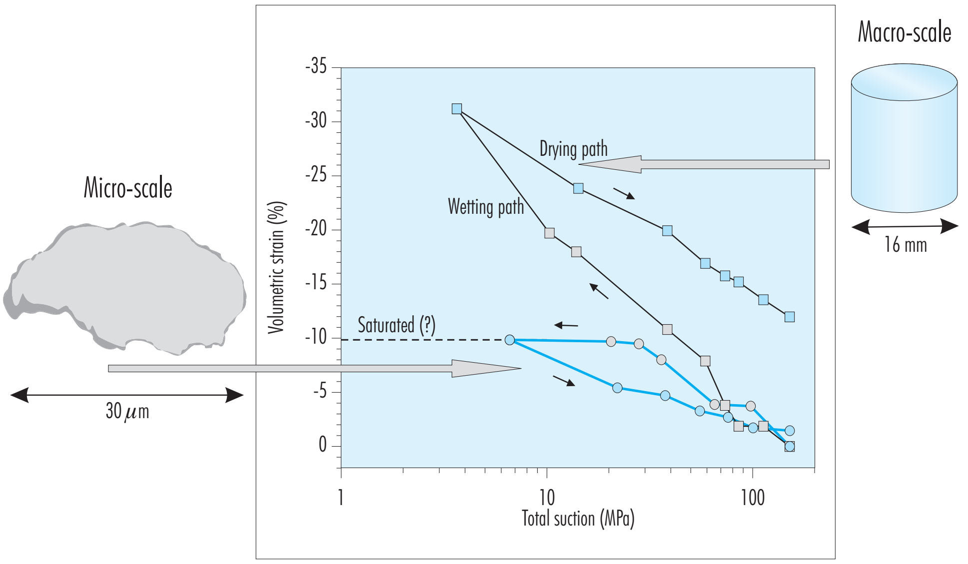

Figure 5.82: Swelling/shrinkage response at micro and macroscale for high-density fabrics.

water inlets were used. The specimens were made from four 2.5-cm thick compacted bentonite blocks (with final dry densities ranging between 1.61 and 1.23 g/cm^3 and initial water contents ranging between 15.0 and 11.7%), some with vertical diametral joints. The main conclusions of this study are as follows:

- ❏ When hydration occurs under a given injection pressure, even if it is low, the volume of water taken up and its distribution inside the clay is controlled by the existence of joints (fissures), their volume and their configuration.
- ❏ The clay takes the water both from the direct hydration surface and from the block joints. Figure 5.83 shows the final distribution of water content in two hydrated tests, in which four half-sectioned specimens were piled and hydrated from the top, illustrating this observation.
- ❏ The volume of water initially taken up depends on hydration pressure.
- ❏ Once the joints have been filled with water, the rate of water intake appears not to depend on injection pressure but on the dry density of the clay.
- ❏ The sealing of a joint, attained after hydration for 24 hours, is effective against hydraulic pressures of up to 5 MPa.
- ❏ Before sealing of the joints is attained, the strain experienced by every slice on saturation is that corresponding to its initial dry density.

5.1.6.2. Joint stiffness

In order to obtain the normal stress *vs*. displacement on joints between bentonite blocks, four unconfined compression tests were performed on compacted cylindrical specimens. Joint displacements were evaluated by comparing the measured strain on a specimen of 78 mm in length and the measured strain on two specimens of 39 mm in length, placed face to face, for the same stress level. The diameter of the specimens was 38 mm. The strains were measured by means of two Hall effect displacement transducers parallel to the longitudinal axis mounted directly on the lateral surface of specimens in order to avoid the bedding effects of the equipment.

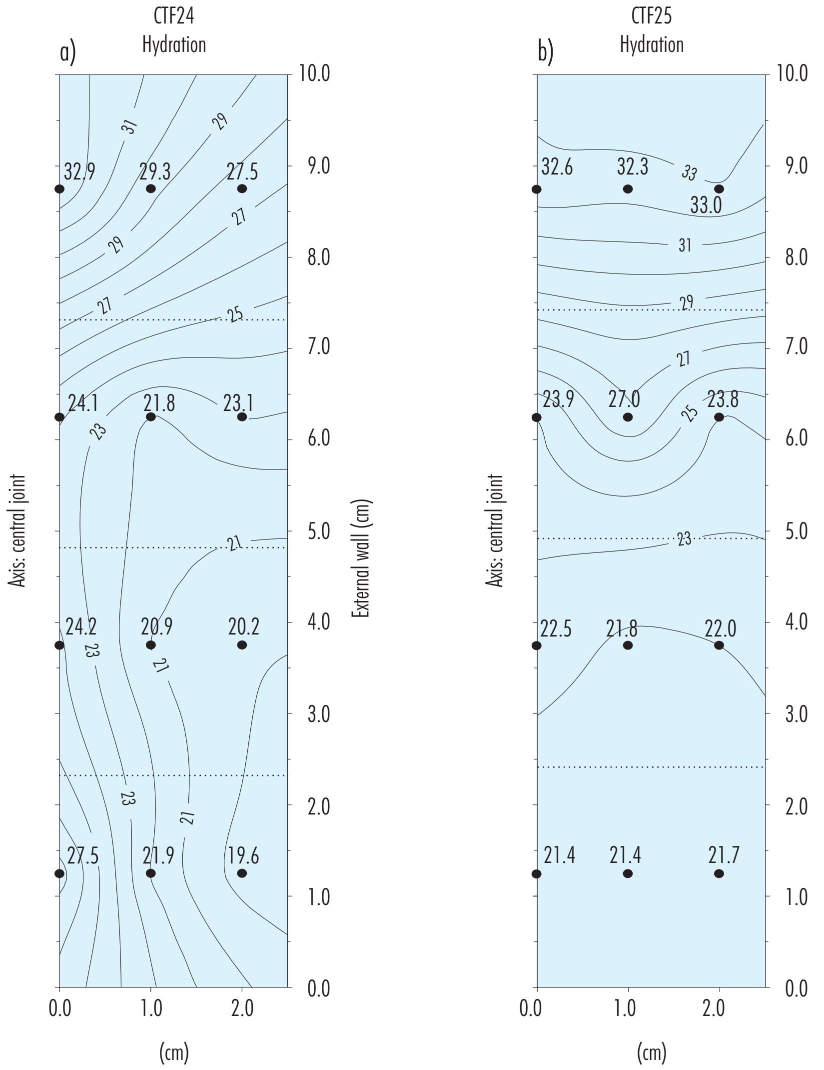

Figure 5.83: Water content distribution of the clay after two sealing tests (piling of four slices) performed under a hydration pressure of 0.5 MPa and lasting a) 1 day, b) 7 days (half section).

Three different degrees of saturation (0.15, 0.45 and 0.85) were imposed on the compacted specimens. Two specimens were compacted at S_r= 0.45. In all cases the bentonite dry density was 1.6 g/cm^3. Figure 5.84 shows the strain-stress relationship measured in specimens with and without joints compacted at a degree of saturation of 0.45. The normal stress-displacement in the joint for two of the tests performed is shown in the Figure 5.85. In Table 5.11 the Young modulus and the unconfined compressive strength of the compacted bentonite specimens are shown.

5.1.7. Variation of properties in the bentonite extracted during partial dismantling

After five years of operation, Heater #1 of the "in situ" test was switched off (Section 4.6). Following cooling of the system for one month, the bentonite barrier was dismantled and the heater extracted. During dismantling many bentonite samples were taken and several determinations were carried out on them. The aim of the thermo-hydro-mechanical

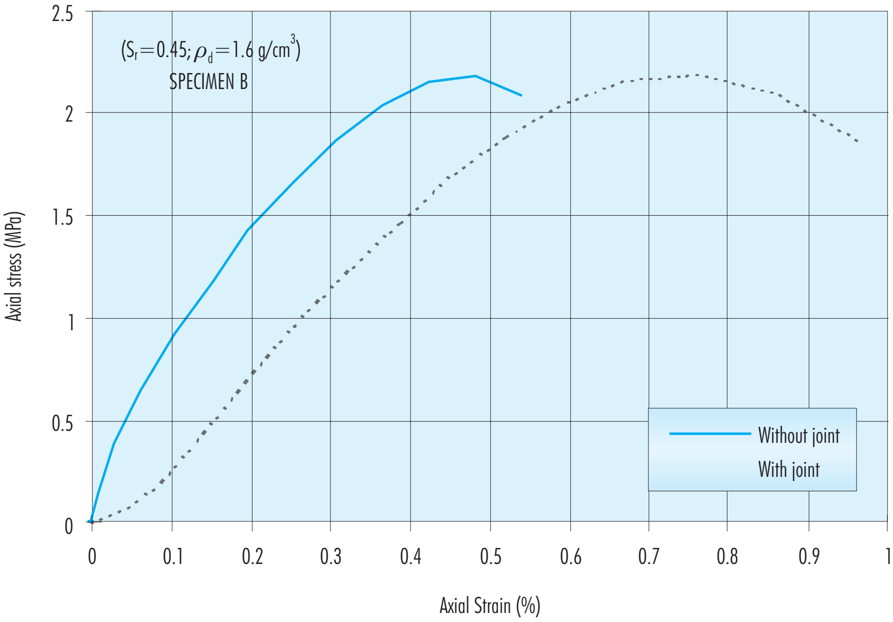

Figure 5.84: Stress-axial strain relationship in specimens compacted at a degree of saturation of 0.45.

tests performed on the samples retrieved from the "in situ" test was twofold: (1) to characterise the actual state of the bentonite and (2) to determine the possible changes in its thermo-hydro-mechanical properties occurring during the test, due to the combined effect of temperature, water content, joints and solutes.

Thermo-hydro-mechanical tests were performed on samples from sections S19, S23, S28 and S31 by CIEMAT, and on samples from section S7, S12, S19 and S28 by CTU (see Figure 4.39 for location of sections). In each sampling section, 9 or 12 complete blocks belonging to 3 or 4 different radii were taken and sent to the different laboratories. Tests on joints were performed by Euro-Géomat on samples taken from sections S11 and S29. EIG EURIDICE performed hydraulic conductivity tests on samples from sections S12 and S19.

Table 5.11
Strength and stiffness of bentonite specimens compacted at a dry density of 1.6 g/cm^3

Degree of saturation	Compressive strength (MPa) With joint	Compressive strength (MPa) Without joint	Young modulus at $\varepsilon=0.5\%$ (MPa) Without joint
0.15	0.82	0.49	78
0.45	2.19	2.18	377
0.45	2.68	2.23	436
0.85	4.43	4.76	601

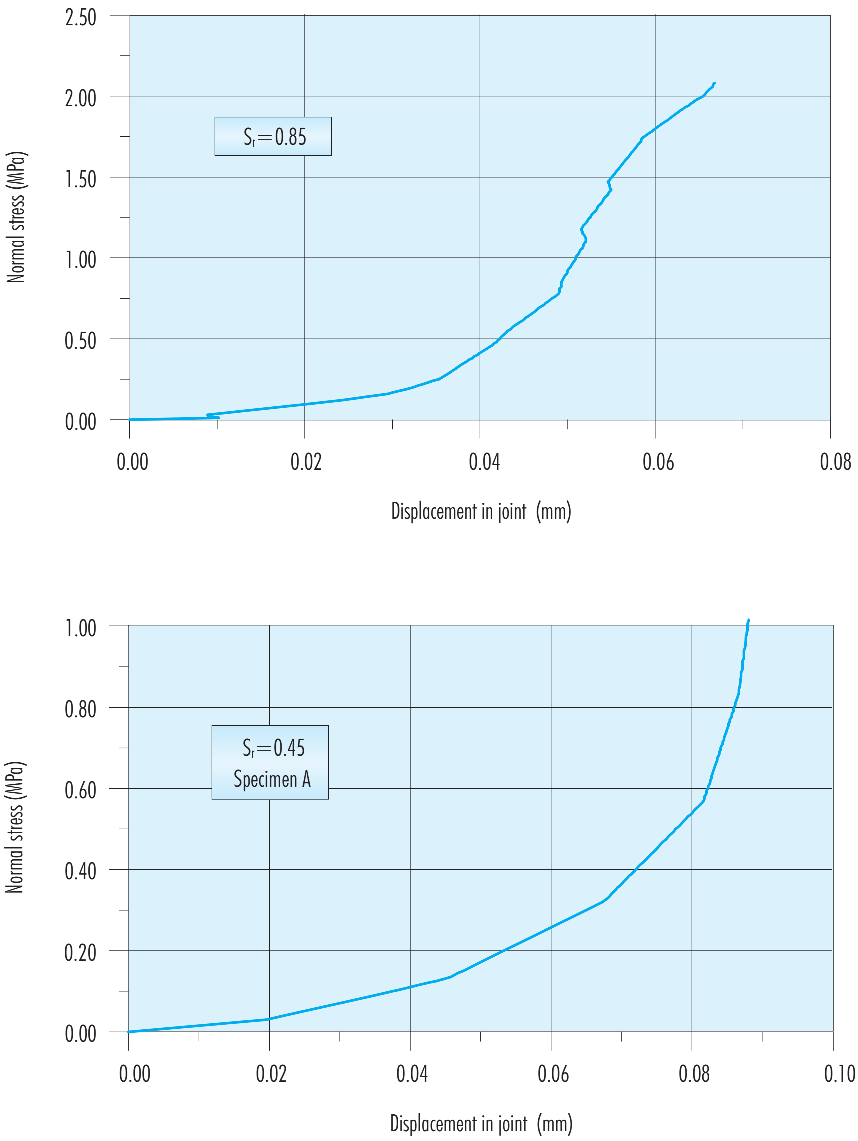

Figure 5.85: Stress-normal displacement relationship in the joints of specimens compacted at various degrees of saturation.

5.1.7.1. Physical properties

Porosity

As described in Chapter 4, the bentonite in the barrier experienced an overall increase of volume after being subjected for five years to repository conditions, which implies an increase of porosity, explained by the swelling and filling of all the construction gaps. The distribution of pore sizes in the bentonite samples was studied by mercury intrusion (CIEMAT) and nitrogen adsorption (INPL and CIEMAT). Despite the different methods employed, all the studies have shown that the treated samples have experienced a decrease in the percentage of the smaller pores. Furthermore, the mercury intrusion showed an overall homogenisation of pore sizes and an increase in average pore size. There is a relative decrease of microporosity with respect to the untreated sample, since the proportion of large pores has increased. These variations, which do not seem to be related to the position of the samples in the barrier, have given rise to a higher degree of uniformity in pore size distribution of the samples after five years of treatment. On the other hand, nitrogen adsorption has revealed that the external surface area of the dismantled bentonite has decreased with respect to the initial area, especially near the heater (see also Section 5.2.5.7).

The interpretation of these results should be accomplished taking into account that, overall, the dry density of the dismantled bentonite is lower than the initial dry density of the blocks, whereas the water content is higher. The saturation experienced by the samples in the barrier and the associated swelling and global increase of volume (which implies a decrease in dry density from that of the compacted blocks –1.70 g/cm^3– to the average dry density of the barrier –1.58 g/cm^3–, see Section 4.4.2.3) is probably responsible for the pore size redistribution [69]

Grain size distribution

CTU determined grain size distribution in samples taken from different sections at the inner, middle and outer ring (36 samples) and in a sample taken from a non-installed block used as a reference [70]. No significant variations were found in the different samples tested (Figure 5.86).

Plasticity

CTU determined the plasticity index on samples taken from different sections at the inner, middle and outer ring (36 samples) and in a sample taken from a non-installed block used as a reference [70].

All the samples showed an extremely high plasticity, the liquid limit of these materials being in the interval 107–138 percent and the plasticity index in the interval 53–85 percent. The latter is closely related to the water content of the samples and thus to their position in the barrier, the plasticity index clearly increasing with water content (Figure 5.87). The lowest values of liquid limit and plasticity index were obtained from blocks subjected to the highest temperature. This increase in plasticity in samples from the outer ring of the barrier might be linked to the

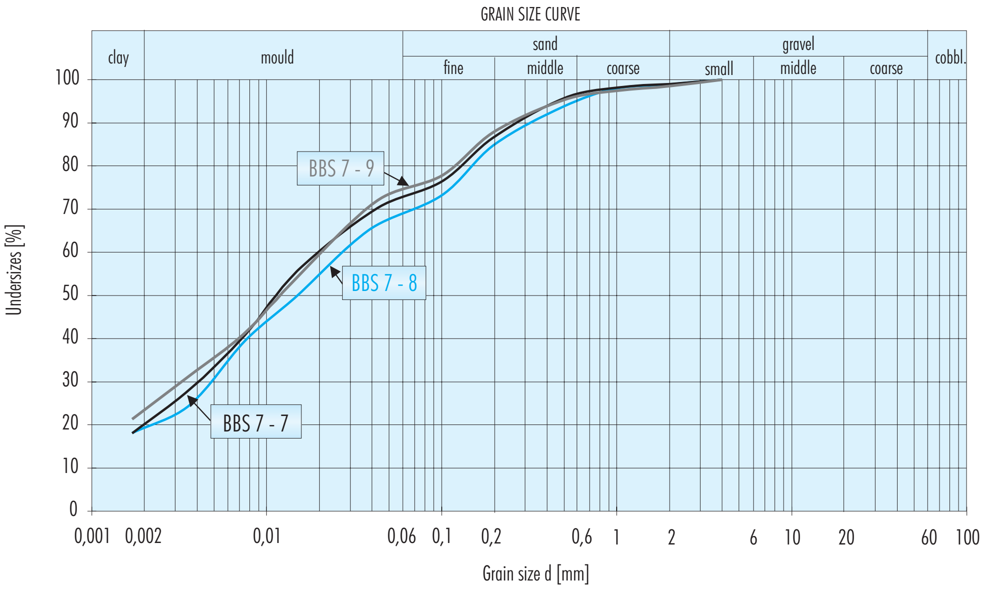

Figure 5.86: Grain size curves of samples from blocks from section S7.

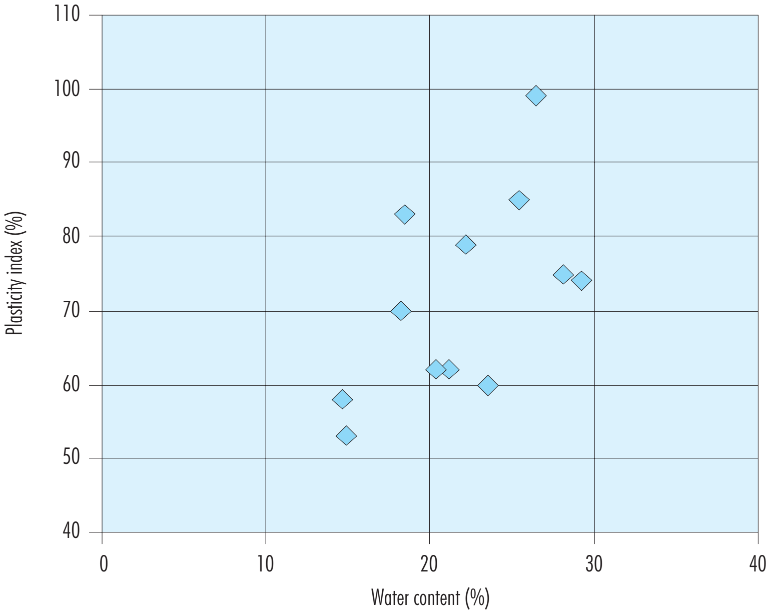

Figure 5.87: Plasticity index of the dismantled bentonite as a function of water content and position along the radius (CTU measurements).

increase in exchangeable sodium that took place near the gallery wall (see Section 5.2.5.3)

5.1.7.2. Thermal properties

The thermal conductivity of intact samples from different sections was measured by CIEMAT and CTU. The results obtained are plotted in Figure 5.88, where the good agreement between the results obtained by both laboratories may be appreciated: the thermal conductivity is higher in the samples with higher water content, *i.e.* those that were placed near the gallery wall. Once remoulded and dried, all the dismantled bentonite showed the same thermal conductivity overall, without any tendency related to the position occupied by the samples in the barrier (Section 4.4.2.4 of [70]).

The comparison of the values obtained in intact samples with those expected for untreated samples of the same dry density and water content revealed a certain decrease in the original thermal conductivity related to heating (Figure 5.89).

5.1.7.3. Hydraulic properties

Permeability

The saturated permeability of the dismantled bentonite remoulded and compacted to different dry densities was measured by Euro-Géomat in samples with and without joints, as well as by CIEMAT and EIG EURIDICE in intact samples. The values obtained do not correspond to the permeability of the bentonite at the moment it was retrieved; in the case of remoulded samples for obvious reasons, and in the case of intact samples, because they have been saturated to perform the determination, and permeability depends greatly on the degree of saturation. The usefulness of this kind of measurements is related to the discovery of irreversible modifications. Euro-Géomat found that the permeability of the samples remoulded from the dismantled bentonite (both with and without joints) is exponentially related to dry density [70]. The results obtained by Euro-Géomat, EIG EURIDICE and CIEMAT are plotted in Figure 5.90, together with the fittings found

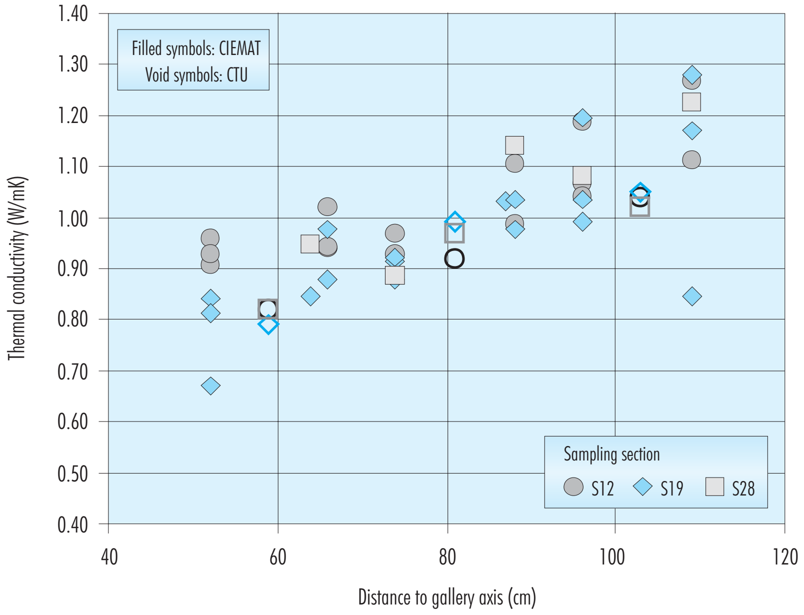

Figure 5.88: Thermal conductivity measured in the dismantled bentonite by CIEMAT and CTU.

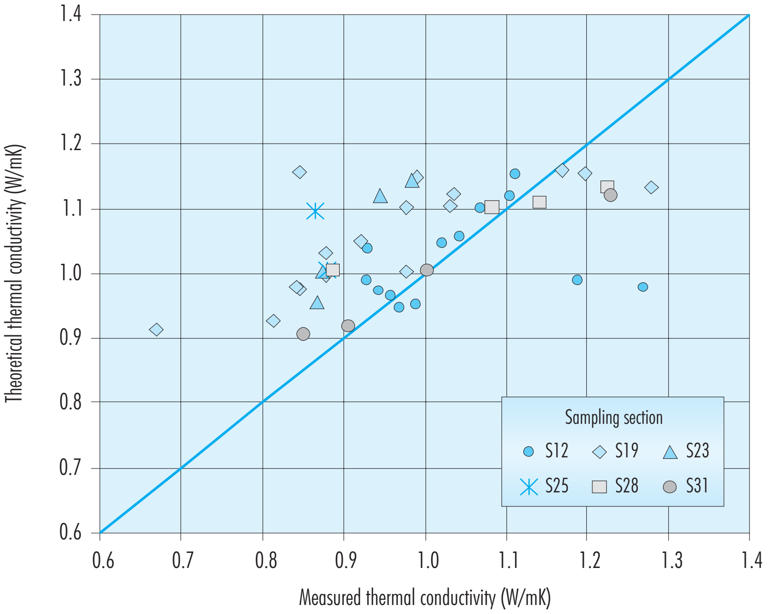

Figure 5.89: Thermal conductivity values measured by CIEMAT, compared to the theoretical values obtained with Equation 5.2 (Section 5.1.1.2).

for the untreated bentonite (Equations 5.7 and 5.8, Section 5.1.2.1). The permeability values measured are low and strongly dependent on dry density. Both the values measured by Euro-Géomat in samples remoulded from the dismantled bentonite and the values measured by EIG EURIDICE in intact samples of the dismantled bentonite are higher than those for untreated samples of similar dry density, especially for the higher densities. However, for intact samples of the dismantled bentonite, CIEMAT found that the permeability has not clearly changed in any sense after the five years of treatment. On the other hand, measurements of hydraulic conductivity performed in specimens of FEBEX bentonite that had been subjected to thermo-hydraulic treatment in cells for periods of time of between 6 and 24 months revealed a slight increase of saturated permeability with respect to the untreated sample (Section 5.1.4.5 "Modification of hydro-mechanical properties" and [67]).

In summary, the hydraulic conductivity of the dismantled bentonite is clearly related to dry density and the latter in turn is related to the position of the block in the barrier. The values of hydraulic conductivity measured for the samples of lower density (more hydrated) are of the same order as the theoretical values, but for samples of higher densities the values obtained are widely dispersed and do not show any clear tendency. This may be due to the complexity of the experimental techniques applied, which increases for the higher densities, giving rise to less accurate values. It is considered that the increase of saturated permeability with respect to the permeability of the untreated FEBEX bentonite found by Euro-Géomat in samples remoulded from the dismantled bentonite, and by EIG EURIDICE in intact samples of the dismantled bentonite, may be a result of the different methodology employed for its determination and of the process of remoulding.

Retention capacity

The retention curve was determined for different samples taken from Grimsel by CIEMAT [70]. The samples were trimmed from blocks and submitted to different relative humidities (suctions) imposed by sulphuric acid solutions. The specimens were unconfined and at laboratory temperature during the determinations.

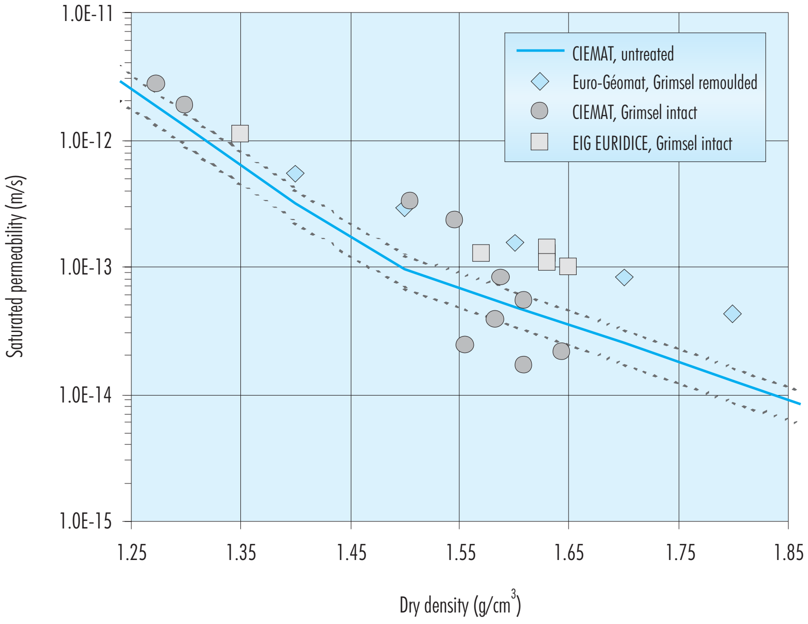

Figure 5.90: Permeability values of the dismantled bentonite (intact and remoulded) and of untreated FEBEX bentonite.

The samples were initially submitted to a suction of 4 MPa, which for most of them meant an increase in water content and a decrease in dry density. Subsequently, they were progressively dried by applying increasingly higher suctions: 14, 33, 75 and 120 MPa. The latter value corresponds approximately to the suction the blocks had prior to their installation in Grimsel (room temperature and relative humidity.)

The samples closer to the gallery wall had initial higher water contents and lower dry densities. After being subjected to a suction of 4 MPa, most of the samples experienced a density decrease and an increase in water content. In the following suction steps the water content of all the samples progressively decreased and the dry density increased. The evolution of all the samples was quite similar, regardless of their positions in the barrier. Moreover, the initial differences attenuated for increasing suction.

The results obtained for the samples from section S23 have been drawn in Figure 5.91 along with the evolution of water content in wetting paths for untreated FEBEX clay obtained with Equation 5.10 (Section 5.1.2.3) for initial dry densities of 1.40 and 1.60 g/cm^3. The results obtained for the samples from section S31 are plotted in Figure 5.92. Although the path followed by the dismantled bentonite has been of sudden wetting (from the initial suction to suction 4 MPa, not shown in the figures) and subsequent drying to suction 120 MPa, it is clear that the evolution of water content experienced by the samples from sections S23 and S31 is of the order of that expected for untreated FEBEX samples of similar initial dry density. The tendency towards a higher retention capacity observed in the dismantled bentonite may be accounted for by hysteresis, since the water content for a given suction is slightly higher in a drying after wetting path than in a wetting path [49, 50, 71]. It may be concluded that the water retention capacity observed in the dismantled bentonite is similar to that of samples of untreated FEBEX clay compacted to the same dry density and subjected to similar suctions.

On the other hand, the relative humidity of some of the dismantled blocks was measured with capacitive sensors in the laboratory. The suction values measured are plotted in Figure 5.93 as a function of position in the barrier. The values registered by the sensors placed in Grimsel in sections C, E1 and F1 just before dismantling (Section 4.5.4.2) are also plotted in the figure. There is good agreement between the measurements taken in the laboratory and those taken "in situ" before dismantling, this corroborating the inertia of the blocks to change their water contents if they are well packed and the reliable performance of the "in situ" instrumentation.

The suction values measured in the laboratory have been related to the water contents determined in the same blocks and in the same positions and are plotted in Figure 5.94 in the form of a retention curve. The curve determined for untreated FEBEX bentonite compacted at dry density 1.60 g/cm^3 in constant volume cells kept in desiccators with sulphuric acid solutions is also plotted in the figure (Figure 5.15). This curve was obtained following a wetting path, which is the same process experienced by the dismantled bentonite. The samples with a dry density lower than 1.60 g/cm^3 have higher water contents for the same suction than the untreated sample with a density of 1.60 g/cm^3, whereas the contrary occurs for samples of higher dry density, which is the expected trend. Overall, the points obtained for the dismantled blocks follow closely the curve for the untreated samples, and no appreciable change of the retention capacity of the FEBEX clay after five years under repository conditions has been detected.

5.1.7.4. Mechanical properties

Swelling capacity

The swelling properties were checked by swelling under load tests performed with intact samples (CIEMAT) and by determination of the swell index and the swelling pressure of remoulded samples (CTU and Euro-Géomat). All these determinations may indicate if there have been irreversible changes in the swelling capacity of the clay, but the values obtained do not correspond to those of the samples when they were placed in the barrier, especially those that have been obtained from remoulded samples.

CIEMAT performed saturation (or swelling) under load tests on twelve samples trimmed from different dismantled bentonite blocks. The samples were saturated in oedometers with deionised water under a vertical pressure of 0.5 MPa at laboratory temperature. The swelling strain experienced by the specimens upon saturation was recorded as a function of time up to stabilisation.

The samples closer to the gallery wall had higher initial water content and lower initial dry density. The swelling capacity is related to both, increasing with initial dry density and decreasing with initial water

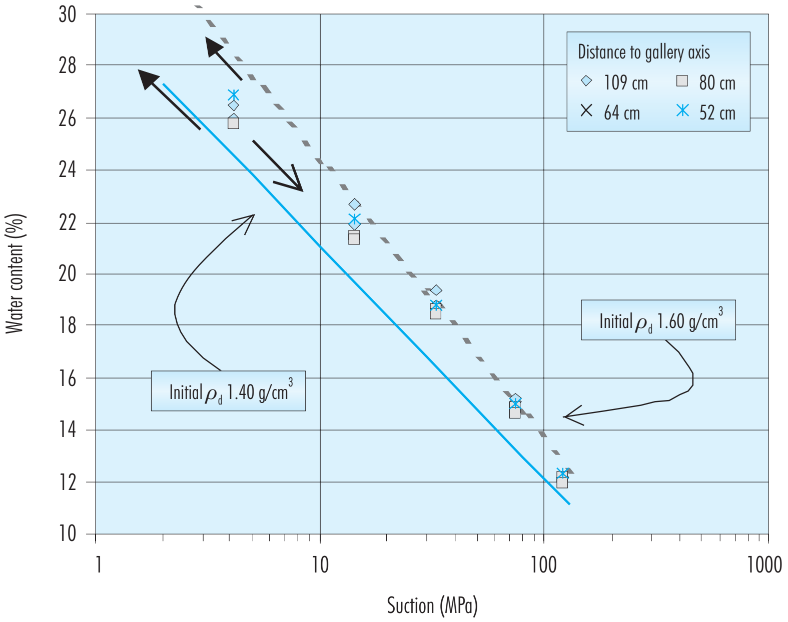

Figure 5.91: Evolution of water content in a drying path for samples from section S23. The lines correspond to untreated FEBEX bentonite in wetting paths (obtained with Equation 5.10).

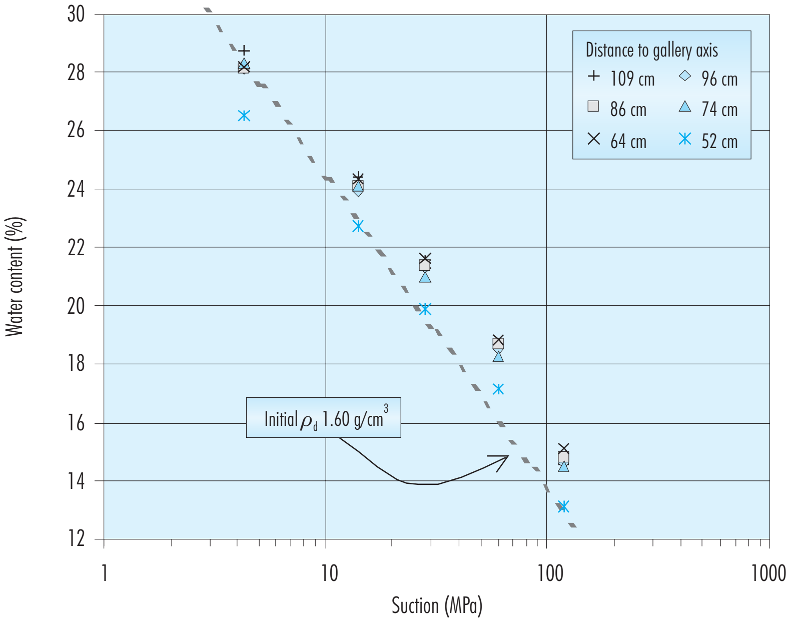

Figure 5.92: Evolution of water content in a drying path for samples from section S31. The line corresponds to untreated FEBEX bentonite in a wetting path (obtained with Equation 5.10).

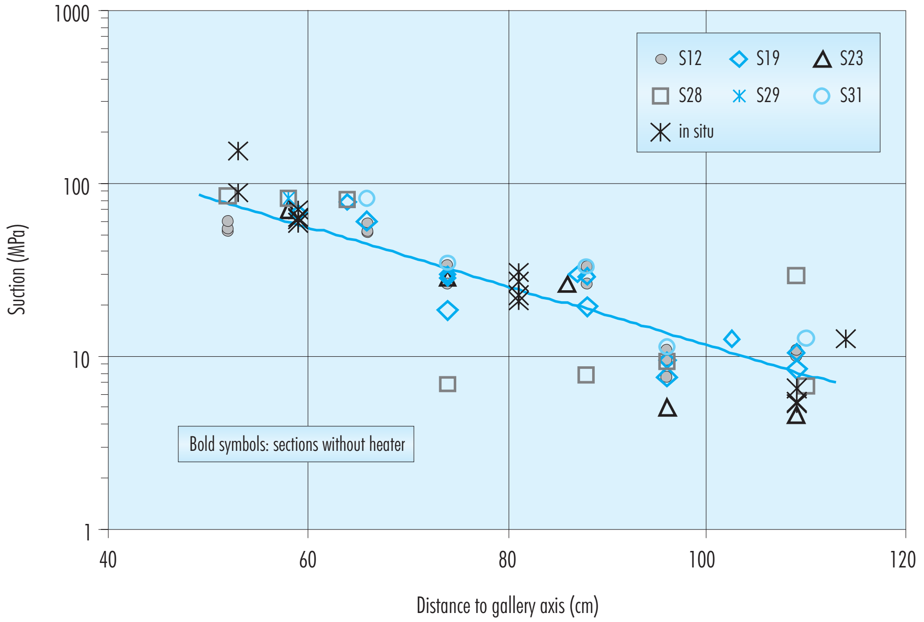

Figure 5.93: Suction values measured with capacitive sensors "in situ" before dismantling (instrumented sections C, E1 and F1) and in laboratory. The line is a fitting for all the laboratory measurements..

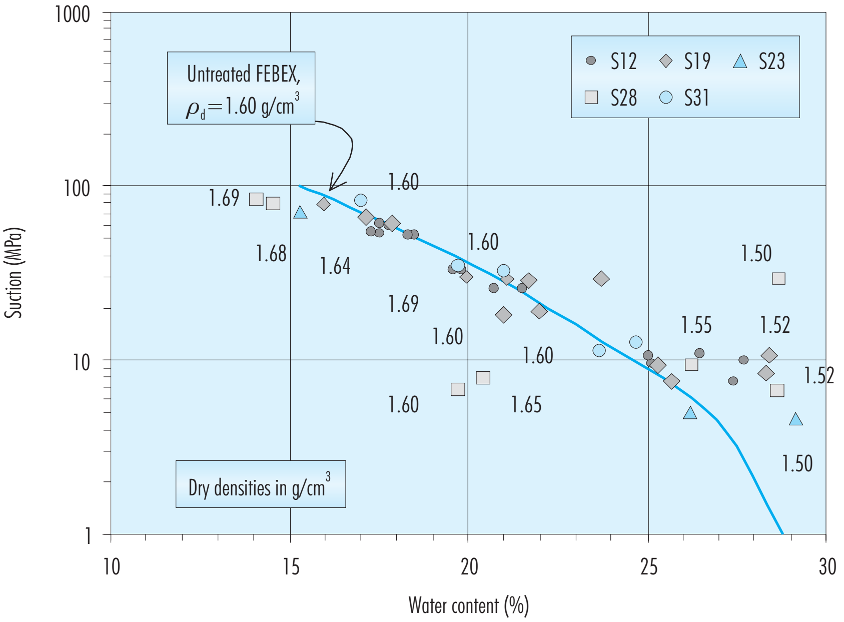

Figure 5.94: Suction/water content relationship as determined from sensor measurements in the laboratory in blocks from different sections (points) and determined in untreated FEBEX samples by control of relative humidity at constant volume (line)

content. For this reason, the final strain of the samples closer to the heater is higher, as may be seen in Figure 5.95.

The vertical strains actually measured in the tests are compared in Figure 5.96 with the theoretical values obtained with Equation 5.21 (Section 5.1.3.4) for untreated FEBEX bentonite compacted at the same initial dry density, with the same water content and saturated under a vertical load of 0.5 MPa. It may be observed that the final swelling strains of the dismantled bentonite are of the order of those expected for the untreated FEBEX bentonite.

The results presented above, obtained from intact samples, show that after five years of being subjected to repository conditions the swelling capacity of the bentonite has not irreversibly changed with respect to the capacity of untreated samples of the same dry density and water content. The results obtained with remoulded samples point in the same direction. Swelling pressure was determined for samples of the dismantled bentonite remoulded and compacted to different dry densities by CTU and Euro-Géomat [70]. The results obtained are plotted in Figure 5.97 together with the correlation determined by CIEMAT for untreated FEBEX samples (Equation 5.16, Section 5.1.3.3). In all cases, the initial water content of the bentonite was hygroscopic. Despite the fact that the methods employed by the different laboratories are quite different, the swelling pressure values obtained in the dismantled bentonite are within the expected range of variation of this property for untreated FEBEX bentonite. The results obtained by Euro-Géomat refer also to samples with joints, since they have not found differences in swelling pressure development in samples with and without joints.

Compressibility

The blocks installed in the FEBEX "in situ" test at Grimsel were manufactured by applying uniaxial vertical pressures of between 40 and 45 MPa (Section 4.3.1.2), which would correspond approximately to the preconsolidation stress of the clay. However, the modification of the structure of the sample – for example as a result of hydration under low load, with which more open structures with higher levels of porosity are obtained – may cause the value of preconsolidation to decrease. This may

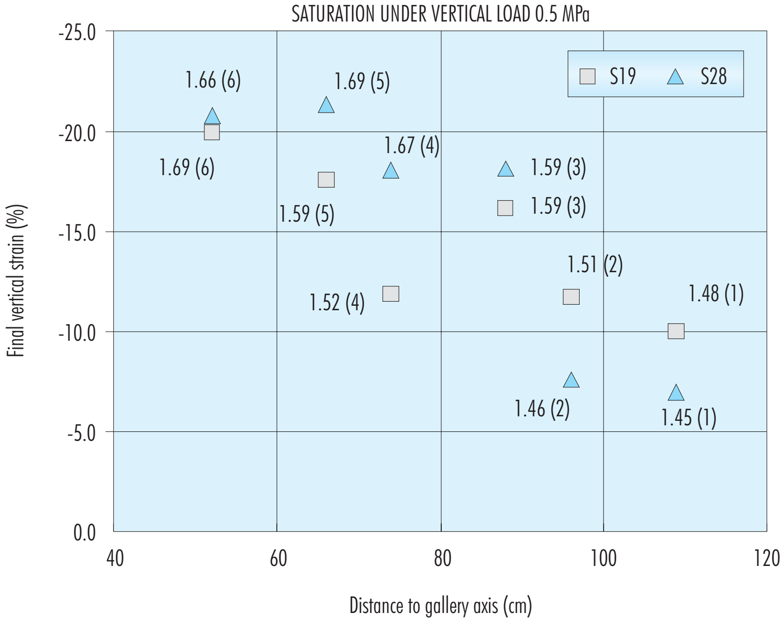

Figure 5.95: Vertical strain after saturation under 0.5 MPa of samples from sections S19 and S28 (the initial dry density of the samples is indicated in g/cm^3 and their position by consecutive numbers from 1 –close to the gallery wall– to 6 –close to the heater–).

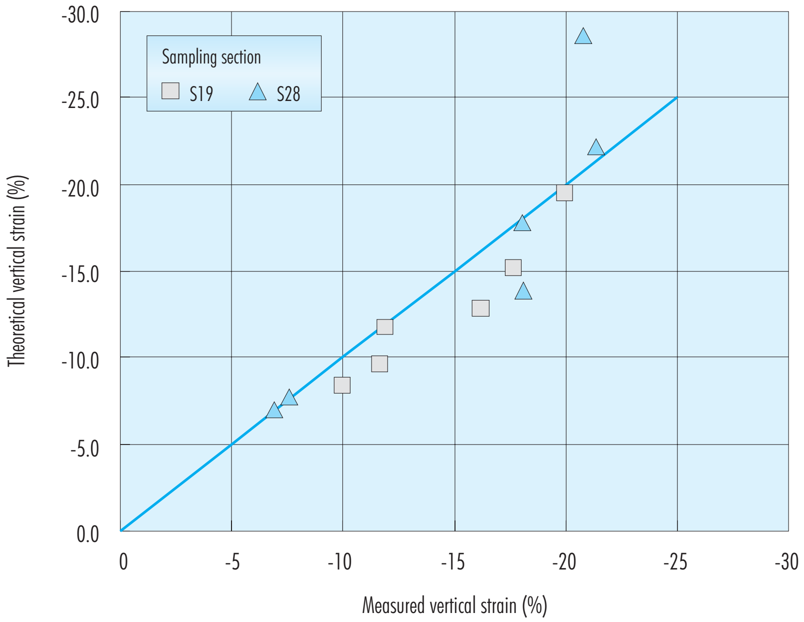

Figure 5.96: Final strain reached in soaking tests under a vertical pressure of 0.5 MPa compared to the theoretical value obtained with Equation 5.21.

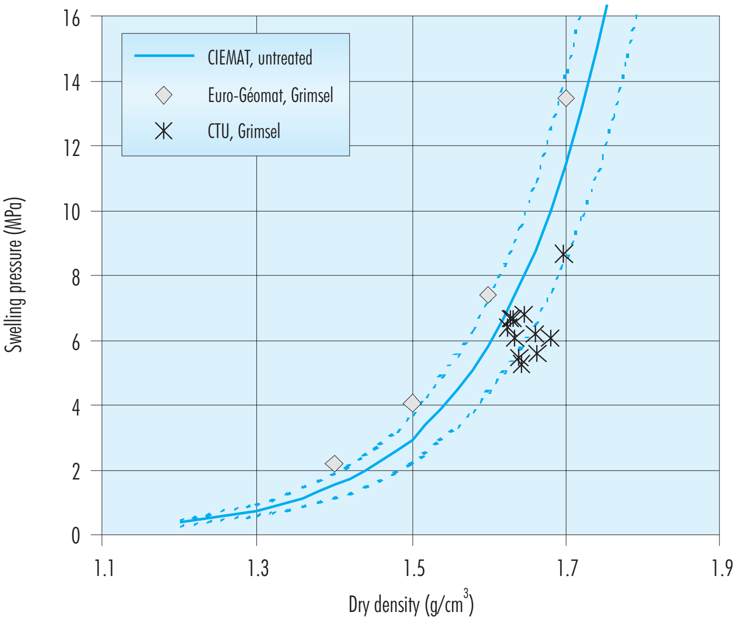

Figure 5.97: Swelling pressure values obtained by different laboratories in samples remoulded from the dismantled bentonite and in untreated bentonite

be analysed through determination of the apparent preconsolidation pressure (σ_p') in graphs showing the evolution of void ratio due to increasing load under constant suction. For this reason, the preconsolidation pressure of the dismantled bentonite was determined under oedometric conditions and with control of suction.

Twelve samples were trimmed from different dismantled blocks and tested under the suction corresponding to their water content, according to the water retention curves (Figure 5.25). Suction was set by means of sulphuric acid solutions. The sample equilibrates at the target suction under a low vertical load. Subsequently, the sample is loaded progressively up to 2, 4, 6, 12 and 20 MPa. The tests were performed at laboratory temperature.

To perform these tests, the sulphuric acid solution oedometric cells were adapted to withstand the high pressure supplied by an oedometric frame equipped with a load cell (Figure 5.98).

One example of the oedometric curves obtained is shown in Figure 5.99. The preconsolidation pressure is lower than 10 Mpa for all the samples, and consequently has decreased with respect to the initial value, this being accounted for by the volume increase experienced by the bentonite during hydration. Furthermore, the preconsolidation stresses found are lower the lower the suction applied during the test, *i.e.* the higher the water content reached during the “in situ” test. These values are plotted as a function of suction in Figure 5.100, in which the apparent preconsolidation stresses found for samples of untreated FEBEX bentonite compacted initially to similar dry densities and subjected to different suctions are also shown [49, 56]. The latter values correspond to the consolidation of samples initially hydrated under low vertical stresses and, since they have swollen during the wetting more than the dismantled bentonite (which was “confined”), their preconsolidation pressures are even lower. On the other hand, the values of the apparent preconsolidation stress obtained in the dismantled bentonite are in agreement with the maximum stresses recorded by load cells in the “in situ” test (Section 4.5.4.3).

Strength

The uniaxial strength of the dismantled bentonite – determined by CTU in slightly dried blocks (Figure 5.101) – is higher in the direction of compaction of

Figure 5.98: Suction controlled oedometer cells installed in the frames for the performance of high-pressure consolidation tests.

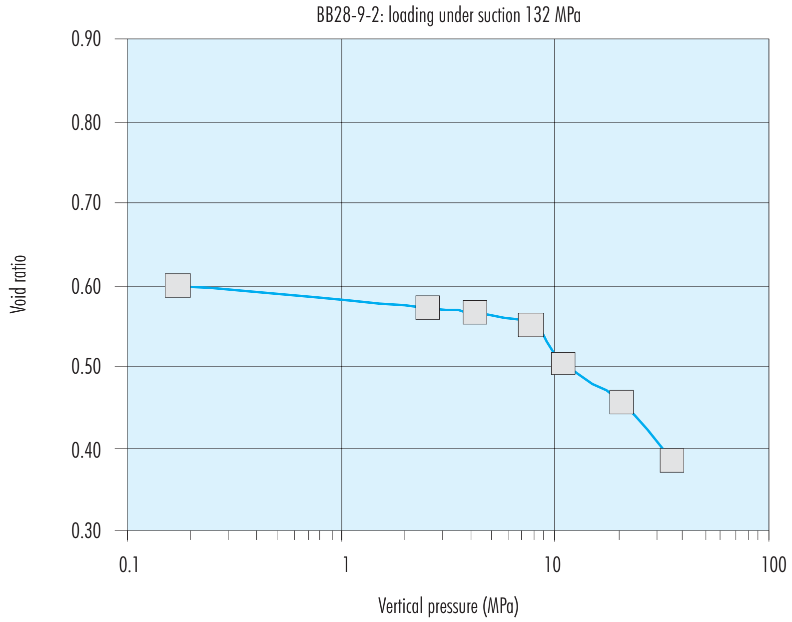

Figure 5.99: Oedometric curve of suction controlled tests performed with the dismantled bentonite.

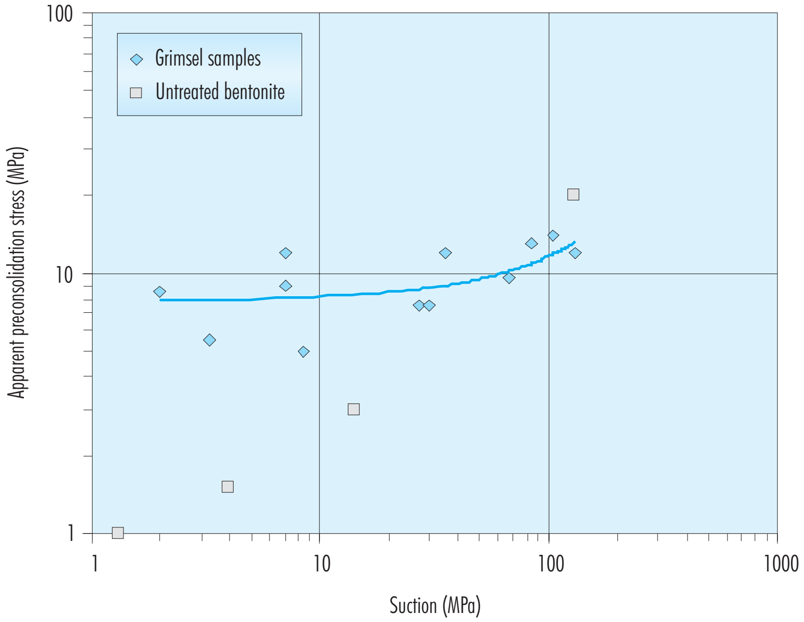

Figure 5.100: Apparent preconsolidation stress of the dismantled bentonite and of untreated bentonite determined under constant suction corresponding to the water content of the clay.

the blocks than in the perpendicular, and tends to be lower for the samples that were subjected to higher temperature.

5.2. THG tests

5.2.1. Pore water chemistry of the bentonite

Knowledge of the pore water chemistry in the clay barrier is essential for performance assessment, since the pore water composition is an important parameter influencing the release and transport of radionuclides, canister corrosion, dissolution of the waste matrix, sorption on mineral surfaces, solubility of radionuclides, etc.

However, the problem of isolating the "true" soil solution to obtain reliable data on the pore water chemistry in very low permeable and scarce water content clay systems, has not yet been solved. Therefore, indirect methods based on geochemical modelling are applied to deduce the chemical composition of the pore water [72, 73, 74, 75, 76, 77, 78, 79, 80, 12, 81].

Thus, the methodology followed to obtain the best possible estimation of the FEBEX bentonite pore water composition under initial repository conditions and at saturation in the compacted state has combined different pore water extraction methods, a detailed physico-chemical and mineralogical characterisation, and geochemical modelling. It has included: a) determination of the physical and physico- chemical properties of the bentonite; b) determination of the accessory and trace minerals in equilibrium with the bentonite pore water; c) aqueous extracts at different S:L ratios to determine the concentration of dissolved and exchangeable ions; d) squeezing tests; e) determination of the cation exchange occupancies using different index cations; and f) determination of selectivity coefficients for the cation exchange reactions.

This investigation has made it possible to gain insight into the water-bentonite interaction processes controlling the physico-chemical parameters and the chemistry of the system and to distinguish between the types of water and their distribution in the clay/water system (adsorbed water, interlayer water and pore water), as well as the respective volumes accessible to cations and anions.

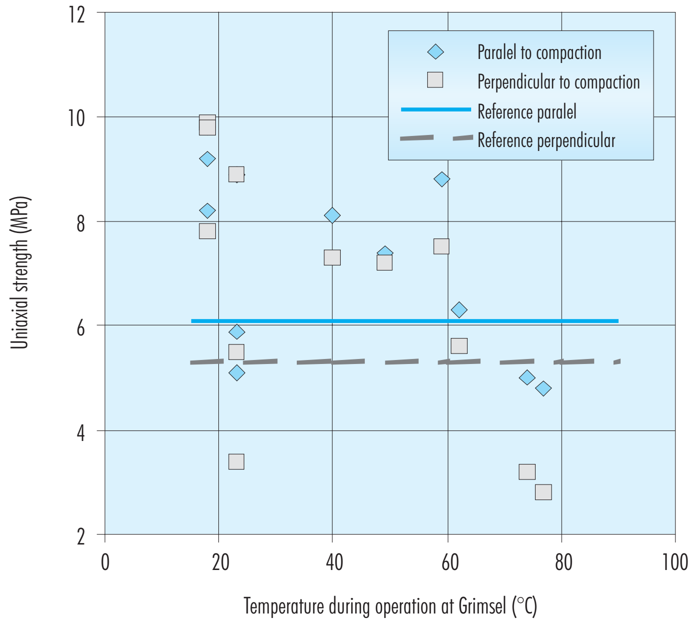

Figure 5.101: Results of the uniaxial strength tests in blocks of dismantled bentonite dried at 70° C for 24 hours.

5.2.1.1. Bentonite pore water extraction and analysis: solid-water interaction processes

A series of bentonite-water interaction laboratory tests was performed [13] with the aim of providing a database for the definition of bentonite pore water. These tests were carried out both with high solid to liquid (S:L) ratios (squeezing tests) and low S:L ratios (aqueous extracts tests). In both types of tests, in addition to the chemical composition, exchangeable cations were analysed in order to determine the selectivity coefficient of the exchange reactions [12, 10].

Pore water obtained by squeezing

The pore water of bentonite samples equilibrated at different water contents (23.8, 26.5 and 30.0 percent, equivalent to S:L ratios of 4.2:1, 3.8:1 and 3.3:1, respectively) was obtained by squeezing at 60 MPa. The water contents chosen correspond to the saturation conditions of the bentonite compacted at a dry density of 1.65, 1.57 and 1.49 g/cm^3, respectively. The contact time of the deionised water and the bentonite (more than three months) and the analysed pore water composition have been considered acceptable, since the results obtained are comparable to those obtained from unaltered core samples from the FEBEX bentonite deposit (Cortijo de Archi-

Table 5.12
Chemical composition of FEBEX bentonite pore water extracted by squeezing for three water contents in mg/L

Dissolved species and physico-chemical parameters	Water content (%)		
	30	26.5	23.8
Cl^-	2200	3600	4000
SO_4^{2-}	603	1100	1260
Br^-	4.9	4.9	9.1
HCO_3^- (1)	67	131	133
SiO_2	10.9	14.4	N.D.
Al^{3+}	0.34	N.D.	0.12
Ca^{2+}	295	450	510
Mg^{2+}	385	410	390
Na^+	800	1725	2100
K^+	7.5	54	15
Sr^{2+}	6.2	6.9	7.5
pH	7.49	7.29	7.38
Conductivity (μS/cm)	7530	11690	13230
Ionic Strength (*M*)	0.11	0.17	0.19
Water type	Na-Mg-Cl	Na-Cl	Na-Cl
S:L ratio	3.3:1	3.8:1	4.2:1

(1) Total alkalinity as mg/L of HCO_3^-; N.D.: not determined.

dona, Spain). However, with this method only a fraction of the total pore water can be extracted.

According to the test results, the pore water of the FEBEX bentonite is an Na-Cl-type water with a high content of magnesium and calcium, high electrical conductivity and neutral pH (Table 5.12).

Aqueous extraction tests

Aqueous extractions were carried out at different low S:L ratios: 1:1, 1:2, 1:4, 1:8, 1:10 and 1:16 with deionised and granitic water (the chemical composition of the latter is shown in Table 5.5), in order to analyse the possible mineral phases controlling the aqueous phase and the behaviour of the exchange cations. The results are shown in Table 5.13 and Table 5.14.

Discussion

Analysis of the results presented above allows the following conclusions to be drawn concerning the processes that govern the water/bentonite interaction [13]:

- ❏ The chemical composition of the pore water depends on the S:L ratios involved in the system, and is basically controlled by ion exchange reactions and dissolution/precipitation reactions of the more soluble trace minerals in the bentonite.

Table 5.13
Aqueous extract chemical composition of FEBEX bentonite in contact with deionised water at different S:L ratios (interaction time = 48 hours) in mg/L

Dissolved species and physico-chemical parameters	Solid to liquid ratio					
	1:1	1:2	1:4	1:8	1:10	1:16
Cl^-	754.0 ± 95.5	312.7 ± 27.1	149.6 ± 11.8	73.4 ± 5.4	55.25 ± 5.0	36.33 ± 1.5
SO_4^{2-}	860.5 ± 97.9	415.1 ± 75.1	200.6±20.3	105.7 ± 9.0	85.0 ± 3.4	50.7 ± 2.9
$HCO_3^{-\ (1)}$	181.8 ± 16.9	164.6 ± 4.3	154.2 ± 5.6	139.0 ± 5.0	138.3 ± 8.7	133.9 ± 3.3
Al^{3+}	1.27 ± 0.60	0.26 ± 0.13	0.52 ± 0.62	1.17 ± 0.66	1.90 ± 1.24	2.07 ± 0.34
Ca^{2+}	47.0 ± 9.6	12.86 ± 2.12	4.27 ± 1.09	3.07 ± 0.06	3.13 ± 0.15	2.70 ± 2.34
Mg^{2+}	30.3 ± 4.7	7.91 ± 0.59	2.86 ± 0.44	1.51 ± 0.28	1.70 ± 0.14	2.60 ± 0.95
Na^+	820.0 ± 50.8	448.6 ± 24.1	246.0 ± 11.0	146.4 ± 5.4	127.5 ± 5.0	93.7 ± 3.8
K^+	14.0 ± 2.4	9.6 ± 2.1	6.1 ± 2.3	3.7 ± 1.1	6.7 ± 5.6	4.0 ± 0.5
Sr^{2+}	0.72 ± 0.07	0.20 ± 0.04	0.08 ± 0.01	N.D.	N.D.	0.03 ± 0.00
Fe^{3+}	1.49 ± 2.53	0.10 ± 0.06	0.20 ± 0.18	0.38 ± 0.25	0.49 ± 0.33	0.54 ± 0.11
SiO_2	22.1 ± 1.3	20.4 ± 1.1	18.6 ± 1.0	15.8 ± 0.3	16.8	17.4 ± 0.1
pH	8.19 ± 0.17	8.35 ± 0.12	8.73 ± 0.16	9.29 ± 0.13	9.48 ± 0.19	9.64 ± 0.21
Cond. (μS/cm)	4027 ± 398	2018 ± 105	1135 ± 45	678 ± 29	619 ± 24	475 ± 40
Clay mass[(2)]/ water (g/mL)	20/20	20/40	10/40	5/40	4/40	2.5/40

(1) Total alkalinity as mg/L of HCO_3^-; (2) Bentonite mass includes 14% of water content; N.D.: not determined

Table 5.14
Aqueous extract chemical composition of FEBEX bentonite in contact with granitic water at different S:L ratios (interaction time = 48 hours) in mg/L

Dissolved species and physico-chemical parameters	Solid to liquid ratio					
	1:1	1:2	1:4	1:8	1:10	1:16
Cl^-	682.5 ± 24.4	331.8 ± 10.6	163.9 ± 3.4	85.0 ± 3.5	70.0 ± 2.7	50.7 ± 8.1
SO_4^{2-}	839.7 ± 70.1	433.0 ± 26.6	207.0 ± 18.1	110.2 ± 1.6	86.7 ± 3.2	68.3 ± 0.6
HCO_3^- (1)	285.7 ± 35.0	256.6 ± 10.5	241.9 ± 8.1	224.4 ± 8.1	226.3 ± 6.7	209.3 ± 4.9
Al^{3+}	1.73 ± 0.23	0.14 ± 0.15	0.43 ± 0.57	0.72 ± 0.48	0.39 ± 0.13	0.31 ± 0.05
Ca^{2+}	49.75 ± 5.25	16.4 ± 3.29	6.05 ± 1.54	3.30 ± 1.47	4.07 ± 0.21	4.70 ± 1.04
Mg^{2+}	34.25 ± 1.26	10.34 ± 1.17	3.81 ± 0.29	2.00 ± 0.10	1.80 ± 0.10	1.73 ± 0.06
Na^+	887.5 ± 26.3	508.0 ± 8.4	290.0 ± 13.4	191.0 ± 8.9	180.0 ± 10.0	166.7 ± 20.8
K^+	15.0 ± 0.82	8.96 ± 0.40	7.96 ± 3.24	4.42 ± 0.78	4.93 ± 0.38	12.9 ± 10.5
Sr^{2+}	0.74 ± 0.04	0.22 ± 0.03	0.09 ± 0.02	N.D.	N.D.	N.D.
Fe^{3+}	0.46 ± 0.07	0.05 ± 0.00	0.18 ± 0.17	0.22 ± 0.14	0.05 ± 0.05	N.D.
pH	8.12 ± 0.14	8.31 ± 0.11	8.53 ± 0.07	8.83 ± 0.06	9.01 ± 0.01	9.00 ± 0.01
Cond. (μS/cm)	4445 ± 114	2402 ± 62	1348 ± 68	883 ± 44	835 ± 43	751 ± 67
Clay mass(2)/ water (g/mL)	20/20	20/40	10/40	5/40	4/40	2.5/40

(1) Total alkalinity as mg/L of HCO_3^-; (2) Bentonite mass includes 14% of water content; N.D.: not determined

- Chlorides and sulphates, as anions, and sodium, calcium and magnesium, as cations, predominate in the pore water chemistry of the bentonite. The ion concentrations are controlled by the dissolution of chlorides, the dissolution/ precipitation of carbonates and sulphates and cation exchange reactions in the smectite.

- The chloride concentration of the bentonite pore water may be estimated from both types of tests, squeezing (high S:L ratios) and aqueous extracts (low S:L ratios) indistinctly; since chloride concentration follows a linear relationship as a function of S:L ratio (Figure 5.102a). The mineral phase possibly controlling the chloride concentration in the aqueous phase is halite and, according to the saturation index values, all the chlorides must be dissolved in the pore water (Figure 5.102b).

- The sulphate concentration is controlled by gypsum solubility. Therefore, the sulphate concentration in the bentonite pore water must be estimated by taking gypsum equilibrium into account.

- The concentration of bicarbonate in the pore water is virtually controlled by equilibrium with calcite, although the partial pressure of CO_2 must be taken into account.

- The cation concentrations in the pore water are basically controlled by the exchange reactions in the smectite. These reactions seem to be induced by the dissolution of the more soluble impurities (calcite and gypsum) in the bentonite, which in turn depends on the S:L ratio. Thus, the exchange complex may be modified by the variation of the pore water in equilib-

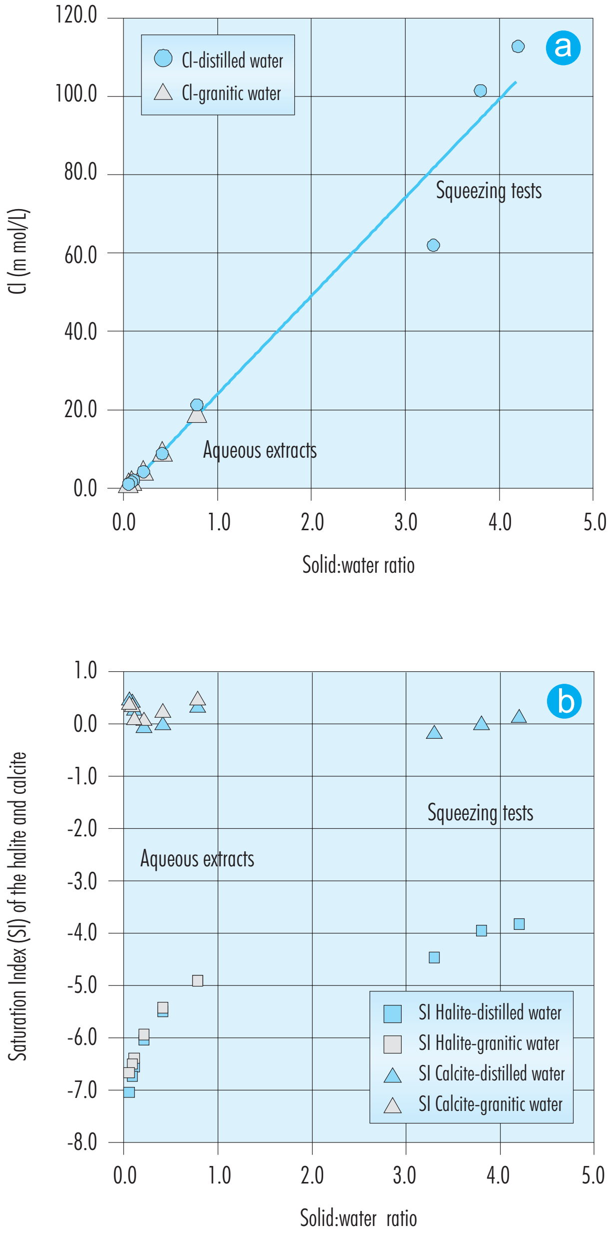

Figure 5.102: a) Chloride concentrations as a function of S:L ratio; b) halite and calcite saturation index as a function of S:L ratio.

rium with the bentonite resulting from the dissolution of trace minerals (Figure 5.103).

- The dissolution of calcite produces a rapid exchange of sodium with calcium in the exchangeable positions of the bentonite. For this reason, this process must be taken into account in the experimental procedure to determine the amount of exchangeable cations, when a bentonite presents a low content of soluble mineral traces (calcite, gypsum), as is the case with the FEBEX bentonite (see Sections 2.3.4 and 5.2.1.4).

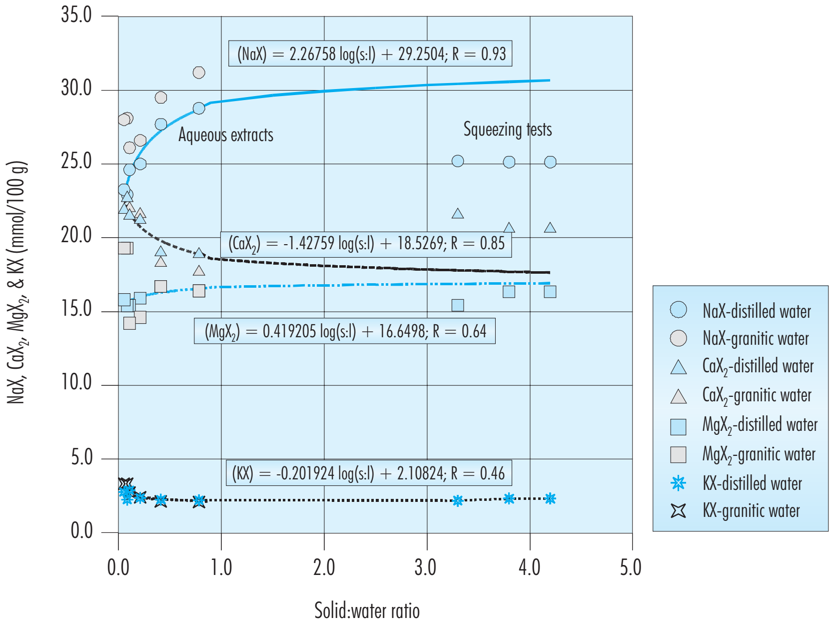

Figure 5.103: Sodium, calcium, magnesium and potassium content at the bentonite exchange positions (NaX, CaX_2, MgX_2 and KX) as a function of S:L ratio.

5.2.1.2. Pore water obtained by squeezing as a function of applied pressure

800 g of FEBEX bentonite were remoulded with deionised water to acquire an initial water content of 30.9 percent. After stabilisation and homogenisation of the solid and liquid phases, 3 months, a squeezing test was performed, in which the pressure was increased by steps from 10 MPa to 100 MPa. The variation of the height of the sample was measured during the test by means of an automatic displacement sensor built in to the hydraulic press. During the test, each pressure step was prolonged to the extent required to obtain all the extractable water. A total amount of water of 65.4 mL was collected after 222 days.

The variation of the dry density of the sample for each pressure step is shown in Figure 5.104, along with empirical correlations between both variables. The variation of the water content of bentonite as a function of its dry density during the squeezing test is plotted in Figure 5.105. In this figure, the theoretical water contents needed to fully saturate the bentonite for each dry density are also plotted. The water contents reached in the squeezing test are similar to the theoretical water contents at saturation for each dry density. This implies that the water collected in each pressure step is the excess water that exists between the saturation water content at an initial and a final dry density, reached when the pressure increases.

The variation of the chemical composition of the pore water as a function of the applied squeezing pressure is shown in Figure 5.106 and Figure 5.107. The concentration of Cl^-, SO_4^{2-}, Na^+ and Ca^{2+} in each step decreases as a function of pressure. This behaviour is not similar to that obtained with consolidated clay rocks composed of non-expansive clays, such as the Opalinus Clay, in which constant concentration is obtained up to pressures of 200 MPa [82].

The bicarbonate concentration increases, indicating some carbonate dissolution process for squeezing pressures above 70 MPa (Figure 5.108). These waters are under-saturated in gypsum and oversaturated in calcite and dolomite.

The overall decrease of chemical concentration with pressure might indicate: i) an ion ultra-filtration through the clay, or 2) a dilution of the ionic con-

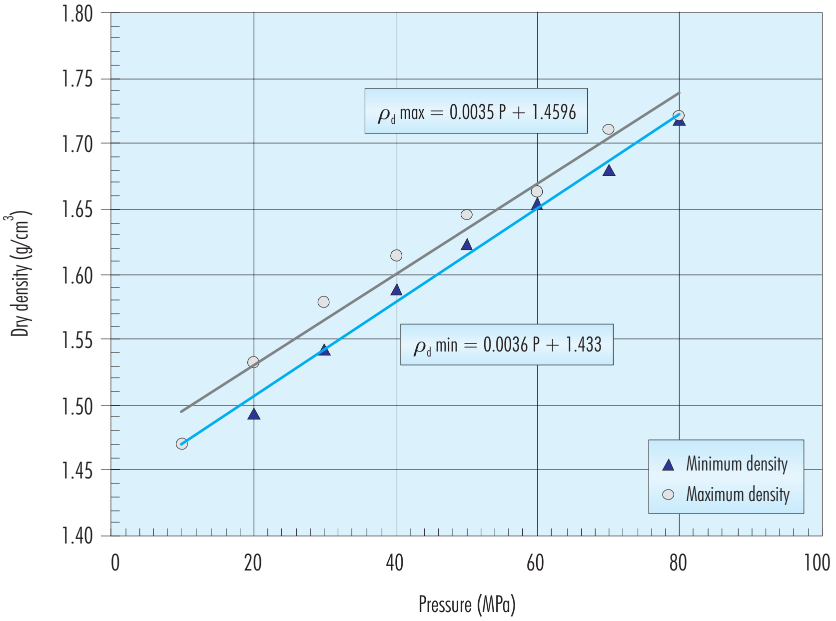

Figure 5.104: Variation of maximum and minimum bentonite dry density (ρ_d) as a function of squeezing pressure (P).

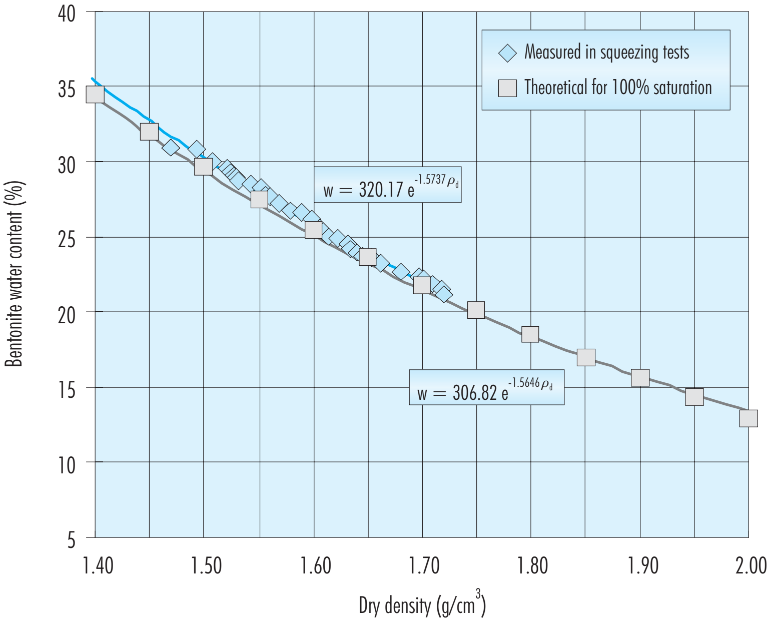

Figure 5.105: Variation of bentonite water content (w) as a function of dry density (ρ_d) of the sample.

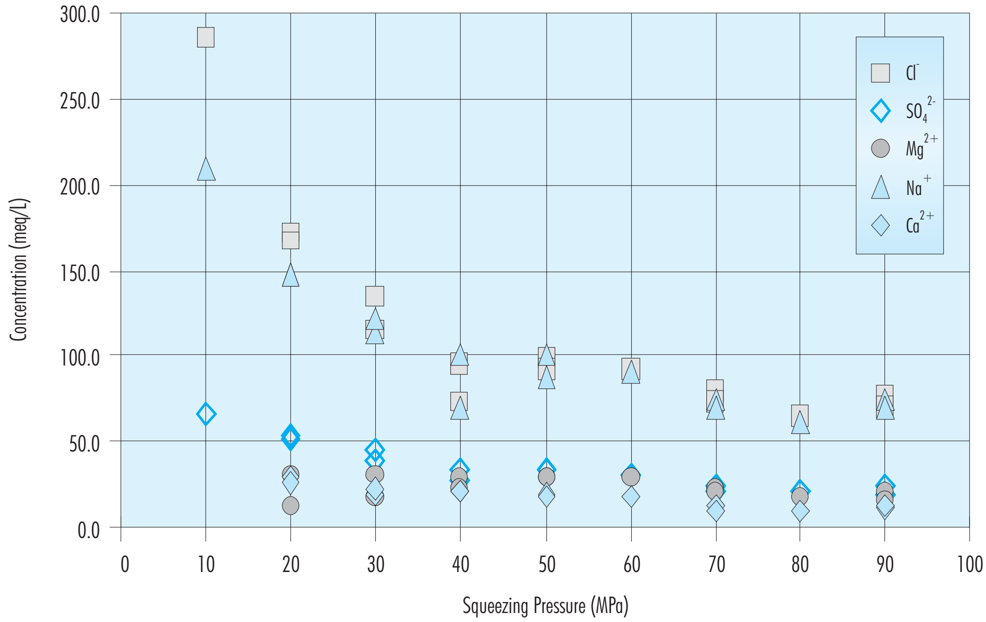

Figure 5.106: Variation of ion content as a function of squeezing pressure

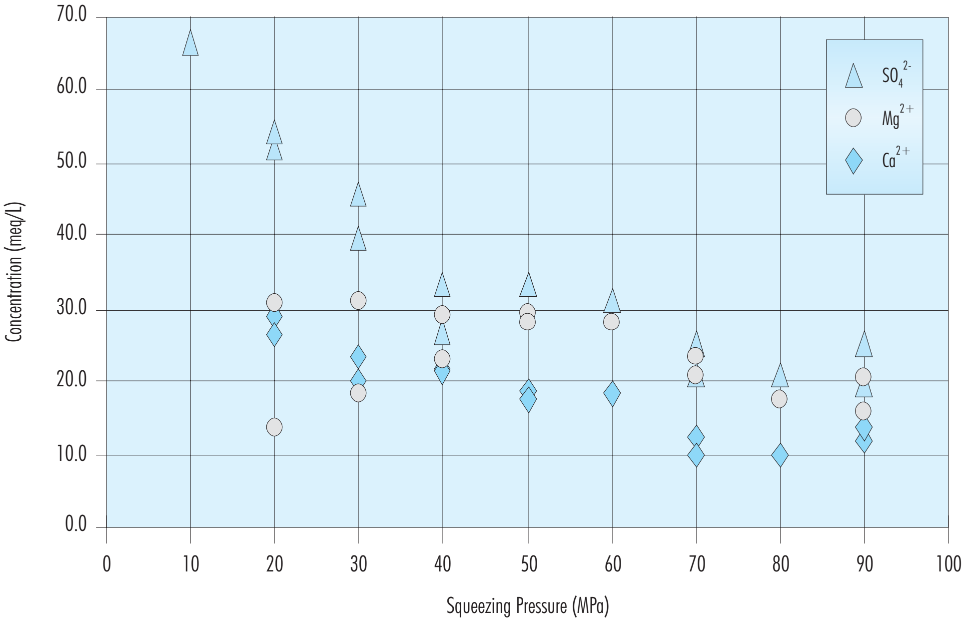

Figure 5.107: Sulphate, magnesium and calcium content as a function of squeezing pressure

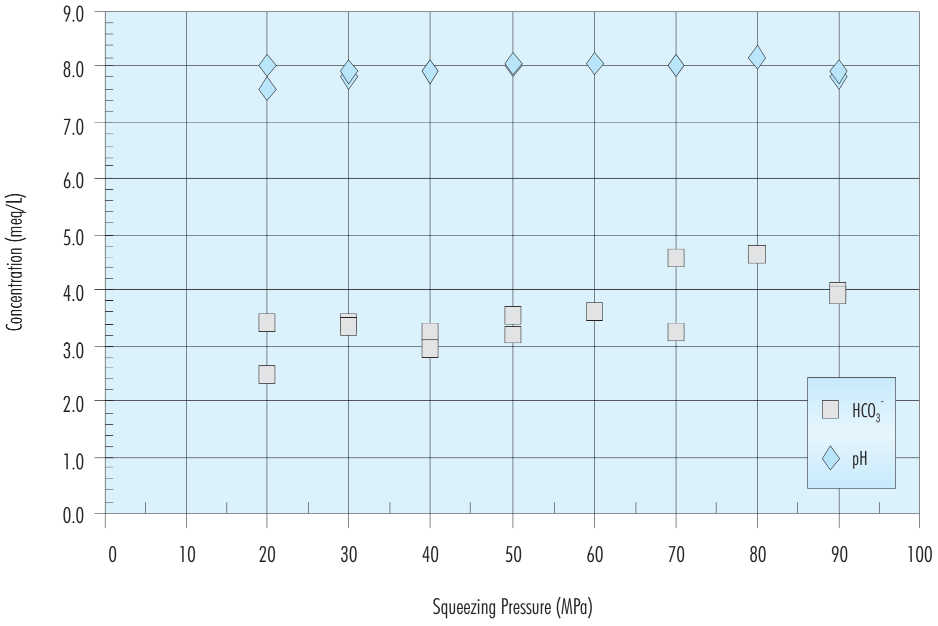

Figure 5.108: Bicarbonate content and pH as a function of squeezing pressure

centrations due to some part of the internal or interlaminar water being extracted when pressure increases. According to the results on the variation of internal/external water as a function of dry density (see Section 5.2.1.3; Figure 5.118), the greater part of the water in the bentonite is internal and, when dry density increases, the amount of water in the pore space decreases (internal + external). For this reason, it is very likely that during squeezing the interlaminar water is released, diluting the chemical composition of the bentonite pore water.

Consequently, the squeezing technique at high pressures is not valid for the acquisition of reliable data on the pore water chemistry of saturated bentonites with high expansible smectite contents, since part of the interlayer water is extracted during the tests, diluting the pore water samples even for pressures of 10-60 MPa.

5.2.1.3. Types and distribution of water in the FEBEX bentonite

Three modes of clay hydration may be distinguished and may take place simultaneously with increasing water activity or relative humidity [83]: a) interlamellar hydration (intracrystalline swelling), which involves the adsorption of limited amounts of water molecules (interlamellar water) on the internal surfaces of primary clay particles; b) osmotic or continuous hydration, which is related to an unlimited adsorption of water (intra-particle water) on the internal and external surfaces of primary particles; and c) capillary condensation of free water (inter-particle water) in meso- and macropores within the clay fabric (*i.e.* in the inter-aggregate and intra-aggregate pores).

The textural and structural features and changes occurring during the intracrystalline swelling of the FEBEX bentonite have been studied by using nitrogen adsorption volumetry, water adsorption and desorption gravimetry and X-ray diffraction under controlled humidity conditions. The results obtained, combined with the analysis of the water adsorption isotherms, have made it possible to identify the types, state and location of water in the FEBEX bentonite.

Nitrogen adsorption/desorption isotherms

Nitrogen adsorption/desorption isotherms of the bentonite were obtained at 77 K using a discontinuous volumetry sorptometer, Micromeritics ASAP

2010. Before measurement, the samples were out-gassed by heating to 90°C under a residual vacuum of 0.01 Pa. Depending on porosity, approximately 0.05 to 0.25 grams of sample were used. The BET micro, meso and total specific surface areas were determined according to *t*-plot and Harkins-Jura methods [84, 85, 86].

Figure 5.109 shows the N_2 adsorption-desorption isotherms obtained from the powdered FEBEX bentonite, expressed in terms of the volume of gas adsorbed per unit of mass, V_a [10]. The adsorption isotherm has the characteristic features of the type-IV isotherm with a very important hysteresis loop due to capillary condensation in mesopores formed between different quasi-crystals. The curves exhibit an H3 hysteresis loop in desorption, which is characteristic of the presence of slit-shaped pores. Table 5.15 shows the relevant parameters deduced from the BET and *t*-plot treatments. The specific surface area calculated from the BET method is 56.4 m^2/g whereas that obtained from the *B* point (P/P_o = 0.057) is 57.0 m^2/g.

The procedure developed by de Boer *et al*. (1966) [85] was used to analyse microporosity. The original slope of the *t*-plot indicates the total specific surface area, 61.5 m^2/g (range *t*: 0-3.35), whereas a positive intercept (converted to liquid volume) indicates the presence of micropores, V_o=8.60·10^{-3} cm^3/g (range *t*: 3.35-6.9) and mesopores, V_o=1.20·10^{-2} cm^3/g (range *t*: 6.9-12.34) having a total volume *i*. The FEBEX bentonite is microporous with microporous volumes accounting for ~43 percent of the BET monolayer capacity.

The average number of clay layers per quasi-crystal was calculated from the nitrogen adsorption data, assuming that the plates (square parallelepipeds = 3000 Å in the lateral direction and a multiple of the *d*001 in height, with a thickness of 9.6 Å) are perfectly stacked. It is possible to determine the mean size of the quasi-crystals using the relationship [86]:

$$S(m^2/g)=56.4=746/n+5.13 \Rightarrow n \approx 14 \text{ layers}$$

When the bentonite is dry, quasi-crystals of about 14 elementary condensed montmorillonite layers are formed on average. As shown in Section 2.2.1, when the FEBEX clay powder is brought to equilibrium with saturated water vapour, the mean size of the quasi-crystals (Scherrer equation) remains constant during the filling of the interlayer spaces, and the size corresponds to particles having a thickness of some six layers with two or three layers of water

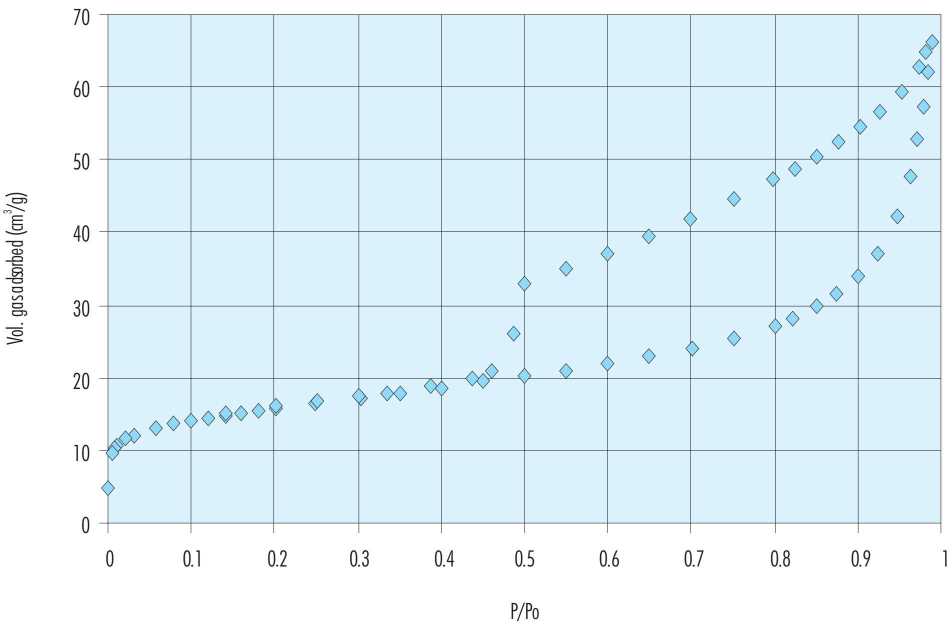

Figure 5.109: Adsorption-desorption isotherms of nitrogen at 77 K onto FEBEX bentonite.

Table 5.15
Parameters deduced from BET and *t*-plot treatment on the adsorption of N_2 at 77K

C_{BET}	V_m (cm^3/g)	S_{BET} (m^2/g)	S_{tot} (m^2/g)	V_{tot} (cm^3/g)	S_{micro} (m^2/g)	V_{micr} (cm^3/g)	$S_{ext\ micro}$ (m^2/g)	$S_{ext\ meso}$ (m^2/g)	V_{meso} (cm^3/g)
388	$1.99 \cdot 10^{-2}$	56.38	61.53	$9.6 \cdot 10^{-2}$	20.73	$8.6 \cdot 10^{-3}$	35.65	29.35	$1.2 \cdot 10^{-2}$

V_m: *Monolayer capacity derived from the BET treatment; expressed as liquid;* S_{BET}: *BET surface area*
S_{tot}: *Total surface area derived from the slope of the straight line passing through the origin of the t-plot*
V_{micr}: *Liquid microporous volume derived from the ordinate at the origin in the second straight line of the t-plot*
$S_{ext\ micro}$: *Surface area of micropores derived from the slope of the second straight line of the t-plot*
V_{tot}: *Total pore volume, derived from the amount of nitrogen adsorbed at* P/P_o *of 0.98*
$S_{ext\ meso}$: *Surface area of mesopores derived from the slope of the third straight line of the t-plot*
V_{meso}: *Liquid mesoporous volume derived from the ordinate at the origin in the third straight line of the t-plot* $S_{micro} = S_{BET} - S_{meso} = S_{BET} - (S_{ext\ micro} - S_{ext\ meso})$: *Surface area of the micropores*

in the interlamellar space. It seems that during the first stage of water adsorption, the original 14-layer thick quasi-crystals are split into smaller ones, approximately 6 layers thick [86].

The analysis of the isotherms by means of the BJH method allows the mesopore volume and the pore size distribution functions to be determined. The pore diameter of the FEBEX bentonite has been estimated using the BJH method [87] based on the Kelvin equation and the *t* values determined by the Frenkel-Halsey-Hill model (FHH) [88]. By application of the Kelvin equation, the minimum radius of pores in which capillary condensation can take place is calculated from the relative pressure at the lower limit of the hysteresis loop. The main parameters calculated from the mesoporous analysis are summarised in Table 5.16, and the distribution of pore size is shown in Figure 5.110 (desorption branch).

Thermogravimetry and X-ray diffraction analyses

The swelling of the bentonite due to interlaminar hydration at different water contents and its shrinkage as a function of temperature were analysed by X-ray diffraction and thermogravimetry (Figure 5.111). Under ambient conditions (*RH* = 50-60 %), the interlayers of the FEBEX smectite contain two layers of water, as deduced from the measured basal spacing of around 15.2 Å. In drying experiments, the basal spacing corresponded to one monolayer of water at 100-110°C and the structure collapsed at a *c*-spacing of 9.6 Å at 150-200°C, *i.e.* essentially no water in the interlayer space. Accordingly, the FEBEX bentonite is not fully dehydrated at the standard temperatures at

Table 5.16
Main parameters calculated by the BJH method

	Desorption branch	Adsorption branch	Total
Accumulated volume (cm^3/g)	$1.05 \cdot 10^{-1}$	$9.47 \cdot 10^{-2}$	$9.60 \cdot 10^{-2}$
Pore surface (m^2/g)	69.21	35.47	56.38 / 61.53
Average pore radius (Å)	30.4	53.4	34.0 / 31.2
Modal pore radius (Å)	19.3	216	—
Porosity at $\rho_d = 1.65\ g/cm^3$ (%)	17.4	15.6	15.8

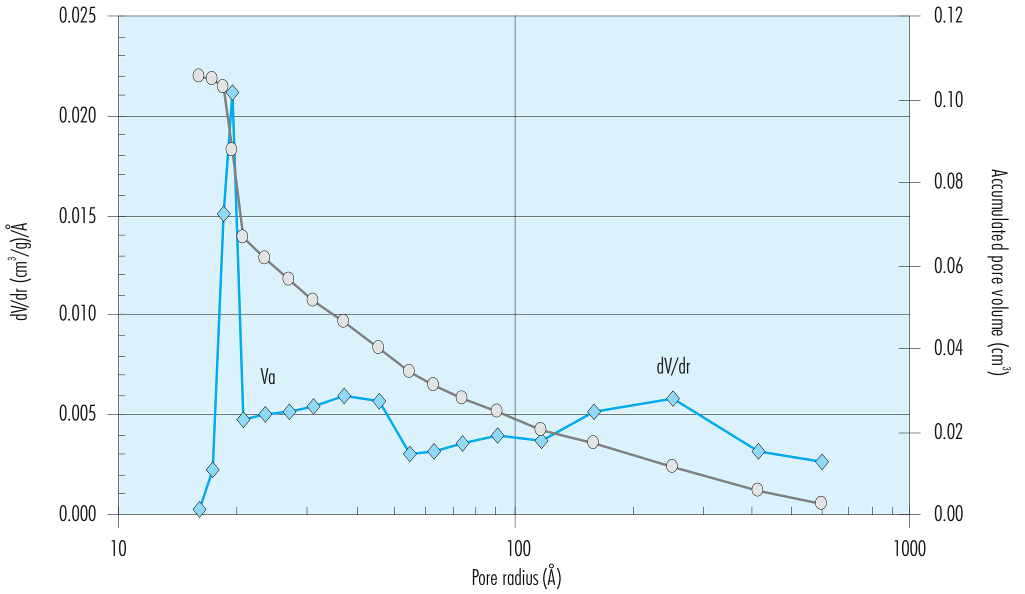

Figure 5.110: Pore size distribution from the desorption branch (cylindrical pores).

which the water content is determined (105-110°C), since one monolayer of water remains at this temperature. Only at temperatures of above 150°C (150-220°C) is the total interlayer water lost. The structural water, or dehydroxylation water, is about 4.3 ±0.6 percent, calculated from mass losses between 300 and 950°C, as determined from TG analysis (discounting CO_2 and SO_2 contents).

X-ray diffraction analysis at different water contents

The basal spacing of powdered FEBEX bentonite samples was also analysed as a function of water content, from an initial water content of 14 percent up to the liquid limit of this bentonite, *i.e.* 102 percent. In these wetting experiments, the FEBEX montmorillonite expands or swells in the c-dimension to an extent equivalent to a maximum of three layers of water in the interlayer space (Figure 5.112).

The basal spacing *d*001 expands due to the hydration of smectite and the formation of successive monomolecular layers of water. The sorption of water into interlamellar space is governed by the hydration energy of the interlayer cations and their degree of polarisation (charge/size relationship), the location of the layer charge of the adjacent silicate sheets, relative vapour pressure, water content and the salinity of the solutions surrounding the clay particles [89, 90, 91, 92, 93, 86]. The apparently continuous change in the c-dimension results from a random alternation of successive discrete hydrates [94, 95]. This may be observed in the X-ray diffraction patterns corresponding to different hydration states of the FEBEX bentonite (Figure 5.112 and Figure 5.113). At a water content of 18 percent the basal spacing is 15.0 Å, which corresponds to two layers of water. The basal spacing is 15.3, 15.7, 16.6 and 17.3 Å at water contents of 28, 34, 38 and 50 percent, respectively. At a water content of 60 percent the basal spacing is 18.5 Å (three layers of water), which is maintained at 18-19 Å up to a water content of 100 percent. This means that, in wetting experiments, the smectite basal spacing increases as a function of water content from two layers of water to a maximum of three layers, but through a continuum of 2°θ distances. Thus, we observe average values from a lattice that contains a random alternation of successive discrete hydrates

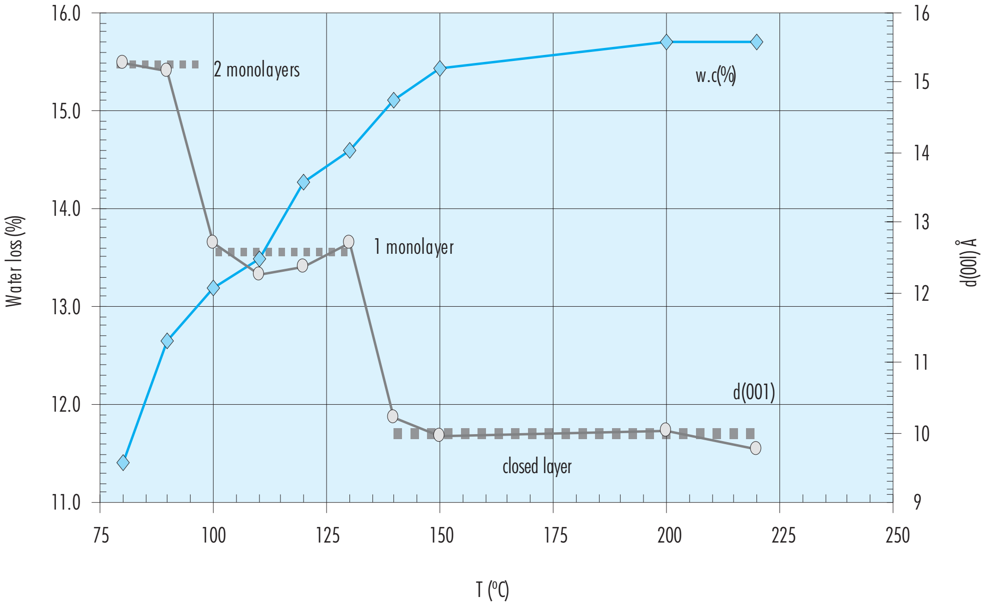

Figure 5.111: Evolution of water loss and basal spacing as a function of temperature.

in bentonite with water contents of from 14 to 100 percent. For this reason, the *d*001 peak may be decomposed in different populations with quasi-crystals formed with two and three layers of water (Figure 5.113). It is worthwhile noting that:

- ❑ According to different tests performed, water adsorption is also a kinetic process. In samples with the same water content but equilibrated over six months, the basal spacing is higher than in samples equilibrated over one week (Figure 5.112).
- ❑ As will be seen later, the bilayer state has two domains. One corresponds to the filling of the second solvation shell (with a basal spacing of ~15.2 Å) and the other to the filling of the free siloxane cavities (~16 Å).

Water vapour adsorption/desorption isotherms

FEBEX bentonite samples, ground to a particle size of < 0.1 mm, were heated at 150°C for 48 h. At this temperature the bentonite was completely dehydrated, without reaching dehydroxylation (the measured basal spacing of the montmorillonite equalled 9.8 Å). Subsequently, 1 to 2 g of the dried bentonite were placed in crucibles and then in desiccators at 20°C in a water vapour atmosphere controlled by means of different saturated salts solutions of different chemical compounds. Having reached equilibrium (after ≈ 1 to 1.5 months, determined by constant weight), the samples were weighed to determine the quantity of water adsorbed. Following this, the basal spacing was immediately determined using XRD. The water vapour adsorption-desorption isotherms for the FEBEX bentonite thus obtained are shown in Figure 5.114 [11, 96, 10].

Types, state and location of waters in FEBEX bentonite powder

The Frenkel, Halsey and Hill (FHH) formalism was used [97] to identify and describe the different states and locations of the water and the mechanisms involved in the water retention phenomenon as a function of the activity of the water, a_w (or P/P_o or relative humidity). The FHH curve is plotted in Figure 5.115, where six domains – related to the different states and location of the water – may be distinguished from an analysis of the slope changes. Moreover, these domains also correspond to the *d*001 spacings

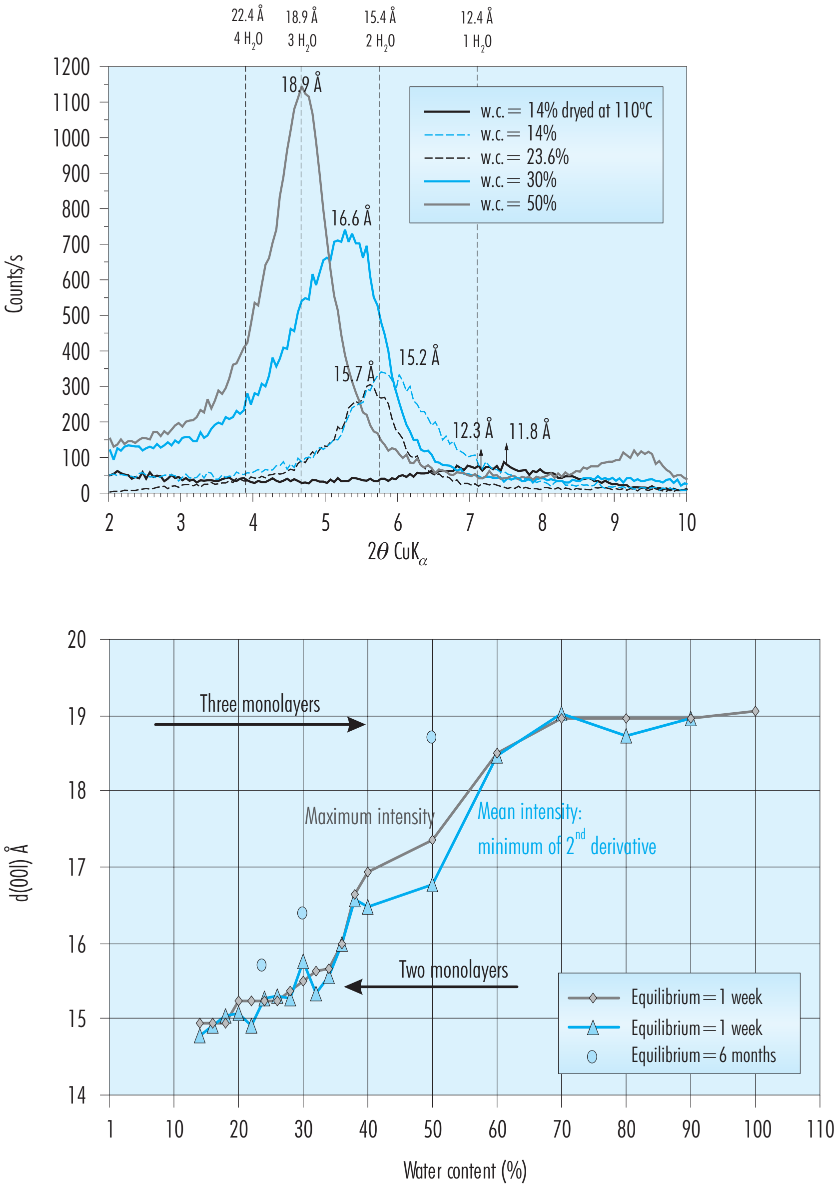

Figure 5.112: Variation of basal spacing, d001, of the FEBEX bentonite as a function of water content.

obtained from XRD measured at each water activity. The amount of water uptake in each domain was quantified (Table 5.17) by means of the Dubinin-Radushkevish equations [98, 99, 87, 88]:

$$W = W_o \exp\left[-\left(\frac{RT}{\beta E_o}\right)^2 ln^2\left(\frac{P_o}{P}\right)\right] \qquad (5.22)$$

$$ln\,W = ln\,W_o - DLn^2\left(\frac{P_o}{P}\right) \qquad (5.23)$$

where, W_o is the total volume of the micropores accessible to the given adsorbate (mmol/g), W represents the volume of the adsorbate condensed within the micropores at temperature T and relative pressure P/P_o (P is the partial pressure of the adsorbate,

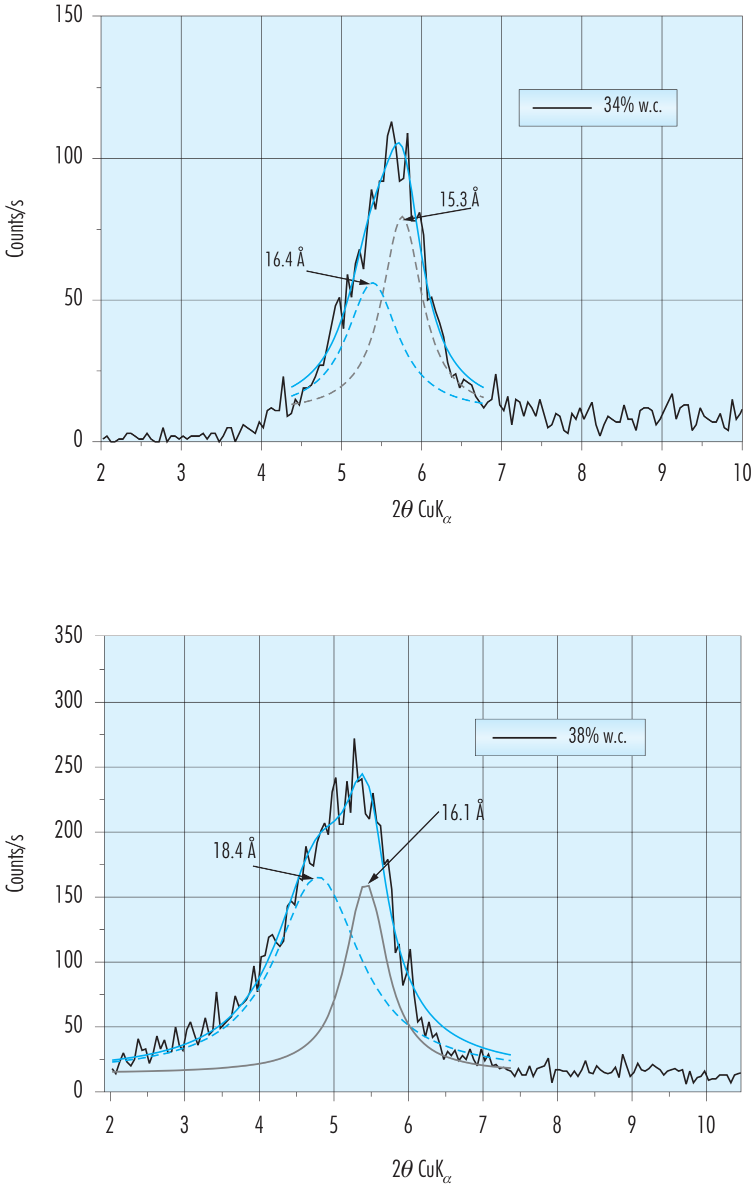

Figure 5.113: Decomposition of the d001 peak for samples of FEBEX bentonite with different water contents.

and P_o is the saturation vapour pressure of the adsorbate), E_o is the characteristic free energy of adsorption for a standard vapour, which depends on both the vapour and the pore system, *i.e.* E varies with pore size; β and n are specific parameters of the adsorbate. β is the similarity coefficient or affinity coefficient and is the ratio of adsorption potentials of the adsorbate to a reference adsorbate, for which a value of 1 has been taken.

Domain A is observed at the lowest values of a_w (0.032-0.069) and corresponds to adsorption on the external surfaces of the stacks, edges and edge surface sites. This domain corresponds to the origi-

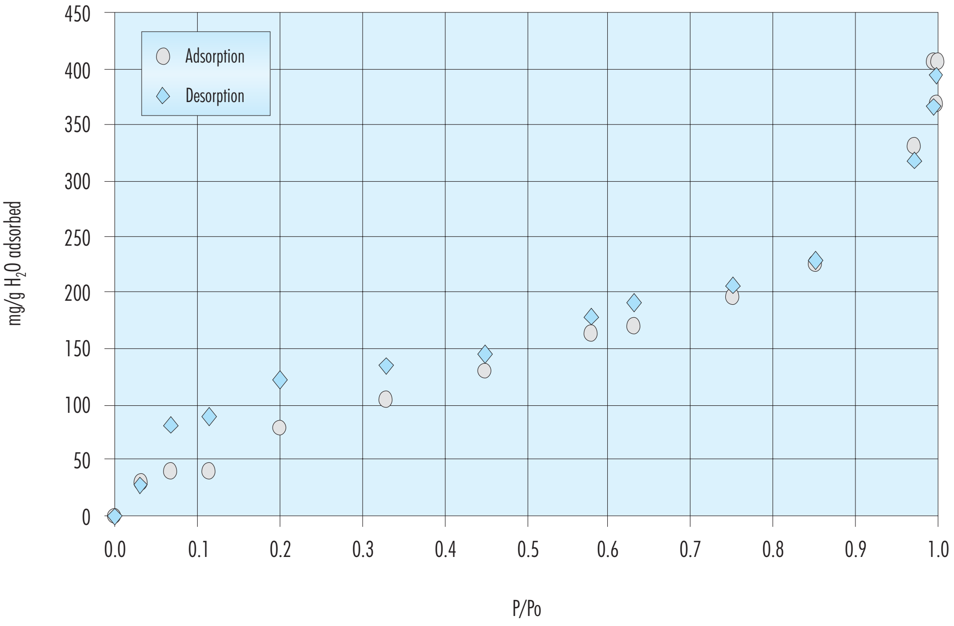

Figure 5.114: Water vapour adsorption-desorption isotherm for the FEBEX bentonite powder.

nal spacing of the montmorillonite in the dry state with virtually no water in the interlayer space (closed state, *d*001 = 9.8 Å). Based on the analysis of the data, the water adsorption on the external surfaces is 60.36 mg/g. Thus, taking into account the adsorption isotherm and the calculated value, the external water has a value of between 3 and 6 percent. This quantity, ~5 percent, is interpreted as the *free water* volume and will be used for the modelling of pore water in the *as received* bentonite.

Domain B (a_w = 0.069-0.1) corresponds to the adsorption of water for the filling of a monolayer of water in the interlayer space. Water is adsorbed around the interlayer cations and the c-spacing increases from 9.6 to 12.1 Å. The amount of interlayer water in the complete one-layer hydrate is 102.4 mg/g, which theoretically covers a surface area of 363 m^2/g.

Domain C (a_w = 0.2-0.58) corresponds to the solvating of interlayer cations (possibly second solvation shell) in the two-layer hydrate (*d*001 = 15.2 Å). The amount of interlayer water in the two layers is 183.4 mg/g, which theoretically covers a surface area of 650 m^2/g.

Domain D (a_w = 0.58-0.97) corresponds to the filling of free siloxane cavities, where no interlayer cations exist, and to multilayer adsorption on external surfaces. In this domain, the spacings between the unit layers remain almost constant (*d*001 = 15.8 Å) but the system continues to adsorb water. Due to the fact that multilayer adsorption on exterior surfaces might occur simultaneously with interlayer adsorption, it is difficult to determine how much water is present in the completed two-layer complex between the unit layers. The total amount of adsorbed water obtained for this domain is 274.2 mg/g, which theoretically covers a surface area of 972 m^2/g.

Domain E (a_w = 0.97-0.99) corresponds to the filling of the three-layer hydrate (*d*001 = 18.8 Å) and the total amount of water adsorbed is 379 mg/g.

Domain F (a_w >0.99), the interlayer space is further filled with water and capillary condensation in intra-aggregates or inter-aggregates begins to occur.

The FEBEX bentonite is in Domain C under laboratory conditions (*RH* = 50 ±10 %) and, for this reason, the amount of external water present in the system corresponds to the adsorbed water in Domain

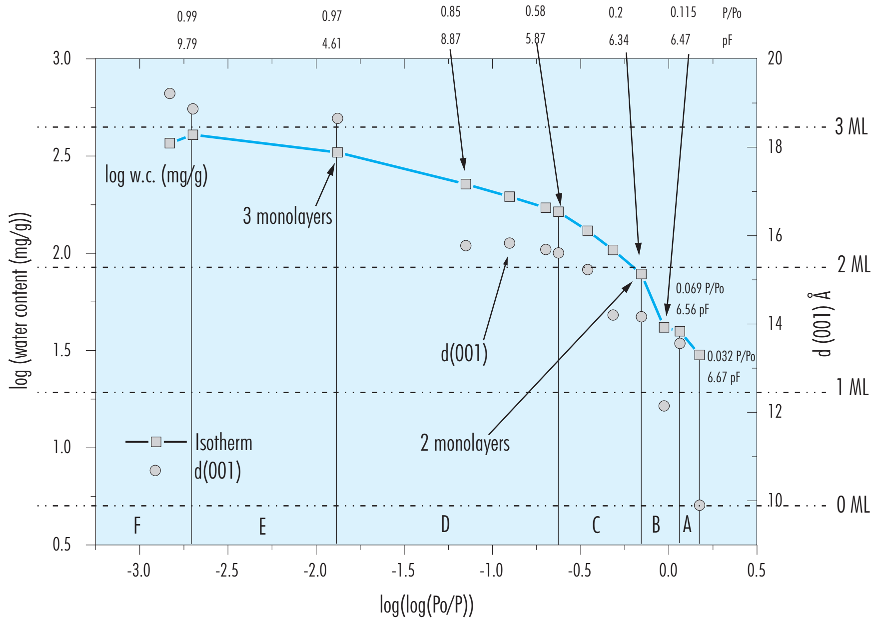

Figure 5.115: FHH water sorption plot obtained for the FEBEX bentonite. A, B, C, D, E and F correspond to domains where water retention is due to different hydration sites and mechanisms. The basal spacings d001 are also shown on the right axis (filled circles).

A. Consequently, the as received bentonite contains 52.6 mL of water per kg of dry clay.

The methods proposed by Cases *et al*. (1992) [86], Laird (1999) [93] and Touret *et al*. (1990) [100] have also been used to obtain the amount and types of water in the FEBEX bentonite.

In the Cases model, if the total external surface determined by nitrogen adsorption/desorption isotherms and the values of the water vapour adsorption isotherms are known, the amount of external, Q_{ext}, and internal water, $Q_{m(i)}$, per gram of montmorillonite may be calculated:

$$Q_{ext} = \theta \frac{S_{ext}}{\sigma N_A} \tag{5.24}$$

$$Q_{m(i)} = i \frac{S_{int}}{2\sigma_i N_A} \tag{5.25}$$

where, S_{ext} is the external surface area, θ is the surface coverage, calculated by means of the adsorbed water film thickness [101], N_A is the Avogadro's number, σ is the cross-sectional area of the water molecule strongly adsorbed on the external surface (~14.8 Å), σ_i is the cross-sectional area of the molecule in the hydrated state considered (being, 7.8 Å for $i=1$ (monolayer state) and 8.7 Å ($i=2$ and $i=3$ for bilayer and three-layer states, respectively), and S_{int} is the internal surface area.

The theoretical amount of water in the interlayer space is 132.5, 239.0 and 358.5 mg/g for the monolayer, bilayer and three-layer state, respectively. The amount of water on the external surface varies as a function of relative humidity, but a small amount of external water always exists in the system. The results are shown in Figure 5.116. Most of the water resides in the interlayer space, whereas there is a small volume of free, external water in the system.

In Laird's model, the hydration of Ca and Mg-saturated expandable 2:1 phyllosilicates may be calculated by means of the following relationship:

$$\theta_w = 0.5\cdot\rho_w\cdot(d-D)\ (S_h-S_x)+\varepsilon\cdot S_x\sigma \tag{5.26}$$

where θ_w is the gravimetric water content, ρ_w is the density of the interlayer water (~$1\cdot10^6$ g/m^3), d is the $d001$ value (m), D is the unit layer thickness

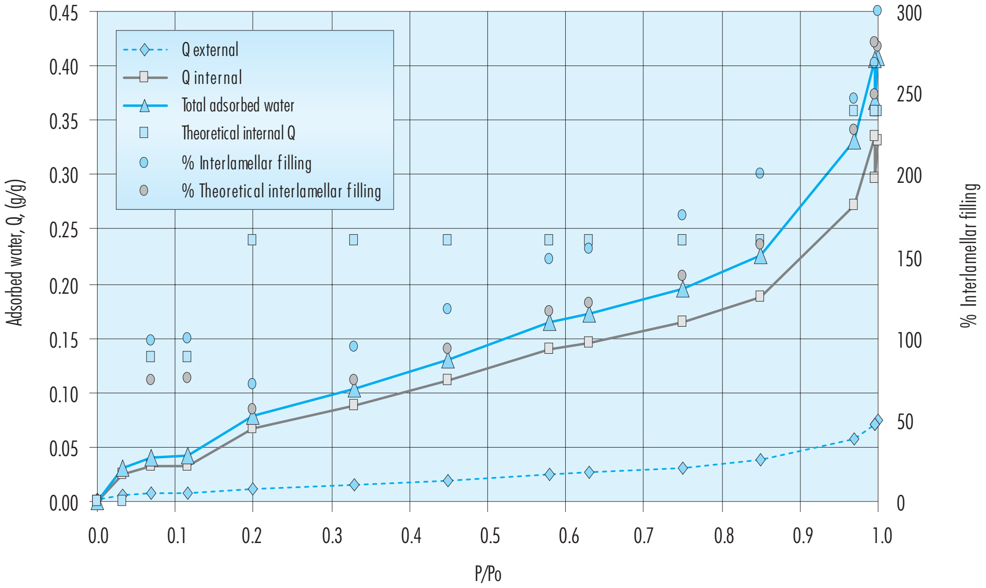

Figure 5.116: Water adsorption isotherm (V adsorbed) for the FEBEX bentonite, expressed as the amount of water adsorbed on the external surface (Q external) and interlamellar space (Q internal).

($9.6 \cdot 10^{-10}$ m), S_h is the hydratable surface area (m^2/g), S_x is the external surface area (m^2/g), ε is the total amount of water per charge site on external surfaces ($7.18 \cdot 10^{-22}$ gH_2O/e) and σ is the surface charge density (e/m^2).

The first term in this equation estimates the quantity of interlayer water and the second term calculates the water retained on the external surfaces. In this model, a restricted multilayer adsorption of water on external surfaces is assumed, in contrast to the Cases model. By applying this model to the case of the FEBEX bentonite, the amount of interlayer water is 322 mg/g and the external water is 38 mg/g. That is, the interlayer water content is ~32 percent and the external water content is ~4 percent.

Table 5.17
Amount of water (w), surface area (S_0), energy (E) and number of water molecules per ion in each domain obtained by Dubinin's equations

Domains	a_w	c-spacing (Å)	w (%)	S_o (m^2/g)	E (kJ/mol)	H_2O molecules/ion
A	0.03-0.07	~9.8	6.0	213.89	10.0285	3.3
B	0.07-0.10	10.3-12.1	10.2	362.83	6.3448	5.6
C	0.20-0.58	15.2	18.3	650.01	3.5521	10.8
D	0.58-0.97	15.8	27.4	971.58	1.5400	14.9
E	0.97-0.99	18.8	38.9	1343.8	0.5502	20.6

In the case of Touret's model, the interlayer or internal water is calculated by the relationship:

$$W_i = \frac{S(M-1)}{2M} x\Delta d(001)\cdot 10^{-4} \qquad (5.27)$$

where M is the number of stacked layers in a quasi-crystal, S is the total specific surface (m^2/g), $\Delta d001$ is $d001$-$d001_{dry}$ (Å), and W_i is the internal water of the particle (g/g). If the total adsorbed water and the internal water are known, the inter-particle water may be calculated. The results are shown in Table 5.18. According to this model, the quantity of interlayer water decreases from 0.33 to 0.28 g/g as the number of stacked layers per quasi-crystal decreases from 14 to 5. In addition, there is no water on the external surfaces up to a relative vapour pressure of 0.97. This marks a difference with respect to the other models, in which a proportion of external water always exists.

The main results obtained using the different methods applied to distinguish the types and distribution of water in the FEBEX bentonite are shown in Table 5.19. The maximum amount of internal or interlayer water in the FEBEX bentonite is ~30-36 percent, once the results obtained with the different methods have been compared. This amount seems to de-

Table 5.18
Inter-particle (inter-aggregate and intra-aggregate) water as a function of the number of stacked layers per quasi-crystal (M)

P/P_o	Total $V_{adsorbed}$ (g/g)	M = 14	M = 7	M = 6	M = 5
1	0.4075	0.082	0.107	0.115	0.13
0.997	0.3680	0.042	0.067	0.076	0.09
0.995	0.4067	0.081	0.106	0.115	0.13
0.97	0.3305	0.005	0.030	0.038	0.05
0.85	0.2268	-0.099	-0.0742	-0.065	-0.05

The negative values indicate the absence of water

Table 5.19
External and internal water obtained by means of different methods (in g/g)

Methods	Total external water	Total internal water	One-layer hydrated	Two-layer hydrated	Three-layer hydrated
BET Method	—	—	0.082	—	—
t-plot Method	0.056	0.311	—	—	—
FHH and Dubinin	0.03-0.06	—	0.102	0.183-0.274	0.379
Cases's Model	0.002-0.075 f(a_w, σ_{H_2O}=10.6 Å) 0.003-0.105 f(a_w, σ_{H_2O}=14.8 Å)	—	0.132	0.239	0.358
Laird's Model	0.038	0.322			
Touret's Model	0.038-0.115 f(M=6)	0.292 f(M=6)			

f(a_w, σ_{H_2O}) indicates values as a function of water activity and the cross-sectional area of the water molecule; f(M) indicates values as a function of the number of stacked lamellae to form a quasi-crystal pend on the number of stacked layers per quasi-crystal. There is an amount of external water of approximately 3-6 percent under the initial conditions (*RH*=50-60%). This external water may increase up to ~8-11percent as a function of relative humidity and the number of stacked layers per quasi-crystal. The Dubinin-Radushkevish equation and the Cases model allow the maximum amount of water in the monolayer, bilayer and three-layer water states to be determined, both results being comparable. According to the review of the literature, the most stable state in smectites is two layers of water, which corresponds to the one formed by the cation solvation shells (first and second shell) and the filling of the free siloxane cavities. The total amount of internal or interlayer water in this state is around 21-27 percent. However, there is always a small fraction of external water.

In summary, the different types of waters in the FEBEX bentonite powder, their state, location and quantity are shown in Table 5.20 [10]. Uptake of water occurs in three discrete stages as the montmorillonite structure expands. The distribution of water in the interlayer or internal space of the FEBEX bentonite powder may be classified in terms of the following states:

- monolayer hydrated state, which corresponds to a water content of 10.2 percent;
- bilayer hydrated state, which may be defined by two sub-states: i) formation of the second solvation shell, which corresponds to a water content of 18.3 percent and, ii) filling of the free siloxane cavities and possible adsorption of water on external surfaces, which corresponds to a water content of 21.4 percent;
- three-layer hydrated state, which corresponds to a water content of 31.9 percent.

Distribution of water as a function of the dry density of the compacted bentonite

In compacted bentonite, the total porosity may be divided into: i) interlayer porosity and ii) external porosity (external water), which corresponds to free water plus DDL water. The external porosity is known as effective porosity [102] or geochemical porosity [103]. The amount of water involved in the geochemical processes in the engineered barrier corresponds to the free water, taking into account that the amount of this water depends on the modifications of the dry density and the salinity concentration in the system. Usually, the geochemical or accessible porosity is assumed to be equivalent to the accessible porosity to chloride in through-diffusion experiments. The chloride anions are excluded from the interlayer space, but they do move relatively easily through compacted bentonite [103, 76, 77].

Table 5.20
Types, state and location of waters in the FEBEX bentonite powder

Method	Type of water	Subdivision	w (%)	E (kJ/mol)	d 001 (Å)	a_w
TG	Structural water	—	4.3 ± 0.6	—	—	—
FHH+Dubinin	Interlayer water	Monolayer of water	10.2	6.34	10-12	0.06-0.1
		Bilayer of water: 2nd solvation shell	18.3	3.55	15.2	0.2-0.58
		Bilayer of water: Filling of free siloxane cavities + external water	21.4-27.4 (1)	1.54	15.8	0.58-0.97
		Three layers of water	31.9-37.9 (1)	0.55	18.8	0.97-0.99
FHH+Dubinin	External water	DDL + free	3-6	10.3	~ 9.8	0.03-0.06

(1) The values 27.4 and 37.9 percent may be overestimated, since accumulated values may be obtained with this method. For this reason, the value in these two states has been calculated by subtracting the amount of external water. Thus, the correct values for bilayer and three layer would be 21.4 and 31.9 percent.

For calculation of the external and internal water in the compacted bentonite in the saturated state, a statistical distribution of monolayers of water as a function of pore volume, fixed by the total porosity, has been performed (Table 5.21) [104, 10]. To accomplish this, the values obtained with the FHH+ Dubinin method have been used. Also, several hypotheses have been considered: 1) in the FEBEX bentonite, a quasi-crystal is formed by seven stacked lamellae, which implies six interlayer spaces to be filled with internal water; 2) the volume of water fixed by the total porosity is distributed between internal and external water; 3) a proportion of external water always exists in the system; 4) the tendency of the bentonite-water system is to fill the maximum number of internal layers of water, which is three.

The results of the statistical distribution are shown in Figure 5.117. As may be observed, the maximum number of water layers in the interlayer space depends on dry density. The total number of layers may be filled with three layers of water up to a dry density of 1.40 g/cm^3. At dry densities higher than 1.40 g/cm^3, a complete uptake of three layers of water is not geometrically possible. However, most of the water is distributed in the interlayer space.

With this distribution, it is possible to determine the internal or interlayer water expressed as a percentage of internal porosity in the system (Figure 5.118) [10]. The internal water distribution is similar to that found by Pusch *et al*. (1990) [102] for the MX-80 bentonite. Also, the amount of external water may be determined. This quantity may be considered similar to the water available for the chemical reactions occurring in the inter-particle pores. These results have been compared to the effective porosity calculated by means of through-diffusion experiments performed on compacted FEBEX bentonite samples [105]. Chloride is excluded from interlayer positions and, for this reason, its concentration depends on the external water (Figure 5.118). The data differ at low densities, due to saline concentration and osmosis, since these diffusion tests were performed with deionised water. Muurinen *et al*. (1987) [106] found that effective porosity increases with the salinity of the injected water in the diffusion tests. At low densities (in this case < 1.40 g/cm^3), where the efficiency of the bentonite functioning as a semi-permeable membrane is much lower than 100 percent, the external fluid composition may have some influence above a certain concentration. However, at high densities and at membrane efficiencies approaching 100 percent, the re-saturating fluid composition plays little or no role [76, 107].

If the system re-saturates under constant volume with dry densities higher than 1.40 g/cm^3, the aforementioned calculations indicate that the swelling resulting from the uptake of different layers of water is sufficient to fill the available porosity. Thus, with an increase in water content, the swelling is sufficiently great to virtually fill all the initially air-filled macroporosity and transform it into predominantly interlayer space. However, a small fraction of external water still exists.

Density of the interlayer water

The density of the adsorbed water may be calculated from measurement of the c-axis spacing and the water content, plus the assumption that the surface area is known and that water is spread uniformly over the area [108].

In the case of the FEBEX bentonite, the X-ray diffraction values as a function of P/P_o have been used to

Table 5.21
Amount of interlayer water in a quasi-crystal formed by six interlayer spaces as a function of the number of hydrated layers (g/g)

6T	5T1B	4T2B	3T3B	2T4B	1T5B	6B	5B1b	4B2b	3B3b	2B4b	1B5b
0.319	0.301	0.284	0.266	0.249	0.231	0.214	0.2085	0.2032	0.1979	0.1926	0.1873
6b	**5b1M**	**4b2M**	**3b3M**	**2b4M**	**1b5M**	**6M**					
0.182	0.169	0.155	0.142	0.129	0.116	0.102					

T = Three layer = 0.37899 – external water; B = Bilayer = 0.27416 – external water (2nd solvation shell + filling of siloxane cavities); b = 0.182 g/g (bilayer of water, only 2nd solvation shell); M = Monolayer of water = 0.10238; External water = 0.06036 g/g (data from Table 5.20)

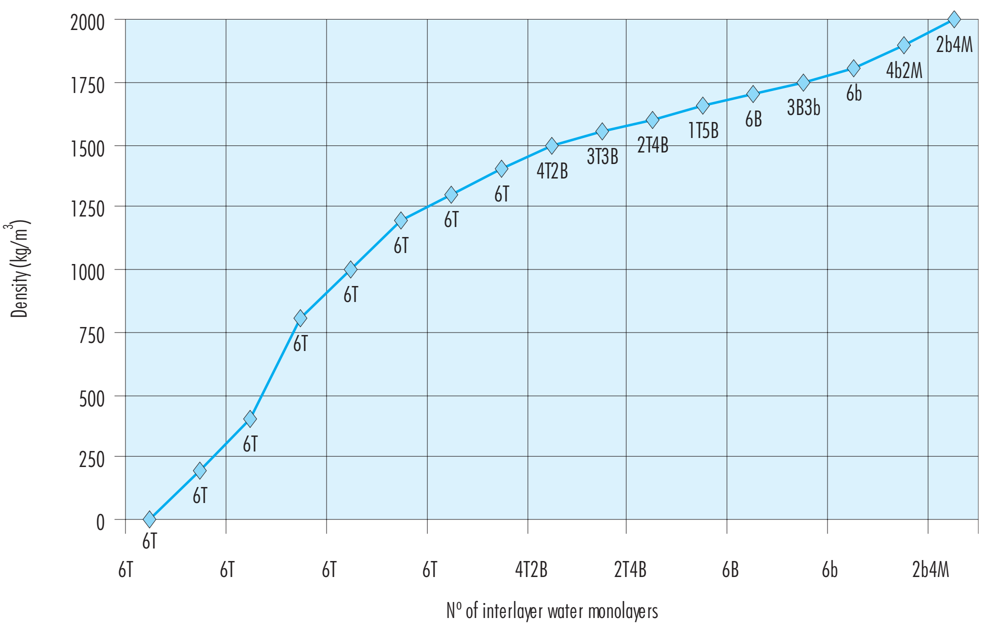

Figure 5.117: Distribution of monolayers of water in the interlayer space as a function of the dry density of compacted FEBEX bentonite (number of lamellae per quasi-crystal =7) (T: Three layers; B=Bilayer, 2nd solvation shell + filling of siloxane cavities; b: bilayer, only 2nd solvation shell); M: Monolayer).

calculate the density of the adsorbed water by means of this equation. The values of internal adsorbed water (S_{int}) for each P/P_o obtained with the Cases' model have been used [86]. The results are shown in Figure 5.119 and Table 5.22. Villar [16, 49] found values of adsorbed water of FEBEX samples at different water content as a function of the dry density of the bentonite greater than 1 g/cm^3; changing the water density from 1.094 g/cm^3 to 1.225 g/cm^3 for dry densities between 1.28 to 1.71 g/cm^3 (see Section 5.1.2.4).

5.2.1.4. Additional characterisation of the solid phase

In order to calculate the FEBEX bentonite pore water composition, the chloride and sulphate inventories and the fractional cation occupancies need to be

Table 5.22
Adsorbed water density for each type of water in the FEBEX bentonite

Location	State	Basal spacing (Å)	$a_w = P/P_o$	ρ_w (g/cm^3)
Zone A, $i=0$	Dry, external water	~9.8	< 0.069	0.97
Zone B, $i=1$	Monolayer	10.3-12.1	0.115-0.33	1.51
Zone C, $i=2$	Bilayer	15.2	0.45	1.23
Zone D, $i=2$	Bilayer + external	15.8	0.58-0.85	1.13
Zone E, $i=3$	Three layer	18.8	>0.97	1.11

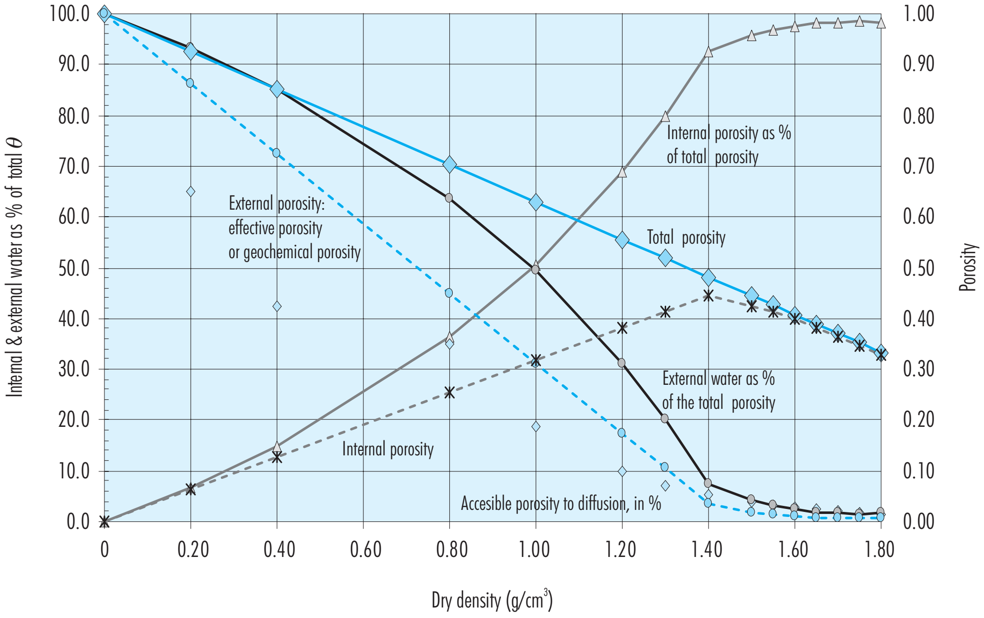

Figure 5.118: Total porosity, external porosity and internal (interlayer) porosity as a function of dry density.

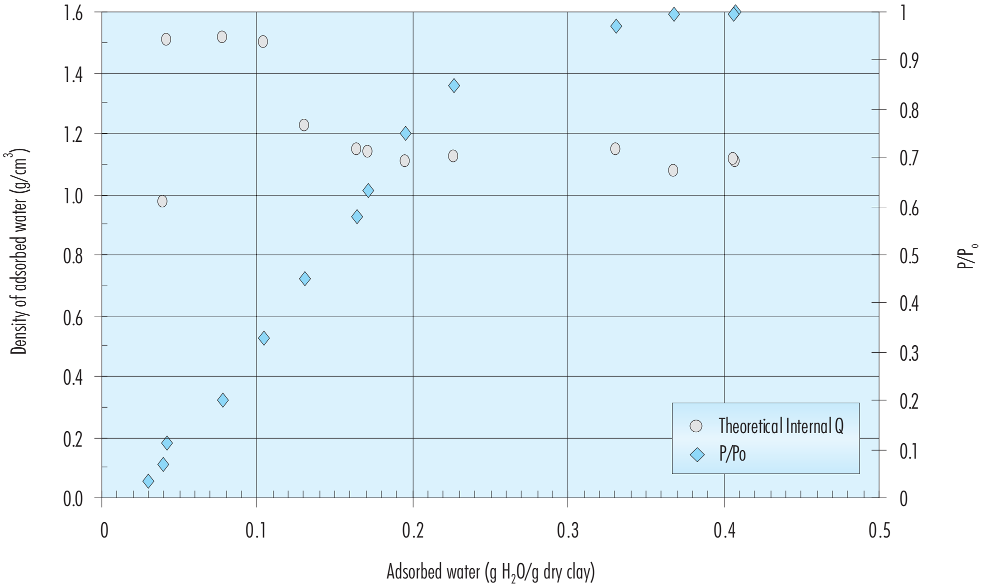

Figure 5.119: Density of adsorbed water for the FEBEX bentonite as a function of the quantity of adsorbed water according to the Cases' model.

determined for the *as received* material. Since these parameters are critical in calculating pore water chemistries in compacted bentonite, a series of investigations were undertaken to measure them once more at another institute (PSI) using different techniques and procedures.

Chloride and sulphate inventories

The chloride and sulphate contents are 21.9 ± 4 and 10.3 ± 7 mmol/kg, respectively (Section 2.2.2). Normally there are no problems associated with chloride determinations, but sulphate measurements may be influenced by kinetic and/or S:L ratio effects, *e.g.* when calcite and dolomite are present [109], or by oxidation in the presence of pyrite. The latter was considered to be a potential open question with respect to the sulphate inventory values given, since the FEBEX bentonite contains pyrite, and the experiments were performed under atmospheric conditions. Consequently, two sets of sulphate extraction tests at an S:L ratio of 0.1 kg/L were carried out in an inert gas glove box and under atmospheric conditions as a function of time. The results are given in Table 5.23 and clearly show that there are no pyrite oxidation effects, and the inventory values given agree well with those taken from Fernández *et al*. [12] (Table 2.7).

CEC, exchangeable cations and fractional occupancies

Different extractions were performed in order to obtain the cation occupancies and cation exchange

Table 5.23
Results of sulphate extraction tests with distilled water (in mmol/kg) on FEBEX bentonite samples (PSI laboratory)

Time	Anoxic	Oxic
1 h	10.1	10.1
5 h	10.0	10.5
1 day	10.1	10.4
4 days	10.2	10.5
11 days	10.3	10.2
33 days	10.1	10.6
75 days	10.4	10.3

Table 5.24
Extraction results for several cations using different displacement ions

Cation	Ni-en displacement (meq/100g)	Cs displacement (meq/100g)
Ca	35.9	35.7
Mg	34.0	32.3
Na	28.9	29.3
K	2.0	2.6
Sr	0.4	0.4
Σ cations	101.3	100.3

capacity of the FEBEX bentonite: i) extractions with Nickel-ethylenediamine (Ni-en) [75] and ii) extractions with 0.5 M $CsNO_3$. Ni-en is a powerful highly selective complex that almost immediately displaces all exchangeable cations from the clay minerals into solution [110, 111]. This process is more rapid than solid phase dissolution reactions [112, 113]. Consequently, the extent of mineral dissolution is reduced via the common ion effect. Thus, the cations displaced from the clay minerals will dominate the solution compositions. Cs may also act as a highly selective cation, and displaces all exchangeable cations from the montmorillonite if its concentration is sufficiently high. The aqueous extracts were carried out at S:L ratios from ~0.15 to ~0.3 kg/L by end-over-end shaking for 1 day.

The cation concentrations released in the Ni-en and Cs extraction solutions are summarised in Table 5.24. These concentrations include contributions from highly soluble salts *e.g.* NaCl and sparingly soluble salts *e.g.* $CaSO_4$ (note that in these tests the S:L ratios were such that the whole sulphate inventory dissolved). The cation occupancies for the raw material, taking into account the corrections for the contributions from NaCl and $CaSO_4$, are given in Table 5.25, along with the fractional cation occupancies.

Selectivity coefficients and protolysis constants

The fractional cation occupancies given in Table 5.25 were used together with the concentrations of Na, K, Mg and Ca measured in each of the aqueous extraction experiments (Section 5.2.1.1) to calculate four sets of selectivity coefficients with respect to sodium, according to the Gaines & Thomas (1953) [114] convention. The procedure followed is

Table 5.25
Summary of cation occupancies (in meq/100g) and fractional cation occupancies, N_B, calculated for the raw bentonite [11]

Cation	PSI	CIEMAT	N_B (1) values	PSI	CIEMAT
Ca	33.1	34.6	N_{Ca}	0.345	0.340
Mg	33.1	34.0	N_{Mg}	0.346	0.334
Na	26.9	31.2	N_{Na}	0.281	0.306
K	2.3	1.9	N_K	0.024	0.019
Sr	0.4		N_{Sr}	0.004	
CEC	96.0	102.0 ± 4.0			

(1) *N_B=loading cation B/CEC*

Table 5.26
Selectivity coefficients for exchange reactions for FEBEX bentonite according to the Gaines-Thomas convention [11]

Exchange reaction	K_C (PSI)	K_C (CIEMAT)
Na-mont + K ⇔ K-mont + Na	10.6 ± 0.1	7.6
2Na-mont + Ca ⇔ Ca-mont + 2Na	12.8 ± 0.9	5.9
2Na-mont + Mg ⇔ Mg-mont + 2Na	10.7 ± 0.8	4.5
2Na-mont + Sr ⇔ Sr-mont + 2Na	12.8 ± 0.9 (1)	

(1) *The selectivity coefficient of Sr with respect to Na was taken to be the same as the Ca-Na value*

Table 5.27
Summary of site types, site capacities, and protolysis constants taken for FEBEX bentonite

Site types	Site capacities (mol/kg) [1]
$\equiv S^{S}OH$	$2.34 \cdot 10^{-3}$
$\equiv S^{W1}OH$	$4.68 \cdot 10^{-2}$
$\equiv S^{W2}OH$	$4.68 \cdot 10^{-2}$
Surface complexation reaction	**log K_{int} [2]**
$\equiv S^{S}OH + H^{+} \Leftrightarrow \equiv S^{S}OH_2^{+}$	4.5
$\equiv S^{S}OH \Leftrightarrow \equiv S^{S}O^{-} + H^{+}$	-7.9
$\equiv S^{W}OH + H^{+} \Leftrightarrow \equiv S^{W}OH_2^{+}$	4.5
$\equiv S^{W}OH \Leftrightarrow \equiv S^{W}O^{-} + H^{+}$	-7.9
$\equiv S^{W2}OH + H^{+} \Leftrightarrow \equiv S^{W2}OH_2^{+}$	6.0
$\equiv S^{W2}OH \Leftrightarrow \equiv S^{W2}O^{-} + H^{+}$	-10.5

[1] *The site capacity values for the FEBEX bentonite have been scaled over their CEC value from the MX-80 CEC value (for MX-80: $\equiv S^{S}OH = 2.0 \cdot 10^{-3}$ mol/kg; $\equiv S^{W1}OH = 4.0 \cdot 10^{-3}$ mol/kg; $\equiv S^{W2}OH = 4.0 \cdot 10^{-3}$ mol/kg; CEC= 78.7 meq/100g [76])*

[2] *Surface complexation constants for the MX-80 bentonite taken from Bradbury & Baeyens [109]*

the same as given in Bradbury & Baeyens [76]. The averaged values are given in Table 5.26, together with the corresponding cation exchange reactions. The cation occupancies, cation exchange capacities and selectivity coefficients found by the PSI laboratory [11] and those taken from Fernández *et al.* [12], which will be used in the pore water chemistry calculations, are compared in Table 5.26 and Table 5.27.

There is a second category of reactive sites associated with montmorillonite that are perceived as being surface hydroxyl groups ($\equiv$SOH) situated along the edges of the clay platelets (edge or broken bond sites). In the surface complexation model developed by Bradbury & Baeyens [109] to describe the titration data on SWy1 montmorillonite and the Ni/Zn sorption edge and isotherm measurements, two protolysis sites ($\equiv S^{W1}OH$ and $\equiv S^{W2}OH$) with the same capacities but with different protolysis constants were required. Here, it has been assumed that the montmorillonite in the FEBEX bentonite has the same characteristics as the SWy1 montmorillonite (Table 5.27).

5.2.1.5. Pore water chemistry modelling

In the interlayer spaces and regions where the individual montmorillonite stacks are in close proximity, double layer overlap will occur and anion exclusion effects will take place. Exclusion will probably be so large that it is highly unlikely that anions can move through these regions [115]. However, Cl^{-} anions do move through compacted bentonite since diffusion rates have been measured in through-diffusion tests [106, 116].

If the Cl^{-} anions cannot move through the interlayer and overlapping double layer regions because of anion exclusion effects, then it is reasonable to propose that the free water must provide the diffusion pathways. Therefore, the hypothesis is that the pore volume associated with the transport of chloride (and other anions) is the free water volume and that this is the pore water in a compacted bentonite. Thus, the chloride accessible porosity measured in through diffusion experiments in compacted bentonites is usually only a small fraction of the original total porosity.

A further hypothesis in the approach proposed is that highly compacted bentonite can function as an efficient semi-permeable membrane [117]. This implies that the re-saturation of compacted bentonite involves predominantly the movement of water molecules and not of solute molecules. Thus, in a first approximation, the composition of the external saturating aqueous phase should be a second order effect that has little influence on the initial compacted bentonite pore water composition [107].

Even if highly compacted bentonite were to function as a less efficient semi-permeable membrane than proposed, there are such large quantities of montmorillonite present compared to the low volumes of free water, that the montmorillonite, together with the other solid phases, will determine the composition of the pore water simply because the ion capacities of the solids are massively greater than those in the aqueous phase. The high exchange capacity of the montmorillonite component acts as a powerful buffer for the composition of the pore water.

The second category of reactive sites associated with montmorillonite, which are perceived as being surface hydroxyl groups (≡SOH), has a capacity of ~10 percent of the CEC and may protonate and deprotonate, such that the concentrations of neutral, protonated and de-protonated edge sites change depending on pH [109]. Using a similar reasoning to the one given above, the hydroxyl groups may function as a powerful pH buffer.

Modelling of the pore water chemistry of the raw FEBEX bentonite

Once the raw bentonite was removed from the quarry and throughout the time it was stored on the surface, it was exposed to atmospheric conditions. At some point, the raw wetted bentonite was processed further on a production line before being stored again, in powdered form, prior to transport. The water content of the powdered FEBEX bentonite, at this stage, had been reduced to about 14 percent (Section 2.3.1). The preparation procedure has conditioned the powdered bentonite to be in equilibrium with air. The cation occupancy data presented in Section 5.2.1.4 result from this atmospheric conditioning. However, probably the most significant effect of all is that the pH in the moist bentonite powder will be that determined by carbonate/sulphate mineral equilibration at air P_{CO_2}, *i.e.* $10^{-3.5}$ bar. The result of this is that the amphoteric hydroxyl groups at the edges of montmorillonite platelets will also have been conditioned to a state reflecting this equilibrium. Furthermore, there is no reason to believe that any subsequent compaction of the powdered bentonite will alter the charge state of these sites.

The hypothesis put forward here is that the bentonite pore water in the compacted material will be buffered to a pH reflecting the protonation/ deprotonation state of the ≡SOH sites because the masses of montmorillonite are much larger than the volumes of free water.

In the calculations it is assumed that there is saturation with respect to calcite, gypsum, celestite and quartz. The concentrations of K, Mg and Ca are determined with respect to the cation exchange equations and selectivity coefficients given in Table 5.26. A further constraint on the system is the mineral inventories, *e.g.* calcite and gypsum. Clearly, the quantity of any mineral phase dissolved must be less than the quantity originally present.

In order to calculate a unique pH for the solution in equilibrium with the air equilibrated bentonite powder ($P_{CO_2} = 10^{-3.5}$ *bar), a* Cl^- concentration needs to be specified. The Cl^- content of the FEBEX powder is 21.9 mmol/kg, and the quantity of free water associated with the raw powder is ~5 percent, yielding a chloride concentration of 0.42 *M* and an S:L ratio of ~19 kg dry FEBEX bentonite/L. The above information, together with the data given in Section 5.2.1.4, allows a unique water chemistry to be calculated for the solution/air equilibrated bentonite powder system [76, 77]. Such calculations were carried out using the geochemical code MINSORB [109] together with the thermodynamic data base compilation from Hummel *et al*. (2002) [118]. The chemistry of the water calculated to be in equilibrium with the FEBEX bentonite powder is given in Table 5.28 and the cation loadings and speciation of the ≡SOH sites are summarised in Table 5.29.

Modelling of the pore water chemistry of FEBEX bentonite compacted at a dry density of 1.65 g/cm^3

In the compacted bentonite the loadings and condition of the ≡SOH sites are taken to be the same as in the powder. However, the compacted system is treated as being closed, which is a reasonable assumption for the calculation of the initial composition of the pore water. As stated previously, the implication is then that the solid phases will determine the chemistry of the pore water because of the very high S:L ratio and the absence of air.

Table 5.28
Calculated pore water compositions in equilibrium with the bentonite powder under atmospheric conditions (M)

$\log P_{CO_2}$ (bar)	-3.50
pH	7.44
Ionic strength	0.66
Na	$3.3 \cdot 10^{-1}$
K	$2.6 \cdot 10^{-3}$
Mg	$8.1 \cdot 10^{-2}$
Ca	$6.8 \cdot 10^{-2}$
Sr	$6.1 \cdot 10^{-4}$
Cl	$4.2 \cdot 10^{-1}$
SO_4	$1.9 \cdot 10^{-2}$
$C_{inorg.}$	$3.1 \cdot 10^{-4}$
Si	$1.8 \cdot 10^{-4}$

Table 5.29
Calculated initial cation loadings and state of the amphoteric ≡SOH sites in FEBEX bentonite powder in equilibrium with air

Exchangeable cations and ≡SOH sites	Concentration (mol/kg)
Na-mont	$2.74 \cdot 10^{-1}$
K-mon	$2.29 \cdot 10^{-2}$
Mg-mont	$1.62 \cdot 10^{-1}$
Ca-mont	$1.66 \cdot 10^{-1}$
Sr-mont	$1.47 \cdot 10^{-3}$
$\equiv S^{W1}OH$	$3.0 \cdot 10^{-2}$
$\equiv S^{W1}OH_2^+$	$3.4 \cdot 10^{-5}$
$\equiv S^{W1}O^-$	$1.0 \cdot 10^{-2}$
$\equiv S^{W2}OH$	$3.9 \cdot 10^{-2}$
$\equiv S^{W2}OH_2^+$	$1.4 \cdot 10^{-3}$
$\equiv S^{W2}O^-$	$3.3 \cdot 10^{-5}$

Note: The charge on the $\equiv SOH_2^+$ *and* $\equiv SO^-$ *sites is compensated by outer sphere complexes that have not been included in the modelling*

A mass balance approach to modelling pore water chemistry in compacted bentonite was adopted. Such an approach automatically takes into account the buffering effects of the exchangeable cations and the amphoteric ≡SOH sites. From the values given in Table 5.29, the mass balance inventories may readily be calculated at any chosen initial dry density. The solubility limiting phases, cation exchange reactions and selectivity coefficients were taken to be the same as those used in the previous section.

The pore water chemistry of the FEBEX bentonite compacted at a dry density of 1.65 g/cm^3 was calculated assuming that the chloride accessible porosity at this density is 5 percent. This value, 0.0303 L of water per kg of dry FEBEX bentonite, together with the chloride inventory, yields a chloride concentration of 0.73 M. The pore water is calculated to be a Na-Ca-Mg chloride type with a high ionic strength, 0.90 M, and a pH of 7.44 (Table 5.30). Thus, pore water chemistries at other initial FEBEX bentonite dry densities may readily be calculated if the corresponding chloride accessible porosity values are available.

Modelling of pore water chemistry for different bentonite dry densities

The same procedure as described above [76] has been followed to calculate pore water chemistry as a function of dry density. The calculations were carried out using the geochemical code PHREEQC2 [119]. The thermodynamic database of the code was modified in order to take into account the high salinities that exist in the FEBEX bentonite-water system. The activity coefficients were calculated according to the Truesdell & Jones equation [120] (valid for solutions with $I<2.5$ M), using the *a* and *b* parameters determined by Parkhurst [121] and Kielland [122] [123]. The Setchenow equation was used for non-charged molecular species, including K_i parameters found in Langmuir (1997).

The main geochemical processes of the FEBEX bentonite-water system to be considered in the modelling come from experimental results obtained from experiments performed at high (squeezing tests) and low (aqueous extract solutions) solid to liquid ratios (Section 5.2.1.1 of [12]):

- Equilibrium with respect to calcite
- Equilibrium with respect to gypsum and celestite
- Equilibrium with respect to chalcedony
- Dilution of chlorides
- Ion exchange reactions
- Surface complexation reactions
- Thermodynamic stability of the clay fraction (smectite) under the expected pH conditions (7<pH<11).

The main input data used for modelling purposes were: i) the chloride inventory; ii) the cation ex-

Table 5.30
Calculated initial pore water chemistry of FEBEX bentonite compacted at a dry density of 1.65 g/cm^3 (*M*)

pH	7.44
Ionic strength	0.90
Na	$3.9 \cdot 10^{-1}$
K	$3.0 \cdot 10^{-3}$
Mg	$9.7 \cdot 10^{-2}$
Ca	$8.2 \cdot 10^{-2}$
Sr	$7.3 \cdot 10^{-4}$
Cl	$7.3 \cdot 10^{-1}$
SO_4	$1.7 \cdot 10^{-2}$
$C_{inorg.}$	$2.4 \cdot 10^{-4}$
Si	$1.8 \cdot 10^{-4}$

change population (Table 5.25); iii) the selectivity coefficients (Table 5.26), and iv) the protolysis constants (Table 5.27).

The external porosity calculated as a function of dry density (Figure 5.118) has been considered as the accessible porosity for free water. The volume of water in the inter-particle pores (external water) and the chloride concentration as a function of dry density are shown in Figure 5.120 and Figure 5.121 (referred to as water isotherm porosity). The values are compared with those obtained from total porosity and chloride accessible porosity determined in through-diffusion tests [105]. As may be observed, the water volume in pores calculated by means of chloride accessible porosity and external porosity are quite similar, considering dry densities between 1.40 and 1.80 g/cm^3. At densities lower than 1.40 g/cm^3, the bentonite water-system is better described by the calculated external porosity, due to the dependence of the through-diffusion experiments on the salinity of the injected water [106]. At densities lower than 1.40 g/cm^3, for which the efficiency of the bentonite functioning as a semi-permeable membrane is much lower than 100 percent, the external fluid composition may have some influence above a certain concentration. As the salinity in the inter-particle water increases, the interlayer tends to expel water until osmotic equilibrium is reached, increasing the amount of external water. If the salinity decreases, the smectite tends to acquire the maximum amount of water it can, decreasing the amount of external water. However, at dry densities higher than 1.80 g/cm^3 and membrane efficiencies approaching 100 percent, the saturating fluid composition plays little or no role [76, 107], and other mechanisms seem to be involved in the compacted FEBEX bentonite-water system.

The ionic strengths of the FEBEX pore waters are greater than 3 M at dry densities of more than 1.8 g/cm^3. This poses a conceptual problem as regards modelling the pore water system and understanding the chemical equilibrium of the bentonite-water system.

The results obtained from the modelling are shown in Figure 5.122 to Figure 5.125. The pore waters are of Na-Cl type with ionic strengths ranging from 0.17 to 3.3 M. The pH values vary from 7.57 to 7.46 as a function of dry density. The variation of sulphate concentration as a function of the free water used in the modelling (external porosity or total

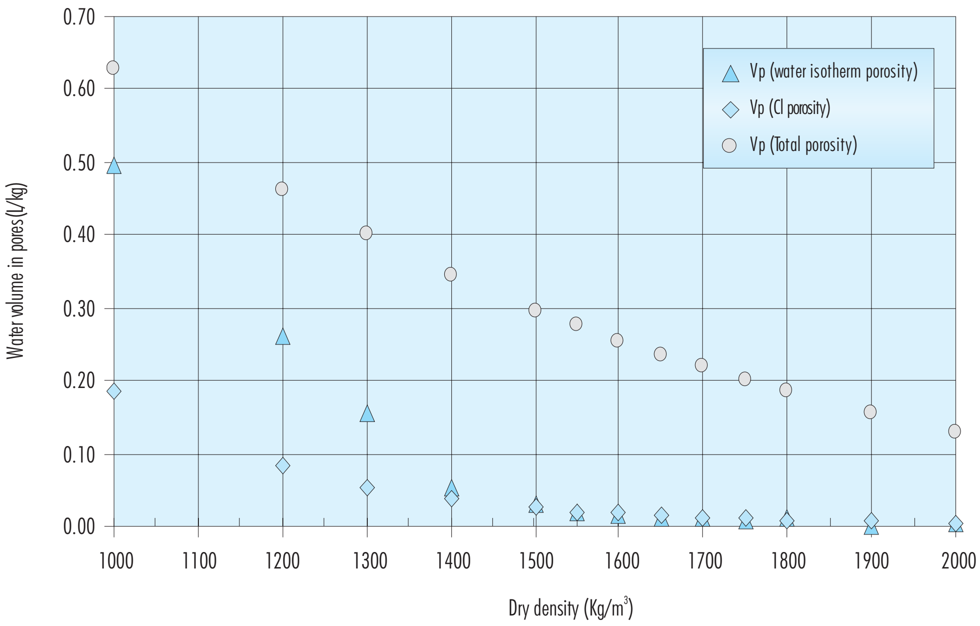

Figure 5.120: Water volume in inter-particle pores as a function of dry density.

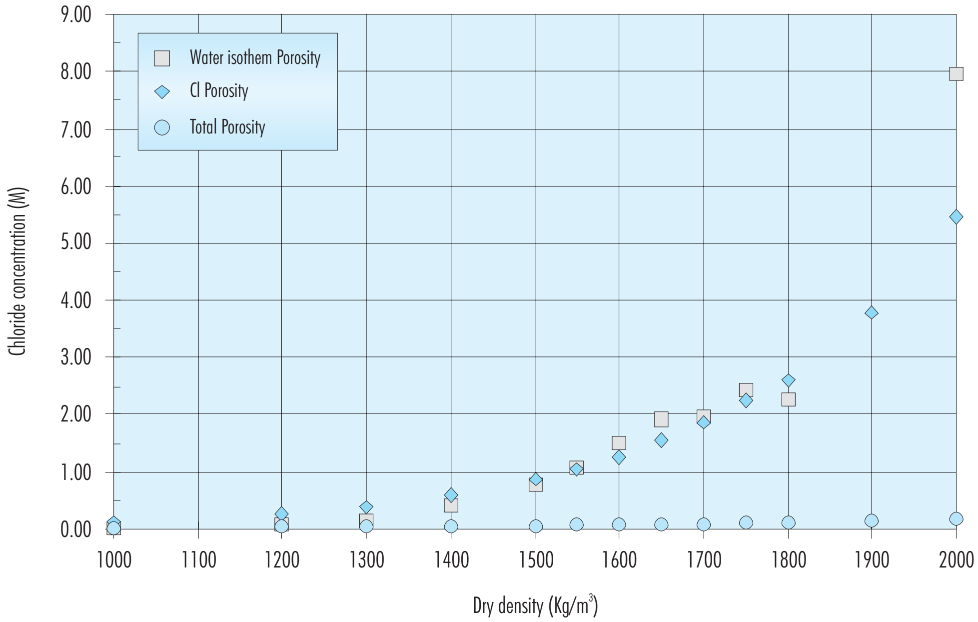

Figure 5.121: Chloride concentration as a function of dry density for different porosities.

porosity) is noteworthy. As was expected, the exchangeable sodium concentration decreases and exchangeable calcium concentration increases when the pore water volume increases in the bentonite-water system.

Properties of the compacted bentonite-water system: surface potential, osmotic potential and swelling pressure

The surface potential of the FEBEX smectite and the double layer thickness in the bentonite-water system have been approximately calculated from the pore water ionic strength and the surface charge density of the FEBEX smectite by applying the Diffuse Double Layer (DDL) theory. As was expected, the DDL thickness decreases when the ionic strength (Figure 5.126) or the dry density (Figure 5.127) increase. In compacted bentonite systems at dry densities of between 1.40 and 1.70 g/cm^3, the calculated DDL thickness is smaller than that of the Stern layer. For this reason, either the application of the DDL models is not valid in these systems, or the DDL water type and free water cannot be differentiated.

According to thermodynamics, the chemical composition of the pore water (mobile water), when expressed in ion activity units, is a measure of the electrochemical potential of ions in the clay/water system. At equilibrium, the chemical potential of all the phases is the same. As the pore water composition was determined taking into account the entire bentonite-water system (smectite, solutes, solid phases, internal water, external water, etc.), the water activity determined in the pore water modelling for each dry density might represent the water activity of the bentonite-water system. The pore water activity as a function of dry density is shown in Figure 5.128. Also, the osmotic potential may be calculated from the chemical composition of the pore water (Figure 5.129). Indeed, the osmotic potential increases with water potential (suction). The swelling pressure of the FEBEX-bentonite system has been calculated taking into account the water activity of the pore water. The results are shown in Figure 5.130 and compared with experimental data obtained in oedometer tests (Section 5.1.3.3). As may be observed, the osmotic pressure in the bentonite-water system explains most of the swelling pressure of the compacted and saturated FEBEX bentonite with dry

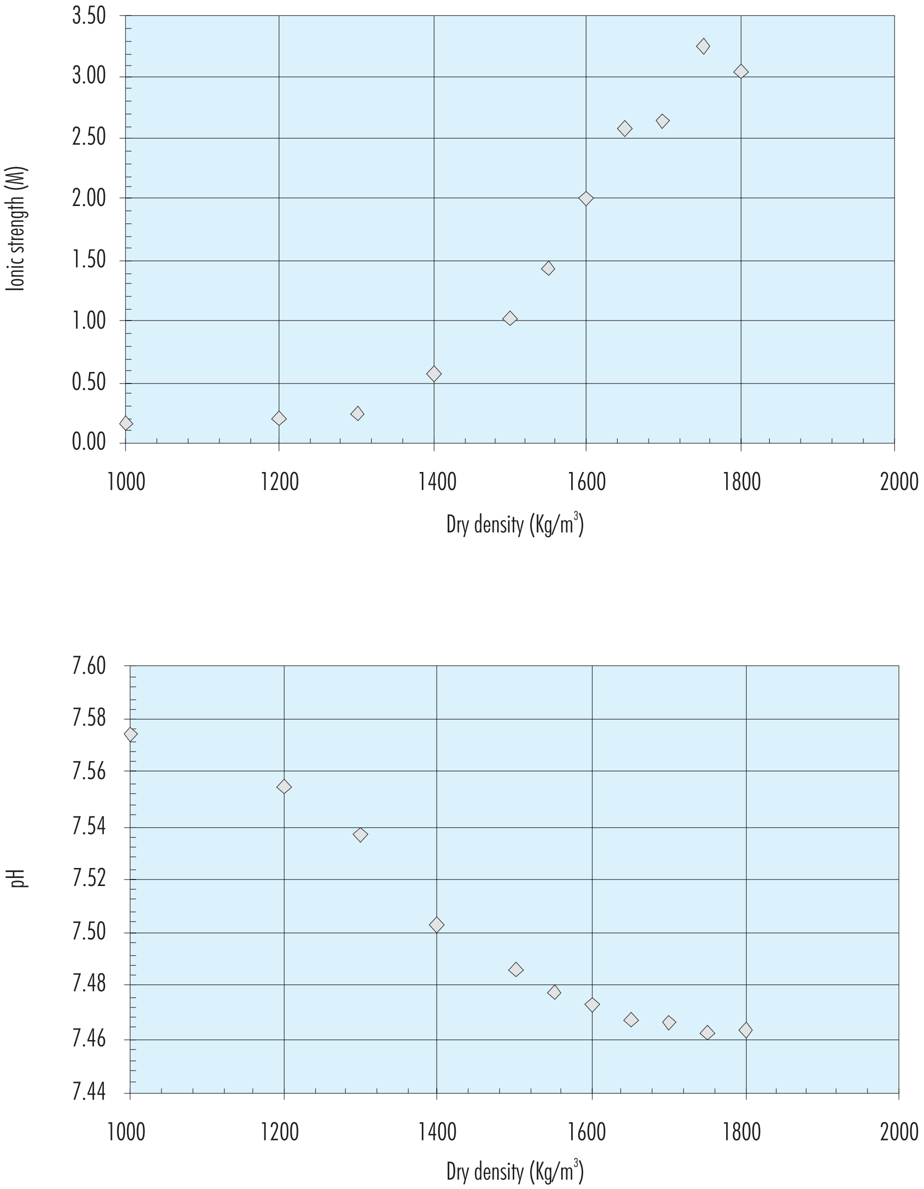

Figure 5.122: Ionic strengths and pH of the pore water as a function of dry density.

densities below 1.65 g/cm^3. The osmotic pressure is related to the concentration of the solvated exchangeable cations in osmotic equilibrium with the salinities of the external pore water. At densities higher than 1.70 g/cm^3, another mechanism seems to occur, which is probably related to the hydration energy of the exchangeable cations. At these high densities, some layers in the quasi-crystals are in a state in which only monolayers of water are present. Thus, the exchangeable cations cannot dehydrate to maintain osmotic equilibrium. Their behaviour might be to uptake water to acquire the second solvation shell, because the hydration energy of the bivalent cations is very high (~500-400 kcal/g). For this reason, the energy to be applied to the system for the bentonite not to be able to adsorb water is very high.

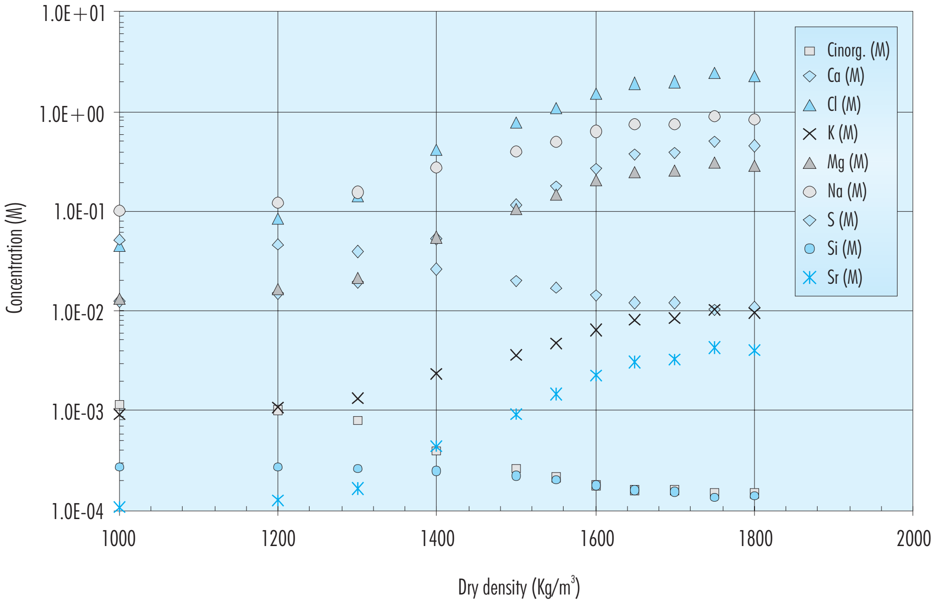

Figure 5.123: Chemical composition of the pore water as a function of dry density.

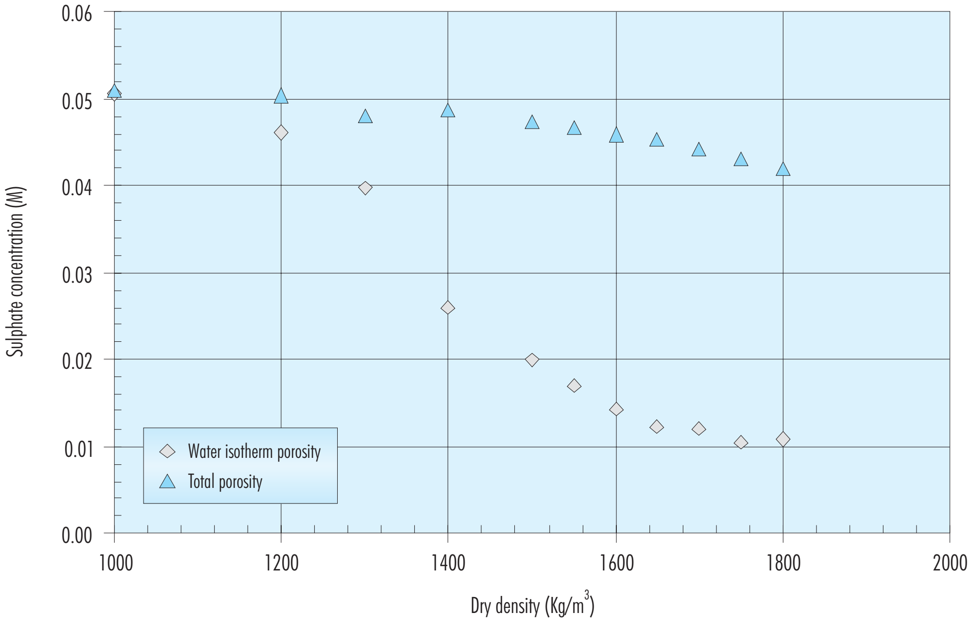

Figure 5.124: Sulphate concentration in the pore water as a function of dry density.

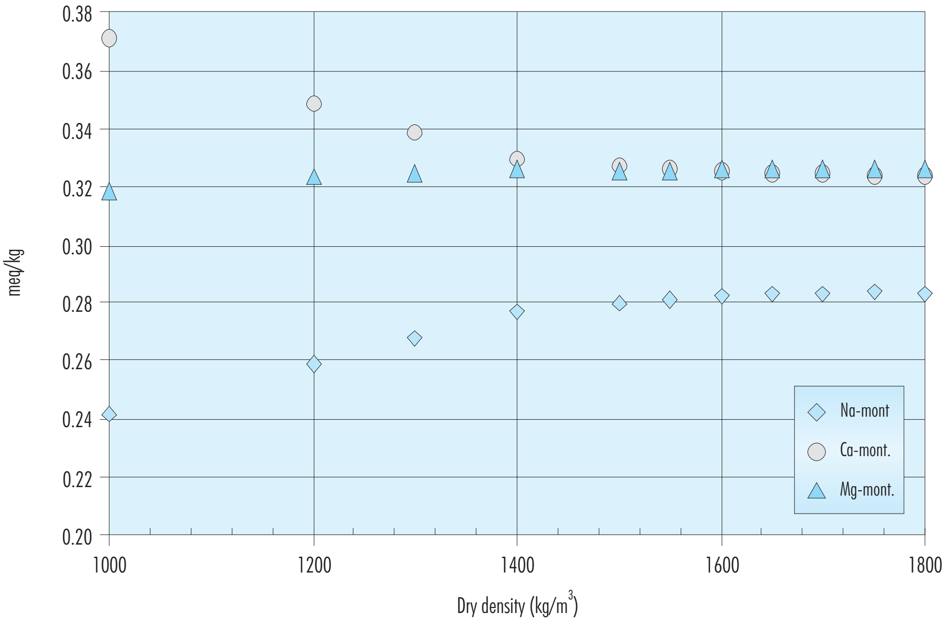

Figure 5.125: Sodium, calcium and magnesium in exchange positions as a function of dry density.

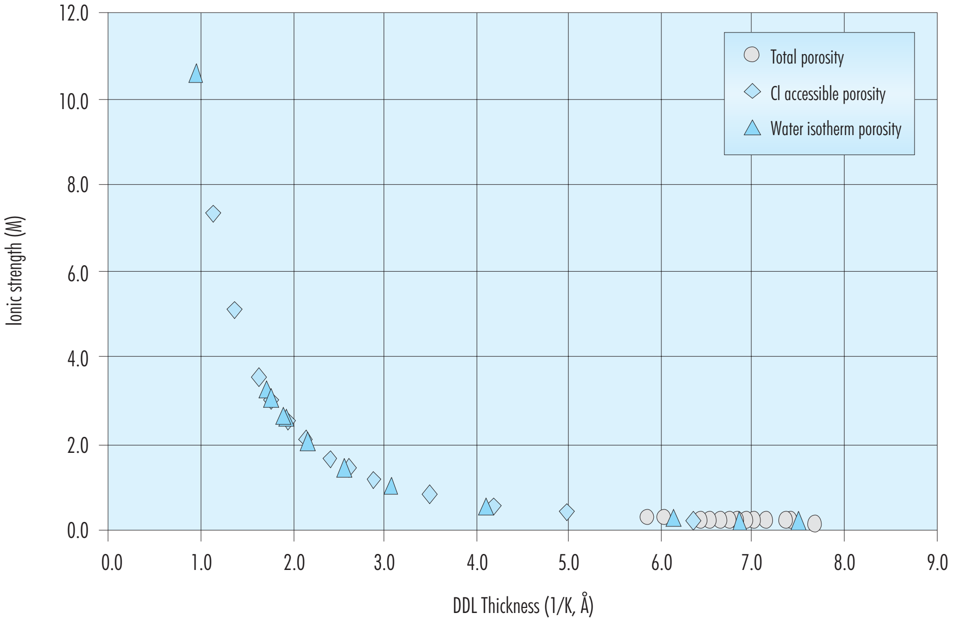

Figure 5.126: Ionic strength versus DDL thickness.

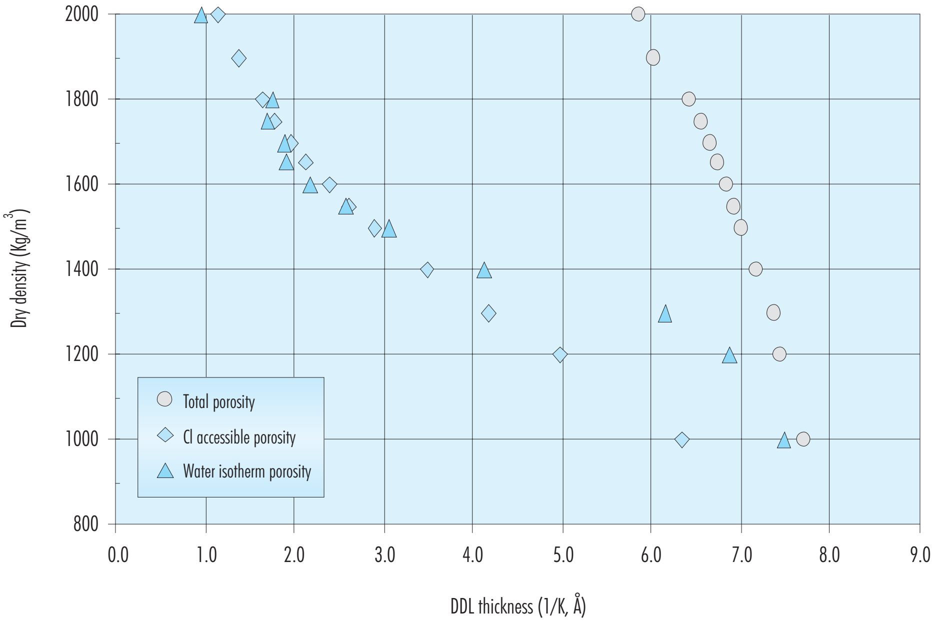

Figure 5.127: Dry density versus DDL thickness in the FEBEX compacted bentonite.

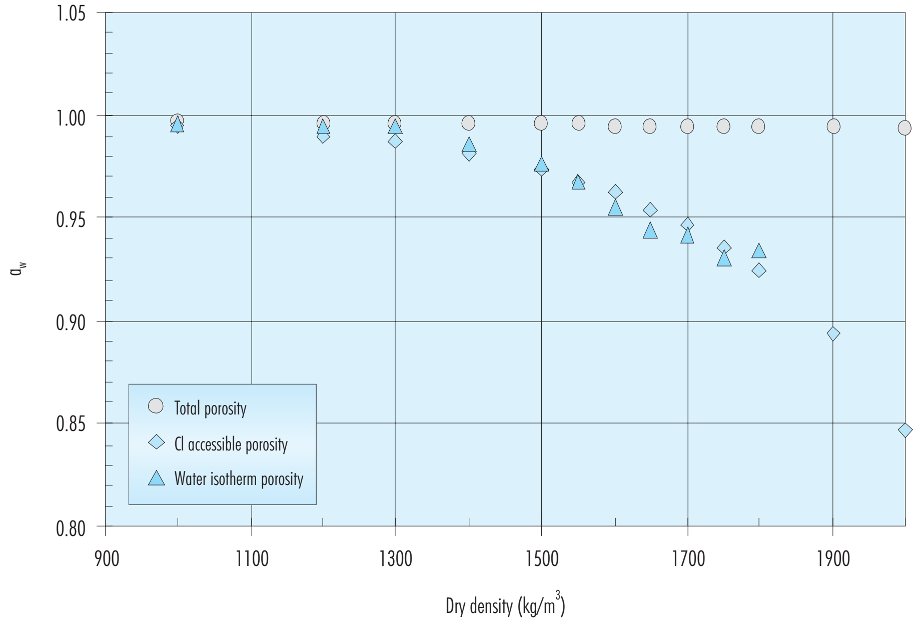

Figure 5.128: Water activity as a function of dry density.

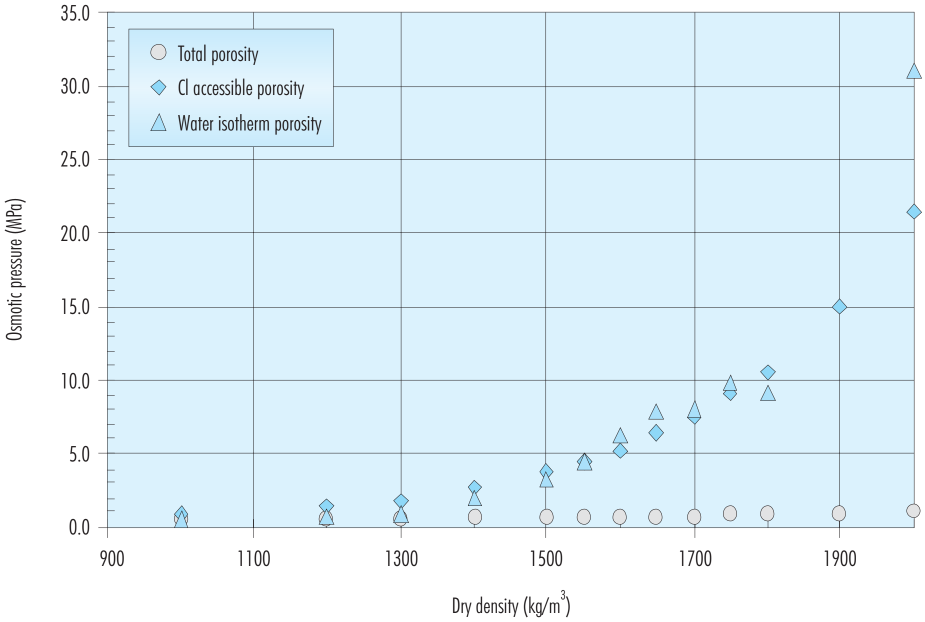

Figure 5.129: Osmotic pressure as a function of dry density.

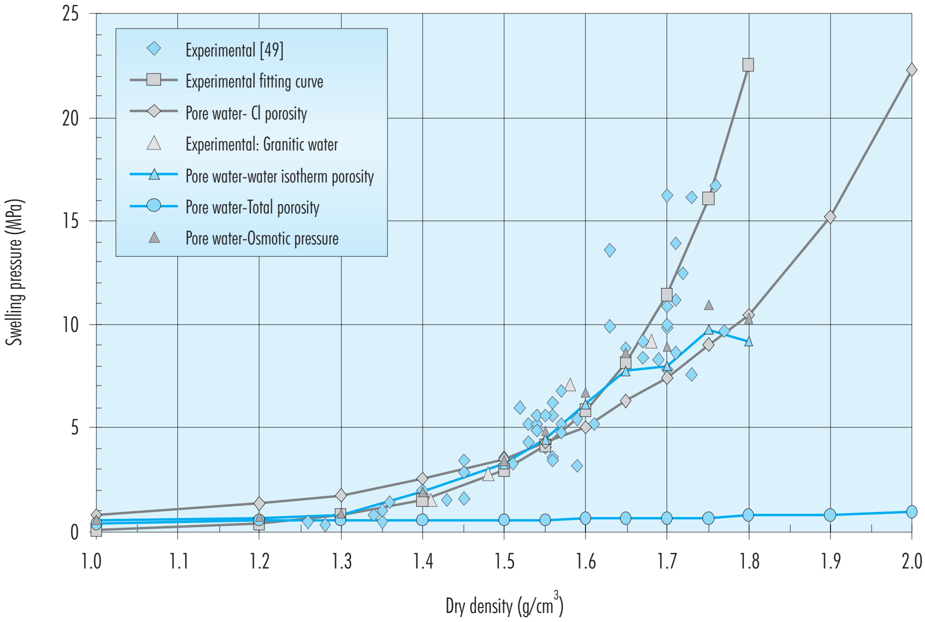

Figure 5.130: Measured and calculated swelling pressure as a function of dry density.

5.2.2. Analysis of solute movement and pore water chemistry in thermo-hydraulic cells

The thermo-hydraulic (TH) tests in cells consist of subjecting the bentonite simultaneously to heating and hydration, in opposite directions, for different periods of time. The objectives of these tests are: a) to analyse the properties of the bentonite and its behaviour under conditions similar to those that will be found in a repository, and b) to make clear what processes and geochemical changes occur when thermal and hydraulic gradients are applied to a compacted bentonite: salt migration, modifications in pore water composition, modification of the cation exchange complex and changes in the fabric. These processes may influence the retention properties (cation exchange capacity and specific surface) and the thermo-hydro-mechanical properties (permeability and swelling capacity) of the clay barrier.

Geochemical modelling also requires the performance of this type of tests to determine the kinetics of ion exchange between the clay and hydration water under different conditions of salinity and temperature. In addition, these experiments are used for the improvement, calibration and validation of the numerical codes developed to obtain predictions regarding the long-term THG evolution of the bentonite barrier.

On completion of the tests, physical, mineralogical and geochemical characterisation of the bentonite was performed. The influence of heating and/or hydration on the physico-chemical and hydro-mechanical properties of the bentonite (hydraulic conductivity and swelling capacity) and the fabric modifications were also tested.

The tests have been performed in cylindrical hermetic cells of different dimensions – 60-cm long, intermediate cells and small cells – described in the following sections.

5.2.2.1.Intermediate cells

In these cells, a single bentonite block measuring 13 cm in height and 15 cm in diameter was heated from the top to 100°C, while being simultaneously hydrated with deionised or granitic water from the bottom, with an injection pressure of 1 MPa (Figure 5.131). The dry density of the bentonite was 1.65 g/cm^3 and in most of the tests it was compacted with its hygroscopic water content. The test program was devised to study the phenomena induced separately by the thermal front and the hydration front, and by the coupling of both fronts, in tests of equal duration. A summary of the characteristics of the tests performed in intermediate cells is given in Table 5.31 and their detailed description and analysis are reported in [124].

Table 5.31
Summary of the tests performed in the intermediate cells

Reference	Test type	Duration (days)	Initial conditions				Water uptake (cm^3)
			Mass (g)	ρ_d (g/cm^3)	Water content (%)	Degree of saturation (%)	
CT-22	Heating+Hydration	26	4298	1.65	13.4	57	275
CT-23	Heating+Hydration	183	4294	1.65	13.3	56	486
CT-24	Heating	168	4690	1.62	26.5	100	---
CT-26	Heating	147	4285	1.65	13.1	55	---
CT-27	Hydration	148	4247	1.65	13.1	55	390
CT-28	Heating+Hydration	307	4315	1.65	13.9	59	399
CT-30	Hydration	362	4274	1.65	13.9	59	439

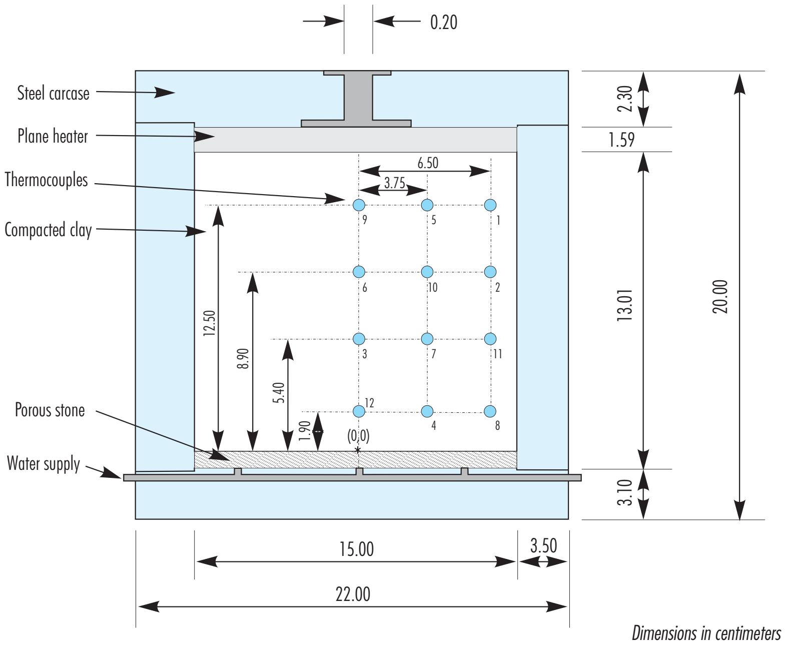

Figure 5.131: Schematic design of the intermediate cells for THG tests.

Figure 5.132 shows the final distribution of water content for various tests. Significant changes in dry density were also observed as a consequence of hydration and heating.

From the geochemical point of view, and based on pore waters extracted by squeezing and the soluble salts determined in 1:4 aqueous extracts, the following relevant processes have been identified [13]:

- Hydration of the bentonite, subjected to heating treatment, produces the dissolution and dilution of the more soluble trace minerals in the bentonite: sulphates, carbonates and chlorides. As a result, saline fronts are generated due to the different mobility of the dissolved ions. The chlorides move as a conservative anion. The movement of sulphates and bicarbonates must basically be regulated by gypsum and calcite equilibrium, respectively.
- The heating treatment without hydration, both with an initial water content of 14 percent (CT-26 test) and an initial water content corresponding to saturated conditions (CT-24 test), seems not to produce a significant movement of the salts. Only an increase of salinity is detected in the heater zone due to the evaporation of water towards cooler zones.
- No significant changes in mass balance have been detected at the end of these thermo-hydraulic tests.
- Under hydration conditions, there is basically an advective transport of chloride and sulphate towards the heater related to hydration front progression (Figure 5.133, Figure 5.134). Chlorides show high mobility. Sulphate concentrates more slowly than chloride towards the heating source, consequently this anion must be affected by gypsum solubility. The dissolution/precipitation processes of the calcite must control bicarbonate movement.
- The main counter ion that follows chloride movement is sodium, which moves following the same pattern shown by chloride. However, the implication of sodium in exchange reactions modifies the relative concentration of both ions: there is an excess of sodium content with respect to that of chloride in the leached

zones, and a default close to the heater. As the hydration front progresses, the dissolution of carbonates and sulphates produces the liberation of calcium. Consequently, the exchange of sodium with calcium in the exchange positions must be induced, changing the relative concentration of the sodium in the aqueous extracts solution. Calcium and magnesium, show a parallel increase, but their concentrations are at least 5-10 times lower than sodium (Figure 5.135). This may be fundamentally related to the different processes in which they are involved: cation exchange reactions and dissolution/precipitation processes of carbonates and sulphates.

Similar conclusions were reached in a set of tests performed in the intermediate cells with the S-2 clay [125].

The chemical composition of the bentonite pore water obtained by squeezing, after being subjected to heating and hydration, depends on the position with respect to the hydration front and on the time elapsed since the process started. There is a depletion of dissolved salts in the more hydrated zones and an enrichment near the heater. A sodium and chloride front is developed in parallel to the hydration front. The sodium content is higher than the chloride concentration in the leached sections, as was observed in the aqueous extracts solutions. The advective transport through the bentonite changes the initial composition of the pore water from sodium-chloride type water ($I \approx 0.2$ *M*) to sodium-sulphate type water ($I \approx 0.02$ *M*) in the more hydrated zones; and to sodium-sulphate-chloride type water ($I \approx 0.07$ *M*) in sections farther from the hydration surface. The different mobility of sulphate with respect to chloride seems to be related to the control of this anion by gypsum solubility. In the driest zone, close to the heating surface, the calculation of the pore water composition shows that it must be an Na-Cl type water, with a maximum saline concentration ($I \approx 1.2$ *M*).

The heating applied to an initially saturated bentonite block (CT-24 test) did not produce significant changes in pore water composition. Only the precipitation of a thin film of anhydrite was detected at the contact with the heating source.

The exchange processes play a fundamental role in the bentonite-water interaction during hydration and heating. The results seem to indicate that there is a general increase in the content of exchangeable calcium and an increase in exchangeable magnesium in the zone closest to the heater, related to a decrease in sodium at the exchangeable positions.

5.2.2.2. Small cells

The main purposes of the small cell tests were to minimise testing time and complement the scale effect on the geochemical processes study. The tests performed made it possible to study the effect of the geochemical environment and the textural modifications produced during the thermohydraulic treatment of the bentonite on its hydraulic and mechanical behaviour. A detailed description of the tests and results is given in [126].

The bentonite specimen measured only 2.5 cm in thickness and 5.0 cm in diameter (Figure 5.136). Saturation was reached after a few days, under an injection pressure of 1 MPa. This allowed a large number of tests of different duration and conditions to be performed. The initial dry density of the bentonite was 1.65 g/cm^3 and the water content was hygroscopic (around 14 percent). Two sets of temperatures (60-35°C and 100-60°C) applied at the heating and hydration ends were examined, in order to ascertain the effect of temperature on the observed processes. The influence of the chemistry of the hydration water on the processes observed was verified by using two types of water: granitic and saline (Table 5.5). This last has a chemical composition similar to that of the bentonite pore water under saturated conditions (Section 5.2.1), but is simplified to include only the major elements. The duration of the tests was related to saturation time. The time needed for saturation was verified previously, and amounts to 16 days for the tests performed at low temperature and to 10 days for the tests at high temperature.

A sodium and chloride enriched water front was developed during the hydration stage, mainly due to the advective transport of these ions inside the bentonite. This process is favoured by an increase in the average temperature and is not dependent on the type of water, saline or granitic. The concentration gradient practically disappeared at complete saturation.

A net decrease in bulk salinity, mainly represented by sodium and chloride variations, was detected from the beginning of the hydration process in the small cells, under both saline and granitic conditions. This decrease is more significant at higher temperatures. Diffusion towards the hydration source must be the predominant transport process after saturation is reached.

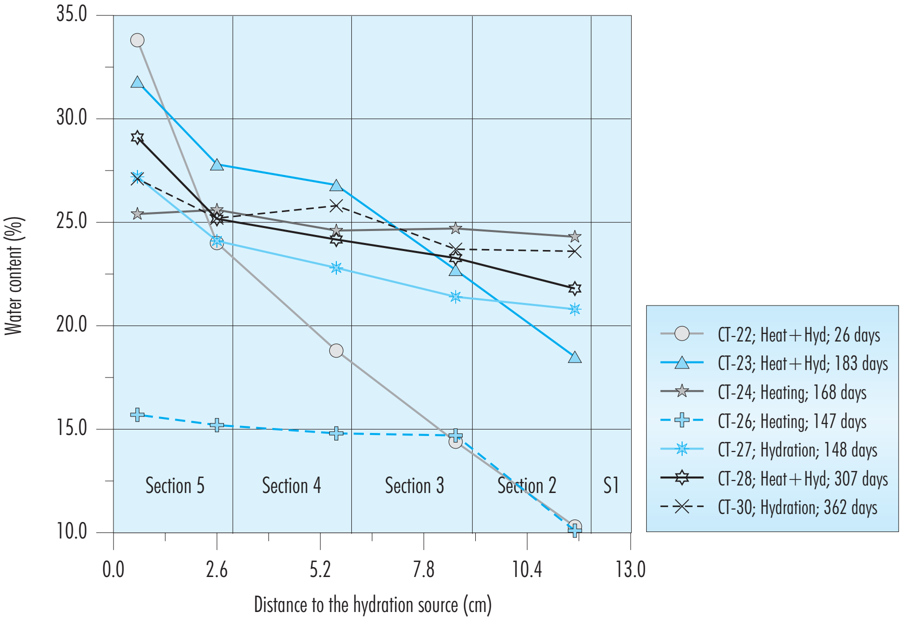

Figure 5.132: Final water content distribution in the intermediate cells tests .

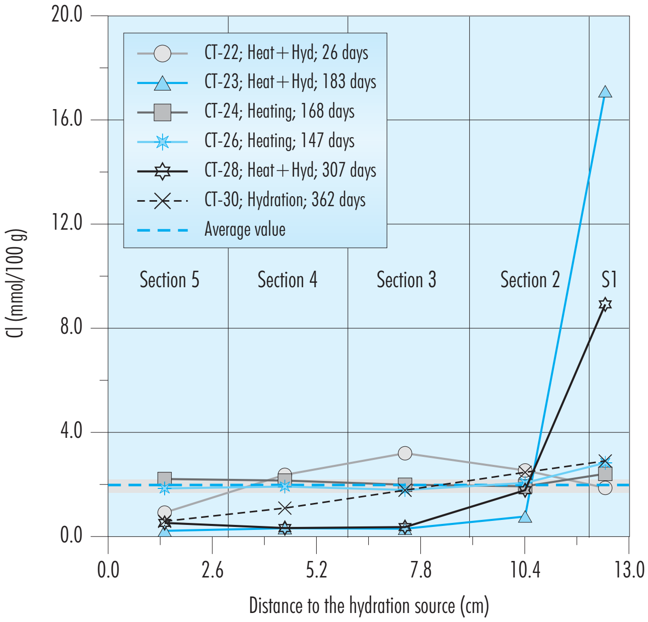

Figure 5.133: Chloride concentration (mmol/100 g of dry bentonite) measured in 1:4 aqueous extracts (the horizontal bar is the average value of the untreated FEBEX bentonite).

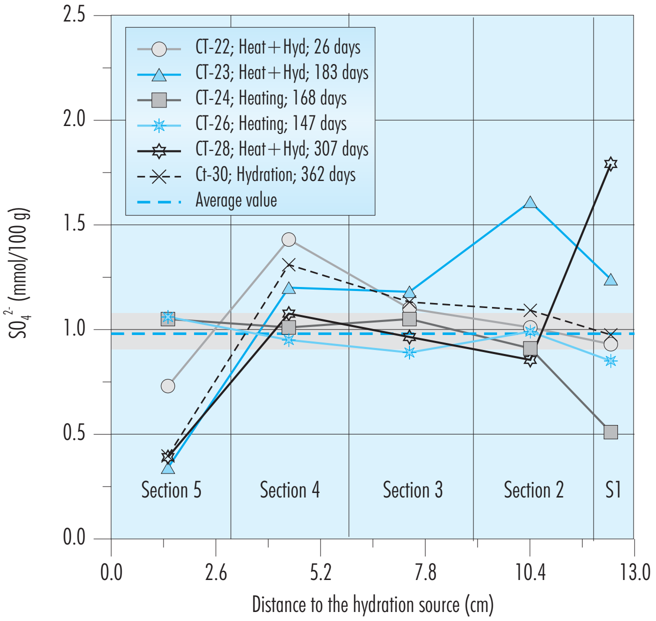

Figure 5.134: Sulphate concentration (mmol/100 g of dry bentonite) measured in 1:4 aqueous extracts (the horizontal bar is the average value of the untreated FEBEX bentonite).

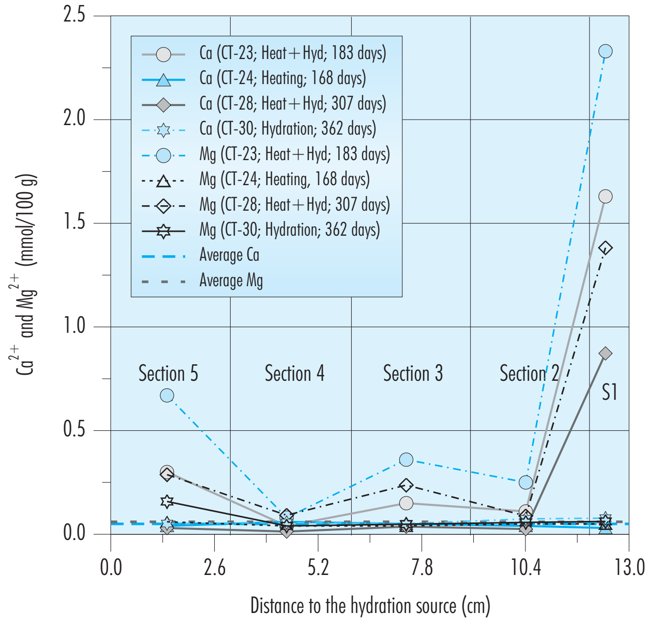

Figure 5.135: Calcium and magnesium concentration (mmol/100 g of dry bentonite) measured in a 1:4 aqueous extract.

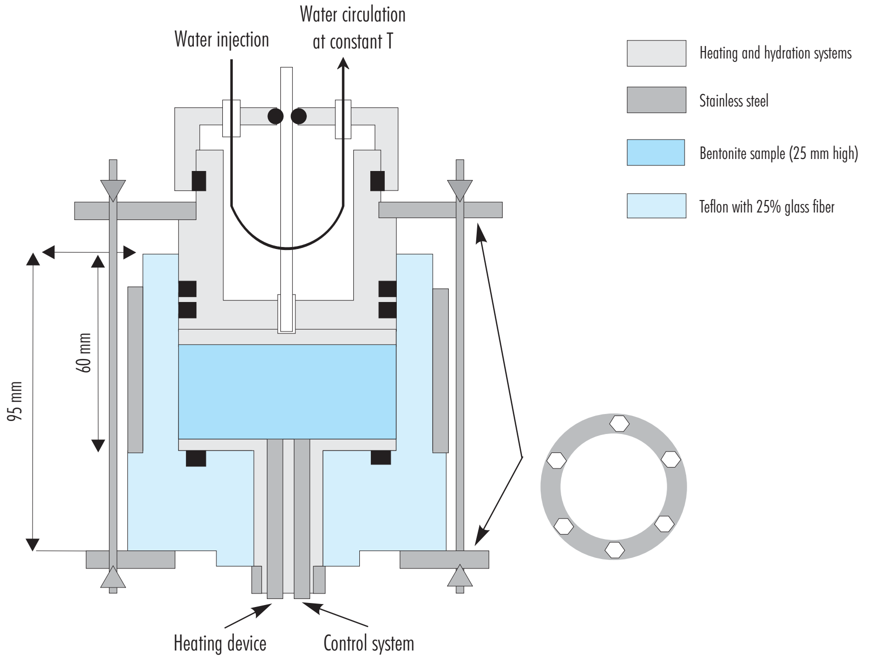

Figure 5.136: Schematic design of the small cells for THG tests.

Apparent diffusion coefficients (D_a) for ions and salts were measured during the homogenisation of concentration profiles in the post-saturated stages. D_a values for Cl^-, SO_4^{2-}, Br^-, Ca^{2+}, Mg^{2+}, Na^+, K^+, Sr^{2+}, and Zn^{2+} were calculated. The values vary in the range of $1.5 \cdot 10^{-10}$ to $4 \cdot 10^{-12}$ m^2/s; the ions Cl^-, Na^+ and Ca^{2+} being of higher mobility [127, 128, 129].

The other geochemical parameters determined show a high degree of invariance:

- Bicarbonates and pH were quite constant in all the tests. These parameters are buffered from calcite equilibrium and their values are 1.5 ± 0.3 mmol/ 100g and pH 8.0 ± 0.2, respectively. Calcite was present in all the samples, and was detected in slightly higher amounts near the heater zone in some tests by X-ray diffraction.
- The constancy of the atomic proportions of the K^+ fixed in the smectite indicates that illite/ smectite inter-stratification did not change during the tests.

The external specific surface of the bentonite presents minor changes at the beginning of treatment, but in most cases the original values are recovered when the bentonite becomes saturated.

The fabric of the bentonite observed by polarising optical microscopy in thin sections is similar in treated and untreated samples. The optically detectable porosity disappears after hydration. Some micro-fissures (1-mm length) inside the clayish macro-aggregates and in the bentonite matrix were identified. They were stained by iron oxides, mainly in the heater zones at complete saturation. Fine-grained calcite was also observed around rigid micro-crystals or vitreous volcanic rock fragments. Clay orientation was higher around rigid and plastic interfaces (micro-crystals and clay aggregates), especially in the longer tests.

Optical microscopy determination of the amount of calcite precipitates showed that calcite had “spread” along the sample. This “spreading” effect is possible by partial dissolution of sparitic crystals and subsequent precipitation elsewhere. Calcite seems to be leached with time in the more diluted granitic environment.

Due to the minor modifications in the bentonite mineralogy, a zero or very low impact on hydraulic conductivity or swelling pressure should be expected during the transient hydration and heating stage. In the short term, a slight increase in the hydraulic conductivity of the clay was observed after TH treatment at high temperature with granitic and, especially, saline water. In the case of saline water, this increase becomes lower with the duration of the treatment, probably due to the general decrease of salinity with time. The swelling capacity of the remoulded clay increases after TH treatment with granitic water, and remains unchanged when saline water is used. This increase might be related to the dissolution of cementing agents by the granitic water, which would bring a disaggregation of bentonite flakes, which seems to be confirmed by the microstructural observations. This is also consistent with the calcite leaching observed by optical microscopy.

5.2.2.3. 60-cm-long cells

The main purpose of the tests performed using the larger cells was to analyse the properties of the bentonite and its behaviour under conditions similar to those that will be found in a repository. In these tests, the thickness of the bentonite and the thermal gradient were similar to those of the real case. Six different tests were performed with this type of cells. Three of them, called FQ, were used to study the effect of the geochemical environment, produced during the TH treatment of the bentonite, on its hydraulic and mechanical behaviour. The others, called HI, were used to analyse the physico-chemical properties and the variation of the chemical composition of the pore water in the bentonite after TH treatment. In addition, the micro-fabric was also analysed by SEM in order to confirm which mineral phases contribute significantly to the composition of the aqueous phase. FQ and HI tests were performed at three different periods of time: 0.5 years, 1 year and 2 years. At the end of the tests, the samples were sliced in 24 vertical sections, each 2.5 cm high, numbered from 1 (near the hydration surface, *i.e.* the top) to 24 (near the heater, *i.e.* the cell bottom).

The experimental setup and results concerning the evolution of temperature throughout the tests, the final distribution of water content and dry density and the repercussion on the HM behaviour of the bentonite are described in Section 5.1.4.5.

The final distribution of soluble salts in the different tests is shown in Figure 5.137. Hydration of the bentonite produces the dissolution and dilution of the more soluble trace minerals in the bentonite (sulphates, carbonates and chlorides). As a result, saline fronts are generated due to the different mobility of the dissolved ions. Chloride moves with water by advection as a conservative anion. For this reason the maximum concentration of chloride in the bentonite block varies as a function of the duration of the test. In addition, close to the heater there is an increase of chloride due to water evaporation. The chloride concentration is diluted at about 5 cm from the heater source, where the evaporated water condenses. This effect depends on the duration of the test. The movement of sulphates and bicarbonates must be basically regulated by gypsum and calcite equilibrium, respectively. Their movement is slower than that of chloride. The increase of the bicarbonate contents close to the hydration source is due to the dissolution of carbonates.

The main counter ion that follows chloride movement is sodium. However, the implication of sodium in exchange reactions modifies the relative concentration of both ions. There is an excess of sodium content with respect to that of chloride in the leached zones. As the hydration front progresses, the dissolution of carbonates and sulphates produces the liberation of calcium. Consequently, the exchange of sodium with calcium in the exchange positions must be induced, changing the relative concentration of the sodium in the aqueous extracts solution. The other major cations, calcium and magnesium, show a parallel increase, but their concentrations are at least 5-10 times lower than sodium. These results are similar to those obtained in tests in intermediate cells (Section 5.2.2.1).

No significant variations have been observed regarding the exchangeable cations (Figure 5.138), neither with time nor as a result of the position of the samples with respect to the heater.

Regarding the chemical composition of the pore water extracted by squeezing at 60 MPa, the distribution of solutes follows the same tendency observed in the aqueous extracts (Figure 5.139). There is an increase of the pore water concentration towards the inner part of the bentonite barrier as a function of the hydration front. The salinity increases also with the distance to the heater as a function of time, in accordance with water movement. In this case, although the pore waters are of Cl-Na type, the content of sodium is lower than chloride. The

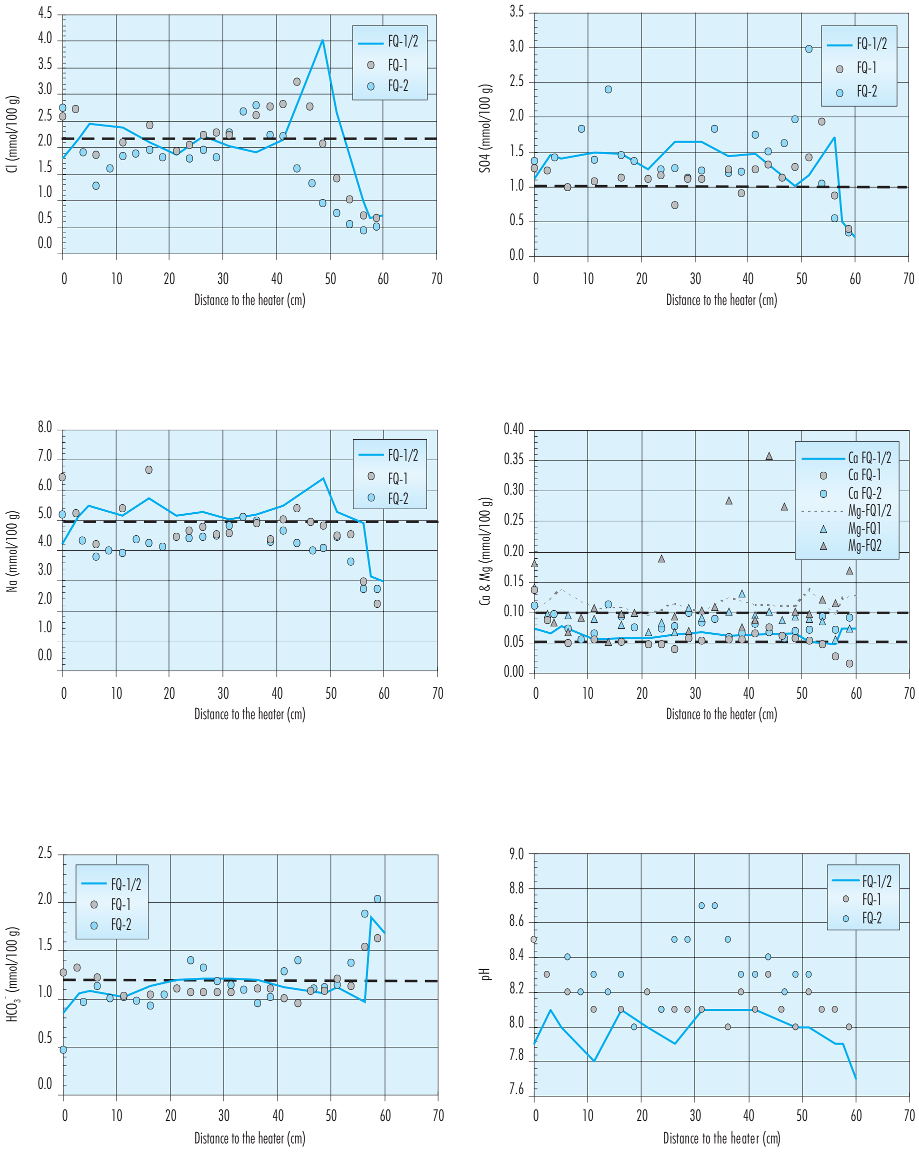

Figure 5.137: Distribution of soluble salts and pH obtained in the 60 cm-long cells by means of aqueous extracts at a 1:4 S:L ratio.

mobility of SO_4^{2-} and HCO_3^- with respect to that of Cl^- is hindered, because these anions are controlled by dissolution/precipitation processes of gypsum and calcite. The pH values are lower than those obtained in the aqueous extracts, the lowest values being those obtained in the 2-year tests.

Regarding the mineralogy, no significant changes were found in the smectitic phase (Figure 5.140). The basal spacing *d*001 of the smectite did not change. In all the tests neo-formed feldspars (sanidine, anortite) were found in the bentonite at the heater contact, where Na-K-Cl salts were also found in the 1-year test.

A study of the bentonite fabric was performed by SEM. The most relevant aspect of this study was the visualisation of the geochemical processes found in

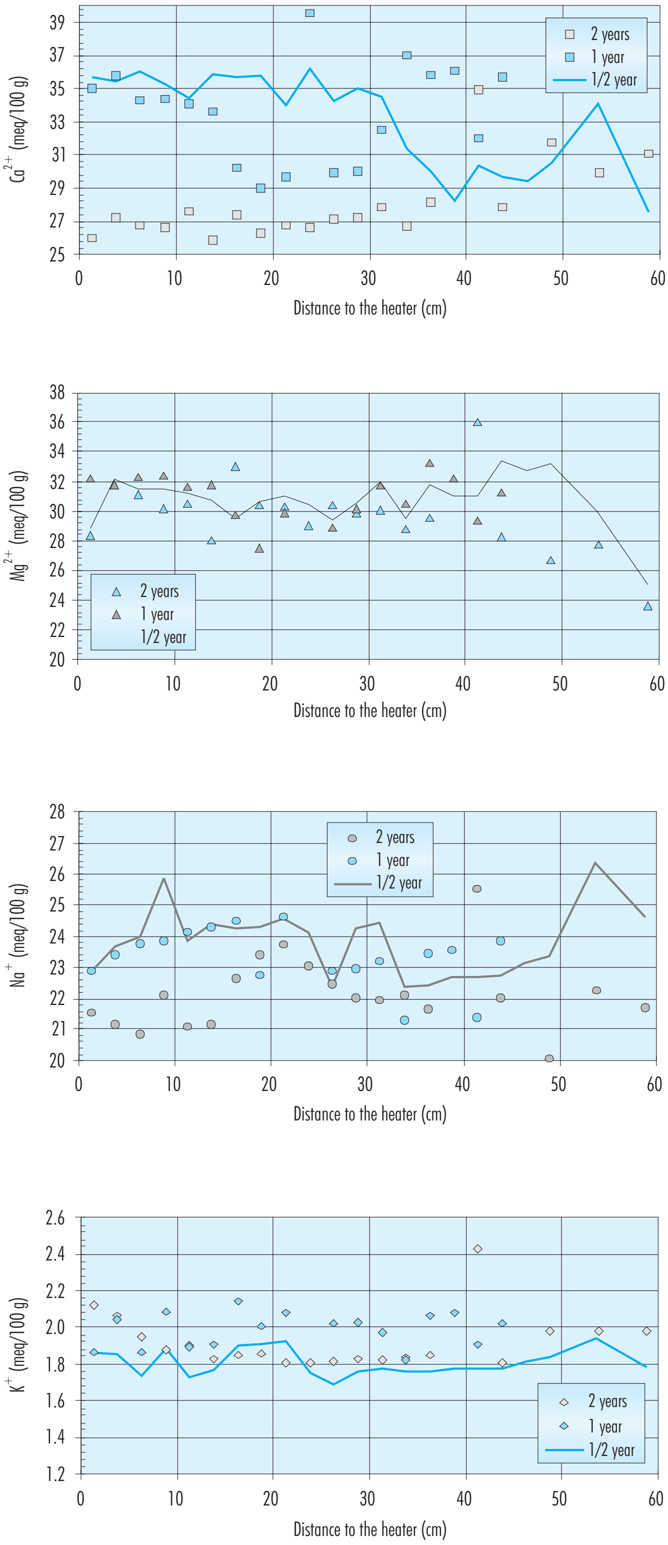

Figure 5.138: Distribution of the exchangeable cations in tests performed in 60 cm-long cells with different duration.

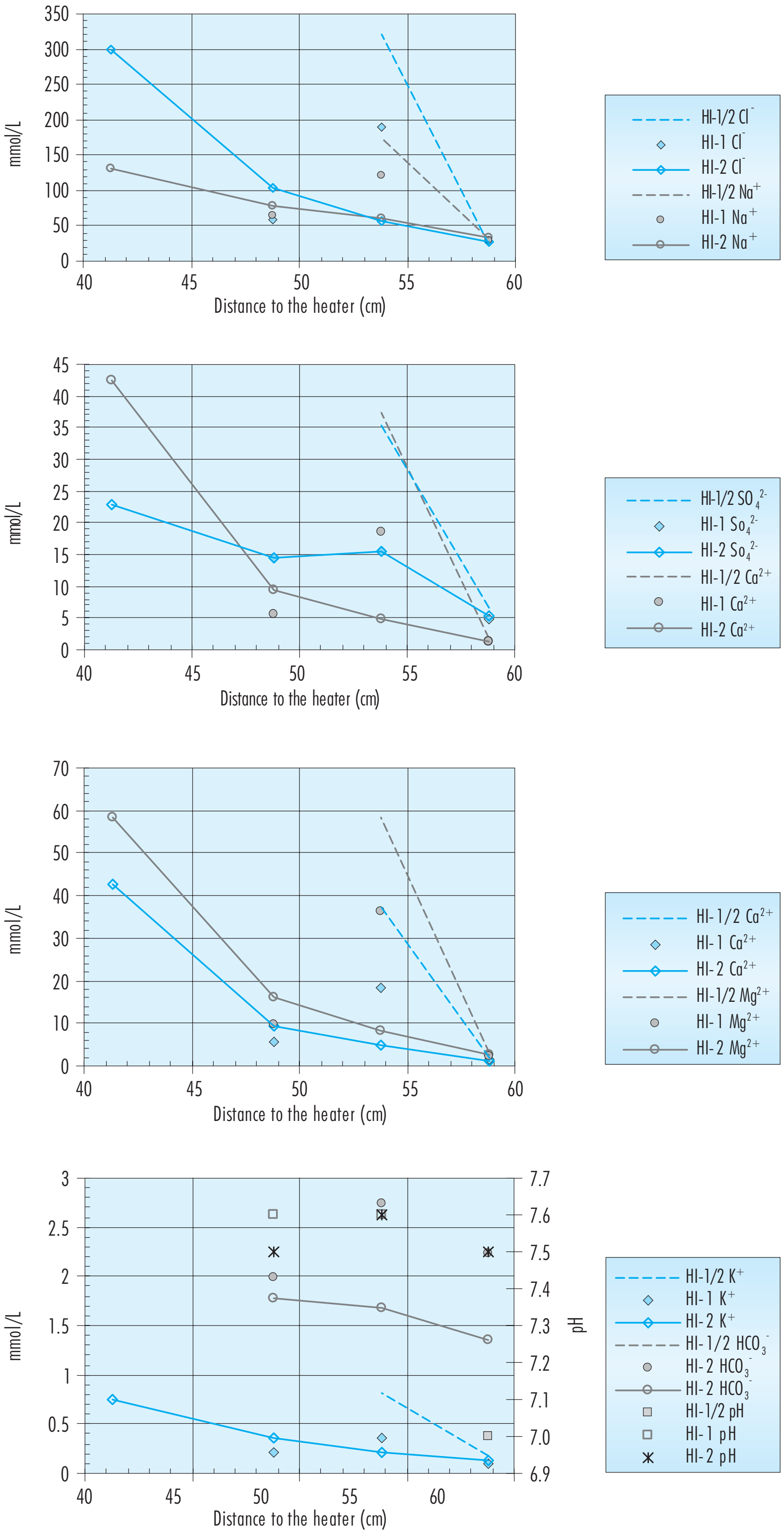

Figure 5.139: Chemical composition of the pore waters obtained by squeezing at 60 MPa after the TH test performed in 60 cm-long cells.

the chemical analyses of the samples (pore water, soluble salts, mineralogy). In the hydration zone (section 1) a leaching of salts is produced, this being distributed to other sections towards the heater (section 24). The location of the different salts depends on the duration of the thermo-hydraulic process and hence, on the advance of the hydration front. The chlorides advance with the water front, followed, at a slower rate, by sulphates and bicarbonates, this being because their movement is limited by the dissolution/precipitation of gypsum and carbonates.

In the 1 year tests, the highest concentration of chlorides was found at about 23 cm from the hydration source (section 9, Figure 5.141), which is the farthest location to which water has arrived (see Figure 5.63). Silica gel with impregnations of chloride was also found at this location. The highest concentration of calcium sulphate was found at about 20 cm from the hydration source (section 8, Figure 5.142), although gypsum was found in section 11 (26 cm from hydration surface). Carbonates have been identified at 20 cm from the hydration surface (section 7, Figure 5.143) and near the hydration surface. In sections 12 and 13 (27-32 cm), there were idiomorphic crystals of Si, Al and K.

In the 6 month test, the same mineral phases were observed but at locations closer to the hydration source. At 9 cm from the hydration surface (section 4), a covering of chloride has been found in some particles. The highest contents in gypsum are located at 8 cm from the hydration surface (section 3, Figure 5.144), where idiomorphic crystals of Si, Al and K were also found. In sections 3 and 4, *i.e.* between 6 and 9 cm from the hydration surface, spherical crystals of silica, tridymite type (Figure 5.145) have been identified. Carbonates have been detected near the hydration surface.

In the 1 and 0.5 year tests, crystals of silica and of some type of feldspar, which seem to be neoformed, have been detected at the heater contact. In addition, in the 1 year test, bacteria were observed at the surface of the bentonite located at the contact to the hydration porous plate.

Mineralogical and geochemical analyses of the FQ tests were also performed at the UAM laboratories. The results obtained are detailed in [66]. The main geochemical processes observed are the inter-

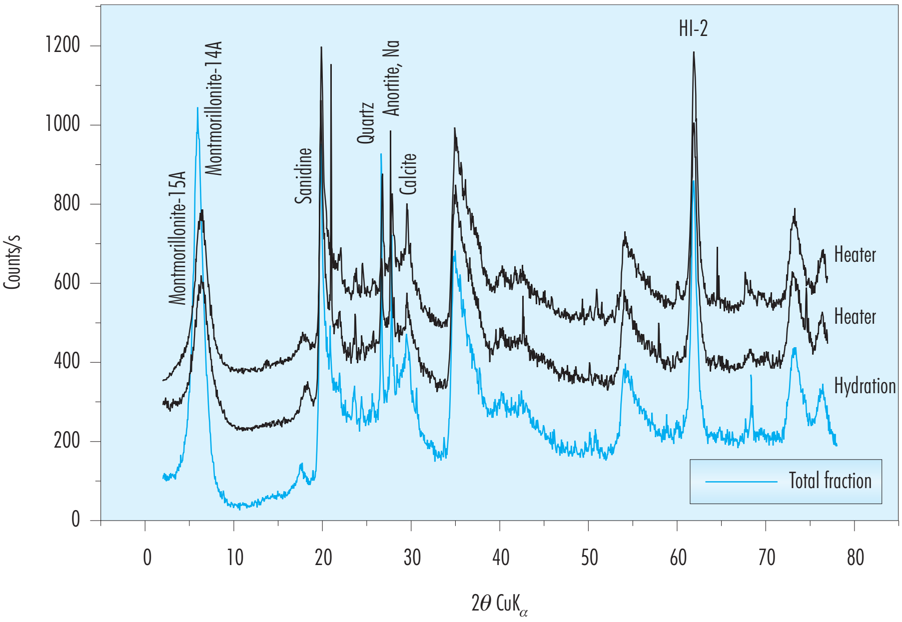

Figure 5.140: XRD pattern of random powder of bentonite samples at different positions after a 2-year test HI2.

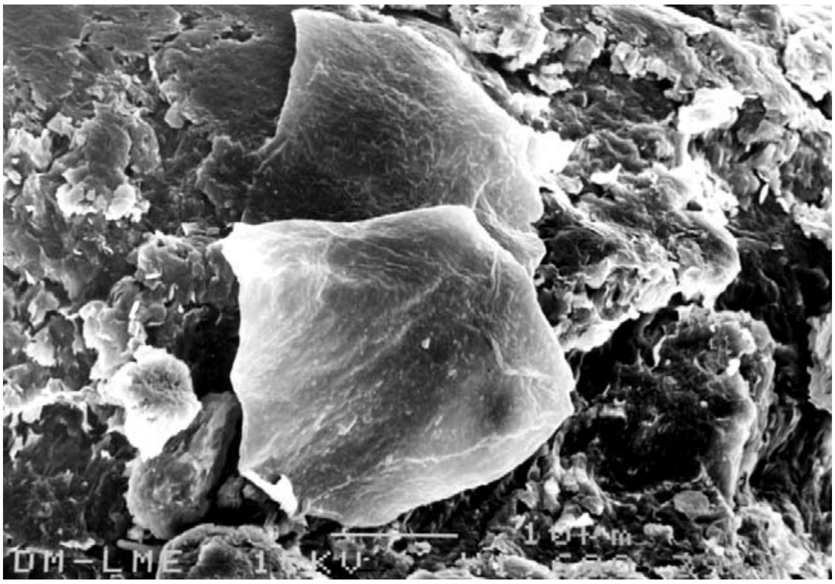

Figure 5.141: K-Na-Cl crystal found in section 9 (22.5 cm from hydration surface) of the 1 year test HI1.

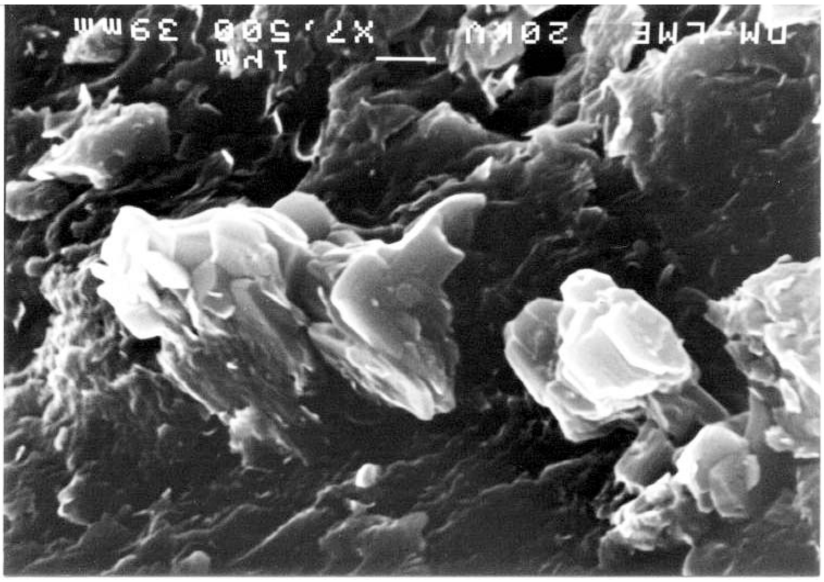

Figure 5.142: Gypsum crystals found in section 8 (20 cm from hydration surface) of the 1 year test HI1.

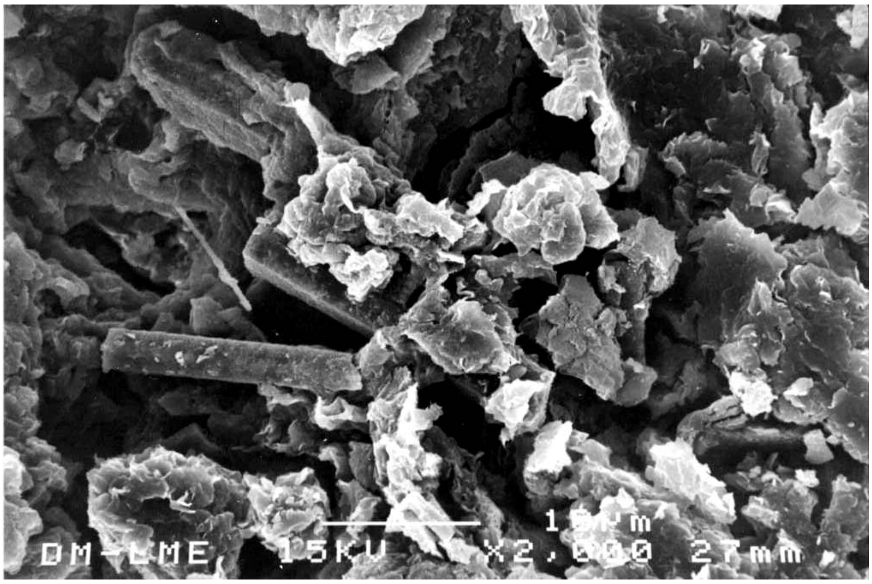

Figure 5.143: Ca-Fe carbonates found in section 7 (16 cm from hydration surface) of the 1 year test HI1.

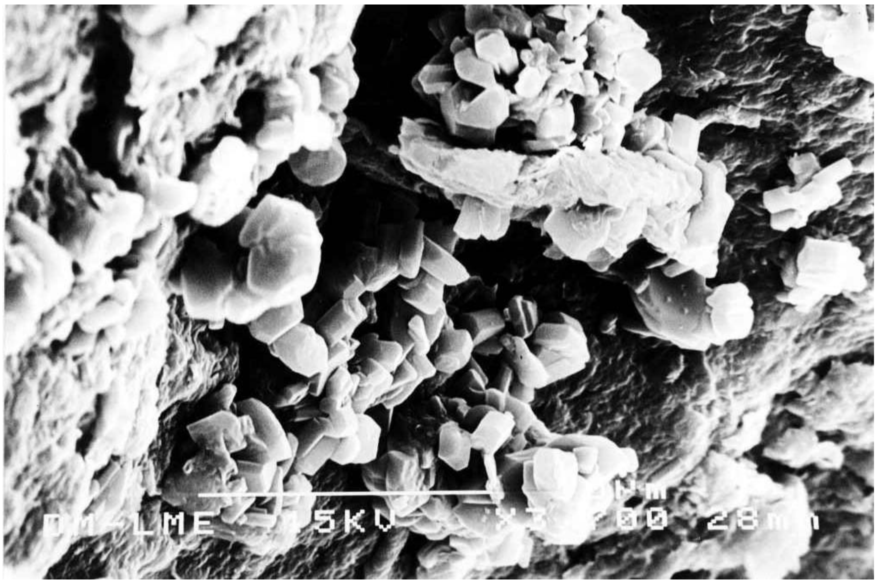

Figure 5.144: $CaSO_4$ crystals found in section 3-4 (6-9 cm from hydration surface) of the 0.5 year test HI1/2.

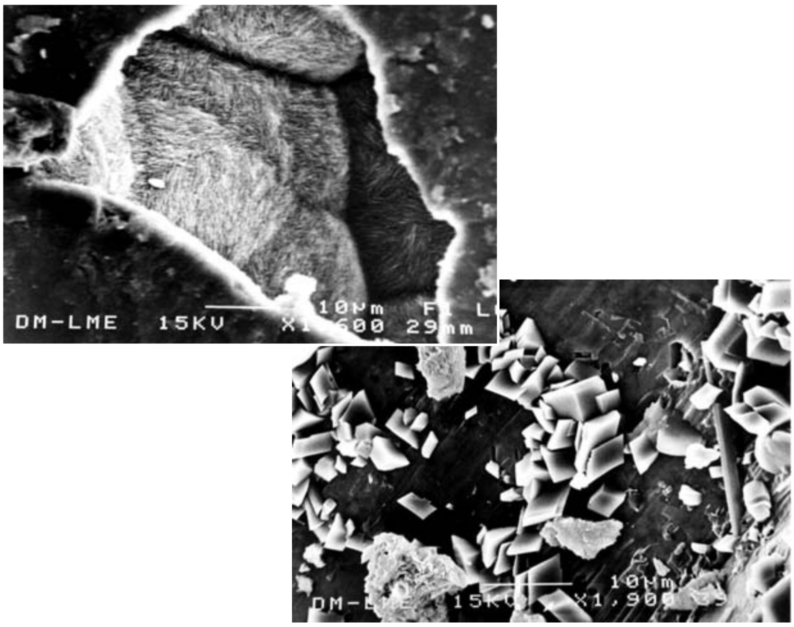

Figure 5.145: Silica surrounded by smectite (left) and neo-formed feldspar crystals (right) found in section 24 (near the heater) of the 0.5 year test HI1/2.

change of Na^+ with Ca^{2+} and the dissolution/precipitation of calcite. Other possible processes are the dissolution of sulphates – whose mobility is conditioned by anionic exclusion –, the formation of colloids (Fe and Ti oxides) and the formation of microcrystalline quartz. No mineralogical changes were detected, except for a slight increase in the size of the smectite crystallites.

5.2.3. Radionuclide sorption and migration in bentonite

The transport of radionuclides through the compacted bentonite is a diffusion-controlled process retarded by sorption, thus, for the performance assessment calculations of a repository, distribution coefficients and apparent and effective diffusion coefficients of relevant radionuclides in bentonite are necessary. A series of small-scale laboratory tests was planned to determine these parameters for several radionuclides and, in particular, for all the elements used in the "mock-up" and "in situ" tests (rhenium, selenium, europium, thorium, uranium, neodymium and caesium). Attention focussed on their diffusion behaviour in clay compacted at 1.65 g/cm^3. Apart from the radionuclides used in these large-scale tests, other radionuclides of interest were investigated (tritium, chlorine, iodine, calcium, strontium and sodium). The diffusion of conservative species, both neutral and anionic, was studied as a function of clay density, in an attempt to clarify the possible effects of anion exclusion. It was observed that the determination of the accessible porosity is often tricky, especially when high clay densities are considered. Therefore, it was very important to analyse different methodologies and compare the results obtained, in order to understand the limitations of each technique and finally provide reliable results. Furthermore, the use of different techniques and the independent determination of each transport parameter could be used to validate the results.

The very different nature of the elements studied (from conservative to highly sorbing) implied the design of different experimental setups in order to obtain transport parameters. As regards the determination of the FEBEX bentonite sorption properties, during the first phase of the project, batch sorption tests on the natural clay were carried out. Distribution coefficients (K_d)

were obtained at different S:L ratios. In the second phase of the project, special cells were designed in an attempt to determine K_d values also in the compacted clay. Since the "K_d-approach" does not allow for the extrapolation of laboratory results to different environments and limits the description of the processes occurring in the medium to an empirical parameter, a new approach, based on the mechanistic description of sorption was also undertaken. The mechanistic approach is expected to improve the understanding of transport processes in compacted bentonite and, therefore, the future predictive capability. Particularly, in the second phase, the sorption mechanisms of Cs and U were analysed. Sorption data obtained for other radionuclides in the FEBEX clay may be found in [130]. In order to carry out this study, it was necessary to work with a simplified and very well characterised system, studying the effects of the most important physico-chemical parameters such as pH, ionic strength and radionuclide concentration, independently. Therefore, purified and homoionised bentonites were used: the FEBEX clay was used by CIEMAT and the SWy1 clay by PSI.

Further information and details on the results described here may be found in [131, 105, 132, 133, 134, 135].

5.2.3.1. Sorption properties of the natural FEBEX bentonite

Table 5.32 summarises the results of the sorption batch tests performed with FEBEX bentonite in water at different solid to liquid (S:L) ratios. The results demonstrated that trivalent cations such as europium and neodymium, along with the tetravalent thorium, were totally sorbed and that the elements present in anionic form, such as rhenium (ReO_4^-), iodine (I^-) and technetium (TcO_4^-), were not sorbed at all. Selenium was not sorbed in its higher valence state (VI, SeO_4^{2-}), but a slight sorption was observed for selenium in a lower valence state (IV, SeO_3^{2-}). Uranium showed small sorption, whereas high / very high K_d values were found for cobalt, strontium and caesium.

These studies showed a dependence of the retention capability on the solid to liquid ratio, since K_d values tend to decrease when the solid to liquid ratio increases (except for strontium). This may be due firstly to the dissolution of salts and impurities contained in the clay, since at higher bentonite contents there is a higher concentration of HCO_3^- and SO_4^{2-}. These ions are well known complexing agents that may contribute to the hindering of sorption. Secondly, with increasing bentonite content there is an increase also in the ionic strength of the water and the content of ions, which are potentially competitive to sorption sites. Ionic strength and the presence of higher concentrations of certain cations in the water would be very important, particularly if sorption occurred via ion exchange or if the surface complexes between the radionuclide and the clay, were of the outer-sphere type.

In addition, the question as to whether or not the sorption behaviour is the same in dispersed and

Table 5.32
Summary of batch tests carried out under oxic conditions on FEBEX bentonite. K_d values in mL/g

Element and concentration	Solid to liquid (S:L) ratio					
	1/100	1/70	1/50	1/40	1/30	1/20
ReO_4^-, I^-, SeO_4^{2-}, TcO_4^-	0% sorption ($K_d = 0$)					
$[Co] = 1.1 \cdot 10^{-8} M$	1100	800	580	470	360	250
$[Cs] = 1.0 \cdot 10^{-9} M$	68500	58000	43000	38000	32000	28800
$[Se]_{IV} = 3.34 \cdot 10^{-8} M$	28	25	24	22	20	17
$[Sr] = 5.0 \cdot 10^{-9} M$	1735	2050	2310	2311	2360	2178
$[U] = 2.27 \cdot 10^{-6} M$	28	26 (1)	23	-	-	15
Eu, Nd, Th	100% sorption ($K_d > 100000$)					

(1) *For S:L = 1:80*

compacted systems was opened. Under repository conditions, the solid to liquid ratio will be high (4:1) and, furthermore the material will be compacted. This should lead to a further decrease in the distribution coefficient. For this reason, it was considered necessary to obtain K_d values by means of tests under conditions as similar as possible to those expected in the repository. Therefore, an attempt was made to determine the K_d values of Cs, Co, Eu, Se, Tc, U, Nd and Th in the FEBEX bentonite compacted to a dry density of 1.65 g/cm^3. In order to do so, an experimental cell was especially designed. The clay was introduced in the cell between two sinters and confined by a stainless ring and two Teflon caps. The cells were located in a vessel filled with water and the caps were open to allow the water to enter into the clay. The time needed to hydrate a clay plug of these dimensions (8x19 mm) is approximately one month. After this time, the water was labelled with the radiotracer, and the concentration in the liquid phase was periodically monitored to check tracer uptake. The evolution of the K_d values obtained during the first year is summarised in Table 5.33.

This method cannot be considered appropriate for the highly-sorbing radionuclides such as Nd, Th and Eu, since these elements are extensively and rapidly sorbed onto the stainless filters and the Teflon cells. Furthermore, K_d for other less sorbing elements increased with time. This suggested that, even after one year, sorption equilibrium was not completely reached.

5.2.3.2. Sorption properties of the homoionised clay

By means of the simple K_d-approach, it is not possible to evaluate the effects on the sorption of the different variable geochemical parameters (for example the evolution of pore water in the medium). For this reason, mechanistic studies were undertaken, in the second phase of the FEBEX project, with Cs and U. Batch sorption tests were carried out using different bentonites that were purified and converted into an homoionised form using the method proposed by Baeyens & Bradbury (1997 [136]) and Bradbury & Baeyens (1997 [109], 1999 [137], 2002a [138]).

The main sorption mechanisms expected in clays are cation exchange and surface complexation. To identify and quantify to what extent these two mechanisms occur, different types of experimental data have to be generated. The sorption has to be represented as a function of pH (*sorption edges*) at constant ionic strength, and as a function of the radionuclide concentration at a constant pH (*sorption isotherms*). The main objective of these tests is to obtain parameters such as *surface complexation constants* and *selectivity coefficients*. These parameters are required for a (quasi)-mechanistic description of sorption and they might be very useful for the mod-

Table 5.33
K_d obtained in compacted bentonite after different periods of time

Element and concentration (M)	K_d (mL/g)			
	60 days	120 days	180 days	350 days
$[^{99}Tc] = 2.35 \cdot 10^{-7}$	0	0	0	0
$[Th] = 2.16 \cdot 10^{-8}$	sorption onto wall and cell, 100% sorption in batch			
$[Nd] = 3.47 \cdot 10^{-6}$	sorption onto wall and cell, 100% sorption in batch			
$[^{152}Eu] = 5.63 \cdot 10^{-10}$	sorption onto wall and cell, 100% sorption in batch			
$[^{60}Co] = 4.72 \cdot 10^{-10}$	18.7±7.7	20.2±3.8	26.3±3.0	29.3±3.0
$[^{137}Cs] = 2.43 \cdot 10^{-9}$	101.6±4.1	528.7±33.5	2120±280	17590±1360
$[^{233}U] = 3.56 \cdot 10^{-7}$	1.05±0.14	1.77±0.07	2.24±0.13	2.82±0.32
$[^{75}Se] = 3.6 \cdot 10^{-8}$	2.04±0.88	0.38±0.94	0.74±1.03	1.11±1.27

elling of sorption/migration results in the compacted system, in strong connection with bentonite pore water studies.

Sorption tests with the homoionised clay were carried out by the two organisations involved in the second phase (CIEMAT and PSI). The data obtained for the same radionuclides by different laboratories were compared taking into account that sorption values were measured under similar conditions but on different purified clays (SWy1 and FEBEX, for PSI and CIEMAT, respectively). The smectite phase of the FEBEX bentonite is actually made up by an illite-smectite mixed layer with a 10-15 percent of illite layers (Section 2.2.1), whereas the SWy1 bentonite contains about one percent of illite [136]. The content of Cs and U in the FEBEX purified clay is lower than the detection limit (<0.2μg/L and <1 μg/L, respectively).

Sorption tests with Cs

Caesium sorption isotherms were carried out at pH 6.5-7 and different ionic strengths (from $1\cdot10^{-3}$ to 1 M in $NaClO_4$). Cs sorption edges were also carried out at different ionic strengths and different Cs concentrations. Kinetic tests were also carried out.

The sorption of caesium was shown to be non-linear over the entire range of concentrations both in the FEBEX and in the SWy1 clay. Since Cs exists in solution only as Cs^+, this behaviour has to be related to the existence of at least two different sorption sites. In the FEBEX clay, the first site has high affinity and low capacity (~$3\cdot10^{-5}$ eq/kg) and the second has a much higher capacity (~1 eq/kg ~ CEC) but lower affinity. The density of the low-density sites may be determined from the isotherms, and the inflexion point coincides with the saturation of these sites.

Since two sites were identified, it was considered useful to analyse the kinetics of sorption using two different Cs concentrations. The kinetic behaviour of Cs sorption in these two regions was different: at "high" Cs concentration (low affinity) the uptake was very rapid (hours or less) whereas at "low" Cs concentration (high affinity) the uptake was significantly slower, and the sorption process was completed within days. This result showed that sorption in the two different sites might be controlled by different mechanisms [139].

The pH dependence of sorption was also analysed at "high" and "low" Cs concentrations. In both cases, almost no influence of pH was observed. On the contrary, a clear effect of the background electrolyte concentration was observed. This uptake behaviour is characteristic of ionic exchange processes.

However, considering the kinetic tests, the adsorption of caesium onto the clay seemed to involve a rapid exchange reaction (hours) and a slower component (days), an anomalous behaviour for ion-exchange reactions. This slow process may be observed only when very low tracer concentrations are used (<$1\cdot10^{-9}$ M), due to the very low density of these sites (~$3\cdot10^{-5}$ eq/kg in the FEBEX clay) compared to the bentonite cation exchange capacity. We interpreted these two processes, in connection with the high affinity and low affinity sites, as adsorption on planar sites (rapid process) and caesium diffusion to less available but highly selective sites (slow process). The existence of "low" and "high" affinity sites for caesium sorption in clays is usually explained by considering that it may be exchanged with hydrated cations in basal/interlayer sites (low affinity sites). Moreover, it may sorb in a highly selective manner at frayed edge sites (FES) [140, 141]. FES sites are high affinity sites not present in expanding clays like smectite, but develop in weathered micas and illite.

The modelling of the data has to be accomplished taking into account the existence of different sorption sites. Two different approaches were followed, one for the FEBEX clay and the other for the SWy1 clay.

A caesium sorption model for argillaceous rocks, based on the idea that illite dominates the Cs uptake in clay rocks, was previously developed by Bradbury & Baeyens [142]. Since the SWy1 montmorillonite contains ~1 percent illite, a similar approach to this model was applied to the SWy1 montmorillonite studied in the FEBEX project. The first assumption of the model is that Cs sorption in SWy1 is governed, in addition to the montmorillonite component, by cation exchange reactions on the illite mineral component. For the purposes of calculating Cs sorption in the SWy1 system, an illite is defined with a cation exchange capacity equal to 0.20 eq/kg. Secondly, the uptake of Cs on illite is envisaged as taking place on three site types, each having different site capacities and affinities [137]. These are denoted as FES, type II and planar sites. The relations between these site capacities are expressed in Bradbury & Baeyens [137] as fixed percentages of the illite CEC. These capacities were scaled to the illite content in the SWy1 system and fixed. Thirdly, selectivity coefficients for Cs-Na were taken from Bradbury & Baeyens [137]. The selectivity coefficients for Cs-Ca were obtained from the best fit to the non-linear part of the isotherms. A summary of the selectivity coefficients used in the modelling for both the Na- and Ca-SWy1 isotherms is presented in Table 5.34. The selectivity of Cs-Na and Cs-Ca on the planar sites of illite are taken to be the same as the K_c values on the planar sites of montmorillonite. From the sorption edge and isotherm data on Na-SWy1, a selectivity coefficient for Cs-Na exchange of 15.1 was obtained.

Finally, with all model parameters fixed, the computer code MINSORB was used to calculate the Cs sorption in Na- and Ca-SWy1 systems. An example of the modelling of Cs data for Na- SWy1 is given in Figure 5.146, together with the curve predicted by the model (continuous line). It may be seen that the predicted isotherm corresponds very well to those measured for the montmorillonites. Very good results were obtained also for data obtained at other ionic strengths and for data on Ca-SWy1 [134, 139].

Although the results were qualitatively very similar in the two montmorillonites (SWy1 and FEBEX), another modelling approach was tested for the FEBEX clay, since the model described above was not totally able to explain the Cs sorption data on FEBEX bentonite. The existence of smectite-illite mixed layer may possibly lead to the existence of FES-like sorption sites in FEBEX bentonite, however the illite in the illite-smectite mixed layer may not behave exactly in the same manner as a pure illite phase.

The sorption of caesium on FEBEX bentonite was therefore interpreted with a 2-site model (2 "generic" sites) considering ion-exchange with both "high" affinity and "low" affinity [140]. The selectivity coefficient value used for the modelling of sorption in the "low affinity" sites is $\log^{Cs}_{Na} K_C = 1.65$, whereas the selectivity coefficient for sorption in the "high affinity" sites is $\log^{Cs}_{Na} K_c = 7.5$. As may be seen in Figure 5.147, with this model, the sorption at the lowest ionic strengths ($1 \cdot 10^{-2}$ and $1 \cdot 10^{-3}$ *M*) is over - predicted. It is clear that at very low Cs concentrations and, above all, when sorption is very high, the magnitude of the experimental errors may be enhanced. However, the deviations observed in the prediction from the experimental data, especially at the low ionic strengths, may be due to the competition of ions like K^+ that may exist in solution. In fact, a non-negligible quantity of potassium ions (up to 2 mg/L) was found in some samples. Therefore, another modelling attempt was carried out considering the possible effect of potassium in solution. The quantity of potassium was fixed to $2 \cdot 10^{-6}$ mol/L for all the samples at the different ionic strengths. The modelling at the lower ionic strengths improved when this contribution was considered.

Sorption tests with U

Sorption edges tests (pH 2 to 11) at different ionic strengths (from $1 \cdot 10^{-1}$ to $1 \cdot 10^{-3}$ *M*) were carried out as well as sorption isotherms ([U]: $1 \cdot 10^{-8}$ to $3 \cdot 10^{-3}$) at different ionic strengths and different pH. All the tests were performed in anoxic condition under N_2 atmosphere.

Qualitatively, similar results were obtained in the two clays studied. In sorption edges, two regions can be clearly distinguished: the first one, at acidic pH, where sorption strongly depends on the ionic strength, and a second one, at basic pH, where sorption does not depend on the ionic strength. These results clearly indicate that two mechanisms are taking place. Ionic exchange is predominant at acid pH, whereas surface complexation seems to be the main sorption mechanism at high pH. Figure 5.148 shows an example of U sorption edge on homoionic Na-montmorillonite (SWy1) at 0.01 and 0.1 *M* $NaClO_4$. Sorption isotherms (obtained at different pH and ionic strengths) showed that sorption is not lineal over the entire range of concentration used.

Table 5.34
Site capacities and selectivity coefficients for illite (CEC = 0.2 eq/ kg)

Site types	FES	Type II sites	Planar sites
Site Capacities: (eq. kg^{-1})	5×10^{-4}	4×10^{-2}	1.6×10^{-1}
$\log^{Cs}_{Na} K_c$	7.0	3.6	1.18
$\log^{Cs}_{Ca} K_c$	13.8	9.5	1.46

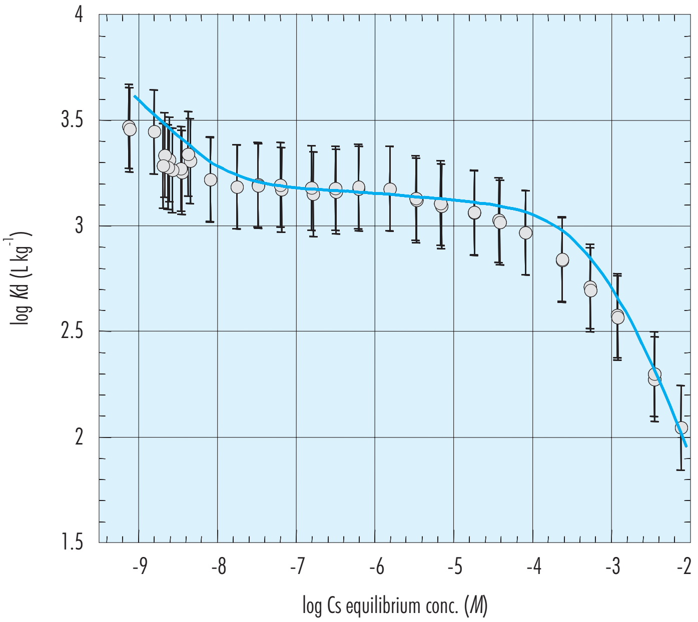

Figure 5.146: Cs sorption isotherm on homoionic Na-montmorillonite (SWy1) at 0.01 M NaClO$_4$, S:L ratio = 1 g L^{-1}, pH = 7.0. The continuous line is the modelling result.

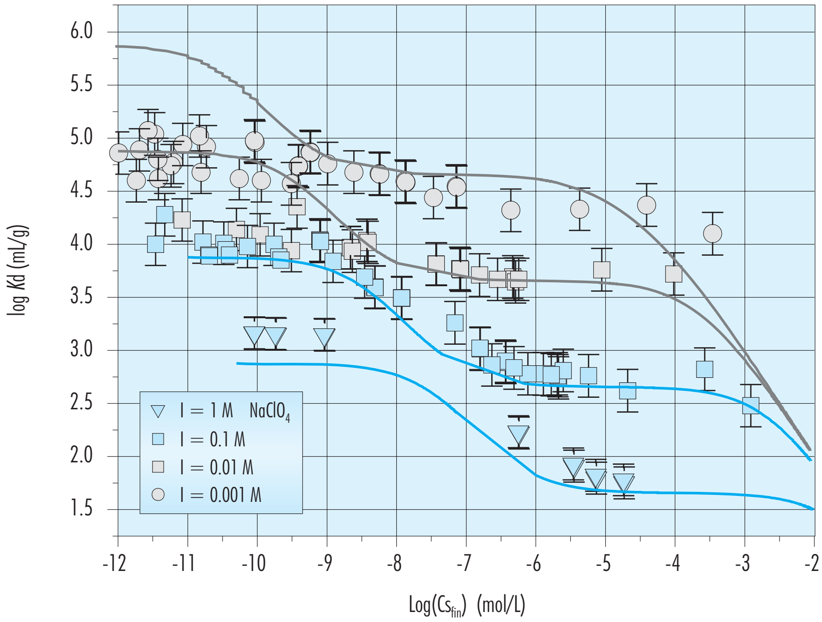

Figure 5.147: Cs sorption isotherms on FEBEX Na-clay and modelling (continuous lines), at different ionic strengths.

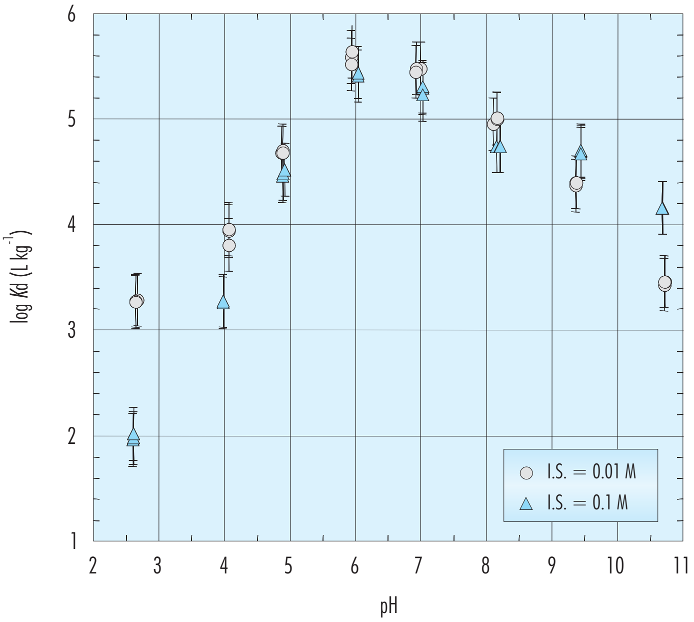

Figure 5.148: Example of U sorption edge on homoionic Na-montmorillonite (SWy1) at 0.01 and 0.1 M $NaClO_4$. Total U concentration = ~10^{7} M, S:L ratio = 1.4 g/L.

It is clear from the experimental results that the modelling has to be carried out considering both ion exchange and surface complexation reactions at the clay surface. In order to model surface complexation reactions it is important to determine the acid – base properties of the SOH groups, which were determined both for SWy1 [143] and FEBEX clay [134]

5.2.3.3. Diffusion tests

The FEBEX clay was compacted at different dry densities (from 1.0 to 1.7 g/cm^3) to determine the accessible porosity (ϕ) and the effective diffusion coefficient (D_e) by means of through-diffusion (TD) tests, and the apparent diffusion coefficient (D_a) by means of in–diffusion (ID) tests. The elements considered were both conservative (HTO, ^{36}Cl, Re, I) and non-conservative (^{75}Se, ^{85}Sr, ^{137}Cs, ^{45}Ca, ^{22}Na, ^{152}Eu, ^{233}U, Nd, Th).

Methodology

As shown in Figure 5.149, different experimental setups were used, depending on the radionuclide and parameter to be determined. All the experimental cells were designed and built at CIEMAT [144].

In the TD tests (Figure 5.149a and Figure 5.149b), a cylindrical stainless-steel diffusion cell is connected to two reservoirs (in and out) where the solution is continuously stirred. The cell contains a ring with the compacted bentonite placed between two stainless steel sinter plates. After the saturation of the clay sample with water, the water in the inlet reservoir is spiked with the tracer and diffusion starts. Two different configurations are used: the first is the variable concentration case (TDV), and the second is the constant concentration gradient (TDC). In the TDV configuration, using in and out reservoirs of 100 mL, the tracer concentration in both reservoirs changes with time and is periodically measured. An example of the results of through-diffusion tests with variable concentration (TDV), which allowed for D_e estimations, is shown in Figure 5.150. The upper experimental points correspond to the concentration evolution in the inlet reservoir, and the lower experimental points correspond to the concentration evolution in the outlet reservoir. When the final concentrations in the in and out reservoirs are quite differ-

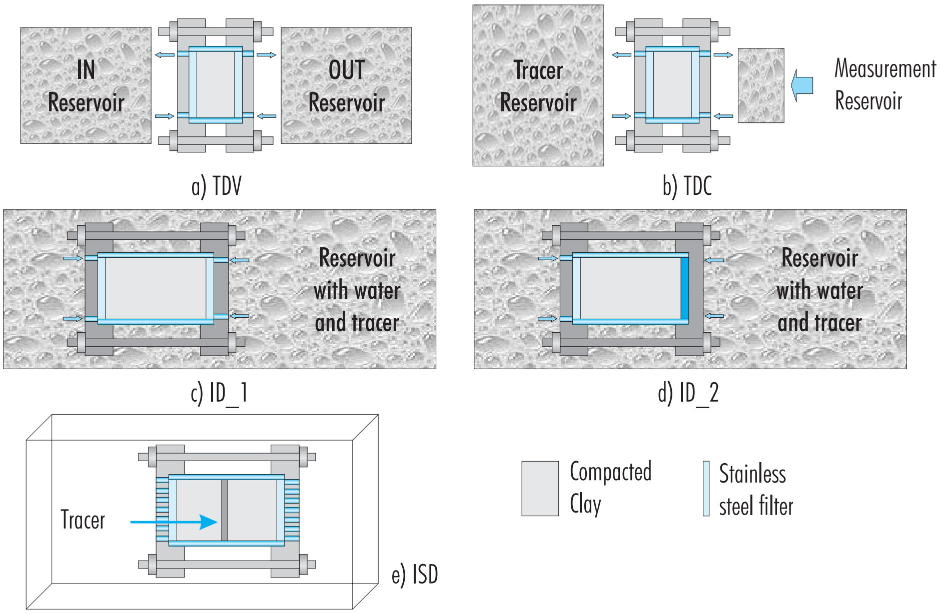

Figure 5.149: Longitudinal section of the experimental setups used for the determination of diffusion coefficients and accessible porosity (TD: through-diffusion, ID: in-diffusion, ISD: internal-source diffusion).

ent, but the tracer concentration in the outlet reservoir is significant, it may be ensured that the concentration profile in the clay plug pore water is linear (PRO tests).

In the first phase of the FEBEX project [131], the variation of concentrations in the two reservoirs was interpreted using the methodology proposed by Wolfrum *et al. [145].*

The second TD configuration is the constant concentration gradient (Figure 5.149b, TDC) case, in which a large (1 L) "in reservoir" and a very small (20 mL) "out reservoir" are used. The "out reservoir" is periodically changed in order to keep the tracer concentration close to zero and, therefore, the concentration gradient approximately constant. Figure 5.151 shows an example of the experimental results of TDC tests with Cl^- (clay density 1.65 g/cm^3) where the linear fit in the steady-state region and the time lag value are indicated. The effective diffusion coefficient may be calculated from the slope of the straight-line fitting the long-term behaviour of the cumulative amount of solute that has passed to the "out" reservoir. The porosity accessible to the tracer may be calculated from the intercept of the fitting straight line to the time-axis, t_e [146].

In in-diffusion tests (Figure 5.149c, d) the stainless-steel diffusion cell is immersed in a reservoir with water for approximately 2.5 months, this being the time required for saturation of the samples. Complete water saturation of the samples is verified at the end of the test by weighing the specimen. After water saturation, the tracer is added to the reservoir. Two different setups were used: in the ID_1 configuration (Figure 5.149c) both sides of the cell are opened so that the tracer can enter from both sides; whereas in the ID_2 configuration one side of the cell is blocked (Figure 5.149d). In in-diffusion tests, after a given time, the diffusion cell is disassembled, the bentonite plug cut into slices (approximately 1-mm thick) and the activity in each slice measured to determine the tracer profile within the clay and calculate the apparent diffusion coefficient, D_a. The ID_1 configuration is also used to find the accessible porosity by means of saturation tests (SAT) or to determine the K_d directly in the compacted clay. In these last two cases, as previously mentioned, the test ends when the concentra-

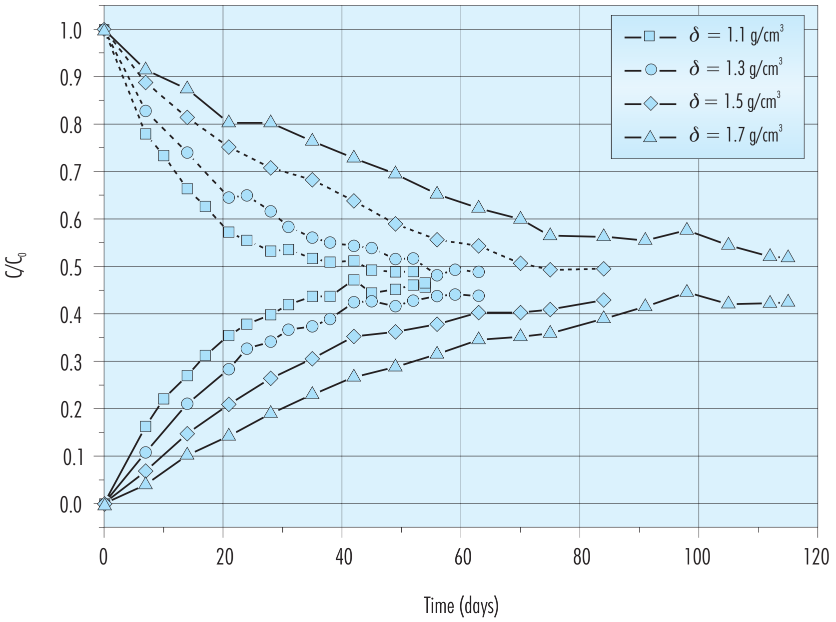

Figure 5.150: HTO concentration evolution for inlet and outlet reservoirs obtained in TDV tests in clay plugs of different densities.

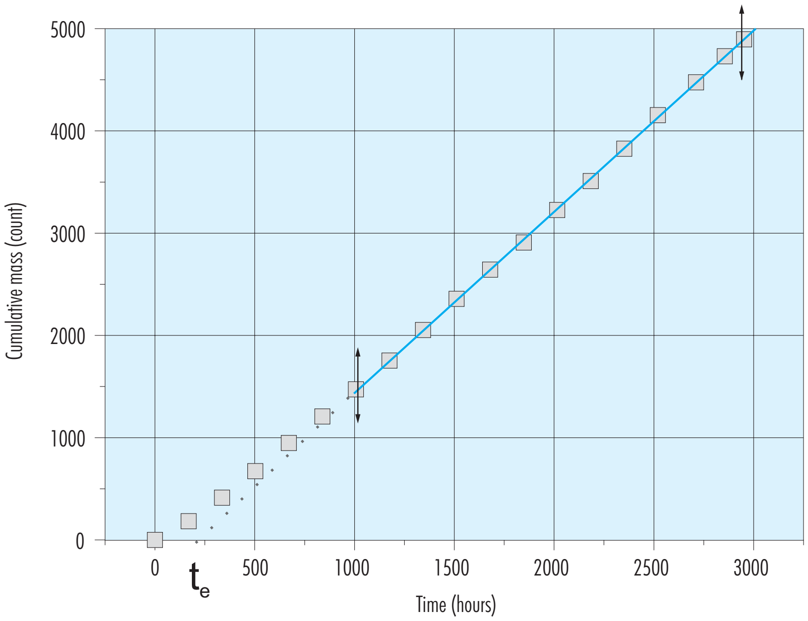

Figure 5.151: TDC test with $^{36}Cl^{-}$; clay dry density 1.65 g/cm^3. The linear fit of the steady-state region and the time lag are indicated.

tion within the plug is uniform and equilibrium is reached.

Figure 5.152 shows the experimental concentration profile in the sample of an in-diffusion test, for a dry density of 1.65 g/cm^3, and the theoretical profiles for three values of D_a.

Accessible porosities for HTO (for all clay densities) and $^{36}Cl^-$ (for clay densities up to 1.2 g/cm^3) were directly obtained by means of saturation tests. In these tests the water-saturated bentonite samples were introduced in a reservoir with the tracer until equilibrium concentration was reached. The measurement of the tracer activity in the clay pore water allowed for direct measurement of the accessible porosity. Alternative estimations of accessible porosity were accomplished in through-diffusion tests with constant concentration and concentration profile tests, which provided redundant, although less precise, methods for its estimation. Similar values of accessible porosities were obtained with the three methods.

Neither through-diffusion or in-diffusion techniques are appropriate for very sorbing tracers. In the first case because the tracer does not elute (in a reasonable time) and in the second because the tracer usually adsorbs significantly in the test cells and in the filters before reaching the clay. Internal-Source Diffusion tests (ISD, Figure 5.149e) were therefore designed for these elements, but this configuration may also be successfully used for less sorbing or conservative elements. In the ISD configuration, the tracer is introduced within the bentonite sample, avoiding contact with anything but the clay. A filter paper or a slice of traced bentonite is sandwiched between two saturated bentonite clay plugs. In this configuration, the symmetrical diffusion profiles are determined at the end of the test after slicing the bentonite sample.

Results: conservative tracers

The main conservative tracers studied were HTO and Cl^- as representative of neutral and anionic species, results for I^- and $SO_4^=$ at dry density of 1.65 g/cm^3 are also presented. The study of ions is of special interest because performance assessment calculations of spent fuel repositories have shown that doses are mainly controlled by non-sorbing anionic species

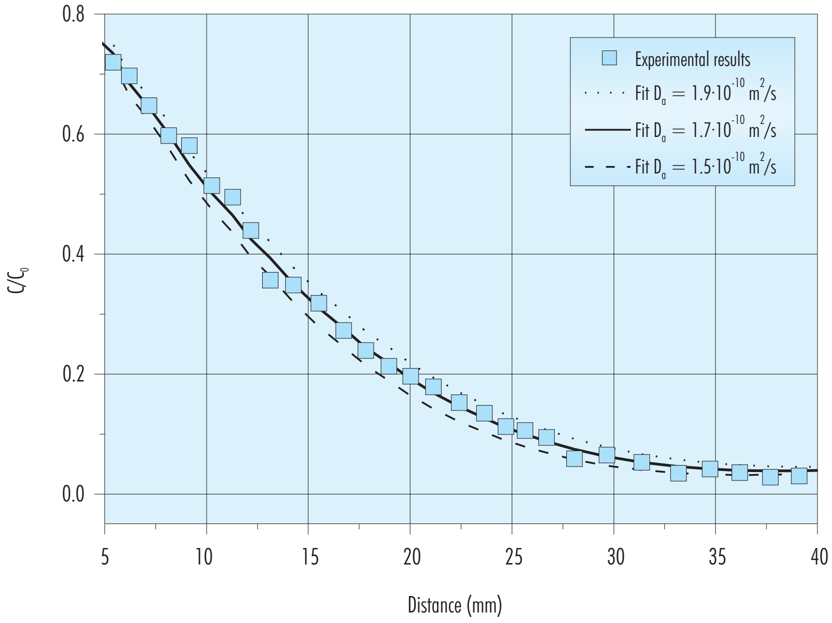

Figure 5.152: ID tests for HTO. The method used for the evaluation of D_a and its error are shown (clay dry density of 1.65 g/cm^3 and experimental time t=190 h).

Table 5.35
Summary of the experimental results for HTO at different clay densities. The experimental method used is indicated. The last column shows the theoretical porosity at the given density

Dry density (g/cm^3)	D_e(m^2/s) TDV	D_a (m^2/s) ID	ϕ (%) SAT	∈ (%)
1.00			65.4	63.0
1.00			64.5	63.0
1.10	$1.92 \cdot 10^{-10}$	—		59.3
1.10	$2.01 \cdot 10^{-10}$	—		59.3
1.10		$3.3 \cdot 10^{-10}$		59.3
1.20			58.3	55.7
1.20			56.6	55.7
1.30	$1.36 \cdot 10^{-10}$	—		51.9
1.30	$1.56 \cdot 10^{-10}$	—		51.9
1.30	—	$3.1 \cdot 10^{-10}$		51.9
1.40			51.9	48.1
1.40			51.0	48.1
1.50	$8.80 \cdot 10^{-11}$	—		44.4
1.50	$8.93 \cdot 10^{-11}$	—		44.4
1.50	—	$2.6 \cdot 10^{-10}$		44.4
1.60			43.3	40.7
1.60			42.8	40.7
1.65	$5.8 \pm 0.2 \cdot 10^{-11}$	—		38.9
1.65	$5.8 \pm 0.2 \cdot 10^{-11}$	—		38.9
1.65	—	$1.7 \cdot 10^{-10}$		38.9
1.65	—	$1.6 \cdot 10^{-10}$		38.9
1.65	—	$1.6 \cdot 10^{-10}$		38.9
1.70	$5.76 \cdot 10^{-11}$	—		37.0
1.70	$4.57 \cdot 10^{-11}$	—		37.0
1.70	—	$2.6 \cdot 10^{-10}$		37.0

Table 5.36
Summary of the experimental results for Cl^-, I^- and $SO_4^=$ at different clay densities. The experimental method used is indicated

Element	Dry density (g/cm^3)	D_e(m^2/s)	ϕ (%)	D_a (m^2/s) (calculated)
$^{36}Cl^-$	1.00	$2.72 \cdot 10^{-11}$ (TDV)	18.0 (SAT)	$1.51 \cdot 10^{-10}$
$^{36}Cl^-$	1.00	$3.68 \cdot 10^{-11}$ (TDV)	15.3 (SAT)	$2.41 \cdot 10^{-10}$
$^{36}Cl^-$	1.20	$1.08 \cdot 10^{-11}$ (TDV)	10.5 (SAT)	$1.03 \cdot 10^{-10}$
$^{36}Cl^-$	1.20	$2.52 \cdot 10^{-11}$ (TDV)	15.2 (SAT)	$1.66 \cdot 10^{-10}$
$^{36}Cl^-$	1.40	$2.9 \cdot 10^{-12}$ (TDV)	5.9 ± 1.8 (PRO)	$4.9 \cdot 10^{-11}$
$^{36}Cl^-$	1.40	$1.7 \cdot 10^{-12}$ (TDV)	3.4 ± 1.4 (PRO)	$5.0 \cdot 10^{-11}$
$^{36}Cl^-$	1.60	$8.7 \cdot 10^{-13}$ (TDV)	2.4 ± 1.1 (PRO)	$3.6 \cdot 10^{-11}$
$^{36}Cl^-$	1.65	$1.1 \cdot 10^{-12}$ (TDC)	2.2 (TDC)	$5.0 \cdot 10^{-11}$
$^{36}Cl^-$	1.65	$7.7 \cdot 10^{-13}$ (TDC)	2.3 (TDC)	$3.3 \cdot 10^{-11}$
$^{36}Cl^-$	1.65	—	2.8 ± 0.4 (PRO)	—
$^{36}Cl^-$	1.65	—	2.5 ± 0.3 (PRO)	—
I^-	1.65	$8.25 \cdot 10^{-13}$ (TDC)	2.7 (TDC)	$3.06 \cdot 10^{-11}$
I^-	1.65	$8.99 \cdot 10^{-13}$ (TDC)	2.2 (TDC)	$4.08 \cdot 10^{-11}$
$^{35}SO_4^=$	1.65	$1.84 \cdot 10^{-13}$ (TDC)	4.6 (TDC)	$4.00 \cdot 10^{-12}$
$^{35}SO_4^=$	1.65	$4.49 \cdot 10^{-14}$ (TDC)	0.8 (TDC)	$5.61 \cdot 10^{-12}$

($^{129}I^-$ and $^{36}Cl^-$). Table 5.35 (HTO) and Table 5.36 (Cl^-, I^- and $SO_4^=$) summarise the experimental results, and the methodology used to obtain each value is also specified. The data in the same row correspond to results obtained in the same cell.

The results included in Figure 5.153 show that the measured accessible porosity for HTO is roughly equal to total porosity in FEBEX bentonite at different dry densities. Since total porosity is easy to calculate, if one of the diffusion coefficients (effective or apparent) is measured, the other coefficient may be calculated. A simple diffusion model in pore water fully explains the experimental results for HTO.

Chloride ions have a very different behaviour from HTO in the FEBEX bentonite. In fact, even at low densities only a fraction of total porosity is accessible for chloride. If dry density increases, the accessible porosity for chloride decreases rapidly and, at a density of 1.65 g/cm^3, its value is between 2 and 3 percent, whereas the total porosity is close to 40 percent. These results show that significant anionic exclusion occurs and that its effects are more pronounced when dry density increases. As a result, only a small fraction of the total porosity is accessible for chloride.

It is usually accepted that anionic exclusion decreases when the ionic strength of the pore water increases. The electrostatic effect may be higher at lower clay densities because the overlapping of the double layers of the pore surfaces does not occur, but at higher clay density the ionic strength effect is expected to be less significant.

As may be seen in Table 5.35, Table 5.36 and Figure 5.153, the effective/apparent diffusion coeffi-

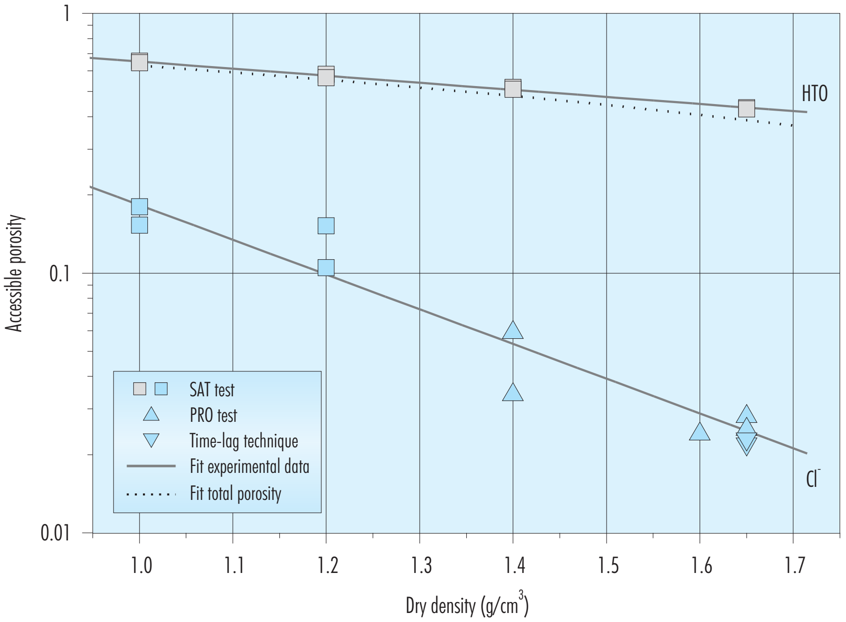

Figure 5.153: Accessible porosities obtained with different methods for HTO and Cl as a function of clay density.

cients and the accessible porosity show an exponential decrease when clay density increases. The decrease is significantly more pronounced in the case of Cl$^-$. Therefore for each parameter the experimental values may be adjusted using exponential functions of the type

$$D_{a,e} = A \cdot e^{-B \cdot \rho_d} \qquad (5.28)$$

where A and B are constants and ρ_d is the bentonite dry density. Accessible porosity, apparent and effective diffusion coefficients in FEBEX bentonite at any dry density may, therefore, be easily estimated by interpolation.

For HTO, the values of D_a , D_e and ϕ measured independently satisfy the relation between effective and apparent diffusion coefficients for conservative tracers ($D_e = D_a \cdot \alpha$). The consistency of the transport parameters measured using different methods confirms that these methods are appropriate and the values obtained are correct.

Results: non-conservative tracers

TDV tests were carried out with ^{85,90}Sr, ^{75}Se, ^{99}Tc, and ^{233}U, and these tests were analysed by the Wolfrum *et al*. [145] method. Also, ID_1 tests were performed with Cs, Tc, Re and Se, and analysed by the Put & Henrion [147] method. Clay plugs with different thickness and compacted at different densities were used. Se and Tc were also studied under anoxic conditions.

ISD tests were used to determine the diffusion coefficients of europium and neodymium as very sorbing tracers. An example of the experimental results obtained by means of the ISD method is shown in Figure 5.154.

Through-diffusion tests, performed according to the Wolfrum *et al*. [145] method, have proven to be an excellent technique for the determination of diffusion coefficients under simple experimental conditions, fundamentally for slightly sorbing species. In contrast, in-diffusion tests seem more suitable for sorbing species, and ISD method for very sorbing tracers.

Table 5.37 summarises the apparent/effective diffusion coefficients obtained with compacted FEBEX bentonite at 1.65 g/cm^3 for different radionuclides.

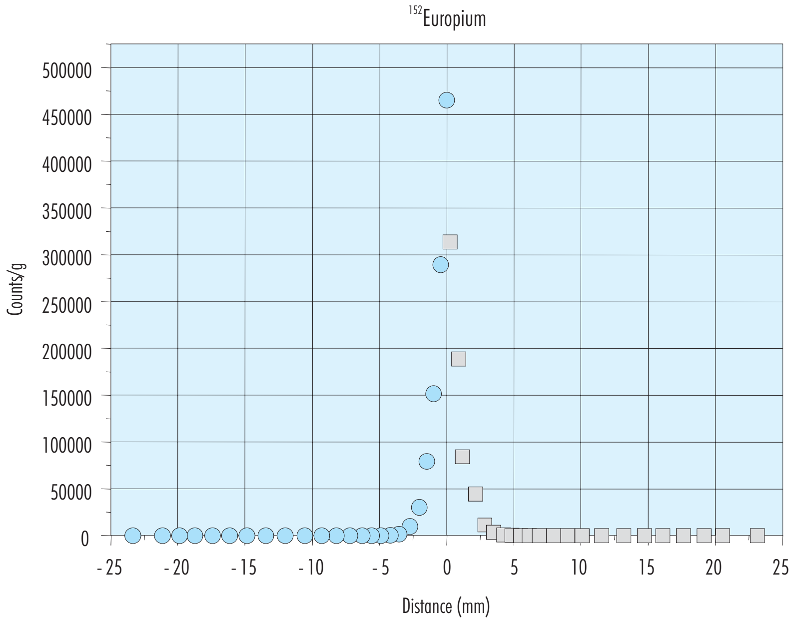

Figure 5.154: Example of the results obtained with Eu in the ISD configuration.

New methodologies to obtain diffusion coefficients

Apart from the completion of the database for transport parameters of conservative and non-conservative tracers, it was considered necessary to develop new methodologies to simultaneously obtain the apparent and effective diffusion coefficient in the same sample, methodologies successfully applied for caesium and uranium [133, 132].

Particularly, in the study performed with caesium, the method allows for the simultaneous determination of effective and apparent diffusion coefficients in compacted bentonite without reaching steady-state conditions. Basically, this method consists of an in-diffusion test in which the concentration profile in the bentonite sample is used to estimate D_a, and the temporal evolution of the solute concentration in the reservoir is used to estimate D_e. This method has several advantages over the typical through-diffusion tests, in particular: a) the test duration is significantly shorter, b) D_a values are measured with greater precision and c) it is not necessary to maintain a constant solute concentration in the reservoir. Figure 5.155 shows the theoretical concentration profiles in the bentonite sample at the end of the test for different values of D_a(Cs) and D_e(Cs) using the analytical solutions for the constant tracer concentration in the reservoir (continuous line) and the instant injection of a pulse at t=0 (dotted lines).

The diffusion coefficients of uranium were also determined using a novel methodology. On the one hand, the comparison of the experimental evolution of the tracer concentration in the “in reservoir” with theoretical curves, for a system with the same geometry, makes it possible to estimate the ratio $D_e/(D_a)^{1/2}$. The fact that the tracer does not reach the “out reservoir” at the end of the test allows for a conservative estimate for D_a. Secondly, by analysing the concentration profile within the bentonite clay, an independent estimation of D_a may be obtained. A calculation of the theoretical concentration evolution in the in and out deposits for different D_e/D_a ratios may be performed, as shown in Figure 5.156.

The range of diffusion coefficients obtained is in agreement with those obtained with more conventional techniques (Table 5.37), confirming the validity of the new approach.

Table 5.37
Summary of the experimental results using different radionuclides. Clay dry density of 1.65 g/cm^3

Element	D_a (m^2/s)	D_e (m^2/s)
Caesium (I)	$(0.9 - 3.3)\cdot10^{-13}$	$(0.1 - 3.0)\cdot10^{-11}$
Uranium (VI)	$(0.1 - 4.0)\cdot10^{-14}$	$(0.6 - 2.2)\cdot10^{-12}$
Strontium (II)	$(1.0 - 2.0)\cdot10^{-11}$	$(1.0 - 4.0)\cdot10^{-10}$
Selenium (IV)	$(1.0 - 3.0)\cdot10^{-13}$	$(6.0 - 8.0)\cdot10^{-12}$
Technetium (VII)		$(2.0 - 4.0)\cdot10^{-13}$
Rhenium (VII)	$(2.0 - 6.0)\cdot10^{-14}$	
Europium (III)	$(6.0\text{-}9.0)\cdot10^{-14}$	
Sodium (I)		$(3.0\text{-}6.0)\cdot10^{-10}$
Calcium (II)		$(4.0\text{-}7.0)\cdot10^{-10}$

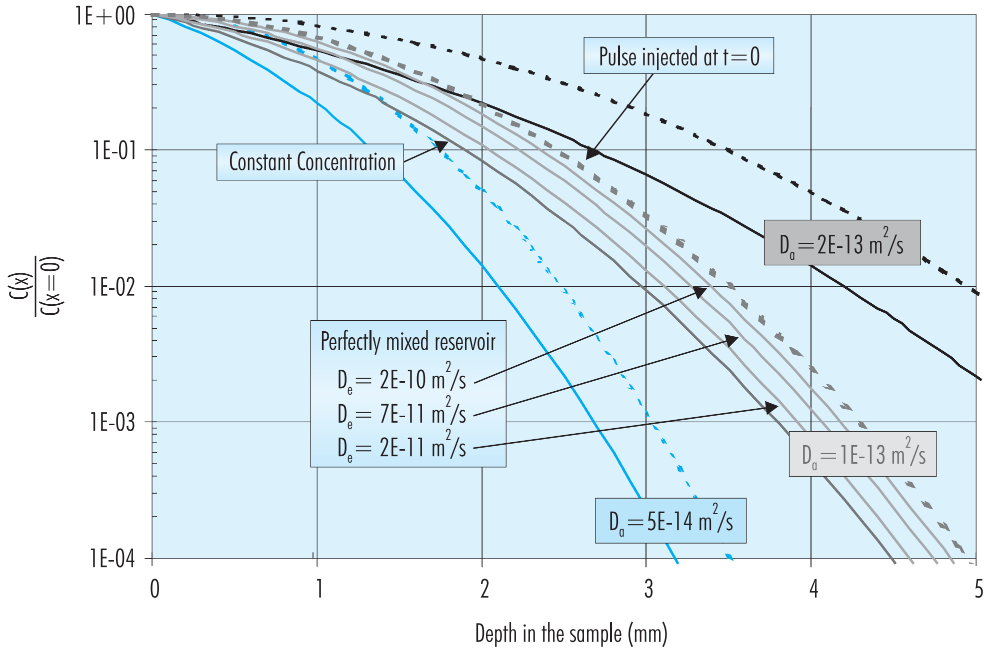

Figure 5.155: Theoretical concentration profile in the bentonite sample for different values of D_a and D_e.

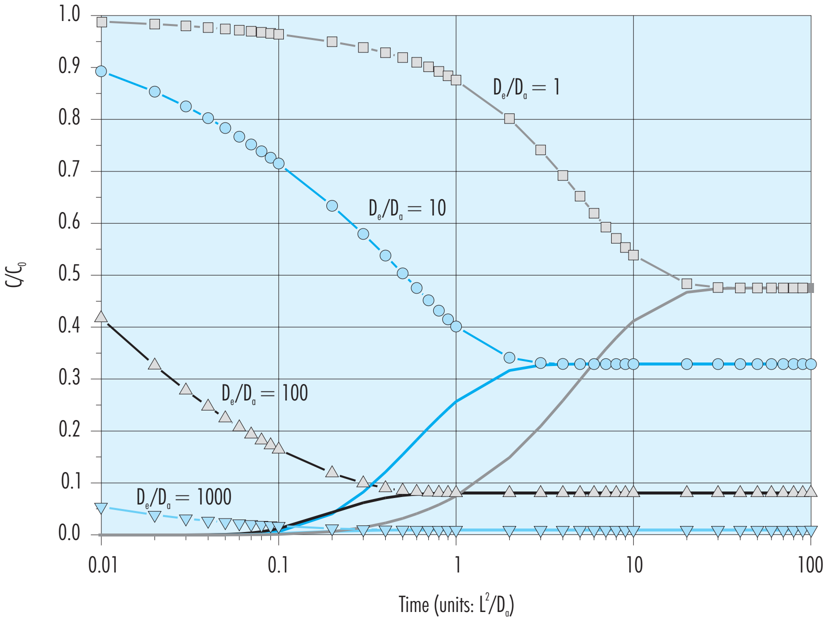

Figure 5.156: Reservoir concentration evolution for different D_e/D_o ratios (points: in deposit, lines: out deposit).

5.2.4. Dissolution processes at the bentonite-solution interface

CSIC performed a set of laboratory tests with the aim of measuring the dissolution rates of smectite and accessory minerals, as a function of pH and temperature, and calculating the kinetic parameters of the dissolution reactions, in order to evaluate the contribution of dissolution reactions to the longevity of the bentonite barrier. The dissolution reactions of smectite and accessory phases release into solution (pore waters) different elements that behave in a mobile (alkaline and alkaline-earth, Si) or immobile (Al, Fe) fashion, which may be transported in solution or precipitated as secondary phases (hydroxides, zeolites, CSH gels, etc.).

Since the most abundant and reactive accessory phases in the bentonite are plagioclase and volcanic glass, these were selected for the dissolution tests. Plagioclase was hand-picked from the FEBEX bentonite under microscope and samples of volcanic glass were collected at the bentonite outcrop. Besides, a smectite sample of the 0.5-4 μm fraction, saturated in K^+ ions, was used. It is composed of more than 99 percent of smectite containing 10-15 percent of non-swelling layers.

The flow-through tests allow for the measurement of the dissolution rate under fixed saturation-state conditions by modifying the flow rate, solid/solution ratio, temperature, pH and composition of the input solutions. The dissolution tests were carried out in flow-through reactors designed and constructed for this purpose (Figure 5.157).

Dissolution rates were calculated based on Al and Si steady-state concentrations, after correction of mass of solid dissolved during the dissolution process [148]. For most of the tests, the dissolution rate error ranged between 12 and 20 percent and is dominated by the uncertainty of the BET surface area measurement (±10% for smectite, and ±15% for glass and plagioclase).

5.2.4.1. Smectite

The variation in composition of the output solutions in two of the dissolution tests as a function of time is shown in Figure 5.158. High Al and Si concentrations are observed at the onset of most of the tests.

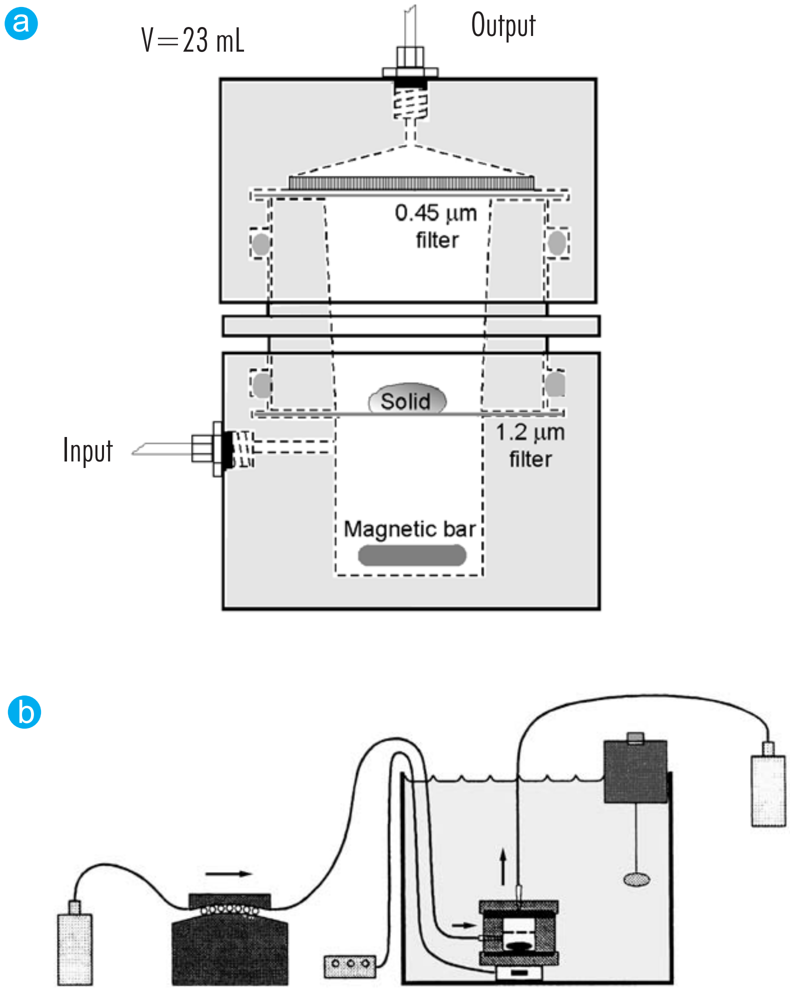

Figure 5.157: a) Sketch of a flow-through cell for dissolution tests. b) General experimental setup of the entire dissolution test system.

Afterwards, Al and Si concentrations decrease until a steady state is approached. Figure 5.159 plots log dissolution rate *vs*. pH at 25, 50, and 70°C. The minimum dissolution rate occurs at a pH of approximately 6.2, and increases with both increasing and decreasing pH within the range studied (pH 4-10). The slope of the log rate vs. pH is the dissolution reaction order with respect to protons (hydroxyls), *n*. An increase of the reaction order with temperature is observed, as was previously the case for other phyllosilicates [149]. Apparent activation energies are shown in Figure 5.160. The V-shape of pH dependence on activation energy shows a minimum value at pH 7 and increases with both increasing and decreasing pH.

The pH values of the pore waters in the barrier and in the interface with the granite host rock are in the range 7-8.5. As was expected, under these conditions smectite dissolution rates are close to the minimum value ($\sim 10^{-14}$ mol/m^{2}s). In addition, the effect of temperature on dissolution rate, measured as apparent activation energy, is minimal in the pH range

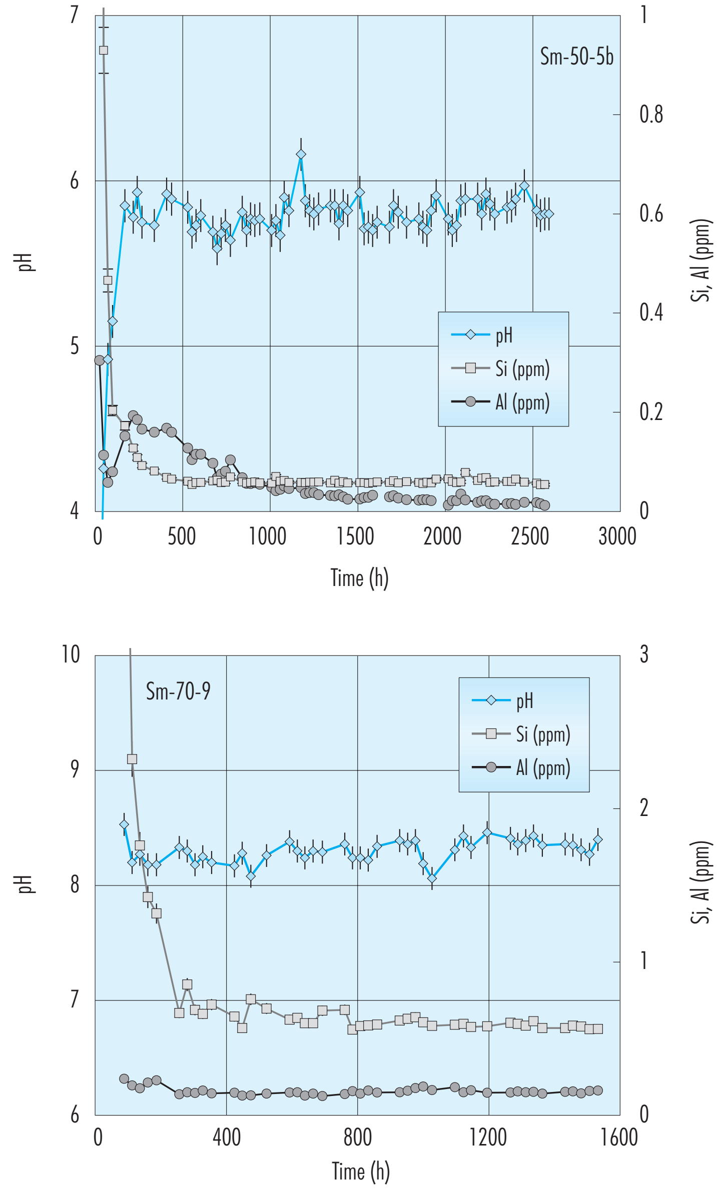

Figure 5.158: Variation of pH, Si and Al concentration as a function of time in the output solutions of some smectite dissolution tests.

7-8.5 (Figure 5.159). The dissolution rates estimated at 70°C range from $10^{-13.7}$ to $10^{-13.5}$ mol/m^{2}s, at pH 7 and 8.5 respectively. It may be derived that the repository conditions provide a suitable environment for preservation of the chemical stability of the bentonite. Such a situation can only be modified locally by the proximity of materials that may induce strong changes in pH, such as alkaline plumes produced by concrete or acid fronts, or by the accumulation of organic matter or microorganisms that may contribute to increasing dissolution through the release of organic acids (ligand-promoted mechanism) or through an increase in acidity.

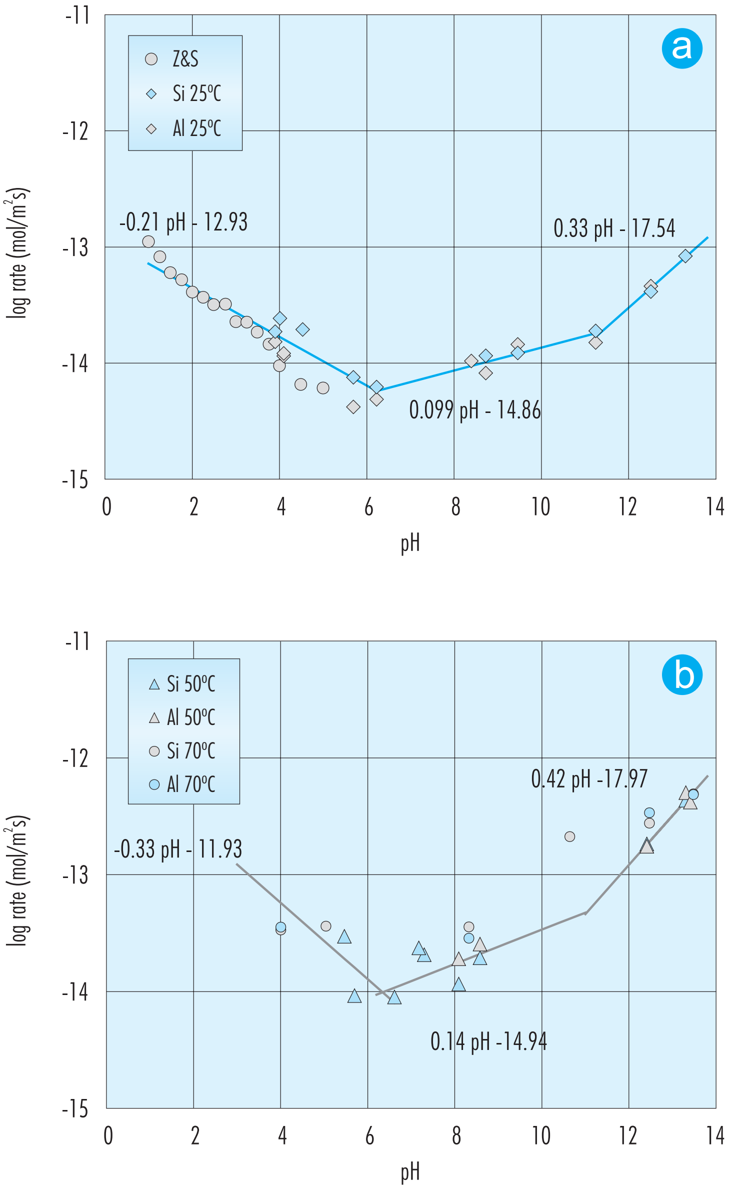

Figure 5.159: pH dependence of the log of smectite dissolution rate at a) 25° C and b) 50 and 70° C. Rates for pH values higher than 11 were included for comparison, as well as those from Zysset & Schindler ([150] at 25° C. Reaction orders were calculated for rates at 25 and 50 °C.

5.2.4.2. Volcanic glass

The variation of pH, Si and Al in the output solutions in glass dissolution tests shows a trend similar to that observed for smectite. Figure 5.161 plots log dissolution rate *vs*. pH at 25 and 50°C. At 25°C there is a minimum of dissolution rate at a pH value of approximately 7-7.5. However, the dissolution rates at 50°C seem to follow a single trend. The reaction orders at 25°C (n=0.39) and 50°C (n=0.36) for pH>8 are inconsistent, as they decreased slightly with temperature instead of increasing, as is nor-

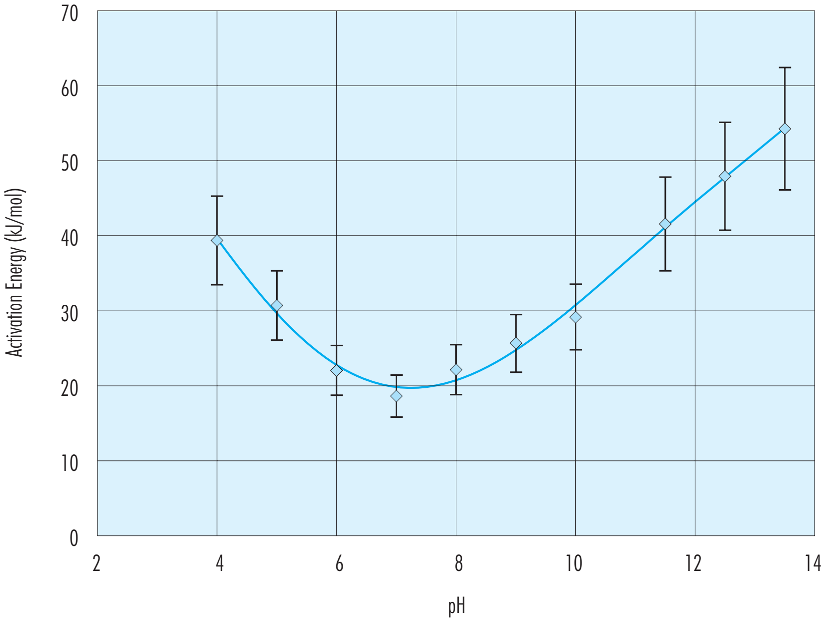

Figure 5.160: Variation of the apparent activation energy of smectite dissolution reaction with pH. Values for pH>11 were included for comparison.

mally observed in silicates. Within the uncertainty of the value, both orders of reaction are the same. This is very improbable, as apparent activation energy in silicates exhibits a minimum close to the minimum of dissolution rate and increases with both increasing and decreasing pH [149]. This behaviour is not clear and additional data would be required to derive any dependence of the rate on pH and temperature.

Thus, within the pH interval 7.0-8.5 at constant temperature, a minor variation in dissolution rate is expected (approximately 0.2-0.3 orders of magnitude). However, comparing the data at 25 and 50°C, an increase in the dissolution rate of one order of magnitude is observed, which is twice that found for the smectite in the same range of temperature. Consequently, glass dissolution is apparently more sensitive to temperature than smectite dissolution.

Furthermore, the glass used for these tests consisted of small spheres (1 mm size) of compact texture, as also revealed by the low specific surface area (1.51 m^2/g). However, the glassy material in the Cortijo de Archidona outcrop is a rhyolitic tuff of a composition similar to the spheres [151]. We do not have a value of the specific surface area of the tuff. If for the tuff surface area, a value of two orders of magnitude greater than that of the compact glass is assumed, the corresponding dissolution rates would also be two orders of magnitude greater. These estimations will be labelled tuff dissolution rates. It indicates that the volcanic glass is a very reactive phase.

5.2.4.3. Plagioclase

The behaviour of plagioclase during dissolution tests is similar to that observed in smectite and glass. Dissolution reaction was frequently non-stoichiometric, which should be attributed to the non-homogeneity and zonation of the bulk mineral, and the faster dissolution of the calcic plagioclase than of the alkaline ones [152], this introducing some additional scattering in the dissolution data.

The plagioclase dissolution rates available are concentrated in the pH region between 7 and 9.5 (Figure 5.162). Only a few differences in rate are observed varying pH or temperature. It is supposed that they are around the pH value for minimum dissolu-

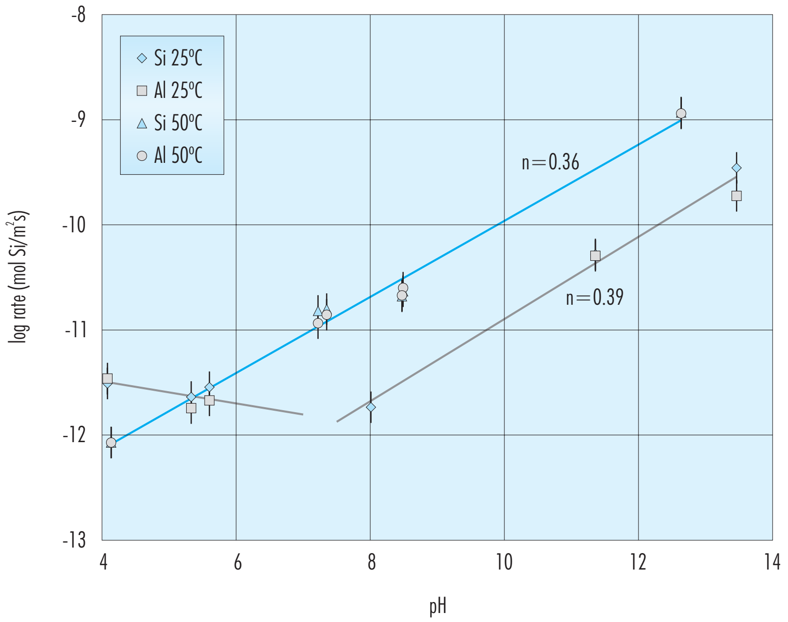

Figure 5.161: pH dependence of the log of volcanic glass dissolution rate at 25 and 50° C. Rates for pH values higher than 11 were included for comparison.

tion rate. In this range, plagioclase dissolves two or three orders of magnitude faster than smectite, molar-based computation, which agrees with previous studies.

5.2.4.4. Conclusions

The tests performed allowed us to measure the dissolution rates of smectite, volcanic glass and plagioclase. Smectite is the main component of bentonite (92 percent in FEBEX bentonite), whereas plagioclase (3 percent) and volcanic glass (tuff, estimated 1-2 percent) correspond to the most abundant and reactive accessory phases.

The change in dissolution rates within the pH range 7.0-8.5 is small, at constant temperature. Important variations are observed or expected outside this interval, corresponding to geochemical conditions not considered within the scope of the FEBEX Project. The most important effect of temperature is observed in the glass and is very small in plagioclase. Only for smectite was it possible to calculate the variation of the apparent activation energy with the pH of the solution.

Some conclusions regarding the stability of the bentonite barrier under repository conditions may be derived assuming that the dissolution rate of the three phases is a reliable proxy of the bulk bentonite, because other accessory phases dissolve much more slowly and have smaller surface areas (quartz) or are trace minerals (pyroxenes, amphiboles).

- ❑ The smectite dissolves slowly within the pH range 7-8.5 and its dissolution rate increases four times when temperature rises from 25 to 50ºC.
- ❑ The accessory phases, plagioclase and glass, are more reactive than the smectite, especially above 25°C. As temperature rises to 50°C, the volcanic glass dissolves faster (one order of magnitude) than smectite. The more reactive accessory minerals being preferentially dissolved, the smectite is preserved from chemical degradation.
- ❑ It should be stressed that the dissolution rates were obtained under conditions far from equilibrium, that is, the fluid flow was high enough to prevent the composition of the solution to equilibrate with smectite. The parameters ob-

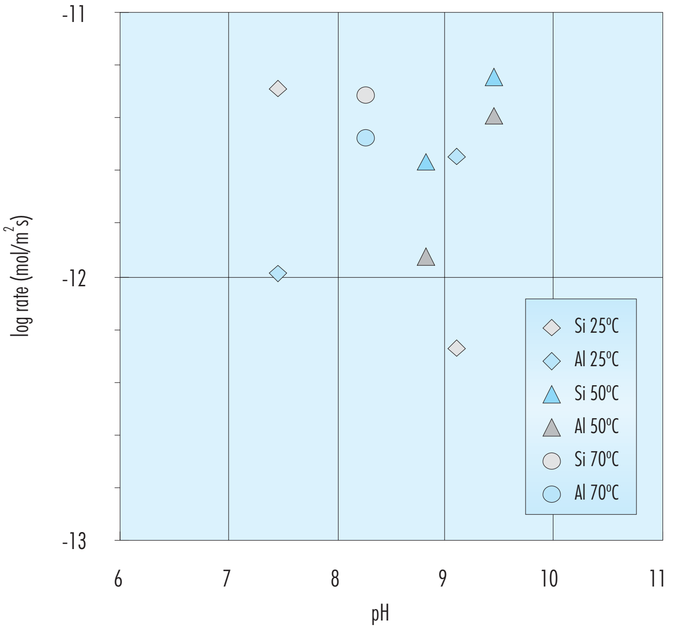

Figure 5.162: pH dependence of the log on plagioclase dissolution rate at 25, 50, and 70° C.

tained under such conditions are necessary to evaluate the effective dissolution rate under barrier conditions of pH, flow, solution composition, temperature, etc. However, limited water flow reduces the dissolution rates by several orders of magnitude as pore water composition approaches equilibrium with smectite. The hydraulic properties of the barrier do not allow for the flux required to produce and maintain a massive dissolution initially, and consequently the smectite should behave as a stable material under repository conditions.

5.2.5. Variation of properties in the bentonite extracted during partial dismantling

The specific goals of the THG characterisation of the bentonite samples retrieved from the "in situ" test dismantling were: 1) to analyse the physical, chemical, mineralogical and textural alterations occurring in the clay as a result of the effect of heat and hydration; 2) to analyse the chemical evolution of the bentonite pore water; and 3) to investigate the geochemical processes and their link to the THM processes within the barrier system.

The samples analysed were taken from section S7 (interface bentonite-concrete), section S12 (without heater), sections S19, S28, S29 (around the heater) and section 31 (bentonite-heater back lid contact) (see Figure 4.39 for location of sections). The laboratories involved in the THG post-mortem bentonite analyses were CIEMAT, INPL/LEM and VTT [153, 154, 155] and the results obtained are summarised in [70].

5.2.5.1. Mineralogy

The mineralogy of the bentonite samples was analysed by INPL/LEM and CIEMAT by X-ray diffraction. The XRD patterns obtained show no significant differences between the treated samples and the reference FEBEX bentonite. The predominant mineral is a smectite with basal spacings d(001) at around 15 Å, which implies a predominance of calcium cations in the interlayer space. The sample BS31-26, that was in contact with the heater rear lid and consequently subjected to the highest temperatures, presents higher peak intensities. There are also minor quantities of quartz, plagioclase, K-feldspars, calcite and cristobalite. A slight increase in carbonates is observed in treated samples.

The basal spacings of the smectite for different treatments were analysed to determine the distribution of water molecules in the clay layers. The oriented aggregates present the same basal spacing line, centred around 14.5 Å. With ethylene glycol saturation, swelling was observed in all the samples, with basal spacings changing to ~16.9 Å. This means that no layer charge modification occurred. Some samples of section S19 were analysed immediately after sampling and without further treatment, *i.e.* in their compacted state and with their original water content. These samples showed, with respect to the results obtained in the dried powder, an increment of water content in interlayer positions, with clay particles formed by quasi-crystals with a random alternation of successive discrete hydrates of two and three layers of water (Table 5.38), especially in the sample closer to the gallery wall (BB19-1).

Calculation of the band width at half-height for the (001) lines did not show any evolution in the thickness of clay particles, and did not reveal any modification of layer stacking ordering. The crystallite thickness (calculated using the Scherrer formulation) is close to 60 Å for treated and untreated samples (INPL/LEM).

Greene-Kelly tests were performed by INPL/LEM on Li-exchanged bentonites. The results indicate that the charge location has not changed for the post-mortem samples.

INPL/LEM also analysed the mineralogy of treated samples by infrared spectroscopy. The spectra obtained for samples from section S-29 are shown in Figure 5.163. No difference was in evidence between the six treated samples and the reference sample (F0). Nevertheless, a slight increase in carbonates contribution was observed, centered at 1440 cm^{-1}.

The unit-cell formulae of the untreated bentonite and of a sample at the contact with the heater were deduced from TEM-EDX analyses by INPL/LEM. The clay minerals (<2μm fraction) did not show any evidence of variation in the composition of the clay particles, *i.e.* the overall chemistry of the montmorillonite remained constant. The calculated interlayer charge is 1.18 and 1.16 for the untreated and the treated samples, respectively; whereas the charge balance is 0.86 and 0.90. In both cases, the smectite is of the Tatatila & Chambers type. The calculated CEC is 113 and 118 meq/100g for the untreated and treated samples, respectively. In addition, a decrease of the K content at the interlayer – balanced by an increase in Mg – has been observed in the sample located in contact with the heater. This release of potassium might be related with the neo-formation of K-feldspar close to the heater (see 5.2.5.7).

5.2.5.2. Chemical composition

The chemical composition of the solid phase of samples from sections S12 and S19 is shown in Table 5.39 and Table 5.40. The most significant changes observed in all the sections are the losses of reduced species with respect to the original FEBEX sample. The ferric iron, Fe_2O_3, is predominant in the treated samples, with very low FeO contents. CIEMAT has also observed a decrease of total SO_2, and a decrease of divalent cations (Ca, Mg, Sr, Ba) with respect to the original FEBEX sample. To illustrate these issues, the chemical composition (major elements) of samples from sections S12, S19 and S31 is plotted in Figure 5.164, together with the results for the untreated sample. In the samples from external positions (BB19-1) there is an in-

Table 5.38
Basal spacing d(001) of the smectite (in Å) for non-dried samples of section S19 (CIEMAT)

Sample	Position[1]	Powder	Compacted
BB19-1	102	14.65	16.86
BB19-2	81	14.90	15.02
BB19-3	59	15.03	15.37

[1] *Distance to gallery axis, in cm*

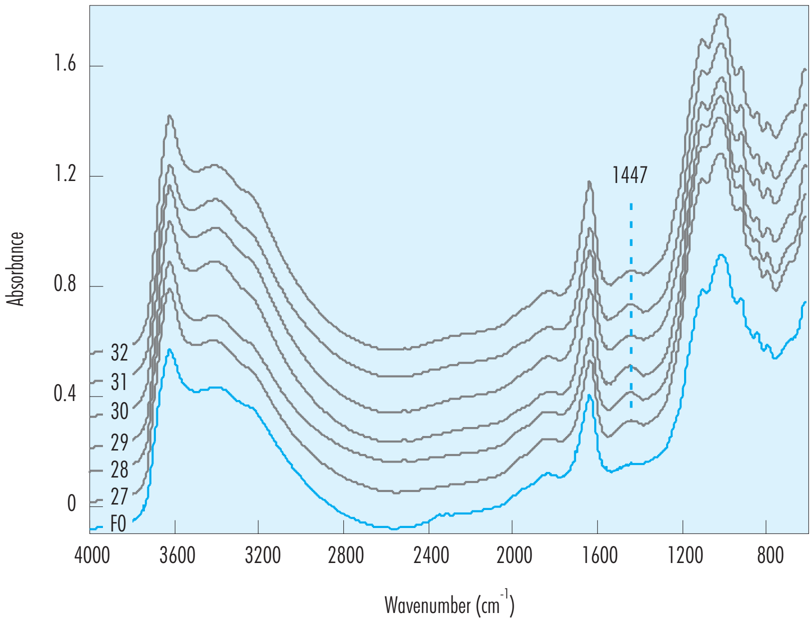

Figure 5.163: IR spectra for untreated sample (F0) and samples from section S29 (INPL/LEM).

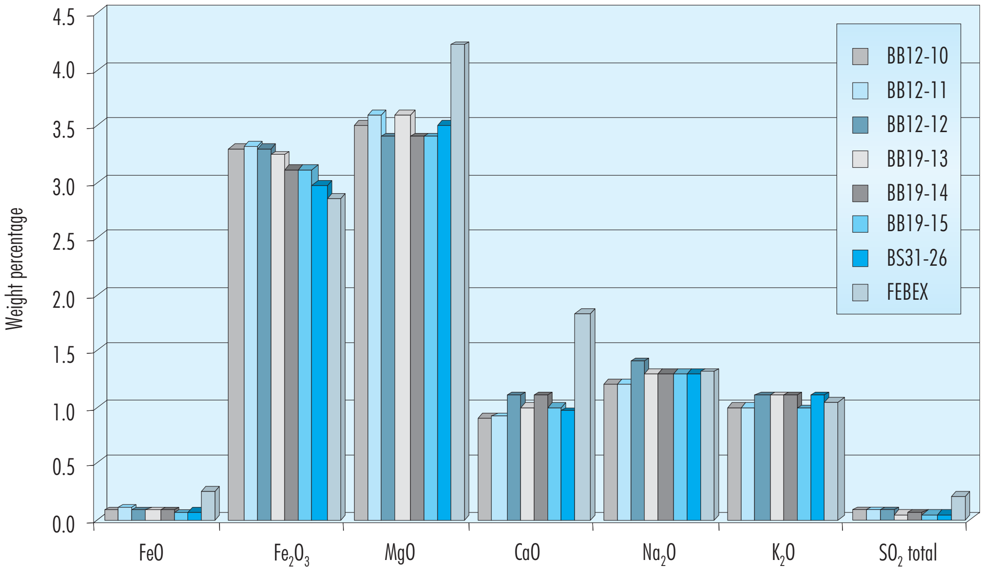

Figure 5.164: Chemical composition of samples from sections S12, S19 and S31 and of the FEBEX untreated sample (CIEMAT).

Table 5.39
Chemical composition of the solid phase of samples from section S12 (CIEMAT)

	Oxides (%)					Element (ppm)			
	BB12-10	BB12-11	BB12-12	FEBEX		BB12-10	BB12-11	BB12-12	FEBEX
Position[1]	103	81	59	—		103	81	59	—
SiO_2	66.37 [2]	66.19 [2]	65.23 [2]	57.89 ± 1.55	Ba	86	95	115	164 ± 25
Al_2O_3	17.38	17.38	18.31	17.95 ± 0.71	Sr	165	155	123	220 ± 23
FeO	0.08	0.1	0.08	0.25 ± 0.10	Ce	43	48	50	74 ± 6
Fe_2O_3	3.30	3.32	3.29	2.84 ± 0.12	Co	9.2	9.7	9.4	9 ± 3
MgO	3.5	3.6	3.4	4.21 ± 0.21	Cr	9.2	8.7	14	8 ± 2
MnO	0.04	0.04	0.05	0.04 ± 0.00	Cu	12	13	11	25 ± 9
CaO	0.9	0.92	1.1	1.83 ± 0.10	La	19	22	23	40 ± 3
Na_2O	1.2	1.2	1.4	1.31 ± 0.09	Mo	<5	<5	<5	—
K_2O	1.0	1.0	1.1	1.04 ± 0.05	Ni	16	17	15	20 ± 3
TiO_2	0.22	0.24	0.24	0.23 ± 0.01	Sn	<10	<10	<10	—
P_2O_5	0.06	0.07	0.06	0.03 ± 0.01	V	9.9	11	10	16 ± 2
H_2O (130°C)	11.70	11.70	11.30	—	W	<25	<25	<25	
H_2O (220°C)	13.08	12.69	12.69	14.1 ± 0.7	Y	13	13	14	25 ± 3
Loss at 950°C [2]	19.00	18.60	18.40	19.5 ± 1.8	Zn	50	49	45	65 ± 4
CO_2 Total	0.51	0.51	0.59	0.61 ± 0.05	Cs	5.9	6	6.9	—
CO_2 organic	0.22	0.22	0.37	0.35 ± 0.05	Eu	—	—	—	—
CO_2 inorganic	0.29	0.29	0.22	0.26 ± 0.06	Se	<0.1	<0.1	<0.1	—
SO_2 total	0.08	0.08	0.08	0.21 ± 0.10	Li	51.0	50.0	47.0	—
H_2O^+ (220-950°C)	5.33	5.32	5.04	4.31 ± 0.41					

[1] Distance to gallery axis, in cm; [2] Calculated to obtain a sum of oxides of 100%

crease of Fe_2O_3 and MgO with respect to samples taken from hotter areas.

5.2.5.3. Exchange capacity

The INPL/LEM and CIEMAT laboratories studied the ion concentration at exchange positions in the clay. Figure 5.165 shows the results obtained for different sections by CIEMAT.

There is an overall increase of Ca content, but especially at the heater and the bentonite-granite contact. Both increments seem to be related to the increase of the water content due to the evaporation

Table 5.40
Chemical composition of the solid phase of samples from section S19 (CIEMAT)

	Oxides (%)					Element (ppm)			
	BB19-1	BB19-2	BB19-3	FEBEX		BB19-1	BB19-2	BB19-3	FEBEX
Position[1]	103	81	59	—		103	81	59	—
SiO_2	58.69	59.16	58.89	57.89 ± 1.55	Ba	138	177	221	164 ± 25
Al_2O_3	17.47	16.68	16.52	17.95 ± 0.71	Sr	154	163	160	220 ± 23
FeO	0.08	0.08	0.06	0.25 ± 0.10	Ce	58	55	50	74 ± 6
Fe_2O_3	3.08	2.95	2.98	2.84 ± 0.12	Co	11	11	10	9 ± 3
MgO	3.6	3.4	3.4	4.21 ± 0.21	Cr	6.9	7.2	5.6	8 ± 2
MnO	0.03	0.03	0.03	0.04 ± 0.00	Cu	12	12	12	25 ± 9
CaO	1.0	1.1	1.0	1.83 ± 0.10	La	21	17	16	40 ± 3
Na_2O	1.3	1.3	1.3	1.31 ± 0.09	Mo	<0.5	<0.5	<0.5	
K_2O	1.1	1.1	0.99	1.04 ± 0.05	Ni	16	16	9.3	20 ± 3
TiO_2	0.24	0.24	0.23	0.23 ± 0.01	Sn	<10	<10	<10	
P_2O_5	0.06	0.06	0.06	0.03 ± 0.01	V	10	11	9.4	16 ± 2
H_2O (130°C)	8.2	10.6	11.7	—	W	<25	<25	<25	—
H_2O (220°C)	9.2	11.92	13.08	14.1 ± 0.7	Y	13	11	10	25 ± 3
Loss at 950°C	14.4	16.8	18	19.5 ± 1.8	Zn	49	49	47	65 ± 4
CO_2 Total	0.48	0.55	0.48	0.61 ± 0.05	Cs	6	6.1	5.5	—
CO_2 organic	0.22	0.26	0.26	0.35 ± 0.05	Eu	2	2.2	1.7	—
CO_2 inorganic	0.26	0.29	0.22	0.26 ± 0.06	Se	<0.1	<0.1	<0.1	—
SO_2 Total	0.04	0.06	0.04	0.21 ± 0.10	Li	<2	<2	<2	—
H_2O^+ (220-950°C)	4.7	4.3	4.4	4.31 ± 0.41					

[1] *Distance to gallery axis, in cm*

or accumulation of water in the heater zone and to the water coming from the granite in the opposite site, respectively. The increase of water favours the dissolution of calcite and the subsequent exchange reaction of sodium by calcite in the smectite, increasing the exchangeable Ca content. Therefore, different processes – linked to high temperature and to hydration – might be responsible for the increment. There is an important increment of potassium in exchange positions with respect to the initial value, more stressed in the external and internal blocks. An increase of sodium and magnesium is observed in the samples closer to the gallery wall. In samples from sections with heaters, S19 and S28,

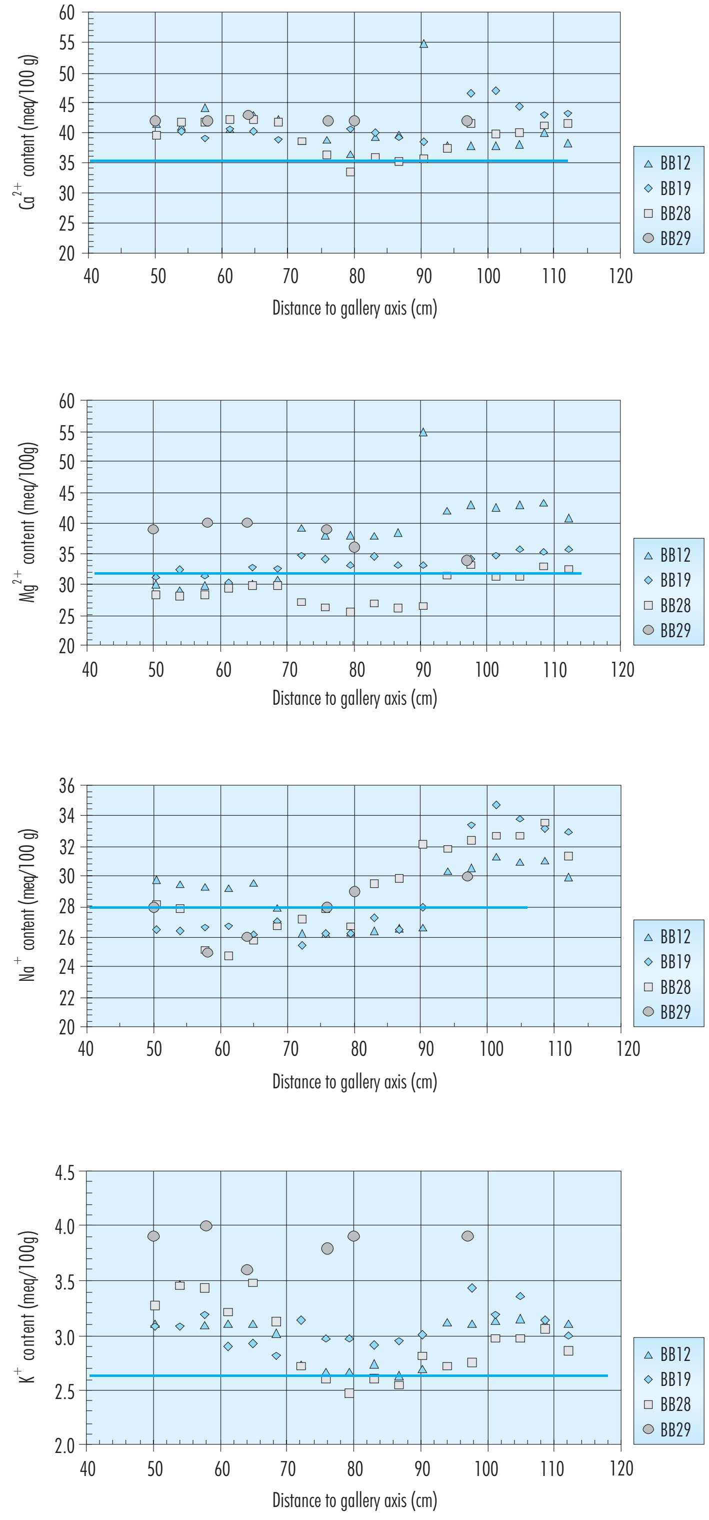

Figure 5.165: Distribution of exchangeable cations along a radius in different sections of the bentonite barrier (the average value for the untreated sample is shown as a line).

the exchangeable sodium content decreases close to the heater contact. INPL/LEM detected an increase of exchangeable magnesium towards the heater contact, which was not observed by CIEMAT. An increase of the sum of exchangeable cations has been detected in most of the samples analysed (Figure 5.166), especially in the samples at the contact with the granite, which have a higher water content. In fact, the CEC values are higher in samples belonging to section S12 – out of the influence of the heater – than in samples belonging to sections subjected to hydration and heating (S19 and S28).

5.2.5.4. Soluble salts: aqueous extracts

The soluble salts were analysed by CIEMAT in aqueous extract solutions at a solid to liquid ratio of 1:4. The distribution of soluble salts along one radius of each section analysed is shown in Figure 5.167. In these figures the results obtained from section S7, at the contact with the concrete plug, are also shown (see Section 5.2.5.8).

There is a lixiviation of chloride and sodium in the bentonite block closer to the gallery wall, the concentrations of these ions increasing towards the inner part of the bentonite barrier above their initial inventories. The maximum values and their location depend on the existence of a thermal gradient. With respect to sulphates, there is also leaching in the most hydrated zones, but sulphate moves more slowly than chloride. There is an increase of bicarbonate both in the bentonite in contact with the granite and in the heater zone, due to calcite-dolomite dissolution. Both increments seem to be related to the increase of the water content because of the evaporation/accumulation of water at the heater zone and of the water coming from the granite.

Therefore, the hydration of bentonite at the external blocks in contact with the granite produces the dissolution and dilution of the more soluble trace minerals in the bentonite (sulphates, carbonates and chlorides). As a result, saline fronts are generated due to the different mobility of the dissolved ions. The chlorides move as a conservative anion. The movement of sulphates and bicarbonates must be basically regulated by gypsum and calcite equilibrium, respectively (see Section 5.2.2).

The main counter-ion that follows chloride movement is sodium. However, the implication of sodium

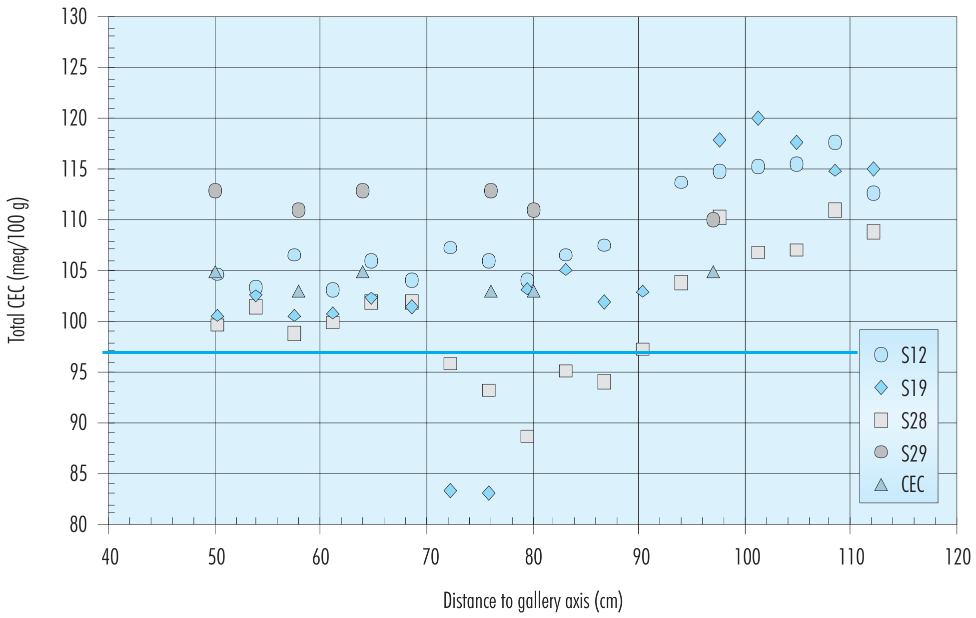

Figure 5-166: Sum of exchangeable cations along a radius in different sections of the bentonite barrier (the average value for the untreated sample is shown as a line). CEC: CEC calculated in S29 from the final concentration of the $Cl_3Co(NH_3)_6$.

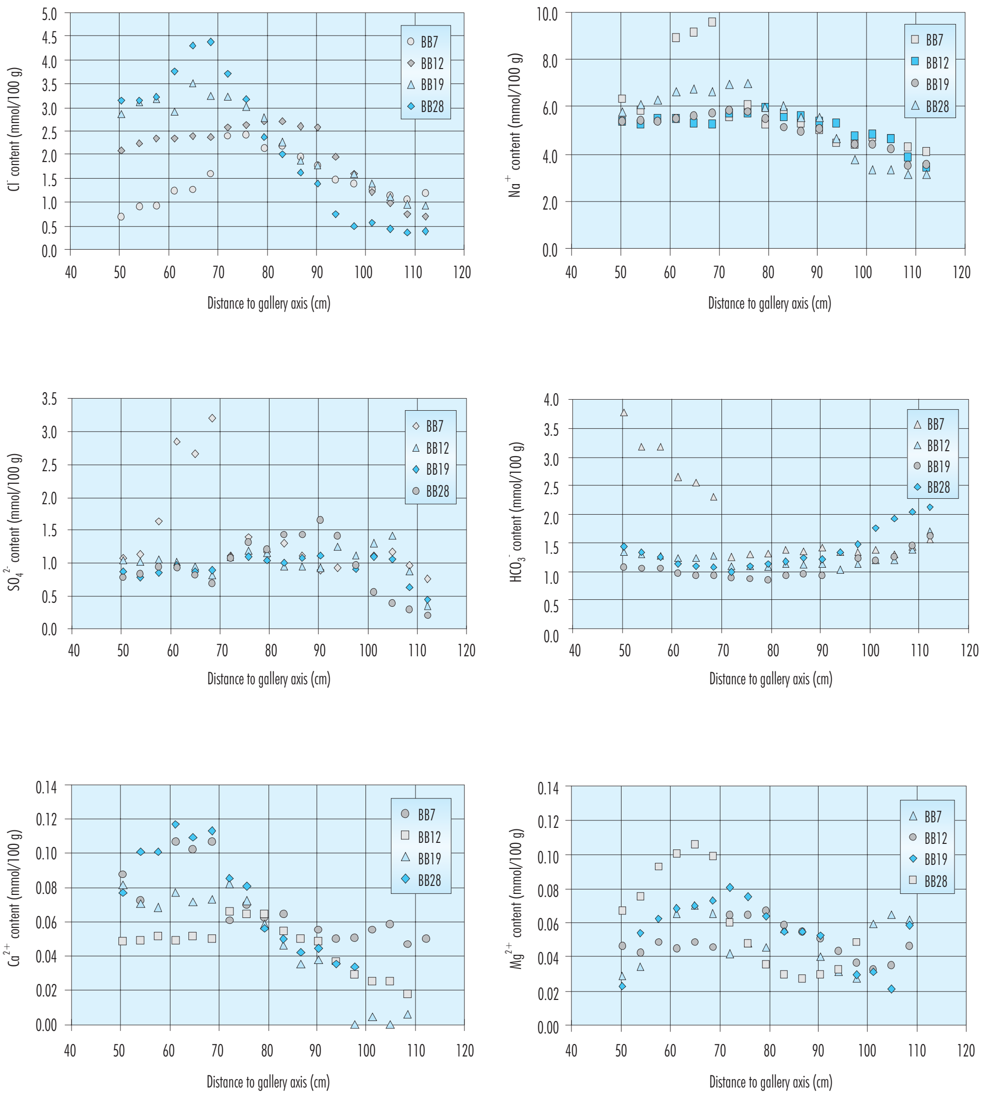

Figure 5.167: Soluble salts measured in 1:4 aqueous extracts in samples taken from different sections. Average values for the untreated sample (in mmol/100g): Cl^-: 1.98, SO_4^{2-}: 0.98, Na^+: 5.02, Ca^{2+}: 0.05, Mg^{2+}: 0.05, K^+: 0.07, HCO_3^-: 1.18) (CIEMAT).

in exchange reactions modifies the relative concentration of both ions. There is an excess of sodium content with respect to that of chloride in the leached zones. As the hydration front progresses, the dissolution of carbonates and sulphates produces the liberation of calcium. Consequently, the exchange of sodium by calcium in the exchange positions must be induced, changing the relative concentration of sodium, bicarbonate and the pH in the aqueous extracts solution.

The other major cations, calcium and magnesium, show a parallel increase, but their concentrations are at least 5-10 times lower than that of sodium. These results are similar to those obtained in tests at intermediate scale ([156]; Section 5.2.2.1).

On the other hand, the salt movement seems to be faster in the heater sections (S19 and S28) than in the zone without a heater (S12 and S7). The highest salt contents have been found in section S28, followed by section S19 and finally section S12 (without heater). Section S28 has the influence of the two heaters.

5.2.5.5. Pore water chemistry: squeezing tests

CIEMAT analysed the chemical composition of the pore water of several blocks taken from a section subjected only to hydration (S12) and another subjected simultaneously to hydration and heating (S19). The method used to extract the pore water from the bentonite was the squeezing technique. As low as possible squeezing pressures were used to avoid ultrafiltration and ionic fractionation phenomena. In turn, the pressure needed to obtain the pore water was higher the lower the initial water content of the bentonite. In fact, the low water content of the internal blocks did not allow pore water to be obtained by squeezing.

The chemical composition of the water obtained from samples of sections S12 and S19 is shown in Table 5.41. Since this extraction technique produces the expulsion of some amount of the interlayer water and, therefore, the dilution of the pore water samples ([10]; Section 5.2.1.1), it is assumed that the content of ions in the true pore water would be higher.

The distribution of solutes in the pore water follows the same tendency as observed in the aqueous extracts (Figure 5.168 and Figure 5.169), *i.e.* the saline fronts detected in the soluble salt distribution are also observed in the squeezing tests. The chemical composition of the pore waters extracted in section S7 (bentonite slice in contact with the concrete plug) is also shown for comparison (section 0). There is an increase of the ionic concentration towards the inner part of the bentonite barrier, linked to the advance of the hydration front. Hence, there is an intense mobilisation of ions towards the most internal part of the bentonite barrier in sections S7 and S12.

The ion concentration of the pore waters obtained in the more heavily leached zones are similar to

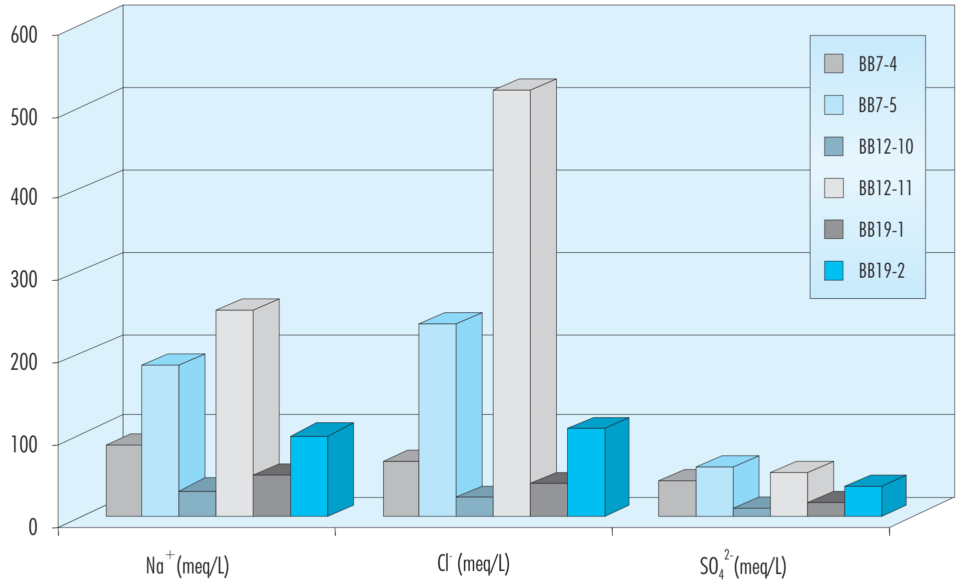

Figure 5.168: Distribution of chloride, sodium and sulphate in the pore water obtained by squeezing in samples from different sections (CIEMAT).

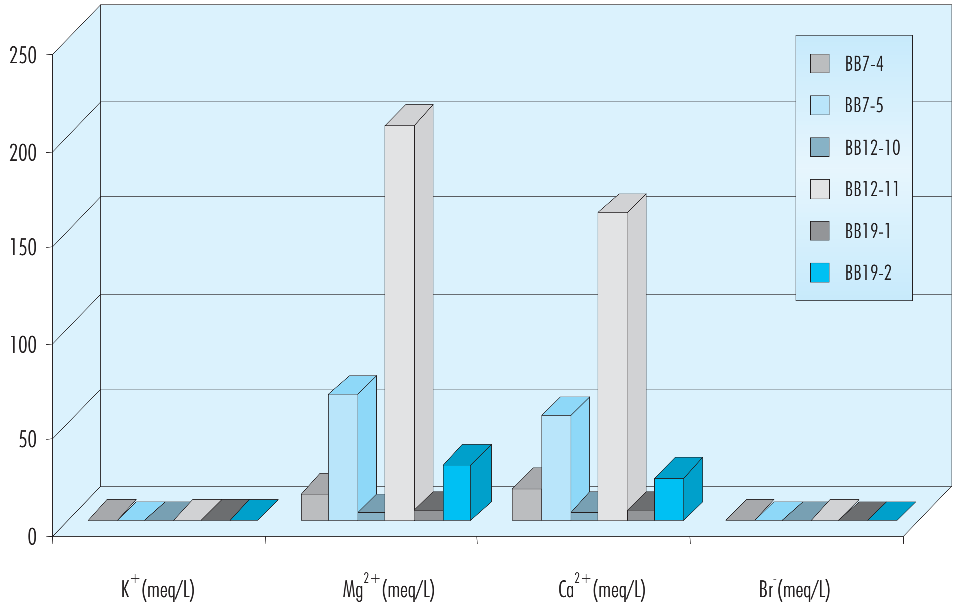

Figure 5.169: Distribution of cations in the pore water obtained by squeezing in samples from different sections (CIEMAT).

those obtained in the gas pipe lines (Section 5.2.5.6), except for section S7.

5.2.5.6. Composition of water obtained from gas pipes

GRS installed in the "in situ" test a number of ceramic pipes to determine the gas content and the gas permeability of the clay buffer (Section 4.3.3.2). Some of these pipes, those at the bentonite/granite interface, were filled with water, which was sampled for analysis. The water analysed was collected from pipes GF-S-L-01, GF-S-L-02 and GF-S-L-03 during three different sampling campaigns: February 1998, December 2001 and January 2002 [70].

A piper diagram of these waters is shown in Figure 5.170, in which they are compared with the granite groundwater obtained at the GTS from different boreholes. The GTS groundwater around the FEBEX drift is Na-Ca-HCO_3-F^- type, very diluted, with low electric conductivities (85 µS/cm), low content of dissolved salts and pH values close to 9 [157, 158, 13].

The salinities and ionic strength of the waters from the gas pipes are far removed from those of a GTS granite groundwater, showing the influence of the bentonite barrier. The GF-SL-01 and GF-SL-02 waters are Na-Cl in type, whereas the GF-SI-03 water is of the Na-Cl-SO_4 type. They show ion concentrations similar to those of a bentonite pore water (Section 5.2.1.5), though slightly more diluted, probably due to the mixing of both types of waters. The pH is between 7.7 and 8.4. The dissolution of the carbonates from the bentonite has buffered the alkaline pH of the GTS groundwater, increasing the bicarbonate content and the sodium content, the latter released by exchange reactions.

The results also show a major variation of the chemical composition with time. The content of all cations and anions increases with time, although the concentrations are, in general, lower than those measured in the pore waters squeezed from bentonite blocks in contact with the gallery wall. It is worth noting the different composition of the samples taken from the gas pipes in December 2001 and in February 2002, when the dismantling operations began, mainly with respect to the redox potential values and Fe(II) contents. The Eh values calculated for the samples taken in December 2001 were 70,

Table 5.41
Chemical composition of the pore water obtained by squeezing in samples from section S12 and section S19 (CIEMAT) in meq/L

Species test conditions and physico-chemical parameters	BB12-10	BB12-11	BB19-1	BB19-2
Na^+	33.2	252.3	52.2	100.0
K^+	0.31	0.56	0.33	0.33
Mg^{2+}	4.28	205.7	5.51	29.0
Ca^{2+}	4.44	159.7	5.29	22.6
Sr^{2+}	0.032	0.87	0.039	0.162
Al^{3+}	—	—	0.07	0.06
Mn^{2+}	0.005	—	0.003	0.015
Cl^-	24.6	521.8	42.3	110.0
SO_4^{2-}	11.8	54.1	18.4	37.5
Br^-	0.02	0.38	0.03	0.09
NO_3^-	0.12	—	0.02	0.61
HCO_3^-	1.43	1.3	2.57	2.64
Initial *w* (%)	24.3	18.9	28.7	23.5
Pressure applied (MPa)	25	70	25	70
pH	7.6	7.4	7.5	7.7
Electrical neutrality (%)	5.4	3.0	0.12	0.50
Ionic strength (*M*)	0.03	0.70	0.06	0.13

100 and 106 mV for the GF-SL-01, GF-SL-02 and GF-SI-03 waters, respectively. These values are much less oxidized than those measured in waters collected in February 2002.

All the waters are close to equilibrium or over-saturated with respect to calcite, except the first sample taken in 1998. The calculated partial pressures of CO_2 are in agreement with the CO_2 contents measured in the gas pipes (Figure 5.171). The P_{CO_2} value increased from the atmospheric value during the initial phase of the "in situ" test, $10^{-3.5}$ atm, to values of between $10^{-2.5}$ and $10^{-1.0}$ atm, the highest values being found in the internal gas pipes.

5.2.5.7. Texture

Microscopic analyses

Samples from section S29 were analysed by INPL/LEM [154] by SEM in order to unravel any modification in the clay layer morphology and identify any new mineral phases that might have been formed during the "in situ" test.

No modifications with respect to the untreated bentonite were noticed in the sample from the external block in contact with the granite. However, some variations in accessory minerals were observed in the

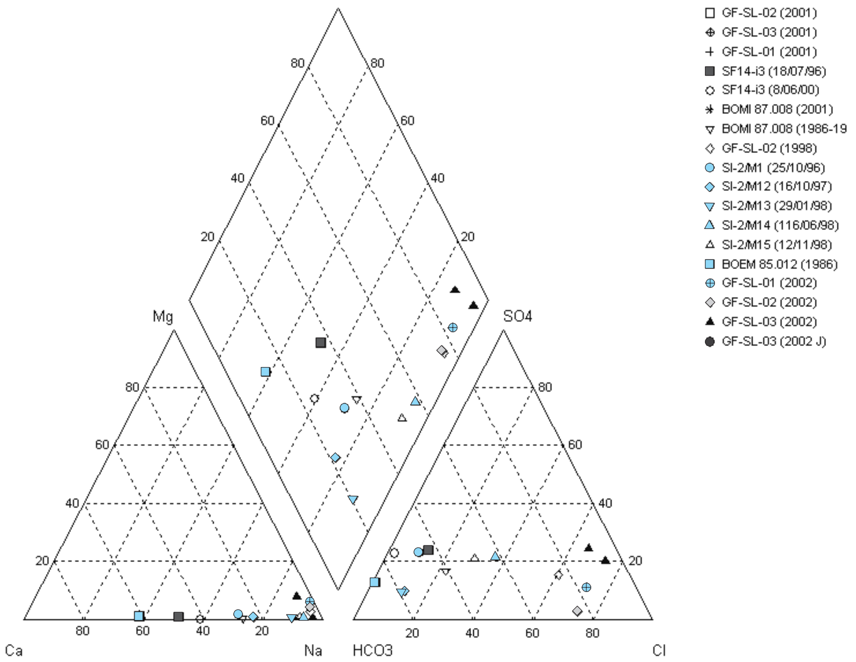

Figure 5.170: Piper diagram of GTS groundwater and water taken from the gas pipes at the FEBEX "in situ" test.

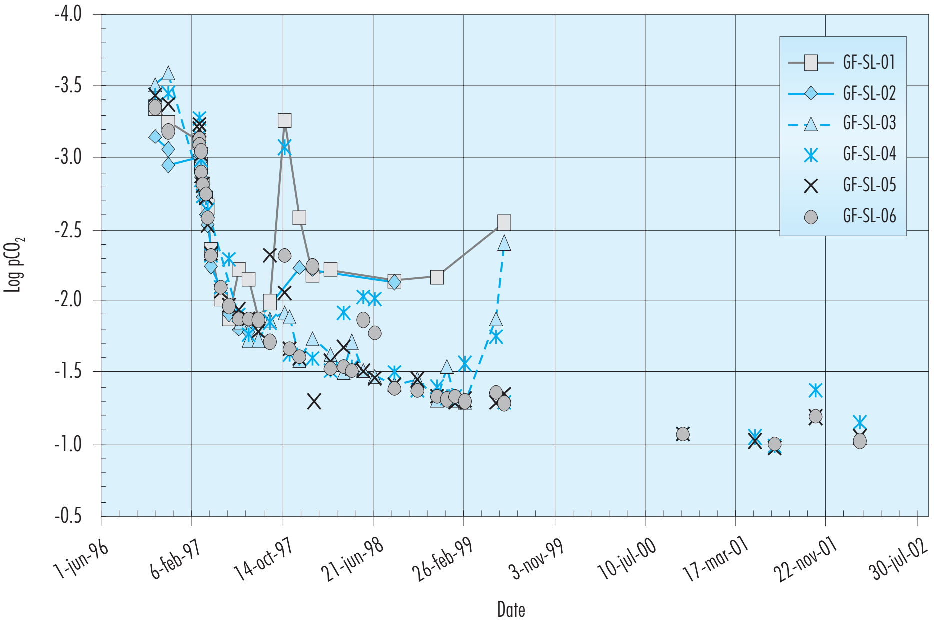

Figure 5.171: Variation of the CO_2 contents in the waters obtained from the gas pipes, expressed as partial pressure of CO_2.

sample located in the internal block in contact with the heater. Potassic feldspars displayed dissolution crevices (Figure 5.172a). Furthermore, near these corroded feldspars, neo-formed minerals were observed, which may be considered as automorph crystals of potassic feldspars (Figure 5.172b). The clay minerals in the vicinity of these feldspars display a filamentous morphology (Figure 5.172b). Biotites are present, but reveal corrosion gulfs. As these corrosion marks were observed for this sample only, they might be explained in terms of this sample being located close to the heater. Neo-formed feldspars were also observed at the contact with the heater in the 60-cm long cell tests (see Section 5.2.2.3).

Nitrogen adsorption/desorption isotherms

Nitrogen adsorption-desorption isotherms were determined by the INPL/LEM and CIEMAT laboratories in powdered samples [70]. Surface areas were determined using the standard BET method, the presence of micropores in the samples and calculations of the external surfaces were assessed using the *t*-plot method and the BJH method was employed for analysis of mesoporosity and pore size distribution.

Figure 5.173 shows the nitrogen adsorption-desorption isotherms obtained by CIEMAT. All of them show the characteristic feature of the type IV isotherm with a very important hysteresis loop due to capillary condensation in mesopores. The curves exhibit an H3 hysteresis loop in desorption, characterising the presence of slit-shaped pores [87]. The volume of gas adsorbed for the samples in contact with the heater is lower than for the other samples. Besides, the end of the adsorption branch reaches higher adsorbed volumes for the treated samples and the hysteresis is less marked, indicating a more continuous distribution in pore size.

From *t*-plot analysis, the specific surface area, which is equivalent to the non-microporous surface area (pore radius > 20 Å), for the FEBEX bentonite is 61.5 m^2/g (Table 5.15), and lower for the treated samples, the most substantial differences being found in the samples in contact with the heater (values from 38 to 28 m^2/g). The reduction of micropores and of the BET surface area in the treated samples is also significant. This might be due to an increase in the number of clay particles per quasi-crystal due to the effect of temperature.

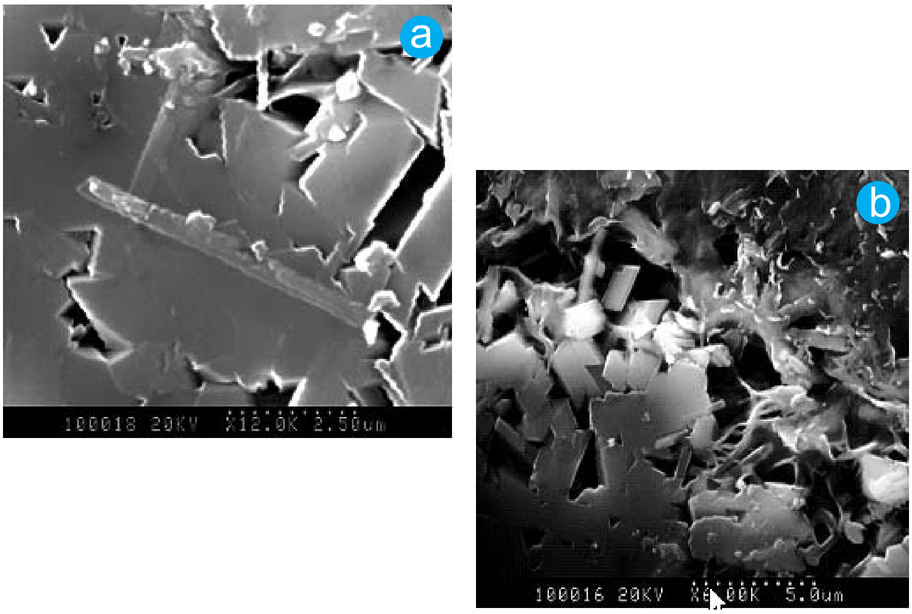

Figure 5.172: SEM microphotographs of a sample located close to the heater: a) K-feldspars; b) K-feldspars and filamentous clays (INPL/LEM).

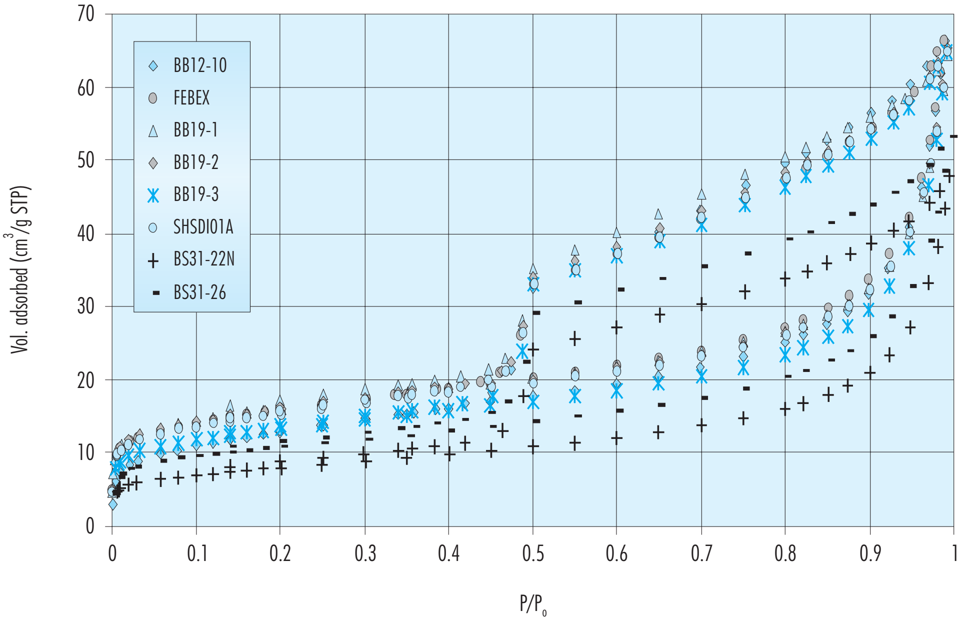

Figure 5.173: Adsorption-desorption isotherm of gas N_2 at 77 K on FEBEX reference bentonite and post-mortem samples. Outgassing conditions: 90ºC for 18 hours, 0.01 Pa (CIEMAT).

INPL/LEM observed an overall decrease of the micropore volume and an increase of the mesopore volume in all the treated samples, irrespective of their position (Figure 5.174).

INPL/LEM also performed the adsorption analyses on compacted, non-powdered samples. Much lower BET surface areas were obtained for compacted samples (between 32 and 40 m^2/g) than for powdered samples (between 64 and 75 m^2/g).

The analysis of mesopores by the BJH method showed an increase in mesopore volume and in the average pore radius in all the samples, but especially in those close to the heater (Figure 5.174b).

5.2.5.8. Effect of the interaction with concrete

CIEMAT and VTT performed studies on the bentonite from section S7, the one in contact with the concrete plug. The study by VTT was more detailed and concentrated on the variations observed in the bentonite as a function of the distance to the concrete surface; whereas the CIEMAT study was more extensive and attempted to establish the differences with those sections of bentonite not under the influence of the concrete.

The fact of being in contact with the concrete may have altered the mineralogical and chemical characteristics of the bentonite in this section, but also provided a different hydraulic context, since the contact surface was intensely hydrated during the construction of the concrete plug and has probably behaved as a preferential water passageway.

According to the results obtained by CIEMAT, the bentonite from section S7 has shown several differences with respect to the other sections analysed and to the reference bentonite. Although its mineralogical composition is similar to that of the untreated FEBEX bentonite, an increase of calcite and gypsum, not observed in other sections, has been detected in one sample. On the other hand, the chemical composition of the bentonite from section S7 is similar to that of the other sections, except for a clear increase in Al. There is also a noticeable increase of Ca, Na and K in exchange positions in all the samples analysed by CIEMAT. The increase is particularly important towards the central part of the bar-

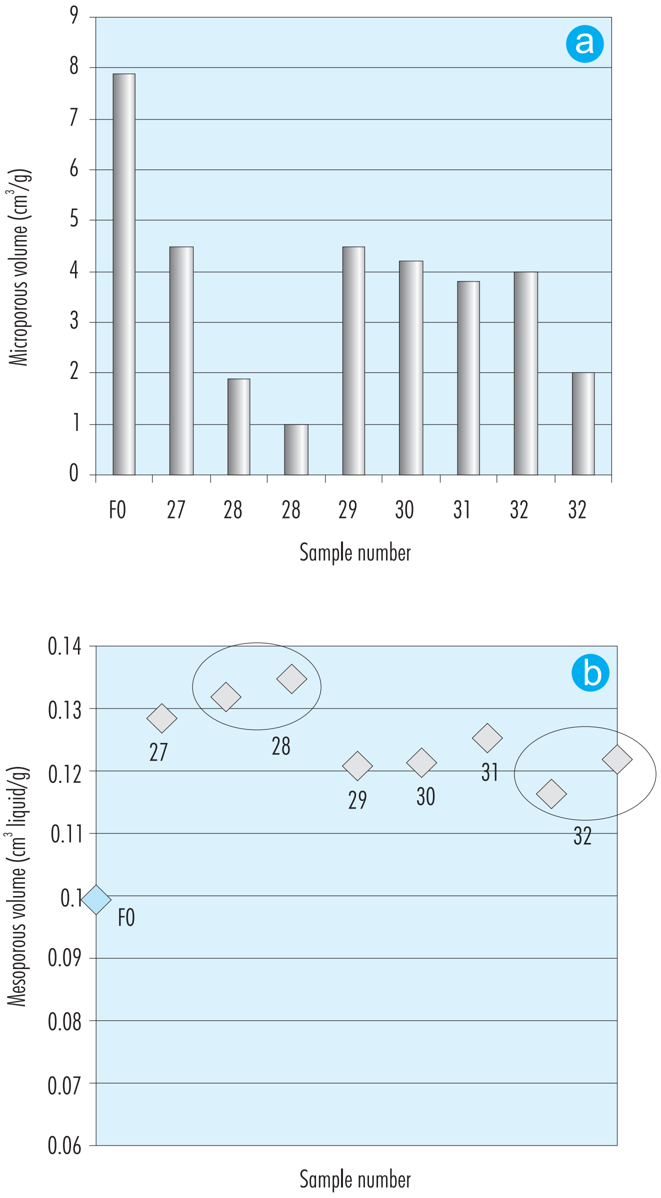

Figure 5.174: Nitrogen adsorption data analysis: micropore volume calculated from t-plot method (a); mesopore volume calculated with the BJH method (F0: untreated sample; sample 27; closest to the heater; sample 32: closest to the gallery wall) (b) (INPL/LEM).

rier, where it is accompanied by a significant decrease in Mg occupation (Figure 5.175). The increase in Ca occupation has also been observed by VTT, especially in those samples taken from close to the concrete. These tendencies have been observed by other authors in tests on the hydrothermal alteration of bentonite by alkaline solutions [159].

However, the main difference observed in section S7 with respect to the other sections is that the salinity of the pore water obtained by squeezing is much higher, especially concerning Cl, Ca, Mg and Na (Figure 5.168 and Figure 5.169). This high salinity has also been measured in the aqueous extracts (Figure 5.167). VTT found an increase of Na^+, Ca^{2+}

and SO_4^{2-} in the pore water of the bentonite directly in contact with the concrete, whereas the content of Mg^{2+} decreases considerably (Table 5.42). The pH values measured close to the concrete interface are not hyperalkaline.

The studies performed in the context of the ECOCLAY I and II projects on the alteration of bentonite by alkaline solutions showed that intense mineralogical and geochemical modifications of the clay occur when it is in contact with concrete solutions at high temperatures; for example, there is an important increase of Mg in octahedral positions that has not been detected in the dismantled bentonite. The fact that no such important changes were observed in section S7 may be explained by the low temperatures experienced by the bentonite in this position (around 18 °C), since the reactivity of bentonite is clearly dependent on temperature, increasing significantly above 75 °C. On the other hand, it seems that these alterations are localised at the contact with the concrete.

5.2.6. Tracers distribution in the “in situ” test

5.2.6.1. Deuterium

Deuterated water (^2H_2O) was used as a conservative tracer for the “in situ” test. Deuterium is a stable isotope that has the unique property of forming part of the water molecule. Therefore, it moves with water as a conservative tracer. However, it will potentially participate in processes that might induce its isotopic fractionation. These processes may include: (1) fractionation due to the water uptake during bentonite hydration; and (2) fractionation due to evaporation/condensation processes in areas close to the heaters.

Five sources containing deuterium in glass ampoules were placed in five bentonite blocks at the external ring of section S29. During dismantling these blocks were taken, along with the four blocks above them completing the two central radii. Most of these blocks were very damaged, probably during extraction. The glass ampoules were found in only three of the five bentonite blocks, and they were broken, although it is not possible to establish whether the breakage occurred during dismantling or during the operation phase of the “in situ” test.

Bentonite pore water was obtained from 18 samples taken from these blocks using the aqueous extract method with low S:L ratio (1:4). The test are described in [160] and summarised in [70]. The results of these analyses do not allow clear conclusions to be drawn due to:

- ❑ Data precision. Although the precision of the deuterium data of aqueous extract samples is 0.8 ‰, this analytical error translates into major errors when bentonite pore water values are computed. If the S:L ratio had been 1:1 instead of 1:4, the error bands would have been much smaller.

Table 5.42
Composition of the pore water squeezed in different slices of the sample C/BS7-16 (meq/L) (VTT)

Sample/slice	Position[1]	pH	Eh (mV)	Na^+	Ca^{2+}	Mg^{2+}	HCO_3^-	Cl^-	SO_4^{2-}
16/1	4	8.25	-58	64.0	13.4	3.0	1.4	52.0	26.8
16/2	13	8.25	-115	57.7	10.4	2.8	1.1	50.3	22.4
16/5	48	8.29	-18	54.6	10.6	7.2	1.2	52.9	22.2
16/8	86	8.32	-52	54.9	9.6	10.0	1.2	54.2	21.8
16/10	124	8.28	-74	55.8	11.6	14.0	1.1	60.3	20.2
Uncertainty		±0.1	±50	±10 %	±15 %	±15 %	±20 %	±15 %	±15 %

[1] *Distance to the concrete/bentonite interface (mm)*

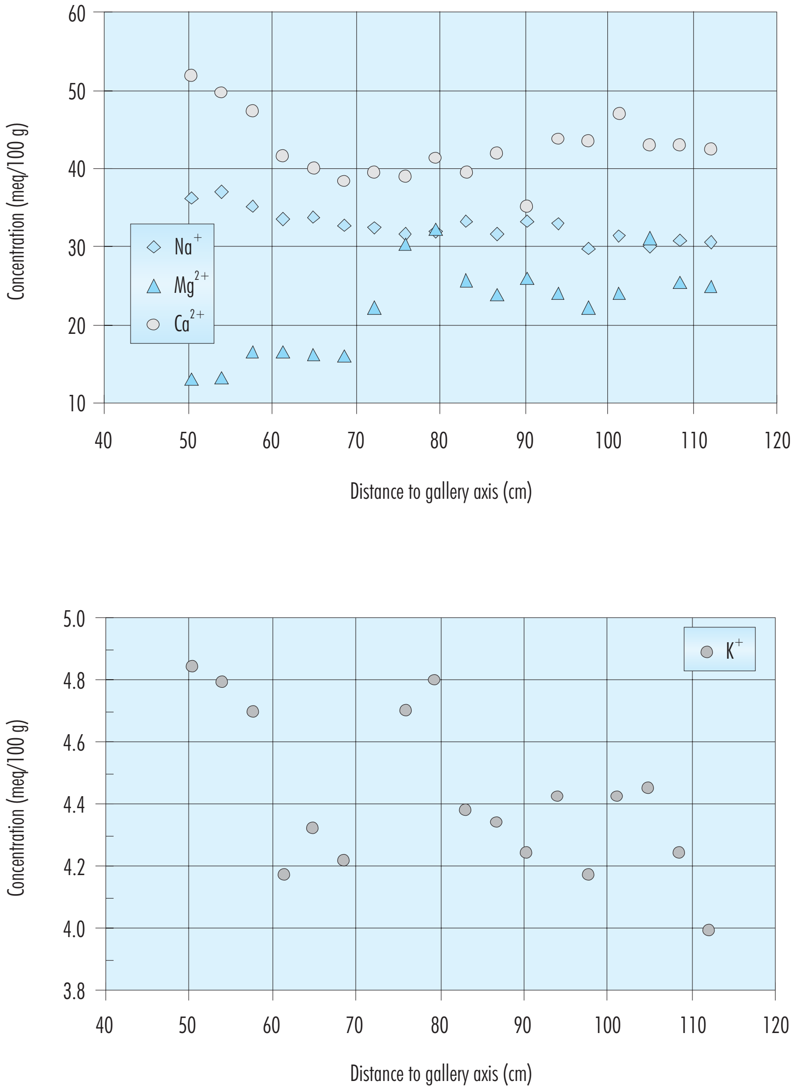

Figure 5.175: Distribution of exchangeable cations in samples taken along a radius of section S7 (Values for untreated sample in Table 2.12) (CIEMAT).

- Uncertainties regarding breakage of the glass ampoules. The most likely thing is that the glass ampoules broke during the operation phase, because if they had broken during dismantling, clay samples near the glass should still show high deuterium ratios. However, since the amount of deuterated water added was not large enough, there is no clear evidence of deuterium migration.

There are also uncertainties in the deuterium data and their interpretation due to the following:

- The preliminary scoping calculations were not fully realistic because they did not account for isotopic fractionation.
- The deuterium mass added to the bentonite blocks was probably not large enough to serve as a tracer for the "in situ" test.
- The bentonite pore water deuterium concentration has been derived from aqueous extract samples. There are uncertainties regarding the

isotopic transfer (fractionation) between internal (interlayer) and external water (double layer water and free water).

- ❑ The deuterium analyses were performed in the liquid phase, and the possibility of measuring deuterium directly in bentonite samples should be explored.

5.2.6.2. Iodide

Iodide was placed in filter papers at the outer part of the barrier, in contact with the granite, in the lamprophyre area, which was covered over a length of 3 meters with 120 iodide-doped papers on the lower right-hand part of the barrier. Three blocks were retrieved by EIG EURIDICE from sampling section S30 during the dismantling operations [161]. Once in the laboratory, 39 samples were taken from the different blocks. Aqueous extraction of these samples was carried out and the solutions obtained were analysed with ICP-MS.

The iodide concentration measured in each sample is plotted in Figure 5.176 as a function of the distance to the gallery axis, *i.e.* following a radius of the barrier. The outer block (in contact with the I-doped sheet) shows an iodide concentration that increases in the direction of the heater, while the highest concentrations are found in the middle block (BB30-2). This is the expected behaviour for a conservative tracer that has moved with the water front, being leached from the filter paper and having concentrated in the further zones reached by the water front.

5.2.6.3. Boron

Block BB-25-2 – located in contact with the gallery wall – was doped with boron (isotopically enriched in ^{10}B) contained in a sintered stainless steel plug placed in the middle of the block. After retrieval during dismantling, the block was cut into 14 slices, one of which contained the source. Only the total boron concentration has been measured in each slice, and it seems quite regular over the whole sampling region. Preliminary analyses indicated an isotope ratio ^{10}B/^{11}B of 35/65, the natural abundance in the bentonite being 20/80. Further isotopic analyses are needed to characterise the tracer movement.

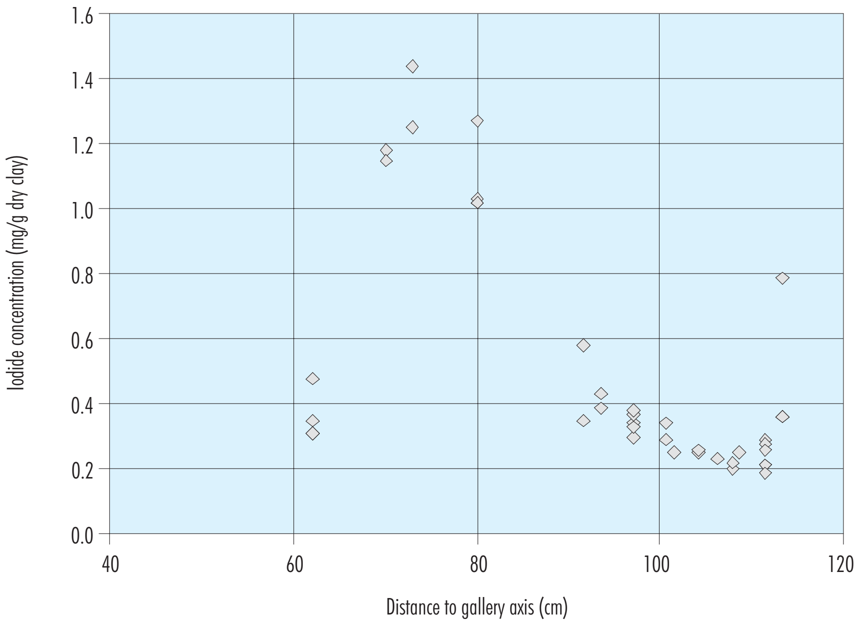

Figure 5.176: Iodide concentration as a function of the distance to the gallery axis in the samples analysed by EIG EURIDICE (section S30).

5.3. Gas generation and migration

The gas production from the bentonite was investigated during the first phase of FEBEX by GRS in laboratory tests performed under defined physical-chemical conditions created inside gastight ampoules: temperature (from 20 to 100°C), humidity (air-dry bentonite or saturated) and type of gas (laboratory air or nitrogen). The duration of the tests was fixed at 100 days. The experimental details of this investigation may be found in ENRESA (2000) [13].

The laboratory measurements on gas release indicated that carbon dioxide is the only gas component of importance released from the backfill material in the temperature range between 20 and 100°C, under aerobic or anaerobic conditions. With decreasing temperature, the velocity of gas generation decreased significantly. In the hygroscopic stage of the bentonite, the amount of carbon dioxide released is lower by a factor of 3 than in the wet stage. The question as to whether air or nitrogen was in contact with the bentonite (aerobic or anaerobic conditions, respectively) did not influence the generation of carbon dioxide. The reason might be that the backfill material had adsorbed oxygen on the internal surfaces of the clay or that air had been trapped in the pore volume during the fabrication and storage of the bentonite. This oxygen would then be consumed by oxidation of the organic material in the bentonite, resulting in the generation of carbon dioxide. This means that for oxidation at 100°C and over a time period of 100 days, no external oxygen is necessary for the thermal oxidation of the organic material in the clay. Furthermore, carbon dioxide may also be generated by thermal decomposition of carbonates in the bentonite.

The amount of methane released varies in the range between 2 mL per 1000 kg and 9 mL per 1000 kg. The storage conditions (temperature, type of gas in contact with the bentonite and additional water) do not seem to have an influence on the amount of methane released. It might be the case that the methane generated by thermal decomposition of the organic material is oxidised instantaneously and that carbon dioxide is generated. Furthermore, the amount of methane found in the residual volume of the ampoules is in the range of the lower detection limit of the analytical system.

During the second phase, GRS continued the studies of gas release in order to determine the influence of time and extrapolate the total amount of gases that might be generated from the bentonite [162]. The tests were performed in gastight ampoules kept at 90°C during exposure times of between 1 and 1000 days. The influence of the quantity of clay employed was investigated, as well as the influence of the presence of water. Formation water from the Grimsel Test Site was used for this purpose. In all the tests the bentonite was in contact with laboratory air.

This investigation indicated once more that carbon dioxide is the only gas generated and released from the bentonite at a temperature of 90°C. The results for the hygroscopic and wet stage as a function of exposure time up to 1000 days are shown in Figure 5.177. These results indicate that the release of carbon dioxide increases with time up to 1.8 m^3 per 1000 kg bentonite in the wet stage and up to 0.4 m^3 per 1000 kg bentonite in the dry stage. The gas generation seems to have reached a plateau for the dry and wet stage. The reason for the difference in the dry and wet stages might be that in the dry stage, carbon dioxide is partly adsorbed to the internal surfaces of the clay. In the wet stage, water is adsorbed, and carbon dioxide is desorbed and released into the residual volume. By increasing the amount of the bentonite in the ampoule from 10 to 100 g the specific amount of the released carbon dioxide decreases, which means that, with a higher concentration of carbon dioxide in the residual volume of the ampoule, back reaction will take place. It is most likely that carbon dioxide is generated by oxidation of the organic components in the clay in the presence of oxygen adsorbed to the clay.

5.4. Corrosion studies

A number of components retrieved during the partial dismantling of the "in situ" test were analysed in order to identify the corrosion processes undergone under the same conditions as those predicted for deep geological disposal in a granitic formation.

The following elements were analysed:

- ❑ Heater #1
- ❑ Liner
- ❑ Corrosion coupons
- ❑ Sensors
- ❑ Bentonite

A description of the studies performed on each element and the results obtained is given below [163].

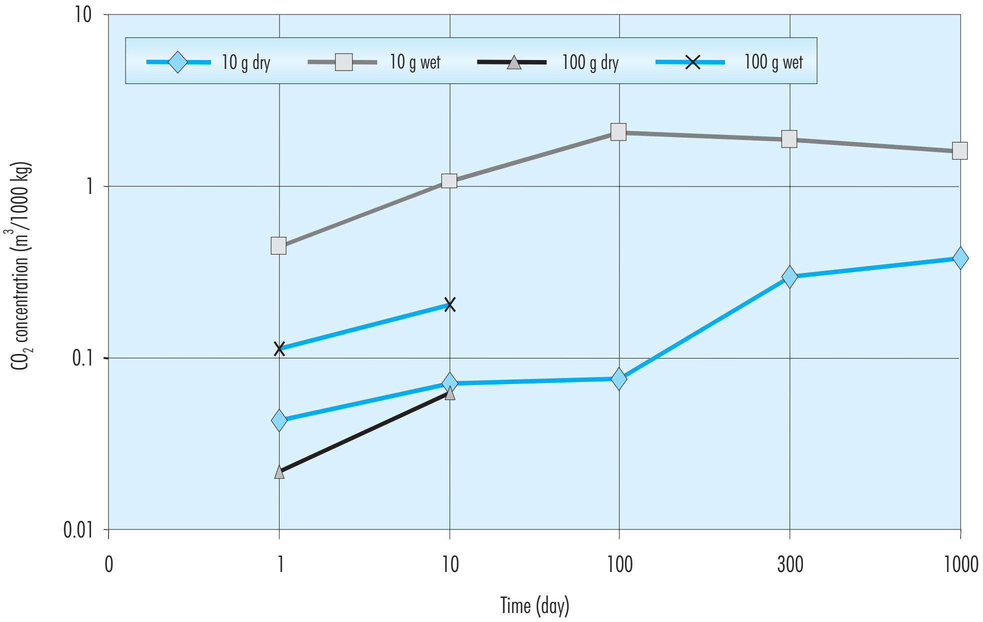

Figure 5.177: Release of carbon dioxide as a function of time from the bentonite at 90° C in the natural dry and in the wet stage.

5.4.1. Heater #1

The heater was made out of carbon steel (Section 4.3.2.1). The sample studied was a section taken from its rear end, consisting of the lid with its welded joints and a 300 mm section of the body. The following analyses were carried out: visual inspection, analysis of corrosion products with energy dispersive spectrometry (EDS) and X-ray diffraction (XRD), metallographic study with optical microscopy, and hardness study.

According to the results from the analysis, the heater underwent very slight generalised corrosion, with oxide layers of less than 20-μm in thickness in all the cases examined and no pitting or any other sign of localised corrosion. The almost complete absence of humidity around the heater as a result of heating, the evolution towards increasingly anoxic conditions within the disposal site, as well as the fact that it was not in direct contact with the bentonite, prevented or slowed down the progression of generalised corrosion, as well as the start and progression of other localised corrosion phenomena.

5.4.2.Liner

The liner was made of carbon steel (Section 4.3.2.2). The sample analysed was one of the three segments retrieved during the dismantling operation. A visual inspection, analyses of corrosion products, and metallographic studies (Figure 5.178) were performed.

This element suffered generalised corrosion that did not advance uniformly, with maximum measured values of corrosion penetration of approximately 130 and 200 μm on the external and internal surfaces, respectively. This penetration was somewhat greater than that suffered by the heater. The test conditions of the liner, in direct contact with the bentonite and with a greater level of humidity in its surroundings, justify the difference in the extent of the generalised corrosion. No localised corrosion phenomena were observed.

5.4.3. Corrosion coupons

Samples of different candidate metals for manufacturing of the containers were analysed. These had

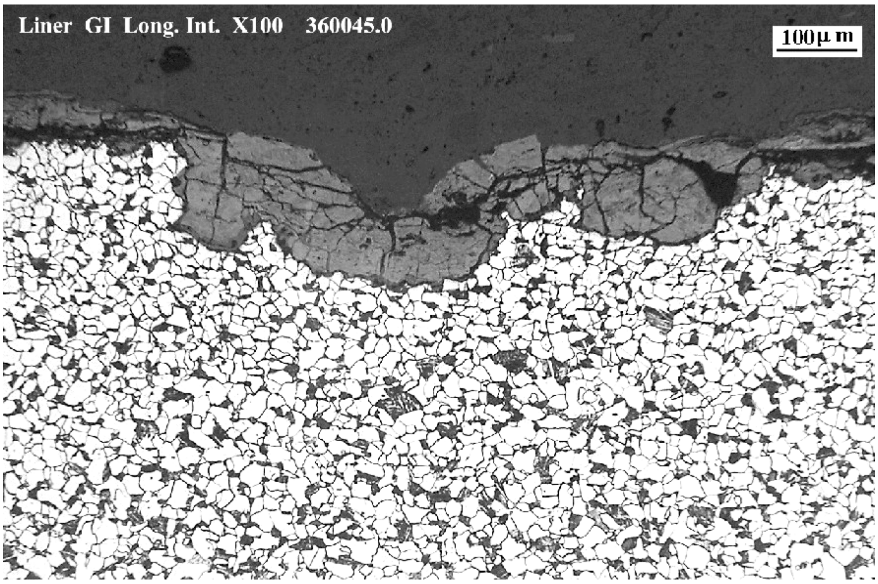

Figure 5.178: Internal surface of the lower part of the liner .

been placed in the clay barrier during the test installation in order to evaluate their behaviour when faced with corrosion phenomena. The corrosion coupons studied consisted of different sized parallelepipeds grouped by materials:

- TStE355 type carbon steel (UNE F 6215), including joints welded by EBW (Electron Beam Welding), FCAW (Flux Cored Arc Welding) and MAGW (Metal Active Gas Welding).
- AISI 316L (UNS S31603) austenitic stainless steel, including joints welded by EBW and GTAW (Gas Tungsten Arc Welding).
- Titanium alloys Grade 2 (UNS R50400), 7 (UNS R52400) and 12 (UNS R53400), including joints welded by EBW and PAW (Plasma Arc Welding).
- Pure copper Cu-ETP (UNS C11000) and cupronickel alloys 70/30 (UNS C71500) and 90/10 (UNS C70600).

Each group of specimens was mounted on a rack, separated by Teflon pieces, and inserted in the bentonite blocks closest to the heater at the bottom side. Four racks were retrieved during the dismantling, one for each group.

Again, a visual inspection of the specimens and an analysis of the corrosion products were carried out. In addition, corrosion rates were calculated according to the ASTM G31 standard "Standard Practice for Laboratory Immersion Corrosion Testing of Metals", Section 11.

No generalised and/or local corrosion was observed on the stainless steel and titanium specimens (Figure 5.179). The carbon steel coupons showed no localised corrosion phenomena, and very slight generalised corrosion, with corrosion rate values of 0.10 μm/year, whereas in laboratory testing values of up to 10 μm/year had been obtained with samples of the same material in contact with saturated bentonite at temperatures of up to 100°C. This may be attributed to the low humidity content of the bentonite housing the samples, as well as to the almost anoxic conditions.

However, the Cu-ETP and Cu-10Ni test pieces underwent similar generalised corrosion rates as those measured in the laboratory tests referred to above. In this case, whilst the oxygen forms cuprite, which is a passive protective oxide, the presence of chlorine – as chloride – generates non-protective species, such as $CuCl_2$. The analyses of bentonite (Section 5.4.5) showed a significant concentration of chlorides, which would justify the corrosion rate values obtained. The corrosion suffered by the Cu30Ni alloy was negligible.

Finally, it should be pointed out that the humidity conditions in the bentonite block where the copper rack was inserted were slightly higher than those of the carbon steel rack.

5.4.4. Sensors

Some of the sensors used to monitor different parameters in the "in situ" test were found to be severely corroded during dismantling (Figure 4.41). Four of these sensors were devoted to corrosion analysis, namely two extensometers measuring the horizontal and vertical displacement of Heater #1 at its front end and two thermocouples. The active element in all cases was protected by an austenitic alloy tube or sheath, and the thermocouples included a magnesia insulating filling. The vertical extensometer was sent for analysis with the bentonite surrounding it at the rock side. The anchoring devices to the rock and liner, which included carbon steel and other metals, were also analysed.

The following analyses were carried out:

- Visual inspection. The extensometers had zones of damage close to the rock and to the liner with extensive pitting on the surface and occasional perforation of the tube wall, along with some cracking in the zone close to the liner. Diffusion of corrosion products could be seen in the surrounding bentonite, as well as pustules or deposits of bentonite and corrosion products built up beneath the sensor surface (Figure 5.180). Significant corrosion damage could be seen on the anchoring devices of the sensors, with significant cracking of the plates on the rock side, and destruction of carbon steel components. Both thermocouples analysed showed some zones of generalised corrosion damage and others with more localised corrosion in the form of pitting. The corrosion progressed from the outer to the inner periphery, perforating the covering sheath, and exposing the magnesia insulation together with

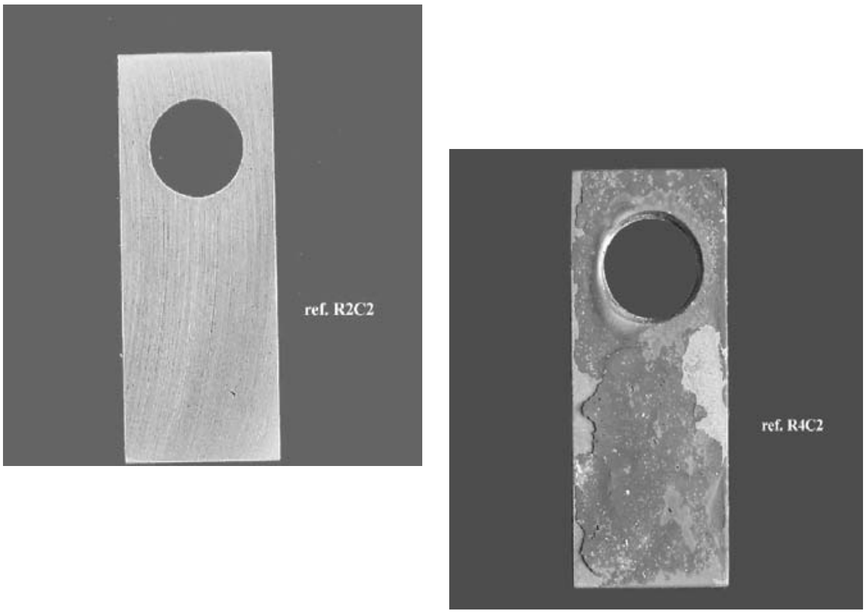

Figure 5.179: AISI 316L stainless steel coupon (left) and Cu-ETP copper coupon (right).

the two wires constituting the thermocouple (Figure 5.181).

- Analysis of corrosion products and/or deposits: the most significant result is the presence of sulphur, sometimes predominant, in almost all the products analysed.
- Metallographic study: the damaged areas described in the visual inspection of the extensometers show significant corrosion penetration of the material, with a clear advance from the outer to the inner periphery. The cracks detected are typical of the stress corrosion cracking of stainless steels.

The four sensors studied were by far the components with the greatest corrosion damage. The most significant feature shown by analysis of the corrosion products generated was a significant presence of sulphur. Microbiological analysis of the bentonite surrounding the sensor revealed a significant content of sulphate reducing bacteria (SRB), which is even higher in the built-up pustules. Therefore, the damage observed may be defined as a local corrosion phenomenon induced by the sulphides generated during the metabolic activity of SRB, as these sulphides create a very corrosive media with the high water content of the bentonite close to the rock. The source of sulphates reduced by the SRB is the bentonite itself. Although the SRB are exclusively anaerobic bacteria, they can develop in aerobic conditions if they are located beneath other aerobic bacterial colonies that create zones deficient in oxygen, as was the case on the sensor surface.

It is not clear that the metabolic activity of the SRB has contributed to the progress of the stress corrosion cracking observed, but both phenomena are quite frequently associated.

In the thermocouples, apart form bacterial induced corrosion, there is corrosion or dissolution of the metal due to the chlorides in the environment.

5.4.5. Bentonite

As the sealing and packing component of the medium, bentonite plays an important role in the corrosion resistance of the materials that it houses. Three bentonite blocks were studied, two of them housing the corrosion coupons and the third surrounding the vertical extensometer. In addition to

Figure 5.180: Full view and detail of corrosion damaged zone of vertical extensometer close to the rock

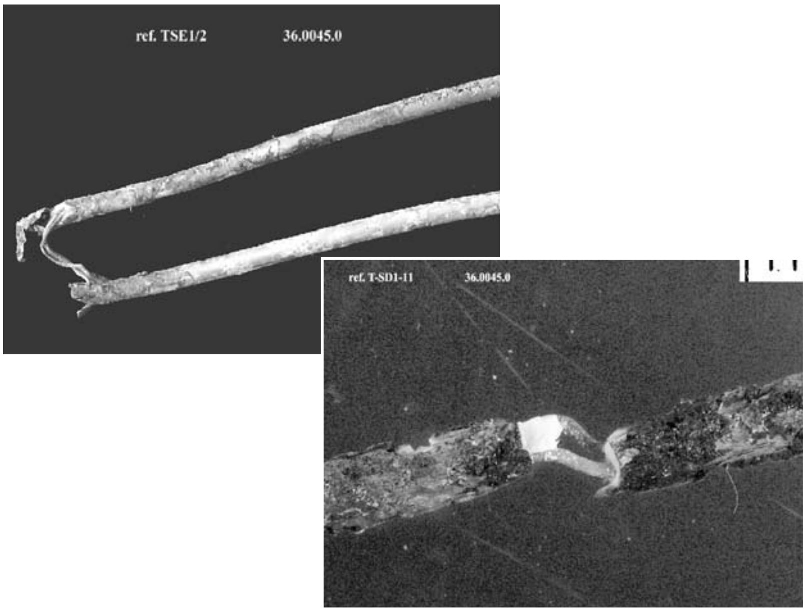

Figure 5.181: Full view and detail of corrosion damaged thermocouple.

the visual inspection, chemical and microbiological characterisations were carried out.

The results obtained show significant bacterial activity, with a major population of SRB, in the block of bentonite housing the extensometer which had a higher degree of humidity. On the contrary, no activity at all may be found in the bentonite close to the liner, which was considerably drier. This may be basically attributed to the high temperatures experienced, given that most bacteria and microorganisms usually involved in microbiological corrosion phenomena, such as SRB, have a "survival" range of between 10 and 50 °C. Furthermore, the absence of humidity inhibits the growth of the bacteria, but does not eliminate them.

5.5. Analysis and recalibration of dismantled sensors

Due to the partial dismantling of the FEBEX "in situ" test, all the instruments contained in the dismantled bentonite buffer section were sampled for analysis. Up to 163 measuring devices were obtained. Discarding the devices used for the gas, which are not strictly sensors, 150 sensors of different types were sampled (Table 5.43). Of these, 72 (47.7 percent), were out of order prior to dismantling. A detailed description of the analysis and recalibration of the sensors may be found in [164].

The obtained sensors were first checked "in situ" to determine their positioning, mechanical damage and corrosion effects (Section 4.6.4.2). The LVDT type clinometers and potentiometers for heater displacement (so-called experimental sensors) failed due to the complete flooding of many of them up to the associated electronics. The remaining sensors were carefully inspected by types in the laboratory to determine the reliability of the data obtained for the operative sensors and the reasons for the failure of the defective sensors.

Also, the total pressure cells cemented at the rock surface of dismantled sections D1, E1 and F1 were checked/calibrated "in situ".

5.5.1. Temperature sensors

Many of the used thermocouples were in operation when retrieved, and only a few (only 7 out of 37) failed due to corrosion processes. According to the calibration data, the behaviour of the operative temperature sensors was excellent and their accuracy had not varied since the time of installation (error below ±1°C).

5.5.2. Humidity sensors

The results of these sensors by type are as follows:

- The capacitive type sensors have widely surpassed the initially expected operative lifetime (13 sensors out of the 27 were on duty) and only two of those in operation showed measurement drift. The readings provided by the remaining operative sensors were still accurate.
- Only four out of the 24 psychrometers retrieved were operative. Most of them failed due to mechanical effects (bentonite swelling or the dismantling operation itself) and also to salty water saturation (contamination by salts), therefore they could not be calibrated.
- The TDRs in the bentonite buffer also proved to be quite fragile for such an environment: only two out of 10 were found to be operative. Furthermore, two distorting effects were identified which have affected the calculated water content and made data re-interpretation necessary: a shift of the registration window with time and with increasing water content in the bentonite, and a change with time in the shape of the reflectogram signals.

5.5.3. Buffer sensors based on the vibrating wire technique

The analysis of bentonite sensors based on the vibrating wire technique (pore pressure sensors, total pressure cells and displacement in bentonite blocks) showed that they displayed very good accuracy after more than five years of operation. Only some small offset drifts were detected in the total pressure cells, such that the pressures registered by some of those sensors were about 3-4 bar lower than the actual pressures.

In general, the vibrating wire sensors also proved to be very robust: only 6 pore pressure sensors out of 24 showed problems, 4 total pressure cells out of 8 were out of order, along with the two heater displacement sensors recovered, whereas all the bentonite block displacement sensors were operative throughout the entire period of operation. The only common difficulty came from the weakness of the embedded thermistor, which failed in some cases. In addition, some corrosion was observed in some of them, especially for the two heater displacement sensors, which were found to be severely damaged by corrosion, this especially affecting the anchoring pieces.

Table 5.43
Sampled sensors by types

Sensor type	Quantity
Thermocouples	37
Capacitive type humidity sensors	27
Psychrometers	24
TDRs	10
Total pressure cells	8
Pore pressure sensors	24
Heater and bentonite displacement sensors	14
Clinometers	6
TOTAL	150

5.5.4. Total pressure cells in rock surface

The tests performed on the rock surface total pressure cells demonstrated a change in the offset (initial reading for null pressure) with regard to the values taken during the installation, in some cases. The application of these new offset values improved the coincidence of pressure evolution for the cells at the same sections.

5.5.5. Conclusions

Thanks to the analysis of sensors carried out the confidence in the recorded and future gathered data has increased significantly, as the results from verified-calibrated sensors showed negligible or very low drift in most cases.

The failure rate for some types of sensors might be minimised for future experiences under similar conditions by avoiding the use of fragile ceramic or metallic filters and weak plastic parts (or if not avoided they should be at least well protected mechanically). The use of corrosion resistant metals (for instance AISI 316L), or if this were not possible, the use of non-corrosive external protections will help to extend the lifetime of several components. Nevertheless, the failures of the experimental sensors did not cause data loss problems, due to the redundancy of the signals obtained by using well-proven sensors in parallel.

6. Thermo-hydro-mechanical (THM) analyses

6. Thermo-hydro-mechanical (THM) analyses

6.1. Introduction

The second objective of the FEBEX project is set out as follows: “the project has sought to study the THM processes in the near-field, especially in the clay barrier, and to improve, verify and validate the existing codes and constitutive equations” (Chapter 1).

The main tool used to achieve this objective has been the performance of coupled THM analyses simulating the “mock-up” and “in situ” tests. To this end, a fully coupled THM formulation and a finite element code based on it have been developed. Verification, validation and continuous updating of the proposed THM framework have been performed throughout the development of the project.

Important THM phenomena take place in the engineered barrier and in the near field due to the combined actions of heating and hydration. For instance, hydration takes place from the external boundary inwards driven by the gradient between the rock water pressure and the suction in the bentonite. Hydration will cause a progressive rise in the degree of saturation. This affects both the temperature field, due to the modifications of thermal conductivity, and the stress/strain distribution, due to suction changes. On the other hand, in the inner part of the buffer, the applied heat causes a temperature rise that moves outwards. Furthermore, water evaporation causes drying of the bentonite. Vapour coming from the inner part of the barrier will diffuse towards the outer regions where it will condense, causing a local rise in the degree of saturation. Water transfer is also affected by the dependence of water viscosity on temperature and by porosity changes arising from variations of stresses and suction. There are additional significant THM couplings in this kind of problem, as discussed in the following sections. Therefore, coupled THM analyses are required to achieve a satisfactory understanding of this problem.

From the perspective of the FEBEX project, coupled THM analyses have been undertaken in a number of phases:

- Previous modelling, during the design of the tests.
- Pre-operational modelling prior to the start of the test.
- Concurrent modelling during the performance of the test.
- Final modelling, after test dismantling.

Another crucial contribution to a better understanding of these complex tests has been the extensive experimental program performed to study the THM behaviour of the engineered barrier components. The behaviour of FEBEX bentonite has been a matter of special attention and has included comprehensive study of the main THM properties and a detailed examination of its fabric. Effort has been devoted to the integration of all these valuable experimental data in a consistent framework via the development, parameter determination and experimental validation of constitutive models for the thermal, hydraulic and mechanical aspects of the problem. These activities include the modelling of oedometer, swelling pressure, permeability, and small and large cell tests, among others. The modelling of these tests is presented in [165]. The final objective has been to propose advanced constitutive models to achieve a closer representation of the actual behaviour of the material.

The FEBEX experiment is not yet finished, as the “mock-up” test and the "in situ" test are still operational. However, during the second phase of the FEBEX project the "in situ" test has been partially dismantled, with the extraction of one heater and part of the clay barrier. This has allowed for the performance of a number of post-mortem comparisons. Indeed, the actions associated with partial dismantling and continuing "in situ" test operation have provided new challenges for THM modelling.

This Chapter is organized in six main sections. Section 2 introduces the main aspects of the basic THM formulation and computer code used in the analyses, while Section 3 contains the adopted constitutive laws and equilibrium restrictions. Section 4 presents and discusses the “mock-up” test numerical analyses. It focuses on comparisons between model predictions and experimental results, and also on the studies undertaken to assist in the interpretation of some unforeseen aspects of the evolution of the “mock-up” test. Section 5 presents the "in situ" test modelling. The comparisons between model predictions and test data are first examined, followed by a description of the modelling of the cooling, excavation and dismantling processes. Comparisons between model predictions and post-mortem data obtained during partial dismantling of the test are also discussed. Section 6 closes the Chapter with the main conclusions from the THM modelling.

6.2. Formulation and computer code

6.2.1. Formulation

A macroscopic approach developed in the context of the continuum theory for porous media has been used in the analyses [62]. It is assumed that the porous medium is made up of three phases: solid, liquid and gas. The liquid phase contains water and dissolved air whereas the gas phase is made up of dry air and water vapour. The formulation incorporates basic thermal, hydraulic and mechanical phenomena in a coupled manner. The hydraulic component should be understood in a generalized way, i.e. including both liquid and gas flow.

The formulation has allowed for the performance of coupled THM analyses within a unified and integrated framework. The approach has also acted as a repository where new advances and developments have been incorporated and integrated. During the development of the project, there has been a growing understanding of the THM behaviour of the clay barrier and the near field components. Therefore, the formulation has been constantly updated as new physical insights, experimental data and application results have become available. In this way, new knowledge does not become a collection of separate items but it is related in a rational and traceable manner to the existing state of the art. The condition is, of course, that the formulation is open, flexible and structured in an accessible manner. The extension of the formulation to double structure media, with the possibility of considering the clay-fabric effects in the simulations, is perhaps the most relevant advance in the THM modelling performed [51]. Other developments allow for the inclusion of a threshold hydraulic gradient or thermo-osmotic effects in the analysis [51].

In this Section the main parts of the basic THM formulation are presented. New developments are introduced at the relevant point in the Chapter, with Sections exclusively devoted to explaining them. Specifically, the basic THM formulation takes into account the following phenomena:

- Heat transport:
    - Heat conduction
    - Heat convection (liquid water)
    - Heat convection (water vapour)
    - Phase changes
- Water flow:
    - Liquid phase
    - Water vapour diffusion
- Air flow:
    - Gas phase
    - Air solution in water
    - Dissolved air diffusion
- Mechanical behaviour:
    - Thermal expansion of materials
    - Behaviour of bentonite dependent on stresses, suction, water pressure and temperature
    - Granite behaviour depending on stresses and temperature (water pressure and suction effects are considered via conventional effective stress)

The problem is approached using a multi-phase, multi-species formulation that expresses mathematically the main THM phenomena in terms of balance equations, which are introduced below. The other main parts of the formulation are the constitutive equations and the equilibrium restrictions, introduced in Section 6.3. Finally, the properties of the fluid phases appear in the balance equations and in the constitutive laws. In general, they depend on the composition of the phase and on the state variables (temperatures and pressures).

6.2.1.1. Balance equations

The compositional approach has been adopted to establish the mass balance equations. This approach consists of balancing the species (mineral, water and air) rather than the phases (solid, liquid and gas). In this way the phase change terms do not appear explicitly, which is particularly useful when equilibrium is assumed. In the notation, the subscript is used to identify the phase (s for solid, *l* for liquid and *g* for gas) and the superscript indicates the species: *w* for water and *a* for air. No symbol is attributed to the mineral species, because it has been assumed that it coincides with the solid phase. The main balance equations are presented in the following paragraphs, a more detailed description may be found elsewhere [62].

Balance of mass of water

$$\frac{\partial}{\partial t}(\theta_l^w S_l \phi + \theta_g^w S_g \phi) + \nabla . (\mathbf{j}_l^w + \mathbf{j}_g^w) = f^w \qquad (6.1)$$

where θ_l^w and θ_g^w are the masses of water per unit volume of liquid and gas phase respectively. ϕ is the porosity and S_α is the volumetric fraction of pore volume occupied by the alpha phase ($\alpha = l, g$). $\mathbf{j}_l^w$ and $\mathbf{j}_g^w$ denote the total mass fluxes of water in the liquid and gas phases with respect to a fixed reference system. f^w is the external mass supply of water per unit volume of medium.

Balance of mass of air

$$\frac{\partial}{\partial t}(\theta_l^a S_l \phi + \theta_g^a S_g \phi) + \nabla.(\mathbf{j}_l^a + \mathbf{j}_g^a) = f^a \qquad (6.2)$$

where θ_l^a and θ_g^a are the masses of air per unit volume of liquid and gas phase respectively. $\mathbf{j}_l^a$ and $\mathbf{j}_g^a$ denote the total mass fluxes of air in the liquid and gas phases with respect to a fixed reference system. f^a is the external mass supply of air per unit volume of medium. Note that dry air is considered as a single species in spite of the fact that it is a mixture of gases. The gaseous phase is assumed to be a mixture of air and water vapour. Air also dissolves in the liquid phase.

Balance of energy

$$\frac{\partial}{\partial t}\left[E_s \rho_s (1-\phi)\right] + \frac{\partial}{\partial t}(E_l \rho_l S_l \phi + E_g \rho_g S_g \phi) +$$

$$\nabla.(\mathbf{i}_c + \mathbf{j}_{Es} + \mathbf{j}_{El} + \mathbf{j}_{Eg}) = f^E \qquad (6.3)$$

The balance of energy has been expressed in terms of internal energy, where E_s is the solid specific internal energy, E_l and E_g are specific internal energies corresponding to the liquid and gas phases respectively. ρ_l and ρ_g are the liquid and gas phase densities of the medium. f^E is the energy supply per unit volume of medium. The most important processes for energy transfer in a porous medium have been considered in (6.3), which are: conduction, advection and phase change. $\mathbf{i}_c$ is the conductive heat flux. $\mathbf{j}_{Es}$, $\mathbf{j}_{El}$ and $\mathbf{j}_{Eg}$ are the energy fluxes due to the motion of phase. In this approach, thermal equilibrium between the three phases has been assumed, therefore the temperature is the same for the phases and only one equation of total energy is required. This assumption is generally valid in low permeability media.

Balance of mass of solid

$$\frac{\partial}{\partial t}\big(\rho_s(1-\phi)\big) + \nabla.\left(\rho_s(1-\phi)\dot{\mathbf{u}}\right) = 0 \qquad (6.4)$$

where $\dot{\mathbf{u}}$ is the solid velocity vector. The variation of porosities in terms of changes in solid density and volumetric deformation of the soil skeleton is obtained from (6.4).

Balance of momentum (equilibrium)

$$\nabla.\sigma_t + \mathbf{b} = 0 \qquad (6.5)$$

where σ_t is the total stress tensor and $\mathbf{b}$ the vector of body forces. In (6.5) inertial terms have been neglected. This assumption is usually accepted because both velocities and accelerations are small, yielding terms that are negligible in comparison with the stress terms. The assumption of small strain rate is also made. Through an adequate constitutive model, the equilibrium equation is transformed into a form expressed in terms of solid velocities, fluid pressures and temperatures.

6.2.2. Computer code

All the analyses have been carried out using the computer code CODE_BRIGHT [63, 166]. It is a finite element code designed to solve thermo-hydro-mechanical problems in geological media. One unknown (state variable) is associated with each of the balance equations presented. The unknowns are obtained by solving the system of PDE's (Partial Differential Equations) numerically in a coupled manner.

The state variables are: solid velocity, $\mathbf{u}$ (one, two or three spatial directions); liquid pressure, P_l ; gas pressure, P_g ; and temperature T. From state variables, dependent variables are calculated using the constitutive equations or the equilibrium restrictions. Strains are defined in terms of displacements. Small strains and small strain rates are assumed for solid deformation. Additionally, advective terms due to solid displacement are neglected after the formulation is transformed in terms of material derivatives (effectively, material derivatives are approximated as eulerian time derivatives).

The numerical approach may be viewed as being divided into two parts: spatial and temporal discretisation. The Galerkin finite element method is used for spatial discretisation while finite differences are used for time discretisation. The discretisation in time is linear and an implicit scheme is used. Finally, since the problem presented here is non-linear, the Newton-Raphson method was adopted as the iterative scheme.

A main feature of the numerical approach is that it can use a wide library of elements including segments, triangles, quadrilaterals, tetrahedrons, triangular prisms and quadrilateral prisms. Linear interpolation functions and, for some elements, quadratic interpolation functions are available. Analytical or numerical integration is used depending on element type. For the mechanical problem, selective integration is used for quadrilateral and quadrilateral prisms (this means that the volumetric part is integrated with a reduced integration of one point).

The program has a scheme for the automatic discretisation of time. A reduction of the time increment may be caused by excessive variation of unknowns per iteration or by an excessive number of iterations to reach convergence or if the correction is larger than in the previous iteration [166]. Convergence criteria are established in terms of forces or flows and of state variables.

Regarding the boundary conditions of the mechanical problem, forces and displacement rate may be prescribed in any spatial direction and at any node. In the hydraulic problem, mass flow rate of water and dry gas may be prescribed at any node, and liquid/gas pressure may be also prescribed at any node. Finally, regarding the thermal problem, heat flow and temperature may be prescribed at any node of the mesh [63, 166].

6.3. Constitutive laws and equilibrium restrictions

6.3.1. Constitutive laws

The constitutive equations establish the link between the unknowns and the dependent variables. There are several categories of dependent variables depending on the complexity with which they are related to the unknowns. The governing equations are finally written in terms of the unknowns when the constitutive equations are substituted in the balance equations. Here, some of the basic constitutive laws are presented, divided into thermal, hydraulic and mechanical. In spite of this distinction between the three basic components of the problem, the constitutive equation in fact provides the links that couple the various phenomena considered in the formulation. In this Section the general expressions of the main constitutive laws for the thermal, hydraulic and mechanical problems are presented. Some additional specific models are introduced when the analyses of the "mock-up" test and the "in situ" test are presented.

6.3.1.1. Thermal

Conductive heat flow is assumed to be governed by Fourier's law:

$$\mathbf{i}_c = -\lambda \nabla T \tag{6.6}$$

where λ is the global thermal conductivity of the porous medium, generally dependent on degree of saturation and porosity. A general expression, based on the geometric mean of the thermal conductivities of the three phases, has been used. The internal energy for the medium has been computed assuming that it is additive in relation to the phases [167].

6.3.1.2. Hydraulic

Advective fluxes are computed using generalized Darcy's law, expressed as:

$$\mathbf{q}_\alpha = -\mathbf{K}_\alpha(\nabla P_\alpha - \rho_\alpha \mathbf{g}); \quad \alpha = l, g \tag{6.7}$$

where P_α is the phase pressure, $\mathbf{K}_\alpha$ is the permeability tensor of α phase and $\mathbf{g}$ is the gravity vector. The permeability tensor is not constant but depends on other variables, according to:

$$\mathbf{K}_\alpha = \mathbf{k}\frac{k_{r\alpha}}{\mu_\alpha}; \quad \alpha = l, g \tag{6.8}$$

where $\mathbf{k}$ is the intrinsic permeability tensor, μ_α is the dynamic viscosity of the α phase and $k_{r\alpha}$ is the α phase relative permeability. Non-advective fluxes of species inside the fluid phases are computed through Fick's law, which expresses them in terms of gradients of mass fraction of species through a hydrodynamic dispersion tensor that includes both molecular diffusion and mechanical dispersion [167]. Finally, the retention curve relates the degree of saturation with suction.

6.3.1.3. Mechanical

A constitutive equation explicitly showing the contributions of strains, temperature and fluid pressures may be expressed generically as:

$$\dot{\sigma} = \mathbf{D}\dot{\varepsilon} + \mathbf{f}\dot{s} + \mathbf{t}\dot{T} \tag{6.9}$$

where σ is the constitutive stress (net or effective stress), ε is the strain vector, s is the matric suction computed as the difference between gas pressure and liquid pressure (p_g- p_l), **D** is the constitutive stiffness matrix, **f** is the generic constitutive vectors relating the changes in the fluid pressures and stresses and **t** is the constitutive vector relating stresses and temperature.

6.3.2. Equilibrium restrictions

It is assumed that phase changes are rapid in relation to the characteristic times typical of this problem. Therefore, they may be considered to be in local equilibrium, giving rise to a set of equilibrium restrictions that must be satisfied at all times. Equilibrium restrictions are given for the concentration of water vapour in the gas phase and for the concentration of dissolved air in the liquid phase.

The vapour concentration in the gaseous phase is governed by the psychometric law, which may be expressed as follows:

$$\theta_g^w = (\theta_g^w)^0 \exp\left(\frac{\psi M_w}{R(273.15+T)\rho_l}\right) \qquad (6.10)$$

where $\theta_g{}^w$ is the vapour concentration in the gas phase; $(\theta_g{}^w)^0$ is the vapour concentration in the gas phase in equilibrium with a liquid at a flat surface (at the sample temperature). ψ is the total water potential of the water (excluding gravity terms); M_w is the molecular mass of the water (0.018 kg/mol) and R the gas constant (8.314 J/mol/°K).

Henry's law is adopted to define the amount of air dissolved in water. This law expresses a linear relationship between the concentration of air in dissolution and the partial pressure of air in the gaseous phase [167].

6.4.Analysis of the "mock-up" test

6.4.1. Introduction

A complete description of the "mock-up" test may be found in Chapter 3. However, it seems convenient to comment here some characteristics that are very relevant to the numerical modelling of the test.

- The test avoids the heterogeneities of the natural system (granite formation).
- The test has a clay barrier with an unlimited availability of hydration water, supplied at constant and controlled pressure.
- The mass of water introduced into the system is continuously measured and recorded.
- The boundary conditions may be better defined than in the "in situ" test.
- The initial conditions are quite well known at the beginning of the heating phase.
- The test is well instrumented, with several sensors located along the barrier registering the evolution of the main THM variables.
- The test has two electrical heaters, symmetrically placed in relation to the central section of the test. This allows for checking of the reliability of measurements by comparing readings of symmetrical sections.

These facts allow for easier identification of the main processes and couplings that take place in a clay barrier submitted to heating and hydration.

One-dimensional axisymmetric and two-dimensional axisymmetric models have been used in the simulations of the "mock-up" test. The 1-D analyses have been helpful in the first stage of the analysis to examine the basic patterns of thermal, hydraulic and mechanical behaviour of the test. Some of these analyses are presented in this section. To obtain a better estimation of the effect of the real geometry of the "mock-up" test, THM analyses have been performed using 2-D axisymmetric longitudinal section. In these simulations only one half of the problem (one heater) is analysed because of symmetry (Figure 6.1).

The THM modelling presented herein refers mainly to the analysis of the behaviour of the "mock-up" test during the operational stage. The evolution of the test is critically examined by comparing the test data and the model results. An apparent decay in the rate of hydration, observed at advanced stages of the experiment, causes differences between model output and measurements. Subsequent studies have been directed towards the identification of other processes or phenomena that may clarify and explain, on a sound physical basis, the observed behaviour of the barrier.

Numerical models have also been used to analyse some particular aspects related to the operation and evolution of the "mock-up" test. For instance, analyses have been performed to study the effect of the loss of one heater over the evolution of the test. However, the most significant contribution in this respect has been the study of the accidental overheating that took place on 26 November 2000. The

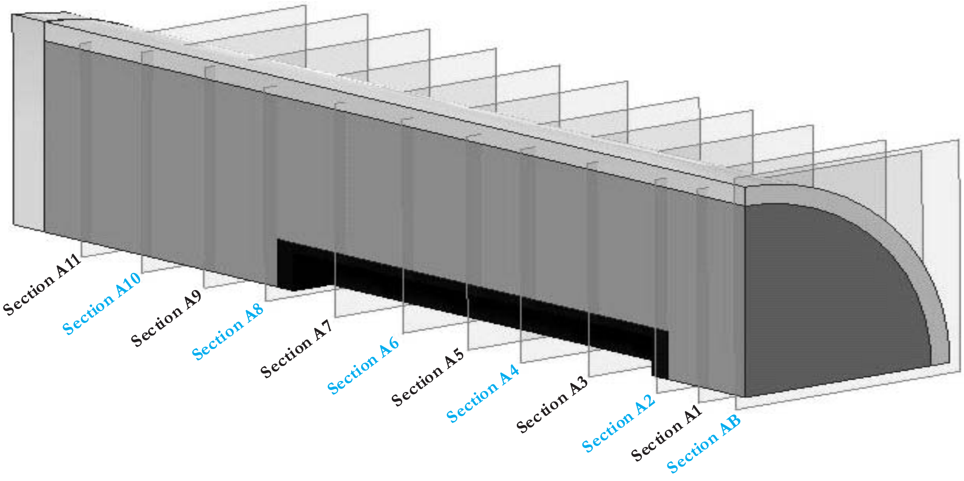

Figure 6.1: A 3-D schematic representation of the barrier.

analysis of this event is very interesting since there was a significant effect of this event on the subsequent evolution of the test. In the reference [167] this episode is analysed in more detail.

This section is organised as follows: first, some of the analyses carried out during the preoperational stage are presented. Afterwards, the initial analysis performed in the operational stage is presented, together with the identification of the apparent hydration deviation observed in the "mock-up" test. Then, the most significant results of the preliminary studies carried out in order to identify the sources of this hydration behaviour are presented. Finally, the double structure framework proposed for a more advanced modelling of the test is presented and the main model results obtained are discussed.

6.4.2. Pre-operational modelling

In the section, a summary of the analysis performed and results obtained in the preoperational modelling of the "mock-up" test is presented. They may be considered as being the best estimate of test performance with the information available before the start of the test. A full description of the analyses is presented in [168]. The preoperational analyses were subject to number of limitations, i.e.:

- ❑ The laboratory test data was still limited. For instance, the number of permeability tests was small and no retention curves had been determined under conditions of zero volume change.
- ❑ The main analyses did not take into account an initial flooding stage, decided after the performance of the computations.
- ❑ The procedure for reaching the prescribed temperature was not fixed at the time of the analysis.

6.4.2.1. Features of the analysis

The 1-D discretisation includes heater, buffer and confining structure [169]. The initial conditions indicated here refer to the state of the "mock-up" test without the initial hydration phase. Therefore, the initial water content is 14.0%. This corresponds to a degree of saturation of 58.6% and, from the retention curve adopted, an initial value of suction of 107.15 MPa [168, 169]. An initially uniform temperature of 21° C is assumed throughout the modelling domain. Finally, for initial stresses, a hydrostatic value of 0.11 MPa has been adopted, approximately equal to the weight of the bentonite at the mid-diameter of the buffer. A value of dry density of ρ_d = 1.7 g/cm^3, equal to the value originally planned, has been adopted as an initial value.

In relation to the boundary conditions, a constant water pressure equal to 0.55 MPa was prescribed at the interface between steel and bentonite (at radius, r = 0.808m). The thermal boundary conditions at: *r* = 0.15 m, radial coordinate of the heater elements are:

- 0 - 6 days constant power 250 W/heater
- 6 days - t_{100} constant power 500 W/heater
- $> t_{100}$ $T = 100$ °C

t_{100} is the time at which the temperature reaches 100 °C at some point in the bentonite. In the analysis presented it is 15.6 days. Depending on the analytical assumptions it ranges between 7.7 and 11.1 days. On the external boundary, a radiation/convection condition proposed by CIEMAT was used. Finally, a stress free boundary was prescribed on the outer surface of the confining structure of the test.

6.4.2.2. Results and comparisons with observations

Perhaps the most relevant study in the pre-operational stage was the parametric analysis performed to verify the effect of a series of parameters. Table 6.1 lists the sensitivity analysis performed and the parameters varied in each case and Figure 6.2 presents a typical example of the results obtained [168, 169]. The following conclusions were reached:

- Heat is mainly transported by conduction. Thermal conductivity is the basic parameter controlling heat transfer.
- Apart from the expected effect of permeability, hydration is extremely sensitive to the shape of the retention curve (Figure 6.2).
- Drying of the bentonite close to the heater requires vapour diffusion.
- Mechanical variables (and especially stress development) depend strongly on the initial dry density of the bentonite.

6.4.3. Operational modeling: the base case

The phase of heating and hydration of the test, known as the ‘operational stage’, started in February 1997 and is on-going at present (almost seven years after switching on the heaters). The numerical analysis presented in this section corresponds to the model coded as the ‘OBC’ model (Operational Base Case). The OBC model attempts to incorporate all available information obtained from laboratory testing of the FEBEX bentonite and available at the beginning of the operational stage. No more adjustments have been made, and the overheating episode has not been considered. This is because the main aim of these analyses is to compare directly the model results with the experimental data. In that context the numerical results shown are real predictions of the OBC model that include a more refined representation of the problem. For instance, the geotextile present between the confining structure and the buffer (installed to ensure a uniform distribution

Table 6.1
Parametric study. “Mock-up” test

Analysis code	Variables modified
BC	Base Case
CT	Thermal conductivity
K	Bentonite permeability
T	Vapour diffusion tortuosity
PR15	Relative permeability of the bentonite
SH	Retention curve of the bentonite
KSH	Permeability and retention curve of the bentonite
M	Dry density of the bentonite

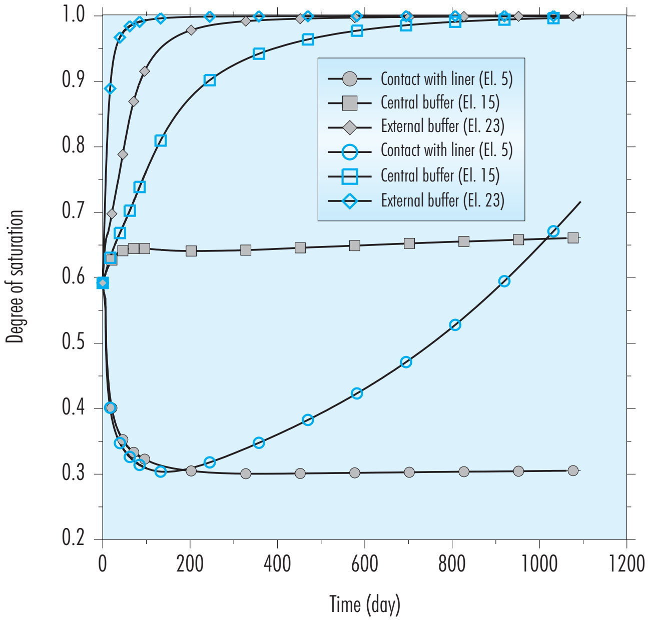

Figure 6.2: Variation of degree of saturation with time, "mock-up" test. SH analysis using an alternative retention curve. The results of the 1-D preoperational Base Case analysis (grey symbols) are provided for comparison [168, 169].

of the hydraulic conditions on the external boundary), has been included in the mesh. The properties of this material have been reported in [170]. Additionally, a series of sensitivity analyses were carried out in order to ensure the independence of the results of the analyses from the mesh used.

The main sections selected for comparison with experimental data are shown in Figure 6.1. The experimental values shown in the comparisons between model results and experimental data have been supplied by CIEMAT. The last records considered in this Chapter were obtained on 18th September 2003, corresponding to day 2417 from the switching on of the heaters (i.e. about 6.62 years).

6.4.3.1.Features of the analysis

Initial conditions

An initially uniform temperature of 20 °C is assumed for the entire domain. This is consistent with CIEMAT data [171].

In relation to the hydraulic problem, the initial water content of the bentonite is 14 %. Before the start of the heating, the barrier was flooded in an attempt to achieve closure of the gaps and joints prior to the performance of the main test [172]. Therefore, the global degree of saturation of the barrier at the beginning of the heating was close to 0.715. An initial suction of 105 MPa has been adopted for the whole barrier, this suction is close to that measured (on average) in the central and internal zones of the barrier before the heater was switched on. According to the retention curve adopted, this implies an initial degree of saturation close to 0.652. In order to ensure that the test and the model have the same initial amount of water at the beginning of the heating, an initial (isothermal) hydration has been simulated until the global degree of saturation of the "mock-up" model reaches the same value of the test (i.e. 0.715).

Finally, for the mechanical problem a hydrostatic value of 0.11 MPa has been adopted, approximately equal to the weight of the bentonite at the mid diameter of the buffer.

Boundary conditions

The thermal boundary conditions at: $r = 0.15$ m (radial coordinate of the heater elements) are the same as indicated in Section 6.4.2.1. On the external boundary a radiation-type boundary condition has been applied [177].

A water pressure of 0.55 MPa is applied in the geotextile (*i.e.* at the interface between steel and bentonite) in accordance with CIEMAT data [171]. The analysis presented herein assumes that the test is airtight. Finally, a stress-free outer boundary has been prescribed on the outside of the steel container.

Constitutive laws adopted in the OBC analysis

The general constitutive laws adopted in the OBC analysis of the "mock-up" test for the thermal, hydraulic and mechanical problems have been presented above. Here some more specific details are given.

The following law has been adopted for the thermal conductivity of FEBEX bentonite:

$$\lambda = \lambda_{sat}^{S_l} \lambda_{dry}^{(1-S_l)} \qquad (6.11)$$

where the values of $\lambda_{sat} = 1.15$ and $\lambda_{dry} = 0.47$ W/m°C have been obtained from the experimental measurements presented in Figure 6.3 [169].

The intrinsic permeability depends on porosity through:

$$\mathbf{k} = k_0 \frac{\phi^3}{(1-\phi)^2} \frac{(1-\phi_0)^2}{\phi_0^3} \mathbf{I} \qquad (6.12)$$

where k_0 is the reference permeability at the reference porosity ϕ_0. Figure 6.4 shows experimental measurements of saturated permeability at different densities and the model results [167].

Figure 6.5 presents the retention curve adopted (based on the expression proposed by van Genuchten, 1978) [173] in the OBC analysis, together with the experimental results obtained for FEBEX bentonite under conditions of constant volume.

Finally, the Barcelona Basic Model, BBM [174] has been selected as the basis for the thermoplastic constitutive model. It is an elasto-plastic law that relates changes in stresses with changes in strains, history variables, matric suction and temperature. The mathematical formulation and model parameters used in the analysis are presented in [167].

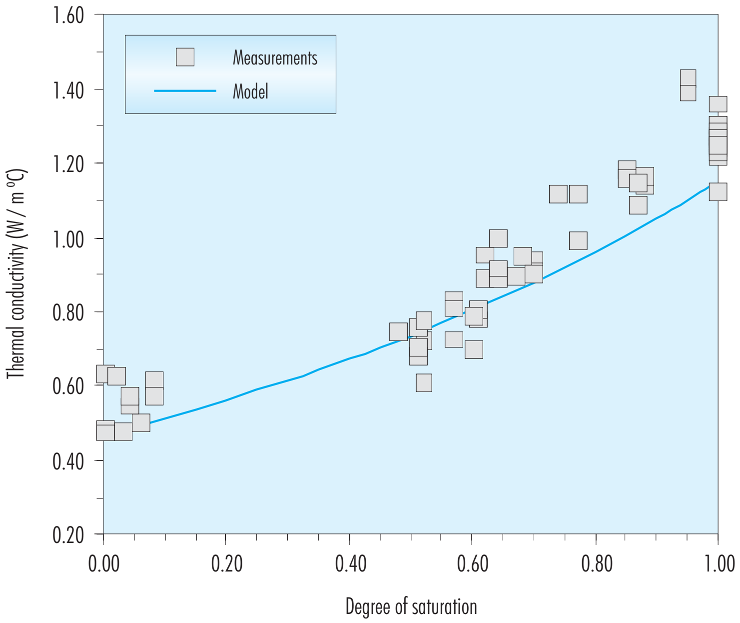

Figure 6.3: Experimental results and adopted thermal conductivity law for the FEBEX bentonite.

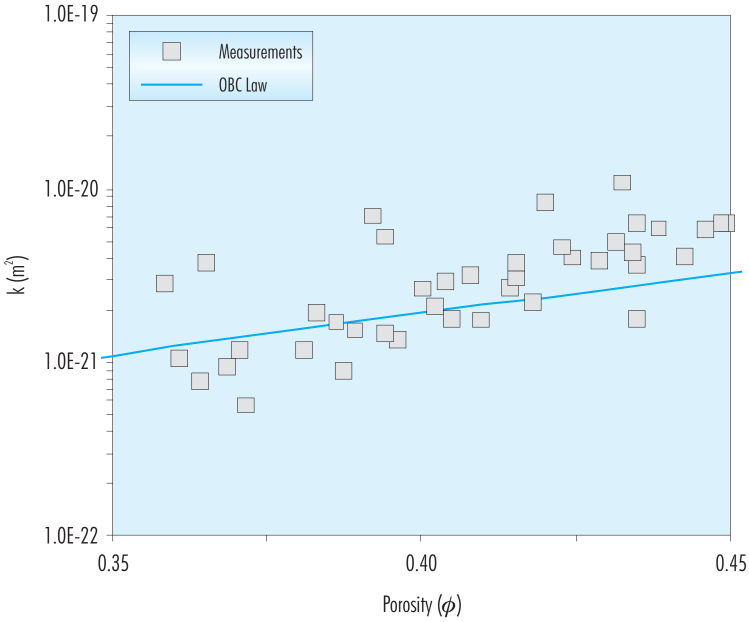

Figure 6.4: Variation of saturated permeability with porosity. Experimental data and adopted model for the intrinsic permeability law of "mock-up" and "in situ" OBC models.

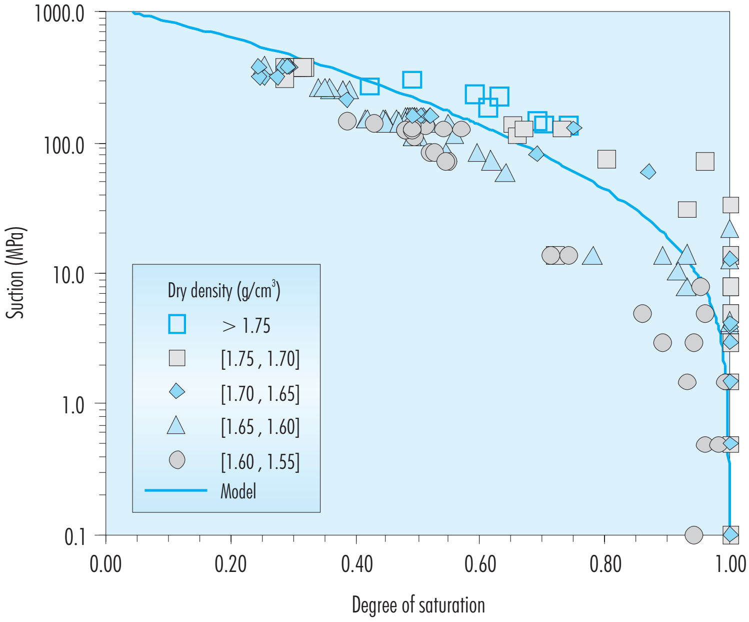

Figure 6.5: Retention curve adopted in the "mock-up" OBC analysis, together with the experimental data of FEBEX bentonite (symbols).

6.4.3.2. Results and comparisons with observations

In this section, both point variables and global test parameters are examined. The evolution of the "mock-up" test is examined considering the thermal, hydraulic and mechanical problem separately, although, of course, the analysis is fully coupled and all three aspects are considered simultaneously. Comparison sections mentioned hereafter are shown in Figure 6.1.

It may be stated that the model yields good results regarding the thermal problem. This is reflected in the evolutions of the power emitted by the heaters, a global variable of the test Figure 6.6. The long-term prediction (20 years) indicates a slow increment of heater power as the barrier is hydrated (Figure 6.7); this is due to the increase of thermal conductivity as saturation increases (Figure 6.3). Good results are also obtained in terms of local variables, such as the evolution of temperatures at different points of the barrier (Figure 6.8). Similar behaviour is observed in other sections [167]. The variation of temperatures along longitudinal and transversal sections is shown in Figure 6.9. It may be noted that the distribution in front of the heaters is reasonably uniform but temperature drops quickly outside this area.

Observing both water entry and the rate of water entry (hydraulic global variables), it may be stated that the OBC model predictions may be considered excellent up to day 900 (approximately), with differences between the model results and test data being less than 10% (Figure 6.10 and Figure 6.11). Regarding the local variables, a similar comment may be made, that is, up to day 900 the model offers a good reproduction of the evolution of relative humidity (Figure 6.12). Up to that time, the overall behaviour of the test is as expected, i.e. an increasing saturation in the zones close to the hydration boundary and an intense drying in the regions close to the heaters followed by slow hydration. The behaviour of zones close to a radius of 0.37 m shows an initial wetting, due to the condensation of the water vapour coming form the inner region, and then a subsequent drying. From about day 900, some differences are observed between the hydraulic behaviour of the test and the model predictions. In terms of water entry, the model results move away progressively from the experimental data. This fact may be clearly detected in terms of the rate of water intake, in which the test data (from day 900 of

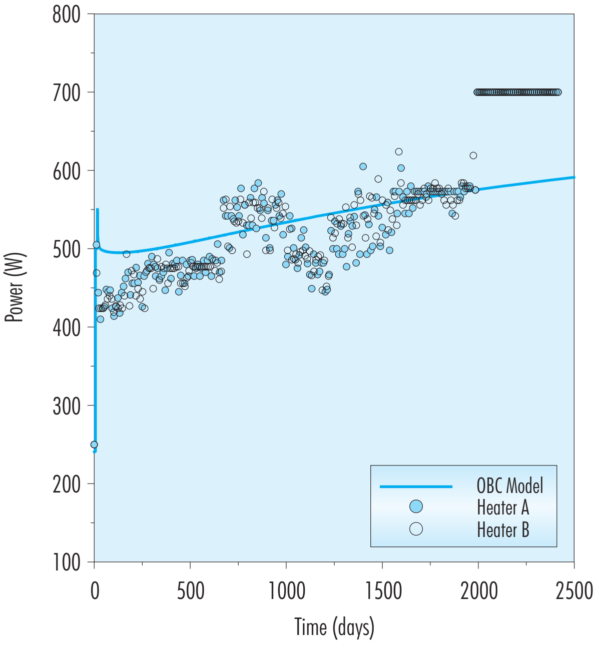

Figure 6.6: Evolution of heater power in the "mock-up" test. Observed and computed values. OBC model.

the test) undergo an important reduction in comparison with the values of the 'OBC' model. A recovery of the observed values of water intake rates may be seen when the overheating episode, on day 1381, took place. Finally the tendency observed before overheating was recovered, i.e. a marked slowing down of the rate of water intake compared to model predictions.

In relation to the evolution of relative humidity in sections involving heaters (for instance, sections A4 and B4, in Figure 6.12) a significant reduction in the rate of relative humidity increase may be observed. The effects of the overheating may be clearly noted in these sections, especially just after this episode has occurred. It seems that the transient period induced by the overheating was practically finished by day 1700. The apparent hydration deviation from the predictions in this section is even more evident when the long-term predictions are observed; a clear tendency to a very slow hydration rate in all of the measured radii may be noted.

On the other hand, when sections away from the heaters are examined (for instance, sections A10 and B10, in Figure 6.12) the hydration deviations are less perceptible. Note that some minor differences between model and test results may also be observed in these sections after day 2000 (approximately). The apparent slow hydration observed in Sections A4 and B4 may be also noted in other sections involving heaters [167].

Figure 6.13 shows the time evolution of stresses in selected positions of the barrier, where: P_T identifies the tangential stress, P_Z the longitudinal stress and P_R the radial stress. Similar trends to those observed in the hydraulic problem appear in the mechanical problem. That is, up to day 900 approximately, there is good agreement between predictions and observations in sections involving the heaters. From that moment on, measured stresses respond to the modifications of the hydration pattern, and a tendency to maintain or reduce the stress values may be observed. This is attributed to the strong hydro-mechanical coupling of the problem. The overheating episode had different influences on mechanical behaviour depending on the sections considered. In sections far from the heaters, the values and tendency recorded before this event were recovered practically immediately (Section A10 and B10), whereas in sections involving heaters, a more permanent influence on the evolution of the stress

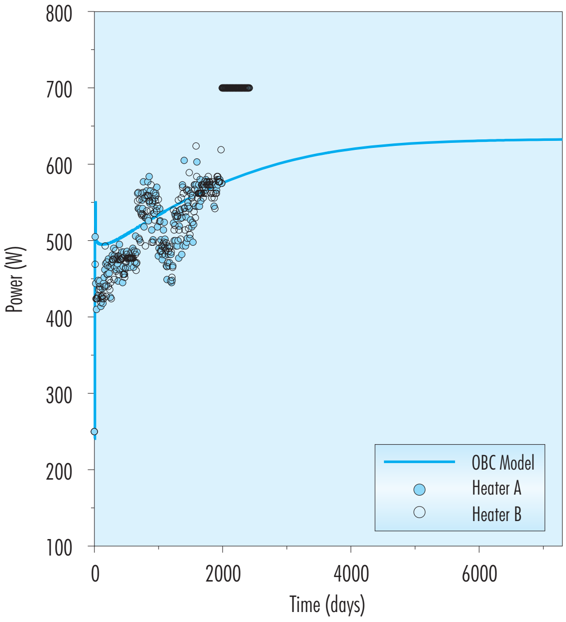

Figure 6.7. Evolution of heater power in the "mock-up" test. Long-term prediction OBC model.

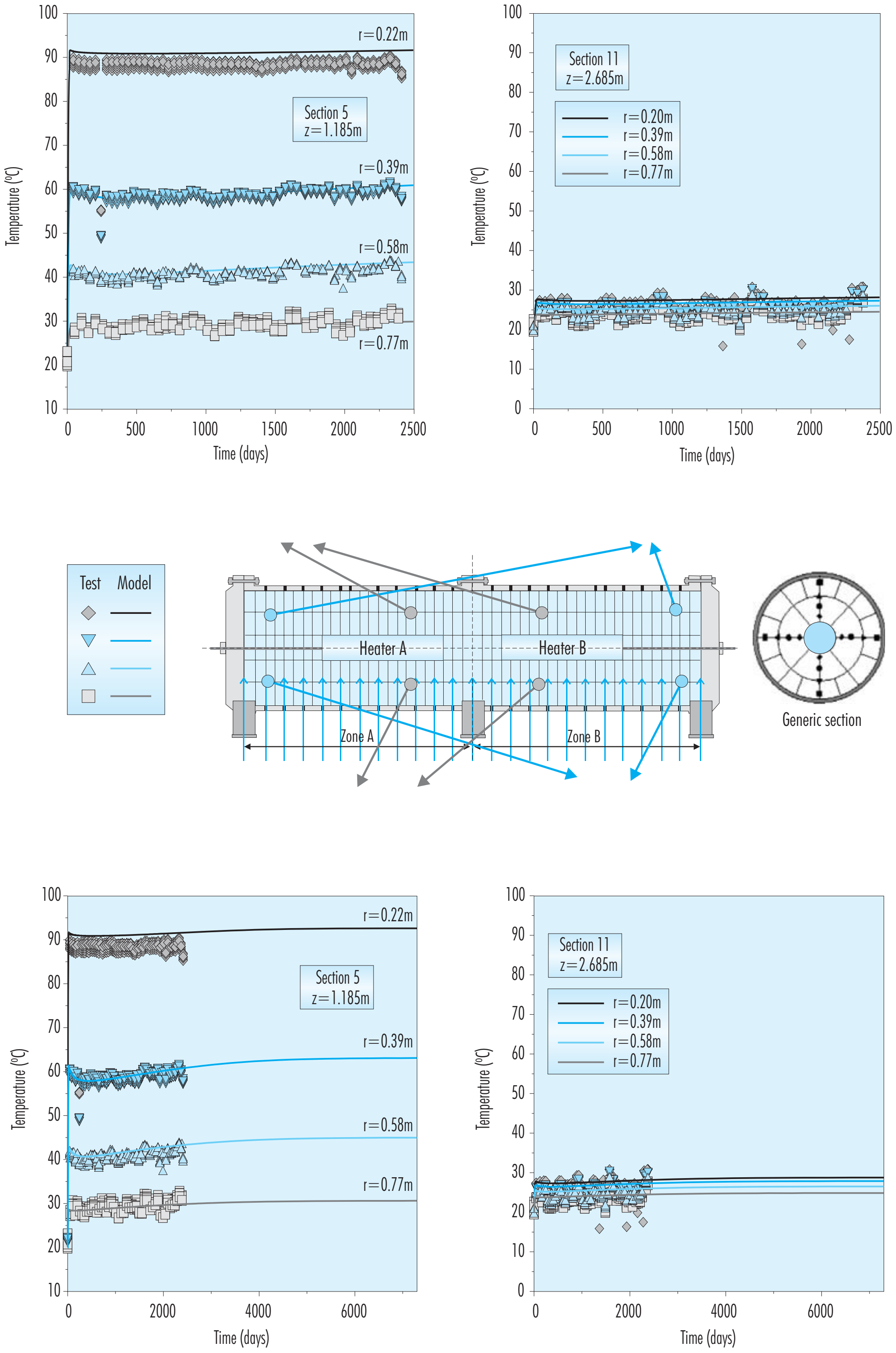

Figure 6.8: Evolution of temperature in the "mock-up" test. Sections A5-B5 ('hot cross-section') and A11-B11 ('cold cross-section'). Observed versus computed values and long-term predictions (OBC model).

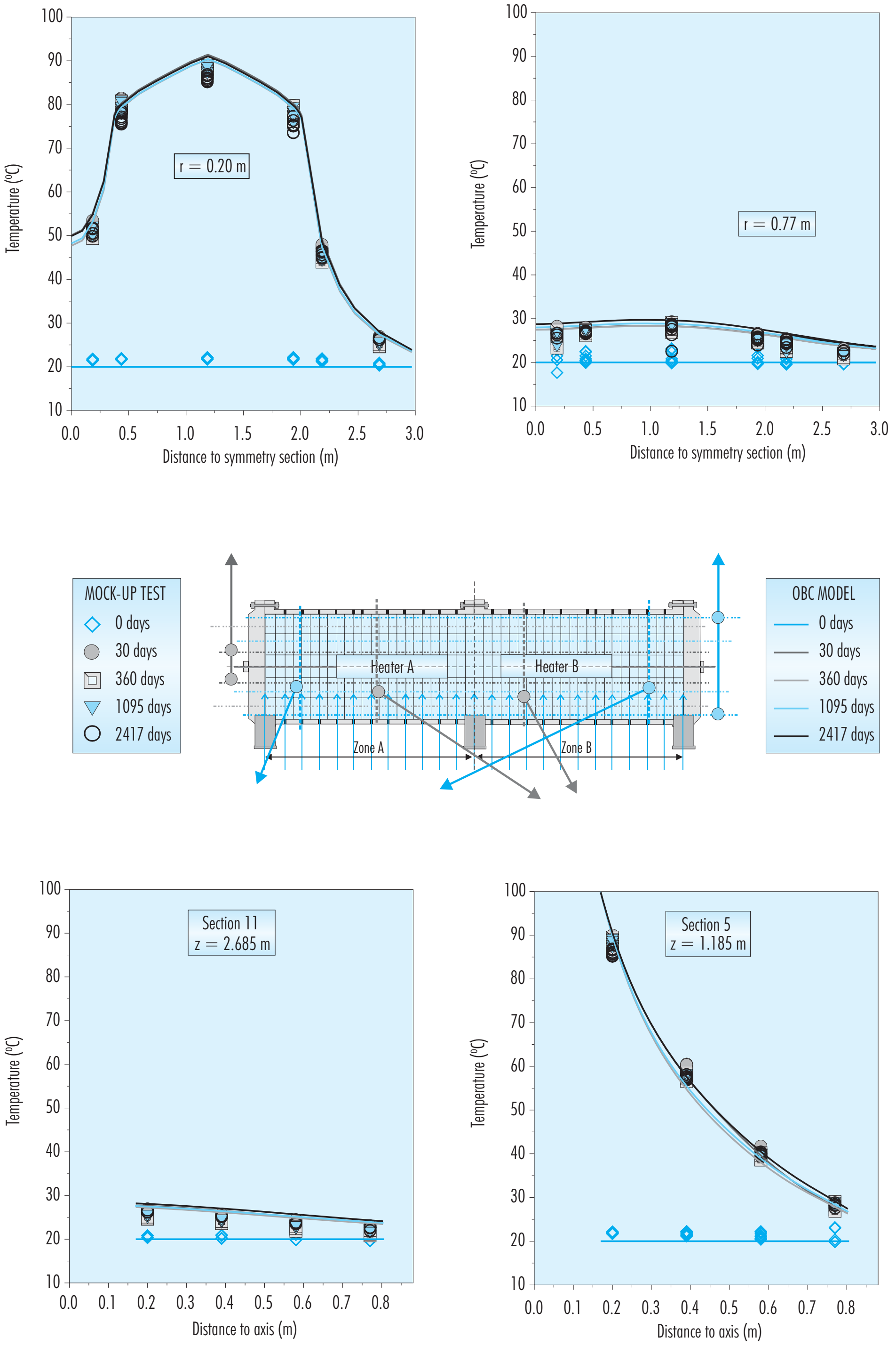

Figure 6.9: Distributions of temperatures in longitudinal and transversal sections of the "mock-up" test. Observed versus computed values (OBC model).

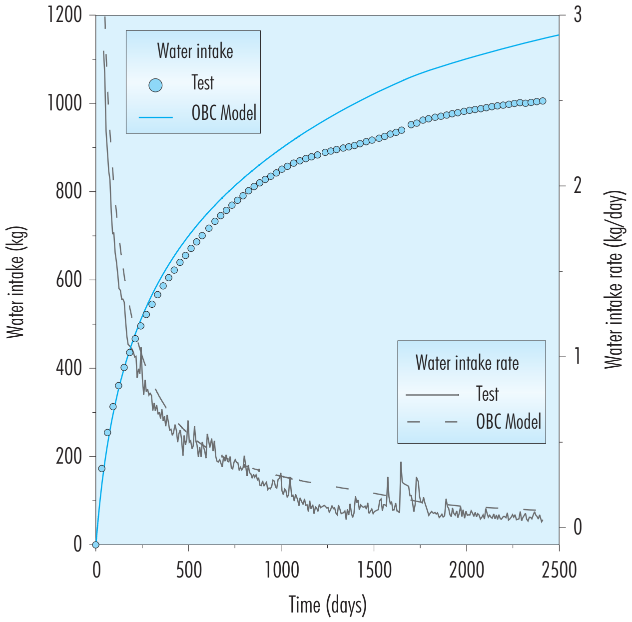

Figure 6.10: Evolution of water entry in the "mock-up" test. Observed and computed values (OBC model).

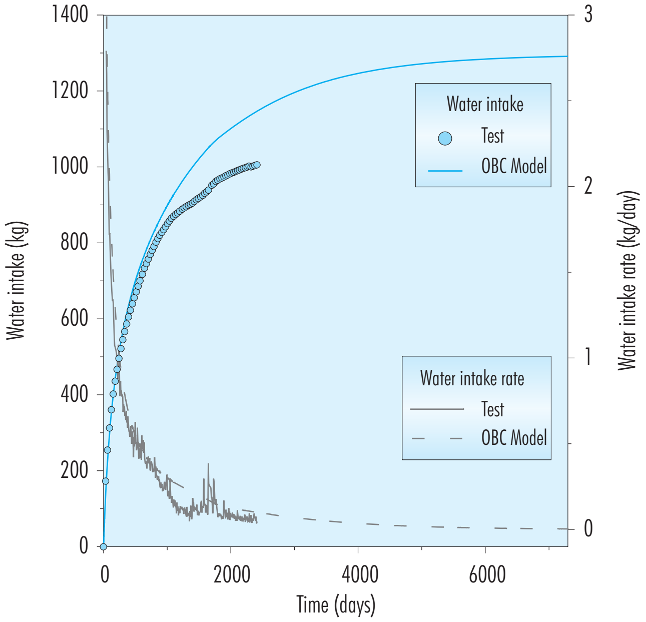

Figure 6.11: Evolution of water entry in the "mock-up" test. Long-term prediction (OBC model).

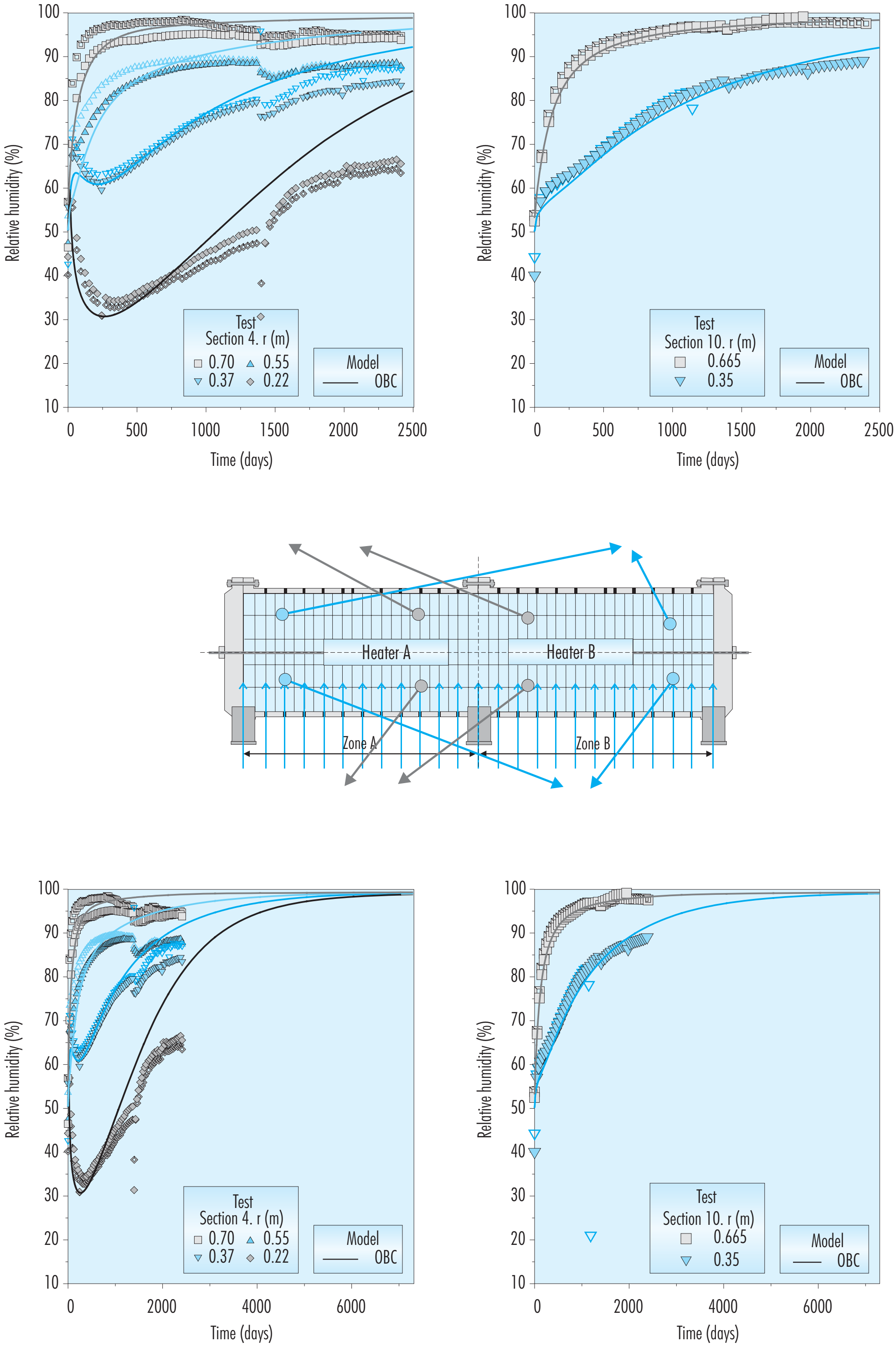

Figure 6.12: Evolution of relative humidity in the "mock-up" test. Sections A4-B4 ('hot cross-section') and A10-B10 ('cold cross-section'). Observed versus computed values and long-term predictions (OBC model).

field may be observed. Stresses are lower compared to those measured before this event (Sections A6 and B6). Arguments based on double structure concepts are presented in [167] to explain this behaviour. Finally, in zones near the ends, the overheating event has no perceptible effects and the model captures very well the measured values of stresses (Section A12 and B12). The long-term analysis predicts a maximum stress of the order of 10 MPa. Similar trends are observed in other sections [167].

6.4.4. Incorporation of new phenomena_

Understanding the apparent decay in the rate of barrier hydration is considered to be an important aspect as regards the performance of reliable long-term predictions. Firstly, attempts were made to determine whether it was possible to explain and reproduce more closely the global evolution of the test with minor modifications of the constitutive laws or their parameters. A far-reaching sensitivity study was carried out to that end, but it proved to be impossible to obtain a set of constitutive laws and materials parameters (with physical meaning) consistent with the observations. An important conclusion of this exercise is that, although changes in some parameters can lead to better agreements locally for some variables, it does not appear that such strategy can lead to a global explanation of the behaviour that includes all the observations made. Some of the analyses performed in this context are described in [175, 167]. Simulations of the "mock-up" test performed by ULC (University of La Coruña) group exhibited difficulties similar to those mentioned in the sections above. Even though the numerical codes are different and the determination of the model parameters was carried out independently, the same tendency is observed, *i.e.*, a growing departure between model predictions and measurements, from 900 days onwards [176].

The hypothesis that problems in the hydration system might affect the normal water supply to the barrier has also been considered. The possibility of either malfunctioning in the hydration system or a geotextile blockage, that might affect the normal hydration of the barrier, was examined. It was confirmed experimentally that there was no obstruction in the hydration system or geotextile, and that the water intake was apparently nearly uniform over the entire hydration front.

As described in Section 6.4.3.2, sections involving heaters (identified hereafter as 'hot-cross section') exhibit behaviour quite different from that observed in sections away from the heater (identified as 'cold-cross section'). The hot-cross sections are characterized by a tendency to very slow hydration, with significant differences between predicted and measured values; whereas in the cold-cross sections, the evolution is quite similar to that predicted. It might be thought that the temperature has an effect on clay properties, affecting the normal hydration of the barrier. But there are some aspects that lessen the possible direct role played by temperature in the unexpected barrier trends. For instance, the departure between the test and model results is detected when the temperature field is well established. There are no important changes in temperature evolution since very shortly after the start of the test (Figure 6.8).

Discarding problems in the water supply and considering that changes in the materials parameters might not explain the unexpected behaviour of the barrier, research was focused on the identification of possible physical processes that might be responsible for the slowing down of barrier hydration. This section presents the extension of the *THM* formulation, and the associated numerical code, to include other phenomena not considered in the original framework. The purpose is to use the code as a tool to investigate the behaviour of the barrier when these phenomena are considered, especially over the long term. Three phenomena have been studied:

- ❑ Existence of an hydraulic threshold gradient
- ❑ Thermo-hydraulic coupled processes
- ❑ Evolution of micro-fabric

The models used in this stage of the analysis are in fact very simplified and each of the possible causes has been considered separately. The three models have been calibrated with the data available on 30th March 2002, (day 1880 of the test, indicated by a vertical dashed line in the following Figures), and the final results of the simulations correspond to 18th September 2003 (day 2417). This implies that the results obtained between those dates are model predictions. It should be noted that all the parameters of the OBC model are maintained in these simulations, only those affected by the 'new phenomena' have been modified (if any). 1-D axisymmetric models have been used in the analyses. The two characteristic sections mentioned above have been considered in the analyses. The results of 1-D 'OBC' model are also included in the Figures to allow for

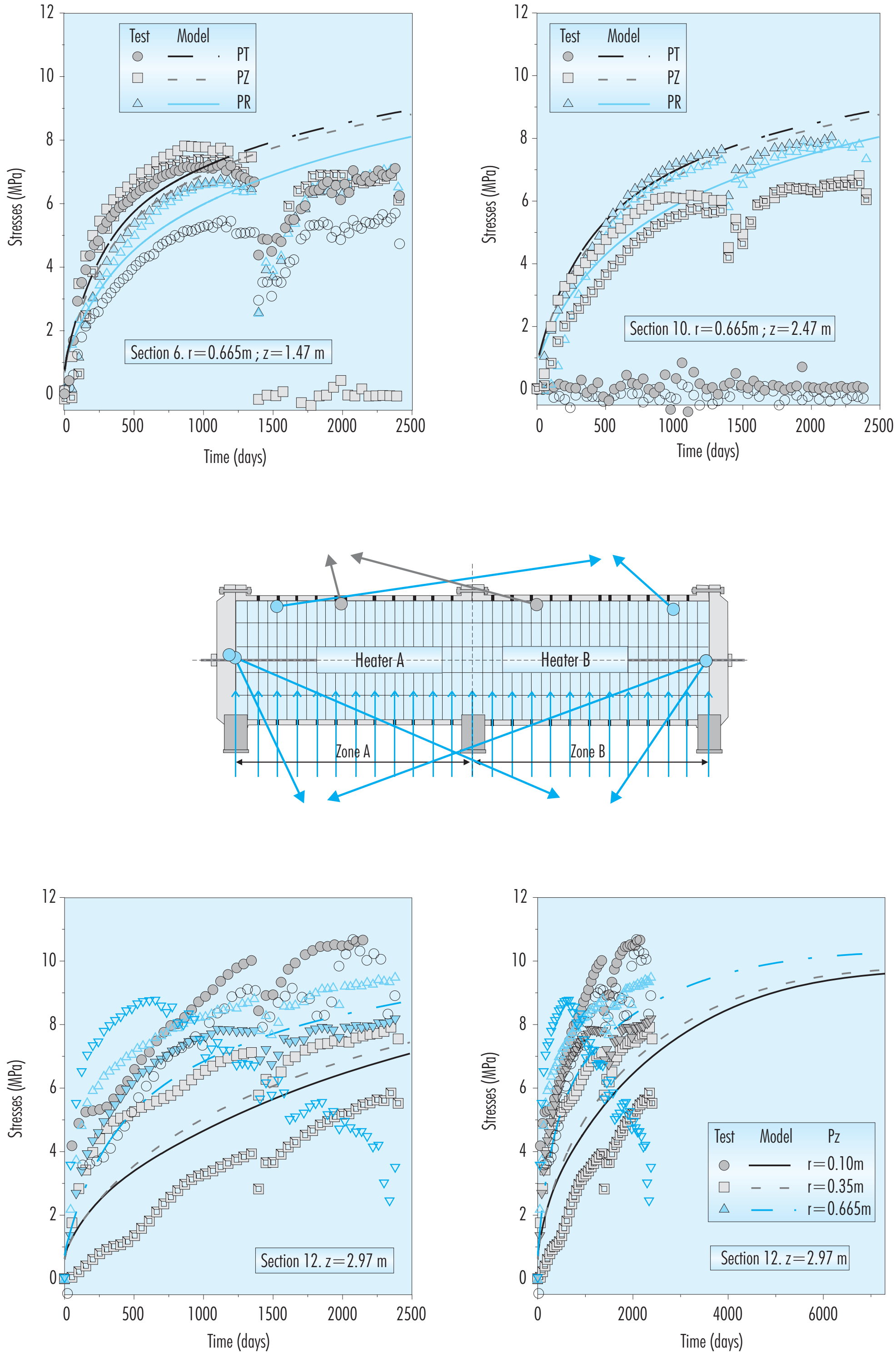

Figure 6.13: Evolution of stresses in the "mock-up" test. Sections A6-B6, and A10-B10 and A12-B12. Observed versus computed values and long-term predictions (OBC model).

comparisons between models. In order to be closer to the actual conditions of the barrier, the analyses with non-standard flow models incorporate the overheating episode.

6.4.4.1. Hydraulic threshold gradient

This section considers the possible effect of a limited applicability of Darcy's law at low hydraulic gradients. Some experimental evidence shows that under low hydraulic gradients (J), Darcy's simple relationship does not govern the liquid flow in some porous media, especially in soils containing active clay minerals. Arguments based on the strong clay-water interactions have been suggested to explain this non-Darcian flow behaviour (*i.e.* Bear, 1972 [177]). There are many models that may be used to describe this phenomenon. A well-known law considers two characteristic gradients (Figure 6.14): the threshold hydraulic gradient (J_o) and the critical hydraulic gradient (J_c). J_o is the hydraulic gradient below which no flow occurs. J_c is the hydraulic gradient below which flow occurs but in a non-Darcian way. If the hydraulic gradient is higher than J_c Darcy's law applies.

When low permeability clays are tested, the main problem is the long time required by the experiments. An established experimental technique to overcome these problems is the application of large hydraulic gradients. A drawback of this practice is that the applied hydraulic gradients are very far from the one measured (or expected) under actual conditions. Consequently, the experimental results obtained may not be realistic in some cases. Dixon et al. (1999) [179] presents a summary of reported hydraulic gradients used in the testing of low permeability soils. Figure 6.15 shows the hydraulic gradient applied and the measured hydraulic permeability for the FEBEX bentonite. The figure presents the results obtained for values of bentonite dry density of between 1.74 and 1.55 g/cm^3 [165].

In the "mock-up" test there is a strong contrast between the predominant hydraulic gradients in the two sections analysed. The section involving the heater presents high hydraulic gradients in zones close to the heater, compared with those prevailing close to the hydration front, while the hydraulic gradient is more uniform in sections away from the heater. The lowest hydraulic gradients are in zones

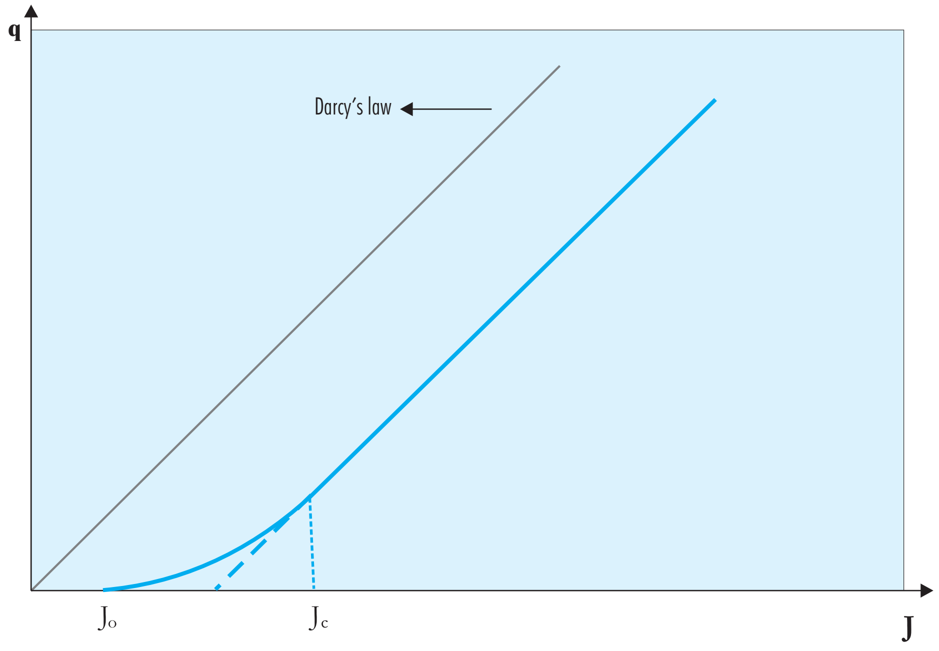

Figure 6.14: Schematic representation of the hydraulic threshold gradient [178].

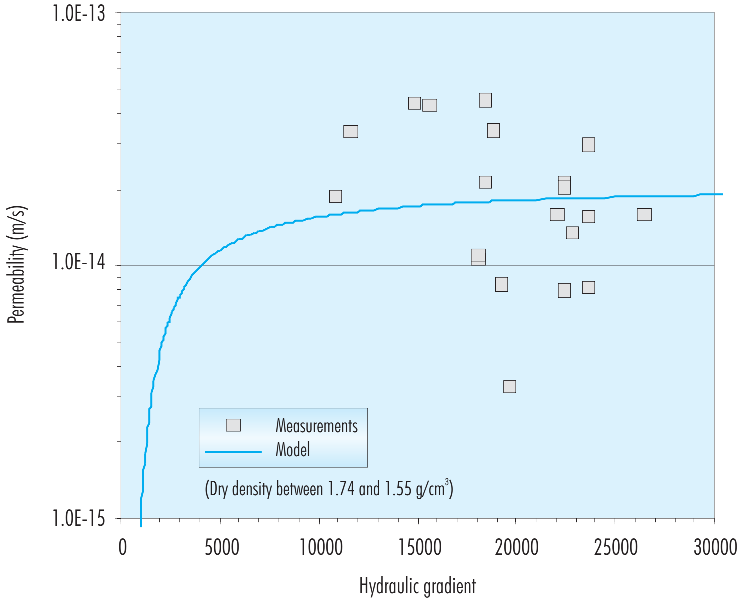

Figure 6.15: Experimental hydraulic gradient vs. saturated permeability [165] and adopted flow model.

near the hydration front. Near to day 900 (when the discrepancies between the model and the test start to appear) the value of the hydraulic gradient is about 2000 [51]. Note that the ranges of the hydraulic gradients applied experimentally are higher than the hydraulic gradients computed in zones close to the hydration boundary. For this reason it is difficult to state whether the apparent decay in the kinetics of hydration of the barrier is due to the existence of a threshold gradient. Moreover, the lack of experimental data at low hydraulic gradient complicates the development of an improved flow model incorporating this phenomenon. Therefore, with the sole aim of exploring the hypothetical influence of this phenomenon on the behaviour of the barrier, a very simple model has been proposed, until such time as more experimental data in this respect become available. The model corresponds to that presented in Figure 6.14. The following considerations have been taken into account:

- A threshold gradient (J_o) equal to 50 (this is a common value found in the literature).
- A critical gradient (J_c) close to 2000. This corresponds to the hydraulic gradient computed at the onset of the discrepancies (at the hydration boundary).
- A power law for the range of hydraulic gradients with non-Darcian flow

In Figure 6.15 it may be observed that the model is consistent with the experimental data available for the FEBEX bentonite (i.e. for high hydraulic gradient).

Figure 6.16 and Figure 6.17 show (with solid lines) the results obtained considering the Threshold Gradient (ThG) model in both reference sections. A good agreement between model and test data may be seen in the hot section, in zones close to the heater. The tendency to a reduction in hydration rate is well captured by the model. The model predictions are also good for the results from day 1880 onwards. In zones near the hydration front the tendency is not so well captured. Regarding the response of the model in the cool sections A10 and B10, the results are also good. It may be seen that the model predicts (after the dashed vertical line) the incipient decay at the inner radii of these sections. Figure 6.18 presents the evolution of water intake for the two models analysed. The presence of a threshold gradient implies a lower rate of water intake, compared with the OBC model. This affects the distribution of water in the barrier and, due to the strong HM coupling, the stress field is also influenced [167]. Figure 6.19 to Figure 6.21 present

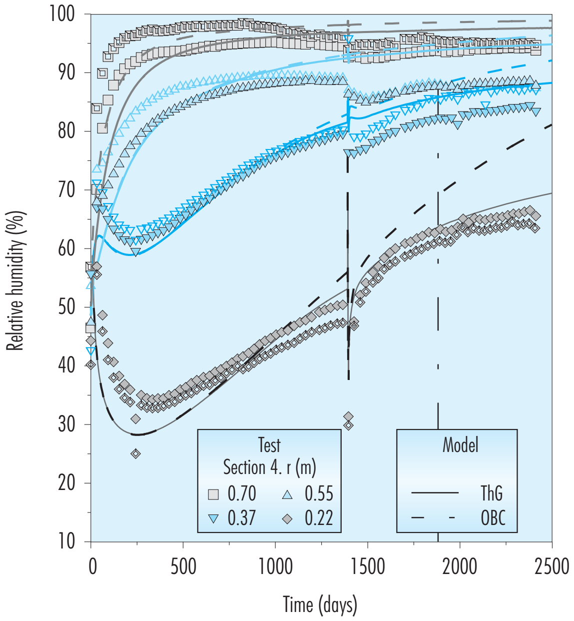

Figure 6.16: Relative humidity. Sections A4-B4. Observed versus computed values of 'ThG' (Threshold Gradient) and 'OBC' models.

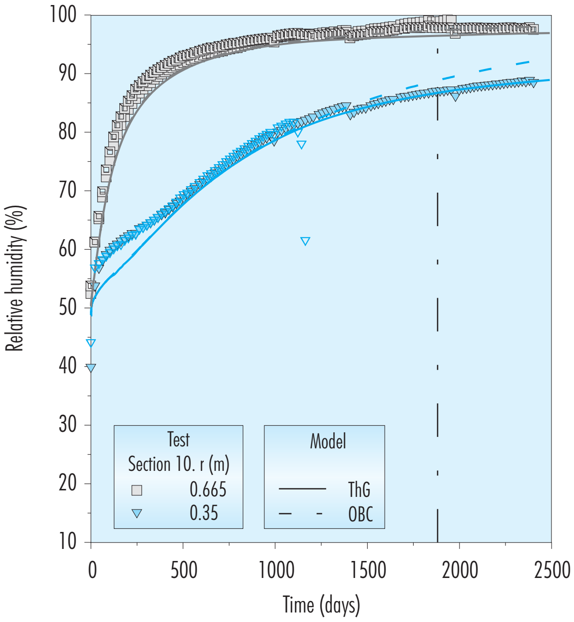

Figure 6.17: Relative humidity. Sections A10-B10. Observed versus computed values of 'ThG' and 'OBC' models.

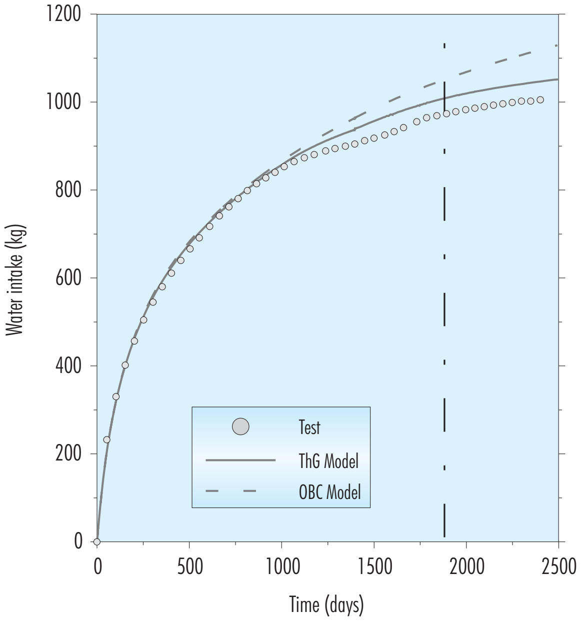

Figure 6.18: Water intake. Observed versus computed values of 'ThG' and 'OBC' models.

long-term predictions. It may be observed that under this hypothesis the barrier does not reach full saturation. Naturally, the relevance of this prediction depends on the existence of a threshold gradient in the FEBEX bentonite and, if this is this case, on the adequacy of the model and parameters adopted here. Therefore, the result obtained should be considered only as an exercise with the object of exploring the hypothetical response of the barrier under these assumptions, until the hypotheses regarding the existence and magnitude of a threshold gradient are independently confirmed experimentally.

6.4.4.2. Thermo-hydraulic coupled processes

The hydraulic gradient is the main thermodynamic force controlling the movement of water in the soils. It is, however, not the only one. Figure 6.22 presents the different kinds of flow that may occur in the porous media and the corresponding gradient responsible for the movements (ignoring the electrical potential). The word 'phenomenon' is used for the diagonal terms associated with the direct flow phenomena, and the name 'coupled process' is reserved for the non-diagonal ones [177, 180]. The Figure also includes the names given to some of these flows. The 'phenomenological coefficient' that links each flow with the corresponding driving force must be measured experimentally [180]. Generally, the non-diagonal coefficients are relatively small and negligible compared to the diagonal terms, and the coupled process may be safely ignored. However there are certain problems in which, due to their particular conditions, the coupled processes may play a more influential role. For example, the thermal conditions imposed on the "mock-up" test correspond to a practically constant thermal gradient during the test and, consequently, a constant thermo-osmotic liquid flow associated with it may exist. In contrast, the hydraulic gradient is very high at the beginning of the test, but diminishes with the hydration of the barrier. The liquid flows associated with these two gradients have opposite directions. Generally, the advective flow due to the pressure gradients (Darcy's law) is the dominant flow. However, at advanced stages of the test (when the hydraulic gradient becomes smaller), it is possible that the flow of liquid due to the coupled

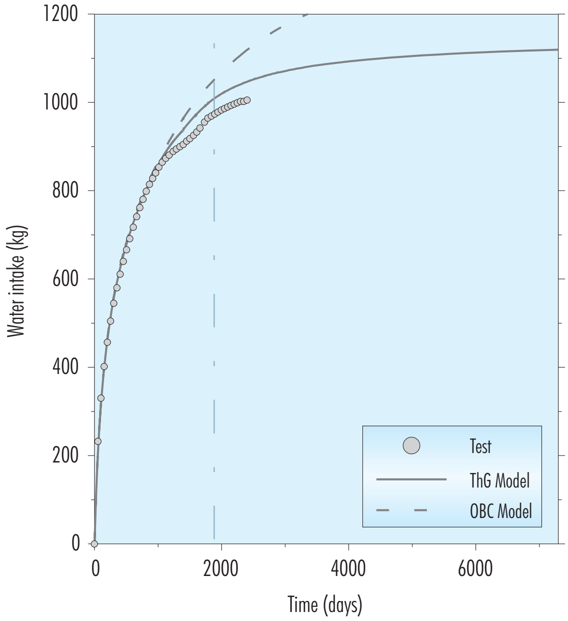

Figure 6.19: Water intake. Long-term predictions 'ThG' and 'OBC' models.

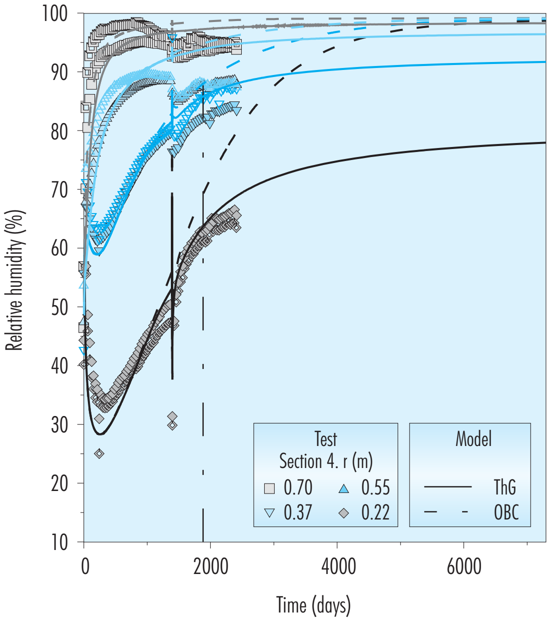

Figure 6.20: Relative humidity. Sections A4-B4. Long-term predictions 'ThG' and 'OBC' models

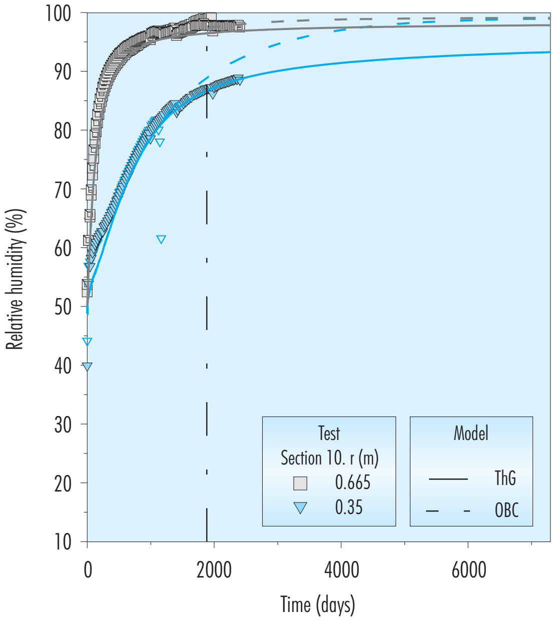

Figure 6.21: Relative humidity. Sections A10-B10. Long-term predictions 'ThG' and 'OBC' models

Flow	Gradients		
	Hydraulic Head	Chemical Concentration	Temperature
Fluid	Darcy's Law (Hydraulic Conduction)	Chemical Osmosis	Thermo Osmosis
Solutes	Ultra Filtration	Fick's Law (Diffusion)	Soret Effect (Thermal Diffusion)
Heat	Thermo Filtration (Isothermal Heat Transfer)	Dufour Effect	Fourier's Law (Thermal Conduction)

Figure 6.22: Direct and coupled flow processes.

process (thermo-osmotic flow) might have a noticeable effect on the behaviour of the test in the hot sections, causing a tendency for hydration to be slowed down in the hot zones close to the heaters.

The magnitude of this effect will depend on the ratio between the gradients of the two mechanisms and on the relationship between the phenomenological coefficients associated with either flow. To check whether this coupled process may help to explain the "mock-up" test observations, a series of analyses including the thermo-osmosis effect were carried out. Mention should be made of the lack of experimental data for the FEBEX bentonite concerning the phenomenological coefficient associated with the thermo-osmotic flow. A thermo-osmotic constant equal to 2.73 $\cdot 10^{-13}$ $m^2/K/s$ has been adopted. This falls within the range of possible values found in the literature [181, 182].

Figure 6.23 and Figure 6.24 show, with solid lines, the results obtained considering the Thermo-osmotic Effects (ToE) for the two reference sections; the dashed lines correspond to the 'OBC' case. In the hot section a somewhat better agreement with the observations may be noted in zones close to the heater, but the behaviour in zones near the hydration front is not so well captured. The responses of sections A10 and B10 do not change under this hypothesis. Figure 6.25 and Figure 6.26 present the long-term predictions. It may be observed that, in the hot sections, it is possible that the clay never reaches full saturation. This fact will of course depend on the real relevance of this phenomenon for the FEBEX bentonite and on test conditions. As for the case of the threshold gradient, the results presented should be considered only as an exercise performed with the aim of investigating the hypothetical response of the barrier under these assumptions, until more experimental evidence on the phenomenon becomes available.

6.4.4.3. Micro-fabric evolution

In this section a preliminary exploration of the influence of the changes on the intrinsic permeability due to changes in the clay fabric during hydration is considered. The microstructure of the compacted clay consists of dense aggregates of clay particles with intra-aggregate pores (micropores) between them. The arrangement of these clay aggregates conforms a granular skeleton of the material with inter-aggregate spaces (macropores). Once hydration starts, the clay aggregates tend to adsorb water and swell. Due to the confinement conditions of the test (overall constant volume conditions practically prevail), the expansion of the microstructure is made possible by reductions of the macropores. This has a significant influence on the permeability value and hence on the hydration of the barrier. These phenomena entail a dynamic character of the clay fabric during wetting,

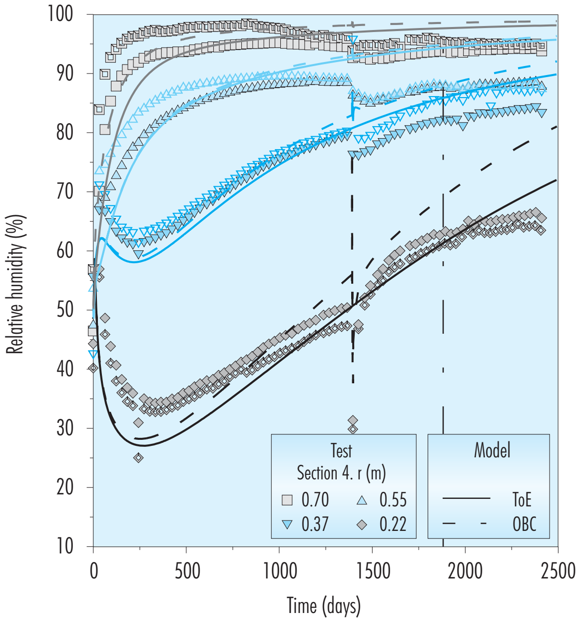

Figure 6.23: Relative humidity. Sections A4-B4. Observed versus computed values of 'ToE' (Thermo-osmotic Effect) and 'OBC' models.

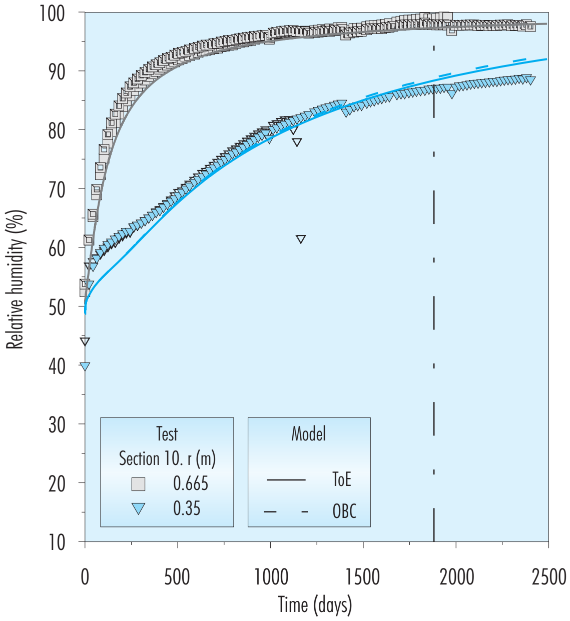

Figure 6.24: Relative humidity. Sections A10-B10. Observed versus computed values of 'ToE' and 'OBC' models.

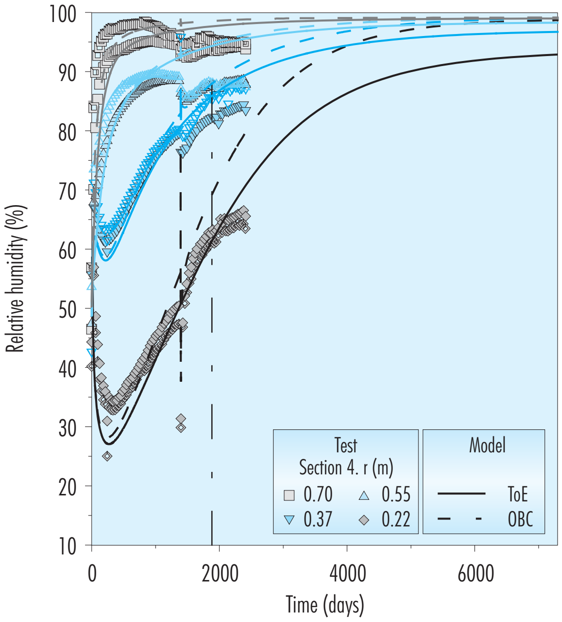

Figure 6.25: Relative humidity. Sections A4-B4. Long-term predictions 'ToE' and 'OBC'.

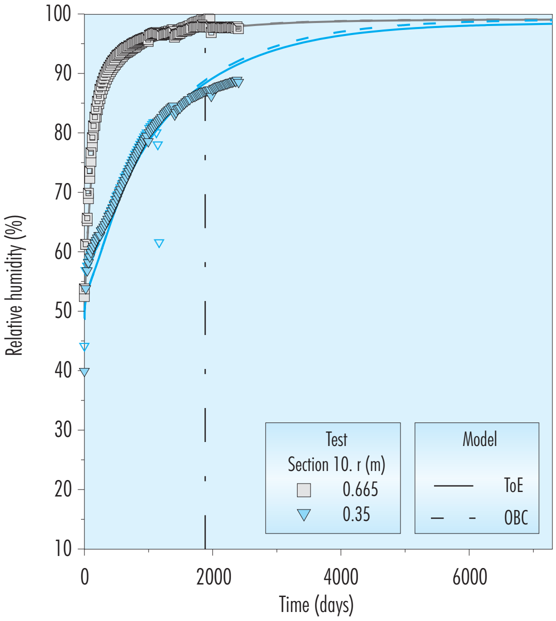

Figure 6.26: Relative humidity. Sections A10-B10. Long-term predictions 'ToE' and 'OBC'.

resulting in a strong coupling between the mechanical and the hydraulic problem. Assuming that the water flow takes place predominately through the macropores, it might be suggested that changes in macroporosity might explain the reduction in the permeability at advanced stages of hydration.

The effect of the clay-fabric changes on the permeability of the FEBEX bentonite has been considered, initially, in a very rough manner. The intrinsic permeability has been reduced in the external (more saturated) zone of the barrier (up to a maximum of 15 % for suctions lower than 2 MPa). Figure 6.27 and Figure 6.28 show the results obtained considering the Micro-fabric evolution effects (MiE) for the two reference sections studied. It may be observed that this model is capable of reproducing the behaviour observed in the barrier better than the OBC model. However, the model predictions are not good (after the dashed vertical line) because the model is incapable of reproducing the more marked decay in hydration rate. Figure 6.29 and Figure 6.30 present the long-term predictions. One difference between this case and the previous ones is that total saturation of the barrier is predicted for the long term. As already mentioned, this is a very simplified model and, for this reason, the results presented here are only qualitative. This phenomenon is treated again, using a more adequate framework, in Section 6.4.5.

6.4.4.4. Final remarks

Explaining the departure of hydration observations from predictions in the "mock-up" test has been approached in a step-by-step manner. The aim is not to exclude in advance some of the possible phenomena that might explain the trends observed in the experiment. A first step of this research is the formulation of the models presented previously. Although they are very simplified, the results obtained are interesting. In this context, this study allows the measurements of an actual test to be compared with the computed barrier response under the hypothetical case in which some of these effects would be present. However, due to the scarcity of experimental data available to formulate these models, and given the preliminary objective of this study, the results presented here can have only a qualitative value. After all, each of these phenomena does not exclude the others and it is possible that an explana-

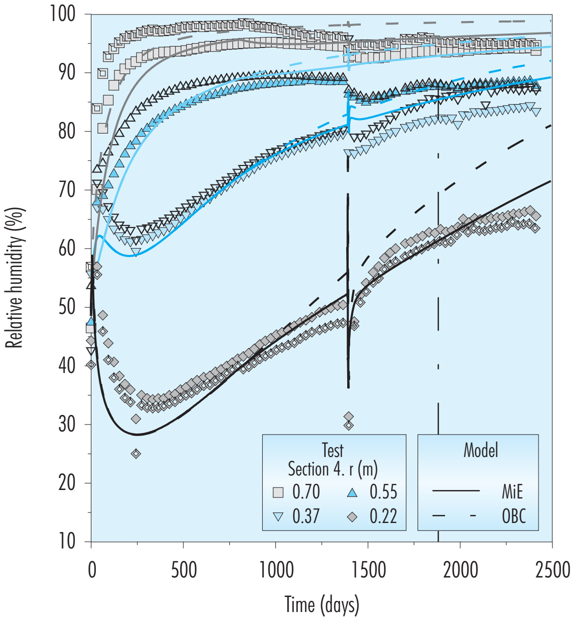

Figure 6.27: Relative humidity. Sections A4-B4. Observed versus computed values of 'MiE' (Microstructure Evolution) and 'OBC' models.

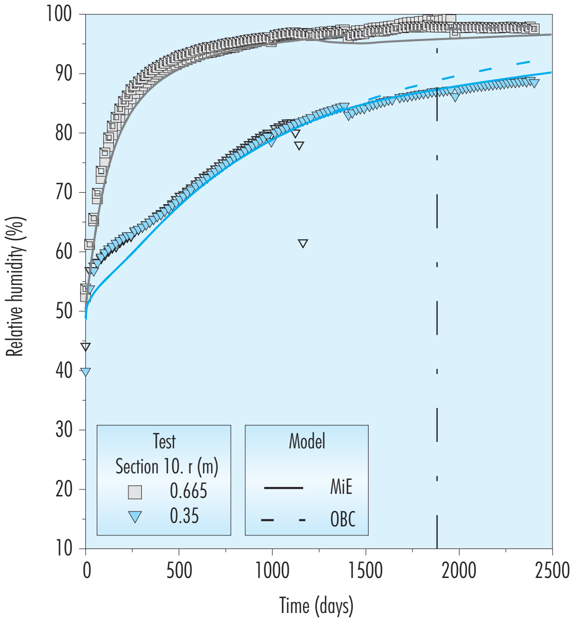

Figure 6.28: Relative humidity. Sections A10-B10. Observed versus computed values of 'MiE' and 'OBC' models.

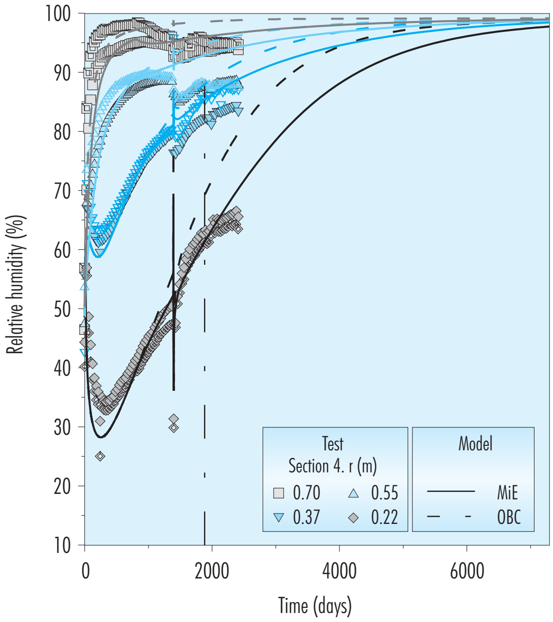

Figure 6.29: Relative humidity. Sections A4-B4. Long-term predictions 'MiE' and 'OBC' models.

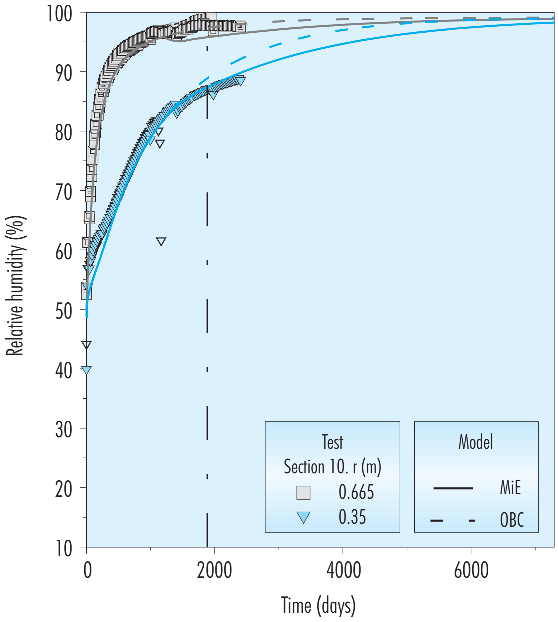

Figure 6.30: Relative humidity. Sections A10-B10. Long-term predictions 'MiE' and 'OBC' models.

tion for the overall behaviour of the barrier might require the combination of some or all of them.

These analyses show the need to improve the 'classical THM formulation' when a complex experiment, such as the "mock-up" test, is studied, especially when long-term predictions are required. However, it should be pointed out that one problem associated with these developments is the scarcity of experimental data available to formulate and to calibrate these new models. New laboratory tests performed with this specific objective should help to develop new models that might incorporate, in a more realistic way, the phenomena deemed to be most relevant. Finally, the "mock-up" test itself may provide relevant information on the phenomena involved, once the consequences of the overheating event are completely overcome and hydration has progressed still further.

6.4.5. Analysis of the "mock-up" test using a THM double structure framework

6.4.5.1. Introduction

Of the phenomena discussed in the previous section, micro-fabric evolution was singled out for further study. The preliminary analyses suggest that this phenomenon might account for the observed hydration behaviour of the "mock-up" test and, furthermore, independent observations of microfabric changes during the wetting and/or drying of compacted bentonite have been made.

The structure of the FEBEX bentonite has been studied using a variety of techniques. For instance, Mercury Intrusion Porosimetry (MIP) observations were performed to examine the pore size distribution of the statically compacted material used in the experimental programme. Figure 6.31 shows the measured incremental pore volume for two samples compacted to quite different values of dry density (ρ_d), 1.5 g/cm^3 and 1.8 g/cm^3. The characteristic bi-modal pore size distribution of compacted expansive materials may be clearly observed. The larger voids would correspond to the inter-aggregate pores. The boundary between the two pore size families appears to be around 0.13 μm, as pores smaller than this magnitude do not seem to be affected by the magnitude of the compaction load. As Figure 6.31 clearly shows, compaction affects mainly the pore structure of the larger inter-aggregate pores. These two dominant pore sizes may be associated with two basic structural levels (Figure 6.32):

- ❑ The macrostructure, composed by arrangements of clay aggregates, with macropores between them.
- ❑ The microstructure, which corresponds to the active clay minerals and their vicinity.

The microstructure is the basis of the basic physical-chemical phenomena occurring at clay particle level. These phenomena underlie the behaviour of expansive soils. On the other hand, deformations due to loading and collapse will have a major effect at the macrostructural level. This macrostructural behaviour may be described by concepts and models of unsaturated non-expansive soils. A proper modelling of expansive clay behaviour also requires consideration of the interactions between the two basic structural levels considered.

The behaviour of unsaturated expansive clays is potentially very complex, since it results from the interaction between the volume change of aggregates made up from a highly expansive clay mineral (microstructural level) and the rearrangement of the granular-like skeleton formed by the aggregates (macrostructural level). Experimental studies of the FEBEX bentonite structure and information on the main mechanisms and phenomena that control the adsorption of water in expansive clays are presented in detail in [165] and [10]. Particularly helpful has been the experimental study related to the changes in the fabric of the FEBEX bentonite during wetting and drying. A systematic study of this issue was performed using a Scanning Electron Microscope (SEM) and an Environmental Scanning Electron Microscope (ESEM).

A key aspect of the behaviour of compacted expansive bentonite is that the clay fabric is not static during hydration, but subject to modifications. For example, changes in the clay structure originated by the progressive wetting of compacted bentonite with an initial dry density of 1.40 g/cm^3 may be observed in Figure 6.33. The progressive occlusion of the inter-aggregate pores due to particle swelling may be easily noted. Although the observations provide mainly qualitative information, the use of this technique allows for improvement of the knowledge of the structural changes due to hydration. As may be observed in Figure 6.33, during hydration the clay fabric exhibits a dynamic character that may strongly affect the kinetics of hydration, especially if confined conditions prevail. Single porosity models

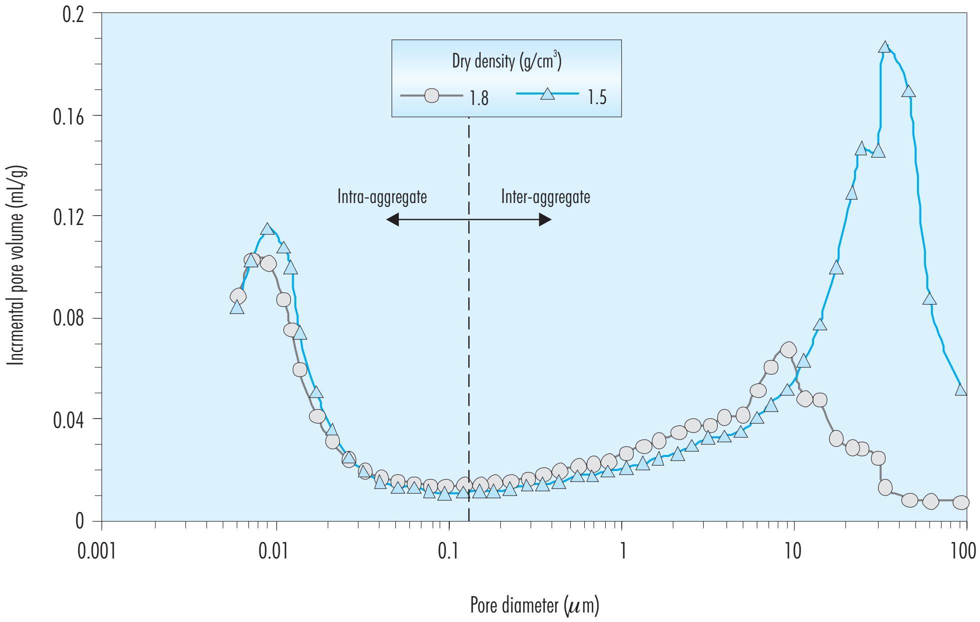

Figure 6.31: Distribution of incremental pore volume for two compacted bentonite samples at different dry densities. Mercury intrusion porosimeter test [56]

(such as the OBC model) are not able to handle properly the potential role of the structure of the swelling clays during hydration. Consequently, and in order to perform a more detailed analysis of the clay fabric effects on the evolution of the "mock-up" test, a double structure THM formulation has been developed.

The aim is to propose a framework suitable for the simulation of problems in which two different pore levels (the macro and micro structure of the FEBEX bentonite) may be clearly distinguished. This approach would allow a conceptual model to be adopted for the hydration of the swelling clays closer to the actual observed behaviour. An addi-

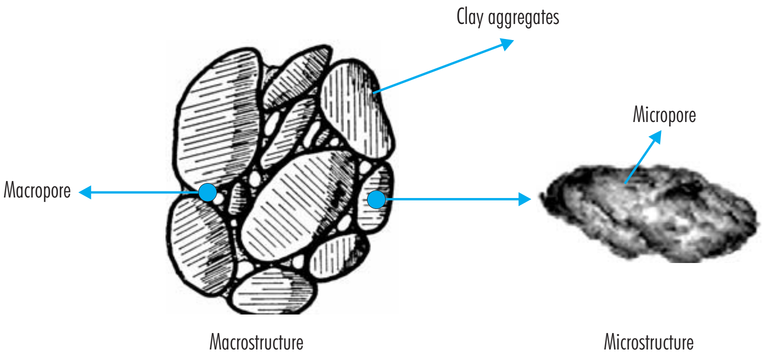

Figure 6.32: Schematic representation of the two structural levels considered.

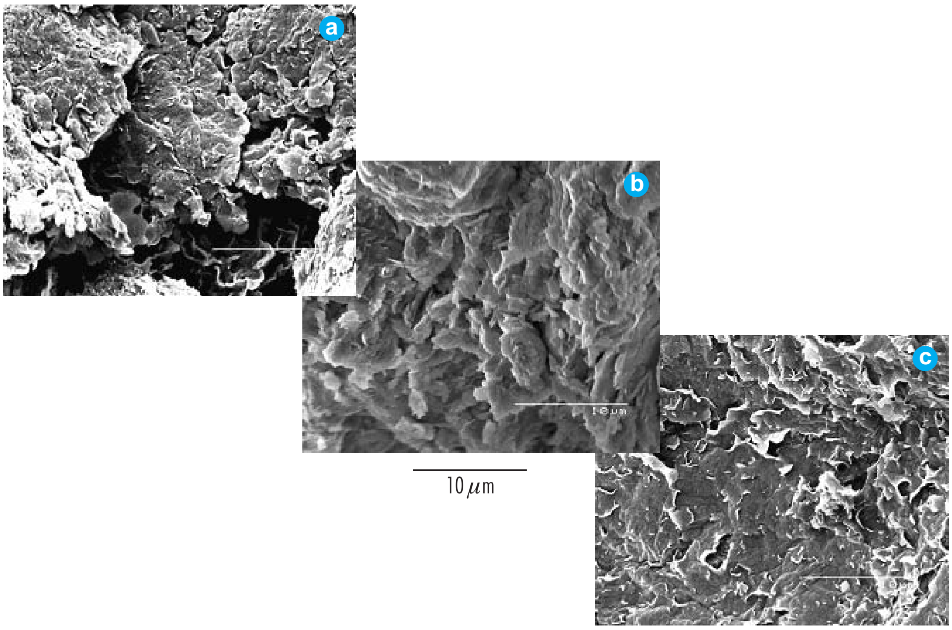

Figure 6.33: Micrographs (SEM, x 6000). a) Compacted with hygroscopic water content to ρ_d=1.40 g/cm^3. b) After application of a suction of 10 MPa under isochoric conditions ($\rho_{d\ final}$=1.46 g/cm^3) on bentonite initially compacted under hygroscopic conditions to ρ_d=1.65 g/cm^3 and c) after saturation under isochoric conditions ($\rho_{d\ final}$ =1.43 g/cm^3) on bentonite initially compacted with hygroscopic water content to ρ_d=1.65 g/cm^3 [165].

tional aim is to provide a general theoretical platform allowing for the inclusion, in a unified and consistent framework, of other phenomena, such as chemical effects or a threshold gradient. The main aspects of the formulation are presented in the next section, more details may be found in [51] and [167].

6.4.5.2. THM double structure formulation

The existing fully coupled THM formulation for single porosity media (presented in Section 6.2) has been extended to include double structure media with the aid of double porosity theory [183]. This theory considers the porous medium as two interacting continuous media coupled through a leakage term that controls the mass transfer between them.

A good schematic representation of the double porosity theory is presented in Figure 6.34. The expansive material with two different pore structures is divided into two overlapping but separate continua. The first is related to the clay particles and the voids inside the aggregates identified as medium '1'. The second is associated with the macrostructure, formed by the clay aggregates (as a whole) and the macropores between them, identified as medium '2'.

The response of the medium overall is obtained from the contribution of the two overlapping porous media, which have different properties. Porosity, fluid pressures, permeability, degree of saturation and other properties are considered separately for each continuum. The generalisation of the THM formulation required is conceptually very simple and it makes it possible to extend most of the well-known laws and models to the case of double structure media.

Some basic aspects of the formulation are summarised as follows:

- ❑ Two overlapping porous media have been considered, with the definitions of two different global porosities.

$$a)\,\phi_1=\frac{V_{v1}}{V};\quad b)\,\phi_2=\frac{V_{v2}}{V};\quad c)\,\phi=\phi_1+\phi_2 \tag{6.13}$$

where ϕ_1 and ϕ_2 are the porosities related to medium one (1) and two (2) respectively, ϕ is the global porosity. V_{v1} and V_{v2} are the volume of voids related to each medium (one and two) and V is the total volume.

- Multiphase, non-saturated flow is considered for each domain.
- Mass transfer processes between the two media are controlled through leakage terms.
- Stress-small strain constitutive laws may be defined for each porous medium.
- Thermal equilibrium between the phases and the media is assumed, this implies that only one energy balance equation is required.
- The relevant THM phenomena are considered in a coupled manner.
- The boundary flow conditions may be prescribed independently for each medium.

The theoretical framework follows the developments presented in Section 6.2, the complete formulation is presented in [51]. As an example, the water mass balance equation for double porosity media is presented. The equation (6.1) is now expressed as

$$\frac{\partial}{\partial t}(\theta_{lj}^{w} S_{lj}\phi_j + \theta_{gj}^{w} S_{gj}\phi_j) + \nabla.(\mathbf{j}_{lj}^{w} + \mathbf{j}_{gj}^{w}) + \\ + (-1)^{j+1}\Gamma^{w} = f_j^{w}; \quad j = 1,2 \qquad (6.14)$$

The same notation has been used, but now, a second subscript, j, is included to identify the medium (1 or 2). Γ^w is the term related to the water mass exchange between the two media. A simple model for this term may be expressed as follows:

$$\Gamma^{w} = \gamma(\psi_1 - \psi_2) \qquad (6.15)$$

where γ is the leakage parameter and ψ_j (j=1,2) represents the variable involved in mass transfer; e.g. the total water potential when water mass transfer is considered. In (6.15) it is implicitly assumed that the process of mass transfer has reached a quasi-steady state [184].

The general framework developed is capable of handling non-saturated multiphase flow in each porous media under non-isothermal conditions and a key aspect of the formulation is the treatment of the strong hydro-mechanical coupling characteristic of expansive clays. The formulation has been implemented in the finite element code, CODE_BRIGHT [63,166]), allowing the incorporation of these concepts in the numerical analyses of the FEBEX test.

6.4.5.3. Mechanical constitutive model for unsaturated expansive clays

Due to the strong influence of the mechanical problem on the swelling clay behaviour, the mechanical constitutive law is a central element in the modelling of these materials. The BBM model presented in Section 6.4.3.1 is not adequate to describe the behaviour of expansive clays. In fact, it was initially developed to model non-expansive materials although some subsequent improvements have been made to allow for the modelling of the swelling behaviour of soils inside the elastic domain. However, a more accurate analysis of this problem requires an improved mechanical constitutive law incorporating some basic characteristics of the behaviour of expansive soils, such as large swelling under wetting, the effect of clay fabric and irreversible deformations inside

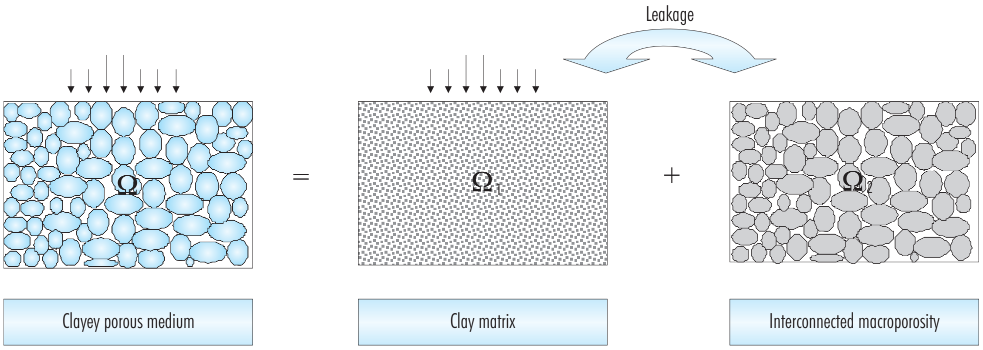

Figure 6.34: Schematic representation of double porosity concepts

the macrostructural elastic domain. A mechanical model for double structure expansive materials has been developed for this purpose.

The mechanical model may be viewed as being the core of the double structure framework presented above. The swelling behaviour of unsaturated expansive clays has often been reproduced through relatively simple and empirical laws, which relate material response to suction changes and applied stresses. However, the model described here integrates the main aspects of expansive clay behaviour in a unified and formal framework. The mechanical law is based on the general approach proposed by Gens & Alonso (1992) [57] and also considers some of the improvements proposed by Alonso et al. (1999) [185]. Particular attention is placed on clay structure and how it may be incorporated in the constitutive modelling of expansive soils. Only the main aspects of the model are presented below, a more extended description of the model with details of the mathematical framework and its implementation in CODE_BRIGHT may be found in [51] and [186].

The mechanical model has been developed using concepts of elasto-plasticity for strain hardening materials. The model is formulated in terms of three stress invariants (*p*, *J*, θ), suction (*s*) and temperature (*T*), where *p* is the mean net stress, *J* is the square root of the second invariant of the deviatoric stress tensor and θ is Lode's angle. A characteristic of this model is the explicit consideration of the two main structural levels identified above (Figure 6.32), as well as the interaction between the two structures. The complete formulation of the model requires the definition of laws to describe the behaviour of: i) the macrostructural level, ii) the microstructural level and iii) the interaction between the structural levels.

The inclusion of the macrostructural level in the analysis allows for consideration of the phenomena that affect the skeleton of the material, for instance deformations due to loading and collapse. These phenomena have a strong influence on the macroscopic response of expansive materials. The macrostructural behaviour may be described by concepts and models of unsaturated non-expansive soils, such as the elasto-plastic Barcelona Basic Model (BBM) [174]. Figure 6.35a) presents a three-dimensional representation of the BBM in space stress invariants.

The microstructure is associated with the active clay minerals, and its behaviour is controlled mainly by the physico-chemical phenomena occurring at this level. It is assumed that these phenomena are basically reversible. The strains arising from microstructural phenomena are considered elastic and volumetric. The microstructural effective stress is defined as:

$$\hat{p} = p + \chi s_t\,; \qquad s_t = s_2 + s_0 \qquad (6.16)$$

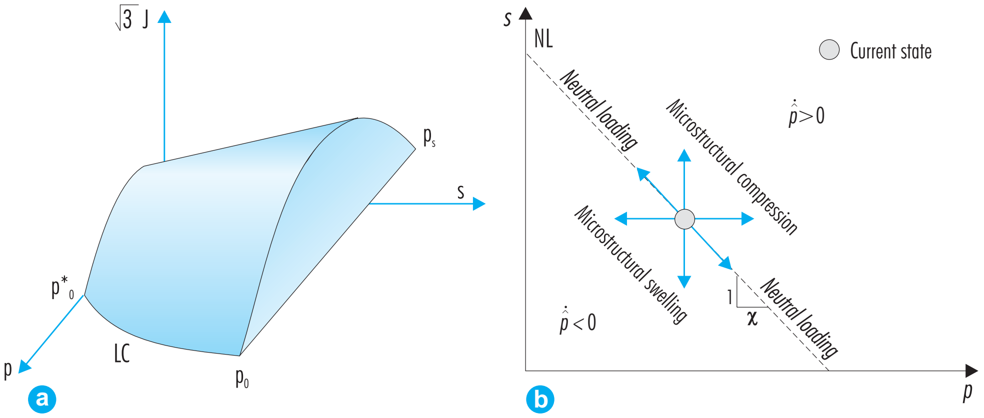

Figure 6.35: a) Three-dimensional representation of the BBM yield surface. b) Definition of the microstructural swelling and contraction directions.

where s_o is the osmotic suction. It is assumed that χ is a constant ($\chi > 0$) and that the total suction (s_t) is equal to the matric suction (s_2), because the effect of the osmotic suction is not considered in this work. In (6.16) hydraulic equilibrium between the water potentials on both structural levels is assumed (this implies $s = s_1 = s_2$). The extension of the constitutive model to handle problems in which this hypothesis is released is described in [51].

On the *p-s* isotropic plane, the line corresponding to constant microstructural effective stresses is referred to as the Neutral Line (*NL*), since no microstructural deformation occurs when the stress path moves on it (Figure 6.35b). According to this, the Neutral Line divides the *p-s* plane into two parts (Figure 6.35b), identified as:

$$\dot{\hat{p}} > 0 \Rightarrow \text{microstructural contraction } (MC)\ ;$$

$$\dot{\hat{p}} < 0 \Rightarrow \text{microstructural swelling } (MS)$$

In expansive soils there are other mechanisms additional to the ones included in the BBM that induce plastic strains. This irreversible behaviour is attributed to the interaction between the macro and microstructures. It is assumed that the microstructural behaviour is not affected by the macrostructure but the opposite is not true, i.e. macrostructural behaviour may be affected by microstructural deformations, generally in an irreversible manner. An assumption of the model is that the irreversible deformations of the macrostructure are proportional to the microstructural strains in a way defined by interaction functions

Note that the material response will depend strongly on the direction of the microstructural stress path relative to the *NL*, which separates two regions of different material behaviour. A proper modelling of this behaviour requires the definition of specific elasto-plastic laws for each domain, in order to describe correctly the material behaviour according to the microstructural stress path followed (*MC* or *MS*). The Generalized Plasticity theory may deal with such conditions, allowing for the consideration of two directions of different behaviour and the formulation of proper elasto-plastic laws for each region [186].

In summary, the behaviour of the macrostructure is modelled in the context of classical plasticity (BBM). The microstructural effects have been modelled using a non-linear elastic model. The interaction between both structural levels has been considered using the general framework of generalised plasticity theory. As described in [51] and [186], the governing small strain-stress equations have been obtained using a general procedure proposed for multi-dissipative materials. Finally, the numerical integration of the model has been performed using a scheme that includes automatic error control.

Before applying the double structure constitutive law to the modelling of the "mock-up" test, it is important to validate it experimentally. Laboratory tests carried out in the context of the FEBEX project have been used for this purpose. Oedometer swelling tests, swelling pressure tests and tests performed to study the structure of the FEBEX bentonite have been used to identify the main model parameters [56].

6.4.5.4. Double structure modelling of the "mock-up" test

Features of the analysis

The "mock-up" test has been analysed using the double structure approach presented above. This analysis is coded 'Dou' hereafter. 1-D axisymmetric models have been developed to analyse the two characteristic sections of the test (the 'hot cross-section' and the 'cold cross-section'). A mesh of one hundred (100) elements has been used. A sensitivity analysis has also been carried out to verify that the model results do not depend on the mesh adopted. The adequacy of 1-D models has been explored in [169].

Here, the work is focused on the behaviour of the FEBEX bentonite during a normal hydration and heating test, and also on how these processes may be interpreted in a double structure context (thus, the overheating event has not been modelled in this analysis). Two sets of comparisons are shown: model output versus experimental data and comparisons between the long-term predictions of the 'OBC' and the double structure model, 'Dou'. The first set of comparisons is presented in order to demonstrate the capacity of the model to reproduce experimental observations and overall trends of behaviour. It is important to remember that the unexpected gradual hydration of the barrier is clearly observed at dates before the overheating event. The second type of comparisons is intended for the analysis of long-term predictions of these two different conceptual models under the same test conditions.

The assumptions of the OBC model have been maintained for the initial conditions of the mechanical and thermal problem (Section 6.4.3.). As regards the hydraulic conditions, the initial suction has been adopted taking into account the records of the relative humidity sensors of the "mock-up" test. Finally, the same mechanical, hydraulic and thermal boundary conditions adopted for the 'OBC' model have been prescribed.

The thermal constitutive laws adopted for the OBC model are assumed for the double structure model, but now considering the contributions of the two structural levels to the thermal behaviour of the medium. Additionally, the specific internal energies of each medium are explicitly considered in the balance energy equation.

In relation to the hydraulic problem, it is assumed that the flow of liquid water takes place mainly through the macropores. In the proposed double structure approach it is possible to consider that the water may also flow through the micro level (pores smaller than 0.13 μm, in the case of FEBEX bentonite, Figure 6.31). However, in this simulation, a very low permeability for the microstructural level has been adopted, considering that the contribution of this level to the total water flow is very small. It is also assumed that the intrinsic permeability is a function of the macro porosity through an exponential law. It is important to bear in mind that, in the double structure framework, the evolution of the clay fabric (macro and micro porosity) is controlled by the changes of the main variables of the problem (displacements, temperature, macro and micro suctions), which are considered in a fully coupled manner through the mechanical model. In this way, the main phenomena that affect the changes in both pore levels and their mutual interactions are taken into account.

In the double structure model the water retention capacity of the soil is obtained considering the water stored in both pore levels. Figure 6.36 presents the retention curves adopted for each medium, in terms of suction and saturation degree of the medium. Additionally, this Figure shows the modelling results of a wetting path (at constant volume) in terms of the global degree of saturation and suction. Even though this model is very simple, it allows for explicit consideration of the amount of water stored at each structural level. This is an active area of research and the present formulation is left open to the incorporation of more sophisticated models.

Different laboratory tests have shown that the swelling of FEBEX bentonite takes place from the very beginning of the wetting process [10, 165]. In the frame-

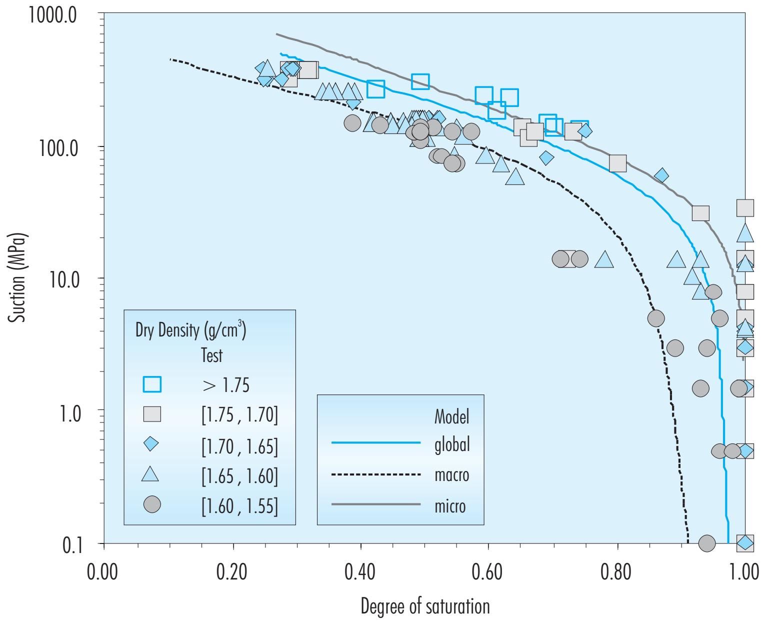

Figure 6.36: Water retention curve, experimental data and adopted models.

work of the double structure model this implies a fast hydration and swelling of the microstructure. Therefore, the water transfer from the macrostructure to the microstructure has been considered as being instantaneous. This implies a low value of the leakage parameter (i.e. $\gamma = 1$ kg s^{-1} m^{-3} MPa^{-1}). Based on experimental observations, a microstructural water density of 1.15 g/cm^3 has been adopted in the analysis [16].

Results and comparisons with observations

Figure 6.37 to Figure 6.40 show the comparisons between model results and test data for a hot cross section and Figure 6.41 to Figure 6.44 present the long-term predictions of the 'OBC' model and of the Double structure model ('Dou'). In relation to the hydraulic problem, it may be observed that the model is capable of capturing qualitatively well the evolution of relative humidity, especially in the inner zones (r = 0.22m and r = 0.37m). In general terms, it may be noted that the trends of the two models are clearly different. This is even more apparent in the comparisons between the long-term predictions of both models. The double structure model predicts a locking of the hydration that implies that important zones of the barrier remain in a non-saturated condition. This is qualitatively in agreement with the tendency observed in the barrier. In relation to the water intake (a global variable), the response of the model is also good when compared with measurements. In the long-term analysis, the 'Dou' model predicts a lower amount of water intake compared to the estimation of the 'OBC' model.

In this work, expressions such as 'zones of the barrier will remain non-saturated' or 'no full saturation is reached' refer to the fact that the rate of water intake is so low that the saturation of the bentonite is delayed for a long time (as may be seen in Figure 6.41 and Figure 6.42). Perhaps, the following information on global water intake may be useful. The experimental value of the water intake rate at day 1400 is close to 0.15 Kg/day (weekly average), while the 'Dou' model computes a rate of 0.17 Kg/day (and the one corresponding to the 'OBC' model is 0.22 Kg/day). This rate reduces drastically for the latest test data available (close to day 2417), with an observed value close to 0.04 Kg/day (weekly average), whereas the rate computed by the 'Dou' model is 0.035 Kg/day (and that estimated

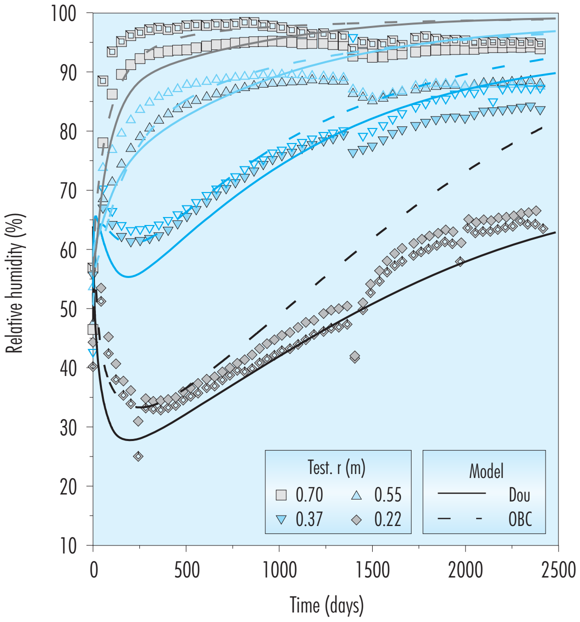

Figure 6.37: Relative humidity in Sections A4-B4. Observed versus computed values of 'Dou' (Double Structure) and 'OBC' models.

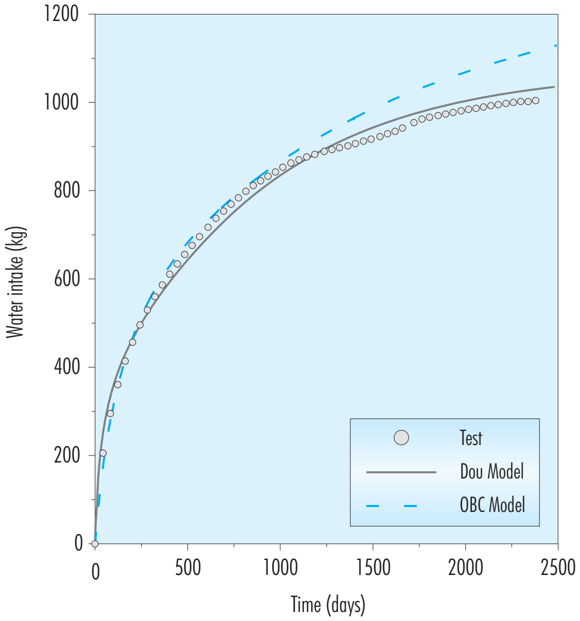

Figure 6.38: Water intake. Observed versus computed values of 'Dou' and 'OBC' models

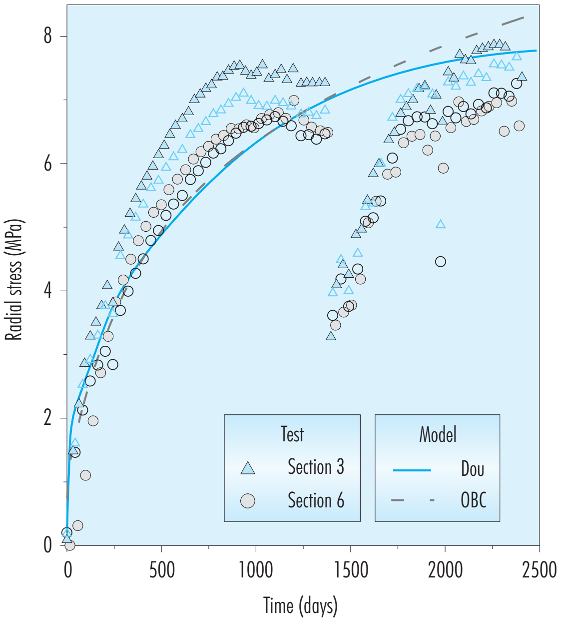

Figure 6.39: Radial stress in Sections A3-B3 and A6-B6. Observed versus computed values of 'Dou' and 'OBC' models.

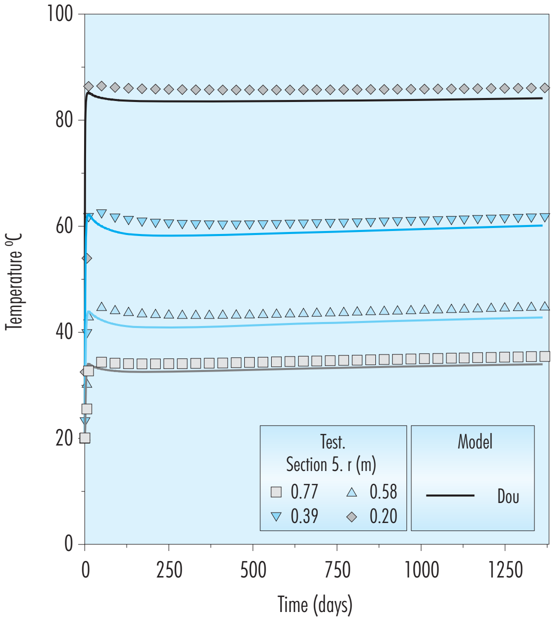

Figure 6.40: Temperature in Section A5. Observed versus computed values of 'Dou' and 'OBC' models

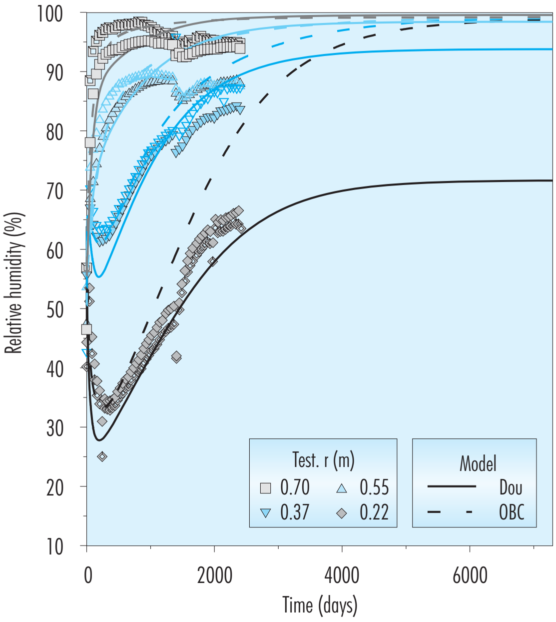

Figure 6.41: Relative humidity. Sections A4-B4. Long-term predictions of 'Dou' (Double Structure) and 'OBC' models.

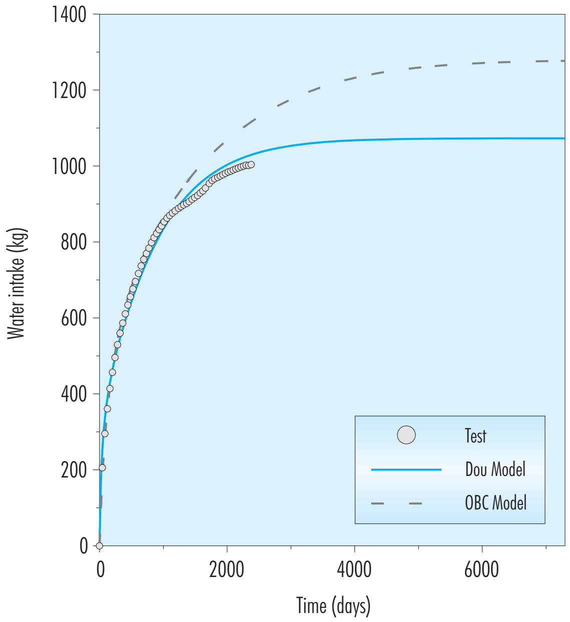

Figure 6.42: Water intake. Long-term predictions of 'Dou' and 'OBC' models

by the 'OBC' model is 0.10 Kg/day). Finally, on the last day of the analysis (7300) the rate of water intake computed by the 'Dou' model is $7.0 \cdot 10^{-6}$ Kg/day. This is a very low value for the water intake rate and implies a very long time to reach the barrier saturation. This result may be exaggerated by the very low permeability used to characterise the microstructural level.

The temperature field is also well captured by the model. Looking at the comparisons of temperatures for the long term, it may be mentioned that no increment in the 'Dou' model predictions is observed (in contrast to the OBC model). The 'Dou' model results show that practically constant temperatures are maintained over time for different radii. This is also a direct consequence of the hydration locking, which implies that the degree of saturation is practically constant after day 2000 and, consequently, the thermal conductivity also remains constant.

Finally, it may be observed that the model captures the strong hydro-mechanical coupling of this problem, reproducing the clear tendency to maintain a practically constant value of the stress level (close to 7 MPa in the test). Some delay in the prediction of the slowing down of stress increment, in relation to the experiment, may be observed. In the test this tendency is detected close to day 1000, whereas in the model it occurs near day 1400. In any case, the trend of the 'Dou' model is closer to the observed behaviour in the "mock-up" test.

Figure 6.45 and Figure 6.46 show the evolution of porosity and intrinsic permeability for two extreme radii computed using the 'OBC' model. A higher porosity (higher permeability for this model) in zones close to the hydration front and a lower porosity in more internal zones are obtained.

Figure 6.47 and Figure 6.48 present, for the same radii, the evolution of the macro porosity, and the intrinsic permeability associated with it, using the 'Dou' model. It may be observed that, in this model, the response is very different, with a tendency to reduce the macro porosity at both locations and, consequently, to reduce also the associated intrinsic permeability. A more external radius (r=0.75m) is also included in the Figure, where it may seen that this effect is more significant in zones near the hydration front. The break observed in Figure 6.47 and Figure 6.48 for a radius of 0.70m close to day 1400 of the test is due to a macrostructural collapse. This is further explained below.

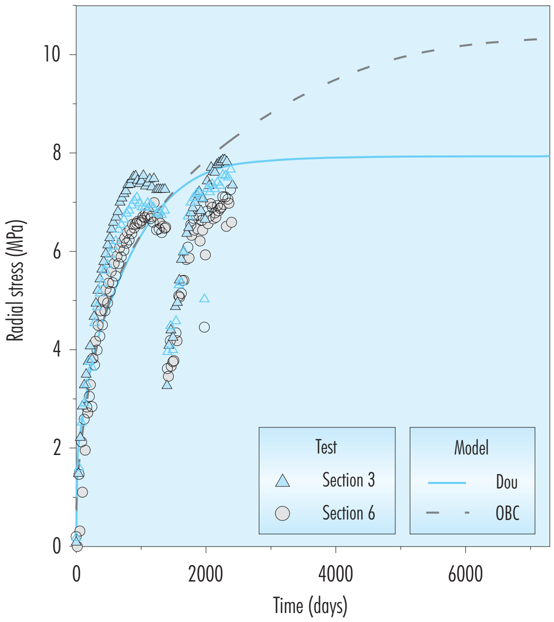

Figure 6.43: Radial stress. Sections A3-B3 and A6-B6. Long-term predictions of 'Dou' and 'OBC' models.

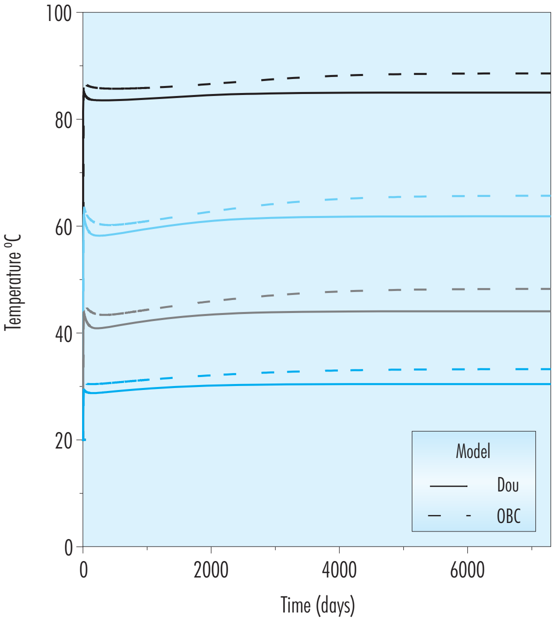

Figure 6.44: Temperature. Section A5. Long-term predictions of 'Dou' and 'OBC' models.

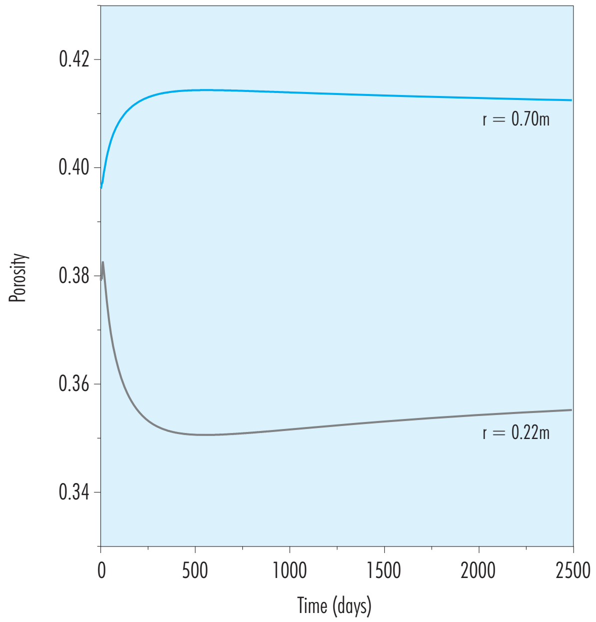

Figure 6.45: Computed evolution of porosity for two extreme radii using the 'OBC' model. Sections A4-B4.

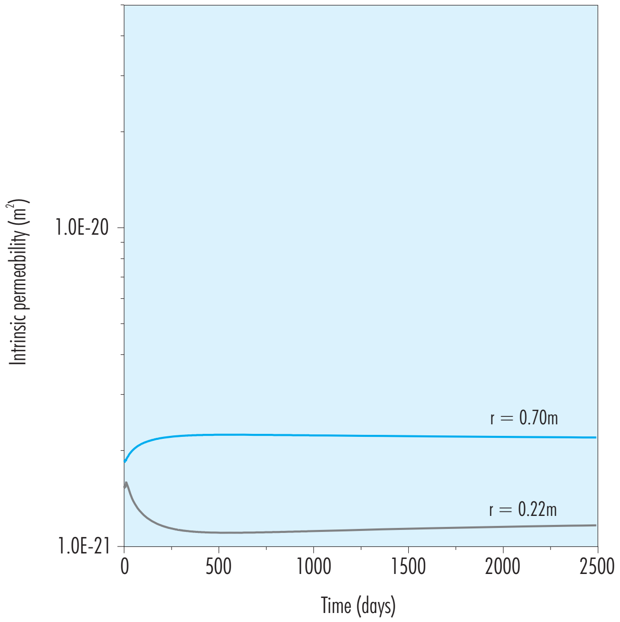

Figure 6.46: Computed evolution of intrinsic permeability for two extreme radii using the 'OBC' model. Sections A4-B4.

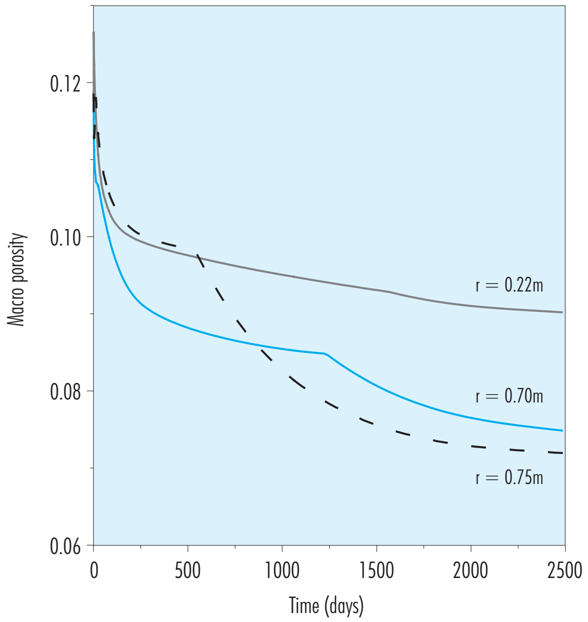

Figure 6.47: Computed evolution of macro porosity for three extreme radii using the 'Dou' model. Sections A4-B4.

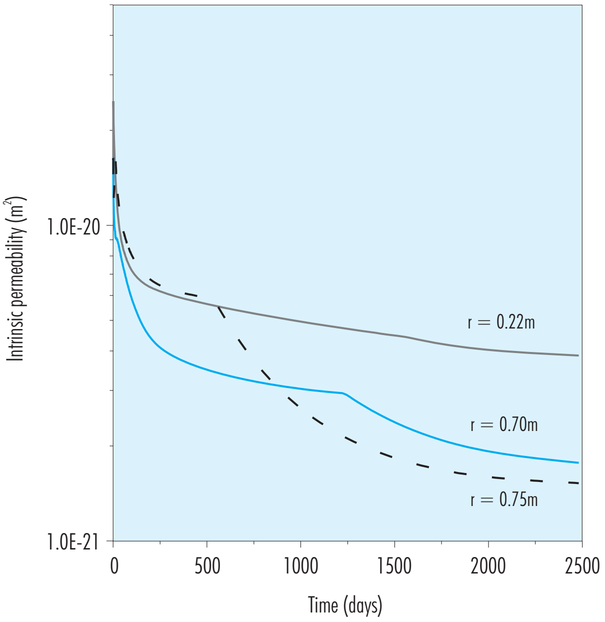

Figure 6.48: Computed evolution of intrinsic permeability for three extreme radii using the 'Dou' model. Sections A4-B4.

According to this simulation, as the barrier is hydrated the pores available for liquid flow undergo progressive reduction. This is due mainly to the microstructure swelling under confined conditions. As a result, full saturation of the barrier is delayed. This kind of hydration-locking is evident in zones close to the heater, because the reduction of the permeability in the zones close to the hydration front reduces the liquid flow supply to the internal zones that are subjected to the heater-induced drying. The final outcome is that the hydration is nearly stopped, with an important zone of the barrier still unsaturated.

Figure 6.49 presents the results obtained in a section away from the heater. It may be observed that the evolution of the relative humidity is not so well reproduced by the model. In the long-term simulations, full saturation of the barrier is predicted in this zone (Figure 6.50).

The analysis of the distribution of certain relevant variables along the barrier computed for different times may help to achieve a more global view of the problem. Figure 6.51 to Figure 6.54 present the isolines of global degree of saturation, macro, micro and global void ratio at different times for a section that includes a heater ('cross-hot section'). The microstructure expands in the external zones due to hydration and contracts in zones close to the heater due to strong drying. The front of swelled microstructure advances progressively inside the barrier as time goes on. As for the macropores, a swelling behaviour may be seen but only at the beginning of the test and for a very thin zone close to the hydration front. This is due to a macrostructural suction reduction and also to the interaction mechanism between structures (in this case microstructural swelling, *ms*, at low load implies a macrostructural expansion). For other times and locations, the values of macro void ratio are lower than the initial ones. This is mainly due to the fact, already discussed, of microstructural expansion under conditions of practically constant volume. The final condition corresponds to significant reductions of the macropores across the barrier, which is more marked in the external zones of the barrier.

Two further aspects should be briefly commented: the first is that macrostructural collapses may be observed along the barrier that progressively move towards more internal zones as hydration proceeds; and the second is that zones close to a radius of 0.35 m are strongly affected by the condensation of

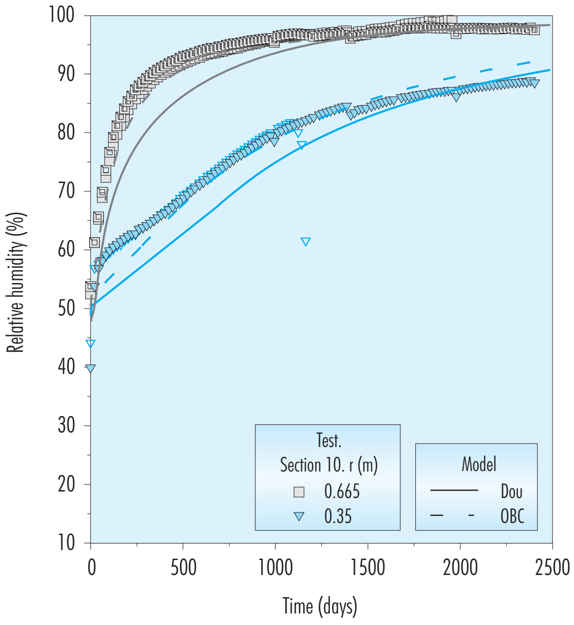

Figure 6.49: Relative humidity. Sections A10-B10. Observed versus computed values of 'Dou' and 'OBC' models

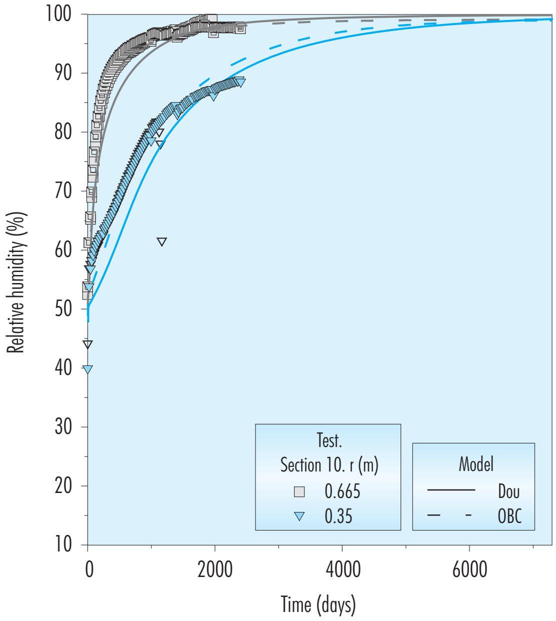

Figure 6.50: Relative humidity. Sections A10-B10. Long-term-predictions of 'Dou' and 'OBC' models

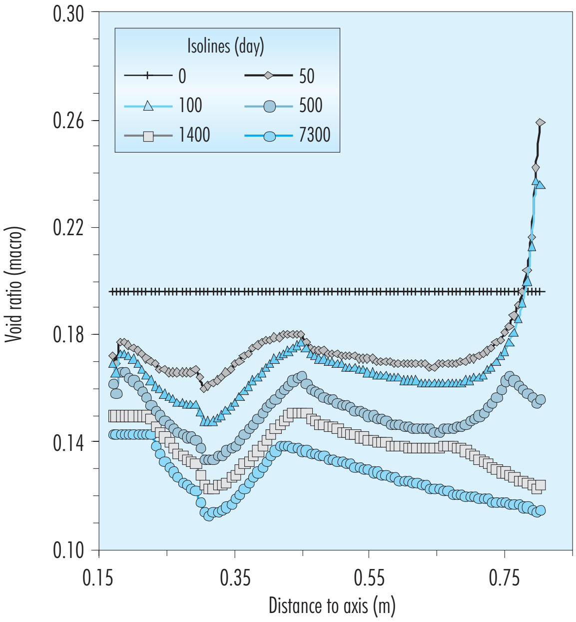

Figure 6.51: Isolines of macro void ratio along a 'hot-cross section'.

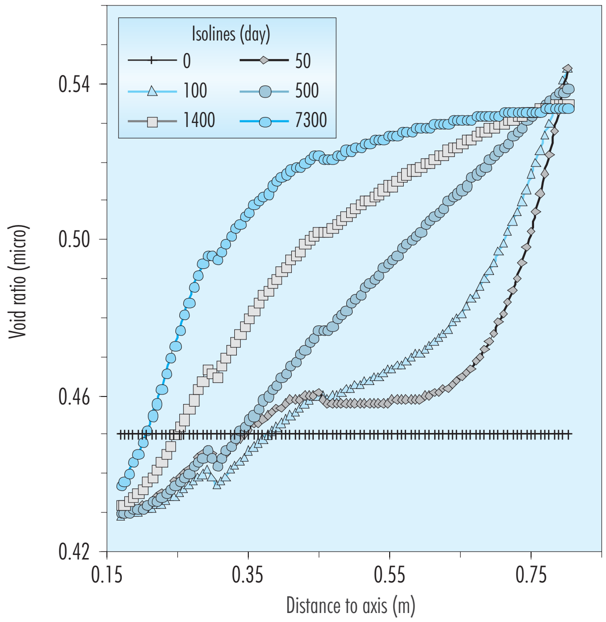

Figure 6.52: Isolines of micro void ratio along a 'hot-cross section'.

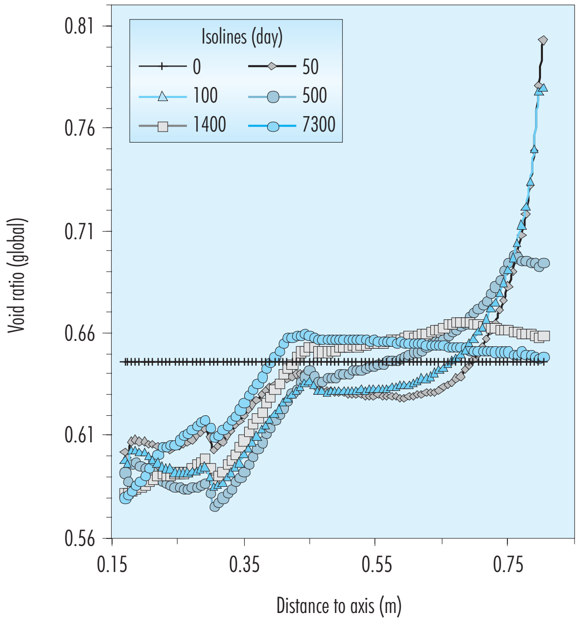

Figure 6.53: Isolines of global void ratio along a 'hot-cross section'.

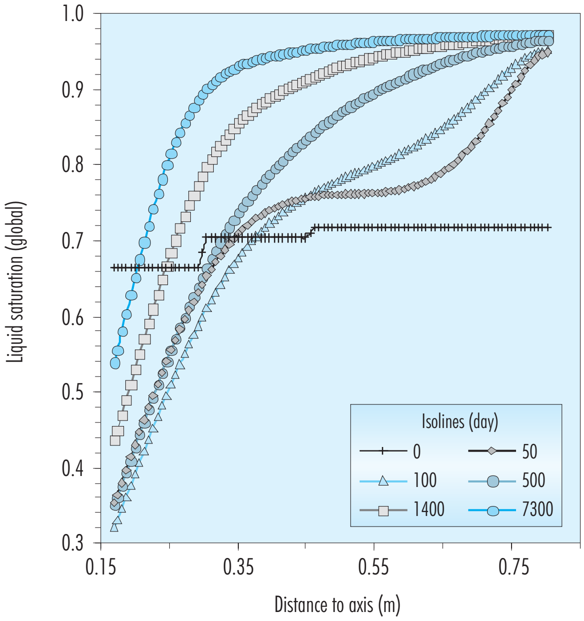

Figure 6.54: Isolines of global liquid saturation along a 'hot-cross section'.

water vapour coming from the inner region of the barrier (Figure 6.51 to Figure 6.54). This local wetting also induces a marked macro void reduction in this region. Regarding the degree of saturation, it may be mentioned that the shape of the hydration front is very similar to the evolution of the micro void ratio. This result is in agreement with the adopted conceptual model, which considers that a large amount of water is stored in the microstructure.

The global void ratio is greater in the outer zones and lower in the inner regions. In that sense, as saturation progresses, the model reproduces a reduction in clay densities in zones close to the hydration front. In contrast to the single porosity model, in this double structure approach, a reduction in clay density implies a reduction of the macropores, the pores available for the main water flow.

In summary, the inclusion in the modelling of the changes in the clay fabric (through the double structure approach) has allowed a more detailed analysis of barrier behaviour to be performed, including the simulation of the main tendencies observed in the two different sections studied ('hot and cold cross sections'). The numerical results may also be considered good in quantitative terms (especially in hot cross sections), although some further improvements are still possible.

It should be noted that most model parameters have been obtained independently from the available experimental data, although they are subject to certain significant limitations. For instance, as pointed out above, the conditions under which some of the laboratory experiments were carried out are different from the actual THM conditions in the "mock-up" test, especially in the case of the permeability tests. The long-term behaviour of FEBEX bentonite has not been explored in sufficient detail either. In this respect, it has been observed that, in expansive clays, there are some microstructural phenomena which are subject to very strong time delays, such as the ageing effects in the microstructure observed by Marcial (2003) [53]. This phenomenon implies a progressive reduction of macroporosity as time goes on. The existence of these two phenomena (threshold gradient and ageing effects in the microstructure) might imply additional restrictions for the hydration of the barrier. If the existence of these phenomena in the FEBEX bentonite is confirmed experimentally, the proposed framework is capable of including them in the simulations.

6.4.6. Constitutive modeling of the overheating event

On day 1391 of the experiment an incident involving an accidental overheating occurred. The heaters attained a temperature of 300 °C in some areas and the contact between the bentonite and the heaters reached a temperature above 200 °C, (i.e. 100°C more than the temperature prescribed in the test). Figure 6.55 and Figure 6.56 present detailed observations of this event. Some separate symbols corresponding to a time of 1000 hours after the event are also shown in the plots.

Figure 6.55 shows the evolution of temperatures at several radii in the barrier. It may be seen that points close to the heater reach temperatures near 200 °C. Afterwards the heaters were switched off and the barrier cooled down rapidly to temperatures close to 45 °C near the heaters. The variation of temperatures away from the heaters is not so large. Eventually the prescribed thermal conditions of the test, *i.e.* a constant temperature of 100 °C at the contact between heaters and clay, were re-established. Figure 6.56 shows the evolution of suction for a point close to the heater derived from the measured values of relative humidity and temperature. It may be observed that suction reduces from 110 MPa to 55MPa due to the passage of the vapour front. Afterwards the thermally induced drying increases the suction to values close to 165 MPa. Finally, there is a tendency to recover the value before the event. The evolution of the radial stress in the barrier is especially interesting. Figure 6.57 shows the evolution of radial stress in two representative sections of the barrier during and just after overheating. At first there is a moderate increment (from 6.6 MPa to 7.2 MPa) followed by a strong reduction to around 2 MPa. The radial stress recovers somewhat subsequently, but remains significantly below the initial values. The net result is a large irreversible reduction of radial stress.

A full understanding of the phenomena occurring during the overheating event requires a coupled THM analysis. A preliminary step, however, is to examine whether the mechanical constitutive model is consistent with the observations of irreversible phenomena just outlined. It should be pointed out that only the constitutive law is tested, so there are no time effects due to the transient phenomena occurring in the barrier. The aim is not to reproduce the

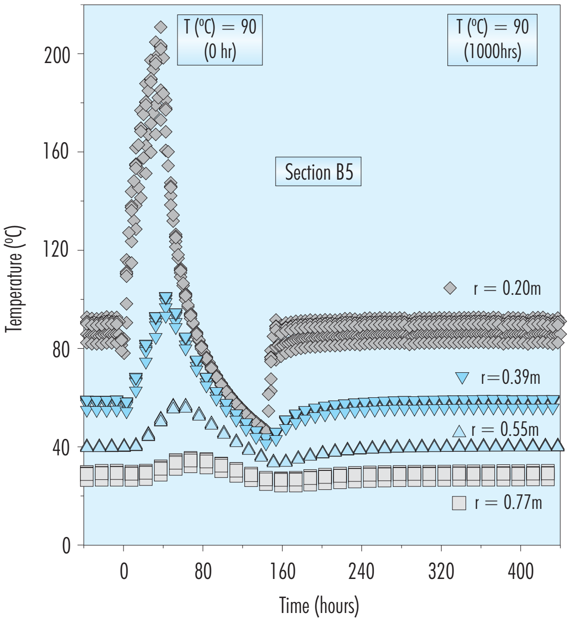

Figure 6.55: Evolution of temperature during and after the overheating event.

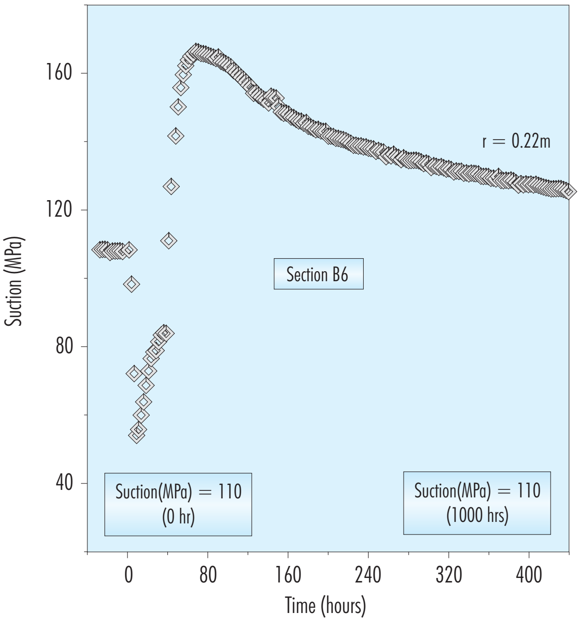

Figure 6.56: Evolution of suction during and after the overheating event.

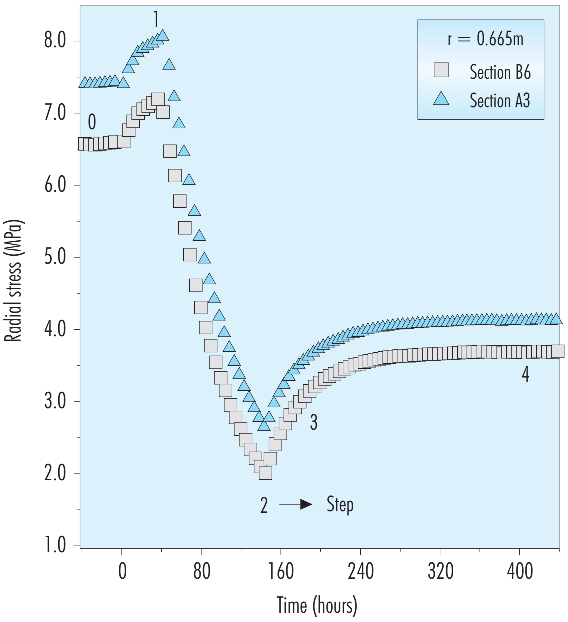

Figure 6.57: Evolution of radial stresses during and after the overheating event.

full behaviour of the barrier but to check whether the main features of the observed mechanical behaviour are a natural outcome of the constitutive model

A synthetic generalised stress path is applied to the constitutive law, corresponding to four major episodes: a wetting due to the passage of a vapour front, an intense drying associated with the increase of temperature, a subsequent cooling due to the switching off of the heaters and, finally, the re-establishment of the prescribed test conditions. The suction and temperature changes are applied under conditions of no volume change, mimicking the confined state of the test [186].

The mechanical model presented in Section 6.4.5.2 has been used in the analysis. Figure 6.58 presents the model results when the generalised loading stages are applied. The four stages of the analysis are also indicated in this Figure. A good correspondence between measured and calculated values of radial stress is observed. Finally, Figure 6.59 shows a three-dimensional representation of the four loading stages adopted and the computed values of radial stress.

The final outcome is that the constitutive model response to this complex generalised stress path is a significant reduction in swelling stress that is not recovered when returning to the initial conditions, the same behaviour as that observed in the test. Naturally, this analysis does not reproduce exactly the conditions of the test, as it involves instantaneous application of the thermal and hydraulic loading without considering the transient phenomena that have occurred in the barrier. It is therefore not surprising that there is a time lag between the test observations and constitutive model predictions. In any case, the main objective of demonstrating the capability of the model to reproduce irreversible behaviour when subjected to a complex THM loading path has been largely achieved.

6.5. Analysis of the "in situ" test

6.5.1. Introduction

A complete description of the "in situ" test is presented in Chapter 4. This section presents some modelling of the pre-operational stage, but focuses

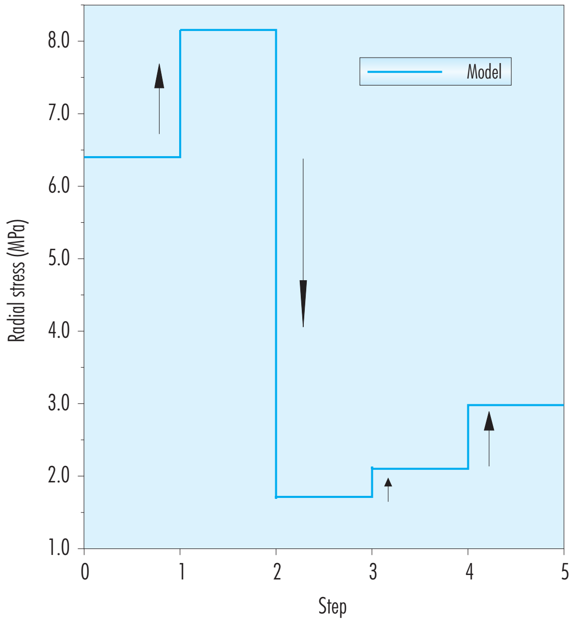

Figure 6.58: Computed values of radial stress during the stress path.

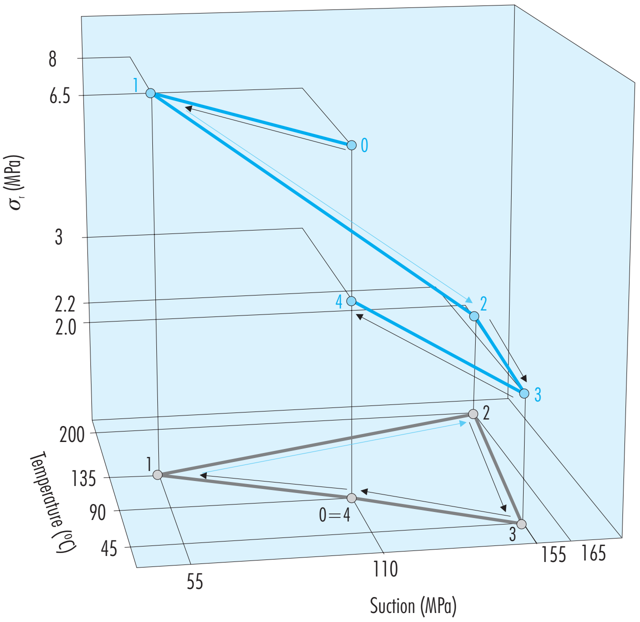

Figure 6.59: Three-dimensional representation of the applied loading stages.

mainly on the operational analyses. As in the "mock-up" test, an operational model was proposed at the beginning of the operational stage. The operational model attempts to integrate all the information available for the various components of the "in-situ" test at the start of the experiment. One of the main activities undertaken in the second phase of the FEBEX project was the partial dismantling of the "in situ" test. This activity involved the removal of one of the heaters (Heater #1) while leaving the other in operation for an as yet undefined period. The analyses performed include the modelling of the main stages of the dismantling, i.e. the switch off of Heater #1; the demolition of the concrete plug; and the step-by step excavation of the clay barrier. A comparison between model predictions and measurements has been made. After dismantling, new sensors have been installed in zones of the barrier not monitored during the initial operation.

This section is organised as follows. Firstly, comparisons between experimental data and the results of the operational model (OBC) for dates prior to the cooling, excavation and extraction of Heater #1 are presented. The aim is to examine the evolution of the test under the design conditions of the test, i.e. natural hydration and two heaters switched on. Afterwards, the main aspects of the modelling of the cooling and excavation stages of Heater #1 are presented. Following this, the analysis for dates subsequent to excavation, including the operation of the test with only one heater, is presented. The comparisons between the model and the measurements obtained in the new instrumented sections are also examined. Finally, some results of the post-mortem study are compared with the model predictions.

Numerical modelling has also been used to assist in devising certain test activities. For instance, modelling has supported the planning of Heater #1 switch off and subsequent excavation. Additionally, some aspects related to the engineering design have been studied, for example, the simulation of assisted hydration to accelerate barrier saturation. These analyses are not included here.

6.5.2. Pre-operational modelling

As in the analysis of the "mock-up" test, in the pre-operational stage only limited data from laboratory tests were available. Also some of the details of the test protocol were modified after the analyses were performed. Here, some selected results of the parametric study are presented. Note that the modelling of the "in situ" test has an additional degree of complexity because of the buffer/host rock interaction. Parametric analyses allow for a better understanding of these phenomena and for an assessment of the relative importance of the different constitutive laws and parameters regarding the expected evolution of the system. The parametric study carried out involved the performance of a significant number of analyses changing parameters, constitutive and boundary conditions. Table 6.2 presents the selected results discussed in this section.

The analysis coded KB has been performed using an intrinsic permeability of $2{\cdot}10^{-20}$ m^2, about three times higher than in the Base Case. The effect of this higher bentonite permeability is striking. As Figure 6.60a shows, a strong desaturation of the granite occurs because the rock is unable to provide the increased inflow of water demanded by the larger hydraulic conductivity of the bentonite. At that point a quasi-impermeable barrier is created that practically prevents the inflow of water into the buffer. As time goes on, the rock becomes saturated again and the progressive hydration of the buffer can then take place. This process may be clearly seen in Figure 6.60b, in which the hydration stoppage due to rock desaturation may be noted. Once resaturation of the granite is achieved, hydration takes place more quickly than in the Base Case because of the greater permeability of the bentonite.

In this context, it is interesting to examine the results of analysis KBPG in which the higher value of bentonite permeability has been used but rock desaturation has been prevented by the use of a high air entry value in the retention curve of the granite. As Figure 6.61 shows, no hydration delay is observed and the higher hydraulic conductivity of the bentonite results is a more hydrated barrier at the end of the test.

The granite intrinsic permeability used in the base case, $8{\cdot}10^{-18} m^2$, was derived as an average value taking into account the rock mass as well as the discontinuities. Although, the overall water entry value into the test area is thus preserved, it is implicitly assumed that this inflow takes place uniformly. An alternative analysis (KG) has been carried out in which the permeability corresponding more closely to the rock mass value ($10^{-18} m^2$) is used. This case would then be more representative of a zone in which water inflow from large discontinuities is absent.

The distributions of degree of saturation obtained using this lower value of rock permeability are shown in Figure 6.62a. It may be noted that granite desaturation initially takes place because the rock is now unable to supply enough water to the bentonite. As in the case described above, the rock finally resaturates and hydration can then proceed (Figure 6.62b). At the end of the analysis, the final state of saturation of the barrier is only just below that of the base case. Performance of other sensitivity analyses has demonstrated that the specific effect of rock permeability is in fact small.

The intricacy of the interaction between buffer and host rock becomes strikingly apparent when examining the effect of the retention curve of the bentonite using only the dry branch of the basic relationship used in the preoperational analysis, without considering any hysteresis effects. The significance of a possible rock desaturation is clear in this case (Figure 6.63). In analysis SH, desaturation of the granite occurs driven by the high suction values associated with the new retention curve. As the desaturation is maintained throughout the analysis, a very limited amount of hydration occurs, the average increase of the degree of saturation is only 4.1%. Contrasting results are obtained in the equivalent analysis where no rock

Table 6.2
Parametric study, "in situ" test

Analysis code	Variables modified
KB, KB1	Permeability of the bentonite
KBPG	Permeability of the bentonite-retention curve of the granite
KG	Permeability of the granite
PGSH	Retention curve of the bentonite-retention curve of the granite

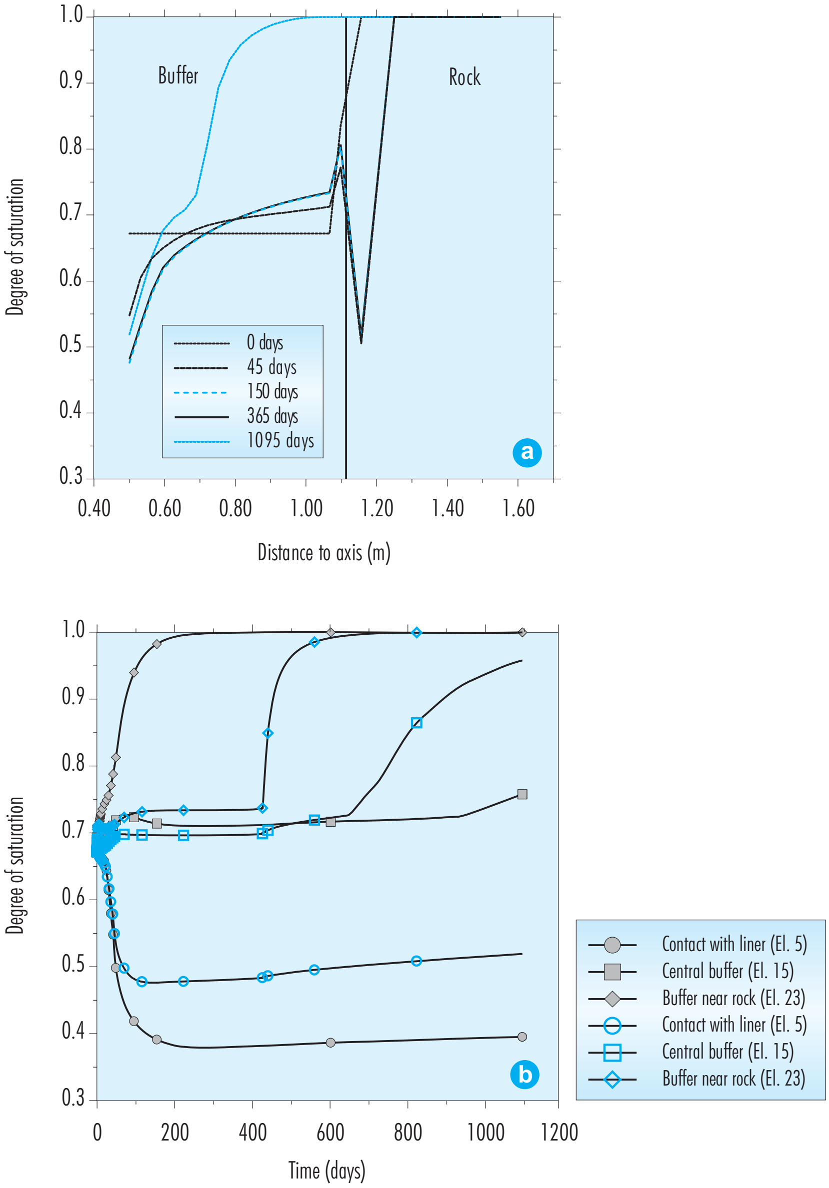

Figure 6.60: "in situ" test. a) Distributions of degree of saturation at various times. KB analysis. b) Variation of degree of saturation with time. KB analysis. The results of the 1-D Base Case analysis (grey symbols) are provided for comparison.

desaturation is allowed (PGSH). Now not only hydration proceeds unimpeded, but also full saturation of the buffer is achieved at the end of the test. The temperature field is also significantly changed due to the increased thermal conductivity associated with saturated bentonite.

In summary, it may be stated that the presence of the rock increases very significantly the complexity of the problem, leading sometimes to apparently paradoxical results. For instance, an increase in permeability may temporarily delay hydration if the enhanced water inflow manages to desaturate the rock. This study has also shown the extreme importance of the role of the retention curve in the analysis. The effects, however, are totally different depending on whether the rock desaturates or not.

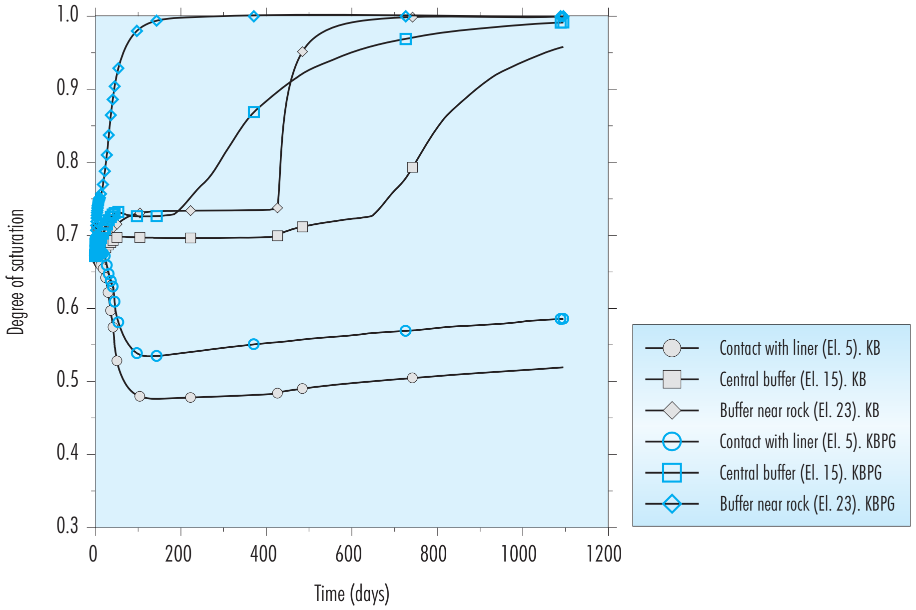

Figure 6.61: "In-situ" test. Variation of degree of saturation with time. KB (granite desaturation) and KBPG (no granite desaturation) analyses.

6.5.3. Operational modelling: the basic case

The installation of the clay barrier was completed on October 15th 1996. The phase of heating of the test, known as the 'operational stage', started on February 27th 1997. The design conditions of the test, with two heaters on were kept unchanged until February 28th 2002. The model results presented in this section include two main phases of the test.

- An initial isothermal hydration of the barrier of 135 days, to account for the hydration taking place in the period between the sealing of the drift and the start of heating.
- A simultaneous natural hydration and heating of the test with two heaters for 1827 days.

The numerical analysis presented in this section corresponds to the model coded as the 'OBC' model (Operational Base Case). As in the "mock-up" modelling, the OBC model attempts to incorporate all available information obtained from laboratory test of FEBEX bentonite at the beginning of the operational stage. No more adjustments have been made. To obtain a closer reproduction of the real geometry, a 2-D axisymmetric longitudinal section has been analysed, in which the most important geometrical features of the "in situ" test are represented [169]. The mesh distribution has been optimised taking advantage of the experienced gained in the study of the "mock-up" test. The outer boundary of the model is placed at a distance of 50 m from the tunnel axis. The geometry also takes into account the presence of the access drift and the concrete plug. The various components of the heater are represented but no gap between liner and buffer has been considered.

In this section the comparisons between experimental and model outputs are presented up to 31/12/2003 (day 2498). The numerical results presented here also include the simulation of the cooling and excavation stage. Therefore, it is possible to analyse the impact of the dismantling operations over the remaining clay barrier and the near field. Long-term predictions are also presented. The detailed modelling of the cooling and dismantling of Heater #1 is presented is Section 6.5.4.

6.5.3.1. Features of the analysis

The analyses performed start by simulating the excavation of the tunnel and subsequently allow suffi-

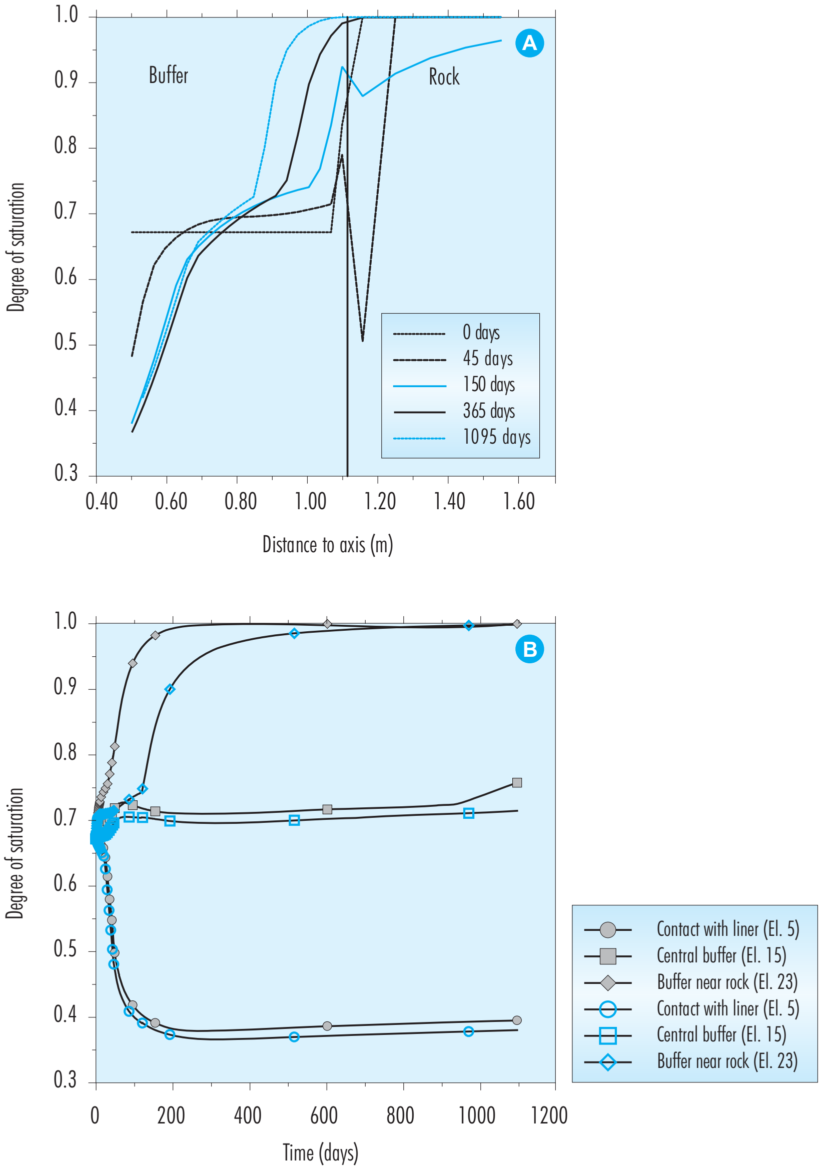

Figure 6.62: "in-situ" test. A) Distribution of degree of saturation at various times. KG analysis. B) Variation of degree of saturation with time. KG analysis. The results of the 1-D Base Case analysis (grey symbols) are provided for comparison.

cient time for both hydraulic and mechanical equilibration. Therefore the initial conditions for the granite correspond to the situation before tunnel excavation. As regards the mechanical variables, an initially uniform and isotropic stress field ($\sigma_r = \sigma_\theta = \sigma_z = 28$ MPa) has been assumed. Initial granite porosity is taken as 0.01.

In accordance with the measurements made during installation, an initial water content of 14% has been assumed for the clay barrier. This corresponds to a global degree of saturation of 0.55 and, from the retention curve adopted, an initial value of suction of 135 MPa. From the available installation data, an average dry density of 1.60 g/cm^3 has been adopted for the analysis. The initial stress in the bentonite is assumed to be isotropic and equal to 0.5 MPa. An initial uniform temperature of 12°C was assumed for the entire domain. A perfect con-

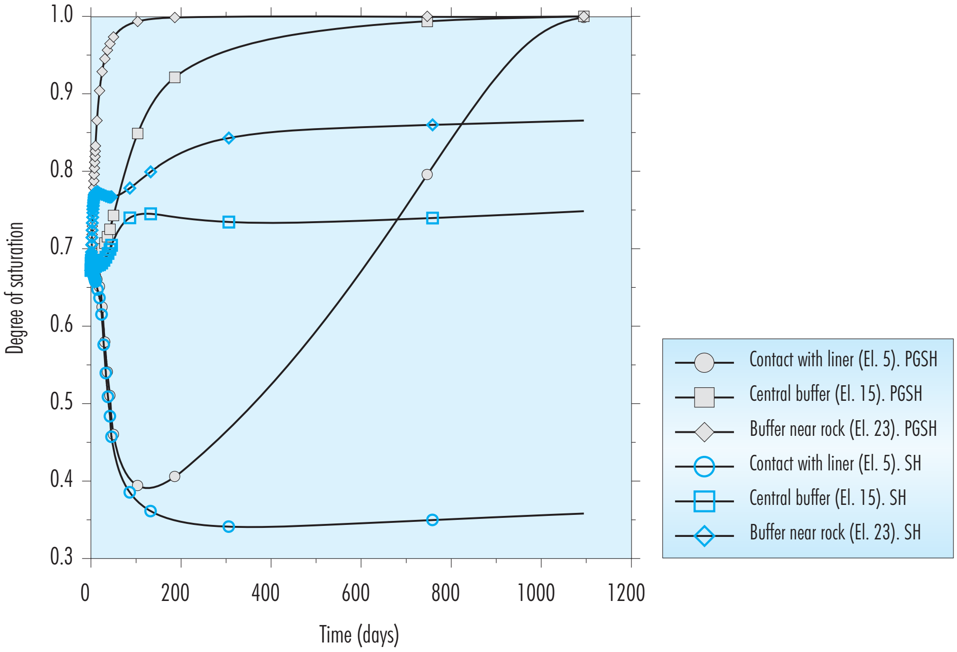

Figure 6.63: "In-situ" test. Variation of degree of saturation with time. Analysis SH (granite desaturation) and PGSH (no granite desaturation).

tact has been assumed between the steel liner and the bentonite and between the bentonite and the rock. According to the observations made, the water flow close to the tunnel is mainly radial, tending gradually towards the regional flow direction over a distance of 50 m. Therefore, it is assumed that the water pressure varies along the boundary, in accordance with water pressure measurements made in borehole sections far away from the test. In contrast to the "mock-up" test, the experiment is not considered airtight and a constant value of gas pressure is assumed.

The thermal and mechanical boundary condition prescribed at r = 50m are:

- Temperature, $T = 12$ °C
- Radial stress, $\sigma_r = 28$ MPa

The thermal boundary conditions applied at the heater location (radius = 0.385m) are:

- 0 -21 days Constant power: 1200W/heater
- 21-42 days Constant power: 2000 W/heater
- 42 days - t_{100} Constant power: 2400 W/heater
- t_{100} - 1827 days $T = 100$ °C

where t_{100} is the time required to reach 100 °C at some point in the bentonite (52 days).

The constitutive laws of the bentonite are practically the same as for the OBC modelling of the "mock-up" test (Section 6.4.3.1.). It has been assumed that the modelling of the "mock-up" test provides the most reliable information on bentonite behaviour. The only differences in bentonite parameters between the two tests are minor variations to account for the different initial densities [167]. Therefore the laws for thermal conductivity, intrinsic permeability and relative permeability of the "mock up" test have been retained in this analysis.

6.5.3.2. Results and comparison with observations

Clay barrier

Selected results of the OBC analysis are presented and compared with observations. Both point variables and global test parameters are considered. In fact, the only global test variable available for comparison is the power supplied to each heater. The results show that the heat power is under-predicted by 18% in Heater #2 and by 10% in Heater #1 [167], approximately. In spite of this, the model captures well the general trend of the test: after the switch from power control to temperature control, a reduction of the power lasting for about 400 days is observed, then power stabilises and, finally, a slight tendency to increase in time is observed. Heater #2 maintains the target temperature of 100 °C at the hottest point of the contact with the bentonite at all times. Therefore, to keep this temperature constant the power requirements at Heater #2 increased by about 5% after the switching off of Heater #1. As may be observed in Figure 6.64, the model predicts well the need for increasing heater power, although by about 10%.

The overall power evolution is well reproduced by the model. This suggests that the physical assumptions of the model are correct and that the differences noted might be due to discrepancies in the parameters adopted, for instance the thermal conductivity of the rock, or, perhaps, some 3-D effects not properly considered in the axisymmetric model.

In relation to the evolution of temperature, the larger influence of the cooling of Heater #1 is observed, as expected, in sections close to this heater (i.e. see Sections G or I) whereas in sections far from Heater #1 the changes are practically negligible (i.e. Sections D2). As in the “mock-up” test, a tendency towards a slight increase of the power of Heater #2 and of the temperature as hydration progresses is predicted in the long-term simulations [167].

In relation to the hydraulic problem, the examination of the evolution of sections *C, E1* (results until just before the cooling of Heater #1) *F2* and *H* (Figure 6.65) makes it possible to conclude that the response of the model is globally satisfactory, taking into account the possible influence of the heterogeneities of the natural system on the hydration of the barrier. Generally the correspondence between computations and measurements is quite good although at some points near the heater the drying observed is somewhat stronger than computed. It may be observed that Section *F2* is not affected by dismantling operations. In the more internal sensors of section *H*, a tendency to a rapid increase in relative humidity may be observed just after the switching off of Heater #1. This fact might relate to a condensation of the water vapour due to the reduction of temperature. The model captures this tendency and the general evolution of the relative humidity. Finally, Figure 6.66 presents the long-term predictions in terms of relative humidity. In this test there is no clear evidence of the slowing down of saturation although there may be some slight indications in the records of the outer relative humidity sensors of some sections [167]. Observations extending over longer times are required to confirm this possibility.

The determination of total stresses in the "in situ" test is subject to important uncertainties that make it difficult to establish reliable comparisons with the results of the analysis. At the beginning, the model results appear to provide an upper bound to measurements that might be consistent with the fact that the stress cells started to give readings sometime after the start of the test. The comparisons between the time variation of the recorded stresses and those obtained from the model are presented for sections *C, E1* (results until just before the cooling of Heater #1), *E2,* and *F2* in Figure 6.67. It is difficult to quantify the behaviour of the model in this area because of the variability of the observations made. The mechanical sensors under operation correspond to sections not significantly affected by the dismantling operations. The model predicts a maximum stress of about 4.5 MPa (Figure 6.68).

Host rock

The under-prediction of temperatures observed in the clay barrier is repeated in the rock mass (Figure 6.69). It is interesting to note that differences vary depending on the borehole direction, i.e. the thermal field is not axisymmetric. Of course this type of variation cannot be reproduced by an axisymmetric model. The effect of the cooling of Heater # 1 is general and affects the whole near field, being more relevant in zones and radii closer to that Heater. The model predicts correctly the measured temperature decay in the granite. Long-term predictions show a tendency towards a very gradual increase of temperatures in the host medium (Figure 6.70).

Water pressure in the rock is also well described by the analysis (Figure 6.71). Pressure values are of the correct order of magnitude and, in particular, rates of pressure recovery are captured well. The dismantling operations do not have a significant effect on rock liquid pressure and the model does not show important changes in this variable. The liquid pressures remain practically constant in the long term.

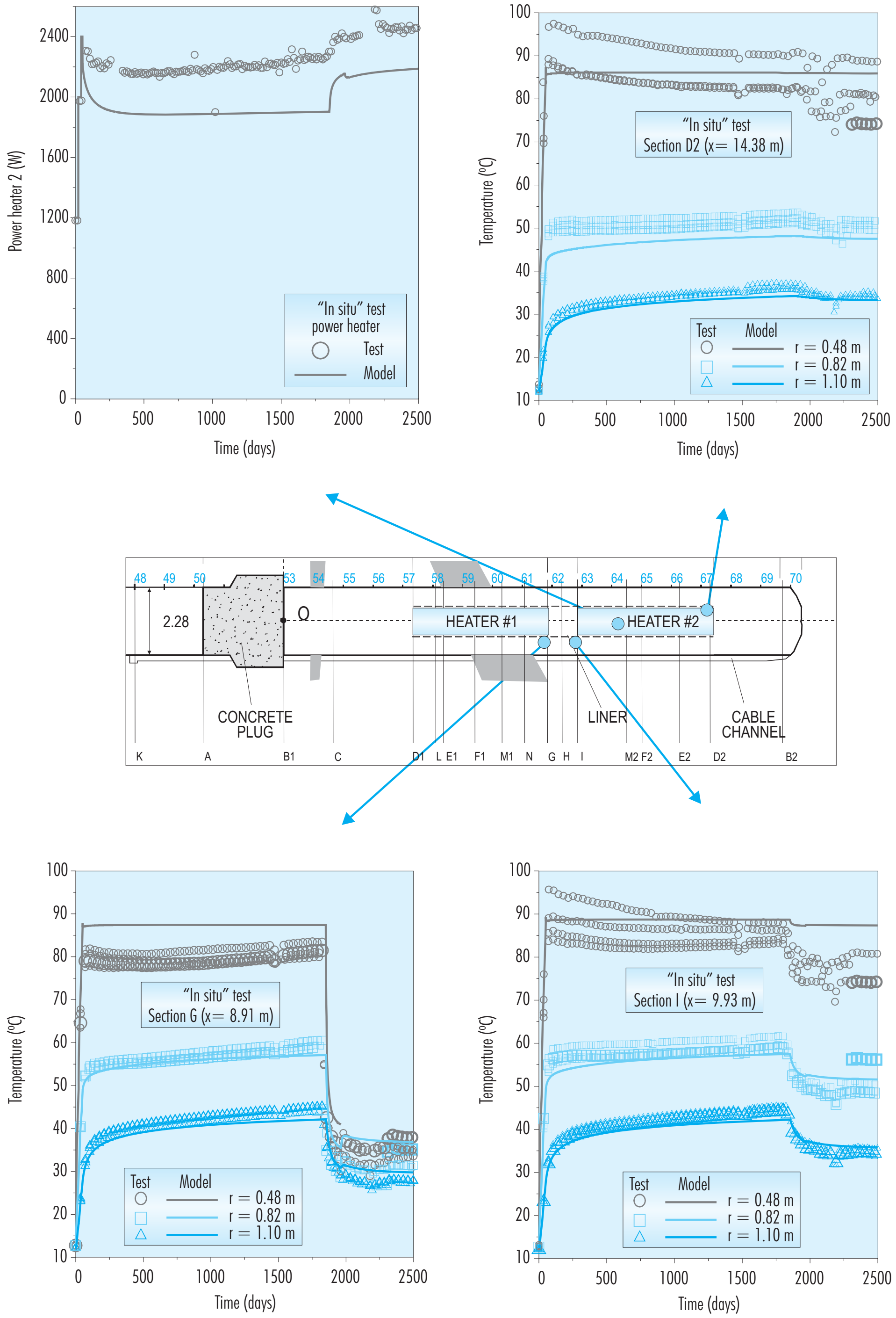

Figure 6.64: Evolution of thermal variables in the "in situ" test. Power of Heater #2 and temperature in sections D2, G and I (clay barrier). Observed versus computed values including operation after partial dismantling (OBC model).

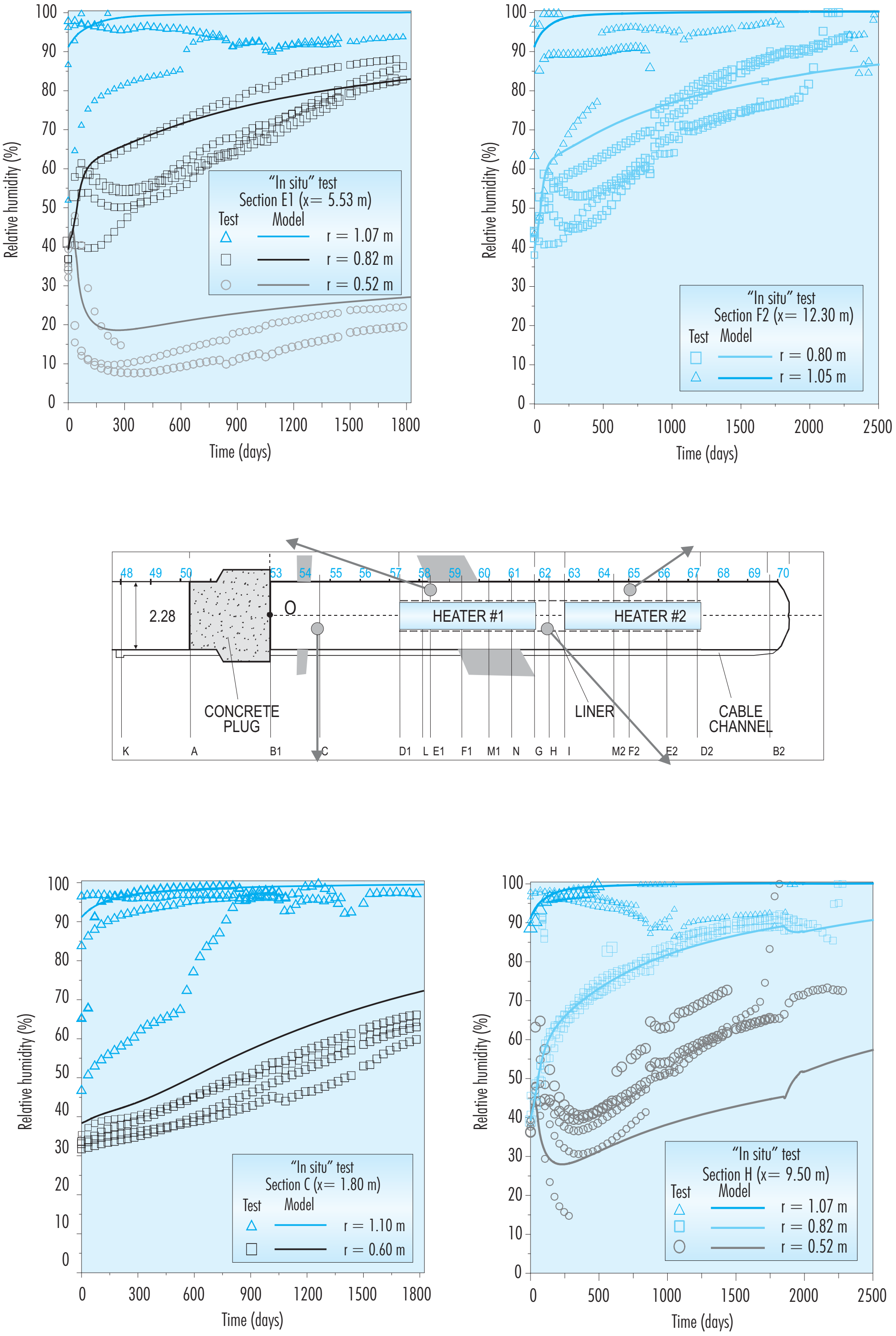

Figure 6.65: Observed versus computed values of relative humidity. Sections E1, F2, C and H (clay barrier) of the "in situ" test (OBC model).

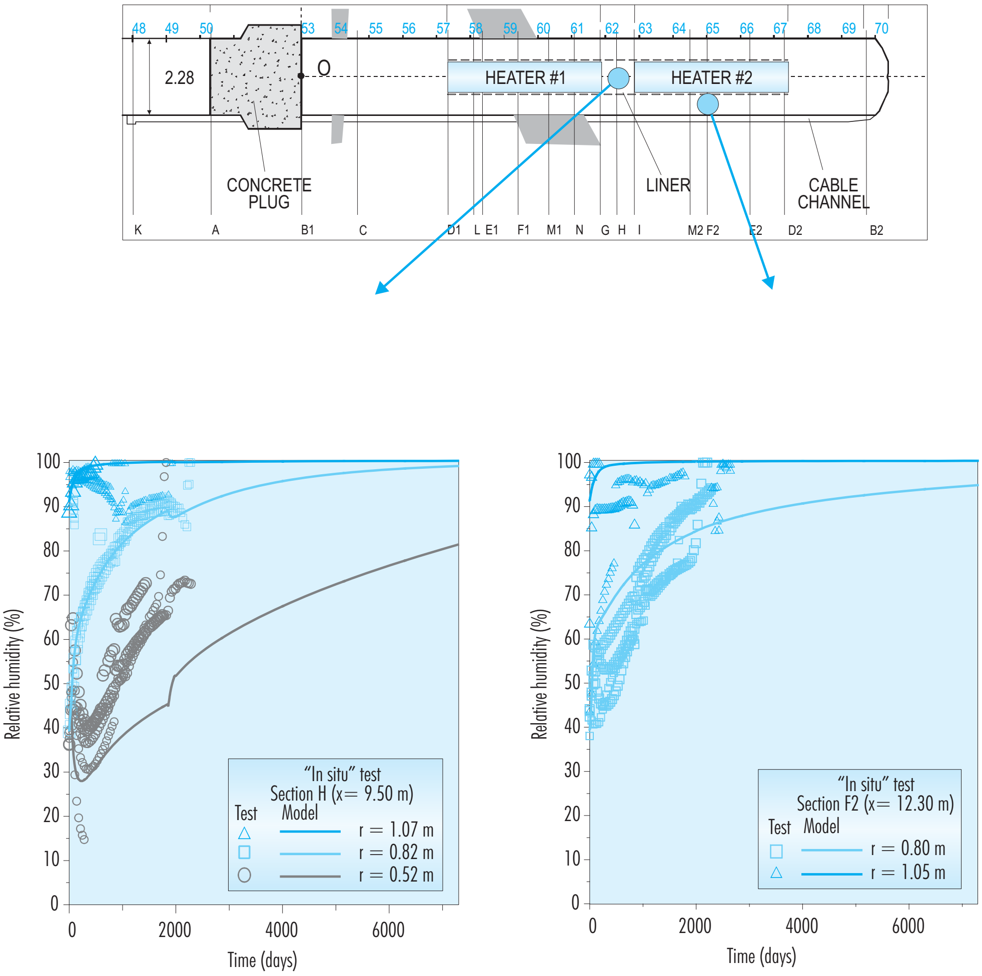

Figure 6.66: Long-term predictions of relative humidity Sections H and F2 (clay barrier) of the "in situ" test (OBC model).

Uncertainties also affect total stress measurements in the rock (Figure 6.72). Some features of the observations appear, however, to be reasonably accounted for:

- Differences between the various stress components are minor (i.e. stress state is not far from hydrostatic).
- Rock normal stresses are higher closer to the buffer, reflecting the variable thermal field.

The measured radial displacements in the rock are very small (Figure 6.73) making it difficult to discern a clear trend. Generally the model also predicts small displacements, although slightly larger than those measured.

The combined effects over the near field of the cooling of Heater # 1 and the excavation of the clay barrier may be clearly observed in the mechanical variables. The model captures well, in qualitative terms, the reduction measured in stresses and radial displacements after the dismantling operations (Figure 6.72 and Figure 6.73). The long-term predictions show a tendency to a slight recovery of these values as time goes on.

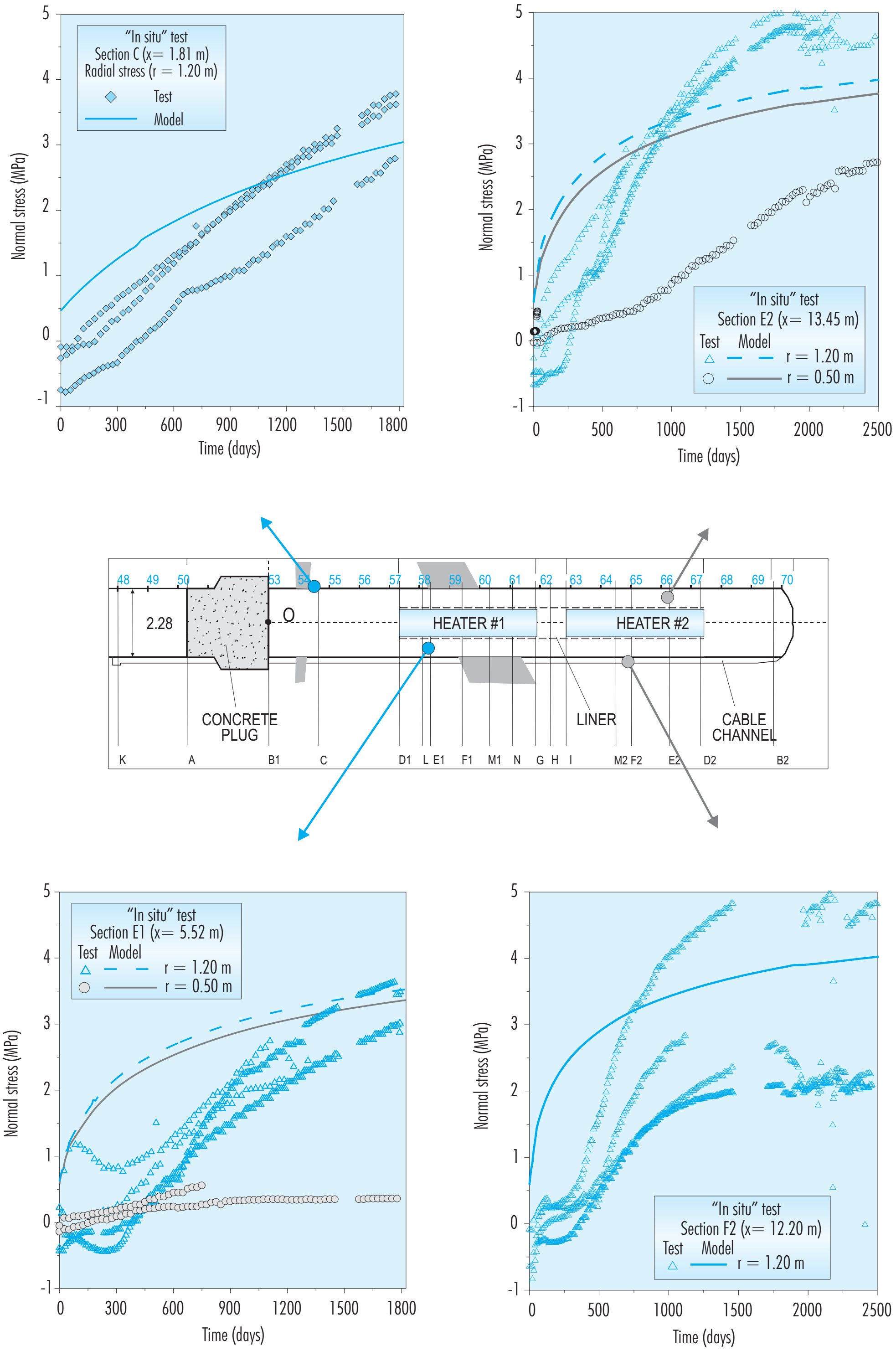

Figure 6.67: Observed versus computed values of stresses. Sections C, E1, E2 and F2 (clay barrier) of the "in situ" test (OBC model).

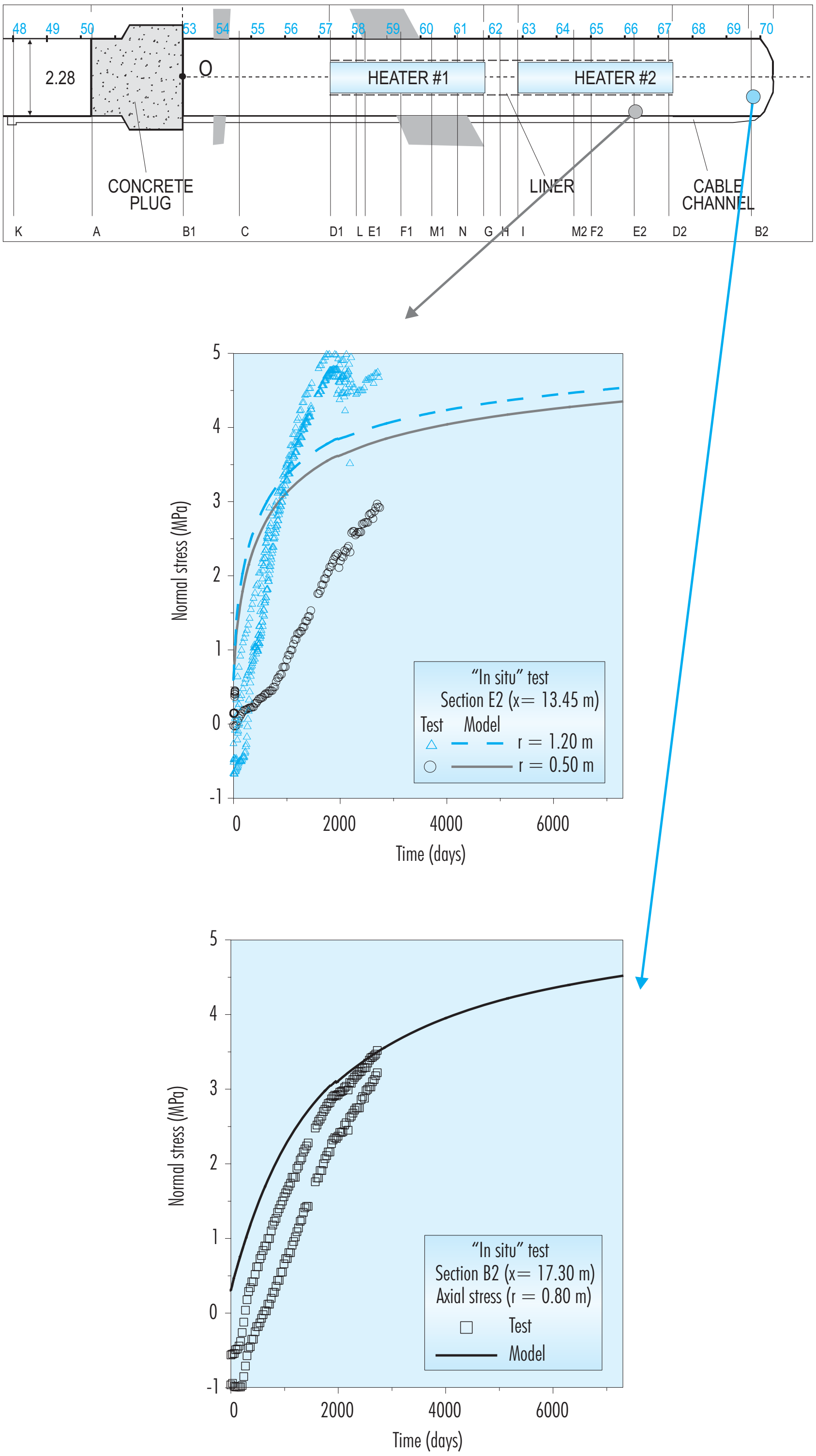

Figure 6.68: Long-term predictions of stresses in the "in situ" test. Sections E2 and B2 (clay barrier). Observed versus computed values (OBC model).

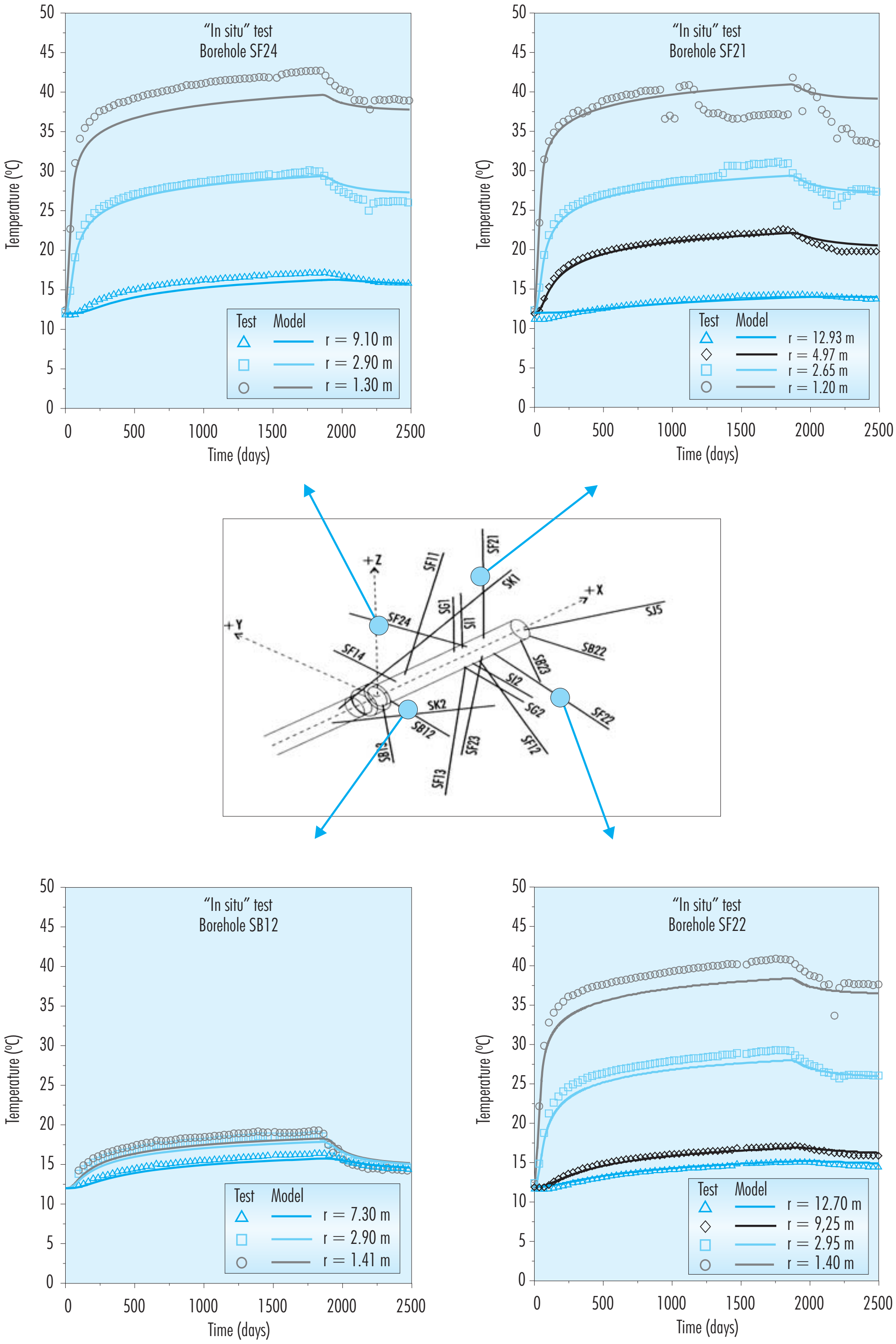

Figure 6.69: Evolution of temperature in the "in situ" test. Sections SF4, SF1, SB12 and SF22 (host rock). Observed versus computed values including operation after partial dismantling (OBC model).

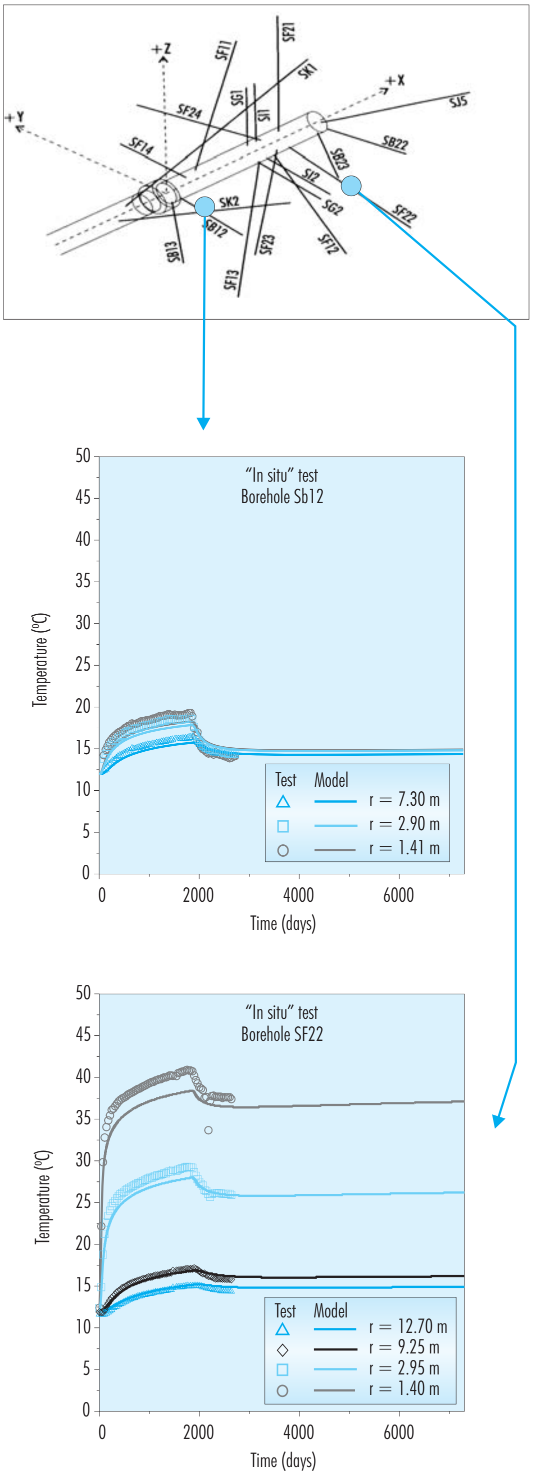

Figure 6.70: Long-term predictions of temperature in the "in situ" test. Sections SB12 and SF22 (host rock). Observed versus computed values including operation after partial dismantling (OBC model).

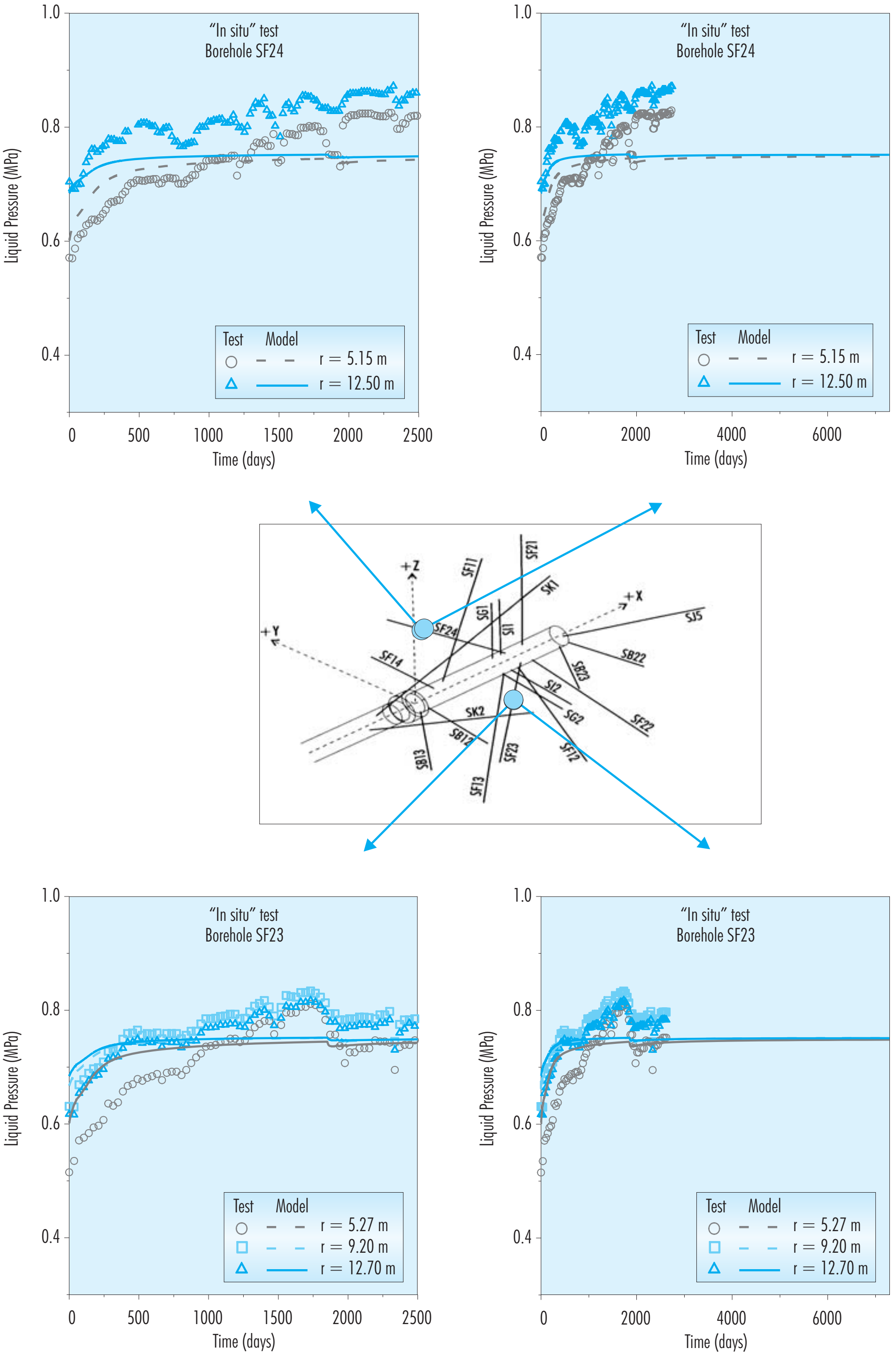

Figure 6.71: Observed versus computed values of liquid pressure and long-term predictions including operation after partial dismantling. Sections SF23 and SF24 (host rock) of the "in situ" test (OBC model).

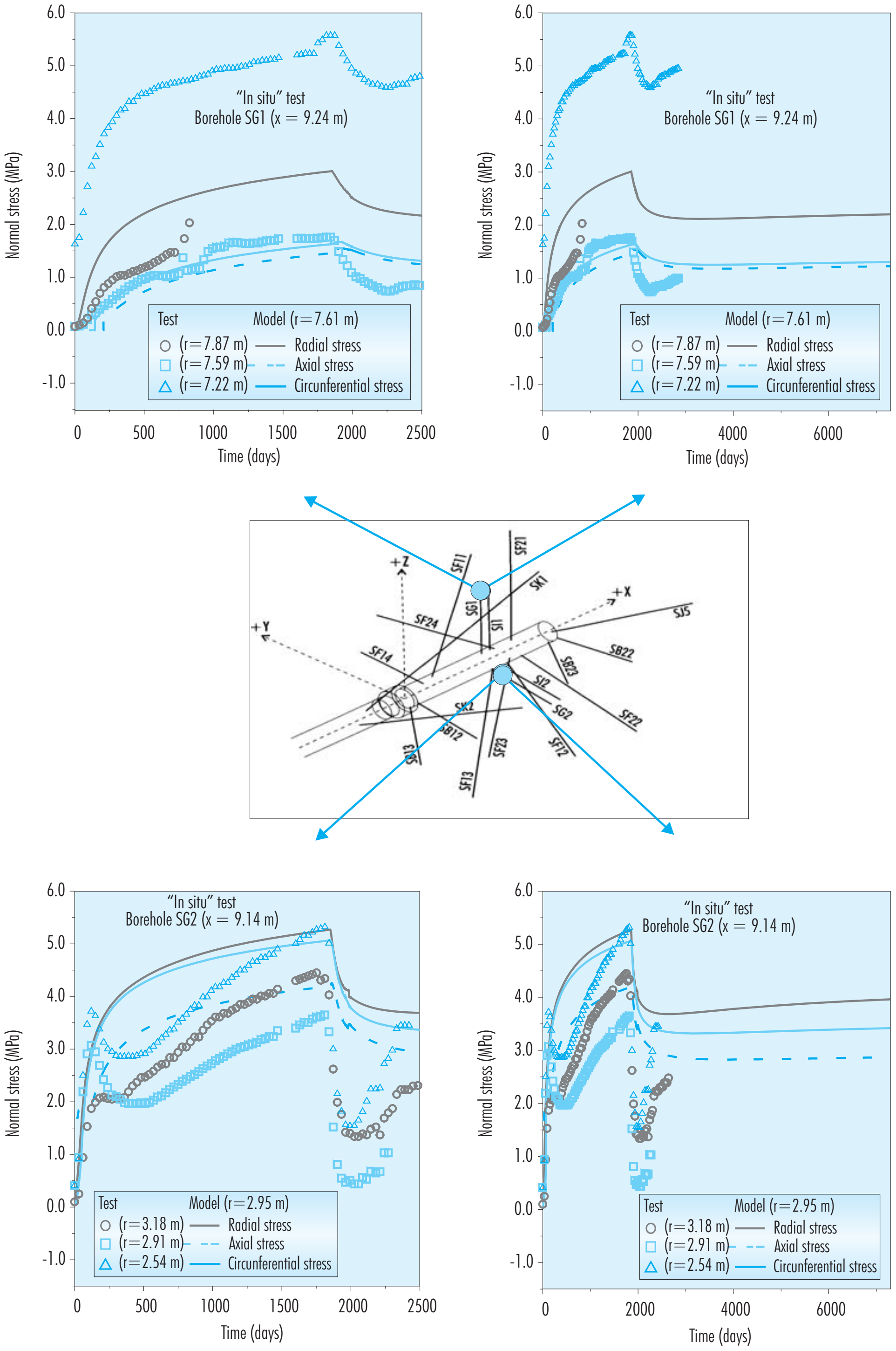

Figure 6.72: Observed versus computed values of stresses and long-term predictions including operation after partial dismantling. Sections SG1 and SG2 (host rock) of the "in situ" test (OBC model).

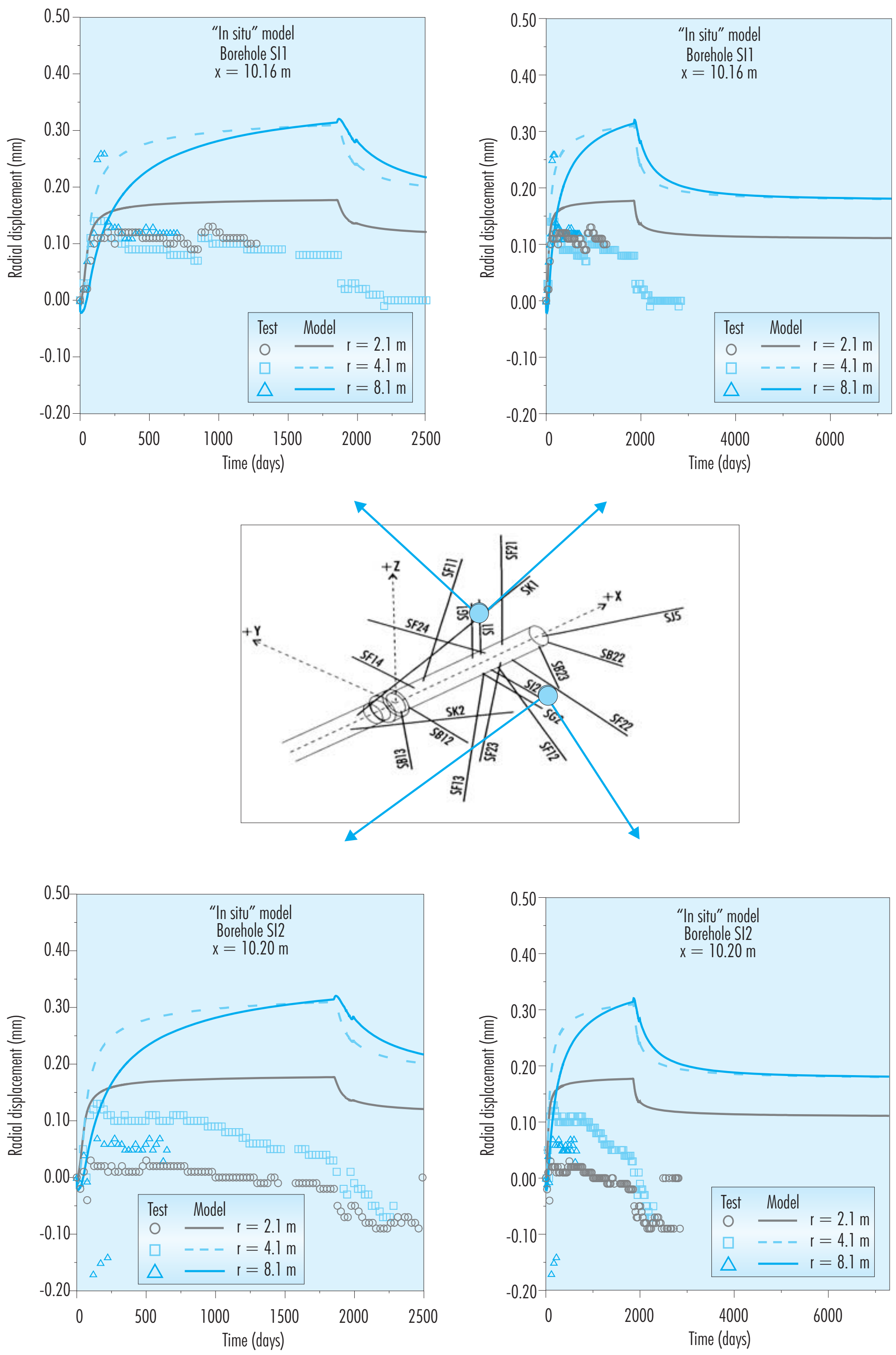

Figure 6.73: Observed versus computed values of radial displacements and long-term predictions including operation after partial dismantling. Sections SI1 and SI2 (host rock) of the "in situ" test (OBC model).

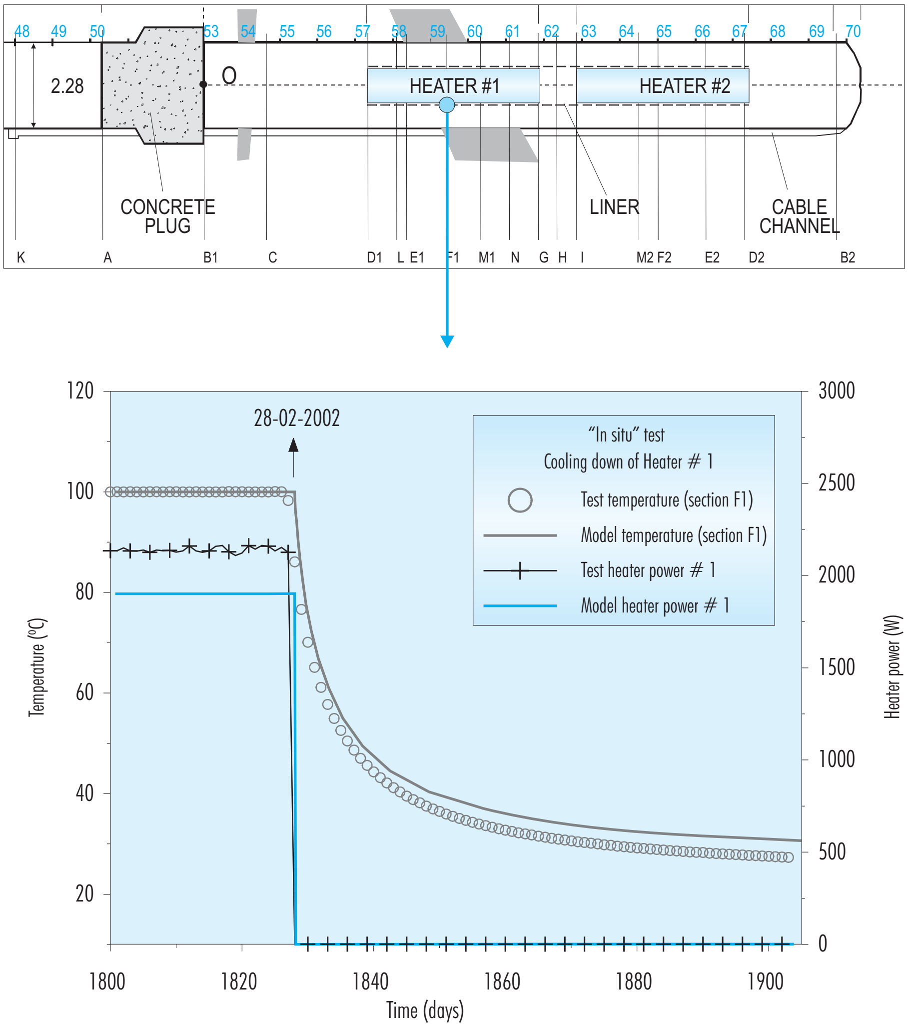

Figure 6.74: Evolution of temperature and power of Heater # 1 during cooling in section F1.

6.5.4. Analysis of cooling and dismantling

The partial dismantling of the "in situ" test was carried out after five years of continuous heating. The operation included the demolition of the concrete plug and the removal of the sections of the barrier corresponding to Heater #1. The objective was to carry out the partial dismantling causing minimum disturbance to the sections of the test in the region of the second heater, which remained in operation at all times. A new concrete plug was constructed immediately after excavation. New instrumented sections have been incorporated in this stage of the project (Chapter 4). Finally, it is important to highlight that the process of data acquisition was maintained throughout all the dismantling operations.

A detailed description of the work performed during the partial dismantling of the "in situ" test may be found in Chapter 4 and reference [187]. Here, a summary of the sequence of dismantling operations is presented as follows:

- ❑ Switching off Heater #1, one month before plug demolition.

- ❑ Demolition of the concrete plug (sampling).
- ❑ Removal of bentonite up to the front of the first heater (sampling).
- ❑ Extraction of Heater #1.
- ❑ Removal of liner and bentonite buffer up to the target point (sampling).
- ❑ Insertion of a one-metre dummy steel cylinder in the central hole.
- ❑ Installation of new instruments.
- ❑ Construction of the shotcrete plug.

After exactly five years of uninterrupted heating, Heater #1 power was switched off on 28/02/2002. Based on the results of numerical analysis [175], it was decided to switch off Heater #1 in a single stage. Figure 6.74 shows the variation of the power of Heater #1 and the temperature in the heater/bentonite interface in section F1. It may be observed that up to day 1827 (28/02/2002) the heating of the test was controlled, a temperature of 100 °C being prescribed at the interface. From this date on, this thermal condition was released and this zone of the barrier cooled down. It may also be observed that the model predicts very well the temperature decay in this section.

The dismantling operations have been modelled assuming the following main stages:

- ❑ Start of plug demolition: 02/04/2002 (day 1860).
- ❑ End of plug demolition: 28/05/2002 (day 1916).
- ❑ Start of bentonite excavation: 29/05/2002 (day 1917).
- ❑ Start of Heater #1 extraction: 19/06/2002 (day 1938).
- ❑ End of excavation: 19/07/2002 (day 1968).

The dates of the stages considered in the analysis correspond to those followed in the field [187]. Figure 6.75 shows schematically the dismantling steps considered. The excavation of the materials, the inclusion of new ones (for instance the dummy canister and the new concrete plug) and the new boundary conditions have been modelled trying to keep as close as possible to the actual test conditions.

A specific computational module has been developed to handle some of the specific characteristics of this test stage, including, for instance, the large swelling of the FEBEX bentonite. Figure 6.76) presents the contours of longitudinal displacement computed in the different excavation stages. It may be observed that the effect of confinement relaxation is quite local and affects only zones close to the excavation front.

New instruments were installed in the remaining part of the test in order to increase the density of measurements in the buffer and also to extend the life expectancy of the monitoring system. The additional instrumentation installed in the buffer consists mainly of relative humidity and total pressure sensors. Details regarding the type of sensor, installation and location may be found in Chapter 4 and reference [187]. The measurements of the total pressure cell in section *G* (at the end of the dummy canister) show a quick increase, while the model predicts a gradual increment of the longitudinal stress in this zone (Figure 6.77). This difference might possibly be attributed to the fact that the model considered a 'normal hydration' whereas, in this zone, there might be a faster hydration due to local water entry associated with the presence of the lamprophyre or, perhaps, to the effects of the dismantling operation. On the other hand, it seems that the total pressure cells in section *F2* are not yet recording load reliably. Finally, Figure 6.78 shows the results from the new relative humidity sensors; it may be observed that the model predictions in these sections are quite good.

During dismantling a large number of samples were extracted from the barrier. The sampling operations and the subsequent transport of the samples were carried out trying to minimise changes in the specimens. A detailed description of the techniques used in these activities is presented in Chapter 4 and reference [187]. The samples obtained from the partial dismantling have been tested in the laboratory to examine the state of the FEBEX bentonite after five years of simultaneous heating and hydration. The tests were aimed at the study of the main thermal, hydraulic, mechanical and chemical properties of this material.

This section focuses on analysis of the water content and dry density measured during the partial dismantling operation and the comparisons of these experimental results with model predictions. All the sampling carried out throughout the dismantling operations was documented with all the relevant aspects graphically recorded with digital photos and video. For example, Figure 6.79 corresponds to a typical section found during the dismantling process. A rather homogeneous material may be observed, with practically complete closure of gaps and joints between blocks. This fact has been confirmed experimentally with the measurements performed in the blocks, because it was not possible to detect any effect of a possible preferential flow of water through the joint between blocks. The water content and density distribution in the blocks follow the pattern imposed by the radial flow that was observed in all drift sections [188]. Therefore, it seems that the assumption made in the modelling, considering a porous medium without joints (between blocks) and gaps, has been experimentally confirmed by the post-mortem observations.

A complete description of the procedures and the experimental techniques followed in the laboratory to measure water content and dry density in samples of FEBEX bentonite is included in [189, 188] and the experimental results presented in this analysis are reported in [188]. As concluded in reference [188], the distribution of the measurements of water content and dry density exhibits a clear radial symmetry. Only minor changes in water content are observed near the drift wall, probably due to a preferential flow of water along the contact of the drift with the transducer wire runs. As an example, Figure 6.80 presents contour maps of water content and dry density obtained from laboratory data [188], in which the radial symmetry of the experimental results may be clearly observed. This implies that the results computed with the axisymmetric model, presented before, may be readily compared with the experimental measurements.

Figure 6.81 and Figure 6.82 present the comparisons between experimental and model data in selected sections. The graphs correspond to values of water content and dry density plotted as a function of the distance to the tunnel axis. A strong reduction in dry density may be observed in the 20 cm nearest to the rock, indicating the swelling of clay in this area associated with an increase in water content. These Figures show that the agreement between the experiment and model predictions is good. Obviously there are some limited differences that might be attributed in part to the fact that it is practically impossible to reproduce exactly with the model the stress paths followed by the material during the sampling and transport processes.

Finally, Figure 6.83 shows the contour map of the degree of saturation obtained experimentally [188] and the contour map of the degree of saturation predicted by the model. A good qualitative agreement may be observed also as regards this variable.

6.6. Conclusions

In this Chapter the work carried out regarding the numerical modelling of the Thermo-Hydro-Mechanical behaviour of the FEBEX experiment has been presented. The analysis has focused on the two large-scale tests: the “mock-up” test and the "in situ" test. One of the main objectives has been to identify the relevant phenomena and processes that control the Thermo-Hydraulic-Mechanical behaviour of the engineered barrier components. A general THM mathematical approach for the analysis of coupled problem in porous media has been developed. An essential aspect of the approach is the description of material behaviour through appropriate constitutive laws. Important efforts have been made to develop these laws for the thermal, mechanical and hydraulic aspects of the general THM problem. The laboratory tests carried out in the context of the FEBEX project have been used to select the constitutive equations and to determine the model parameters.

In relation to the “mock-up” test, the operational model (OBC) was formulated using a full THM approach for a single porosity medium, in which all the processes and couplings deemed relevant at the time were considered. The comprehensive laboratory work carried out within the context of the FEBEX project has allowed for the identification of the main model parameters required for a ‘standard THM model’. However, the results obtained with this model cannot be considered completely satisfactory, because the simulation over-predicts the hydration rate of the barrier during the later stages of the test. Comparing experimental data versus model results, a slowing down in the hydration kinetics of the test may be observed. A tendency to maintain a very low rate of water intake and nearly constant values of the main variables at different radii of the barrier may be observed in all the sections of the test, with a more marked trend in the cross-sections that include a heater. Changes in the constitutive laws or their parameters could not reproduce accurately the test evolution. Similar difficulties were identified by other groups, using different numerical codes to simulate the evolution of the barrier.

It is possible that a ‘standard THM model’ may have some shortcomings when reproducing the barrier behaviour described above. Generally, the formulation considers a progressive increment of hydraulic conductivity as saturation goes on, especially due to the increment of relative permeability. However, experimental evidence reflects that the behaviour of expan-

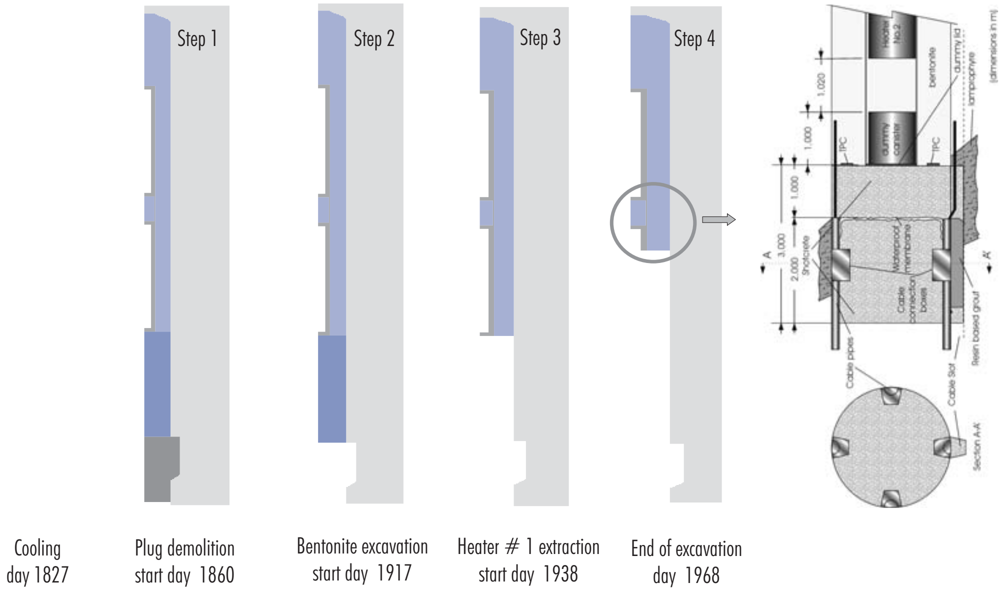

Figure 6.75: Excavation stages considered in the modelling.

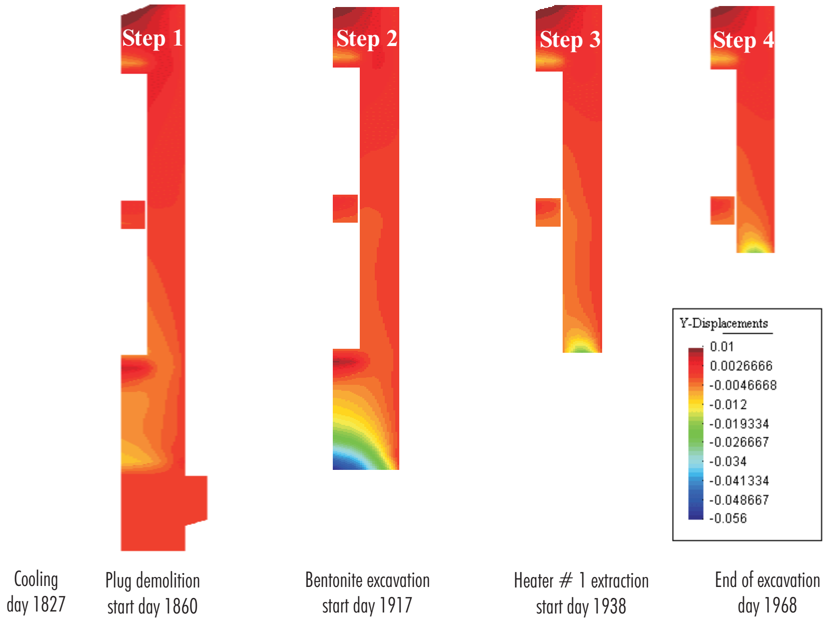

Figure 6.76: Axial Displacement during excavation.

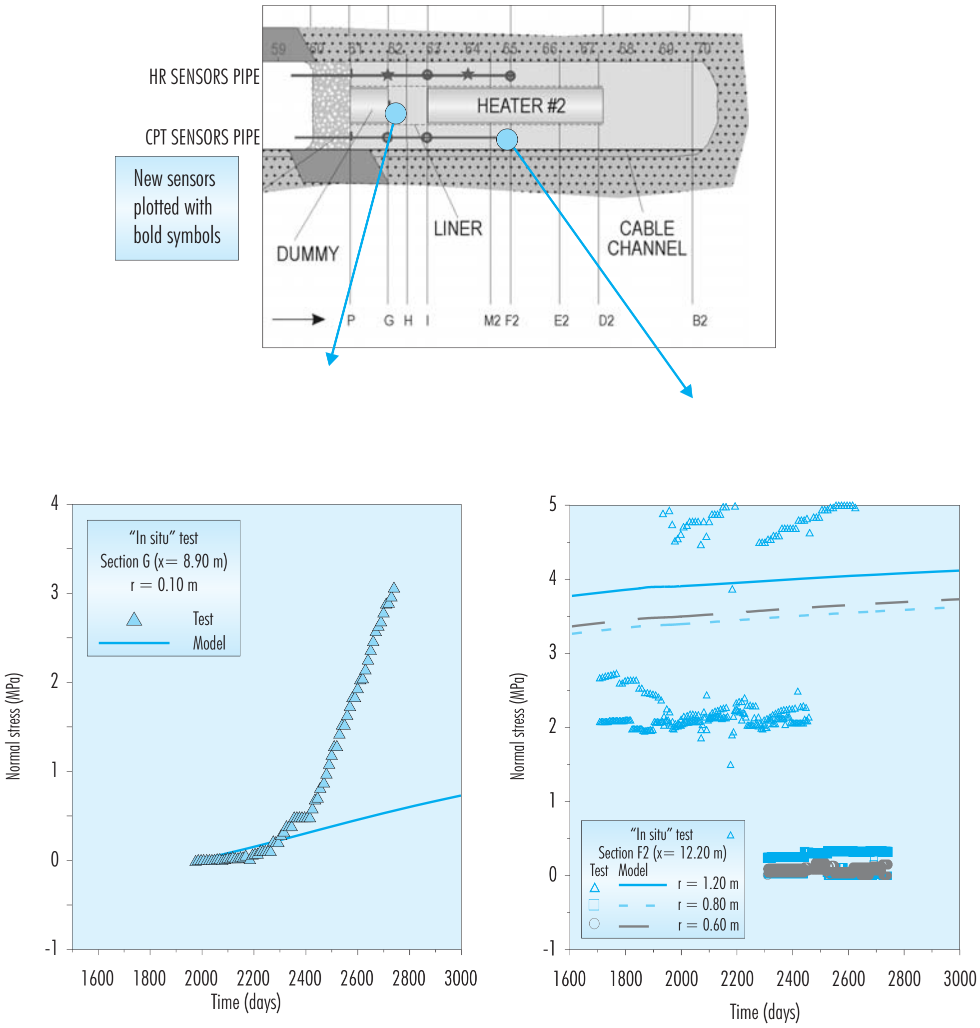

Figure 6.77: Computed and measured values of stresses from the new sensors. Sections G and F2 (clay barrier) of the "in situ" test (OBC model).

sive clays under hydration is more complex. The simulation difficulties of the "mock-up" test might be ascribed to the presence of other processes or phenomena, which were not contemplated in the 'OBC' model. A series of developments have been carried out in order to include in the analyses additional phenomena that might explain, with physical bases, the observed barrier behaviour. Each of the proposed mechanisms may explain, to some extent, the observed response of the experiment.

In this context, a double structure framework has been developed and applied to the simulation of the THM behaviour of the "mock-up" test. The explicit consideration of two structural levels provides an opportunity to define separate properties and constitutive laws, in order to consider the main processes that take place in each pore level, and to take into account the coupling between both pore structures. In the case of the FEBEX bentonite these two levels of pores have been identified. The modelling results may be considered to reproduce satisfactorily to a large extent the main tendencies of the observed behaviour. In this framework, the mechanical constitutive law may be viewed as being the core of the model, because stresses and void ratios (macro and

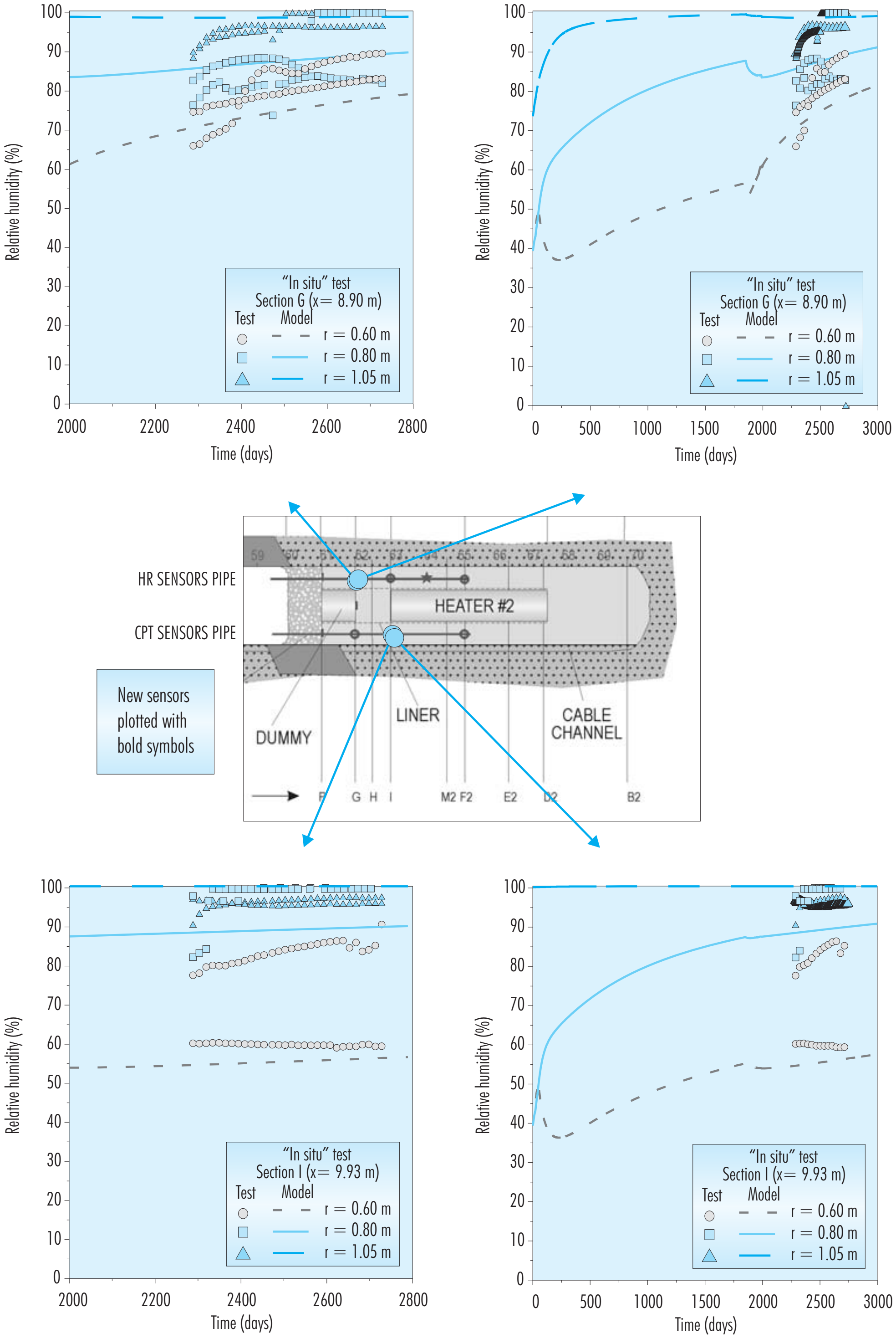

Figure 6.78: Computed and measured values of relative humidity from the new sensors. Sections G and I (clay barrier) of the "in situ" test (OBC model).

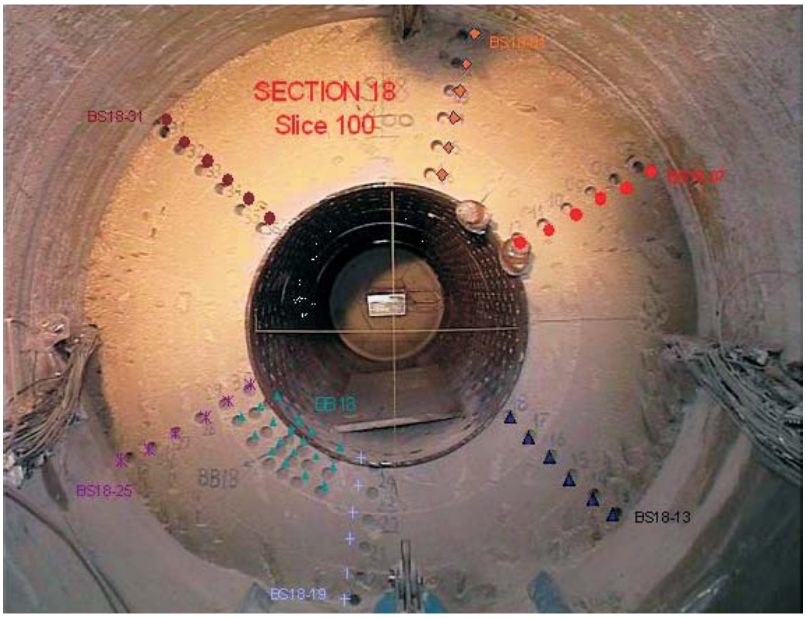

Figure 6.79: Photograph of a typical section including the position of samples [188].

micro) are updated using this law when changes in the state variables of the problem (suctions, temperature and deformations) occur. In addition, the permeability field depends on the pore structure.

The analysis shows, in an integrated way, how changes in the state variables of the problem affect the evolution of the main variables, and helps to better understand some trends of the observed barrier evolution. According to the model results, as the barrier hydration advances, the pores available for the main liquid flow undergo a progressive reduction, mainly due to the swelling of the microstructure under confined conditions. As a result, the full saturation of the barrier is delayed very significantly. This type of hydration-locking is evident in zones close to the heater, because the reduction of the permeability in the zones close to the hydration front reduces the liquid supply to the inner zones that are subjected to heater-induced drying. On the other hand, it is important to bear in mind that the temperature has been maintained constant in the contact between the heater and the bentonite (equal to 100 °C) throughout the analysis, but, under real repository conditions, the waste temperature will reduce progressively as time elapses. Consequently, the conclusions of the analysis presented here should not be directly extrapolated to other situations.

Finally, it may be concluded that standard models, such as OBC, allow for understanding and reproduction of the main THM phenomena in the clay barrier. This kind of models shows good agreements with the experimental results, especially in the short term, and in general the qualitative results are satisfactory. When medium and long-term responses are analysed, however, it may be necessary to incorporate other physical phenomena (i.e. microstructural changes, threshold gradient, chemical coupling) in the formulation to achieve a closer representation of the actual behaviour of expansive clays. The availability of laboratory tests conducted under similar conditions to the ones expected in a repository is a crucial requirement in order to develop models better adapted to the material behaviour under the expected THM and geochemical conditions.

The modelling of the "in situ" test has also led to advances in the understanding of the main *THM* processes and of the phenomena that take place in the clay barrier and near field under actual field conditions. In this experiment the problem is more com-

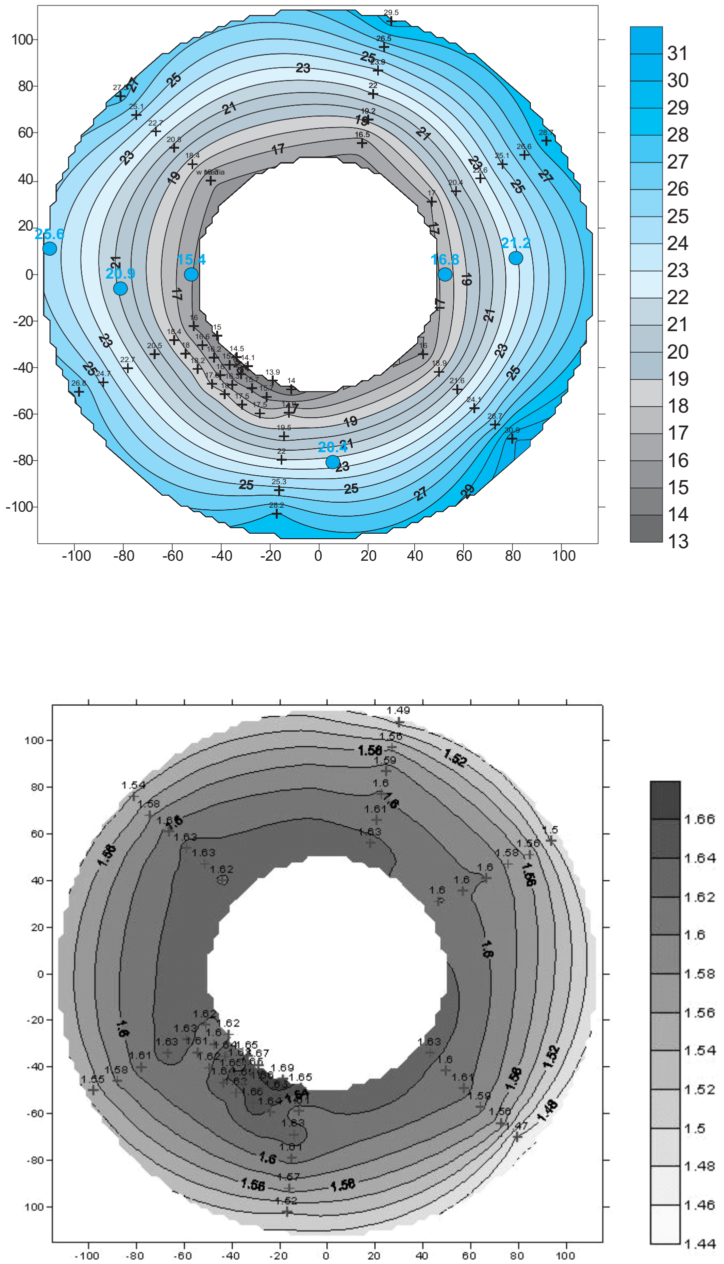

Figure 6.80: Contour maps of water content and dry density obtained from experimental data [188].

plex than in the case of the "mock-up" test due to the heterogeneities and uncertainties inherent to a natural system. In any case, the operational model has been able to explain and to reproduce the main tendencies observed in the experiment, both in the clay barrier and in the host rock. It seems that, in spite of the presence of heterogeneities in the host medium, the homogeneous axisymmetric model is capable of satisfactorily predicting the main tendencies observed in the rock. In relation to the clay barrier, the experiment may show a tendency to a slower hydration in some sections, similar to that

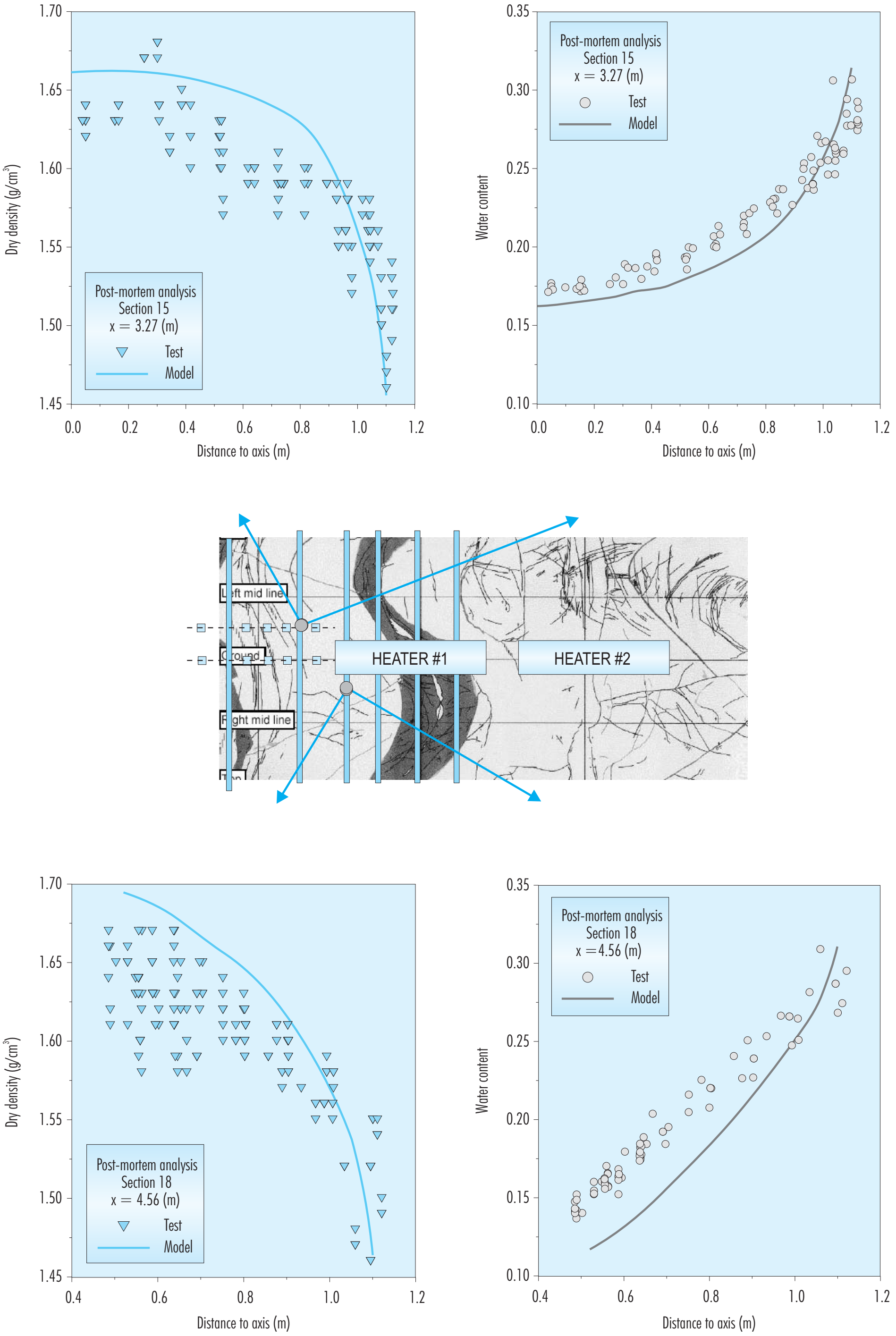

Figure 6.81: Computed and measured values of dry density and water content in sections 15 and 18. Post-mortem analysis of "in situ" test (OBC model).

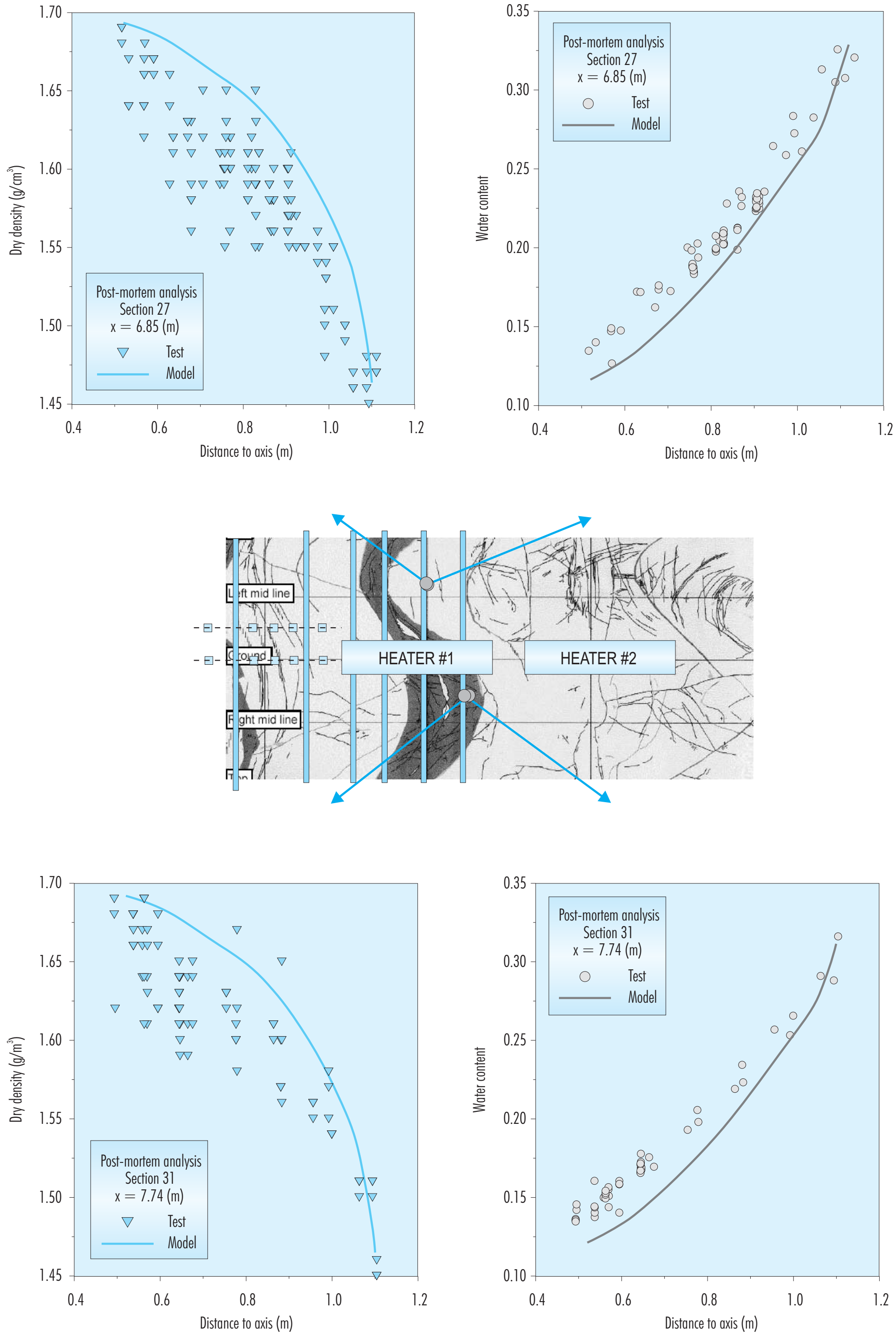

Figure 6.82: Computed and measured values of dry density and water content in sections 27 and 31. Post-mortem analysis of "in situ" test (OBC model).

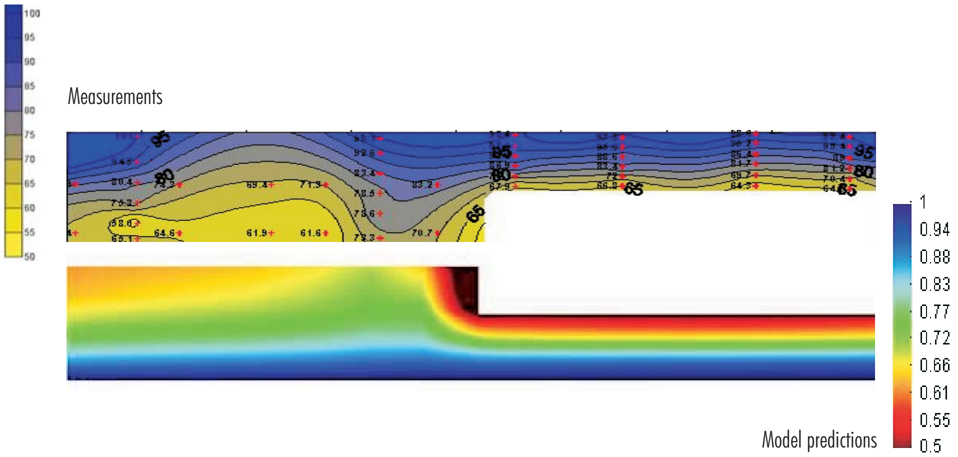

Figure 6.83: Contour maps of degree of saturation. Model predictions and experimental data [188].

observed in the "mock-up" test. However, this trend is now much less clear, at least as far as the measurements obtained up to the partial dismantling of the test is concerned. Note that the global density of the bentonite in this test is lower than that in the "mock-up" test. This fact might imply either that these kinds of phenomena are less noticeable or that they appear at more advanced stages of hydration. The difference in geometry might also be a factor. It is expected that the long-term evolution of the "in situ" test will help to clarify this issue.

The analysis of the partial dismantling of the "in situ" test has also contributed to a better understanding of the behaviour of this kind of system. From a modelling point of view it was necessary to develop special numerical tools to simulate the excavation of highly expansive materials. Satisfactory model predictions have been obtained in the modelling of the different stages of the partial dismantling: cooling, excavation and post-mortem analysis. This study confirms the reliability of the formulation and computer code to predict the THM behaviour of the engineered barrier components under different scenarios and generalized stress-paths. Finally, the dismantling observations of the "in situ" test have also confirmed some of the hypotheses of the modelling of the FEBEX tests, such as the assumption of barrier homogeneity and the axial symmetry of the problem.

Throughout this modelling work, developments affecting the formulation, code and constitutive laws have been continuous. The basic THM approach and computer program, initially developed during the phase of 'previous modelling', have been significantly improved up to the present time. Changes have centred on the inclusion of new THM phenomena in order to allow for a more complete representation of the problem, with special attention given to the possibility of considering the effects of the clay structure and its evolution.

In summary, it may be stated that the formulation and computer code used in the analysis are capable of modelling the THM behaviour in the clay barrier and near field. This is probably a consequence of having based the formulation on sound physical bases and appropriate constitutive laws. The basic formulation provides a robust nucleus with sufficient flexibility to incorporate changes as required by the contrast with reality. Thus, the developments and modifications introduced during the project have added to the central core of the formulation and code in a structured and consistent manner. As a general outcome of the project, it is possible to conclude that a THM model of the experiments with a very high degree of demonstrated reliability is now available. Undoubtedly, the good performance of the two large-scale heating tests spanning a long period of time (more than seven years), with continuous monitoring of the main THM variables, has made it possible to check the predictive capability of the codes and the identification of key THM processes on the basis of a large number of relatively long term observations.

7. Thermo-hydro-geochemical analyses

7. Thermo-hydro-geochemical analyses

7.1. Introduction

7.1.1. Objectives of FEBEX regarding THG

One of the objectives of the FEBEX Project is the study, identification and modelling of the possible geochemical alterations that might occur in the bentonite due to the combined effect of high temperatures and water flow [47, 190, 13]. For this purpose, a detailed and extensive laboratory program was carried out in the first phase of the project in order to provide thermo-hydro-geochemical (THG) parameters and identify the processes triggered by temperature and water flow.

Inasmuch as geochemical processes are linked and affected by other thermal, hydrodynamic and mechanical processes, the study, identification and modelling of geochemical alterations require a coupled THG analysis [47, 190, 13]. In such complex systems as that of the clay barrier, this analysis must be performed with THG numerical models, which must be solved using appropriate THG codes. Significant developments have been achieved as regards the capabilities of THG codes for coupled non-isothermal multiphase water and air flow and multi-component and reactive solute transport. Existing codes were improved and a new multiphase non-isothermal multi-component reactive solute transport code has been developed.

In the second phase of the project, the objectives were focused on updating THG conceptual models, improving THG numerical models and codes, testing such improvements on supporting laboratory experiments, updating the THG models of the "mock-up" and "in situ" tests and comparing calculated with measured geochemical data from partial dismantling of the "in situ" test to validate THG models.

7.1.2. Approach

The following approach was adopted, with a view to achieving the objectives of the project. Available data from FEBEX and other similar projects and materials were compiled and analysed. Based on this information, flow, thermal, transport and geochemical conceptual models were postulated, which were later tested using lab data. In some cases these data suggested the rejection of some candidate models. Only conceptual models not rejected by the experimental evidence were retained. By following this approach, a THG conceptual model has been postulated which is the basis for the THG numerical models of the tests carried out within the FEBEX Project. A significant development in the capabilities of UDC codes for water flow, heat transfer and reactive solute transport was achieved in order to solve these numerical models. Subsequently, different laboratory tests were modelled to estimate parameters and identify processes. For the "mock-up" test THG predictions of tracer migration were performed for iodide, a tracer added with the hydration water, and also of the THG evolution of the barrier. In the case of the "in situ" test, THG predictions for tracers added to the test (deuterium and iodide) and for the geochemical evolution of the bentonite were performed. Finally, these THG predictions were compared with measured data from the Heater #1 dismantling of the "in situ" test.

7.1.3. Scope

This chapter contains the tasks performed on THG analyses within the FEBEX project. THG conceptual models, on which numerical models are based, are described first in Section 7.2. Major developments in codes and computing tools are described afterwards in Section 7.3. Most of the development of THG models is based on their application to modelling lab tests. A wide range of lab tests have been modelled for the following purposes: a) obtaining key THG parameters, b) identifying geochemical and transport processes and c) testing their performance. Section 7.4 describes applications of THG models to lab tests. Sections 7.5 and 7.6 present THG predictions of tracer migration and the geochemical evolution of both large-scale tests, "mock-up" and "in situ", respectively. In the case of the "in situ" test, the predictions are compared with geochemical data from partial dismantling of Heater #1 to validate the THG models. The chapter ends with a discussion of the main conclusions and the requirements of future work in Section 7.7.

7.2. THG conceptual models

7.2.1. Flow model

The main features of the conceptual model for water flow through the clay barrier are as follows [190, 13, 191]:

- Darcy's Law is applicable in its most general form, that is, written in terms of pressure head and intrinsic permeability. Compacted bentonite may exhibit non-Darcian behaviour especially under low water potential gradients. However, the available data do not allow clear conclusions to be drawn regarding the relevance of this process. Therefore, such non-Darcian behaviour has not been taken into account.
- The bentonite is expected to experience an increase in water content, and eventually become fully saturated. Therefore, water flow occurs under variably saturated conditions. Once the clay barrier is saturated, water flow through the bentonite occurs under saturated conditions and water velocities are much smaller than those taking place during the hydration of the barrier.
- Water flow depends on the degree of saturation and temperature. Heaters induce a thermal gradient across the barrier. The temperature gradient affects flow parameters such as hydraulic conductivity (through changes in water viscosity and density) and vapour diffusion.
- High temperatures near the heaters cause water evaporation during the early and intermediate stages of the hydration process. Water vapour diffuses towards cooler areas where it condenses. This process affects the overall water distribution.
- Chemical and thermal osmosis might be two additional driving forces for water flow. However, since chemical osmosis pressure is only a small portion of total liquid pressure, this process is not likely to affect water flow.
- Dependence of water flow on water density variations. Due to the evaporation near the heater, solute concentrations increase in that location. Therefore, water density should reach high values (up to 1.01 or 1.02 g/cm^3). However, for the salinities computed with current THG models, water density is smaller than these values. Therefore, the effect of water density changes on water flow is not relevant and is not taken into account.

In addition to vapour flow, there is air flow. The relevance of air flow depends on the boundary conditions for the gaseous phase. Under air-tight conditions the air initially present in the bentonite is trapped and might affect water flow. However, this effect is expected to be of minor importance in both the "mock-up" and "in situ" tests and is not considered.

7.2.2. Thermal model

The major heat transport processes are convection throughout the liquid and gas phases and conduction throughout all the phases. The thermal conductivity of unsaturated bentonite is a volume-weighted average of the conductivities of pure water and clay. Heat transfer associated with the gaseous phase (vapour diffusion) and evaporation and condensation processes are also significant thermal processes [47, 206, 13, 207].

7.2.3. Transport model

The main transport processes through bentonite and granite are [190, 13, 191]:

- Advective transport. This is relevant especially during the initial stages when water uptake is more important. There is evidence of the fact that water may flow through the largest pores corresponding to the mobile porosity. Therefore, both single and double porosity models have been tested.
- Dispersive transport. There are no direct measurements of dispersivities. However, early numerical analyses clearly indicated that mechanical dispersion was not a relevant process [47]. Numerical analyses performed subsequently also confirm this statement.
- Role of joints between blocks and the voids resulting from the instrumentation of the barrier. These heterogeneities may act as fast transport paths as long as they remain open. However, once joints are sealed, they are no longer preferential pathways.
- Diffusive transport. The relevance of this process increases as solute advection decreases. There is evidence of the possible existence of restrictions for the diffusion of negatively charged species. For these, diffusion accessible porosity is smaller than total porosity. Moreover, cross-diffusion, which affects charge balance, may also affect the transport of chemical species. Its relevance has been evaluated in the model of the "mock-up" test [191].

The main solute transport parameters for the clay barrier include: accessible porosity, effective molecular diffusion coefficient and dispersivity. Most of these parameters have been determined as described in Chapter 5.

7.2.4. Geochemical model

Modelling of the variety of tests performed during the project requires the construction of a sound conceptual model for the most relevant geochemical processes. The conceptual geochemical model (CGM) is defined in terms of relevant geochemical processes and chemical composition of pore water bentonite at a given water content (usually under dry conditions of 14%). Special attention has been paid to the geochemical characterisation of the bentonite (reported in Chapters 2 and 5) and to the checking of data consistency.

Different conceptual geochemical models have been proposed depending on the type of data used in their construction: squeezing and/or aqueous extract data (see Chapter 5). The conceptual model used by UDC initially relied on squeezing data for the THG modelling of FEBEX tests and is denoted as CGM-0 [190, 13]. This model was compared with the geochemical model derived by Ciemat [12] for the FEBEX bentonite using aqueous extract and squeezing data. This model is referred to as CGM-Ciemat. Both models present similar results.

During the second phase of the project, attempts were made to develop a conceptual model capable of simultaneously reproducing squeezing and aqueous extract data. An alternative model was developed using only aqueous extract data [191, 192, 193]. This is denoted as model CGM-1. Modifications were introduced in this model in order to fit not only aqueous extract but also squeezing data. This modified model is termed CGM-2. Therefore, up to four conceptual geochemical models have been proposed for the FEBEX bentonite, which include CGM-Ciemat and models CGM-0, CGM-1 and CGM-2 [191, 192, 193].

The main features of the geochemical conceptual models are as follows [191, 193]:

- ❑ Models CGM-0, CGM-1 and CGM-2 consider the following geochemical processes: aqueous complexation, acid-base, mineral dissolution/precipitation with chemical equilibrium or kinetics, cation exchange, and gas dissolution/ex-solution (except for CGM-0).
- ❑ The chemical species considered in the three models are shown in Table 7.1. Primary species, aqueous complexes and exchangeable cations are the same in models CGM-0, CGM-1 and CGM-2. In relation to minerals, model CGM-0 does not consider dolomite and assumes chemical equilibrium for all mineral phases in the system. The difference between models GCM-1 and CGM-2 is the assumption of a gypsum/anhydrite initial concentration in

Table 7.1
Chemical species considered in models CGM-0, CGM-1 and CGM-2

	CGM-0	CGM-1	CGM-2
Primary species	H_2O, H^+, Ca^{2+}, Mg^{2+}, Na^+, K^+, Cl^-, SO_4^{2-}, HCO_3^-, $SiO_{2(aq)}$		
Aqueous complexes	OH^-, $CaSO_{4(aq)}$, $CaCl^+$, $MgCl^+$, $NaCl_{(aq)}$, $MgHCO_3^+$, $NaHCO_{3(aq)}$, $CaHCO_3^+$, $MgCO_{3(aq)}$, $CaCO_{3(aq)}$, $CO_{2(aq)}$, CO_3^{2-}, KSO_4^-, $MgSO_{4(aq)}$, $NaSO_4^-$, $H_2SiO_4^{2-}$, $HSiO_3^-$		
Minerals	Calcite (equilibrium), Chalcedony (equilibrium) Gypsum/Anhydrite (equilibrium, only precipitation)	Calcite (kinetic), Dolomite (kinetic) Chalcedony (equilibrium) Gypsum/Anhydrite (equilibrium)	Calcite (kinetic), Dolomite (kinetic) Chalcedony (equilibrium) Gypsum/Anhydrite (equilibrium, only precipitation)
Exchangeable cations	H^+, Ca^{2+}, Mg^{2+}, Na^+, K^+ (selectivity coefficients)		
Gas	No condition on $CO_{2(g)}$	Fixed pressure of $CO_{2(g)}$	

the first and no gypsum/anhydrite present initially in the second. CGM-0 presents no gas condition.

- The most relevant solid phases considered in THG models are calcite, dolomite, chalcedony and, anhydrite or gypsum. They are assumed to be present as pure phases.
- The main silica-bearing phases present in the bentonite are smectite, plagioclase, potassium feldspar, quartz and cristobalite. The minor difference in the solubility products of quartz, cristobalite (the phases which will dissolve in the rock), and chalcedony and the proximity of this mineral to amorphous silica (the phase that will eventually precipitate from the solution) justifies the assumption of adopting chalcedony as a reasonable constraint of silica in the system.
- Aluminium-bearing phases have not been considered in the THG models due to the fact that data on aluminium concentrations are limited.
- Data on the gypsum and halite content of the bentonite are available that indicate that these phases are present in the bentonite, especially in dry bentonite samples (Chapter 2). Anhydrite is the stable calcium sulphate at temperatures above 60 °C. Therefore, this phase is more appropriate than gypsum whenever temperatures are above this value. This is the case for the greater part of the "in situ", "mock-up" and thermo-hydraulic tests. For this reason, anhydrite was selected as the sulphate-bearing mineral phase in the numerical models of these tests.
- The kinetics of mineral dissolution/precipitation is not considered to be a relevant process in reactive transport modelling of the "in situ", "mock up" and thermo-hydraulic tests. However, it has been considered in lab tests of shorter duration, such as the exchange tests and the aqueous extracts tests at different times (up to 30 days) [193].
- For the reactivity of gas phases, and particularly for the role of $CO_{2(g)}$, the bentonite system is considered in all cases to be closed. This assumption depends on the experimental set up and particularly affects the carbonate system and ion exchange behaviour. However, the closed system environment is not guaranteed when clay is sampled and squeezed to extract its water.

7.3. THG codes and numerical tools

7.3.1. Developments

Significant developments have been achieved during the FEBEX Project in terms of the capabilities of UDC codes for water flow, heat transfer and reactive solute transport.

During the first phase two new codes were developed: CORE-LE-2D v0.0a and FADES-CORE-LE V0.0a [194, 195, 196, 197, 198].

During the second phase an extended version of CORE-LE-2D v0.0a was developed, yielding a new code: CORE^{2D}. Of the different versions of this code, CORE^{2D} V4 [199] was mainly used in the THG analyses of the FEBEX tests. Other new codes developed within this phase of the project are: FADES-CORE V1 [200], (an updated version of FADES-CORE-LE V0.0a); and INVERSE-FADES-CORE V0 [201], (an updated version of FADES-CORE V1 which consider the automatic estimation of parameters involved in reactive transport models).

These numerical tools have been used to: 1) interpret various lab tests for the purpose of proper parameter estimation, 2) interpret lab tests for the purpose of identifying relevant geochemical processes, 3) predict the transport patterns of artificial tracers added in the "in situ" and "mock-up" tests, and 4) predict the thermo-hydro-geochemical performance of the clay barrier for the "in situ" and "mock-up" tests.

7.3.2. Code description

7.3.2.1. CORE-LE-2D V0.0a

This is a COde for modelling water flow (saturated and unsaturated), heat transport and multi-component REactive solute transport under Local chemical Equilibrium conditions [194]. The code is an extended, widely verified and improved version of a previous reactive transport code, TRANQUI [195]. Some of the major changes introduced into CORE-LE-2D V0.0a which are not shared by TRANQUI are:

- Unsaturated water flow.
- Time varying real recharge and boundary parameters for both water flow and solute transport.

- A thorough verification of non-isothermal reactive transport.
- Anion exclusion for both saturated and non-saturated water flow.
- Retardation by means of the K_d concept.
- Modelling of radioactive decay processes.
- Gas dissolution/ex-solution.
- Upwinding numerical algorithm for the solution of advective-dominated transport problems, in order to avoid numerical oscillations.
- Implementation of several sequential iterative approaches (SIA) for solving coupled transport + chemistry equations.

The program is able to simulate simultaneously groundwater flow, heat transport and multi-component reactive solute transport under the following conditions:

- 2-D confined or unconfined, saturated or non-saturated steady-state or transient groundwater flow. General boundary conditions are allowed.
- Transient heat transport, considering conduction, heat dispersion and convection processes.
- Chemical equilibrium, reactions including: aqueous complexation, acid-base, redox, mineral dissolution/precipitation, cation exchange, surface adsorption and gas dissolution/ex-solution.

CORE-LE-2D is based on the sequential iteration approach (SIA) and solves coupled hydrological transport processes and hydro-geochemical reactions. In this approach the transport and chemical equilibrium equations are considered to be two different subsystems. These subsystems are solved separately in a sequential manner in accordance with an iterative procedure. At any given iteration, the chemical sink/source term is assumed to be known (or taken to be equal to the value at the previous iteration) for the purpose of solving the transport equations. This renders the differential equations linear, which allows for the use of fast numerical methods for the solving of linear systems of equations. After solving the transport equations, the set of chemical equations is solved on a node-basis. Solution of these non-linear equations is carried out using Newton-Raphson iterative procedures. After convergence, the chemical source term is updated. The whole iterative process (transport + chemistry) is repeated until overall convergence is attained.

The solute transport processes included in the code are advection, molecular diffusion and mechanical dispersion. Solute transport boundary conditions include: (1) specified solute mass fluxes, (2) specified solute concentrations and (3) solute sources associated with fluid sources. The code is capable of handling the following types of reactions under the local equilibrium assumption: aqueous complexation, acid-base, redox, mineral dissolution/precipitation, gas dissolution/ex-solution, cation exchange and adsorption via surface complexation (using the constant capacitance model). CORE-LE-2D is capable of taking into account any number of aqueous, exchanged and sorbed species, minerals and gases.

The input of aqueous species, minerals, gases and adsorbed species requires only that their names be specified. Thermodynamic data and stochiometric coefficients of the reactions are read directly from a database. The database is built from the EQ3NR database [198]. The data for surface adsorption reactions are implemented in the database.

7.3.2.2. FADES-CORE-LE V0.0a

The need to cope with multiphase flow (which cannot be handled by CORE-LE-2D v0.0a) led to the development of a multiphase, non-isothermal, multi-component reactive solute transport code: FADES-CORE-LE v0.0a [196]. The code is the result of adding reactive transport to an existing multiphase-flow code, FADES [197], which in addition to flow accounts for soil deformation and heat transport. Solute transport and chemical reactions have been added to the FADES code, resulting in a new code known as FADES-CORE-LE V0.0a.

FADES-CORE-LE V0.0a shares all the geochemical capabilities of CORE-LE and provides additional options for solute transport, such as the possibility of different molecular diffusion coefficients for each primary species, and the geochemical effects of evaporation and condensation.

7.3.2.3. CORE^{2D} V4

CORE^{2D} V4 [199] is a finite element code that solves for groundwater flow, heat transport and multi-component reactive solute transport. It accounts for the following chemical equilibrium reactions: aqueous complexation, acid-base, redox, mineral dissolution/precipitation, cation exchange, surface adsorption via surface complexation and Kd-approach and gas dissolution/ex-solution. It also considers chemical kinetics for the dissolution/precipitation of minerals as well as radioactive decay.

CORE^{2D} V4 incorporates a set of additional features compared to those of the CORE-LE-2D V0.0a which include:

- ❑ Adding kinetics for redox processes, mineral precipitation/dissolution and sorption reactions.
- ❑ Automatic time stepping algorithm.
- ❑ An improved Sequential Iteration Approach (SIA-1).
- ❑ Accounting for anisotropic diffusion.
- ❑ Accounting for different expressions of diffusion.
- ❑ Allowing each chemical species to have different transport properties.
- ❑ Accounting for solutes undergoing exclusion.
- ❑ Improving the checking of mass balance errors.
- ❑ Accounting for water evaporation.
- ❑ Introducing improvements in the input files.
- ❑ Allowing for the use of thermodynamic databases other than those used previously by CORE-LE-2D V0.0a.

7.3.2.4. FADES-CORE V1

This multiphase, non-isothermal and multi-component reactive solute transport code is an updated version of FADES-CORE-LE V0.0a. Features added to FADES-CORE V1 during the second phase of the project [200] are the following :

- ❑ Implementing subroutines for mass and charge balance.
- ❑ Incorporating a constitutive law for permeability as a function of pore water ionic strength.
- ❑ Adding a subroutine to avoid gas pressure oscillations when the medium becomes fully saturated.
- ❑ Including the chemical kinetics of mineral dissolution/precipitation.
- ❑ Accounting for Pitzer equations to calculate the activity coefficient for aqueous solutions of high salinity.
- ❑ Taking into account chemical and thermal osmosis.
- ❑ Considering double porosity models.
- ❑ Implementing the capabilities for solving the inverse problem of optimum estimation of any THG parameter. This has led to the development of INVERSE-FADES-CORE V0.

7.3.2.5. INVERSE-FADES-CORE V0

INVERSE-FADES-CORE V0 [201] is an updated version of FADES-CORE V1 that solves the inverse problem by minimising a generalised least-squares criterion by means of a Gauss-Newton-Levenberg-Marquardt method.

This code makes it possible to estimate a wide range of parameters by taking into account different types of observations, including: 1) liquid and gas pressure, 2) concentrations of chemical species, 3) total concentration in the solid and liquid phases, 4) water inflows, 5) water content, 6) exchanged cations, and 7) temperature [200].

The following parameters may be estimated: intrinsic permeability, parameters of the relative permeability curve, parameters of the retention curve, such as parameters m, n, and a of the van Genuchten retention curve, vapour tortuosity and diffusion coefficient, thermal conductivity, dispersivity, accessible porosity, distribution coefficient, initial concentrations of chemical species including pH and pE, boundary concentrations of chemical species, selectivity coefficients of exchangeable cations, cation exchange capacity (CEC), specific surface of minerals and initial volume fraction of minerals.

7.4. THG modelling of laboratory tests

7.4.1. Modelling for parameter estimation and process identification

7.4.1.1. Numerical interpretation of diffusion tests

Different types of diffusion and permeation tests were carried out by CIEMAT (Chapter 5). These tests were performed to estimate transport and sorption parameters, such as total and kinematic porosities, molecular diffusion coefficients (effective and apparent) and retardation coefficients. The tests were interpreted by means of the available analytical solutions by CIEMAT (Chapter 5). The conditions of some tests are not taken into account by these solutions. The use of numerical models for test interpretation overcomes the limitations of the analytical solutions.

Diffusion and permeation tests were interpreted numerically using CORE-LE-2D V0.0 and an improved version of the code that allows for automatic parameter estimation [202]. The results of the numerical interpretation of through-diffusion (TD) and in-diffusion (ID) tests as well as permeation (P) tests are shown in Table 7.2.

Two types of diffusion tests have been interpreted. The first is the so-called through-diffusion test, in which the clay sample is placed between two water reservoirs. A tracer is initially added to only one of the reservoirs (the upstream reservoir). Neither the clay nor the sinters contain this tracer. The gradient in tracer concentration induces a diffusive flux from the upstream to the downstream reservoir through the clay sample. Several sets of through-diffusion (TD) tests were performed on clay samples having a total porosity of 0.56, which amounts to a dry density of 1.18 g/cm^3, using tritiated water (HTO). HTO was used in three TD tests, which lasted about 50 days, a period of sufficient length for the test to achieve steady concentrations. HTO tests were used to test the estimation algorithms and to explore the role of the sinters. The computed results indicate that the sinters should be taken into account for proper interpretation of the tests. Otherwise, bentonite diffusion coefficients may be underestimated by a factor of 3. Based on this finding, the sinters were considered for the interpretation of all the tests. In general, the numerical solution is able to reproduce fairly well the tracer data observed in both reservoirs (Figure 7.1). Effective diffusion coefficients for tritium range from 1.17 to 1.40·10^{-10} m^2/s, being these values within the range of published values for this tracer in bentonites. The best fit is obtained with diffusive porosities ranging from 0.44 to 0.5 (Table 7.2:), which are slightly smaller than the total porosity. This result might be an indication of a slight correlation between the estimates of porosity and diffusion caused by a weak lack of parameter identifiability. The tortuosity factor ranges from 0.76 to 0.79.

Four tests were performed using strontium, Sr^{2+}. This tracer has a large sorption capacity. In fact, the tracer does not reach the downstream reservoir after

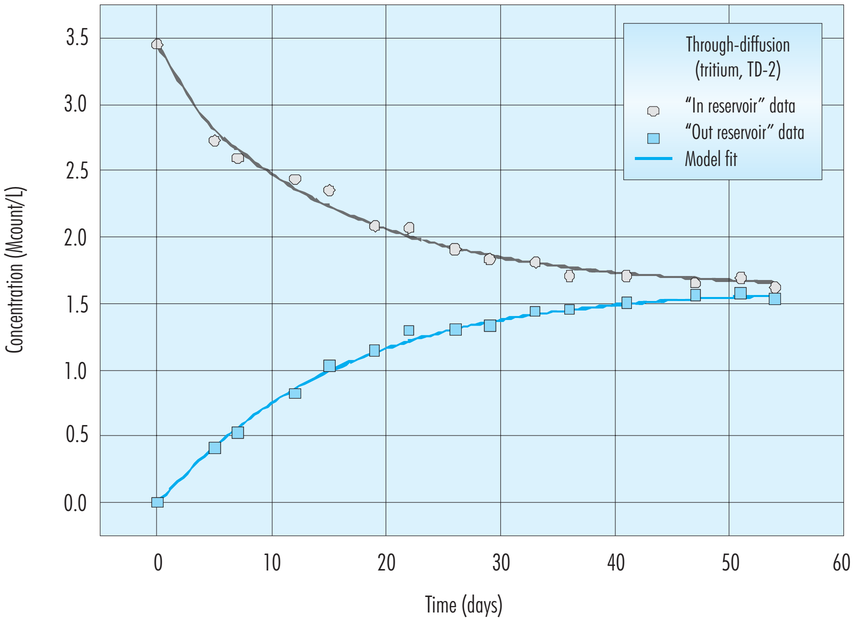

Figure 7.1: Numerical interpretation of through-diffusion test TD-2 (with tritiated water). Upstream (IN reservoir) and downstream (OUT reservoir) reservoir concentrations are shown.

Table 7.2
Numerical results of the diffusion tests

Species	Test number	$ø^{(1)}$	D_e $^{(2)}$ (m^2/s)	D_a $^{(3)}$ (m^2/s)	K_d $^{(4)}$ (mL/g)
HTO	TD-1	0.56*	$1.41 \cdot 10^{-10}$	$2.52 \cdot 10^{-10}$	
		0.50	$1.41 \cdot 10^{-10}$	$2.82 \cdot 10^{-10}$	
	TD-2	0.56*	$1.24 \cdot 10^{-10}$	$2.21 \cdot 10^{-10}$	
		0.45	$1.24 \cdot 10^{-10}$	$2.74 \cdot 10^{-10}$	
	TD-3	0.56*	$1.18 \cdot 10^{-10}$	$2.10 \cdot 10^{-10}$	
		0.44	$1.17 \cdot 10^{-10}$	$2.67 \cdot 10^{-10}$	
	P-1	0.44/0.19	$3.50 \cdot 10^{-9}$		
	P-2	0.60/0.20	$2.33 \cdot 10^{-9}$		
Strontium	TD-Sr-5	0.56*	$1.12 \cdot 10^{-9}$	$1.51 \cdot 10^{-12}$	626.0
		0.62	$1.11 \cdot 10^{-9}$	$1.51 \cdot 10^{-12}$	621.3
	TD-Sr-6	0.56*	$7.57 \cdot 10^{-10}$	$1.15 \cdot 10^{-12}$	557.4
		0.64	$7.61 \cdot 10^{-10}$	$1.17 \cdot 10^{-12}$	549.9
	TD-Sr-7	0.56*	$1.74 \cdot 10^{-9}$	$1.46 \cdot 10^{-12}$	975.4
		0.52	$1.71 \cdot 10^{-9}$	$1.46 \cdot 10^{-12}$	995.1
	TD-Sr-8	0.56*	$8.50 \cdot 10^{-10}$	$1.21 \cdot 10^{-12}$	594.0
		0.63	$8.35 \cdot 10^{-10}$	$1.16 \cdot 10^{-12}$	609.1
Cesium	ID-Cs-9	0.42*	$8.03 \cdot 10^{-10}$	$3.34 \cdot 10^{-13}$	925.1
		0.49	$8.05 \cdot 10^{-10}$	$3.32 \cdot 10^{-13}$	931.8
	ID-Cs-10A	0.42*	$3.30 \cdot 10^{-10}$	$1.37 \cdot 10^{-13}$	924.1
		0.49	$3.44 \cdot 10^{-10}$	$1.43 \cdot 10^{-13}$	924.4
	ID-Cs-10B	0.42*	$7.57 \cdot 10^{-10}$	$3.21 \cdot 10^{-13}$	907.9
		0.45	$8.81 \cdot 10^{-10}$	$3.39 \cdot 10^{-13}$	999.6
Selenium	ID-Se-17	0.42*	$4.35 \cdot 10^{-13}$	$6.51 \cdot 10^{-14}$	2.41
		0.21	$1.73 \cdot 10^{-13}$	$3.40 \cdot 10^{-14}$	1.87
	ID-Se-18	0.42*	$1.39 \cdot 10^{-13}$	$2.29 \cdot 10^{-14}$	2.17
		0.25	$1.23 \cdot 10^{-13}$	$2.23 \cdot 10^{-14}$	2.02

(1) ø denotes diffusion-accessible porosity; (2) D_e is the effective diffusion coefficient; (3) D_a is the apparent diffusion coefficient, and (4) K_d is the distribution coefficient in mL/g).
** Means that the parameter is fixed and therefore not estimated*

almost 200 days, even though it has been fully flushed from the upstream reservoir after that time. These tests were interpreted in two stages. First, the porosity was fixed to a value of 0.56 while K_d and D_o were estimated. In the second stage, porosity was also estimated, resulting in an excellent fit to the measured data (Figure 7.2). The best fit is obtained with diffusive porosities slightly greater than total porosity. The mean diffusive porosity is 0.6. Estimated porosities greater than the total porosity might be caused by tracer exchange. This hypothesis requires further testing. Effective diffusion coefficients D_e range from $7.6 \cdot 10^{-10}$ to $1.71 \cdot 10^{-9}$ m^2/s, with a mean value of $1.1 \cdot 10^{-9}$ m^2/s. The estimated values of K_d also show a wide range (from 550 to 995 cm^3/g) with a mean of 691 cm^3/g. Apparent diffusion coefficients, which take into account the effect of sorption, show much lower scatter (from $1.15 \cdot 10^{-12}$ to $1.51 \cdot 10^{-12}$ m^2/s) with a mean value of $1.33 \cdot 10^{-12}$ m^2/s). These values are within the range of published values for this tracer in bentonites. Estimated values of K_d and D_e show a positive correlation, i.e., the larger D_e the greater is K_d. The fact that the apparent diffusion coefficients, D_a, obtained from different tests are quite stable leads to the conclusion that TD tests for sorbing tracers allow only D_a to be estimated. The estimates of K_d and D_e may contain significant uncertainty.

The second type of diffusion tests is the so-called in-diffusion (ID) test, in which two clay samples of identical dimensions are immersed in a reservoir containing a tracer that is initially not present either on the clay or on the sinters. The gradient in tracer concentration induces a diffusive flux from the reservoir into the clay samples. Several sets of ID tests were performed on clay samples having a total porosity of 0.42, which amounts to a dry density of 1.57 g/cm^3 using radioactive cesium (^{137}Cs) and selenite, SeO_3^{2-}. Tracer activity in the reservoir was monitored throughout the duration of the test. At the end of the test, clay samples were sliced and total tracer concentration was measured in each slice.

Two cesium tests were available (ID-Cs-9 and ID-Cs-10). In one of them, the behaviour of the sample is not symmetric, i.e. the tracer diffuses more on one of the faces. In this case, data from each side of the sample were interpreted separately. The tests were interpreted in two stages. First, the porosity was fixed to a value of 0.42 while K_d and

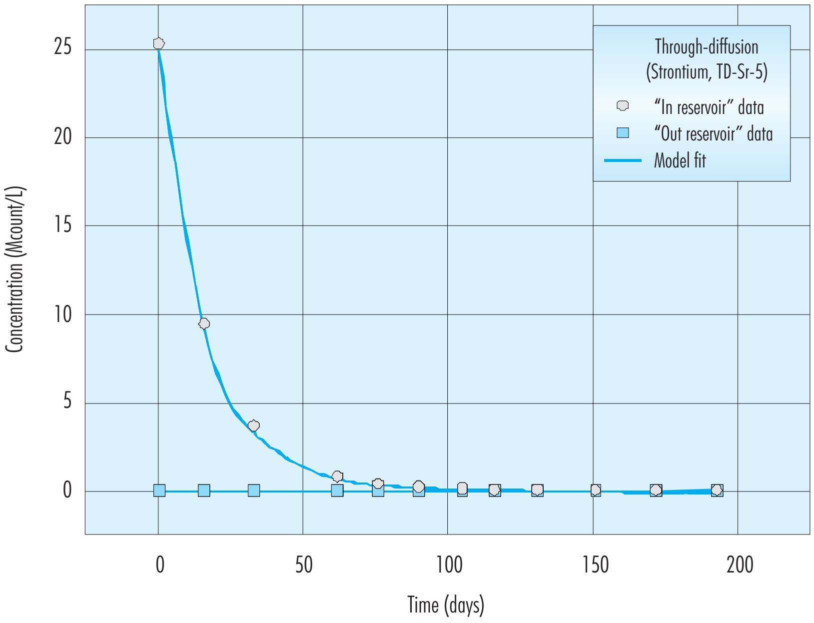

Figure 7.2: Numerical interpretation of through-diffusion test TD-Sr-5 (with strontium). Upstream (IN reservoir) and downstream (OUT reservoir) reservoir concentrations are shown.

D_o were estimated. In the second stage, porosity was also estimated, resulting in an excellent fit to measured final concentration data. Some discrepancies are observed in the time evolution of tracer activity in the reservoir, these being attributed to uncertainties in the initial activity and to the lack of well-mixed conditions in the reservoir. A detailed sensitivity analysis was performed to evaluate the effects of several sources of uncertainty, which include: (1) the initial concentration in the sinters, (2) the appropriate boundary condition for the reservoir, (3) the initial concentration in the reservoir, and (4) the effective volume of the reservoir. The results of this analysis indicate that the estimated parameters are very sensitive to the properties and conditions prevailing in the reservoir. Therefore, for the proper interpretation of this type of tests it is suggested that: (1) only one clay sample should be located in each reservoir, (2) the initial concentration should be measured as accurately as possible, (3) special care should be taken in measuring the activities of the slices located near the faces of the clay samples. The best fit is obtained with diffusive porosities slightly higher than total porosity. Diffusive porosities range from 0.45 to 0.49. The effective diffusion coefficient D_e ranges from $3.30 \cdot 10^{-10}$ to $8.81 \cdot 10^{-10}$ m^2/s. The estimated values of K_d range from 924.4 to 999.6 cm^3/g. Apparent diffusion coefficients, which take into account the effect of sorption, show some scatter. They range from $1.37 \cdot 10^{-13}$ to $3.39 \cdot 10^{-13}$ m^2/s. These values are within the range of published values for this tracer in bentonites. Again, numerical solutions satisfactorily reproduce the measured data (Figure 7.3).

Two selenite, SeO_3^{2-}, tests were performed on clay samples of 2.5 cm, half the length of the Cs cells. Again, the tests were interpreted in two stages. First, the porosity was fixed to a value of 0.42 while K_d and D_o were estimated. In the second stage, porosity was also estimated, resulting in an excellent fit to both final concentration data and to the time evolution of tracer activity in the reservoir. A better fit is obtained with diffusive porosities, which are much lower than total porosity. As in the case of what was observed for tritiated water, this result might be the result of parameter unidentifiability. Diffusive porosities are equal to 0.21 and 0.25. The effective diffusion coefficients D_e range from $1.23 \cdot 10^{-13}$ to $1.73 \cdot 10^{-13}$ m^2/s. The estimated values of K_d range from 1.87 to 2.02 cm^3/g. Apparent diffusion coefficients, which take into account the effect of sorption, range from $2.23 \cdot 10^{-14}$ to $6.50 \cdot 10^{-14}$ m^2/s. The

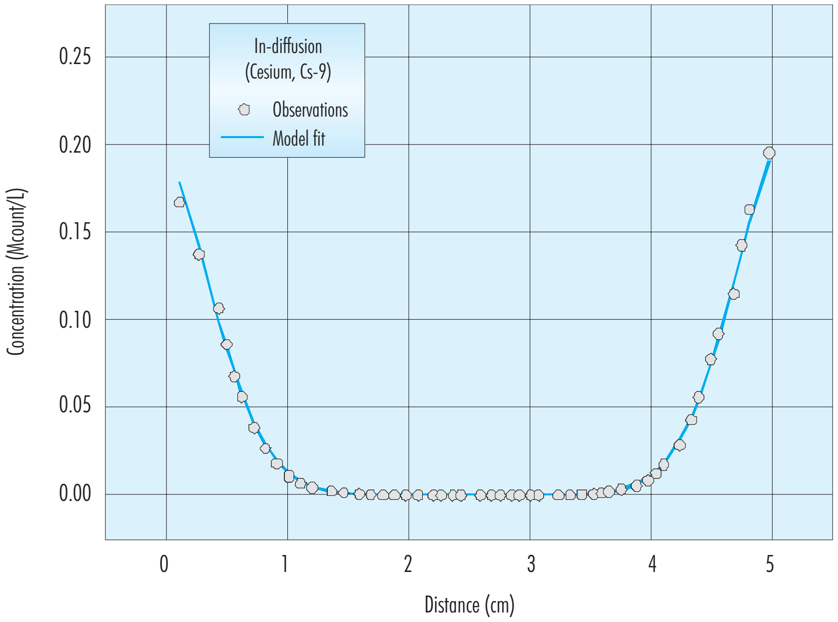

Figure 7.3: Numerical interpretation of in-diffusion test Cs-9 (with cesium). Final total concentrations in the clay sample are shown.

estimated values of K_d, D_e and D_a are within the range of published values for Se in bentonites.

Contrary to in- and through-diffusion tests, permeation tests involve advective solute transport in addition to diffusive processes. These tests are intended to provide information on dispersivities and kinematic porosity, which measures the volume of well-connected pores. Several permeation tests were performed using tritiated water and Se. Only the results of the interpretation of HTO permeation tests are presented here. The results of the Se tests show unpredictable and difficult to explain patterns. Following the parsimony principle, the classic single-porosity model was tested first. For the first permeation test (P-1) a convergent but sub-optimal solution is obtained with a porosity of 0.35. The fit of the second test is very poor, in fact, the estimation algorithm fails to attain a convergent solution. Given the limitations of the single-porosity model, a more complex double-porosity model was also considered. With this model the fit of the tests is excellent (Figure 7.4). However, since the double porosity model involves four parameters, the issue of parameter unidentifiability becomes more of a problem, especially for the parameters of the immobile phase. Kinematic or mobile porosity is 0.2. The effective diffusion coefficient in the mobile phase ranges from 2.32 to $3.50 \cdot 10^{-9}$ m^2/s, while that of the immobile phase is almost three orders of magnitude smaller.

The numerical interpretation of diffusion and permeation tests has been useful for the identification of certain issues that should be analysed in greater depth in future projects. These issues include: 1) the role and properties of the sinters, their effective diffusion properties should be measured; 2) the initial tracer concentration in the reservoirs, which should be measured as accurately as possible; 3) the effective volume of the reservoir in in-diffusion tests and 4) the activities of the slices located near the faces of the clay samples in in-diffusion tests, which should be measured as accurately as possible; and 5) the appropriate duration of the test which should depend on the sorbing properties of the tracer.

Some suggestions for future tests are as follows: 1) only one clay sample should be located in each reservoir for in-diffusion tests; 2) special care should be taken in measuring the activities of the slices located

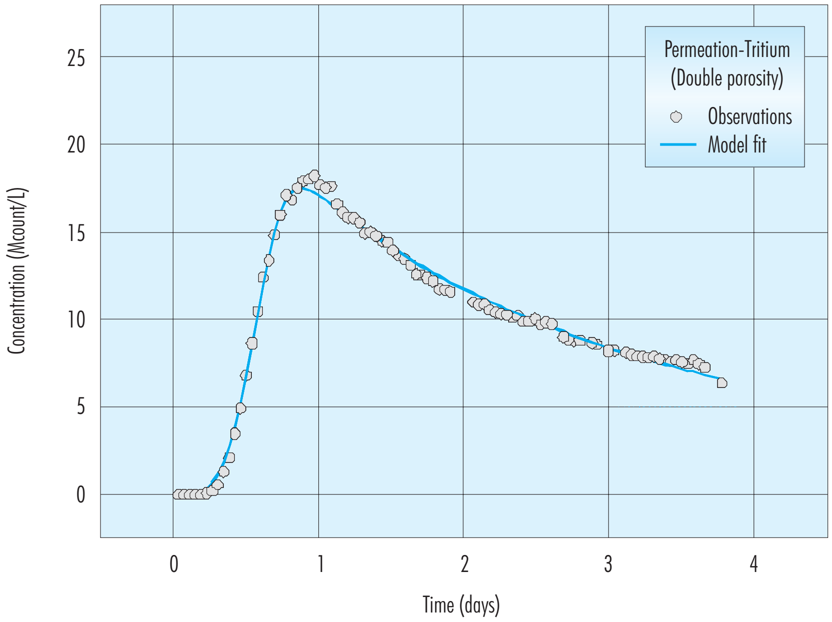

Figure 7.4:Numerical interpretation of permeation test P-1 (tritiated water). Computed concentrations (line) satisfactorily reproduce the measured data (symbols).

near the faces of the clay samples; 3) the duration of the tracer pulse should be much smaller than the duration of permeation tests, otherwise, the concentration of the inflow water should be carefully measured; 4) additional diffusion tests under non-saturated conditions are required to explore the variation of anion exclusion (excluded porosity) with water content; and 5) radial diffusion tests should be performed in order to better identify the retardation coefficients of compacted bentonite.

7.4.1.2. Modelling of exchange tests

Exchange isotherms

Selectivity coefficients depend on a variety of factors, one of them being the exchanger composition. Exchange isotherms for the bentonite were determined in order to improve the modelling of ion exchange processes [203]. Homosodic bentonite was first prepared and then placed in contact with several aqueous solutions with different Na/K, Na/Mg, and Na/Ca ratios, until saturation was reached with respect to Ca, K, and Mg. To ensure the reproducibility of the results, two independent series of batch tests were performed, 10 points per series and for each of the three isotherms (Na/K, Na/Mg, and Na/Ca) [203].

Figures 7.5, 7.6 and 7.7 show the Vanselow selectivity coefficients for Na/K, Na/Mg, and Na/Ca exchange as a function of the composition of the exchange complex. These results were fitted to a third-order polynomial taking into account the experimental uncertainty brackets, although equal weight was assigned to each datum:

$$\ln^{M}_{Na} k_V = a_0 + a_1 \cdot E_M + a_2 \cdot E_M^2 + a_3 \cdot E_M^3$$

E_M denotes the equivalent fraction of cation M exchanging with sodium (M = Ca, Mg, and K) and k_V is the selectivity coefficient according to the Vanselow convention. Fitting coefficients are given in Table 7.3.

It may be seen that the exchange coefficients are not constant. This dependency on exchanger composition has to be considered in geochemical modelling. Moreover, the FEBEX bentonite shows the following decreasing sequence of selectivities: calcium,

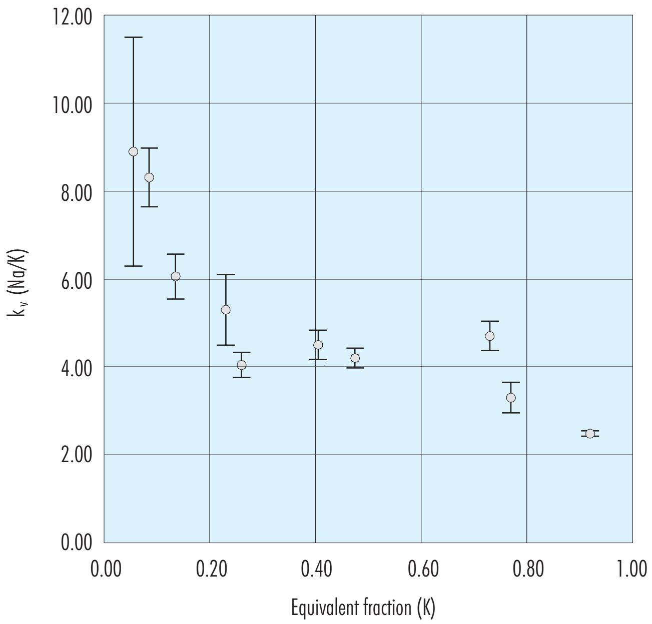

Figure 7.5: Vanselow selectivity coefficients for Na/K exchange in the FEBEX bentonite. Bars represent the experimental uncertainty brackets.

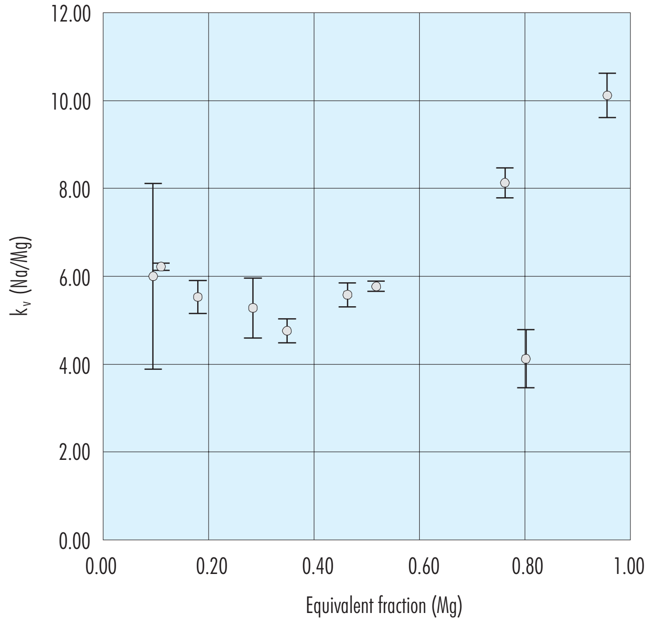

Figure 7.6: Vanselow selectivity coefficients for the Na/Mg exchange in the FEBEX bentonite. Bars represent the experimental uncertainty brackets.

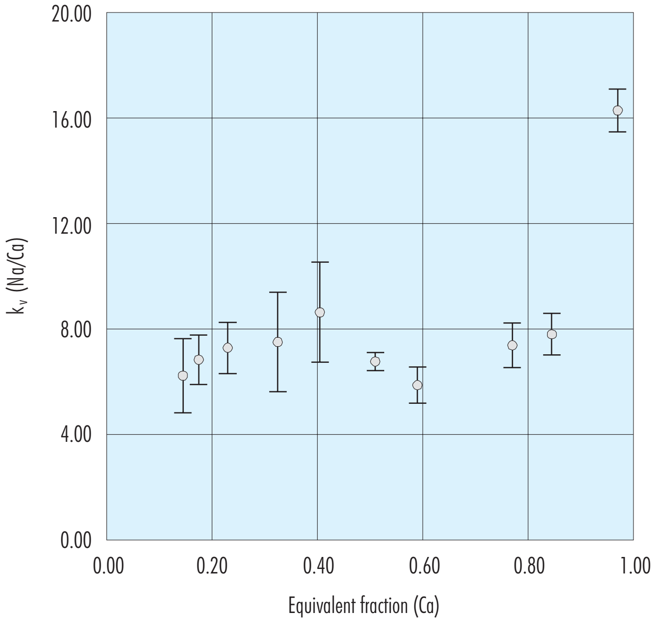

Figure 7.7: Vanselow selectivity coefficients for the Na/Ca exchange in the FEBEX bentonite. Bars represent the experimental uncertainty brackets.

Table 7.3
Fitting coefficients and their corresponding standard deviation for the Na/K, Na/Mg, and Na/Ca exchange isotherms

Coefficient	Na/K	$\sigma_{Na/K}$	Na/Mg	$\sigma_{Na/Mg}$	Na/Ca	$\sigma_{Na/Ca}$
a_0	2.436	0.174	1.735	0.293	0.959	0.307
a_1	-6.035	1.698	0.339	2.518	8.244	2.274
a_2	12.288	4.24	-2.387	5.732	-19.055	4.696
a_3	-8.187	2.958	2.670	3.710	12.894	2.849

magnesium, potassium and sodium. Therefore, a significant release of exchanged sodium (and to a lesser extent of potassium and magnesium) is expected during the test, this being replaced by calcium.

CSIC-Zaidín - exchange experiments

Exchange experiments were performed in order to explore possible geochemical alterations of the clay, gain insight into the kinetics of cation exchange and evaluate its temperature dependence [204]. In short, five grams of dry powder of bentonite were placed inside dialysis bags, which were in turn placed inside PFA reactors filled with 125 mL of water of a given chemical composition (Moody, Grimsel, and bentonitic-granitic type waters). The PFA reactors containing the water and the clay powder were heated to different temperatures (from room temperature up to 80 °C) for a period of time ranging from one day to one year. Water was renewed according to a prescribed schedule, but not the clay, which remained in place throughout the entire duration of each test. After each water renewal, major cations, silica, total inorganic carbon (TIC), and pH were analysed. At the end of each test, the exchange complex and the CEC of the bentonite were measured.

Numerical modelling of these tests could have been done using CORE-LE-2D V0.0a [194]. However, since hydrodynamic transport was lacking (water does not flow in a continuous manner but is instead renewed periodically) it was more expeditious to use standard hydrochemical codes, such as EQ3/6 [198]. A conveniently modified version of the EQ3/6 software package was used in which ion exchange reactions were formulated as half reactions [205].

It was necessary to take into account the dissolution kinetics of minerals present in the bentonite (calcite, dolomite), due to the fact that they play a significant role in the carbonate-pH system. Calcite and dolomite dissolution are assumed to take place under kinetically-controlled conditions. Kinetic rate laws used for calcite and dolomite dissolution/precipitation require knowledge of their reactive wet surface. No measurements of the reactive surface area of calcite and dolomite in the bentonite are available. Therefore, an educated guess was made and a sensitivity analysis was performed on the results, due to this uncertainty.

These tests were modelled using the measured data on the initial composition of the exchange complex for each sample, which vary from one sample to another and may not coincide with reported average values [204, 205].

Highly soluble salts such as sulphates and chlorides were assumed to dissolve instantaneously during initial contact between the water and the bentonite, causing a sharp increase in dissolved calcium, sodium and sulphate. This process takes place only once at the beginning of the test.

Since the chemical composition of all the renewal waters is constant and always undersaturated with respect to calcite and dolomite, these never reach equilibrium within the renewal period. Consequently they always dissolve. However, the amount of carbonates present in the bentonite guarantees that, even for the longest tests, they are never exhausted.

Cation exchange tests were performed at several temperatures and using different types of waters. The experimental data indicate that cation exchange is nearly independent of temperature. For the purpose of examining chemical processes and testing THG models, only a few tests performed at 20 °C were modelled. Here modelling results are shown only for tests performed with Moody water.

Figures 7.8 and 7.9 illustrate the time evolution of dissolved and exchanged Ca, respectively. It may be seen that Ca is depleted from the solution and enriched in the bentonite. The rate of such depletion in the water is higher during the first 40 days than later. This is due to the lack of equilibrium between the initial water and the bentonite. As ion exchange proceeds, the bentonite approaches a state of equilibrium with water. The inflexion point, located after 40 days, coincides in time with the balance between dissolved sodium and the sodium in the bentonite (Figures 7.10 and 7.11). Since Ca has a greater selectivity for the bentonite than either magnesium, sodium or potassium, these cations are displaced from the exchanger by calcium, at a slow rate.

The measured data and computed results show that during the first 40 days sodium is displaced from the exchanger by both dissolved Ca and Mg, because both have greater selectivity than sodium. During this time magnesium competes with calcium in depleting the sodium in the bentonite. However, once sodium reaches equilibrium with water, the higher selectivity of calcium with respect to magnesium causes a depletion of exchanged magnesium in the bentonite (Figures 7.12 and 7.13 for the time evolution of magnesium in the water and bentonite, respectively). Potassium shows a rather similar pattern of evolution (Figures 7.14 and 7.15).

Since PFA reactors behave like a closed system, CO_2 has been modelled accordingly. The effect of calcite and dolomite dissolution under kinetic constraint is quite striking (Figure 7.16), resulting in a characteristic saw-tooth pattern with a period of 7 days (the renewal period).

In general, the model results agree fairly well with the experimental data, especially for dissolved cations. The computed values of exchanged concentrations also reproduce the measurements, although in some cases they deviate from them. Such deviations are partly attributed to the effect of ionic strength on the values of the selectivity coefficients, for which there are no data. Experimental data should be collected to confirm such ionic strength dependence. If so proved, numerical THG models should then account for such dependence. In other cases, deviations might be caused by measurement uncertainties in exchanged cation concentrations.

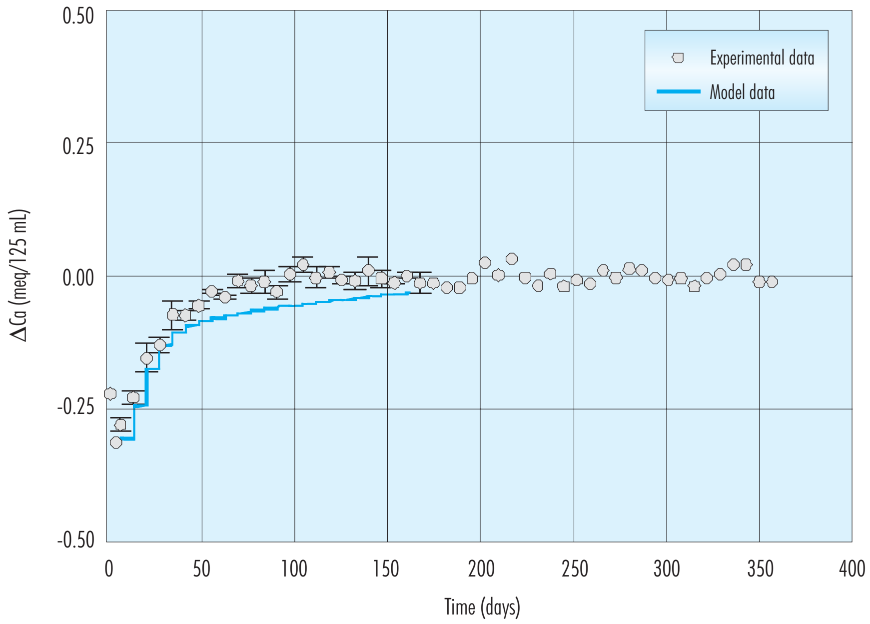

Figure 7.8: Time distribution of ΔCa in the solution (Ca_{water}-Ca_{Moody}). Bars represent uncertainty brackets.

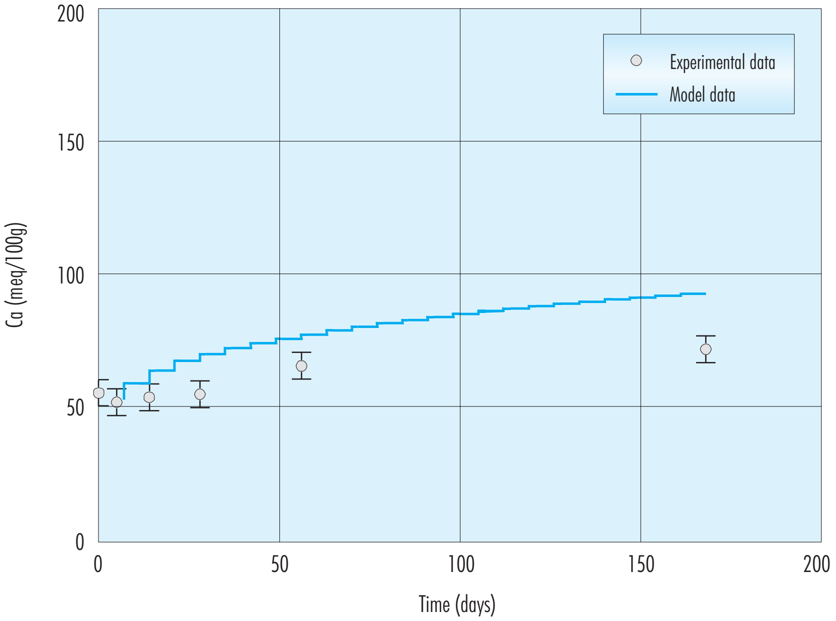

Figure 7.9: Time distribution of Ca in the bentonite. Bars represent uncertainty brackets.

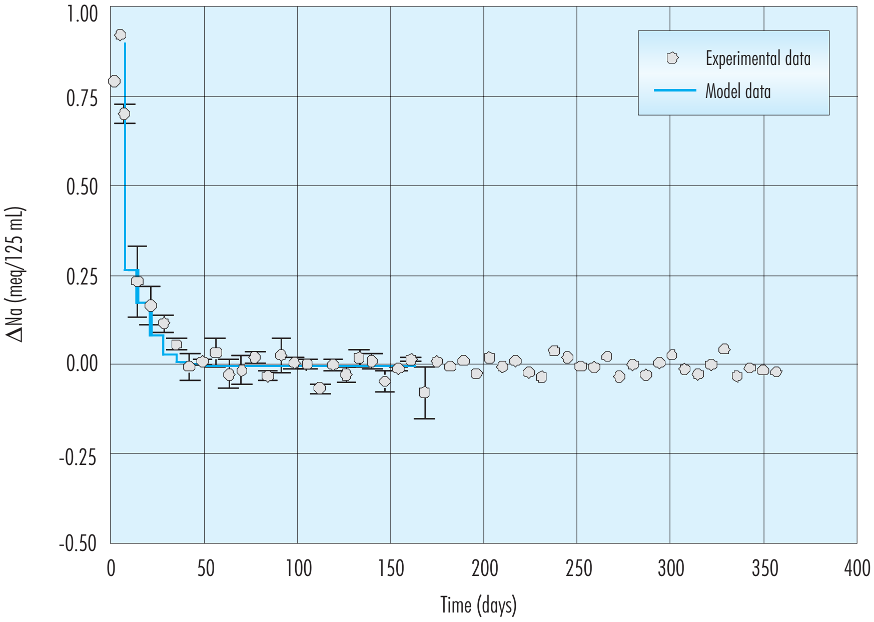

Figure 7.10: Time distribution of ΔNa in the solution (Na_{water}-Na_{Moody}). Bars represent uncertainty brackets.

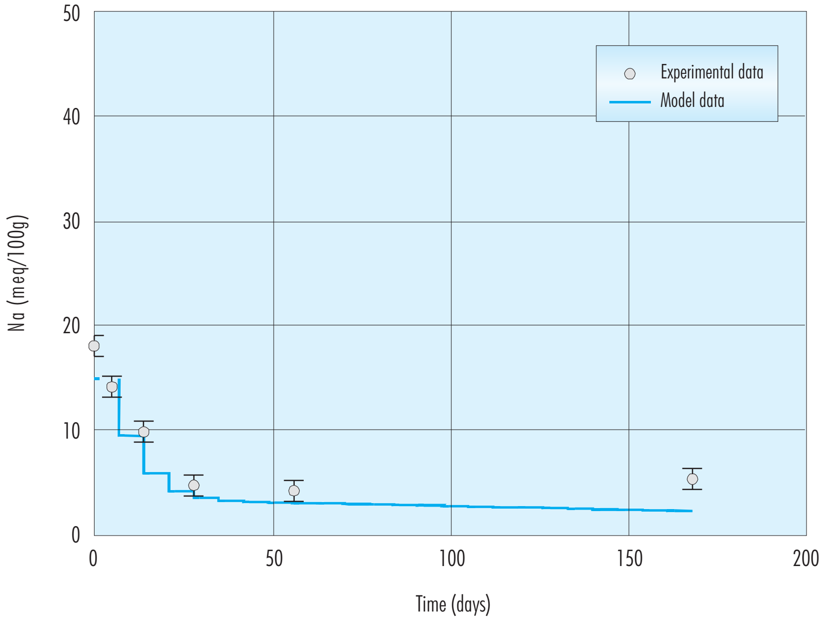

Figure 7.11: Time distribution of Na in the bentonite. Bars represent uncertainty brackets.

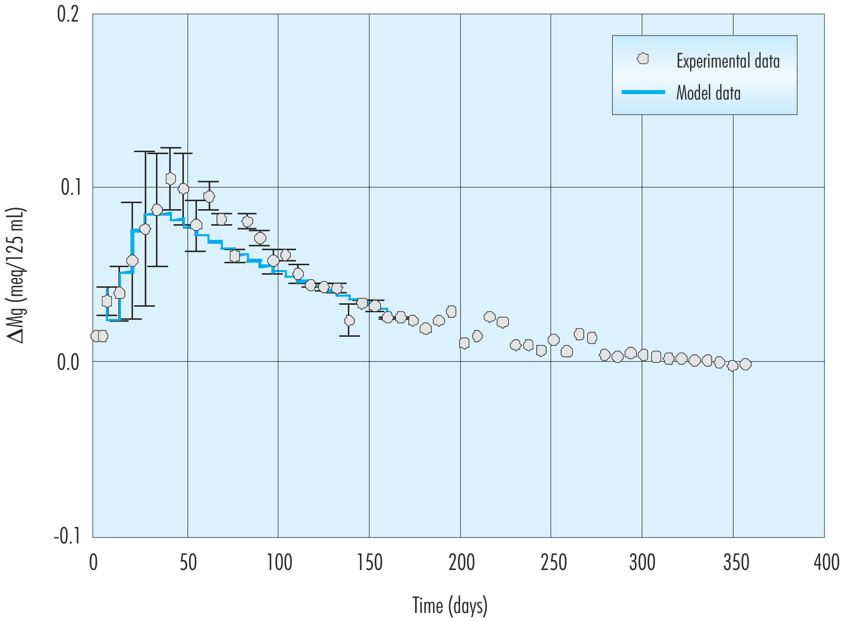

Figure 7.12: Time distribution of ΔMg in the solution (Mg_{water}-Mg_{Moody}). Bars represent uncertainty brackets.

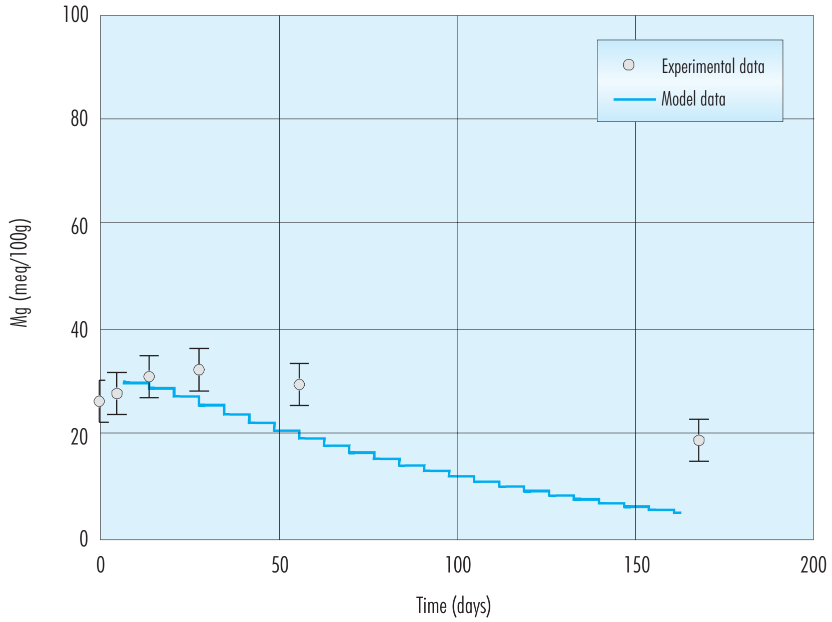

Figure 7.13: Time distribution of Mg in the bentonite. Bars represent uncertainty brackets.

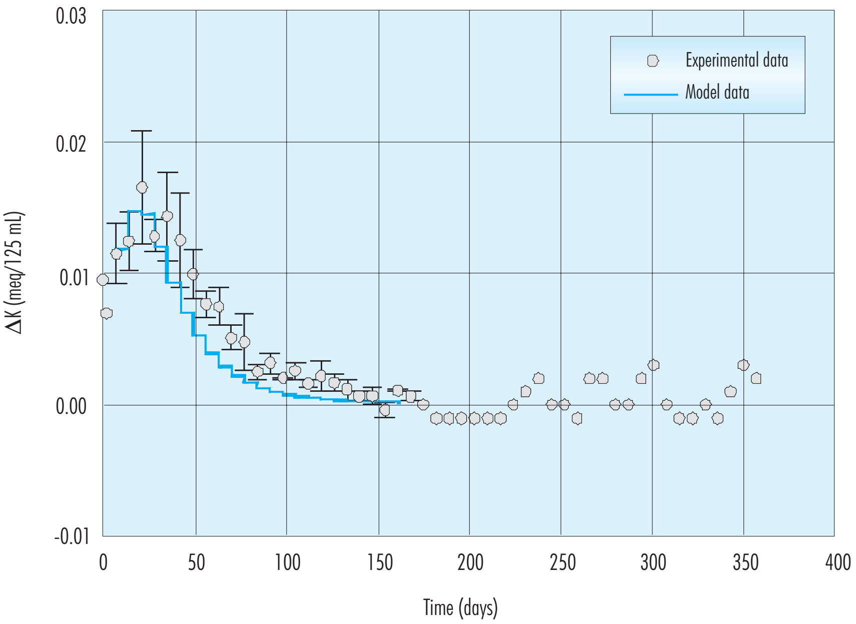

Figure 7.14: Time distribution of ΔK in the solution (K_{water}-K_{Moody}). Bars represent uncertainty brackets.

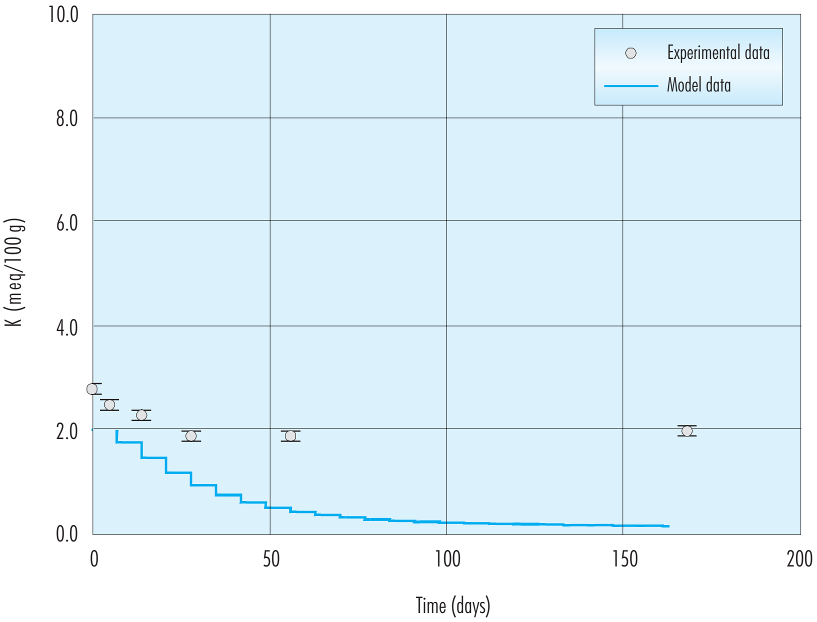

Figure 7.15: Time distribution of K in the bentonite. Bars represent uncertainty brackets.

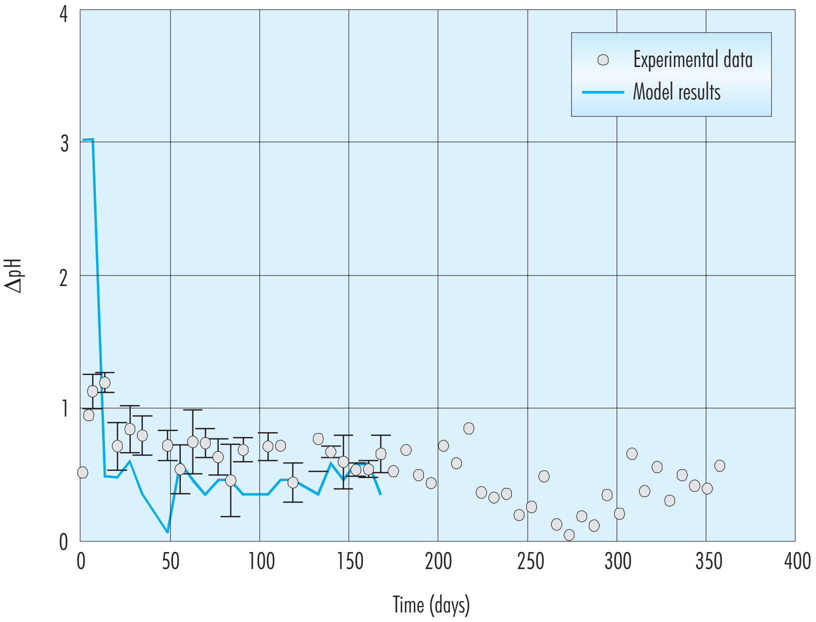

Figure 7.16: Time distribution of ΔpH (pH_{water}-pH_{Moody}). Bars represent uncertainty brackets.

The fact that the numerical results reproduce the observed patterns of the exchange tests indicates that the conceptual model adopted is appropriate. Some features of the geochemical evolution of these tests also take place in the "mock-up" and "in situ" tests. Therefore, understanding and modelling of the CSIC-Zaidín exchange experiments has proven to be most useful for the development of THG models.

7.4.1.3. Modelling of aqueous extraction and squeezing tests

A methodology based on different conceptual geochemical models (CGM) described in Section 7.2.4 has been developed to interpret the chemical analyses of FEBEX bentonite pore water obtained by squeezing and aqueous extraction tests for different S/L ratios performed by CIEMAT (see Chapter 5, Tables 5.12 and 5.13).

Figure 7.17 to Figure 7.22 show the computed results of aqueous extracts tests for different S/L ratios with distilled water using model CGM-1 [191, 193]. The computed values of chloride in Figure 7.17 follow a straight line, indicating that this species is conservative. The model reproduces all the measured data except that of 1:1. Sulphate also shows conservative behaviour (Figure 7.18). Ca^{2+}, Mg^{2+}, Na^{+} and K^{+} are affected by mineral dissolution/precipitation and cation exchange. Therefore, their trends deviate from the straight lines of conservative species. The computed values for these cations match the measured data (Figure 7.19 to Figure 7.22).

Figure 7.23 illustrates that computed bicarbonate concentrations show a trend opposite to that of measured data, possibly due to sample CO_2(g) degassing during aqueous extract tests. Degassing causes calcite precipitation and a decrease of bicarbonate concentration. It should be pointed out that the model considers a fixed pressure of CO_2(g) during the test and, therefore, cannot reproduce measured bicarbonate data. This figure also shows the sensitivity of computed bicarbonate to changes in CO_2(g) pressure. The measured data are between the curves corresponding to CO_2(g) pressures of $10^{-4.4}$ y 10^{-3} bar. These results tend to indicate that measured bicarbonate at different S/L ratios might be reproduced by using different gas pressures for each S/L ratio.

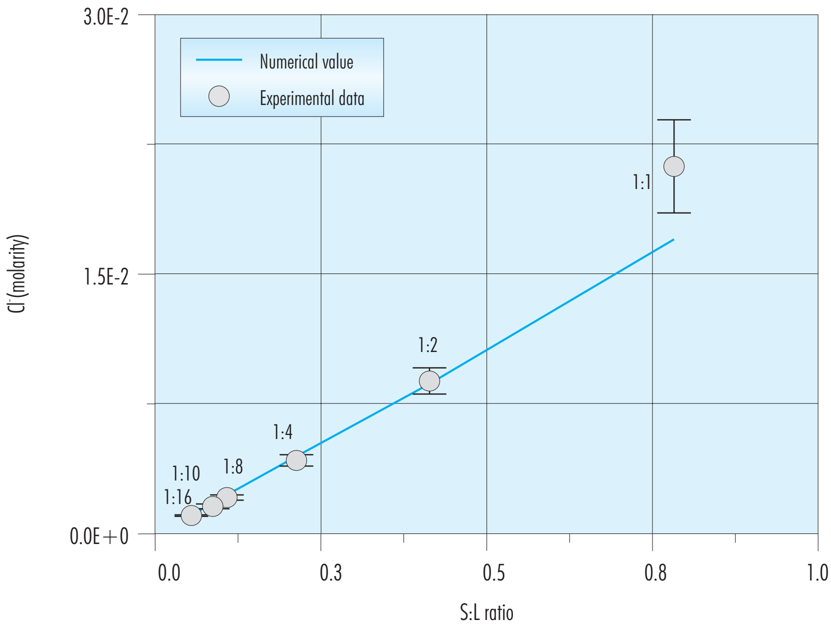

Figure 7.17: Cl^- computed and measured aqueous extract data at different S/L ratios. Values of 1:R (See Section 7.4.1.4.) are given within the squares.

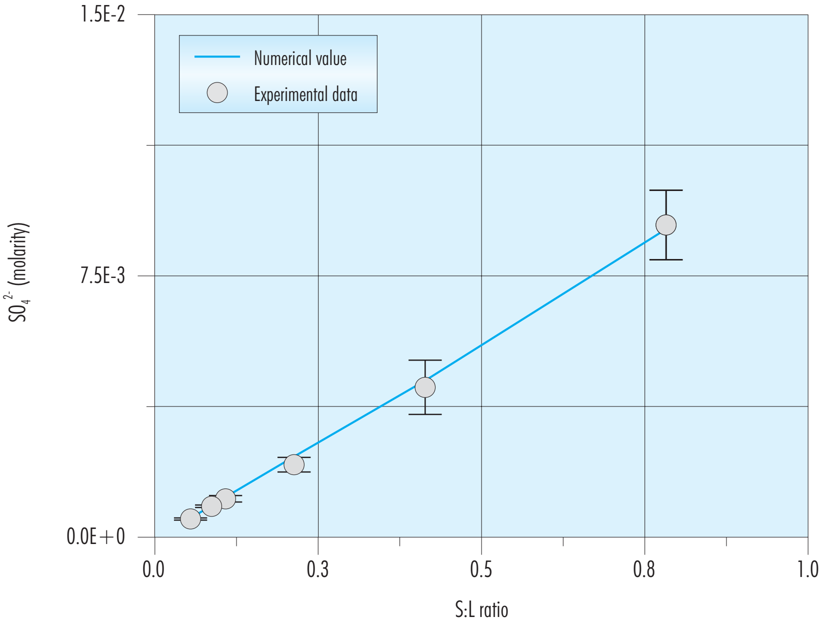

Figure 7.18: SO_4^{2-} computed and measured aqueous extract data at different S/L ratios.

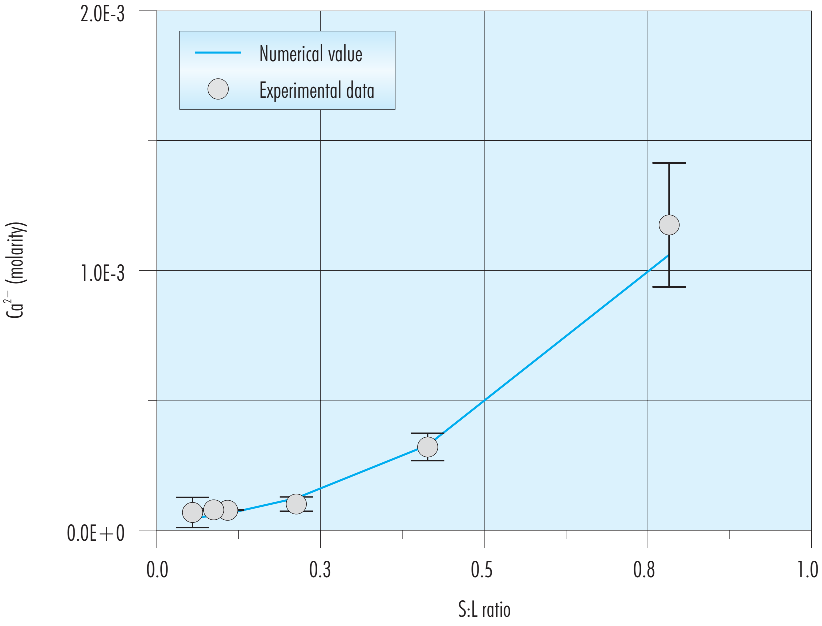

Figure 7.19: Ca^{2+} computed and measured aqueous extract data at different S/L ratios.

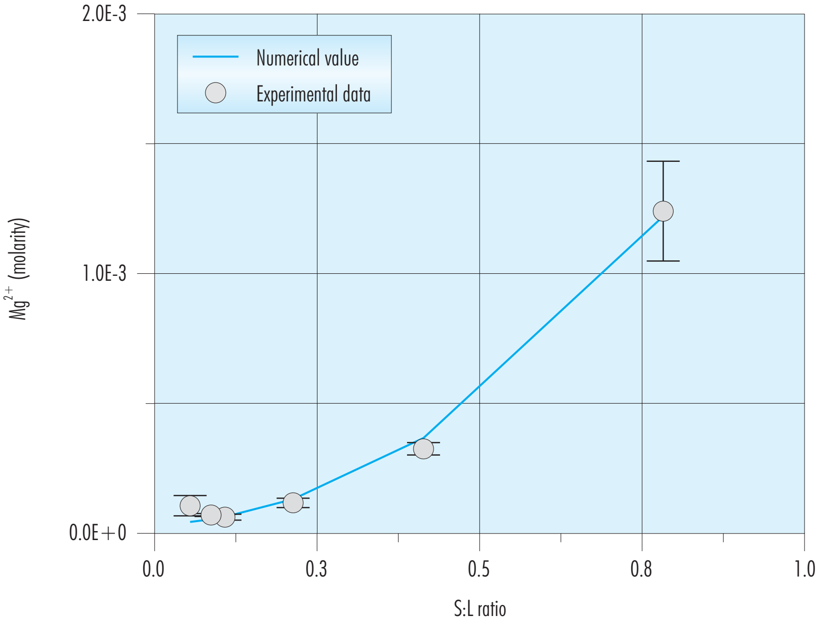

Figure 7.20: Mg^{2+} computed and measured aqueous extract data at different S/L ratios.

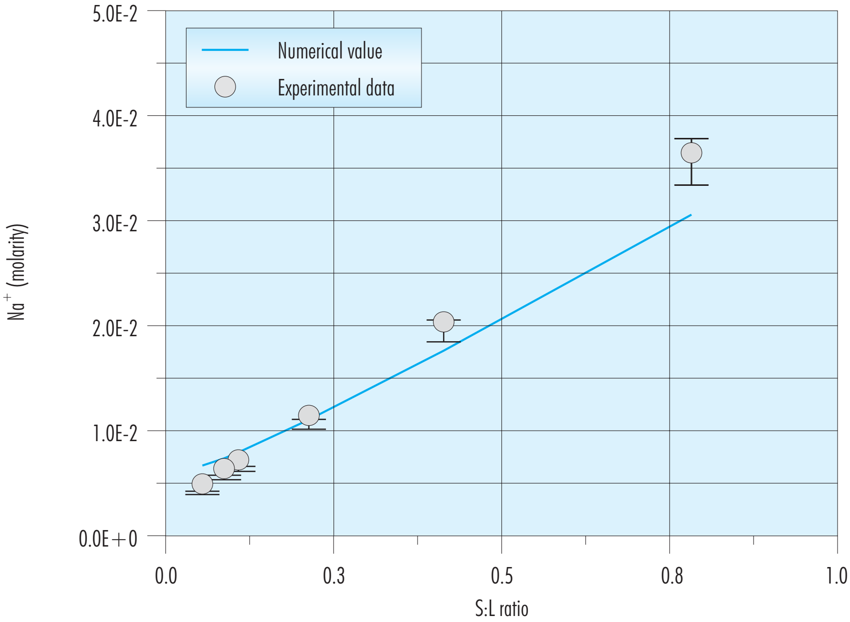

Figure 7.21: Na^+ computed and measured aqueous extract data at different S/L ratios.

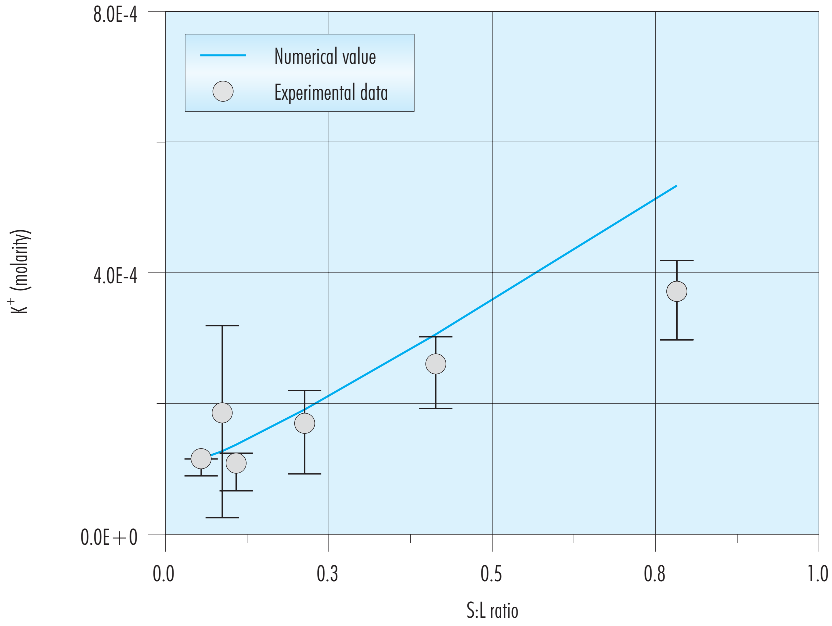

Figure 7.22: K^+ computed and measured aqueous extract data at different S/L ratios.

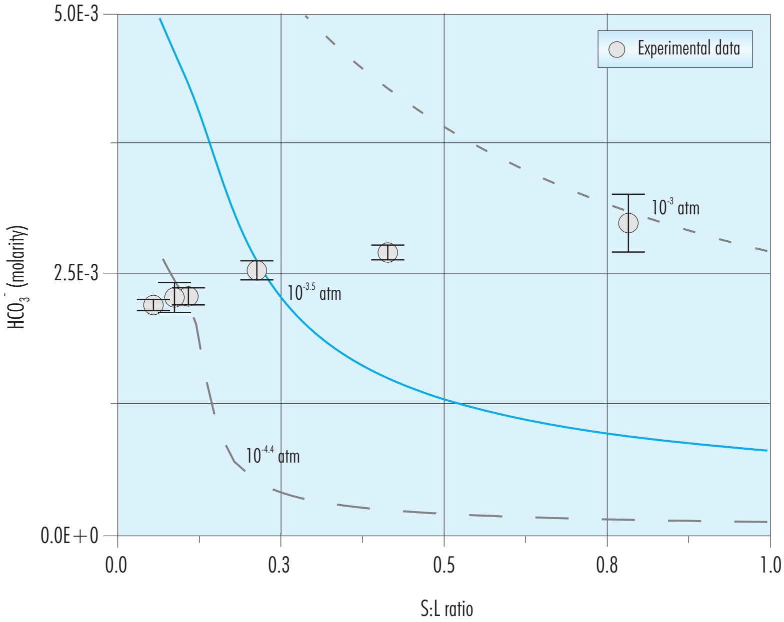

Figure 7.23: HCO_3^- computed and measured aqueous extract data at different S/L ratios. Also shown is the sensitivity of computed HCO_3^- concentrations to changes in prescribed $CO_2(g)$ pressures.

Figure 7.24 shows that calculated pH agrees well with the measured data at high S/L ratios, however, at low S/L ratios the computed values deviate from experimental data, possibly also due to CO_2(g) degassing. Current THG models assume either a constant CO_2(g) pressure or no gas flow. None of these assumptions seems to hold under the conditions of the aqueous extracts tests. Future studies should address this limitation of current THG models.

When model CGM-1, which is based on aqueous extract data, is used to model squeezing data at w = 23.5 and 30% it is found that the computed sulphate concentrations largely over predict the measured squeezing data (Figure 7.25), due possibly to an excessive dissolution of gypsum.

In order to overcome this discrepancy, a modified version of model CGM-1 was postulated which assumes that initially no gypsum is present in the clay sample at w = 14%. In this modified model, which is denoted as CGM-2, the concentration of sulphate at w = 14% is assumed to be smaller than that of model CGM-1 [191, 193]. Optimum concentrations of other species at w = 14% were derived by trial and error hydro-geochemical modelling using CORE^{2D} V4 [199]. Chloride, calcium and magnesium concentrations at w = 14% for CGM-2 are greater than those of CGM-1.

Figure 7.25 to Figure 7.31 show the comparison of concentrations computed with models CGM-1 and CGM-2 at different S/L ratios and their fit to the experimental data. Figure 7.25 shows the results for sulphate. While model CGM-1, which considers the presence of gypsum in the system, is able to fit aqueous extract data, it fails to match measured squeezing data. On the other hand, the concentrations of sulphate computed with model CGM-2, which does not consider gypsum in the system (although it allows for its precipitation), match the measured squeezing data but largely under predict measured aqueous extract data. For chloride both models give similar results, although model CGM-1 under predicts squeezing data (Figure 7.26).

In general, model CGM-2 fits better the aqueous extract and squeezing calcium and sodium data than does model CGM-1 (Figure 7.27 and Figure 7.30). The curves of computed calcium concentrations for models CGM-1 and CGM-2 cross each other at a ratio of S/L = 6, which corresponds to w = 16.6%.

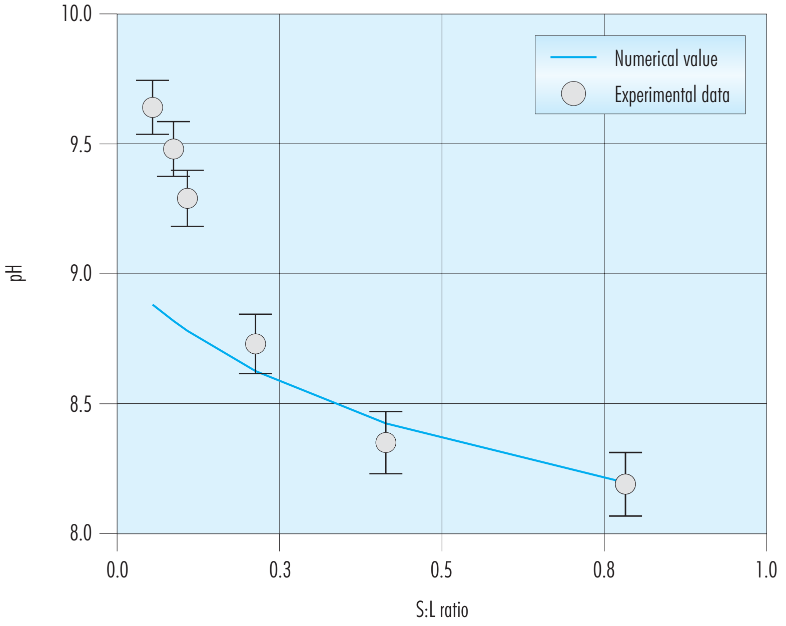

Figure 7.24: pH computed and measured aqueous extract data at different S/L ratios.

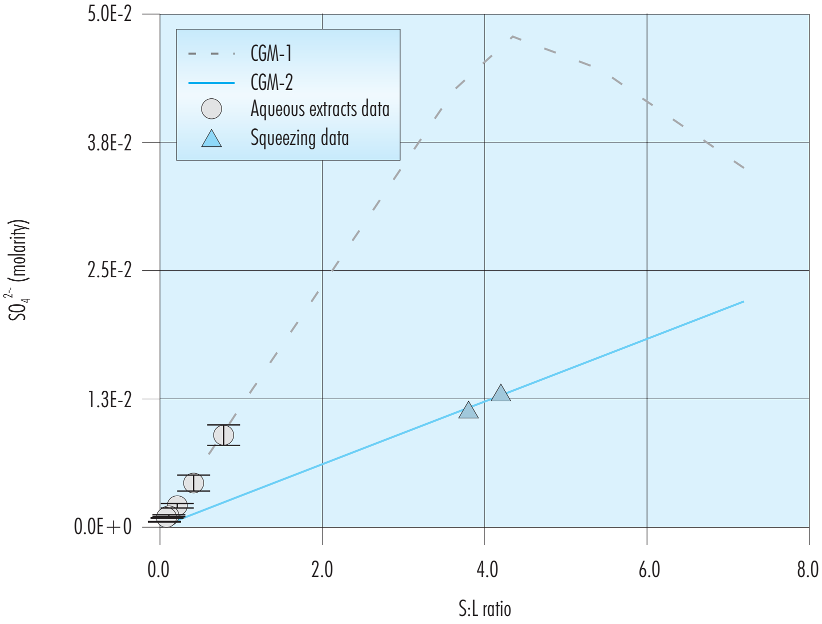

Figure 7.25: SO_4^{2-} computed (lines) and measured (symbols) squeezing and aqueous extract concentrations at different S/L ratios for models CGM-1 and CGM-2.

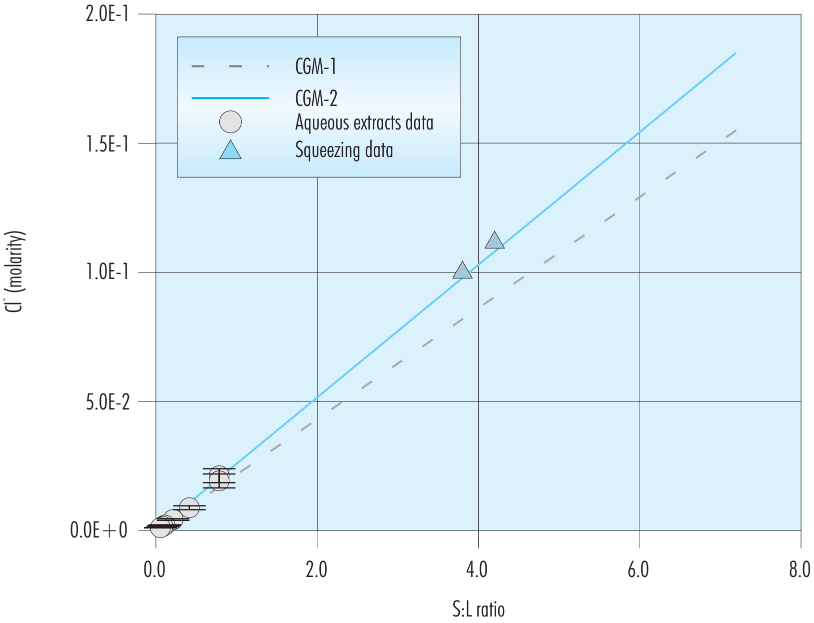

Figure 7.26: Cl^- computed (lines) and measured (symbols) squeezing and aqueous extract concentrations at different S/L ratios for models CGM-1 and CGM-2.

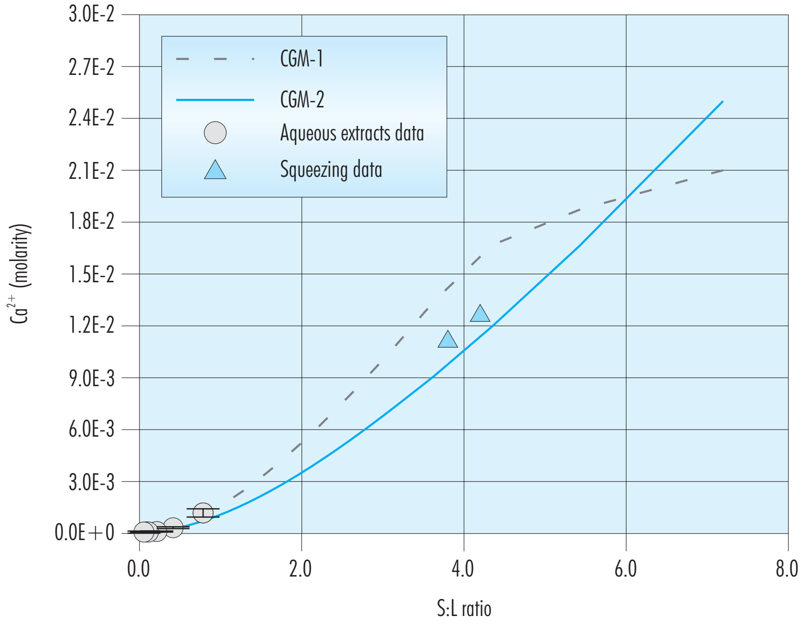

Figure 7.27: Ca^{2+} computed (lines) and measured (symbols) squeezing and aqueous extract concentrations at different S/L ratios for models CGM-1 and CGM-2.

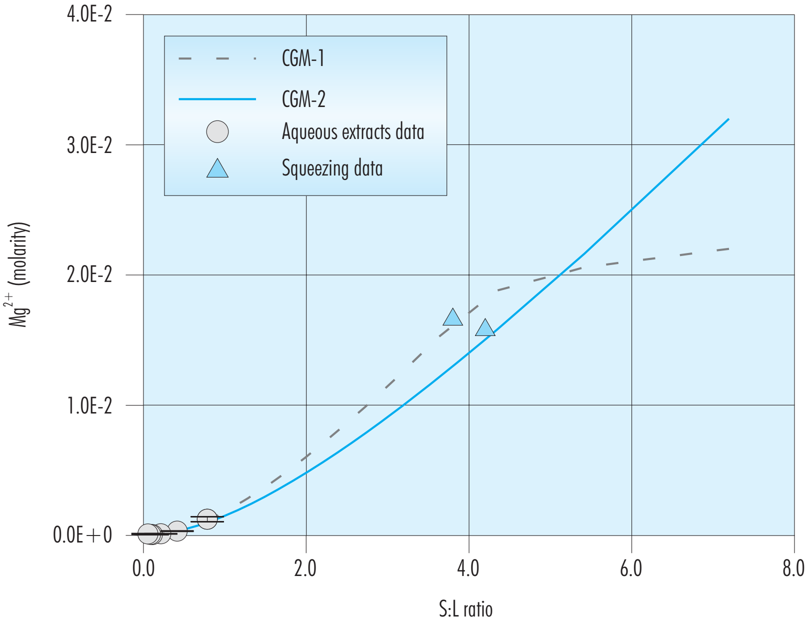

Figure 7. 28:Mg^{2+} computed (lines) and measured (symbols) squeezing and aqueous extract concentrations at different S/L ratios for models CGM-1 and CGM-2.

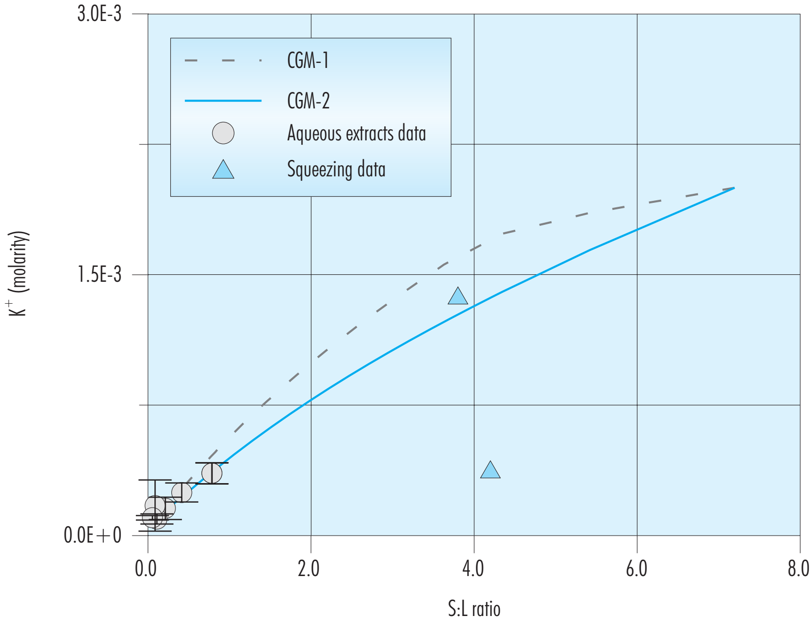

Figure 7.29: K$^+$ computed (lines) and measured (symbols) squeezing and aqueous extract concentrations at different S/L ratios for models CGM-1 and CGM-2.

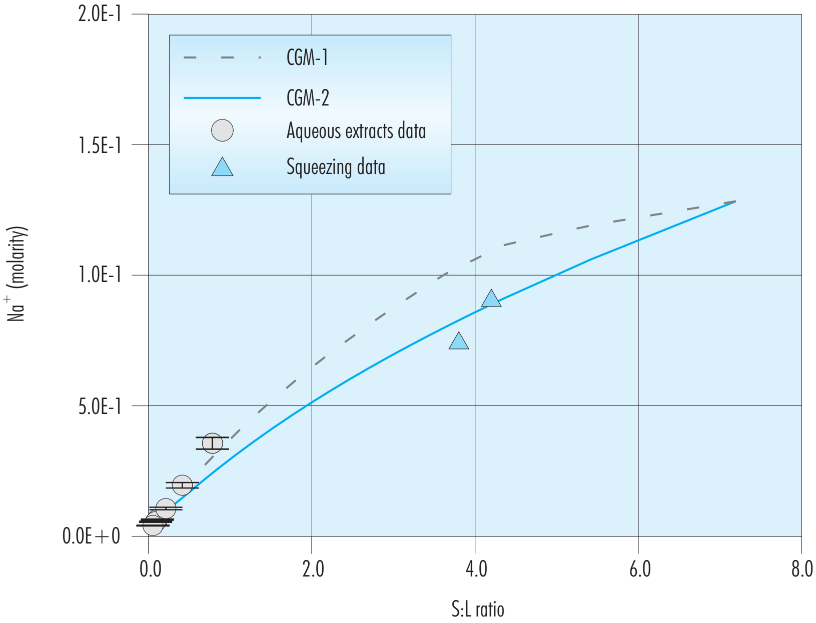

Figure 7.30: Na$^+$ computed (lines) and measured (symbols) squeezing and aqueous extract concentrations at different S/L ratios for models CGM-1 and CGM-2.

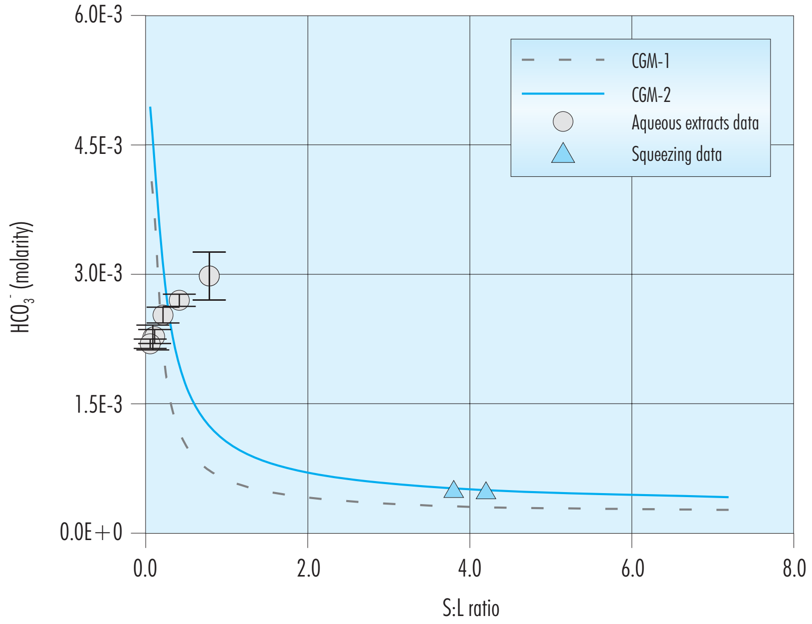

Figure 7.31: HCO_3^- computed (lines) and measured (symbols) squeezing and aqueous extract concentrations at different S/L ratios for models CGM-1 and CGM-2.

Magnesium shows a similar pattern (Figure 7.28). Figure 7.30 clearly illustrates that even though the initial concentration (at w = 14%) is similar in both models, the evolutions of sodium concentration with increasing S/L ratios predicted by the two models are different. Figure 7.31 illustrates that both models predict a decrease of bicarbonate concentration with increasing S/L ratio.

In summary, model CGM-1, derived from aqueous extract data, fits the measured data at different S/L ratios for most of the chemical species. However, it fails to reproduce the trend of bicarbonate, possibly due to changes in the pressure of CO_2(g), which are not considered in the model. The results computed with model CGM-1 show slight deviations for the 1:1 data of chloride, sodium and potassium. In general this model cannot fit squeezing data [191, 193].

Model CGM-2 fits simultaneously aqueous extract and squeezing data, although it presents some clear deviations for sulphate and bicarbonate. The measured data tend to reject the hypothesis of a constant pressure of CO_2(g) during the tests. This hypothesis needs to be revised in the future [191, 193].

7.4.1.4 Modelling of bentonite porewater chemistry

One of the major uncertainties in the geochemical conceptual model is the chemical composition of the FEBEX bentonite pore water at 14% water content. This is the chemical composition needed for THG modelling of the large tests. Geochemical characterisation of clays can be performed in-situ (field techniques) and ex-situ by means of laboratory techniques (squeezing and aqueous extraction tests). The problem of isolation of the “true” pore water to obtain reliable data on pore water chemistry has not yet been solved. A great deal of effort has been made by CIEMAT to improve the water extraction methods, and by UDC in developing numerical interpretation methods, in order to achieve consistency between the analytical evidence (obtained after squeezing clay samples or from aqueous extraction tests) and geochemical knowledge of the processes taking place in the bentonite (based on mineralogy, exchange complex composition, selectivity coefficients or exchange isotherms, determination of the correct hypothesis regarding openness/closeness of the geochemical system, relevance of chemical kinetics, etc). These processes governing pore water chemistry in the bentonite are the same, regardless of whether they take place in the thermo-hydraulic cells, in the "mock-up", at the "in situ" barrier, in exchange tests or in the tests conducted to extract the pore waters from the bentonite.

Squeezing at high pressures and aqueous extracts, which have been used to obtain pore water from compacted FEBEX bentonite, may alter the water-clay system in several ways and introduce sampling artefacts in measured data. Squeezing at high pressures may induce the oxidation and dissolution of accessory minerals of the bentonite, the deggassing of $CO_2(g)$, and chemical fractionation. Furthermore, squeezing does not allow pore water to be extracted from bentonites with water contents below 20%. The squeezing method cannot be used to characterise bentonite under ambient conditions with a water content of 14%. For these conditions the aqueous extract technique must be used.

The aqueous extract technique provides a method for quantification of the total content of soluble salts because it works with a low solid-to-liquid ratio. A 1:R aqueous extract test consists of adding to a mass M of clay sample a mass of distilled water equal to R times M [191, 193]. The mixture of solid and water is allowed to react over a period of time (usually 2 days). Subsequently, the liquid and solid phases are separated by centrifugation. Chemical analyses are performed on the supernatant solution. It should be pointed out that the solid-to-liquid ratio S/L is equal to the aqueous extract ratio 1:R when the clay sample is completely dry. If the clay sample has an initial gravimetric water content, w_0, then the ratio S/L is given by [191, 193]:

$$\frac{S}{L}=\frac{1}{w_0+R(1+w_0)} \qquad (7.1)$$

During the extraction, the mineral dissolution of various soluble minerals (halite, carbonates and gypsum) and cation exchange processes take place, affecting the concentrations of the dissolved species. These processes complicate the interpretation of aqueous extract data.

Since the laboratory techniques used to obtain bentonite pore water may alter the geochemical system and introduce sampling artefacts, indirect methods based on hydro-geochemical modelling are needed in order to infer the chemical composition of bentonite pore water. Different methods have been developed to interpret chemical analyses of FEBEX bentonite pore water obtained by aqueous extract tests. These methods have been applied to model different aqueous extract tests carried out by CIEMAT on intact FEBEX bentonite samples at the following 1:R ratios: 1:1, 1:2, 1:4, 1:8, 1:10 and 1:16 with distilled and granitic water (see Chapter 5, Tables 5.13 and 5.14). Tests were also performed with different reaction times, ranging from 2 to 30 days, for a 1:4 ratio in order to evaluate the kinetics of mineral dissolution/precipitation. The results obtained from these tests were compared to values derived from squeezing tests carried out by CIEMAT (see Chapter 5, Table 5.12).

The initial bentonite pore water chemical composition was obtained by inverse hydro-geochemical modelling using the reactive transport code CORE^{2D} V4 [199]. Starting with the initial chemical composition of bentonite pore water at a water content of 14%, distilled water is added until the appropriate S/L ratio of the test is attained. The distilled water added to the bentonite samples has a pH of 7 and the chemical concentration of all species is 10^{-20} mol/L. $CO_2(g)$ is fixed at atmospheric pressure ($10^{-3.5}$ bar). Cation exchange was modelled using

Table 7.4
Selectivity coefficients and cation exchange capacity used in the model

	Selectivity coefficients	Exchangeable cations (meq/100g)
NaX	1	26.95
KX	$1.43\cdot10^{-1}$	2.29
Mg_2X	$4.40\cdot10^{-1}$	33.15
Ca_2X	$5.63\cdot10^{-1}$	33.1
HX	$8.40\cdot10^{-6}$	1

selectivity coefficients calculated in accordance with the Gaines-Thomas convention. Table 7.4 shows selectivity coefficients and cation exchange capacity (CEC) values.

Tables 7.5 and 7.6 show the chemical compositions of FEBEX bentonite pore water under ambient (w = 14%) and saturated conditions (w = 23.8%) inferred with different conceptual geochemical models CGM-0, CGM-1 and CGM-2 [191, 193]. These chemical compositions were derived from hydro-geochemical modelling of different aqueous extracts and squeezing tests. These tables also contain the values calculated using model CGM-Ciemat. In general, the inferred concentrations at w = 14% with different models are similar. At saturation, w = 23.8%, there are discrepancies, which are significant for sulphate, bicarbonate and calcium [191, 193].

7.4.2. Modelling permeability tests

The experimental column used for the permeability test consists of a stainless steel cell in which a sam-

Table 7.5
Inferred chemical composition (mol/L) and pH of FEBEX bentonite pore water at 14% water content obtained with different conceptual geochemical models

	CGM-0	CGM-1	CGM-2	CGM-Ciemat
Cl^-	$1.8\cdot10^{-1}$	$1.55\cdot10^{-1}$	$1.85\cdot10^{-1}$	$1.6\cdot10^{-1}$
SO_4^{2-}	$2.1\cdot10^{-2}$	$3.1\cdot10^{-2}$	$2.2\cdot10^{-2}$	$3.2\cdot10^{-2}$
HCO_3^-	$5.7\cdot10^{-4}$	$3.9\cdot10^{-4}$	$4.1\cdot10^{-4}$	$4.1\cdot10^{-4}$
Ca^{2+}	$1.1\cdot10^{-2}$	$2.1\cdot10^{-2}$	$2.5\cdot10^{-2}$	$2.2\cdot10^{-2}$
Mg^{2+}	$1.4\cdot10^{-2}$	$2.2\cdot10^{-2}$	$3.2\cdot10^{-2}$	$2.3\cdot10^{-2}$
Na^+	$1.8\cdot10^{-1}$	$1.28\cdot10^{-1}$	$1.28\cdot10^{-1}$	$1.3\cdot10^{-1}$
K^+	$1.6\cdot10^{-3}$	$2.3\cdot10^{-3}$	$2.3\cdot10^{-3}$	$1.7\cdot10^{-3}$
pH	7.86	7.62	7.62	7.72

Table 7.6
Inferred chemical composition (mol/L) and pH of FEBEX bentonite porewater at 23.8% water content obtained with different conceptual geochemical models

	CGM-0	CGM-1	CGM-2	CGM-Ciemat
Cl^-	$1.12\cdot10^{-1}$	$1.10\cdot10^{-1}$	$1.39\cdot10^{-1}$	$1.13\cdot10^{-1}$
SO_4^{2-}	$1.27\cdot10^{-2}$	$4.37\cdot10^{-2}$	$1.65\cdot10^{-2}$	$4.30\cdot10^{-2}$
HCO_3^-	$6.45\cdot10^{-4}$	$4.15\cdot10^{-4}$	$4.55\cdot10^{-4}$	$1.54\cdot10^{-3}$
Ca^{2+}	$6.34\cdot10^{-3}$	$1.92\cdot10^{-2}$	$1.66\cdot10^{-2}$	$1.54\cdot10^{-2}$
Mg^{2+}	$8.82\cdot10^{-3}$	$2.14\cdot10^{-2}$	$2.16\cdot10^{-2}$	$1.94\cdot10^{-2}$
Na^+	$1.14\cdot10^{-1}$	$1.20\cdot10^{-1}$	$1.06\cdot10^{-1}$	$1.29\cdot10^{-1}$
K^+	$1.04\cdot10^{-3}$	$2.15\cdot10^{-3}$	$1.64\cdot10^{-3}$	$1.24\cdot10^{-3}$
pH	7.94	7.65	7.69	7.43

ple of compacted clay is subject to water flow (Figure 7.32). The internal diameter of the cell is 5 cm and the length is 2.5 cm. An HPLC pump injects a solution at a pressure of 4 MPa through a porous stainless steel filter, providing a flow rate that after stabilisation reaches a nearly constant value of approximately $2.0 \cdot 10^{-3}$ L/month. The out-flowing water emerges through another stainless steel filter, is recovered at the end of the compacted clay and sampled inside a syringe [191, 206, 207]. The main characteristics of this test are listed in Table 7.7.

The chemical composition of the inflow granitic water is listed in Table 7.8 [206]. The initial pore water chemical composition of the FEBEX compacted bentonite at a dry density of 1.65 g/cm^3 depends on the conceptual geochemical model used in THG modelling.

Hydrodynamic and chemical data were monitored throughout the duration of the experiment. Nearly $2 \cdot 10^{-3}$ L were needed for a complete chemical analysis; therefore samples could only be taken once the cell delivered a sufficient amount of water. The first sample of $2 \cdot 10^{-3}$ L was obtained after 69 days, the second after 107 days and the rest of the aliquots were obtained, regularly, each month with an approximate flow rate of $2 \cdot 10^{-3}$ L/month.

The clay sample has a dry density of 1.65 g/cm^3 and a porosity of 0.39. A total volume of $9.113 \cdot 10^{-2}$ L was collected after 1177 days. The quasi steady-state hydraulic conductivity of the clay is $2.7 \cdot 10^{-14}$ m/s.

Table 7.7
Main characteristics of the permeability test

Initial time	Initial dry density (g/cm^3)	Initial gravimetric water content (%)	Total clay weight (Kg)	Pore volume (m^3)	Injection pressure (MPa)
29/9/98	1.65	23.1	$9.97 \cdot 10^{-2}$	$1.909 \cdot 10^{-5}$	4

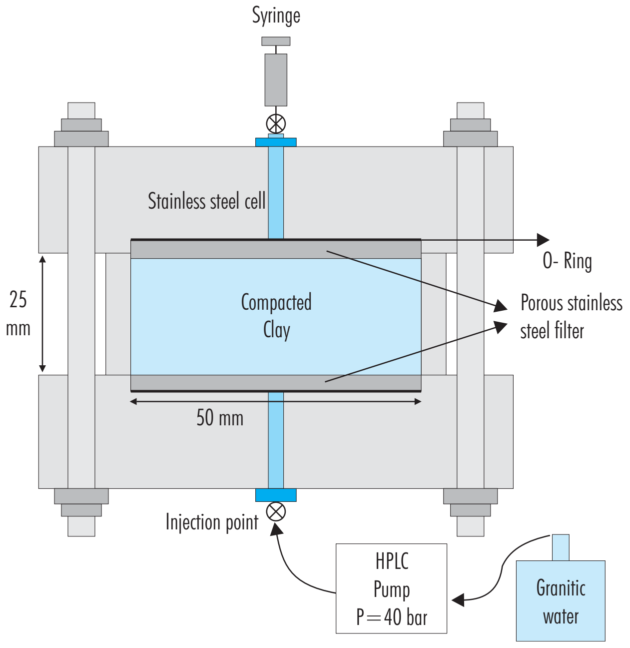

Figure 7.32: Schematic design of the permeability test [206].

Table 7.8
Chemical composition (mg/L) of the inflow granitic water (1)

Cations	Concentration	Anions	Concentration
Na^+	11.5 ± 0.7	F^-	0.20
K^+	1.0 ± 0.00	Cl^-	13.5 ± 0.7
Ca^{2+}	40 ± 7.1	Br^-	<0.10
Mg^{2+}	8.9 ± 0.7	NO_2^-	<0.10
Sr^+	0.09 ± 0.01	NO_3^-	4.3 ± 0.7
Ba^+	0.04 ± 0.01	HCO_3^-	144.5 ± 0.7
Cs^+	$5.6 \cdot 10^{-3}$	SO_4^{2-}	14 ± 0.0
Al^{3+}	$80 \cdot 10^{-3}$	PO_4^{3-}	<0.10
B^{3+}	$31 \cdot 10^{-3} \pm 41 \cdot 10^{-3}$	SiO_2	22.1 ± 0.1
Mn^{2+}	<0.03	I^-	$10.7 \cdot 10^{-3} \pm 3 \cdot 10^{-3}$

(1) pH=8.15±0.21; Eh=262 mV; EC=291 μS/cm.

The electrical conductivity of the effluent water decreased from 15536 in the first aliquot to 700 μS/cm in the last. Most chemical species show clear dilution trends, which are shown below. Chloride, for instance, decreases from 3500 to 64 mg/L [206].

7.4.2.1. Uncertainties in interpretation of the permeability cell test

There are uncertainties in interpretation of the permeability test related to the conceptual geochemical model. The test was modelled using the three conceptual models. The modelling results with these three conceptual geochemical models reproduce the general trends of the measured data. The models fail, however, to capture the long tails of most species. The concentrations of some species are overestimated from 200 to 600 days. There are uncertainties in the initial concentration of some species, such as calcium. These limitations were overcome by estimating initial concentrations and diffusion coefficients. Another uncertainty is related to proton adsorption/desorption. Numerical results show that proton adsorption/desorption is very important for pH evolution over time, while this is not the case for bicarbonate (Figures 7.33 and 7.34). Another source of uncertainty is related to the relevance of double porosity.

7.4.2.2. Numerical model and results

Single porosity model: forward model

In the single porosity model, the system is divided into two material zones, one for the bentonite and another for the stainless steel filter. The parameters used for these two material zones are summarised in Table 7.9. Transport porosity, density and saturated hydraulic conductivity were taken from the experimental results. Diffusion coefficients were taken from those used for the coupled thermo-hydro-geochemical models of the “mock-up” and “in situ” tests [13, 191, 206, 207]. Dirichlet flow boundary conditions have been used. The calculated water outflow is compared to the measured outflows in Figure 7.35. For solute transport a Neuman transport boundary condition was used, according to which solute flux is equal to the product of solute

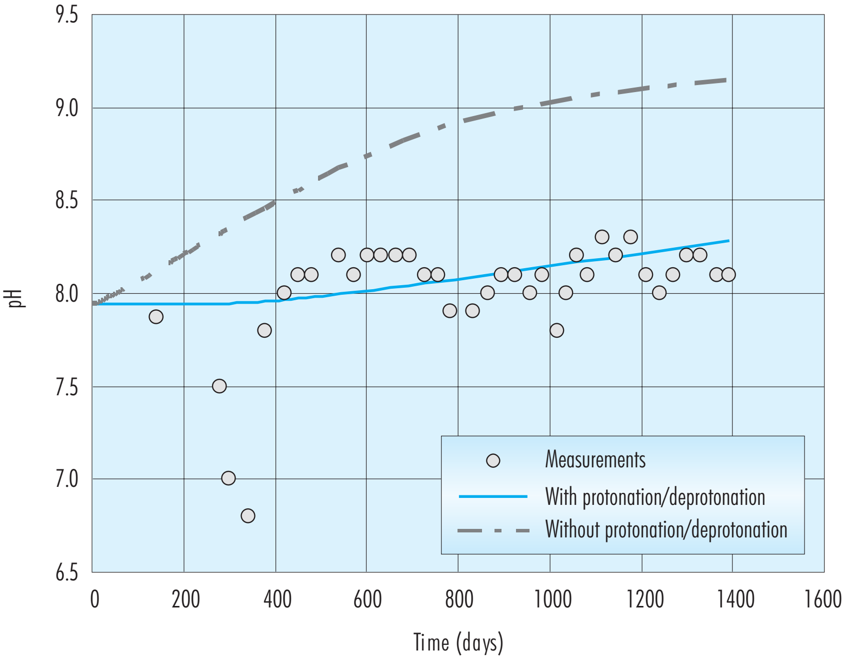

Figure 7.33: Sensitivity of computed pH to protonation/deprotonation.

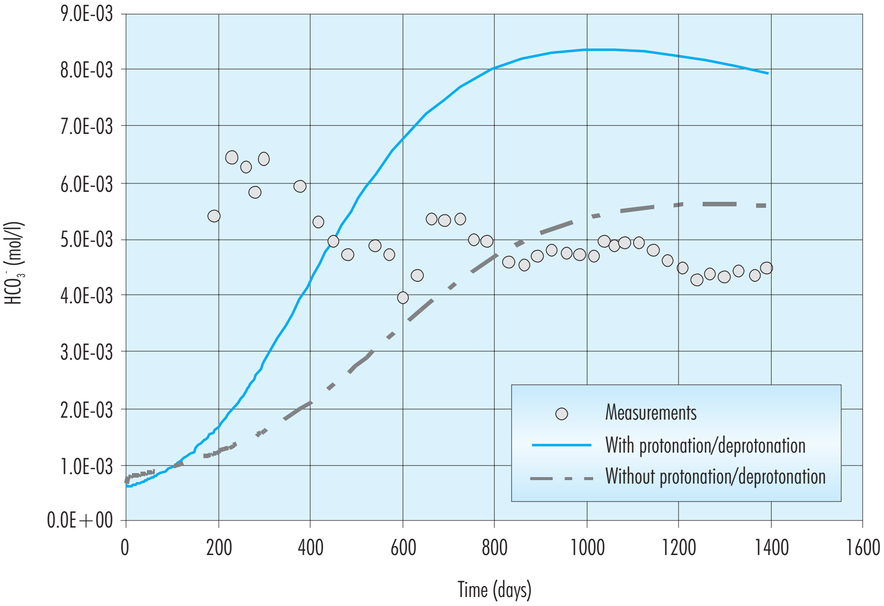

Figure 7.34: Sensitivity of computed bicarbonate to protonation/deprotonation..

concentration times water flux. The permeability test was modelled using CORE^{2D} V4 [199]. Using model CGM-0 and considering protonation/deprotonation, a forward reactive transport model has been performed [207].

Single porosity model: inverse model

Chloride, which undergoes anion exclusion, was analysed separately by estimating its accessible porosity and diffusion coefficient. The estimation results are shown in Table 7.10. Breakthrough curves of chloride computed with and without anion exclusion are compared to measured data in Figure 7.36. Although the overall fit of the model results to the measured data is good, a semi-log plot of concentrations (Figure 7.37) reveals that this model does not reproduce well the long tail of the curve. The model tends to underestimate concentrations later in time.

The inverse problem was modelled using INVERSE-CORE^{2D} V1 and solved in two steps. In the first step, the initial concentrations of Ca^{2+}, Mg^{2+}, Na^+, K^+, SO_4^{2-} and HCO_3^- were estimated. In the second step, initial concentrations of Ca^{2+}, Mg^{2+}, Na^+, K^+, SO_4^{2-}, HCO_3^- together with the diffusion coefficient were estimated simultaneously. Table 7.11 shows the estimated initial concentrations and effective diffusion coefficient for these two steps.

Model results improve by estimating initial concentrations and effective diffusion coefficients. However, there are discrepancies for bicarbonate, which are especially noticeable in the early stages. As stated above, bicarbonate concentrations are very sensitive to changes in CO_2(g) pressure. The reason for the poor fit of the bicarbonate data is, therefore, related to an inadequate definition of CO_2(g) pressure in the model.

Table 7.9
Parameters of FEBEX compacted bentonite and stainless steel filter

Parameters	Bentonite	Stainless steel filter
Saturated hydraulic conductivity, m/s	$2.93 \cdot 10^{-14}$	$2.93 \cdot 10^{-8}$
Total transport porosity	0.39	0.80
Molecular diffusion coefficient, m^2/s	$5.70 \cdot 10^{-11}$	$5.70 \cdot 10^{-11}$
Longitudinal dispersivity, m	0.01	0.01
Transverse dispersivity, m	0.01	0.01
Dry density, g/cm^3	1.65	1.20
Tortuosity	$\theta^{7/3} / \phi^{2}$ (1)	$\theta^{7/3} / \phi^{2}$ (1)

(1) *where θ is water content and ϕ is porosity*

Table 7.10
Estimated effective diffusion coefficient and accesible porosity for chloride

Parameters	Estimated values
Effective diffusion coefficient, m^2/s	$6.33 \cdot 10^{-12}$
Accesible porosity	0.237

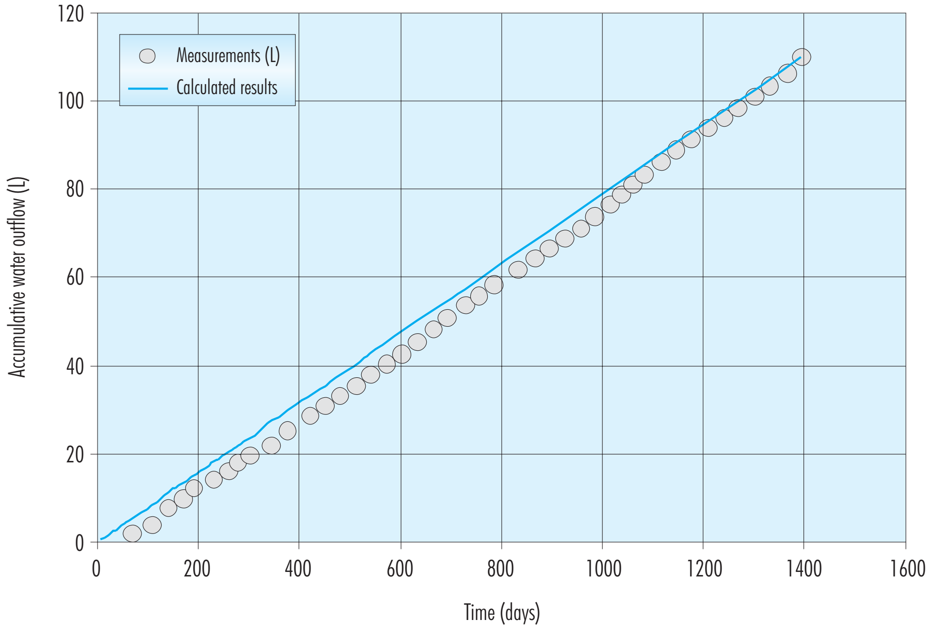

Figure 7.35: Modelling results of cumulative water outflow volume with Dirichlet flow boundary condition.

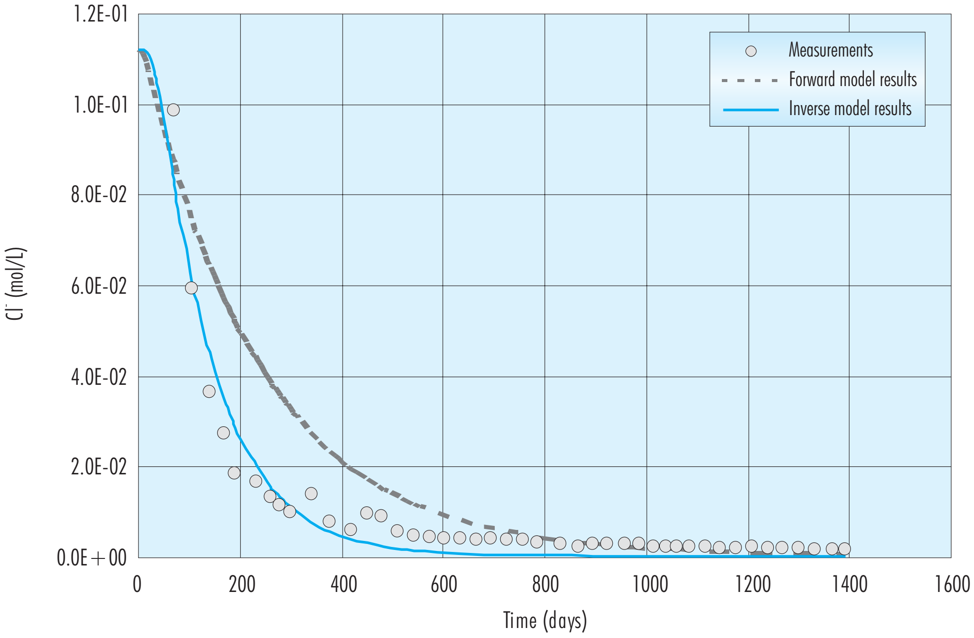

Figure 7.36: Measured and computed breakthrough curve of chloride.

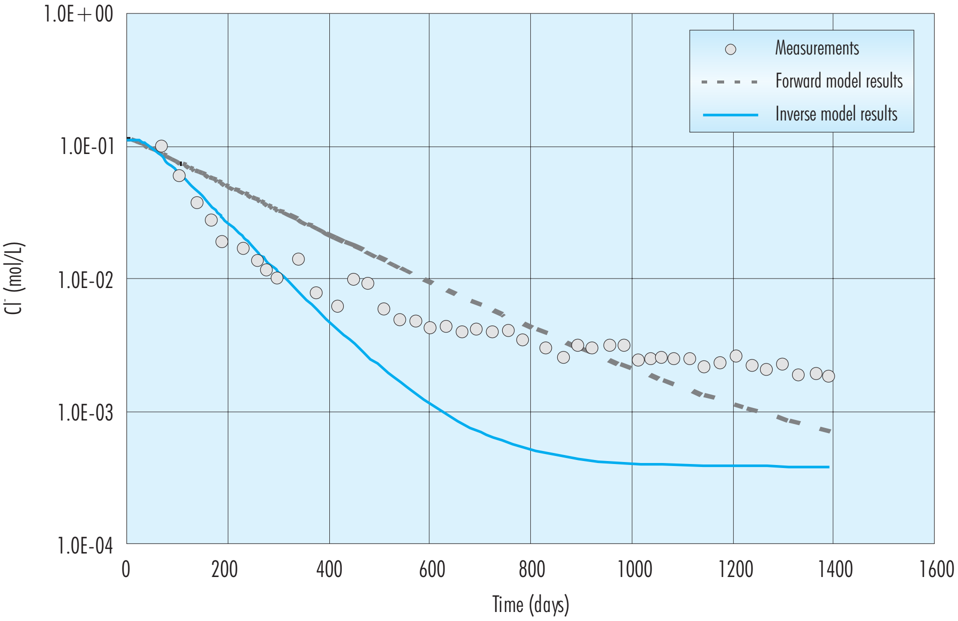

Figure 7.37: Breakthrough curve of chloride on a semi-logarithmic scale.

Double porosity model

Generally the term 'double porosity' is used to represent a conceptual model in which, based on the microscopic heterogeneities, the medium is divided into two or more domains, coupled by an interaction term for the modelling of flow and solute transport. This kind of conceptual model may be called 'dual-domain', 'dual region', 'multi-region', etc., and the sub-regions may be two or more mobile regions or one mobile region and one immobile region [191, 206, 207]. Dual or double porosity models assume that a porous medium consists of two separate but connected continua. Of these, one

Table 7.11
Estimated effective diffusion coefficient (m^2/s) and initial concentrations (mol/L)

Parameters	Estimated values in step 1	Estimated values in step 2
Effective diffusion coefficient	-	$9.51 \cdot 10^{-12}$
Ca^{2+}	$1.64 \cdot 10^{-2}$	$1.44 \cdot 10^{-2}$
Mg^{2+}	$2.00 \cdot 10^{-2}$	$1.80 \cdot 10^{-2}$
Na^{+}	$1.14 \cdot 10^{-1}$	$1.04 \cdot 10^{-1}$
K^{+}	$5.74 \cdot 10^{-4}$	$5.94 \cdot 10^{-4}$
SO_4^{2}	$4.04 \cdot 10^{-2}$	$3.84 \cdot 10^{-2}$
HCO_3^{-}	$6.45 \cdot 10^{-2}$	$6.85 \cdot 10^{-3}$

continuum is associated with a system or network of fractures, fissures, macropores, or intra-aggregate pores, while the other continuum involves the porous matrix blocks or soil aggregates. Hence, dual porosity models usually involve two flow/transport equations, coupled by means of a sink/source term to account for water/solute transfer between the pore systems.

The dual-porosity concept has been commonly used to describe the preferential movement of water and solutes at the macroscopic scale, a phenomenon that is widely believed to occur in most natural (undisturbed) media. This double porosity model has been used to predict water flow in fractured reservoirs or solute transport during both steady-state flow and transient flow.

Compacted clay also exhibits a double porosity behaviour. As shown in Figure 7.38, the double porosity model includes two parts: macro-pores through which water flows, this consequently being considered the mobile part, and micro-pores through which there is no flow, which may be considered as the immobile part. An increased level of complexity may be built into the single porosity model by assuming that equilibrium is not reached between the mobile part (macro-pores) and the immobile part (micro-pores which may not be well connected). Furthermore, it is assumed that almost all of the water flows through the mobile part, although mass transfer (by molecular diffusion) exists between the mobile and immobile parts. In order to account for the two regions in CORE^{2D} V4 [199], three material zones were defined: material 1 which corresponds to the mobile part; material 2 for the immobile part, while material 3 is used to model the two stainless steel filters located upstream and downstream of the clay sample (Figure 7.39).

Let f_m and f_{im} be the fractions of the total volume of the sample occupied by the mobile and immobile domains, respectively. By trial and error we estimated that $f_m = 0.3$ and $f_{im} = 0.7$. In other words, the mobile zone occupies 30% of the total volume of the sample, while the immobile zone of the clay sample is 70%.

It should be noticed that in our formulation of the double porosity, model porosities for mobile and immobile zones (materials 1 and 2) are not global porosities, but relative porosities. Let ϕ_m and ϕ_{im} be the relative porosities of the mobile and immobile zones, which are defined as the ratio of void volume

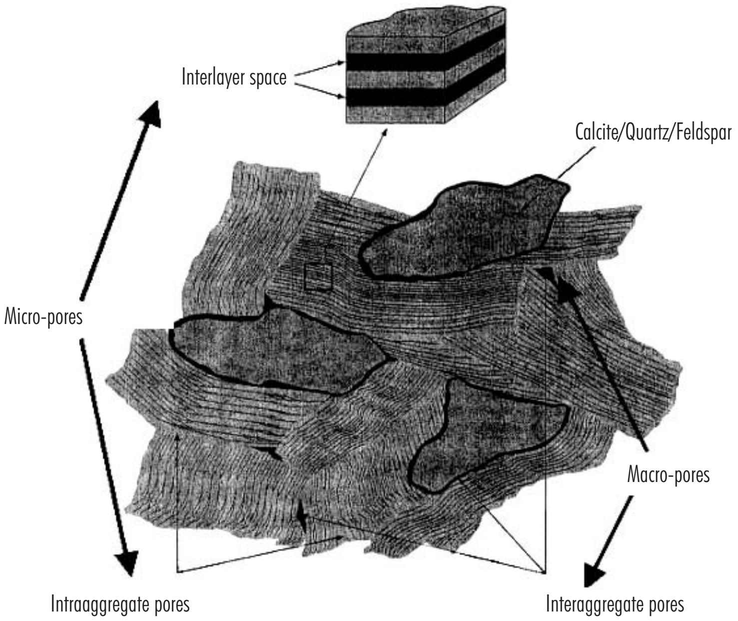

Figure 7.38: Schematic representation of the 'macro-pores', and 'micro-pores' in the double porosity model [207].

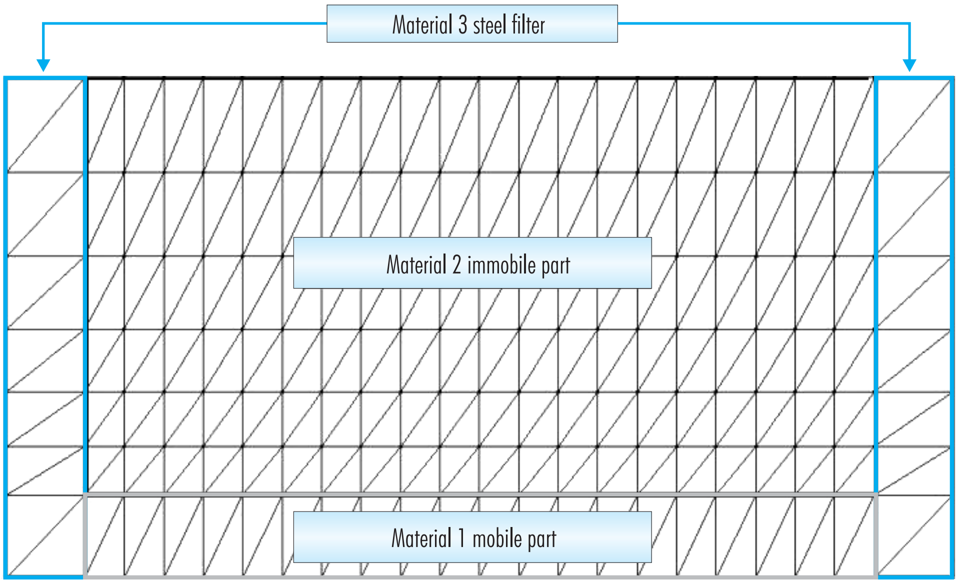

Figure 7.39: Mesh used in the double porosity model.

to the total volume of each domain. According to this approach, the total porosity of the sample is given by $\phi=\phi_m f_m+\phi_{im} f_{im}$. Parameters ϕ_m and ϕ_{im} have a clear physical meaning, although they are hard to measure. It should be noticed that the overall porosity of the mobile region may be computed as $\phi_m f_m$. Similarly, $\phi_{im} f_{im}$ represents the overall porosity of the immobile region. According to our experience, this way of parameterising double porosity is not affected by the geometry adopted in the model. Therefore, the values $\phi_m f_m$ and $\phi_{im} f_{im}$ are independent of the model geometry. The hydrodynamic parameters used in the double porosity model, and the corresponding physical values, are shown in Table 7.12.

The double porosity behaviour of chloride was studied first. Based on the measurement of chloride, total porosity for each domain was estimated, this being used for the rest of the species. In addition, the effective diffusion coefficient and accessible porosity for chloride of each domain were estimated. Anion exclusion was considered for chloride in both the mobile and immobile parts. Effective diffusion coefficients for chloride are shown in Table 7.13. The effective diffusion coefficient of the mobile domain is very similar to the values measured by CIEMAT [191, 205]. The double porosity model leads to results that are better than those of the best inverse single porosity model (Figure 7.40).

There are several uncertainties regarding the double porosity behaviour of reactive species, mineral phases and exchangeable cations for each domain. However, as a first attempt, diffusion coefficients for each reactive species were estimated (Table 7.13). The modelling results are compared with the best results of the single porosity model in Figure 7.40 to Figure 7.47. Some figures are shown on a semi-logarithm scale to illustrate the calculation of the tails of the curves.

7.4.3. THG modelling of heating and hydration cells

A large number of laboratory tests have been conducted by CIEMAT in thermo-hydraulic CT cells (see Chapter 5, Table 5.31). These tests reproduce the effect of simultaneous heating and hydration of bentonite under conditions similar to those of the “in situ” and “mock up” tests. However, some differences are observed between the numerical results

Table 7.12
Material zone parameters for double porosity models

Material	K_1⁽¹⁾ (m/s)	K_2⁽¹⁾ (m/s)	ϕ, ϕ_m, ϕ_{im}⁽¹⁾	DS_L⁽¹⁾ (m)	DS_T⁽¹⁾ (m)
1	$9.75 \cdot 10^{-14}$	$9.75 \cdot 10^{-14}$	0.7	$2.50 \cdot 10^{-3}$	$5.00 \cdot 10^{-4}$
2	$2.93 \cdot 10^{-17}$	$2.93 \cdot 10^{-17}$	0.257	$2.50 \cdot 10^{-3}$	$5.00 \cdot 10^{-4}$
3	$2.93 \cdot 10^{-7}$	$2.93 \cdot 10^{-7}$	0.8	$1.00 \cdot 10^{-3}$	$1.00 \cdot 10^{-3}$
Physical value	$2.93 \cdot 10^{-14}$	$2.93 \cdot 10^{-14}$	0.39	$2.50 \cdot 10^{-3}$	$5.00 \cdot 10^{-4}$

(1) K_1 is hydraulic conductivity in the direction of the flow while K_2 is the conductivity in the transverse direction. ϕ, ϕ_m, ϕ_{im} are total porosity, porosity of mobile domain and porosity of inmobile domain, respectively. DS_L and DS_T are longitudinal and transverse dispersivities.

Table 7.13
Effective diffusion coefficients for the double porosity model

Species	Effective diffusion coefficients, m^2/s		
	Material 1	Material 2	Material 3
H^+	$8.86 \cdot 10^{-11}$	$3.25 \cdot 10^{-17}$	$1.48 \cdot 10^{-8}$
Ca^{2+}	$8.86 \cdot 10^{-11}$	$3.25 \cdot 10^{-17}$	$1.48 \cdot 10^{-8}$
Mg^{2+}	$8.86 \cdot 10^{-11}$	$3.25 \cdot 10^{-17}$	$1.48 \cdot 10^{-8}$
Na^+	$8.86 \cdot 10^{-11}$	$3.25 \cdot 10^{-17}$	$1.48 \cdot 10^{-8}$
K^+	$8.86 \cdot 10^{-11}$	$3.25 \cdot 10^{-17}$	$1.48 \cdot 10^{-8}$
Cl^-	$1.35 \cdot 10^{-12}$	$7.29 \cdot 10^{-15}$	$1.48 \cdot 10^{-8}$
SO_4^{2-}	$8.86 \cdot 10^{-11}$	$3.25 \cdot 10^{-17}$	$1.48 \cdot 10^{-8}$
HCO_3^-	$8.86 \cdot 10^{-11}$	$3.25 \cdot 10^{-17}$	$1.48 \cdot 10^{-8}$

for the CT cells and the “in situ” and “mock up” tests. These differences may be attributed to scale factors (both in space and time). Tests performed on CT-18, CT-23 and CT-24 were modelled [190, 13, 191, 208]. Here only the results of thermohydraulic cell CT-23 are presented.

During the initial FEBEX work, the modelling of thermo-hydraulic cell CT-23 was performed using FADES-CORE-LE V0.0a [196]. As a general procedure for modelling CT cells, first a two-dimensional model was run in order to calibrate flow and transport using the available data and parameters. Once the thermo-hydraulic (TH) model had been calibrated, a one-dimensional numerical model was used for the purpose of full thermo-hydro-geochemical (THG) modelling. In addition to the base or reference model, sensitivity analyses were also performed with respect to key parameters such as diffusion coefficients, vapour tortuosity, and selectivity coefficients.

The most relevant transport processes occurring in the cell may be deduced from the behaviour of a conservative species such as chloride (Figure 7.48). For the purpose of better illustrating the transient behaviour of water flow, solute transport and geochemical reactions, space and time have been nor-

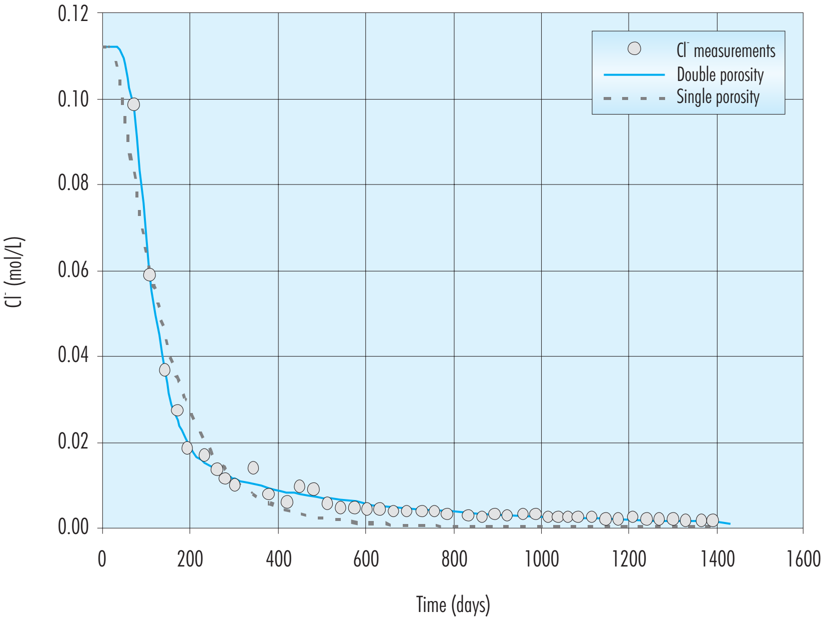

Figure 7.40: Modelling results for chloride with single and double porosity models.

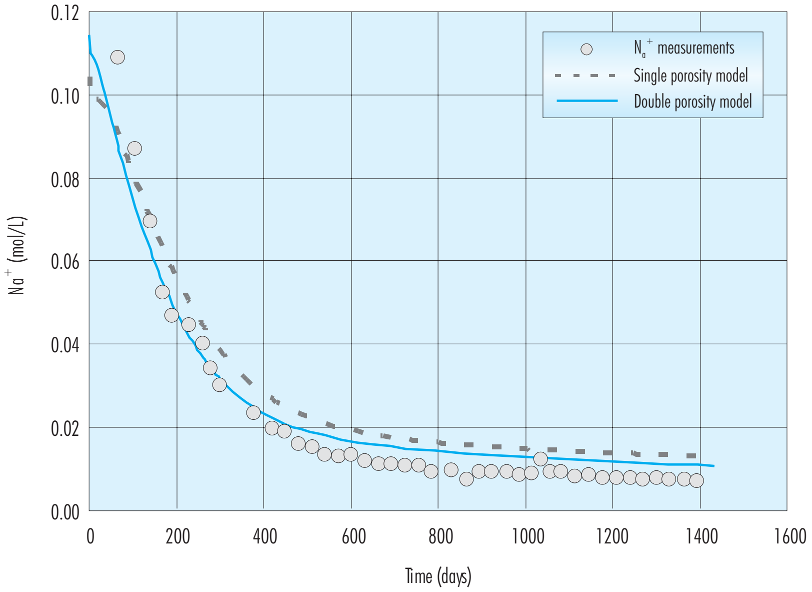

Figure 7.41: Modelling results for sodium with single and double porosity models.

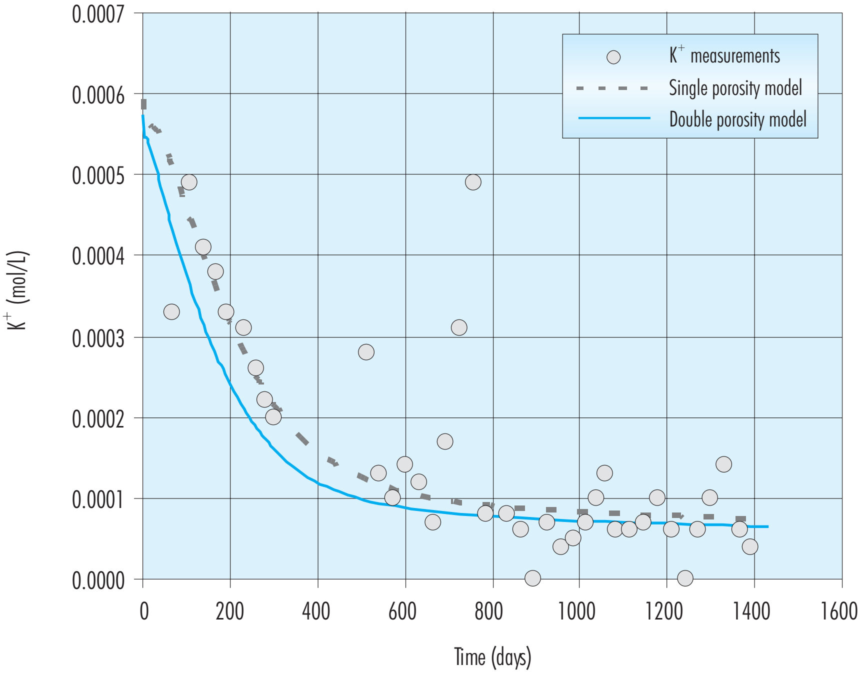

Figure 7.42: Modelling results for potassium with single and double porosity models.

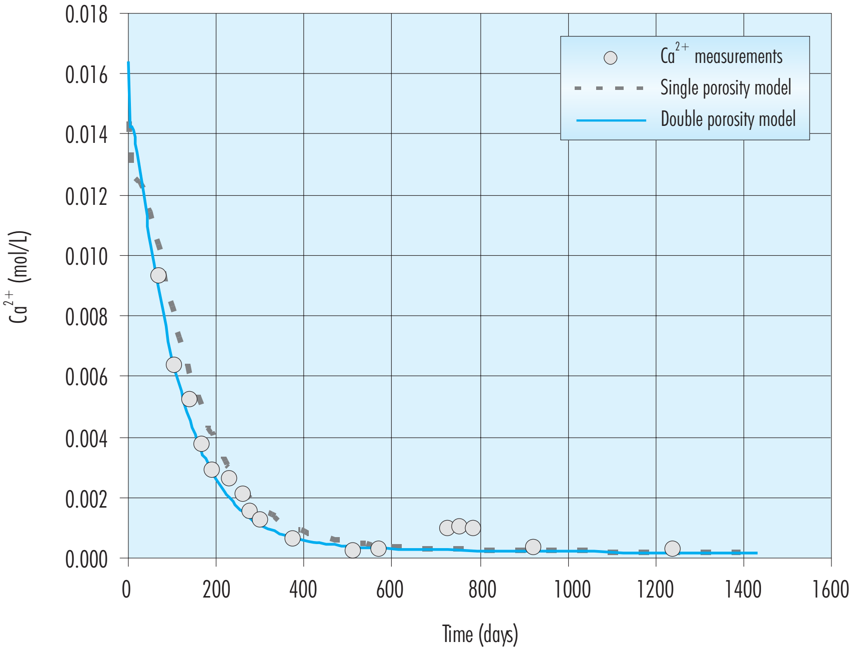

Figure 7.43: Modelling results for calcium with single and double porosity models.

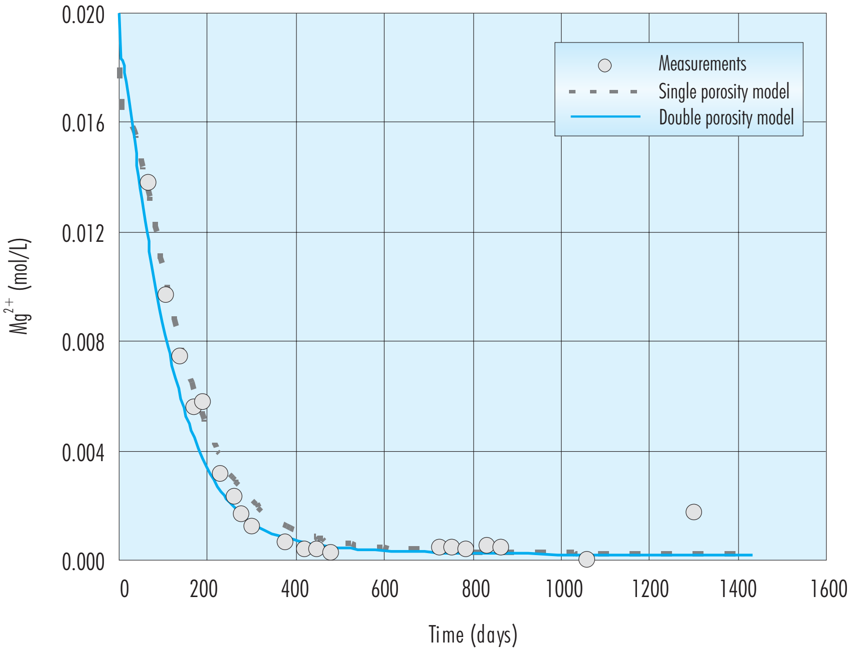

Figure 7.44: Modelling results for magnesium with single and double porosity models.

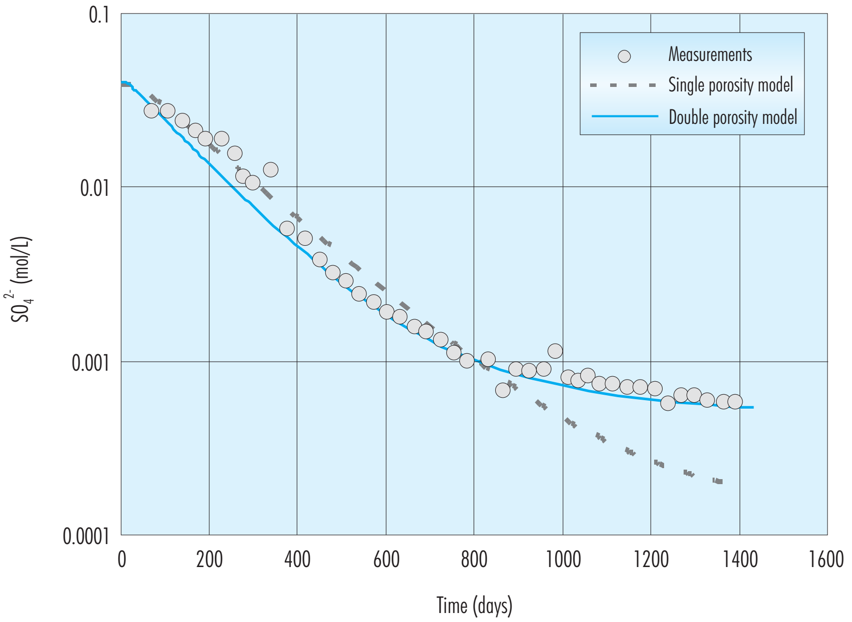

Figure 7.45: Modelling results for sulphate with single and double porosity models.

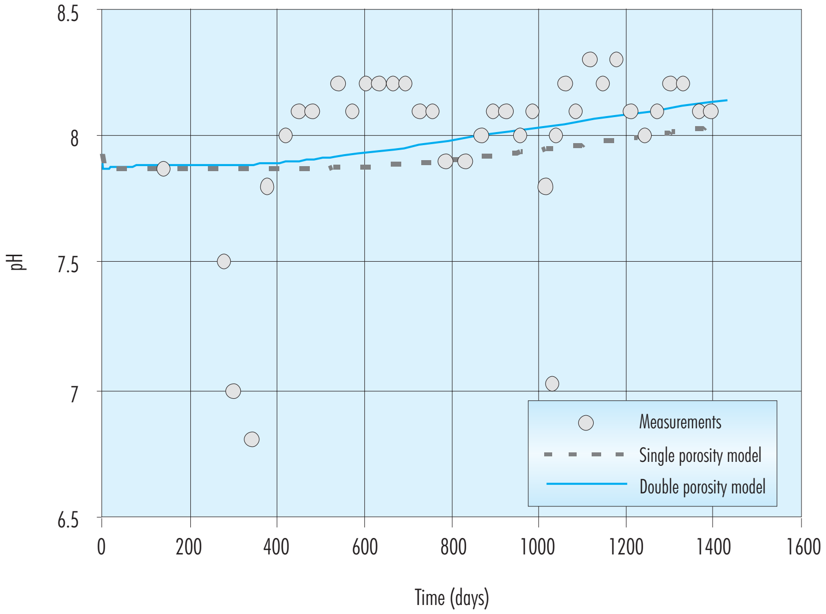

Figure 7.46: Modelling results for pH with single and double porosity models.

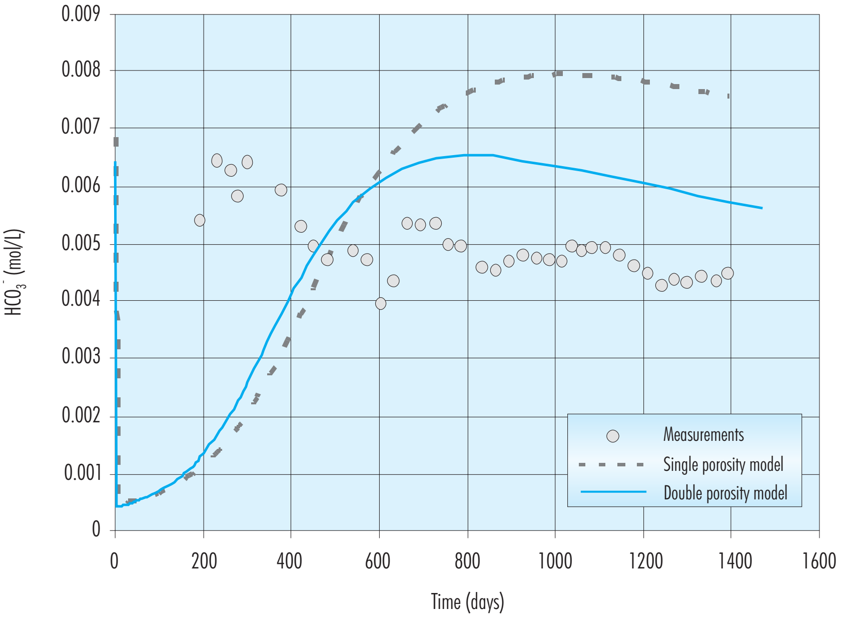

Figure 7.47: Modelling results for bicarbonate with single and double porosity models.

malised from 0 to 1. The values computed at the end of the experiment, that is at 183 days, (t = 1) are compared to the available data [190, 13].

This conservative anion increases its concentration close to the heater (right part of Figure 7.48) due to water evaporation (the vapour condenses at a certain distance from the heater, thus diluting the local chloride content). Near the water inlet, concentrations decrease due to water hydration. Both processes develop a concentration gradient that triggers back-diffusion of chloride from the hot end to the cold side. This diffusion takes place in the opposite direction from advective flow. This is the reason why this diffusion is known as backwards diffusion.

At the end of the test the concentration profile along the cell is still not flat, meaning that the system has not yet reached chemical and transport steady-state. Computed values at the end of the test capture the trends of experimental data.

Transport mechanisms for other chemical species are similar. However, their concentration patterns are more complex, as these species are affected by dissolution/ precipitation and ion exchange.

The THG model of thermo-hydraulic cell CT-23 was improved and updated by UDC during the second phase of FEBEX [191]: 1), this including the updating of TH parameters according to the THG model of the "mock-up" test, 2) debugging oscillations in gas pressures, 3) checking mass and charge balance errors, 4) evaluating the relevance of Pitzer equations for the calculation of activity coefficients and 5) performing sensitivity analysis to determine diffusion coefficient and accessible porosity. The code INVERSE-FADES-CORE V0 [201] was used to estimate the following parameters: accessible porosity, diffusion coefficient and vapour tortuosity [191, 201]. Given the uncertainties in the thermal conditions along the external surface of the cell, the updated TH model considers only the central part of the cell.

Table 7.14 shows the parameters and boundary conditions of the previous and updated TH. The computed values of water content and cumulative water inflow are shown in Figures 7.49 and 7.50, respectively.

Oscillations in gas pressures were observed in the TH models under two conditions: 1) the medium be-

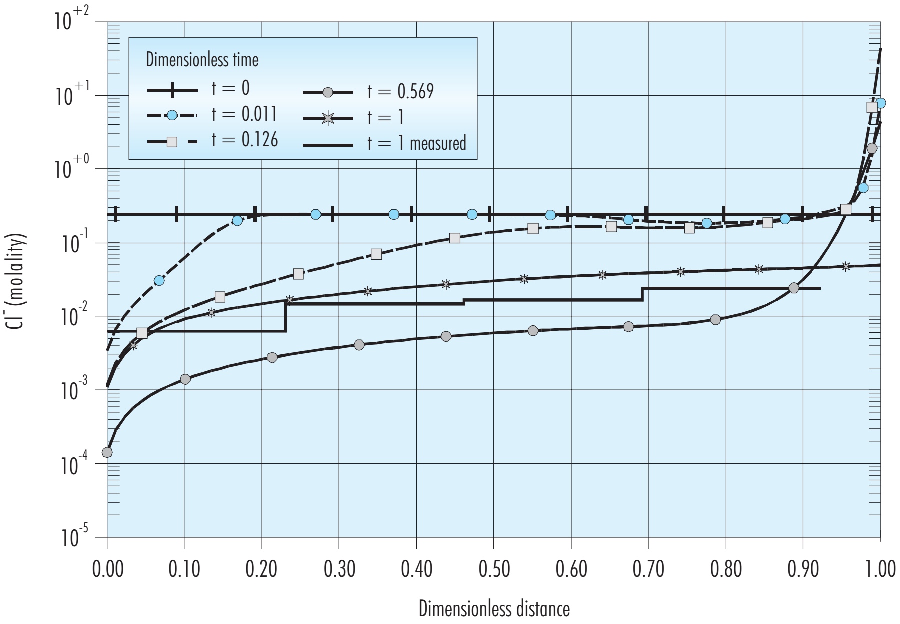

Figure 7.48: Spatial distribution of chloride in the pore water at different times for cell CT-23. Space and time have been normalised from 0 to 1. Computed values at the end of the experiment (t=1) are compared to available data. Note that the water inlet corresponds to x=0.

Table 7.14
Parameters and boundary conditions of previous and updated TH models of cell CT-23

Parameters/boundary condition	Updated TH model	Previous TH model
Intrinsic permeability of liquid	$2.75\cdot10^{-21}$ m^2	$k_{il} = k_{il}^0 \cdot \left(\frac{\phi}{\phi_0}\right)^3 \cdot \left(\frac{1-\phi_0}{1-\phi}\right)^2$ with $k_{il}^0 = 10^{-20}$ m^2 and $\phi_0 = 0.41$
Retention curve	$S_l = (1-\psi/1100000)^{1.1} / (1+(5\cdot10^{-5}\psi)^{1/0.82})^{0.18}$	$S_l = 1/(1+(1.43\cdot10^{-4}\psi)^{1/0.65})^{0.35}$
Porosity	0.43	0.41
Grain density (g/cm^3)	2.693	2.78
Heat boundary condition	83 °C	75 °C

comes fully saturated; 2) a closed system is used for the gas phase. Such problems were found in the TH models of cell CT-23 and in the "in situ" test. The reason for this oscillation is that when the medium switches from non-saturated to fully saturated, the program continues to calculate gas pressures as under non-saturated conditions. In order to avoid such oscillations, a subroutine for the calculation of gas pressure was implemented in FADES-CORE V1 [200] and INVERSE-FADES-CORE V0 [201].

When the medium is fully saturated, neither the mass nor the volume of dissolved air change with time. Thus, changes in the absolute pressure of dissolved air, P_a, due to changes in temperature T may be computed from the following equation:

$$P_{a2} = \frac{T_2}{T_1} P_{a1} \tag{7.2}$$

Numerical solutions are free of oscillations in gas pressures by implementing this equation in the code. It should be noticed that both water content and water inflow are affected by such oscillations, as is shown in Figures 7.49 and 7.50 [191, 201]. Oscillations in gas pressures were observed also in the TH model of the "in situ" test. However, they do not have a large effect on the model results of water content.

The analysis of computed concentrations reveals large mass balance errors for chloride and sulphate. The possible reasons for such errors, include: 1) the numerical scheme used for solving of the transport and chemical equations (sequential partly iterative approach, SPIA, versus the general sequential iterative approach, SIA), 2) the correction term used to update the activity of water and 3) the process of anion exclusion, which is relevant for chloride. It should be remembered that only 75% of total porosity is accessible to chloride. Mass balance errors for chloride are found to be small when SIA is used and the correction term is fixed to a value equal to 1. However, charge balance errors are still large [191, 209].

The numerical analysis of the effect of cross-diffusion processes and anion exclusion on charge balance indicates that anion exclusion is the main cause of charge balance errors. Cross-diffusion phenomena affect computed concentrations, but do not improve charge balance [191, 210].

Since the ionic strength of pore water near the heater may reach values too high to make the use of Debye-Huckel equations valid for the calculation of activity coefficients, Pitzer equations were implemented in FADES-CORE V1 [200] and INVERSE-FADES-CORE V0 [201]. The effect of using Pitzer equations on the model results was evaluated.

Activity coefficients computed with Pitzer (P) and Debye-Huckel (DH) equations generally have similar values. The largest differences occur for Ca^{2+} and Mg^{2+}. Activity coefficients which would be near one for an infinitely diluted solution, take values of around 0.8 for monovalent ions such as H^+, Na^+, K^+, Cl^- and HCO_3^-, and are usually smaller for divalent anions (SO_4^{2-}) and cations (Ca^{2+} and Mg^{2+}). Attention is called to the extremely low activity coef-

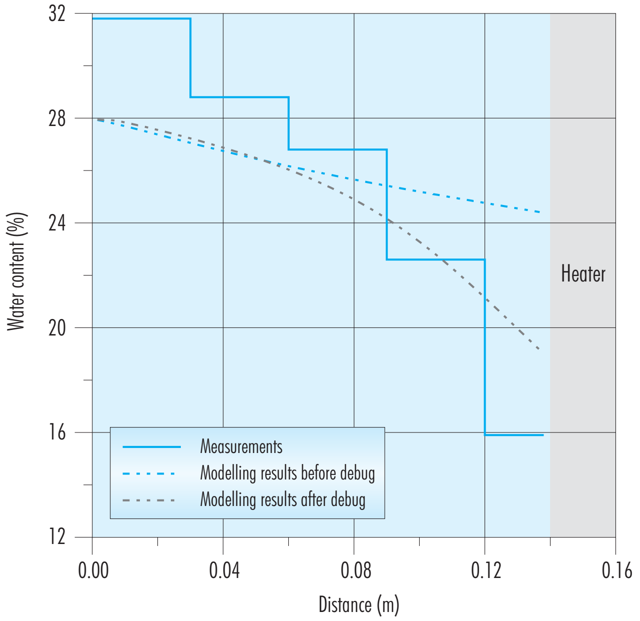

Figure 7.49: Comparison of modelling results of water content prior to and after debugging. The measurements are the data measured at a radial distance of 3.75 cm from the centre of the sample.

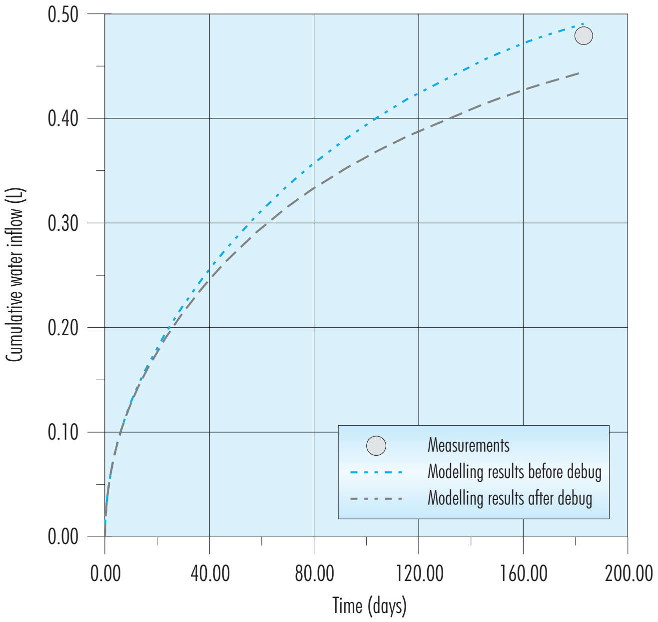

Figure 7.50: Comparison of modelling results of water inflow prior to and after debugging.

ficient of SO_4^{2-} near the heater at both 80 (Table 7.15) and 180 days.

Figure 7.51 shows the time evolution of ionic strength near the heater, which is where this parameter reaches its highest values [191]. Here ionic strength increases with time and reaches a maximum value after 80 days. The peak value for Debye-Huckel equations is slightly higher than that of Pitzer equations. The computed concentrations at the end of the experiment with Debye-Huckel and Pitzer equations do not show significantly difference for most of the monovalent ions. For Ca^{2+} and Mg^{2+} there are noticeable differences. Figures 7.52 and 7.53 are presented in order to better illustrate the difference in the results obtained using Debye-Huckel and Pitzer equations. These figures show the ratios of computed concentration with Debye-Huckel (C_{DH}) and Pitzer (C_P) equations for anions and cations. The Mg^{2+} and Ca^{2+} concentrations obtained using Debye-Huckel equations are around 15 to 30% higher than those computed with Pitzer. For other ions, the differences are smaller than 10%.

It is well known that Pitzer equations are relevant for highly concentrated solutions with ionic strengths greater than 1 M. Since the ionic strength of the pore water solution in cell CT-23 is lower than 0.3 M in most of the cell except at the contact with the heater, the use of Pitzer equations to calculate activity coefficients leads to almost the same results as those given by the Debye-Huckel equation.

Diffusion coefficient and accessible porosity are the key transport parameters in the THG modelling of CT-23. Taking advantage of the recent development of the code INVERSE-FADES-CORE V0 [201] (which solves the inverse problem of non-isothermal multiphase flow), optimum values of the diffusion coefficient and accessible porosity were obtained for Cl^-. Figure 7.54 shows the comparison of Cl^- spatial distribution model results with measured squeezing and aqueous extract data [191].

There are some differences in the concentrations computed in the initial phase of FEBEX [190, 13] (Figure 7.48) and those computed using the updated model in the second phase (see Figure 7.54), these being related to changes in TH parameters, diffusion coefficient and accessible porosity.

The model results indicate that concentrations are more sensitive to D_0 and ϕ_a than they are to vapour tortuosity. The results of the inverse model lead to a (pure water) diffusion coefficient of around $2.08 \cdot 10^{-10}$ to $2.61 \cdot 10^{-10}$ m^2/s and an accessible porosity equal to 80% of total porosity for chloride. These values provide an effective diffusion coefficient for chloride under saturated conditions which ranges from $3.2 \cdot 10^{-11}$ to $4.0 \cdot 10^{-11}$ m^2/s. These values are an order of magnitude larger than those

Table 7.15
Activity coefficients calculated with Debye-Huckel and Pitzer equations at 80 days at a point located at radial distance of 0.074 m from the water inlet

Species	γ_{DH}	γ_{Pitzer}
H_2O	0.998	0.998
H^+	0.843	0.779
Ca^{2+}	0.440	0.335
Mg^{2+}	0.478	0.354
Na^+	0.797	0.786
K^+	0.785	0.780
Cl^-	0.785	0.820
SO_4^{2-}	0.397	0.384
HCO_3^-	0.797	0.794

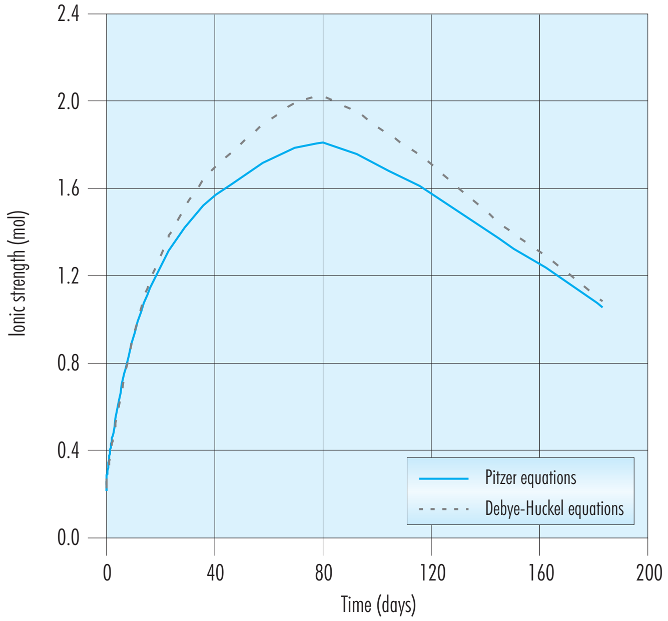

Figure 7.51: Time evolution of ionic strength at a point located at a radial distance of 0.139 m from the water inlet (near the heater).

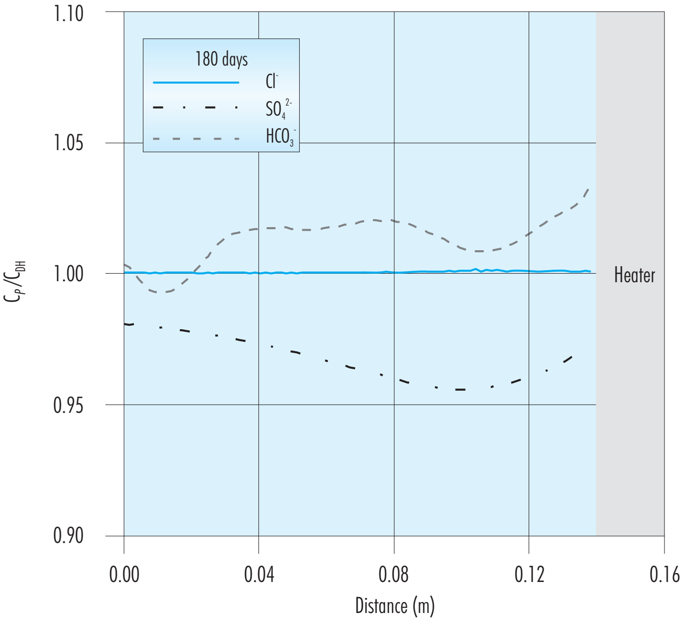

Figure 7.52: Ratio of the concentrations computed with Pitzer and Debye-Huckel equations (C_P/C_{DH}) for anions at 180 days. Distances are measured from the hydration side of the cell (see Chapter 5, Figure 5.131).

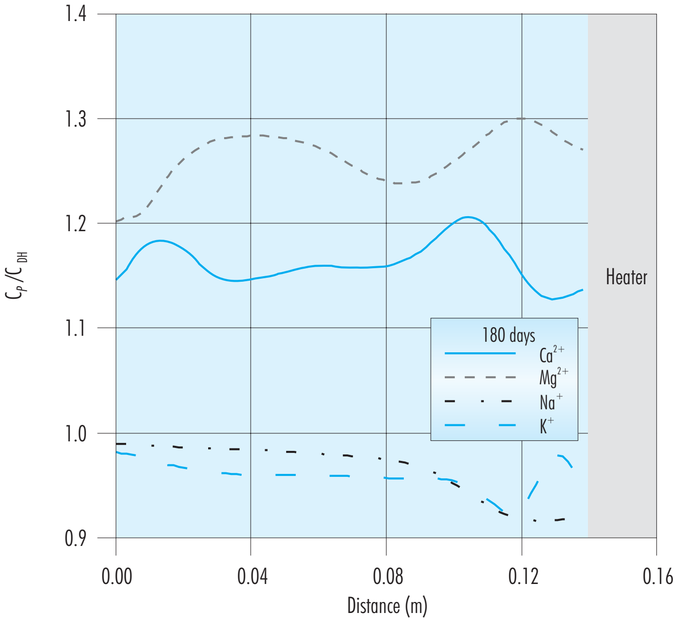

Figure 7.53: Ratio of the concentrations computed with Pitzer and Debye-Huckel equations (C_P/C_{DH}) for cations at 180 days. Distances are measured from the hydration side of the cell (see Chapter 5, Figure 5.131).

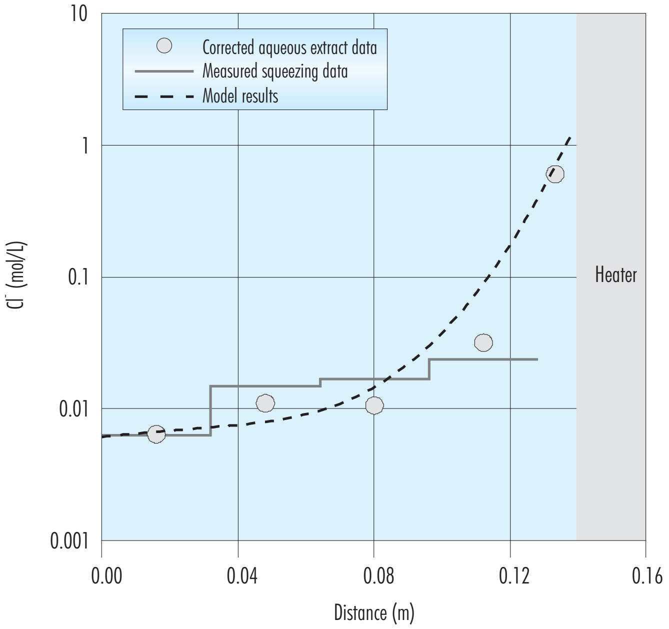

Figure 7.54: Comparison of Cl^- measurements with inverse modelling results for the optimum run. The inverse problem is solved using squeezing data. Corrected aqueous extract data are shown for comparison purposes.

obtained by CIEMAT from diffusion experiments performed on small saturated samples (see Chapter 5). This discrepancy seems to indicate that chloride diffusion may be faster in partly-saturated bentonite than in fully-saturated bentonite. Such a discrepancy might be overcome by using a double porosity model.

7.5. THG modelling of the "mock-up" test

7.5.1. TH model

The hydration of the barrier in the "mock-up" test commenced with water filling all the joints and macro gaps (in the periphery, between blocks and in the bentonite due to machining for the locations of cables and sensors, etc.). To accomplish this, the clay barrier was flooded with water under pressure. Available water on the external surface of the clay barrier can flow uniformly in the radial direction or can take a preferential path through the joints between blocks. Water will flow through the joints as long as they remain open. The time period during which joints are open depends not only on the hydration process, but also on the swelling of the bentonite in the blocks. Once joints are closed, bentonite hydration takes place, fundamentally from outside to inside. The laboratory tests performed by CIEMAT on sealing of the blocks clearly show that, during the beginning of the test, a significant part of the injected water flowed along the joints, flooding them, and causing their sealing. This means that after the sealing of the joints by the swelling of the bentonite, the water can only flow from the peripheral surface.

During the initial phase of FEBEX a boundary condition of constant pressure flow equal to 0.55 MPa was adopted for the periphery of the clay barrier. The conceptual hydration model assumed that, during the first 6 days, 550 L of water entered through the transversal block joints (which represent the majority of the volume of gaps and are those that show the greatest spatial continuity). After the initial period of hydration, it is assumed that the joints are sealed and, therefore, that from that time hydration may take place only radially from the external surface of the barrier [47, 190, 13].

The thermo-hydrodynamic model of the "mock-up" test during the initial phase was constructed based mainly on the parameters and constitutive laws proposed in the pre-operational report [47]. Some parameters were later adjusted once data from the "mock-up" test were available. The adjusted parameters include: gas and liquid intrinsic permeabilities, gas boundary condition (open or closed conditions), the retention curve and the thermal conductivity of the bentonite. The model is sensitive to variations in these parameters. This allows for good calibration of the model parameters. The optimum parameter values adopted for the reference model are: intrinsic permeability of bentonite for liquid $2.75 \cdot 10^{-21}$ m^2, intrinsic permeability of bentonite for gas $5 \cdot 10^{-10}$ m^2, vapour tortuosity 0.5, the exponent of the Irmay equation 3 and open-to-gas boundary conditions.

The reference model leads to results which reproduce well the observed water inflows (Figure 7.55), water flow rates, temperatures and relative humidities. This result is a clear indication of the "validity" of the TH model. However, the possibility of other parameter combinations leading to similar fits cannot be precluded.

Predictions of the rate of hydration of the "mock-up" test were performed up to 10 years. After this time the barrier is almost under saturation conditions, although full water saturation is not yet reached.

7.5.1.1. Analysis of unexpected trends

The TH model of the "mock-up" test reproduces the trend of measured cumulative water inflow for almost the first 800 days of hydration, as is shown in Figures 7.55 and 7.56 [190, 13]. However, since November 1999 (almost 3 years after the beginning of the hydration) the measured cumulative water inflow increased at a slower rate than computed values (Figure 7.56). Such unexpected deviations were also partly confirmed by relative humidity data. In order to explain such deviations, during the second phase of FEBEX [191], the following hypotheses were postulated and analysed:

- ❑ Variation of intrinsic permeability with ionic strength
- ❑ Coupled fluid transport process such as chemical and thermal osmosis

Variation of intrinsic permeability with ionic strength

The diffuse double layer theory and some experimental results indicate that hydraulic conductivity may be influenced by the concentration of dissolved species in the permeating liquid. In FEBEX, the ben-

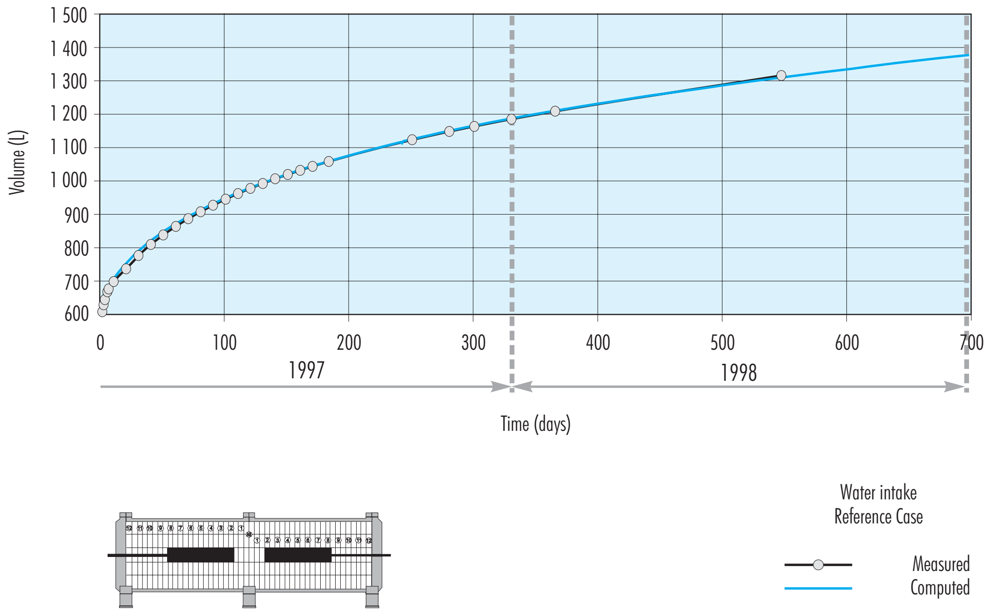

Figure 7.55: Comparison of computed and measured cumulative injected water volumes in the "mock-up" test.

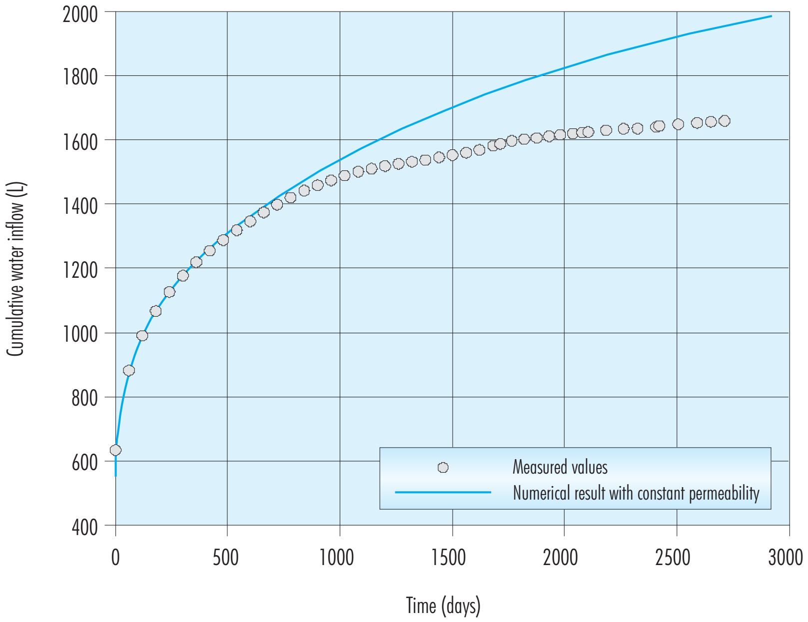

Figure 7.56: Discrepancy between computed and measured cumulative water inflow in the "mock-up" test.

tonite pore water concentration decreases due to the inflow of less saline granite water. A variation of intrinsic permeability with ionic strength may account for the discrepancy in water inflow. Expressions relating hydraulic conductivity to ionic strength were reviewed from published references [191, 210]. Subsequently, during the second phase these expressions were implemented in FADES-CORE V1 [200]. Finally, the THG model of the "mock-up" test was run using a constitutive law of variable intrinsic permeability as a function of ionic strength. The published data may be fitted to the following general expression with homogeneous dimensions [191]:

$$\frac{K}{K_0} = a\left(\frac{I}{I_0}\right)^n \tag{7.3}$$

where K is the liquid intrinsic permeability, I is the ionic strength, K_0 and I_0 are reference values of K and I, and a is a dimensionless constant having a value close to 1. Several values of the exponent n have been proposed within the range of 0.5 to 1.8. Two possible alternatives for this expression were tested, with different values for a and n, the value of K_0 being $2.75{\cdot}10^{-21}$ m^2 for the FEBEX compacted bentonite at a dry density of 1.65 g/cm^3 at I_0 of pore water under dry ambient conditions of 0.2578 M. The following two possible alternatives for the constitutive law of variable intrinsic permeability as a function of ionic strength were tested:

$$\frac{K}{K_0} = a_1\left(\frac{I}{I_0}\right)^{0.5} \tag{7.4}$$

$$\frac{K}{K_0} = 1.7698 \times \left(\frac{I}{I_0}\right)^{1.72} \tag{7.5}$$

Figure 7.57 to Figure 7.61 show model results taking into account constant and variable permeability using Equation (7.5). The discrepancy between computed and measured water inflow occurs at 1250 days (Figure 7.57). Figure 7.58 to Figure 7.61 illustrate computed and measured relative humidities. Near the heater (Figure 7.58), numerical results underestimate the measured data. In the centre of the bentonite buffer, the numerical results reproduce the trend of the measured data.

To provide a better picture of how the bentonite buffer hydrates, plots of the time evolution of volumetric water content were prepared. It should be

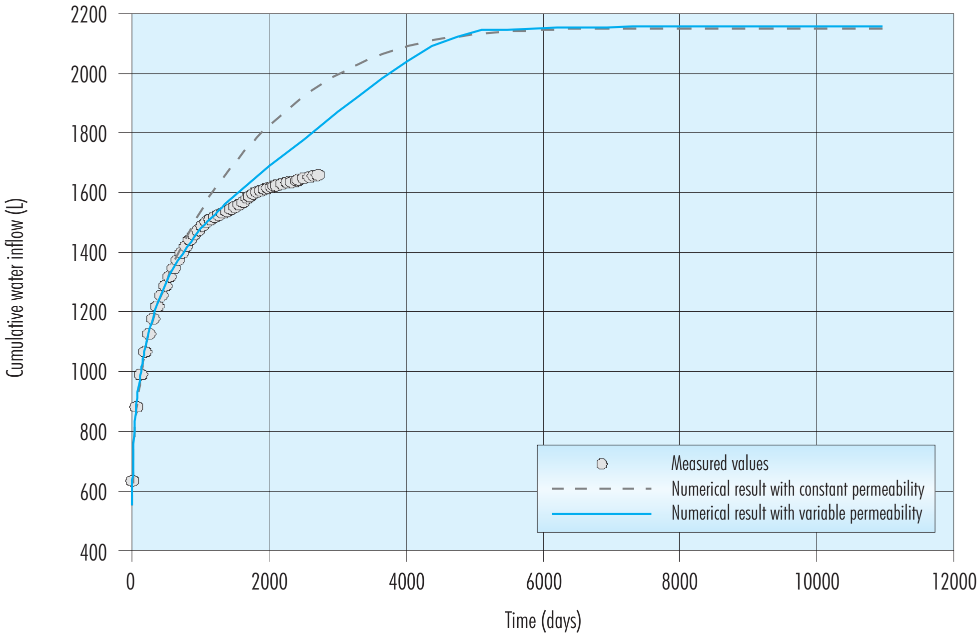

Figure 7.57: Measured (symbols) and predicted cumulative water inflow with constant and variable permeability using Equation (7.5).

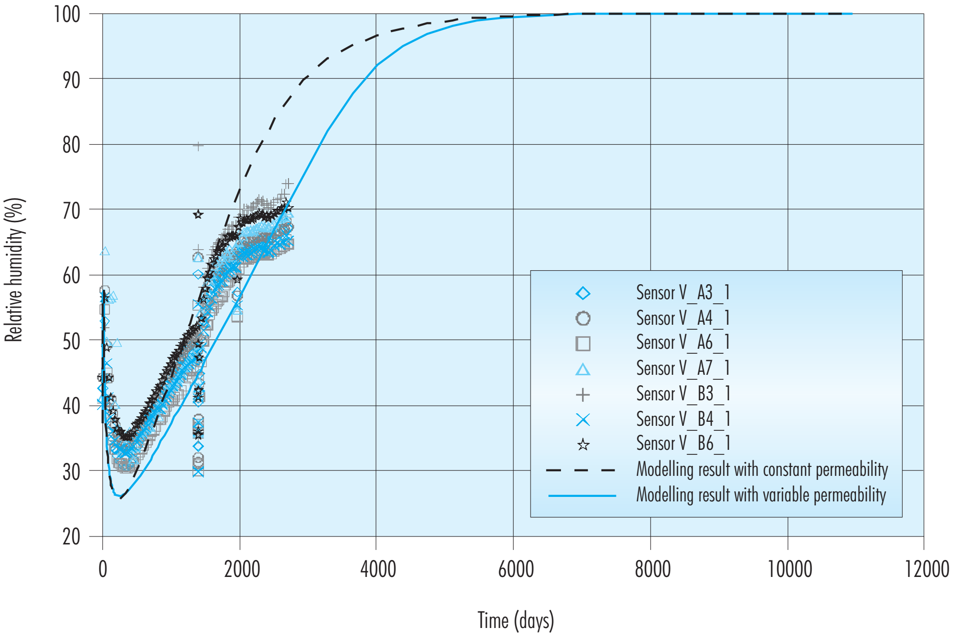

Figure 7.58: Measured and computed relative humidities with constant and variable permeability (Equation 7.5) at a radial distance of 0.22 m in the "mock-up" test.

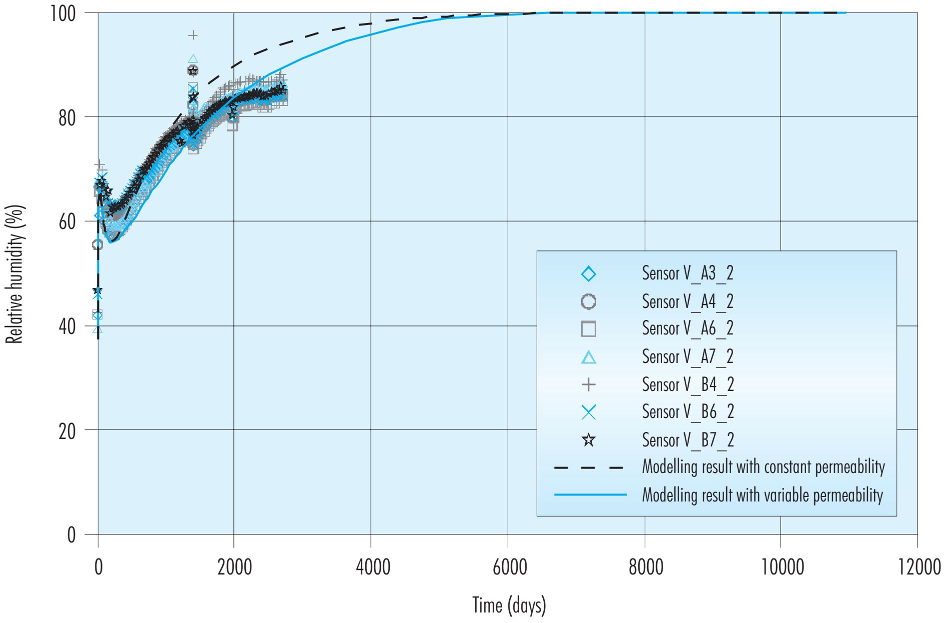

Figure 7.59: Measured and computed relative humidities with constant and variable permeability (Equation 7.5) at a radial distance of 0.37 m in the "mock-up" test.

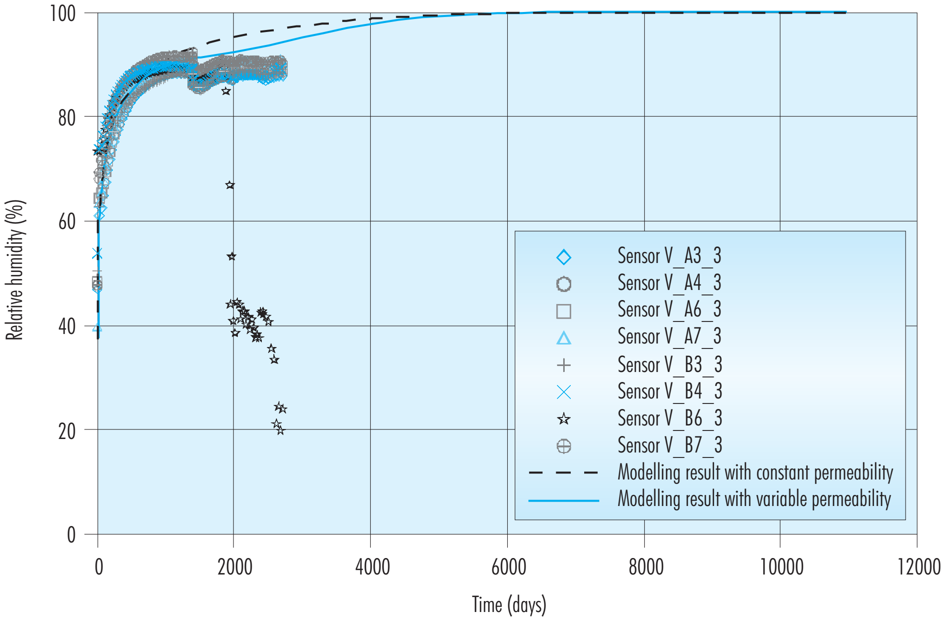

Figure 7.60: Measured and computed relative humidities with constant permeability and variable permeability (Equation 7.5) at a radial distance of 0.55 m in the "mock-up" test.

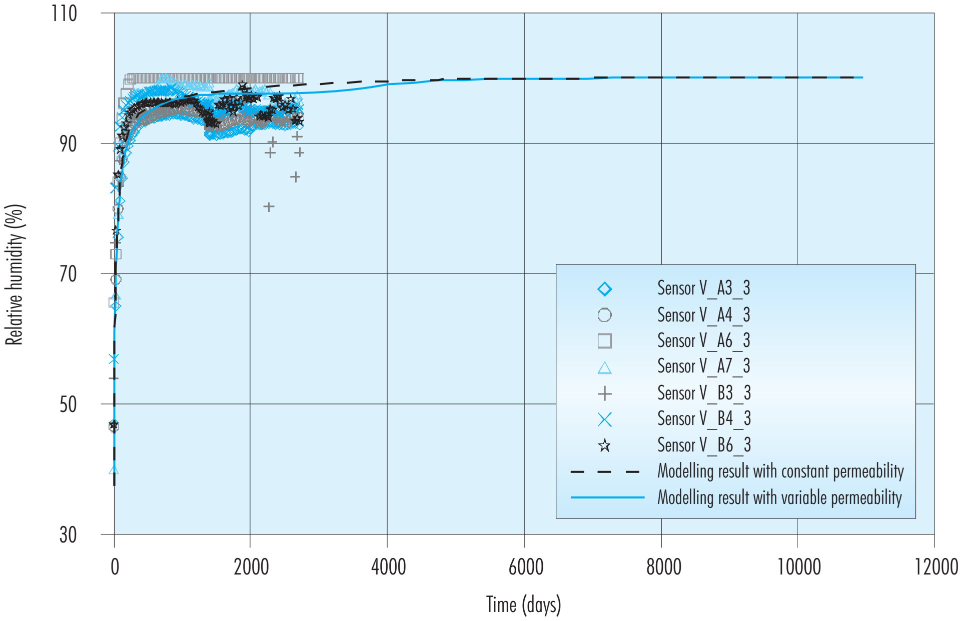

Figure 7.61: Measured and computed relative humidities with constant permeability and variable permeability (Equation 7.5) at a radial distance of 0.70 m in the "mock-up" test.

noted that the numerical model solves for liquid and gas pressure, P_l and P_g, respectively. Suction, $-(P_l-P_g)$, is computed from relative humidity RH through:

$$P_l\text{-}P_g = \ln(RH) \times \rho_l\, RT/M_w \qquad (7.6)$$

where ρ_l is liquid density (kg/L), R is the gas constant (8.314 J/mol/K) and M_w is the molecular mass of the water (0.018 kg/mol).

The degree of liquid saturation is related to suction through the retention curve:

$$S_l = \frac{(1-(P_g-P_l)/c)^d}{\left(1+(a \times (P_g-P_l))^{\left(1/(1-b)\right)}\right)^b} \qquad (7.7)$$

where a, b, c and d are experimental parameters of the retention curve. It should be noticed that the temperatures have to be known in order to calculate water content. Given the symmetry of the temperature field in the “mock-up” test, the average temperatures of sections T_A5 and T_B5 were used to calculate the temperatures at sections V_A3, V_A4, V_A6, V_A7, V_B3, V_B4, V_B6, V_B7 (see Chapter 3).

The measured data on relative humidity, RH, are translated into saturation degree values by using equations 7.6 and 7.7. These saturation values are then expressed as volumetric water content. Such water contents are here called pseudo-measured water content data. Figure 7.62 to Figure 7.65 show the comparison of computed and pseudo-measured water content data at several locations within the barrier for the model of variable permeability as a function of ionic strength (see Equation 7.4). Near the heater, the model results with constant permeability overestimate the pseudo-measured water content data, while those computed with a variable permeability underestimate pseudo-measured water contents. In the centre of the barrier, the model results reproduce water content data. It may be seen that the patterns of water content are similar to those of relative humidity.

Effect of chemical and thermal osmosis

It is well known that clays can act as semi-permeable membranes when double layers of adjacent

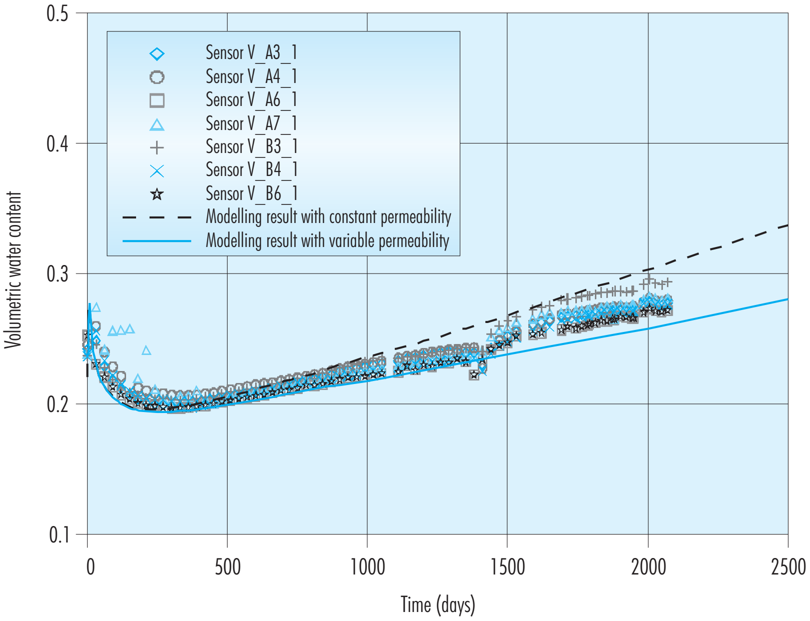

Figure 7.62: Recalculated and computed water content with constant and variable permeability (using Equation 7.4) at a radial distance of 0.22 m in the “mock-up” test.

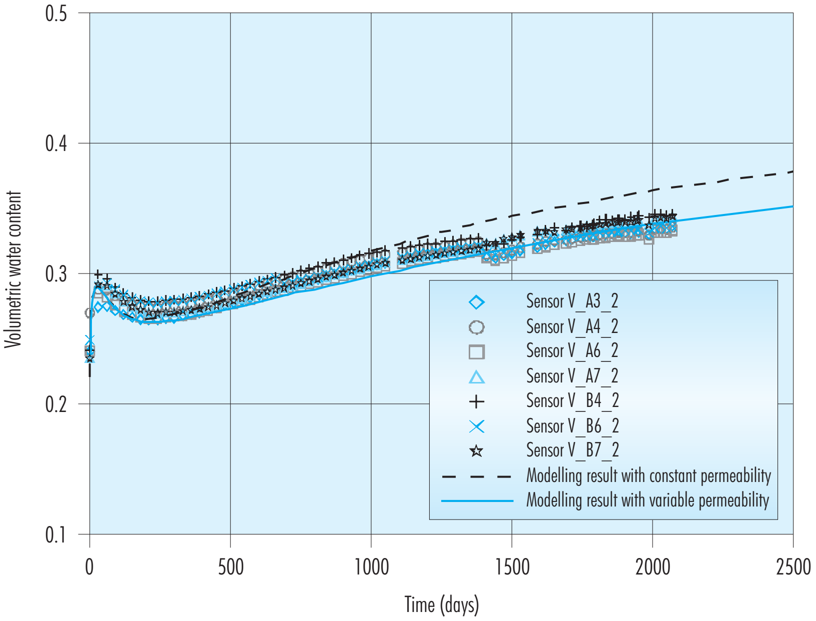

Figure 7.63: Recalculated and computed water content with constant and variable permeability (using Equation 7.4) at a radial distance of 0.37 m in the "mock-up" test.

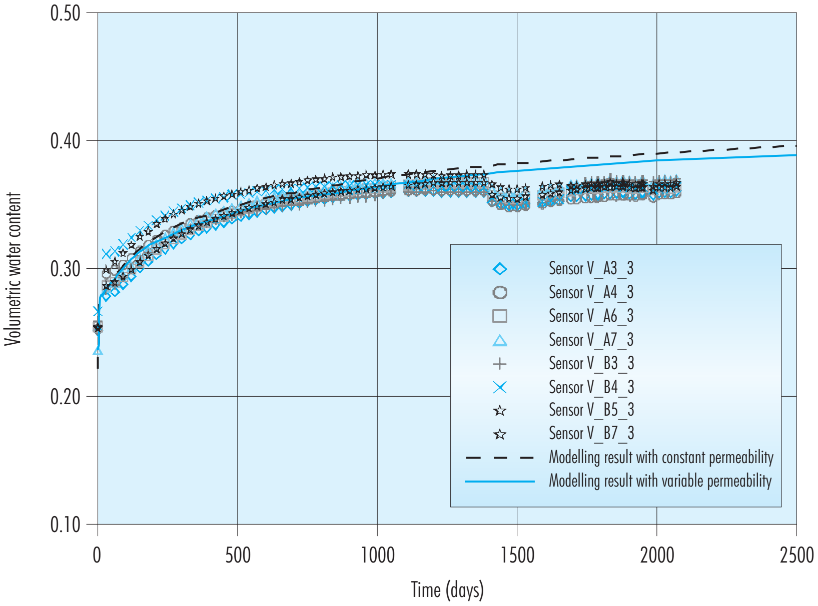

Figure 7.64: Recalculated and computed water content with constant and variable permeability (using Equation 7.4) at a radial distance of 0.55 m in the "mock-up" test.

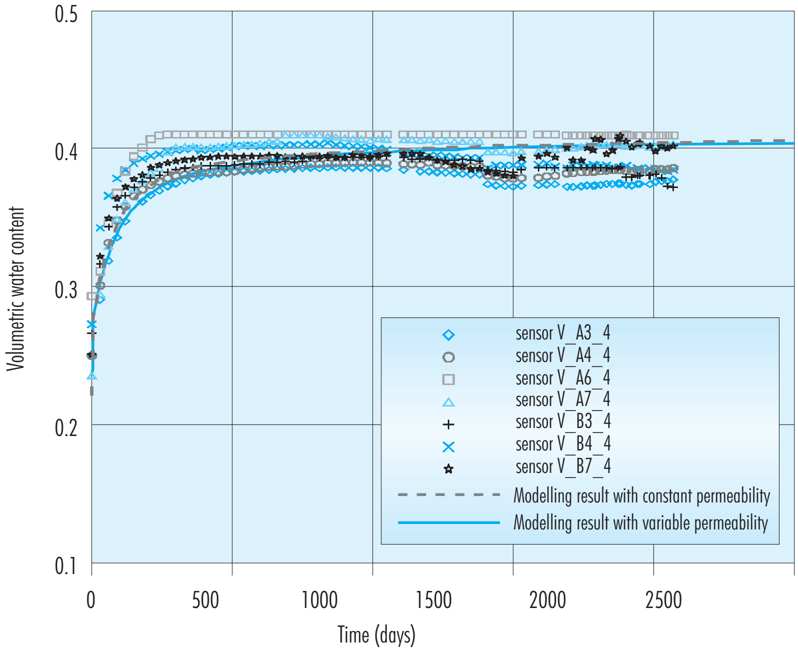

Figure 7.65: Recalculated and computed water content with constant and variable permeability (using Equation 7.4) at a radial distance of 0.70 m in the "mock-up" test.

clay particles overlap and both cations and anions are excluded from pores, but water and uncharged solutes have free access to all pores. The flux of water induced by chemical osmosis may be expressed by applying an analogue of Darcy's law modified by a reflection coefficient, σ. Possible expressions relating osmotic pressure to porewater chemical composition have been reviewed [191].

Thermal osmosis is another coupled process that can produce a fluid flux. Significantly mass transport through clay membranes due to temperature gradient has been observed in laboratory experiments. Both coupled processes, thermal and chemical osmosis have been implemented in FADES-CORE V1 [200].

The key parameter for chemical osmosis is the reflection coefficient, which measures the non-ideality of a membrane and is defined as the ratio of the applied osmotic pressure to the hydraulic pressure developed after equilibrium is reached (i.e. at zero solution flux). An ideal membrane has a reflection coefficient of one, whereas for non-ideal membranes its value varies between zero and one. Measured values of reflection coefficient σ range from 0.001 to 0.03 for bentonite, while theoretical values might range from 0.002 to 0.27 [191].

Numerical analyses of the THG model of the "mock-up" test performed with reflection coefficients equal to 0.002, 0.02 and 0.2 indicate that chemical osmosis does not have a significant effect on liquid flow in the bentonite. The explanation of this result is that under non-saturated conditions, osmotic suction accounts only for a very small proportion of total suction (Figure 7.66). In the greater part of the bentonite barrier, osmotic suction accounts for less than 1% percent of the total suction, even when the reflection coefficient is equal to 2.

Due to the uncertainty in thermo-osmotic permeability, several values have been tested in the THG model of the "mock-up" test. Figure 7.67 shows computed water inflow with thermo-osmotic permeabilities of $1 \cdot 10^{-13}$, $5 \cdot 10^{-13}$ and $1 \cdot 10^{-12}$ m^2/K·s. Figure 7.68 shows the computed relative humidity at a radial distance of 0.22 m with a thermo-osmotic permeability of $5 \cdot 10^{-13}$ m^2/K·s. It may be seen that the computed water inflow and relative humidity may be improved significantly by properly adjusting thermal permeability. When thermal osmosis is con-

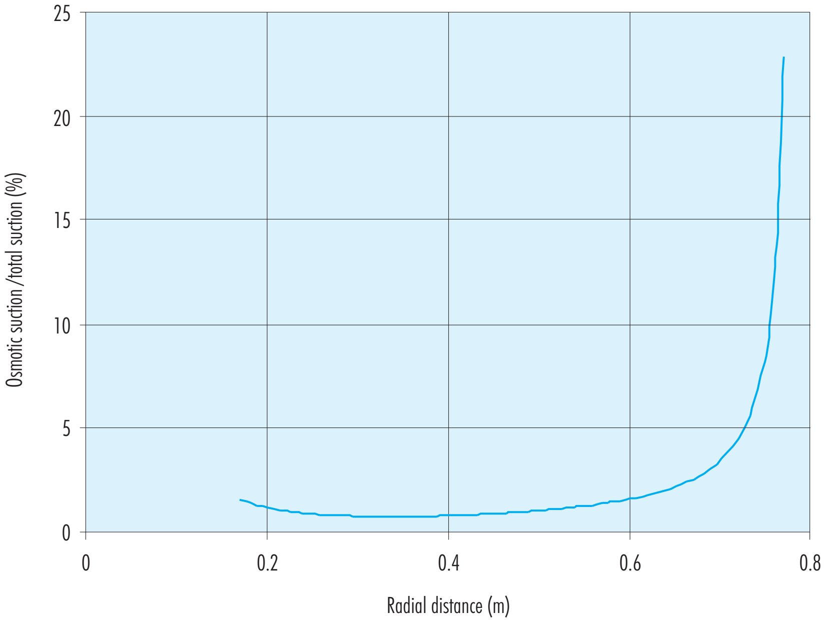

Figure 7.66: Ratio of osmotic suction to total suction at 1825 days.

sidered, the water inflow rate decreases (Figure 7.67); the concentration of chloride increases only slightly [191].

7.5.1.2. Modelling the overheating episode

An overheating episode occurred in November 2000 (days 1392 and 1393), as is explained in Chapter 3. After overheating, the temperatures decreased up to day 1397, recovering the values existing prior to overheating. At the same time, relative humidities and fluid pressures decreased sharply after overheating. At day 1395 they reached their lowest values, subsequently increasing and recovering the values existing prior to overheating. This overheating phenomenon was simulated by modifying the thermal boundary condition of the THG model of the "mock-up" test.

Computed temperatures, water inflow and relative humidities have been compared to measured data. Figure 7.69 to Figure 7.72 show model results for temperature at some selected points. In general, the model results reproduce the measured data. Near the heater, however, the model results underestimate the peak measured temperature and overestimate the minimum value. Computed cumulative water inflow is the same with and without consideration given to overheating. During overheating, the large increment of vapour transport slowed down the infiltration of water. However, since overheating lasted for only two days, water inflow was almost unaffected.

Figures 7.73 and 7.74 show model results for relative humidity with and without overheating. Near the heater (Figure 7.73), the model results reproduce the sharp decrease and the recovery phase of the measured data. In the centre of the barrier (Figure 7.74), the model results fail to capture the slow recovery phase of the measured data. The numerical model of the overheating episode indicates that this episode affected hydrodynamic conditions, although only slightly because of its short duration. The model captures the trends of measured temperatures, although it lacks the capacity to reproduce the sharp temperature profile. The model reproduces the trend of measured relative humidities. In the middle part of the barrier, however, the model fails to reproduce the slow recovery phase following overheating.

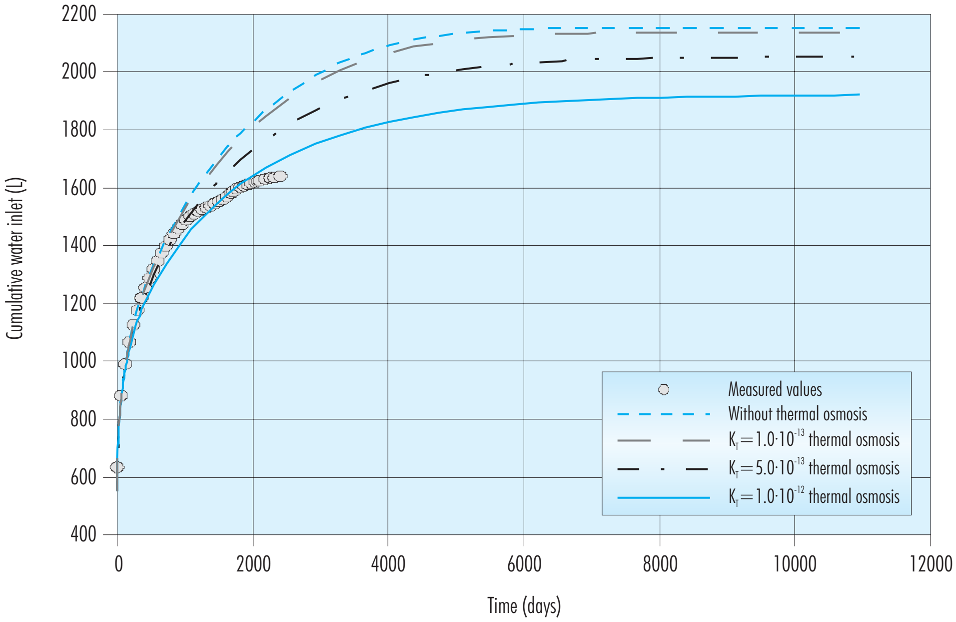

Figure 7.67: Computed cumulative water inflow considering thermal osmosis with different thermo-osmotic permeabilities.

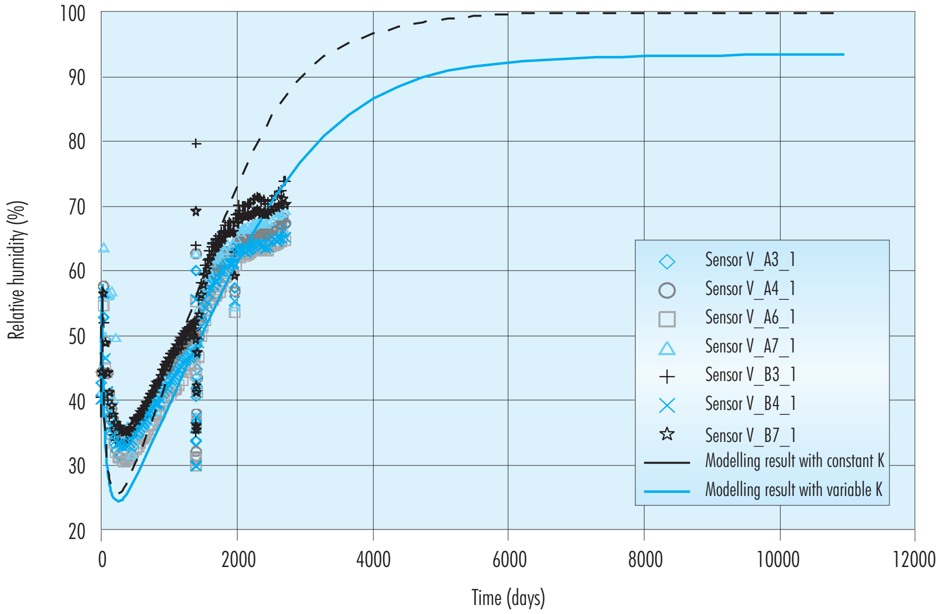

Figure 7.68: Measured and computed relative humidities with and without thermal osmosis at a radial distance of 0.22 m in the "mock-up" test.

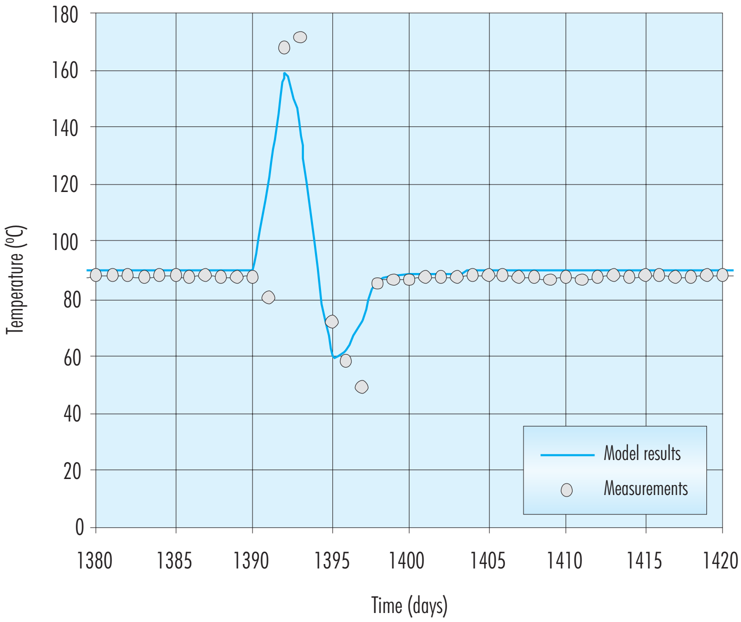

Figure 7.69: Computed and measured temperature during overheating at a point located at a radial distance of 0.22 m.

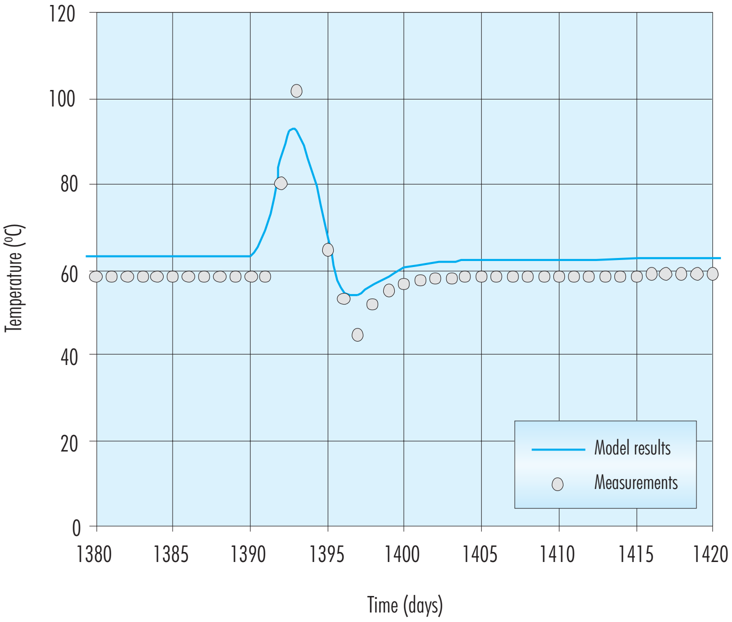

Figure 7.70: Computed and measured temperature during overheating at a point located at a radial distance of 0.35 m.

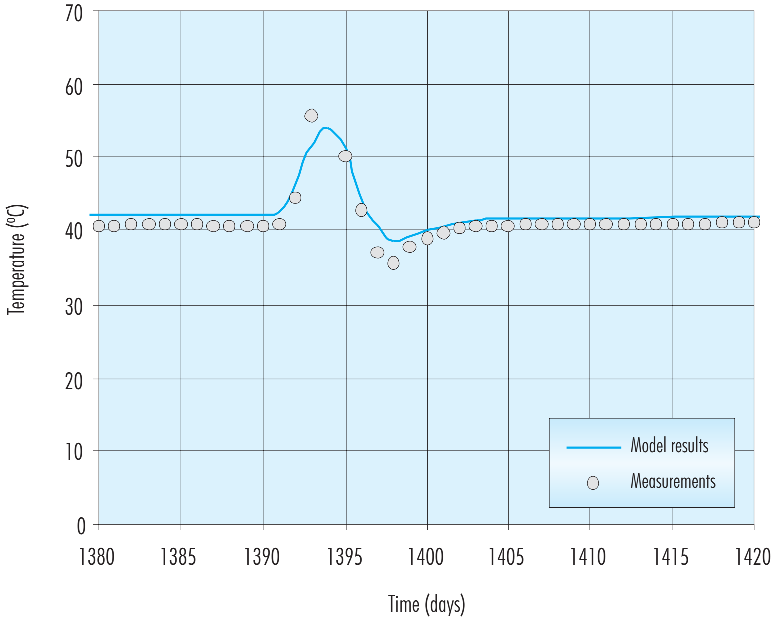

Figure 7.71: Computed and measured temperature during overheating at a point located at a radial distance of 0.55 m.

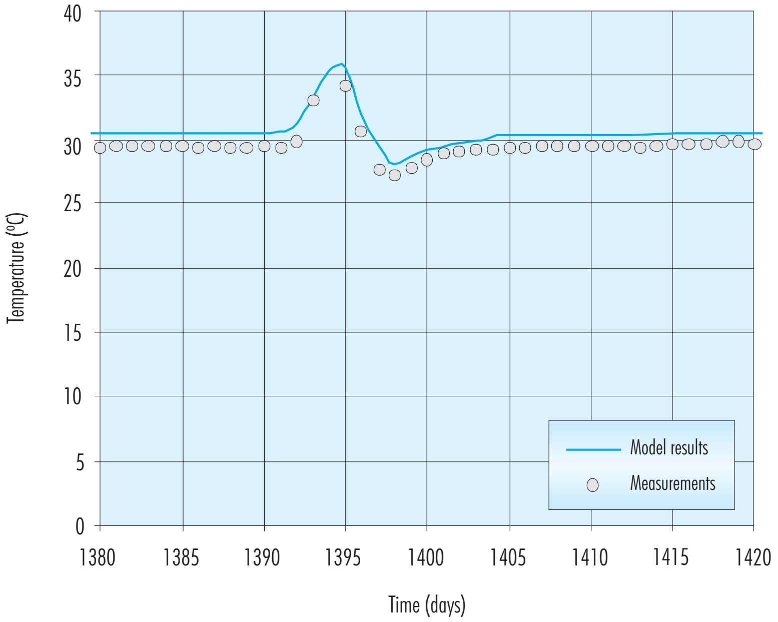

Figure 7.72: Computed and measured temperature during overheating at a point located at a radial distance of 0.75 m.

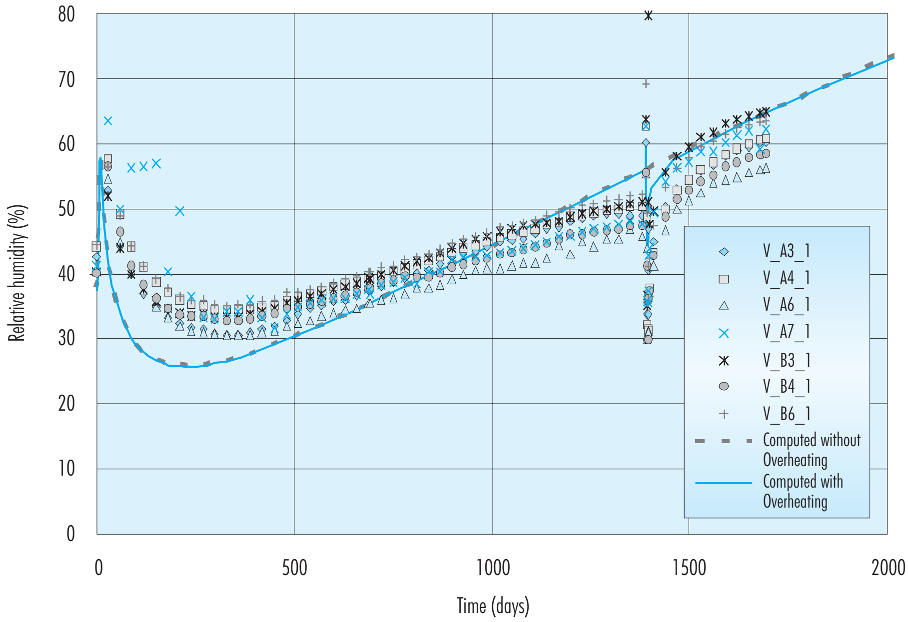

Figure 7.73: Computed and measured relative humidity at a point near the heater (r= 0.22 m) with and without overheating.

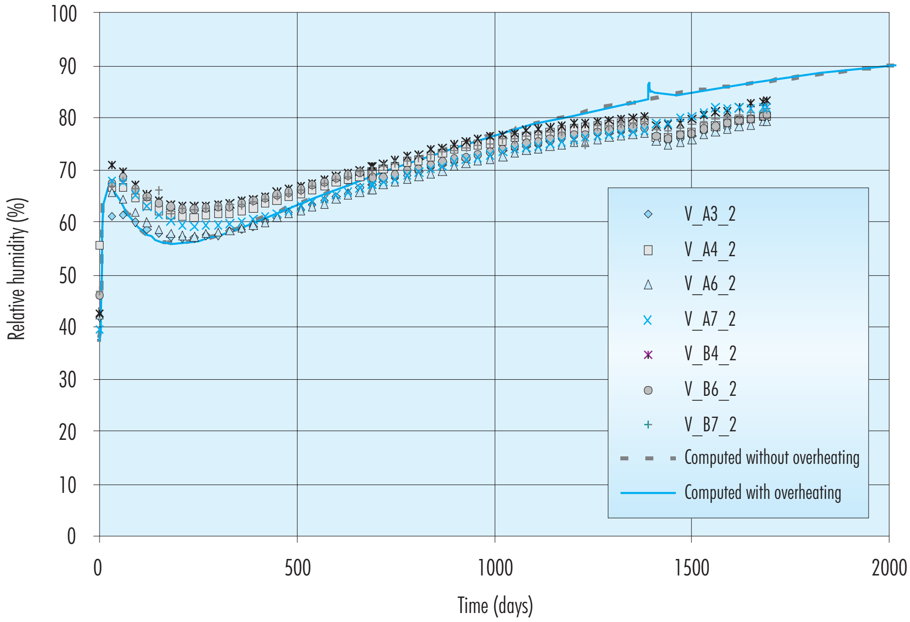

Figure 7.74:Computed and measured relative humidity at r = 0.37 m with and without overheating

7.5.2. Numerical modelling of tracer migration

In order to obtain information on the geochemical processes and transport mechanisms, conservative and non-conservative artificial chemical and isotopic tracers were placed at single points, in the interior, and distributed along the periphery of the bentonite barrier in both large-scale tests [211, 212]. These tracers include: iodine, rhenium, selenium, boron, deuterium, europium, cesium, thorium, uranium, and neodymium. Selected tracers include conservative and non-conservative tracers. Iodide and borate may be partially retained and are not considered to be fully conservative. Selenate and perrhenate, in addition to being sensitive to the redox process, may be excluded from a part of the total porosity. The rest of the tracers are clearly non-conservative, as indicated by their large K_d values. Iodide and deuterium were added with the hydration water. The rest of the tracers were emplaced using the following methods: within sintered metallic capsules, SSS; mixed with bentonite in plugs of compacted bentonite, CP; and in impregnated filter paper, FP [211, 212].

During the first phase of FEBEX two possible types of boundary conditions were adopted for modelling of the transport of the tracers added to the hydration water [190, 13]. The first of these conditions consists of assuming that the mass flow of the injected tracer is equal to the product of the volume of water flow and the concentration of the tracer in the injected water. The second type of boundary condition is of the Dirichlet type, where the concentration at the exterior limit of the barrier is assumed to be constant and equal to that of the injected water.

The concentration of iodide in the water used to hydrate the bentonite buffer of the "mock-up" test was of 0.0133 mol/L. A one-dimensional mesh of axial symmetry was used for the modelling of iodide transport, adopting a boundary condition of mixed transport or Cauchy type (mass flow of tracer intake is given by the advective flow of the tracer). Figure 7.75 shows the spatial distribution of the iodide ion concentration after 1100 days, for two values of the distribution coefficient ($K_d = 0$ and $K_d = 0.73$ mL/g). The effect of the iodide undergoing retention is shown by the great delay. For $K_d = 0$, the tracer front penetrates almost 40 cm into the barrier, whereas with $K_d = 0.73$ mL/g, the tracer penetrates

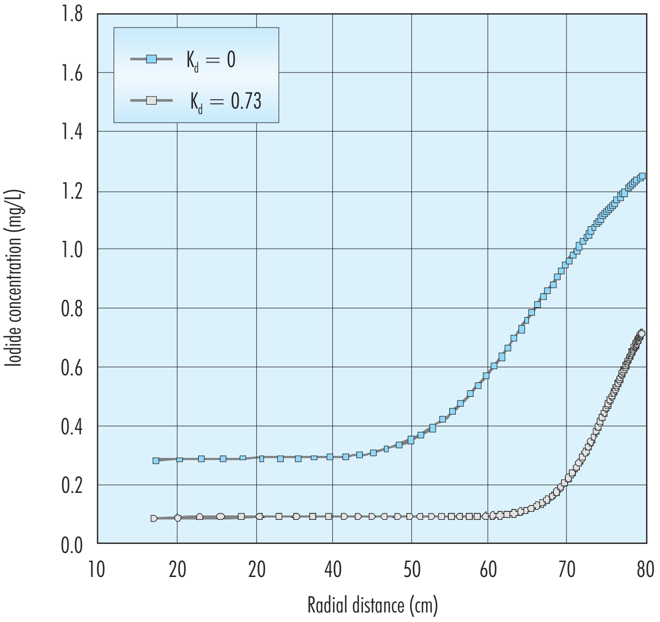

Figure 7.75: Spatial distribution of the iodide ion in the clay barrier at 1100 days. For two values of K_d.

only 15 cm in the same time period. Furthermore, the tracer concentration in the pore water of the bentonite is approximately three times less when the effect of delay is considered, due to the fact that an important part of the tracer is retained in the solid phase.

For the point tracers (those applied in the form of capsules or plugs), two-dimensional meshes were used. Figure 7.76 shows the spatial distribution of the concentrations calculated for the perrhenate ion at 50 and 1100 days.

During the second phase, predictions of iodide migration using a Dirichlet boundary condition have been updated using the revised TH model [191]. In this model, molecular diffusion coefficient and accessible porosity are those estimated by the inverse model for iodide migration for the "in situ" test (see Section 7.6.2.2). The molecular diffusion coefficient is $2.27\cdot10^{-11}$ m^2/s, accessible porosity is equal to 56% of total porosity (0.41) and the effective diffusion coefficient is 10^{-12} m^2/s. Figure 7.77 shows the iodide model predictions at different times using a $K_d = 0$. It should be noticed that the predictions of migration performed during the first phase were obtained with a model that assumed neither vapour flow nor evaporation near the heater. This is the main reason for the large differences in the predicted concentration profiles of Figures 7.75 and 7.77.

7.5.3. THG model

During the initial FEBEX work, predictive modelling of the geochemical evolution of the "mock up" test was performed using the parameters, processes, solid phases, and reactions identified in small-scale laboratory heating and hydration cells (CT-18 and CT-23).

THG predictions for the "mock-up" test have been updated during the second phase [191, 213]. Several improvement have been introduced in the THG model of the "mock-up" test, including: 1) accounting for the dependency of permeability on ionic strength, 2) updating cation exchange data, which are listed in Table 7.16, and 3) using Pitzer equations for the calculation of activity coefficients.

Selectivity coefficients corresponding to the exchangeable cation data of Table 7.16 are listed in Table 7.17. Model CGM-0 was used for updating THG predictions (see Section 7.2.4).

Table 7.16
Exchangeable cations in FEBEX bentonite in meq/100g

Cations	Deduced at w=14%
NaX	31.18
CaX_2	34.62
MgX_2	34.01
KX	1.94
CEC	102

Table 7.17
Calculated selectivity coefficients from exchangeable cation data in Table 7.16

Species	Selectivity
Ca^{2+}	0.292
Mg^{2+}	0.288
Na^+	1
K^+	0.138

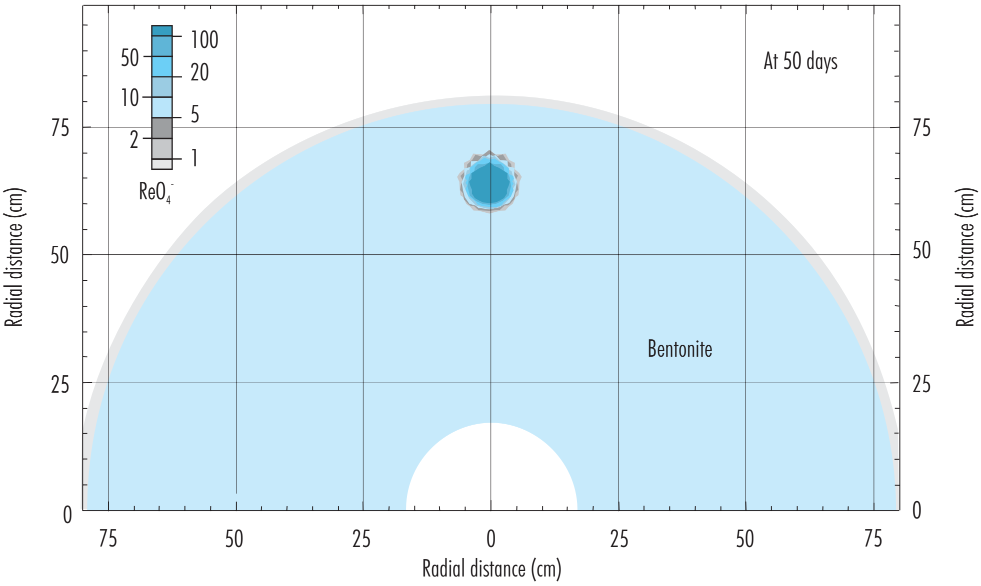

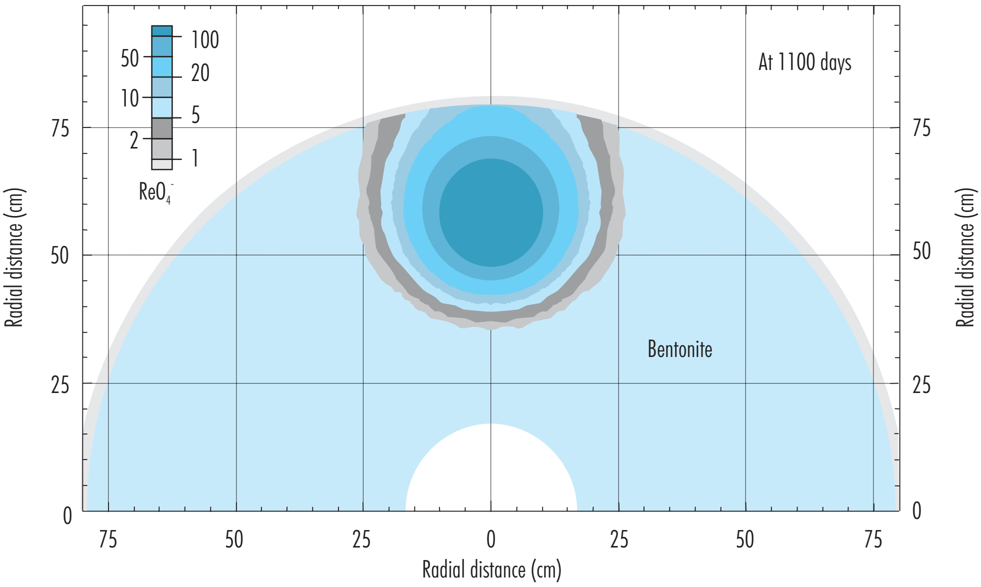

Figure 7.76: Spatial distribution, in a section perpendicular to the barrier axis, of perrhenate ion concentration at 50 days (top) and 1100 days (bottom).

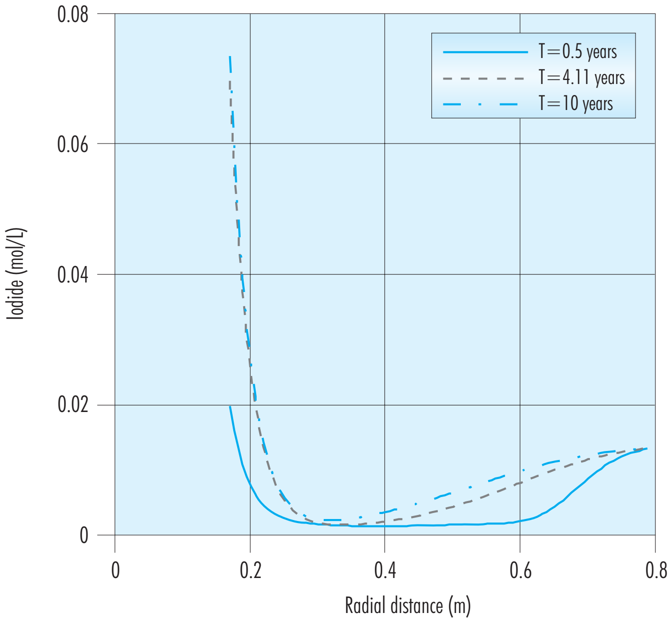

Figure 7.77: Spatial distribution of iodide at different times using Dirichlet boundary condition with $C_0 = 0.01339$ mol/L ($K_d = 0$).

Figure 7.78 shows the THG predictions of chloride concentrations computed during the initial phase. Such predictions were updated during the second phase (see Figure 7.79). It may be seen that the most recent predictions show sharper concentration profiles because the value of the diffusion coefficient adopted in the second phase is an order of magnitude smaller than that used in the initial phase.

Dilution of chloride concentration is induced by the initial flooding and hydration, while near the heater chloride concentration increases due to the condensation caused by the evaporation of bentonite pore water. These are the two main processes that lead to the spatial distribution of this conservative species. After four years, chloride concentration decreases near the heater due to the combined effect of the arrival of the hydration front, which dilutes bentonite pore water, and molecular diffusion. Compared with the prediction of the first phase [190, 13], chloride concentrations near the heater are larger when the variable permeability function is used because less water enters into the bentonite barrier and consequently the water content near the heater is lower. At 30 years the chloride pattern is flat. For the same reason, the time needed to reach the steady state is longer than the prediction of the first phase. In the previous model, steady-state concentration was achieved in 10 years [190, 13]. In the updated model, steady concentrations are attained after 20 years (Figure 7.80).

Dissolved cations (Ca^{2+}, Mg^{2+}, Na^{+}, K^{+}) generally show similar patterns to those of Cl^{-}. Even though these species are subject to chemical reactions (mineral dissolution/precipitation and cation exchange), these processes are not sufficiently strong, compared to dilution and condensation processes, for their concentration patterns to be changed. (Figure 7.81 to Figure 7.84).

Figure 7.85 shows the THG predictions of sulphate spatial distribution. Sulphate concentration of bentonite pore water decreases due to the dilution effect of inflow granitic water. Near the heater, the combined effect of water evaporation and anhydrite precipitation produces a depletion of dissolved sulphate. After 10 years, when the hydration front reaches the vicinity of the heater, anhydrite dissolves (time 30 years in Figure 7.85) and the sulphate content of bentonite pore water increases.

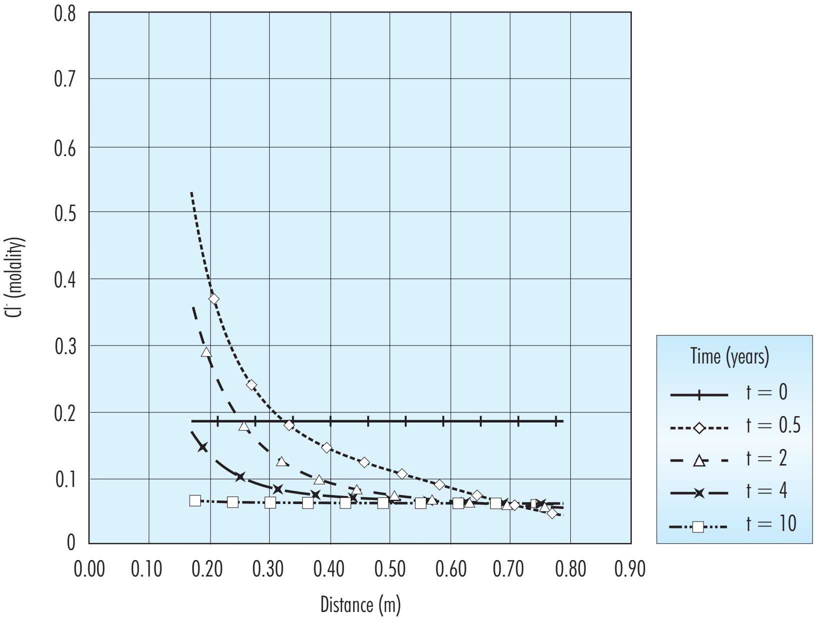

Figure 7.78: Predicted time evolution of the spatial distribution of chloride concentrations in pore water in the "mock-up" test in the initial phase.

Figure 7.86 shows THG predictions of bicarbonate. The bicarbonate content of bentonite pore water undergoes a sudden increase during the first 6 days due to the initial flooding with water for filling of the joints (630 L) during the first 10 days. This injection of granitic water has a bicarbonate concentration greater than the initial bentonite pore water. After 10 days when heaters are switched on, bicarbonate concentrations show a pattern in which concentrations decrease towards the heater. This is due to two effects: 1) The fact that the hydration water has a bicarbonate concentration greater than the initial bentonite pore water, and 2) Calcite solubility decreases with increasing temperature. Therefore, calcite dissolves near to the hydration side and precipitates near the heater (Figure 7.88).

THG predictions of pH (Figure 7.87) show an initial proton dilution (increase in pH) of bentonite pore water due to the inflow of granitic water with a lower proton concentration than the initial bentonite pore water. After 10 days the granitic hydration water that enters the system is responsible for pH increasing, while near the heater pH decreases due to calcite precipitation (Figure 7.88) and proton concentration due to the evaporation of bentonite pore water. After four years pH increases near the heater due to the combined effect of the arrival of the hydration front, which dilutes bentonite pore water, and molecular diffusion.

The spatial distribution of computed exchanged cations (Na^+, K^+, Ca^{2+} and Mg^{2+}) at different times is shown in Figure 7.90 to Figure 7.93. The changes in the composition of the bentonite exchange complex used in the "mock-up" test are greater near the heater than near the hydration side. Anhydrite and calcite precipitation (due to evaporation) induce a depletion of dissolved calcium, which is compensated by calcium released from the exchange complex (Figure 7.92). This release of exchanged calcium causes a gain in exchanged sodium (Figure 7.90). After 10 years, when the hydration front reaches the vicinity of the heater, anhydrite dissolves (time 30 years in Figure 7.89) and the calcium content of bentonite pore water increases. This leads to an increase in exchanged calcium (Figure 7.92) and a decrease in exchanged sodium (Figure 7.90) at 30 years. Exchanged magnesium (Figure 7.93) and potassium (Figure 7.91) show similar behaviour to calcium and sodium, respectively.

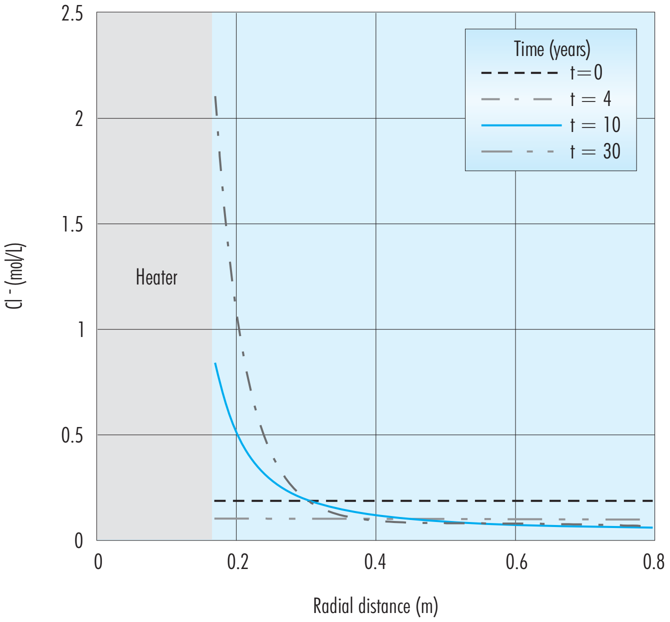

Figure 7.79: Spatial distribution of computed chloride concentrations at different times during the second phase.

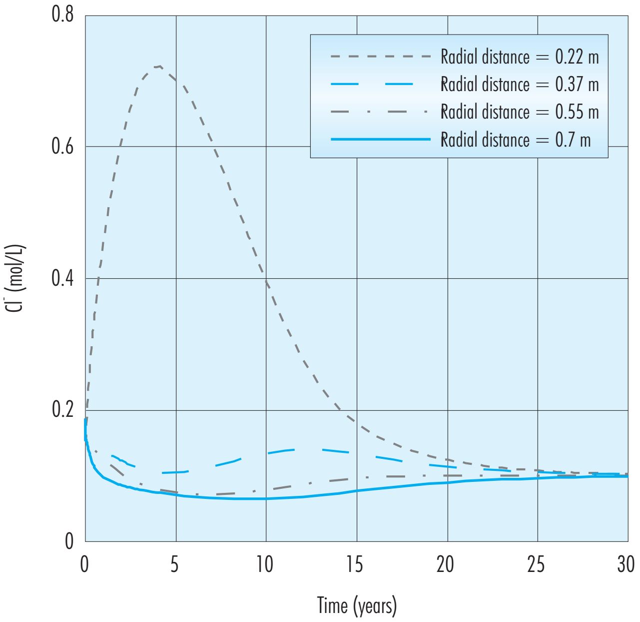

Figure 7.80: Time evolution of computed chloride concentrations at points located at different radial distances.

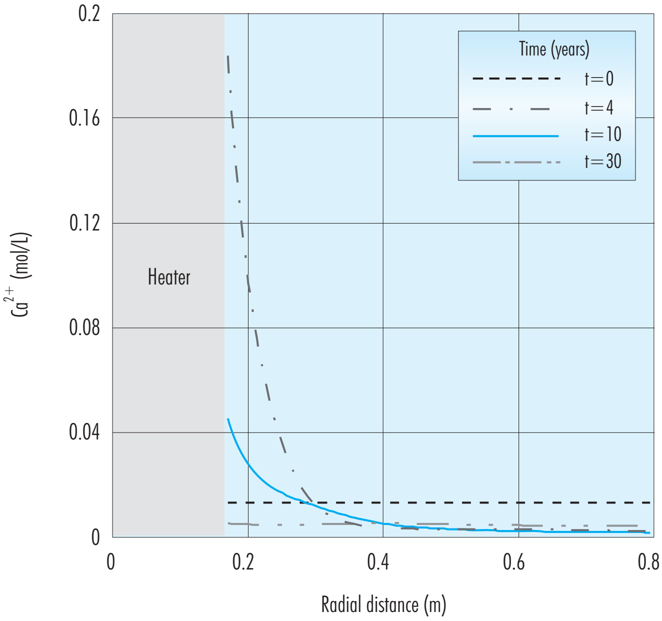

Figure 7.81: Spatial distribution of computed calcium concentrations at different times.

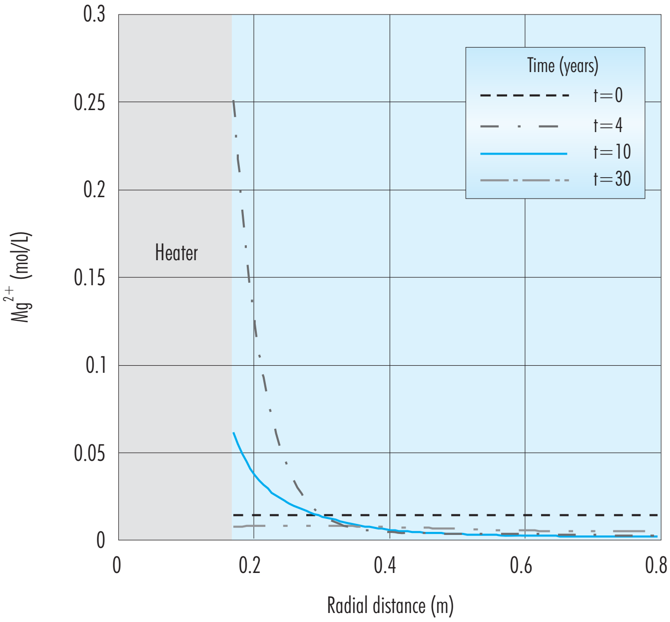

Figure 7.82: Spatial distribution of computed magnesium concentrations at different times.

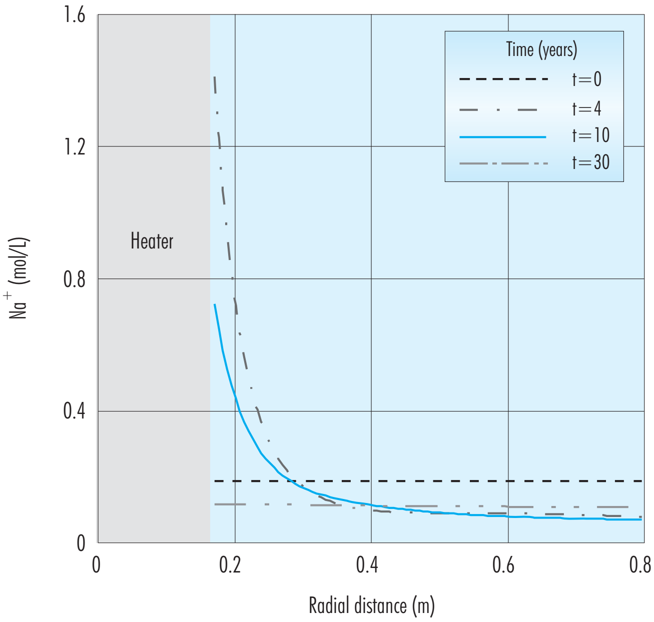

Figure 7.83: Spatial distribution of computed sodium concentrations at different times.

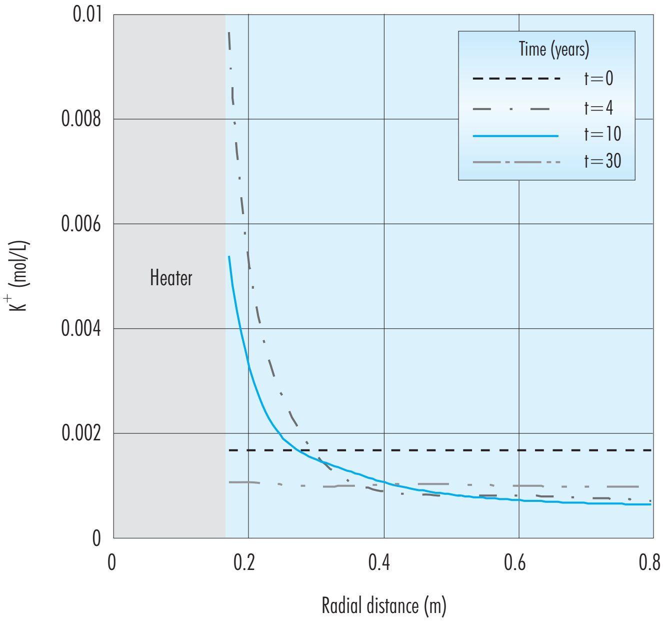

Figure 7.84: Spatial distribution of computed potassium concentrations at different times.

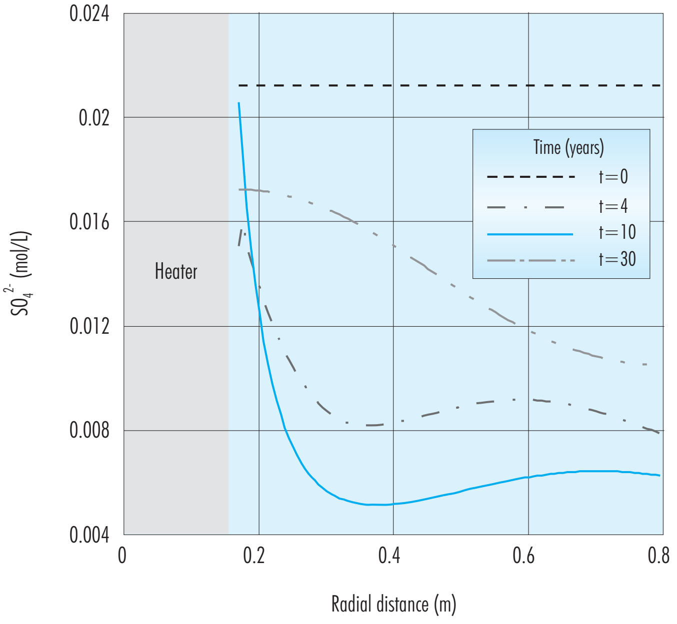

Figure 7.85: Spatial distribution of computed sulphate concentrations at different times.

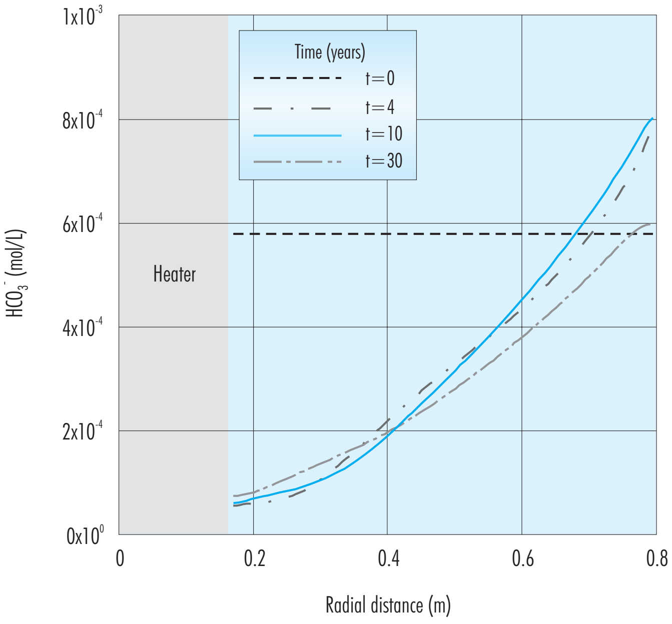

Figure 7.86: Spatial distribution of computed bicarbonate concentrations at different times.

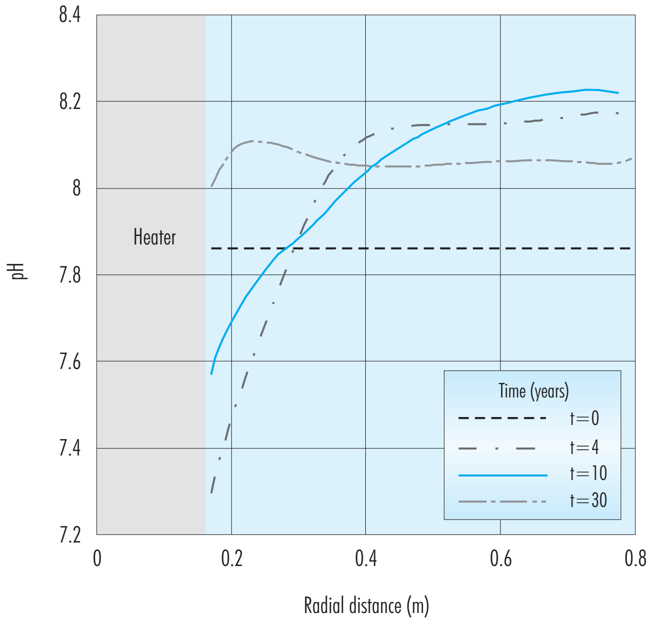

Figure 7.87: Spatial distribution of computed pH at different times.

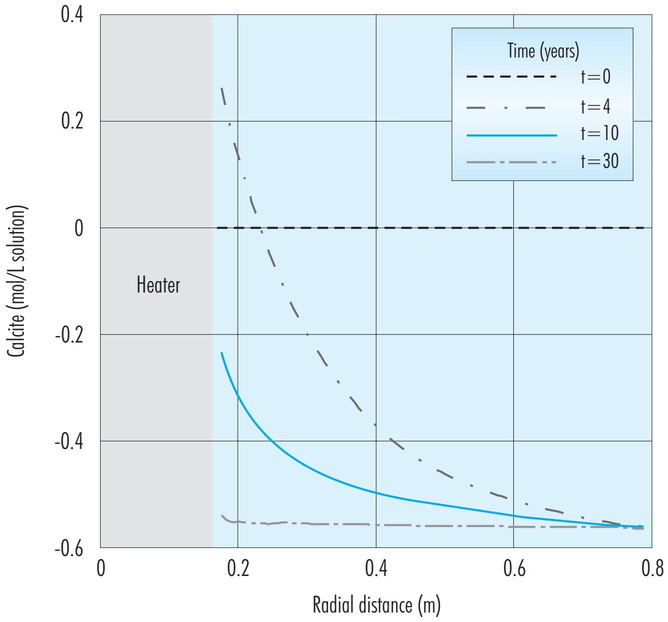

Figure 7.88: Spatial distribution of computed cumulative calcite dissolution (negative)/precipitation (positive).

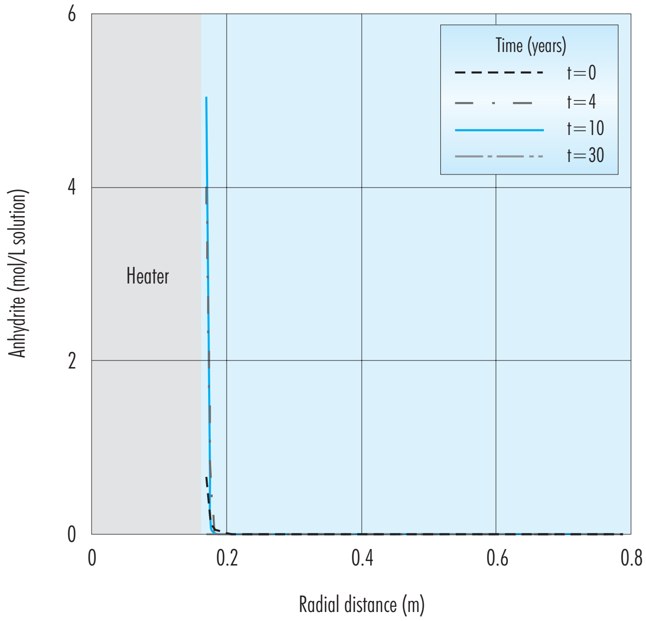

Figure 7.89: Spatial distribution of computed cumulative anhydrite dissolution (negative)/precipitation (positive).

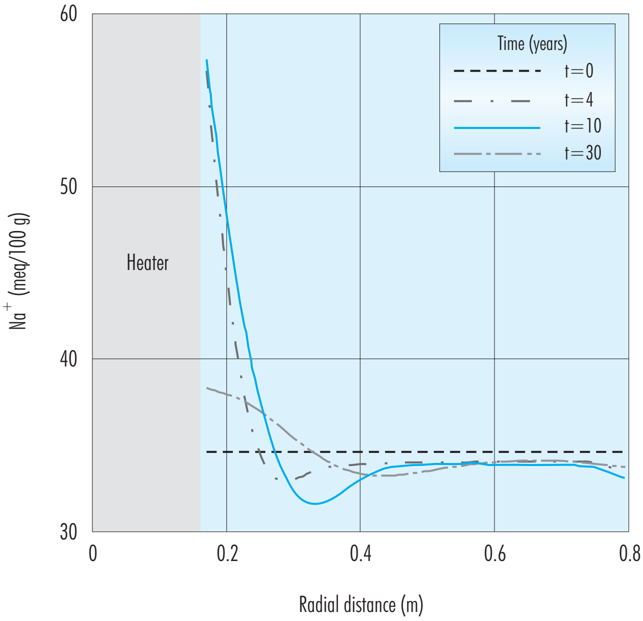

Figure 7.90: Spatial distribution of computed exchanged sodium at different times.

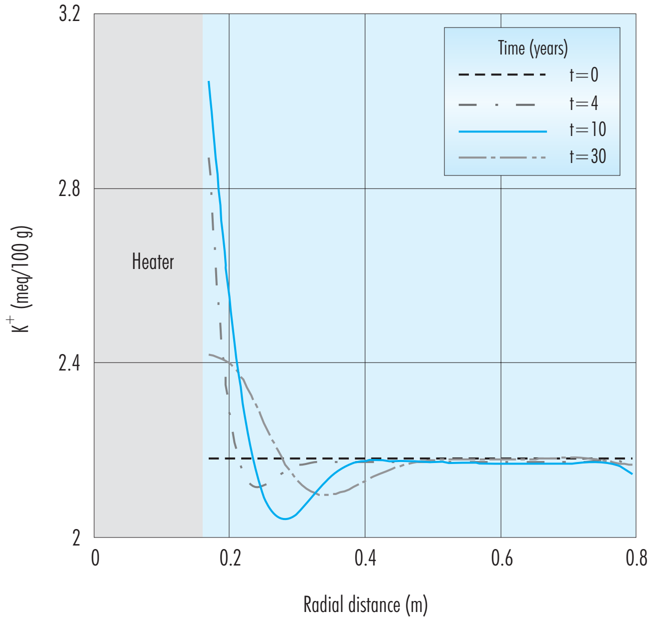

Figure 7.91: Spatial distribution of computed exchanged potassium at different times.

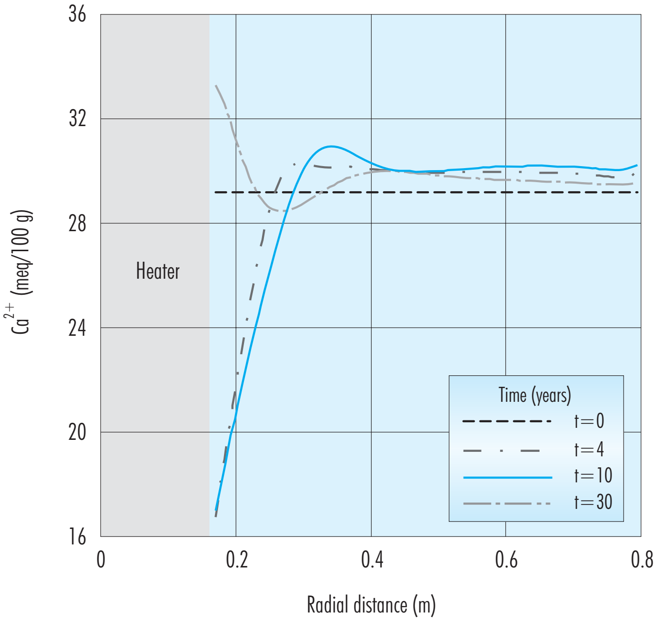

Figure 7.92: Spatial distribution of computed exchanged calcium at different times.

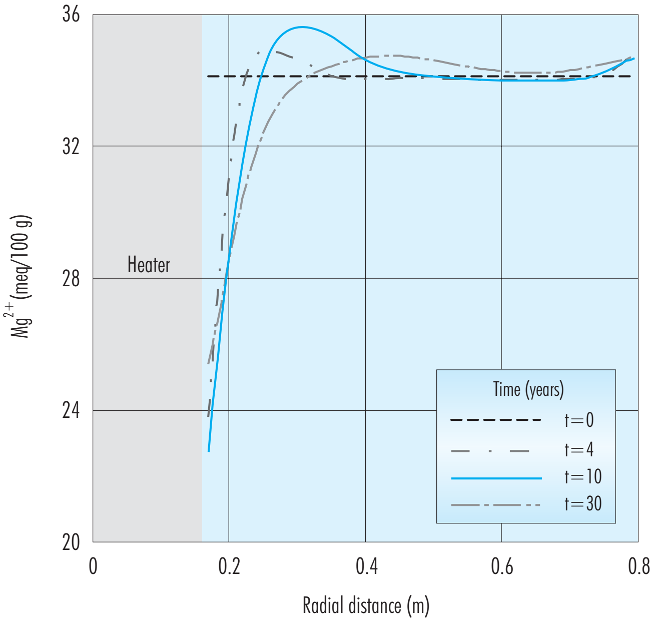

Figure 7.93: Spatial distribution of computed exchanged magnesium at different times.

7.6. THG modelling of the “in situ” test

The THG model for the “in situ” test shares most of the features of the THG model for the “mock-up” test. The same bentonite parameters and processes apply equally well to both tests. The main difference between the models is related to the external boundary condition of the clay buffer. While in the “mock-up” test such boundary conditions are controlled artificially, in the “in situ” test they are imposed by the surrounding granitic rock mass.

7.6.1. TH model

The TH model of the “in situ” test performed during the first phase of FEBEX is based on the same thermo-hydrodynamic parameters and assumptions for the bentonite as the TH model for the “mock-up” test. The parameters and boundary conditions for the granite were derived from available data [47]. However, some of the parameters were slightly modified during the calibration process in order to reproduce the observed thermal and hydrodynamic evolution of the test. The parameters calibrated include: intrinsic permeability for liquid and thermal conductivity of the granite. The model is highly sensitive to variations in these parameters. The base or reference model was calibrated with an intrinsic permeability of 5.38 $\cdot 10^{-17}$ m^2 for water and a thermal conductivity of 4.6 W/m °C for the granite [208]. Both of these parameters are within the range of the measured data.

The model properly captures the temperatures and relative humidities in the bentonite and reproduces the observed spatial distribution of temperatures in the granite after 250 days (Figure 7.94), although at later times computed temperatures tend to slightly overestimate the measured values [208].

During the second phase, both the thermal parameters and the boundary conditions were slightly modified during the calibration process in order to reproduce the observed thermal and hydrodynamic evolution of the test [191]. Computed temperatures are sensitive to the thermal conductivity of granite. Its optimum value of 1.5 W/m·°C was determined by model calibration and assuming a prescribed temperature of 97 °C at the heater surface. This value is within the range of the published thermal conductivities for granite.

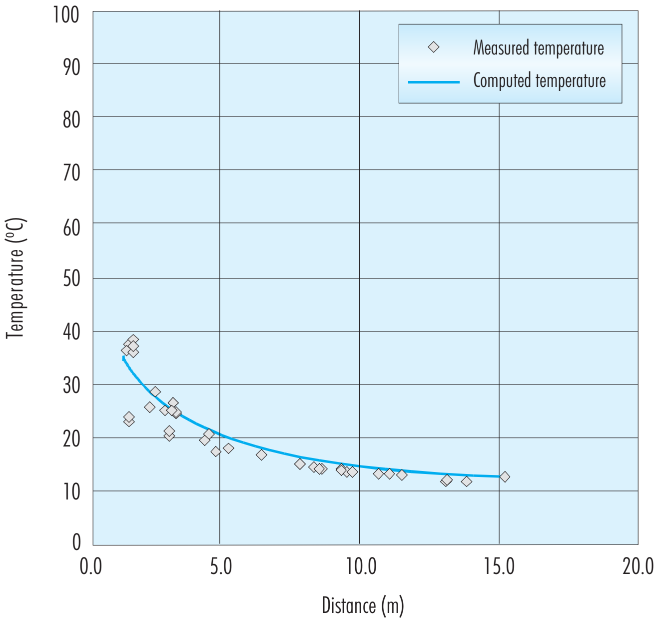

Figure 7.94: Comparison of the measured and computed temperatures in the granite around the "in situ" test after 250 days.

The model properly reproduces temperatures in the bentonite and granite at 1827 days, which coincides with the date on which Heater #1 was switched off (Figure 7.95), but overestimates temperatures near the heater at 1930 days, corresponding to dismantling (Figure 7.96). After 1930 days, the model captures the observed relative humidities at the bentonite barrier, although it overestimates the relative humidity near the heater (Figure 7.97).

Figure 7.98 shows a comparison of modelling results for water content with measured data for hot and cold sections in the "in situ" test. The measured data show an increase in water content above the value corresponding to 100% saturation (23%) due to bentonite swelling. The current TH model does not account for swelling and cannot, therefore, reproduce such large water content values near the granite-bentonite interface (right part of the figure) in the hot and cold sections after 1930 days, at dismantling. The model tends to overpredict the water content near the heater (left part of the figure). This is due to the fact that the model is 1-D axisymmetric and has a fixed temperature at the heater which is equal to the average value of measured temperatures at the heater surface, which range from 75 to 100 °C. Imposing a higher temperature of 100 °C at the heater-bentonite interface, the model provides a better fit to measured water contents near the heater [191, 214].

7.6.2 Numerical modelling of tracer migration

Similar to what occurred in the "mock-up" test, in the "in situ" test artificial chemical and isotopic tracers were placed at single points inside the bentonite barrier and distributed along its periphery, in order to obtain information on the geochemical processes and transport mechanisms. Both conservative and non-conservative tracers were used, including: iodine, rhenium, selenium, boron, deuterium, europium and cesium [212, 215]. In this Section THG predictions of deuterium and iodide migration are presented and compared with measured data.

7.6.2.1 Deuterium

Sampling of selected bentonite blocks (BB29-5 to BB29-13) was carried out at CIEMAT in October 2002. It should be pointed out that glass ampoules were found only in three of the five bentonite blocks:

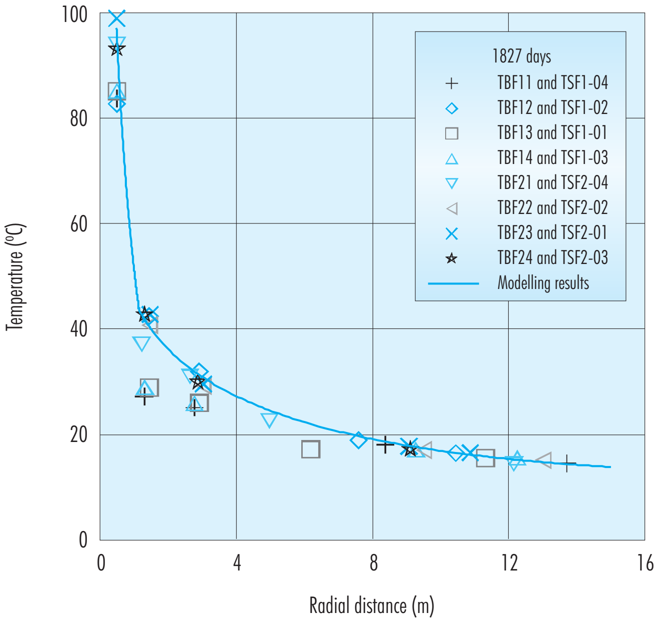

Figure 7.95: Comparison of measured and computed temperatures in the bentonite and granite for the "in situ" test after 1827 days, when Heater #1 was switched off.

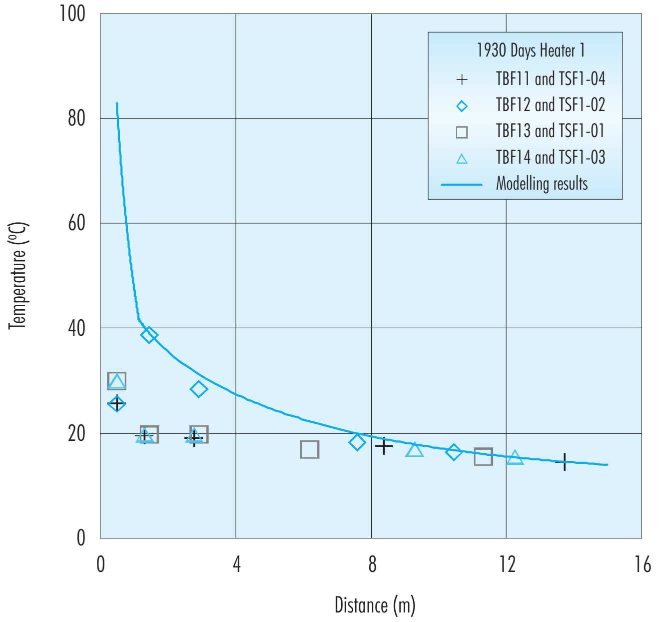

Figure 7.96: Comparison of measured and computed temperatures in the bentonite and granite for the "in situ" test after 1930 days, at dismantling.

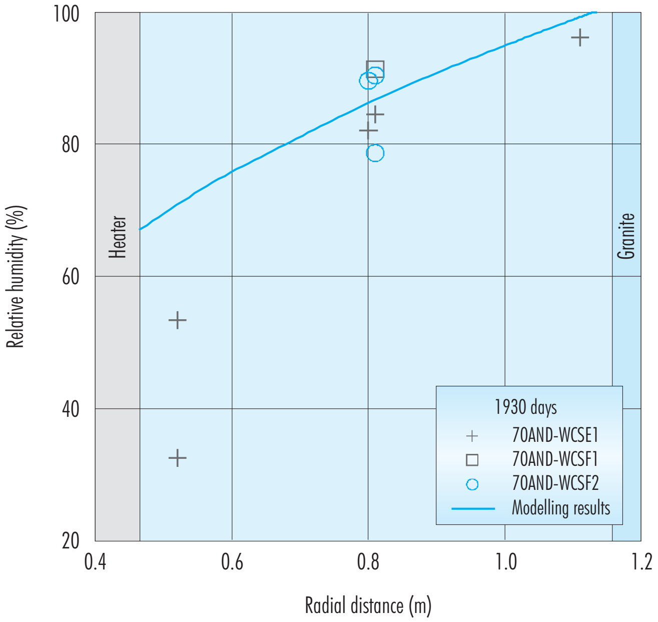

Figure 7.97: Comparison of measured and computed relative humidities in the bentonite for the "in situ" test after 1930 days, at dismantling.

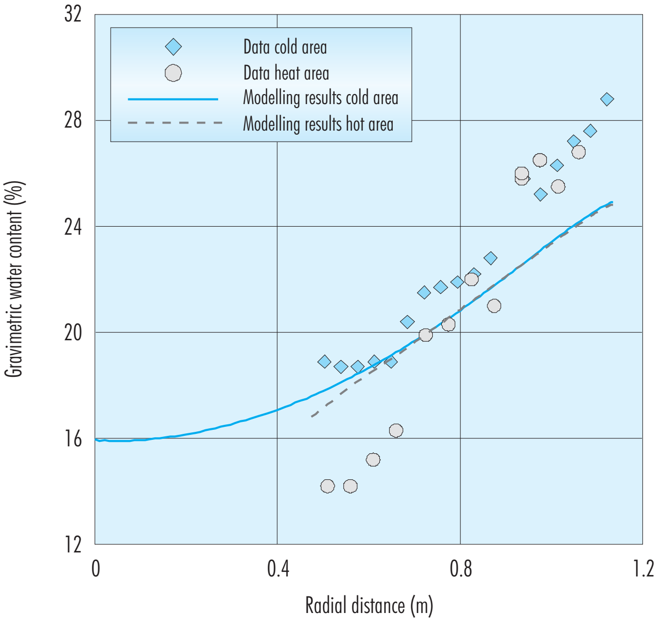

Figure 7.98: Comparison of measured and computed gravimetric water content in the bentonite in sections located in cold and hot areas of the "in situ" test after 1930 days, at dismantling.

BB29-7, BB29-8 and BB29-9. Most of the selected bentonite blocks were very damaged, probably during in situ extraction at Grimsel. Glass ampoules, if found, were broken. All the pieces of the glass ampoule were found only in the case of block BB29-7 [160]. Bentonite pore water for deuterium isotopic determination was obtained from 18 samples of the blocks BB29-7, BB29-12 and BB29-11 using the aqueous extract method with a low solid to liquid (S/L) ratio (1:4). The supernatant solutions were sent for isotopic and chemical analysis. Two additional water samples, one from another section (BB19-14) without deuterium and another of the bidistilled water used in the aqueous extracts, were analysed. Deuterium concentrations (δD values performed with Isotope Ratio Mass Spectrometry) of aqueous extract samples at 1:4 ratio were transformed into δD values of bentonite pore water [160]. Figure 7.99 shows that the error bands for a 1:4 ratio are excessively large. The error bands would have been smaller if the samples had been prepared with a 1:1 ratio

Testing predictions with inferred deuterium data

Glass ampoules containing deuterium were located at the centre of five blocks. They were found broken in bentonite blocks BB29-7, BB29-8 and BB29-9. It is not possible to ascertain whether the ampoules broke during dismantling or during the hydration phase. Due to this uncertainty in sampling, predictions of deuterium transport were made in accordance with two hypotheses. In the first it is assumed that the ampoules broke during the early stages of the "in situ" test, while the second hypothesis assumes they broke during dismantling. The predictions assume that deuterium is conservative and suffers no isotopic fractionation.

The best estimate of δD (deuterium ratio referred to SMOW standard) for the bentonite porewater is -31‰. This value corresponds to a D/H ratio of $1.5213\cdot10^{-4}$. Similarly, the granitic porewaters have a δD of -90‰, which amounts to a D/H ratio of $1.4287\cdot10^{-4}$. Deuterium predictions were obtained using the TH model calibrated with data from the "mock-up" test and using a longitudinal dispersivity of 0.03 m for the bentonite and the granite and a molecular diffusion coefficient (in water), of $1.59\cdot10^{-10}$ m^2/s. Predictions were also made by assuming that 10 mL of deuterium having a D/H ratio of $2.355\cdot10^{-4}$ were added initially at the centre of the external block. Adding this mass is equivalent to

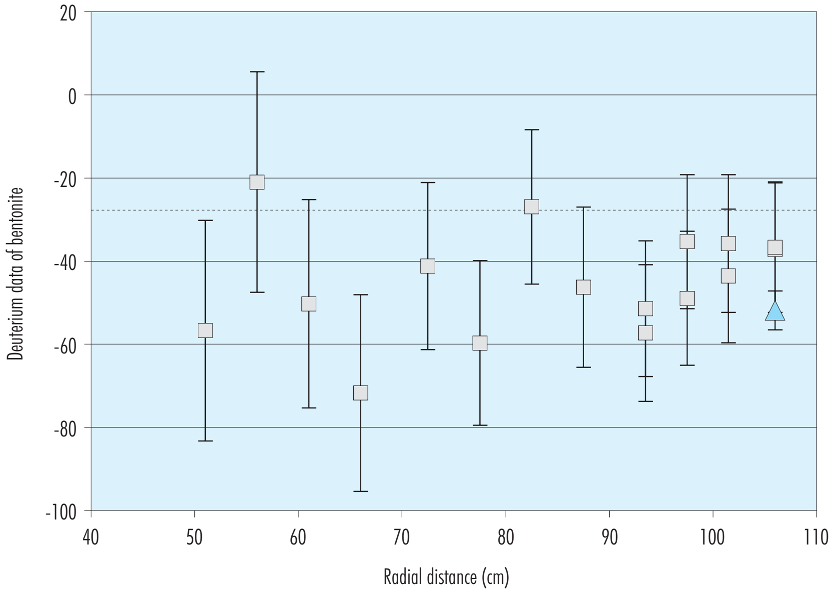

Figure 7.99: Delta values of bentonite porewaters versus radial distance (r= 0 corresponds to heater axis). Error bands have been computed by multiplying the lab precision of 0.8 ‰ by the multiplicative error factor [160]. Deuterium data for intact bentonite porewater (-27.71 ‰) is also shown.

specifying an initial ratio of $3.66 \cdot 10^{-4}$. A deuterium pulse develops in addition to the isotopic dilution caused by the flow of granitic water into the bentonite. Predictions of deuterium derived with both hypotheses, assuming ampoules broke during dismantling and at an early time, are compared to measurements in Figure 7.100.

The available deuterium data do not allow clear conclusions to be drawn because of their precision. Although the precision of the deuterium data on aqueous extract samples is 0.8 ‰, this analytical error translates into large errors for bentonite pore water values. There are uncertainties regarding the breakage of the glass ampoules. Only three were found broken. The most likely thing is that the glass ampoules broke during the test, because if they had broken during dismantling, clay samples near the glass should still show high deuterium ratios. However, since the amount of deuterated water added was not large enough there is no clear evidence of deuterium migration [160].

7.6.2.2. Iodide

Iodide was emplaced in a filter paper located in the outer rings of the bentonite barrier at the central section of Heater #1. During the initial phase of FEBEX, a 1-D mesh of axial symmetry was used for the model predictions of the migration of this tracer in the “in situ” test [190, 13]. Figure 7.101 shows the spatial distribution of the concentration of the ion iodide at 1100 days for the two hypotheses of the magnitude of anionic exclusion (no exclusion and 50% exclusion) and of the distribution coefficient ($K_d = 0$ and $K_d = 0.73$ mL/g). Iodide retention leads to a large retardation. In fact, for $K_d = 0$, the position of the peak of the tracer penetration curve is almost 10 cm farther into the barrier than for the case of $K_d = 0.73$ mL/g. Furthermore, the concentrations of iodide in the pore water are much smaller when adsorption of the tracer is considered. If an anionic exclusion of 50% (one-half of the volume of the pores are not accessible to the iodide) and a $K_d = 0$ are considered, the iodide tracer is displaced much more rapidly (the peak of the curve penetrates 10 cm farther into the barrier than in the case in which exclusion is not considered) and shows weaker dispersion (caused by the reduction in the effective diffusion coefficient). The effect of anionic exclusion depends on the value of the distribution coefficient. For $K_d = 0.73$ mL/g, the effect of anionic exclusion results in a tracer penetration curve that is more peaked (less diffusion), although the position of the peak almost coincides with that corresponding to the hypothesis of non-exclusion.

During the second phase, model predictions of iodide migration in the “in situ” test were updated based on the revised TH model [191]. It was assumed that the tracer was readily available to migration through the bentonite at $t = 0$. This was achieved by assigning a high initial iodide concentration to the nodes located at the bentonite-granite interface.

There are uncertainties regarding the value of the diffusion coefficient, D_0, and accessible porosity, ϕ_a. Published effective diffusion coefficient D_e ranges from $7.7 \cdot 10^{-13}$ to $5 \cdot 10^{-10}$ m^2/s. A set of sensitivity runs was performed around the reference values of $D_0 = 8.3 \cdot 10^{-12}$ m^2/s and $\phi_a = 0.75 \cdot \phi$, where ϕ is total porosity (0.41), corresponding to a value of D_e of $9.7 \cdot 10^{-13}$ m^2/s, which is the average of these two measurements in Table 5.36 of Chapter 5. Modelling results are more sensitive to accessible porosity than to the diffusion coefficient.

An inverse model (inverse model 1) was used to derive optimum estimates of the diffusion coefficient and accessible porosity. It should be noted that accessible porosity is expressed as its ratio to total porosity, for example, 0.614 means accessible porosity is 61.4% of total porosity (0.41). In inverse model 1, the tortuosity of vapour was taken to be equal to 0.5. It should be noted that the code estimates the value of molecular diffusion coefficient in pure water D_0 instead of the effective diffusion coefficient D_e. In the numerical model, D_e is calculated using the equation: $D_e = \phi_a \cdot \tau_a \cdot D_0$, τ_a being tortuosity for transport. The estimated values are $D_0 = 1.6 \cdot 10^{-11}$ m^2/s and $\phi_a = 0.56 \cdot \phi$ (corresponding an effective diffusion coefficient of $7.0 \cdot 10^{-13}$ m^2/s). The modelling results are shown in Figure 7.102.

The results of this run indicate that there is too much evaporation near the heater. Therefore, a new inverse run was performed in which, in addition to the diffusion coefficient and accessible porosity, vapour tortuosity was also estimated (inverse model 2). The estimated parameters in this case are tortuosity equal to 0.1, $D_0 = 2.27 \cdot 10^{-11}$ m^2/s and $\phi_a = 0.56 \cdot \phi$, which amount to an effective diffusion coefficient of $7.0 \cdot 10^{-13}$ m^2/s. This value is consistent with the diffusion coefficient derived by CIEMAT from diffusion experiments performed on small bentonite samples (see Chapter 5). Figure 7.103: shows inverse modelling results.

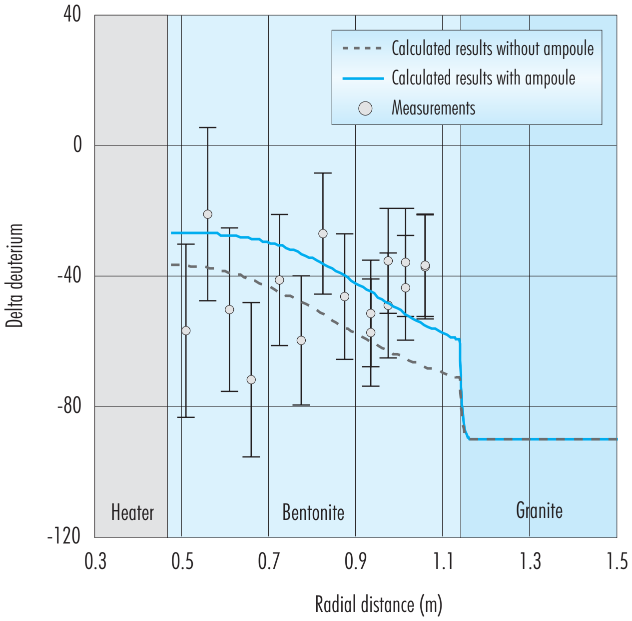

Figure 7.100: Predicted δD assuming ampoules broke during dismantling (without ampoule) and at an early time (with ampoule) and comparison to measured data after 1930 days of heating (June 2002).

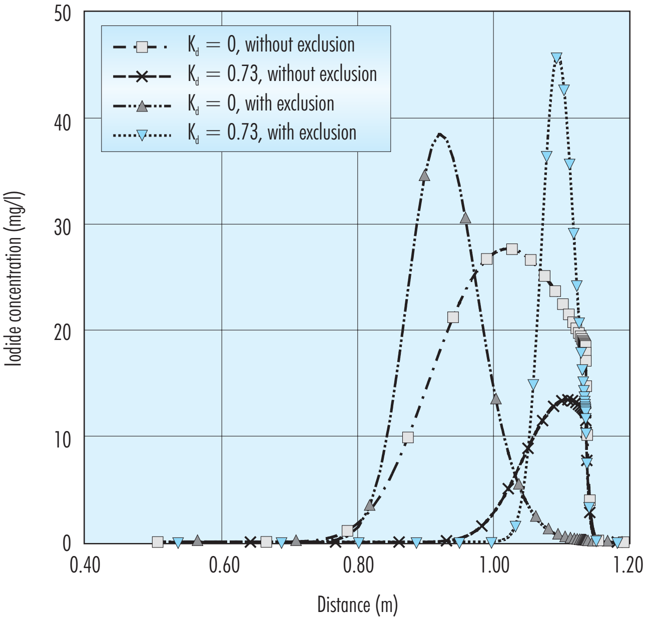

Figure 7.101: Spatial distribution of iodine ion in the clay barrier at 1100 days, for various retention and exclusion hypotheses.

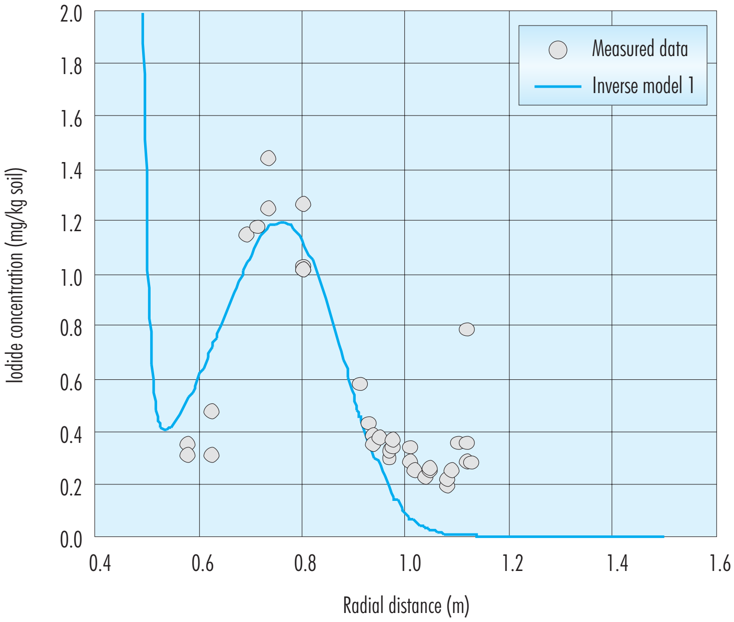

Figure 7.102: Modelling results of inverse model 1.

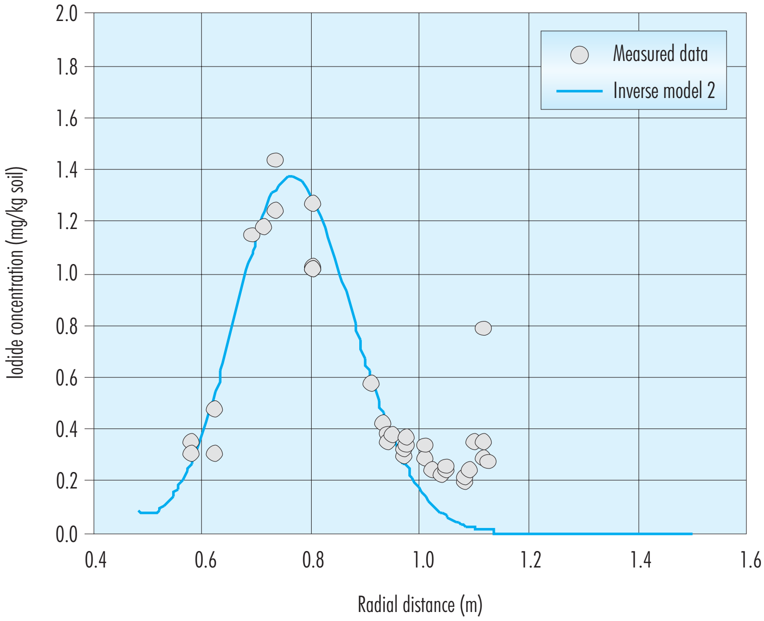

Figure 7.103: Modelling results of inverse model 2.

By reducing vapour tortuosity from 0.5 to 0.1, water evaporation near the heater is greatly reduced and the computed iodide concentration near the heater approximates to the measured values. Computed concentrations capture the peak of the tracer distribution. There are, however, some discrepancies near the bentonite-granite interface that might be attributed to the initial iodide concentration in the bentonite. The initial concentration of iodide in the bentonite and granite is 20 ppb, which amounts to $2.87 \cdot 10^{-3}$ mg/kg of bentonite. However, the sensitivity analyses at the initial concentration indicate that the discrepancies near the bentonite-granite interface are not caused by an inadequate initial concentration of iodide in the bentonite. Other possible processes which might explain the high iodide concentration near the bentonite-granite interface include:

- ❑ The double porosity behaviour of bentonite. The transfer of iodide mass from macro-pores to relatively stagnant micro-pores might lead to a high iodide concentration in micro-pores.
- ❑ Bentonite swelling. The water involved in clay swelling is not available for solute transport.

These limitations might be overcome by using a THMG double porosity model.

7.6.3. THG model

During the initial phase of FEBEX, predictive modelling of the "in situ" test was carried out using the same parameters, processes, solid phases, and reactions as those of the "mock up" test [190, 13]. However, there is a minor difference in the initial temperature of both tests which affects the initial geochemical conditions. Figure 7.104 shows the spatial distribution of chloride. There is important dilution at the granite/bentonite interface due to water hydration. Similar to the heating and hydration cells, the concentration of most of the ions increases around the heater, due to water evaporation. Inward displacement of the hydration front, together with diffusion processes, leads to rather homogeneous – but still not flat – concentration profiles at the end of the modelling period (1550 days, i.e. four years and three months). This result is an indication of the fact that the transport and chemical processes have not yet reached the steady state.

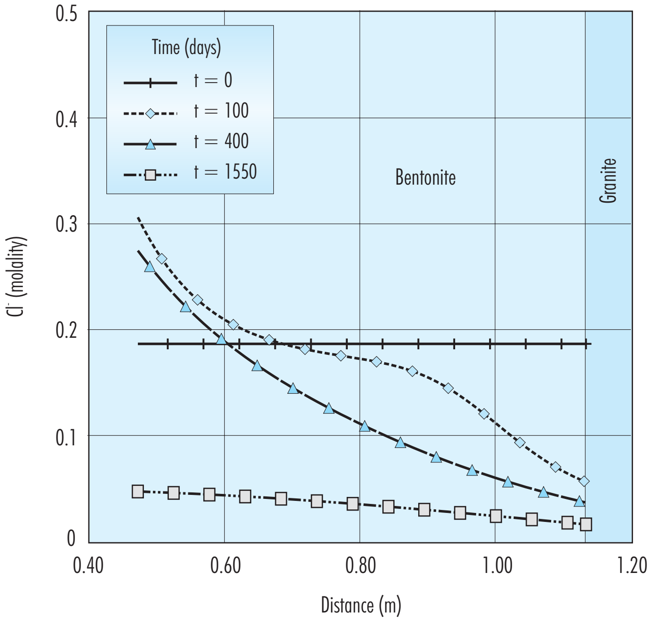

Figure 7.104: Predicted time evolution of the spatial distribution of chloride concentrations in pore water in the "in situ" test

It should be noted that the THG model assumes that the fractured granitic rock may be represented by an equivalent porous medium having a low porosity of 0.01. This assumption makes the backward diffusion of ions from the clay barrier to the rock very unlikely.

7.6.3.1. Measured geochemical dismantling data

During the second phase, supernatant solutions of aqueous extract tests performed on samples from sections 29 and 12, which are situated respectively in hot (surrounding the heater) and cold (far from the heater) areas, were subjected to chemical analysis (Chapter 5).

7.6.3.2. Inferred chemical composition of bentonite pore water

The chemical composition of bentonite pore water at different water contents was estimated using an inverse methodology [191, 193, 201]. Tables 7.18 and 7.19 show the inferred pore water chemical composition of bentonite samples BB29-7/1-12 and BB29-11/2-3 with water contents of 26% (almost saturated) and 14.2% (similar to ambient conditions), respectively, together with calculated aqueous extract data. All the conceptual models are capable of reproducing the measured data, except for model CGM-1 which is unable to accurately reproduce the bicarbonate calculated concentration [191, 214]. This model shows some limitations when used for the interpretation of the "in situ" test data. It should be noticed that all models lead to similar inferred results for all chemical species, except for bicarbonate and sulphate. Models CGM-0 and CGM-2, which were derived from squeezing data [191, 193], provide similar results except for bicarbonate. For this species, the inferred concentrations obtained with model CGM-0 are almost two orders of magnitude greater than those of models CGM-1 and CGM-2. Following a similar procedure to that of section 29, the chemical composition of samples of section 12 was inferred from aqueous extract data. The inferred chemical concentrations are shown in Tables 7.18 and 7.19 for section BB29.

7.6.3.3. Comparison of THG predictions with inferred geochemical data

THG predictions are compared to geochemical data inferred from the data collected during the dismantling of Heater #1 of the "in situ" test. Such a comparison is the way to test and validate current THG models of the engineered barrier system [191, 214].

In hot areas, aqueous extract data are available in sections 30, 29, 28 and 19. There are some differ-

Table 7.18
Inferred (26% water content) and calculated and measured aqueous extract resulting data (1:4 ratio) chemical composition (mol/L) of bentonite sample BB29-7/1-12

	CGM-0		CGM-1		CGM-2		
	Inferred	Calculated	Inferred	Calculated	Inferred	Calculated	Measured
Ca^{2+}	$8.3\cdot10^{-3}$	$2.5\cdot10^{-5}$	$7.8\cdot10^{-3}$	$2.7\cdot10^{-5}$	$6.3\cdot10^{-3}$	$2.4\cdot10^{-5}$	$2.5\cdot10^{-5}$
Cl^{-}	$1.9\cdot10^{-2}$	$9.2\cdot10^{-4}$	$2.0\cdot10^{-2}$	$9.7\cdot10^{-4}$	$1.9\cdot10^{-2}$	$9.2\cdot10^{-4}$	$9.3\cdot10^{-4}$
HCO_3^{-}	$4.6\cdot10^{-2}$	$2.2\cdot10^{-3}$	$1.1\cdot10^{-4}$	$7.2\cdot10^{-4}$	$1.7\cdot10^{-4}$	$1.2\cdot10^{-3}$	$2.2\cdot10^{-3}$
K^{+}	$1.1\cdot10^{-3}$	$7.6\cdot10^{-5}$	$1.1\cdot10^{-3}$	$8.0\cdot10^{-5}$	$1.0\cdot10^{-3}$	$7.6\cdot10^{-5}$	$7.6\cdot10^{-5}$
Mg^{2+}	$1.5\cdot10^{-2}$	$4.4\cdot10^{-5}$	$1.5\cdot10^{-2}$	$4.9\cdot10^{-5}$	$1.3\cdot10^{-2}$	$4.6\cdot10^{-5}$	$4.5\cdot10^{-5}$
Na^{+}	$1.2\cdot10^{-1}$	$8.0\cdot10^{-3}$	$1.2\cdot10^{-1}$	$8.4\cdot10^{-3}$	$1.0\cdot10^{-1}$	$8.1\cdot10^{-3}$	$8.0\cdot10^{-3}$
SO_4^{2-}	$5.7\cdot10^{-2}$	$2.7\cdot10^{-3}$	$6.0\cdot10^{-2}$	$2.9\cdot10^{-3}$	$5.7\cdot10^{-2}$	$2.7\cdot10^{-3}$	$2.7\cdot10^{-3}$

Table 7.19
Inferred (14.2% water content) and calculated and measured aqueous extract resulting data (1:4 ratio) chemical composition (mol/L) of bentonite sample BB29-11/2-3

	CGM-0		CGM-1		CGM-2		
	Inferred	Calculated	Inferred	Calculated	Inferred	Calculated	Measured
Ca^{2+}	$5.1\cdot10^{-2}$	$1.9\cdot10^{-4}$	$4.3\cdot10^{-2}$	$2.0\cdot10^{-4}$	$5.0\cdot10^{-2}$	$2.1\cdot10^{-4}$	$2.0\cdot10^{-4}$
Cl^{-}	$3.2\cdot10^{-1}$	$9.8\cdot10^{-3}$	$3.2\cdot10^{-1}$	$9.8\cdot10^{-3}$	$3.2\cdot10^{-1}$	$9.8\cdot10^{-3}$	$9.8\cdot10^{-3}$
HCO_3^{-}	$6.7\cdot10^{-2}$	$2.1\cdot10^{-3}$	$1.4\cdot10^{-4}$	$8.2\cdot10^{-4}$	$1.4\cdot10^{-4}$	$9.1\cdot10^{-4}$	$2.0\cdot10^{-3}$
K^{+}	$2.5\cdot10^{-3}$	$1.8\cdot10^{-4}$	$2.4\cdot10^{-3}$	$1.8\cdot10^{-4}$	$2.5\cdot10^{-3}$	$1.8\cdot10^{-4}$	$1.8\cdot10^{-4}$
Mg^{2+}	$5.1\cdot10^{-2}$	$2.1\cdot10^{-4}$	$4.0\cdot10^{-2}$	$2.2\cdot10^{-4}$	$4.6\cdot10^{-2}$	$2.1\cdot10^{-4}$	$2.2\cdot10^{-4}$
Na^{+}	$1.7\cdot10^{-1}$	$1.3\cdot10^{-2}$	$1.6\cdot10^{-1}$	$1.3\cdot10^{-2}$	$1.7\cdot10^{-1}$	$1.3\cdot10^{-2}$	$1.3\cdot10^{-2}$
SO_4^{2-}	$3.5\cdot10^{-2}$	$1.9\cdot10^{-3}$	$2.0\cdot10^{-2}$	$2.0\cdot10^{-3}$	$3.3\cdot10^{-2}$	$1.9\cdot10^{-3}$	$2.0\cdot10^{-3}$

ences between the measured data in these sections that warrant additional analysis.

Aqueous extract data from section 29, located in the middle of Heater #1, were inferred and used for the purpose of testing THG predictions because these data were the first to be delivered. Additional data from sections 30, 28 and 19 became available after completion of the THG model. A preliminary analysis of data from these four sections reveals certain significant differences between the data in different sections, which should be analysed in the future.

Since squeezing pore water chemistry data are not available at this section, data from section 19 were used, where data from both techniques, aqueous extract and squeezing, are available [216]. As regards the cold section, aqueous extract and squeezing data of section 12 were used.

THG predictions of the "in situ" test have been performed using INVERSE-FADES-CORE V0 [201], a code which preserves all the capabilities of FADES-CORE V1 [200] and is capable of performing automatic parameter estimation.

The thermal and hydrodynamic parameters of the THG model were calibrated from TH data from the "mock-up" and "in situ" tests. A longitudinal dispersivity of 0.03 m was used for the bentonite and the granite [191].

THG predictions were performed with the three conceptual geochemical models CGM-0, CGM-1 and CGM-2 described in Section 7.2.4. A comparison of the modelling results for water content with measured data for hot and cold sections in the "in situ" test after 1930 days, at dismantling, has been shown in Figure 7.98 (see Section 7.6.1).

Predictions of concentrations were performed by assuming the same diffusion coefficient (in pure water) for all chemical species, equal to $2\cdot10^{-10}$ m^2/s. Although the diffusion coefficient may be smaller for species undergoing anion exclusion, such as chloride, the sensitivity runs performed with smaller diffusion coefficients and anion exclusion provide worse results (not shown here).

Comparison of THG predictions with inferred geochemical data in hot areas

Figure 7.105 to Figure 7.110 show THG predictions after 1930 days of heating (which corresponds to the dismantling date) in the hot section [191, 214]. These predictions are compared to data inferred from aqueous extracts at section 29 [216]. In addition, the values obtained at section 19 are shown, at which both squeezing and aqueous extract data are available. Table 7.20 shows a comparison between the measured chemical composition using squeezing and inferred aqueous extract

Table 7.20
Comparison of chemical composition at section 19 as obtained by squeezing and inferred aqueous extract. Concentrations in mol/L

	BB19-1 (Squeezing)	BB19-2 (Squeezing)	BB19-13/2.1 (Aqueous extract)
w (%)	28.7	23.5	26.9
pH	7.5	7.7	7.65
Na^+	$5.21 \cdot 10^{-2}$	$1.00 \cdot 10^{-1}$	$8.67 \cdot 10^{-2}$
K^+	$3.32 \cdot 10^{-4}$	$3.32 \cdot 10^{-4}$	$9.40 \cdot 10^{-4}$
Mg^{2+}	$2.75 \cdot 10^{-3}$	$1.45 \cdot 10^{-2}$	$1.14 \cdot 10^{-2}$
Ca^{2+}	$2.65 \cdot 10^{-3}$	$1.13 \cdot 10^{-2}$	$4.26 \cdot 10^{-3}$
Cl^-	$4.22 \cdot 10^{-2}$	$1.10 \cdot 10^{-1}$	$5.26 \cdot 10^{-2}$
SO_4^{2-}	$9.20 \cdot 10^{-3}$	$1.87 \cdot 10^{-2}$	$4.00 \cdot 10^{-2}$
HCO_3^-	$2.57 \cdot 10^{-3}$	$2.64 \cdot 10^{-3}$	$3.63 \cdot 10^{-4}$

data at section 19. By comparing samples BB19-1 (squeezing) and BB19-13/2.1 (inferred aqueous extracts), which have similar water contents, it may be seen that the squeezing method leads to lower concentrations for sulphate, magnesium, sodium, and potassium than those of the aqueous extract method.

The comparison of THG predictions and re-calculated data indicates that for the most part the THG model reproduces the trends of the inferred data. Chloride concentrations are larger near the heater and decrease with radial distance (Figure 7.105). Although the model tends to overpredict chloride concentrations near the granite interface at section 29, available data at section 19 fall closer to the band of values computed with models CGM-0, CGM-1 and CGM-2. Calcium (Figure 7.106) shows similar trends to those of chloride. Aqueous extract data from section 29 show an increase of calcium concentrations near the granite-bentonite interface. Such an increase, however, is not observed at section 19. Models CGM-1 and CGM-0 seem to fit the measured calcium data better than model CGM-2.

Measured aqueous extract data from samples located near the bentonite-granite interface show exceedingly large cation concentrations that, according to CIEMAT, might be an artefact caused by colloidal particles.

Magnesium (Figure 7.107), sodium (Figure 7.108) and potassium (Figure 7.109) also show a general pattern of higher concentrations near the heater and lower concentrations at the bentonite-granite interface. The results computed with models CGM-0, CGM-1 and CGM-2 reproduce the general trends of measured data. The available data at section 19 fall closer to the band of values computed with the three models. Only squeezing values for potassium at section 19 are smaller than expected, for reasons yet to be ascertained. Sulphate aqueous extract data (Figure 7.110) show different trends. Model predictions are more coherent with squeezing data from section 19 than with aqueous extract data. The uncertainties of the conceptual geochemical models for sulphate should be borne in mind [191,193].

Comparison of THG predictions with inferred geochemical data in cold areas

Figure 7.111 to Figure 7.117 show THG predictions after 1930 days of heating (which corresponds to the dismantling date) in the cold section [191, 214]. These predictions are compared to data in-

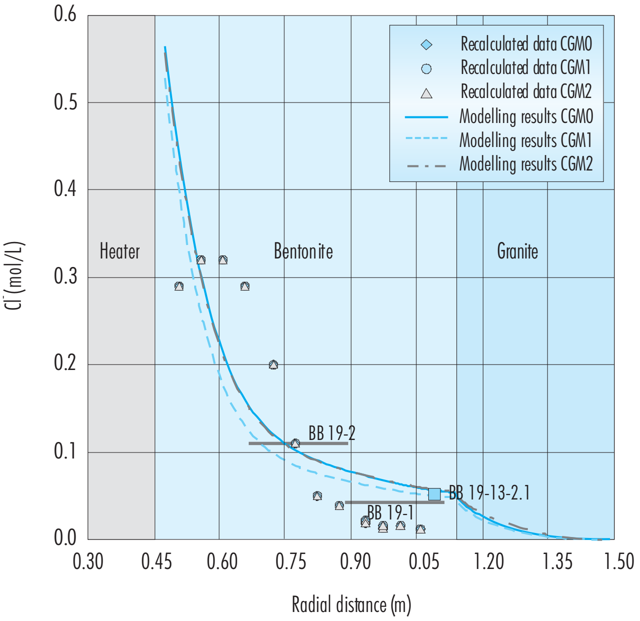

Figure 7.105: Comparison of predictions of Cl with inferred aqueous extract data at section 29 (symbols) after 1930 days of heating. Also shown are the values obtained at section 19 with squeezing (horizontal lines) and aqueous extract (symbol).

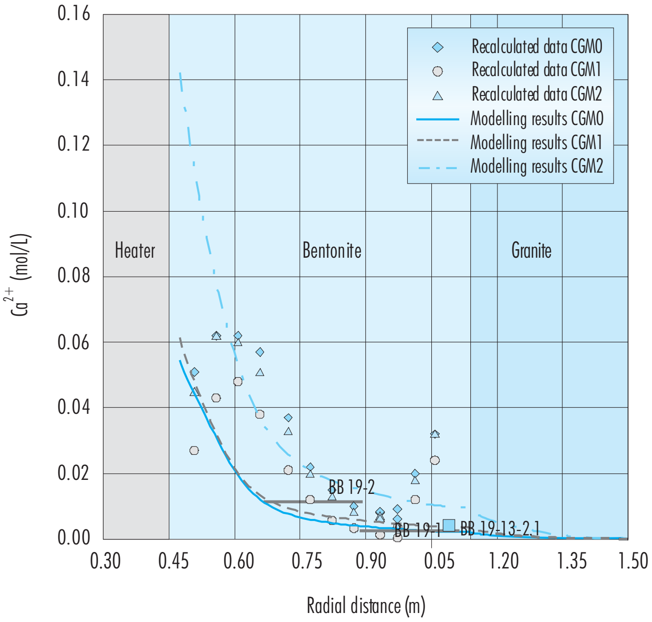

Figure 7.106: Comparison of predictions of Ca^{2+} with inferred aqueous extract data at section 29 (symbols) after 1930 days of heating. Also shown are the values obtained at section 19 with squeezing (horizontal lines) and aqueous extract (symbol).

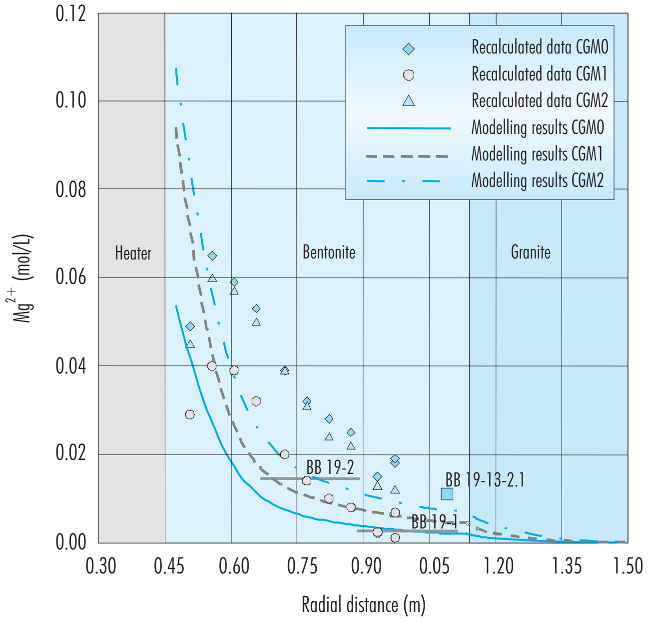

Figure 7.107: Comparison of predictions of Mg^{2+} with inferred aqueous extract data at section 29 (symbols) after 1930 days of heating. Also shown are the values obtained at section 19 with squeezing (horizontal lines) and aqueous extract (symbol).

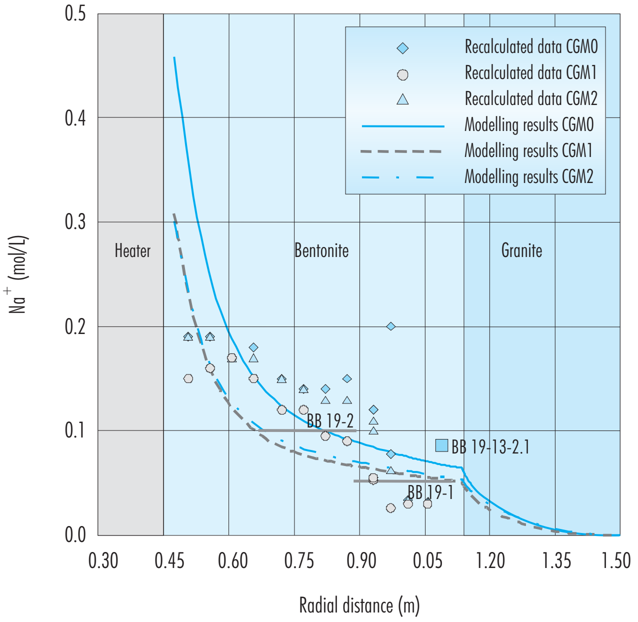

Figure 7.108: Comparison of predictions of Na^{+} with inferred aqueous extract data at section 29 (symbols) after 1930 days of heating. Also shown are the values obtained at section 19 with squeezing (horizontal lines) and aqueous extract (symbol).

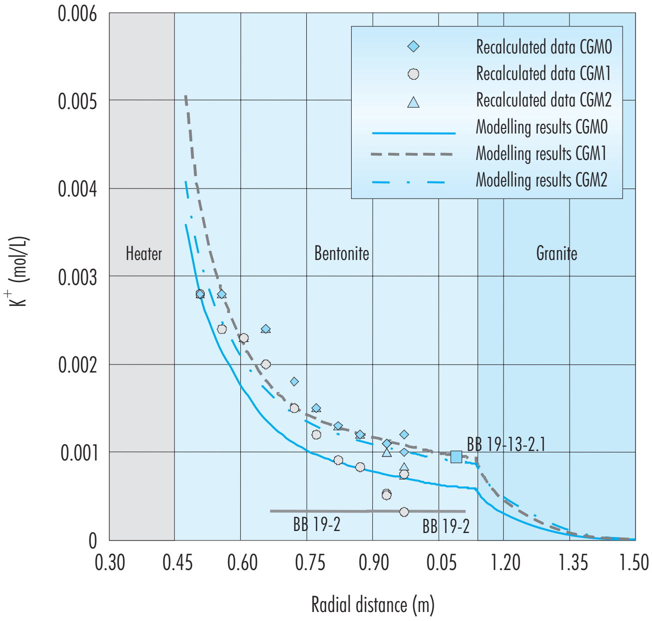

Figure 7.109: Comparison of predictions of K^+ with inferred aqueous extract data at section 29 (symbols) after 1930 days of heating. Also shown are the values obtained at section 19 with squeezing (horizontal lines) and aqueous extract (symbol).

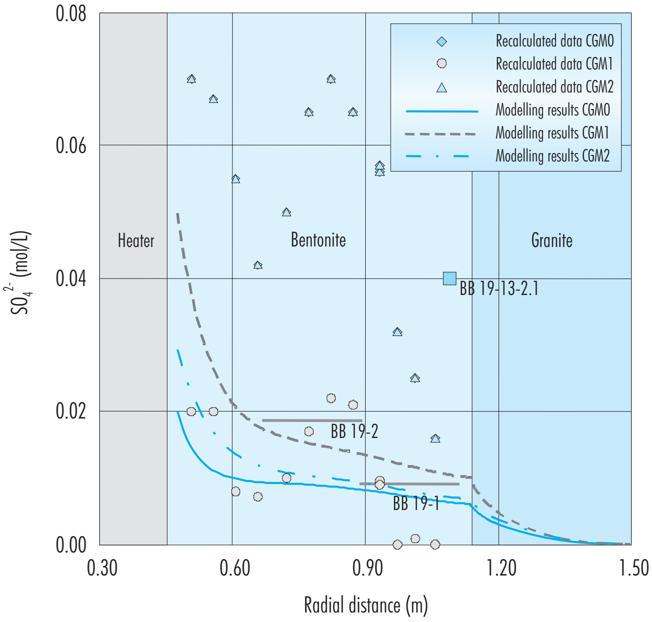

Figure 7.110: Comparison of predictions of SO_4^{2-} with inferred aqueous extract data at section 29 (symbols) after 1930 days of heating. Also shown are the values obtained at section 19 with squeezing (horizontal lines) and aqueous extract (symbol).

ferred from aqueous extracts at section 12 [216]. Squeezing data obtained at this section are also shown in the figures.

Chloride (Figure 7.111) concentrations are higher near the heater, but lower than in Figure 7.105 for hot section, and decrease with radial distance. Near the granite interface the available squeezing data fall closer to the band of values computed and re-calculated with models CGM-0, CGM-1 and CGM-2. The predictions reproduce the general trend of the measured data, but overestimate observed concentrations at the interface granite-bentonite, which might be attributed to the underestimation of water content (Figure 7.98) or to anion exclusion. In the central part of the bentonite barrier, all three models overestimate measured data.

THG predictions of Ca^{2+} (Figure 7.112) with model CGM-0 do not fit the measured data, but those performed with CGM-1 and CGM-2 reproduce the trend of these data. Such a discrepancy might be related to the role of anhydrite.

Measured Mg^{2+} concentrations fall within the band of predictions with three CGM's (Figure 7.113). It should be noted that the CGM obtained from squeezing data (CGM-0) reproduces the squeezing data, while the models obtained from aqueous data (CGM-1 and CGM-2) reproduce aqueous extract data. Here attention is called to the differences in concentration provided by squeezing and aqueous extract method.

Predictions of Na^+ concentrations reproduce the general trend of aqueous extract data and fall within the band of squeezing data (Figure 7.114). Predictions of K^+ concentrations reproduce the measured data at the granite interface but overestimate them in the middle of the bentonite barrier (Figure 7.115).

The computed sulphate results underpredict the re-calculated data (Figure 7.116). The re-calculated aqueous extract data for sulphate do not show any clear trend. Model predictions are more coherent with squeezing data from this section 12 than with aqueous extract data, as in the case of the hot sections. Uncertainties regarding bicarbonate (Figure 7.117) calculation are significant not only in the inference of aqueous extract data but also in THG prediction.

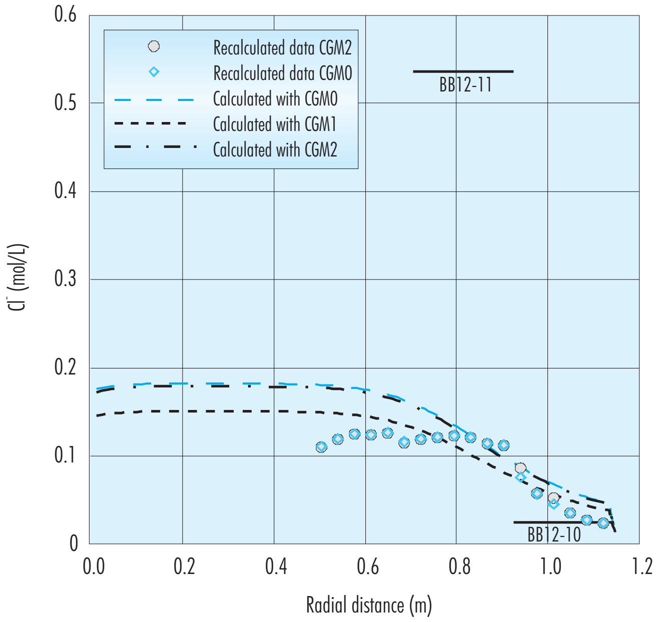

Figure 7.111: Comparison of predictions of Cl^- with inferred aqueous extract data at section 12 (symbols) after 1930 days of heating. Also shown are the values obtained at section 12 with squeezing (horizontal lines).

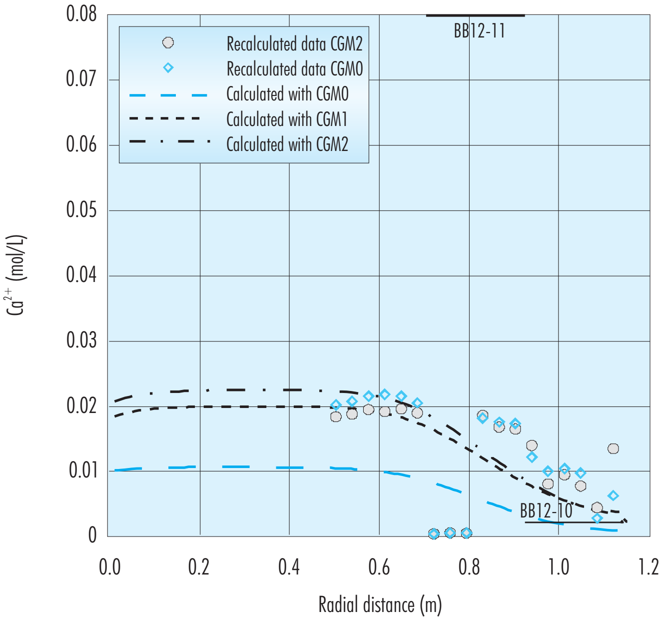

Figure 7.112: Comparison of predictions of Ca^{2+} with inferred aqueous extract data at section 12 (symbols) after 1930 days of heating. Also shown are the values obtained at section 12 with squeezing (horizontal lines).

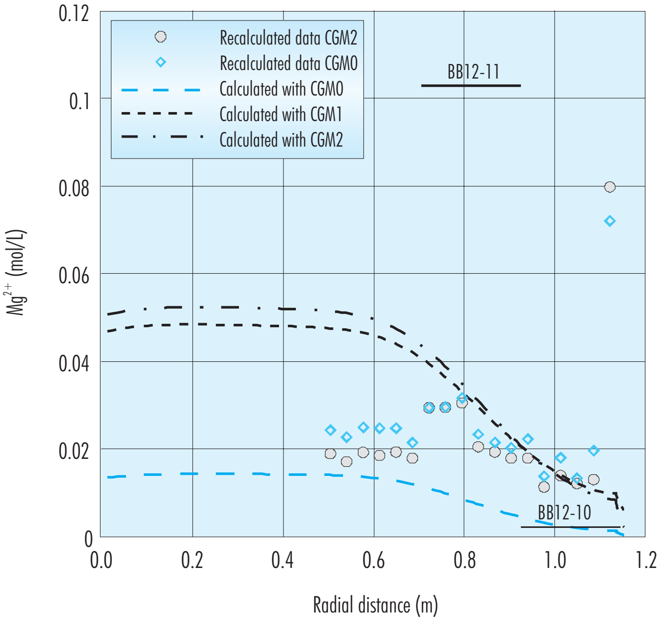

Figure 7.113: Comparison of predictions of Mg^{2+} with inferred aqueous extract data at section 12 (symbols) after 1930 days of heating. Also shown are the values obtained at section 12 with squeezing (horizontal lines).

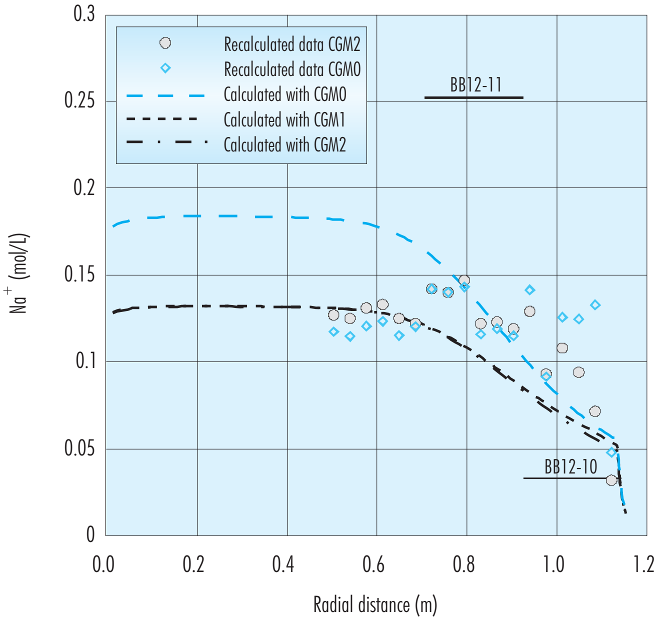

Figure 7.114: Comparison of predictions of Na^+ with inferred aqueous extract data at section 12 (symbols) after 1930 days of heating. Also shown are the values obtained at section 12 with squeezing (horizontal lines).

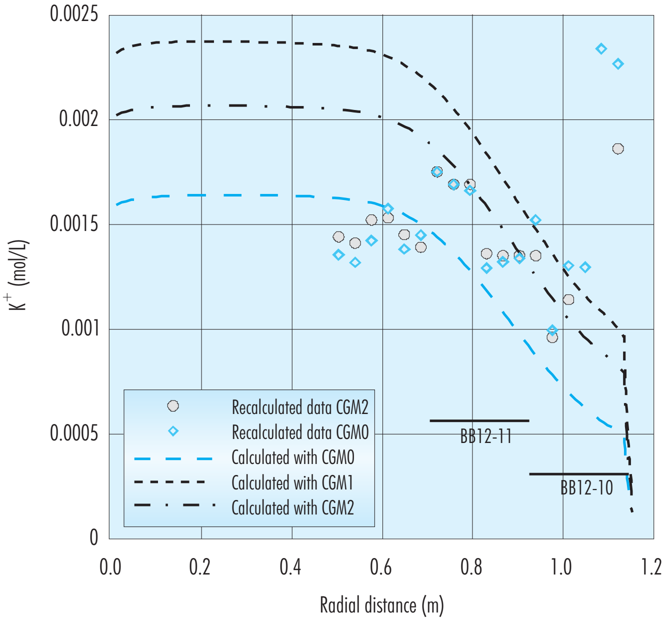

Figure 7.115: Comparison of predictions of K^+ with inferred aqueous extract data at section 12 (symbols) after 1930 days of heating. Also shown are the values obtained at section 12 with squeezing (horizontal lines).

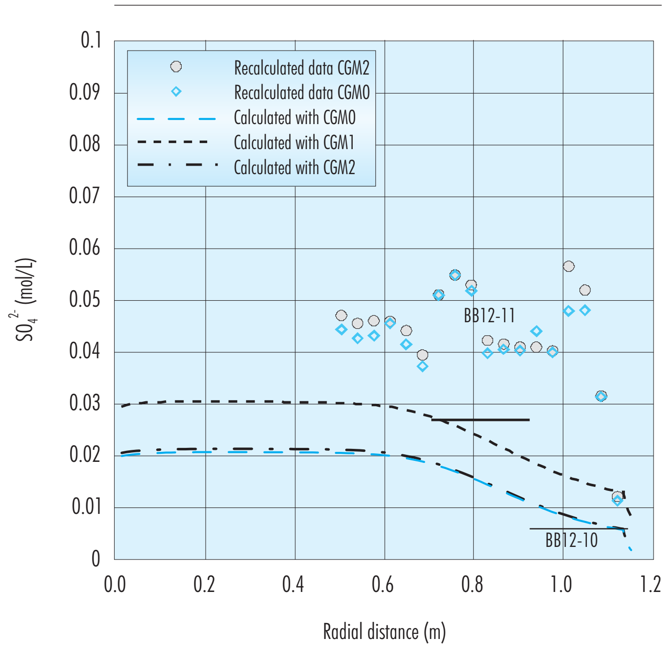

Figure 7.116: Comparison of predictions of SO_4^{2-} with inferred aqueous extract data at section 12 (symbols) after 1930 days of heating. Also shown are the values obtained at section 12 with squeezing (horizontal lines).

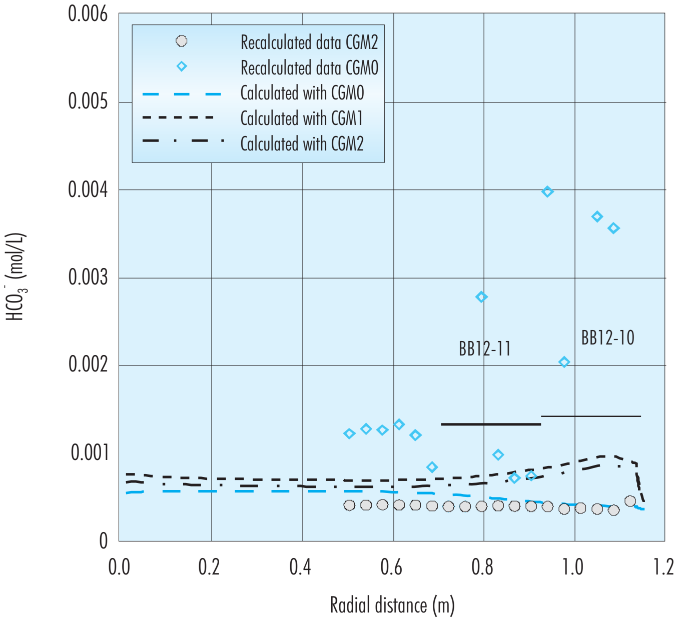

Figure 7.117: Comparison of predictions of HCO_3^- with inferred aqueous extract data at section 12 (symbols) after 1930 days of heating. Also shown are the values obtained at section 12 with squeezing (horizontal lines).

7.7. Conclusions

7.7.1. Major achievements

A significant improvement in Thermo-Hydro-Geochemical (THG) modelling of the clay barrier has been achieved during the FEBEX Project. The THG codes available at the beginning of the project were capable of handling only non-isothermal multiphase flow and transport with no geochemical processes or isothermal saturated flow and reactive transport. Novel numerical methodologies and sophisticated THG codes have been developed during the course of the project, capable of handling in a general manner the observed thermo-hydro-geochemical couplings, and account for the most relevant features of the THG conceptual model. Such codes are at the cutting-edge of coupled THG models for porous media. THG models have been constructed using such codes and relying on: 1) Data provided by a wide range of small-scale lab tests; 2) Thermal and hydrodynamic data from the "mock-up" test and; 3) Thermal, hydrodynamic and geochemical data from partial dismantling of the "in situ" test. The ability of the models to reproduce most of the observed THG patterns under such a large number of conditions enhances confidence in their predictive capabilities.

Modelling in future stages should address the needs described in the last section (7.7.8) of this chapter. There are major expectations that, by so doing, it might be possible to construct numerically verified, scientifically sound and thoroughly tested THG computer codes and numerical models.

7.7.2. Conclusions on THG parameters

A large number of laboratory tests performed for the purpose of deriving THG parameters have been interpreted numerically, including: 1) Batch tests to derive distribution coefficients, 2) Through- and in-diffusion tests to estimate accessible porosity, distribution coefficients and effective diffusion coefficients, 3) Permeation tests aimed at exploring dual porosity structures and dispersive parameters, 4) Infiltration tests devised to estimate relative hydraulic conductivity, and 5) Exchange isotherm tests. Data from the two large-scale tests have also been used to derive hydrodynamic and thermal parameters.

The interpretation and THG numerical analysis of the FEBEX tests allows the following conclusions to be drawn regarding water flow, heat transport, solute transport and geochemical parameters:

1 Relative hydraulic conductivity (K_r) of the bentonite is a key bentonite parameter that cannot be measured directly. It must be derived indirectly from the interpretation of lab tests. Several functions such as those of Irmay and van Genuchten have been tested and compared. In general they provide different results in terms of water fluxes and solute distributions. The automatic numerical interpretation of infiltration tests leads to the conclusion that Irmay's model is more consistent with actual water fluxes than the van Genuchten model.

2 Vapour tortuosity controls the amount of water evaporation near the heaters, which in turn induces sharp increases in solute concentrations. Several assumptions regarding vapour tortuosity were tested numerically. Numerical analyses of the "in situ" and "mock-up" tests lead to apparently conflicting conclusions regarding vapour tortuosity. On the one hand, large tortuosity factors lead to iodide tracer concentrations much higher than the values measured near the heater of the "in situ" test. On the other hand, the best fit to observed relative humidities in both "in situ" and "mock-up" tests are obtained with vapour tortuosities ranging from 0.5 and 1.

3 Available data on gas pressures and permeabilities are conflicting in some cases. The current understanding of the role of the gas phase in the overall THG behaviour of the clay barrier is as yet inadequate.

4 Diffusive solute transport is the most relevant transport process after the early stages of hydration. Diffusion and permeation tests performed with a wide range of tracers and radionuclides on water-saturated samples have been effectively interpreted using an automatic interpretation method. Contrary to standard analytical methods, which fail to account for some experimental conditions such as the presence of porous sinters, numerical methods allow for efficient, fast and optimal interpretation of these tests. It has been found that failing to account for some experimental conditions may lead to misleading effective diffusion coefficients. Numerical methods have proven to be useful for the detection of experimental flaws, pin-pointing identification problems and suggesting possible improvements in experimental conditions.

5 Molecular diffusion is a process that depends on a large number of properties of bentonite: thermal (temperature), mechanical (bulk density, porosity), physical (tortuosity, connectivity), hydrodynamic (water content) and chemical (surface charge phenomena, ionic strength, size, charge and type of species). While the dependence of molecular diffusion on most of these parameters has been already incorporated in current THG models, available data on some hydrodynamic and chemical parameters are limited. There is a clear lack of diffusion data for non-saturated bentonite.

6 Most reactive transport models assume that all chemical species have the same diffusion coefficient. However, it is well known that major chemical species have different diffusion coefficients. Accounting for different diffusion coefficients requires considering cross-diffusion terms in order to preserve charge balance. The relevance of cross diffusion has been evaluated numerically for the heating and hydration test CT-23 and the "mock-up" test. The numerical results indicate that model results change significantly due to cross diffusion. Cross diffusion coefficients are especially relevant for chloride and sodium. However, accounting for cross-diffusion terms does not always ensure charge balance preservation.

7 In the bentonite pore water the concentrations of most species are greater than those of the hydration water. Therefore, diffusion of solutes against the direction of water flow (backward diffusion) is likely to occur. Backward diffusion has been demonstrated numerically to be relevant for lab heating and hydration experiments and the "in situ" test.

8 Anionic tracers such as Cl, I and Re show very low diffusion coefficients due to significant anion exclusion effects. These effects, which have been observed under saturated conditions, are expected to play a more significant role under the partly-saturated conditions prevailing in the clay barrier during the hydration phase. Several conceptual models have been postulated and tested using chloride data. It has been found that anion exclusion is a relevant process for chloride transport. Models without exclusion fail to reproduce the observed data. Measured data for iodide, an artificial tracer added in the "in situ" test, also attest to anion exclusion effects.

9 Similar to other clays, bentonite exhibits a complex porosity structure. Two types of porosities may be distinguished: a kinematic or mobile porosity along which pore water flows, and an immobile porosity, where water does not flow. The results of permeation and long-term permeability tests performed on saturated samples indicate that for large and moderate water fluxes corresponding to Peclet numbers greater than 0.1 (this number measures the ratio of advective to dispersive transport), the bentonite behaves as a double-porosity medium. For a small water flux and a sufficiently large time (of the order of months), the clay behaves as a single-porosity medium. Except for permeation and permeability tests, most THG models of the clay barrier carried out within the project assume a single porosity for bentonite.

10 Types of water in bentonite. Bentonite can hold different types of water, including: 1) interlayer water, 2) double-layer water and 3) free or pore water. There are major differences regarding the role of each of these waters on reactive solute transport. While adhesive water is strongly tight to clay surfaces, pore water may flow under the presence of a hydraulic gradient. Although significant progress has been achieved in the FEBEX project on experimental characterisation and quantification of their amounts on powder clay samples, there are no conceptual models yet available for the interactions between these different types of water for compacted bentonite under the dynamic conditions of the clay barrier. So far, THG models have been based on the assumption that measured values of water content represent the amount of free water.

7.7.3. Conclusions of THG conceptual model

Lab tests performed by CIEMAT and CSIC-Zaidín to identify hydrochemical processes and geochemical alterations have been useful for deriving appropriate THG conceptual models. These experiments include: 1) Cation exchange tests, 2) Heating tests devised to study the effect of temperature on chemical processes, 3) Hydration tests to analyse chemical processes triggered by dilution, 4) Long-term permeability tests to investigate transport parameters and chemical processes and 5) Heating and hydration tests on small and medium cells aimed at exploring the geochemical behaviour of the bentonite and possible alterations under the simultaneous effects of a thermal gradient and hydration.

Laboratory exchange tests indicate that cation exchange is a fast process which shows no temperature dependence. The exchange complex is enriched in Ca^{+2}, while it is depleted in K^{+}, Na^{+} and Mg^{+2}. Depletion in K^{+} means that no illitisation takes place. One of the contributions of the project has been the derivation of global selectivity coefficients for Ca^{+2}, K^{+}, Na^{+} and Mg^{+2} exchange, which were obtained from exchange isotherm tests.

Quantitative characterisation of the chemical composition of bentonite pore water is a fundamental requirement for THG modelling. Two methods have been tested for two different solid-to-liquid ratios: 1) Sample squeezing by strong compaction and 2) Saturation extraction methods based on mixing a clay sample with a larger mass of water (usually four times the mass of the sample). The former is thought to provide more representative results because the solid-to-liquid ratio is similar to that of real conditions. However, squeezing tests last too long, can be used only for samples near water saturation and sample only a fraction of the total pore water. Extraction tests are much faster, but their results are more prone to interpretation errors.

Different conceptual geochemical models (CGM) may be derived depending on the type of data used to construct them: squeezing and/or aqueous extract data. Three CGM's have been developed to account in a realistic manner for the experimental conditions of the laboratory methods. The first model (CGM-0), which relies only on squeezing data, was used during the early stages of the project. An inverse numerical method has been developed for the interpretation of aqueous extract tests, which accounts for the geochemical processes experienced by clay samples during the extraction tests. A second conceptual geochemical model, CGM-1, has been derived from aqueous extract tests of various durations and solid-to-liquid ratios. Model CGM-1 adequately reproduces the measured data of tests performed at different durations (up to 30 days). Most chemical species reach steady concentrations before 10 days. Therefore, calcite and dolomite kinetics are rather fast. Although model CGM-1 fits measured extraction data at different solid-to-liquid ratios, it fails to reproduce bicarbonate and pH data and cannot fit squeezing data.

Based on model CGM-1, a modified model CGM-2 has been derived in order to fit simultaneously squeezing and aqueous extract data. Model CGM-2 does not consider initial gypsum in the system but its precipitation is allowed. This model CGM-2 fits simultaneously both squeezing and aqueous extract measured concentrations for most chemical species, although it presents some clear deviations for sulphate. Measured data tend to reject the hypothesis of a constant pressure of $CO_{2(g)}$ during the tests.

The major geochemical processes controlling the chemistry of the clay barrier during the hydration process are acid-base reactions, aqueous complexation, cation exchange, proton surface complexation, dissolution/ex-solution of CO_2 and dissolution/precipitation of calcite, dolomite, chalcedony and gypsum/anhydrite. All these processes have been assumed to take place under equilibrium conditions. Exchange tests carried out by CSIC-Zaidín indicate clearly that cation exchange is not affected by temperature. This is not the case for mineral dissolution-precipitation, which shows a significant dependence on temperature.

The interpretation of a long-term permeability test has been performed numerically with single and dual porosity models and using three conceptual geochemical models. The model results lead to the following conclusions:

1 Measured data fall within the bands of computed breakthrough curves with conceptual models CGM-0, 1 and 2 and using a single porosity model.

2 Major discrepancies between model results and measured data are found for bicarbonate. They might be related to changes in the pressure of $CO_{2(g)}$ which have not been considered in the THG model.

3 Chloride and sodium data are coherent with a double porosity model. The relevance of double porosity for other species remains to be ascertained.

The analysis and numerical interpretation of heating and hydration tests reveals that the main hydrochemical processes taking place during heating and hydration are:

1 During the early stages the thermal pulse causes the precipitation of calcite, dolomite and gypsum because their solubilities decrease with temperature. The behaviour of

chalcedony is the opposite because its solubility increases with temperature.

2 At intermediate stages, water entering the system, which has much lower solute concentrations, causes dilution, which in turn induces the dissolution of all minerals.

3 In the early and intermediate stages, water evaporation near the heater causes a strong increase in solute concentrations, which in turn causes mineral precipitation. Large concentrations near the heaters cause the solutes to diffuse away from the heater.

4 As hydration progresses, the effect of dilution and mineral dissolution extends to most of the cell. Once the hydration front reaches the vicinity of the heater, precipitated minerals start to re-dissolve.

5 During the final stages, when the cell reaches water saturation, concentration gradients dissipate due to the effect of molecular diffusion.

7.7.4. Achievements on THG codes

A significant development in the capabilities of UDC codes for water flow, heat transfer and reactive solute transport has been achieved during the FEBEX project. Starting from the original code CORE-LE-2D v0.0a [194], updated versions of the code were developed such as CORE V1 [200] and FADES-CORE-LE V0.0a [196]. The latter is capable of solving for coupled multiphase non-isothermal flow and reactive transport. The most recent and powerful version, INVERSE-FADES-CORE V0 [201], can solve both direct and inverse coupled THG problems. These codes have been used to: 1) Interpret different lab tests for estimating parameters and identifying relevant geochemical processes, 2) Predict transport patterns of artificial tracers added in the “in situ” and “mock-up” tests and 3) Predict the THG performance of the clay barrier.

THG predictions of the “in situ” test have been performed with INVERSE-FADES-CORE V0 [201], a code which preserves all the capabilities of FADES-CORE V1 [200] and is capable of performing automatic parameter estimation. In addition to extensive code debugging, thorough verification against TOUGH-REACT and detailed checking of mass and charge balance, the following improvements have been implemented in INVERSE-FADES-CORE^{2D}: 1) Different diffusion coefficients for each dissolved chemical species, 2) Cross-diffusion processes, 3) Additional constitutive laws for bentonite thermal conductivity as a function of water content and bentonite permeability as a function of the ionic strength of the porewater, 4) Pitzer equations to calculate activity coefficients for high ionic strength porewaters, 5) Chemical osmosis, 6) Thermal osmosis, 7) Double porosity models and 8) Solution of the inverse problem for automatic estimation of THG parameters.

7.7.5. Conclusions derived from the THG model of the “mock-up” test

2-D and 3-D axisymmetric THG models of the “mock-up” test have been constructed which have been used to calibrate key thermal and hydrodynamic bentonite parameters. While the model reproduces the observed trends of cumulative water inflow and relative humidities for the first 1000 days, model predictions after this date systematically overestimate measured inflows and humidities. Possible explanations for these discrepancies have been evaluated including: 1) The implementation of a constitutive law for intrinsic permeability as a function of ionic strength; 2) Chemical osmosis and 3) Thermal osmosis. It has been found that chemical osmosis is not relevant for the conditions of the “mock-up” test. Thermal osmosis is a process that might explain the observed behaviour. However, there are no measured data on thermal osmosis coefficients, which are extremely difficult to measure.

A THG model with a variable permeability as a function of ionic strength improves the fit of cumulative water inflow and relative humidity. However, discrepancies still remain. It is believed that the combination of dual-porosity and swelling of clay (not accounted for in current THG models) has the potential to overcome such discrepancies.

The overheating episode, which occurred in November 2000, has been modelled. The model results indicate that the overheating affected the hydrodynamic conditions only slightly, due to its short duration. The model captures the trends of measured temperatures and relative humidities. In the middle part of the barrier, however, it fails to reproduce the slow recovery phase after overheating.

Long-term predictions of tracer migration and hydrodynamic and hydrochemical evolution of the barrier have been updated using the revised THG model. With the updated model, steady concentrations are attained after 20 years. Except for bicarbonate, chemical species show patterns similar to those of chloride, even though such species are subject to chemical reactions. Changes in the bentonite exchange complex are largest near the heater.

7.7.6. Conclusions derived from the THG model of the "in situ" test

The THG model of the "in situ" test has been revised and updated by incorporating the conclusions drawn from the model of the "mock-up" test. The predictions of the "in situ" test have been compared to measured tracer and geochemical data collected after dismantling of Heater #1.

Available tracer data for deuterium and iodide have been interpreted numerically. Deuterium data do not allow clear conclusions to be drawn regarding deuterium migration due to: 1) Low data precision, 2) The insufficient mass of added deuterium, 3) Uncertainties regarding the breakage of the glass ampoules (only 3 out of 5 were found broken; the most likely thing is that the glass ampoules broke during the test, because, if they had broken during dismantling, clay samples near the glass should have shown deuterium ratios higher than those measured after dismantling) and 4) Isotopic fractionation between interlayer and external water.

Iodide is a tracer which was added at the bentonite-granite interface. Iodide data clearly show a peak located 40 cm inwards from this interface, thus confirming the advective migration of iodide due to water inflow towards the heater. These data have been used to solve the inverse problem and derive optimum estimates of accessible porosity, effective diffusion and vapour tortuosity. The optimum estimate of tortuosity is 0.1, a value that is 5 times smaller than that derived from the THG model of the "mock-up" test. A tortuosity of 0.5 would lead to computed iodide concentrations near the heater much greater than the measured values.

THG predictions of the "in situ" test have been compared to measured geochemical data collected after dismantling of Heater #1 in sections 29 (hot area) and 12 (cold area). The available data include a few squeezing data (which take a long time) and aqueous extract data, which contain uncertainties associated with the fact that aqueous extract tests must be interpreted by means of geochemical models to account for the geochemical processes undergone by bentonite samples during aqueous extraction. Noticeable differences have been found between squeezing and aqueous extract chemical data obtained at the same location, especially in section 12. Additional geochemical data from sections 19, 28 and 30 became available after completion of the THG model. A preliminary analysis of such data reveals significant differences between sections.

Measured aqueous extract data from samples located near the bentonite-granite interface show exceedingly large cation concentrations that, according to CIEMAT, might be an artefact caused by colloidal particles.

Three conceptual models have been used to interpret aqueous extract data. All three models reproduce measured data, except for CGM-1, which is unable to accurately fit bicarbonate data. All models lead to similar inferred results for all chemical species except for bicarbonate and sulphate. Models CGM-0 and CGM-2, which were derived from squeezing data, provide similar results except for bicarbonate.

The re-interpreted aqueous extract concentrations of most species near the heater are larger than in the granite-bentonite interface, where dilution is much more pronounced. Dissolved cations (Ca^{2+}, Mg^{2+} Na^{+}, K^{+}) show trends similar to those of chloride. Although these species are subject to mineral dissolution/precipitation and cation exchange reactions, these reactions are not sufficiently strong compared to the dilution and evaporation processes to produce concentration patterns different from those of chloride.

THG model predictions of the "in situ" test performed with three conceptual geochemical models have been compared to the measured data. The comparison of predicted and inferred values using data from a section at the heater location (29) and a section far from the heater (section 12) indicates that:

1 Thermo-hydrodynamic predictions of the "in situ" test capture the general trends of measured transient temperatures and relative humidities. The model accurately represents the trend of measured water contents after dismantling, but underestimates measured values near the bentonite-granite interface and overestimates measured water contents near the heater. These discrepancies are caused by clay swelling/shrinking phenomena which are not taken into account in current THG models

2 Geochemical predictions capture the general trend of aqueous extract and squeezing data of most chemical species in hot and cold areas, except for sulphate and bicarbonate data. THG predictions reproduce the chemical dilution pattern caused by bentonite hydration.

3 Predicted concentrations systematically overestimate measured values near the heater and show gradients which are sharper than those of measured data in section 29. This deviation of chemical predictions from measured data might occur only in this section because the available data on sections 19, 28 and 30 do not show such a trend.

4 The fact that predicted concentrations near the heater systematically overestimate measured values and show gradients much sharper than those of measured values may point to water evaporation being overestimated by the THG model. This is consistent with the results of the interpretation of iodide data, which indicate that current THG models may overestimate vapour tortuosity.

5 Predicted chloride concentrations near the granite-bentonite interface at section 29 overestimate measured values. This discrepancy might be associated with the fact that the THG model does not account for changes in porosity caused by swelling/shrinking phenomena. However, computed values in section 19 are close to the aqueous extract and squeezing data.

6 The computed results for magnesium, sodium and potassium obtained with the three models reproduce the general trends of aqueous extract data in sections 29 and 12.

7 No clear conclusion may be drawn on which CGM performs the best. CGM-1 shows limitations for the interpretation of bicarbonate data. While models CGM-0 and CGM-1 fit calcium data in hot section 29 better than model CGM-2, models CGM-1 and CGM-2 perform better in cold section 12. Such a discrepancy might be related to the role of gypsum/anhydrite.

8 Predicted sulphate concentrations are consistent with squeezing data, but systematically underestimate aqueous extract data.

The fact that THG models derived from small-scale lab tests reproduce the overall trends of measured concentrations for most chemical species in the "in situ" test provides an indication of the lack of scale effects

7.7.7 Uncertainties

Partial dismantling of the "in situ" test provided a unique opportunity to test the predictive capabilities of the THG models. The models of the "in situ" test accurately represent measured water content and temperature data and capture the trends of most chemical species. However, some discrepancies between predictions have been observed which may be attributed to a combination of the following factors: 1) Overestimation of water evaporation at the heater-bentonite interface, 2) Clay swelling/shrinking phenomena that are not taken into account in current THG models and 3) the need for a dual-porosity model.

Parameters and processes which require additional characterisation include:

1 Relative hydraulic conductivity (K_r). Additional infiltration tests with the injection of tracers should be performed to derive appropriate relative conductivity functions. These tests should be repeated at various temperatures to derive the variation of K_r with temperature.

2 Gas phases. Evaluating gas flow parameters such as gas permeability and vapour tortuosity and studying the role of gaseous phases such as $CO_{2(g)}$ in chemical processes. The detected contradictions on vapour tortuosity values derived from calibration of the TH model of the "mock up" test and iodide data from the "in situ" test should be further analysed.

3 Molecular diffusion coefficients under partly saturated conditions. Diffusion tests should be performed under non-saturated conditions to make up for the current lack of solute diffusion data for non-saturated bentonite.

4 The relevance of cross-diffusion processes requires further analysis.

5 Additional diffusion tests should be performed to characterise the dependence of diffusion coefficients on ionic strength, ion size and charge.

6 Additional diffusion and permeation tests should be designed and performed in order to avoid parameter identification problems. Performing radial diffusion tests is highly recommended for future stages of the project.

7 Anion exclusion. Additional diffusion tests are needed to quantify anion exclusion under non-saturated conditions.

8 Proton surface complexation. Tests performed during the second phase of the FEBEX project have provided firm evidence of the relevance of proton surface complexation for buffering pH. Future THG models should account for this process.

9 Uncertainties still remain regarding the couplings of THG and mechanical processes.

10 Types of water in bentonite. Current THG models assume that measured values of water content represent the amount of free water. However, multiple-porosity models, in which a distinction is made between intra-aggregate and inter-aggregate water, will be needed to explain model deviations in water inflow and relative humidities of the “mock up” test and in geochemical data of the “in situ” test.

11 A detailed analysis of geochemical data collected after dismantling of Heater #1 is required to ascertain the differences observed in different sections.

12 There are uncertainties related to CO_2 conditions (open or closed system), the role of K-feldspars and the effect of heater corrosion, which have not been yet considered in THG models. There is experimental evidence indicating a decrease of exchanged cations near the heaters, which might be attributed to the exchange of certain corrosion products, such as Cu and Zn. Additional experimental data are needed in order to understand and model the interaction of corrosion products and bentonite.

7.7.8. Future needs

Future THG models should incorporate mechanical and geochemical couplings (thus leading to fully coupled THMG models) and account for porosity changes caused by swelling phenomena. They should also consider more sophisticated conceptual geochemical models in which a distinction is made between intra-aggregate and inter-aggregate water for the purpose of hydro-geochemical modelling. Dual porosity models using the dual continuum model (DCM) approach should be developed. Such models should consider two transport equations with a coupling interaction term to describe solute transfer across the interface of macro- and micro-pores.

Most of the THG analysis effort has been devoted to constructing thermo-hydro-geochemical models for the main geochemical processes controlling the geochemical evolution of the clay barrier in terms of major ion composition, pH and alkalinity. There are some processes which are relevant for performance assessment such as redox and the interactions of corrosion products which have not been addressed in the FEBEX project. Experimental data as well as numerical analyses on the role of these processes should be undertaken in the future.

8. EDZ (Excavation Damaged Zone) studies in the drift of the “in situ” test

8. EDZ (Excavation Damaged Zone) studies in the drift of the “in situ” test

8.1. Introduction

The test drift is 70.40 m long and has a circular cross section of 2.28 m in diameter. It was excavated in 1995 using a tunnel-boring machine (TBM). The test area (heated zone) was isolated from the rest of the drift (service area) by a 2.70 m-thick concrete plug placed at a distance of 17.40 m from the drift dead-end. The drift is intersected by two lamprophyre dikes in the test area, intruded in the granite rock mass (for a detailed description, see Chapter 4).

After the partial dismantling of the "in situ" test, a study was performed on the mechanisms of creation of the potential damaged zone around the test drift and its evolution after a period of more than five years of heating, within the framework of the second phase of the project. The research program included laboratory and in-situ investigations as well as the numerical modelling of the observed phenomena.

8.2. Laboratory investigations

Several types of tests were performed on the core samples taken from the test area (heated zone), and from the service area: microfracturing and porosity tests, gas permeability tests and acoustic investigations.

8.2.1. Microfracturing and porosity tests

The objective of the work performed was to analyse the porosity and microfracturing (Figures 8.1, 8.2 and 8.3), both quantitatively and qualitatively. The ^{14}C-PMMA (^{14}C-polymethyl-methacrylate) technique was applied for study of the spatial distribution of porosity. In addition, complementary microscopy and scanning electron microscopy (SEM) studies were performed for qualitative investigation of the pore apertures and minerals in porous regions.

No clear increased porosity zone was found adjacent to the drift wall with the ^{14}C-PMMA method in the granite samples. The total porosities of the samples varied between 0.6-1.2%. Grain boundary pores and trans-granular porosity were detected. The samples from the unplugged region did not differ from the samples from the plugged region.

A clear increase in porosity to depths of 10-15 mm from the drift wall was detected in lamprophyre

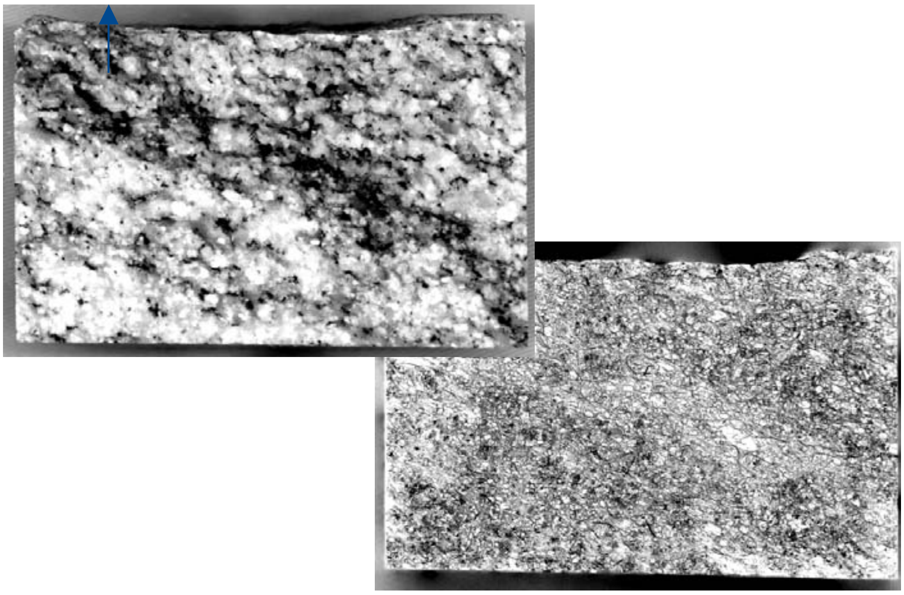

Figure 8.1: Photo image of granite (left) and corresponding autoradiograph (right) from the unplugged region in the FEBEX drift. The excavated surface is on top. Sample width is 10.6 cm.

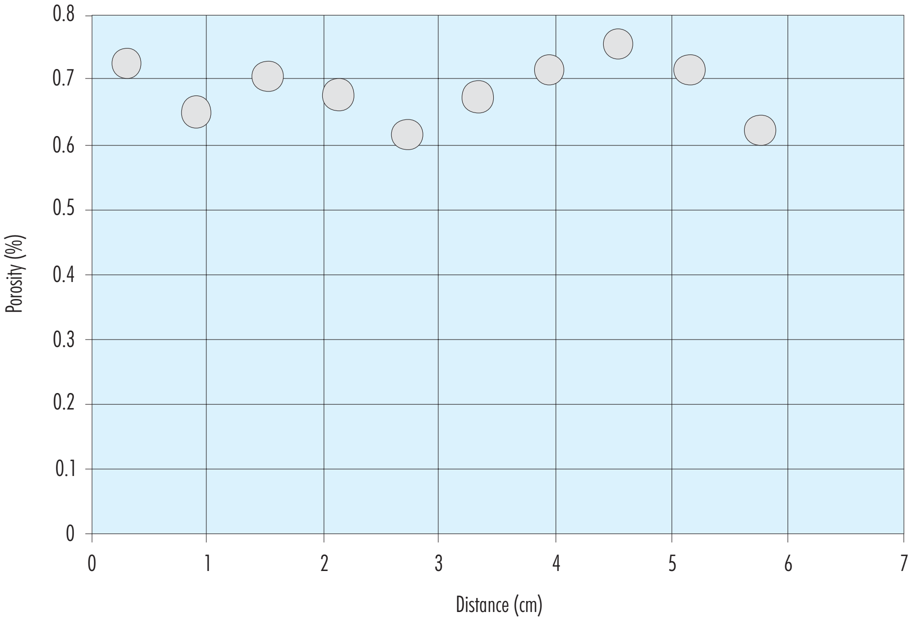

Figure 8.2: Porosity is calculated with respect to the distance from the drift wall and presented as a porosity histogram.

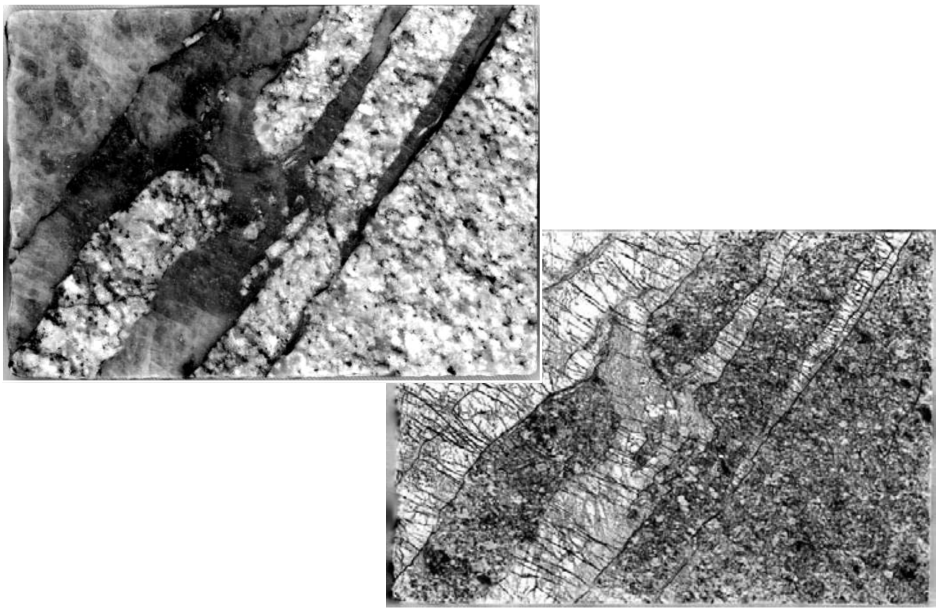

Figure 8.3: Photo image of the granite (left) and corresponding auto-radiograph (right) from the unplugged region in the FEBEX drift. The excavated surface is on the left. Sample width is 14 cm

samples. The EDZ consisted of micro fractures perpendicular to the drift wall. Strong fracturing was found in some lamprophyre samples at depths of several cm from the drift wall. Some samples contained quartz inclusions, where plenty of micro fractures transacted the mineral grains parallel to the drift wall and numerous intra-granular fissures transacted the quartz grains. The quartz grains were found to be porous, having a porosity value of 0.5%. The granite matrix, which was surrounded by the quartz inclusion adjacent to the drift wall, had clearly higher total porosity (i.e. 1.3-1.5%) than the granite matrix at depths of 10 cm from the drift wall, which was 0.9-1.1%.

According to the SEM/EDX analyses, the EDZ in the granite matrix extended to depths of 1 - 3 mm from the wall surface. A few quartz grains were crushed and some micro fractures were found. Some transgranular fissures were found parallel to the wall surface, with apertures of around 5-30 μm. The micro-fracture apertures varied between 20-50 μm in the EDZ of lamprophyre samples, trending to depths of 5-25 mm from the drift wall.

8.2.2. Gas permeability test

The permeability measurement (Figures 8.4 and 8.5) is a good indicator for assessment of the existence and evolution of the EDZ. Gas permeability tests were carried out on two core samples measuring approximately one metre in length, each taken from the granite wall perpendicular to the drift. The first sample was cored in the service area distant from the heated zone and the second at the level of Heater #1. Core samples were first machined in order to obtain hollow cylinders with an internal diameter of 24mm. The tests were performed at constant gas pressure by setting a steady-state radial flow through a section of one centimetre in width isolated by means of four mini-packers. By moving the mini-packers along the sample, the profile of gas permeability may be established according to the length of the core.

The magnitude of the permeability measured ranges between $6.5\cdot10^{-18}$ and $8.4\cdot10^{-19}$ m^2, pointing to the absence of marked damage. The highest value is obtained on the sample taken in the service area and corresponds to a natural sealed joint.

Although the flow rate profile corresponding to the sample taken from the heated area shows an increase in permeability over the first 20 centimetres, this evolution cannot be linked to the existence of a damaged zone. Indeed, whereas natural rock heterogeneities provide greater variation, the maximum discrepancy in terms of permeability continues to be less than one order of magnitude.

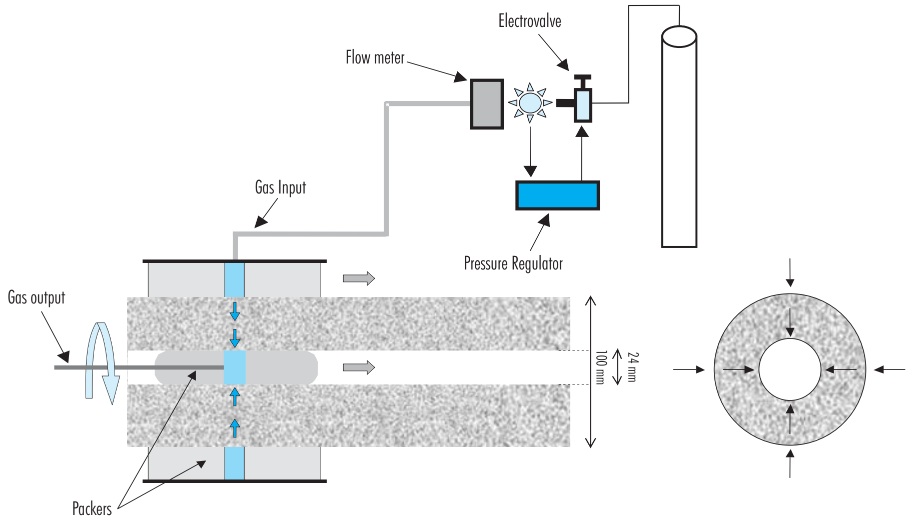

Figure 8.4: Gas permeability measurement set-up.

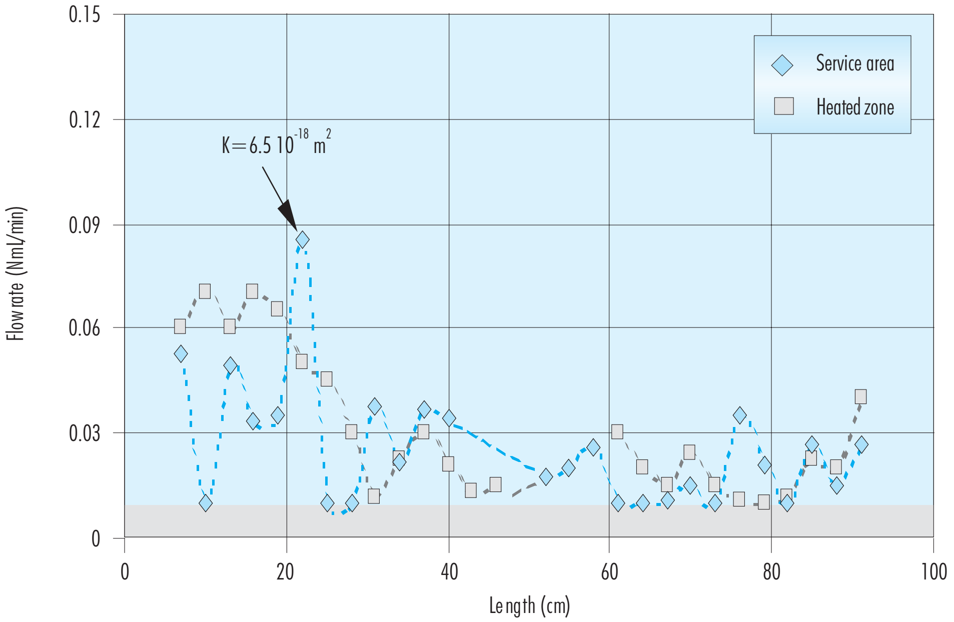

Figure 8.5: Results of gas permeability tests.

8.2.3. Acoustic investigations

Measurements of the travel times of ultrasonic waves through a cylindrical granite block have been performed. The aim of this test has been to quantify the variations in propagation velocities of acoustic waves through the rock. The cylindrical granite block was taken from the service area, and measures 38.8 cm in diameter and 40 cm in length (from the drift wall towards the rock mass). For this study, the block was analysed along 2D transversal sections in six radial directions (section 1 (R1-R7) coincides with the FEBEX drift direction). More than 900 measurements were taken by combining different positions of the transmitter-receiver pairs.

Different inverse tomographic strategies have been used to analyse the measured data. By studying signal propagation velocities through horizontal trajectories (Figure 8.6), a preferential direction R2-R8 with higher velocities may be observed, although the velocity differences are not significant. The 2D tomographic inversion (Figure 8.7) shows some heterogeneity in propagation velocity through the granite. However, no special decrease of velocity towards the drift wall (top part of the sections) is appreciated. Therefore, no evidence of the existence of an EDZ has been found in the analysed sample. The anomalous highest velocities are associated with measurement artefacts, since there were broken parts in the granite sample where measurements were not taken.

The results have been contrasted with those of the FEBEX site geologic characterisation report [217]. The sampled block is not intersected by any of the fracture traces of the cartography of the FEBEX drift (Figure 8.8 left), and a visual analysis of this granite block does not show any fracture or fissure. Moreover, pole distributions of the fracture families (Figure 8.8 bottom) are not correlated with the pole of the preferential direction R2-R8. Therefore, this preferential direction might be due to any heterogeneity in the fabric of the granite.

8.3. In situ investigations

To characterise the hydraulic connectivity of the potential fracture networks in the drift near field and to determine the permeability distribution along artificial/natural fractures intersecting the tunnel, the BGR

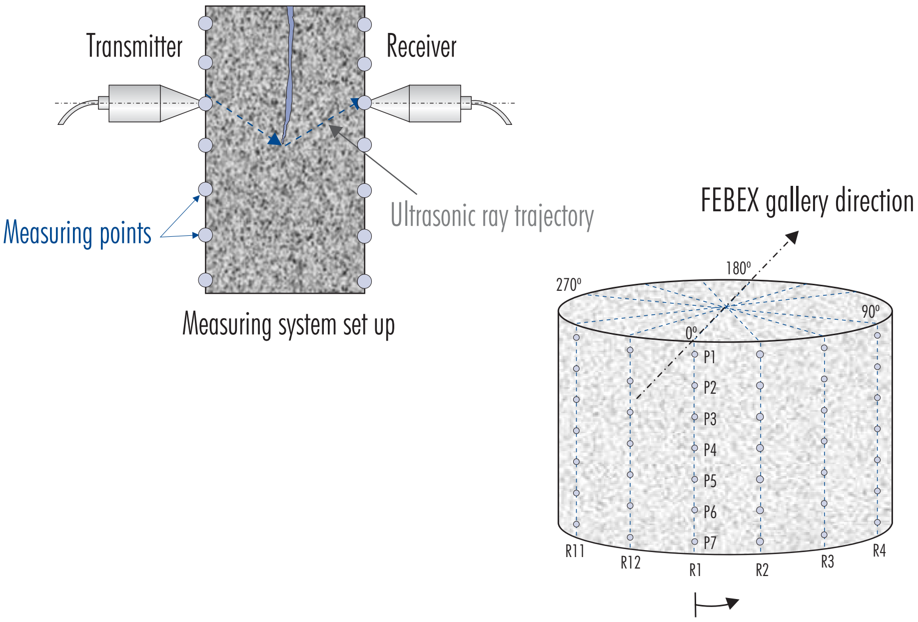

Figure 8.6: Measuring system set up with a static transmitter and a portable receiver (left), and measuring points grid in the granite sample (right).

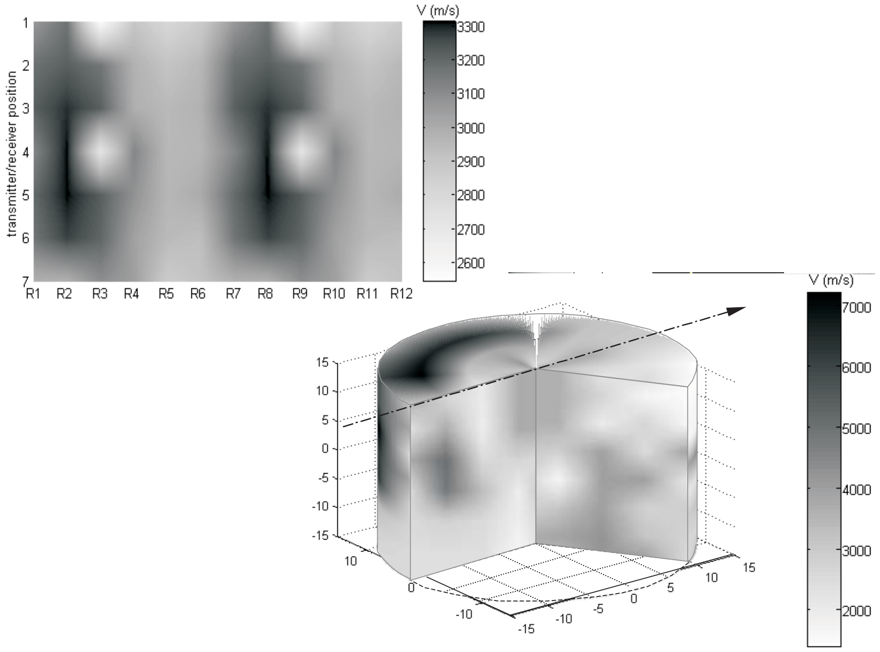

Figure 8.7: 2D velocities graph, where a preferential direction (R2-R8) with higher velocities may be located (right); and 3D interpolation of the tomographic inverse problem 2D results in sections 1-6

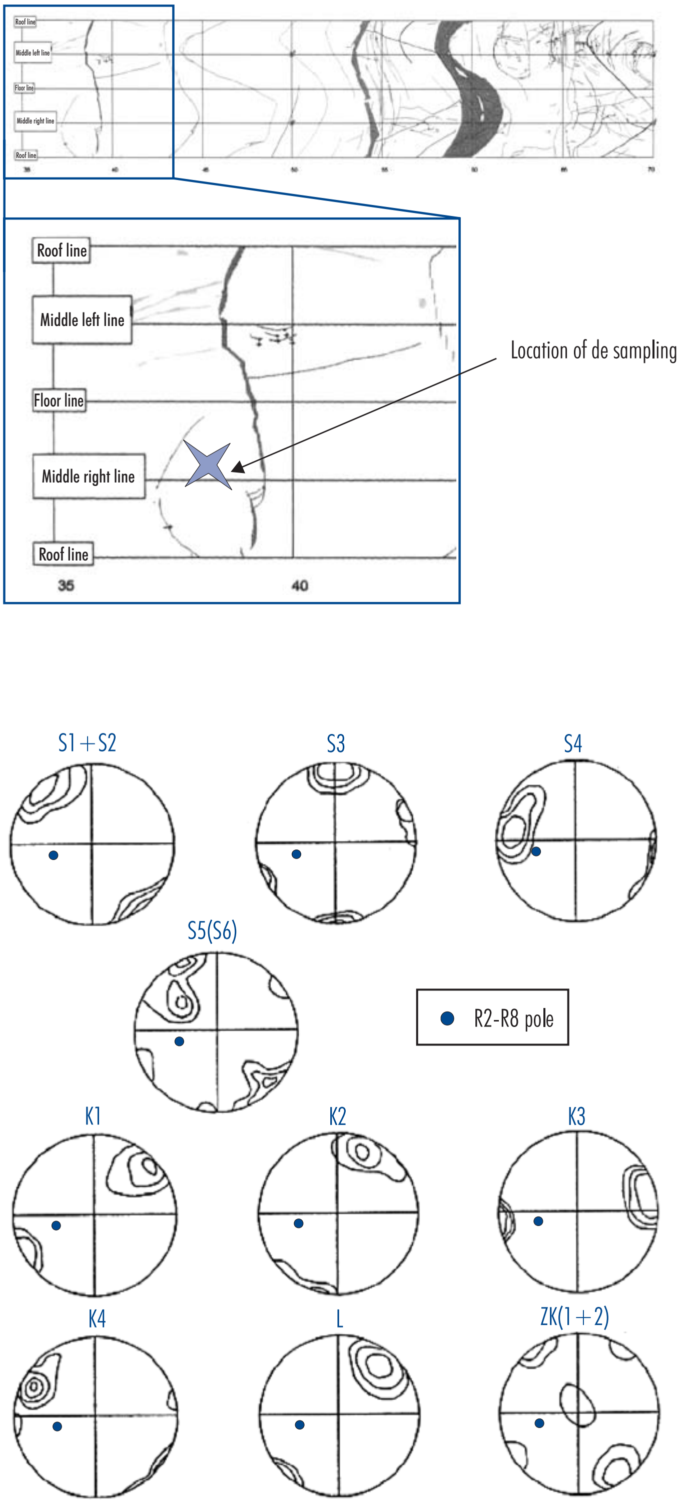

Figure 8.8: Location of the granite sample in the FEBEX drift (top) and pole distributions of the fracture families and preferential direction R2-R8 (bottom) [217]

surface packer system was developed and used in the FEBEX drift.

On the basis of the geological circumstances and from the viewpoint of the possible mechanical influences of the excavation processes, seventeen locations, including granite matrix and lamprophyre dykes in the heated area (11) and in the service zone (6) have been selected and tested. In the matrix area with lower permeability a pulse test was carried out, using pressurised air with stepwise pressure increases, to determine gas entry pressure. In the fractured area, a gas constant flow rate injection test was conducted.

Only two locations with higher permeability were detected: one is a natural fracture in the lamprophyre dyke and the other is the interface between the lamprophyre and granite. To interpret the experimental results, the numerical code RockFlow for one and two phase flow was applied. The permeability measurements obtained on the granite wall are comparable to those corresponding to the undisturbed rock mass ($<5.0\cdot10^{-19}$ m^2).

The thermal (temperature on the tunnel wall of about 40 °C) and mechanical (swelling pressure of about 4 MPa) loadings during the heating period and hydration have no significant influence on hydraulic parameters (permeability and porosity) but may affect the residual water saturation of the granite in the EDZ and long-term re-saturation. However the distribution of the hydraulic parameters around the tunnel cannot be correlated with the re-distribution of the stress state. The investigations show that attention should further be focused mainly on the natural fracture system with relative higher permeability, which intersects the drift.

8.4. Numerical investigations

2D and 3D thermo-hydro-mechanical and thermo-mechanical analyses have been performed in order to assess the effects of the excavation and the heating phases on the possible development of an EDZ around the drift.

In the 2D analysis, the main hypotheses adopted were as follows:

1. Homogeneous porous medium
2. Isotropic mechanical state conditions
3. Axisymmetric conditions

It may be observed (Figure 8.9) that the maximum developed stresses are around 22 MPa after the excavation phase and 62 MPa at the end of the hypothetical worst case heating phase, leading to the conclusion that no mechanical reason exists for the development of an EDZ in the FEBEX drift.

In order to take into account the strong anisotropy of the initial state of stress, a 3D modelling was performed. According to the in-situ measurements, the compressive tectonic regime leads to a horizontal stress 4 or 5 times larger than the vertical lithostatic pressure (9-12 MPa). In addition, there is a difference of more than 10 MPa between the minimum and the maximum horizontal stress, forming an angle of 60° with the drift axis. The rock mass, concrete plug, heaters and bentonite buffer were modelled. The excavation phase, followed by the thermo-mechanical loading of the test drift were simulated.

The maximum stress developed around the drift wall compared to the yielding criterion (Drucker Prager) shows (Figure 8.10) that the state of stresses induced by the excavation and the heating phases remains far below the critical curve.

8.5. Conclusions

All the experimental results show that the granite matrix has not been damaged either by the excavation or by the THM loading experienced by the rock mass. Except for a zone of about three millimeters in depth, underlined by the SEM/EDX analyses, the granite seems to preserve its mechanical and hydraulic properties. The evidence of a potential EDZ concerns only the lamprophyre area and the interface between the lamprophyre and granite.

The absence of an EDZ in the Grimsel granite matrix is also confirmed by the numeric simulation, which shows that the maximum stress developed is much lower than the minimum resistance of the rock. Even some uncertainty may exist regarding the behaviour of the natural joints at the local scale, the creation of a continuous pathway for radionuclide migration along the drift seems to be highly improbable.

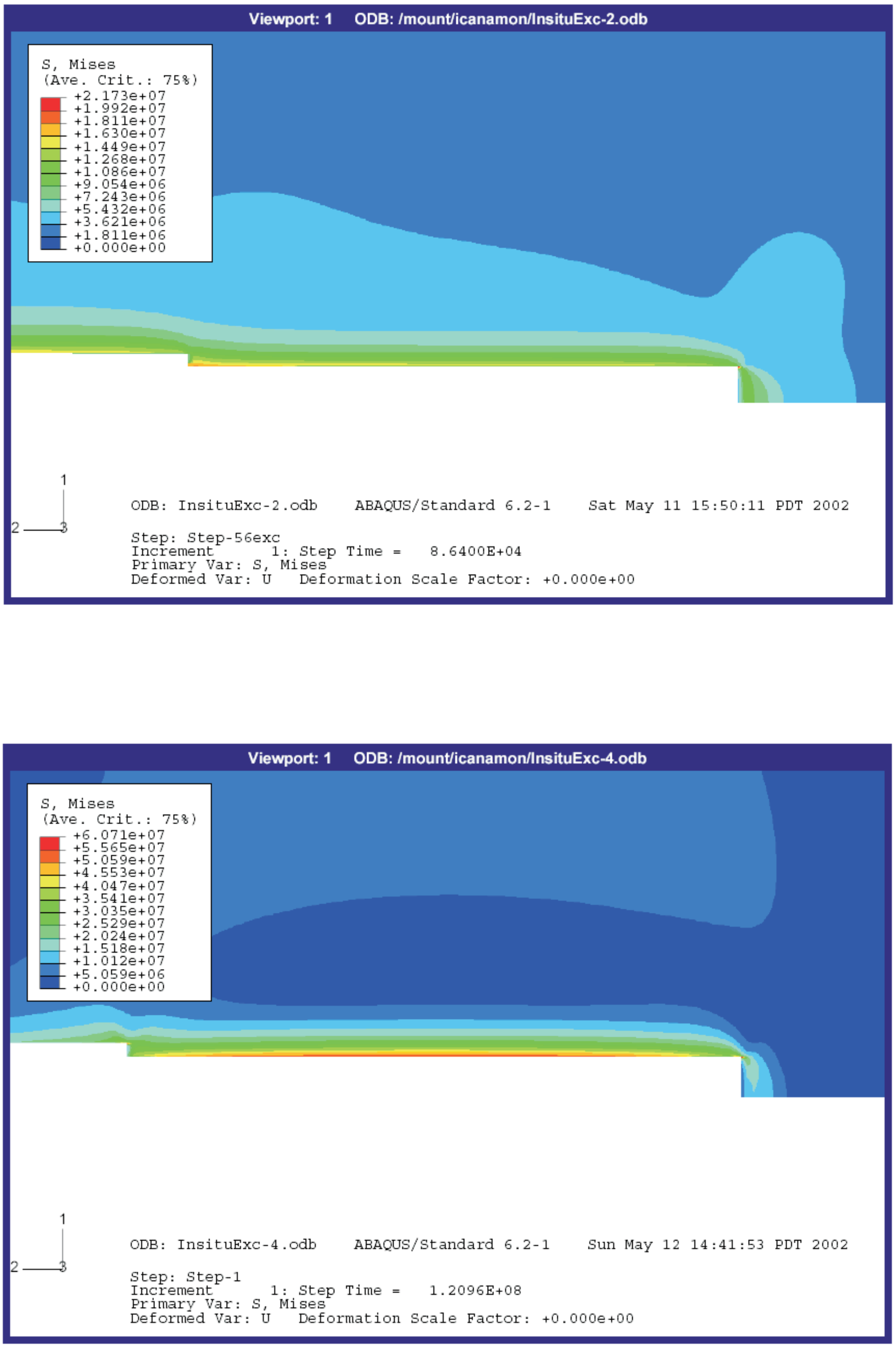

```
ODB: InsituExc-2.odb    ABAQUS/Standard 6.2-1    Sat May 11 15:50:11 PDT 2002

Step: Step-56exc
Increment       1: Step Time =    8.6400E+04
Primary Var: S, Mises
Deformed Var: U   Deformation Scale Factor: +0.000e+00
```

```
ODB: InsituExc-4.odb    ABAQUS/Standard 6.2-1    Sun May 12 14:41:53 PDT 2002

Step: Step-1
Increment       1: Step Time =    1.2096E+08
Primary Var: S, Mises
Deformed Var: U   Deformation Scale Factor: +0.000e+00
```

Figure 8.9: Results of 2D thermo-mechanical calculation: Von Mises stresses after excavation (top) and after more than five years heating period (bottom).

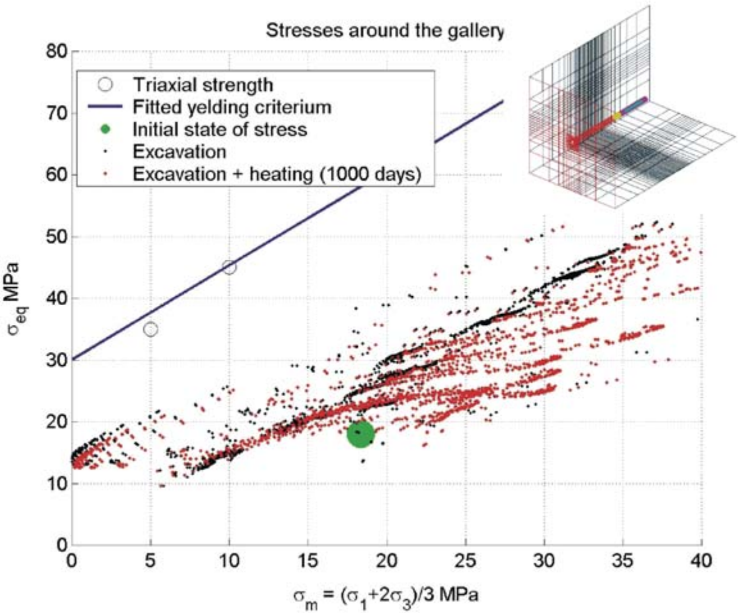

Figure 8.10: Stresses around the test drift compared to Drucker Prager yielding criterion.

9. Quality assurance/quality control programme

9. Quality assurance/quality control programme

9.1. General

Although the FEBEX project (throughout its several phases) was basically an R&D project, ENRESA decided to apply a Quality Assurance (QA) Programme to it for the reasons given below.

QA programmes are usually implemented in large manufacturing processes or in large engineering projects. The requirements of Quality Assurance must be in proportion to the degree of complexity of the project. In general, the intent in applying a quality programme is to ensure that the work is accomplished in a planned and systematic manner in order to decrease the probability of errors and malfunctions resulting from the complex interrelations existing between the various organisations participating in the project.

The QA programme applied to the project is described in summary below. For details of the programme applied in the first phase of the project, see reference [218].

9.2. Quality assurance in ENRESA

ENRESA is a Spanish public company whose mission is the management of radioactive wastes; therefore, it has established a quality assurance system based on nuclear regulations. The application of this system is obligatory only to the activities related to nuclear safety and radiological protection of the installations operated by the company, as well as to the transportation of radioactive wastes. Furthermore, ENRESA is registered as an AENOR certified firm, since its quality system is also based on the UNE-EN-ISO-9001 standard, which has a broader application. ENRESA is also in possession of an environmental system management certification.

From the above, it may be concluded that application of the quality system at ENRESA is mandatory or voluntary depending on the nature of the project. Generally speaking the ENRESA R&D projects, in general, are not subject to a quality assurance system. Nevertheless, application of the quality system to the FEBEX project was decided, for the following reasons:

- ❑ During the operational stages of this experiment it would be impossible to maintain, repair or replace some of the fundamental components of the two large-scale tests. Under these conditions, it was considered advisable to apply a QA programme in order to increase the quality control in the fabrication and in the installation of the two phases of components of the tests, and thus reduce the probability of failures during the operational stages.
- ❑ The complex interrelations existing among the numerous participating organisations (this number was actually increased in the second phase of the project), in the phases of design, fabrication, installation, testing and interpretation of the results. As a tool for project management, it was considered advisable to implement a QA programme to regulate the activities and relations between the working groups. In the second phase of the project Work Package Leaders were appointed, thus achieving the decentralisation of responsibilities in several project management activities.
- ❑ High financial cost.

9.3. Quality assurance in the FEBEX project

The basic aim of the project QA programme was to increase the probability of success being achieved in reaching its demonstration and of modelling objectives. However, since the decision to apply the QA system was taken after the project had begun, some difficulties were experienced in its implementation, as indicated below.

9.3.1. Anticipated difficulties

The following difficulties were taken into account in relation to the implementation of the QA Programme:

- ❑ Suspicion of a probable lack of familiarity (subsequently confirmed) by the majority of the organisations participating in the first phase of the project, and the new second project phase participants, with the Quality Assurance programmes, requirements, and procedures.
- ❑ Potential difficulties were anticipated in the supply of elements required to be subjected to QA controls, due to the lack of commercial availability of such elements with the specified characteristics. The actual difficulties proved to be fewer than anticipated.

- ❑ The uncertainties in defining some of the necessary characteristics of the instrumentation for the large-scale tests (isolation, expected life, range of measurements, etc.).
- ❑ The uncertainties in determining the type and values of stresses and other variables for the design of the large-scale tests.
- ❑ The uncertainties in determining the values of some parameters or constants to be used in the modelling.
- ❑ The difficulties in managing the interrelations between the different organisations participating in the project.
- ❑ Application of the programme once the project had started.

9.3.2. Elements of the quality assurance system

As has previously been stated, ENRESA decided to apply a QA programme to the FEBEX project after the design of many of the project components had begun. In fact, the application of the programme was initiated in the last quarter of 1995. The Test Plan of the "in situ" test [1] had been issued in June 1995, and that of the "mock-up" test [2] was practically complete by that time.

A QA programme must contain the elements for the control of the design; consequently it should have been issued prior to the commencement of the work. It is quite clear that this condition has not been met. Other aspects, such as supply controls, etc. were similarly affected.

In summary, it was not possible to apply a QA programme in its entirety. Nevertheless, from the beginning of its implementation, consideration was given to the method of applying the basic elements, such that to the greatest possible degree it would be possible to meet the goal of a quality programme: "work performed in a systematic and planned manner".

For this reason, the criteria of quality assurance were applied simultaneously with development of the project. As a result, application of the programme was prioritised on the basis of the necessity of the work, rather than in the habitual order. The different elements of the system are described below, in the chronological order of application.

This problem did not occur in the second phase of the project. The Monitoring System panel re-installation, and installation of the second "in situ" test after partial dismantling were completely covered by the QA programme in their instruments design and supply phases.

9.3.2.1. Document control

First, the procedure for project documentary control was issued. The intent was to achieve the highest possible degree of homogeneity and systematisation in the coding, issuing, distribution, use and cancellation of the documents issued by the different participating organisations. This had become urgent due to the large volume of documentation being generated. Furthermore, it was necessary to make the distribution of the documentation among the different participating organisations for information or comments a systematic affair. Therefore, this procedure was applied prior to the issuing of the QA programme for the project.

This procedure was revised during the project second phase, in order to include the new second phase participants and the new project stages created with the second phase of the FEBEX project: monitoring system panels removal and re-installation, first cooling, partial dismantling, second installation (instrumentation, second shotcrete plug, and second heating into the second operational stage).

During the second project phase a Sample Control procedure was also issued in order to control the partial dismantling sample extraction, handling, storage, and transportation processes.

9.3.2.2. QA Programme

Following the Document Control procedure, the QA Programme was written and was issued in January 1996 in rev. 0, following revision by the participating organisations.

The QA Programme is based fundamentally on the capability already acquired by ENRESA from its own quality system. The rest of the participating organisations (particularly the universities and research organisations) did not, in general, have their own quality systems. The FEBEX programme is, therefore, based on the ENRESA system and extended to the rest of the organisations. In the case of the non-Spanish organisations (in particular, GRS and G.3S, since the participation of ANDRA, from the quality point of view, was limited to the acquisition of instruments for measuring humidity), the programme was delivered to them, but the quality of their work was their own responsibility and is not described herein.

Throughout the rest of the project, the participating Spanish organisations developed their own procedures (in accordance with the procedure for document control described above) to a greater or lesser extent depending on the volume of their activities. Only in the case of AITEMIN was an in-house quality manual, based on the UNE-EN-ISO-9001 standard, approved and implemented during this initial stage of the project.

The QA Programme was also revised with the second phase of the project in order to include the new participating organisations, and the new stages of the project. As several non-Spanish organisations were added in the second phase, a new approach was tried in order to subject Quality Assurance uniformly to their activities. The main new feature of this revision was to include a requirement for every participating organisation (new and old) to draw up a specific Quality Plan for the activities assigned within the project second phase to each of them. Thus, specific Quality Plans were issued by GRS, VTT, CEG, CIEMAT, BRGM, CSIC, CT, PSI and UPC. As in the first stage of the project, AITEMIN issued global Quality Plans in the format of Inspection Points Programmes for the several activities led by them, included in this second phase of the project, and consisting mainly of the removal of the monitoring panels from the tunnel, partial dismantling and the second installation.

The main aspects that were intended to be covered, and that are included in the QA Programme, are described below.

The project organisation was defined, including the lines of communication and authority to be used by the various participating organisations. In general, the information had, in the first phase, been satisfactorily centralised by the Technical Secretariat of the project. In the second phase of the project information was first gathered and filtered by the Work Package Leaders, prior to the final coordination activities performed by the Technical Secretariat.

In addition, the QA Programme includes a description of the project responsibilities (principal or secondary) of the participating organisations in the various phases of the project. This has made it possible to determine the main responsible figure for each activity.

The programme includes not only the scope of QA requirements applicable to each of the successive stages of the project, but also explains in detail the significance of each of the requirements and how they are to be applied to the project and to what applicable participating organisations.

The programme contains other useful information, such as:

- ❑ Description of the interventions of the ENRESA Quality Management Department (which has undertaken to carry out the non-conformance and audit control functions for the entire project, due to the aforementioned lack of quality organisations within the participating organisations)
- ❑ Definition of the quality records to be generated by the project, etc.

9.3.2.3. Administrative procedures

Drafts of administrative procedures were subsequently issued by ENRESA, the aim being for each participating organisation to be able to prepare its own procedures, adapted to its idiosyncrasies and particular circumstances. One exception was the procedure for document control that, as explained above, was issued by ENRESA for application to all the participating organisations, with a view to ensuring the highest possible level of uniformity. The other exception was the procedure for sample control, also issued by ENRESA, to ensure that all the participating organisations designated the samples uniformly and were able to maintain their traceability.

It was not possible to implement QA design control of the physical components, since a large part of the design had been performed prior to issuing of the QA Programme. Procedures for software control were, however, issued by the universities in charge of the modelling. Design control activities were implemented however for the second concrete plug in the second phase of the project.

AITEMIN implemented procedures for supplies control that were applied to the main components of the “in situ” test. CIEMAT, on the other hand, had the suppliers implement a quality control in the fabrication of some of the components of the “mock-up” test.

Procedures for the control of tests and control of measuring, and testing equipment were established by the various organisations responsible for these activities.

For the documentation governing the installation of the two large-scale tests, the panel movement, the partial dismantling and the second installation, as well as the corresponding equipment reception, calibration, and functional and acceptance tests, the decision was taken to use Quality Plans (Inspection Point Programmes, IPP) as a guide for the performance of these activities. Their use proved to be satisfactory during the implementation of these activities

9.3.2.4. Design control

Since some of the designs had already been completed [1, 2] when the QA Programme was approved, the only option open to ensure quality was review of the design by ENRESA. Basically this review was directed at analysing the design inputs, the standards applied, and the calculation methods used. A summary of these aspects in the design of the components for the two large-scale tests is presented below.

The drift design specification and the hydro-geological boring specification for the "in situ" test were performed based on pre-existing information, and in general, through the analysis and design conditions of the ENRESA generic Granite Deep Geological Waste Repository (AGP) project design, performed in accordance with a QA programme. The design of the heaters was intended also to be very similar (in dimensions and weight) to those of the reference canisters of the "AGP" project.

There was no detailed design for the concrete plug in the "AGP" project. The preliminary design was made by UPM. The detailed design, developed by AITEMIN with expert help, was reviewed by ENRESA.

The second concrete plug (installed after the partial dismantling of the first heater), was not anchored to the drift, as was the first, but instead opposed the "in situ" test internal pressure resting on the friction forces developed between the wall of the drift and the plug. Another difference with respect to the first plug was the use of shotcrete instead of conventional concrete. This new design complemented the original demonstration objective of the FEBEX project with a more realistic installation procedure in the real repository. In this case the basic design was assigned to DM Iberia, the detailed design and fabrication specification again being assigned to AITEMIN, as in the case of the first plug. The new design of the plug proved to be effective to in stopping the leakage across the cable penetrations suffered by the first plug.

For the instrumentation, the selection (type), range of conditions, expected life – i.e., the capacity to withstand the environmental conditions (and isolation) – suitability, and calibration possibilities were reviewed and discussed. The cabling was designed with a Teflon cover for isolation from the surroundings. In general, and due to the lack of commercial precedents, no formal control of the instrument design could be established. The instruments installed in the second installation profited from the lessons learned in the dismantling analyses, especially with regard to anti-corrosion performance.

Neither were there any precedents in relation to the design of the electric power system. The main design input in this case was not the real power of the fuel elements, but the boundary condition of constant temperature at the surface of the heaters. AITEMIN performed the detailed design of the power control and of the monitoring and control systems for the "in situ" test. There were three resistances in both of the two heaters.

Certain modifications were made to the design, such as, for instance, the diameter of the drift. The diameter was reduced by a few centimetres in order to allow for the use the tunnelling machine (TBM) available at the desired time.

For the "mock-up" test, also lacking in precedents, CIEMAT had to develop the mechanical design from the basic data, such as, for example, the design pressure (obtained by adding the swelling pressure to the water injection pressure).

Consequently, the confining structure and the heaters of the "mock-up" test were designed, in accordance with the basic data mentioned above and using Division 2 of Section VIII of the ASME code. The tanks of the hydration system also were designed in accordance with Section VIII of the ASME code. Given the aforementioned problem of scheduling, an internal review by ENRESA replaced formal control of the design.

Both the instrumentation and the power control system have characteristics similar to those of the "in situ" test, although there are major differences in the solutions adopted in each case for the power control, this allowing a comparative analysis to be performed at the end of the project. The "in situ" solution has proven to be more convenient (power control based on wave chopping on a single operating resistance) than the one used in the "mock-up" (power control based on time chopping on the three resistances operating simultaneously).

For the monitoring and control system, the same basic design was used as in the "in situ" test.

9.3.2.5. Control of Suppliers

The ENRESA QA Department evaluated the quality of the Spanish organisations participating in the project. As has been pointed out above, with the exception of AITEMIN, the participating organisations did not have their own quality systems; consequently, the evaluation was fundamentally directed at checking the availability of procedures, material, and human resources for the performance of their activities. The evaluations indicated that the level of quality was satisfactory for the characteristics of the project.

In addition, the intention was to implement procurement control, but only in relation to the acquisition of the main components of the two large-scale tests. In the case of the "in situ" test, the main components subjected to QA were the drift; the steel liner; the heaters; the bentonite blocks; the concrete plug; the instrumentation (excluding the TDR's, that are experimental in nature); the cabling; and the power control, monitoring and control and data acquisition systems. For the "mock-up" test, the main components were the same as in the "in situ" test, except for the obvious lack of the drift, the concrete plug, and the steel liner, but with the addition of the confining structure and its hydration system.

For the "in situ" test, AITEMIN implemented quality control using their internal administrative procedures. It should be noted that the heaters and the steel liner were fabricated in accordance with a QA programme and in accordance with IPP's complying with Division 1 of Section VIII of the ASME code. The plan for the assembly and testing of the control panels for the power control system was revised to incorporate additional tests aimed at improving quality in manufacturing. The purchase orders for the instrumentation were revised to incorporate requirements related to isolation, calibration, and stability in harsh environments. The fabrication of the bentonite blocks was subject to specifications and fabrication procedures issued by AITEMIN.

As a result of scheduling constraints, revision of the supply plans relating to the "mock-up" test was possible only once the manufacturing of the main components was already in progress. In all cases, corrective actions were implemented whenever features possibly susceptible to problems were detected. The confining structure for the "mock-up" test was fabricated in accordance with an IPP that complied with Division 1 of Section VIII of the ASME code. The heaters were fabricated according to the code, but, in order to perform weld radiography and thus assure the quality of the welding, it was necessary to modify the design of the welds between the heater shell and its back end cover. The hydration system tanks were fabricated in accordance with Division 1 of Section VIII of the ASME code, and tested in accordance with the Spanish regulations for pressure vessels ("Reglamento de Aparatos a Presión"). Purchase orders for the instrumentation were revised to add requirements relating to calibration and stability in harsh environments. The fabrication of the bentonite blocks was subject to quality control.

9.3.2.6. Installation of the two large-scale tests

As has already been commented above, the installation of both tests was documented using IPP´s. These programmes made reference to the installation procedures and/or to tests to be performed and proved to be particularly useful: first, as an aid in the planning and independent review of all the tasks and, second, for clarification and documentation of the implementation of those tasks.

Prior to beginning the installation of the physical components of the "in situ" test, some activities having quality implications were performed. One of these activities was the installation of a concrete replica of a drift section to verify the viability of bentonite block installation. Reception inspections and calibrations of the instrumentation, as well as the preliminary assembly of the control panels, were also performed. Another documented activity with quality implications was the chronological shipping of all the necessary material to Switzerland, following careful planning,

The installation of the physical components of the "in situ" test commenced in early summer, 1996, and, as the site is accessible by road only from May to November, the final date for transporting the equipment was in November 1996. For this reason, the planning was very important, especially in view of AITEMIN's needs concerning coordination with other participating organisations, such as GRS, G.3S, and NAGRA.

The installation activities with major quality implications were as follows:

- ❑ Documentation of the location of the instrumentation, as well as its verification both before and after installation.

- ❑ Documentation of the density of the bentonite installed in the slices of blocks.
- ❑ Installation of the steel liner segments and their alignment.
- ❑ Reduction of the humidity in the drift environment, to avoid swelling of the bentonite during its installation.
- ❑ Insertion of the heaters into the steel liner.
- ❑ Construction of the concrete plug, including tests for controlling the concrete, and the penetrations for cable bundles.
- ❑ Connection of the cables to the control panels, their functional testing, the tests on the monitoring and control system and the final overall tests.
- ❑ Determination of the parameters of the power control system.

During the spring of 2001 the panels of the monitoring and control system, originally situated in the drift immediately in front of the plug, were removed and re-installed out of the drift. This operation was performed to allow for the removal without interferences of the first heater during the partial dismantling phase to be performed the following year. The disconnection of the electrical cables from the cabinet terminals and subsequent reconnection, the functional checks and the recording operations were of considerable quality importance for the success of the test in its partial dismantling stage. An IPP was followed for these activities.

The switching-off of the heaters took place in January 2002. Later in the spring of that year, the partial dismantling of the "in situ" experiment began. The dismantling activities with major quality implications were as follows:

- ❑ Careful demolition (to avoid harming instruments) of the first concrete plug.
- ❑ Selective acquisition of samples (including instruments, and the first heater).
- ❑ Handling, packaging, temporary storage and shipping of samples.
- ❑ New instrumentation installation.
- ❑ Second 3 m-long concrete plug installation. (Only 1 m was constructed in 2002. The rest of the plug was installed during the summer of 2003).

All these activities were guided by the use of the applicable IPP´s, and in the case of the sample acquisition the process was also governed by the "Sampling Plan", a document issued by AITEMIN, where samples and instruments to be retired in each section were described, along with specific integrity instructions for the removal of samples and instruments. Format records for each section were also included in the Sampling Plan.

During partial "in situ" experiment dismantling, "in situ" measurements of water and moisture content of bentonite samples for each section were performed, in order to achieve results quickly, before alteration of the samples could occur.

In the installation of the "mock-up" test, the activities with major quality implications were the following:

- ❑ Hydration system tests.
- ❑ Documentation of the location of the instrumentation, as well as its verification both before and after installation.
- ❑ Documentation of the density of the bentonite installed in the slices of blocks.
- ❑ Insertion of the heaters.
- ❑ Cable penetrations through the confining structure and its sealing.
- ❑ Connections of cables to the control panels, functional testing, testing of the monitoring and control system and the final overall tests.
- ❑ Flooding of the clay barrier.
- ❑ Determination of the parameters of the power control system.

The only design modification worth mentioning occurring in the "mock up" test consisted of installing flow integrators in the hydration system in order to be able to determine the water mass actually swallowed.

All the details of the previously described features are in the Final Data Dossiers for the "in situ" test phases and for the "mock-up" test.

9.3.2.7. Maintenance and periodic calibration plans

From a quality point of view, operation manuals for the two large-scale tests were needed in the operational stages. As periodical instrument calibrations were impossible to perform, the maintenance plans focused mainly on the power supply systems for both tests. In fact, the power supply and power control systems are the systems in which most of the Non-Conformances appeared during the operational stages of both tests, all of which were conveniently resolved.

9.3.2.8. Modelling

Procedures have been issued for the software design control documentation. These procedures describe the issue of the Requirements and Design specifications of the different modelling codes developed by the modelling organisations, their plans for their verification and validation, the reports on these activities and the user manuals. The procedures were issued by the organisations in charge of the development of the models and of the modelling activities: UPC-DIT and UPM, for the THM and EDZ modelling and ULC for the THG modelling.

Many modelling predictions and activities were performed during the pre-operational and operational stages. The cooling and the second heating after partial dismantling of the “in situ” experiment, as well as several operational transients such as the overheating and underheating “mock-up” transients, provided additional opportunities for model validations against experimental data. The results obtained are detailed in the Modelling Chapters of this report.

Several modifications have been implemented on the THM and THG codes, concerning not only parameter adjustments but also improvement of the constitutive equations. New capabilities have also been incorporated into the codes.

A configuration control of the status of the codes has also been performed by the modelling organisations.

9.3.2.9. Laboratory tests

During both project phases, laboratory tests were performed for the determination of modelling parameters. From the point of view of quality, each laboratory test is subjected to test control, this implying its documentation through the testing procedure, the conservation of its generated records and the implementation of controls relating to the inspection, measurement and testing equipment.

Post-mortem laboratory analyses for the samples obtained in the partial dismantling of the “in situ” test have also been performed. The results are detailed in the Tests Chapter of this report.

9.3.2.10. Periodic interventions of the ENRESA QA Department

The QA Department of ENRESA, in accordance with the QA Programme of the project, has received the assignment of performing the internal audits within ENRESA and the external audits of the Spanish participating organisations. The Non-Conformances found during the experiments have been resolved satisfactorily in all cases.

A special audit has been performed on the “in situ” partial dismantling sample gathering process. This special audit has focused on all the organisations participating in partial dismantling and has been performed by an appointed inter-organisational audit team formed by SKB, RAWRA, and ENRESA. This audit was performed in June 2002, with satisfactory results.

In addition, this department has undertaken supervision and inspections during the fabrication of the major components of the large-scale tests (confining structure of the “mock-up” test and heaters for both), the calibrations of the instrumentation, the assembly and testing of the control panels and the installation and final testing of the two large-scale experiments, instrument panel movement, dismantling activities and the installation of the two concrete plugs.

The QA Department has managed the documented non-conformances generated during the project.

9.3.3 Problem areas

As had been anticipated, difficulties were detected in the application of the QA programme. This was due, in many cases, to the haste imposed in the performance of the project; in others, the difficulties appeared due to the lack of information on the new fields to which it was applied.

Perhaps the greatest difficulty affecting the project, from the quality point of view, was the lack of familiarity by those participating in the project with the terminology, elements, procedures, activities, and programmes of Quality Assurance. During the second phase of the project this lack of familiarity affected only some of the new participants, since those participating in the first phase had by then acquired quite a lot of quality experience.

The difficulties in implementing the quality programme have led to problems, such as those summarised below:

- ❑ Use of out-of-date standards for design and/or fabrication.
- ❑ Minor discrepancies in the fabrication standards requirements, caused by a deficient flow of information.
- ❑ Problems in the design of the heaters, relating to compliance with certain standards requirements.
- ❑ Selection of Teflon as the protection for the cables. The Teflon solved the problem of the chemical interaction with the environment but caused problems in sealing of the cable passages.
- ❑ Design for the cables passing through the first concrete plug. This problem was resolved with the new concrete plug terminal connections design within the second concrete plug.
- ❑ Problems with the "mock-up" power control system design choice. Problems with the electrical isolation of the power supply conductors of the "mock up" heater resistances.
- ❑ Managing to get some almost exclusive suppliers to meet certain requirements or international standards.
- ❑ Changes in design that caused information to be lost between participating organisations, since no formal design control existed.
- ❑ Change in the form of initial hydration of the clay barrier in the "mock-up" test.
- ❑ Difficulties in achieving the expected Quality Control requirements specified in the fabrication specification, during the two different installations of the second concrete plug.
- ❑ Progressive loss of instruments & sensors due to the actual operational lifetime of both tests exceeding that projected. These lost sensors have had very little impact on the overall performance of both tests. Possibly the worst case was the loss of one of the two thermocouples responsible for the power control of the "in situ" test. The applicable corrective action consisted of provisions for a possible substitution with a different thermocouple with a different setpoint.

All the difficulties and problems that were encountered during the project have constituted an opportunity to learn and have in all cases been satisfactorily resolved.

9.4. Conclusions

From the experience obtained in applying a QA programme during the two phases of the FEBEX project, a set of conclusions was drawn that should be useful as a lesson learned for other R&D projects. Among the most important conclusions are the following:

1. It has been confirmed that a quality programme is applicable to an R&D project, even though its application was initially in doubt. However, the peculiarities of a research project and those of the working groups dedicated to this type of activity can, and must, be taken into account in working out future R&D activities subjected to a QA programme.

   This conclusion is particularly relevant, since any research project, whose results are to be used as input data for a project subjected to quality assurance, should also be subjected to such a requirement.

2. The QA Programme has been very useful in the FEBEX project, specifically in the following three aspects:

   - ➪ As an aid to project management, particularly due to the regulation of documents, coding of samples, and definition of the interrelations among groups.
   - ➪ Achieving a reasonably good Quality Assurance & Control in the design, fabrication, and installation of main components in the two large-scale tests.
   - ➪ Achieving a systematic procedure for the application of Preventive and Corrective Actions following the appearance of operational Non-Conformances.

   Although the programme was initiated after the design had started, the degree of success in its application has been greater than anticipated.

3. The application of the programme in the project has evidently contributed to the quality of the results from the installation and operation of both large-scale tests, the laboratory tests, model development, and the modelling of the two large-scale tests.
4. It is evident that, for its goals to be to accomplished, a quality programme should be applied from the very beginning of the project (conceptualisation Phase).
5. The application of a Quality Assurance Programme in all cases implies an increase in the project budget that has to be conveniently analysed during the programming phases of an R&D project.
6. Both large-scale tests remain operational and will continue to be useful for the validation of other R&D projects that will not be subjected to quality assurance. Nevertheless the database information gathering for both large scale tests and their final dismantling are the two remaining areas in which a QA programme application would greatly profit from the application of the FEBEX QA Programme, especially from the FEBEX project QA records generated.

10. Conclusions

10. Conclusions

10.1. Conclusions relating to the first objective (demonstration of handling and construction of the EBS)

10.1.1. Feasibility of constructing the engineered barriers system (EBS)

The design, fabrication, handling and installation of the various components of the "in situ" test accomplished a major part of the initial objective of the experiment – demonstration of the feasibility of constructing the EBS in accordance with the Spanish reference concept for crystalline rock (AGP Granito). Specifically it has been demonstrated that it is feasible to fabricate and handle the bentonite blocks, on an industrial scale, that a clay barrier can be constructed with the average dry density required and that, consequently, the average volume of the construction gaps between the blocks, canisters and rock may be predicted and are of magnitudes compatible with the swelling of the bentonite, such that the barrier has the specified swelling pressure and permeability.

10.1.2. Experience acquired in relation to the design of a repository

Although, as stated in Chapter 1, the "in situ" test is not an exact replica of the AGP Granito concept (especially in the size and weight of the bentonite blocks and the installation method), the experience acquired is described below, since it may be useful in some aspects for the design of a future repository.

- The disposal drift diameter of 2.40 m, as in the AGP Granito, is quite limiting. It is considered that a drift of this diameter is viable, but will require a very refined design for the handling and transportation equipment. The equipment must be very compact, while at the same time, accurate, powerful and robust.
- The majority of the specifications and procedures adopted in FEBEX for the industrial fabrication of the bentonite blocks are, in principle, applicable to blocks of greater dimensions (properties of raw bentonite, characteristics of the molds, fabrication tolerances, quality assurance system, etc). Although the FEBEX blocks have an approximate mass of only 25 kg, the experience acquired during the fabrication and handling of these blocks leads to the conclusion that larger blocks are feasible without any special problems. In fact, O-ring shaped blocks of compacted bentonite with an inner diameter of 1.07 m, an outer diameter of 1.65 m, a height of 0.5 m and a weight of more than 1000 kg have been manufactured by SKB for its KBS-3-Prototype Repository design project. The technical feasibility of these large size blocks, as regards handling, have also been tested within the framework of the Prototype project.
- The handling required for the installation of larger sized blocks may present difficulties. The installation equipment (by robot or remotely operated) for the blocks must be designed such that the blocks are subjected to compression stresses compatible with their strength (2 to 3 MPa) and to basically zero tension. Even more importantly, the gap between the blocks and the steel liner, especially in the lower part, is practically non-existent, as a result of which the equipment must hold each block only by its front face.
- A very important factor that must be taken into account is the influence of relative humidity on the mechanical integrity of the bentonite blocks. Adequate control of this humidity is necessary at the storage sites and during the handling and installation of the blocks. This issue must be studied in detail, to establish the allowable humidity limits as a function of exposure time. The presence of a film of water on the walls of the drift does not, however, seem to produce any problems from the point of view of the installation.
- A critical factor during insertion of the canisters is the alignment of the steel liner with respect to the axis of the drift. For this reason, the liner may be a hindrance rather than an aid as regards insertion of the canister. This aspect of the barrier should be studied, since in the case of a real repository it would be constructed using larger size blocks.
- The type of concrete plug performed during the first phase required special attention as regards the following two aspects: the form of over excavation for the key and the concreting, to obtain a good contact between the plug and the rock across the entire peripheral surface. For these reasons, the plug developed following the dismantling of Heater #1 was made of shotcrete; this may prove to be an adequate solution, although further tests will be required.

A part of the demonstration objective was to gain insight into the state of the barrier after it has been subjected to hydration and heating. This part of the objective has been attained during the dismantling of Heater # 1 of the "in situ" test. In general terms, the behaviour of the buffer has been as expected. That is, the hydration is progressing homogenously from the outer part in contact with rock to the inner and hotter part, and this hydration has produced the closure of all the gaps and joints existing after the installation. Also, the state of the instrumentation system has been evaluated during the partial dismantling. The laboratory analysis of the instruments retrieved indicates that they still operate correctly, without any loss of accuracy.

Laboratory and in situ tests as well as THM modelling indicate that, to all practical intents and purposes, there is no EDZ in the FEBEX drift.

Also the studies have shown that there has been no modification in the original hydraulic properties of the rock as a result of either the excavation or the test.

10.1.3. Experience acquired in relation to the behaviour of the instruments during the two large-scale tests

Various areas entailing problems or uncertainties were considered during the design and installation of the two large-scale tests (Chapter 1). Among these, consideration was given to the possibility of failure of the heating system (heaters, temperature sensors and cables) and the instrumentation system (sensors and cables).

In both tests, however, the behaviour of the heating system has been excellent. The clay barrier and rock instrumentation systems have also shown a high degree of reliability, higher in fact than was expected by the suppliers. After five years of heating and hydration, 80% of the instruments in the "in situ" test and 90% in the "mock-up" continue to be operational.

The data acquisition and heater control systems have also operated correctly, including the remote control system for the "in situ" test.

The good behaviour shown thus far by these systems does not, however, allow their final duration to be predicted. Given the impossibility of making such predictions, the advisability of having information with respect to this issue and the good behaviour observed to date, it would be recommendable to continue with the large-scale tests as long as possible.

10.1.4. Quality Assurance (QA) Programme

Another part of the first objective is the development and implementation of a QA programme. Although the application of the programme was initiated after a large part of the physical components had been designed, it has contributed to improving quality control during the fabrication and the installation of the components for the two large-scale tests. Nevertheless, it is obvious that for this part of the project the application of a QA programme is similar to that of any industrial process. Its application was necessary to reduce the probability of failure of the fundamental elements, since they would be inaccessible in the event of malfunctioning for either repair or replacement.

The most important conclusion is the confirmation that a QA programme is applicable to all the research process. However, due to the peculiarities of a research process and, consequently, of the scientists and engineers in charge of its development, the quality programme must include mechanisms allowing for adaptation to the discoveries and innovations that occur during the process. This conclusion is important, since, if the results are used as design data for another project that must be subjected to a quality assurance programme, then the research project must also be subjected to that requirement.

10.2. Conclusions relating to the second objective (THM modelling)

The study of the THM processes in the near field (especially the clay barrier) was the second objective of the project. The ultimate objective was to develop and validate a numerical model capable of quantitatively describing and predicting the THM processes occurring.

The numerical model used is CODE-BRIGHT, developed prior to FEBEX. During the project, formulation of the model and the code were modified and significantly improved, although the core, based on a solid formulation of physical laws, has not required any change. Laboratory tests carried out during the project have been used for the improvement of the model.

From the beginning of the project to the end of the first phase of FEBEX, three complete modellings of the two large-scale tests have been carried out.

The conclusion of the first, performed at the beginning of the project with few real data on the bentonite parameters, did however make it possible to understand the THM processes, determine heater power and define the distribution of the sensors for measurement of the THM variables of interest.

The second modelling was carried out at the end of the pre-operational stage (that is to say, before any test monitoring data was available). In this case, characterisation parameters were already available for the clay barrier and the rock mass (for the "in situ" test). This modelling led to two conclusions: on the one hand determination, by means of sensitivity analysis, of which laws and parameters had the greatest influence on the results, this making it possible to develop a laboratory testing program suitable for the demands of the model; and on the other, using the parameters and laws considered to be most realistic with the information available at the time, prediction of the behaviour of the large-scale tests ("blind" prediction), with a view to subsequently contrasting the results with the monitoring data.

The last modelling of the first phase was performed after checking the degree of fitness between the previous "blind" prediction and the monitoring data, obtained after almost two years of hydration and heating of the two large-scale tests. The "blind" prediction reproduced all the processes well, albeit with quantitative deviations with respect to the monitoring data, due to the fact that, as of the date of modelling, adequate results on certain critical parameters were not yet available from the laboratory testing. This third modelling was performed using the parameters and information obtained from laboratory testing over two years of the operational stage. In fact, modelling was performed until the best possible fit with the monitoring data was achieved, with the condition that the values of the parameters were within the range of those obtained from laboratory testing. The conclusion of this modelling was that with CODE-BRIGHT it is possible to reproduce with reasonable accuracy the results of the measures performed during the two large-scale tests and, consequently, increase the degree of confidence in its capacity to predict the near-field THM behaviour of a repository.

Naturally there were still uncertainties, but the modelling performed, using the available data, led to the conclusion that to bracket the uncertainties detected it was necessary to complete the foreseen program of laboratory tests and, if possible, the performance of other specific tests. It was also concluded that it would be particularly useful to prolong the operational stage of both large-scale tests for as long as possible, since it was seen that with time, as the degree of saturation of the barrier increases, the dispersion of the measure of certain variables (such as pressures) decreases. This would allow a more reliable contrast to be made between the monitoring data and modelling results. The conclusions of the analyses performed on the results of this modelling, finally, led to a second phase of FEBEX.

Various overall modellings of the two large-scale tests were also performed during the second phase.

The first was performed using the previous model, the aim being to compare the results with the monitoring data obtained after almost three years since the beginning of heating. The results of the "mock-up" modelling led to a surprise regarding the hydraulic problem: up to approximately day 900 of the test, the modelling provided a suitable reproduction of the data on water ingress into the "mock-up" and the distribution of relative humidity; as from this moment, however, differences were observed between the hydraulic behaviour of the test and the model predictions. It was concluded that analysis of these differences should receive preferential attention: understanding and explaining the apparent reduction in the actual rate of hydration was considered an important aspect relating to the long-term prediction capacity.

Following several initial attempts, the research focused on the identification of other processes not considered in the model available. The following lines of research were explored: the existence of a threshold gradient, the effects of thermocoupling and evolution of the microfabric. In view of the results obtained it may be stated that, to some extent, each of these phenomena explains the unexpected response of the test. However, the changes in the microfabric are considered to be the most promising phenomenon as regards explanation of the behaviour of the bentonite barrier; consequently, a more detailed analysis was performed on the effects of changes in the fabric of the clay, using the double-structure concept. The results of the modelling are fairly satisfactory, inasmuch as the main trends observed in the behaviour of the test have been reproduced.

At the end of the second phase – after more than six years of heating and hydration on the "mock-up" and more than seven on the "in situ" test – overall modellings were performed. In addition, the overheating of the "mock-up" has been modelled, along with the stage of cooling and excavation of the partial dismantling of the "in situ" test.

In summary, and as a final conclusion, it may be stated that CODE-BRIGHT is capable of modelling the THM behaviour of the clay barrier and the near field of the rock. However, there are still some gaps in knowledge of the processes, as is demonstrated by the persisting differences between the monitoring data and the results of the modelling as regards the trend of relative humidity, especially in the most hydrated zone of the barrier. Consequently, it is necessary to continue investigating these divergences – which may have consequences for other variables depending on hydration – unless they are shown to be irrelevant.

10.3. Conclusions relating to the third objective (THG modelling)

This objective refers to study of the THG processes in the near field and to their effects on the hydrodynamic, mechanical and hydrochemical properties of the bentonite. The ultimate aim is to develop analysis tools and methods, among them the construction and validation of a THG numerical model as a tool for application to evaluation of the geochemical behaviour of the near field.

The probability assigned to achievement of this objective was lower than those of the other two, due not only to the greater complexity of the geochemical processes but also to the lower degree of initial development of the THG model, compared to the THM. Nevertheless, to date great progress has been made in developing a THG model, in understanding and evaluating the processes involved and in parameter acquisition by means of the laboratory tests.

The laboratory testing program was drawn up and has been performed in coordination between experimenters and modellers, such that the results serve as a basis for construction and partial validation of the THG model; furthermore, certain laboratory tests by themselves allow certain conclusions to be drawn in relation to the possible chemical and mineralogical transformation of the bentonite and the composition of the pore water in the clay barrier. Perhaps the most important result is that obtained from the ion exchange tests. These tests have demonstrated that there is no potassification of the bentonite, this being the first step towards transformation into illite. Consequently, it may be stated that, at least for temperatures of up to 80°C (the maximum test temperature), montmorillonite does not transform into illite. During these tests (and also during the hydration and heating tests in small-scale cells), it has been seen that the exchange complex is modified: calcium or magnesium increases and sodium and potassium decrease in the hottest areas. This exchange complex modification does not, however, appreciably influence the mechanical and hydraulic properties of the bentonite (swelling and permeability), as has been demonstrated through testing of samples from the cells. Progress has been made also in determining sorption and transport processes and parameters and in the chemical analysis of the pore water.

The THG codes have been continuously improved from TRANQUI (developed prior to FEBEX) to CORE-LE and FADES-CORE-LE (first phase of the project), finishing in the second phase with the most recent and powerful version: INVERSE-HFADES-CORE. These codes have been applied to the following analyses: 1) interpretation of various laboratory tests for parameter estimation; 2) interpretation of laboratory tests for the identification of relevant geochemical processes; 3) prediction of the transport patterns of the artificial tracers positioned in the two large-scale tests; and 4) prediction of the THG behaviour of the clay barriers in the "mock-up" and "in situ" tests.

From the aforementioned application of the codes it may be concluded that in general they reproduce fairly well most of the observed patterns of geochemical behaviour of a large number of laboratory tests and of the results obtained from the laboratory analyses on samples taken during partial dismantling of the "in situ" test, this generating confidence in their predictive capacity. The models have been constructed on the basis of small-scale tests and for system states in specific discrete times. There is no geochemical instrumentation in either the small or large-scale tests. However, the fact that THG models derived from small-scale lab tests reproduce the overall patterns of measured concentrations for most chemical species in the "in situ" test provides an indication for the lack of the scale effects.

Nevertheless, certain discrepancies have been observed between the modelling results and the data on behaviour of the clay barrier. Among these is the same hydraulic problem described in relation to THM modelling. From the chemical point of view, mention should be made of the major disagreement between the prediction and the measurement data for sulphate and carbonate. There are also certain processes that were not taken into account.

In conclusion, it is considered that future THG models should incorporate mechanical and geochemical couplings (thus leading to fully coupled THMG models) and account for porosity changes caused by swelling phenomena. They should also consider more sophisticated conceptual geochemical models in which a distinction is made between intra-aggregate and inter-aggregate water for the purpose of hydrogeochemical modelling. Dual porosity models using the dual continuum model (DCM) approach should be developed. Such models should consider two transport equations with a coupling interaction term to describe solute transfer across the interface of macro- and micro-pores.

Most of the THG analysis effort has been devoted to constructing thermo-hydrogeochemical models for the main geochemical processes controlling the geochemical evolution of the clay barrier in terms of major ion composition, pH and alkalinity. There are some processes that are relevant for performance assessment, such as redox and the interactions of corrosion products, which have not been addressed in the FEBEX project. Experimental data as well as numerical analyses on the role of these processes should be undertaken in the future.

There are major expectations that by acting in accordance with what is recommended above it might be possible to construct numerically verified, scientifically sound and thoroughly tested THG computer codes and numerical models.

10.4. Conclusions of a general nature

The most relevant general conclusions drawn are methodological in nature.

There is confirmation of ENRESA's idea that, following the partial research carried out in previous R&D plans, with a view to establishing the viability of the reference concept and making progress in the understanding and evaluation of behaviour in the near field (especially the clay barrier), it was necessary to perform a very complete experiment such as FEBEX (Chapter 1). There is a demonstrated synergy achievement from the simultaneous, integrated performance of tests on three scales within the FEBEX project: real-scale testing under natural conditions; testing at almost real scale and eliminating the complexities of the rock mass; and laboratory tests of a type and complexity adapted to the requirements of the overall experiment. In other words, the combination of the three experimental scales and the modelling has been seen not only to provide a more complete database but also to multiply the information obtained from each test or group of tests.

It might be argued that complementary information could also be obtained by means of different independent research projects. However, this is not so effective, for various reasons. On the one hand, the type and number of the small-scale laboratory tests have been modified during the project as the process of interpretation, by modelling the behaviour of the large-scale tests, defined those constitutive laws or parameters that were most critical due to their effects on the results. In certain cases it has even been necessary to carry out specific tests that were unthinkable previously, such as those performed in order to take the decision regarding the initial hydration of the "mock-up". Furthermore, the coordination and integration of the information generated by the different working groups with experimental or modelling responsibilities is difficult enough within one same project, and impossible in the case of independent, non-simultaneous projects.

11. References

11. References

[1] ENRESA. FEBEX. Full-scale Engineered Barriers Experiment in Crystalline Host Rock. Test Plan, "In situ" Test. Version 1. Madrid, July, 1995.

[2] ENRESA. FEBEX. Full-scale *Engineered* Barriers Experiment in Crystalline Host Rock. Test Plan, "Mock-up" Test. Version 1. Madrid, January, 1996.

[3] 70-UPC-H-5-2. UPC-DIT. Plan de Trabajo de la Experimentación Termo-Hidro-Mecánica durante la Etapa Operacional del Proyecto FEBEX. Revisión 0. Barcelona, septiembre 1997.

[4] 70-ULC-H-5-1. ULC. Plan de Trabajo Integrado de la Modelización y Experimentación Termo-hidro-geoquímica. Revisión 0. La Coruña, septiembre 1997.

[5] P.T. núm. 11/95. ENRESA. Almacenamiento Geológico Profundo de Residuos Radiactivos de Alta Actividad (AGP). Diseños Conceptuales Genéricos. Madrid, noviembre 1995.

[6] ENRESA, 1998. FEBEX. Bentonite: origin, properties, and fabrication of blocks. Publicación Técnica ENRESA 4/98. 146 pp. Madrid.

[7] 70-IMA-M-0-2. CIEMAT. Caracterización Geoquímica de Bentonita Compactada: Efectos Producidos por Flujo Termohidráulico. Revisión 1. Madrid, abril 1997.

[8] Fernández Soler, J.M., 1992. El volcanismo calco-alcalino de Cabo de Gata (Almería). Ph. D. Thesis. Universidad de Granada. 243 pp.

[9] Delgado, A., 1993. Estudio isotópico de los procesos diagenéticos e hidrotermales relacionados con la génesis de bentonitas (Cabo de Gata, Almería). Ph. D. Thesis. Universidad de Granada. 413 pp.

[10] Fernández A.Mª., 2003. Caracterización y modelización del agua intersticial en materiales arcillosos. Estudio de la bentonita de Cortijo de Archidona. Ph.D. Thesis. Universidad Autónoma de Madrid, 505 pp.

[11] Fernández, A.Mª., Baeyens, B., Bradbury, M., Rivas, P., 2004. Analysis of the pore water chemical composition of a Spanish compacted bentonite used in an engineered barrier. Physics and Chemistry of the Earth, Vol. 29/1, pp. 105-118. ISSN: 1474-7065.

[12] Fernández, A.Mª., Cuevas, J., Rivas, P., 2001. Pore water chemistry of the FEBEX bentonite. Mat. Res. Soc. Symp. Pro. 663, pp. 573-588.

[13] ENRESA, 2000. FEBEX Project. Full-scale engineered barriers experiment for a deep geological repository for high level radioactive waste in crystalline host rock. Final Report. Publicación Técnica ENRESA 1/2000. 354 pp. Madrid.

[14] Sing, K.S.W., Everett, D.H., Haul, R.A.W., Moscou, L., Pierotti, R.A., Rouquérol, J. & Siemieniewska, T., 1985. Reporting physisorption data for gas/solid systems with special reference to the determination of surface area and porosity. Pure & Appl. Chem. 57(4), 603-619. IUPAC.

[15] Lloret, A., Romero, E., Villar, M.V., 2004. FEBEX II Project Final Report on thermo-hydro-mechanical laboratory tests. Publicación Técnica ENRESA 10/04. 180 pp. Madrid.

[16] Villar, M.V., 2000. Caracterización termo-hidro-mecánica de una bentonita de Cabo de Gata. Ph.D. Thesis. Universidad Complutense de Madrid. 387 pp. Madrid.

[17] Rhoades J. D., 1982. Cation Exchange Capacity. In: Methods of Soil Analysis, Part 2. Chemical and Microbiological Properties. Agronomy Monograph nº 8 (2nd Edition). ASA-SSSA, 677. Madison.

[18] Thomas, G.W., 1982. Exchange cations. In: Methods of Soil Analysis, Part 2. Chemical and Microbiological Properties. Agronomy Monograph nº 9 (2nd Edition). ASA-SSSA, 677. Madison. pp. 159-165.

[19] Sawhney, B. L., 1970. Potassium and caesium ion selectivity in relation to clay mineral microstructure. Clays Clay Minerals, 18, 47-52.

[20] Sawhney, B. L., 1972. Selective sorption and fixation of cations by clay minerals: A review. Clays Clay Minerals, 20, 93-100.

[21] 70-IMA-M-9-4. CIEMAT. Ensayo en maqueta: informe final. Instalación y operación. Versión 0. Madrid, Junio 199.

[22] 70-IMA-L-9-108. CIEMAT. 24th Data Report. Final Project Report: Mock-up test. Project Deliverable D15-L. Madrid, July 2004.

[23] Martín, P.L., Barcala, J.M. 2001 a. Report on over-heating failure. Mock-up test. Informe técnico. CIEMAT/DIAE/54520/1/2003.

[24] Martín, P.L. Barcala, J.M. 2004. 24 the Data Report: Final Report Mock-up Test. CIEMAT/DIAE/54520/ /06/04 (70-IMA-L-9-108).

[25] Fredlund, D.C., Rahardjo, H. Soil Mechanics for Unsaturated Soils. John Willey & Sons, INC., New York 1993.

[26] Cañamón, I., Calle, O., Elorza, F.J., Rodríguez, R. Borregón, J.L., 2001. Aplicación del análisis espectral a la modelización acoplada Termo-hidro-mecánica. XVII Congreso de Ecuaciones Diferenciales y Aplicaciones y VII Congreso de Matemática Aplicada. Universidad de Salamanca, 24-28 de septiembre de 2001. Pp. 687. L. Ferragut y A. Santos. Salamanca.

[27] Cañamón, I., Elorza, F.J., Rodríguez, R., Valeriano, L., López Iraza, V., 2002. Técnicas de análisis de datos en experimentos relacionados con el almacenamiento de residuos radiactivos de alta actividad.

[28] Norbert, N., Wieczorek, K., GRS. Investigation of Gas Generation, Release and Migration. FEBEX final report 1996-1999: GRS contribution. Braunschweig, 1999.

[29] 70-AIT-M-4-01. AITEMIN. Diseño Final y Montaje del Ensayo "In situ" en Grimsel. Revision 0. Madrid, June 1997.

[30] 70-AIT-L-5-20. AITEMIN. Sensors data report No. 14 (20.February.97 to 31.March.99). Revision 0. Madrid, April 1999.

[31] 70-AND-L-5-01. ANDRA. Review of the capacitive humidity sensors: data interpretation in the FEBEX "in situ" test. Version 0. Chatenay-Malabry, July 1998.

[32] Bazargan-Sabet, B., Ghoreychi, M., G.3S. Rock and bentonite barrier displacement sensors in the FEBEX in-situ test. Palaiseau, September, 1999

[33] Kickmaier, W., Marschall, P., NAGRA. TDR measurements. Wettingen, September 1999.

[34] ENRESA, FEBEX Full-scale engineered barriers test in crystalline rock: Dismantling of the Heater #1 at the FEBEX "in situ" test, Pub. Técnica de ENRESA 9/03, Madrid, 2003.

[35] 70-AIT-L-6-08. AITEMIN. "Instruments analisys report". Version 0. Project deliverable D14. Madrid, march 2004.

[36] ENRESA. FEBEX Project. Post-mortem Analysis: Corrosion study. Publicación Técnica de ENRESA 08/2004. Madrid, agosto 2004.

[37] 70-UPC-M-0-1001. UPC-DIT. Hydrogeological Characterization and Modelling. Version 0. Barcelona, March, 1997.

[38] 70-IMA-L-2-28. CIEMAT. Caracterización Hidrogeoquímica de las Aguas del Túnel FEBEX del Grimsel Test Site (GTS). Revision 1. Madrid, noviembre 1996.

[39] 70-IMA-M-2-01. CIEMAT. Caracterización Geológica de la Zona de Ensayo FEBEX (Grimsel-Suiza). Revision 0. Madrid, mayo 1997. (Borrador.)

[40] Fuentes-Cantillana, J.L., García-Siñeriz, J.L., Bárcena, I. and Tuñón, S. "Sampling Plan for Dismantling of Section 1 of "in situ" Test". AITEMIN February 2002. FEBEX Report 70-AIT-G-6-27 Rev. 2.

[41] Huertas, F. and Martínez, M.A. "Sample Identification and Control within the FEBEX project". ENRESA February 2002. FEBEX Report 070-PC-TA-0002.

[42] Fuentes-Cantillana, J.L. and García-Siñeriz, J.L. "FEBEX: Final Design and Installation of the "In Situ" Test at Grimsel". ENRESA Technical Publication 12/98.

[43] AITEMIN - "Data Sensor Report nº 22". FEBEX Report 70-AIT-L-5-29. June 2001.

[44] N. Jockwer. "Report on the installation of the draining pipe systems for gas sampling and permeability measurements. GRS. March 31, to April 07. 2003.

[45] Fuentes-Cantillana, J.L. and Velasco, M. "Design of a new plug for FEBEX II". AITEMIN. FEBEX Report 70-AIT-L-6-01. May 2002.

[46] Fuentes-Cantillana, J.L. "Specification for FEBEX II Concrete Plug". AITEMIN. FEBEX Report 70-AIT-H-6-03 Rev. 5. July 2003.

[47] Huertas, F. et al. "FEBEX-Pre-operational Stage. Summary report". ENRESA Technical Publication 01/98. Madrid, January 1998.

[48] AITEMIN "Ajuste del Sistema de Control por temperaturas internas del calentador". FEBEX Report 70-AIT-L-7-04. Mayo 2004, Madrid.

[49] Villar, M.V., 2002. Thermo-hydro-mechanical characterisation of a bentonite from Cabo de Gata. A study applied to the use of bentonite as sealing material in high level radioactive waste repositories. Publicación Técnica ENRESA 04/2002. 258 pp. Madrid, April 2002.

[50] Lloret, A.; Villar, M.V. & Pintado, X., 2002: Ensayos THM: Informe de síntesis. Internal report CIEMAT/DIAE/54111/9/99. FEBEX report 70-UPC-M-0-04. 97 pp. Barcelona.

[51] Sánchez, M., 2004. Thermo-hydro-mechanical coupled analysis in low permeability media. Ph.D. Thesis. Universidad Politécnica de Cataluña. Barcelona.

[52] Skipper, N.T., Refson, K. & McConnell J.D.C., 1991. Computer simulation of interlayer water in 2:1 clays. J. Chem. Phys. 94 (11), 7434-7445.

[53] Marcial, D., 2003. Comportement hydromécanique et microstructural des matériaux de barrière ouvragée. Ph.D. Thesis. École Nationale des Ponts et Chausées, Paris. 316 pp. (In French).

[54] Villar, M.V. & Lloret, A., 2004a. Influence of temperature on the hydro-mechanical behaviour of a compacted bentonite. Applied Clay Science 26, 337-350.

[55] Villar, M.V. & Lloret, A., 2004b. Temperature influence on the mechanical behaviour of a compacted bentonite. In: Stephansson, O.; Hudson, A. & Jing, L.(eds.): Coupled thermo-hydro-mechanical processes in geo-systems. Fundamentals, modelling, experiments and applications. Elsevier Geo-engineering Book Series. Vol 2. Elsevier. Amsterdam. pp. 305-310.

[56] Lloret, A., Villar, M.V., Sánchez, M., Gens, A., Pintado, X., & Alonso, E. 2003. Mechanical behaviour of heavily compacted bentonite under high suction changes. Géotechnique, 53(1): 27-40.

[57] Gens, A. & Alonso, E., 1992. A framework for the behaviour of unsaturated clay. *Can. Geotech. J.* 29: 1013-1032.

[58] Alonso, E.E., Gens, A. & Hight, D.W., 1987. Special problem soils. General report. Proc. 9th Eur. Conf. SMFE, 3, 1087-1146.

[59] Pintado, X., 2002. Caracterización del comportamiento termo-hidro-mecánico de arcillas expansivas. Ph.D. Thesis. Universitat Politécnica de Catalunya. Barcelona. (In Spanish).

[60] Romero, E., Villar, M.V. & Lloret, A., 2005. Thermo-hydro-mechanical behaviour of two heavily overconsolidated clays. Eng. Geol. 81: 255-268.

[61] Hueckel, T. & Borsetto, M., 1990. Thermoplasticity of saturated soils and shales: constitutive equation s. J. Geotech. Eng. ASCE 116(12), 1765-1777.

[62] Olivella, S., Carrera, J., Gens, A. & Alonso, E.E., 1994. Nonisothermal Multiphase Flow of Brine and Gas through Saline Media. Transport in Porous Media 15: 271-293.

[63] Olivella, S., Gens, A., Carrera, J. & Alonso E.E., 1996. Numerical formulation for a simulator (CODE-BRIGHT) for the coupled analysis of saline media. Engineering Computations 13: 87-112.

[64] Pintado, X., Ledesma, A., Lloret, A. 2002. Back analysis of thermohydraulic bentonite properties from laboratory tests. Engineering Geology, 64. 91–115.

[65] Villar, M.V., 2001. Ensayos termohidráulicos en celdas grandes: Propiedades hidro-mecánicas. Informe FEBEX 70-IMA-L-0-76 rev. 0. Marzo 2001. 65 pp.

[66] Martín, M., 2002. Procesos geoquímicos y modificaciones texturales en bentonita FEBEX compactada sometida a un gradiente termohidráulico. Ph. Thesis. Universidad Autónoma de Madrid. 293 pp.

[67] Villar, M.V., Martín, P.L. & Barcala, J.M., 2005. Modification of physical, mechanical and hydraulic properties of bentonite by thermo-hydraulic gradients. Eng. Geol. 81, 284-297.

[68] Romero, E., Gens, A. & Lloret, A., 1999. Water permeability, water retention and microstructure of unsaturated Boom clay. Eng. Geol. 54, 117-127.

[69] Tessier, D., 1984. Etude expérimentale de l'organisation des matériaux argileux. Hydratation, gonflement et structuration au cours de la dessication et de la réhumectation. Ph.D. Thesis. Université de Paris VII. 361 pp. Paris. (In French).

[70] Villar, M.V., Fernández, A.M., Rivas, P., Lloret, A., Daucausse, D., Montarges-Pelletier, E., Devineau, K. , Villieras, F. , Hynková, E. , Cechova, Z. , Montenegro, L. , Samper, J. , Zheng, L., Robinet, J.-C., Muurinen, A., Weber, H.P., Börgesson, L. & Sandén, T., 2004: Task 141: Postmortem bentonite analysis. EC Contract FIKW-CT-2000-00016, Deliverable D11. FEBEX Technical Report 70-IMA-M-6-7 v0. CIEMAT. 159 pp. Madrid.

[71] Villar, M.V.; Martín, P.L.; Lloret, A. & Romero, E., 2002b, 2nd Report on Termo-hydro-mechanical laboratory tests. Deliverable D-17/2. September 00-March 02. May 2002. CIEMAT/DIAE/ 54520/ 06/02. FEBEX report 70-IMA-L-0-97. 53 pp. Madrid.

[72] Wanner, H., Wersin, P., Sierro, N., 1992. Thermodynamic modelling of bentonite-groundwater interaction and implications for near field chemistry in a repository for spent fuel. SKB 92-37, 28 pp.

[73] Curti, E. 1993. Modelling bentonite pore waters for the Swiss High-level Radioactive Waste Repository. Nagra Technical Report NTB 93-45. 85 pp.

[74] Wieland, E., Wanner, H., Albinsson, Y., Wersin, P., Karland, O., 1994. A surface chemical model of the bentonite-water interface and its implications for modelling the near field chemistry in a repository for spent fuel. SKB Technical Report 94-26. 64 pp.

[75] Bradbury, M.H., Baeyens, B., 1998. A physico-chemical characterisation and geochemical modelling approach for determining pore water chemistries in argillaceous rocks. Geochim. Cosmochim. Acta 62, pp. 783-795.

[76] Bradbury, M.H., Baeyens, B., 2002b. Pore water chemistry in compacted re-saturated MX-80 bentonite: Physico-chemical characterisation and geochemical modelling. PSI Bericht Nr. 02-10 Paul Scherrer Institut, Villigen, Switzerland and Nagra Technical Report NTB 01-08, Nagra, Wettingen, Switzerland.

[77] Bradbury, M.H., Baeyens, B., 2003. Pore water chemistry in compacted resaturated MX-80 bentonite. J. Contaminant Hydrology, 61, 329-338.

[78] Muurinen, A., Lehikoinen, J., 1999. Pore water chemistry in compacted bentonite. Engineering Geology, 54, pp. 207-214.

[79] Pusch, R., Muurinen, A., Lehikoinen, J., Bors, J., Eriksen, T. 1999. Microstructural and chemical parameters of bentonite as determinants of waste isolation efficiency. European Commission. Nuclear Science and Technology. Project Report EUR 18950 EN.

[80] Bruno, J., Arcos, D., Duro, L., 1999. Processes and features affecting the near field hydrochemistry. Groundwater-bentonite interaction. SKB Tech. Rep. 99-29.

[81] Wersin, P., 2003. Geochemical modelling of bentonite pore water in high-level waste repositories. Journal of Contaminant Hydrology 61, pp. 405-422.

[82] Pearson, F.J., Arcos, D., Bath, A., Boisson, J. Y., Fernández, A.Mª, Gäbler, H-E, Gaucher, E., Gautschi, A., Griffault, L., Hernán, P., Waber, H.N., 2003. Geochemistry of water in the Opalinus Clay Formation at the Mont Terri Rock Laboratory. Swiss Federal Office for Water and Geology Series, Nº 5, 500 pp.

[83] Güven, N., Low, P.F., Mitchell, J.K., Sposito, G., van Olphen, H., 1993. Clay-Water interface and its rheological implications. CMS Workshop Lectures. Volume 4. R.E., Ferrel Editor. The Clay Minerals Society. Colorado. USA.

[84] Brunauer, S., Emmett, P.H., Teller, E., 1938. Adsorption of gases in multimolecular layers. J. Am. Chem. Soc. 60, 309.

[85] de Boer, J.H., Lippens, B.C., Linesen, B.G., Brokhoff, J.C.P., Van der Heuvel, A., Osinga., J., 1966. The t-curve of multimolecular N_2 adsorption. J. Colloid Inrerface Sci., 21, pp. 405-414.

[86] Cases, J.M., Bérend, I., Besson, G., Francois, M., Uriot, J.P., Thomas, F., Poirier, J.E., 1992. Mechanism of adsorption and desorption of water vapor by

homoionic montmorillonite. 1. The sodium-exchanged form. Langmuir, 8, 2730-2739.

[87] Gregg, S. J., Sing, K.S.W., 1982. Adsorption, surface area and porosity. Academic Press. 303 pp.

[88] Webb, P.A., Orr, C., 1997. Analytical Methods in Fine Particle Technology. Micromeritics Instrument Corporation. Norcross, GA USA. 301 pp.

[89] Norrish, K., 1954. The swelling of montmorillonite. Discuss. Faraday Soc. 18, 120-133.

[90] van Olphen, 1977. An introduction to Clay Colloid Chemistry for clay technologies, geologists and soil scientists. John Wiley, N.Y., 318 pp.

[91] Sposito, G., 1983. The surface chemistry of soils. Oxford University Press, N.Y., 234 pp.

[92] Newman, A.C.D., 1987. Chemistry of Clays and Clay Minerals. Mineral Society. Monograph Nº 6. Longman Scientific & Technical, 480 pp.

[93] Laird, D.A., 1999. Layer charge influences on the hydration of expandable 2:1 phyllosilicates. Clays and Clay Minerals, vol. 47, 5, pp. 630-636.

[94] Grim, R.E., 1968. Clay Mineralogy, 2nd edition. McGraw-Hill. New York. 596 pp.

[95] MacEwan, D.M.C., Wilson, M., 1980. Interlayer and intercalation complexes of clay minerals. In: Crystal Structures of Clay minerals and their X-ray identification. F.W. Brindley and G. Brown eds. Mineral Soc. Monogr. 5, London, pp. 197-248.

[96] Fernández A.Mª, Rivas P., 2003. Analysis of types and distribution of waters in the FEBEX bentonite used as an engieneered barrier. Proceedings of the International Conference of the European Clay Group Association. EUROCLAY 2003, Módena (Italy). June 22-26, pp. 96-97.

[97] Prost, R., Koutit, T., Benchara, A., Huard, E., 1998. State and location of water adsorbed on clay minerals: Consequences of the hydration and swelling-shrinkage phenomena. Clays and Clay Minerals, 46, 117-131.

[98] Dubinin, M.M., 1967. Adsorption in micropores. J. Colloid Interface Sci., 23, 487-499.

[99] Kraehenbuehl, F., Stoeckli, H.F., Brunner, F., Kahr, G., Mueller-Vonmoos, M., 1987. Study of the water-bentonite system by vapour adsorption, immersion calorimetry and X-ray diffraction techniques: I. Micropore volumes and internal surface areas, following Dubinin´s theory. Clay Minerals 22, 1-9.

[100] Touret, O., Pons, C.H., Tessier, D. et Tardy, Y., 1990. Etude de la reparticion de l'éau dans des argiles saturees Mg^{2+} aux fortes teneurs en eau. Clay Minerals 25, 217-233.

[101] Hagymassy J., Brunauer S. and Mikhail R., 1969. Pore structure analysis by water vapor adsorption. I. t-curves for water vapor. J. Colloid Interface Sci., 29, pp. 485-491.

[102] Pusch, R., Karnland, O. & Hökmark, H., 1990. GMM-A general microstructural model for qualitative and quantitative studies on smectite clays. SKB Technical Report 90-43. Stockholm. 94 pp.

[103] Pearson, F.J., 1998. Geochemical and other porosity types in clay-rich rocks. Water-Rock interaction, Arehart & Hulston (eds.), pp. 259-262. Balkema. Rotterdam.

[104] Fernández, A. Mª, Rivas, P., 2005. Analysis and distribution of waters in the compacted FEBEX bentonite: Pore water chemistry and adsorbed water properties. In: Alonso and Ledesma. Proceedings of a Workshop on Large scale field tests in granite - Field emplacement and instrumentation techniques. Sitges 2003. A.A. Balkema Publishers. Leiden, The Netherlands. 257-275.

[105] García-Gutiérrez, M., Cormenzana, J.L., Missana, T., Mingarro, M., 2004a. "Diffusion coefficients and accessible porosity for HTO and 36Cl in compacted FEBEX bentonite" Applied Clay Science, 26, p. 65-73.

[106] Muurinen, A., Penttila-Hiltunen, P., Rantanen, J., Uusheimo, K., 1987. Diffusion of uranium and chloride in compacted Na-bentonite. Report YJT-87-14. Nuclear waste Commission of Finnish Power Companies, Helsinki, Finland.

[107] Dixon, D.A., 2000. Pore water salinity and the development of swelling pressure in bentonite based buffer and backfill materials. POSIVA Report 2000-04, Posiva Oy, Helsinki, Finland.

[108] Martin, R.T., 1962. Adsorbed water on clay: a review. Clay and Clay Minerals, v. 9, pp. 28-70.

[109] Bradbury, M.H., Baeyens, B., 1997. A mechanistic description of Ni and Zn sorption on Na-montmorillonite. Part II: Modelling. J. Contaminant Hydrology 27(3-4), pp. 223-248.

[110] Peigneur, P. 1976. Stability and adsorption affinity of some transition metal-amine complexes in aluminosilicates. Ph.D Thesis, Univ. Leuven, Belgium.

[111] Maes, A., Cremers, A., 1986. High selective ion exchange in clay minerals and zeolites. In Geochemical Processes at Mineral Surfaces. Eds. J.A. Davis and K.F. Hayes. ACS Symp. Series 323, 254-295.

[112] Wollast, R., 1990. Rate and mechanism of dissolution of carbonates in the system $CaCO_3$-$MgCO_3$. In: Aquatic Chemical Kinetics. Ed. W. Stumm. Wiley Interscience.

[113] Dreybrodt, W., Lauckner, J., Zaihua, Liu, Svensson, U., Buhmann D., 1996. The kinetics of the reaction $CO_2 + H_2O \Leftrightarrow H^+ + HCO_3^-$ as one of the rate limiting steps for the dissolution of calcite in the system H_2O-CO_2-$CaCO_3$. Geochim. Cosmochim. Acta 60, 3375-3381.

[114] Gaines, G.I., Thomas, H.C., 1953. Adsorption studies on clay minerals. II. A formulation of the

thermodynamics of exchange adsorption. J. Chem. Phys. 21, 714-718.

[115] Bolt, G.H., De Haan, F.A.M., 1982. Anion exclusion in soil. in soil chemistry B. Physico-chemical Models. Ed. G. H. Bolt. Vol. 5B, Chap. 5, Elsevier.

[116] Muurinen, A., 1994. Diffusion of anions and cations in compacted sodium bentonite. Technical research centre of Finland. VTT publications 168, 75 pp.

[117] Horseman, S.T., Higgo, J.J., Alexander, J., Harrington, J.F., 1996. Water, gas and solute movement through argillaceous media. Report CC-96/1. Nuclear Energy Agency, OECD, Paris, France.

[118 Hummel, W., Berner, U., Curti, E., Pearson, F.J., Thoenen, T., 2002. Nagra/PSI chemical thermodynamic data base 01/01. Nagra Technical Report NTB 02-16, Nagra, Wettingen, Switzerland and Universal Publishers/uPublish.com, Parkland, Florida.

[119] Parkhurst D.L., Appelo C.A.J., 1999. PHREEQC2 - A computer program for speciation reaction-path, 1D-Transport and inverse geochemical calculations. U.S. Geological Survey.

[120] Truesdell, A.H., Jones, B.F., 1974. WATEQ, A computer program for calculating chemical equilibria of natural waters: Journal of Research, U.S. Geological Survey, v. 2, p. 233-274.

[121] Parkhurst, D. L., 1990. Ion-Association models and mean activity coefficients of various salts. In: Chemical modelling of aqueous systems II, ed. D.C. Melchior and R.L. Bassett, Am. Chem. Soc. Symp. Ser. 416, pp. 30-43. Washington DC.

[122] Kielland, A.G., 1937. Individual activity coefficients of ions in aqueous solutions. J. Am. Chem. Soc. 59, pp. 1675-1735.

[123] Langmuir, D., 1997. Aqueous Environmental Geochemistry. 600 pp. Prentice Hall. New Jersey.

[124] Fernández, A.M.ª, Cuevas, J., Rivas, P., 1999. THG tests in intermediate cells: Study of the pore water composition. Technical Report FEBEX 70-IMA-L-0-41.

[125] Villar, M.V., Cuevas, J., Fernández, A.Mª., 1997. Caracterización geoquímica de bentonita compactada: efectos producidos por flujo termohidráulico. Interim Report FEBEX 70-IMA-M-0-2. CIEMAT. Madrid, España.

[126] Cuevas, J., Villar, M.V., Martín, M., Cobeña, J.C., Leguey S., Rivas, P., 2000. Termo-hydro-geochemical tests on small cells. Internal report CIEMAT/DIAE/54111/4/99 v1. FEBEX report 70-IMA-M-0-5. 46 pp. Madrid.

[127] Martín, M., Cuevas, J., Leguey, S., 2000. Diffusion of soluble salts under a temperature gradient after the hydration of compacted bentonite. Applied Clay Science, 17, pp. 55-70.

[128] Cuevas, J., Villar, M.V., Martín, M., Cobeña, J.C., Leguey S., 2002. Thermo-hydraulic gradients on bentonite: distribution of soluble salts, microstructure and modification of the hydraulic and mechanical behaviour. Applied Clay Science. 8.467-484.

[129] Leguey, S., Cuevas, J., Martín, M., Vigil de la Villa, R., Ramírez, S., García, R., 2002a. Procesos geoquímicos y modificaciones texturales en bentonita FEBEX compactada sometida a un gradiente termohidráulico. Publicación Técnica de ENRESA 10/2002. 154 pp. Madrid. (In Spanish).

[130] Missana, T., García-Gutiérrez, M., Fernández, V., Gil, P., 2003 "Application of surface complexation modelling to sorption onto clays. Part I: Titration experiments and sorption of Cs, Sr and Ca in Na -montmorillonite." CIEMAT Technical report CIEMAT/DIAE/ 54610/01/03.

[131] García-Gutiérrez, M., Missana, T., Mingarro, M., Samper, J., Dai, Z., Molinero, J., 2001. "Solute transport properties of compacted Ca-bentonite used in FEBEX project" J. of Contaminant Hydrology 47, p.127-137.

[132] García-Gutiérrez, M., Cormenzana, J.L., Missana, T., Mingarro, M., Alonso, Ú., 2004b. "Analysis of Uranium Diffusion Coefficients in compacted FEBEX Bentonite" Mat. Res. Soc. Vol. 807, p. 603-608, Scientific Basis for Nuclear Waste Management XXVII. ISBN-1-55899-752-0.

[133] Cormenzana, J.L., García-Gutiérrez, M., Missana, T., Junghanns, A., 2003. "Simultaneous estimation of effective and apparent diffusion coefficients in compacted bentonite" Journal of Contaminant Hydrology, 61, p. 63-72.

[134] Missana, T., García-Gutiérrez, M., Alonso, Ú., 2004a. "Kinetics and irreversibility of caesium and uranium sorption onto bentonite colloids in a deep granitic environment" Appl. Clay Science 26, 137-150.

[135] Bradbury, M.H. and Baeyens, B., 2005. "Modelling the sorption of Mn(II), Co(II), Ni(II), Cd(II), Eu(III), Am(III), Sn(IV), Th(IV), Np(V) and U(VI) on montmorillonite: linear free energy relationships and estimate of surface binding constants for some selected heavy metals and actinides" Geoch. Cosm. Acta 69, 875-892.

[136] Baeyens, B., Bradbury, M.H., 1997. "A mechanistic description of Ni and Zn sorption on Na-montmorillonite. Part I. Titration and sorption measurements" J. Cont. Hydrol. 27 (3-4), 199-222.

[137] Bradbury, M.H., Baeyens, B., 1999. "Modelling the sorption of Zn and Ni on Ca-montmorillonite" Geochim. et Cosmochim Acta 63 (3-4): 325-336.

[138] Bradbury, M.H., Baeyens, B., 2002a. "Sorption of Eu on Na- and Ca-montmorillonites: Experimental investigations and modelling with cation exchange and surface complexation" Geochim. et Cosmochim Acta 66 (13), 2325-2334.

[139] Missana, T., Fernández, A.Mª., García-Gutiérrez, M., Mingarro, M., Rivas, P., Caballero, E., Huertas, F.J., García-Palma, S., Jiménez de Cisneros, C.,

Linares, J., Rozalén, M.L., Baeyens, B., Bradbury, M.H., Muurinen, A., Cormenzana, J.L., 2004b. FEBEX II Project: THG Laboratory experiments. Publicación Técnica ENRESA 09/2004. 137 pp.

[140] Zachara, J.M., Smith, S.C., Liu, C., McKinley, J. P., Serne, R.J., Gassman, P.L., 2002. "Sorption of Cs^+ to micaceous subsurface sediments from the Hanford site, USA" Geochim. Cosmochim. Acta 66(2), 193-211.

[141] Poinssot, C., Baeyens, B., Bradbury, M.H., 1999. "Experimental and modelling studies of caesium sorption on illite", Geochim. Cosmochim Acta 63, 3217-3227.

[142] Bradbury, M.H. and Baeyens, B., 2000. " A generalised sorption model for the concentration dependent uptake of caesium by argillaceous rocks "J. Contaminant Hydrology, 42 141-163.

[143] Baeyens, B. and Bradbury, M.H., 1995. "A quantitative Mechanistic description of Ni, Zn and Ca sorption on Na-montmorillonite" Technical report :PSI Bericht Nr 95-10/11/12.

[144] García-Gutiérrez, M., Martín, P.L., 1996. "Celdas y técnicas para los estudios de difusión y coeficiente de distribución en arcillas compactadas". CIEMAT/ IMA/54B50/5/96.

[145] Wolfrum, C., Lang, H., Moser, H., Jordan, W., 1988. "Determination of Diffusion Coefficients Based on Ficks Second Law for Various Boundary Conditions" Radichim. Acta 44/45, p.245-249.

[146] Bourke, P.J., Jefferies, N.L., Lever, D.A., Lineham, T.R., 1993. "Mass transfer mechanisms in compacted clays" in Geochemistry of Clay-Pore Fluid Interactions, Eds. by D.A.C. Manning, P.L. Hall and C.R. Hughes, Chapman & Hall, London.

[147] Put, M., Henrion, P., 1992. "Modelling of radionuclide migration and heat transport from an HLW-repository in Boom clay" EUR-14156.

[148] Cama, J., Ganor, J., Ayora, C. and Lasaga, A.C., 2000. Smectite dissolution kinetics at 80°C and pH 8.8. Geochimica Cosmochimica Acta 64, 2701-2717.

[149] Carroll, S.A. and Walther, J.V., 1990. Kaolinite dissolution at 25°, 60° and 80°C, American Journal of Science 290, 797-810.

[150] Zysset, M. & Schlinder, P.W., 1996. The proton promoted dissolution kinetics of K-montmorillonite. Geochim. Cosmochim. Acta 60, 921-931.

[151] de la Fuente, S., 2000. Estudio experimental de la formación de un interestratificado esmectita-ilita por alteración hidrotermal de una toba volcánica, PhD Thesis, University of Granada, pp 189.

[152] Bloom, A.E. and Stillings, S.L., 1995. Felspars dissolution kinetics. In Chemical Weathering Rates of Silicate Minerals, A.W. White and S.L. Brantley, eds. Reviews in Mineralogy 31, 291-352.

[153] Fernández, A.Mª., Rivas, P., 2004. Task 141: Postmortem bentonite analyses. Geochemical behaviour. FEBEX report 70-IMA-L-0-109.

[154] Montarges-Pelletier, E., Devineau, K., Villieras, F., Bouquet, E., Pelletier, M., Razafitianamaharavo, A., Barres, O., Lambert, P., 2003. Postmortem FEBEX bentonite samples. Mineralogical and textural analysis. Final report LEM. 34 pp. Vandoeuvre-lPs-Nancy.

[155] Muurinen, A., 2004. Analysis of the samples from the cement-bentonite interface of the FEBEX in situ experiment. VTT processes. FEBEX study 70-VTT-I-6-02. 14 pp. Helsinki.

[156] Cuevas, J., Villar, M.V., Fernández, A.Mª., Gómez, P., Martín, P.L., 1997. Pore waters extracted from compacted bentonite subjected to simultaneous heating and hydration. Applied Geochemistry, 12 pp. 473-481.

[157] Bradbury, M., 1989. Laboratory investigations in support of the migration experiments. Nagra Technical Report 88-23.

[158] Eikenberg, J., Baeyens, B. and Bradbury, M.H., 1991. The Grimsel migration experiment: a hydrogeochemical equilibrium test. Nagra Technical Report 90-39.

[159] Leguey, S., Cuevas, J., Ramírez, S., Vigil, R. & Martín, M., 2002b. Alteración alcalina hidrotermal de la barrera de bentonita por aguas intersticiales de cementos. *Publicación Técnica ENRESA* 03/2002. 172 pp. Madrid.

[160] Montenegro, L., Samper, J., Zheng, L., Fernández, A.Mª. & Rivas, P., 2004. Sampling, laboratory analyses and numerical modelling of deuterium in the in situ FEBEX experiment. *FEBEX report* 70-ULC-L-6-03. 65 pp. La Coruña.

[161] Verstricht, J., 2004. Work Package 1. Task 1.4 Post-mortem analysis. Bentonite. Technical Report 70-EIG-L-6-02. ESV EURIDICE GIE. 24 pp. Mol.

[162] Jockwer, N. & Wieczorek, K., 2004. Gas sampling and analysis report. 2nd operational phase. FEBEX Deliverable D09b. 32 pp. Braunschweig.

[163] Madina, V. & Azkárate, I., 2004. FEBEX Project. Post-mortem analysis: corrosion study. Publicación Técnica ENRESA 08/2004. 87 pp. Madrid.

[164] García-Siñeriz, J.L., Bárcena, I., Fernández, P., Sanz, F.J., 2004. Instruments Analysis Report. FEBEX report 70-AIT-L-6-8. AITEMIN. 79 pp. Madrid. Unpublished report.

[165] FEBEX II Report, 2004. "Final report on thermo-hydro-mechanical laboratory tests". Deliverable D17/3. UPC-L-7-13.

[166] CODE_BRIGHT User's Manual, 2005. *UPC Geomechanical Group.*

[167] Sánchez, M. & Gens, A., 2005. "Final Report on THM modelling" FEBEX II. *UPC Geomechanical Group. ENRESA Report: 70-UPC-L-7-014.Deliverable D19/3.*

[168] FEBEX Report, 1998. "Preoperational Thermo-Hydro-Mechanical (THM) modelling of the 'mock-up' test". *Publicación Técnica Nº 10/98. ENRESA*. Madrid.

[169] FEBEX Report, 2000. "Full-scale engineered barriers experiment for a deep geological repository for high level radioactive waste in crystalline host rock". *Final project report*. EUR 19612 EN, European Commission, Brussels.

[170] Martin, P.L., & Villar, M.V., 1997. "Propiedades hidráulicas del geotextil utilizado en el ensayo de maqueta del proyecto FEBEX". Informe Técnico *ENRESA: 70-IMA-L-3-32.*

[171] CIEMAT Report, 2002. "19th Data Report Mock-Up test". *Informe 70-IMA-L-9-96. CIEMAT*. Madrid.

[172] ENRESA, 1997. "Reunión de urgencia para analizar incidencias durante la hidratación de la maqueta y decidir eventuales actuaciones". *Acta de Reunión 70-ST-C-9-27*. Madrid.

[173] van Genuchten, R., 1978. "Calculating the unsaturated hydraulic permeability conductivity with a new closed-form analytical model". *Water Resource Research*. 37(11), pp. 21-28.

[174] Alonso, E., Gens, A. & Josa, A., 1990. "A constitutive model for partially saturated soils". *Géotechnique,* 40, 3, pp. 405-430.

[175] Sánchez, M. & Gens, A., 2001. "Report on THM modelling results. FEBEX II". *UPC Geomechanical Group. ENRESA Report: 70-UPC-L-5-010.*

[176] Samper, J., Montenegro, L., & Zheng, L., 2002. "ULC contribution to the FEBEX II project meeting of September 26th, 2002". E.T.S. Ingenieros de Caminos Universidad de La Coruña. *ENRESA Report: 70-ULC-D-6-03.*

[177] Bear, J., 1972. "Dynamics of fluids in porous media". *Dover Edit.*, 164 pp.

[178] Dixon, D., Gray, M. & Hatiw. 1992. "Critical gradients and pressures in dense swelling clays". *Can. Geotech. Jnl.,* 29, pp. 1113-1119.

[179] Dixon, D., Graham, J. & Gray, M. 1999. "Hydraulic conductivity of clays in confined tests under low hydraulic gradients". *Can. Geotech. Jnl.,* 36, pp. 815-825.

[180] Mitchell, J., 1993. "Fundamentals of soil behaviour". *2nd ed. John Wiley & Sons*, 437 pp.

[181] Soler, J., 1999. "Coupled transport phenomena in the opalinus clay: implications for radionuclide transport". Paul Scherrer Institut Nº 99-07- ISSN 1019-0643.

[182] Djeran, I., 1993. "Étude des diffusions thermique et hydraulique dans una argile soumise á un champ de température". *Sciences et techniques nucléaires rapport*. Commission des Communautés européennes, ISBN 1018-5593.

[183] Aifantis, E., 1980. "On the problem of diffusion in solids". *Actha Mechanica*, Vol 37, Nº 3-4, pp. 265-296.

[184] Huyakorn, B., Lester & Faust, C., 1983. "Finite element techniques for modelling groundwater flow in fractured aquifers". *Water Resources Research,* Vol. 19, Nº 4, pp.1019-1035.

[185] Alonso, E., Vaunat, J. & Gens, A., 1999. "Modelling the mechanical behaviour of expansive clays". *Engineering Geology*, 54, pp. 173-183.

[186] Sánchez, M., Gens, A., Guimarães, L., & Olivella, S., 2005. "A double structure generalized plasticity model for expansive materials". *Int. Jnl. Numer. Anal. Meth. Geomech (in print).*

[187] Bárcena, I., Fuentes-Cantillana, J. & García-Siñeriz, J., 2003. "Dismantling of heater Nº 1 at the FEBEX in-situ test". Descriptions of operations 70-AIT-L-6-03.

[188] FEBEX II Report, 2003. "Results of in-situ .measurements of water content and dry density". 70-UPC-L-5-012.

[189] FEBEX II Report, 2002. "Procedimiento para la obtención de la humedad y densidad seca sobre muestras de bentonita in-situ.". 70-UPC-G0-19.

[190] Full-scale engineered barriers experiment for a deep geological repository in crystalline host rock (FEBEX Project). European Commission, EUR 19147 EN. 2000. 403 pp.

[191] 70-UDC-M-6-002. Final THG modelling report (Deliverable D25). Version 0. FEBEX Final Report. UDC. 2005, 211 pp.

[192] 70-UDC-L-6-01. Modelización hidrogeoquímica de ensayos de laboratorio para la identificación de la composición química. FEBEX Technical Report. 2003. 64 pp.

[193] Samper, J., Vázquez, A., Montenegro, L., 2005. Inverse hydrochemical modelling of aqueous extract experiments for the estimation of FEBEX bentonite pore water chemistry. In Alonso, E.E. & Ledesma, A. Advances in Understanding Engineered Clay Barriers. Proceedings of the International Symposium on Large Scale Field Tests in Granite, Sitges, Barcelona (Spain), 12-14 November. A.A. Balkema Publishers. Leiden, The Netherlands. 553-563.

[194] Samper, J., Juncosa, R., Delgado, J., Montenegro, L., 1998. CORE-LE-2D: A code for water flow and reactive solute transport. Users Manual, Draft Version. UDC. 207 pp.

[195] ENRESA, 1995. Multicomponent reactive solute transport models. ENRESA Final Report. UDC-CSIC. 1995.

[196] 70-ULC-H-5-006. Manual del usuario de FADES-CORE V0.0a. Informe FEBEX. UDC. 2000. 150 pp.

[197] Navarro, V., 1997. Modelo de comportamiento mecánico e hidráulico de suelos no saturados en condiciones no isotermas. Ph.D. Dissertation. UPC. 329 pp.

[198] Wolery, T.J., 1979. Calculation of chemical equilibrium between aqueous solutions and minerals: The

EQ3/6 software package. Lawrence Livermore National Laboratory. UCRL-52658 Report.

[199] Samper, J., Juncosa, R., Delgado, J., Montenegro, L., 2000. CORE2D: A code for non-isothermal water flow and reactive solute transport. Users Manual, Version 2. ENRESA Technical Report 6/2000. 131 pp.

[200] Samper, J., Zheng, L., 2003. Users Manual of FADES-CORE V1. UDC. Internal Report. 61 pp.

[201] 70-UDC-M-6-001. Improved THG model and numerical code (Deliverable D23). Version 0. FEBEX Final Report. UDC. 2005. 96 pp.

[202] 70-ULC-L-5-011. Numerical interpretation of difusion and permeation experiments. Version 0. UDC. 1999.

[203] 70-ULC-L-5-014. Isotermas de intercambio de la bentonita FEBEX. Version 0. UDC. 1999.

[204] 70-ZAI-L-03-08. Proceso de intercambio iónico entre los cationes interlaminares de la montmorillonita y soluciones graníticas. Granada, 1999.

[205] 70-ULC-L-5-013. Interpretación y modelización de los ensayos de intercambio: Resultados preliminares. Version 0. UDC. 1999.

[206] 70-UDC-L-6-02 Reactive transport model of a long-term permeation experiment. FEBEX Technical Report. UDC-CIEMAT. 2003. 12 pp.

[207] Samper, J., Zheng, L., Montenegro, L., Fernández, A.Mª., Rivas, P., Dai, Z., 2005. Direct and inverse modelling of multicomponent reactive transport in single and dual porosity media. In Alonso, E.E. & Ledesma, A. Advances in Understanding Engineered Clay Barriers. Proceedings of the International Symposium on Large Scale Field Tests in Granite, Sitges, Barcelona (Spain), 12-14 November. A.A. Balkema Publishers. Leiden, The Netherlands. 493-503.

[208] 70-ULC-M-5-001. Modelización termo-hidro-geoquímica del proyecto FEBEX. Vol. 2. Version 0. UDC. 1999.

[209] 70-UDC-L-5-15 Revisión y actualización de los modelos THG de los ensayos de laboratorio de hidratación y calentamiento. Informe Técnico FEBEX. UDC. 2000. 43 pp.

[210] Samper, J., Zheng, L., Molinero, J., Montenegro, L., Fernández, A.Mª., Rivas, P., 2005. Reactive solute transport mechanisms in nonisothermal unsaturated compacted clays. In Alonso, E.E. & Ledesma, A. Advances in Understanding Engineered Clay Barriers. Proceedings of the International Symposium on Large Scale Field Tests in Granite, Sitges, Barcelona (Spain), 12-14 November. A.A. Balkema Publishers. Leiden, The Netherlands. 525-533.

[211] 70-ULC-M-0-001. Termo-hydro-geochemical modelling of the mock-up FEBEX experiment. Version 2. UDC. 1998.

[212] 70-IMA-L-0-33. Tracers in the FEBEX project. CIEMAT. 1997.

[213] 70-UDC-L-5-22. Update of the thermo-hydro-geochemical model of the mock-up test. Version 1. FEBEX Technical Report. UDC. 2001. 123 pp.

[214] Samper, J., Zheng, L., Montenegro, L., Vázquez, A., Fernández, A.Mª., Rivas, P., 2005. Testing coupled thermo-hydro-geochemical models with geochemical data from FEBEX in situ test. In Alonso, E.E. & Ledesma, A. Advances in Understanding Engineered Clay Barriers. Proceedings of the International Symposium on Large Scale Field Tests in Granite, Sitges, Barcelona (Spain), 12-14 November. A.A. Balkema Publishers. Leiden, The Netherlands. 565-576.

[215] 70-ULC-M-0-002. Termo-hydro-geochemical modelling of the in situ FEBEX experiment. Version 2. UDC. 1998.

[216] 70-IMA-L-0-109. Task 141: Post-mortem bentonite analyses. Geochemical behaviour. FEBEX Technical Report. Version 0. CIEMAT. 2003 (in press).

[217] Pardillo, J., Campos, R., Guimerá, J. Caracterización geológica de la zona del ensayo FEBEX (Grimsel-Suiza). CIEMAT Tech. Report: 70-IMA-M-2-01. May 1997 (Draft).

[218] 70-ST-M-0-02. ENRESA. Garantía de Calidad en el Proyecto FEBEX.

PUBLICACIONES TÉCNICAS

1991

01 *REVISIÓN SOBRE LOS MODELOS NUMÉRICOS RELACIONADOS CON EL ALMACENAMIENTO DE RESIDUOS RADIACTIVOS.*
02 *REVISIÓN SOBRE LOS MODELOS NUMÉRICOS RELACIONADO CON EL ALMACENAMIENTO DE RESIDUOS RADIACTIVOS. ANEXO 1. Guía de códigos aplicables.*
03 *PRELIMINARY SOLUBILITY STUDIES OF URANIUM DIOXIDE UNDER THE CONDITIONS EXPECTED IN A SALINE REPOSITORY.*
04 *GEOESTADÍSTICA PARA EL ANÁLISIS DE RIESGOS. Una introducción a la Geoestadística no paramétrica.*
05 *SITUACIONES SINÓPTICAS Y CAMPOS DE VIENTOS ASOCIADOS EN "EL CABRIL".*
06 *PARAMETERS, METHODOLOGIES AND PRIORITIES OF SITE SELECTION FOR RADIOACTIVE WASTE DISPOSAL IN ROCK SALT FORMATIONS.*

1992

01 *STATE OF THE ART REPORT: DISPOSAL OF RADIACTIVE WASTE IN DEEP ARGILLACEOUS FORMATIONS.*
02 *ESTUDIO DE LA INFILTRACIÓN A TRAVÉS DE LA COBERTERA DE LA FUA.*
03 *SPANISH PARTICIPATION IN THE INTERNATIONAL INTRAVAL PROJECT.*
04 *CARACTERIZACIÓN DE ESMECTITAS MAGNÉSICAS DE LA CUENCA DE MADRID COMO MATERIALES DE SELLADO. Ensayos de alteración hidrotermal.*
05 *SOLUBILITY STUDIES OF URANIUM DIOXIDE UNDER THE CONDITIONS EXPECTED IN A SALINE REPOSITORY. Phase II*
06 *REVISIÓN DE MÉTODOS GEOFÍSICOS APLICABLES AL ESTUDIO Y CARACTERIZACIÓN DE EMPLAZAMIENTOS PARA ALMACENAMIENTO DE RESIDUOS RADIACTIVOS DE ALTA ACTIVIDAD EN GRANITOS, SALES Y ARCILLAS.*
07 *COEFICIENTES DE DISTRIBUCIÓN ENTRE RADIONUCLEIDOS.*
08 *CONTRIBUTION BY CTN-UPM TO THE PSACOIN LEVEL-S EXERCISE.*
09 *DESARROLLO DE UN MODELO DE RESUSPENSIÓN DE SUELOS CONTAMINADOS. APLICACIÓN AL ÁREA DE PALOMARES.*
10 *ESTUDIO DEL CÓDIGO FFSM PARA CAMPO LEJANO. IMPLANTACIÓN EN VAX.*
11 *LA EVALUACIÓN DE LA SEGURIDAD DE LOS SISTEMAS DE ALMACENAMIENTO DE RESIDUOS RADIACTIVOS. UTILIZACIÓN DE MÉTODOS PROBABILISTAS.*
12 *METODOLOGÍA CANADIENSE DE EVALUACIÓN DE LA SEGURIDAD DE LOS ALMACENAMIENTOS DE RESIDUOS RADIACTIVOS.*
13 *DESCRIPCIÓN DE LA BASE DE DATOS WALKER.*

Publicaciones no periódicas

PONENCIAS E INFORMES, 1988-1991.
SEGUNDO PLAN DE I+D, 1991-1995. TOMOS I, II Y III.
SECOND RESEARCH AND DEVELOPMENT PLAN, 1991-1995, VOLUME I.

1993

01 *INVESTIGACIÓN DE BENTONITAS COMO MATERIALES DE SELLADO PARA ALMACENAMIENTO DE RESIDUOS RADIACTIVOS DE ALTA ACTIVIDAD. ZONA DE CABO DE GATA, ALMERÍA.*
02 *TEMPERATURA DISTRIBUTION IN A HYPOTHETICAL SPENT NUCLEAR FUEL REPOSITORY IN A SALT DOME.*
03 *ANÁLISIS DEL CONTENIDO EN AGUA EN FORMACIONES SALINAS. Su aplicación al almacenamiento de residuos radiactivos*
04 *SPANISH PARTICIPATION IN THE HAW PROJECT. Laboratory Investigations on Gamma Irradiation Effects in Rock Salt.*
05 *CARACTERIZACIÓN Y VALIDACIÓN INDUSTRIAL DE MATERIALES ARCILLOSOS COMO BARRERA DE INGENIERÍA.*
06 *CHEMISTRY OF URANIUM IN BRINES RELATED TO THE SPENT FUEL DISPOSAL IN A SALT REPOSITORY (I).*
07 *SIMULACIÓN TÉRMICA DEL ALMACENAMIENTO EN GALERÍA-TSS.*
08 *PROGRAMAS COMPLEMENTARIOS PARA EL ANÁLISIS ESTOCÁSTICO DEL TRANSPORTE DE RADIONUCLEIDOS.*
09 *PROGRAMAS PARA EL CÁLCULO DE PERMEABILIDADES DE BLOQUE.*
10 *METHODS AND RESULTS OF THE INVESTIGATION OF THE THERMOMECHANICAL BEAVIOUR OF ROCK SALT WITH REGARD TO THE FINAL DISPOSAL OF HIGH-LEVEL RADIOACTIVE WASTES.*

Publicaciones no periódicas

SEGUNDO PLAN DE I+D. INFORME ANUAL 1992.

PRIMERAS JORNADAS DE I+D EN LA GESTIÓN DE RESIDUOS RADIACTIVOS. TOMOS I Y II.

1994

01 *MODELO CONCEPTUAL DE FUNCIONAMIENTO DE LOS ECOSISTEMAS EN EL ENTORNO DE LA FÁBRICA DE URANIO DE ANDÚJAR.*
02 *CORROSION OF CANDIDATE MATERIALS FOR CANISTER APPLICATIONS IN ROCK SALT FORMATIONS.*
03 *STOCHASTIC MODELING OF GROUNDWATER TRAVEL TIMES*
04 *THE DISPOSAL OF HIGH LEVEL RADIOACTIVE WASTE IN ARGILLACEOUS HOST ROCKS. Identification of parameters, constraints and geological assessment priorities.*
05 *EL OESTE DE EUROPA Y LA PENÍNSULA IBÉRICA DESDE HACE -120.000 AÑOS HASTA EL PRESENTE. Isostasia glaciar, paleogeografías paleotemperaturas.*
06 *ECOLOGÍA EN LOS SISTEMAS ACUÁTICOS EN EL ENTORNO DE EL CABRIL.*
07 *ALMACENAMIENTO GEOLÓGICO PROFUNDO DE RESIDUOS RADIACTIVOS DE ALTA ACTIVIDAD (AGP). Conceptos preliminares de referencia.*
08 *UNIDADES MÓVILES PARA CARACTERIZACIÓN HIDROGEOQUÍMICA*
09 *EXPERIENCIAS PRELIMINARES DE MIGRACIÓN DE RADIONUCLEIDOS CON MATERIALES GRANÍTICOS. EL BERROCAL, ESPAÑA.*
10 *ESTUDIOS DE DESEQUILIBRIOS ISOTÓPICOS DE SERIES RADIACTIVAS NATURALES EN UN AMBIENTE GRANÍTICO: PLUTÓN DE EL BERROCAL (TOLEDO).*
11 *RELACIÓN ENTRE PARÁMETROS GEOFÍSICOS E HIDROGEOLÓGICOS. Una revisión de literatura.*
12 *DISEÑO Y CONSTRUCCIÓN DE LA COBERTURA MULTICAPA DEL DIQUE DE ESTÉRILES DE LA FÁBRICA DE URANIO DE ANDÚJAR.*

Publicaciones no periódicas

SEGUNDO PLAN I+D 1991-1995. INFORME ANUAL 1993.

1995

01 *DETERMINACIÓN DEL MÓDULO DE ELASTICIDAD DE FORMACIONES ARCILLOSAS PROFUNDAS.*
02 *UO_2 LEACHING AND RADIONUCLIDE RELEASE MODELLING UNDER HIGH AND LOW IONIC STRENGTH SOLUTION AND OXIDATION CONDITIONS.*
03 *THERMO-HYDRO-MECHANICAL CHARACTERIZATION OF THE SPANISH REFERENCE CLAY MATERIAL FOR ENGINEERED BARRIER FOR GRANITE AND CLAY HLW REPOSITORY: LABORATORY AND SMALL MOCK UP TESTING.*
04 *DOCUMENTO DE SÍNTESIS DE LA ASISTENCIA GEOTÉCNICA AL DISEÑO AGP-ARCILLA. Concepto de referencia.*
05 *DETERMINACIÓN DE LA ENERGÍA ACUMULADA EN LAS ROCAS SALINAS FUERTEMENTE IRRADIADAS MEDIANTE TÉCNICAS DE TERMOLUMINISCENCIA. Aplicación al análisis de repositorios de residuos radiactivos de alta actividad.*
06 *PREDICCIÓN DE FENÓMENOS DE TRANSPORTE EN CAMPO PRÓXIMO Y LEJANO. Interacción en fases sólidas.*
07 *ASPECTOS RELACIONADOS CON LA PROTECCIÓN RADIOLÓGICA DURANTE EL DESMANTELAMIENTO Y CLAUSURA DE LA FÁBRICA DE ANDÚJAR.*
08 *ANALYSIS OF GAS GENERATION MECHANISMS IN UNDERGROUND RADIACTIVE WASTE REPOSITORIES. (Pegase Project).*
09 *ENSAYOS DE LIXIVIACIÓN DE EMISORES BETA PUROS DE LARGA VIDA.*
10 *2º PLAN DE I+D. DESARROLLOS METODOLÓGICOS, TECNOLÓGICOS, INSTRUMENTALES Y NUMÉRICOS EN LA GESTIÓN DE RESIDUOS RADIACTIVOS.*
11 *PROYECTO AGP- ALMACENAMIENTO GEOLÓGICO PROFUNDO. FASE 2.*
12 *IN SITU INVESTIGATION OF THE LONG-TERM SEALING SYSTEM AS COMPONENT OF DAM CONSTRUCTION (DAM PROJECT). Numerical simulator: Code-Bright.*

Publicaciones no periódicas

TERCER PLAN DE I+D 1995-1999.

SEGUNDAS JORNADAS DE I+D. EN LA GESTIÓN DE RESIDUOS RADIACTIVOS. TOMOS I Y II.

1996

01 *DESARROLLO DE UN PROGRAMA INFORMÁTICO PARA EL ASESORAMIENTO DE LA OPERACIÓN DE FOCOS EMISORES DE CONTAMINANTES GASEOSOS.*
02 *FINAL REPORT OF PHYSICAL TEST PROGRAM CONCERNING SPANISH CLAYS (SAPONITES AND BENTONITES).*
03 *APORTACIONES AL CONOCIMIENTO DE LA EVOLUCIÓN PALEOCLIMÁTICA Y PALEOAMBIENTAL EN LA PENÍNSULA IBÉRICA DURANTE LOS DOS ÚLTIMOS MILLONES DE AÑOS A PARTIR DEL ESTUDIO DE TRAVERTINOS Y ESPELEOTEMAS.*
04 *MÉTODOS GEOESTADÍSTICOS PARA LA INTEGRACIÓN DE INFORMACIÓN.*
05 *ESTUDIO DE LONGEVIDAD EN BENTONITAS: ESTABILIDAD HIDROTERMAL DE SAPONITAS.*
06 *ALTERACIÓN HIDROTERMAL DE LAS BENTONITAS DE ALMERÍA.*
07 *MAYDAY. UN CÓDIGO PARA REALIZAR ANÁLISIS DE INCERTIDUMBRE Y SENSIBILIDAD. Manuales.*

Publicaciones no periódicas

EL BERROCAL PROJECT. VOLUME I. GEOLOGICAL STUDIES.

EL BERROCAL PROJECT. VOLUME II. HYDROGEOCHEMISTRY.

EL BERROCAL PROJECT. VOLUME III. LABORATORY MIGRATION TESTS AND IN SITU TRACER TEST.

EL BERROCAL PROJECT. VOLUME IV. HYDROGEOLOGICAL MODELLING AND CODE DEVELOPMENT.

1997

01 *CONSIDERACIÓN DEL CAMBIO MEDIOAMBIENTAL EN LA EVALUACIÓN DE LA SEGURIDAD. ESCENARIOS CLIMÁTICOS A LARGO PLAZO EN LA PENÍNSULA IBÉRICA.*
02 *METODOLOGÍA DE EVALUACIÓN DE RIESGO SÍSMICO EN SEGMENTOS DE FALLA.*
03 *DETERMINACIÓN DE RADIONUCLEIDOS PRESENTES EN EL INVENTARIO DE REFERENCIA DEL CENTRO DE ALMACENAMIENTO DE EL CABRIL.*
04 *ALMACENAMIENTO DEFINITIVO DE RESIDUOS DE RADIACTIVIDAD ALTA. Caracterización y comportamiento a largo plazo de los combustibles nucleares irradiados (I).*
05 *METODOLOGÍA DE ANÁLISIS DE LA BIOSFERA EN LA EVALUACIÓN DE ALMACENAMIENTOS GEOLÓGICOS PROFUNDOS DE RESIDUOS RADIACTIVOS DE ALTA ACTIVIDAD ESPECÍFICA.*
06 *EVALUACIÓN DEL COMPORTAMIENTO Y DE LA SEGURIDAD DE UN ALMACENAMIENTO GEOLÓGICO PROFUNDO EN GRANITO. Marzo 1997*
07 *SÍNTESIS TECTOESTRATIGRÁFICA DEL MACIZO HESPÉRICO. VOLUMEN I.*
08 *III JORNADAS DE I+D Y TECNOLOGÍAS DE GESTIÓN DE RESIDUOS RADIACTIVOS. Pósters descriptivos de los proyectos de I+D y evaluación de la seguridad a largo plazo.*
09 *FEBEX. ETAPA PREOPERACIONAL. INFORME DE SÍNTESIS.*
10 *METODOLOGÍA DE GENERACIÓN DE ESCENARIOS PARA LA EVALUACIÓN DEL COMPORTAMIENTO DE LOS ALMACENAMIENTOS DE RESIDUOS RADIACTIVOS.*
11 *MANUAL DE CESARR V.2. Código para la evaluación de seguridad de un almacenamiento superficial de residuos radiactivos de baja y media actividad.*

1998

01 *FEBEX. PRE-OPERATIONAL STAGE. SUMMARY REPORT.*
02 *PERFORMANCE ASSESSMENT OF A DEEP GEOLOGICAL REPOSITORY IN GRANITE. March 1997.*
03 *FEBEX. DISEÑO FINAL Y MONTAJE DEL ENSAYO "IN SITU" EN GRIMSEL.*
04 *FEBEX. BENTONITA: ORIGEN, PROPIEDADES Y FABRICACIÓN DE BLOQUES.*
05 *FEBEX. BENTONITE: ORIGIN, PROPERTIES AND FABRICATION OF BLOCKS.*
06 *TERCERAS JORNADAS DE I+D Y TECNOLOGÍAS DE GESTIÓN DE RESIDUOS RADIACTIVOS. 24-29 Noviembre, 1997. Volumen I*
07 *TERCERAS JORNADAS DE I+D Y TECNOLOGÍAS DE GESTION DE RESIDUOS RADIACTIVOS. 24-29 Noviembre, 1997. Volumen II*
08 *MODELIZACIÓN Y SIMULACIÓN DE BARRERAS CAPILARES.*
09 *FEBEX. PREOPERATIONAL THERMO-HYDRO-MECHANICAL (THM) MODELLING OF THE "IN SITU" TEST.*
10 *FEBEX. PREOPERATIONAL THERMO-HYDRO-MECHANICAL (THM) MODELLING OF THE "MOCK UP" TEST.*
11 *DISOLUCIÓN DEL UO_2(s) EN CONDICIONES REDUCTORAS Y OXIDANTES.*
12 *FEBEX. FINAL DESIGN AND INSTALLATION OF THE "IN SITU" TEST AT GRIMSEL.*

1999

01 *MATERIALES ALTERNATIVOS DE LA CÁPSULA DE ALMACENAMIENTO DE RESDIUOS RADIACTIVOS DE ALTA ACTIVIDAD.*
02 *INTRAVAL PROJECT PHASE 2: STOCHASTIC ANALYSIS OF RADIONUCLIDES TRAVEL TIMES AT THE WASTE ISOLATION PILOT PLANT (WIPP), IN NEW MEXICO (U.S.A.).*
03 *EVALUACIÓN DEL COMPORTAMIENTO Y DE LA SEGURIDAD DE UN ALMACENAMIENTO PROFUNDO EN ARCILLA. Febrero 1999.*
04 *ESTUDIOS DE CORROSIÓN DE MATERIALES METÁLICOS PARA CÁPSULAS DE ALMACENAMIENTO DE RESIDUOS DE ALTA ACTIVIDAD.*
05 *MANUAL DEL USUARIO DEL PROGRAMA VISUAL BALAN V. 1.0. CÓDIGO INTERACTIVO PARA LA REALIZACION DE BALANCES HIDROLÓGICOS Y LA ESTIMACIÓN DE LA RECARGA.*
06 *COMPORTAMIENTO FÍSICO DE LAS CÁPSULAS DE ALMACENAMIENTO.*
07 *PARTICIPACIÓN DEL CIEMAT EN ESTUDIOS DE RADIOECOLOGÍA EN ECOSISTEMAS MARINOS EUROPEOS.*

Títulos publicados

08 PLAN DE INVESTIGACIÓN Y DESARROLLO TECNOLÓGICOPARA LA GESTIÓN DE RESIDUOS RADIACTIVOS 1999-2003.OCTUBRE 1999.

09 ESTRATIGRAFÍA BIOMOLECULAR. LA RACEMIZACIÓN/EPIMERIZACIÓN DE AMINOÁCIDOS COMO HERRAMIENTA GEOCRONOLÓGICA Y PALEOTERMOMÉTRICA.

10 CATSIUS CLAY PROJECT. Calculation and testing of behaviourof unsaturarted clay as barrier in radioactive waste repositories. STAGE 1: VERIFICATION EXERCISES.

11 CATSIUS CLAY PROJECT. Calculation and testing of behaviourof unsaturarted clay as barrier in radioactive waste repositories. STAGE 2: VALIDATION EXERCISES AT LABORATORY SCALE.

12 CATSIUS CLAY PROJECT. Calculation and testing of behaviour of unsaturarted clay as barrier in radioactive waste repositories. STAGE 3: VALIDATION EXERCISES AT LARGE “IN SITU” SCALE.

2000

01 FEBEX PROJECT. FULL-SCALE ENGINEERED BARRIERS EXPERIMENT FOR A DEEP GEOLOGICAL REPOSITORY FOR HIGH LEVEL RADIOACTIVE WASTE IN CRYISTALLINE HOST ROCK. FINAL REPORT.

02 CÁLCULO DE LA GENERACIÓN DE PRODUCTOS RADIOLÍTICOSEN AGUA POR RADIACIÓN α. DETERMINACIÓN DE LA VELOCIDAD DE ALTERACIÓN DE LA MATRIZ DEL COMBUSTIBLE NUCLEAR GASTADO.

03 LIBERACIÓN DE RADIONUCLEIDOS E ISÓTOPOS ESTABLES CONTENIDOS EN LA MATRIZ DEL COMBUSTIBLE. MODELO CONCEPTUAL Y MODELO MATEMÁTICO DEL COMPORTAMIENTO DEL RESIDUO.

04 DESARROLLO DE UN MODELO GEOQUÍMICO DE CAMPO PRÓXIMO.

05 ESTUDIOS DE DISOLUCIÓN DE ANÁLOGOS NATURALES DE COMBUSTIBLE NUCLEAR IRRADIADO Y DE FASES DE (U)VI-SILICIO REPRESENTATIVAS DE UN PROCESO DE ALTERACIÓN OXIDATIVA.

06 CORE2D. A CODE FOR NON-ISOTHERMAL WATER FLOW AND REACTIVE SOLUTE TRANSPORT. USERS MANUAL VERSION 2.

07 ANÁLOGOS ARQUEOLÓGICOS E INDUSTRIALES PARA ALMACENAMIENTOS PROFUNDOS: ESTUDIO DE PIEZAS ARQUEOLÓGICAS METÁLICAS.

08 PLAN DE INVESTIGACIÓN Y DESARROLLO TECNOLÓGICO PARA LA GESTIÓN DE RESIDUOS RADIACTIVOS 1999-2003. REVISIÓN 2000.

09 IV JORNADAS DE INVESTIGACIÓN Y DESARROLLO TECNOLÓGICO EN GESTIÓN DE RESIDUOS RADIACTIVOS. POSTERS DIVULGATIVOS.

10 IV JORNADAS DE INVESTIGACIÓN Y DESARROLLO TECNOLÓGICO EN GESTIÓN DE RESIDUOS RADIACTIVOS. POSTERS TÉCNICOS.

11 PROGRAMA DE INVESTIGACIÓN PARA ESTUDIAR LOS EFECTOS DE LA RADIACIÓN GAMMA EN BENTONITAS CÁLCICAS ESPAÑOLAS.

12 CARACTERIZACIÓN Y LIXIVIACIÓN DE COMBUSTIBLES NUCLEARES IRRADIADOS Y DE SUS ANÁLOGOS QUÍMICOS.

2001

01 MODELOS DE FLUJO MULTIFÁSICO NO ISOTERMO Y DE TRANSPORTE REACTIVO MULTICOMPONENTE EN MEDIOS POROSOS.

02 IV JORNADAS DE INVESTIGACIÓN Y DESARROLLO TECNOLÓGICO EN GESTIÓN DE RESIDUOS RADIACTIVOS. RESÚMENES Y ABSTRACTS.

03 ALMACENAMIENTO DEFINITIVO DE RESIDUOS DE RADIACTIVIDAD ALTA. CARACTERIZACIÓN Y COMPORTAMIENTO A LARGO PLAZO DE LOS COMBUSTIBLES NUCLEARES IRRADIADOS (II).

04 CONSIDERATIONS ON POSSIBLE SPENT FUEL AND HIGH LEVEL WASTE MANAGEMENT OPTIONS.

05 LA PECHBLENDA DE LA MINA FE (CIUDAD RODRIGO, SALAMANCA), COMO ANÁLOGO NATURAL DEL COMPORTAMIENTO DEL COMBUSTIBLE GASTADO. Proyecto Matrix I.

06 TESTING AND VALIDATION OF NUMERICAL MODELS OF GROUNDWATER FLOW, SOLUTE TRANSPORT AND CHEMICAL REACTIONS IN FRACTURED GRANITES: A QUANTITATIVE STUDY OF THE HYDROGEOLOGICAL AND HYDROCHEMICAL IMPACT PRODUCED.

07 IV JORNADAS DE INVESTIGACIÓN Y DESARROLLO TECNOLÓGICOEN GESTIÓN DE RESIDUOS RADIACTIVOS. Volumen I.

08 IV JORNADAS DE INVESTIGACIÓN Y DESARROLLO TECNOLÓGICO EN GESTIÓN DE RESIDUOS RADIACTIVOS. Volumen II.

09 IV JORNADAS DE INVESTIGACIÓN Y DESARROLLO TECNOLÓGICO EN GESTIÓN DE RESIDUOS RADIACTIVOS. Volumen III

10 IV JORNADAS DE INVESTIGACIÓN Y DESARROLLO TECNOLÓGICO EN GESTIÓN DE RESIDUOS RADIACTIVOS. Volumen IV

2002

01 FABRICACIÓN DE BLANCOS PARA LA TRANSMUTACIÓN DE AMERICIO: SÍNTESIS DE MATRICES INERTES POR EL MÉTODO SOL-GEL. ESTUDIO DEL PROCEDIMIENTO DE INFILTRACIÓN DE DISOLUCIONES RADIACTIVAS.

02 ESTUDIO GEOQUÍMICO DE LOS PROCESOS DE INTERACCIÓN AGUA-ROCA SOBRE SISTEMAS GEOTERMALES DE AGUAS ALCALINAS GRANITOIDES.

03 ALTERACIÓN ALCALINA HIDROTERMAL DE LA BARRERA DE BENTONITA POR AGUAS INTERSTICIALES DE CEMENTOS.

04 THERMO-HYDRO-MECHANICAL CHARACTERISATION OF A BENTONITE FROM CABO DE GATA. A study applied to the use of bentonite as sealing material in high level radioactive waste repositories.

05 ESTUDIOS GEOLÓGICO-ESTRUCTURALES Y GEOFÍSICOS EN MINA RATONES (PLUTÓN DE ALBALÁ).

06 IMPACTO DE LA MINA RATONES (ALBALÁ, CÁCERES) SOBRE LAS AGUAS SUPERFICIALES Y SUBTERRÁNEAS: MODELIZACIÓN HIDROGEOQUÍMICA.

07 CARACTERIZACIÓN PETROLÓGICA, MINERALÓGICA, GEOQUÍMICA Y EVALUACIÓN DEL COMPORTAMIENTO GEOQUÍMICO DE LAS REE EN LA FASE SÓLIDA (GRANITOIDES Y RELLENOS FISURALES) DEL SISTEMA DE INTERACCIÓN AGUA-ROCA DEL ENTORNO DE LA MINA RATONES.

08 MODELLING SPENT FUEL AND HLW BEHAVIOUR IN REPOSITORY CONDITIONS. A review of th state of the art.

09 UN MODELO NUMÉRICO PARA LA SIMULACIÓN DE TRANSPORTE DE CALOR Y LIBERACIÓN DE MATERIA EN UN ALMACENAMIENTO PROFUNDO DE RESIDUOS RADIACTIVOS.

10 PROCESOS GEOQUÍMICOS Y MODIFICACIONES TEXTURALES EN BENTONITA FEBEX COMPACTADA SOMETIDA A UN GRADIENTE TERMOHIDRÁULICO.

2003

01 CONTRIBUCIÓN EXPERIMENTAL Y MODELIZACIÓN DE PROCESOS BÁSICOS PARA EL DESARROLLO DEL MODELO DE ALTERACIÓN DE LA MATRIZ DEL COMBUSTIBLE IRRADIADO.

02 URANIUM(VI) SORPTION ON GOETHITE AND MAGNETITE: EXPERIMENTAL STUDY AND SURFACE COMPLEXATION MODELLING.

03 ANÁLOGOS ARQUEOLÓGICOS E INDUSTRIALES PARA ALMACENAMIENTO DE RESIDUOS RADIACTIVOS: ESTUDIO DE PIEZAS ARQUEOLÓGICAS METÁLICAS (ARCHEO-II).

04 EVOLUCIÓN PALEOAMBIENTAL DE LA MITAD SUR DE LA PENÍNSULA IBÉRICA. APLICACIÓN A LA EVALUACIÓN DEL COMPORTAMIENTO DE LOS REPOSITORIOS DE RESIDUOS RADIACTIVOS.

05 THE ROLE OF COLLOIDS IN THE RADIONUCLIDE TRANSPORT IN A DEEP GEOLOGICAL REPOSI8TORY. Participation of CIEMAT in the CRR project.

06 V JORNADAS DE INVESTIGACIÓN Y DESARROLLO TECNOLÓGICO EN GESTIÓN DE RESIDUOS RADIACTIVOS. Resúmenes de ponencias.

07 V JORNADAS DE INVESTIGACIÓN Y DESARROLLO TECNOLÓGICO EN GESTIÓN DE RESIDUOS RADIACTIVOS. Sinopsis de pósteres.

08 V JORNADAS DE INVESTIGACIÓN, DESARROLLO TECNOLÓGICO Y DEMOSTRACIÓN EN GESTIÓN DE RESIDUOS RADIACTIVOS. Pósteres técnicos.

09 DISMANTLING OF THE HEATER 1 AT THE FEBEX "IN SITU" TEST. Descriptions of operations

10 GEOQUÍMICA DE FORMACIONES ARCILLOSAS: ESTUDIO DE LA ARCILLA ESPAÑOLA DE REFERENCIA.

11 PETROPHYSICS AT THE ROCK MATRIX SCALE: HYDRAULIC PROPERTIES AND PETROGRAPHIC INTERPRETATION.

2004

01 PLAN DE INVESTIGACIÓN, DESARROLLO TECNOLÓGICO Y DEMOSTRACIÓN PARA LA GESTIÓN DE RESIDUOS RADIACTIVOS 2004-2008.

02 ESTUDIO DE LOS PRODUCTOS DE CORROSIÓN DE LA CÁPSULA Y SU INTERACCIÓN CON LA BARRERA ARCILLOSA DE BENTONITA "CORROBEN".

03 EFECTO DE LA MAGNETITA EN LA RETENCIÓN DE LOS RADIONUCLEIDOS EN EL CAMPO PRÓXIMO: CESIO, ESTRONCIO, MOLIBDENO Y SELENIO.

04 V^{as} JORNADAS DE INVESTIGACIÓN Y DESARROLLO TECNOLÓGICO EN GESTIÓN DE RESIDUOS RADIACTIVOS. Volumen I.

05 V^{as} JORNADAS DE INVESTIGACIÓN Y DESARROLLO TECNOLÓGICO EN GESTIÓN DE RESIDUOS RADIACTIVOS. Volumen II.

06 V^{as} JORNADAS DE INVESTIGACIÓN Y DESARROLLO TECNOLÓGICO EN GESTIÓN DE RESIDUOS RADIACTIVOS. Volumen III.

07 V^{as} JORNADAS DE INVESTIGACIÓN Y DESARROLLO TECNOLÓGICO EN GESTIÓN DE RESIDUOS RADIACTIVOS. Volumen IV.

08 FEBEX PROJECT. POST-MORTEM ANALYSIS: CORROSION STUDY.

09 FEBEX II PROJECT. THG LABORATORY EXPERIMENTS.

10 FEBEX II PROJECT. FINAL REPORT ON THERMO-HYDRO-MECHANICAL LABORATORY TEST.

11 FEBEX II PROJECT. POST-MORTEM ANALYSIS EDZ ASSESSMENT.

2005

01 DEVELOPMENT OF A MATRIX ALTERATION MODEL (MAM).

02 ENGINEERED BARRIER EMPLACEMENT EXPERIMENT IN OPALINUS CLAY FOR THE DISPOSAL OF RADIOACTIVE WASTE IN UNDERGROUND REPOSITORIES.

03 USE OF PALAEOHYDROGEOLOGY IN RADIOACTIVE WASTE MANAGEMENT.

04 METODOLOGÍAS DE CARACTERIZACIÓN RADIOLÓGICA DE BULTOS DE RESIDUOS RADIACTIVOS DESARROLLADAS POR ENRESA

05 ANÁLOGOS NATURALES DE LA LIBERACIÓN Y MIGRACIÓN DEL UO_2 Y ELEMENTOS METÁLICOS ASOCIADOS

06 FLUJO RADIAL EN MEDIOS HETEROGÉNEOS

07 VENTILATION EXPERIMENT IN OPALINUS CLAY FOR THE MANAGEMENT OF RADIOACTIVE WASTE

08 INFORME FINAL. IMPACTO ECONÓMICO DEL DESMANTELAMIENTO DE LA CENTRAL NUCLEAR VANDELLÒS I

2006

01 PLAN DE INVESTIGACIÓN, DESARROLLO TECNOLÓGICO Y DEMOSTRACIÓN PARA LA GESTIÓN DE RESIDUOS RADIACTIVOS 2004-2009. REVISIÓN 2006

02 SEPARACIÓN DE ELEMENTOS TRANSURÁNICOS Y ALGUNOS PRODUCTOS DE FISIÓN PRESENTES EN LOS COMBUSTIBLES NUCLEARES IRRADIADOS. PROGRAMA 2005

03 CONTRIBUCION A LA SELECCIÓN Y EVALUACIÓN DEL COMPORTAMIENTO DEL MATERIAL DE RELLENO INTERNO DEL CONTENEDOR DE RESIDUOS DE ALTA ACTIVIDAD. INFORME FINAL. FASE 1

04 INVENTARIO DE RESIDUOS RADIACTIVOS Y COMBUSTIBLE GASTADO. EDICIÓN 2004

Full-scale Engineered Barriers Experiment

Updated Final Report 1994-2004

PUBLICACIÓN TÉCNICA 05-0/2006

Para más información, dirigirse a:

enresa

Departamento de Soportes de Información
C/ Emilio Vargas, 7
28043 MADRID

http://www.enresa.es

Diciembre 2006